

H A N D B O O K
O F

Surface
and
Colloid
Chemistry

Second Edition

H A N D B O O K
O F

Surface
and
Colloid
Chemistry

Second Edition

Edited by
K.S. Birdi



CRC PRESS

Boca Raton London New York Washington, D.C.

Library of Congress Cataloging-in-Publication Data

Handbook of surface and colloid chemistry / edited by K.S. Birdi.--2nd ed.

p. cm.

Includes bibliographical references and index.

ISBN 0-8493-1079-2 (alk. paper)

1. Surface chemistry. 2. Colloids. I. Birdi, K. S., 1934-

QD508 .H36 2002

541.3'3--dc21

2002025923

CIP

This book contains information obtained from authentic and highly regarded sources. Reprinted material is quoted with permission, and sources are indicated. A wide variety of references are listed. Reasonable efforts have been made to publish reliable data and information, but the authors and the publisher cannot assume responsibility for the validity of all materials or for the consequences of their use.

Neither this book nor any part may be reproduced or transmitted in any form or by any means, electronic or mechanical, including photocopying, microfilming, and recording, or by any information storage or retrieval system, without prior permission in writing from the publisher.

All rights reserved. Authorization to photocopy items for internal or personal use, or the personal or internal use of specific clients, may be granted by CRC Press LLC, provided that \$1.50 per page photocopied is paid directly to Copyright Clearance Center, 222 Rosewood Drive, Danvers, MA 01923 USA. The fee code for users of the Transactional Reporting Service is ISBN 0-8493-1079-2/03/\$0.00+\$1.50. The fee is subject to change without notice. For organizations that have been granted a photocopy license by the CCC, a separate system of payment has been arranged.

The consent of CRC Press LLC does not extend to copying for general distribution, for promotion, for creating new works, or for resale. Specific permission must be obtained in writing from CRC Press LLC for such copying.

Direct all inquiries to CRC Press LLC, 2000 N.W. Corporate Blvd., Boca Raton, Florida 33431.

Trademark Notice: Product or corporate names may be trademarks or registered trademarks, and are used only for identification and explanation, without intent to infringe.

Visit the CRC Press Web site at www.crcpress.com

© 2003 by CRC Press LLC

No claim to original U.S. Government works

International Standard Book Number 0-8493-1079-2

Library of Congress Card Number 2002025923

Printed in the United States of America 1 2 3 4 5 6 7 8 9 0

Printed on acid-free paper

Preface

The science related to the subject of surface and colloid chemistry has expanded in the past decade at a rapid pace. This area of science has been especially important in such new areas as environmental control, wastewater processing, nanotechnology, pharmacy, and biotechnology. The applications of nanoparticles in pharmacy products are very significant. Initially, the subject arose over 50 years ago when theoretical understanding of surface and colloid systems developed. The amount of information published since has increased steadily; consider that there are at present some half a dozen different specialty journals related mainly to surface and colloid chemistry. The applications of this subject have developed rapidly in both the industrial and biological areas.

During the last few decades, many empirical observations have been found to be based in the fundamental laws of physics and chemistry. These laws have been extensively applied to the science of surface and colloid chemistry, which gave rise to investigations based on molecular description of surfaces and reactions at interfaces. Especially during the last decade, theoretical analyses have added to the understanding of this subject with increasing molecular detail. These developments are moving at a much faster pace with each decade.

The application area of surface and colloid science has increased dramatically during the past decades. For example, the major industrial areas have been soaps and detergents, emulsion technology, colloidal dispersions (suspensions, nanoparticles), wetting and contact angle, paper, cement, oil recovery, pollution control, fogs, foams (thin liquid films), the food industry, biomembranes, drug delivery (vesicles), membrane technology, and the pharmaceutical industry. Recently, new areas of applications are developing, two of which are synthetic transplants and biological monitors. These trends show the importance of this field of science in everyday life.

Thus, a group of experts from the United States, Europe, and worldwide wrote a handbook that covered this subject extensively in 1997 (*Handbook of Surface and Colloid Chemistry*, CRC Press, Boca Raton, FL). However, since 1997 the number of publications related to surface and colloid science has grown exponentially. Accordingly, a new group of experts decided that at this stage there is an urgent need for a second edition of the handbook, which should make theoretical and experimental information on the systems related to surfaces and colloids readily available. The purpose of this second edition of the handbook is to bring the reader up-to-date with the most recent developments in this area. The second edition of this handbook both updates the first edition and includes new areas of research. Hence, the two editions combined cover an extensive range of research subjects. In this edition of the handbook a unifying theme of information on surface and colloid chemistry is presented by a team of international experts. The subject content is presented such that the reader can follow through the physical principles that are needed for applications, and extensive references are included for understanding the related phenomena. Thus, the two editions together become a gateway to a vast number of literature references. This is unique in the current literature.

As the subject area and the quantity of knowledge are immense, there is always a need for a team of experts to join together and compile a handbook. It is therefore an honor for me to be able to arrange and present to the reader chapters written by experts on various subjects pertaining to this science, with bibliographical references well in excess of 2000.

It is most impressive to discover how theoretical knowledge has led to some fascinating developments in the technology. The purpose of this handbook is also to further this development. The scope of the second edition of this handbook is consciously different from that of any existing volume on the same subject. The molecular description of liquid surfaces has been obtained from

surface tension (under static and dynamic conditions) and adsorption studies. Thin-film formation and emulsion formation and stability are described by interfacial film structures. The surfaces of solids are characterized by contact angle and adsorption studies. Foams are described by the bilayer arrangement of the detergent and other amphiphile molecules in the thin films. The ultimate in interfaces are molecular films and molecular self-assemblies. Many questions about monomolecular films on solids are answered with the use of modern scanning probe microscopes (SPMs). The impact of the scanning tunneling microscope (STM) and the atomic force microscope (AFM) is delineated. This has indeed led to such new scientific fields as nanotechnology. In the past decade developments in increased sensitivity and innovation in instruments have added much knowledge. Colloidal structures and their stability have been found to be of much interest, as described extensively in this second edition of the handbook. The theoretical basis of colloids and their stability is thoroughly described.

The chapters are arranged such that the information is basically needed for the whole handbook. The organization allows the reader to follow the subject area smoothly, with the extensive data provided in the form of tables and figures supporting this aim.

The Editor

Professor K. S. Birdi received his undergraduate education (B.Sc. Hons. Chem.) from Delhi University; Delhi, India, in 1952. He also majored in chemistry at the University of California at Berkeley. After graduation in 1957, he joined Standard Oil of California, Richmond.

In 1959, Dr. Birdi became chief chemist at Lever Brothers in Denmark. He became interested in surface and colloid chemistry and joined the Institute of Physical Chemistry as an assistant professor. He initially did research on surface science aspects (e.g., thermodynamics of surfaces, detergents, micelle formation, adsorption, Langmuir monolayers, biophysics). During the early exploration and discovery stages of oil and gas in the North Sea, Dr. Birdi became involved in Danish Research Science Foundation programs, with other research institutes around Copenhagen, in the oil recovery phenomena and surface science. Later, research grants on the same subject were awarded from European Union projects. These projects involved extensive visits to other universities and an exchange of guests from all over the world. Professor Birdi was appointed Research Professor in 1985 (Nordic Science Foundation), and was then appointed, in 1990, to the School of Pharmacy, Copenhagen, as professor in physical chemistry. Since 1999, Professor Birdi has been actively engaged in consultancy to both industrial and university projects.

Professor Birdi is a consultant to various national and international industries. He is and has been a member of various chemical societies, and a member of organizing committees of national and international meetings related to surface science. He has been a member of selection committees for assistant professor and professor, and was an advisory member (1985 to 1987) of the ACS journal *Langmuir*.

Professor Birdi has been an advisor for some 90 advanced student projects and various Ph.D. projects. He is the author of some 100 papers and articles (and a few hundred citations).

To describe these research observations and data he realized that it was essential to write books on the subject of surface and colloid chemistry. His first book on surface science was published in 1984: *Adsorption and the Gibbs Surface Excess*, Chattorraj, D.K. and Birdi, K.S., Plenum Press, New York. This book remains the only one of its kind in the present decade. Further publications include *Lipid and Biopolymer Monolayers at Liquid Interfaces*, K.S. Birdi, Plenum Press, New York, 1989; *Fractals — In Chemistry, Geochemistry and Biophysics*, K.S. Birdi, Plenum Press, New York, 1994; *Handbook of Surface and Colloid Chemistry*, CRC Press, Boca Raton, FL, 1997 (CD-ROM, 1999), and *Self-Assembly Monolayer*, Plenum Press, New York, 1999. Surface and colloid chemistry has remained his major research interest throughout these years.

Contributors

Anne Marit Blokhus

Department of Chemistry
University of Bergen
Bergen, Norway

Krassimir D. Danov

Laboratory of Chemical Physics and
Engineering
Faculty of Chemistry
University of Sofia
Sofia, Bulgaria

Nikolai D. Denkov

Laboratory of Chemical Physics and
Engineering
Faculty of Chemistry
University of Sofia
Sofia, Bulgaria

Abdelhamid Elaissari

Macromolecular Systems and
Human Immunology
CNRS–bioMérieux
Lyon, France

Byron Gates

Department of Chemistry
University of Washington
Seattle, Washington

Charles M. Hansen

FORCE Technology
Brøndby, Denmark

Harald Høiland

Department of Chemistry
University of Bergen
Bergen, Norway

Georgios M. Kontogeorgis

Department of Chemical Engineering
Technical University of Denmark
Lyngby, Denmark

Peter A. Kralchevsky

Laboratory of Chemical Physics and
Engineering
Faculty of Chemistry
University of Sofia
Sofia, Bulgaria

S. Krishnakumar

Unilever Research US
Edgewater, New Jersey

Mika Lindén

Department of Physical Chemistry
Åbo Akademi University
Åbo (Turku), Finland

B. Markovic

International Specialty Products
Wayne, New Jersey

Clarence A. Miller

Department of Chemical Engineering
Rice University
Houston, Texas

Thomas Oberholzer

Institut für Polymere
ETH-Zentrum
Zürich, Switzerland

Costas G. Panayiotou

Department of Chemical Engineering
University of Thessaloniki
Thessaloniki, Greece

Jarl B. Rosenholm

Department of Physical Chemistry
Åbo Akademi University
Åbo (Turku), Finland

P. Somasundaran

Langmuir Center for Colloids and Interfaces
Columbia University
New York, New York

C.M. Sorensen

Department of Physics
Kansas State University
Manhattan, Kansas

Yugang Sun

Department of Chemistry
University of Washington
Seattle, Washington

Manuel G. Velarde

Instituto Pluridisciplinar
Universidad Complutense
Madrid, Spain

Michèle Vignes-Adler

Laboratoire de Physique des Matériaux Divisés
et des Interfaces
Université de Marne-la-Vallée
Marne-la-Vallée, France

D.T. Vu

Technical University of Denmark
Lyngby, Denmark

Younan Xia

Department of Materials Science and
Engineering
University of Washington
Seattle, Washington

Yadong Yin

Department of Chemistry
University of Washington
Seattle, Washington

X. Yu

International Specialty Products
Wayne, New Jersey

Contents

Chapter 1

Introduction to Surface and Colloid Chemistry

K.S. Birdi

Chapter 2

Hydrogen Bonding in Solutions: The Equation-of-State Approach

Costas G. Panayiotou

Chapter 3

Surface Tension and Interfacial Tension of Liquids

K.S. Birdi

Chapter 4

Surface Waves and Dissipative Solitons Sustained by the Marangoni Effect

Michèle Vignes-Adler and Manuel G. Velarde

Chapter 5

Chemical Physics of Colloid Systems and Interfaces

Peter A. Kralchevsky, Krassimir D. Danov, and Nikolai D. Denkov

Chapter 6

Solubilization in Aqueous Surfactant Systems

Harald Høiland and Anne Marit Blokhus

Chapter 7

Colloid Systems and Interfaces — Stability of Dispersions through Polymer and Surfactant Adsorption

P. Somasundaran, B. Markovic, X. Yu, and S. Krishnakumar

Chapter 8

Controlled Synthesis and Processing of Ceramic Oxides — A Molecular Approach

Jarl B. Rosenholm and Mika Lindén

Chapter 9

Solubilization in Surfactant Systems

Clarence A. Miller

Chapter 10

Cohesion Energy Parameters Applied to Surface Phenomena

Charles M. Hansen

Chapter 11

Self-Assembly of Monodispersed Spherical Colloids into Complex Structures

Younan Xia, Byron Gates, Yadong Yin, and Yugang Sun

Chapter 12

Thermally Sensitive Latex Particles: Preparation, Characterization, and Application in the Biomedical Field

Abdelhamid Elaissari

Chapter 13

Nucleic Acid-Dependent Enzymatic Reactions in Conventional Liposomes and Giant Vesicles

Thomas Oberholzer

Chapter 14

Scattering and Absorption of Light by Particles and Aggregates

C.M. Sorensen

Chapter 15

Application of Scanning Probe Microscopy (Scanning Tunneling Microscopy and Atomic Force Microscopy) in Colloid and Surface Chemistry

K.S. Birdi and D.T. Vu

Chapter 16

Thermodynamics of Polymer Solutions

Georgios M. Kontogeorgis

1 Introduction to Surface and Colloid Chemistry

K. S. Birdi

Matter exists as gas, liquid, and solid phases, as has been recognized by classical science. The molecules that are situated at the interfaces (e.g., between gas–liquid, gas–solid, liquid–solid, liquid₁–liquid₂, solid₁–solid₂) are known to behave differently from those in the bulk phase.¹⁻¹⁷ It is also well known that the molecules situated near or at the interface (i.e., liquid–gas) are situated differently with respect to each other than are the molecules in the bulk phase. The intramolecular forces acting would thus be different in these two cases. Furthermore, it has been pointed out that, for a dense fluid, the repulsive forces dominate the fluid structure and are of primary importance. The main effect of the repulsive forces is to provide a uniform background potential in which the molecules move as hard spheres. The molecules at the interface would be under an asymmetric force field, which gives rise to the so-called surface tension or interfacial tension (Figure 1.1).¹⁶

The resultant force on molecules varies with time because of the movement of the molecules; the molecules at the surface will be pointed downward into the bulk phase. The nearer the molecule is to the surface, the greater the magnitude of the force due to asymmetry. The region of asymmetry plays a very important role. Thus, when the surface area of a liquid is increased, some molecules must move from the interior of the continuous phase to the interface. The surface of a liquid can thus be regarded as the plane of potential energy. An analogous case would be when the solid is crushed and the surface area increases per unit gram. Further, molecular phenomena at the surface separating the liquid and the saturated vapor are appreciably more complex than those that occur in the bulk homogeneous fluid phase. Especially, some amphiphiles exhibit the *self-assembly* characteristic. This phenomenon is known to be the basic building block of many natural assemblies.

The designation *colloid* is used for particles that are of some small dimension that cannot pass through a membrane with a pore size $\sim 10^{-6}$ m ($= \mu\text{m}$) (Thomas Graham described this about a century ago). The nature and relevance of colloids are among the main current research topics.¹⁶

Colloids are an important class of materials, intermediate between bulk and molecularly dispersed systems. The colloid particles may be spherical, but in some cases one dimension can be much larger than the other two (as in a needle shape). The size of particles also determines whether they can be seen by the naked eye. Colloids are not visible to the naked eye or under an ordinary optical microscope. However, the scattering of light can be used to see such colloidal particles (such as dust particles, etc.) easily. The size of colloidal particles then may range from 10^{-4} to 10^{-7} cm. The units used are as follows:

$$1 \mu\text{m} = 10^{-6} \text{ m}$$

$$1 \text{ \AA} (\text{angstrom}) = 10^{-8} \text{ cm} = 0.1 \text{ nm} = 10^{-10} \text{ m}$$

The angstrom unit is named for the famous Swedish scientist, and currently the nm (10^{-9}) unit is mainly used. Because colloidal systems consist of two or more phases and components, the interfacial area-to-volume ratio becomes very significant. Colloidal particles have a high ratio of surface area to volume compared with bulk materials. A significant proportion of the colloidal

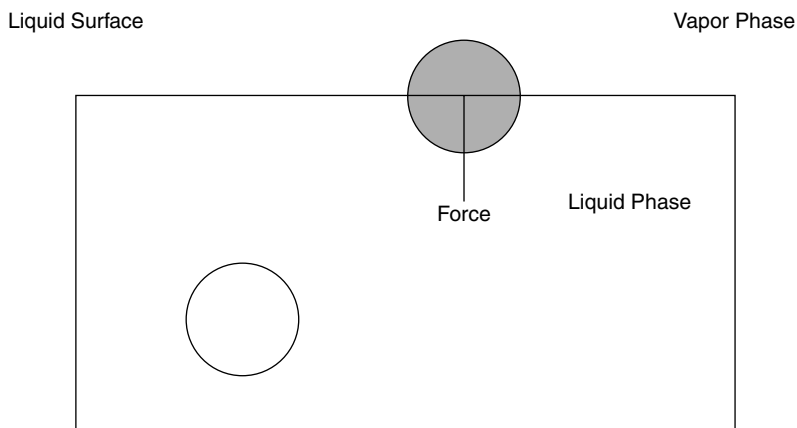


FIGURE 1.1 Intermolecular forces around a molecule in the bulk liquid and around a molecule in the surface layer (schematic).

molecules lie within, or close to, the interfacial region. Hence, the interfacial region has significant control over the properties of colloids. To understand why colloidal dispersions can be either stable or unstable, we need to consider the following:

- The effect of the large ratio of surface area to volume
- The forces operating between the colloidal particles

There are some very special characteristics that must be considered regarding colloidal particle behavior: size and shape, surface area, and surface charge density. The *Brownian motion* of the particles is a much-studied field, and the fractal nature of surface roughness has recently been shown to be important. Recent applications have been reported employing nanocolloids.

The definitions generally employed are as follows. *Surface* is a term used when considering the dividing phase between

Gas–Liquid
Gas–Solid

Interface is the term used when considering the dividing phase:

Solid–Liquid
Liquid₁–Liquid₂
Solid₁–Solid₂

In other words, surface tension may be considered to arise because of a degree of unsaturation of bonds that occurs when a molecule resides at the surface and not in the bulk. The term *surface tension* is used for solid–vapor or liquid–vapor interfaces. The term *interfacial tension* is more generally used for the interface between two liquids, two solids, or a liquid and a solid.

It is, of course, obvious that in a one-component system the fluid is uniform from the bulk phase to the surface, but the orientation of the surface molecules will be different from the molecules in the bulk phase. The question we may ask, then, is how sharply the density changes from that of being fluid to that of gas. Is this transition region a monolayer deep or many layers deep?

TABLE 1.1
Typical Colloidal Systems

Phases		
Dispersed	Continuous	System Name
Liquid	Gas	Aerosol fog, spray
Gas	Liquid	Foam, thin films, froth, fire extinguisher foam
Liquid	Liquid	Emulsion (milk), mayonnaise, butter
Solid	Liquid	Sols, AgI, photography films, suspension wastewater, cement
Biocolloids		
Corpuscles	Serum	Blood
Hydroxyapatite	Collagen	Bone
Liquid	Solid	Solid emulsion (toothpaste)
Solid	Gas	Solid aerosol (dust)
Gas	Solid	Solid foam — expanded (polystyrene), insulating foam
Solid	Solid	Solid suspension/solids in plastics

Many reports are found where this subject has been investigated.^{13,14} The Gibbs adsorption theory considers the surface of liquids to be monolayer. The experiments that analyze the spread monolayers are also based on one molecular layer. The subject related to self-assembly monolayer (SAM) structures has been treated extensively.^{14,16} However, there exists no procedure that can provide information by a direct measurement; this subject is described later in this handbook. The composition of the surface of a solution with two components or more requires additional comments.¹⁵ In Table 1.1 are given typical colloidal suspensions that are found in everyday life.

Colloidal systems are widespread in their occurrence and have biological and technological significance. There are three types of colloidal systems:¹⁶

1. In simple colloids, clear distinction can be made between the disperse phase and the disperse medium, e.g., simple emulsions of oil in water (o/w) or water in oil (w/o).
2. Multiple colloids involve the coexistence of three phases of which two are finely divided, e.g., multiple emulsions of water in oil in water (w/o/w) or oil in water in oil (o/w/o).
3. Network colloids have two phases forming an interpenetrating network, e.g., polymer matrix.

Colloidal stability is determined by the free energy (surface free energy or the interfacial free energy) of the system. The main parameter of interest is the large surface area exposed between the dispersed phase and the continuous phase. Because the colloid particles move about constantly, their dispersion energy is determined by Brownian motion. The energy imparted by collisions with the surrounding molecules at temperature $T = 300$ K is $\frac{3}{2} k_B T = \frac{3}{2} \times 1.38 \times 10^{-23} \times 300 = 10^{10-20}$ J (where k_B is the Boltzmann constant). This energy and the intermolecular forces would thus determine the colloidal stability. The idea that two species should interact with one another, so that their mutual potential energy can be represented by some function of the distance between them, has been described in the literature.

Furthermore, colloidal particles frequently adsorb (and even absorb) ions from their dispersing medium. Sorption that is much stronger than expected from dispersion forces is called *chemisorption*, a process that is of both chemical and physical interest.

These considerations are important in regard to many different systems: paints, cements, adhesives, photographic products, water purification, sewage disposal, emulsions, chromatography, oil recovery, the paper and print industry, microelectronics, soap and detergents, catalysts, food products, pharmaceutical products, and biology (cell, virus).

REFERENCES

1. a) Bakker, G., *Kapillarität und Oberflächenspannung Handbuch der Experimentalphysik*, 3rd ed., Leipzig, 1928; b) Freundlich, H., *Colloid and Capillary Chemistry*, Methuen, London, 1926.
2. Adam, N.K., *The Physics and Chemistry of Surfaces*, Clarendon Press, Oxford, 1930.
3. Bancroft, W.D., *Applied Colloid Chemistry*, McGraw-Hill, New York, 1932.
4. Partington, J.R., *An Advanced Treatise of Physical Chemistry*, Vol. II, Longmans, Green, New York, 1951.
5. Harkins, W.D., *The Physical Chemistry of Surface Films*, Reinhold, New York, 1952.
6. Davies, J.T. and Rideal, E.K., *Interfacial Phenomena*, Academic Press, New York, 1963.
7. Defay, R. et al., *Surface Tension and Adsorption*, Longmans, Green, London, 1966.
8. Gaines, G.L., Jr., *Insoluble Monolayers at Liquid-Gas Interfaces*, Wiley-Interscience, New York, 1966.
9. Matijević, E., Ed., *Surface and Colloid Science*, Vol. 1–9, Wiley-Interscience, New York, 1969–1976.
10. Aveyard, R. and Hayden, D.A., *An Introduction to Principles of Surface Chemistry*, Cambridge University Press, London, 1973.
11. Fendler, J.H. and Fendler, E.J., *Catalysis in Micellar and Macromolecular Systems*, Academic Press, New York, 1975.
12. a) Adamson, A.W., *Physical Chemistry of Surfaces*, 5th ed., Wiley-Interscience, New York, 1990; b) Faraday Symposia of the Chemical Society, No. 16, *Structure of the Interfacial Region*, Faraday Society, London, 1981.
13. Chattoraj, D.K. and Birdi, K.S., *Adsorption and the Gibbs Surface Excess*, Plenum Press, New York, 1984.
14. a) Birdi, K.S., *Lipid and Biopolymer Monolayers at Liquid Interfaces*, Plenum Press, New York, 1989; b) Birdi, K.S., *Self-Assembly Monolayer (SAM) Structures*, Plenum Press, New York, 1999.
15. a) Feder, J., *Fractals: Physics of Solids and Liquids*, Plenum Press, New York, 1988; b) Avnir, D., Ed., *The Fractal Approach to Heterogeneous Chemistry*, Wiley, New York, 1989; c) Birdi, K.S., *Fractals — In Chemistry, Geochemistry and Biophysics*, Plenum Press, New York, 1993.
16. Birdi, K.S., Ed., *Handbook of Surface and Colloid Chemistry*, CRC Press, Boca Raton, FL, 1997.
17. Birdi, K.S., Ed., *Handbook of Surface and Colloid Chemistry — CD ROM*, CRC Press, Boca Raton, FL, 1999.

2 Hydrogen Bonding in Solutions: The Equation-of-State Approach

Costas G. Panayiotou

CONTENTS

- 2.1 Introduction
- 2.2 The Essentials of Hydrogen Bonding Formalism
 - 2.2.1 The Combinatorial Formalism
 - 2.2.2 A First Application to Aqueous Systems
 - 2.2.3 Preferential Adsorption
 - 2.2.4 Macromolecular Ultrafiltration
- 2.3 Solubility Parameter Revisited
 - 2.3.1 Pure van der Waals Fluids
 - 2.3.2 Mixtures of van der Waals Fluids
 - 2.3.3 Hydrogen-Bonded Mixtures
 - 2.3.4 Applications
- 2.4 Rubber Swelling: Gels and Hydrogels
- 2.5 Intramolecular Hydrogen Bonding
 - 2.5.1 Applications
- 2.6 Hydrogen Bonding Cooperativity
 - 2.6.1 The Cooperativity Formalism
 - 2.6.2 The Gibbs Free Energy Equation
 - 2.6.3 The Case of Cyclic Associates
 - 2.6.4 An Application to Water

References

Appendix 2.A: The Equation-of-State Frameworks

- 2.A.1 The Lattice-Fluid Framework
- 2.A.2 The Quasi-Chemical Lattice Fluid (QCLF) Framework
- 2.A.3 Other Equation-of-State Frameworks

References to Appendix 2.A

Appendix 2.B: The Algorithm for Obtaining the Number of Hydrogen Bonds

Appendix 2.C: Implications of the Equation for Relative Adsorption

References to Appendix 2.C

2.1 INTRODUCTION

Hydrogen bonding is a subject of remarkable diversity as it is present in and dictates the behavior of an enormous number of systems including aqueous solutions, systems of biological/biomedical interest, pharmaceuticals, colloids and surfactants, physical networks and gels, adhesives and pastes, extractives and binders, polymer alloys and blends. There are many reviews of the subject in the

open literature¹⁻¹⁶ each addressing, usually, one aspect or type of application of hydrogen bonding. Because of its many-faceted character, unified approaches of treatment of hydrogen bonding are particularly useful, especially in areas at the interface of various scientific branches, such as colloid and interface science.

The focus in this chapter is on the thermodynamic aspects of hydrogen bonding in pure fluids and their mixtures. For the treatment of hydrogen bonding in associated fluids and mixtures, a variety of different approaches are popular. We could divide the overwhelming majority of these approaches into two groups: the *association* models^{8,17-22} and the *combinatorial* models.^{16,23-26} Association models invoke the existence of multimers or association complexes and seek expressions for their population. Combinatorial models do not invoke the existence of association complexes but, instead, they focus on the donor–acceptor contacts and seek combinatorial expressions for the number of ways of forming hydrogen bonds in systems of given proton-donor and proton-acceptor groups. Both types of models imply that the molecules tend to be distributed in the system nonrandomly for more efficient hydrogen bonding interaction.

A few years ago,¹⁶ we presented a review of the thermodynamic models for the treatment of hydrogen bonding in fluids and their mixtures. In that work, we gave an account of the association models and reviewed the work that was done to that time with models adopting the combinatorial approach. The two approaches were compared and applied to the description of phase equilibria and mixture properties of systems of fluids. The key conclusion was that, in the systems where both approaches apply, they prove to be essentially equivalent. However, the combinatorial approach has a much broader field of applications as it can be applied even to systems forming three-dimensional hydrogen bonding networks.

The present review is, in a sense, a continuation of the 1994 review. Here, we do not deal with the association models. Instead, we focus on the combinatorial approach and review the recent progress. We provide the essentials of this approach to make the chapter self-sufficient.

It should become clear at the outset that, in general, hydrogen bonding makes a *contribution* only and is not sufficient for the complete evaluation of the various thermodynamic properties of fluids and their mixtures. Thus, hydrogen bonding formalisms are usually combined with thermodynamic models, which account for all other contributions. For the purposes of this chapter, we use two such thermodynamic models of fluids: the simple lattice fluid (LF) model²⁷⁻²⁹ and the recently developed QCLF (quasi-chemical lattice fluid) model.^{30,31} The latter model takes into account the nonrandom distribution of free volume in the system by using Guggenheim's *quasi-chemical* approach.^{32,33} These two equation-of-state frameworks are briefly presented in Appendix 2.A. By adopting this type of thermodynamic framework, our approach to hydrogen bonding becomes an *equation-of-state* approach, which means that it is applicable to fluids over an extended range of external conditions encompassing liquids, vapors, gases, as well as the supercritical state. In addition, because it can handle in a consistent manner linear, branched, as well as three-dimensional (network formation) association, it is suitable for treating complex systems such as aqueous systems, polymer mixtures, and (hydro)gels.

In the following, after an exposition of the essentials of the combinatorial hydrogen bonding formalism, we present some applications to preferential adsorption at liquid interfaces and to gels (chemically cross-linked systems). We subsequently examine its extension to account for intramolecular association (as opposed to intermolecular association), and for hydrogen bonding cooperativity. The way the hydrogen bonding component of the solubility parameter can be evaluated is also presented. Throughout the presentation, examples of calculations in systems of practical interest are given.

2.2 THE ESSENTIALS OF HYDROGEN BONDING FORMALISM

According to our approach, known in the literature as the LFHB (lattice fluid hydrogen bonding) approach, the system partition function can be factored into a “physical” and a “chemical” or hydrogen bonding term:

$$Q = Q_P Q_H \quad (2.1)$$

The focus here is on the Q_H term. We give expressions for this term by adopting the combinatorial approach. As already mentioned, two alternative versions of the physical term Q_P are presented in Appendix 2.A. Of course, the combinatorial approach of this section is not bound to the models of Appendix 2.A and can be combined with any other appropriate thermodynamic model able to describe the nonhydrogen bonding contributions to the thermodynamic properties of the studied systems.

2.2.1 THE COMBINATORIAL FORMALISM

Combinatorial formalism originated primarily from thermodynamic studies of water and aqueous solutions. In a seminal paper, Levine and Perram²³ presented a statistical mechanical treatment of hydrogen bonding in water. They point out that the focus should be on the correct counting of the number of arrangements of hydrogen bonds and not of the distribution of the association complexes or *associates*. In a similar context, Luck²⁴ has pointed out that the only equilibrium to be considered is that of the formation and rupture of hydrogen bonds and not of the equilibrium formation of the various associates. Along these lines, Veytsman²⁵ considered systems of molecules with one type of proton-donor group and one type of proton-acceptor group and proposed an approximate combinatorial expression for the number of ways of forming hydrogen bonds in the system without invoking the existence of associates. Recently,^{16,26} we have extended the combinatorial expression of Veytsman²⁵ to systems of molecules with any number and type of hydrogen bonding groups by emphasizing the enumeration of pair interactions between various hydrogen bonding acceptor and donor groups. This section is heavily based on our previous work,^{16,26} and reviews the essentials of the generalized combinatorial formalism.

Let us consider a system consisting of N_1 molecules of type 1, N_2 molecules of type 2, ..., N_t molecules of type t under a pressure P and a temperature T . Let us assume that there are m different kinds of hydrogen bonding donors and n kinds of hydrogen bonding acceptors. Let d_i^k be the number of hydrogen bond donors of type i ($i = 1, m$) in each molecule of type k ($k = 1, t$) and α_j^k the number of hydrogen bond acceptors of type j ($j = 1, n$) in each molecule of type k . The total number N_d^i of hydrogen bond donors i in the system is

$$N_d^i = \sum_k d_i^k N_k \quad (2.2)$$

and the total number N_a^j of hydrogen bond acceptors j in the system is

$$N_a^j = \sum_k \alpha_j^k N_k \quad (2.3)$$

The potential energy of the system due to hydrogen bonding is *in excess* of that due to physical interactions. The total energy E_H of the system due to hydrogen bonding is given by

$$E_H = \sum_i^m \sum_j^n N_{ij} E_{ij}^0 \quad (2.4)$$

where N_{ij} is the number of hydrogen bonds between hydrogen bond donors of type i and hydrogen-bond acceptors of type j , and E_{ij}^0 is the corresponding hydrogen bonding energy of the i - j interaction.

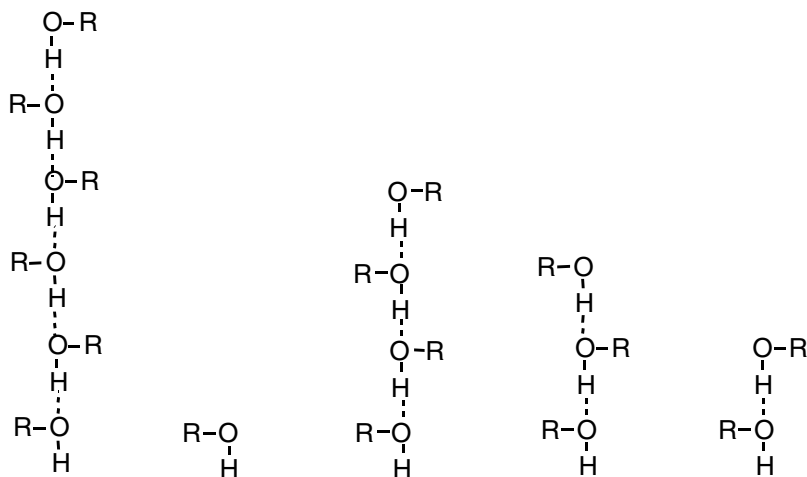


FIGURE 2.1 One configuration of a system with $N = 16$ and $N_{11} = 11$.

The total number of hydrogen bonds in the system is

$$N_H = \sum_i^m \sum_j^n N_{ij} \quad (2.5)$$

What is now required is the number of ways Ω of distributing the N_{ij} bonds among the functional groups of the system. Let us briefly summarize the rationale for this enumeration process and apply it, first, to the simple case of a system of *molecules with one proton donor and one acceptor group which self-associate*. An example of such systems is that of molecules with hydroxyl $-\text{OH}$ groups.

To find the different number of isoenergetic configurations of our system (number of the different ways of forming or distributing the hydrogen bonds in the system) we have to do the following:

1. Find the number of different ways of selecting the associated donor sites out of the donor population.
2. Find the number of different ways of selecting the associated acceptor sites out of the acceptor population.
3. Find the number of different ways of making hydrogen bonds between the selected donor and acceptor sites.

The number of configurations of the system is the product of these three terms.

As a simple example, let us have a system with N molecules each having one donor and one acceptor site (1) with N_{11} hydrogen bonds among them. In Figure 2.1, group 1 is $-\text{O}-\text{H}$. The number of ways of selecting the N_{11} associated donors out of the donor population N is just the binomial coefficient $N!/(N - N_{11})!N_{11}!$. Similarly, the number of ways of selecting the N_{11} associated acceptors out of the acceptor population N is again the binomial coefficient $N!/(N - N_{11})!N_{11}!$. The free donor groups in the system are $N - N_{11} = N_{10}$. This is also the number of free acceptor groups in this particular system. Now, a specific donor can hydrogen bond with any of the N_{11} acceptors, a second donor can hydrogen bond with any of the remaining $N_{11} - 1$ acceptors, and so on. The number of ways that N_{11} bonds can be formed between N_{11} donors and N_{11} acceptors is just $N_{11}!$. Thus, the

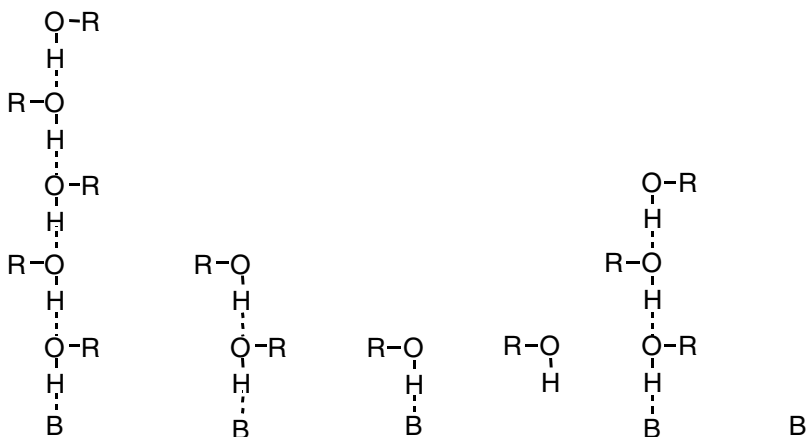


FIGURE 2.2 One configuration of a system with $N_1 = 12$, $N_2 = 5$, $N_{11} = 7$, $N_{12} = 4$.

total number of ways that N_{11} bonds can form between N donors and N acceptors is the product of the above three terms, or

$$\Omega = \frac{N!}{(N - N_{11})! N_{11}!} \frac{N!}{(N - N_{11})! N_{11}!} N_{11}! = \frac{N!}{N_{10}!} \frac{N!}{N_{10}! N_{11}!} \quad (2.6)$$

As a second example, let us consider the case of N_1 molecules or groups (1) that self-associate and N_2 molecules or groups (2) that cross-associate only with groups (1) (Figure 2.2).

Let in the system be N_{11} and N_{12} bonds of type 1-1 and 1-2, respectively (in Figure 2.2 the groups 1 and 2 are 1 = -O-H, 2 = B). Then, the free donors 1 are $N_1 - N_{11} - N_{12} = N_{10}$ (the inner lower index is the donor) and the free acceptors 2 are $N_2 - N_{12} = N_{02}$. Following the above enumeration procedure, we must select first, out of the donor population N_1 , the N_{11} and N_{12} donors participating in hydrogen bonds 1-1 and 1-2, respectively. This can be done in $N_1!/[N_{10}! N_{11}! N_{12}!]$ ways. The N_{11} associated acceptors 1 can be selected in $N_1!/[N_{11}!(N_1 - N_{11})!]$ ways, and the N_{12} associated acceptors 2 in $N_2!/[N_{12}!(N_2 - N_{12})!]$ ways. Now, the bonds N_{11} between the N_{11} donors and the N_{11} acceptors can be done again in $N_{11}!$ ways and, similarly, the N_{12} bonds can be done in $N_{12}!$ ways. Thus, Ω in this case is

$$\begin{aligned} \Omega &= \frac{N_1!}{N_{10}! N_{11}! N_{12}!} \frac{N_1!}{(N_1 - N_{11})! N_{11}!} \frac{N_2!}{(N_2 - N_{12})! N_{12}!} N_{11}! N_{12}! \\ &= \frac{(N_1!)^2 N_2!}{N_{10}! (N_1 - N_{11})! N_{11}! (N_2 - N_{12})! N_{12}!} \end{aligned} \quad (2.7)$$

These arguments, when extended to the general case of multigroup molecules, lead to the following equation:^{16,26}

$$\Omega = \prod_i^m \frac{N_d^i!}{N_{i0}! N_{i1}! \dots N_{in}!} \prod_j^n \frac{N_a^j!}{N_{0j}! N_{1j}! \dots N_{mj}!} \prod_i^m \prod_j^n N_{ij}! = \prod_i^m \frac{N_d^i!}{N_{i0}!} \prod_j^n \frac{N_a^j!}{N_{0j}!} \prod_i^m \prod_j^n \frac{1}{N_{ij}!} \quad (2.8)$$

where N_{i0} is the number of free (nonhydrogen bonded) donor groups of type i and N_{j0} the respective number of free acceptor groups of type j ;

$$N_{i0} = N_d^i - \sum_j^n N_{ij} \quad (2.9)$$

$$N_{0j} = N_a^j - \sum_i^m N_{ij} \quad (2.10)$$

However, to form a hydrogen bond, the two interacting groups must be proximate. The mean field probability P_{ij} that a specific acceptor j will be proximate to a given donor i is proportional to the volume of the acceptor group divided by the total system volume; that is, $P_{ij} \sim 1/V$. Even spatial proximity does not guarantee that a bond will form. Bond formation requires that donor and acceptor adopt a unique spatial orientation with respect to one another. Formation of the bond is also accompanied by a loss of rotational degrees of freedom. Steric considerations will also come into play in bond formation. In general and in the LF framework, for a donor i -acceptor j pair, this probability is given by²⁶

$$P_{ij} = e^{S_{ij}^0/R} \frac{\tilde{\rho}}{rN} \quad (2.11)$$

where S_{ij}^0 is the entropy loss (intrinsically negative) associated with hydrogen bond formation of an (i,j) pair. The last term $\tilde{\rho}/rN$ in Equation 2.11 comes from the estimation of the volume V by the model framework for the physical term (see Appendix 2.A). r in Equation 2.11 is the average number of segments per molecule; $\tilde{\rho}$ is the reduced density in the system and can be calculated from the equation of state (see below).

With these definitions we may now write for the canonical partition function for hydrogen bonding the following equation:

$$Q_H(T, N_0, \{N_k\}, \{N_{ij}\}) = \left(\frac{\tilde{\rho}}{rN} \right)^{N_H} \prod_i^m \frac{N_d^i!}{N_{i0}!} \prod_j^n \frac{N_a^j!}{N_{0j}!} \prod_i^n \prod_j^n \frac{\exp(-N_{ij}F_{ij}^0/RT)}{N_{ij}!} \quad (2.12)$$

$$F_{ij}^0 = E_{ij}^0 - TS_{ij}^0 \quad (2.13)$$

The total partition function of the system in the P, T ensemble and in its maximum term approximation is given by

$$\Psi(T, P, \{N_k\}) = Q_P(T, N_0, \{N_k\}) Q_H(T, N_0, \{N_k\}, \{N_{ij}\}) \exp\left(\frac{-PV}{RT}\right) \quad (2.14)$$

where V is the total volume of the system and is given by

$$V = V_P + V_H = V_P + \sum_i^m \sum_j^n N_{ij} V_{ij}^0 \quad (2.15)$$

V_{ij}^0 is the volume change accompanying a i - j hydrogen bond formation.

The free energy of the system will be given by

$$G = -kT \ln \Psi \quad (2.16)$$

A direct consequence of our approach for the factorization of the partition function is the division of the Gibbs free energy, G , into a physical term and a chemical or hydrogen bonding term:

$$G = G_p + G_H \quad (2.17)$$

The chemical (hydrogen bonding) contribution to the free energy of the system is given by

$$\frac{G_H}{kT} = rN \left\{ \sum_i^m \sum_j^n v_{ij} \left[1 + \frac{G_{ij}^0}{RT} + \ln \left(\frac{\tilde{v} v_{ij}}{v_{i0} v_{0j}} \right) \right] + \sum_i^m v_d^i \ln \frac{v_{i0}}{v_d^i} + \sum_i^m v_a^j \ln \frac{v_{0j}}{v_a^j} \right\} \quad (2.18)$$

where

$$v_{ij} \equiv \frac{N_{ij}}{rN} \quad v_{i0} \equiv \frac{N_{i0}}{rN} \quad v_d^i \equiv \frac{N_d^i}{rN} \quad \text{etc.} \quad (2.19)$$

and

$$G_{ij}^0 = F_{ij}^0 + PV_{ij}^0 = E_{ij}^0 + PV_{ij}^0 - TS_{ij}^0 \quad (2.20)$$

The expression for the physical contribution to free energy G_p depends on the adopted thermodynamic framework for the physical term. Examples are given in Appendix 2.A.

For a system at equilibrium, the free energy is at a minimum. We may then write the following minimization conditions:

$$\left(\frac{\partial G}{\partial \tilde{v}} \right)_{T,P,\{N_k\},\{N_{ij}\}} = 0 \quad (2.21)$$

$$\left(\frac{\partial G}{\partial N_{ij}} \right)_{T,P,\{N_k\},\{N_{rs}\}} = 0 \quad (2.22)$$

When adopting the LF framework, from minimization condition 2.21 we obtain the LFHB equation of state:²⁶

$$\tilde{\rho}^2 + \tilde{P} + \tilde{T} \left[\ln(1 - \tilde{\rho}) + \tilde{\rho} \left(1 - \frac{1}{\tilde{r}} \right) \right] = 0 \quad (2.23)$$

where \tilde{P} is the reduced pressure defined as

$$\tilde{P} = \frac{P}{P^*} = \frac{Pv^*}{\varepsilon^*} \quad (2.24)$$

\tilde{T} is the reduced temperature

$$\tilde{T} = \frac{T}{T^*} = \frac{RT}{\varepsilon^*} \quad (2.25)$$

and the modified chain length is given by

$$\frac{1}{\tilde{r}} = \frac{1}{r} - \sum_i^m \sum_j^n v_{ij} = \frac{1}{r} - v_H \quad (2.26)$$

where v_H is the fraction of hydrogen bonds in the system, or

$$v_H = \frac{N_H}{rN}$$

By the second minimization condition, Equation 2.22, the following equations are obtained:

$$\frac{v_{ij}}{v_{i0}v_{0j}} = \tilde{\rho} \exp\left(-\frac{G_{ij}^0}{RT}\right) \text{ for all } i,j \quad (2.27)$$

or

$$v_{ij} = \left[v_d^i - \sum_k^n v_{ik} \right] \left[v_a^j - \sum_k^m v_{kj} \right] \tilde{\rho} \exp\left(-\frac{G_{ij}^0}{RT}\right) \quad (2.28)$$

which is a system of $(m \times n)$ quadratic equations for v_{ij} . This system must be solved in combination with the LFHB equation of state (Equation 2.23) and thus we are finally left with a system of $(m \times n + 1)$ coupled nonlinear equations for $\tilde{\rho}$ and v_{ij} . v_{ij} in these equations are again fractions of hydrogen bonds, or

$$v_{ij} = \frac{N_{ij}}{rN}$$

and similarly for v_{i0} and v_{0j} .

The chemical potential of component k is given by

$$\mu_k = \mu_{k,P} + \mu_{k,H} = \left(\frac{\partial G_P}{\partial N_k} \right)_{T,P,N_j, \tilde{v}, \{N_{ij}\}} + \left(\frac{\partial G_H}{\partial N_k} \right)_{T,P,N_j, \tilde{v}, \{N_{ij}\}} \quad (2.29)$$

On the basis of the above we have for the hydrogen bonding contribution to the chemical potential:

$$\frac{\mu_{k,H}}{RT} = r_k v_H - \sum_i^m d_i^k \ln \frac{v_d^i}{v_{i0}} - \sum_j^n a_j^k \ln \frac{v_a^j}{v_{0j}} \quad (2.30)$$

The expression for the physical contribution to the chemical potential depends on the adopted framework. Examples can again be found in Appendix 2.A.

This formalism is applicable to a variety of systems of practical interest varying in complexity from simple self-associated systems, such as the alkanols, up to highly complex systems forming three-dimensional interpenetrating hydrogen bonding networks, such as the multicomponent hydrogels

and the self- and cross-associating polymer blends. In our previous review¹⁶ we applied the above formalism, in combination with the LF framework for the physical term, to a number of systems including alkanol + alkane mixtures, polymer solutions and polymer + polymer mixtures. In this chapter, we give new examples of applications. In the subsection, we confine ourselves to a recent application to aqueous systems over an extended range of external conditions.³¹ In this application the QCLF framework (see Appendix 2.A) was adopted for the evaluation of the physical contributions to the various thermodynamic properties.

2.2.2 A FIRST APPLICATION TO AQUEOUS SYSTEMS

In this section we apply the above model for the description of the volumetric behavior of water and water + inert solvent mixtures at moderate to high temperatures and pressures. In this range of conditions we do not expect any predominance of the well-known picture of icebergs valid for the lower range of conditions. The formation of icebergs will be discussed in a later section.

In each water molecule we have two proton donors and two proton acceptor sites and only one type of hydrogen bond. In this case we have only one minimization condition (Equation 2.28) which, when solved for the number of hydrogen bonds, gives the physically meaningful solution:

$$v_{11} = \frac{4 + B - \sqrt{B(B+8)}}{2} \quad (2.31)$$

where

$$B = r\tilde{v} \exp\left(\frac{G^H}{RT}\right) \quad (2.32)$$

To perform these calculations we must first determine the parameters of the model. There are two types of constants that must be determined: the equation-of-state scaling constants (T^* , P^* , ρ^* , or, equivalently, ϵ^* , v^* , r) and the hydrogen bonding constants (E^H , V^H , S^H), in total, six parameters for pure water. They will be obtained, as usual, by a least squares fit to the experimental data. From such a procedure we may obtain a multitude of sets that describe the experimental data equally well. To simplify this procedure we have set $r = 1$; that is, water has been considered as a simple monosegmental molecule. Because V^H and ρ^* are interrelated, we have set $\rho^* = 1.00 \text{ g/cm}^3$ and, thus, we have fixed $v^* = 18.02 \text{ cm}^3/\text{mol}$. E^H and S^H are also interrelated and, thus, we have fixed $S^H = -26.5 \text{ J}/(\text{mol K})$ as for hydroxyl interactions. In this way, from the value of E^H we will have a direct comparison of the strength of the water–water hydrogen bond with that of the OH–OH interaction. The estimated values for the remaining parameters are $E^H = -19.9 \text{ kJ/mol}$ and $\epsilon^* = RT^* = P^*v^* = 3359 \text{ J/mol}$.

This is, certainly, an oversimplified picture and, as expected, to have an adequate description of the volumetric behavior of water, the remaining V^H parameter must vary with both temperature and pressure. For this purpose we have adopted a simple relation analogous to that proposed by Marcus,³⁴ namely,

$$V^H = (V_0^H - \beta P) \left(1 + \alpha \frac{(T - 373.15)^3}{|T - 373.15|} \right) \quad (2.33)$$

with $V_0^H = -0.51 \text{ cm}^3/\text{mol}$, $\beta = 2.03 \times 10^{-9} \text{ m}^3/\text{MPa}$, and $\alpha = -5.66 \times 10^{-5} \text{ K}^{-2}$.

Before proceeding, some comments are in order regarding the values of the above parameters. The energy change upon formation of one water–water hydrogen bond is significantly lower

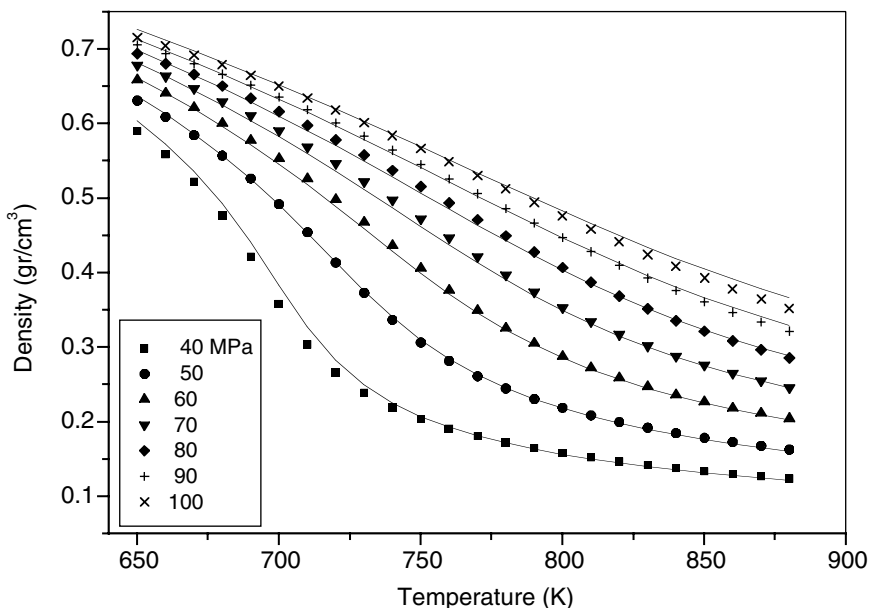


FIGURE 2.3 Experimental³⁵ and calculated densities of supercritical water, as calculated by the QCLFHB model.

compared to the corresponding energy for the OH–OH interaction in alkanols (–25.6 kJ/mol).²⁰ One should keep in mind, however, that each water oxygen can participate in two hydrogen bonds with protons from other water molecules. The estimated value for V^H is negative and almost one order of magnitude smaller compared to the corresponding value for OH–OH interaction in alkanols (–5.6 cm³/mol).^{19,20} If our focus were on the densities at the lower range of T – P conditions, we would even expect a positive value for V^H . At high temperatures, however, the degree of hydrogen bonding per water molecule is expected to be significantly lower than 2 and, thus, the lack of persistence of long-range order and the associated geometric constraints will no longer lead to a positive volume change upon hydrogen bond formation. Thus, it is essential to have an estimation of the degree of hydrogen bonding of water at the studied range of T – P conditions.

Figure 2.3 compares the calculated densities of water over an extended range of supercritical conditions with the calculations by Duan’s expressions,³⁵ which are essentially experimental data. In view of the significant variation in temperature and pressure, the agreement is again rather satisfactory.

As mentioned before, it is essential to have an estimation of the degree of hydrogen bonding of water at supercritical conditions. The maximum number of hydrogen bonds per molecule as calculated by Equation 2.50 is 2, which is the expected value. Thus, the percent degree of hydrogen bonding, N_{HB} , in the system is simply equal to $100 \times v_{11}/2$.

Figure 2.4 shows the calculated degrees of hydrogen bonding of water over an extended range of supercritical conditions. Experimental data at these conditions are sparse. To have an alternative estimation of this degree, we have conducted molecular dynamics (MD) calculations for water with the MSI Cerius2 suite of Molecular Simulations, Inc., and by using the Dreiding 2.11 force field. A qualitative agreement was obtained between the calculations with the two methods. The equation-of-state calculations and the MD calculations have a similar trend but the former are systematically higher than the MD calculations.

The above formalism can easily be extended to aqueous mixtures. In the case of water + inert solvent mixtures we do not need any additional hydrogen bonding parameters. However, the equation giving the number of hydrogen bonds (Equation 2.31) must now change to the equation:

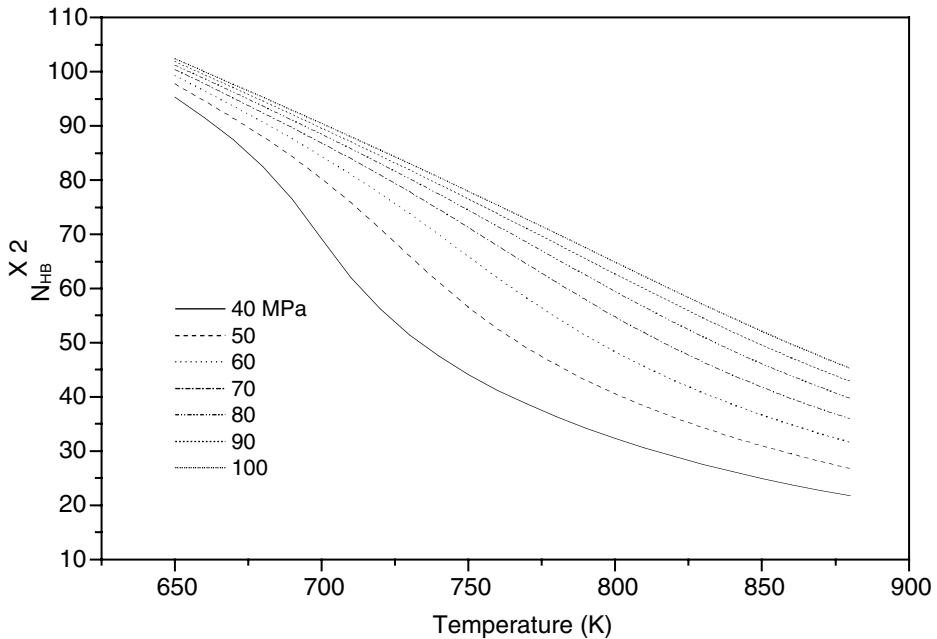


FIGURE 2.4 The degree of hydrogen bonding in supercritical water as a function of temperature and pressure as calculated by the equation-of-state model.

$$v_{11} = \frac{4x_1 + B - \sqrt{B(B + 8x_1)}}{2} \quad (2.31a)$$

where x_1 is the mole fraction of water. B is given by Equation 2.32 but now the average number of segments per molecule, r , is given by (see Appendix 2.A)

$$r = x_1 r_1 + x_2 r_2$$

Because no additional parameters are needed, the model can be used for the prediction of the volumetric behavior of water + inert solvent mixtures. In Figures 2.5 and 2.6 we compare experimental and predicted molar volumes for the water + *n*-pentane and for the water + methane mixture, respectively. The scaling constants used for these calculations are as follows: for *n*-pentane, $T^* = 485$ K, $P^* = 274$ MPa, $\rho^* = 755$ kg/m³; and for methane, $T^* = 212$ K, $P^* = 252$ MPa, $\rho^* = 489$ kg/m³. As observed in the figures, in both cases there is satisfactory agreement between theory and experiment. We have applied the model to a number of mixtures with equally satisfactory results.

The physical picture that has been adopted in this application for hydrogen bonding in water is a rather oversimplified one. At near-critical and supercritical conditions, as the degree of hydrogen bonding diminishes drastically, this infinite structure breaks down to a structure of small, varying in size clusters of hydrogen-bonded water molecules. We have considered here one-state hydrogen bonding and attributed to it a small but negative value for the volume change upon its formation. This picture may be justifiable for the relatively high temperatures of interest in this work, but it is not expected that it will be appropriate for the low-temperature region. In the dense state (low temperature, high pressure), this model treats water as an infinite three-dimensional hydrogen bonding network or as a collection of large clusters of hydrogen-bonded molecules. For the latter, the picture of cooperative hydrogen bonding with positive volume change is more appropriate. We discuss this in a later section. However, this introduces additional parameters in the model and

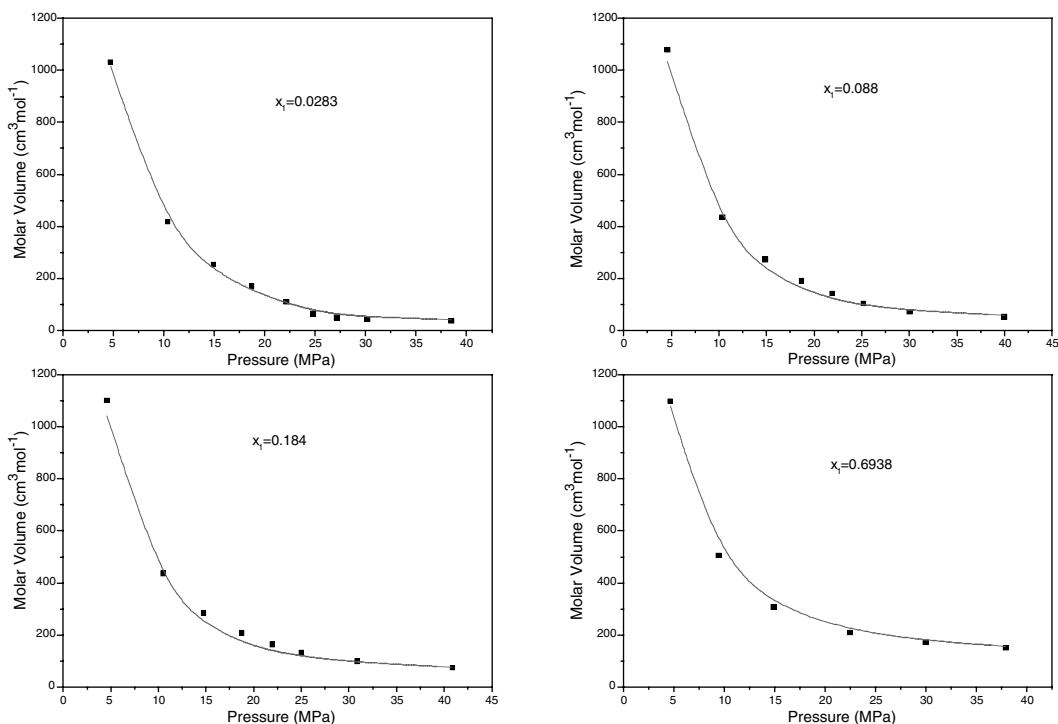


FIGURE 2.5 Molar volumes of pentane(1) + water(2) mixture at 647.05 K. Symbols are experimental data.³⁶ Lines are predictions of the QCLFHB model.

some complexity in the formalism. The complex nature of water might justify such a complexity in the formalism but this may not be necessary, as long as we confine ourselves to the region of interest in this work. This is why we have preferred, rather arbitrarily, to fix three of the six model parameters here instead of forcing them to describe the thermodynamic properties of water at low temperatures as well.

2.2.3 PREFERENTIAL ADSORPTION

In this section we present an application of the above hydrogen bonding model for the estimation of preferential adsorption at liquid interfaces.

In a binary mixture, the relative adsorption of component 2 at the liquid–air interface is defined by

$$\Gamma_{2,1} = - \left(\frac{d\sigma}{d\mu_2} \right)_T = - \left[\left(\frac{d\sigma}{dx_2} \right) \left(\frac{dx_2}{d\mu_2} \right) \right]_T \quad (2.34)$$

where μ_2 is the chemical potential of component 2 in the mixture. It is clear from this equation that the calculation of the relative adsorption requires knowledge of the variation with composition of both the surface tension and the chemical potential. Experimental data for the variation of surface tension with composition can be found in the literature for a number of systems. We have measured^{38,39} this property for the hydrogen-bonded systems that appear in [Table 2.1](#). These correspond to two classes of hydrogen-bonded systems. In the first, a self-associated substance (alkanol) is mixed with an inert solvent (alkane). In the second, a self-associated substance (alkanol) is mixed with a weakly self-associated substance (alkylamine), which can cross-associate strongly with the former. The hydrogen bonding parameters for these interactions are reported in [Table 2.2](#).

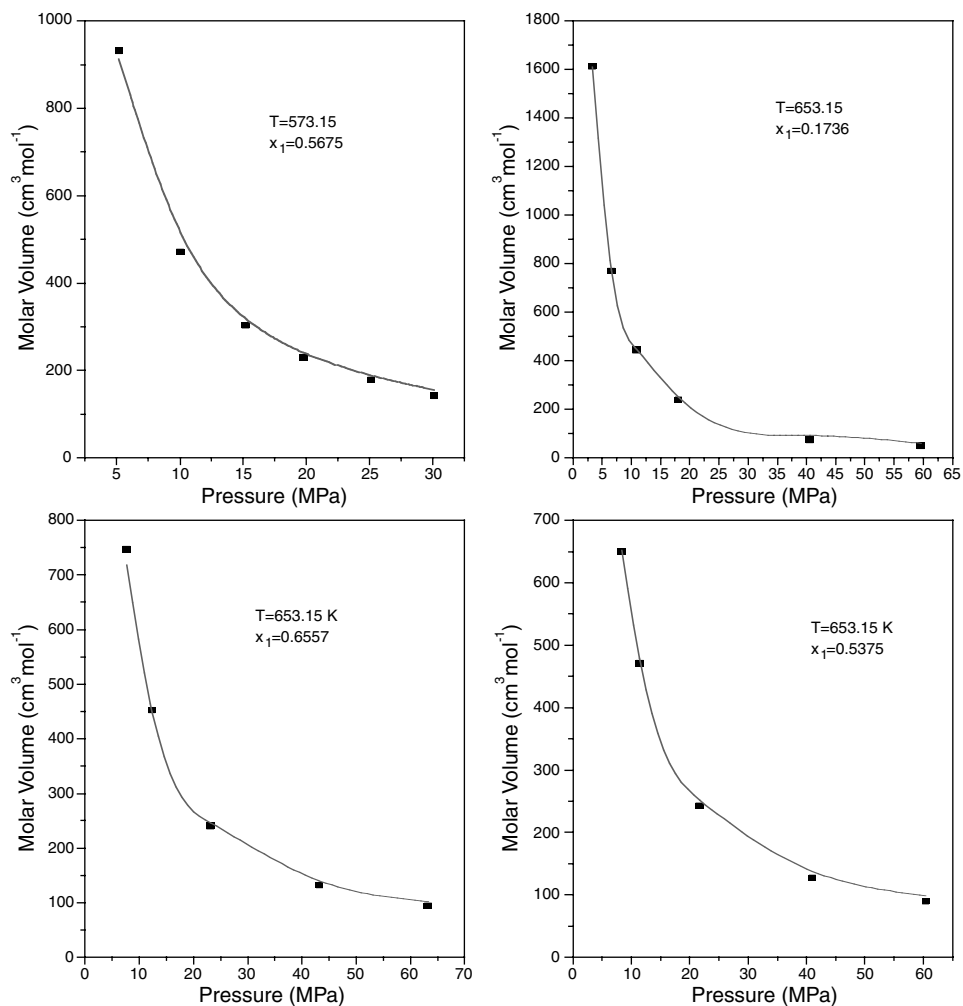


FIGURE 2.6 Molar volumes of CH₄(1) + water(2) mixture at various temperatures and mole fractions. Symbols are experimental data.³⁷ Lines are predictions of the QCLFHB model.

TABLE 2.1
Extreme Values of Excess Surface Tensions^{38,39}

System	σ^E (mN/m)
Hexane(1) + ethanol(2)	-1.84
Hexane(1) + propanol(2)	-1.91
Heptane(1) + ethanol(2)	-1.17
Heptane(1) + propanol(2)	-1.50
Propanol(1) + propylamine(2)	0.89
Methanol(1) + butylamine(2)	1.33
Ethanol(1) + butylamine(2)	0.87
Propanol(1) + butylamine(2)	0.64
Butanol(1) + butylamine(2)	0.53

TABLE 2.2
Hydrogen Bonding Parameters

Interaction	E^0 (kJ/mol)	S^0 (J/K/mol)	V^0 (cm ³ /mol)
OH-OH	-25.1	-26.5	-5.6
NH-NH	-13.2	-22.2	-2.2
OH-NH	-39.3	-62.0	-7.0

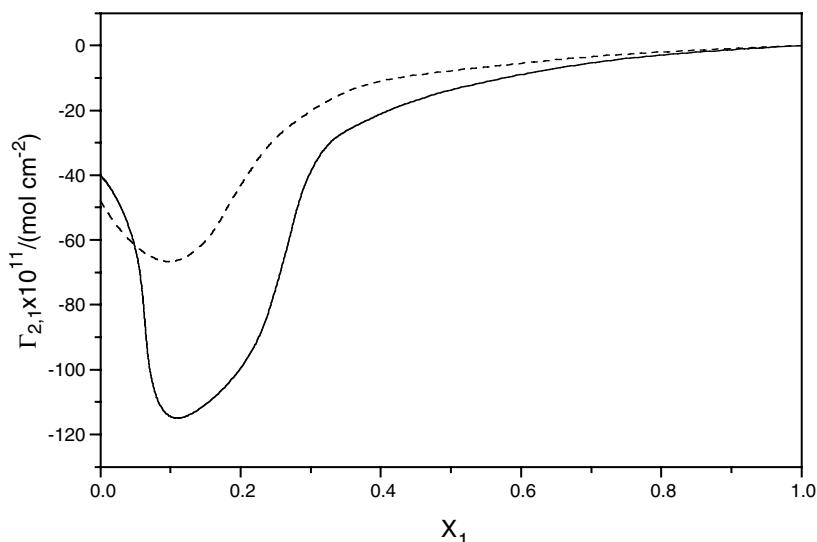


FIGURE 2.7 The preferential adsorption in hexane(1) + 1-propanol(2) (solid line) and heptane(1) + 1-propanol(2) (dashed line) mixtures at 25°C.

The LFHB model or the former LFAS (lattice fluid associated solution) model²⁰ can provide the needed equations for the chemical potential as a function of composition. The picture that emerges from application of the LFHB and LFAS models in this case is, essentially, identical. For the chemical potential, Equation 2.30 can be combined with Equation 2.A23 of Appendix 2.A to provide the required expression. On the other hand, the experimental data can be correlated to provide the appropriate expressions $\sigma(x_2)$ for the surface tension.^{38,39}

Figures 2.7 and 2.8 are typical ones showing the relative adsorptions at the liquid–air interface of the two classes of our systems as calculated by Equation 2.34. As observed in these figures, the variation of the relative adsorptions with composition follows distinctively different patterns in the two classes of systems. In alkanol + alkane mixtures, the relative adsorption of alkanol is negative with a pronounced minimum in the alkanol-rich region. In the alkanol + alkylamine systems, the relative adsorption of alkanol is both positive and negative with a pronounced maximum in the alkanol-rich region and a shallow minimum in the amine-rich region. The role of hydrogen bonding in the observed patterns is very important.

The alkanol + alkane mixtures have, in general, the following properties in common: positive enthalpies and volumes of mixing (the extreme values $H^E = 619.5$ J/mol, $V^E = 0.463$ cm³/mol for the heptane + ethanol mixture are typical), positive deviations from Raoult’s law, and negative excess surface tensions (see Table 2.1). The alkanol + alkylamine mixtures have in common the

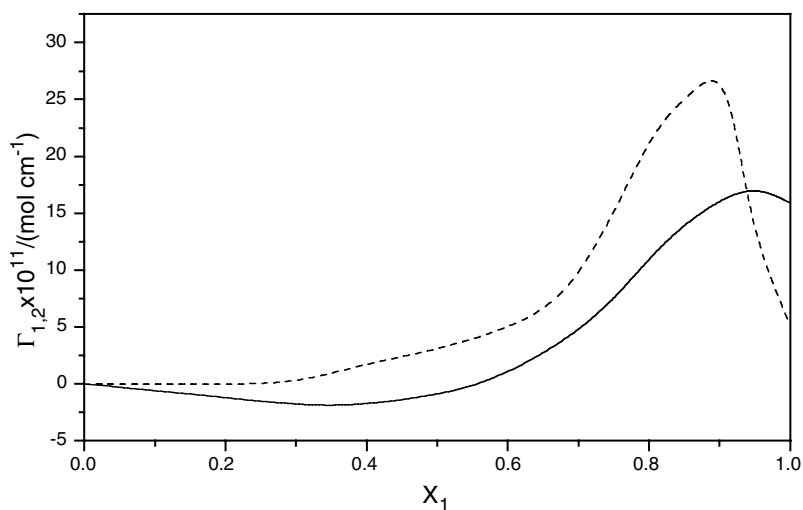


FIGURE 2.8 The preferential adsorption in ethanol(1) + *n*-butylamine (2) (dashed line) and 1-propanol(1) + *n*-propylamine(2) (solid line) mixtures at 25°C.

following properties: relatively large negative enthalpies and volumes of mixing (the extreme values $H^E = -2914$ J/mol, $V^E = -1.288$ cm³/mol for the ethanol + butylamine mixture are typical), and positive excess surface tensions (Table 2.1). These distinct differences as well as the differences in the calculated relative adsorptions shown in Figures 2.7 and 2.8 are the outcomes of the distinctively different types of intermolecular interactions in the two classes of systems.

As the hydrogen bonding parameters of Table 2.2 indicate, the alkanol prefers to interact with alkanol in the alkanol + alkane mixtures, but in the case of alkanol + alkylamine systems both the alkanol and the amine prefer to interact with each other rather than with themselves. On the basis of these, one could explain the observed patterns in Figures 2.7 and 2.8 for the relative adsorptions in our systems.

For alkanol + alkane mixtures, there are two synergistic factors that force the alkanol molecules to preferentially avoid the interface: the lower surface tension of the alkane and the fact that the hydrogen bonding interaction can be accomplished more efficiently in the bulk liquid phase rather than in the interface. The role of *n*-alkanes in the alkanol-rich region is essentially the breaking of the “structure” of the hydrogen-bonded alkanol chains. This is a highly endothermic process as we can verify from the positive enthalpy of mixing. This explains the tendency to keep the interfacial region rich in alkane rather than in alkanol especially in the alkanol-rich region.

The picture is different in the case of alkanol + alkylamine mixtures. In these systems, due to the strength of the OH–NH interaction, both compounds tend to prefer the bulk liquid phase rather than the interface where they can accomplish this hydrogen bond more efficiently. Thus, in both diluted regions of the composition, the less abundant component will tend to prefer the bulk, giving rise to S-shaped curves of preferential adsorptions. This is particularly noticeable in the alkanol-rich region in Figure 2.8. One should contrast Figure 2.8 to Figure 2.7, where the inert alkane in the alkanol-rich region exhibits a strong preference for the interface, whereas the cross-associated amine in the corresponding region in Figure 2.8 strongly prefers the bulk. This tendency, however, will be moderated by the tendency of the component with the lower surface tension (an outcome of physical interactions as well) to be preferentially adsorbed at the interface. It is the interplay of these factors that may explain in qualitative terms the behavior observed in Figures 2.7 and 2.8.

Equation 2.34 has many implications and can be used in various ways, as explained in Appendix 2.C In all these applications we may use the above formalism to account for the hydrogen bonding in the solution.

2.2.4 MACROMOLECULAR ULTRAFILTRATION

A widely used method for the separation of macromolecules from solution is ultrafiltration — a pressure-driven membrane process. Because of the formation of a “gel” layer of rejected macromolecules on the surface of the membrane, in most ultrafiltration processes the permeate flux becomes independent of the applied pressure for sufficiently high pressures. It is very important for this membrane process to have a method for predicting this “gel” concentration. Karode⁴⁰ has used LFHB to predict this concentration for a PEG–water system. He has constructed the temperature vs. polymer volume fraction phase diagram for the system (a UCST-type diagram in this case). The left side branch (polymer lean) of this diagram is the solubility limit line for the macromolecule, and the right side branch (polymer rich) is the gel concentration line. For a given temperature we can find the pair of points in the two branches by the classical phase equilibrium calculation, namely, the equality of the chemical potentials of polymer and solvent in the two phases α and β (rich and lean):

$$\mu_1^\alpha = \mu_1^\beta \quad \text{and} \quad \mu_2^\alpha = \mu_2^\beta \quad (2.35)$$

For these calculations Karode⁴⁰ combined Equation 2.30 with Equation 2.A23 of Appendix 2.A. The solubility limit for PEG of molecular weight 6000 Da was predicted to be $\sim 340 \text{ kg/m}^3$. The corresponding osmotic pressure from van't Hoff's law was estimated to be $\sim 2.8 \text{ MPa}$.

On the basis of these calculations, Karode was able to explain the experimental findings of Bhattacharjee and Bhattacharya⁴¹ for this system. In their experiments and simulations, the maximum wall concentration was always far below the above calculated limit of 340 kg/m^3 . As a consequence, no gel layer was formed on the membrane surface. In addition, it is reasonable to expect the wall concentration to be a function of the operating parameters such as the operating pressure, the stirring speed, etc. In practical applications of PEG ultrafiltration, the filtration would be osmotically limited and one could never expect the formation of a gel layer. The formation of such a layer would require application of pressures higher than $\sim 30 \text{ atm}$.

2.3 SOLUBILITY PARAMETER REVISITED

The solubility parameter, δ , is one of the most useful concepts in the physical chemistry and thermodynamics of solutions. Originally introduced by Hildebrand and Scott,⁴² it remains today one of the key parameters for selecting solvents or predicting solubilities and degrees of rubber swelling.⁴³⁻⁴⁵ There is today much interest in utilizing solubility parameter for rationally designing new processes, such as the supercritical extraction⁴⁶ and the coating process,⁴⁵ or new materials such as drugs and polymer alloys.^{14,45} In these cases it is usually necessary to have an estimation of the separate contributions to δ of nonspecific or van der Waals and specific intermolecular interactions.⁴⁵

One closely related concept to δ is the cohesive energy E , which is defined as the increase in the internal energy per mole of the system upon removal of all intermolecular interactions. When E is divided by the molar volume V , we obtain the cohesive energy density (ced), E/V , of the system. The solubility parameter is simply the square root of this cohesive energy density. A thorough discussion of the definition of δ and its relation to internal pressure may be found in the comprehensive review by Barton.⁴³

Although simple in its definition, the evaluation of δ is not always straightforward. In many applications we need to know the effect of temperature and pressure on δ . If in addition the system is not volatile (such as the high polymers), the evaluation of δ is difficult. The difficulty increases when we further need to know the separate contribution to δ of intermolecular dispersion forces and of specific forces such as hydrogen bonding.

Recently,⁴⁷ starting from the original definition of cohesive energy density and solubility parameter, we have proposed a systematic approach for estimating the latter. The potential energy E and the volume V of the system were obtained from the LFHB model. The model is able to provide with estimations of E and V over extended ranges of external conditions, for pure fluids as well as for mixtures, for simple systems as well as for highly nonideal systems, such as the hydrogen-bonded systems. In the latter systems the approach provides estimations of the separate components of the solubility parameter, namely, the “hydrogen bonding” contribution and the “van der Waals” contribution. The approach provides a straightforward procedure for the consistent estimation of the effect of temperature and pressure on the solubility parameter components of pure fluids, including high polymers and their mixtures. In the following we briefly present this approach.

As already mentioned, the starting point is the combination of one of the thermodynamic frameworks of Appendix 2.A with the above hydrogen bonding formalism. For simplicity of presentation we use the LF framework and we confine ourselves to the case of one self-associated (e.g., $\text{OH}\equiv\text{OH}$) and one cross-associated (e.g., $\text{OH}\equiv\text{O}(\text{ether})$) hydrogen bonding interaction.

2.3.1 PURE VAN DER WAALS FLUIDS

According to the LF model,²⁷⁻²⁹ the lattice potential energy of the system is

$$-E = rN\tilde{\rho}\tilde{\epsilon}^* \quad (2.36)$$

and the volume of the system:

$$V = rN\tilde{v}v^* \quad (2.37)$$

It is worth pointing out that, with the above definitions, $-E$ in Equation 2.36 is simply the cohesive energy of the system. The cohesive energy density, then, is given by

$$\text{ced} = \frac{-E}{V} = \frac{rN\tilde{\rho}\tilde{\epsilon}^*}{rN\tilde{v}v^*} = \tilde{\rho}^2 \frac{\tilde{\epsilon}^*}{v^*} = \tilde{\rho}^2 P^* \quad (2.38)$$

As a consequence, the solubility parameter of the fluid is given by the simple equation:

$$\delta = \sqrt{\text{ced}} = \tilde{\rho}\sqrt{P^*} \quad (2.39)$$

The unknown in Equation 2.39 is the reduced density. If the density is known, the reduced density is obtained by dividing the density with the characteristic density ρ^* of the fluid. If the density is not known, the reduced density may be obtained directly from the LF equation of state (see Appendix 2.A):

$$\tilde{P} + \tilde{\rho}^2 + \tilde{T} \left[\ln(1 - \tilde{\rho}) + \tilde{\rho} \left(1 - \frac{1}{r} \right) \right] = 0 \quad (2.40)$$

As is clear from Equation 2.39, the dependence of δ on temperature and pressure arises from the dependence of density on these external conditions.

The component of solubility parameter due to dispersion or van der Waals forces is usually approximated in the literature through the homomorph concept. The hydrocarbon homomorph of

the studied substance has a characteristic pressure P_{hm}^* (found in tabulations, such as in Reference 16). As Equation 2.39 indicates, to find this component δ_{hm} we must bring the homomorph to a condition where the reduced density is equal to that of the studied fluid, or

$$\delta_{\text{hm}} = \tilde{\rho} \sqrt{P_{\text{hm}}^*} \quad (2.39a)$$

2.3.2 MIXTURES OF VAN DER WAALS FLUIDS

Let us now consider a mixture of N_1 molecules of type 1 with N_2 molecules of type 2 characterized by the LF scaling constants $T_1^*, P_1^*, \rho_1^*, r_1^*, v_1^*, \epsilon_1^*$ and $T_2^*, P_2^*, \rho_2^*, r_2^*, v_2^*, \epsilon_2^*$, respectively. Mixing and combining rules, like those reported in Appendix 2.A, are now needed for ϵ^* and v^* of the mixture. On the basis of these mixing and combining rules we may further define the scaling constants of the mixture (in the one-fluid approach). With the above definitions we may write for the lattice potential energy of the mixture an equation identical in form to Equation 2.36. The same holds true for the total volume of the system (Equation 2.37) and for the equation of state. Of course, in these equations we must replace the corresponding quantities for the mixtures. Equation 2.39, then, is valid for mixtures as well, if we use the mixture quantities for P^* and reduced density.

2.3.3 HYDROGEN-BONDED MIXTURES

To avoid a lengthy presentation, we present directly the formalism for hydrogen-bonded binary mixtures. Pure hydrogen-bonded fluids is just a limiting case ($\phi_2 = 0$).

Let us consider a mixture of N_1 and N_2 molecules of type 1 and 2, respectively, at temperature T and external pressure P . Both types of molecules are assumed to possess two types of hydrogen bonding groups. The first (type 1) is a proton-donor and proton-acceptor or self-associated group (e.g., $-\text{OH}$, $-\text{NH}$) and the second (type 2) is proton acceptor only (e.g., $-\text{O}-$, $-\text{C}=\text{O}$). By applying the above hydrogen bonding formalism to this case we may write for the hydrogen bonding terms of E and V of the system:

$$E_H = N_{11} \cdot E_{11}^H + N_{12} \cdot E_{12}^H \quad (2.41)$$

and

$$V_H = N_{11} \cdot V_{11}^H + N_{12} \cdot V_{12}^H \quad (2.42)$$

The unknowns in the above equations are the N_{ij} , which are obtained from the corresponding free energy minimization conditions as before. The average number of segments, r , in the equation of state must be replaced now by the modified average chain length, \bar{r} , which is given by

$$\frac{1}{\bar{r}} = \frac{1}{r} - \frac{N_{11} + N_{12}}{rN} = \frac{1}{r} - v_{11} - v_{12} = \frac{1}{r} - v_H \quad (2.43)$$

With these definitions we may write for the cohesive energy density of the hydrogen-bonded system:

$$\text{ced} = \frac{rN\tilde{\rho}\epsilon^* - (N_{11}E_{11}^H + N_{12}E_{12}^H)}{rN\tilde{v}v^* + (N_{11}V_{11}^H + N_{12}V_{12}^H)} = \frac{\tilde{\rho}\epsilon^* - (v_{11}E_{11}^H + v_{12}E_{12}^H)}{\tilde{v}v^* + (v_{11}V_{11}^H + v_{12}V_{12}^H)} \quad (2.44)$$

TABLE 2.3
LF Scaling Parameters for Pure Fluids

Fluid	T^* (K)	P^* (MPa)	δ^* (kg/m ³)
1-Propanol	478	320	858
1-Butanol	494	320	863
1-Hexanol	534	301	867
CO ₂	294	703	1661
SF ₆	281	565	2933
<i>n</i> -Octane	502	308	815
Benzene	523	444	994
Poly(vinyl phenol)	649	425	1106
Diethylene glycol	604	451	1183
Triethylene glycol	585	456	1130

Equation 2.44 reduces to Equation 2.38 when hydrogen bonding is absent.

The total solubility parameter of our system is obtained from the square root of δ_{total} — Equation 2.44. The hydrogen bonding component of the solubility parameter is obtained from the equation:

$$\delta_{\text{hb}} = \sqrt{\frac{-(v_{11}E_{11}^H + v_{12}E_{12}^H)}{\tilde{v}v^* + (v_{11}V_{11}^H + v_{12}V_{12}^H)}} \quad (2.45)$$

The homomorph concept may also be used here in the case of hydrogen-bonded liquids. Equation 2.39a provides the component δ_{hm} . In principle, then, we may obtain the “polar” component of the solubility parameter as follows:

$$\delta_p = \sqrt{(\delta^2 - \delta_{\text{hb}}^2 - \delta_{\text{hm}}^2)} \quad (2.46)$$

2.3.4 APPLICATIONS

In this section we apply the above formalism for the evaluation of solubility parameters, first, of pure components and, subsequently, of mixtures. For all these calculations we need the characteristic LF scaling constants or equation-of-state parameters of pure components. A compilation of these parameters may be found in Reference 16. Scaling constants of typical fluids used in this work are reported in Table 2.3.

As already mentioned, the solubility parameter is a function of both temperature and pressure. Table 2.4 presents the calculated solubility parameters for a number of pure substances wherein only “physical” interactions are operating. The table also includes literature values for comparison purposes. Concerning the agreement with literature values it should be kept in mind that for the latter there is always an uncertainty, which, even for low molecular weight liquids may sometimes be as large as 0.5 Hild⁴⁸ (1 Hild = 1 cal^{0.5} cm^{-1.5}). The corresponding uncertainty for polymers is, of course, much larger. In the case of polymers, their processing occurs usually at high temperatures and varying pressures. As observed in the table, the solubility parameter of polymers depends on the external temperature and pressure. This should be kept in mind when mixing high polymers. Under appropriate conditions, homogeneous polymer mixture structures, if formed at processing conditions, may be frozen in the glassy state at ambient conditions.

TABLE 2.4
Solubility Parameters of Pure Nonhydrogen-
Bonded Substances as Calculated by the Present
Model (1 Hild = 1 cal^{0.5} cm^{-1.5} = 0.4889 MPa^{1/2})

Liquid	<i>T</i> (K)	<i>P</i> (MPa)	δ (Hild)	δ lit. (Ref.)
<i>n</i> -Hexane	298.15	0.1	7.2	7.3 (1)
	318.15	0.1	7.0	
<i>n</i> -Heptane	298.15	0.1	7.4	7.4 (1)
	318.15	0.1	7.2	
Cyclohexane	298.15	0.1	8.3	8.2 (1)
	318.15	0.1	8.1	
Benzene	298.15	0.1	9.1	9.2 (1)
	318.15	0.1	8.9	
PE linear	453.15	50.0	8.9	7.7–8.4 ^a (2)
	453.15	100.0	9.2	
PE branched	453.15	50.0	8.3	7.7–8.4 ^a (2)
PP	543.15	0.1	6.9	8.2–9.2 ^a (2)
	543.15	20.0	7.1	
PIB	333.15	0.1	8.5	7.8–8.1 ^a (2)
	363.15	100.0	8.8	
PS	403.15	0.1	8.4	8.5–9.3 ^a (2)
	453.15	100.0	8.7	
PVA	323.15	0.1	10.1	9.4–11.1 ^a (2)
PMMA	453.15	20.0	9.8	9.1–12.8 ^a (2)
PVME	300.15	0.1	8.7	
PAN	423.15	1.0	10.5	12.5–15.4 ^a (2)
PVC	403.15	0.1	9.0	9.4–10.8 ^a (2)
	423.15	100.0	9.4	
PDMS	298.15	0.1	7.5	7.3–7.6 (2)
PTFE	613.15	0.1	6.5	6.2 ^a (2)
	613.15	20.0	7.0	

References:

1. Barton, A., *Chem. Rev.*, 75, 731, 1975.

2. van Krevelen, D.W., *Properties of Polymers*, 2nd ed., Elsevier, Amsterdam, 1976, chap. 7.

^a At 298 K and 0.1 MPa.

Table 2.5 shows the calculated solubility parameters, δ , for hydrogen-bonded substances along with their “hydrogen bonding” component δ_{hb} . The nonhydrogen-bonding component, δ_{vdW} , may be found from the equation:

$$\delta_{\text{vdW}}^2 = \delta^2 - \delta_{\text{hb}}^2 \quad (2.47)$$

The table also shows the literature values for comparison purposes. It is worth pointing out that this table includes substances in which the hydrogen bonds form three-dimensional networks, indicating that the present approach is applicable even to rather complex systems.

In the case of pure alkanols or polymers with only –OH hydrogen bonding groups (1-1 type interaction only, $a_1 = d_1$ groups), Equation 2.28 reduces to one simple equation for the number of hydrogen bonds in the system:

TABLE 2.5
Solubility Parameters of Hydrogen-Bonded Substances
at 298.15 K and 0.1 MPa as Calculated by the Present Model

Liquid	δ				
	(Hild)	δ_{hb}	δ_{hm}	δ lit (Ref.)	δ_{hb} lit (Ref.)
Methanol	14.4	11.8	8.2	14.5 (1)	10.9 (1)
Ethanol	12.6	9.7	8.2	13.0 (1)	9.5 (1)
1-Propanol	11.7	8.6	8.2	11.9 (1)	8.5 (1)
1-Butanol	11.1	7.8	8.1	11.4 (1)	7.7 (1)
1-Pentanol	10.7	7.1	7.9	10.6 (2)	6.8 (2)
1-Hexanol	10.3	6.6	8.1		
1-Octanol	9.8	5.9	8.1	10.3 (1)	5.8 (1)
1-Decanol	9.5	5.3	8.0	10.0 (2)	4.9 (2)
Diethylene glycol	14.7	10.3	8.1	14.6 (1)	10.0 (1)
Triethylene glycol	13.4	8.6	8.0	13.5 (1)	9.1 (1)
Poly(vinyl phenol)	10.7 ^a	4.6 ^a	—	—	—

References:

1. Barton, A., *Chem. Rev.*, 75, 731, 1975.
2. Hansen, C.M. and Skaarup, K., *J. Paint Tech.* 39, 511, 1967.

^a At 453 K and 50 MPa.

$$r\nu_H = \frac{A_{11} + 2a_1 - \sqrt{A_{11}(A_{11} + 4a_1)}}{2} \quad (2.48)$$

where

$$A_{11} = r\tilde{v} \exp(G_{11}^H/RT) \quad (2.49)$$

In the case of systems possessing two types of interacting groups, such as the diethylene glycol and triethylene glycol (—OH and —O—groups, 1-1 and 1-2 interactions), the number of each type of hydrogen bonds is obtained by a simple algorithm as explained in Appendix 2.B For these calculations we need the values for the energy, entropy, and volume change upon mixing for each type of hydrogen bond. These values were obtained from the literature⁴⁹⁻⁵¹ and are as follows: for the OH≡OH interaction, $E_{11}^H = -25.1$ kJ/mol, $S_{11}^H = -26.5$ J/(K·mol), $V_{11}^H = -5.6$ cm³/mol; for the OH≡O interaction, $E_{12}^H = -22$ kJ/mol, $S_{12}^H = -52$ J/(K·mol), and $V_{12}^H = 0.0$ cm³/mol.

As already mentioned, in evaluating the dispersive component of the solubility parameter in the literature, reference is usually made to the “homomorph” concept. The homomorph is typically the hydrocarbon with the structure closest to the studied substance. The homomorph of *n*-pentanol, for example, is *n*-hexane and of isopropanol is isobutane. The homomorph concept may be used with the present approach as well. Equation 2.36 indicates how to use it: The homomorph and the studied substance should be brought at the same reduced density — a type of “corresponding states.” Table 2.5 also includes the calculated “homomorph” component, δ_{hm} , of the solubility parameter.

Figure 2.9 shows the typical temperature and pressure dependence of the solubility parameter of alkanols. As observed, both effects are by no means negligible. These two effects are much more pronounced in the case of supercritical systems. Figure 2.10 shows these two effects for the supercritical CO₂. This type of figure is particularly useful for selecting the appropriate external

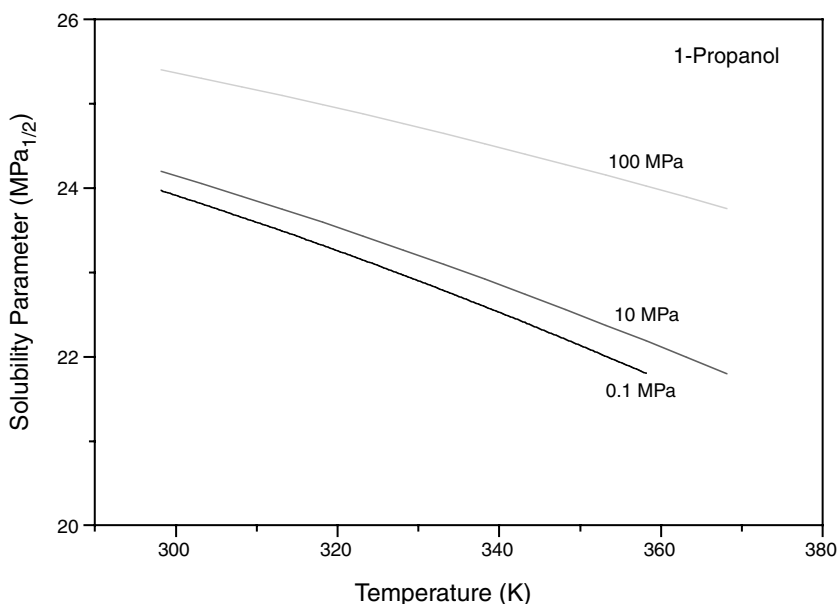


FIGURE 2.9 The solubility parameter of 1-propanol as a function of temperature at various pressures.

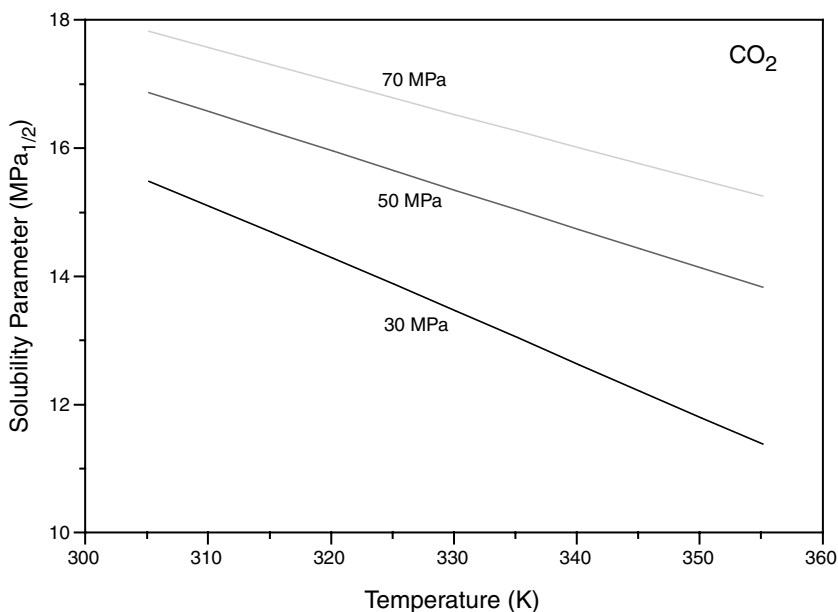


FIGURE 2.10 The solubility parameter of CO₂ as a function of temperature at various pressures.

conditions to reach a given solubility capacity (e.g., a given δ). As observed, under appropriate conditions of temperature and pressure, CO₂ may exhibit solubility capacity comparable to *n*-hexane (for example, at ~60°C and 40 MPa) or even to benzene (for example, ~35°C and 85 MPa).

It is common practice in supercritical extraction to use a “modifier” or an “entrainer” with the main supercritical fluid (e.g., CO₂) to increase the polarity of the system and concomitantly its solubility parameter. Table 2.6 reports the solubility parameters for the system CO₂ + *n*-propanol

TABLE 2.6
Solubility Parameters for the
System CO₂(1)–1-Propanol(2)

<i>T</i> (K)	<i>P</i> (MPa)	<i>X</i> ₁	δ (Hild)	δ_{hb} (Hild)
305	40	0.98	8.1	1.1
350	40	0.98	6.5	0.7
310	30	0.99	7.4	0.6
310	30	0.95	7.8	1.9
350	30	0.95	6.2	1.3
320	40	0.97	7.2	1.2
320	60	0.97	8.2	1.4
320	80	0.97	8.7	1.4
305	60	0.97	8.7	1.5
305	80	0.97	9.0	1.6
305	90	0.97	9.2	1.6
305	90	0.95	9.3	2.2
315	40	0.97	7.8	1.3
325	40	0.97	7.5	1.2
335	40	0.97	7.1	1.1
355	40	0.97	6.4	0.9
355	40	0.99	6.3	0.3

at varying external conditions. As observed, the concentration of the system in alkanol is an important additional parameter for the rational design of the supercritical extraction process.

The pressure dependence of solubility parameter and its hydrogen bonding component for this system, at $T = 37^\circ\text{C}$ and at a 0.02 mole fraction of 1-propanol, are shown in Figure 2.11. As observed, the hydrogen bonding contribution, even at very low alkanol concentration, is significant in this system.

In summary, then, we could say that the approach presented in this section is a straightforward procedure for estimating the solubility parameters of substances of varying complexity ranging from simple nonpolar solvents to hydrogen-bonded high polymers. The calculations are in rather satisfactory agreement with literature values. The equation-of-state character of the approach permits the evaluation of solubility parameters over extended ranges of external conditions.

The model used may evaluate the hydrogen bonding component of the solubility parameter directly and with no recourse to ambiguous concepts such as the homomorph concept. Apart from this, the model does not distinguish between the remaining polar and nonpolar contributions to δ .

The hydrogen bonding component δ_{hb} in the present work has been obtained by assigning specific values to the energy and entropy change upon hydrogen bond formation widely used in the literature. In principle, these values may be obtained directly from carefully conducted spectroscopic experiments. In this case, δ_{hb} may be considered an “experimental” value. By combining, then, this information with the homomorph component δ_{hm} , the model may give the dependence on temperature and pressure of all three components δ_{hm} , δ_p , and δ_{hb} of the solubility parameter.

2.4 RUBBER SWELLING: GELS AND HYDROGELS

Of significant interest is the swelling of network structures either by ordinary solvents or by solvents in the near-critical or supercritical state. The development in this case is based on the assumption that the partition function of our system may be factored into three contributions: the two factors already considered (one due to physical and the other due to hydrogen bonding interactions) and

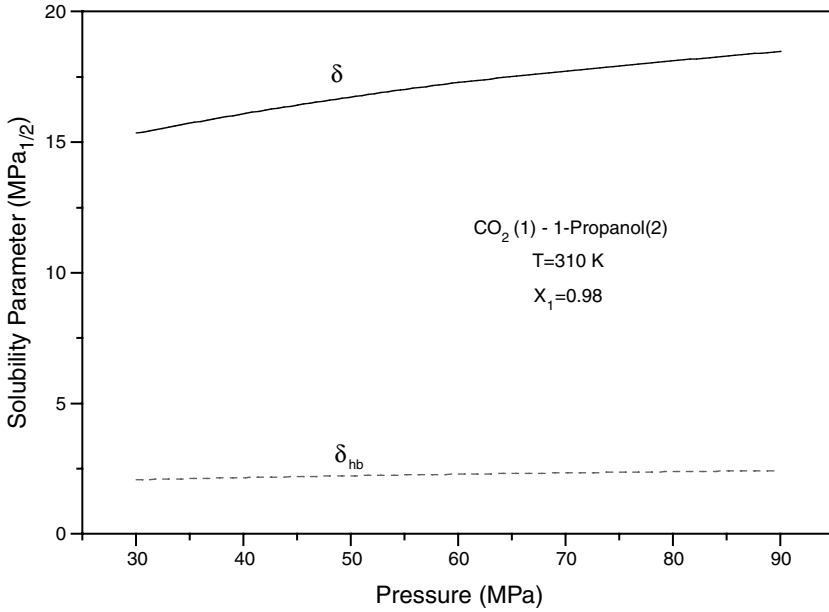


FIGURE 2.11 The effect of pressure on the solubility parameter and its hydrogen bonding component for the mixture CO₂ + 1-propanol.

a third factor due to rubber elasticity. This is equivalent to writing the following equation for the Gibbs free energy of the system:

$$G = G_p + G_H + G_{el} \quad (2.50)$$

For the elastic term we use here the interpolation expression of Birshtein and Pryamitsyn:⁵²

$$G_{el} = kT \frac{3v_e}{2} \left(\alpha_s^2 + \frac{1}{\alpha_s^2} - 2 + \ln \alpha_s \right) \quad (2.51)$$

where, α_s^3 is the swelling ratio, or, the ratio of the total volume to the volume of pure polymer:

$$\alpha_s^3 = \frac{V}{V_2} = \frac{rN\tilde{v}v^* + \sum_i \sum_j N_{ij} V_{ij}^H}{r_2 N_2 \tilde{v}_2 v_2^* + \sum_i \sum_j N_{ij,2} V_{ij,2}^H} = \frac{V_{LF} + V_{HB}}{V_2} \quad (2.52)$$

v_e in Equation 2.51 is the effective number of cross-links in the rubber network. V_{LF} and V_{HB} are the LF and the hydrogen bonding contributions, respectively, to the total volume of the system.

The consequence of Equation 2.51 is that there is an “elastic” contribution in the basic thermodynamic quantities of the system. The contribution to the equation of state (the extra term to be added in the right-hand side of Equation 2.40) is

$$\tilde{T} \left[v^* \frac{v_e}{V_2} \left(\alpha_s^2 - \frac{1}{\alpha_s^2} + \frac{1}{2} \right) \frac{1}{\alpha_s^3} \right] \quad (2.53)$$

Thus, the full equation of state (Equation 2.23) is now

$$\tilde{P} + \tilde{T} \left[\ln(1 - \tilde{\rho}) + \tilde{\rho} \left(1 - \frac{1}{\tilde{r}} \right) + \frac{s}{2} \ln \Gamma_{00} + \left[v^* \frac{v_e}{V_2} \left(\alpha_s^2 - \frac{1}{\alpha_s^2} + \frac{1}{2} \right) \frac{1}{\alpha_s^3} \right] \right] = 0 \quad (2.23a)$$

where, as before:¹⁶

$$\frac{1}{\tilde{r}} = \frac{1}{r} - \sum_{i=1}^m \sum_{j=1}^n v_{ij} \quad (2.54)$$

The presence, of course, of the elastic term changes the minimization conditions, Equation 2.27, which now become

$$\frac{v_{ij}}{v_{i0} v_{0j}} = \tilde{\rho} \exp \left(\frac{-G_{ij}^H}{RT} - \frac{v_e}{V_2} \left(\alpha_s^2 - \frac{1}{\alpha_s^2} + \frac{1}{2} \right) \frac{V_{ij}^H}{\alpha_s^3} \right) = \frac{r}{A_{ij}} \quad \text{for all } (i,j) \quad (2.27a)$$

The contribution to the chemical potential of the solvent (component 1) due to the elastic term is now

$$r_1 \tilde{v} v_1^* \frac{v_e}{V_2} \left(\alpha_s^2 - \frac{1}{\alpha_s^2} + \frac{1}{2} \right) \frac{1}{\alpha_s^3} \quad (2.55)$$

These contributions are valid for the most common case of tetrafunctional cross-links. In the general case of f -functional cross-links the $\frac{1}{2}$ in the parentheses in Equations 2.53 and 2.55 should be replaced by the ratio $2/f$.

If the (hydro)gel is charged, we must add the electrostatic contribution to the above formulae. If there is a small charge density, we may use the van't Hoff equation for the electrostatic effect, namely,

$$G_{\text{ion}} = -kTm v_e \ln rN \quad (2.56)$$

where m is the number of charged segments per network chain. There is no contribution to the equation-of-state term, but there is one for the chemical potential, namely,

$$-m r_1 \tilde{v} v_1^* \frac{v_e}{V_2} \frac{V}{V_{\text{LF}} \alpha_s^3} \quad (2.57)$$

where, V_{LF} is the LF contribution to the total volume of the system. If, in addition, the surrounding water of the charged (hydro)gel is a dilute electrolyte solution, we may use the classical Donnan equilibrium theory to correct the expression for the chemical potential.

As usual, the equilibrium swelling ratio is obtained by setting $\mu_1 - \mu_1^0 = 0$ and solving for ϕ_2 . Let us now apply the above formalism to experimental rubber swelling data.

Lele et al.⁵³ have reported careful experimental data on the swelling capacity of poly(ethylene oxide) (PEO) gels in chloroform as a function of temperature. Four systems with varying cross-linking densities from 600 to 2050 mol/m³ were prepared and studied. The parameters needed for

TABLE 2.7
Parameters for the PEO–CHCl₃ System

	T*/K	P*/MPa	ρ*/kg/m ³
CHCl ₃	499	476	1709
PEO	541	605	1172
	E ⁰ /J·mol ⁻¹	S ⁰ /J·K ⁻¹ ·mol ⁻¹	V ⁰ /cm ³ ·mol ⁻¹
Cl ³ CH=O	-10410	-6.11	-0.85

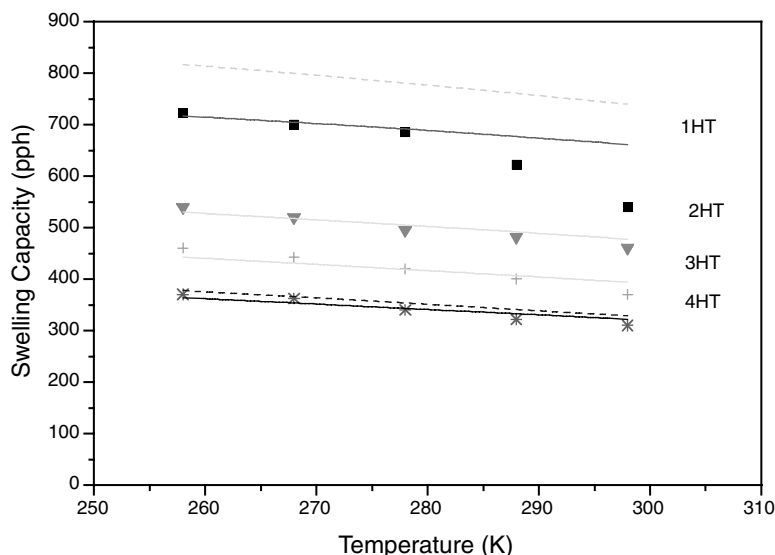


FIGURE 2.12 The swelling capacities of PEO gels of different cross-link densities in chloroform as a function of temperature. Symbols are experimental data.⁵³ The two dashed lines are the predictions of the model for the lowest (upper curve) and the highest (lower curve) cross-link densities. Solid lines are calculated by slightly varying the ζ binary parameter as shown in Table 2.8.

applying our model to these systems are known from our previous work^{16,26} and are reported in Table 2.7. By using these parameters we may predict the swelling capacity of the PEO–CHCl₃ system. Figure 2.12 shows these predictions for the two extreme cases of the cross-linking density. In view of the complexity of the systems, these predictions are rather satisfactory. In addition to other causes, the discrepancy might be attributed to the uncertainty in the values of the cross-linking densities reported by Lele et al.⁵³ Of course, we may slightly vary the ζ_{12} LF binary interaction parameter and fit the experimental data as shown in Figure 2.12 by the solid lines. Table 2.8 reports the values of the ζ_{12} parameter used for this data fit.

Experimental data are also available⁵³ for the swelling capacity of the above cross-linked PEOs in water. We already have the scaling constants for water and PEO as well as the hydrogen bonding parameters for the self-association of water. For simplicity we will use here the one-state hydrogen bonding model for water. However, to apply the above formalism to the PEO hydrogels we also need the hydrogen bonding parameters for the water–PEO (ether oxygen) cross-association. We set for simplicity $V^H = 0$, and the remaining energy and entropy parameters are obtained by applying the QCLFHB model to the experimental data of Malcolm et al.⁵⁴ for the activity of water in the

TABLE 2.8
The Cross-Link Densities
and the ζ_{12} Parameter

Symbol	Cross-Link Density (mol/m ³)	ζ_{12}
1HT	600	0.991
2HT	1050	0.992
3HT	1400	0.993
4HT	2050	0.999

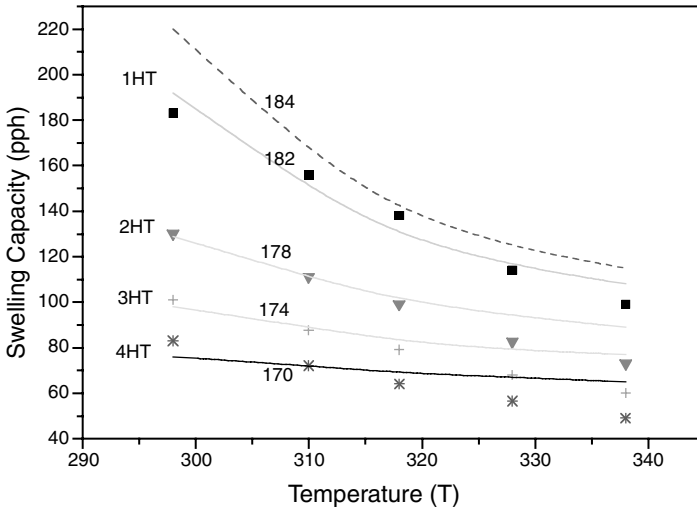


FIGURE 2.13 The swelling capacities of PEO gels of different cross-link densities in water as a function of temperature. Symbols are experimental data.⁵³ The dashed line is the predictions of the model for the lowest cross-link density assuming availability for hydrogen bonding of all oxygens of PEO chains. Solid lines are calculated by varying the number of available oxygen sites per PEO chain (numbers near each line).

water + linear PEO system. The water molecule is a relatively small molecule and can form two hydrogen bonds per oxygen atom with itself. It is assumed that it can also form two bonds per oxygen atom in PEO chains. Thus, for a molecular weight of 4050, the maximum number of hydrogen bonds per PEO chain is $2 \times 92 = 184$. This is the value used for the calculation of water activities. The obtained values for the hydrogen bonding parameters are $E^H = -16,500$ J/mol; $S^H = -15.0$ J/K/mol. By using these parameters we may now calculate the swelling capacity of the PEO hydrogels. It is expected that the number of oxygen sites available for hydrogen bonding will diminish as we increase the degree of cross-linking of the PEO chains. This number is not known but the model could be used for estimating it.

The dashed line Figure 2.13 presents the predictions of the model for the swelling capacity of lightly cross-linked PEO chains by assuming that all (284) oxygen sites are available for hydrogen bonding. As observed, the model slightly overpredicts this swelling capacity. The experimental data could be better reproduced by diminishing the available oxygen sites to 182, as shown by the corresponding solid line in this figure. In a similar manner, we can estimate the numbers of available oxygen sites with the other cross-linking densities. These estimations are shown in Figure 2.13 near the corresponding solid lines. The values are quite reasonable for these cross-linking densities. The ζ_{12} parameter was set equal to 1 in all the above calculations.

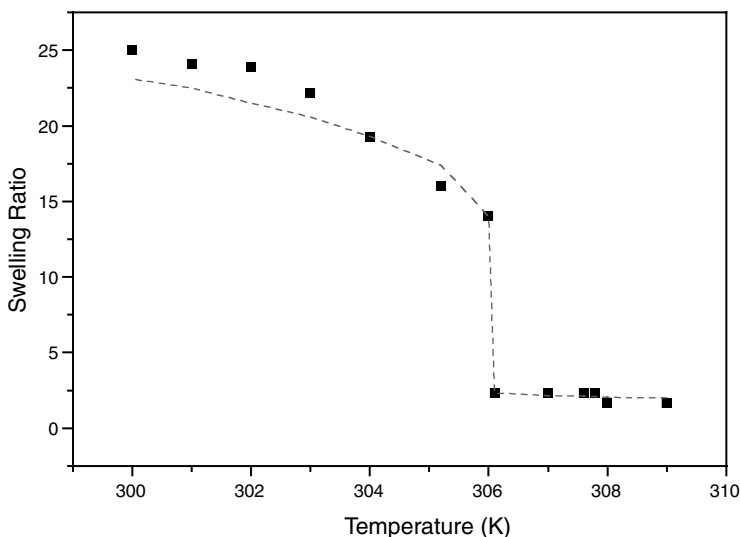


FIGURE 2.14 The swelling ratio of water + NIPA gel as a function of temperature. Symbols are experimental data from Marchetti et al.⁵⁵ The dashed line represents the LFHB model calculations by Lele et al.⁵³ (Adapted from Lele, A.K. et al., *Chem. Eng. Sci.*, 59, 3535, 1995.)

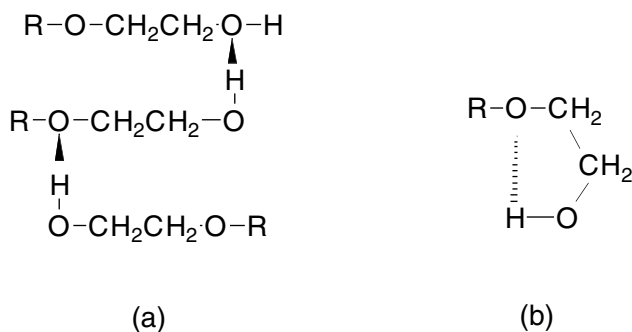


FIGURE 2.15 Intermolecular (a) and intramolecular (b) hydrogen bonding.

Another system of significant interest is the poly(*n*-isopropyl acrylamide) (PNIPA) hydrogel. Safe calculations cannot be performed at present for this system because neither the LF scaling constants for PNIPA nor the hydrogen bonding parameters for the water–PNIPA interactions are available. Lele et al.⁵³ have assumed that the LF scaling parameters of PNIPA are equal to those for poly(methyl methacrylate) and were able to calculate by the LFHB model the swelling ratio as a function of temperature. Their calculations are compared with experimental data⁵⁵ in Figure 2.14. As observed, the model can reproduce the volume phase transition (gel collapse) near 306 K.

2.5 INTRAMOLECULAR HYDROGEN BONDING

So far, we have confined ourselves to *intermolecular* hydrogen bonding, that is, hydrogen bonding between different molecules. However, in molecules possessing both proton donor and proton acceptor groups, *intramolecular* association (Figure 2.15) may occur as long as the location of the association groups does not prohibit such an interaction. Intramolecular hydrogen bonding is often

an important contribution to the overall hydrogen bonding in fluid systems, especially in systems of biological interest. Of interest is the case of very dilute systems in inert solvents where intermolecular hydrogen bonding is absent and the only observed hydrogen bonds are the intramolecular ones. In this section we first extend the above hydrogen bonding formalism to account for intramolecular association. Subsequently, we apply the model to recent⁵⁶ relevant experimental data of alkoxyethanol + hydrocarbon mixtures.

For simplicity, we confine ourselves to the case of molecules with one donor group (such as $\equiv\text{OH}$) and w equivalent proton acceptor sites (such as ether oxygen $-\text{O}-$) per molecule. This type of system (polyethoxyalcohols) is of key importance in the study of nonionic surfactants. The formalism can easily be extended to more complex cases. Once again, we focus on the chemical or hydrogen bonding term, Q_H , of the partition function:

$$Q = Q_P Q_H \quad (2.1)$$

This term may, in general, be written as

$$Q_H = \left(\frac{\tilde{\rho}}{rN} \right)^{N_H} \Omega \exp\left(-\frac{\sum N_{ij} G_{ij}^0}{kT} \right) \quad (2.58)$$

All symbols have their usual meaning. Of specific interest here is the factor Ω .

As before, the pre-exponential factor Ω in Equation 2.58 is the number of different ways of distributing the hydrogen bonds in the system without requiring that donor and acceptor groups be neighbors. This requirement of donor/acceptor proximity is taken into account by the first term on the right-hand side of Equation 2.58. The focus now is on the statistical derivation of Ω . The method will be explained by applying it to a classical case.

Case: Polyethoxy alcohol (PEA) with w ether oxygen sites

Let us consider a system with N_1 PEA molecules and N_2 molecules of an inert solvent ($N = N_1 + N_2$). The number of proton donors of type 1 ($-\text{OH}$) is N_1 , of proton acceptors of type 1 ($-\text{OH}$) is N_1 , and of proton acceptors of type 2 ($-\text{O}-$) is wN_1 . Let there be N_{11} hydrogen bonds $\text{OH}\equiv\text{OH}$, N_{12} intermolecular bonds $\text{OH}\equiv\text{O}-$, and B intramolecular bonds $\text{OH}\equiv\text{O}-$ in the system. The number of free proton donors is

$$N_{10} = N_1 - N_{11} - N_{12} - B \quad (2.59)$$

The number of different ways of distributing the above hydrogen bonds in the system can be found by applying the above rationale of the LFHB model.^{16,26} According to this rationale, to find the different number of isoenergetic configurations of our system, we have to do the following:

1. Find the number of different ways of selecting the associated donor sites out of the donor population.
2. Find the number of different ways of selecting the associated acceptor sites out of the acceptor population.
3. Find the number of different ways of making hydrogen bonds between the selected donor and acceptor sites.

The number of configurations of the system is the product of these three terms.

Let us apply the above procedure to our case. We have first to select the N_{11} , N_{12} , B , and N_{10} donors out of the N_1 donor population. From simple combinatorics, this can be done in

$N_1/[B!N_{11}!N_{12}!N_{10}!]$ ways. In a second step we have to select the N_{11} acceptors 1 out of the N_1 acceptor population. This can be done in $N_1/[N_{11}!(N_1 - N_{11})!]$ ways. In a third step we have to select the B acceptors 2 out of the wN_1 acceptor population. However, once we have selected the B proton donors that participate in intramolecular bonds, we have also selected the molecules with the acceptor 2 sites that participate in the B intramolecular bonds. We will assume for simplicity that all w acceptor sites are equivalent for the intramolecular bonds. In each of these B molecules we must now select the acceptor 2 site for the intramolecular bond out of the w acceptor 2 population. For each molecule this can be done in $w/[1!(w - 1)!]$ ways. Thus, for the B molecules it can be done in $\{w/[1!(w - 1)!]\}^B = w^B$ ways. Having selected the B acceptor 2 sites we must now select, out of the remaining $(wN_1 - B)$ acceptor 2 population, the N_{12} that will participate in the intermolecular bonds. This can be done in $(wN_1 - B)/[(wN_1 - B - N_{12})!N_{12}!]$ ways. The N_{11} and N_{12} bonds can be done in $N_{11}!N_{12}!$ ways while the B bonds in only one way after we have selected both the donor and the acceptor site in each molecule. Thus, the number of configurations in the hydrogen-bonded system is

$$\begin{aligned}\Omega &= \frac{N_1!}{B!N_{11}!N_{12}!N_{10}!} \frac{N_1!}{N_{11}!(N_1 - N_{11})!} \left(\frac{w!}{(w - 1)!} \right)^B \\ &\quad \times \frac{(wN_1 - B)!}{(wN_1 - B - N_{12})!N_{12}!} N_{11}!N_{12}! \\ &= \frac{w^B (N_1!)^2 (wN_1 - B)!}{B!N_{11}!N_{12}!N_{10}!(N_1 - N_{11})!(wN_1 - B - N_{12})!}\end{aligned}\quad (2.60)$$

In our case, there are three types of hydrogen bonds: N_{11} 1-1 bonds with free energy of bond formation G_{11}^0 , N_{12} 1-2 intermolecular bonds with free energy of bond formation G_{12}^0 , and B 1-2 intramolecular bonds with free energy of bond formation G_B^0 . The free energy of the i - j bond formation can be resolved as follows:

$$G_{ij}^0 = E_{ij}^0 + PV_{ij}^0 - TS_{ij}^0 \quad (2.61)$$

E_{ij}^0 , V_{ij}^0 , S_{ij}^0 are the energy, volume, and entropy change of the i - j bond formation, respectively.

Thus, the hydrogen bonding term Q_H of the partition function in Equation 2.58 can then be written as follows:

$$\begin{aligned}Q_H &= \left(\frac{\tilde{p}}{rN} \right)^{N_{11}+N_{12}} c^B \frac{w^B (N_1!)^2 (wN_1 - B)!}{B!N_{11}!N_{12}!N_{10}!(N_1 - N_{11})!(wN_1 - B - N_{12})!} \\ &\quad \times \exp\left(-\frac{N_{11}G_{11}^0 + N_{12}G_{12}^0 + N_B G_B^0}{kT} \right)\end{aligned}\quad (2.62)$$

The hydrogen bonding part of the free energy of the system is obtained from the equation

$$G_H = -kT \ln Q_H \quad (2.63)$$

By minimizing this equation with respect to the unknowns N_{11} , N_{12} , and B we obtain the following coupled equations:

$$\frac{B(wN_1 - B)}{(wN_1 - B - N_{12})N_{10}w} = c \exp\left(-\frac{G_B^0}{kT}\right) = K_B \quad (2.64)$$

$$\frac{N_{11}}{(N_1 - N_{11})N_{10}} = \frac{\tilde{\rho}}{rN} \exp\left(-\frac{G_{11}^0}{kT}\right) = \frac{K_{11}}{N} \quad (2.65)$$

$$\frac{N_{12}}{(wN_1 - B - N_{12})N_{10}} = \frac{\tilde{\rho}}{rN} \exp\left(-\frac{G_{12}^0}{kT}\right) = \frac{K_{12}}{N} \quad (2.66)$$

The coupled Equations 2.64 through 2.66 must be solved simultaneously by an appropriate iteration scheme. After some algebra the above three equations lead to the following equations:

$$N_{12} = \frac{K_{12}}{K_B N w} B(wN_1 - B) \quad (2.67)$$

$$N_{11} = \frac{K_{11}}{K_B N w + B(K_{11} - K_{12})} B N_1 \quad (2.68)$$

$$B = \frac{(N w K_B - K_{12} B)}{N} \left[N_1 - B - B \frac{K_{12}}{w K_B} \frac{w N_1 - B}{N} - N_1 \frac{K_{11} B}{w N K_B + B(K_{11} - K_{12})} \right] \quad (2.69)$$

The last equation contains only the unknown B and it can be solved numerically by successive substitutions. The solution for B can then be replaced in Equations 2.67 and 2.68 to obtain N_{12} and N_{11} , respectively.

In the limiting case of highly dilute systems, we have $N_{11} = N_{12} = 0$ and, consequently, Equation 2.64 becomes

$$\frac{B}{(N_1 - B)w} = K_B \quad \text{or} \quad \frac{B}{N_1} = \frac{K_B}{1 + w K_B} \quad (\text{very dilute system}) \quad (2.70)$$

This is a useful equation, which can be used for determining K_B from experimental (such as spectroscopic) information on the degree of hydrogen bonding B/N_1 .

With the aid of classical thermodynamics we may use Equation 2.1 for obtaining equations for all basic thermodynamic quantities for both pure components and mixtures. For example, if the LF framework (see Appendix 2.A) is used for Q_p the equation for the heat of mixing of the binary system becomes

$$\begin{aligned} H^E &= x_1 r_1 \tilde{\rho}_1 \varepsilon_1^* + x_2 r_2 \tilde{\rho}_2 \varepsilon_2^* - r \tilde{\rho} \varepsilon^* \\ &+ N_{11} E_{11}^0 + N_{12} E_{12}^0 + B E_B^0 - x_1 (n_{11}^0 E_{11}^0 + N_{12}^0 E_{12}^0 + B^0 E_B^0) \end{aligned} \quad (2.71)$$

where the symbols have their usual meaning.

TABLE 2.9
LF Scaling Constants and Hydrogen Bonding Parameters

Fluid	LF Scaling Constants		
	T^* (K)	P^* (MPa)	ρ^* (kg/m ³)
2-Methoxyethanol	522	509	1062
2-Ethoxyethanol	514	441	1030

Interaction	Hydrogen Bonding Parameters		
	E^0 /J/mol	S^0 /J/K/mol	V^0 /cm ³ /mol
1-1 (OH \equiv OH)	-28,100	-26.5	0
1-2 (OH \equiv O Inter)	-19,000	-24.0	0
B (OH \equiv O Intra)	-10,470	-16.0	0

2.5.1 APPLICATIONS

Recently⁵⁶ we have reported new spectroscopic data for the intermolecular and intramolecular hydrogen bonding in 2-methoxyethanol + *n*-hexane and in 2-ethoxyethanol + *n*-hexane mixtures. The solutions were studied at 30, 40, and 50°C and at concentrations where either only intramolecular association is observed or where both intermolecular and intramolecular associations are present as two competing types of hydrogen bonds. These data are ideally suited for testing the above model.

The required parameters for the application of the model are reported in Table 2.9. Two hydrogen bonding sites per ether oxygen in alkoxyethanols were assumed in the calculations. As expected, the presence of the electron-drawing ether oxygen in the alkoxyethanol molecules strengthens the O–H \equiv OH interaction relative to the corresponding interaction in alkanols as can easily be visualized by semiempirical quantum mechanical calculations of point charge distribution and bond order in an alkanol (e.g., ethanol) and in an alkoxyalkanol (e.g., 2-methoxyethanol). Thus, we expect E_{11}^0 in alkoxyalkanols to have more negative values than -25,100 J/mol, which corresponds to alkanols.²⁶ This is indeed the case in the data reported in Table 2.9.

The ability of the model to describe the degree of hydrogen bonding in the mixtures of alkoxyethanols with *n*-hexane can be appreciated from Figure 2.16, where our spectroscopic data are compared with the calculated ones. The number of hydrogen bonds per mole in the system has been calculated with Equations 2.67 through 2.70.

We have not found in the open literature experimental data on the heat of mixing for the two binary systems examined in this work. However, the parameters reported in Table 2.9 should, in principle, be valid for all mixtures of alkoxyethanols with inert hydrocarbons. Figure 2.17 compares the calculated heats of mixing with the experimental ones for the system of 2-ethoxyethanol with *n*-octane at 25°C. A similar picture is obtained for the mixture of 2-ethoxyethanol with cyclohexane. A number of comments regarding the above experimental data and the calculations are in order.

The experiment as well as the calculations show that a large fraction of the –OH groups of alkoxyethanol molecules in the very dilute mixtures with *n*-hexane are associated via intramolecular hydrogen bonding. In both systems, as the temperature increases, the overall degree of hydrogen bonding diminishes. This trend is also followed by the degree of intermolecular hydrogen bonding. However, the degree of intramolecular hydrogen bonding increases as the temperature is increased. The explanation provided by the model is the following: As the temperature increases there is a drastic decrease of intermolecular hydrogen bonds due to the relatively large entropy change upon formation of these bonds. Upon destruction of intermolecular hydrogen bonds, more –OH groups are available for intramolecular association. Thus, although the negative entropy change upon

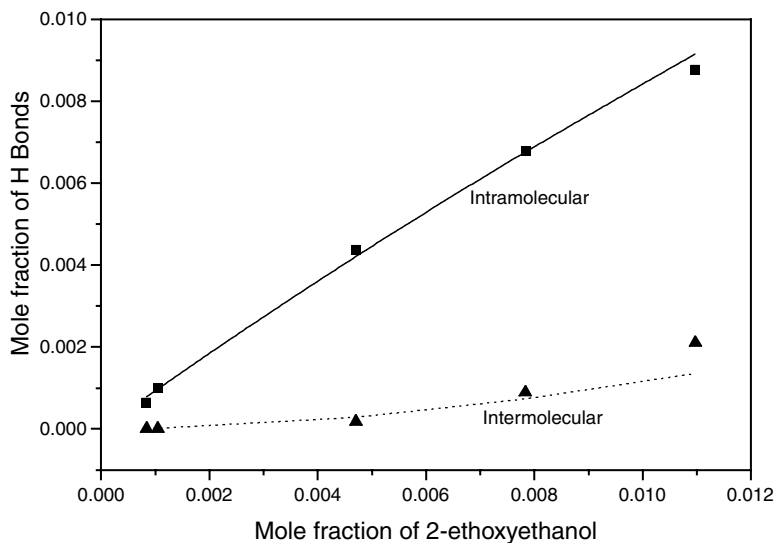


FIGURE 2.16 Experimental,⁵⁶ \blacktriangle , and calculated (dotted line), degree of intermolecular and experimental,⁵⁶ \blacksquare , and calculated (solid line), degree of intramolecular hydrogen bonding in the mixture: 2-ethoxyethanol + *n*-hexane at 30°C.

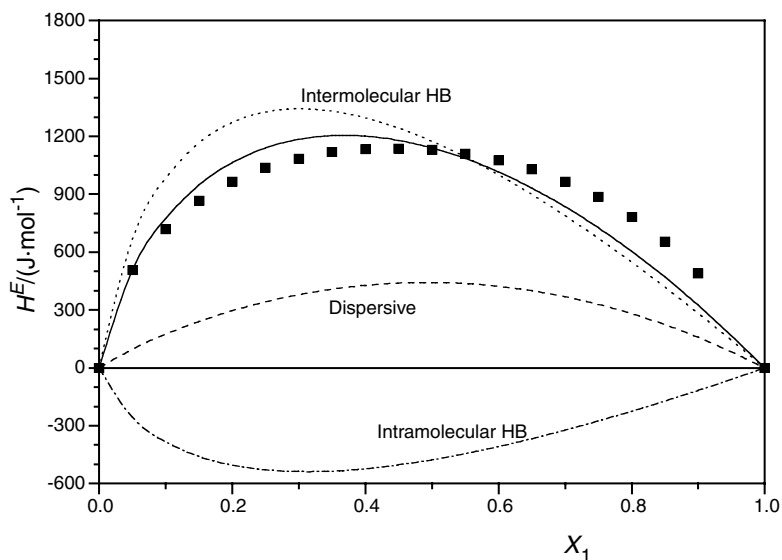


FIGURE 2.17 Experimental,⁵⁷ \blacksquare , and calculated (solid line), heats of mixing for the system 2-ethoxyethanol(1) + *n*-octane(2) at 25°C. The contributions from dispersive interactions (dashed line), intermolecular hydrogen bonds (dotted line), and intramolecular hydrogen bonds (dash-dot line) are shown.

formation of this bond tends to reduce the number of hydrogen bonds, the increased population of available $-OH$ groups overruns this trend and finally increases the number of intramolecular hydrogen bonds.

An interesting point comes from Figure 2.17. As observed, the contribution of the intramolecular hydrogen bonds to the heats of mixing of the system is by no means negligible. The important point is that its contribution is negative (exothermic) while that of intermolecular hydrogen bonding

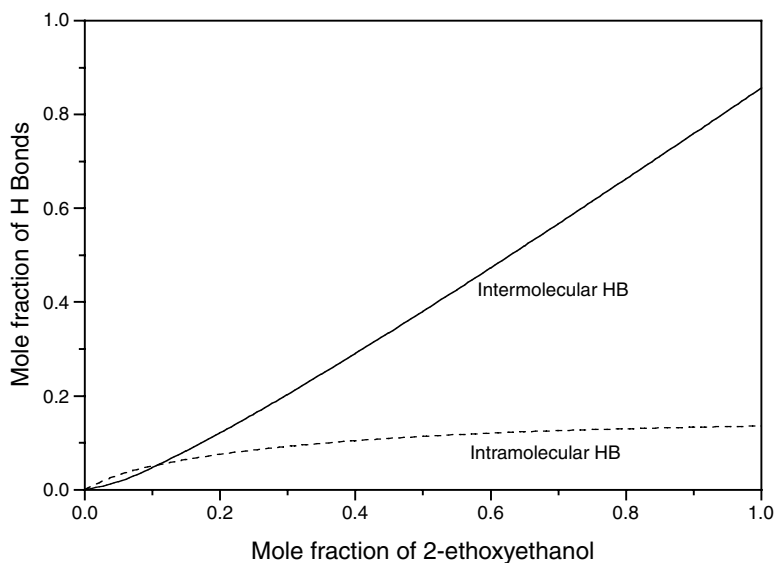


FIGURE 2.18 The calculated degree of intermolecular (solid line) and intramolecular (dashed line) hydrogen bonding in the mixture: 2-ethoxyethanol + *n*-octane at 25°C over the full composition range.

as well as that of the van der Waals dispersive interactions are positive (endothermic). An explanation of this behavior may come from Figure 2.18 where the degree of hydrogen bonding is estimated over the full composition range for a typical system. As observed, there is a positive deviation from linearity for the intramolecular bonding. This excess of intramolecular bonds is responsible for the negative contribution to the heat of mixing because the formation of an intramolecular bond is an exothermic process (negative E_B^0).

At low concentrations the degree of intramolecular hydrogen bonding is increasing with increasing mole fraction of the alkoxyethanol much stronger than the degree of intermolecular hydrogen bonding, as shown in Figure 2.16. This is because in this concentration region the inert solvent does not influence essentially the intramolecular hydrogen bonds while it greatly influences the formation of the intermolecular bonds as the interacting molecules must come close together (proximity condition). Of course, at higher concentrations, the –OH groups prefer to bond intermolecularly and thus the number of intramolecular hydrogen bonds levels off as shown in Figure 2.18.

Before judging the overall performance of the model, it is essential to keep in mind that a single set of hydrogen bonding parameters is used for all alkoxyethanol systems and for all thermodynamic properties. In view of this, the ability of the model to describe the diverse properties of these systems is rather satisfactory.

As shown previously, the above formalism can be integrated to any equation-of-state framework, such as those presented in Appendix 2.A, leading to an equation-of-state theory of hydrogen-bonded systems. The formalism can also be extended in a straightforward manner to the case of more complex systems with more than one proton donor group per molecule. However, we must keep in mind that, due to steric and other interactions, the acceptor sites may not be equivalent.⁵ This is important when estimating equilibrium constants and hydrogen bonding energies. In the case of polyethoxyalcohol molecules, the strength of the intermolecular OH≡O– bond is expected to be close to the corresponding intramolecular OH≡O– bond only when the two interacting groups are sufficiently far apart.^{4,5} In general, however, we are not justified in neglecting the difference in strength between intermolecular and intramolecular hydrogen bonds⁴⁹ as is also clear from the present work.

The findings of this work may be summarized in the following conclusions:

1. The thermodynamic properties of alkoxyethanol + hydrocarbon mixtures are dictated by the interplay of *dispersive forces*, *intermolecular* hydrogen bonding, and *intramolecular* hydrogen bonding.
2. The intramolecular hydrogen bonds are the weakest hydrogen bonds in the system. They increase rapidly with concentration at very low alkoxyethanol concentrations and level off at higher concentrations.
3. The self-associations (OH≡OH interactions) are the strongest in the system.
4. The contribution of the intermolecular hydrogen bonds to the heat of mixing is endothermic, whereas that of intramolecular bonds is exothermic.
5. The new theoretical model can, at least qualitatively, describe the spectroscopic and calorimetric data for these systems.

2.6 HYDROGEN BONDING COOPERATIVITY

So far in this presentation we have attributed one set of hydrogen bonding parameters or, equivalently, one equilibrium constant for each type of hydrogen bond, be it monomer–monomer, monomer–dimer, dimer–multimer. Careful spectroscopic studies over the last few decades have revealed that it is not always possible to explain the experimental data with one association equilibrium constant only.^{1,3,6,9,11,15} Very often, spectroscopists use two, instead of one, equilibrium constants for the above association — one for the monomer/dimer association (K_d) and one for the equilibria among the higher complexes (K_∞). Usually K_d is several times smaller than K_∞ and the effect is called *hydrogen bond cooperativity*. The first theoretical justification for this came from the statistical treatment of associated solutions by Sarolea-Mathot,⁵⁸ who predicted that K_d should be smaller than K_∞ by a factor f , where f is the number of possible energetically equivalent orientations of the monomer. Thus, this difference is ascribed to an entropy factor: the entropy loss when two monomers form a dimer is greater than when only one monomer and a higher multimer unite.

Apart from the classical association approach, two complementary theoretical approaches for hydrogen bond cooperativity have appeared recently in the literature.^{59,60} The new approach of Veytsman⁵⁹ focuses on the combinatorial problem in the simplest possible case: a fluid whose molecules have one donor group and one acceptor group with association constants K_d and K_∞ for the formation of dimers and higher multimers, respectively. The problems associated with the general case are also discussed in earlier work.²⁵

Hydrogen bond cooperativity is treated in the work of Sear and Jackson,⁶⁰ by including in the association energy a three-body term which either increases or decreases the strength of the bonds in chains of three or more molecules. Their model (in essence, an association model) is able to account for the effect of density on the degree of association and, thus, it can describe vapor–liquid equilibria.

Recently,⁶¹ we have examined this cooperativity hypothesis and proposed a straightforward manner of integrating it in the framework of the LFHB equation-of-state model. This integration was done without altering the basic rationale of the LFHB model for the enumeration of hydrogen bond configurations for the self-association and cross-association in the system. In the following we briefly present the cooperativity formalism. As we will see, the model can accommodate hydrogen bond cooperativity in complex systems, even polymer mixtures forming three-dimensional networks of hydrogen bonds, and permits its study over an extended range of temperatures and pressures. It can also handle the formation of cyclic associates.

2.6.1 THE COOPERATIVITY FORMALISM

The systems of interest here are systems containing molecules with groups of type (1) having one donor and one acceptor site (self-associating groups), such as the –OH groups. In the system there

may be molecules with groups of type (2) with one acceptor site, such as $-\text{C}=\text{O}$ or R_3N . If the same molecule has various groups (1) and (2), we assume for simplicity that they are sufficiently far apart, so that they remain unaffected by the association of other groups of the molecule. Thus, in the frame of this work, we will have hydrogen bonds of the types 1-1 and 1-2 for the self-association and cross-association, respectively.

As in the LFHB model, the partition function Q of our system is factored into a physical, Q_p , and a chemical or hydrogen bonding, Q_H , term, or

$$Q = Q_p Q_H \quad (2.1)$$

We focus first on the chemical factor. According to the LFHB model, this term may, in general, be written as

$$Q_H = \left(\frac{\tilde{p}}{rN} \right)^{N_H} \Omega \exp \left(- \frac{\sum N_{ij} G_{ij}^0}{kT} \right) \quad (2.58)$$

The pre-exponential factor Ω is the number of different ways of distributing the hydrogen bonds in the system without requiring that donor and acceptor groups be neighbors. This requirement of donor/acceptor proximity is taken into account by the first term in the right hand side of the above equation.^{16,26} The focus now is on the statistical derivation of Ω . The method will be explained by applying it to three representative cases of practical interest.

To find the different number of isoenergetic configurations of our system (number of the different ways of forming or distributing the hydrogen bonds in the system), we have to follow the steps 1 through 3 of Section 2.2.1, namely,

1. Find the number of different ways of selecting the associated donor sites out of the donor population.
2. Find the number of different ways of selecting the associated acceptor sites out of the acceptor population.
3. Find the number of different ways of making hydrogen bonds between the selected donor and acceptor sites.

Let us apply this procedure to hydrogen bond cooperativity.

Case 1: Molecules or groups whose self-association is cooperative

Let us consider a system of N molecules with one proton donor and one acceptor site ($-\text{O}-\text{H}$ groups), which self-associate forming N_{11} bonds. However, the first dimer bond, now, is weaker than any subsequent bond in a multimer (trimer, tetramer, etc.) complex. In fact, it is not important for the enumeration of bonds whether the dimer bond is weaker or stronger than the others; it suffices for it to be distinguishable.

The strength of a bond is assumed to depend on the state of the acceptor site. Thus, the acceptor sites of the molecules with the $N - N_{11} = N_{10}$ free donors (elements of the lowest row in Figure 2.19) are interacting weakly. All other acceptor sites (acceptors above the first row in Figure 2.19) are assumed to be interacting with bonds of higher but the same strength. N_d of the N_{10} weak acceptors participate in the weak bonds of the system (initial dimerlike bonds)

Following the enumeration method of LFHB, we must first choose the donors that will be bonded in N_{11} bonds. It can be done in $N!/(N_{10}!N_{11}!)$ ways. Having selected the N_{10} free donors, we have also selected the N_{10} “weak” acceptors 1 (the same OH group). Of these N_{10} weak acceptors we must choose the N_d acceptors that participate in the (weak) hydrogen bonds. This can be done

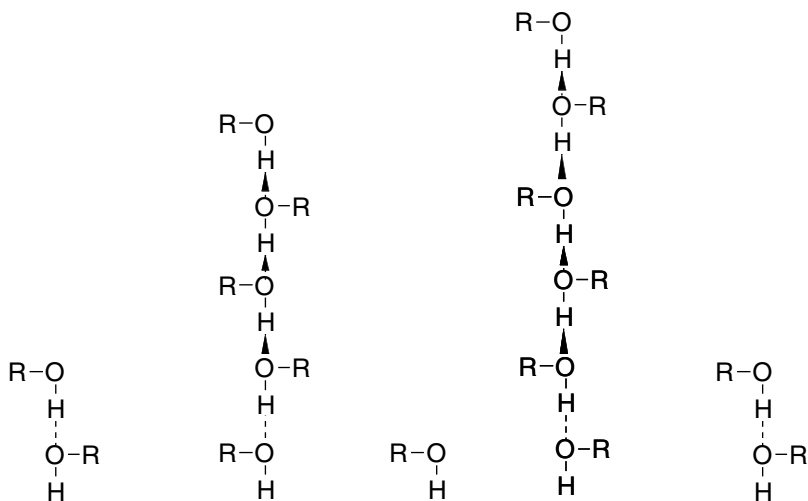


FIGURE 2.19 One configuration of a system with $N = 16$, $N_{11} = 11$. Out of the 11 bonds there are $N_d = 4$ weak dimerlike bonds marked with dashed lines.

in $N_{10}!/[N_d!(N_{10} - N_d)!]$ ways. Because we recognized that the acceptors in the groups with the free donors are weak, we must choose, out of the remaining $N - N_{10} = N_{11}$ acceptors, the associated $N_{11} - N_d$ ones that will participate in the strong bonds. This can be done in $N_{11}!/[N_d!(N_{11} - N_d)!]$ ways. Because we have strong and weak acceptors, we must choose, out of the N_{11} associated donors, the N_d that will associate with the weak acceptors and the $N_{11} - N_d$ that will interact with the strong acceptors. This can be done in $N_{11}!/[N_d!(N_{11} - N_d)!]$ ways. Having selected the interacting donors and acceptors, the number of different ways that they can interact to form the N_d weak 1-1 bonds and the $N_{11} - N_d$ strong 1-1 bonds is $N_d!(N_{11} - N_d)!$. Thus, Ω is the product of the above terms, or

$$\begin{aligned} \Omega &= \frac{N!}{N_{10}!N_{11}!} \frac{N_{10}!}{N_d!(N_{10} - N_d)!} \frac{N_{11}!}{(N_{11} - N_d)!N_d!} \frac{N_{11}!}{(N_{11} - N_d)!N_d!} N_d!(N_{11} - N_d)! \\ &= \frac{N!N_{11}!}{(N_{10} - N_d)!(N_{11} - N_d)!(N_d!)^2} \end{aligned} \quad (2.72)$$

Case 2: Molecules or groups that self-associate and cross-associate but there is cooperativity in self-association 1-1

Let us have again N_1 and N_2 molecules (groups) between which there are N_{11} self-association and N_{12} cross-association bonds ($1 = -\text{O}-\text{H}$, $2 = B$). However, now, the bond for dimer formation is weaker than any subsequent bond of the multimer complex.

For simplicity we consider that in a complex 1-1-1 ... -1-1-2, the bond 1-1 next to the 1-2 bond is as strong as any other 1-1 bond beyond the first dimer bond in a 1-1-1 ... -1-1 multimer (bond cooperativity), as shown in Figure 2.20. In the system there are $N_{10} = N_1 - N_{11} - N_{12}$ free donors of type 1 and $N_{11} + N_{12}$ “strong” acceptor groups of type 1. These acceptors are shown in Figure 2.20 located above the lowest row of acceptors. The strength of the 1-2 bonds is not important; it suffices for it to be the same for all 1-2 bonds.

In this case, Ω can be obtained as follows: The N_{11} and N_{12} interacting donors 1 can be selected in $N_1!/[N_{10}!N_{11}!N_{12}!]$ ways. As in the previous case, with the selection of the N_{10} free donors we have also selected the N_{10} weak acceptors 1. Of these, the associated N_{d1} acceptors can be selected

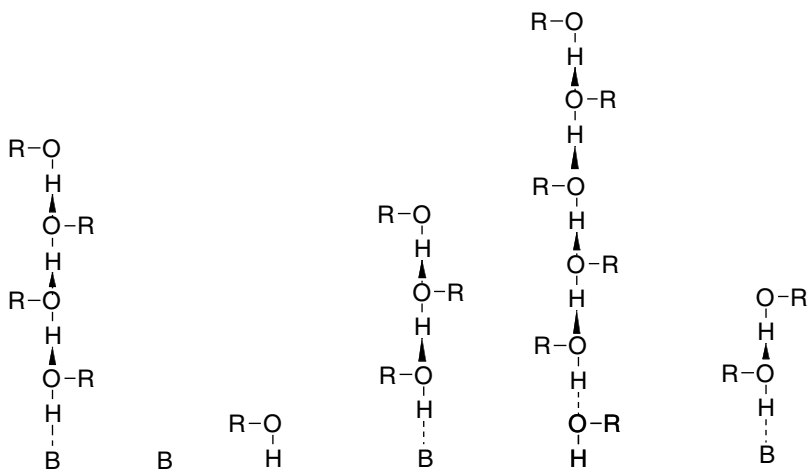


FIGURE 2.20 One configuration of a system with $N_1 = 16$, $N_2 = 4$, $N_{11} = 11$, $N_{12} = 3$. Out of the 11 1-1 bonds the $N_{d1} = 1$ is a weak dimerlike bond marked with dashed line.

in $N_{10}!/[N_{d1}!(N_{10} - N_{d1})!]$ different ways. Because the N_{10} acceptors 1 (at the groups of the free donors) have been recognized to be weak, we are left to choose, of the remaining $N_1 - N_{10}$ acceptors 1, the acceptors that will participate in the $N_{11} - N_{d1}$ strong bonds. It can be done in $(N_1 - N_{10})!/[N_{d1}!(N_{11} - N_{d1})!(N_{11} - N_{d1})!]$ ways. Of the N_{11} interacting donors 1 we must select the N_{d1} and $N_{11} - N_{d1}$, which associate with the weak and the strong acceptors, respectively. This can be done in $N_{11}!/[N_{d1}!(N_{11} - N_{d1})!]$ different ways. The N_{12} interacting acceptors 2 can be chosen in $N_2!/[N_{d2}!(N_2 - N_{d2})!]$ ways. The N_{11} and N_{12} interacting donors can be combined with the N_{d1} weak acceptors 1, the $N_{11} - N_{d1}$ strong acceptors 1, and the N_{12} acceptors 2, in $N_{d1}!(N_{11} - N_{d1})!N_{12}!$ ways. Thus, Ω is given by

$$\begin{aligned} \Omega &= \frac{N_1!}{N_{10}!N_{11}!N_{12}!} \frac{N_{10}!}{N_{d1}!(N_{10} - N_{d1})!} \frac{(N_{11} + N_{12})!}{(N_{11} - N_{d1})!(N_{12} + N_{d1})!} \\ &\quad \times \frac{N_{11}!}{N_{d1}!(N_{11} - N_{d1})!} \frac{N_2!}{N_{d2}!(N_2 - N_{d2})!} N_{d1}!(N_{11} - N_{d1})!N_{12}! \quad (2.73) \\ &= \frac{N_1!N_2!(N_{11} + N_{12})!}{N_{d1}!N_{12}!(N_{10} - N_{d1})!(N_{12} + N_{d1})!(N_{11} - N_{d1})!(N_2 - N_{d2})!} \end{aligned}$$

Case 3: Same as case 2 but, now, there is cooperativity in both self-association and cross-association

Let us have again N_1 and N_2 molecules (groups) 1 and 2, between which there are N_{11} self-association and N_{12} cross-association bonds. However, now, the 1-1 bond for dimer formation is weaker than any subsequent bond of the multimer complex. In addition, the 1-2 bond is becoming stronger (bond fortification) when it is associated with a multimer complex of molecules of type 1. To simplify the situation, we will consider that in a complex 1-1-1 ... -1-1-2, the bond 1-1 next to the 1-2 bond is equally strong as any other 1-1 bond beyond the first dimer bond in a 1-1-1 ... -1-1 multimer (Figure 2.21). Thus, in the system we have N_{11} 1-1 bonds distributed in N_{d1} multimers of the 1-1-1 ... 1-1 type and N_{d2} multimers of the 1-1-1 ... 1-1-1-2 type. In addition, we have N_{12} 1-2 bonds, $N_{12} - N_{d2}$ of which are dimers 1-2 (with no bond fortification). In the system there are $N_{10} = N_1 - N_{11} - N_{12}$ molecules (groups) 1 with the N_{10} free donor sites 1 and the N_{10} weak acceptor sites 1.

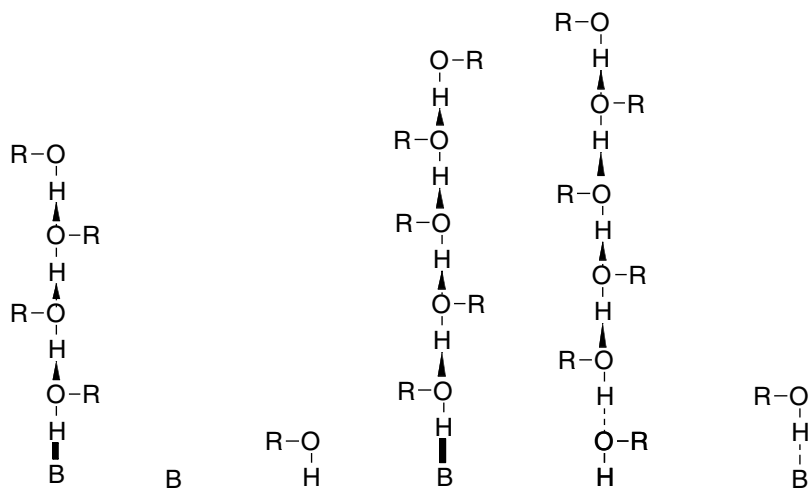


FIGURE 2.21 One configuration of a system with $N_1 = 17$, $N_2 = 4$, $N_{11} = 12$, $N_{12} = 3$. Of the 12 1-1 bonds the $N_{d1} = 1$ is a weak dimerlike bond marked with dashed line. Of the 3 1-2 bonds the $N_{d2} = 2$ are fortified 1-2 bonds marked with a heavy solid line.

To calculate Ω , we must first select, of the donor population N_1 , the N_{11} and N_{12} donors 1, which will participate in hydrogen bonds. This can be done in $N_1!/[N_{10}!N_{11}!N_{12}!]$ different ways. In each such selection we select not only the $N_{10} = N_1 - N_{11} - N_{12}$ free donors but, also, the N_{10} “weak” acceptors 1, which belong to the groups with the free donors. Of these weak acceptors we must select the N_{d1} participating in hydrogen bonds. It can be done in $N_{10}!/[N_{d1}!(N_{10} - N_{d1})!]$ ways. Of the remaining $N_1 - N_{10} = N_{11} + N_{12} = N_H$ “strong” acceptors 1, we must select the $N_{11} - N_{d1}$ that participate in hydrogen bonds. It can be done in $(N_1 - N_{10})!/[N_{11}!(N_{11} - N_{d1})!(N_{12} + N_{d1})!]$ ways. The N_{12} acceptors 2, which participate in hydrogen bonds, can be selected from the population N_2 in $N_2!/[N_{d2}!(N_2 - N_{d2})!]$ ways. However, now, the N_{12} bound acceptors 2 are differentiated in N_{d2} acceptors participating in “fortified” 1-2 bonds and in $N_{12} - N_{d2}$ acceptors participating in the weak 1-2 bonds. Their selection can be done in $N_{12}!/[N_{d2}!(N_{12} - N_{d2})!]$ different ways. Of the N_{11} donors 1 we must select the N_{d1} and $N_{11} - N_{d1}$ donors that associate with the weak and the strong acceptors 1, respectively and, of the N_{12} donors 1, we must select the N_{d2} and $N_{12} - N_{d2}$ that participate in fortified and weak 1-2 bonds, respectively. This can be done in $N_{11}!N_{12}!/[N_{d1}!(N_{11} - N_{d1})!N_{d2}!(N_{12} - N_{d2})!]$ ways. Again, all the above N_{d1} , $N_{11} - N_{d1}$, N_{d2} , and $N_{12} - N_{d2}$ different types of bonds can be done in $N_{d1}!(N_{11} - N_{d1})!N_{d2}!(N_{12} - N_{d2})!$ ways. Thus, Ω in this case is

$$\begin{aligned} \Omega &= \frac{N_1!}{N_{10}!N_{11}!N_{12}!} \frac{N_{10}!}{N_{d1}!(N_{10} - N_{d1})!} \frac{N_H!}{(N_{11} - N_{d1})!(N_{12} + N_{d1})!} \frac{N_2!}{N_{d2}!(N_2 - N_{d2})!} \\ &\times \frac{N_{12}!}{N_{d2}!(N_{12} - N_{d2})!} \frac{N_{11}!N_{12}!}{N_{d1}!(N_{11} - N_{d1})!N_{d2}!(N_{12} - N_{d2})!} N_{d1}!(N_{11} - N_{d1})!N_{d2}!(N_{12} - N_{d2})! \quad (2.74) \\ &= \frac{N_1!N_2!(N_{11} + N_{12})!}{N_{d1}!N_{d2}!(N_{10} - N_{d1})!(N_{11} - N_{d1})!(N_{12} + N_{d1})!(N_2 - N_{d2})!(N_{12} - N_{d2})!} \end{aligned}$$

which reduces to Equation 2.73 by setting $N_{d2} = 0$.

Case 4: A more general case

The above enumeration method can be extended easily to the more general case of a system of N_1, N_2, \dots, N_t molecules of type 1, 2, \dots, t , respectively, which may have both donor/acceptor groups of type 1 and acceptor groups of type 2. Let each molecule of type i have d_1^i donors 1, a_1^i acceptors 1, and a_2^i acceptors 2. The total number of donors 1 in the system is

$$N_d^1 = \sum_{i=1}^t N_i d_1^i \quad (2.2a)$$

Similarly, the total number of acceptors 1 in the system is

$$N_a^1 = \sum_{i=1}^t N_i a_1^i = N_d^1 \quad (2.75)$$

and the acceptors of type 2

$$N_a^2 = \sum_{i=1}^t N_i a_2^i \quad (2.76)$$

Let there be in this system N_{11} and N_{12} hydrogen bonds of type 1-1 and 1-2, respectively. The free donors 1 are

$$N_{10} = N_d^1 - N_{11} - N_{12} = N_d^1 - N_H \quad (2.77)$$

the free acceptors 1 are

$$N_{01} = N_a^1 - N_{11} \quad (2.78)$$

and the free acceptors 2 are

$$N_{02} = N_a^2 - N_{12} \quad (2.79)$$

Let the (weak) dimerlike bonds 1-1 be N_{d1} , and the fortified 1-2 bonds be N_{d2} . By following the above enumeration method, we obtain for Ω the following expression:

$$\Omega = \frac{N_d^1! N_a^2! (N_{11} + N_{12})!}{N_{d1}! N_{d2}! (N_{10} - N_{d1})! N_{02}! (N_{12} - N_{d2})! (N_{d1} + N_{12})! (N_{11} - N_{d1})!} \quad (2.80)$$

which is the generalization of Equation 2.74. This equation can cope with more complex associates, such as the one shown in [Figure 2.22](#). It can be applied, for example, to hydrogen bonding networks of polyoxyalcohols or to mixtures of polyalcohols and polyethers or polyesters.

2.6.2 THE GIBBS FREE ENERGY EQUATION

Let us now return to Equation 2.58 and find the expression for the free energy G_H for the above general case of a hydrogen-bonded system with bond cooperativity. In this case, there are four types of hydrogen bonds: N_{d1} (weak) 1-1 bonds with free energy of bond formation G_{d1}^0 , $N_{11} - N_{d1}$ (strong) 1-1 bonds with free energy of bond formation G_{11}^0 , N_{d2} (strong) 1-2 bonds with free energy

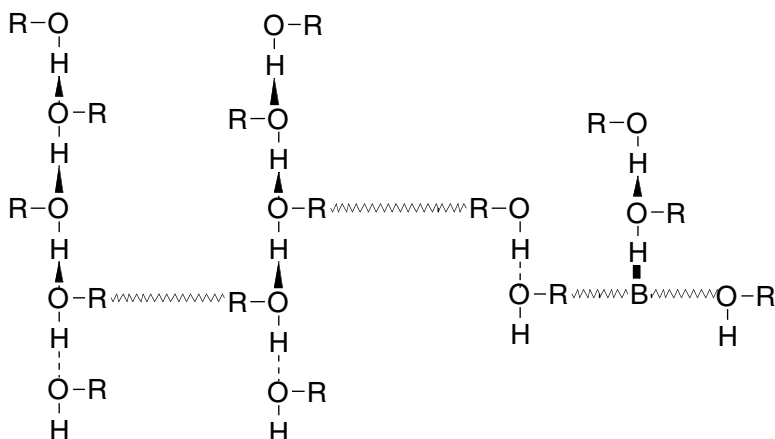


FIGURE 2.22 One complex associate of a system with $N_1 = 15$, $N_2 = 1$, $N_{11} = 10$, $N_{12} = N_{d2} = 1$. Of the 10 1-1 bonds the $N_{d1} = 3$ are weak dimerlike bonds marked with dashed lines. The 1-2 bond is fortified (heavy solid line). The springs connect different hydrogen bonding groups of the same molecule.

of bond formation G_{d2}^0 , and $N_{12} - N_{d2}$ (weak) 1-2 bonds with free energy of bond formation G_{12}^0 . The free energy of the i - j bond formation can be resolved as follows:

$$G_{ij}^0 = E_{ij}^0 + PV_{ij}^0 - TS_{ij}^0 \quad (2.81)$$

where E_{ij}^0 , V_{ij}^0 , S_{ij}^0 are the energy, volume, and entropy change of the i - j bond formation, respectively. The hydrogen bonding term Q_H of the partition function in Equation 2.58 can then be written as follows:

$$Q_H = \left(\frac{\tilde{p}}{rN} \right)^{N_H} \frac{N_d^1! N_d^2! N_H!}{N_{d1}! N_{d2}! (N_{10} - N_{d1})! N_{02}! (N_{12} - N_{d2})! (N_{d1} + N_{12})! (N_{11} - N_{d1})!} \times \exp \left(- \frac{N_{d1} G_{d1}^0 + (N_{11} - N_{d1}) G_{11}^0 + N_{d2} G_{d2}^0 + (N_{12} - N_{d2}) G_{12}^0}{kT} \right) \quad (2.82)$$

where $N = \sum N_i$ is the total number of molecules in the system.

The hydrogen bonding part of the free energy of the system is obtained from the equation:

$$G_H = -kT \ln Q_H \quad (2.83)$$

By minimizing this equation with respect to the unknowns N_{11} , N_{12} , N_{d1} , N_{d2} , we obtain the following coupled equations:

$$\frac{N_{11} - N_{d1}}{(N_{11} + N_{12})(N_{10} - N_{d1})} = K_{11} \quad (2.84)$$

$$\frac{(N_{12} - N_{d2})(N_{d1} + N_{12})}{N_{02}(N_{11} + N_{12})(N_{10} - N_{d1})} = K_{12} \quad (2.85)$$

$$\frac{N_{d1}(N_{d1} + N_{12})}{(N_{10} - N_{d1})(N_{11} - N_{d1})} = \frac{K_{d1}}{K_{11}} \quad (2.86)$$

$$\frac{N_{d2}}{N_{12} - N_{d2}} = \frac{K_{d2}}{K_{12}} \quad (2.87)$$

where the equilibrium constant K_{ij} for the formation of the bond $i-j$ is given by the equation:

$$K_{ij} = \frac{\tilde{\rho}}{r} \exp\left(-\frac{G_{ij}^0}{kT}\right) \quad (2.88)$$

The coupled Equations 2.84 through 2.87 must be solved simultaneously by an appropriate iteration scheme. This solution can be facilitated by replacing Equation 2.86 with the ratio of Equations 2.84 and 2.85, leading to the new equation

$$\frac{N_{02}(N_{11} - N_{d1})}{(N_{12} - N_{d2})(N_{d1} + N_{12})} = \frac{K_{11}}{K_{12}} \quad (2.85a)$$

By using these minimization conditions (Equations 2.84 through 2.87) in Equation 2.83, we obtain for the G_H :

$$\frac{G_H}{kT} = N_H + N_d^1 \ln\left(1 - \frac{N_H + N_{d1}}{N_d^1}\right) + N_a^2 \ln\left(1 - \frac{N_{12}}{N_a^2}\right) \quad (2.89)$$

Equation 2.89 can be integrated to any equation-of-state framework, such as those reported in Appendix 2.A, leading to an equation-of-state theory of hydrogen-bonded systems. The procedure used in the LFHB model^{16,26} can be applied directly here to obtain full expressions for the total free energy of the system:

$$G = G_p + G_H$$

2.6.3 THE CASE OF CYCLIC ASSOCIATES

Cyclic associates can be handled in a straightforward manner in the LFHB frame. Let us consider a simple case with one type of cyclic associates — cyclic tetramers. Let in the above case 1, in addition to linear associates, there be also N_q cyclic tetramers. There are N_{11} bonds in the system, $4N_q$ of which belong to the cyclic tetramers and N_d to the weak dimerlike bonds shown in Figure 2.23. In the system there are $N_{10} = N - N_{11}$ free donor groups. The strength of a hydrogen bond in the tetramer may or may not be the same as in the strong bonds of the linear associates.

In the enumeration process we have first to find the number of ways of selecting from the N donor population the $4N_q$ donors that participate in the cyclic tetramer bonds, and the $N_{11} - 4N_q$ that participate in the hydrogen bonds of the linear associates. This can be done in $N! / [(4N_q)! N_{10}! (N_{11} - 4N_q)!]$ ways. Having selected the $4N_q$ donors of the cyclic associates we have also selected the $4N_q$ acceptors that participate in the hydrogen bonds of the cyclic associates (the same OH group). As previously, having selected the N_{10} free donors, we have also selected the N_{10} “weak” acceptors (the same OH group). Of these N_{10} weak acceptors we must choose the N_d acceptors that participate in the (weak) hydrogen bonds. This can be done in $N_{10}! / [N_d! (N_{10} - N_d)!]$

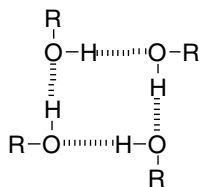


FIGURE 2.23 A cyclic tetramer.

ways. Because we recognized that the acceptors in the groups with the free donors are weak, we must choose, of the remaining $N - N_{10} - 4N_q = N_{11} - 4N_q$ acceptors, the associated $N_{11} - 4N_q - N_d$ ones that will participate in the strong bonds of the linear associates. This can be done in $(N_{11} - 4N_q)!/[N_d!(N_{11} - 4N_q - N_d)!]$ ways. Because we have strong and weak acceptors in the linear associates, we must choose, of the $N_{11} - 4N_q$ associated donors, the N_d that will associate with the weak acceptors and the $N_{11} - 4N_q - N_d$ that will interact with the strong acceptors. This can be done in $(N_{11} - 4N_q)!/[N_d!(N_{11} - 4N_q - N_d)!]$ ways. Having selected the interacting donors and acceptors, the number of different ways that they can interact to form the N_d weak 1-1 bonds, the $4N_q$ bonds in the cyclic associates, and the $N_{11} - 4N_q - N_d$ strong 1-1 bonds in the linear associates is $N_d!(4N_q)!(N_{11} - 4N_q - N_d)!$. Thus, Ω is the product of the above terms, or

$$\begin{aligned} \Omega &= \frac{N!}{N_{10}!(4N_q)!(N_{11} - 4N_q)!} \frac{N_{10}!}{N_d!(N_{10} - N_d)!} \frac{(N_{11} - 4N_q)!}{(N_{11} - 4N_q - N_d)!N_d!} \\ &\quad \times \frac{(N_{11} - 4N_q)!}{(N_{11} - 4N_q - N_d)!N_d!} N_d!(4N_q)!(N_{11} - 4N_q - N_d)! \quad (2.90) \\ &= \frac{N!(N_{11} - 4N_q)!}{(N_{10} - N_d)!(N_{11} - 4N_q - N_d)!(N_d!)^2} \end{aligned}$$

The exponential term in the partition function (see Equations 2.58 and 2.82) now becomes

$$\exp\left(-\frac{N_d G_d^0 + (N_{11} - 4N_q - N_d)G_{11}^0 + 4N_q G_q^0}{kT}\right)$$

As previously, from the minimization conditions we may obtain the values of N_{11} , N_d , and N_q at equilibrium.

2.6.4 AN APPLICATION TO WATER

The well-known formation of icelike cage structures in water could also be treated as a cooperative process much like the previous case of formation of cyclic associates. By adopting a scheme similar to that proposed by John et al.,⁶² we could assume that in the fluid water we may distinguish two types of hydrogen bonding states in equilibrium: State A is much like the ordinary linear hydrogen bonding structures and is the denser state. State B corresponds to the iceberg or cagelike cluster formation, which is the less dense structure. Each iceberg is formed cooperatively by a number of water molecules.

We could proceed as in the previous section by setting q around 46, as suggested by Nemethy and Scheraga,⁶³ and by assuming that all donors and acceptors in each iceberg are involved in hydrogen bonding. However, we can also follow an alternative simple procedure. For simplicity,

we will make no distinction between the molecules at the interior and at the surface of the icebergs. This will permit us to divide the total number M of hydrogen bonds in the system into M_A bonds corresponding to state A and M_B bonds corresponding to the cagelike state B . Because each water molecule has two donor and two acceptor sites, in a system of N water molecules we will have $2N - M$ free donor sites and an equal number of free acceptor sites.

Following the rationale of the previous section, we may write now for the hydrogen bonding partition function:

$$Q_H = \left(\frac{\tilde{p}}{rN} \right)^{(M_A + M_B)} \frac{[(2N)!]^2}{[(2N - M_A - M_B)]^2 M_A! M_B!} \exp\left(-\frac{M_A G_A^0 + M_B G_B^0}{kT} \right) \quad (2.91)$$

The numbers M_A and M_B at equilibrium may be obtained from free energy minimization with respect to them leading to the following two equations:

$$\frac{(2N - M)^2}{M_A} = rN\tilde{v} \exp \frac{G_A}{kT} = \frac{N}{K_A} \quad (2.92)$$

and

$$\frac{(2N - M)^2}{M_B} = rN\tilde{v} \exp \frac{G_B}{kT} = \frac{N}{K_B} \quad (2.93)$$

This is a system of two equations with two unknowns, M_A and M_B . It can be solved easily in terms of the association constants K_A and K_B and the physically meaningful solutions are

$$\frac{M_A}{K_A} = \frac{M_B}{K_B} = N \frac{4(K_A + K_B) + 1 - \sqrt{1 + 8(K_A + K_B)}}{2(K_A + K_B)^2} \quad (2.94)$$

On the basis of Equation 2.91 we may obtain for the hydrogen bonding contribution to the chemical potential:

$$\frac{\mu_H}{kT} = r\nu_H + 4 \ln \left(\frac{2 - r\nu_H}{2} \right) \quad (2.95)$$

where

$$\nu_H = \frac{M_A + M_B}{rN} \quad (2.96)$$

This formalism can be coupled now to an equation-of-state formalism resulting in a quite versatile model of water. Let us use the QCLF framework to implement the above formalism.

As before, to perform the calculations we need the scaling constants and the hydrogen bonding constants, a total of nine constants in this case. To reduce the number of parameters, we have assumed, as previously, that $r = 1$ for water and that the entropy change upon hydrogen bond formation for the state A is equal to -26.5 J/K/mol, that is, the same as for the $\text{OH}\equiv\text{OH}$ interaction. In addition we assume that the volume change upon formation of this bond is zero. These assump-

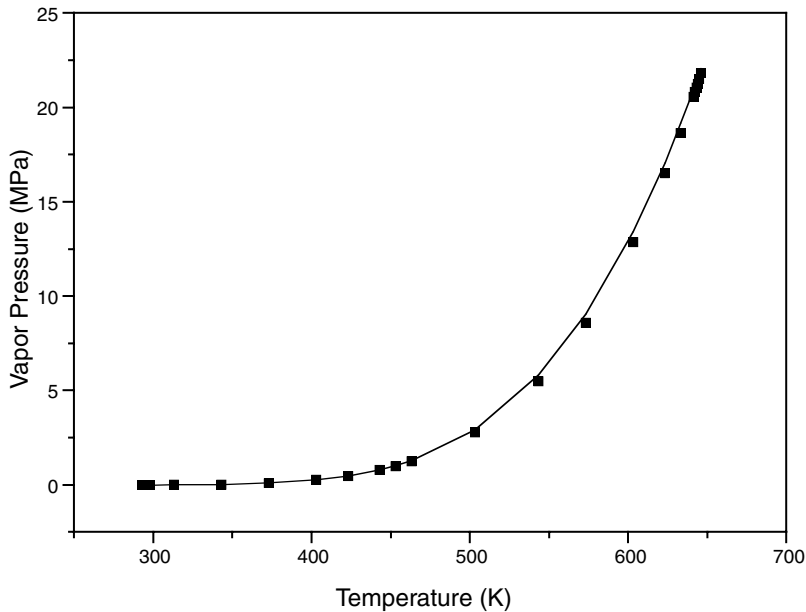


FIGURE 2.24 Experimental (symbols)⁶⁴ and calculated (line) vapor pressures of water up to the critical point.

tions reduce the number of parameters from nine to six. Because state B is the preferred state up to $\sim 4^\circ\text{C}$, we may further impose that the free energy changes for the two states be equal at this temperature, or

$$(E^H - 277.2S^H)_{\text{state A}} = (E^H - 277.2S^H)_{\text{state B}}$$

This condition reduces to five the number of parameters.

We have applied the model over an extended range of external conditions from the triple point up to the critical point of water. Figure 2.24 compares the experimental⁶⁴ (steam tables) vapor pressures with the calculated ones. The two sets of values are practically identical. Figure 2.25 compares the corresponding values for the orthobaric densities of water. As observed, the density is well described over the full range.

The parameters that were used for the above calculations (obtained from a least squares fit) are as follows:

$$\varepsilon^* = RT^* = 2093 \text{ J/mol}; r = 1, \rho^* = 1.1637 \text{ g/cm}^3$$

$$E^H = -19,380 \text{ J/mol}; S^H = -26.5 \text{ J/K mol}; V^H = 0.0 \text{ cm}^3/\text{mol} \text{ (state A)}$$

$$E^H = -22,500 \text{ J/mol}; S^H = -37.8 \text{ J/K mol}; V^H = 1.25 \text{ cm}^3/\text{mol} \text{ (state B)}$$

It is worth observing the value of the volume change upon formation of a hydrogen bond in the cagelike state B that the cooperativity model calculates. As expected, it is significant and positive. On the other hand, the significantly more negative value of the entropy change for state B indicates that these bonds will disappear faster than the state A bonds as we raise the temperature. We should keep in mind, however, that the above set of parameters is by no means unique.

In the above calculations we have imposed a number of restrictions to reduce the number of required parameters. If we relax these restrictions, we end up with a quite flexible molecule for water.

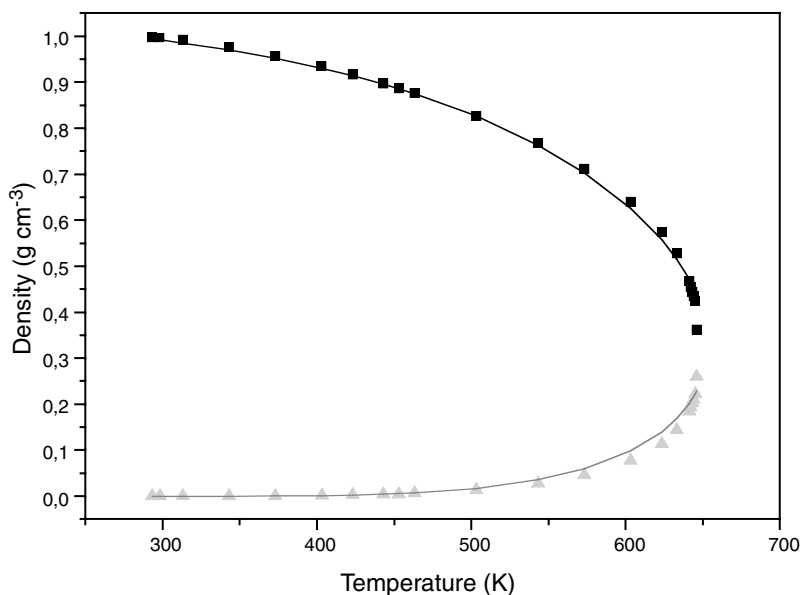


FIGURE 2.25 Orthobaric densities of water as calculated (line) by the cooperativity model. Symbols are experimental data.⁶⁴

REFERENCES

1. Frank, H.S. and Wen, W.-Y., *Disc. Faraday Soc.*, 24, 133, 1957.
2. Pimentel, G.C. and McClellan, A.L., *The Hydrogen Bond*, W.H. Freeman, San Francisco, 1960.
3. LaPlanche, L.A., Thompson, H.B., and Rogers, M.T., *J. Phys. Chem.*, 69(5), 1482, 1965.
4. Vinogradov, S. and Linnell, R., *Hydrogen Bonding*, Van Nostrand Reinhold, New York, 1971.
5. Joesten, M.D. and Saad, L.J., *Hydrogen Bonding*, Marcel Dekker, New York, 1974.
6. Huyskens, P.L.J., *Am. Chem. Soc.*, 99, 2578, 1977.
7. Walter, H., Brooks, D., and Fisher, D., Eds., *Partitioning in Aqueous Two-Phase Systems*, Academic Press, New York, 1985.
8. Marsh, K. and Kohler, F., *J. Mol. Liquids*, 30, 13, 1985.
9. Kleeberg, H., Klein, D., and Luck, W.A.P., *J. Phys. Chem.*, 91, 3200, 1987.
10. Bourrel, M. and Schechter, R.S., Eds., *Microemulsions and Related Systems*, Marcel Dekker, New York, 1988.
11. Hobza, P. and Zahradnik, R., *Intermolecular Complexes*, Academia, Praha, 1988.
12. Reichardt, C., *Solvent and Solvent Effects in Organic Chemistry*, VCH Verlagsgesellschaft mbH, Weinheim, FRG, 1988.
13. Burchard, W. and Ross-Murphy, S.B., Eds., *Physical Networks, Polymers, and Gels*, Elsevier Applied Science, London, 1990.
14. Coleman, M.M., Graf, J.F., and Painter, P.C., *Specific Interactions and the Miscibility of Polymer Blends*, Technomic, Lancaster, PA, 1991.
15. Maes, G. and Smets, J., *J. Phys. Chem.*, 97, 1818, 1993.
16. Sanchez, I.C. and Panayiotou, C., in *Models for Thermodynamic and Phase Equilibria Calculations*, S. Sandler, Ed., Marcel Dekker, New York, 1994.
17. Acree, W.E., *Thermodynamic Properties of Nonelectrolyte Solutions*, Academic Press, New York, 1984.
18. Prausnitz, J.M., Lichtenthaler, R.N., and de Azevedo, E.G., *Molecular Thermodynamics of Fluid Phase Equilibria*, 2nd ed., Prentice-Hall, New York, 1986.
19. Heintz, A., *Ber. Bunsenges. Phys. Chem.*, 89, 172, 1985.
20. Panayiotou, C., *J. Phys. Chem.*, 92, 2960, 1988.

21. Panayiotou, C., *J. Solution Chem.*, 20, 97, 1991.
22. Panayiotou, C. and Sanchez, I.C., *Macromolecules*, 24, 6231, 1991.
23. Levine, S. and Perram, J.W., in *Hydrogen Bonded Solvent Systems*, A.K. Covington, and P. Jones, Eds., Taylor & Francis, London, 1968.
24. Luck, W.A.P., 1980, *Angew. Chem.*, 92, 29, 1980.
25. Veytsman, B.A., *J. Phys. Chem.*, 94, 8499, 1990.
26. Panayiotou, C. and Sanchez, I.C., *J. Phys. Chem.*, 95, 10090, 1991.
27. Sanchez, I.C. and Lacombe, R., *J. Phys. Chem.*, 80, 2352, 1976.
28. Sanchez, I.C. and Lacombe, R., *Macromolecules*, 11, 1145, 1978.
29. Panayiotou, C., *Macromolecules*, 20, 861, 1987.
30. Taimoori, M. and Panayiotou, C., *Fluid Phase Equilibria*, Vol. 192, 155–169, 2001.
31. Vlachou, Th. et al., *Ind. Eng. Chem. Res.*, Vol. 41, 1057–1063, 2002.
32. Guggenheim, E.A., *Mixtures*, Clarendon Press, Oxford, 1952.
33. Panayiotou, C. and Vera, J.H., *Polym. J.*, 14, 681, 1982.
34. Marcus, Y., *Phys. Chem. Chem. Phys.*, 2, 1465, 2000.
35. Duan, Z., Moller, N., and Weare, J.H., *Geochim. Cosmochim. Acta*, 56, 2605, 1992.
36. Abdulagatov, I.M. et al., A.E., *J. Chem. Eng. Data*, 43, 451, 1998.
37. Abdulagatov, I.M., Bazaev, A.R., and Ramazanov, A.E., *Int. J. Thermophys.*, 14, 231, 1993.
38. Papaioannou, D. et al., *J. Colloid Interface Sci.*, 156, 52, 1993.
39. Papaioannou, D. and Panayiotou, C., *J. Chem. Eng. Data*, 39, 457, 1994.
40. Karode, S., *J. Membr. Sci.*, 171, 131, 2000.
41. Bhattarjee, C. and Bhattacharya, P.K., *J. Membr. Sci.* 72, 137, 1992.
42. Hildebrand, J. and Scott, R.L., *Regular Solutions*, Prentice-Hall, Englewood Cliffs, NJ, 1962.
43. Barton, A.F.M., *Chem. Rev.*, 6, 731, 1975.
44. van Krevelen, D.W., *Properties of Polymers*, 2nd ed., Elsevier, Amsterdam, 1976, chap. 7.
45. Hansen, C.M., in *Handbook of Surface and Colloid Chemistry*, Birdi, K.S. Ed., CRC Press, Boca Raton, FL, 1997.
46. Tehrani, J., *Am. Lab.*, February, 40hh, 1993.
47. Panayiotou, C., *Fluid Phase Equilibria*, 131, 21, 1997.
48. Allen, G., Gee, G., and Wilson, G.J., *Polymer*, 1(4), 456, 1960.
49. Missopolinou, D. and Panayiotou, C., *Fluid Phase Equilibria*, 110, 73, 1995.
50. Nagata, I. and Tamura, K., *Thermochim. Acta*, 57, 331, 1982.
51. Renon, H. and Prausnitz, J.M., *Chem. Eng. Sci.*, 22, 299, 1967.
52. Birshstein, T.M. and Pryamitsyn, V.A., *Vysokomol. Soedin.*, 29A, 1858, 1987.
53. Lele, A.K. et al., *Chem. Eng. Sci.*, 59, 3535, 1995.
54. Malcolm, G.N. et al., *J. Polym. Sci.*, A-2 7, 1495, 1969.
55. Marchetti, M., Prager, S., and Cussler, E.L., *Macromolecules*, 23, 1760, 1990.
56. Missopolinou, D. et al., *Z. Phys. Chem.*, in press.
57. Ohji, H. et al., *J. Chem. Thermodyn.*, 30, 761, 1998.
58. Sarolea-Mathot, L., *Trans. Faraday Soc.*, 49, 8, 1953.
59. Veytsman, B.A., *J. Phys. Chem.*, 97, 7144, 1993.
60. Sear, R.P. and Jackson, G., *J. Chem. Phys.*, 105, 1113, 1996.
61. Missopolinou D. and Panayiotou, C., *J. Phys. Chem. A*, 102(20), 3574, 1998.
62. John, M.S. et al., *Chem. Phys.*, 44, 1465, 1966.
63. Nemethy, G. and Scheraga, H., *J. Chem. Phys.*, 41, 680, 1964.
64. Perry, R. and Green, D., *Chemical Engineers' Handbook*, CD ed., McGraw-Hill, New York, 1999.

APPENDIX 2.A: THE EQUATION-OF-STATE FRAMEWORKS

In this appendix we briefly present the two thermodynamic models that have been used as frameworks for the incorporation of the hydrogen bonding formalism presented in the main text. As discussed here, the two thermodynamic models are used for the evaluation of the “physical” or “van der Waals” contribution (as opposed to the “chemical” or hydrogen bonding contribution). In other words, these models provide the physical term Q_p of the partition function $Q = Q_p Q_c$ of our system.

2.A.1 THE LATTICE-FLUID FRAMEWORK

According to lattice fluid (LF) theory,¹⁻³ each fluid i is characterized by three scaling constants: a characteristic temperature T_i^* , a characteristic pressure P_i^* , and a characteristic density ρ_i^* . These three constants are enough for full description of the equation-of-state behavior of the fluid, as long as the operating intermolecular forces are of the van der Waals type. If M_i is the molecular weight of the fluid, we may define alternative equivalent sets of scaling constants. The LF model treats each molecule as divided into r_i segments, each having a hard core volume v_i^* and a mean intersegmental interaction ϵ_i^* . These alternative scaling constants are related through the equations:

$$P_i^* v_i^* = RT_i^* = \epsilon_i^* \quad (2.A1)$$

and

$$M_i / \rho_i^* = r_i v_i^* \quad (2.A2)$$

The mixture is also characterized by the corresponding scaling constants T^* , P^* , ρ^* , and alternatively, ϵ^* , v^* , r . The latter set is obtained from the appropriate mixing and combining rules. In this section we will present the multicomponent version of the LF model.

Let us consider a system consisting of N_1 molecules of type 1, N_2 molecules of type 2, ..., N_t molecules of type t at temperature T and external pressure P . According to the LF theory, the molecules are considered arranged on a quasi-lattice of N_r sites, N_0 of which are empty. Every molecule of type k consists of r_k segments of volume v_k^* each. The total number of segments in the system is

$$\sum_k^t r_k N_k = N \sum_k^t r_k x_k = rN \quad (2.A3)$$

where N is the total number of molecules and x_k is the mole fraction of component k . The total number of sites in the lattice is

$$N_r = rN + N_0 \quad (2.A4)$$

The mean interaction energy per segment for molecules of type k is

$$\epsilon_k^* = \frac{s\epsilon_{kk}}{2} \quad (2.A5)$$

where ϵ_{kk} is the interaction energy for a k - k contact and s is the mean coordination number of the lattice.

For the mixture and in the one-fluid approximation the following mixing and combining rules are adopted:

$$v^* = \sum_i^t \phi_i v_i^* \quad (2.A6)$$

$$\epsilon^* = \frac{1}{2} \sum_i^t \sum_j^t \phi_i \phi_j \epsilon_{ij} \quad (2.A7)$$

where ϕ_i is the segment fraction of component i which is equal to:

$$\phi_i = \frac{r_i N_i}{rN} = \frac{x_i r_i}{r} \quad (2.A8)$$

and

$$\epsilon_{ij} = \xi_{ij} \sqrt{\epsilon_{ii} \epsilon_{jj}} \quad (2.A9)$$

The binary parameter ξ_{ij} assumes values close to one.

For a binary mixture, Equation 2.A7 assumes the simpler form:

$$\epsilon^* = \phi_1 \epsilon_1^* + \phi_2 \epsilon_2^* - \phi_1 \phi_2 RTX_{12} \quad (2.A10)$$

where

$$X_{12} = \frac{\epsilon_1^* + \epsilon_2^* - 2\epsilon_{12}^*}{RT} \quad (2.A11)$$

The total volume of the system is

$$V_{LF} = N_r v^* = rN v^* \tilde{v} = V^* \tilde{v} \quad (2.A12)$$

where V^* is the close-packed volume of the system and $\tilde{v} = 1/\tilde{\rho}$ is the reduced volume ($\tilde{\rho}$ is the reduced density).

The total energy of the system due to physical interactions is

$$-E_{LF} = rN\tilde{\rho}\epsilon^* \quad (2.A13)$$

The segment fractions, ϕ_k , should not be confused with the site fractions f_k , which are given by

$$f_k = \frac{r_k N_k}{N_r} = \frac{r_k N_k}{rN} \frac{rN}{N_r} = \phi_k \tilde{\rho} \quad (2.A14)$$

With these definitions, the physical term of the partition function of the system is

$$\begin{aligned} Q_p(T, N_0, \{N_k\}) &= (1/f_0)^{N_0} \prod_k^t (\omega_k/\phi_k)^{N_k} \exp(-E_{LF}/RT) \\ &= (1-\tilde{\rho})^{-N_0} \tilde{\rho}^{-N} \prod_k^t (\omega_k/\phi_k)^{N_k} \exp(-rN\tilde{\rho}\varepsilon^*/RT) \end{aligned} \quad (2.A15)$$

where ω_k is related to the number of possible conformations of an r_k -mer.

The free energy of the system is given by

$$G_p = -kT \ln Q_p = G_{LF} \quad (2.A16)$$

Combining Equations 2.A15 and 2.A16 we obtain for the LF (physical) contribution to free energy:

$$\frac{G_{LF}}{kT} = rN \left\{ -\frac{\tilde{\rho}}{\tilde{T}} + \frac{\tilde{P}\tilde{v}}{\tilde{T}} + (\tilde{v}-1) \ln(1-\tilde{\rho}) + \frac{1}{r} \ln \tilde{\rho} + \sum_k^t \frac{\phi_k}{r_k} \ln \left(\frac{\phi_k}{\omega_k} \right) \right\} \quad (2.A17)$$

For a system at equilibrium, the free energy is at a minimum. The minimization condition:

$$\left(\frac{\partial G}{\partial \tilde{v}} \right)_{T,P,N} = 0 \quad (2.A18)$$

may then be used for obtaining the LF equation of state for our system:

$$\tilde{\rho}^2 + \tilde{P} + \tilde{T} \left[\ln(1-\tilde{\rho}) + \tilde{\rho} \left(1 - \frac{1}{\tilde{r}} \right) \right] = 0 \quad (2.A19)$$

where \tilde{P} is the reduced pressure defined as

$$\tilde{P} = \frac{P}{P^*} = \frac{Pv^*}{\varepsilon^*} \quad (2.A20)$$

\tilde{T} is the reduced temperature

$$\tilde{T} = \frac{T}{T^*} = \frac{RT}{\varepsilon^*} \quad (2.A21)$$

The chemical potential of component k is obtained from

$$\mu_k = \mu_{k,LF} = \left(\frac{\partial G_{LF}}{\partial N_k} \right)_{T,P,N_{j \neq k}} \quad (2.A22)$$

or

$$\begin{aligned} \frac{\mu_{k,LF}}{RT} = & \ln \frac{\phi_k}{\omega_k} + \left(1 - \frac{r_k}{r}\right) + r_k \left\{ \frac{-\tilde{\rho} + \tilde{P}_k}{\tilde{T}_k} + (\tilde{\nu} - 1) \ln(1 - \tilde{\rho}) + \frac{1}{r_k} \ln \tilde{\rho} \right\} \\ & + r_k \tilde{\rho} \left\{ \sum_{i=1}^t \phi_i X_{ik} - \sum_{k < j}^t \sum_j^t \phi_k \phi_j X_{kj} \right\} \end{aligned} \quad (2.A23)$$

2.A.2 THE QUASI-CHEMICAL LATTICE FLUID (QCLF) FRAMEWORK

Recently^{4,5} we have presented a quasi-chemical equation-of-state model that accounts for the nonrandom distribution of free volume in pure nonpolar fluids as well as in their mixtures. The model has proved successful in describing the phase equilibria of these systems, especially at the near-critical region. The essentials of this model follow.

Let us consider first a system of N molecules of a pure r -mer fluid at temperature T and external pressure P . The molecules are considered arranged on a quasi-lattice of N_r sites, N_0 of which are empty. The empty sites, however, are not considered distributed randomly throughout the volume of the system. In a general way we may consider that the partition function of our system can be written as follows:

$$Q(N, T, P) = Q_R Q_{NR} \quad (2.A24)$$

where Q_R is the partition function for the hypothetical system where there is a random distribution of the empty sites and Q_{NR} is a correction factor for the actual nonrandom distribution of the empty sites. As already mentioned, for the first factor we use here the simple LF expression,¹⁻³ which was presented in the previous section. For the second factor we use Guggenheim's quasi-chemical approach⁶ as adapted to the problem previously,^{7,8} namely,

$$Q_{NR} = \frac{N_{rr}^0! N_{00}^0! \left[\left(\frac{N_{r0}^0}{2} \right)! \right]^2}{N_{rr}! N_{00}! \left[\left(\frac{N_{r0}}{2} \right)! \right]^2} \quad (2.A25)$$

N_{rr} in Equation 2.A25 is the number of external contacts between the segments of the molecules. N_{00} is the number of contacts between the empty sites, whereas N_{r0} is the number of contacts between a molecular segment and an empty site. Superscript 0 refers to the case of randomly distributed empty sites.

As before, the molecules of the pure fluid are considered divided into r segments of volume v^* each. The same volume is assigned to the empty site as well. Thus, the total volume of the system is given by

$$V = Nr v^* + N_0 v^* = N_r v^* = V^* + N_0 v^* \quad (2.A26)$$

According to the LF model presented in the previous paragraph and to Equation 2.A15, the partition function Q_R in the present case may be written as:

$$Q_R = \left(\frac{1}{f_0} \right)^{N_0} \left(\frac{\omega}{f} \right)^N \exp \left(- \frac{E + PV}{RT} \right) \quad (2.A27)$$

where the site fractions f_0 and f are for the empty sites and the molecular segments, respectively, namely,

$$f_0 = \frac{N_0}{N_r} = \frac{N_r - rN}{N_r} = 1 - f \quad (2.A28)$$

ω in Equation 2.A27 is a characteristic quantity for the fluid that takes into account the flexibility and the symmetry of the molecule, which will cancel in all applications of our interest and will not be given any further consideration.

The potential energy E arises from the intermolecular interactions in the system. It will be assumed that only first-neighbor segment–segment contacts contribute to it while the contacts of an empty site with a segment or with another empty site are assigned a zero interaction energy. If s is the average number of external contacts per segment (either molecular or empty sites) and ϵ the segment–segment interaction energy, the potential energy of the system is given by

$$-E = N_{rr} \epsilon \quad (2.A29)$$

In the random case N_{rr} is given by the equation:¹⁻³

$$N_{rr}^0 = \frac{1}{2} Nrs \frac{Nr}{N_r} = \frac{1}{2} Nrsf \quad (2.A30)$$

The average per segment interaction energy in the absence of empty sites is now

$$\epsilon^* = \frac{s}{2} \epsilon \quad (2.A5a)$$

In the random case, the number of contacts between empty sites is given, in analogy to Equation 2.A30, by the equation:

$$N_{00}^0 = \frac{1}{2} N_0s \frac{N_0}{N_r} = \frac{1}{2} N_0sf_0 = \frac{1}{2} N_0s(1 - \tilde{\rho}) \quad (2.A31)$$

while the number of contacts between a segment and an empty site is given by

$$N_{r0}^0 = rNs \frac{N_0}{N_r} = N_0s \frac{rN}{N_r} = rNs(1 - \tilde{\rho}) = N_0s\tilde{\rho} \quad (2.A32)$$

In the nonrandom case, following our previous practice,^{7,8} we will write for the number of contacts in the system the following equations:

$$\begin{aligned} N_{rr} &= N_{rr}^0 \Gamma_{rr} \\ N_{00} &= N_{00}^0 \Gamma_{00} \\ N_{r0} &= N_{r0}^0 \Gamma_{r0} \end{aligned} \quad (2.A33)$$

The nonrandom Γ factors in Equation 2.A33 are, of course, equal to one in the random case. These numbers must satisfy the following material balance equations:^{7,8}

$$\begin{aligned} 2N_{00} + N_{0r} &= N_0s \\ 2N_{rr} + N_{0r} &= rsN \end{aligned} \quad (2.A34)$$

By combining the last three equations, we obtain

$$\begin{aligned} (1 - \tilde{\rho})\Gamma_{00} + \tilde{\rho}\Gamma_{r0} &= 1 \\ \tilde{\rho}\Gamma_{rr} + (1 - \tilde{\rho})\Gamma_{r0} &= 1 \end{aligned} \quad (2.A35)$$

Thus, the three nonrandom Γ factors are not independent. When one is known, the other two are obtained from Equation 2.A35. The reduced density must, of course, be known prior to using Equation 2.A35. It will be obtained from the equation of state of the system.

As before, the free energy of our system is obtained from the partition function as follows:

$$G = -RT \ln Q \quad (2.A36)$$

At equilibrium, the number of empty sites in the system or, equivalently, the reduced density is obtained from the minimization condition:

$$\left(\frac{\partial G}{\partial \tilde{\rho}} \right)_{T,P,N,N_{r0}} = 0 \quad (2.A18a)$$

while the number of contacts N_{r0} or, equivalently, the nonrandom factor Γ_{r0} is obtained from the minimization condition:

$$\left(\frac{\partial G}{\partial N_{r0}} \right)_{T,P,N,\tilde{\rho}} = 0 \quad (2.A37)$$

The first minimization condition, Equation 2.A18a, leads to the equation of state:

$$\tilde{P} + \tilde{T} \left[\ln(1 - \tilde{\rho}) + \tilde{\rho} \left(1 - \frac{1}{r} \right) + \frac{s}{2} \ln \Gamma_{00} \right] = 0 \quad (2.A38)$$

In the random case ($\Gamma_{rr} = \Gamma_{00} = 1$) this equation reduces to the familiar LF equation of state,^{1,2} Equation 2.A19. The second minimization condition, Equation 2.A37, leads to the equation:

$$\frac{4N_{rr}N_{00}}{N_{r0}^2} = \frac{4\Gamma_{rr}\Gamma_{00}}{\Gamma_{r0}^2} = \exp\left(\frac{\epsilon}{RT}\right) = A \quad (2.A39)$$

By replacing from Equation 2.A35 in Equation 2.A39, we obtain a quadratic equation for Γ_{r0} whose physically meaningful solution is

$$\Gamma_{r0} = \frac{2}{1 + [1 - 4\tilde{\rho}(1 - \tilde{\rho})(1 - A)]^{1/2}} \quad (2.A40)$$

Equations 2.A35, 2.A38, and 2.A39 are coupled equations and must be solved simultaneously for the reduced density or the nonrandom factors.

From the expression for the free energy we obtain by derivation the following equation for the chemical potential:

$$\frac{\mu}{RT} = r(\tilde{v} - 1)\ln(1 - \tilde{\rho}) + \ln \frac{\tilde{\rho}}{\omega} - \frac{r\tilde{\rho}}{\tilde{T}}\Gamma_{rr} + r\frac{\tilde{P}\tilde{v}}{\tilde{T}} + \frac{rs}{2}[\ln \Gamma_{rr} + (\tilde{v} - 1)\ln \Gamma_{00}] - r\frac{1 - \tilde{\rho}\Gamma_{rr}}{\tilde{T}} \quad (2.A41)$$

This set of equations is sufficient for performing the basic thermodynamic calculations for pure fluids.

Let us now consider a binary system of N_1 and N_2 molecules of components 1 and 2, respectively, with r_1 and r_2 segments and of segmental volume v_1^* and v_2^* , respectively. The total number N_r of lattice sites is now

$$N_r = N_1r_1 + N_2r_2 + N_0 = rN + N_0 = N(x_1r_1 + x_2r_2) + N_0 \quad (2.A42)$$

where $N = N_1 + N_2$ is the total number of molecules in the system and x_1 and x_2 the mole fractions of components 1 and 2, respectively.

For the mixture, and in the one-fluid approach, the combining and mixing rules, Equations 2.A6 and 2.A7, are assumed to be valid here as well.

Because only segment–segment interactions contribute to the potential energy E , we may write:

$$E = N_{11}\epsilon_{11} + N_{12}\epsilon_{12} + N_{22}\epsilon_{22} \quad (2.A43)$$

The number of intersegmental contacts N_{ij} will be obtained by applying the quasi-chemical approach. The key assumption that is now adopted is the following: The empty sites are distributed nonrandomly and make no distinction between their neighbor molecular segments. This means that for nonrandom distribution a number of intersegmental contacts satisfy the following equations:

$$\begin{aligned} N_{11} &= N_{11}^0\Gamma_{rr} \\ N_{22} &= N_{22}^0\Gamma_{rr} \\ N_{12} &= N_{12}^0\Gamma_{rr} \\ N_{rr} &= N_{11} + N_{12} + N_{22} \\ N_{rr} &= N_{rr}^0\Gamma_{rr} = \frac{s}{2}Nr\tilde{\rho}\Gamma_{rr} \\ N_{00} &= N_{00}^0\Gamma_{00} \\ N_{r0} &= N_{r0}^0\Gamma_{r0} \end{aligned} \quad (2.A44)$$

The above assumption implies that Equation 2.A25 is also valid for the case of our mixture but with the N_{ij} obtained from Equation 2.A44. The Q_R term in Equation 2.A24 for the mixture is similar to Equation 2.A27 and is given by

$$Q_R = \left(\frac{1}{f_0}\right)^{N_0} \left(\frac{\omega_1}{f_1}\right)^{N_1} \left(\frac{\omega_2}{f_2}\right)^{N_2} \exp\left(-\frac{E + PV}{RT}\right) \quad (2.A45)$$

The equation of state for the mixture is obtained by the minimization procedure discussed previously. The result is an equation of state identical in form to Equation 2.A38. Similarly, the quasi-chemical condition for the mixture is identical in form to Equation 2.A39, and the material balance equations are identical in form to Equations 2.A34 or 2.A35. Of course r , s , ϵ , and $\tilde{\rho}$ in these equations are now quantities pertinent to the mixture.

The chemical potential of each component in the mixture is obtained by a procedure analogous to that used for deriving Equation 2.A41, and is given by

$$\begin{aligned} \frac{\mu_1}{RT} = & \ln \phi_1 + \left(1 - \frac{r_1}{r_2}\right) \phi_2 + r_1 \tilde{\rho} X_{12} \theta_2^2 \Gamma_{rr} + r_1 (\tilde{v} - 1) \ln(1 - \tilde{\rho}) \\ & + \ln \frac{\tilde{\rho}}{\omega_1} - \frac{r_1 \tilde{\rho}}{\tilde{T}_1} \Gamma_{rr} + r_1 \frac{\tilde{P}\tilde{v}}{\tilde{T}} \frac{v_1^*}{v^*} + \frac{r_1 s_1}{2} [\ln \Gamma_{rr} + (\tilde{v} - 1) \ln \Gamma_{00}] - r_1 \frac{\theta_1}{\phi_1} \frac{1 - \tilde{\rho} \Gamma_{rr}}{\tilde{T}} \end{aligned} \quad (2.A46)$$

2.A.3 OTHER EQUATION-OF-STATE FRAMEWORKS

The above frameworks are by no means unique. Any other equation-of-state model, which can provide an expression for the Q_p term of the partition function or the corresponding G_p term of the free energy can be used, in principle, as such a framework. Models, such as those of Prigogine et al.,⁹⁻¹¹ of Patterson et al.,^{12,13} of Flory et al.,¹⁴⁻¹⁶ of Simha et al.,^{17,18} of Kleintjens and Koningsveld,¹⁹ of Nose,²⁰ of Panayiotou and Vera⁸ — just to name a few — can serve this purpose.

REFERENCES TO APPENDIX 2.A

1. Sanchez, I.C. and Lacombe, R., *J. Phys. Chem.*, 80, 2352, 1976.
2. Sanchez, I.C. and Lacombe, R., *Macromolecules*, 11, 1145, 1978.
3. Panayiotou, C., *Macromolecules*, 20, 861, 1987.
4. Taimoori, M. and Panayiotou, C., *Fluid Phase Equilibria*, Vol. 192, 155–169, 2001.
5. Vlachou, Th. et al., *Ind. Eng. Chem. Res.*, Vol. 41, 1059–1063, 2002.
6. Guggenheim, E.A., *Mixtures*, Clarendon Press, Oxford, 1952.
7. Panayiotou, C. and Vera, J.H., *Fluid Phase Equilibria*, 5, 55, 1980.
8. Panayiotou, C. and Vera, J.H., *Polym. J.*, 14, 681, 1982.
9. Prigogine, I. and Mathot, V., *J. Chem. Phys.*, 20, 49, 1952.
10. Prigogine, I., Trappeniers, N., and Mathot, V., *Discuss. Faraday Soc.*, 15, 93, 1953.
11. Prigogine, I. (with the collaboration of V. Mathot and A. Bellemans), *The Molecular Theory of Solutions*, North Holland, Amsterdam, 1957.
12. Patterson, D., *Polym. Sci. C*, 16, 3379, 1968.
13. Patterson, D. and Delmas, G., *Discuss. Faraday Soc.*, 49, 98, 1970.
14. Flory, P.J., Orwoll, R.A. and Vrij, A., *J. Am. Chem. Soc.*, 86, 3515, 1964.
15. Flory, P.J., *J. Am. Chem. Soc.*, 87, 1833, 1965.
16. Eichinger, B.E. and Flory, P.J., *Trans. Faraday Soc.*, 64, 2035, 1968.
17. Nanda, V.S. and Simha, R., *J. Phys. Chem.*, 68, 3158, 1964.
18. Simha, R. and Somcynsky, T., *Macromolecules*, 2, 342, 1969.
19. Kleintjens, L.A. and Koningsveld, R., *Colloid Polym. Sci.*, 258, 711, 1980.
20. Nose, T., *Polym. J.*, 2, 124 and 196, 1971.

APPENDIX 2.B:

THE ALGORITHM FOR OBTAINING THE NUMBER OF HYDROGEN BONDS

In this appendix we explain how the equations for the number of hydrogen bonds in the system can be solved numerically to obtain physically meaningful solutions. In the general case we must solve the equations (see Equations 2.38 and 2.39 of the main text):

$$\frac{v_{ij}}{v_{i0}v_{0j}} = \tilde{\rho} \exp\left(-\frac{G_{ij}^0}{RT}\right) = \frac{r}{A_{ij}} \quad \text{for all } i,j \quad (2.B1)$$

or

$$v_{ij} = \left[v_a^i - \sum_k^n v_{ik} \right] \left[v_a^j - \sum_k^m v_{kj} \right] \tilde{\rho} \exp\left(-\frac{G_{ij}^0}{RT}\right) \quad (2.B2)$$

which is a system of $(m \times n)$ quadratic equations for v_{ij} . This system must be solved in combination with the equation of state since the reduced density $\tilde{\rho}$ is needed in the calculations. We should keep in mind that v_{ij} in these equations are fractions of hydrogen bonds, or $v_{ij} = N_{ij}/rN$ and similarly for v_{i0} and v_{0j} . These fractions can be calculated from the following $(m \times n)$ equations:

$$rv_{ij} = \frac{1}{2} \left\{ P_{ij} - \sqrt{(P_{ij}^2 - 4Q_{ij})} \right\} \quad \text{for all } i,j \text{ pairs} \quad (2.B3)$$

where

$$P_{ij} = A_{ij} + \sum_k d_i^k x_k + \sum_k a_j^k x_k - \sum_{m \neq j} rv_{im} - \sum_{n \neq i} rv_{nj} \quad (2.B4)$$

and

$$Q_{ij} = \left(\sum_k d_i^k x_k - \sum_{m \neq j} rv_{im} \right) \left(\sum_k a_j^k x_k - \sum_{n \neq i} rv_{nj} \right) \quad (2.B5)$$

The numerical procedure for solving these equations is as follows. We assume some initial values (usually small) for the v_{ij} terms and calculate the P_{ij} and Q_{ij} terms. By using Equation 2.B3, we now do the first calculation of the v_{ij} terms. This set of v_{ij} terms is used for calculating the second set of P_{ij} and Q_{ij} terms, which in turn is used for the second calculation of the v_{ij} terms. This procedure is repeated until two consecutive calculations of the v_{ij} terms differ by less than a preset tolerance.

The above procedure is implemented in the following FORTRAN code in the case of a binary system of molecules both having two types of donor groups and three types of acceptor groups. The subroutine returns with the calculated values of A_{ij} terms, which correspond to rv_{ij} terms for the donor i and acceptor j pair. $Y_{ij}(k)$ in this subroutine is the corresponding value of the rv_{ij} for the i - j pair, as calculated in the k th iteration. The calculations are made at a mixture compositions given by the mole fraction X_1 of component 1. The numbers D_{kl} of donors of type k in the molecule of type l and the numbers AC_{mn} of acceptors of type m in the molecule of type n are provided by

the COMMON block DONACC of the subroutine. Similarly, the A_{ij} terms (see Equation 2.B1) are provided by the COMMON block AL.

This is a very stable algorithm, which converges rapidly to the solution.

The FORTRAN code

```

SUBROUTINE MSOLVER(X1,AM11,AM12,AM13,AM21,AM22,AM23)
IMPLICIT DOUBLE PRECISION (A-H,O-Z)
COMMON/DONACC/D11,D12,D21,D22,AC11,AC12,AC21,AC22,AC31,AC32
COMMON/AL/A11,A12,A13,A21,A22,A23
DIMENSION Y11(302),Y12(302),Y13(302),Y21(302),Y22(302),
1  Y23(302)
Y11(1)=0.005
Y12(1)=0.005
Y13(1)=0.005
Y21(1)=0.005
Y22(1)=0.005
Y23(1)=0.005
4  X2=1.0-X1
DO1=D11*X1+D12*X2
DO2=D21*X1+D22*X2
AC1=AC11*X1+AC12*X2
AC2=AC21*X1+AC22*X2
AC3=AC31*X1+AC32*X2
I=2
1  P11=DO1+AC1+A11-Y12(I-1)-Y13(I-1)-Y21(I-1)
Q11=(DO1-Y12(I-1)-Y13(I-1))*(AC1-Y21(I-1))
R11=P11**2-4.0*Q11
IF(R11.LT.0.0) GO TO 5
Y11(I)=(P11-DSQRT(R11))/2.
P12=DO1+AC2+A12-Y11(I-1)-Y13(I-1)-Y22(I-1)
Q12=(DO1-Y11(I-1)-Y13(I-1))*(AC2-Y22(I-1))
R12=P12**2-4.0*Q12
IF(R12.LT.0.0) GO TO 5
Y12(I)=(P12-DSQRT(R12))/2.
P13=DO1+AC3+A13-Y12(I-1)-Y11(I-1)-Y23(I-1)
Q13=(DO1-Y12(I-1)-Y11(I-1))*(AC3-Y23(I-1))
R13=P13**2-4.0*Q13
IF(R13.LT.0.0) GO TO 5
Y13(I)=(P13-DSQRT(R13))/2.
P21=DO2+AC1+A21-Y22(I-1)-Y23(I-1)-Y11(I-1)
Q21=(DO2-Y22(I-1)-Y23(I-1))*(AC1-Y11(I-1))
R21=P21**2-4.0*Q21
IF(R21.LT.0.0) GO TO 5
Y21(I)=(P21-DSQRT(R21))/2.
P22=DO2+AC2+A22-Y21(I-1)-Y23(I-1)-Y12(I-1)
Q22=(DO2-Y21(I-1)-Y23(I-1))*(AC2-Y12(I-1))
R22=P22**2-4.0*Q22
IF(R22.LT.0.0) GO TO 5
Y22(I)=(P22-DSQRT(R22))/2.
P23=DO2+AC3+A23-Y21(I-1)-Y22(I-1)-Y13(I-1)
Q23=(DO2-Y21(I-1)-Y22(I-1))*(AC3-Y13(I-1))

```

```
R23=P23**2-4.0*Q23
IF(R23.LT.0.0) GO TO 5
Y23(I)=(P23-DSQRT(R23))/2.
```

```
T=DABS(Y11(I)-Y11(I-1))+DABS(Y12(I)-Y12(I-1))+DABS(Y13(I)-
1 Y13(I-1))+DABS(Y21(I)-Y21(I-1))+DABS(Y22(I)-Y22(I-1))+
2 DABS(Y23(I)-Y23(I-1))
```

```
IF(T.LT.0.0000001) GO TO 2
```

```
I=I+1
```

```
IF(I.GT.300) THEN
```

```
WRITE(*,*) I,T
```

```
GO TO 2
```

```
ENDIF
```

```
GO TO 1
```

```
2 AM11=Y11(I)
```

```
AM12=Y12(I)
```

```
AM13=Y13(I)
```

```
AM21=Y21(I)
```

```
AM22=Y22(I)
```

```
AM23=Y23(I)
```

```
5 RETURN
```

```
END
```


APPENDIX 2.C: IMPLICATIONS OF THE EQUATION FOR RELATIVE ADSORPTION

Equation 2.34 of the main text, which we rewrite here for ease of reading,

$$\Gamma_{2,1} = - \left(\frac{d\sigma}{d\mu_2} \right)_T = - \left[\left(\frac{d\sigma}{dx_2} \right) \left(\frac{dx_2}{d\mu_2} \right) \right]_T \quad (2.34)$$

has significant implications and may be the starting point for development of thermodynamic models of surface properties. The derivatives in the right hand side of this equation may be calculated in various ways. The derivative involving the chemical potential can be obtained from equations for the activity or activity coefficients, which in turn may be obtained, as an example, from correlation of phase equilibrium data. The derivative involving the surface tension may be obtained either directly from correlations of experimental data or from model equations for the variation of surface tension with composition. In what follows, we give an example of how Equation 2.34 could be used for a rough estimation of the thickness of the surface layer at the liquid–vapor interface in a solution.

For generality, let us consider a mixture of two components 1 and 2 varying in size and characterized by molar volumes v_1 and v_2 , respectively. In this case, it is preferable to rewrite Equation 2.34 in terms of the volume fractions rather than the mole fractions:

$$\Gamma_{2,1} = - \left(\frac{d\sigma}{d\mu_2} \right)_T = - \left[\left(\frac{d\sigma}{d\phi_2^b} \right) \left(\frac{d\phi_2^b}{d\mu_2} \right) \right]_T \quad (2.C1)$$

where ϕ_2^b is the volume fraction of component 2 in the bulk (liquid) phase, and is defined in general as

$$\phi_2^b = \frac{n_2^b v_2}{n_1^b v_1 + n_2^b v_2} = 1 - \phi_1^b \quad (2.C2)$$

where n is the number of moles.

By adopting an equation for the chemical potential of the Flory–Huggins type:¹

$$\frac{\mu_2 - \mu_2^0}{RT} = \ln \phi_2^b + \left(\frac{v_2}{v_1} - 1 \right) \phi_1^b + \chi (\phi_1^b)^2 \quad (2.C3)$$

we obtain for the derivative:

$$\frac{\partial \phi_2^b}{\partial \mu_2} = 1 / \left[\frac{1}{\phi_2^b} + \left(\frac{v_2}{v_1} - 1 \right) - 2\chi(1 - \phi_2^b) \right] \quad (2.C4)$$

χ in these equations is the well-known Flory–Huggins interaction parameter.¹

An interesting application arises when the surface tension is correlated in terms of the volume fractions at the interface (superscript s) instead of the corresponding fractions in bulk. Often, a simple linear correlation of the Eberhart type:²⁻⁴

$$\sigma = \phi_1^s \sigma_1 + \phi_2^s \sigma_2 \quad (2.C5)$$

is adequate for representing the surface tension over the full composition range. The link between volume fractions in bulk and in interface is usually obtained from semiempirical or semitheoretical expressions. Recently, Pineiro et al.,⁴ by extending the Langmuir isotherm, have provided such an expression:

$$\phi_2^s = \frac{\beta \phi_2^b}{1 + (\beta - 1) \phi_2^b} = 1 - \phi_1^s \quad (2.C6)$$

where β is Henry's constant for two dimensions and measures the lyophobicity of the solute, i.e., its tendency to be adsorbed by the surface.⁴ Once accurate experimental data of the variation of surface tension with composition are available, we may select appropriate combinations of relations of the type of Equations 2.C5 and 2.C6 and adjust their parameters (like the parameter β) so that they reproduce satisfactorily the experimental data. Of course, if volume fractions at the surface are going to be used, Equation 2.34 must be cast in the appropriate form, or

$$\Gamma_{2,1} = - \left(\frac{d\sigma}{d\mu_2} \right)_T = - \left[\left(\frac{d\sigma}{d\phi_2^s} \right) \left(\frac{d\phi_2^s}{d\phi_2^b} \right) \left(\frac{d\phi_2^b}{d\mu_2} \right) \right]_T \quad (2.C7)$$

In addition, $\Gamma_{2,1}$ may also be expressed in terms of the volume fractions at the interface. This is not a straightforward step, however. It is well known that the liquid–vapor interface of a liquid is a discontinuous region in which the field forces acting on the molecules of the fluid are nonhomogeneous. This results in a modification in this region of the number density of molecules of the fluid, their time average orientation, and their lateral interactions. It is essential to remember that the real surface layer is not a homogeneous “phase,” but there is a gradual change in concentration with distance from the surface. However, for the development of semiempirical models of interfacial properties it is often useful to think of a fictitious homogeneous phase, to which one could attribute an effective “thickness.” Also, the experimental attempts to determine the surface excess, like the famous microtome or railroad method of McBain and Humphreys⁵ and the radioactivity technique of Nilsson,⁶ give average (number of moles/area) results, which, when translated into concentrations, give average concentrations as if the interfacial layer were a homogeneous phase (with an average concentration, mole or volume fractions). For such a homogeneous interfacial layer, the relative adsorption can be expressed in terms of the volume fractions at the interface by recalling the meaning of this quantity in the Gibbs convention: If t is the thickness of the interfacial layer, the volume corresponding to an area A is $t \times A$. In this volume, the number of moles of component 1 is (assuming that the molar volumes in bulk and in interface are the same)

$$n_1^s = \frac{tA\phi_1^s}{v_1} \quad (2.C8)$$

and, similarly,

$$n_2^s = \frac{tA\phi_2^s}{v_2} \quad (2.C9)$$

To obtain the relative adsorption of component 2 we must obtain first a volume from the bulk containing n_1^s moles of component 1 and find how many moles of component 2 are contained in the same volume. By neglecting volume changes upon mixing and by replacing in the definitions of volume fractions, Equations 2.C2 and 2.C6, we obtain

$$n_2^b = n_2^s \frac{\phi_1^s \phi_2^b}{\phi_2^s \phi_1^b} \quad (2.C10)$$

By definition,

$$\Gamma_{2,1} = \frac{n_2^s - n_2^b}{A} \quad (2.C11)$$

Combining the last three equations, we obtain

$$\Gamma_{2,1} = \frac{n_2^s}{A} \left[1 - \frac{\phi_1^s \phi_2^b}{\phi_1^b \phi_2^s} \right] = \frac{t \phi_2^s}{v_2} \left[1 - \frac{\phi_1^s \phi_2^b}{\phi_1^b \phi_2^s} \right] \quad (2.C12)$$

This equation can be replaced in Equation 2.C7 to obtain one additional equation relating the compositions in bulk and in interface. If Equations 2.C3, 2.C5, and 2.C6 are adopted, Equation 2.C7 combined with Equation 2.C12 gives for the “thickness” of the interfacial layer:

$$t = \frac{(\sigma_1 - \sigma_2) v_2}{\left[1 + (\beta - 1) \phi_2^b \right] \left[1 + \left(\frac{v_2}{v_1} - 1 \right) \phi_2^b - 2\chi \phi_2^b (1 - \phi_2^b) \right]} \quad (2.C13)$$

This is a useful equation relating the thickness of the supposedly homogeneous interfacial layer to properties of pure components (surface tensions and molar volumes), to the bulk composition, and to the interaction parameters β and χ . It is worth observing that the more negative the χ parameter (the more favorable the interaction between components 1 and 2), the smaller the thickness of the interfacial layer. If the thickness is estimated from independent studies, Equation 2.C13 could be used for obtaining the lipophobicity constant or the composition of the interfacial layer.

If hydrogen bonding is involved, both Equations 2.C3 and 2.C5 must be replaced by more appropriate equations. In this case the above derivatives may not lead to analytical expressions and numerical differentiation may be needed. Still, however, Equations 2.C7 and 2.C12 can be used for making a rough estimation of the effective interfacial layer thickness, which could prove useful for development of semiempirical models.²⁻⁴

REFERENCES TO APPENDIX 2.C

1. Flory, P.J., *Principles of Polymer Chemistry*, Cornell University Press, Ithaca, NY, 1953.
2. Eberhart, J.G., *J. Phys. Chem.*, 70, 1183, 1996.
3. Connors, K.A. and Wright, J.L., *Anal. Chem.*, 61, 194, 1989.
4. Pineiro, A. et al., *Langmuir*, 17, 4261, 2001.
5. McBain, J.W. and Humphreys, C.W., *J. Phys. Chem.*, 36, 300, 1932.
6. Nilsson, G., *J. Phys. Chem.*, 61, 1135, 1957.

3 Surface Tension and Interfacial Tension of Liquids

K. S. Birdi

CONTENTS

- 3.1 Introduction
 - 3.2 The Parachor
 - 3.3 Heat of Surface Formation and Heat of Evaporation
 - 3.4 Effect of Temperature and Pressure on the Surface Tension of Liquids
 - 3.4.1 Corresponding States Theory
 - 3.5 Surface Tension of Liquid Mixtures
 - 3.6 Solubility of Organic Liquids in Water and Water in Organic Liquids
 - 3.6.1 The Hydrophobic Effect
 - 3.7 Interfacial Tension of Liquids
 - 3.7.1 Introduction
 - 3.7.2 Liquid-Liquid Systems — Work of Adhesion
 - 3.7.3 Interfacial Tension Theories of Liquid-Liquid Systems
 - 3.7.4 Hydrophobic Effect on the Surface Tension and Interfacial Tension
 - 3.7.5 Heat of Fusion in the Hydrophobic Effect
 - 3.7.6 Analysis of the Magnitude of the Dispersion Forces in Water (γ_D)
 - 3.7.6.1 Liquid-Solid Systems (Contact Angle)
 - 3.8 Surface Tension and Interfacial Tension of Oil-Water Systems
- References

3.1 INTRODUCTION

The liquid state of matter plays a very important role in everyday life, and the liquid surface has a dominant role in many phenomena. In fact, about 70% of the surface of Earth is covered by water. The most fundamental characteristic of liquid surfaces is that they tend to contract to the smallest surface area to achieve the lowest free energy. Whereas gases have no definite shape or volume, completely filling a vessel of any size containing them, liquids have no definite shape but do have a definite volume, which means that a portion of the liquid takes the shape of that part of a vessel containing it and occupies a definite volume, with the free surface plane except for capillary effects where it is in contact with the vessel. This is evident in rain drops and soap films, in addition to many other systems that will be mentioned later. The cohesion forces present in liquids and solids and the condensation of vapors to liquid state indicate the presence of much larger intermolecular forces than the gravity forces. Furthermore, the dynamics of molecules at interfaces are important in a variety of areas, such as biochemistry, electrochemistry, and chromatography. The degree of sharpness of a liquid surface has been the subject of much discussion in the literature.

There is strong evidence that the change in density from liquid to vapor (by a factor of 1000) is exceedingly abrupt, in terms of molecular dimensions. The surface of a liquid was analyzed by

light reflectance investigations, as described by Fresnel's law. Various investigators indeed found that the surface transition involves just one layer of molecules. In other words, surfaces and investigations related to this part of a system are actually just a molecular layer. However, there exists one system that clearly shows that the "one molecule thick" layer of surface is the surface of a liquid; thus, the monolayer studies of lipids spread on water and studied by Langmuir balance.^{1a} The surface thermodynamics of these monolayers is based on a unimolecular layer at the interface, which thus confirms the thickness of the *surface*.

The molecules of a liquid in the bulk phase are in a state of constant unordered motion like those of a gas, but they collide with one another much more frequently owing to the greater number of them in a given volume:

GAS PHASE.....molecules in gas
 -----(INTERMEDIATE PHASE)-----
 LIQUID SURFACE.....surface molecules
 BULK LIQUID PHASE.....molecules inside liquid

It is important to note that the *intermediate* phase is present only between the gas phase and the liquid phase. Although we do not often think about how any interface behaves at equilibrium, the liquid surface demands special comment. The surface of a liquid is under constant agitation, but there are few things in nature presenting an appearance of more complete repose than a liquid surface at rest. On the other hand, kinetic theory tells us that molecules are subject to much agitation.

This is apparent if we consider the number of molecules that must evaporate each second from the surface to maintain the vapor pressure. At equilibrium, the number of liquid molecules that evaporate into the gas phase is equal to the number of gas molecules that condense at the liquid surface (which will take place in the intermediate phase). The number of molecules hitting the liquid surface is considered to condense irreversibly.^{1b} From the kinetic theory of gases, this number can be estimated as follows:

$$\text{mass/cm}^2/\text{second} = \rho_G (k_B T / 2\pi m_m)^{0.5} = 0.0583 p_{\text{vap}} (M/T) \quad (3.1)$$

where k_B is the Boltzmann constant (1.3805×10^{-16} erg/deg, m_m is the mass of molecule, ρ_G is the density of the gas, and M is the molecular weight.

If we consider water, at 20°C the vapor pressure of this liquid is 17.5 mm, which gives 0.25 g/s/cm² from Equation 3.1. This corresponds to 9×10^{21} molecules of water per second. While from consideration of the size of each water molecule we find that there are $\sim 10^{15}$ molecules, so that it can be concluded that the average life of each molecule in the surface is only about one eight-millionth of a second ($1/8 \times 10^{-6}$ s). This must be compounded with the movement of the bulk water molecules toward the surface region. It thus becomes evident that there is extremely violent agitation in the liquid surface. In fact, this turbulence may be considered analogous to the movement of the molecules in the gas phase. This is vividly evident in a cognac glass.

In the case of an interface between two immiscible liquids due to the presence of interfacial tension, the interface tends to contract. The magnitude of interfacial tension is always lower than the surface tension of the liquid with the higher tension. The liquid-liquid interface has been investigated by specular reflection of X rays to gain structural information at angstrom ($\text{Å} = 10^{-8}$ cm = 0.10 nm) resolution.²⁻⁴

The term *capillarity* originates from the Latin word *capillus*, a hair, describing the rise of liquids in fine glass tubes. Laplace showed that the rise of fluids in a narrow capillary was related to the difference in pressure across the interface and the surface tension of the fluid:⁵⁻⁷

$$\begin{aligned}\Delta P &= \gamma(\text{curvature}) = \gamma(1/\text{radius of the curvature}) \\ &= 2\gamma(1/\text{radius of the capillary})\end{aligned}\tag{3.2}$$

This means that when a glass tube of a hair-fine diameter is dipped in water, the liquid meniscus will rise to the very same height. The magnitude of rise is rather large, i.e., 3 cm if the bore is of 1 mm for water. This equation also explains what happens when liquid drops are formed at a faucet. Although it may not be obvious here, the capillary force can be very dominating in different processes. The capillary phenomenon thus means that it will play an important role in all kinds of systems where liquid is in contact with materials with pores or holes. In such systems the capillary forces will determine the characteristics of liquid–solid systems. Some of the most important are as follows:

- All kinds of fluid flow inside solid matrices (ground water; oil recovery)
- Fluid flow inside capillary (oil recovery; groundwater flow; blood flow)

It was recognized at a very early stage that only the forces from the molecules in the surface layer act on the capillary rise. The flow of blood in all living species is dependent on the capillary forces. The oil recovery technology in reservoirs is similarly dependent on capillary phenomena. Actually, the capillary forces become very dominating in such systems.

Furthermore, virtually all elements and chemical compounds have a solid, liquid, and vapor phase. A transition from one phase to another phase is accompanied by a change in temperature, pressure, density, or volume. In a recent study, the cascade of a structure in a drop falling from a faucet was investigated.⁸ In fact, fluid in the shape of drops (as in rain, sprays, fog, emulsions) is a common natural phenomenon and has attracted the attention of scientists for many decades.

A molecular explanation can be useful to consider in regard to surface molecules. Molecules are small objects that behave as if of definite size and shape in all states of matter, e.g., gas (G), liquid (L), and solid (S).⁹ The volume occupied by a molecule in the gas phase is some 1000 times larger than the volume occupied by a molecule in the liquid phase, as follows:

Volume per Mole in Gas or Liquid Phase and Distance between Molecules in Gas and Liquid Phases

Molar volume of water (at 20°C):

$$V_{\text{gas}} = \sim 24,000 \text{ ml as gas}$$

$$V_{\text{liquid}} = \sim 18 \text{ ml as liquid}$$

Ratio:

$$V_{\text{gas}} : V_{\text{liquid}} = \sim 1000$$

Distance (D) between molecules in gas (D_G) or liquid (D_L) phase:

$$\text{Ratio } D_G : D_L = (V_G : V_L)^{1/3} = (1000)^{1/3} = 10$$

As shown above, the volume of 1 mol of a substance — for example, water in the gas phase (at standard temperature and pressure), V_G ($\sim 24,000$ cc/mol) — is some 1000 times its volume in the liquid phase, V_L (~ 18 cc/mol). The distance between molecules, D , will be proportional to $V^{1/3}$ such that the distance in the gas phase, D_G , will be approximately 10 ($= 1000^{1/3}$) times larger than in the liquid phase, D_L . The finite compressibility and the relatively high density, which characterize liquids in general, point to the existence of repulsive and attractive intermolecular forces. The same forces that are known to be present in the gaseous form of a substance may be imagined also to play a role in the liquid form. The mean speed of the molecules in the liquid is the same as that

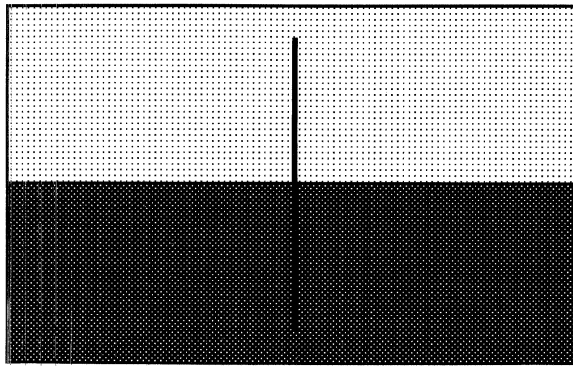


FIGURE 3.1 Tension in liquid surface.

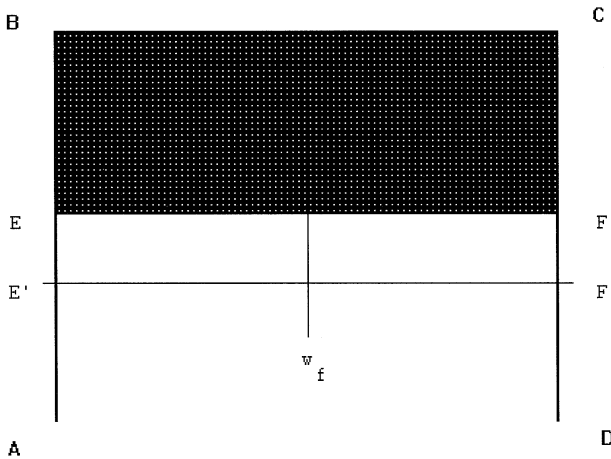


FIGURE 3.2 Stretching of a thin liquid film.

of the molecules in the gas; at the same temperature, the liquid and gas phase differ mainly by virtue of the difference in the density between them.

The magnitude of surface tension, γ , is determined by the internal forces in the liquid; thus it will be related to the internal energy or cohesive energy. The surface tension or the capillary phenomenon was mentioned in the literature at a very early stage by Leonardo da Vinci.^{10,11}

The phenomenon of surface tension can be explained by assuming that the surface behaves like a stretched membrane, with a *force of tension* acting in the surface at right angles, which tends to pull the liquid surface away from this line in both directions (Figure 3.1).

Surface tension thus has units of force/length = mass distance/time² distance = mass/time.² This gives *surface tension* in units as mN/m or dyn/cm or Joule/m² (mN m/m²). As another example, we can imagine a rectangular frame with a sliding wire, EF, fitted with a scale pan (Figure 3.2). If the frame is dipped into a soap (or any detergent) solution, a surface film (denoted as EBCF) will be formed. The surface tension would give rise to a tendency for the film to contract, to achieve a minimum in free energy. The weight, w_f thus required to balance this force would be

$$w_f = 2\gamma[EF] \quad (3.3)$$

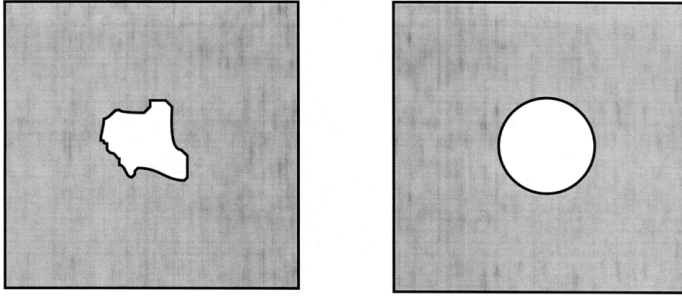


FIGURE 3.3 Surface tension causes the equilibrium in the right drawing, where a circular shape is present.

Factor 2 in Equation 3.3 arises from the two sides of the film. If the film is stretched to a new EBCF point, the work done on the system is

$$\begin{aligned}
 \text{work} &= w_f [EE'] \\
 &= 2\gamma [EF.EE'] \\
 &= 2\gamma [E'EFF'] \\
 &= 2\gamma (\text{increase in area})
 \end{aligned}
 \tag{3.4}$$

Gibbs¹² defined surface tension as the *free energy* excess per unit area:

$$\begin{aligned}
 \gamma &= \left(G - (G^a = G^b) \right) / \text{area} \\
 &= G_{\text{surface}} / \text{area}
 \end{aligned}
 \tag{3.5a}$$

where G is the free energy of the two-phase system (phases a and b). The liquid and vapor phases are separated by a surface region.¹²⁻¹⁷

It is also seen that other thermodynamic quantities would be given as^{1a}

$$\text{surface energy} = U_{\text{surface}} = U / \text{area}
 \tag{3.5b}$$

$$\text{surface entropy} = S_{\text{surface}} = S / \text{area}
 \tag{3.5c}$$

and from this we can obtain

$$\gamma = U_{\text{surface}} - S_{\text{surface}}
 \tag{3.5d}$$

Hence, the surface tension is also equal to the work spent in forming the unit surface area (m^2 or cm^2). This work increases the potential energy or *free surface energy*, G_s ($\text{J}/\text{m}^2 = \text{erg}/\text{cm}^2$) of the system. This can be further explained by different observations we make in everyday life, where liquid drops contract to attain minimum surfaces. If a loop of silk thread is laid carefully on a soap film and the inside of the loop is pricked with a needle, the loop takes up a circular shape, which provides a minimum in the energy for the system (Figure 3.3). Indeed, the concept of surface tension was accepted as early as around the year 1800. The observations such as a floating metal

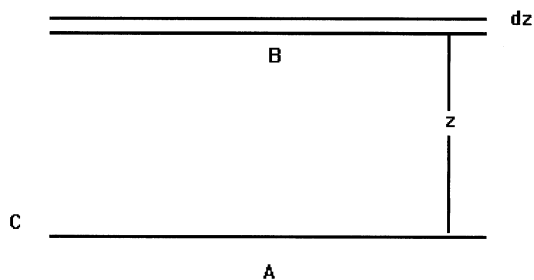


FIGURE 3.4 Pressure gradient in the surface region. (A and B are two parts of fluid divided by plane C; dz is an imaginary thin layer in the z axis.)

pin on the surface of water have been a common experience to all youngsters. In fact, a great many aquatic insects survive by floating on the surface of water in lakes due to surface forces.

It is well known that the attraction between two portions of a fluid decreases very rapidly with the distance and may be taken as zero when this distance exceeds a limiting value, R_c , the so-called range of molecular action. According to Laplace,¹⁸⁻²¹ surface tension, γ , is a force acting tangentially to the interfacial area, which equals the integral of the difference between the external pressure, p_{ex} , and the tangential pressure, p_t :

$$\gamma = \text{integral} (p_{ex} - p_t) dz \quad (3.6)$$

The z -axis is normal to the plane interface and goes from the liquid to the gas (Figure 3.4). The magnitude of work that must be exerted to remove a unit area of a liquid film of thickness t will be proportional to the tensile strength (latent heat of evaporation) of the liquid \times thickness. In the case of water, this would give approximately 25,000 atm of pressure ($600 \text{ cal/g} \propto 25.2 \times 10^9 \text{ erg} = 25,000 \text{ atm}$).

However, different theoretical procedures used to estimate γ by using Equation 3.6 have been subject to much difficulty, and some of these procedures have been analyzed in a review.²⁰ In this review, the energetics and hydrostatic forces were analyzed. The change in density that occurs near the interface was also discussed.

Further, due to the asymmetry of surface force fields as mentioned here, the outermost layer of surface molecules in a liquid will be expected to be highly structured, for example, in the case of water, leading to well-defined structural orientations such as *polychair* or *polyboat* surface networks.²² In the same way, surface tension can be described by quantitative structure–property relationship (QSPR) or the so-called parachor (as described in the following section).

3.2 THE PARACHOR

In all kinds of technology, it is most useful to be able to predict the physical property of a molecule from some theoretical criteria. Many physical properties of molecules in the bulk phase can be related to their composition and structure.²³ This is very convenient when we need to be able to predict the properties of any molecule and also from a theoretical viewpoint, which gives us a more molecular understanding of the different forces present in any system. At a very early stage, it was accepted that the same could be expressed for surface tension and bulk characteristics. The most significant observation was that the expression relating surface tension with density was independent of temperature:

$$\gamma^{1/4} / (p_L - p_G) = C_{\text{para}} \quad (3.7)$$

TABLE 3.1
Quantitative Structural Relationships for Estimating the Parachor Values

Reference	Parachor Values									
	C	H	O	F	Cl	Br	I	N	S	P
i(24)	4.8	17.1	20	25.7	54.3	68	91	12.5	48.2	38.2
ii(25)	7.2	16.2	20	25	53.5	68	90	13	48.5	37
iii(26)	4.8	16	20	25	54.3	68	90	12.5	48.2	39.2

Reference	Parachor Values									
	CH ₃	CH ₂	C ₆ H ₅	COO	COOH	OH	NH ₂	NO ₂	NO ₃	CONH ₂
iv(23)	55.5	40.1	189.6	63.8	73.8	29.8	42.5	74	93	91.7

was useful in the determination of molecular properties.²⁴ After multiplication of both sides by the molecular weight, M_w , the constant, C_{para} , is called the parachor (P_{para}):

$$P_{para} = C_{para} M_w = M_w \gamma^{1/4} / (p_L - p_G) \quad (3.8)$$

The parachor quantity, P_{para} , is primarily an additive term such that each group of molecules contributes to the same extent in a homologous series. If one neglects p_G in comparison to p_L (an error of less than 0.1%), then we obtain:

$$\begin{aligned} P_{para} &= M_w \gamma^{1/4} / p_L \\ &= V_m \gamma^{1/4} \end{aligned} \quad (3.9)$$

where V_m is the molar volume of the liquid. The adaptivity of parachors is thus equivalent to that of atomic volumes measured under unit surface tension, which is regarded to be approximately the same as under equal internal pressures.

The atomic and constitutional parachor values are given in Table 3.1.²⁵⁻²⁷ Furthermore, the parachor values for single bond (sb); coordinate bond (cb); double bond (db); triple bond (tb); single-electron bond (seb); 3-, 4-, 5-, 6-, 7-, or 8-membered rings (3r, etc.); and a naphthalene ring (na) were given as follows:²³

Parachor Values											
seb	sb	cb	db	tb	3r	4r	5r	6r	7r	8r	na
-11.6	0	-1.6	23.2	46.6	16.7	11.6	8.5	6.1	4.6	2.4	12.2

As an example, the calculated value for toluonitrile, C₆H₄CH₃CN, is found as:

$$8 \times 4.8 + 7 \times 17.1 + 1 \times 12.5 + 46.6 + 3 \times 23.2 + 6.1 = 292.9$$

The measured values of parachor are 290.6 for the ortho, 295.5 for the meta, and 294.4 for the compound.

A parachor relation between refractive index, n , and surface tension, γ , was also formulated as follows:^{28a}

TABLE 3.2
Parachor from Refractive Index

	Acetone	Ethyl-iodide	Ethanol	<i>n</i> -Octane	Nitromethane
$\gamma_{\text{calculate}}$	23.35	28.05	21.92	21.30	35.38
γ_{measure}	23.09	28.10	22.03	21.32	35.6

$$(P) = R_1 \gamma^{1/4} / (n_2 - 1) / (n_2 + 2) \quad (3.10)$$

where R_1 is the Lorentz–Lorenz molecular fraction relation:

$$R_1 = n_2 - 1 / n_2 + 2(M/d) \quad (3.11)$$

Some typical parachor calculated values are given in Table 3.2.

Parachors in solution can also be estimated, but it has been reported to be more difficult. This arises from the fact that the composition of the surface is different from that of the bulk phase. The present state of analysis is not very satisfactory.²³ Furthermore, the parachor theory for interfacial tension remains to be investigated; therefore, some suggestions will be developed in this chapter. However, many data are found in literature where surface tension for various mixed systems is given along with density, refractive index, and viscosity:^{28b}

- Density and surface tension of aqueous H_2SO_4 at low temperature^{28b}
- Density, viscosity, and surface tension of sodium carbonate + sodium bicarbonate buffer solutions in the presence of glycerine, glucose, and sucrose from 25 to 40°C^{28b}
- Density, surface tension, and refractive index of aqueous ammonium–oxalate solutions from 293 to 333 K^{28b}
- Surface tensions, refractive indices, and excess molar volumes of hexane + 1-alkanol mixtures at 298.15 K^{28b}
- Densities, viscosities, refractive indices, and surface tensions of 4-methyl-2-pentanone + ethyl benzoate mixtures at 283.15, 293.15, and 303.15 K^{28b}

3.3 HEAT OF SURFACE FORMATION AND HEAT OF EVAPORATION

All natural phenomena are dependent on temperature and pressure. As mentioned earlier, energy is required to bring a molecule from the bulk phase to the surface phase of a liquid. In the bulk phase, the number of neighbors (six near neighbors for hexagonal packing if considering only two-dimensional packing) will be roughly twice the molecules at the surface (three near neighbors, when discounting the gas phase molecules) (Figure 3.5).

The interaction between the surface molecules and the gas molecules will be negligible as the distance between molecules in the two phases will be very large. Furthermore, as explained elsewhere, these interaction differences disappear at the critical temperature. It was argued^{15,29} that when a molecule is brought to the surface of a liquid from the bulk phase (where each molecule is symmetrically situated with respect to each other), the work done against the attractive force near the surface will be expected to be related to the work spent when it escapes into the vapor phase. It can be shown that this is just half for the vaporization process (see Figure 3.5).

The density, viscosity, and surface tension of liquid quinoline, naphthalene, biphenyl, decafluorobiphenyl, and 1,2-diphenylbenzene from 300 to 400°C, have been reported.⁹⁶

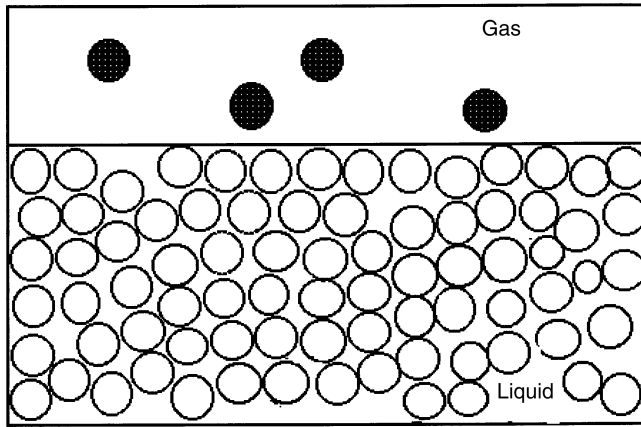


FIGURE 3.5 Molecular packing in two dimensions in bulk (six near neighbors) and surface (three near neighbors) molecules.

In the earlier literature, several attempts were made to find a correlation between the latent heat of evaporation, L_{evap} , and γ or the specific cohesion, a_{co}^2 ($2\gamma/p_L = 2\gamma v_{\text{sp}}$), where p_L = density of the fluid and v_{sp} is the specific volume. The following correlation was given:³⁰

$$L_{\text{evap}}(V_m)^{3/2}/a_{\text{co}}^2 = 3 \quad (3.12)$$

However, later analyses showed that this correlation was not very satisfactory for experimental data. From these analyses it was suggested that there are 13,423,656 layers of molecules in 1 cm³ of water. In [Table 3.3](#) are given some comparisons of this model of a liquid surface as originally described by Stefan.²⁹

It is found that substances that have nearly spherical molecules have Stefan ratios (γ/L_{evap}) of approximately half (three near neighbors at the surface/six near neighbors in the bulk phase). On the other hand, substances with polar groups on one end give much smaller ratios. This suggests that the molecules are oriented with the nonpolar end toward the gas phase and the polar end toward the bulk liquid phase. At this stage, more detailed analysis is needed to describe these relations in more molecular detail. This also requires a method of measuring the molecular structure, which is lacking at this stage. In spite of this, what we conclude is that the molecular analysis is valid as regards the surfaces of liquids. Hence, any changes in surface properties would require only molecules at surfaces, as described below.

It is well known that both the heat of vaporization of a liquid, ΔH_{vap} , and the surface tension of the liquid, γ , are dependent on temperature and pressure, and they result from various intermolecular forces existing within the molecules in the bulk liquid.

To understand the molecular structure of liquid surfaces, we may consider this system in a somewhat simplified model. The molecular surface energy, Σ_{mse} , was defined by Eotvos³¹ (in 1886) as the surface energy on the face of a cube containing 1 mol of liquid:

$$\Sigma_{\text{mse}} = \gamma (M_w v_{\text{sp}})^{2/3} \quad (3.13)$$

where v_{sp} is the specific volume and M_w is the molecular weight. The molar internal heat of evaporation, L_{evap} , can be given as

TABLE 3.3
Enthalpy of Surface Formation, h_s
(10^{-14} erg/molecule), and Ratios of
Evaporation, L_{evap} (10^{-14} erg/molecule),
at a Reduced Temperature ($T/T_c = 0.7$)

Molecule	h_s	h_s/L_{evap}
Nitrogen	3.84	0.51
Oxygen	4.6	0.50
CCl_4	18.2	0.45
C_6H_6	18.4	0.44
Diethylether	15.6	0.42
ClC_6H_5	20.3	0.42
Methyl formamate	15.4	0.40
Ethyl acetate	18.3	0.4
Acetic acid	11.6	0.34
Water	14.4	0.28
Ethyl alcohol	11.2	0.19
Methyl alcohol	8.5	0.16
Mercury	20	0.64

Source: Adapted from Stefan, J., *Ann. Phys.*, 27, 448, 1886.

$$L_{\text{evap}} = L_e - pM_w(v_G - v_L) \quad (3.14)$$

and

$$\gamma(M_w v_{\text{sp}})^{2/3} = 12L_{\text{evap}} \quad (3.15)$$

The correct value for the molar surface energy is probably not the face of a cube representing the molecular volume:

$$\text{molecular volume} = M_w(v)^{2/3} \quad (3.16)$$

but rather the area of the sphere containing 1 mol of the liquid:

$$\begin{aligned} \text{molecular surface area} &= 4\pi(3/4\pi)^{2/3}(M_w v)^{2/3} \\ &= 4.836(M_w v)^{2/3} \end{aligned} \quad (3.17)$$

The amount of heat required to convert 1 g of a pure liquid into saturated vapor at any given temperature is called the latent heat of evaporation or latent heat of vaporization, L_{evap} . It has been suggested that

$$\begin{aligned} \text{latent heat of evaporation}/2\gamma &= L_{\text{evap}}/2\gamma \\ &= \text{area occupied by all molecules} \\ &\text{if they lie in the surface} = A_{\text{mol}} \end{aligned} \quad (3.18)$$

Then we can write:

$$\text{diameter } A_{\text{mol}} = v_{\text{sp}} \quad (3.19)$$

Hence,

$$\text{diameter} = 2\gamma v_{\text{sp}} / L_{\text{evap}} \quad (3.20)$$

For example, for water,

$$\begin{aligned} L_{\text{evap}} &= 600 \text{ g cal} \\ &= 600 \times 42,355 \text{ g cm} = 25,413,000 \\ v_{\text{H}_2\text{O}} &= \sim 1 \text{ g/cc} \\ \gamma_{\text{oc}} &= 88 \text{ dyn/cm} = 0.088 \text{ N/m} \end{aligned} \quad (3.21)$$

From this, we find

$$\begin{aligned} \text{diameter of water molecule} &= 2 \times 0.088 \times 1 / (2,541,300) = 0.7 \times 10^{-8} \text{ cm} \\ &= 0.7 \text{ \AA} = 0.07 \text{ nm} \end{aligned} \quad (3.22)$$

which is of the right order of magnitude.

In a later investigation,³² a correlation between heat of vaporization, ΔH_{vap} , and the effective radius of the molecule, R_{eff} , and surface tension, γ , was given:

$$\Delta H_{\text{vap}} = C_1 \gamma R_{\text{eff}}^2 + C_2 \quad (3.23)$$

These analyses show that a correlation between enthalpy and surface tension exists that is dependent on the size of the molecule. It thus confirms the molecular model of liquids. More investigations are required at this stage before a molecular model can be delineated.

3.4 EFFECT OF TEMPERATURE AND PRESSURE ON THE SURFACE TENSION OF LIQUIDS

As already mentioned, all natural processes are dependent on the temperature and pressure variations in the environment. The molecular interactions in the surface (two dimensional) are by one order of magnitude less than in the bulk (three dimensional). As the temperature increases, the kinetic energy of the molecules increases. This effect thus provides the means of obtaining information about molecular interactions in different systems and interfaces. Molecular phenomena at the surface separating the liquid and the saturated vapor (or the liquid and the walls of its containing vessel) are appreciably more complex than those that occur inside the homogeneous liquid, and it is difficult to state much of a rigorous qualitative nature concerning them. The essential difficulty is that from the microscopic standpoint there is always a well-defined surface of separation between the two phases, but on the microscopic scale there is only a surface zone, in crossing which the structure of the fluid undergoes progressive modification. It is in this surface zone that the dynamic equilibrium between the molecules of the vapor and those of the liquid is established. Owing to

the attractive forces exerted by the molecules of the liquid proper on one another, only the fast moving molecules can penetrate the layer and escape into the vapor; in the process, they lose kinetic energy and, on average, attain the same velocity as the molecules in the vapor.

Further, the number of molecules escaping cannot, on the average, exceed the number entering from the much rarer vapor. From a statistical point of view, the density of the fluid is the most important variable in the surface area; it does not, of course, suffer an abrupt change but varies continuously in passing through the surface zone from its value in the liquid to the generally much lower value in the vapor (a decrease by a factor of ~ 1000). In consequence, it is possible to specify only rather arbitrarily where the liquid phase ends and the gaseous phase begins. It is convenient to some extent to define the interface as a certain surface of constant density within the surface zone such that if each of the two phases remains homogeneous up to the surface, the total number of molecules would be the same.^{15,16}

The work required to increase the area of a surface is the work required to bring additional molecules from the interior to the surface. This work must be done against the attraction of surrounding molecules. Because cohesive forces fall off very steeply with distance, we can consider as a first approximation interactions between neighboring molecules only. There is strong evidence that the change of density from the liquid phase to vapor is exceedingly abrupt, as transitional layers are generally only one or two molecules thick.

Perhaps the most convincing evidence is that derived from the nature of the light reflected from the surfaces of liquids. According to Fresnel's law of reflection, if the transition between air and a medium of refractive index, n , is absolutely abrupt, the light is completely plane polarized if the angle of incidence is the Brucetarian angle. But, if the transition is gradual, the light is elliptically polarized. It was found^{5,33} that there is still some small amount of residual ellipticity in the cleanest surfaces of water and that these scatter light to some extent.

The structure of liquid surfaces has been described by using a hybrid approach of thermodynamics and super liquids.³ Even though the surface tension phenomenon of liquids has been extensively studied, the transition region where surface tension is present has not been successfully described.

3.4.1 CORRESPONDING STATES THEORY

To understand the molecular structure of liquid surfaces, it is important to be able to describe the interfacial forces as a function of temperature and pressure. As temperature increases, the kinetic energy increases due to the increase in the molecular movement. This effect on the change in surface tension gives information on the surface entropy. Although a large number of reports are found in the literature at this stage, complete understanding of surface energy and entropy has not been achieved. In the following some of these considerations will be delineated.

The magnitude of γ decreases almost linearly with temperature within a narrow range:^{17,19,23}

$$\gamma_t = \gamma_o (1 - k_o t) \quad (3.24)$$

where k_o is a constant and t is temperature ($^{\circ}\text{C}$). It was found that the coefficient k_o is approximately equal to the rate of decrease of density (ρ) with rise of temperature:

$$\rho_t - \rho_o (1 - k_d t) \quad (3.25)$$

Values of constant k_d were found to be different for different liquids. Furthermore, the value of k_d was related to T_c (critical temperature) and critical pressure.¹⁸

The following equation relates surface tension of a liquid to the density of liquid, ρ_L , and vapor, ρ_V :³⁴

TABLE 3.4
Typical Data of Variation
of Surface Tension with
Temperature of Different Liquids

Fluid	T (K)	γ (mN/m)	$\delta\gamma/\delta T^a$ (dyn/cm/K)
H ₂ O	293.2	72.8	-0.16
NaCl	1076	114	-0.07
Zn	693.2	782	-0.17
Hg	235.2	498	-0.2

^a Equal to $-s_s$ surface entropy.

Source: Adapted from Takahashi, R., *Jpn. J. Appl. Phys.*, 2(1), 17, 1983.

$$\gamma / (\rho_L - \rho_V)^{2/3} = C_{mc} = \sim 3 \quad (3.26a)$$

where the value of constant C_{mc} is only nonvariable for organic liquids, while it is not constant for liquid metals.

The effect of temperature (at constant pressure) on surface tension is different for different fluids (Table 3.4).⁵ This is the surface entropy, s_s ($-d\gamma/dT$). Thus, we can obtain much useful information from this regarding thermodynamics and the molecular interactions. As shown later, the effect of temperature can also give information about the surface orientation of the molecules.

These data are given here merely to indicate how surface tension is characteristic for a given fluid, as we can estimate from the effect of temperature. We clearly observe the range in γ and the variation in s_s for the various types of fluids.

At the critical temperature, T_c , and the critical pressure, P_c , p of liquid and vapor is identical; the surface tension, γ , and total surface energy, like the energy of vaporization, must be zero.

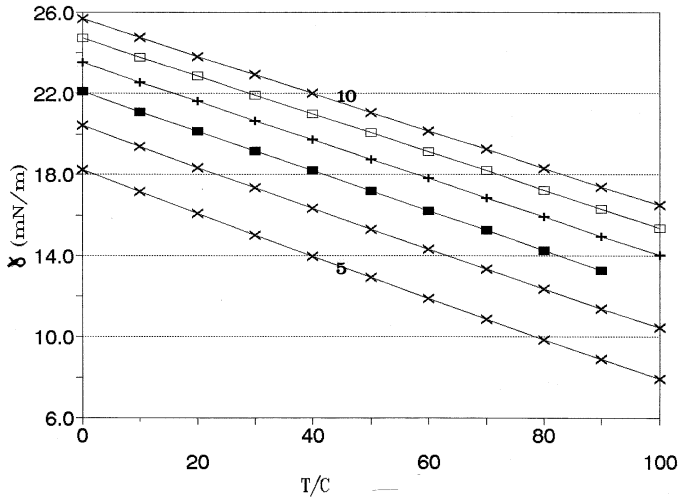
At critical temperature, T_c , and critical pressure, P_c :

$$(d\gamma/dT)_{T \rightarrow T_c, P \rightarrow P_c} = 0 \quad (3.26b)$$

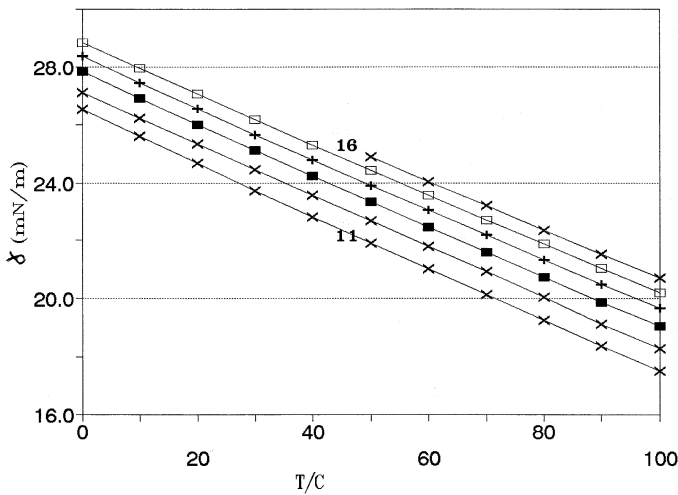
In current literature erroneously the term P_c is omitted in this equation.^{34a} It also needs to be emphasized that T_c and P_c exist simultaneously, by definition.

At temperatures below the boiling point, which is $2/3T$, the total surface energy and the energy of evaporation are nearly constant. The surface tension, γ , variation with temperature is given in [Figure 3.6](#) for different liquid n -alkanes with a number of carbon atoms from 5 (C_5) to 18 (C_{18}).³⁵

These data clearly show that the variation of γ with temperature is a very characteristic physical property of a given liquid, analogous to other bulk properties such as boiling point, heat of vaporization, density, viscosity, compressibility, and refractive index. In other words, the molecules at the surface of the alkanes exhibit dependence on chain length, which can be related to some of these bulk properties. The surface entropy is almost a linear function of n_c ([Table 3.5](#)). These data provide very useful information about the molecular structures at the surface. This observation becomes even more important when considering that the sensitivity^{16,17} of γ measurements can be as high as approximately ± 0.001 dyn/cm (mN/m). It is seen that the magnitude of the extrapolated value of γ at $T = 0^\circ\text{C}$ increases with alkane chain length, n_c . This means that γ increases with



(a)



(b)

FIGURE 3.6 Variation of γ vs. temperature for n_c for n -alkanes. (a) For n_c from 5 to 10; (b) for n_c from 11 to 16.³⁵

increasing van der Waals interactions between chains, analogous to heat of vaporization, melting point, and other molecular properties. The data thus show how such useful physical measurements can be related to the molecular property of a homologous series of molecules.

These data clearly show that the magnitude of γ is proportional to the chain length of the alkanes. This is to be expected based on the previous relation given by Stefan on the dependence of the magnitude of γ on the heat of evaporation. The data of surface tension vs. temperature can be analyzed as follows. It is well known that the corresponding states theory can provide much useful information about the thermodynamics and transport properties of fluids. For example, the most useful two-parameter empirical expression that relates the surface tension, γ , to the critical temperature is given as^{18b}

TABLE 3.5
Linear Equation^a for Data of γ vs. Temperature
for *n*-Alkanes in Figure 3.6

Alkane (n_c)	A_o	$B_{s,s}$ ($-d \gamma/dT$)	Extrapolated Value of γ^b
5	18.25	0.1102	77
6	20	0.1022	75
7	22.10	0.098	76
8	23.52	0.0951	75
9	24.72	0.0935	75
10	25.67	0.092	75
11	26.46	0.0901	75
12	27.12	0.08843	75
13	27.73	0.0872	75
14	28.30	0.0869	75
15	29	0.08565	75
16	29	0.0854	75
17	29	0.0846	75
18	30	0.08423	75
19	30	0.0837	75
20	31	0.0833	75

^a $\gamma = A_o - B_{s,s} T$, where T is $^{\circ}\text{C}$. Magnitude of A_o is the extrapolated value of γ at $T = 0^{\circ}\text{C}$.

^b At $T = -540^{\circ}\text{C}$ (see text).

$$\gamma = k_o \left(1 - T/T_c\right)^{k_1} \quad (3.27)$$

where k_o and k_1 are constants. van der Waals derived this equation and showed that the magnitude of constant $k_1 = 3/2$, although the experiments indicated that $k_1 = \sim 1.23$. Guggenheim³⁶ has suggested that $k_1 = 11/9$.

Moreover, the quantity $k_o = (V_c)^{2/3}/T_c$ was suggested³⁷ to have a universal value² of ~ 4.4 ; however, for many liquids, the value of k_1 lies between $6/5$ and $5/4$. Thus, the *correct* relation is given as

$$\gamma = (V_c)^{2/3} / T_c \left(1 - T/T_c\right)^{k_1} \quad (3.28)$$

It is thus seen that surface tension is related to T_c and V_c . van der Waals^{17,19,23} also found that k_o was proportional to $(T_c)^{1/3} (P_c)^{2/3}$.

The above equation, when fit to the surface tension, γ , data of liquid CH_4 , has been found to give the following relation:^{38a}

$$\gamma_{\text{CH}_4} = 40.52 \left(1 - T/190.55\right)^{1.287} \quad (3.29)$$

where $T_{c,\text{CH}_4} = 190.55 \text{ K}$. This equation has been found to fit the γ data for liquid methane from 91 to -190°C , with an accuracy of $\pm 0.5 \text{ mN/m}$. Although the theory predicts that the exponent is

valid only asymptotically close to the critical point, the surface tension corresponding states theory with additional expansion terms has been shown to be valid for many pure substances over their entire liquid range.^{38a}

In a different context, the surface tension of a fluid, γ_a , can be related to that of a reference fluid, γ_{ref} , as follows:^{38b}

$$\gamma_a(T) = \left(T_{a,c}/T_{\text{ref},c}\right) \left(V_{\text{ref},c}/V_{a,c}\right)^{2/3} \gamma_{\text{ref}} \left(T_{\text{ref},c}/T_{a,c}\right) \quad (3.30)$$

where T is the temperature, $T_{a,c}$ and $V_{a,c}$ are the critical temperature and volume of fluid under consideration, respectively. Similarly, the terms $T_{\text{ref},c}$ and $V_{\text{ref},c}$ refer to the critical temperature and volume of the reference fluid, respectively. This procedure was found to predict the temperature dependence of γ of various fluids and mixtures (such as CO_2 , ethane, butane, hexane, octane, hexane + ethane, hexane + CO_2). The variation of γ of a mixture of hexane + ethane was almost linear with the mole fraction of hexane, x_{C_6} :

$$\gamma_{\text{C}_6+\text{C}_2} = 0.64 + 17.85x_{\text{C}_6} \quad (3.31)$$

This means that we can estimate the concentration of dissolved ethane from such γ measurements. Similar analyses of $\text{C}_6 + \text{CO}_2$ data gives almost the same relationship as for $\text{C}_6 + \text{C}_2\text{H}_6$. This indicates that in a mixed system the addition of a gas to a fluid simply reduces the magnitude of γ in the mixture, as the extrapolated plot tends toward almost zero at a mole fraction of the fluid = 0. That the magnitude of γ of fluids can be measured with a very high accuracy¹⁷ suggests that the solubility of gas (or gases) can be investigated by the γ change. A change in mole fraction by 0.1 unit will give a change in γ of the solution of ~ 2 mN/m. This quantity can be measured with an accuracy of ± 0.001 mN/m, suggesting a gas solubility sensitivity of $\pm 10^{-4}$.

The variation of γ of a large variety of liquids (more than a hundred) is available in literature.^{1a,35} The different homologue series will provide information about the stabilizing forces in these fluids. For example, while alkanes are stabilized mainly by van der Waals forces, the alcohols would be mainly stabilized by both van der Waals forces and hydrogen bonds; the latter is stronger than the former.

To analyze such thermodynamic relations of different molecules, we will take the model system to be a homologous series of normal alkanes and alkenes, as very reliable and accurate data are available in the literature. Linear hydrocarbon chains, n -alkanes, are among the most common blocks of organic matter. They form part of the organic and biological molecules of lipids, surfactants, and liquid crystals and determine their properties to a large extent. As major constituents of oils, fuels, polymers, and lubricants, they also have immense industrial importance. Accordingly, their bulk properties have been extensively studied.

The measured variation in γ with temperature data, near room temperature, was almost linear with temperature for all the alkanes with carbon atoms, n_{C} , from 5 to 18. This means that the magnitude of surface entropy is constant over a range of temperature. A similar observation is made from the analyses of other homologue series of organic fluids (over 100 different molecules):

1. Alkenes³⁵
2. n -Alcohols³⁵
3. CO_2 in liquid state³⁸

The γ data of alkanes were analyzed using Equation 3.27. The constants, k_o (between 52 and 58) and k_1 (magnitude ranging between 1.2 and 1.5), were found to be dependent on the number of carbon atoms, n_{C} ; since T_c is also found to be dependent on n_{C} , the expression for all the different

TABLE 3.6
Calculated γ^a and Measured Values
of Different n -Alkanes at Various Temperatures

n -Alkane	Temperature (C°)	γ (measured)	γ (calculated)
C ₅	0	18.23	18.25
	50	12.91	12.8
C ₆	0	20.45	20.40
	60	14.31	14.3
C ₇	30	19.16	19.17
	80	14.31	14.26
C ₉	0	24.76	24.70
	50	19.97	20.05
	100	15.41	15.4
C ₁₄	10	27.47	27.4
	100	19.66	19.60
C ₁₆	50	24.90	24.90
C ₁₈	30	27.50	27.50
	100	21.58	21.60

^a From Equation 3.33.

Source: Adapted from Birdi, K.S., *Lipid and Polymer Monolayers at Liquid Interfaces*, Plenum Press, New York, 1989; Birdi, K.S., *Self-Assembly Monolayer Structures*, Plenum Press, New York, 1999.

alkanes which individually were fit to Equation 3.31 gave rise to a general equation where γ was a function of n_c and T :¹⁷

$$\gamma = \text{function of } T, n_c \quad (3.32)$$

$$= (41.41 + 2.731n_c - 0.192n_c^2 + 0.00503n_c^3)$$

$$\left(1 - T / \left(273 + -99.86 + 145.4(\ln(n_c)) + 17.05(\ln(n_c^2)^{k_1}) \right) \right) \quad (3.33)$$

where

$$k_1 = 0.9968 + 0.04087n_c - 0.00282(n_c)^2 + 0.000844(n_c)^3 \quad (3.34)$$

The estimated values from the above equation for γ of different n -alkanes were found to agree with the measured data within a few percent: γ for n -C₁₈H₃₈, at 100°C, was 21.6 mN/m, both measured and calculated. This shows that the surface tension data of n -alkanes fit the corresponding state equation very satisfactorily (Table 3.6). In this analysis the pressure is assumed to be constant. Furthermore, by using this relationship, we do not need any elaborate tables of data. Especially by using a computer program we can find γ values rapidly and accurately, as a function of both n_c and T . However, the effect of pressure must not be considered negligible, as delineated later. More

TABLE 3.7
Comparison of Measured and Estimated^a Values
of $T_{c,1atm}$ at $\gamma = 0$ for Different n -Alkanes^b

n_c	$T_{c,\gamma=0}$ (C°) (estimated)	$T_{c,at P_c}$ (measured)	Δ^d	Δ/n_c^e	P_c /bar (measured)
5	166	197	31	6	33.2
6	200	234	34	6	30.1
7	216	267	51	7	27.4
8	240	296	56	7	24.9
9	260	320	60	7	23.4
10	279	344	65	6.5	21.2
11	294	364	70	6.3	19.9
12	307	385	78	6	18.5
13	318	403	85	6	17.2
14	326	420	94	6	14.4
15	336	434	98	6	15.2
16	342	449	107	6	14.1
17	350	460	110	6	13
18	356	475	119	6	12
19	361	483	121	6	11.1
20	367	494	127	6	11

^a From γ vs. T data to $\gamma = 0$.

^b Extrapolated from data in Figure 3.6.

^c See Reference 39.

^d $T_{c,\gamma>0} - T_{c,estimated}$.

^e $T_{c,\gamma>0} - T_{c,estimated}/n_c$.

studies are needed on similar homologue series of liquids, to understand the relation between molecules and surface tension.

The physical analyses of the constants k_0 and k_1 have not been investigated at this stage. Further, as QSPR models can predict relations between molecular structures and boiling points,³⁹⁻⁴¹ it should be possible to extend these models to surface tension prediction based on the above relation. A general and semiempirical correlation between the alkane chain length and surface tension has been described.⁴²

It is worth mentioning that the equation for the data of γ vs. T for polar (and associating) molecules such as water and alcohols, when analyzed by the above equation, gives magnitudes of k_0 and k_1 that are significantly different from those found for nonpolar molecules such as alkanes, etc. This observation therefore requires further analysis to understand the relation among γ , surface entropy, and T_c (as well as P_c and V_c).

The critical constants of a compound are of both fundamental and practical interest. Furthermore, sometimes the critical constants are not easily measured, due to experimental limitation. In Table 3.7, the estimated data for $\gamma_t = 0$ (at $t = 0^\circ\text{C}$) and the magnitude of $d\gamma/dT$ (surface entropy) for a variety of liquids are given. For a very practical approximate estimation of T_c we can use these data as

$$T_c = \gamma_{t=0} / (d\gamma/dT) \quad (3.35)$$

where T is in °C. The calculated value for water $T_c = 75.87/0.1511 + 273 = 502$ K. This compares with the measured value of 647 K. The data for C_6H_6 give $T_{c,C_6H_6} = 226.4^\circ\text{C}$ (499 K), as compared with the measured value of 561 K. The estimated values are lower, as expected.

In the case of n -alkanes, the linear part (see Figure 3.6) was extrapolated to $\gamma = 0$ to estimate $T_{c,c}$. The analyses of the alkane data for C_5 to C_{20} is of much interest in this context, from both a theoretical and practical point of view. If we merely extrapolate the linear part of the measured data (at 1 atm), then the estimated $T_{c,1\text{atm}}$ is found to be somewhat lower (~10%, dependent on n_c) than the directly measured values (Table 3.7). As we observe here, the magnitudes of T_c for these alkanes can be very high. This may lead, in some cases, to decomposition of the substance if measurements are made directly. On the other hand, if we can use the present surface tension data to estimate $T_{c,c}$, then it can provide much useful information.

The difference between the estimated T_c (lower in all cases) and the measured T_c (range measured from 200 to 500°C at P_c) per carbon atom is found to be 6°. This gives values of estimated T_c within a 5% error for alkanes with n_c from 5 to 20. This finding is of great significance.

One of the most important consequences is that, in the case of fluids that are unstable at high temperatures, we need only measure the variation of surface tension with temperature, from which we can estimate the value of T_c . The correction required arises from the effect of P_c on γ .

We can thus show from these data that for n -alkanes:

$$T_{c,\gamma 0} = T_c - n_c 6$$

Or, we can rewrite

$$T_c = T_{c,\gamma 0} + n_c 6 \quad (3.36)$$

This shows convincingly that an increase in pressure gives rise to an increase in surface tension, i.e., $d\gamma/dP = +$. However, the need for this correction is expected; if we consider the fact that at the critical point the pressure is not 1 atm but P_c , then a correction would be needed. For example, the T_c and P_c for alkanes of n_c equal to 12 and 16 are 658 K and 18 atm and 722 K and 14 atm, respectively (Table 3.7). In fact, all the relations as found in the literature that neglect critical pressure are in error.

To modify the data of γ vs. T at 1 atm to include the effect of pressure, P_c , then this would give an increase in surface tension, as the quantity $d\gamma/dP$ is positive for liquids.¹⁷ In other words, the analyses of surface tension vs. temperature data must be reformulated to include the effect of P_c on the surface tension data, as shown in Figure 3.7. The measured γ data is obtained at 1 atm.

The extrapolated line is moved from 1 atm to P_c and moved up by a value that corresponds to $d\gamma/dP$ (positive). It is thus possible to estimate the magnitude of $d\gamma/dP$ from such data.

The correction required based on the above is as follows:

$$T_c = \left(\gamma_{t,\text{ref}} + s_s t_{\text{ref}} \right) / s_s + 6(n_c) \quad (3.37)$$

where $\gamma_{t,\text{ref}}$ is surface tension at a given temperature (and at 1 atm) and s_s is the surface entropy. The correction term, second on the right-hand side, arises from the correction necessary to obtain γ at T_c at pressure equal to P_c . Previous studies have shown that an increase in the hydrostatic pressure over gas–water systems can produce marked changes in the surface tension by virtue of enhanced adsorption of the gaseous component at the interface.

It is obvious that when more systematic surface tension data become available, a more detailed molecular description of the significance of this observation can be given. For example, there exists

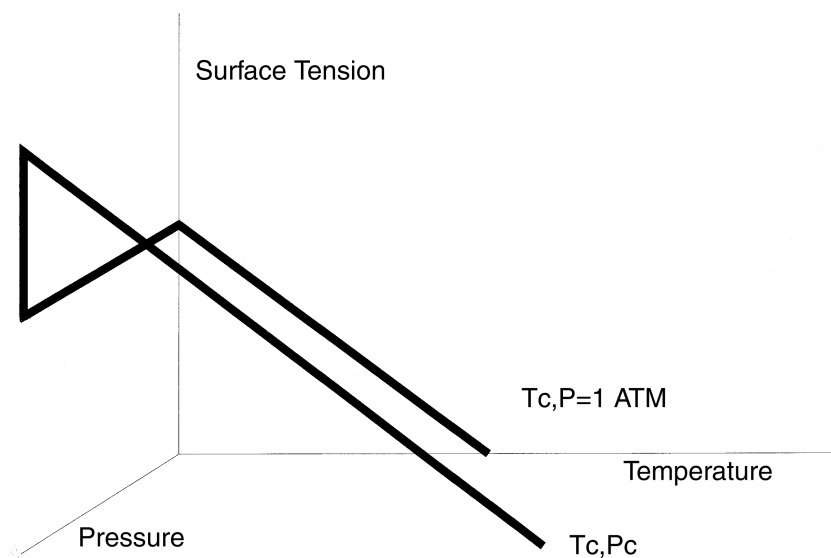


FIGURE 3.7 Variation of surface tension γ vs. temperature (T) and pressure (P).

no such analysis of alkane mixtures (of two or more components). These latter systems are of much interest in enhanced oil-recovery processes.

The γ vs. temperature data for the homologous series n -alkanes and n -alkenes show some unique characteristics. The data for alkanes, on extrapolation to a hypothetical supercooled region, converge at $T_{sc} =$ approximately -540°C , and $\gamma_{sc} = 75 \text{ mN/m}$.^{1a} The calculated values of γ_{sc} are given in Table 3.7 for a homologous series of alkanes. The magnitude of γ_{sc} is estimated as $\sim 75 \text{ mN/m}$ in all cases.

This shows that the alkane molecules in their hypothetical supercooled state at T_{sc} ($-540^\circ\text{C} \gg 2(-273^\circ\text{C})$) exhibit the same surface tension ($\gamma_{sc} = 75 \text{ mN/m}$) regardless of chain length. To analyze this in more detail, the surface tension data of alkenes were investigated.^{1a}

These data also exhibit a super cooled temperature, T_{sc} (approximately -540°C), where all the alkene molecules have the same γ_{sc} (75 mN/m). This characteristic property can be ascribed to the fact that long molecule axes will tend to lie along a preferred direction at the interface. This is well recognized in such structures as liquid crystal phases. Thus, at the *supercooled state* at T_{sc} (-540°C), the attractive forces and the repulsive forces in different alkanes exhibit a supercooled state where the dependence on n_c disappears. In other words, all alkanes behave as pseudomethane. Another possibility could be that the *holes* in the alkanes are all filled at a supercooled state, T_{sc} , as expected from Eyring's^{43a} theory for liquids.

From these observations, we can rewrite Equation 3.36 in the case of n -alkanes data relating T_c to s_s and the above supercooled point:

$$\begin{aligned} T_c &= \gamma_{sc}/s_s + 6n_c + T_{sc} \\ &= 75/s_s + 6n_c - 540 \end{aligned} \quad (3.38)$$

where $T_{sc} = -540^\circ\text{C}$. From this relation, we can estimate the values of T_c (within a few percentage accuracy) if we know s_s (or if variation of γ is known for any temperature). Because the change in γ with temperature can be measured with a very high sensitivity ($\pm 0.001 \text{ mN/m}$), then we can estimate T_c with very high accuracy. Of course, currently these analyses have been found to be valid only for n -alkanes with chain lengths from $n_c = 5$ to 20. This observation has many useful

TABLE 3.8
Effect of Alkyl Chain Length (n_c) on the Variation of γ vs. T for Homologous Series of Alkanes or Alkenes and Other Fluids

Homologous Series	Variation of γ with Temperature and n_c
Alkanes	Convergence (at $\gamma = 75$ mN/m and -540°C)
Alkenes	Convergence (at $\gamma = 75$ mN/m and -540°C)
Complicated	Divergence at lower temperature
Alkyl-derivatives	Convergence at $\sim 120^\circ\text{C}$ and $\gamma = \sim 30$ mN/m

aspects. It shows that the concepts as described here regarding the molecular structures of liquids is fairly accurate. Further, the correlation between surface entropy and critical temperature has much theoretical value, especially in all kinds of theoretical model considerations.

The variation of surface entropy for molecules with complex stabilizing forces other than alkanes requires extensive analysis at this stage, although preliminary analysis shows that for more complicated molecules such as alkyl-naphthalene or alkyl-diester homologous series the plots of γ vs. temperature intersect at ~ 30 dyn/cm and 150°C .^{1a}

The γ vs. temperature data for complicated homologue series molecules also showed that molecular packing changes as the alkyl chain changes in a manner different from that in the case of simple alkane molecules. This is as expected, because the molecules are interacting under different kinds of forces. The effect of a change in the alkyl chain length will also be different from that in the case of linear alkanes. The data plots do not converge at lower temperatures, as was observed for alkanes and alkenes. The data, however, do indeed show that the molecules at the surface exhibit the same magnitude of surface tension (i.e., ~ 30 mN/m at 120°C) regardless of the alkyl chain length. Observation of a variety of homologous series of molecules allows us to conclude that the hydrophobic effect arising from the addition of each CH_2 group gives rise to three general types of γ vs. temperature data plots (Table 3.8).

The following observations are important when considering the effect of hydrophobicity on γ and s_s :

1. *n*-Alkanes and *n*-alkenes: Surface tension increases from 18.25 to 29.18, while surface entropy decreases from 0.11 to 0.0854 for C_5 to C_{16} .
2. Alkyl-phosphonates: Surface tension decreases from 39.15 to 30.73, while surface entropy decreases from 0.126 to 0.0869 for C_1 to C_8 phosphonates.
3. Dialkyl-phosphonates and alkyl-diester: Same trend as for alkyl-phosphonates.

These observations require further theoretical analysis at this stage; however, it is sufficient to stress that the method to extrapolate the data to hypothetical states is justified in the case of alkanes and alkenes.

Surface tension of any fluid can be related to various interaction forces, e.g., van der Waals, hydrogen bonding, dipole, and induction. The above analyses of the alkanes thus provide information about the van der Waals forces only. In other homologous series, such as alcohols, we can expect that there are both van der Waals and hydrogen bonding contributions. We can thus combine these two kinds of homologous series of molecules and analyze the contribution from each kind of interaction.

The magnitude of surface tension, γ , has also been calculated from statistical theory and molecular orientations at the free surface in nematic liquid crystals.^{43b}

These calculations were carried out based on a model of the mean field approximation in the system of rodlike molecules interacting via attraction as well as hard-core repulsion. Excluded volume effect was found to give favorable results regarding the alignment of molecules at the free surface. Experimental data⁴⁴ have shown a jump in the surface tension, T_c ; however, the estimation of the jump in surface tension was considerably larger than the experimental data.

As the shape of molecules is known to affect the thermodynamic properties of real fluids and fluid mixtures, more investigations are necessary. This arises from the fact that all intramolecular forces are dependent on the distance between the molecules. Hence, in the case of nonspherical or asymmetrically shaped molecules the distance will be dependent on the nonsymmetric surfaces of the molecule. Surface tension measurements are thus found to provide much useful information about this aspect.

In the studies of surface tension of liquids we need data for calibration of instruments at different temperatures. The variation of γ for water with temperature, $t(^{\circ}\text{C})$, is given as follows by various investigators.

By Harkins,¹⁴

$$\gamma_{\text{water}} = 75.680 - 0.138t - 0.05356t^2 + 0.0647t^3 \quad (3.39)$$

The high accuracy is important in such data, as we use these for calibration purposes. More recent and reliable data by Cini et al.⁴⁵ indicate that

$$\gamma_{\text{water}} = 75.668 - 0.1396t - 0.2885 \cdot 10^{-3}t^2 \quad (3.40)$$

The surface entropy, S_s , corresponding to the above equation is

$$S_s = -d\gamma/dT = k_1 k_o (1 - T/T_c) k_1 - 1/(T_c) \quad (3.41)$$

and the corresponding expression for surface enthalpy, H_s , is

$$\begin{aligned} H_s &= \gamma - T(d\gamma/dT) \\ &= k_o (1 - T/T_c) k_1 - 1 \left(1 + (k_1 - 1) T/T_c \right) \end{aligned} \quad (3.42)$$

Surface tension is a type of Helmholtz free energy, and the expression for surface entropy is $s_s = -d\gamma/dT$. Hence, an amount of heat (H_s) must be generated and absorbed by the liquid when the surface is extended. The reason heat is absorbed upon extending a surface is that the molecules must be transferred from the interior against the inward attractive force to form the new surface. In this process, the motion of the molecules is retarded by this inward attraction, so that the temperature of the surface layers is lower than that of the interior, unless heat is supplied from outside.^{15,18b}

These analyses thus confirm the assumptions made regarding the molecular structure of the interfacial region as compared with the bulk phase. The surface entropy provides a very useful description of the molecular interactions in the interface of a liquid. The values of surface entropy ($-d\gamma/dT$ at 0°C) for a range of liquids are given in [Table 3.9](#). The data clearly show how the surface entropy describes the molecular properties of the different liquids. The magnitude of surface entropy varies from 0.07 to 0.16 mN/mT.

The following surface tension data for benzene, C_6H_6 , and ethyl ether are analyzed by using the above relations for estimating T_c . The surface tension data measured under pressure close to

TABLE 3.9
Magnitudes of Surface Tension, γ (mN/m) and Surface Entropy^a
for Different Liquids

Liquid	Surface Tension	$-d\gamma/dT$	Liquid	Surface Tension	$-d\gamma/dT$
H ₂ O	75.87	0.1511	[CH ₂ Cl] ₂	35.31	0.139
CS ₂	35.71	0.1607	[CH ₂ Br] ₂	40.51	0.131
CH ₃ OH	23.5	0.071	CH ₃ NO ₂	36.69	0.146
C ₂ H ₅ OH	23.3	0.080	C ₂ H ₅ NO ₂	34.92	0.120
C ₃ H ₇ OH	25.32	0.081	Methyl-formate	28.50	0.157
C ₄ H ₉ OH	26.11	0.081	Ethyl-formate	26.30	0.136
C ₂ H ₄ (OH) ₂	49.34	0.0935	Ethyl-acetate	26.84	0.127
Glycerol	65.28	0.0598	Amyl-acetate	27.04	0.098
[C ₂ H ₅] ₂ O	19.31	0.117	Ethyl-propionate	5.73	0.111
C ₆ H ₆	31.7	0.140	Ethyl-malonate	33.6	0.100
Toluene	30.76	0.115	C ₆ H ₅ CN	40.9	0.117
<i>o</i> -Xylene	31.06	0.107	Furfural	43.5	0.096
<i>m</i> -Xylene	29.7	0.106	Thiophene	33.5	0.113
<i>p</i> -Xylene	29.31	0.115	Pyridine	38.1	0.136
Hexane	21.31	0.1032	Picoline	36.6	0.118
Octane	23.36	0.092	Quinoline	47.0	0.122
Decane	23.76	0.084	Piperidine	30.6	0.118
CHCl ₃	28.77	0.1134	Benzamide	47.20	0.070
C ₂ H ₅ I	33.53	0.137	Phenyldiazine	44.02	0.076

^a $-d\gamma/dT$ at 0°C.

Source: Adapted from Partington, J.R., *An Advanced Treatise on Physical Chemical*, Vol. II, Longmans, Green, London, 1951.

T_c are compared with the estimated values (Table 3.10). This analysis clearly shows that more investigations are necessary in this area of research.

In a recent study,¹⁹ a new model of fluids was described by using the generalized van der Waals theory. Actually, van der Waals over 100 years ago suggested that the structure and thermodynamic properties of simple fluids could be interpreted in terms of neatly separate contributions from intermolecular repulsions and attractions. A simple cubic equation of state was described for the estimation of the surface tension. The fluid was characterized by the Lennard–Jones (12–6) potential. In a recent study the dependence of surface tension of liquids on the curvature of the liquid–vapor interface has been described.^{36a}

3.5 SURFACE TENSION OF LIQUID MIXTURES

All industrial liquid systems are made up of more than one component, which makes the studies of mixed liquid systems important. The analyses of surface tension of liquid mixtures (for example, two or three or more components) has been the subject of studies in many reports.^{16,36,37,46-52} According to Guggenheim's³⁶ model of liquid surfaces, the free energy of the molecule is

$$G_i = k_B T \ln(a_i) \quad (3.43)$$

where a_i is the absolute activity. This latter term can be expressed as

TABLE 3.10
Surface Tension Data of C₆H₆ and Ethylether
at Different Temperatures^a

Temperature (°C)	Surface Tension			
	C ₆ H ₆		(C ₂ H ₅) ₂ O	
	Measured (under pressure)	Estimated (at 1 atm)	Measured	Estimated
0	31.7	31.7	19.31	19.31
20	28.88	30.06	17.01	16.97
50	—	—	13.60	13.46
61	23.61	23.16	—	—
110	—	—	7.00	6.44
120	16.42	14.9	—	—
140	—	—	4.00	2.93
170	—	—	1.42	-0.58
180	9.56	6.5	—	—
240	3.47	-1.9	—	—
T _c = 288.5	0	-8.7	—	—
T _c = 193	—	—	0	-3.3

^a Measured and estimated from data in Table 3.9.

$$a_i = N_i g_i \quad (3.44)$$

where N_i is the mole fraction (unity for pure liquids) and g_i is derived from the partition function.

The free energy can thus be rewritten as

$$\begin{aligned} G_i &= g_i s_i \\ &= k_B T \ln(a_i/a_1^s) \end{aligned} \quad (3.45)$$

where s_1 is the surface area per molecule. This is the free energy for bringing the molecule, a_1 , from the bulk to the surface, a_1^s .

In a mixture consisting of two components, 1 and 2, we can then write the free energy terms as follows for each species:

$$\gamma s_1 = k_B T \ln(N_1 g_1/N_1^s/g_1^s) \quad (3.46)$$

and

$$\gamma s_2 = k_B T \ln(N_2 g_2/N_2^s/g_2^s) \quad (3.47)$$

where N^s is the mole fraction in the surface such that

$$N_1^s + N_2^s = 1 \quad (3.48)$$

As a first approximation we may assume that $s = s_1 = s_2$; that is, the surface area per molecule of each species is approximately the same. This will be reasonable to assume in such cases as mixtures of hexane + heptane, for example. This gives

$$\gamma_s = k_B T \left(\ln(N_1 g_1 g_1^s) + \ln(N_2 g_2 / g_2^s) \right) \quad (3.49)$$

Or, in combination with Equation 3.42, we can rewrite as follows:

$$\exp(-\gamma_s / k_B T) = N_1 \exp(-\gamma_1 s / k_B T) + N_2^2 \exp(-g_2 s / k_B T) \quad (3.50)$$

Hildebrand and Scott³⁷ have given a more expanded description of this derivation.

Using the regular solution theory,³⁶ the relation between activities was given as

$$RT \ln f_1 = -a_1 N_2^2; \quad RT \ln f_2 = -a_1 N_1^2 \quad (3.51)$$

where f_i denotes the activity coefficient. Other analyses by later investigators⁴⁸ gave a different relationship:

$$\gamma_{12} = \gamma_1 N_1 + \gamma_2 N_2 - \beta N_1 N_2 \quad (3.52)$$

where β is a semiempirical constant.

The surface tensions of a variety of liquid mixtures such as carbontetrachloride-chloroform, benzene-diphenylmethane, and heptane-hexadecane⁴⁷ have been reported.

In the case of some mixtures, a simple linear relationship has been observed:

1. Water-*m*-dihydroxy-benzene (resorcinol) in the range of 0.1 to 10.0 *M* concentration gives the following relationship:^{53a}

$$\gamma = 72.75 - 8.0(M_{\text{resorcinol}}) \quad (\text{at } 20^\circ\text{C}) \quad (3.53)$$

2. iso-Octane-benzene mixtures: The surface tension changes gradually throughout. This means that the system behaves almost as an ideal.
3. Water-electrolyte mixtures: The example of water-NaCl shows that the magnitude of surface tension increases linearly from ~72 to 80 mN/m for 0- to 5-*M* NaCl solution ($d\gamma/d \text{ mol NaCl} = 1.6 \text{ mN/mol NaCl}$):^{53b}

$$\gamma_{\text{NaCl}} = 72.75 + 1.6(M_{\text{NaCl}}) \quad (\text{at } 20^\circ\text{C}) \quad (3.54a)$$

In another system: for water-NH₄NO₃:

$$\gamma_{\text{NH}_4\text{NO}_3} = 72.75 + 1.00(M_{\text{NH}_4\text{NO}_3}) \quad (\text{at } 20^\circ\text{C}, m < 2m) \quad (3.54b)$$

It is seen that increase in γ per mol added NaCl is much larger than that for NH₄NO₃. In general, the magnitude of surface tension of water increases on the addition of electrolytes, with a very few exceptions. This indicates that the magnitude of the surface

TABLE 3.11
Surface Tension of *n*-Butanol Solutions at 25°C

	Surface Tension (mol)							
	0.00329	0.00658	0.01320	0.0264	0.0536	0.1050	0.2110	0.4330
γ	72.80	72.26	70.82	68.00	63.14	56.31	48.08	38.87

Source: Adapted from Harkins, R.W. and Wamper, J., *Am. Chem. Soc.*, 53, 850, 1931.

TABLE 3.12
Aqueous Solutions of *n*-Hexanoic Acid Mixtures at 19°C

	Aqueous solutions (mol)						
	0.00212	0.0064	0.0128	0.0212	0.0425	0.068	0.085
γ	70.	63	56	49	40	34	31

Source: Adapted from Lange, A.A. and Forker, G.M., *Handbook of Chemistry*, 10th ed., McGraw-Hill, New York, 1967.

excess term is different for different solutes. In other words, the state of solute molecules at the interface is dependent on the solute. In a recent study a surface tension model for concentrated electrolyte solutions by the Pitzer equation was described.^{53b}

4. *n*-Butanol–water and *n*-hexanoic acid–water mixture data are given in Tables 3.11 and 3.12.^{54,55}

Further, the necessary condition that the local chemical potential difference be constant throughout the interface provides the following expression for the surface tension:^{51a}

$$\gamma \sim l/k_T \left[\left(1 + (d^2 S_{cc}) \right) / \left[(N/V) k_B T k_T \right] \right] - 1 \quad (3.55)$$

where l is the thickness of the liquid surface, d is the size factor, S_{cc} is the concentration fluctuation in the bulk liquid mixture surface, and k_T is the bulk compressibility. However, there is a need for investigations that should help in the usefulness of this relation and data.^{51b}

The data of other diverse mixtures include the following:

1. Ethanol–water mixtures and hydrogen bonding: The ethanol–water mixture is known to be the most extensively investigated system. The addition of even small amounts of ethanol to water gives rise to contraction in volume.⁵⁶ A remarkable decrease of the partial molar volume of ethanol with a minimum at an ethanol molar fraction of 0.08 was observed. The same behavior is observed from heat-of-mixing data. The surface tension drops rather appreciably when 10 to 20% ethanol is present, while the magnitude of surface tension slowly approaches that of the pure ethanol.
2. Surface tension of hydrocarbon + alcohol mixtures: The surface tension of the binary hydrocarbon (benzene, toluene, cyclohexane, methyl-cyclohexane) + alcohol (ethanol, *t*-pentyl alcohol) mixtures were reported⁵⁷ at 303.15 K (30°C).

The effect of temperature on the surface tension of mixtures of *n*-propanol/*n*-heptane has been investigated.^{58,59a} The variation of surface tension by temperature (K) for pure components was

$$\gamma_{\text{propanol}} = 25.117 - 0.0805(T - 273.15) \quad (3.56)$$

$$\gamma_{\text{heptane}} = 22.204 - 0.1004(T - 273.15) \quad (3.57)$$

It is seen that the effect of temperature is lower on a more stable structure as propanol (due to hydrogen bonding) than in heptane, as expected. In a recent study the refractive indices and surface tensions of binary mixtures of 1,4-dioxane + *n*-alkanes at 298.15 K were analyzed.^{59b}

The surface tension of binary mixtures of water + monoethanolamine and water + 2-amino-2-methyl-1-propanol and tertiary mixtures of these amines with water from 25 to 50°C have been reported.^{59c} The surface tension of aqueous solutions of diethanolamine and triethanolamine from 25 to 50°C have been analyzed.^{59d}

3.6 SOLUBILITY OF ORGANIC LIQUIDS IN WATER AND WATER IN ORGANIC LIQUIDS

The process of solubility of one compound into another is of fundamental importance in everyday life; examples are industrial applications (paper, oil, paint, washing) and pollution control (oil spills, waste control, toxicity, biological processes such as medicine). Accordingly, many reports are found in the literature that describe this process both on a theoretical basis and by using simple empirical considerations. As already described here, the formation of a surface or interface requires energy; however, how theoretical analyses can be applied to curvatures of a molecular-sized cavity has not been satisfactorily developed. It is easy to accept that any solubility process is in fact the procedure where a solute molecule is placed into the solvent where a cavity has to be made. The cavity has both a definite surface area and volume. The energetics of this process is thus a surface phenomenon, even if of molecular dimensions (i.e., nm²). Solubility of one compound, S, in a liquid such as water, W, means that molecules of S leave their neighbor molecules (SSS) and surround themselves by WWW molecules. Thus, the solubility process means formation of a cavity in the water bulk phase where a molecule, S, is placed (WWWSWWW). Langmuir¹⁷ (and some recent investigators) suggested that this cavity formation is a surface free energy process for the formation of the cavity.

The solubility of various liquids in water, and vice versa, is of much interest in different industrial and biological phenomena of everyday importance (Table 3.13).⁶⁰ In any of these applications, we would encounter instances where a prediction of solubility would be of interest; the following such applications are mentioned for general interest. Furthermore, solubilities of molecules in a fluid are determined by the free energy of solvation. In more complicated processes such as catalysis, the reaction rate is related to the desolvation effects.

A correlation between the solubility of a solute gas and the surface tension of the solvent liquid was described⁶¹ based on the curvature dependence of the surface tension for C₆H₆, C₆H₁₂, and CCl₄. This was based on the model that a solute must be placed in a hole (or cavity) in the solvent. The change in the free energy of the system, ΔG_{sol} , transferring a molecule from the solvent phase to a gas phase is then

$$\Delta G_{\text{sol}} = 4\pi r^2 \gamma_{\text{aq}} - \epsilon_i \quad (3.58)$$

where ϵ_i is the molecular interaction energy. By applying the Boltzmann distribution law,

TABLE 3.13
Solubilities of Water (w) in Organic Liquids (o) and
Vice Versa, at 298°C

Liquid (o)	X_o in Water	X_w in Organic Phase
<i>n</i> -Pentane	9.5×10^{-6}	0.48×10^{-3}
<i>n</i> -Hexane	1.98×10^{-6}	0.351×10^{-3}
<i>n</i> -Heptane	0.57×10^{-6}	0.61×10^{-3}
<i>n</i> -Octane	0.096×10^{-6}	0.65×10^{-3}
<i>n</i> -Decane	2×10^{-8} ^a	0.572×10^{-3}
<i>n</i> -Dodecane	0.5×10^{-8} ^a	0.615×10^{-3}
Cyclopentane	40.8×10^{-6}	0.553×10^3
Cyclohexane	11.8×10^{-6}	0.47×10^3
Benzene	409.5×10^{-6}	2.74×10^3
<i>n</i> -Butanol	19.2×10^{-3}	0.515
2-Butanol	33.6×10^{-3}	0.765
2-Methyl-1-ol	26.3×10^{-3}	0.456
2-Methyl		
Propan-1-ol (miscible)		
1-Pentanol	4.56×10^{-3}	0.284
2-Pentanol	9.50×10^{-3}	0.396
3-Pentanol	11.1×10^{-3}	0.308
<i>n</i> -Hexanol	1.23×10^{-3}	0.313
1-Heptanol	0.28×10^{-3}	0.3 ^a
1-Octanol	0.745×10^{-4}	0.3 ^a

^a Approximate value.

Source: Adapted from McAuliffe, C., *J. Phys. Chem.*, 70, 1267, 1966.

$$c_g^s/c_g = \exp(-\Delta G_G/k_B T) \quad (3.59)$$

where c_g^s is the concentration of gas molecules in the solvent phase and c_g is their concentration in the gas phase. Combining these equations, we obtain:

$$\ln(c_g^s/c_g) = (-4\pi r^2 g_{aq}/k_B T) + e_i/k_B T \quad (3.60)$$

This model was tested from the solubility data of argon in various solvents (Figure 3.8), where a plot of log (Oswald coefficient) vs. surface tension is given. In the literature, similar linear correlations were reported for other gas (e.g., He, Ne, Kr, Xe, O₂) solubility data.

The solubility of water in organic solvents does not follow any of these aforementioned models. For example, while the free energy of solubility, ΔG_{sol} , for alkanes in water is linearly dependent on the alkyl chain, there exists no such dependence of water solubility in alkanes (see Table 3.13). If the microscopic interfacial tension determines the work of forming a cavity in alkane, then this should be almost the same as the cavity needed in alkane for dissolution of water. Furthermore, very few data in the literature are available concerning the effect of temperature or pressure on solubility.

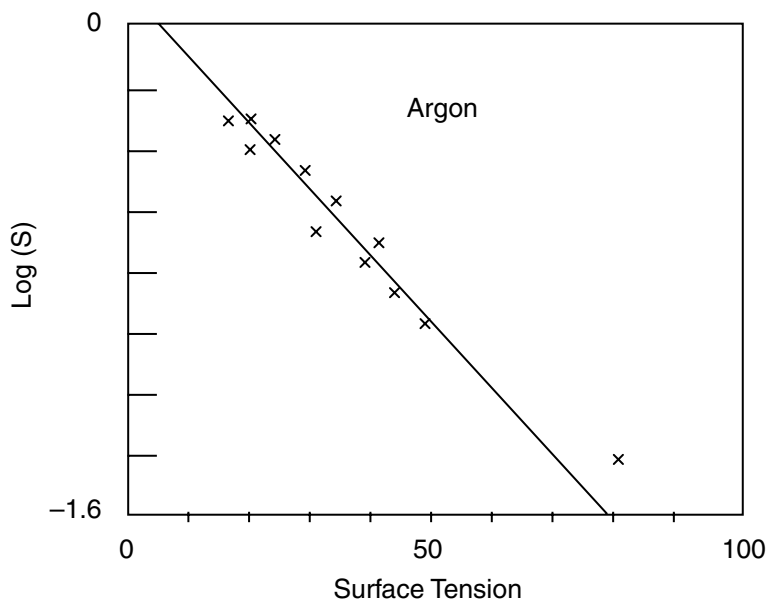


FIGURE 3.8 Solubility of gas, Ar, vs. surface tension, γ , of liquids.⁶¹

3.6.1 THE HYDROPHOBIC EFFECT

All natural processes are in general dependent on the physicochemical properties of water. Amphiphile molecules, such as long-chain alcohols or acids, lipids, or proteins, exhibit polar/apolar characteristics, and the dual behavior is given this designation. The solubility characteristics in water are determined by the alkyl or apolar part of these amphiphiles, which arise from hydrophobic effect.^{17,62-64} Hydrophobicity plays an important role in a wide variety of phenomena, such as solubility in water of organic molecules, oil–water partition equilibrium, detergents, washing and all other cleaning processes, biological activity, and chromatography techniques. Almost all drugs are designed with a particular hydrophobicity as determined by the partitioning of the drug in the aqueous phase and the cell lipid membrane.

The ability to predict the effects of even simple structural modifications on the aqueous solubility of an organic molecule could be of great value in the development of new molecules in various fields, e.g., medical or industrial. There exist theoretical procedures to predict solubilities of nonpolar molecules in nonpolar solvents⁵ and for salts or other highly polar solutes in polar solvents, such as water or similar substances.^{65a} However, the prediction of solubility of a nonpolar solute in water has been found to require some different molecular considerations.

Furthermore, the central problems of living matter comprise the following factors: recognition of molecules leading to attraction or repulsion, fluctuations in the force of association and in the conformation leading to active or inactive states, the influence of electromagnetic or gravitational fields and solvents including ions, and electron or proton scavengers. In the case of life processes on Earth, we are mainly interested in solubility in aqueous media.

The unusual thermodynamic properties of nonpolar solutes in aqueous phase were analyzed,^{65b} by assuming that water molecules exhibit a special ordering around the solute. This water-ordered structure was called the iceberg structure.

The solubility of semipolar and nonpolar solutes in water has been related to the term molecular surface area of the solute and some interfacial tension term.⁶⁶ This model was later analyzed by various investigators in much greater detail.^{16,67-70}

Based on the Langmuir–Herman–Amidon model, the solubility, X_{solute} , in water was given by the following expression:

$$RT(\ln X_{\text{solute}}) = -(\text{surface area of solute})(\gamma_{\text{sol}}) \quad (3.61)$$

where surface tension, γ_{sol} , is some interfacial tension term at the solute–water (solvent) interface. The quantity surface area of a molecule is the cavity dimension of the solute when placed in the water media.

The conformational potential energy of a molecule is, in general, given by⁷¹

$$V = V_{\text{nb}} + V_{\text{es}} + V_{\text{se}} + Vt_t + V_f + V_{\text{hb}} \quad (3.62)$$

with the subscripts defined as nb = the nonbonded energy, es = the electrostatic energy, se = the strain energy associated with the stretching of bonds, t = the strain energy due to bending of bonds, f = the torsional potential, and hb = the hydrogen bond formation energy. The quantity V_{nb} is the sum of two terms, a van der Waals attraction term and a repulsive term. For example, in the simple hydrocarbons, as there is not very much stretching or bending deformation, the van der Waals interactions are the most important. The rotations about near-single bonds, the nonbonded interactions, make the major contributions to the torsional potential. The surface areas of the solutes have been calculated by computer programs.⁶⁹⁻⁷²

The data of solubility, total surface area (TSA), and hydrocarbon surface area (HYSA) are given in [Table 3.14](#) for some typical alkanes and alcohols. The relationship between different surface areas of contact between the solute solubility (sol) and water were derived as⁷⁰

$$\begin{aligned} \ln(\text{sol}) &= -0.043 \text{ TSA} + 11.78 \\ \Delta G_{o,\text{sol}} &= -RT \ln(\text{sol}) = 25.5 \text{ TSA} + 11.78 \end{aligned} \quad (3.63)$$

where sol is the molar solubility and TSA is in \AA^2 .

The quantity 0.043 ($RT = 25.5$) is some microsurface tension. The microsurface tension has not been analyzed exhaustively at the molecular level. It is also important to mention that at the molecular level there cannot exist any surface property that can be uniform in magnitude in all directions. Hence, the microsurface tension will be some average value. The effect of temperature must also be investigated.

In the case of alcohols, assuming a constant contribution from the hydroxyl group, the hydrocarbon surface area (HYSA) = TSA – hydroxyl group surface area:

$$\ln(\text{sol}) = -0.0396 \text{ HYSA} + 8.94 \quad (3.64)$$

However, we can also derive a relationship that includes both HYSA and OHSA (hydroxyl group surface area):

$$\ln(\text{sol}) = -0.043 \text{ HYSA} - 0.06 \text{ OHSA} + 12.41 \quad (3.65)$$

The relations described above correlate with the measured data, which were satisfactory (~0.4 to 0.978). The following relationship was derived based on the solubility data of both alkanes and alcohols, which gave correlations on the order of 0.99:

TABLE 3.14
Solubility Data, Boiling Point, Surface Areas,^a and Predicted Solubility^b
of Different Molecules in Water^c

Compound	Solubility Measured (molal)	TSA	OHSA	Boiling Point	Solubility Predicted (molal)
<i>n</i> -Butane	2.34E-3	255.2	—	—	1.43E-3
Isobutane	2.83E-3	249.1	—	—	1.86E-3
<i>n</i> -Pentane	5.37E-4	287	—	—	3.65E-4
2-Methyl-butane	6.61E-4	274	—	—	6.21E-4
3-Methyl-pentane	1.48E-4	300	—	—	2.08E-4
Neopentane	7.48E-4	270	—	—	7.52E-4
Cyclohexane	6.61E-4	279	—	—	5.11E-4
Cycloheptane	3.05E-4	301.9	—	—	1.92E-4
Cyclooctane	7.05E-5	322.6	—	—	7.89E-5
<i>n</i> -Hexane	1.11E-4	310	—	—	1.23E-4
<i>n</i> -Heptane	2.93E-5	351	—	—	2.33E-5
<i>n</i> -Octane	5.79E-6	383	—	—	5.87E-6
<i>n</i> -Butanol	1.006	272	59	118	0.82
2-Butanol	1.07	264	43	100	1.5
<i>n</i> -Pentanol	0.255	304	59	138	0.21
<i>n</i> -Hexanol	0.06	336	59	157	0.053
Cyclohexanol	0.38	291	50	161	0.43
<i>n</i> -Heptanol	0.016	368	59	176	0.014
1-Octanol	4.5E-3	399	59	195	3.45E-3
1-Nonanol	0.001	431	59	213	8.8E-4
1-Decanol	2.0E-4	463	59	230	2.24E-4
1-Dodecanol	2.3E-5	527	59	—	1.43E-5
1-Tetradecanol	1.5E-6	591	59	264	9.4E-7
1-Pentadecanol	5E-7	623	59	—	2.4E-7

Note: Å = 10⁻¹⁰ m; TSA = total surface area; OHSA = hydroxyl group surface area.

^a TSA and OHSA in Å² units.

^b From Equation 3.65.

^c At 25°C.

Source: Adapted from Amidon, G.L.L. et al., *Pharmaceut. Sci.*, 63, 3225, 1974.

$$\ln(\text{sol}) = 0.043 \text{ HYSA} + 8.003 \text{ IOH} - 0.0586 \text{ OHSA} + 4.42 \quad (3.66)$$

where the IOH term equals 1 (or the number of hydroxyl groups) if the compound is an alcohol and 0 if the hydroxyl group is not present.

The term HYSA, thus, can be assumed to represent the quantity that relates to the effect of the hydrocarbon part on the solubility. The effect is negative, and the magnitude of t is 17.7 erg/cm². The magnitude of OHSA is found to be 59.2 Å². As an example, the surface areas of each carbon atom and the hydroxyl group in the molecule 1-nonanol were estimated (Table 3.15). It is seen that the surface area of the terminal methyl group (84.9 Å²) is approximately three times larger than the methylene groups (31.82 Å², or 31.82 × 10⁻²⁰ m²).

The solubility model was tested for the prediction of a complex molecule such as cholesterol.⁷⁰ The experimental solubility of cholesterol is reported to be ~10⁻⁷ M. The predicted value was ~10⁻⁶ (TSA = 699 Å²). It is obvious that further refinements are necessary for predicting the solubilities of such complex organic molecules.

TABLE 3.15
Surface Areas (A²) of Each Methylene
and Methyl Group in 1-Nonanol
 $\text{CH}_3\text{-CH}_2\text{-CH}_2\text{-CH}_2\text{-CH}_2\text{-CH}_2\text{-CH}_2\text{-CH}_2\text{-OH}$

Group	Surface Area at the Interface between Solute and Solvent
OH	59.15
C ₁	45.43
C ₂	39.8
C ₃	31.82
C ₄	31.82
C ₅	31.82
C ₆	31.82
C ₇	31.82
C ₈	42.75
C ₉	84.92

Source: Adapted from Scamehorn, J.F., Ed., *Phenomena in Mixed Surfactant Systems*, ACS Symp. Ser., No. 311, American Chemical Society, Washington, D.C., 1986.

The molecular surface areas are still not easily available, even though computer computations have been carried out to some extent.⁷⁰⁻⁷² However, all these analyses were reported at some temperature in the vicinity of room temperature. The effect of temperature and other parameters such as pressure has not been extensively reported.

Computer simulation techniques have been applied to such solution systems.^{71b,c} The Monte Carlo statistical mechanics have provided much useful information about the energetics, structure, and molecular interactions. The computations suggested that at the hexanol–water interface minimal water penetration into the hydrocarbon regions takes place.

The surface area model for solubility in water or any solvent can be further investigated by measuring the effect of temperature or added salt. Preliminary measurements indicate that some of the above models are not satisfactory. We find that the solubility of butanol in water decreases while the magnitude of surface tension of aqueous NaCl solution increases. These kinds of data are important for such systems as EOR (enhanced oil recovery).

As is well known,¹⁷ the bilayer structure of cell membranes exhibits hydrophobic properties in the hydrocarbon part. This means that those molecules that must interact with the membrane interior must be hydrophobic. Anesthesia is brought about by the interaction between some suitable molecule and the lipid molecules in the biological membrane at the cell interface. The effect of pressure has been reported to be due to the volume change of membranes, which reverses the anesthesia effect. Local anesthetics are basically amphiphile molecules of tertiary amines, and some have colloidal properties in aqueous solution. The anesthetic power is determined by the hydrophobic part of the molecule. Surface tension measurements showed a correlation with the anesthetic power for a variety of molecules: dibucane < tetracaine < bupivacaine < mepivacaine < lidocaine < procaine (all as HCl salts).⁷³

3.7 INTERFACIAL TENSION OF LIQUIDS

3.7.1 INTRODUCTION

The interfacial forces present between two phases, such as immiscible liquids, are important from a theoretical standpoint, as well as in regard to practical systems. The liquid₁–liquid₂ interface is

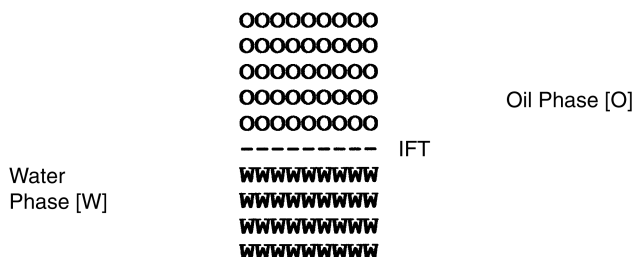


FIGURE 3.9 Interfacial region at two liquids (O = oil phase; W = water phase).

an important one as regards such phenomena as chemical problems, extraction kinetics, phase transfer, emulsions (oil–water), fog, and surfactant solutions. In the case of primary oil production, we have to take into consideration the surface tension of oil. On the other hand, during a secondary or tertiary recovery, the interfacial tension between the water phase and oil phase becomes an important parameter. For example, the *bypass* and other phenomena such as snap-off are related to the interfacial phenomena.⁷⁴ Analogous examples can be given for other systems, such bi-liquid flow through porous media, where again interfacial tension considerations would be required (groundwater pollution control). It is thus obvious that other multicomponent flow systems will be quite complicated phenomena. This is also relevant in the case of blood flow through arteries. Despite this, data on interfaces and interfacial tension are not found in many textbooks that cover important aspects of liquids.²³ Furthermore, although the concept of hydrophobicity in single-component systems such as alkanes has been extensively described, these properties for two-phase systems, such as oil–water, have almost not been described in detail in the current literature.^{1a} The problem of liquid₁–liquid₂ interfaces is of interest to both theoreticians and experientialists.

Indeed, over the past decades great effort has been expended in trying to understand and give plausible theories from a statistical-mechanical point of view.¹⁹

The interface can be considered the location where the molecules of different phases meet and the asymmetric forces are present (Figure 3.9).

The molecules in the bulk phases are surrounded by like molecules. However, at the interface the molecules are subjected to interactions with molecules of phase O and from phase W. Because the molecules in both phases are situated at the interface, the orientations may not exactly be the same as when inside the bulk phase.

Interfacial tension (IFT) between two liquids is less than the surface tension of the liquid with the higher surface tension, because the molecules of each liquid attract each other across the interface, thus diminishing the inward pull exerted by that liquid on its own molecules at the surface.

The precise relation between the surface tensions of the two liquids separately against theory vapor and the interfacial tension between the two liquids depends on the chemical constitution and orientation of the molecules at the surfaces. In many cases, a rule proposed by Antonow holds true with considerable success.¹⁹

The various kinds of interfacial forces have been described in the literature.^{16,17} The interface at the water and simple aromatic hydrocarbons hydrogen bonding has been considered.⁷⁵⁻⁷⁹ The IFT of water–alkanes and water–aromatic hydrocarbons have been extensively analyzed. These analyses have been considered for two different kinds of forces: the short-range and long-range work of adhesion.

3.7.2 LIQUID–LIQUID SYSTEMS — WORK OF ADHESION

The free energy of interaction between dissimilar phases is the work of adhesion, W_A (energy per unit area):

$$W_A = W_{AD} + W_{AH} \quad (3.67)$$

where W_A is expressed as the sum of different intermolecular forces, e.g.,^{16,77}

- London dispersion forces, D
- Hydrogen bonds, H
- Dipole–dipole interactions, DD
- Dipole-induced interactions, DI
- Π bonds, Π
- Donor–acceptor bonds, DA
- Electrostatic interactions, EL

It is also easily seen that the W_{AD} term will always be present in all systems (i.e., liquids and solids), while the other contributions will be present to a varying degree as determined by the magnitude and nature of the dipole associated with the molecules.

To simplify the terms given by the above equation, one procedure has been to compile all the intermolecular forces arising from the dipolar nature of W_{AP} :

$$W_A = W_{AD} + W_{AP} \quad (3.68)$$

where

$$W_{AP} = W_{AH} + W_{ADD} + W_{AID} \quad (3.69)$$

The molecular description of dispersion forces has been given in much detail in the literature. The expression for dispersion forces between two molecules as a function of distance, r_D , center-to-center, is, according to London,⁷⁷

$$\epsilon_{a,12} = k_1 a^2 / r_D \quad (3.70)$$

where

$$k_1 = 3a_i I_1 I_2 / 2(I_1 + I_2) + u_i^2 \quad (3.71)$$

and a_p , I_p , and u_i are polarizability, ionization potential, and dipole moment, respectively. To determine how theoretical treatment agrees with experimental data, the surface tension of *n*-octane is found, as given below:

$$\gamma_{\text{octane}} = \gamma_{LD} \quad (3.72)$$

$$= 0.3\pi N_i^2 c_i f_i \lambda_i / \epsilon_i D_i^2 \quad (3.73)$$

In the case of a molecule such as *n*-octane, $\gamma_{LP} = 0$ for any nonpolar molecule; N_i is the density of CH_2 or CH_3 groups (3.1×10^{22} groups/cm³); c_i is the interaction energy; $f_i = \sim 9$; $\lambda_i = 0.87$; $a_i = 2.12 \times 10^{-24}$ cm³; $I_i = 10.55$ V; $D_i = 4.6$ Å; and $\epsilon_i = 1.05$. The calculated value for γ of octane = 19.0 mN/m, while the measured value is 21.5 mN/m, at 20°C. The real outcome of this example is that such theoretical analyses do indeed predict the surface dispersion forces, γ_{LD} , as measured experimentally, to good accuracy. In a further analysis, the Hamaker constant, A_p for liquid alkanes is found to be related to γ_{LD} as

$$A_i = 3 \times 10^{-14} (\gamma_{LD})^{11/12} \quad (3.74)$$

This was further expanded to include components at an interface between phases I and II:

$$A_{I,II} = 3 \times 10^{-14} / \epsilon_2 \left(\sqrt{\gamma_I^D} - \sqrt{\gamma_{II}^D} \right)^{11/6} \quad (3.75)$$

where ϵ_2 is the dielectric constant of phase II; however, in some cases, forces other than dispersion forces would also be present.⁷⁷

The manifestation of intermolecular forces is a direct measure of any interface property and requires a general picture of the different forces responsible for bond formation, as discussed in the following.

1. Ionic bonds: The force of attraction between two ions is given as

$$F_{ion} = (g^+ g^-) / r^2 \quad (3.76)$$

and the energy, U_{ion} , between two ions is related to r_{ion} by the equation as

$$U_{ion} = (g^+ g^-) / r_{ion} \quad (3.77)$$

where two charges (g^+ , g^-) are situated at a distance of r_{ion} .

2. Hydrogen bonds: Based on molecular structure, those conditions under which hydrogen bonds might be formed are (a) presence of a highly electronegative atom, such as O, Cl, F, and N, or a strongly electronegative group such as $-CCl_3$ or $-CN$, with a hydrogen atom attached; (b) in the case of water, the electrons in two unshared sp^3 orbitals are able to form hydrogen bonds; (c) two molecules such as $CHCl_3$ and acetone (CH_3COCH_3) may form hydrogen bonds when mixed with each other, which is of much importance in interfacial phenomena.
3. Weak-electron sharing bonding: In magnitude, this is of the same value as the hydrogen bond. It is also the Lewis acid–Lewis base bond (comparable to Brønsted acids and bases). Such forces might contribute appreciably to cohesiveness at interfaces; a typical example is the weak association of iodine (I_2) with benzene or any polyaromatic compound. The interaction is the donation of the electrons of I_2 to the electron-deficient aromatic molecules (π -electrons).
4. Dipole-induced dipole forces: In a symmetric molecule, such as CCl_4 or N_2 , there is no dipole ($\mu_a = 0$) through the overlapping of electron clouds from another molecule with dipole, μ_b , with which it can interact with induction.

The typical magnitudes of the different forces are given in [Table 3.16](#) for comparison. It will thus be clear that various kinds of interactions would have to be taken into consideration whenever we discuss interfacial tensions of liquid–liquid or liquid–solid systems.^{16,77-79}

3.7.3 INTERFACIAL TENSION THEORIES OF LIQUID–LIQUID SYSTEMS

As shown above, various types of molecules exhibit different intermolecular forces, and their different force and potential-energy functions can be estimated.¹⁶ If the potential-energy function were known for all the atoms or molecules in a system, as well as the spatial distribution of all

TABLE 3.16
Intermolecular and Interatomic
Forces between Molecules Energy

	Force (kJ/mol)
Chemical bonds	
Ionic	590–1050
Covalent	60–700
Metallic	100–350
Intermolecular forces	
Hydrogen bonds	50
Dipole-Dipole	20
Dispersion	42
Dipole-induced dipole	2.1

Source: Adapted from Chatteraj, D.K. and Birdi, K.S., *Adsorption and the Gibbs Surface Excess*, Plenum Press, New York, 1984.

atoms, it could in principle then be possible to add up all the forces acting across an interface. Further, this would allow us to estimate the adhesion or wetting character of interfaces. Because of certain limitations in the force field and potential-energy functions, this is not quite so easily attained in practice. Further, the microscopic structure at a molecular level is not currently known. For example, to calculate the magnitude of surface tension of a liquid, we need knowledge of the radial pair-distribution function. However, for the complex molecule, this would be highly difficult to measure, although data for simple liquids such as argon have been found to give the desired result. The intermolecular force in saturated alkanes arise only from London dispersion forces. Now, at the interface, the hydrocarbon molecules are subjected to forces from the bulk molecule, equal to γ (we denote phase I as the hydrocarbon in Figure 3.9). Also, the hydrocarbon molecules are under the influence of London forces due to molecules in phase II. It has been suggested that the most plausible model is the geometric means of the force due to the dispersion attraction, which should predict the magnitude of the interaction between any dissimilar phases. As described earlier, the molecular interactions arise from different kinds of forces, which means that the measured surface tension, γ , arises from a sum of dispersion, γ_D , and other polar forces, γ_P :

$$\gamma = \gamma_D + \gamma_P \quad (3.78)$$

Here, γ_D denotes the surface tensional force solely determined by the dispersion interactions, and γ_P arises from the different kinds of polar interactions (Equation 3.72). Some values of typical liquids are given in Table 3.17.

The interfacial tension between hydrocarbon (HC) and water (W) can be written as

$$\gamma_{HC,W} = \gamma_{HC} + \gamma_W - 2(\gamma_{HC}\gamma_{W,D})^{1/2} \quad (3.79)$$

where subscripts HC and W denote the hydrocarbon and water phases, respectively. Considering the solubility parameter analysis of mixed-liquid systems, we find that the geometric mean of the attraction forces gives the most useful prediction values of interfacial tension. Analogous to that analysis in the bulk phase, the geometric mean should also be preferred for the estimation of intermolecular forces at interfaces. The geometric mean term must be multiplied by a factor of 2

TABLE 3.17
Values of the Surface Tension (γ)
Components of Some Test
Liquids 20°C

Liquids	γ_l	γ_D	γ_{lp}
<i>o</i> l-Br-Naphthalene	44.4	44.4	~0
Diiodomethane	50.8	50.8	~0
Dimethyl sulfoxide	44	36	8
Ethylene glycol	48	29	19
Glycerol	64	34	30
Formamide	58	39	19
Water	72	21.8	51

Source: Adapted from Kwok, D.Y. et al.,
Langmuir, 10, 1323, 1994.TFS

as the interface experiences this amount of force by each phase. However, the relation in Equation 3.79 was alternatively proposed by Antonow:

$$\begin{aligned}\gamma_{12} &= \gamma_1 + \gamma_2 - 2(\gamma_1\gamma_2)^{1/2} \\ &= \left((\gamma_1)^{1/2} - (\gamma_2)^{1/2} \right)^2\end{aligned}\quad (3.80)$$

This relation is found to be only an approximate value for such systems as fluorocarbon–water or hydrocarbon–water interfaces, and not applicable to polar organic liquid–water interfaces. The effect of additives such as *n*-alkanols on the interfacial tension of alkane–water interfaces has been investigated in much detail.⁸⁰

To analyze these latter systems, a modified theory was proposed. The expression for interfacial tension was given as^{81,82}

$$\gamma_{12} = \gamma_1 + \gamma_2 - 2\Phi(\gamma_1\gamma_2)^{1/2} \quad (3.81)$$

where the value of Φ varied between 0.5 and 0.15. Φ is a correction term for the disparity between molar volumes of v_1 and v_2 :

$$\Phi_{12} = 4(v_1v_2)^{1/2} / (v_1^{0.5} + v_2^{0.5})^2 \quad (3.82)$$

In Table 3.18 some representative data are given which were used to verify experimental data.

3.7.4 HYDROPHOBIC EFFECT ON THE SURFACE TENSION AND INTERFACIAL TENSION

In most systems, it is of interest to determine how a change in the alkyl part of the organic molecule (i.e., the hydrophobic part) affects the surface and interfacial tension. In spite of its importance (both in biology and technical industry), no such systematic analysis is found in the current literature. These molecular considerations are pertinent in any reaction where the hydrophobicity might be of major importance in the system, e.g., surfactant activity, EOR, protein structure and activity, and pharmaceutical molecules and activity.

TABLE 3.18
Prediction of Interfacial Tension for Hydrogen Bonding Organic Liquids (o) vs. Water (w) (20°C)

Organic Liquid (o)	γ_{ow}	γ_o	X_o	X_w	Φ	$\gamma_{ow,calc}$
<i>n</i> -Butyl alcohol	1.8	24.6	0.500	0.0188	1.00	2.2
iso-Butyl alcohol	2.0	23.0	0.449	0.0195	1.01	3.0
<i>n</i> -Amyl alcohol	4.4	25.7	0.357	0.0046	1.00	4.0
iso-Amyl alcohol	4.8	23.2	0.326	0.0055	1.00	5.0
<i>n</i> -Hexyl alcohol	6.8	25.8	0.288	0.0011	0.98	5.1
<i>n</i> -Heptyl alcohol	7.7	25.8	0.267	0.00028	0.98	5.8
<i>n</i> -Octyl alcohol	8.5	27.5	0.25	0.00	0.97	5.1
Cyclohexanol	3.9	32.7	0.406	0.008	0.99	2.3
Diethyl ether	11.0	17.0	0.345	0.0177	0.95	6.0
Diisopropyl ether	17.9	17.3	0.0333	0.00187	0.99	17.2
Ethyl acetate	6.8	23.9	0.139	0.0163	1.03	8.6
Methyl- <i>n</i> -propyl ketone	9.6	24.7	0.152	0.0132	0.98	8.0
Methyl- <i>n</i> -butyl ketone	9.6	25.0	0.176	0.005	0.98	7.5
Methyl- <i>n</i> -amyl ketone	12.4	26.2	0.123	0.0031	0.96	8.4
Isovaleric acid	2.7	25.5	0.39	0.0082	0.99	3.7
Aniline	5.8	42.9	0.218	0.0073	0.97	2.2

Note: X_w = mole fraction in the water phase; X_o = mole fraction in the oil phase; calc = calculated.

Source: Adapted from Good, C.J., in *Chemistry and Physics of Interfaces*, Ross, S., Ed., American Chemical Society, Washington, D.C., 1965.

The hydrophobic interactions are known to control many aspects of self-assembly and stability of macromolecular and supramolecular structures.¹⁶ This has obviously been useful in both theoretical analysis and technical development of chemical structures. Furthermore, the interaction between nonpolar parts of amphiphiles and water is an important factor in many physicochemical processes, such as surfactant micelle formation and adsorption or protein stability. To make the discussion short, this interaction will be discussed in terms of the measured data of the surface and interfacial tension of homologous series. Analyses have shown that there is no clear correlation; therefore, different homologous series will be discussed separately.

Data concerning the interfacial tension of an alkane–water system deserves detailed analysis for various basic theoretical reasons. Not only are these systems of fundamental importance in oil recovery processes and emulsion formation, but such molecules also form the basis of structures in complex biological and industrial molecules.

These systems also provide an understanding of the molecular basis of interfaces, since the amphiphile molecules consist of alkyl chains and hydrophilic groups. Thermodynamic analyses on surface adsorption and micelle formation of an anionic surfactants in water were described by surface tension (drop volume) measurements.¹⁶ These data are analyzed in Table 3.19. These data show that at 20°C (Table 3.20) the magnitude of surface tension changes nonlinearly (varying from 1.7 to 0.7 mN/m per CH₂) with alkyl chain length.

Interfacial tension changes linearly with a magnitude of 0.3 mN/m (dyn/cm) per CH₂ group (Figure 3.10). These data can be compared (Table 3.21) with a homologue series of aromatic compounds. Surface tension changes with a magnitude of ~0.3 mN/m per CH₂ group. This is much lower than for *n*-alkanes. The change in interfacial tension per CH₂ group is rather large in comparison with the alkane vs. water data.

TABLE 3.19
Variation of γ with Alkyl Chain Length and Temperature

$n_c/T(^{\circ}\text{C})$	20	25	27.5	30	32.5	35	37.5
5	50.24	—	—	—	—	—	—
6	50.8	50.41	50.16	49.92	49.74	49.49	49.24
7	51.23	50.77	—	50.28	—	—	—
8	51.68	51.22	51.02	50.78	50.57	50.31	50.12
10	52.30	—	—	—	—	—	—
12	52.78	52.46	52.21	51.99	51.74	51.50	51.28
14	53.32	52.92	52.69	52.46	52.27	52.04	51.83
16	53.77	53.30	53.09	52.9	—	—	—

Source: Adapted from Good, R.J., in *Chemistry and Physics of Interfaces*, Ross, S., Ed., American Chemical Society, Washington, D.C., 1965.

TABLE 3.20
Surface and Interfacial Tension
of n -Alkane/Water Systems

Organic Liquid	Surface Tension (ST)	Interfacial Tension (IFT)	$d\gamma/\text{CH}_2$	$\Delta\gamma\text{IFT}/\text{CH}_2$
$n\text{-C}_6$	18.0	50.7	—	—
$n\text{-C}_7$	19.7	51.2	1.7	0.5
$n\text{-C}_8$	21.4	51.5	1.7	0.3
$n\text{-C}_{10}$	23.5	52.0	1.1	0.3
$n\text{-C}_{12}$	25.1	52.2	0.8	0.1
$n\text{-C}_{14}$	25.6	52.8	0.3	0.3
$n\text{-C}_{16}$	27.3	53.3	0.85	0.3

Source: Adapted from Good, R.J., in *Chemistry and Physics of Interfaces*, Ross, S., Ed., American Chemical Society, Washington, D.C., 1965.

The latter values are approximately five times larger. This shows that the simple dependence of the hydrophobic effect on the number of carbon atoms becomes rather complicated when considering the interfacial properties. These differences thus may be suggestive of the differences in orientation of the alkyl chains at the interfaces. This subject has been recently investigated by measuring surface tension and interfacial tension near the freezing point of the oil (alkanes) phase under supercooled measurements, as described further below.

In Table 3.22 are data of interfacial tension of the alcohol vs. water system analyzed. The variation of interfacial tension with a change in alkyl chain length for different organic liquids vs. water is given in Table 3.23.

These data are analyzed here for the first time in the literature and clearly show that simple hydrophobic correlations with alkyl chain length as observed in bulk phases^{16,62a} are not found at interfaces and require further analysis. Interfacial tension analysis of organic mixtures has been reported.^{62b}

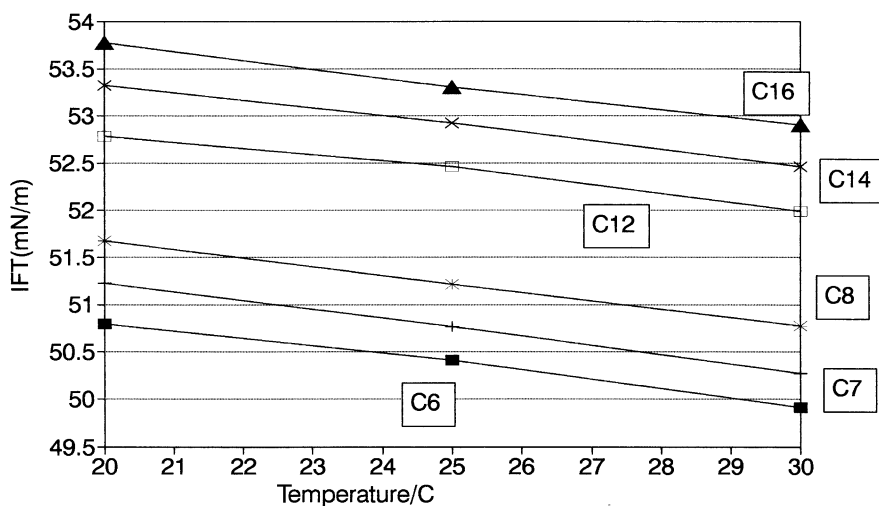


FIGURE 3.10 Variation in interfacial tension (IFT) of alkanes (C₆, C₇, C₈, C₁₂, C₁₄, C₁₆) vs. water at different temperatures.^{1a,81}

TABLE 3.21
Surface and Interfacial Tension of Aromatic Compounds vs. Water

Organic Liquid	Surface Tension (ST)	Interfacial tension (IFT)	$\Delta\gamma_{ST}/CH_2$	$\Delta\gamma_{IFT}/CH_2$
C ₆ H ₆	28.88	33.90	—	—
CH ₃ C ₆ H ₅	28.5	36.1	-0.38	2.2
C ₂ H ₅ C ₆ H ₅	29.2	38.4	+0.7	2.3
C ₃ H ₇ C ₆ H ₅	28.99	39.60	-0.2	1.2

TABLE 3.22
Surface and Interfacial Tension of Alcohol vs. Water System

Organic Liquid	Surface Tension (ST)	Interfacial Tension (IFT)	$\Delta\gamma_{ST}/CH_2$	$\Delta\gamma_{IFT}/CH_2$
<i>n</i> -Butyl alcohol	24.6	1.8	—	—
<i>n</i> -Amyl alcohol	25.7	4.4	1.1	2.6
<i>n</i> -Hexyl alcohol	24.5	6.8	-1.2	2.4
<i>n</i> -Heptyl alcohol	25.8	7.7	1.3	0.9
<i>n</i> -Octyl alcohol	27.5	8.5	1.7	0.8

The protein molecules exhibit hydrophobicity due to polar and apolar side chains.¹⁷ The protein denaturation process has been analyzed by considering the enthalpy of fusion of the hydrophobic groups when undergoing transfer from the liquid organic phase to water phase.^{83,84} The hydrophobic effect is recognized to play an important role in such biological systems.

TABLE 3.23
A Summary of Variation of Interfacial Tension (IFT) for Various Organic Liquids vs. Water

Organic Liquid	Change in IFT/CH ₂ Group		
	Short	Long	
Alkanes	0.5	0.3	1.7–0.9
Alcohols	2.5	1	1
Phenyl	2.2	—	—

3.7.5 HEAT OF FUSION IN THE HYDROPHOBIC EFFECT

In some studies⁸⁴ it has been pointed out that, when calculating the hydrophobic effect in protein denaturation, the enthalpy of fusion of the hydrophobic groups should be considered. A similar analysis had been given in earlier hydrophobic interactions analysis.⁸³

In a later study, a model for absolute free energy of solvation of organic, small inorganic, and biological molecules in aqueous media was described.⁸⁵ From the Monte Carlo simulation studies of aqueous solvation and the hydrophobic effect, we assume that some 250 or more solvent molecules are involved in the process.^{86–88} To resolve this problem, the so-called self-consistent field (SCF) solvation model for the hydrophobic effect was described.⁸⁵

3.7.6 ANALYSIS OF THE MAGNITUDE OF THE DISPERSION FORCES IN WATER (γ_D)

Because water plays such a very important role in a variety of systems encountered in everyday life, its physicochemical properties are of much interest. Therefore, the magnitude of water γ_D has been the subject of much investigation and analysis. By using Equation 3.79 and the measured data of interfacial tension for alkanes–water, the magnitude of γ_D has generally been accepted to be 21.8 mN/m. This value, however, has been questioned by other investigators. The criticism arises from the observation that data of interfacial tension and Equation 3.72 do not give a linear plot for $(\gamma_2 - \gamma_{12})/\gamma_1$ vs. $\gamma_1 - 1$, and the plots did not seem to intercept the theoretical origin at 0, -1.

Additionally, it has been shown that the value of γ_{LD} as calculated from Equation 3.83 for water is not independent of the alkane chain length; however, other investigators⁸⁹ have shown that the following relationship is valid. A plot of $W_A = 2 (\gamma_{1,LD}^{1/2} \gamma_{2,LD})^{1/2}$ vs. $\gamma^{1/2}$ is linear:

$$W_A = 6.6\gamma_1 + 12.0 \quad (3.83)$$

where γ_1 is in mN/m units. These observations are consistent with a value of $\gamma_{2,D} = 10.9$ mN/m and the presence of a residual interaction over the interface, possibly resulting from the Debye forces of 12.0 mN/m. However, this appears unlikely since theoretical calculations¹⁶ convincingly give a value of 19.2 mN/m for $\gamma_{2,D}$ ($\gamma_{\text{water},D}$), and Debye forces could only contribute about 2 mN/m.

Assuming that alkane molecules lie flat at the interface, the additive contributions from the $-\text{CH}_3$ and $-\text{CH}_2$ group to W_A are given by⁸⁹

$$W_A = \left(2W_{\text{CH}_3} - \sigma_{\text{CH}_3} + (N-2)\sigma_{\text{CH}_2} W_{\text{CH}_2} \right) / \left((N-2)\sigma_{\text{CH}_3} + 2\sigma_{\text{CH}_2} \right) \quad (3.84)$$

where N is the number of carbon atoms in the alkane chain and σ denotes the surface area for $-\text{CH}_3$ (0.11 nm²) or $-\text{CH}_2$ (0.05 nm²) groups. The values for the work of adhesion for $-\text{CH}_3$ and

$-\text{CH}_2$ groups are estimated to be $30 \text{ mN/m} = W_{\text{CH}_3}$ and $52 \text{ mN/m} = W_{\text{CH}_2}$, respectively. The plots of γ_{12} vs. N using Equation 3.84 show that the relation given in Equation 3.86 for a flat alkane orientation model at the interface is in agreement with the experimental data. This suggests that the magnitude of γ_D for water is 19.5 mN/m , which is in agreement with the experimental data.

To obtain any thermodynamic information of such systems it is useful to consider the effect of temperature on the interfacial tension. The alkane–water interfacial tension data have been analyzed (Figure 3.10). These data show that the interfacial tension is lower for C_6 (50.7 mN/m) than for the other higher chain length alkanes. The slopes (interfacial entropy: $-d\gamma/dT$) are all almost the same, $\sim 0.09 \text{ mN/m}$ per CH_2 group. This means that water dominates the temperature effect, or that the surface entropy of the interfacial tension is determined predominantly by the water molecules. Further, as described earlier, the variation of surface tension of alkanes varies with chain length. This characteristic is not present in interfacial tension data; however, it is worth noting that the slopes in the interfacial tension data are lower than those of both pure alkanes and water. The molecular description must be analyzed.

It may be safe to conclude that the magnitude of different interfacial tensions (for example, dispersion tension of water) might be constant; however, there is great need for a more thorough analysis.

As mentioned earlier, simple specular reflection profiles can yield detailed interfacial structural information.⁹⁰ X-ray and neutron reflectometers have been developed specifically to investigate the liquid surfaces.^{90,91} The problem is to be able to study the buried interfacial region by x-ray methods.

The beam of x-rays or thermal neutrons is thus required to impinge on the sample at low angles ($< 10^\circ$). This also requires that the top phase be made as thin as possible to avoid significant absorption or incoherent scattering. The systems studied were⁹⁰

1. Cyclohexane–water
2. Cyclohexane–water (with surfactant)

These studies showed that the interfacial region is very diffuse and that the major excess electron density arises from the nonaqueous phase of the interface. The thickness of the layer in the presence of a surfactant was found to be of the magnitude 15.4 \AA (1.54 nm).

In a recent study,⁹² the liquid(A)–liquid(B) interface was described in terms of the Lennard–Jones potential:

$$u_{\text{AB},rij} = 4\epsilon\beta \left(\left(\frac{\sigma}{r_{ij}} \right)^{12} - \alpha \left(\frac{\sigma}{r_{ij}} \right)^6 \right) \quad (3.85)$$

and

$$u_{\text{AA},rij} = u_{\text{BB},rij} = 4\epsilon \left(\left(\frac{\sigma}{r_{ij}} \right)^{12} - \left(\frac{\sigma}{r_{ij}} \right)^6 \right) \quad (3.86)$$

where u_{AA} and u_{AB} are the respective interaction potentials. The parameter β will, of course, be determined by the degree of miscibility of liquids A and B. The expression for the interfacial tension, γ_{AB} , is

$$\gamma_{\text{AB}} = 1/(4A) \sum_{i=1}^N \sum \left(3z_{ij}^2 - r_{ij}^3 \right) 1/r_{ij} \left(du/dr_{ij} \right) \quad (3.87)$$

The main criterion here is that the normal component of the pressure must remain constant as the surface line is approached, as required by the mechanics. The deficiency of tension in the transverse tensor should be analyzed.

3.7.6.1 Liquid–Solid Systems (Contact Angle)

The state of a liquid in contact with a solid surface is very important in many everyday phenomena (detergency, adhesion, wetting, flotation, suspensions, solid emulsions, erosion, printing, pharmaceutical products).

If we consider two systems, such as a drop of liquid (water) placed on different solid surfaces (glass, Teflon), we observe the following. The contact angle, θ , as defined by the balance between surface forces (surface tensions) between the respective phases, solid, liquid and LS (liquid–solid):^{92c}

$$\gamma_s = \gamma_{SL} + \gamma_{\text{liquid}} \cos(\theta) \quad (3.88)$$

In the case of water–glass and water–Teflon, we find that the magnitude of θ is 30° and 105° , respectively. Because the liquid is the same, then the difference in contact angle arises from the different solid surface tensions. From this we can therefore easily see that the surface tension of a solid is an important surface parameter. A more extensive analyses can be found elsewhere.^{92b,96}

In recent years a great many studies have reported on the dynamic systems where a drop of liquid is placed on a smooth solid surface.^{92c} The system liquid drop–solid is a very important system in everyday life, for example, rain drops on tree leaves or other surfaces. It is also significant in all kinds of systems where a spray of fluid is involved, such as in sprays or combustion engines. The dynamics of liquid drop evaporation rate is of much interest in many phenomena. The liquid–solid interface can be considered as follows. Real solid surfaces are, of course, made up of molecules not essentially different in their nature from the molecules of the fluid. The interaction between a molecule of the fluid and a molecule of the boundary wall can be regarded as follows. The molecules in the solid state are not as mobile as those of the fluid. It is therefore permissible for most purposes to regard the molecules in the solid state as stationary. However, complexity arises in those liquid–solid systems where a layer of fluid might be adsorbed on the solid surface, such as in the case of water–glass.

Systematic studies have been reported in the literature on the various modes of liquid drop evaporation when placed on smooth solid surfaces.^{92c}

In these studies the rate of the mass and contact diameter of water and *n*-octane drops placed on glass and Teflon surfaces were investigated. It was found that the evaporation occurred with a constant spherical cap geometry of the liquid drop. The experimental data supporting this were obtained by direct measurement of the variation of the mass of droplets with time, as well as by the observation of contact angles. A model based on the diffusion of vapor across the boundary of a spherical drop has been considered to explain the data. Further studies were reported, where the contact angle of the system was $\theta < 90^\circ$. In these systems, the evaporation rates were found to be linear and the contact radius constant. In the latter case, with $\theta > 90^\circ$, the evaporation rate was nonlinear, the contact radius decreased and the contact angle remained constant.

As a model system, we may consider the evaporation rates of fluid drops placed on polymer surfaces in still air.^{92d} The mass and evaporating liquid (methyl acetoacetate) drops on polytetrafluoroethylene (Teflon) surface in still air have been reported. These studies suggested two pure modes of evaporation: at constant contact angle with diminishing contact area and at constant contact area with diminishing contact angle. In this mixed mode, the drop shape would vary resulting in an increase in the contact angle with a decrease in the contact circle diameter, or, sometimes a decrease

in both quantities. These investigators developed a theory to predict the evaporation rate and residual mass at any time in the life of the drop based on the spherical cap geometry. A later study^{92d} investigated the change in the profile of small water droplets on polymethylmethacrylate (PMMA) due to evaporation in open air. The drops were observed to maintain a constant contact radius over much of the evaporation time. Measurements were carried out on q and the drop height, h_d , as a function of time in the regime of constant contact radius.

The results showed that the initial contact angle was $< 90^\circ$. No attempt was made to obtain measurements for the final rapid stages of evaporation where the mixed mode of evaporation occurred. It was also noted that the earlier models^{92c} did not distinguish between the two principal radii of curvature occurring at the contact line: these two radii do not have the same values. The latter studies, therefore, extended the model to a two-parameter spherical cap geometry, which was able to explain why the experimentally observed change in contact angle should appear linear in time.

We can describe the state of a liquid drop placed on a smooth solid surface in terms of the radius, height of the drop, and the contact angle, θ . The liquid drop when placed on a smooth solid can have a spherical cap shape, which will be the case whenever the drop volume is approximately $10 \mu\text{l}$ or less. In the case of much larger liquid drops, ellipsoidal shapes may be present, and a different geometric analysis will have to be implemented. On the other hand, in the case of rough surfaces, we may have much difficulty in explaining the dynamic results. However, we may also expect that there will be instances where the drop is nonspherical. This parameter will need to be determined before any analyses can be carried. Let us assume the case where a spherical cap drop shape is present. In the case of a liquid drop that is sufficiently small and where surface tension dominates over gravity, the drop can be assumed to form a spherical cap shape. A spherical cap shape can be characterized by four different parameters, the drop height (h_d), the contact radius (r_b), the radius of the sphere forming the spherical cap (R_s), and the contact angle (θ). By geometry, the relationships between the two radii, the contact angle, and the volume of the spherical cap (V_c) are given as:^{92d}

$$r_b = R_s \sin(\theta) \quad (3.89)$$

and

$$R_s = \left[(3V_c) / (\rho b) \right]^{1/3} \quad (3.90)$$

where

$$b = (1 - \cos\theta)^2 (2 + \cos\theta) = 2 - 3\cos\theta + \cos 3\theta \quad (3.91)$$

The height of the spherical cap above the supporting solid surface is related to the two radii and the contact angle, θ , by

$$h = R_s (1 - \cos\theta)$$

and

$$h = r_b \tan(\theta/2) \quad (3.92)$$

A spherical cap-shaped drop can be characterized by using any two of these four parameters. When the horizontal solid surface is taken into account, the rate of volume decrease by time is given as,⁸⁻¹⁰

$$-(dV_c/dt) = (4pR_s D)/(r_L)(c_s - c_\infty)f(\theta) \quad (3.93)$$

where t is the time (s), D is the diffusion coefficient (cm²/s), c_s is the concentration of vapor at the sphere surface (at R_s distance) (g/cm³), c_∞ is the concentration of the vapor at infinite distance (R_s distance) (g/cm³), r_L is the density of the drop substance (g/cm³), and $f(\theta)$ is a function of contact angle of the spherical cap. In the literature we find a few solutions of this relationship.^{92d} By using the analogy between the diffusive flux and electrostatic potential, the exact solution has been derived.

The approximate solution for $f(\theta)$ was given as:^{92d}

$$f(\theta) = (1 - \cos(\theta))/2 \quad (3.94)$$

while other investigators gave the following relationships:^{92d}

$$f(\theta) = (\cos(\theta))/(2 \ln(1 - \cos(\theta))) \quad (3.95)$$

It was shown that only in some special cases the magnitude of θ remains constant under evaporation, such was in water-glass systems. In this latter case, where the contact angle remains constant during evaporation, the following relation can be written:

$$V_c^{2/3} = V_{ct}^{2/3} - 2/3 Kf(\theta)t \quad (3.96)$$

Some limited experimental results have been reported that fit this relationship. However, more detailed investigations are needed to understand fully the evaporation phenomena. Only one case^{92c} has reported on the fate of the liquid film that remains after most of the liquid has evaporated. It was shown that we could estimate the degree of porosity of solid surfaces from these data. Thus, we find a new method of determination of porosity of solids, without the use of mercury porosimeter.^{92c} The latter studies are much more accurate, as these were based on measurements of change of weight of drop vs. time under evaporation. At this stage in the literature, therefore, there is a need for more studies on this dynamic system of liquid drop-solid.

3.8 SURFACE TENSION AND INTERFACIAL TENSION OF OIL-WATER SYSTEMS

The oil-water interface is one of the most important systems. The liquid-liquid interface constitutes a phase separation where two different molecules meet. We can directly measure the magnitude of the surface tension, with rather high precision. It would thus seem that much useful information can be obtained if we could measure a dynamic parameter of the interface, such as the freezing phenomenon. It is widely known that liquids can be cooled below their freezing temperature without solidification (supercooled fluid) and that they can be heated above their boiling temperature without vaporization (superheated liquid).

The behavior of liquid surfaces near the freezing point or under supercooled conditions has not been investigated in much detail. Although the subject is fundamental and of considerable intrinsic importance in science and technology, it remains severely underinvestigated because the

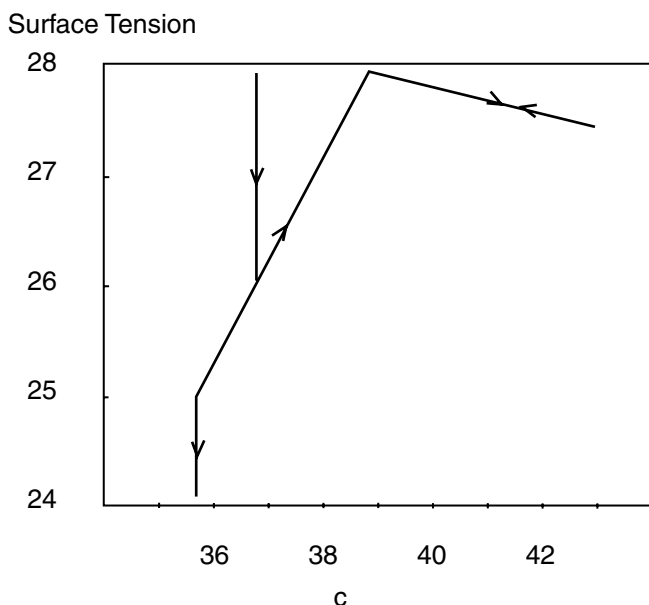


FIGURE 3.11 Variation of γ of long chain alkane in heating and cooling cycles. The arrows indicate the temperature scan direction.

traditional techniques have been difficult to apply definitively. As is well known, most liquids will undergo supercooling when the temperature is lowered slowly below the freezing point, so much so that liquids such as water will not freeze until -40°C under strictly controlled conditions and purity. Other fluids exhibit similar supercooled behavior: benzene to -8°C and glycerol to -40°C . Under these conditions the liquid remains homogeneous beyond the line of phase equilibrium into the so-called metastable region.

This is important, as it is well recognized that supercooled liquids may be regarded as legitimate representatives of the liquid state.⁹³ The limit of supercooling has also been of some interest, as surely liquids must solidify before absolute temperature. In fact, the liquid state in comparison to the gas state is stabilized due to gravity forces. Thus, the supercooled state is a quite legitimate phase of interest for the fundamental understanding of phase equilibria. Furthermore, the crystallization requires the necessary orientation prior to the phase change.

It has been argued⁹⁴ that supercooled liquids should be considered legitimate representatives of the liquid state. The fact that a phase exists with a lower Gibbs energy than the liquid, so that a spontaneous transformation (i.e., crystallization) is possible, although in some cases it may even be slow, is not an inherent property of the liquid state and according to some views may be discarded. The analysis given above on the surface tension of alkanes, alkenes, and other liquids thus provides support for these postulates.

As mentioned above, the surface tension of all liquids decreases with a rise of temperature. On the other hand, it was also observed that the surface tension of a supercooled liquid passes continuously through the freezing point.⁹⁵

Recent studies have shown that the surface tension of fluids near their freezing point can provide useful molecular information.^{96a,b} From both x-ray scattering and γ measurements, it was concluded that abrupt formation of a crystalline monolayer on the surface of *n*-alkanes, *n*- $\text{C}_{20}\text{H}_{44}$, took place above their bulk melting temperatures.^{96a} The abrupt change in γ at 38.6°C was suggested to indicate the solid monolayer formation. The bulk solidification was observed at 35.6°C , after which the Wilhelmy plate provides no useful information. In Figure 3.11 a schematic description is given. From these studies it was concluded that a layering transition on the free surface of fluid alkanes

at temperatures a few degrees above their solidification is observed. The surface exhibited a single monolayer of alkane forms in an apparently first-order transition with hexagonal packing structure and chains oriented vertically.

It was also found that the freezing of lower chain alkanes, such as hexadecane, $C_{16}H_{34}$, did not show abnormal surface tension behavior. The data for hexadecane^{1a,96b} were described elsewhere. The crystallization of a mixture of 90% C_{16} + 10% C_{14} was also investigated. These data showed that crystallization takes place at 15.5°C, which is lower than that for pure C_{16} .

The interfacial tension of the water–alcohol (with 10 to 15 carbon atoms) interface was investigated near the crystallization temperature.⁹⁷ The water–undecanol data⁹⁸ indicated that a phase transition occurred a few degrees above the melting point (11°C) of the alcohol. Furthermore, the process of melting should be regarded as the transition of a substance from a state of order to one of disorder among the molecules.

In a recent investigation,^{96b} the effects of additives to the aqueous phase on the interfacial tension, γ , vs. temperature curves near the freezing point of *n*-hexadecane were reported. The aim of these investigations was to determine the effect of additives such as proteins that are surface active on the supercooled region and the interfacial tension. This would reveal the effect of the adsorbed protein molecule on the interfacial tension of the water–alkane system and could be used as a model for cell membranes.¹⁷

The interfacial tension vs. temperature curves for different systems were investigated: C_{16} vs. water, C_{16} vs. an aqueous solution with protein (BSA; casein). These data showed that the freezing of *n*-hexadecane takes place at 18°C; however, supercooling is observed down to 16.6°C. In contrast, surface tension measurements at the air–liquid interface showed no supercooling behavior.^{1a}

The slope of the data, dy/dT , is of the same value (approximately -0.09 mN/m) as reported in the literature for a C_{16} –water system. In other words, the magnitude of the interfacial tension of the system increases as temperature decreases. After reaching the supercooled temperature, 16.6°C, as the crystallization starts the temperature increases. C_{16} is still in a liquid state, as the value of the interfacial tension also abruptly decreases until it reaches the freezing point, 18°C. These data show, for the first time, that fluids crystallize in the bulk phase in a different way than in the surface. The large change in interfacial tension after freezing is due to the solidification and inability of the Wilhelmy plate method to provide any useful information for such solid–oil systems. The abrupt change observed under the supercooled process must be investigated by high-speed measurements. This could provide information about the dynamics of surface molecules. The data also show that the scatter in the plots is reduced after freezing initiates at $\sim 16.5^\circ\text{C}$. Very fast data acquisition has been attempted on these systems. The rate of crystallization is very rapid and could not be determined successfully.

Crystallization is known to initiate at the interface. It is thus obvious that the crystallization will then be dependent on the magnitude of IFT. The water–hexadecane interface will not be able to freeze exactly at the freezing point of hexadecane (18°C) because of the neighboring water molecules. However, at the supercooled temperature of 16°C, it seems that water molecules have no effect or a lesser effect on the packing of the hexadecane chains at the interface, which means that the bulk structure of hexadecane and the interfacial phase are similar, and freezing can take place.

The supercooling is also observed with protein (BSA, casein, lactoglobulin) in addition to the aqueous phase– C_{16} system, but the freezing point of hexadecane increases to 18.2°C. This indicates that the crystallization of the hexadecane is affected by the presence of surface-active molecules. The supercooling will have extensive dependence on various interfaces, such as emulsions, oil recovery, and immunological systems. The adsorption of proteins from aqueous solutions on surfaces has been studied by neutron reflection.^{99a}

It is known that polymer/surfactant complexes are formed at the water–air interface, as studied by surface tension and x-ray reflectivity studies.^{99b} Furthermore, the effect of surface tension on the stability of proteins has been described in terms of a molecular thermodynamics model.^{99c}

Further studies are needed before a more plausible description can be given regarding how the protein molecules affect the freezing point. Preliminary studies using very fast data acquisition have indeed indicated that the transition from liquid to solid at interfaces is very complex.^{1a}

These studies provide a view of the structure and molecular interactions in interfacial regions of more complicated systems, such as monolayer, bilayer, and bi-phase systems. The two-dimensional assemblies are thus subject to the water molecule effect in the packing energetics.

In the future, the rate of the supercooled region should be investigated in more detail. This has much interest for physicochemical understanding of the kinetics of phase change processes. That velocity is related to cluster formation might be useful in the estimation of impurities.

REFERENCES

1. a) Birdi, K.S., Ed., *Handbook of Surface and Colloid Chemistry*, CRC Press, Boca Raton, FL, 1997; b) Birdi, K.S., *Self-Assembly Monolayer (SAM) Structures*, Plenum Press, New York, 1999; Langmuir, I., *Phys. Rev.*, 2, 331, 1913.
2. Parratt, I.G., *Phys. Rev.*, 95, 359, 1954.
3. Penfold, J. and Thomas, R.K., *J. Phys. Cond. Matter*, 2, 1369, 1990.
4. Roser, S.J., Felici, R., and Eaglesham, A., *Langmuir*, 10, 3853, 1994.
5. Takahashi, R., *Jpn. J. Appl. Phys.*, 2(1), 17, 1983.
6. Vogelsberger, W., Sonnefeld, J., and Rudakoff, G., *Z. Phys. Chem. (Leipzig)*, 266, 225, 1985.
7. Adamson, A.W., *Physical Chemistry of Surfaces*, 5th ed., John Wiley & Sons, New York, 1990.
8. Shi, X.D., Brenner, M.P., and Nagel, S.R., *Science*, 265, 219, 1994.
9. Newman, F.H. and Searle, V.H., *The General Properties of Matter*, Butterworths Scientific, London, 1957; Green, H.S., *The Molecular Theory of Fluids*, Dover Publications, New York, 1970.
10. Leonardo da Vinci, Libri, *Histoire des Sciences Mathematiques en Italie, Paris*, 3, 54, 1838–1841.
11. Pogendorff, F., *Ann. Phys.*, 101, 551, 1857.
12. Gibbs, J.W., *The Collected Works of J.W. Gibbs*, Vol. I, *Thermodynamics*, Yale University Press, New Haven, CT, 1957.
13. Adam, N.K., *The Physics and Chemistry of Surfaces*, Clarendon Press, Oxford, 1930.
14. Harkins, W.D., *The Physical Chemistry of Surface Films*, Reinhold, New York, 1952.
15. Defay, R., Prigogine, I., and Bellemans, A., *Surface Tension and Adsorption*, Longmans, Green, London, 1966.
16. Chattoraj, D.K. and Birdi, K.S., *Adsorption and the Gibbs Surface Excess*, Plenum Press, New York, 1984; Fu, D. et al., *Ind. Eng. Chem. Res.*, 39(2), 320, 2000; Hisatomi, M. et al., *Langmuir*, 16, 1515, 2000.
17. Birdi, K.S., *Lipid and Biopolymer Monolayers at Liquid Interfaces*, Plenum Press, New York, 1989.
18. a) Bakker, G., *Kapillarität und Oberflächenspannung Handbuch der Experimentalphysik*, 3rd ed., Leipzig, 1928; b) Partington, J.R., *An Advanced Treatise on Physical Chemistry*, Vol. II, Longmans, Green, London, 1951.
19. Rowlinson, J.S. and Widom, B., *Molecular Theory of Capillarity*, Clarendon Press, Oxford, 1982; Abbas, S. and Nordholm, S., *J. Colloid Interface Sci.*, 166, 481, 1994.
20. Burshtein, A.A., *Adv. Colloid Interface Sci.*, 11, 315, 1979.
21. Young, T., *Trans. R. Soc. London*, 95, 65, 1805.
22. Garflas, F.J., *J. Phys. Chem.*, 83, 3126, 1979.
23. Reid, R.C., Prausnitz, J.M., and Poling, B.E., *The Properties of Gases and Liquids*, McGraw-Hill, New York, 1987.
24. Sugden, S., *J. Chem. Soc.*, 125, 32, 1924; Sugden, S., *The Parachor and Valency*, G. Routledge & Sons, London, 1930; Knotts, T.A. et al., *J. Chem. Eng. Data*, 46, 158, 2001.
25. Pearson, D. and Robinson, E., *J. Chem. Soc. Faraday Soc.*, 736, 1934.
26. Mumford, N. and Philips, L., *J. Am. Chem. Soc.*, 52, 5295, 1930.
27. Quale, O.R., *Chem. Rev.*, 53, 439, 1953.
28. a) Tripathi, R., *J. Indian Chem. Soc.*, 18, 411, 1941; b) Saastad, O.W., *J. Chem. Eng. Data*, 43, 617, 1998; Navaza, J.M., *J. Chem. Eng. Data*, 43, 128, 1998; Navaza, J.M., *J. Chem. Eng. Data*, 43, 158, 1998; Jiménez, E. et al., *J. Chem. Eng. Data*, 45, 862, 2000; Tsierkezos, N.G., Kelarakis, A.E., and

- Molinou, I.E., *J. Chem. Eng. Data*, 45, 776, 2000; Tsierkezos, N.G., Kellarakis, A.E., and Palaiologou, M.M., *J. Chem. Eng. Data*, 45, 395, 2000; Lee, J.-W., Park, S.-B., and Lee, H.; Den, *J. Chem. Eng. Data*, 45, 166, 2000; Watts, L.A., in *Solvent Systems and Experimental Data on Thermal Conductivity and Surface Tension*, G.G. Aseyev, Ed., Begell House, New York, 1998; Jimenez, E., *J. Chem. Eng. Data*, 44, 1435 1999.
29. Stefan, J., *Ann. Phys.*, 29, 655, 1886.
 30. Waterston, C., *Philos. Mag.*, 15, 1, 1858.
 31. Eotovos, R., *Ann. Phys.*, 27, 448, 1886.
 32. Keeney, M. and Hecklen, J., *J. Inorg. Nucl. Chem.*, 41, 1755, 1979.
 33. Raman, C.V. and Ramdas, L.A., *Philos. Mag.*, 3, 220, 1927.
 34. a) McLeod, D.B., *Trans. Faraday Soc.*, 19, 8, 1923; b) Straub, J. and Grigull, U., *Wärme- und Stoffübertragung*, 13, 241, 1980.
 35. Timmerman, J., *Physico-Chemical Constants of Pure Organic Compounds*, Elsevier, New York, 1950; *Selected Properties of Hydrocarbons and Related Compounds*, Vol. 1, API Project 44, Thermodynamics Research Center, Houston, TX, 1966.
 36. a) Guggenheim, E.A., *Trans. Faraday Soc.*, 41, 150, 1945; b) Fenelonov, V.B., Kodenov, G.G., and Kostrovsky, V.G., *J. Phys. Chem. B*, 105, 1050, 2001.
 37. Hildebrand, J.H. and Scott, R.L., *Solubility of Nonelectrolytes*, Reinhold, New York, 1950.
 38. a) Somyajulu, G.R., *Int. J. Thermophys.*, 9, 559, 1988; b) Murad, S., *Chem. Eng. Commun.*, 24, 353, 1983.
 39. Reid, R.C. and Sherwood, T.K., *The Properties of Gases and Liquids — Their Estimation and Correlation*, McGraw-Hill, New York, 1996.
 40. Lyman, W.J., Reehl, W.J., and Rosenblatt, D.H., Eds., *Handbook of Chemical Property Estimation Methods*, American Chemical Society, Washington, D.C., 1990.
 41. Le, T.D. and Weers, J.G., *J. Phys. Chem.*, 99, 6739, 1995.
 42. Wooley, R.J., *Chem. Eng.*, March, 109, 1986; Nordholm, S., *Langmuir*, 14, 396, 1998; Carroll, F.A., *Langmuir*, 16, 6689, 2000.
 43. a) Eyring, H. and Jhon, M.S., *Significant Liquid Structures*, John Wiley & Sons, London, 1969; b) Kimura, H. and Nakano, H.J., *J. Phys. Soc. Jpn.*, 54, 1730, 1985; Rey, A.R., *Langmuir*, 16, 845, 2000.
 44. Gannon, M.G.J., *Faber Philos. Mag.*, A37, 117, 1978.
 45. Cini, R., Loglio, G., and Ficalbi, A., *J. Colloid Interface Sci.*, 41, 287, 1972.
 46. Gaines, G.L., *Insoluble Monolayers at Liquid-Gas Interfaces*, Wiley Interscience, New York, 1966.
 47. Koefoed, J. and Villadsen, J.V., *Acta Scand.*, 12, 1124, 1958.
 48. Hoar, T.P. and Mellord, D.A., *Trans. Faraday Soc.*, 53, 315, 1957.
 49. Jansen, H.R.S. and Sogor, L., *J. Colloid Interface Sci.*, 40, 424, 1972.
 50. Jain, D.V.S., Singh, S., and Wadi, R.K., *J. Chem. Soc. Faraday Trans.*, 70(I), 961, 1974.
 51. a) Bhatia, A.B., March, N.H., and Sutton, J., *J. Chem. Phys.*, 69(5), 2258, 1978; b) Henderson, J.R., *Mol. Phys.*, 39, 709, 1980; c) Nohira, H., *Langmuir*, 14, 4330, 1998.
 52. Carey, B.S., Scriven, L.E., and Davis, H.T., *AIChE J.*, 26(5), 705, 1980; Good, R.J. and Buff, F.P., in *The Modern Theory of Capillarity*, Goodrich, F.C. and Tusanov, A.I., Eds., Akademie-Verlag, Berlin, 1981.
 53. a) Sheehan, W.F., *Physical Chemistry*, 2nd ed., Allyn & Bacon, Boston, 1970; b) Kumar, A., *J. Phys. Chem. B*, 104, 9505, 2000; Kumar, A., *Ind. Eng. Chem. Res.*, 38, 4135, 1999.
 54. Harkins, R.W. and Wamper, J., *Am. Chem. Soc.*, 53, 850, 1931.
 55. Lange, N.A. and Forker, G.M., *Handbook of Chemistry*, 10th ed., McGraw-Hill, New York, 1967.
 56. Franks, F. and Ives, D.J.C., *Q. Environ. Chem. Soc.*, 20, 1, 1966.
 57. Myers, R.S. and Clever, H.L., *J. Chem. Thermodyn.*, 6, 949, 1974.
 58. McLure, I.A., Sipowska, J.T., and Pegg, I.L., *J. Chem. Thermodyn.*, 14, 733, 1982.
 59. a) McLure, I.A. et al., *Langmuir*, 9, 2190, 1993; b) Penas, A. et al., *J. Chem. Eng. Data*, 45, 682, 2000; c) Romero, E., *J. Chem. Eng. Data*, 42, 57, 1997; d) Navaza, J.M., *J. Chem. Eng. Data*, 41, 806, 1996.
 60. McAuliffe, C., *J. Phys. Chem.*, 70, 1267, 1966.
 61. Choi, D.S., Jhon, M.S., and Eyring, H., *J. Chem. Phys.*, 531, 2608, 1970.
 62. a) Tanford, C., *The Hydrophobic Effect*, 2nd ed., John Wiley & Sons, New York, 1980; b) Yarranton, H.W. and Masliyah, J.H., *J. Phys. Chem.*, 100, 1786, 1996.

63. Ben-Naim, A., *Hydrophobic Interactions*, Plenum Press, New York, 1980.
64. Birdi, K.S., The hydrophobic effect, *Trans. Faraday Soc.*, 17, 194, 1982.
65. a) Gurney, R.W., *Ionic Processes in Solution*, Dover, New York, 1953; b) Frank, H.S. and Evans, M.W., *J. Chem. Phys.*, 13, 507, 1945.
66. Langmuir, I., *Third Colloid Symp. Monogr.*, 48, 1925.
67. Uhlig, H.H., *J. Phys. Chem.*, 41, 1215, 1937.
68. Herman, R.B., *J. Phys. Chem.*, 76, 2754, 1972.
69. Ishikawa, S., Hada, S., and Funasaki, N., *J. Phys. Chem.*, 99, 11508, 1995.
70. Amidon, G.L., Yalkowsky, H., and Leung, S.J., *Pharmaceut. Sci.*, 63, 3225, 1974; Amidon, G.L.L. et al., *J. Phys. Chem.*, 79, 2230, 1975.
71. a) Ramachadran, G.N. and Sasisekharan, V., *Adv. Protein Chem.*, 23, 283, 1968; b) Gao, J. and Jorgensen, W.L., *J. Phys. Chem.*, 92, 5813, 1988; c) Wallqvist, A. and Covell, D.G., *J. Phys. Chem.*, 99, 13118, 1995.
72. Gill, S.J. et al., *J. Phys. Chem.*, 89, 3758, 1985.
73. Matsuki, H., Hashimoto, S., and Kaneshina, S., *Langmuir*, 10, 1882, 1994.
74. Birdi, K.S. Vu, D.T., and Winter, A., in *Proc. 4th Eur. Symp. Enhanced Oil Recovery*, Hamburg, Germany, October, 1987.
75. Fowkes, F.M., *J. Adhes. Sci. Technol.*, 1, 7, 1987.
76. Fowkes, F.M., *J. Phys. Chem.*, 67, 2538, 1963.
77. Fowkes, F.M., *Ind. Eng. Chem.*, 12, 40, 1964; *J. Phys. Chem.*, 84, 510, 1980.
78. Wu, W., Giese, R.F., and van Oss, C.J., *Langmuir*, 11, 379, 1995.
79. Kwok, D.Y., Li, D., and Neumann, A.W., *Langmuir*, 10, 1323, 1994.
80. Aveyard, R. and Briscoe, B.J., *J. Chem. Soc. Faraday Trans.*, 68, 478, 1972.
81. Good, R.J., in *Chemistry and Physics of Interfaces*, Ross, S., Ed., American Chemical Society, Washington, D.C., 1965.
82. Good, R.J., in *Wetting*, van Oss, C.J., Ed., Plenum Press, New York, 1992.
83. Bello, J., *J. Theor. Biol.*, 68, 139, 1977; Bello, J., *Int. J. Peptide Res.*, 12, 38, 1978; Bello, J., *J. Phys. Chem.*, 82, 1607, 1978.
84. Herzfeld, H., *Science*, 88, 256, 1992.
85. Cramer, C.J. and Truhlar, D.G., *Science*, 256, 213, 1992.
86. Jorgensen, W.L. et al., *Am. Chem. Soc. Symp. Ser.*, 353, 200, 1987.
87. van Gunsteren, W.F. and Berendsen, H.J.C., in *Molecular Dynamics and Protein Structure*, Hermans, J., Ed., Polycrystal, Western Springs, IL, 1985.
88. Harte, W.E. and Anderson, E.T., *Proc. Natl. Acad. Sci. U.S.A.*, 87, 8864, 1990.
89. Aveyard, R., *J. Colloid Interface Sci.*, 52, 621, 1975.
90. Roser, S.J. Felici, R., and Eaglesham, A., *Langmuir*, 10, 3853, 1994.
91. Cosgrove, T., Phipps, J., and Richardson, R.M., *Colloids Surf.*, 62, 199, 1992.
92. a) Mareschat, M., Meyer, M., and Turq, P., *J. Phys. Chem.*, 95, 10723, 1991; b) Willard, N.P., *Langmuir*, 14, 5907, 1998; Kramer, E.J., *Macromolecules*, 30, 1906, 1997; Orban, J.M., *Macromolecules*, 29, 7553, 1996; Schwarz, S.A., *Macromolecules*, 29, 899, 1996; Menke, T.J. et al., *Macromolecules*, 33, 6120, 2000; Hernáinz, F. and Caro, A., *J. Chem. Eng. Data*, 46, 107, 2001; c) Birdi, K.S., Vu, D.T., and Winter, A., *J. Phys. Chem.*, 93, 3702, 1989; Birdi, K. S. and Vu, D.T., *Adhes. Sci. Technol.*, 7, 485, 1993; Schwartz, L.W., *Langmuir*, 15(5), 1859, 1999; Chen, L.-J. et al., *J. Phys. Chem.*, 98, 1910, 1994; d) Picknett, R.G. and Bexon, R., *J. Colloid Interface Sci.*, 61, 336, 1977; Rowan, S.M., Newton, M. L., and McHale, G., *J. Phys. Chem.*, 99, 13268, 1995; Erbil, H.Y., Surface tension of polymers, in *Handbook of Surface and Colloid Chemistry*, Birdi, K.S., Ed., CRC Press, Boca Raton, FL, 1997; Erbil, H.Y., *Z Phys, Chem. B*, 102, 9234, 1998; Erbil, H.Y., *J. Adhes. Sci. Technol.*, 13, 1405, 1999; Erbil, H.Y. et al., *Adhes. Sci. and Technol.*, 13, 1375, 1999, *Langmuir*, 15, 7378, 1999; Erbil, H.Y. and Dogan, M., *Langmuir*, 16, 9267, 2000.
93. Angell, C.A., *J. Chem. Educ.*, 47, 583, 1970; *J. Phys. Chem.*, 70, 2793, 1966.
94. Kauzmann, W., *Chem. Rev.*, 43, 219, 1948.
95. Hock, R., *Wien Ber.*, 108(AII), 1516, 1899.
96. a) Wu, X.Z. et al., *Science*, 261, 1018, 1993; b) Birdi, K.S., *Colloids Surf.*, 123, 543, 1997; c) Back, D.D., *J. Chem. Eng. Data*, 41, 446, 1996.
97. Salajan, M. et al., *J. Colloid Interface Sci.*, 164, 387, 1994.

4 Surface Waves and Dissipative Solitons Sustained by the Marangoni Effect

Michèle Vignes-Adler and Manuel G. Velarde

CONTENTS

- 4.1 [Introduction.](#)
- 4.2 [The Marangoni Effect](#)
- 4.3 [Nonlinear Surface Waves](#)
- 4.4 [Nonlinear Wave Properties and the Marangoni Effect](#)
- 4.5 [Experiments](#)
 - 4.5.1 [Waves, Patterns, and Interfacial Turbulence](#)
 - 4.5.2 [Experimental Evidence for Solitonic Behavior](#)
 - 4.5.2.1 [Wave Characteristics](#)
 - 4.5.2.2 [Characterization of the Collisions](#)
 - 4.5.2.2.1 [Oblique Collisions between Pinned Waves](#)
 - 4.5.2.2.2 [Head-On Collisions between Free Waves](#)
 - 4.5.2.2.3 [Overtaking Collisions](#)
 - 4.5.3 [Wave Collisions and Patterns](#)
 - 4.5.3.1 [Quasi-Elastic and Inelastic Collisions](#)
 - 4.5.3.2 [Patterns](#)
- 4.6 [Conclusion](#)
- [References](#)

4.1 INTRODUCTION

A liquid layer heated from below is stratified: it may not be stable, and above a certain instability threshold, rolls and stationary hexagonal cells are produced. This is the well-known Bénard convection. Now, when the liquid layer is heated from above, it is stratified and stable, but the variation of surface tension can lead to oscillatory surface convection, to stationary or traveling surface waves. Mass transfer through the interface between two stratified liquid layers can also produce similar surface waves when the latter results in a lowering of the interfacial tension. Namely, in the 1960s Linde and Schwarz¹ observed patterns at the surface of a shallow octane layer heated from above. Similarly, Orell and Westwater² observed stationary and propagating patterns, stripes, and ripples produced at an ethylene glycol–ethyl acetate interface by the interfacial transfer of acetic acid from the glycol phase. In both cases, the authors measured the wavelength and wave velocities, and from a simplified linear stability theory, the oscillation frequencies of the convective cells and the instability threshold could be fairly predicted.³

In the 1990s, this problem of surface structuration was revisited in the light of recent theoretical findings obtained on nonlinear surface waves.⁴ It could be established that the waves sustained by a Marangoni effect, as observed by Linde and Schwarz and Orell and Westwater, are relevant to a nonlinear theory. They have solitonic properties and the patterns that structure the surface are produced by their collision.⁵ The description and analysis of these nonlinear waves sustained by a solutal Marangoni effect are the subject of this chapter.

4.2 THE MARANGONI EFFECT

The Marangoni effect transforms physicochemical energy into flow whose form and evolution depend on the sign of the thermal or solutal gradient and the transport properties of the adjacent fluids. It is associated with two surface phenomena. The first is the motion in a fluid interface due to the local variation of interfacial tension caused by differences in composition or temperature induced, for example, by dissolution (or evaporation). The second is the departure from equilibrium tension that is produced by deformation of an interface.⁶ The pioneering work of Sternling and Scriven⁷ provided the basis for the interfacial hydrodynamics incorporating these two surface phenomena effects. Their analysis was based on the Gibbs–Boussinesq description for approximating the behavior of real interfaces as the two-dimensional analogue of the three-dimensional fluid dynamics for Newtonian fluids. In the same way that pressure gradients generate flow in the bulk of a liquid, surface tension gradients generate interfacial convection accompanied by bulk motions. The major difference is that pressure gradient–driven motions can occur in inviscid fluids, whereas surface tension gradient–driven motions are always dissipative because the Marangoni effect induces shear viscous stresses.

Sternling and Scriven⁷ wrote the interfacial boundary conditions on nonsteady flows with free boundary and they analyzed the conditions for hydrodynamic instability when some surface-active solute transfer occurs across the interface. In particular, they predicted that oscillatory instability demands suitable conditions crucially dependent on the ratio of viscous and other (heat or mass) transport coefficients at adjacent phases. This was the starting point of numerous theoretical and experimental studies on interfacial hydrodynamics (see Reference 4, and references therein). Instability of the interfacial motion is decided by the value of the Marangoni number, Ma , defined as the ratio of the interfacial convective mass flux and the total mass flux from the bulk phases evaluated at the interface. When diffusion is the limiting step to the solute interfacial transfer, it is given by

$$Ma = \frac{\partial \sigma}{\partial C} L^2 \frac{\frac{\partial C}{\partial z} |_{z=\text{interface}}}{\mu D} \quad (4.1)$$

where $C(x,y,z,t)$ is the solute concentration distribution in the bulk, $\sigma = \sigma(C)$ is the surface state equation of the interfacial tension, μ is the bulk dynamic shear viscosity, D is the diffusion coefficient of the transferring substance, and L is a characteristic length scale of the solute transfer toward the interface. This expression (Equation 4.1) is the dimensionless concentration gradient obtained from the adimensionalization of the system of equations describing the bulk and interfacial hydrodynamics. It is also a (surface) Reynolds number, or a (mass) Péclet number, based on the scale of the velocity induced by the surface tension gradients. Other pertinent nondimensional parameters of the problem are $Sc = \mu/\rho D$ (the Schmidt number), $Ca = \mu D/\sigma L$ (the capillary number), and $Bo = \rho g L^2/\sigma$ (the static Bond number). Under appropriate circumstances, interfacial instability can excite (transverse) gravitocapillary waves or (longitudinal) dilational waves propagating at the liquid surface. The former demand surface deformation, whereas the latter do not. In the following we illustrate how gravitocapillary waves can be excited to a striking nonlinear level.

4.3 NONLINEAR SURFACE WAVES

Assume that a capillary wave of wavelength λ is generated by a localized deformation η (pulse) of the free surface of a liquid layer of thickness h . If $h \ll \lambda$ and $\eta \ll h$, the wave propagation occurs with a linear phase velocity $c_o = \sqrt{gh}$; this is a result typical of waves in shallow waters. If the free surface deformation η , although small compared with the wavelength, is not regarded as infinitesimal, the nonlinearity cannot be neglected. Then, the propagation in, say, the x -direction of this weakly nonlinear and dispersive shallow water wave can be modeled by the Boussinesq–Korteweg–de Vries (BKdV) equation.^{4,8} In a reference frame moving with velocity c_o , the BKdV equation for an inviscid liquid is

$$\eta_t + a_1 \eta \eta_x + a_3 \eta_{xxx} = 0 \quad (4.2)$$

$$\text{with } a_1 = \frac{3}{2} \frac{c_o}{h} \quad \text{and} \quad a_3 = \frac{c_o}{6} \left(h^2 - \frac{3\sigma}{\rho g} \right) = \frac{c_o h^2}{6} (1 - 3B_o^{-2})$$

where ρ and σ are the liquid density and surface tension, and g is gravity. For simplicity, we have only considered waves traveling in one direction, say, right-moving waves. Consideration of waves propagating in both directions, right and left, brings a second time derivative term rather than the first derivative in Equation 4.2 together with higher-order space derivatives.

The nonlinear term $\eta \eta_x$ accounts for wave peaking as higher waves travel with higher velocities. The peaking and possible breaking is balanced by the dispersive term η_{xxx} (making velocity dependent on wavelength) related to gravity and surface tension (via the Bond number). When both terms (nonlinearity and dispersion) are in (local) dynamic balance, which depends on whether the ratio a_1/a_3 is of order unity, a wave or a pulse may become permanent, thus traveling with no deformation. Indeed, the BKdV Equation 4.2 is known to possess particular solutions in the form of solitary waves and periodic cnoidal waves trains. The steady, permanent solution called the solitary wave is

$$\eta = \eta_o \operatorname{sech}^2 \left[\frac{3\eta_o}{4h^3} (x - Vt) \right]$$

where due to nonlinearity the phase velocity V is amplitude dependent; η_o is the wave amplitude and its width depends on the quantity $\sqrt{4h^3/3\eta_o}$.

An important property is that the BKdV solitary waves have particle-like properties when colliding with each other as first shown by Zabusky and Kruskal,⁹ who showed that, upon collision, such solitary waves cross each other without apparent deformation, hence the name *solitons*. Moreover, depending on the angle before collision, they experience, at most, a displacement in their trajectories originating in a temporary change in wave velocity, which is called a *phase shift*.⁴

4.4 NONLINEAR WAVE PROPERTIES AND THE MARANGONI EFFECT

A solvent dissolution, a vapor adsorption, any kind of surface-active substance exchange between the surface and the adjacent subphase, or heating makes the surface tension locally vary, thus generating Marangoni stresses and convection. Then, gravitocapillary waves (wavelength λ and amplitude η) excited and sustained by the Marangoni effect in the shallow water waves approximation can be described by the equation:

$$\eta_t + a_1 \eta \eta_x + a_2 \eta_{xx} + a_3 \eta_{xxx} + a_4 \eta_{xxxx} + a_5 (\eta \eta_x)_x = 0 \quad (4.3)$$

where the coefficients a_i ($i = 1$ to 5) depend on the dimensionless parameters defined above. Thus, Equation 4.3 is the natural generalization of Equation 4.2 accounting for the Marangoni effect, the concomitant dissipation, and hence the appropriate (local) dynamic (input–output) energy balance. The cumbersome explicit forms of the coefficients a_i can be found in Reference 10. It seems pertinent to recall their origin and the role of the various terms of Equation 4.3 on the wave propagation.

The new coefficients a_1 and a_3 , that now also depend on Schmidt and capillary numbers in addition to the Bond number, have exactly the same role as in Equation 4.2 when their ratio a_1/a_3 is of order unity. The coefficient a_2 depends on Schmidt and Marangoni numbers, a_4 depends on capillary, Schmidt, and Bond numbers, and although a_5 depends only on the Schmidt number, the term $(\eta\eta_x)_x$ is a genuine contribution of the Marangoni stresses. The role of the a_2 term, whose sign changes as the Marangoni number increases, is to create the instability and subsequently at supercritical Marangoni numbers to provide continuous energy input for the flow.⁴ This energy brings the wave motion in the long wavelength range and in part it is dissipated by viscosity at the opposite side of the spectrum, i.e., at short waves. The a_4 term, proportional to η_{xxxx} , takes care of this viscous dissipation. The a_5 term helps energy redistribution over the wave spectrum.

Note that waves obeying Equation 4.2 can only be the result of initial conditions like with standard wave makers in the laboratory. They can also take all possible amplitudes or phase velocities. In contrast, waves obeying Equation 4.3 can only have a single amplitude or velocity, depending on the conditions of the experiment. The latter case corresponds to the waves reported here. This is a property generally valid for all dissipative structures whether steady patterns or waves. Thus, if a wave is excited above or below the required level imposed by the Marangoni number, it is expected that in the course of time its amplitude and corresponding velocity will evolve toward a given terminal value set by the Marangoni effect. Hence, initial conditions play a negligible role.

To see this result, the time variation of the (free) energy of the surface wave is calculated by multiplying Equation 4.3 by η , and integrating over a wavelength or over the entire surface with, say, vanishing values of η at both boundaries ($x \rightarrow \pm\infty$). It gives

$$\frac{1}{2} \frac{\partial}{\partial t} \int_{-\infty}^{+\infty} \eta^2 dx = -a_2 \int_{-\infty}^{+\infty} \eta\eta_{xx} dx - a_4 \int_{-\infty}^{+\infty} \eta\eta_{xxxx} dx \quad (4.4)$$

In Equation 4.4, for simplicity, a_5 is neglected. Note also the fact that both a_1 and a_3 terms vanish *separately* by suitable integration by parts. For steady, permanent waves of Equation 4.3, the left-hand side term vanishes but, as none of the right-hand side terms vanishes separately, the only possibility to obtain the dynamic (free) energy dynamic balance early mentioned is for both to vanish combined. This is possible if they have opposite signs, which only occurs when the Marangoni number is above critical. The vanishing value of a_2 defines the critical value of the Marangoni number for the onset of overstability and the generation of surface waves by the Marangoni effect. Past the instability threshold, we expect these waves to be sustained by Equation 4.4. Experimental evidence has confirmed this qualitative prediction and, in particular the (solitonic) particle-like behavior in surface tension gradient (Marangoni)–driven waves.⁴

It is also worth recalling that when simultaneously a_3 and a_4 vanish (we also disregard a_5) Equation 4.3 reduces to the Burgers equation,⁴ which is known to possess (Taylor–Burgers) shocks. In this case there is an energy balance between the nonlinear a_1 term and the dissipative a_2 term. Shocks are also known to possess solitonic-like properties, a phenomenon already discovered long ago by Mach and collaborators (for an historical account see e.g., References 4 and 11).

Thus, according to the relative values taken by the coefficients a_i ($i = 1$ to 5), Equation 4.3 is expected to provide different solutions in the form of humps (bumps) or shocks (kinks, bores,

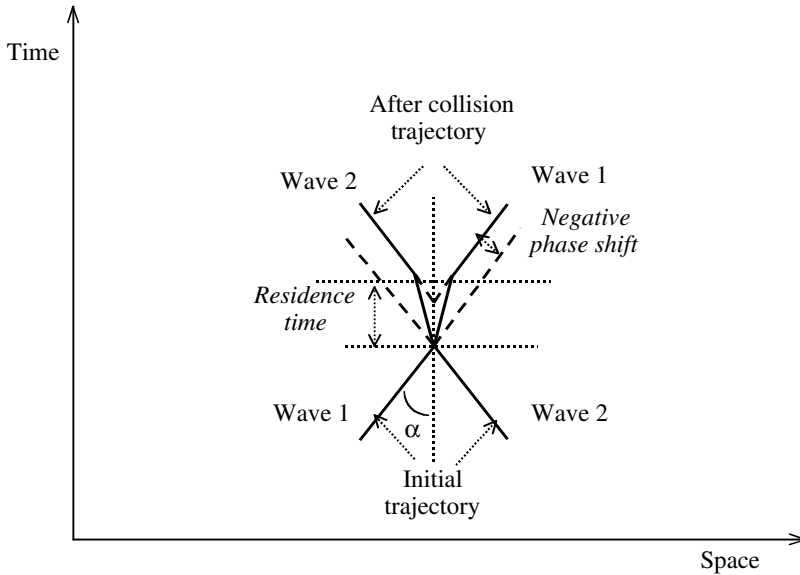


FIGURE 4.1 Space–time plot of a head-on collision with negative phase shift: the waves are temporarily decelerated due to collision and they reappear delayed.

mascarets, or hydraulic jumps). The former comes from the BKdV equation as sech^2 -like solutions or periodic cnoidal waves whereas the latter come from the Burgers equation as \tanh -like solutions.

There is also numerical evidence of the above given solitonic properties of nonlinear waves. For the particular case of Equation 4.3 and related two-side propagating wave equations, Christov and Velarde¹³ have calculated wave profiles and discussed the kinematics of the collisions of solitonic surface waves in two extreme limiting cases.

Case A: The production-dissipation part of Equation 4.3 (a_2, a_4, a_5 terms), hence the free-energy balance, is taken as a small perturbation to the BKdV equation. Hump shape solutions after interaction experience a decrease in amplitude (slow “aging”) while keeping their sech^2 -like shape to a large extent. However, if the interaction triggers enough production, the sech^2 evolves until it reaches a shape of higher amplitude in accordance with the energy balance.

Case B: The production-dissipation part of Equation 4.3 is predominant. This corresponds to negligible dispersion. Although a hump shape solution may exist, it is not stable and a space and time chaotic regime may occur. Then, shocks (\tanh -like) can exist that share features of solitons but their interactions appear almost completely inelastic: after collision the waves may stick to each other and form a single structure, or have trajectories that drastically depart from their original ones. Generally, dissipative waves exhibit inelasticity upon collisions.

Finally, solitary waves are characterized by their collisions. There exist two main types of wave collisions, *oblique* and *head-on collisions*, which generate different patterns in the liquid surface. Head-on collisions are better analyzed in a space–time diagram, whereas oblique collisions can be easily analyzed in real space.

Head-on collisions are such that two waves approaching each other emerge after collision, accelerate, and keep moving away from each other with almost the same velocity as before collision. The analysis of the collision is achieved by plotting vs. time the position x of several points of the moving front in an Euclidean frame of reference (Figure 4.1). The velocity changes are measured by the angle between the pre- and postcollision trajectories. By convention *positive* (respectively, *negative*) *phase-shift* corresponds to a temporary acceleration (respectively, deceleration) of the wave caused by the collision, after which the wave appears slightly in advance (respectively, delayed) relative to its initial position. and after a time called the *residence time*.

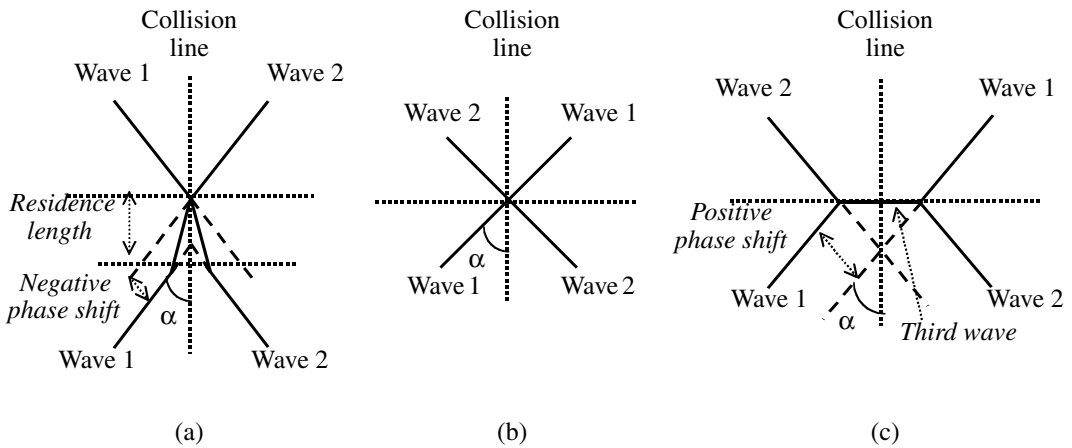


FIGURE 4.2 Schematic classification of oblique collisions according to the collision angle α represented in the real space: (a) $2\alpha < \pi/2$ oblique acute collision, (b) $2\alpha \sim \pi/2$ neutral collision, (c) $2\alpha > \pi/2$ Mach–Russell oblique collision.

When two solitary waves or shocks collide at an initially oblique angle, the result depends on the actual value of this angle (Figure 4.2). If it is small and acute enough, the trajectories experience a delay opposite to the case of wide, obtuse-enough collisions. There is, indeed, a critical value of the collision angle at which no appreciable change of trajectories exists (Figure 4.2b). When the angle is acute, there is formation of a dead zone on a residence length where the waves strongly interact (Figure 4.2a). When the angle is wide enough, there is formation of a third wave that after collision emerges forward, phase locked with the two other waves (Figure 4.2c). This is called the Mach–Russell stem or third wave, a phenomenon observed by Mach in 1875, and earlier by Russell and others for the case of oblique reflections at walls.^{4,11,12} We can observe a change in real trajectories leading to a phase shift that follows the above convention defined in the space–time representation for head-on collisions. A residence length is defined by analogy with the residence time in the space–time representation for the head-on collisions.

4.5 EXPERIMENTS

4.5.1 WAVES, PATTERNS, AND INTERFACIAL TURBULENCE

Experiments show a rich variety of phenomena as illustrated below. Santiago-Rosanne et al.^{14,15} observed a daisy flower–like pattern generated by the dissolution of a nitroethane drop with a lower surface tension than that of water and partially soluble in water carefully deposited at a water surface (Figure 4.3). As soon as the nitroethane droplet is deposited, it spreads under the action of gravity and capillary forces with formation of a central cap surrounded by a thin circular primary film ending in a rim. The drop deposition generates circular dimples, a form of rapidly damped gravitocapillary waves appearing over the entire open surface of the aqueous solution extending beyond the surface wetted by the nitroethane (Figure 4.3a). Then, a petal-like pattern like a daisy occurs in the primary film (Figure 4.3b). Finally, the daisy pattern breaks (Figure 4.3c) and evolves toward a seemingly spatially chaotic state, which is usually called interfacial turbulence (Figure 4.3d). The time taken for the droplet to be completely dissolved by the mixing process is about 5 s.

Linde et al.^{16–18} observed by shadowgraphy traveling surface waves in an annular container from the absorption of a solvent vapor, e.g., pentane, by another solvent layer, e.g., toluene, which has a higher surface tension. The time evolution of the surface convection is opposite to the one observed

by Santiago-Rosanne et al. When the absorption process starts there is immediately a strong interfacial turbulence with irregular traveling and breaking waves, which evolve toward more and more regular periodic wave trains.

These opposite time evolutions of the surface motions are related to the Marangoni number variations. In the Santiago-Rosanne et al. experiments, at the contact surface between the central cap and the aqueous layer there is an excess of nitroethane; the first molecular water layer is immediately saturated with nitroethane and the interfacial tension decreases from $\sigma_w = 73$ mN/m to $\sigma_{n/w} = 14.65$ mN/m. Because the nitroethane is very easily dissolved in water in the limit of its miscibility, its adsorption kinetics at the interface is not expected to be a limiting step at any time of the experiment, as no surface tension gradient can develop there as long as the central cap exists. For the same reason there is no surface or interfacial tension gradients in the primary film either, as long as there is an excess of nitroethane. Gradients can only exist when there has been some nitroethane depletion in the solution surface. This happens when the nitroethane primary film has sufficiently diffused in the solution. Besides, as the geometry of the experiment is axisymmetric, the nitroethane concentration decreases as the distance from the central cap increases. Hence, the interfacial transfer (characterized by the Marangoni number) depends on the location and changes in time during the experiment, hence the transient although relatively long lasting character of the patterns and related phenomena in an unsteady experiment.

In the Linde et al. experiments,¹⁶ at the start of the experiment, the concentration gradient is very high and so is the Marangoni number leading to strong interfacial turbulence. They decrease further with time as the vapor absorption slows giving rise to quasi-stationary periodic waves with steady wavelength and frequency until thermodynamic equilibrium between the vapor and liquid phases is achieved. During the transient phase, the Marangoni number does not depend on the location in the surface, and no pattern is observed.

4.5.2 EXPERIMENTAL EVIDENCE FOR SOLITONIC BEHAVIOR

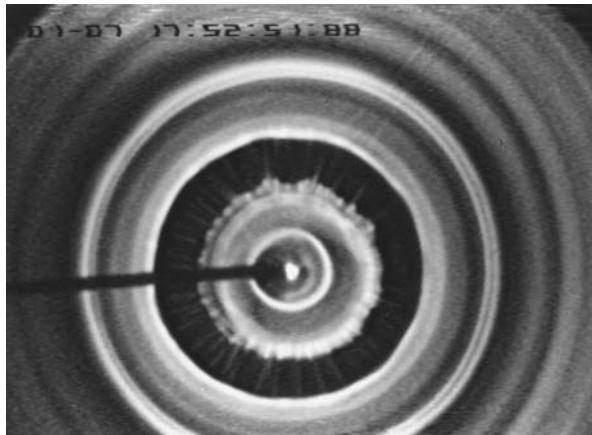
As stated above, their shape, their velocity, and their collisions characterize soliton-like waves. In the present state of knowledge, comparison between theoretical analysis and experimental data can be obtained in two basic situations when there is predominance of the nonlinearity dispersion balance, as in BKdV solitons (case A) and when the (free)-energy production dissipation terms dominate (case B).¹³

Surface waves only appear when the (local) Marangoni number Ma is higher than a critical value, i.e., past an instability threshold. Usually the actual value of Ma cannot be easily measured, and it is estimated. In the Santiago-Rosanne experiments, near the central cap, Ma is practically zero and case A of surface waves is expected. Far from it the surface tension gradients are much more important, Ma is large and case B should occur. Remarkable enough is that both limiting cases can be found for the same wave but at different positions along the front, which illustrates the local, space-time dependence of the parameters influencing the wave motion.

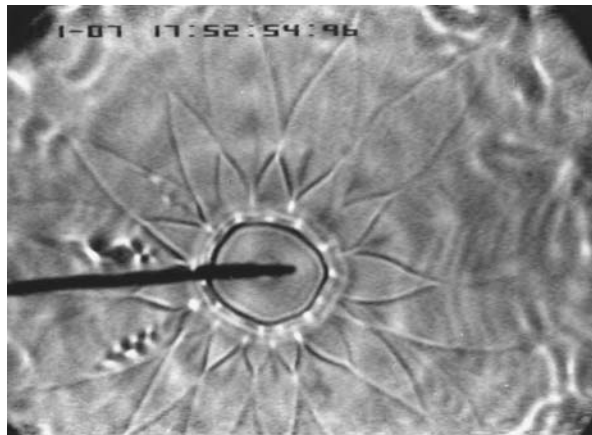
4.5.2.1 Wave Characteristics

The deformations of the liquid surface induced by the waves are usually in the submillimetric range, and they can be optically measured by means of a Schlieren technique.^{14,15} The wave velocity is obtained by following the trajectory of several points of the moving wave in the laboratory reference identified by their curvilinear coordinate d along the wave in sequences of frames taken every 0.02 s. The position, d , is plotted as a function of time. A resulting straight line indicates constant velocity of propagation of the wave.

Two examples of wave profiles are given in [Figures 4.4](#) and [4.5](#); they were obtained from an experiment like the one displayed in [Figure 4.3](#).¹⁴



(a)



(b)

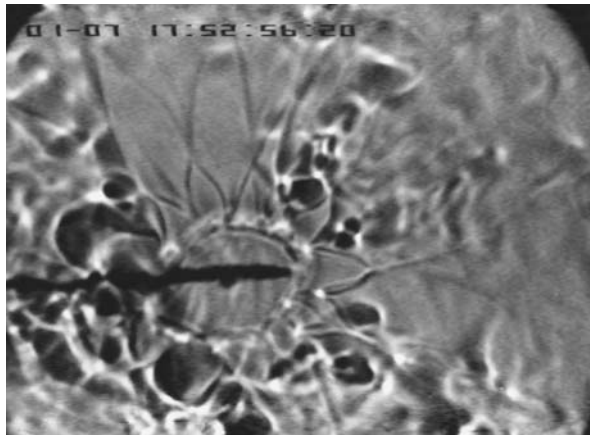
FIGURE 4.3 Photograph showing the surface phenomena arising when a drop of nitroethane is carefully deposited on the free surface of a water layer. The solvent drop spreads as a central cap surrounded by a primary film. The pattern formation and evolution (surface waves and their interactions) in the primary film are visualized with a Schlieren device sensitive to density gradients and surface deformations. The sequence of events is as follows: (a) traveling ripples following drop deposition on the water surface with subsequent drop spreading; (b) petal-like unsteady structure appearing in the primary film due to surface wave collisions; (c) transition to the chaotic behavior with transient formation of “coherent” structures; (d) interfacial turbulence. (Modified from Santiago-Rosanne, M. et al., *J. Colloid Interface Sci.*, 191, 65, 1997.)

Figure 4.4a shows the evolution in a moving frame (variable x) of the profile of a wave measured at a few millimeters near the central cap where the surface tension gradients are small. It is well fitted to a sech^2 function:

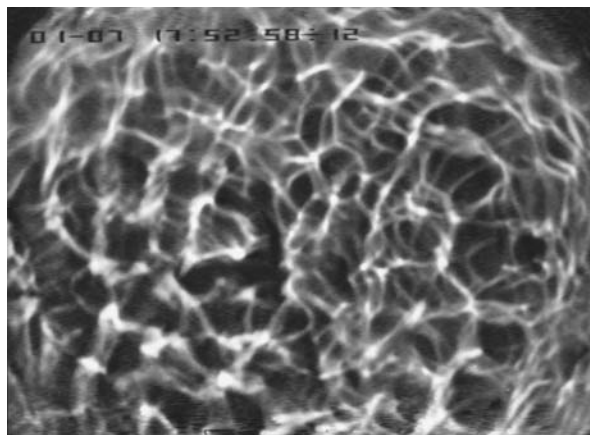
$$z(x) = \text{sech}^2[(x - c \cdot t)\beta]$$

traveling with a constant phase velocity $c = 7.4$ mm/s. It keeps its sech^2 -like shape during its propagation. However, its width in the x -direction $\beta = \beta(t)$ evaluated at $z = 0$ changes with time (Figure 4.4b); sequentially, it decreases, increases, and decreases again.

Far from the central cap, where the surface tension gradients are large, the profile of the same wave evolves to a *tanh-like* function:



(c)



(d)

FIGURE 4.3 (CONTINUED)

$$z(x) = \tanh[(x - c \cdot t)\delta]$$

δ accounts for the width where the jump occurs in the experiment (Figure 4.5a). This tanh-like wave travels with a constant velocity $c = 34$ mm/s, and it experiences an increase in velocity, preserves its shape and its width δ during propagation (i.e., δ is time independent) (Figure 4.5b).

The two wave profiles displayed in Figures 4.4 and 4.5 are very much like the numerical ones reported by Christov and Velarde.¹³ As earlier described, the stable sech²-like profile corresponds to case A, when there is a low level in the energy production dissipation part of Equation 4.3; hence, dissipation is a small perturbation to the BKdV equation. Two stages of evolution could be predicted: (1) first, the amplitude and the width of the sech²-like profiles decrease; (2) then, when the energy input is large enough, the amplitude of the wave increases while its width decreases. With the Schlieren the absolute measurement can only be done in one direction, here, x ; hence, the absolute value of the amplitude cannot be obtained in the z -direction but the x distances are absolute. Figure 4.4b shows that the width of the sech²/hump increases and decreases in time as predicted by the numerical analysis.

Numerical tanh/shock profiles correspond to case B where the level in the energy production dissipation balance in Equation 4.3 is predominant compared with the viscous-free BKdV terms.

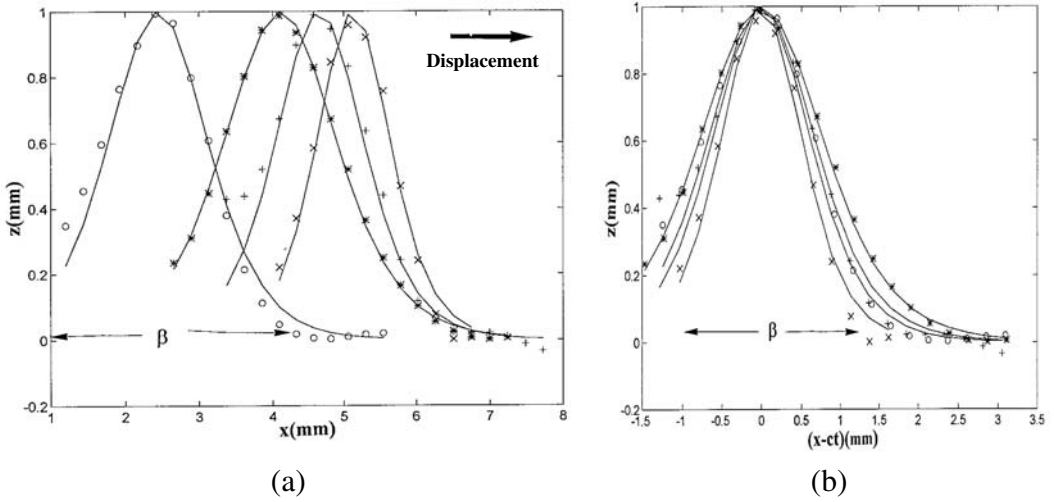


FIGURE 4.4 Normalized surface wave sech-like profiles obtained, as the nonlinearity induced by the dispersion term in Equation 4.3 is predominant: (a) time evolution of a sech-like profile near the central cap; (b) shift of the origin on the x -axis to compare all shape profiles together. (o , $t = t_0$; $*$, $t = t_0 + 0.16$ s; $+$, $t = t_0 + 0.28$ s; \times , $t = t_0 + 0.36$ s.) (From Santiago-Rosanne, M. et al., *J. Colloid Interface Sci.*, 191, 65, 1997. With permission.)

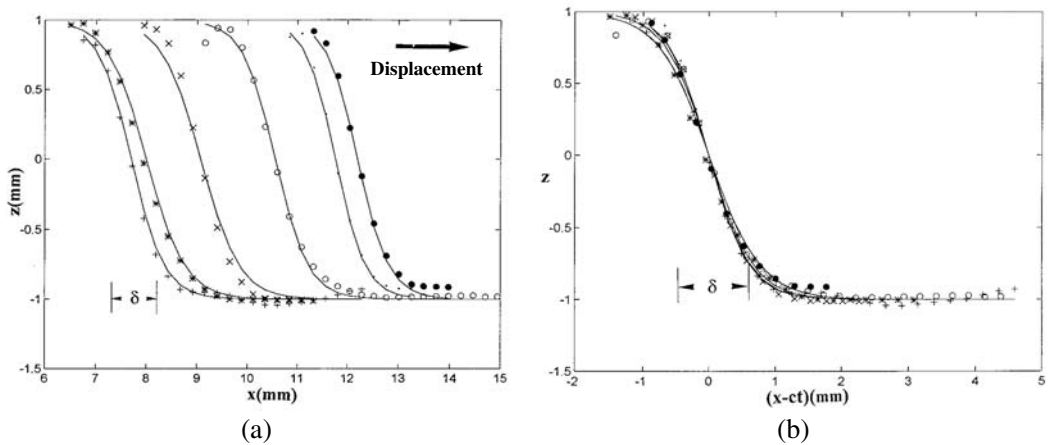


FIGURE 4.5 Normalized surface wave tanh-like profiles: (a) time evolution of a tanh-like profile far from the central cap; (b) shift of the origin on the x -axis through the change of variables $x' = x - c \cdot t$ to compare all shape profiles together. ($*$, $t = t_0$; $+$, $t = t_0 + 0.04$ s; \times , $t = t_0 + 0.08$ s; o , $t = t_0 + 0.12$ s; \cdot , $t = t_0 + 0.16$ s; \bullet , $t = t_0 + 0.24$ s.) (From Santiago-Rosanne, M. et al., *J. Colloid Interface Sci.*, 191, 65, 1997. With permission.)

Stable tanh-like profiles were found far from the central cap, where, indeed, Ma seems to be large enough.

A wave can be pinned or completely free to travel until it meets some obstacle, namely, a wall. The former case occurs when the wave is tied to some point, for example, when it is tied to the central cap in Figure 4.3b. At the pinning point, $Ma = 0$ since there is no interfacial mass flux below the central cap; hence, the wave velocity is also zero there. The value of Ma slightly departs from zero very near the central cap and increases as we move away from it. Then, when $Ma \neq 0$, the wave travels with a velocity that depends on the distance to the pinning point. The latter case is

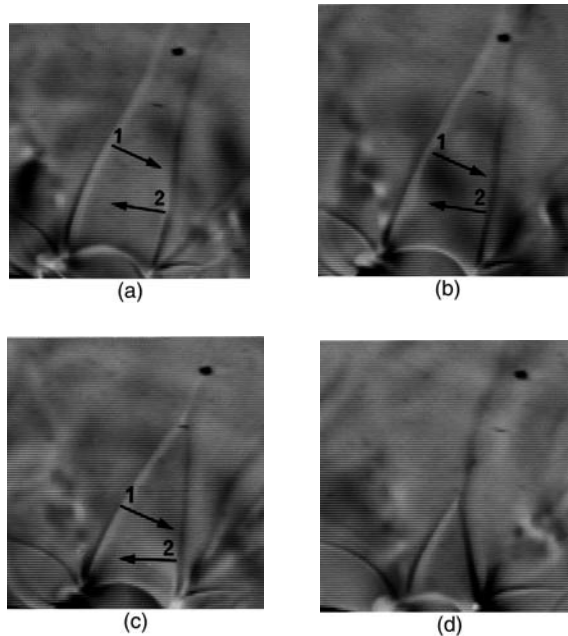


FIGURE 4.6 Standard collision of pinned waves: (a and b) before interaction; (c) during interaction; (d) after interaction. Arrows indicate the direction of propagation of both waves. The dust in the optical system acts as a fixed reference frame for better observation of the propagation. (From Santiago-Rosanne, M. et al., *J. Colloid Interface Sci.*, 191, 65, 1997. With permission.)

beautifully shown by the Linde et al. experiments, all waves obtained in an annular cell are free to travel either clockwise or counterclockwise.¹⁶ In a square container they can be reflected upon collision with the wall.^{5,19}

4.5.2.2 Characterization of the Collisions

In the simple experiment of the deposited nitroethane drop, we can observe several types of collisions. However, in view of the unsteady character (solvent dissolution, etc.) of this kind of experiment, the occurrence of a given type of interaction has a random character. However, we can safely say that each event depends on the local value of parameters such as the local Ma , and not on the initial conditions of the experiment.

4.5.2.2.1 Oblique Collisions between Pinned Waves

We can observe

- Neutral oblique collisions (Figure 4.6)
- Oblique collisions with negative phase shift and formation of a “dead zone” (vanishing wave velocity) (Figure 4.7)
- Collisions with positive phase shift and formation of a Mach–Russell-like third wave (Figure 4.8) obtained when a layer of nitroethane condenses on the aqueous surface before deposition of the droplet

The trajectories of pinned waves are observed in the (x, y) surface plane. Wave crossings are denoted with α_d for pinned waves with a dead zone and with α_r for pinned waves producing a third (Mach–Russell) wave upon collision. In the scheme in Figure 4.7 we observe a sudden deceleration of the waves after collision (Figure 4.7a), hence the appearance of a dead zone (corresponding to

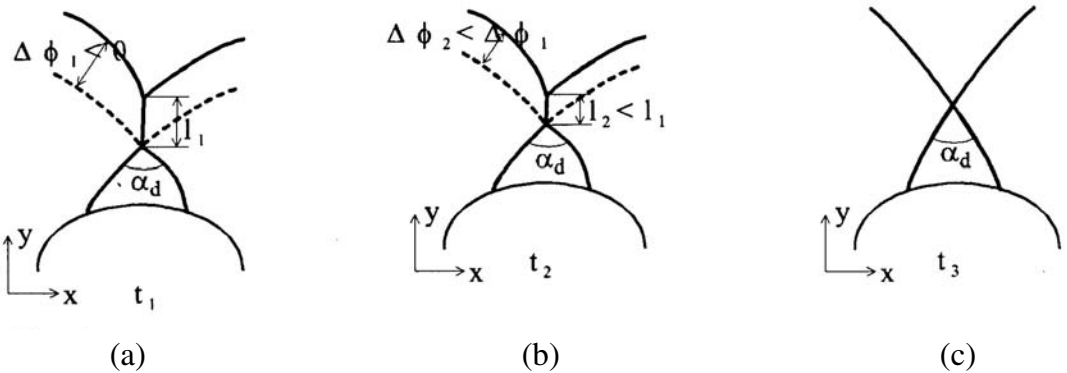
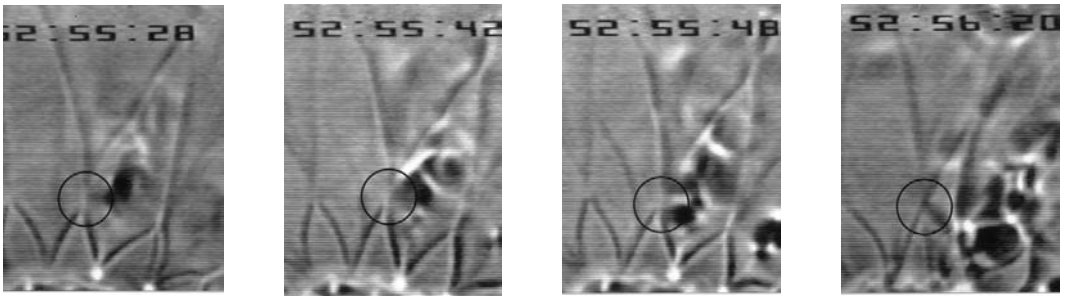


FIGURE 4.7 Oblique collision of pinned waves with formation of a dead zone where waves have vanishing velocity (same experiment as in Figure 4.3 with a higher time resolution). Details of the evolution of the dead zone are in the encircled area. Scheme shows the evolution of the negative phase shift and the length, l , of the dead zone. (a, b, c from Santiago-Rosanne, M. et al., *J. Colloid Interface Sci.*, 191, 65, 1997. With permission.)

the residence length) where locally wave velocities vanish. Then there is a process of reacceleration (Figure 4.7b) and the dead zone disappears (Figure 4.7c). The critical angle at which the dead zone disappears is about 23° . In Figure 4.8, we observe collisions of pinned waves with formation of a “third” wave (Mach–Russell stem). In this case there is an increase in velocity (Figure 4.8a). The length of the third wave, L , and the angle, α_p , decrease with time (Figure 4.8b). Then, the third wave disappears and there is no velocity change at a critical angle about 82° (Figure 4.8c). Similar phenomena were reported by Weidman et al.⁵

4.5.2.2.2 Head-On Collisions between Free Waves

Figure 4.9 shows the head-on collision of two waves. Local collisions at several distances d from the wave origin at the central cap are analyzed in the space–time diagram.

- $d = 14.8$ mm (scheme a): The faster wave experiences no velocity change, whereas the slower wave reappears with still lower velocity.
- $d = 7.22$ mm (scheme b): The faster wave experiences no velocity change, whereas the initially slower wave reappears with higher velocity.
- $d = 23.4$ mm (scheme c): Very far from the central cap is a situation where both waves reappear after collision with the same velocity.

A common feature of these three collisions is that one wave keeps its initial velocity while the second wave is accelerated (positive phase shift) (scheme a), decelerated (negative phase shift) (scheme b), or its velocity remains constant (scheme c). The last steady situation has been numerically

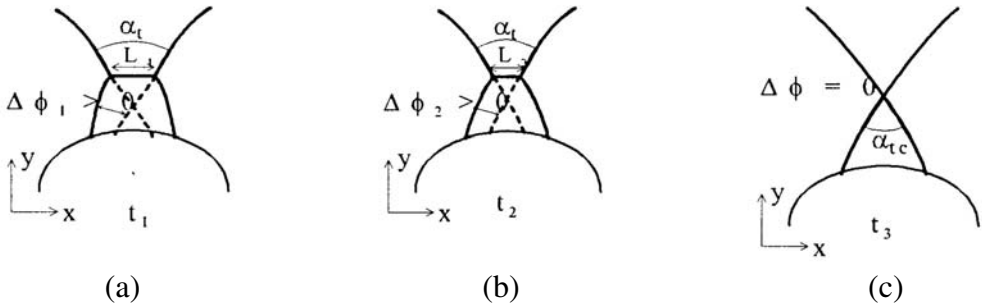
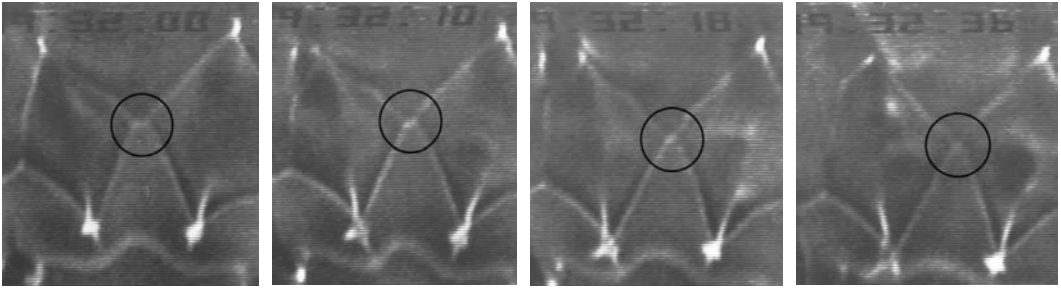


FIGURE 4.8 Oblique collision of pinned waves with formation of a Mach–Russell-like wave. The evolution of the Mach–Russell wave can be followed in the encircled area. The scheme shows the evolution of the positive phase shift and length, L , of the Mach–Russell wave. (Photos modified from Santiago-Rosanne, M. et al., *J. Colloid Interface Sci.*, 191, 65, 1997. a, b, c from Santiago-Rosanne, M. et al., *J. Colloid Interface Sci.*, 191, 65, 1997; with permission.)

obtained in Reference 13 when the (free)-energy balance Equation 4.4 operates. The two first cases correspond to an unsteady process where likely the dissipated energy is not balanced by the amount provided by the Marangoni effect. As far as we know there is no numerical simulation of this kind of collision. It is amazing that the nature of the collision changes along the waves; this is due to the spatial variation of the (local) Marangoni number as the distance from the central cap increases.

4.5.2.2.3 Overtaking Collisions

Overtaking collisions occur when two waves with very different velocities are traveling in the same direction (Figure 4.10). The faster wave collides with the slower one; then they join together forming a single wave structure that propagates with a still higher velocity, a phenomenon reminiscent of a numerical finding by Christov and Velarde when the production dissipation part of Equation 4.3 is predominant (case B).¹³

4.5.3 WAVE COLLISIONS AND PATTERNS

4.5.3.1 Quasi-Elastic and Inelastic Collisions

As far as the production dissipation part of Equation 4.3 can be taken as a small perturbation to the BKdV equation (case A), wave collisions are essentially elastic, and patterns¹⁴ or wave trains in an annular container¹⁶ can be obtained. On the other hand, the increase of production dissipation can be so important (case B) that the waves evolve toward a chaotic regime, as was numerically shown in Reference 13.

Figure 4.11 depicts the space–time plot of a head-on quasi-elastic collision with positive phase shifts between two waves of unequal velocity. The slower wave experiences the larger change in wave velocity. Both waves travel with higher velocities after the collision. This situation is reminiscent

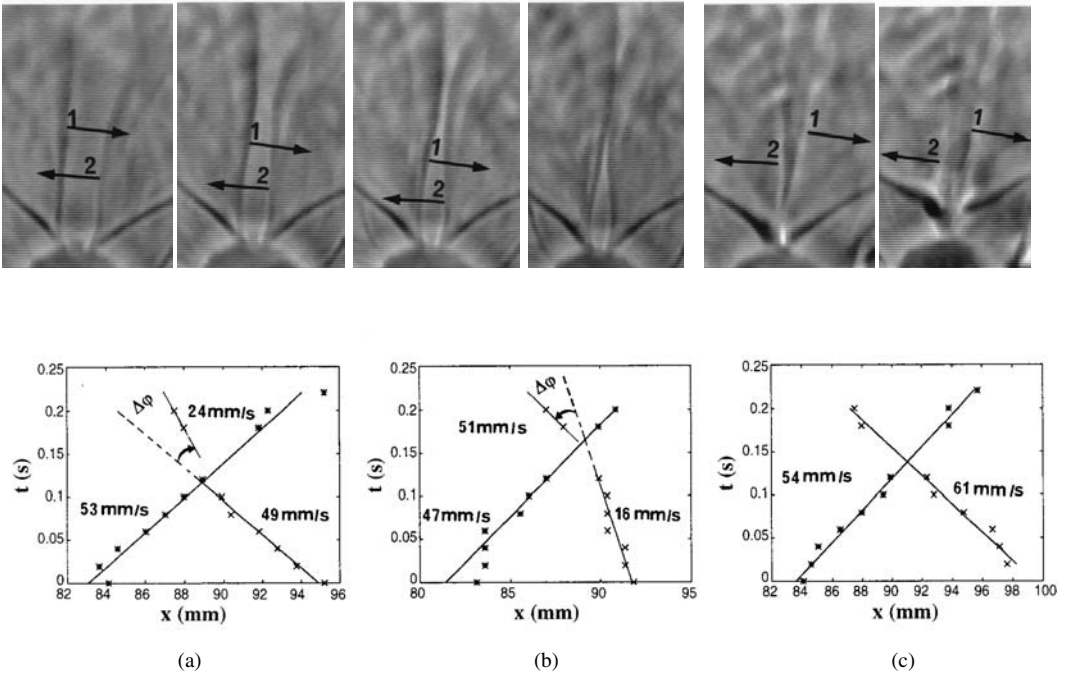


FIGURE 4.9 Head-on collision of free waves. Arrows show direction of propagation. Scheme represents the collision in a space–time representation at different locations of the waves: (a) the phase shift is negative; (b) the phase shift of the slower wave is positive; (c) zero phase shift. (Photos modified from Santiago-Rosanne, M. et al., *J. Colloid Interface Sci.*, 191, 65, 1997. a, b, c from Santiago-Rosanne, M. et al., *J. Colloid Interface Sci.*, 191, 65, 1997; with permission.)

of case A; the dissolution is, however, large enough to enhance the value of the (local) Marangoni number. Everything happens as if the energy production a_2 term in Equation 4.3 were dominating the a_4 dissipative term since an acceleration of the waves is observed. If they had balanced as in Equation 4.4, the collision would have been elastic and the waves would have recovered their initial velocities.

Figure 4.12 depicts two situations in which the production dissipation is so important to provide completely inelastic collisions. In Figure 4.12a the collision is so drastically inelastic that there is annihilation of both waves followed by interfacial turbulence after interaction. In Figure 4.12b the slower wave disappears while the faster experiences no change in velocity. Image processing is not easy, and it cannot be excluded in this case that the slower wave does not annihilate but rather sticks up to the faster wave, as happens in the numerical study of Equation 4.3 when dissipation is very high (term a_4 predominates relative to the others).

4.5.3.2 Patterns

Patterns are due to wave collisions. In the experiments by Linde and Schwarz¹ or Orell and Westwater,² the observed polygonal cells are patterns obtained as two traveling wave trains cross each other. Actually, the second train corresponds to the reflection of the first train against a wall.^{17,20}

Inspection of the pictures in Figure 4.3 shows that the “petals” are patterns due to collisions between two sets of pinned waves, one set traveling clockwise and the other counterclockwise (Figure 4.13). Indeed, the formation of one surface wave is simultaneously accompanied by the formation of its mirror image, a symmetric one. A wave and its symmetric companion never interact because they always travel in opposite azimuthal directions. Then, only waves traveling in one direction collide with waves traveling in the opposite direction.

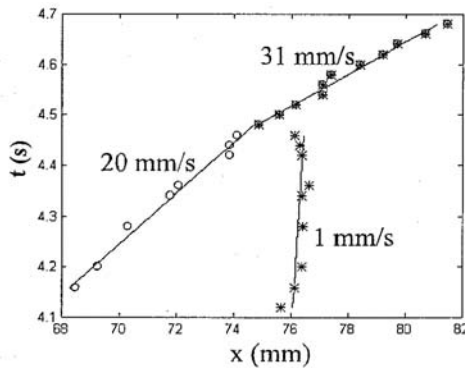
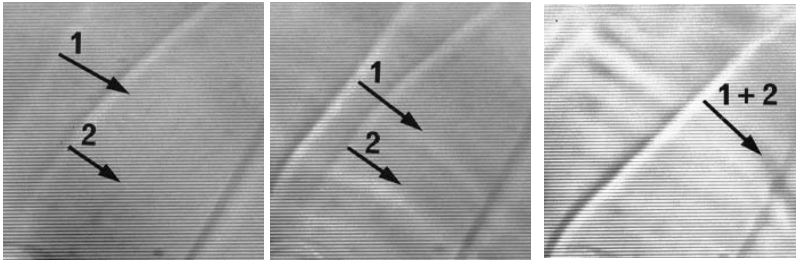


FIGURE 4.10 Example of strongly inelastic overtaking collision of free waves. Arrows show the direction of propagation. Faster wave (1) overtakes the slower wave (2). Space-time plot of the collision. (From Santiago-Rosanne, M. et al., *J. Colloid Interface Sci.*, 191, 65, 1997. With permission.)

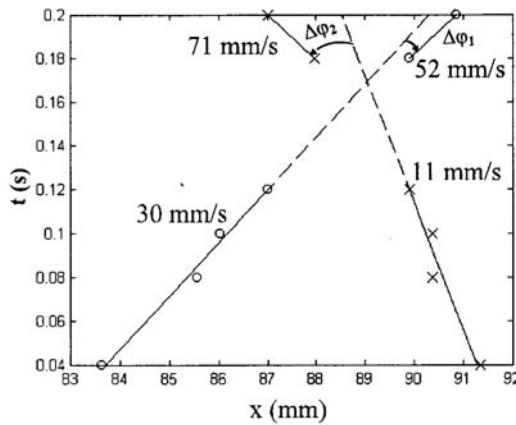


FIGURE 4.11 Quasi-elastic head-on collisions with positive phase shift. (From Santiago-Rosanne, M. et al., *J. Colloid Interface Sci.*, 191, 65, 1997. With permission.)

Whatever the boundary conditions, the aspect and the regularity of the pattern depend on the shape, the size of the container, and the local value of the Marangoni number.

4.6 CONCLUSION

Progress in understanding the surface structuration accompanying heat or mass interfacial transfer has been considerable. Data analysis of the waves follows the theoretical guide given by Christov

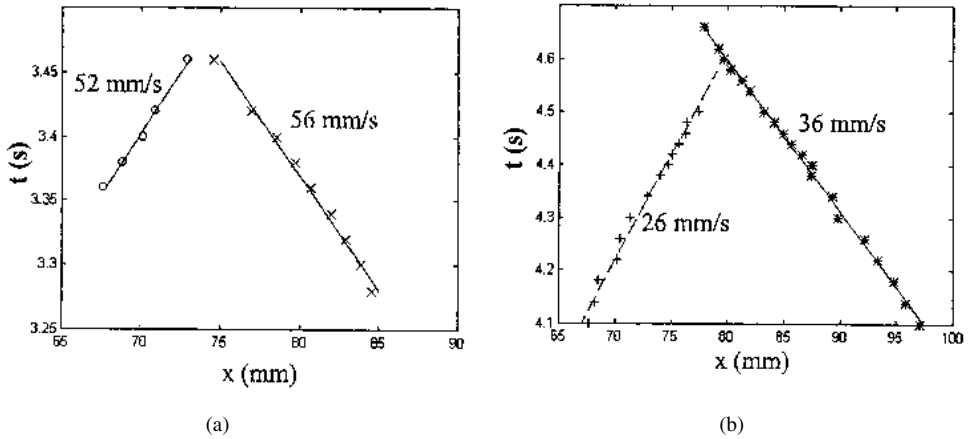


FIGURE 4.12 Highly inelastic head-on collisions with annihilation of both waves (a) or one wave (b). (From Santiago-Rosanne, M. et al., *J. Colloid Interface Sci.*, 191, 65, 1997. With permission.)

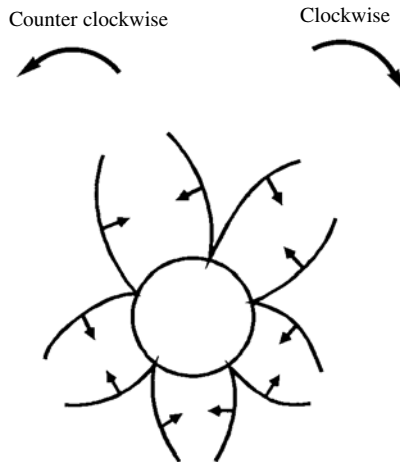


FIGURE 4.13 Formation of a daisy pattern due to the appearance of many pinned waves and their collisions with a dead zone. Rotating waves in the clockwise direction collide with counter-clockwise rotating waves. (From Santiago-Rosanne, M. et al., *J. Colloid Interface Sci.*, 191, 65, 1997. With permission.)

and Velarde.¹³ It is now well established that patterns result from the interactions of nonlinear surface waves sustained by a Marangoni effect, which have properties characterizing solitons. However, the comparison can only be qualitative for obvious reasons. Model equations such as BKdV (Equation 4.2) or the dissipation-modified Equation 4.3 come from such drastically simplifying assumptions as long wavelength, small amplitude, shallow layers, and last but not least, only one characteristic (local and global) Marangoni number, and steady boundary conditions. Although good qualitative agreement with numerics exists, clearly much remains to be done from the theoretical side.⁴

REFERENCES

1. Linde, H. and Schwarz, E., *Z. Phys. Chem.*, 224, 331–352, 1963.
2. Orell, A. and Westwater, J.W., Spontaneous interfacial cellular convection accompanying mass transfer: ethylene glycol–acetic acid–ethyl acetate, *AIChE J.*, 8, 350–356, 1962.
3. Reichenbach, J. and Linde, H., Linear perturbation analysis of surface-tension-driven convection at a plane interface (Marangoni instability), *J. Colloid Interface Sci.*, 84, 433–443, 1981.
4. Nepomnyashchy, A.A., Velarde, M.G., and Colinet, P., *Interfacial Phenomena and Convection*, CRC Press/Chapman & Hall, London, 2002.
5. Weidman, P.D., Linde, H., and Velarde, M.G., Evidence for solitary wave behavior in Marangoni-Bénard convection, *Phys. Fluids A*, 4, 921–926, 1992.
6. Levich, B., *Physicochemical Hydrodynamics*, Prentice-Hall, Englewoods Cliffs, NJ, 1962.
7. Sternling, C.V. and Scriven, L.E., Interfacial turbulence: hydrodynamic instability and the Marangoni effect, *AIChE J.*, 5, 514–523, 1959.
8. Drazin, P.G. and Johnson, R.S., *Solitons: An Introduction*, Cambridge University Press, Cambridge, U.K., 1989.
9. Zabusky, N.J. and Kruskal, M.D., Interaction of solitons in a collisionless plasma and the recurrence of initial states, *Phys. Rev. Lett.* 15, 240–243, 1965.
10. Nepomnyashchy, A.A. and Velarde, M.G., A three-dimensional description of solitary waves and their interaction in Marangoni-Bénard layers, *Phys. Fluids*, 6, 187–198, 1994.
11. Krehl, P. and van der Geest, M., The discovery of the Mach reflection effect and its demonstration in an auditorium, *Shock Waves*, 1, 3–15, 1991.
12. Courant, R. and Friedrichs, K.O., *Supersonic Flow and Shock Waves*, Wiley-Interscience, New York, 1948.
13. Christov, C.I. and Velarde, M.G., Dissipative solitons, *Physica D*, 86, 323–347, 1995.
14. Santiago-Rosanne, M., Vignes-Adler, M., and Velarde, M.G., Dissolution of a drop on a liquid surface leading to surface waves and interfacial turbulence, *J. Colloid Interface Sci.*, 191, 65–80, 1997.
15. Santiago-Rosanne, M., Vignes-Adler, M., and Velarde M.G., A pathway to interfacial turbulence, in *Fluid Physics, Lecture Notes of Summer Schools*, M.G. Velarde and C.I. Christov, Eds., World Scientific, Singapore, 1994, 275.
16. Linde, H. et al., Interfacial wave motions due to Marangoni instability. I. Traveling periodic wave trains in square and annular containers, *J. Colloid Interface Sci.*, 188, 16–26, 1997.
17. Linde, H. et al., Interfacial wave motions due to Marangoni instability. III. Solitary waves and [periodic] wave trains and their collisions and reflections leading to dynamic network [cellular] patterns in large containers, *J. Colloid Interface Sci.*, 236, 214–224, 2001.
18. Wierschem, A., Linde, H., and Velarde, M.G., Properties of surface wave trains excited by mass transfer through a liquid surface, *Phys. Rev. E*, 64, 022601-1-4, 2001.
19. Linde, H., Chu, X.L., and Velarde, M.G., Oblique and head-on collisions of solitary waves in Marangoni-Bénard convection, *Phys. Fluids A*, 5, 1068–1070, 1993.
20. Linde, H. et al., Wall reflections of solitary waves in Marangoni-Bénard convection, *Phys. Fluids A*, 5, 3162–3166, 1993.

5 Chemical Physics of Colloid Systems and Interfaces

Peter A. Kralchevsky, Krassimir D. Danov, and Nikolai D. Denkov

CONTENTS

- 5.1 Introduction
- 5.2 Surface Tension of Surfactant Solutions
 - 5.2.1 Static Surface Tension
 - 5.2.1.1 Nonionic Surfactants
 - 5.2.1.1.1 Types of Adsorption Isotherms
 - 5.2.1.1.2 Derivation from First Principles
 - 5.2.1.2 Ionic Surfactants
 - 5.2.1.2.1 The Gouy Equation
 - 5.2.1.2.2 Contributions from the Adsorption and Diffuse Layers
 - 5.2.1.2.3 The Effect of Counterion Binding
 - 5.2.1.2.4 Dependence of Adsorption Parameter K on Salt Concentration
 - 5.2.1.2.5 Comparison of Theory and Experiment
 - 5.2.2 Dynamic Surface Tension
 - 5.2.2.1 Adsorption under Diffusion Control
 - 5.2.2.2 Small Initial Perturbation
 - 5.2.2.3 Large Initial Perturbation
 - 5.2.2.4 Generalization for Ionic Surfactants
 - 5.2.2.5 Adsorption under Barrier Control
- 5.3 Capillary Hydrostatics and Thermodynamics
 - 5.3.1 Shapes of Fluid Interfaces
 - 5.3.1.1 Laplace and Young Equations
 - 5.3.1.2 Solutions of Laplace Equations for Menisci of Different Geometry
 - 5.3.1.2.1 Meniscus Meeting the Axis of Revolution
 - 5.3.1.2.2 Meniscus Decaying at Infinity
 - 5.3.1.2.3 Meniscus Confined between Two Cylinders ($0 < R_1 < r < R_2 < \infty$)
 - 5.3.1.3 Gibbs–Thomson Equation
 - 5.3.1.4 Kinetics of Ostwald Ripening in Emulsions
 - 5.3.2 Thin Liquid Films and Plateau Borders
 - 5.3.2.1 Membrane and Detailed Models of a Thin Liquid Film
 - 5.3.2.2 Thermodynamics of Thin Liquid Films
 - 5.3.2.3 The Transition Zone between Thin Film and Plateau Border
 - 5.3.2.3.1 Macroscopic Description
 - 5.3.2.3.2 Micromechanical Description
 - 5.3.2.4 Methods for Measuring Thin Film Contact Angles

- 5.3.3 Lateral Capillary Forces between Particles Attached to Interfaces
 - 5.3.3.1 Particle–Particle Interactions
 - 5.3.3.2 Particle–Wall Interactions
- 5.4 Surface Forces
 - 5.4.1 Derjaguin Approximation
 - 5.4.2 van der Waals Surface Forces
 - 5.4.3 Electrostatic Surface Forces
 - 5.4.3.1 Two Identically Charged Planes
 - 5.4.3.2 Two Nonidentically Charged Planes
 - 5.4.3.3 Two Charged Spheres
 - 5.4.4 DLVO Theory
 - 5.4.5 Non-DLVO Surface Forces
 - 5.4.5.1 Ion Correlation Forces
 - 5.4.5.2 Steric Interaction
 - 5.4.5.2.1 Physical Background
 - 5.4.5.2.2 Thickness of the Polymer Adsorption Layer
 - 5.4.5.2.3 Overlap of Adsorption Layers
 - 5.4.5.3 Oscillatory Structural Forces
 - 5.4.5.3.1 Origin of the Structural Forces
 - 5.4.5.3.2 Oscillatory Solvation Forces
 - 5.4.5.3.3 Depletion Forces
 - 5.4.5.3.4 Colloid Structural Forces
 - 5.4.5.4 Repulsive Hydration and Attractive Hydrophobic Forces
 - 5.4.5.4.1 Repulsive Hydration Forces
 - 5.4.5.4.2 Hydrophobic Attraction
 - 5.4.5.5 Fluctuation Wave Forces
 - 5.4.5.5.1 Undulation Forces
 - 5.4.5.5.2 Peristaltic Force
 - 5.4.5.6 Protrusion Force
- 5.5 Hydrodynamic Interactions in Dispersions
 - 5.5.1 Basic Equations and Lubrication Approximation
 - 5.5.2 Interaction between Particles of Tangentially Immobile Surfaces
 - 5.5.2.1 Taylor and Reynolds Equations, and Influence of the Particle Shape
 - 5.5.2.2 Interactions among Nondeformable Particles at Large Distances
 - 5.5.2.3 Stages of Thinning of a Liquid Film
 - 5.5.2.4 Dependence of Emulsion Stability on the Droplet Size
 - 5.5.3 Effect of Surface Mobility
 - 5.5.3.1 Diffusive and Convective Fluxes at an Interface — Marangoni Effect
 - 5.5.3.2 Fluid Particles and Films of Tangentially Mobile Surfaces
 - 5.5.3.3 Bancroft Rule for Emulsions
 - 5.5.3.4 Demulsification
 - 5.5.4 Interactions in Nonpreequilibrated Emulsions
 - 5.5.4.1 Surfactant Transfer from Continuous to Disperse Phase (Cyclic Dimpling)
 - 5.5.4.2 Surfactant Transfer from Disperse to Continuous Phase (Osmotic Swelling)
 - 5.5.4.3 Equilibration of Two Droplets across a Thin Film
 - 5.5.5 Hydrodynamic Interaction of a Particle with an Interface
 - 5.5.5.1 Particle of Immobile Surface Interacting with a Solid Wall
 - 5.5.5.2 Fluid Particles of Mobile Surfaces
 - 5.5.6 Bulk Rheology of Dispersions

- 5.6 Kinetics of Coagulation
 - 5.6.1 Irreversible Coagulation
 - 5.6.2 Reversible Coagulation
 - 5.6.3 Kinetics of Simultaneous Flocculation and Coalescence in Emulsions
- 5.7 Mechanisms of Antifoaming
 - 5.7.1 Location of Antifoam Action — Fast and Slow Antifoams
 - 5.7.2 Bridging-Stretching Mechanism
 - 5.7.3 Role of the Entry Barrier
 - 5.7.3.1 Film Trapping Technique
 - 5.7.3.2 Critical Entry Pressure for Foam Film Rupture
 - 5.7.3.3 Optimal Hydrophobicity of Solid Particles
 - 5.7.3.4 Role of the Pre-spread Oil Layer
 - 5.7.4 Mechanisms of Compound Exhaustion and Reactivation
- 5.8 Electrokinetic Phenomena in Colloids
 - 5.8.1 Potential Distribution at a Planar Interface and around a Sphere
 - 5.8.2 Electroosmosis
 - 5.8.3 Streaming Potential
 - 5.8.4 Electrophoresis
 - 5.8.5 Sedimentation Potential
 - 5.8.6 Electrokinetic Phenomena and Onzager Reciprocal Relations
 - 5.8.7 Electric Conductivity and Dielectric Response of Dispersions
 - 5.8.7.1 Electric Conductivity
 - 5.8.7.2 Dispersions in Alternating Electrical Field
 - 5.8.8 Anomalous Surface Conductance and Data Interpretation
 - 5.8.9 Electrokinetic Properties of Air–Water and Oil–Water Interfaces
- 5.9 Optical Properties of Dispersions and Micellar Solutions
 - 5.9.1 Static Light Scattering
 - 5.9.1.1 Rayleigh Scattering
 - 5.9.1.2 Rayleigh–Debye–Gans Theory
 - 5.9.1.3 Theory of Mie
 - 5.9.1.4 Interacting Particles
 - 5.9.1.4.1 Fluctuation Theory of Static Light Scattering
 - 5.9.1.4.2 Zimm-Plot (Method of Double Extrapolation)
 - 5.9.1.4.3 Interpretation of the Second Osmotic Virial Coefficient
 - 5.9.1.5 Depolarization of Scattered Light
 - 5.9.1.6 Polydisperse Samples
 - 5.9.1.7 Turbidimetry
 - 5.9.2 Dynamic Light Scattering
 - 5.9.2.1 DLS by Monodisperse, Noninteracting Spherical Particles
 - 5.9.2.1.1 Spectrum Analyzer
 - 5.9.2.1.2 Correlator
 - 5.9.2.2 DLS by Polydisperse, Noninteracting Spherical Particles
 - 5.9.2.3 DLS by Nonspherical Particles
 - 5.9.2.4 Effect of the Particle Interactions
 - 5.9.2.5 Concentrated Dispersions: Photon Cross-Correlation Techniques, Fiber-Optics DLS, and Diffusing Wave Spectroscopy
 - 5.9.3 Application of Light Scattering Methods to Colloidal Systems
 - 5.9.3.1 Surfactant Solutions
 - 5.9.3.1.1 Critical Micellar Concentration, Aggregation Number, Second Virial Coefficient

- 5.9.3.1.2 Diffusion Coefficient, Size, Shape, and Polydispersity of Micelles
- 5.9.3.1.3 Intermicellar Interactions
- 5.9.3.1.4 Microemulsions
- 5.9.3.2 Dispersions
 - 5.9.3.2.1 Size, Shape, and Polydispersity of Particles
 - 5.9.3.2.2 Static and Dynamic Structure Factors
 - 5.9.3.2.3 Kinetics of Coagulation and Structure of the Formed Aggregates

Acknowledgment

References

5.1 INTRODUCTION

A *colloidal system* represents a multiphase (heterogeneous) system, in which at least one of the phases exists in the form of very small particles: typically smaller than 1 μm but still much larger than the molecules. Such particles are related to phenomena like Brownian motion, diffusion, and osmosis. The terms *microheterogeneous system* and *disperse system* (dispersion) are more general because they also include bicontinuous systems (in which none of the phases is split into separate particles) and systems containing larger, non-Brownian, particles. The term *dispersion* is often used as a synonym of colloidal system.

A classification of the colloids with respect to the state of aggregation of the *disperse* and the *continuous* phases is shown in [Table 5.1](#). Some examples follow:

1. Examples of *gas-in-liquid* dispersions are the foams or the boiling liquids. *Gas-in-solid* dispersions are the various porous media such as filtration membranes, sorbents, catalysts, and isolation materials.
2. Examples of *liquid-in-gas* dispersions are the mist, the clouds, and other aerosols. *Liquid-in-liquid* dispersions are the emulsions. At room temperature there are only four types of mutually immiscible liquids: water, hydrocarbon oils, fluorocarbon oils, and liquid metals — Mercury (Hg) and gallium (Ga). Many raw materials and products in food and petroleum industries exist in the form of oil in water or water in oil emulsions. The soil and some biological tissues can be considered *liquid-in-solid* dispersions.
3. Smoke, dust, and some other aerosols are examples of *solid-in-gas* dispersions. The *solid-in-liquid* dispersions are termed *suspensions* or *sols*. The pastes and some glues are highly concentrated suspensions. The *gels* represent *bicontinuous* structures of solid and liquid. The pastes and some glues are highly concentrated suspensions. *Solid-in-solid* dispersions are some metal alloys, many kinds of rocks, some colored glasses, etc.

Below we consider mostly liquid dispersions, i.e., dispersions with liquid continuous phase, such as foams, emulsions, and suspensions. Sometimes these are called *complex fluids*.

In general, the area of the interface between the disperse and continuous phases is rather large. For example, 1 cm^3 of dispersion with particles of radius 100 nm and volume fraction 30% contains an interface area about 10 m^2 . This is the reason the interfacial properties are of crucial importance for the properties and stability of colloids.

The *stabilizing* factors for dispersions are the repulsive surface forces, the particle thermal motion, the hydrodynamic resistance of the medium, and the high surface elasticity of fluid particles and films.

On the other hand, the factors *destabilizing* dispersions are the attractive surface forces, the factors suppressing the repulsive surface forces, the low surface elasticity, gravity, and other external forces tending to separate the phases.

TABLE 5.1
Types of Disperse Systems

Disperse Phase	Continuous Phase		
	Gas	Liquid	Solid
Gas	—	G in L	G in S
Liquid	L in G	L ₁ in L ₂	L in S
Solid	S in G	S in L	S ₁ in S ₂

Below, in Sections 5.2 and 5.3, we consider effects related to the surface tension of surfactant solution and capillarity. In Section 5.4 we present a review of the surface forces due to intermolecular interactions. In Section 5.5 we describe the hydrodynamic interparticle forces originating from the effects of bulk and surface viscosity and related to surfactant diffusion. Section 5.6 is devoted to the kinetics of coagulation in dispersions. Section 5.7 regards foams containing oil drops and solid particulates in relation to the antifoaming mechanisms and the exhaustion of antifoams. Finally, Sections 5.8 and 5.9 address the electrokinetic and optical properties of dispersions.

5.2 SURFACE TENSION OF SURFACTANT SOLUTIONS

5.2.1 STATIC SURFACE TENSION

As a rule, the fluid dispersions (emulsions, foams) are stabilized by adsorption layers of amphiphile molecules. These can be ionic^{1,2} and nonionic³ surfactants, lipids, proteins, etc. All have the property to lower the value of the surface (or interfacial) tension, σ , in accordance with the *Gibbs adsorption equation*:^{4,6}

$$d\sigma = - \sum_i \Gamma_i d\mu_i \quad (5.1)$$

where Γ_i is the surface concentration (adsorption) of the i th component and μ_i is its chemical potential. The summation in Equation 5.1 is carried out over all components. Usually an equimolecular dividing surface with respect to the solvent is introduced for which the adsorption of the solvent is set to zero by definition.^{4,5} Then the summation is carried out over all other components. Note that Γ_i is an excess surface concentration with respect to the bulk; Γ_i is positive for surfactants, which decrease σ in accordance with Equation 5.1. On the contrary, Γ_i is negative for aqueous solutions of electrolytes, whose ions are repelled from the surface by the electrostatic image forces;⁵ consequently, the addition of electrolytes increases the surface tension of water.⁶ For surfactant concentrations above the CMC (critical micellization concentration) $\mu_i = \text{const.}$ and, consequently, $\sigma = \text{const.}$; see Equation 5.1 of this handbook.

5.2.1.1 Nonionic Surfactants

5.2.1.1.1 Types of Adsorption Isotherms

Consider the boundary between an aqueous solution of a nonionic surfactant and a hydrophobic phase, air or oil. The dividing surface is usually chosen to be the equimolecular surface with respect to water, that is $\Gamma_w = 0$. Then Equation 5.1 reduces to $d\sigma = -\Gamma_1 d\mu_1$, where the subscript 1 denotes the surfactant. Because the bulk surfactant concentration is usually not too high, we can use the expression for the chemical potential of a solute in an ideal solution: $\mu_1 = \mu_1^{(0)} + kT \ln c_1$, where k is the Boltzmann constant, T is the absolute temperature, c_1 is the concentration of nonionic

surfactant, and $\mu_1^{(0)}$ is its standard chemical potential, which is independent of c_1 . Thus, the Gibbs adsorption equation acquires the form:

$$d\sigma = -kT\Gamma_1 d \ln c_1 \quad (5.2)$$

The surfactant adsorption isotherms, expressing the connection between Γ_1 and c_1 , are usually obtained by means of some molecular model of adsorption. Table 5.2 contains the six most popular surfactant adsorption isotherms, those of Henry, Freundlich,⁷ Langmuir,⁸ Volmer,⁹ Frumkin,¹⁰ and van der Waals.¹¹ For $c_1 \rightarrow 0$ all isotherms (except that of Freundlich) reduce to the Henry isotherm: $\Gamma_1/\Gamma_\infty = Kc_1$. The physical difference between the Langmuir and Volmer isotherms is that the former corresponds to a physical model of *localized* adsorption, whereas the latter corresponds to *nonlocalized* adsorption. The Frumkin and van der Waals isotherms generalize, respectively, to the Langmuir and Volmer isotherms for the case in which the interaction between neighboring adsorbed molecules is not negligible. (If the interaction parameter β is set to zero, the Frumkin and van der Waals isotherms reduce to the Langmuir and Volmer isotherms, correspondingly.) The comparison between theory and experiment shows that for air–water interfaces $\beta > 0$, whereas for oil–water interfaces we can set $\beta = 0$.^{12,13} The latter facts lead to the conclusion that for air–water interfaces β takes into account the van der Waals attraction between the hydrocarbon tails of the adsorbed surfactant molecules across air; such attraction is missing when the hydrophobic phase is oil. (Note that in the case of ionic surfactants it is possible to have $\beta < 0$; see the next section.) The adsorption parameter K in Table 5.2 characterizes the surface activity of the surfactant: the greater the K , the higher the surface activity. K is related to the standard free energy of adsorption, $\Delta f = \mu_1^{(0)} - \mu_{1s}^{(0)}$, which is the energy gain for bringing a molecule from the bulk of the aqueous phase to a diluted adsorption layer.^{14,15}

$$K = \frac{\delta_1}{\Gamma_\infty} \exp\left(\frac{\mu_1^{(0)} - \mu_{1s}^{(0)}}{kT}\right) \quad (5.3)$$

The parameter δ_1 characterizes the thickness of the adsorption layer; δ_1 can be set (approximately) equal to the length of the amphiphilic molecule. Γ_∞ represents the maximum possible value of the adsorption. In the case of localized adsorption (Langmuir and Frumkin isotherms) $1/\Gamma_\infty$ is the area per adsorption site. In the case of nonlocalized adsorption (Volmer and van der Waals isotherms) $1/\Gamma_\infty$ is the excluded area per molecule.

As already mentioned, the Freundlich adsorption isotherm, unlike the others in Table 5.2, does not become linear at low concentrations, but remains convex to the concentration axis. Moreover, it does not show a saturation or limiting value. Hence, for the Freundlich adsorption isotherm in Table 5.2 Γ_∞ is a parameter scaling the adsorption (rather than saturation adsorption). This isotherm can be derived assuming that the surface (as a rule solid) is heterogeneous.^{16,17} Consequently, if the data fit the Freundlich equation, this is an indication, but not a proof, that the surface is heterogeneous.⁶

The *adsorption* isotherms in Table 5.2 can be applied to both fluid and solid interfaces. The *surface tension* isotherms in Table 5.2, which relate σ and Γ_1 , are usually applied to fluid interfaces, although they could also be used for solid–liquid interfaces if σ is identified with the Gibbs⁴ *superficial* tension. (The latter is defined as the force per unit length that opposes every increase of the wet area without any deformation of the solid.)

The surface tension isotherms in Table 5.2 are deduced from the respective adsorption isotherms in the following way. Integration of Equation 5.2 yields

$$\sigma = \sigma_0 - kTJ \quad (5.4)$$

TABLE 5.2
Types of Adsorption and Surface-Tension Isotherms

Type of Isotherm

Surfactant Adsorption Isotherms
(for nonionic surfactants: $a_{1s} \equiv c_1$)

Henry	$Ka_{1s} = \frac{\Gamma_1}{\Gamma_\infty}$
Freundlich	$Ka_{1s} = \left(\frac{\Gamma_1}{\Gamma_\infty}\right)^{1/m}$
Langmuir	$Ka_{1s} = \frac{\Gamma_1}{\Gamma_\infty - \Gamma_1}$
Volmer	$Ka_{1s} = \frac{\Gamma_1}{\Gamma_\infty - \Gamma_1} \exp\left(\frac{\Gamma_1}{\Gamma_\infty - \Gamma_1}\right)$
Frumkin	$Ka_{1s} = \frac{\Gamma_1}{\Gamma_\infty - \Gamma_1} \exp\left(-\frac{2\beta\Gamma_1}{kT}\right)$
van der Waals	$Ka_{1s} = \frac{\Gamma_1}{\Gamma_\infty - \Gamma_1} \exp\left(\frac{\Gamma_1}{\Gamma_\infty - \Gamma_1} - \frac{2\beta\Gamma_1}{kT}\right)$

Surface Tension Isotherm $\sigma = \sigma_0 - kTJ + \sigma_d$
(for nonionic surfactants: $\sigma_d \equiv 0$)

Henry	$J = \Gamma_1$
Freundlich	$J = \frac{\Gamma_1}{m}$
Langmuir	$J = -\Gamma_\infty \ln\left(1 - \frac{\Gamma_1}{\Gamma_\infty}\right)$
Volmer	$J = \frac{\Gamma_\infty \Gamma_1}{\Gamma_\infty - \Gamma_1}$
Frumkin	$J = -\Gamma_\infty \ln\left(1 - \frac{\Gamma_1}{\Gamma_\infty}\right) - \frac{\beta\Gamma_1^2}{kT}$
van der Waals	$J = \frac{\Gamma_\infty \Gamma_1}{\Gamma_\infty - \Gamma_1} - \frac{\beta\Gamma_1^2}{kT}$

Note: The surfactant adsorption isotherm and the surface tension isotherm, which are combined to fit experimental data, obligatorily must be of the same type.

where σ_0 is the interfacial tension of the pure solvent and

$$J \equiv \int_0^{c_1} \Gamma_1 \frac{dc_1}{c_1} = \int_0^{\Gamma_1} \Gamma_1 \frac{d \ln c_1}{d \Gamma_1} d\Gamma_1 \quad (5.5)$$

TABLE 5.3
Elasticity of Adsorption Monolayers at a Fluid Interface

Type of Isotherm (see Table 5.2)	Gibbs Elasticity E_G
Henry	$E_G = kT\Gamma_1$
Freundlich	$E_G = kT \frac{\Gamma_1}{m}$
Langmuir	$E_G = kT\Gamma_1 \frac{\Gamma_\infty}{\Gamma_\infty - \Gamma_1}$
Volmer	$E_G = kT\Gamma_1 \frac{\Gamma_\infty^2}{(\Gamma_\infty - \Gamma_1)^2}$
Frumkin	$E_G = kT\Gamma_1 \left(\frac{\Gamma_\infty}{\Gamma_\infty - \Gamma_1} - \frac{2\beta\Gamma_1}{kT} \right)$
van der Waals	$E_G = kT\Gamma_1 \left[\frac{\Gamma_\infty^2}{(\Gamma_\infty - \Gamma_1)^2} - \frac{2\beta\Gamma_1}{kT} \right]$

Note: The above expressions are valid for both nonionic and ionic surfactants.

The derivative $d \ln c_1/d\Gamma_1$ is calculated for each adsorption isotherm, and then the integration in Equation 5.5 is carried out analytically. The obtained expressions for J are listed in Table 5.2. Each surface tension isotherm, $\sigma(\Gamma_1)$, has the meaning of a *two-dimensional equation of state* of the adsorption monolayer, which can be applied to both *soluble* and *insoluble* surfactants.^{6,18}

An important thermodynamic property of a surfactant adsorption monolayer is its Gibbs (surface) elasticity:

$$E_G \equiv -\Gamma_1 \left(\frac{\partial \sigma}{\partial \Gamma_1} \right)_T \quad (5.6)$$

Expressions for E_G , corresponding to various adsorption isotherms, are shown in Table 5.3. Gibbs elasticity characterizes the lateral fluidity of the surfactant adsorption monolayer. At high values of Gibbs elasticity the adsorption monolayer behaves as tangentially immobile. In such case, if two emulsion droplets approach each other, the hydrodynamic flow pattern, as well, the hydrodynamic interaction, is almost the same as if the droplets were solid. For lower values of the surfactant adsorption the so-called Marangoni effect appears, which is equivalent to appearance of gradients of surface tension due to gradients of surfactant adsorption: $\nabla_s \sigma = -(E_G/\Gamma_1) \nabla_s \Gamma_1$ (here ∇_s denotes the surface gradient operator). The Marangoni effect can considerably affect the hydrodynamic interactions of fluid particles (drops, bubbles); see Section 5.5 below.

5.2.1.1.2 Derivation from First Principles

Each surfactant adsorption isotherm (that of Langmuir, Volmer, Frumkin, etc.), and the related expressions for the surface tension and surface chemical potential, can be derived from an expression for the surface free energy, F_s , which corresponds to a given physical model. This derivation helps us obtain (or identify) the self-consistent system of equations, referring to a given model, which is to be applied to interpret a set of experimental data. Combination of equations corresponding to different models (say, Langmuir adsorption isotherm with Frumkin surface tension isotherm) is incorrect and must be avoided.

TABLE 5.4
Free Energy and Chemical Potential for Surfactant Adsorption Layers

Type of Isotherm

Surface Free Energy $F_s(T, A, N_1)$ ($M = \Gamma_\infty A$)	
Henry	$F_s = N_1 \mu_{1s}^{(0)} + kT [N_1 \ln(N_1/M) - N_1]$
Freundlich	$F_s = N_1 \mu_{1s}^{(0)} + \frac{kT}{m} [N_1 \ln(N_1/M) - N_1]$
Langmuir	$F_s = N_1 \mu_{1s}^{(0)} + kT [N_1 \ln N_1 + (M - N_1) \ln(M - N_1) - M \ln M]$
Volmer	$F_s = N_1 \mu_{1s}^{(0)} + kT [N_1 \ln N_1 - N_1 - N_1 \ln(M - N_1)]$
Frumkin	$F_s = N_1 \mu_{1s}^{(0)} + kT [N_1 \ln N_1 + (M - N_1) \ln(M - N_1) - M \ln M] + \frac{\beta \Gamma_\infty N_1^2}{2M}$
van der Waals	$F_s = N_1 \mu_{1s}^{(0)} + kT [N_1 \ln N_1 - N_1 - N_1 \ln(M - N_1)] + \frac{\beta \Gamma_\infty N_1^2}{2M}$
Surface Chemical Potential μ_{1s} ($\theta \equiv \Gamma_1/\Gamma_\infty$)	
Henry	$\mu_{1s} = \mu_{1s}^{(0)} + kT \ln \theta$
Freundlich	$\mu_{1s} = \mu_{1s}^{(0)} + \frac{kT}{m} \ln \theta$
Langmuir	$\mu_{1s} = \mu_{1s}^{(0)} + kT \ln \frac{\theta}{1-\theta}$
Volmer	$\mu_{1s} = \mu_{1s}^{(0)} + kT \left(\frac{\theta}{1-\theta} + \ln \frac{\theta}{1-\theta} \right)$
Frumkin	$\mu_{1s} = \mu_{1s}^{(0)} + kT \ln \frac{\theta}{1-\theta} - 2\beta \Gamma_1$
van der Waals	$\mu_{1s} = \mu_{1s}^{(0)} + kT \left(\frac{\theta}{1-\theta} + \ln \frac{\theta}{1-\theta} \right) - 2\beta \Gamma_1$

The general scheme for derivation of the adsorption isotherms is the following:

(i) With the help of statistical mechanics an expression is obtained, for example, for the canonical ensemble partition function, Q , from which the surface free energy F_s is determined:¹¹

$$F_s(T, A, N_1) = -kT \ln Q(T, A, N_1) \quad (5.7)$$

where A is the interfacial area and N_1 is the number of adsorbed surfactant molecules; see Table 5.4.

(ii) Differentiating the expression for F_s , we derive expressions for the *surface pressure*, π_s , and the *surface chemical potential* of the adsorbed surfactant molecules, μ_{1s} :¹¹

$$\pi_s \equiv \sigma_0 - \sigma = - \left(\frac{\partial F_s}{\partial A} \right)_{T, N_1}, \quad \mu_{1s} = \left(\frac{\partial F_s}{\partial N_1} \right)_{T, A} \quad (5.8)$$

Combining the obtained expressions for π_s and μ_{1s} , we can deduce the respective form of the Butler equation;¹⁹ see Equation 5.16 below.

(iii) The surfactant adsorption isotherm (Table 5.2) can be derived by setting the obtained expression for the surface chemical potential μ_{1s} equal to the bulk chemical potential of the surfactant molecules in the subsurface layer (that is, equilibrium between surface and subsurface is assumed):¹¹

$$\mu_{1s} = \mu_1^{(0)} + kT \ln(a_{1s} \delta_1 / \Gamma_\infty) \quad (5.9)$$

Here a_{1s} is the activity of the surfactant molecule in the subsurface layer; a_{1s} is scaled with the volume per molecule in a dense (saturated) adsorption layer, $v_1 = \delta_1 / \Gamma_\infty$, where δ_1 is interpreted as the thickness of the adsorption layer, or the length of an adsorbed molecule. In terms of the subsurface activity, a_{1s} , Equation 5.9 can be applied to ionic surfactants and to dynamic processes. In the simplest case of nonionic surfactants and equilibrium processes, we have $a_{1s} \approx c_1$, where c_1 is the bulk surfactant concentration.

First, let us apply the above general scheme to derive the *Frumkin isotherm*, which corresponds to *localized* adsorption of *interacting* molecules. (Expressions corresponding to the Langmuir isotherm can be obtained by setting $\beta = 0$ in the respective expressions for the Frumkin isotherm.) Let us consider the interface as a two-dimensional lattice having M adsorption sites. The corresponding partition function is¹¹

$$Q(T, M, N_1) = \frac{M!}{N_1! (M - N_1)!} [q(T)]^{N_1} \exp\left(-\frac{n_c w N_1^2}{2kTM}\right) \quad (5.10)$$

The first multiplier in the right-hand side of Equation 5.10 expresses the number of ways N_1 indistinguishable molecules can be distributed among M labeled sites; the partition function for a single adsorbed molecule is $q = q_x q_y q_z$, where q_x , q_y , and q_z are one-dimensional harmonic-oscillator partition functions. The exponent in Equation 5.10 accounts for the interaction between adsorbed molecules in the framework of the Bragg–Williams approximation.¹¹ w is the nearest-neighbor interaction energy of two molecules and n_c is the number of nearest-neighbor sites to a given site (for example, $n_c = 4$ for a square lattice). Next, we substitute Equation 5.10 into Equation 5.7 and using the known Stirling approximation, $\ln M! = M \ln M - M$, we obtain the expression for the surface free energy corresponding to the Frumkin model:

$$F_s = kT [N_1 \ln N_1 + (M - N_1) \ln (M - N_1) - M \ln M - N_1 \ln q(T)] + \frac{n_c w N_1^2}{2M} \quad (5.11)$$

Note that

$$M = \Gamma_\infty A, \quad N_1 = \Gamma_1 A \quad (5.12)$$

where Γ_∞^{-1} is the area per one adsorption site in the lattice. Differentiating Equation 5.11 in accordance with Equation 5.8, we deduce expressions for the surface pressure and chemical potential:¹¹

$$\pi_s = -\Gamma_\infty kT \ln(1 - \theta) - \beta \Gamma_1^2 \quad (5.13)$$

$$\mu_{1s} = \mu_{1s}^{(0)} + kT \ln \frac{\theta}{1 - \theta} - 2\beta \Gamma_1 \quad (5.14)$$

where we have introduced the notation:

$$\theta = \frac{\Gamma_1}{\Gamma_\infty}, \quad \beta = -\frac{n_c w}{2\Gamma_\infty}, \quad \mu_{1s}^{(0)} = -kT \ln q(T) \quad (5.15)$$

We can check that Equation 5.13 is equivalent to the Frumkin's surface tension isotherm in Table 5.2 for a nonionic surfactant. Furthermore, eliminating $\ln(1 - \theta)$ between Equations 5.13 and 5.14, we obtain the Butler¹⁹ equation in the form:

$$\mu_{1s} = \mu_{1s}^{(0)} + \Gamma_\infty^{-1} \pi_s + kT \ln(\gamma_{1s} \theta) \quad (\text{Butler equation}) \quad (5.16)$$

where we have introduced the surface activity coefficient

$$\gamma_{1s} = \exp\left[-\frac{\beta \Gamma_\infty \theta (2 - \theta)}{kT}\right] \quad (\text{for Frumkin isotherm}) \quad (5.17)$$

(In the special case of Langmuir isotherm we have $\beta = 0$, and then $\gamma_{1s} = 1$.) The Butler equation is used by many authors^{12,20-22} as a starting point for development of thermodynamic adsorption models. It should be kept in mind that the specific form of the expressions for π_s and γ_{1s} , which are to be substituted in Equation 5.16, is not arbitrary, but must correspond to the *same* thermodynamic model (to the same expression for F_s — in our case Equation 5.11). At last, substituting Equation 5.16 into Equation 5.9 we derive the Frumkin adsorption isotherm in Table 5.2, where K is defined by Equation 5.3.

Now, let us apply the same general scheme, but this time to the derivation of the *van der Waals isotherm*, which corresponds to *nonlocalized* adsorption of *interacting* molecules. (Expressions corresponding to the Volmer isotherm can be obtained by setting $\beta = 0$ in the respective expressions for the van der Waals isotherm.) Now the adsorbed N_1 molecules are considered a two-dimensional gas. The corresponding expression for the canonical ensemble partition function is

$$Q(T, M, N_1) = \frac{1}{N_1!} q^{N_1} \exp\left(-\frac{n_c w N_1^2}{2kTM}\right) \quad (5.18)$$

where the exponent accounts for the interaction between adsorbed molecules, again in the framework of the Bragg–Williams approximation. The partition function for a single adsorbed molecule is $q = q_{xy} q_z$, where q_z is a one-dimensional (normal to the interface) harmonic-oscillator partition function. On the other hand, the adsorbed molecules have free translational motion in the xy plane (the interface); therefore, we have¹¹

$$q_{xy} = \frac{2\pi\tilde{m}kT}{h_p^2} \hat{A} \quad (5.19)$$

where \tilde{m} is the molecular mass, h_p is the Planck constant and $\hat{A} = A - N_1 \Gamma_\infty^{-1}$ is the area accessible to the moving molecules; the parameter Γ_∞^{-1} is the excluded area per molecule, which accounts for the molecular size. Having in mind that $M \equiv \Gamma_\infty A$, we can bring Equation 5.18 into the form:

$$Q(T, M, N_1) = \frac{1}{N_1!} q_0^{N_1} (M - N_1)^{N_1} \exp\left(-\frac{n_c w N_1^2}{2kTM}\right) \quad (5.20)$$

where

$$q_0(T) \equiv \frac{2\pi\tilde{m}kT}{h_p^2\Gamma_\infty} q_z(T) \quad (5.21)$$

Further, we substitute Equation 5.20 into Equation 5.7 and, using the Stirling approximation, we determine the surface free energy corresponding to the van der Waals model:^{11,18,23}

$$F_s = kT \left[N_1 \ln N_1 - N_1 - N_1 \ln q_0(T) - N_1 \ln(M - N_1) \right] + \frac{n_c w N_1^2}{2M} \quad (5.22)$$

Again, having in mind that $M \equiv \Gamma_\infty A$, we differentiate Equation 5.22 in accordance with Equation 5.8 to deduce expressions for the surface pressure and chemical potential:

$$\pi_s = \Gamma_\infty kT \frac{\theta}{1-\theta} - \beta \Gamma_1^2 \quad (5.23)$$

$$\mu_{1s} = \mu_{1s}^{(0)} + kT \left(\frac{\theta}{1-\theta} + \ln \frac{\theta}{1-\theta} \right) - 2\beta\Gamma_1 \quad (5.24)$$

where $\mu_{1s}^{(0)} = -kT \ln q_0(T)$ and β is defined by Equation 5.15. We can check that Equation 5.23 is equivalent to the van der Waals surface tension isotherm in Table 5.2 for a nonionic surfactant. Furthermore, combining Equations 5.23 and 5.24 we obtain the Butler (Equation 5.16), but this time with another expression for the surface activity coefficient:

$$\gamma_{1s} = \frac{1}{1-\theta} \exp \left[- \frac{\beta\Gamma_\infty\theta(2-\theta)}{kT} \right] \quad (\text{for van der Waals isotherm}) \quad (5.25)$$

In the special case of Volmer isotherm we have $\beta = 0$, and then $\gamma_{1s} = 1/(1 - \theta)$. Finally, substituting Equation 5.24 into Equation 5.9 we derive the van der Waals adsorption isotherm in Table 5.2, with K defined by Equation 5.3.

In Table 5.4 we summarize the expressions for the surface free energy, F_s , and chemical potential μ_{1s} , for several thermodynamic models of adsorption. We recall that the parameter Γ_∞ is defined in different ways for the different models. On the other hand, the parameter K is defined in the same way for all models, specifically by Equation 5.3. The expressions in Tables 5.2 through 5.4 can be generalized for multicomponent adsorption layers.^{18,27}

At the end of this section, let us consider a general expression, which allows us to obtain the surface activity coefficient γ_{1s} directly from the surface pressure isotherm $\pi_s(\theta)$. From the Gibbs adsorption isotherm, $d\pi_s = \Gamma_1 d\mu_{1s}$, it follows that

$$\left(\frac{\partial \mu_{1s}}{\partial \Gamma_1} \right)_T = \frac{1}{\Gamma_1} \left(\frac{\partial \pi_s}{\partial \Gamma_1} \right)_T \quad (5.26)$$

By substituting μ_{1s} from the Butler Equation 5.16 into Equation 5.26 and integrating, we can derive the sought-for expression:

$$\ln \gamma_{1s} = \int_0^\theta \left(\frac{(1-\theta)}{\Gamma_\infty kT} \frac{\partial \pi_s}{\partial \theta} - 1 \right) \frac{d\theta}{\theta} \quad (5.27)$$

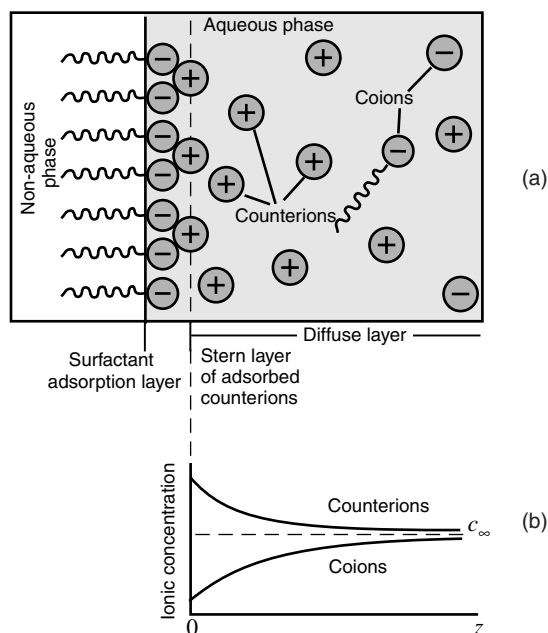


FIGURE 5.1 Electric double layer in the vicinity of an adsorption layer of ionic surfactant. (a) The diffuse layer contains free ions involved in Brownian motion, whereas the Stern layer consists of adsorbed (bound) counterions. (b) Near the charged surface there is an accumulation of counterions and a depletion of coions.

We can check that a substitution of π_s from Equations 5.13 and 5.23 into Equation 5.27 yields, respectively, the Frumkin and van der Waals expressions for γ_{1s} , specifically Equations 5.17 and 5.25.

5.2.1.2 Ionic Surfactants

5.2.1.2.1 The Gouy Equation

The thermodynamics of adsorption of *ionic* surfactants^{13,24-28} is more complicated (in comparison with that of nonionics) because of the presence of long-range electrostatic interactions and, in particular, of an electric double layer (EDL) in the system (Figure 5.1). The electrochemical potential of the ionic species can be expressed in the form:²⁹

$$\mu_i = \mu_i^{(0)} + kT \ln a_i + Z_i e \psi \quad (5.28)$$

where e is the elementary electric charge, ψ is the electric potential, Z_i is the valency of the ionic component “ i ,” and a_i is its activity. In the EDL (Figure 5.1) the electric potential and the activities of the ions are dependent on the distance z from the phase boundary: $\psi = \psi(z)$, $a_i = a_i(z)$. At equilibrium the electrochemical potential, μ_i , is uniform throughout the whole solution, including the EDL (otherwise diffusion fluxes would appear).²⁹ In the bulk of solution ($z \rightarrow \infty$) the electric potential tends to a constant value, which is usually set equal to zero, that is, $\psi \rightarrow 0$ and $\partial\psi/\partial z \rightarrow 0$ for $z \rightarrow \infty$. If the expression for μ_i at $z \rightarrow \infty$ and that for μ_i at some finite z are set equal, from Equation 5.28 we obtain a Boltzmann-type distribution for the activity across the EDL:²⁹

$$a_i(z) = a_{i\infty} \exp \left[- \frac{Z_i e \psi(z)}{kT} \right] \quad (5.29)$$

where $a_{i\infty}$ denotes the value of the activity of ion “ i ” in the bulk of solution. If the activity in the bulk, $a_{i\infty}$, is known, then Equation 5.29 determines the activity $a_i(z)$ in each point of the EDL. A good agreement between theory and experiment can be achieved^{12,13,27} using the following expression for $a_{i\infty}$:

$$a_{i\infty} = \gamma_{\pm} c_{i\infty} \quad (5.30)$$

where $c_{i\infty}$ is the bulk concentration of the respective ion, and the activity coefficient γ_{\pm} is calculated from the known formula:³⁰

$$\log \gamma_{\pm} = - \frac{A |Z_+ Z_-| \sqrt{I}}{1 + B d_i \sqrt{I}} + bI \quad (5.31)$$

which originates from the Debye–Hückel theory; I denotes the ionic strength of the solution:

$$I \equiv \frac{1}{2} \sum_i Z_i^2 c_{i\infty} \quad (5.32)$$

where the summation is carried out over all ionic species in the solution. When the solution contains a mixture of several electrolytes, then Equation 5.31 defines γ_{\pm} for each separate electrolyte, with Z_+ and Z_- the valences of the cations and anions of *this* electrolyte, but with I the *total* ionic strength of the solution, accounting for all dissolved electrolytes.³⁰ The log in Equation 5.31 is decimal, d_i is the ionic diameter, A , B , and b are parameters, whose values can be found in the book by Robinson and Stokes.³⁰ For example, if I is given in moles per liter (M), the parameters values are $A = 0.5115 \text{ M}^{-1/2}$, $B d_i = 1.316 \text{ M}^{-1/2}$, and $b = 0.055 \text{ M}^{-1}$ for solutions of NaCl at 25°C.

The theory of EDL provides a connection between surface charge and surface potential (known as the Gouy equation^{31,32} or Graham equation^{33,34}), which can be presented in the form:^{27,35}

$$\sum_{i=1}^N z_i \Gamma_i = \frac{2}{\kappa_c} \left\{ \sum_{i=1}^N a_{i\infty} [\exp(-z_i \Phi_s) - 1] \right\}^{1/2} \quad (\text{Gouy equation}) \quad (5.33)$$

where Γ_i ($i = 1, \dots, N$) are the adsorptions of the ionic species, $z_i = Z_i/Z_1$, the index $i = 1$ corresponds to the surfactant ions,

$$\kappa_c^2 \equiv \frac{2 Z_1^2 e^2}{\epsilon_0 \epsilon kT}, \quad \Phi_s \equiv \frac{Z_1 e \psi_s}{kT} \quad (5.34)$$

ϵ is the dielectric permittivity of the medium (water), and $\psi_s = \psi(z = 0)$ is the surface potential. Note that the Debye parameter is $\kappa^2 = \kappa_c^2 I$.

For example, let us consider a solution of an ionic surfactant, which is a symmetric 1:1 electrolyte, in the presence of a symmetric, 1:1, inorganic electrolyte (salt). We assume that the counterions due to the surfactant and salt are identical. For example, this can be a solution of sodium dodecyl sulfate (SDS) in the presence of NaCl. We denote by $c_{1\infty}$, $c_{2\infty}$, and $c_{3\infty}$ the bulk concentrations of the surface active ions, counterions, and coions, respectively (Figure 5.1). For the special system of SDS with NaCl $c_{1\infty}$, $c_{2\infty}$, and $c_{3\infty}$ are the bulk concentration of the DS⁻, Na⁺,

and Cl^- ions, respectively. The requirement for the bulk solution to be electroneutral implies $c_{2\infty} = c_{1\infty} + c_{3\infty}$. The multiplication of the last equation by γ_{\pm} yields

$$a_{2\infty} = a_{1\infty} + a_{3\infty} \quad (5.35)$$

The adsorption of the coions of the nonamphiphilic salt is expected to be equal to zero, $\Gamma_3 = 0$, because they are repelled by the similarly charged interface.^{27,36-38} However, the adsorption of surfactant at the interface, Γ_1 , and the binding of counterions in the Stern layer, Γ_2 , are different from zero (Figure 5.1). For this system the Gouy Equation 5.33 acquires the form:

$$\Gamma_1 - \Gamma_2 = \frac{4}{\kappa_c} \sqrt{a_{2\infty}} \sinh\left(\frac{\Phi_s}{2}\right) \quad (Z_1:Z_1 \text{ electrolyte}) \quad (5.36)$$

5.2.1.2.2 Contributions from the Adsorption and Diffuse Layers

In general, the *total* adsorption $\tilde{\Gamma}_i$ of an ionic species include contributions from *both* the adsorption layer (surfactant adsorption layer + adsorbed counterions in the Stern layer), Γ_i , and the diffuse layer, Λ_i .^{13,24,26,27}

$$\tilde{\Gamma}_i = \Gamma_i + \Lambda_i \quad \text{where} \quad \Lambda_i \equiv \int_0^{\infty} [a_i(z) - a_{i\infty}] dz \quad (5.37)$$

$\tilde{\Gamma}_i$ represents a surface excess of component “*i*” with respect to the *uniform* bulk solution. As the solution is electroneutral, we have $\sum_{i=1}^N z_i \tilde{\Gamma}_i = 0$. Note, however, that $\sum_{i=1}^N z_i \Gamma_i \neq 0$; see the Gouy Equation 5.33. Expressions for Λ_i can be obtained by using the theory of EDL. For example, because of the electroneutrality of the solution, the right-hand side of Equation 5.36 is equal to $\Lambda_2 - \Lambda_1 - \Lambda_3$, where

$$\Lambda_2 = 2a_{2\infty} \kappa^{-1} [\exp(\Phi_s/2) - 1]; \quad \Lambda_j = 2a_{j\infty} \kappa^{-1} [\exp(-\Phi_s/2) - 1], \quad j = 1, 3 \quad (5.38)$$

($\kappa^2 = \kappa_c^2 J$; $Z_1:Z_1$ electrolyte). In analogy with Equation 5.37, the interfacial tension of the solution, σ , can be expressed as a sum of contributions from the adsorption and diffuse layers:^{24,27,32}

$$\sigma = \sigma_a + \sigma_d \quad (5.39)$$

where

$$\sigma_a = \sigma_0 - kTJ \quad \text{and} \quad \sigma_d = -\epsilon_0 \epsilon \int_0^{\infty} \left(\frac{d\psi}{dz}\right)^2 dz \quad (5.40)$$

Expressions for J are given in Table 5.2 for various types of isotherms. Note that Equations 5.39 and 5.40 are valid under both equilibrium and dynamic conditions. In the special case of SDS + NaCl solution (see above), *at equilibrium*, we can use the theory of EDL to express $d\psi/dz$; then from Equation 5.40 we derive^{24,27,32}

$$\sigma_d = -\frac{8kT}{\kappa_c} \sqrt{a_{2\infty}} \left[\cosh\left(\frac{\Phi_s}{2}\right) - 1 \right] \quad (Z_1:Z_1 \text{ electrolyte, at equilibrium}) \quad (5.41)$$

Analytical expressions for σ_d for the cases of 2:1, 1:2, and 2:2 electrolytes can be found in References 27 and 35.

In the case of ionic surfactants, Equation 5.1 can be presented in two alternative, but equivalent, forms^{27,35}

$$d\sigma = -kT \sum_{i=1}^N \tilde{\Gamma}_i d \ln a_{i\infty} \quad (T = \text{const.}) \quad (5.42)$$

$$d\sigma_a = -kT \sum_{i=1}^N \Gamma_i d \ln a_{is} \quad (T = \text{const.}) \quad (5.43)$$

where $a_{is} = a_i(z=0)$ is the “subsurface” value of activity a_i . From Equations 5.29 and 5.34 we obtain

$$a_{is} = a_{i\infty} \exp(-z_i \Phi_s) \quad (5.44)$$

The comparison between Equations 5.42 and 5.43 shows that the Gibbs adsorption equation can be expressed either in terms of σ , $\tilde{\Gamma}_i$, and $a_{i\infty}$ or in terms of σ_a , Γ_i , and a_{is} . Note that Equations 5.42 and 5.44 are valid under *equilibrium* conditions, whereas Equation 5.43 can be used also for the description of *dynamic* surface tension (Section 5.2.2) in the case of surfactant adsorption under diffusion control, assuming local equilibrium between adsorptions Γ_i and subsurface concentrations of the respective species.

The expression $\sigma_a = \sigma_0 - kTJ$, with J given in Table 5.2, can be used for description of both static and dynamic surface tension of ionic and nonionic surfactant solutions. The surfactant adsorption isotherms in this table can be used for both ionic and nonionic surfactants, with the only difference that in the case of ionic surfactant the adsorption constant K depends on the subsurface concentration of the inorganic counterions;²⁷ see Equation 5.48 below.

5.2.1.2.3 The Effect of Counterion Binding

As an example, let us consider again the special case of SDS + NaCl solution. In this case, the Gibbs adsorption equation takes the form:

$$d\sigma_a = -kT(\Gamma_1 d \ln a_{1s} + \Gamma_2 d \ln a_{2s}) \quad (5.45)$$

where, as before, the indices “1” and “2” refer to the DS⁻ and Na⁺ ions, respectively. The differentials in the right-hand side of Equation 5.45 are independent (one can vary independently the concentrations of surfactant and salt), and moreover, $d\sigma_a$ is an exact (total) differential. Then, according to the Euler condition, the cross derivatives must be equal:²⁷

$$\frac{\partial \Gamma_1}{\partial \ln a_{2s}} = \frac{\partial \Gamma_2}{\partial \ln a_{1s}} \quad (5.46)$$

A surfactant adsorption isotherm, $\Gamma_1 = \Gamma_1(a_{1s}, a_{2s})$, and a counterion adsorption isotherm, $\Gamma_2 = \Gamma_2(a_{1s}, a_{2s})$, are *thermodynamically compatible* only if they satisfy Equation 5.46. The counterion adsorption isotherm is usually taken in the form:

$$\frac{\Gamma_2}{\Gamma_1} = \frac{K_2 a_{2s}}{1 + K_2 a_{2s}} \quad (\text{Stern isotherm}) \quad (5.47)$$

where K_2 is a constant parameter. The latter equation, termed the *Stern isotherm*,³⁹ describes Langmuirian adsorption (binding) of counterions in the Stern layer. It can be proved that a sufficient condition Γ_2 from Equation 5.47 to satisfy the Euler condition (Equation 5.46), together with one of the surfactant adsorption isotherms for Γ_1 in Table 5.2, is²⁷

$$K = K_1(1 + K_2 a_{2s}) \quad (5.48)$$

where K_1 is another constant parameter. In other words, if K is expressed by Equation 5.48, the Stern isotherm 47 is thermodynamically compatible with every of the surfactant adsorption isotherms in Table 5.2. In analogy with Equation 5.3, the parameters K_1 and K_2 are related to the respective standard free energies of adsorption of surfactant ions and counterions $\Delta\mu_i^{(0)}$:

$$K_i = \frac{\delta_i}{\Gamma_\infty} \exp\left(\frac{\Delta\mu_i^{(0)}}{kT}\right) \quad (i = 1, 2) \quad (5.49)$$

where δ_i stands for the thickness of the respective adsorption layer.

5.2.1.2.4 Dependence of Adsorption Parameter K on Salt Concentration

The physical meaning of Equation 5.48 can be revealed by chemical-reaction considerations. For simplicity, let us consider *Langmuir*-type adsorption; i.e., we treat the interface as a two-dimensional lattice. We will use the notation θ_0 for the fraction of the free sites in the lattice, θ_1 for the fraction of sites containing adsorbed surfactant ion S^- , and θ_2 for the fraction of sites containing the complex of an adsorbed surfactant ion + a bound counterion. Obviously, we can write $\theta_0 + \theta_1 + \theta_2 = 1$. The adsorptions of surfactant ions and counterions can be expressed in the form:

$$\Gamma_1/\Gamma_\infty = \theta_1 + \theta_2; \quad \Gamma_2/\Gamma_\infty = \theta_2 \quad (5.50)$$

Following Kalinin and Radke,²⁵ we consider the “reaction” of adsorption of S^- ions:



where A_0 symbolizes an empty adsorption site. In accordance with the rules of the chemical kinetics we can express the rates of adsorption and desorption in the form:

$$r_{1,ads} = K_{1,ads}\theta_0 c_{1s}, \quad r_{1,des} = K_{1,des}\theta_1 \quad (5.52)$$

where, as before, c_{1s} is the subsurface concentration of surfactant and $K_{1,ads}$ and $K_{1,des}$ are constants. In view of Equation 5.50 we can write $\theta_0 = (\Gamma_\infty - \Gamma_1)/\Gamma_\infty$ and $\theta_1 = (\Gamma_1 - \Gamma_2)/\Gamma_\infty$. Thus, with the help of Equation 5.52 we obtain the net adsorption flux of surfactant:

$$Q_1 \equiv r_{1,ads} - r_{1,des} = K_{1,ads}c_{1s}(\Gamma_\infty - \Gamma_1)/\Gamma_\infty - K_{1,des}(\Gamma_1 - \Gamma_2)/\Gamma_\infty \quad (5.53)$$

Next, let us consider the reaction of counterion binding:



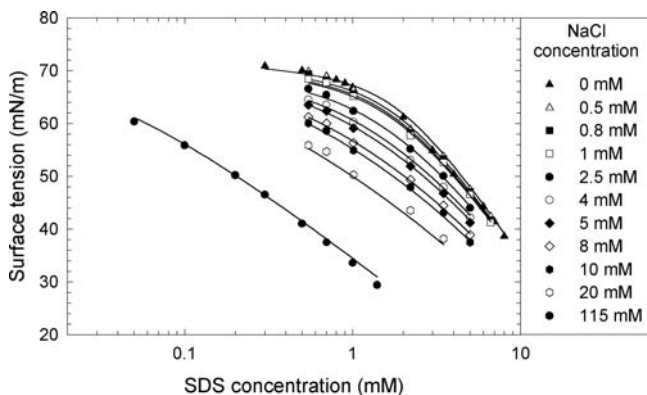


FIGURE 5.2 Plot of the surface tension σ vs. the concentration of SDS, $c_{1\infty}$, for 11 fixed NaCl concentrations. The symbols are experimental data by Tajima et al.^{38,40,41} The lines represent the best fit⁴² with the full set of equations specified in the text, involving the van der Waals isotherms of adsorption and surface tension (Table 5.2).

The rates of the direct and reverse reactions are, respectively,

$$r_{2,\text{ads}} = K_{2,\text{ads}} \theta_1 c_{2s}, \quad r_{2,\text{des}} = K_{2,\text{des}} \theta_2 \quad (5.55)$$

where $K_{2,\text{ads}}$ and $K_{2,\text{des}}$ are the respective rate constants, and c_{2s} is the subsurface concentration of counterions. Having in mind that $\theta_1 = (\Gamma_1 - \Gamma_2)/\Gamma_\infty$ and $\theta_2 = \Gamma_2/\Gamma_\infty$, with the help of Equation 5.55 we deduce an expression for the adsorption flux of counterions:

$$Q_2 \equiv r_{2,\text{ads}} - r_{2,\text{des}} = K_{2,\text{ads}} c_{2s} (\Gamma_1 - \Gamma_2)/\Gamma_\infty - K_{2,\text{des}} \Gamma_2/\Gamma_\infty \quad (5.56)$$

If we can assume that the reaction of counterion binding is much faster than the surfactant adsorption, then we can set $Q_2 \equiv 0$, and Equation 5.56 reduces to the Stern isotherm (Equation 5.47), with $K_2 \equiv K_{2,\text{ads}}/K_{2,\text{des}}$. Next, a substitution of Γ_2 from Equation 5.47 into Equation 5.53 yields³⁵

$$Q_1 \equiv r_{1,\text{ads}} - r_{1,\text{des}} = K_{1,\text{ads}} c_{1s} (\Gamma_\infty - \Gamma_1)/\Gamma_\infty - K_{1,\text{des}} (1 + K_2 c_{2s})^{-1} \Gamma_1/\Gamma_\infty \quad (5.57)$$

Equation 5.57 shows that the adsorption flux of surfactant is influenced by the subsurface concentration of counterions, c_{2s} . At last, if there is equilibrium between surface and subsurface, we have to set $Q_1 \equiv 0$ in Equation 5.57, and thus we obtain the Langmuir isotherm for an ionic surfactant:

$$Kc_{1s} = \Gamma_1/(\Gamma_\infty - \Gamma_1), \quad \text{with} \quad K \equiv (K_{1,\text{ads}}/K_{1,\text{des}})(1 + K_2 c_{2s}) \quad (5.58)$$

Note that $K_1 \equiv K_{1,\text{ads}}/K_{1,\text{des}}$. This result demonstrates that the linear dependence of K on c_{2s} (Equation 5.48) can be deduced from the reactions of surfactant adsorption and counterion binding (Equations 5.51 and 5.54). (For $I < 0.1$ M we have $\gamma_{\pm} \approx 1$ and then activities and concentrations of the ionic species coincide.)

5.2.1.2.5 Comparison of Theory and Experiment

As illustration, we consider the interpretation of experimental isotherms by Tajima et al.^{38,40,41} for the surface tension σ vs. SDS concentrations at 11 fixed concentrations of NaCl (Figure 5.2). Processing the set of data for the interfacial tension $\sigma = \sigma(c_{1\infty}, c_{2\infty})$ as a function of the bulk concentrations of surfactant (DS⁻) ions and Na⁺ counterions, $c_{1\infty}$ and $c_{2\infty}$, we can determine the

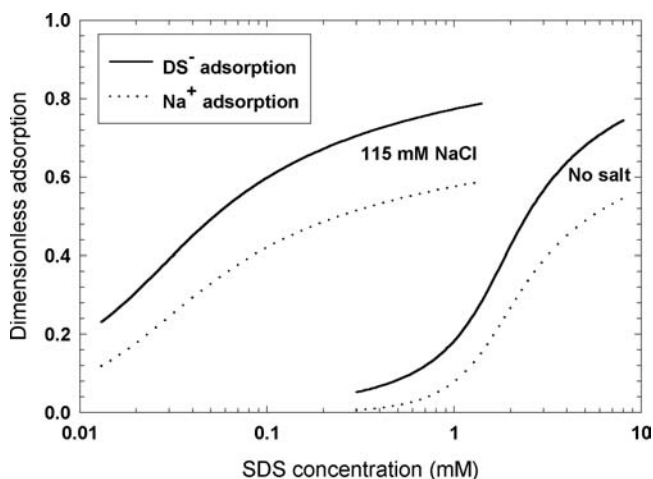


FIGURE 5.3 Plots of the dimensionless adsorptions of surfactant ions Γ_1/Γ_∞ (DS^- , the full lines), and counterions Γ_2/Γ_∞ (Na^+ , the dotted lines), vs. the surfactant (SDS) concentration, $c_{1\infty}$. The lines are calculated⁴² for NaCl concentrations 0 and 115 mM using parameter values determined from the best fit of experimental data (Figure 5.2).

surfactant adsorption, $\Gamma_1(c_{1\infty}, c_{2\infty})$, the counterion adsorption, $\Gamma_2(c_{1\infty}, c_{2\infty})$, the surface potential, $\Psi_s(c_{1\infty}, c_{2\infty})$, and the Gibbs elasticity $E_G(c_{1\infty}, c_{2\infty})$ for every desirable surfactant and salt concentrations.

The theoretical dependence $\sigma = \sigma(c_{1\infty}, c_{2\infty})$ is determined by the following *full set of equations*: Equation 5.44 for $i = 1, 2$; the Gouy Equation 5.36, Equation 5.39 (with σ_d expressed by Equation 5.41 and J from Table 5.2), the Stern isotherm (Equation 5.47), and one surfactant adsorption isotherm from Table 5.2, say, the van der Waals isotherm. Thus, we get a set of six equations for determining six unknown variables: σ , Φ_s , a_{1s} , a_{2s} , Γ_1 , and Γ_2 . (For $I < 0.1 M$ the activities of the ions can be replaced by the respective concentrations.) The principles of the numerical procedure are described in Reference 27.

The theoretical model contains four parameters, β , Γ_∞ , K_1 , and K_2 , whose values are to be obtained from the best fit of the experimental data. Note that all 11 curves in Figure 5.2 are fitted simultaneously.⁴² In other words, the parameters β , Γ_∞ , K_1 , and K_2 are the same for all curves. The value of Γ_∞ , obtained from the best fit of the data in Figure 5.2, corresponds to $1/\Gamma_\infty = 31 \text{ \AA}^2$. The respective value of K_1 is $82.2 \text{ m}^3/\text{mol}$, which in view of Equation 5.49 gives a standard free energy of surfactant adsorption $\Delta\mu_1^{(0)} = 12.3 kT$ per DS^- ion, that is, 30.0 kJ/mol . The determined value of K_2 is $8.8 \times 10^{-4} \text{ m}^3/\text{mol}$, which after substitution in Equation 5.49 yields a standard free energy of counterion binding $\Delta\mu_2^{(0)} = 1.9 kT$ per Na^+ ion, that is, 4.7 kJ/mol . The value of the parameter β is positive, $2\beta \Gamma_\infty/kT = +2.89$, which indicates attraction between the hydrocarbon tails of the adsorbed surfactant molecules. However, this attraction is too weak to cause two-dimensional phase transition. The van der Waals isotherm predicts such transition for $2\beta \Gamma_\infty/kT > 6.75$.

Figure 5.3 shows calculated curves for the adsorptions of surfactant, Γ_1 (the full lines), and counterions, Γ_2 (the dotted lines), vs. the SDS concentration, $c_{1\infty}$. These lines represent the variation of Γ_1 and Γ_2 along the experimental curves, which correspond to the lowest and highest NaCl concentrations in Figure 5.2, that is, $c_{3\infty} = 0$ and 115 mM . We see that both Γ_1 and Γ_2 are markedly greater when NaCl is present in the solution. The highest values of Γ_1 for the curves in Figure 5.3 are $4.2 \times 10^{-6} \text{ mol/m}^2$ and $4.0 \times 10^{-6} \text{ mol/m}^2$ for the solutions with and without NaCl, respectively. The latter two values compare well with the saturation adsorptions measured by Tajima et al.^{40,41} for the same system by means of the radiotracer method, that is, $\Gamma_1 = 4.3 \times 10^{-6} \text{ mol/m}^2$ and $3.2 \times 10^{-6} \text{ mol/m}^2$ for the solutions with and without NaCl.

For the solution *without* NaCl the occupancy of the Stern layer, Γ_2/Γ_1 rises from 0.15 to 0.73 and then exhibits a tendency to level off. The latter value is consonant with data of other authors,⁴³⁻⁴⁵ who have obtained values of Γ_2/Γ_1 up to 0.70 to 0.90 for various ionic surfactants; pronounced evidences for counterion binding have been obtained also in experiments with solutions containing surfactant micelles.⁴⁶⁻⁵⁰ As could be expected, both Γ_1 and Γ_2 are higher for the solution *with* NaCl. These results imply that the counterion adsorption (binding) should be always taken into account.

The fit of the data in Figure 5.2 also gives the values of the surface electric potential, ψ_s . For the solutions with 115 mM NaCl, the model predicts surface potentials varying in the range $|\psi_s| = 55$ to 95 mV within the experimental interval of surfactant concentrations, whereas for the solution without salt the calculated surface potential is higher: $|\psi_s| = 150$ to 180 mV (for SDS ψ_s has a negative sign). Thus, it turns out that measurements of surface tension, interpreted by means of an appropriate theoretical model, provide a method for determining the surface potential ψ_s in a broad range of surfactant and salt concentrations. The described approach could be also applied to solve the inverse problem, that is, to process data for the surface potential. In this way, the adsorption of surfactant on solid particles can be determined from the measured zeta-potential.⁵¹

5.2.2 DYNAMIC SURFACE TENSION

If the surface of an equilibrium surfactant solution is disturbed (expanded, compressed, renewed, etc.), the system will try to restore the equilibrium by exchange of surfactant between the surface and the subsurface layer (adsorption-desorption). The change of the surfactant concentration in the subsurface layer triggers a diffusion flux in the solution. In other words, the process of equilibration (relaxation) of an expanded adsorption monolayer involves two consecutive stages:

1. Diffusion of surfactant molecules from the bulk solution to the subsurface layer
2. Transfer of surfactant molecules from the subsurface to the adsorption layer; the rate of transfer is determined by the height of the kinetic barrier to adsorption

(In the case of desorption the processes have the opposite direction.) Such interfacial expansions are typical for foam generation and emulsification. The rate of adsorption relaxation determines whether or not the formed bubbles/drops will coalesce upon collision and, in final reckoning; how large the foam volume and the emulsion drop-size will be.^{52,53} Below, we focus on the relaxation time of surface tension, τ_σ , which characterizes the interfacial dynamics.

The overall rate of surfactant adsorption is controlled by the slowest stage. If it is stage (1), we deal with *diffusion control*, whereas if stage (2) is slower, the adsorption occurs under *barrier (kinetic) control*. The next four subsections are dedicated to processes under diffusion control (which are the most frequently observed), whereas in Section 5.2.2.5 we consider adsorption under barrier control.

Various experimental methods for dynamic surface tension measurements are available. Their operational timescales cover different time intervals.^{54,55} Methods with a *shorter* characteristic operational time are the oscillating jet method,⁵⁶⁻⁵⁸ the oscillating bubble method,⁵⁹⁻⁶² the fast-formed drop technique,^{63,64} the surface wave techniques,⁶⁵⁻⁶⁸ and the maximum bubble pressure method.⁶⁹⁻⁷⁴ Methods of *longer* characteristic operational time are the inclined plate method,^{75,76} the drop-weight/volume techniques,⁷⁷⁻⁸⁰ the funnel⁸¹ and overflowing cylinder⁸² methods, and the axisymmetric drop shape analysis (ADSA),^{83,84} see References 54, 55, and 85 for a more detailed review.

In this section, devoted to dynamic surface tension, we consider mostly *nonionic* surfactant solutions. In Section 5.2.2.4 we address the more complicated case of *ionic* surfactants. We will restrict our considerations to the simplest case of *relaxation of an initial uniform interfacial dilatation*. The more complex case of simultaneous adsorption and dilatation is considered elsewhere.^{54,70,74,82,85}

5.2.2.1 Adsorption under Diffusion Control

Here we consider a solution of a *nonionic* surfactant, whose concentration, $c_1 = c_1(z, t)$, depends on the position and time because of the diffusion process. (As before, z denotes the distance to the interface, which is situated in the plane $z = 0$.) Correspondingly, the surface tension, surfactant adsorption and the subsurface concentration of surfactant vary with time: $\sigma = \sigma(t)$, $\Gamma_1 = \Gamma_1(t)$, $c_{1s} = c_{1s}(t)$. The surfactant concentration obeys the equation of diffusion:

$$\frac{\partial c_1}{\partial t} = D_1 \frac{\partial^2 c_1}{\partial z^2} \quad (z > 0, t > 0) \quad (5.59)$$

where D_1 is the diffusion coefficient of the surfactant molecules. The exchange of surfactant between the solution and its interface is described by the boundary conditions:

$$c_1(0, t) = c_{1s}(t), \quad \frac{d\Gamma_1}{dt} = D_1 \frac{\partial c_1}{\partial z}, \quad (z = 0, t > 0) \quad (5.60)$$

The latter equation states that the rate of increase of the adsorption Γ_1 is equal to the diffusion influx of surfactant per unit area of the interface. Integrating Equation 5.59, along with Equation 5.60, we can derive the equation of Ward and Tordai:⁸⁶

$$\Gamma_1(t) = \Gamma_1(0) + \sqrt{\frac{D_1}{\pi}} \left[2c_{1\infty} \sqrt{t} - \int_0^t \frac{c_{1s}(\tau)}{\sqrt{t-\tau}} d\tau \right] \quad (5.61)$$

Solving Equation 5.61 together with some of the adsorption isotherms $\Gamma_1 = \Gamma_1(c_{1s})$ in Table 5.2, we can in principle determine the two unknown functions $\Gamma_1(t)$ and $c_{1s}(t)$. Because the relation $\Gamma_1(c_{1s})$ is nonlinear (except for the Henry isotherm), this problem, or its equivalent formulations, can be solved either numerically⁸⁷ or by employing appropriate approximations.^{70,88}

In many cases it is convenient to use asymptotic expressions for the functions $\Gamma_1(t)$, $c_{1s}(t)$, and $\sigma(t)$ for *short times* ($t \rightarrow 0$) and *long times* ($t \rightarrow \infty$). A general asymptotic expression for the short times can be derived from Equation 5.61 substituting $c_{1s} \approx c_{1s}(0) = \text{const.}$:

$$\Gamma_1(t) = \Gamma_1(0) + 2\sqrt{D_1/\pi} [c_{1\infty} - c_{1s}(0)]\sqrt{t} \quad (t \rightarrow 0) \quad (5.62)$$

Analogous asymptotic expression can be obtained also for the long times, although the derivation is not so simple. Hansen⁸⁹ derived a useful asymptotics for the subsurface concentration:

$$c_{1s}(t) = c_{1\infty} - \frac{\Gamma_{1e} - \Gamma(0)}{\sqrt{\pi D_1 t}} \quad (t \rightarrow \infty) \quad (5.63)$$

where Γ_{1e} is the equilibrium value of the surfactant adsorption. The validity of the Hansen Equation 5.63 was confirmed in subsequent studies by other authors.^{90,91}

Below we continue our review of the asymptotic expressions considering separately the cases of *small* and *large* initial perturbations.

5.2.2.2 Small Initial Perturbation

When the deviation from equilibrium is small, then the adsorption isotherm can be linearized:

$$\Gamma_1(t) - \Gamma_{1e} \approx \left(\frac{\partial \Gamma_1}{\partial c_1} \right)_e [c_{1s}(t) - c_e] \quad (5.64)$$

Here and hereafter the subscript e means that the respective quantity refers to the equilibrium state. The set of linear equations, 5.59, 5.60, and 5.64, has been solved by Sutherland.⁹² The result, which describes the relaxation of a *small* initial interfacial dilatation, reads

$$\frac{\sigma(t) - \sigma_e}{\sigma(0) - \sigma_e} = \frac{\Gamma_1(t) - \Gamma_{1e}}{\Gamma_1(0) - \Gamma_{1e}} = \exp\left(\frac{t}{\tau_\sigma}\right) \operatorname{erfc}\left(\sqrt{\frac{t}{\tau_\sigma}}\right) \quad (5.65)$$

where

$$\tau_\sigma \equiv \frac{1}{D_1} \left(\frac{\partial \Gamma_1}{\partial c_1} \right)_e^2 \quad (5.66)$$

is the characteristic relaxation time of surface tension and adsorption, and

$$\operatorname{erfc}(x) \equiv \frac{2}{\sqrt{\pi}} \int_x^\infty \exp(-x^2) dx \quad (5.67)$$

is the so-called complementary error function.^{93,94} The asymptotics of the latter function for small and large values of the argument are^{93,94}

$$\operatorname{erfc}(x) = 1 - \frac{2}{\sqrt{\pi}} x + O(x^3) \quad \text{for } x \ll 1; \quad \operatorname{erfc}(x) = \frac{e^{-x^2}}{\sqrt{\pi}x} \left[1 + O\left(\frac{1}{x^2}\right) \right] \quad \text{for } x \gg 1 \quad (5.68)$$

Combining Equations 5.65 and 5.68 we obtain the short-time and long-time asymptotics of the surface tension relaxation:

$$\frac{\sigma(t) - \sigma_e}{\sigma(0) - \sigma_e} = \frac{\Gamma_1(t) - \Gamma_{1e}}{\Gamma_1(0) - \Gamma_{1e}} = 1 - \frac{2}{\sqrt{\pi}} \sqrt{\frac{t}{\tau_\sigma}} + O\left[\left(\frac{t}{\tau_\sigma}\right)^{3/2}\right] \quad (t \ll \tau_\sigma) \quad (5.69)$$

$$\frac{\sigma(t) - \sigma_e}{\sigma(0) - \sigma_e} = \frac{\Gamma_1(t) - \Gamma_{1e}}{\Gamma_1(0) - \Gamma_{1e}} = \sqrt{\frac{\tau_\sigma}{\pi t}} + O\left[\left(\frac{\tau_\sigma}{t}\right)^{3/2}\right] \quad (t \gg \tau_\sigma) \quad (5.70)$$

Equation 5.70 is often used as a test to verify whether the adsorption process is under diffusion control: data for $\sigma(t)$ are plotted vs. $1/\sqrt{t}$ and we check if the plot complies with a straight line; moreover, the intercept of the line gives σ_e . We recall that Equations 5.69 and 5.70 are valid in the case of a *small* initial perturbation; alternative asymptotic expressions for the case of *large* initial perturbation are considered in the next subsection.

With the help of the thermodynamic Equations 5.2 and 5.6 we derive

$$\frac{\partial \Gamma_1}{\partial c_1} = \frac{\partial \Gamma_1}{\partial \sigma} \frac{\partial \sigma}{\partial c_1} = \frac{\Gamma_1^2 kT}{c_1 E_G} \quad (5.71)$$

Thus, Equation 5.66 can be expressed in an alternative form:³⁵

$$\tau_\sigma = \frac{1}{D_1} \left(\frac{\Gamma_1^2 kT}{c_1 E_G} \right)^2 \quad (5.72)$$

Substituting E_G from Table 5.3 into Equation 5.72 we can obtain expressions for τ_σ corresponding to various adsorption isotherms. In the special case of the Langmuir adsorption isotherm we can present Equation 5.72 in the form:³⁵

$$\tau_\sigma = \frac{1}{D_1} \frac{(K\Gamma_\infty)^2}{(1 + Kc_1)^4} = \frac{1}{D_1} \frac{(K\Gamma_\infty)^2}{(1 + E_G/(\Gamma_\infty kT))^4} \quad (\text{for Langmuir isotherm}) \quad (5.73)$$

Equation 5.73 visualizes the very strong dependence of the relaxation time τ_σ on the surfactant concentration c_1 ; in general, τ_σ can vary with many orders of magnitude as a function of c_1 . Equation 5.73 shows also that high Gibbs elasticity corresponds to short relaxation time, and vice versa.

As a quantitative example let us take typical parameter values: $K_1 = 15 \text{ m}^3/\text{mol}$, $1/\Gamma_\infty = 40 \text{ \AA}^2$, $D_1 = 5.5 \times 10^{-6} \text{ cm}^2/\text{s}$, and $T = 298 \text{ K}$. Then with $c_1 = 6.5 \times 10^{-6} \text{ M}$, from Table 5.3 (Langmuir isotherm) and Equation 5.73 we calculate $E_G \approx 1.0 \text{ mN/m}$ and $\tau_\sigma \approx 5 \text{ s}$. In the same way, for $c_1 = 6.5 \times 10^{-4} \text{ M}$ we calculate $E_G \approx 100 \text{ mN/m}$ and $\tau_\sigma \approx 5 \times 10^{-4} \text{ s}$.

To directly measure the Gibbs elasticity E_G , or to precisely investigate the dynamics of surface tension, we need an experimental method, whose characteristic time is smaller compared with τ_σ . Equation 5.73 and the latter numerical example show that when the surfactant concentration is higher, the experimental method should be faster.

5.2.2.3 Large Initial Perturbation

By definition, we have *large initial perturbation* when at the initial moment the interface is clean of surfactant:

$$\Gamma_1(0) = 0, \quad c_{1s}(0) = 0 \quad (5.74)$$

In such a case, the Hansen Equation 5.63 reduces to

$$c_{1s}(t) = c_{1\infty} - \frac{\Gamma_{1e}}{\sqrt{\pi D_1 t}} \quad (t \rightarrow \infty) \quad (5.75)$$

By substituting $c_{1s}(t)$ for c_1 in the Gibbs adsorption Equation 5.2, and integrating, we obtain the long-time asymptotics of the surface tension of a nonionic surfactant solution after a large initial perturbation:

$$\sigma(t) - \sigma_e = \left(\frac{\Gamma_1^2 kT}{c_1} \right) \left(\frac{1}{\pi D_1 t} \right)^{1/2} \quad (\text{large initial perturbation}) \quad (5.76)$$

with the help of Equation 5.72 we can bring Equation 5.76 into another form:

$$\sigma(t) - \sigma_e = E_G \left(\frac{\tau_\sigma}{\pi t} \right)^{1/2} \quad (\text{large initial perturbation}) \quad (5.77)$$

where E_G is given in Table 5.3. It is interesting to note that Equation 5.77 is applicable to both nonionic and ionic surfactants with the only difference that for nonionics τ_σ is given by Equation 5.66, whereas for ionic surfactants the expression for τ_σ is somewhat longer; see References 35 and 95.

The above equations show that in the case of adsorption under diffusion control the long-time asymptotics can be expressed in the form:

$$\sigma = \sigma_e + S t^{-1/2} \quad (5.78)$$

In view of Equations 5.70 and 5.77, the slope S of the dependence σ vs. $t^{-1/2}$ is given by the expressions:⁹⁵

$$S_s = [\sigma(0) - \sigma_e] \left(\frac{\tau_\sigma}{\pi} \right)^{1/2} \quad (\text{small perturbation}) \quad (5.79)$$

$$S_l = E_G \left(\frac{\tau_\sigma}{\pi} \right)^{1/2} \quad (\text{large perturbation}) \quad (5.80)$$

As known, the surfactant adsorption Γ_1 monotonically increases with the rise of the surfactant concentration, c_1 . In contrast, the slope S_l is a nonmonotonic function of c_1 : S_l exhibits a maximum at a certain concentration. To demonstrate that we will use the expression

$$S_l = \frac{\Gamma_1^2 kT}{c_1 \sqrt{\pi D_1}} \quad (5.81)$$

which follows from Equations 5.76 and 5.78. In Equation 5.81 we substitute the expressions for c_1 stemming from the Langmuir and Volmer adsorption isotherms (Table 5.2 with $c_1 = a_{1s}$); the result reads

$$\tilde{S}_l = \theta(1 - \theta) \quad (\text{for Langmuir isotherm}) \quad (5.82)$$

$$\tilde{S}_l = \theta(1 - \theta) \exp\left(-\frac{\theta}{1 - \theta}\right) \quad (\text{for Volmer isotherm}) \quad (5.83)$$

where θ and \tilde{S}_l are the dimensionless adsorption and slope coefficient:

$$\theta = \Gamma_1 / \Gamma_\infty, \quad \tilde{S}_l = \frac{S_l \sqrt{\pi D_1}}{kT K \Gamma_\infty^2} \quad (5.84)$$

Figure 5.4 compares the dependencies \tilde{S}_l (θ) given by Equations 5.82 and 5.83; we see that the former is symmetric and has a maximum at $\theta = 0.5$, whereas the latter is asymmetric with a

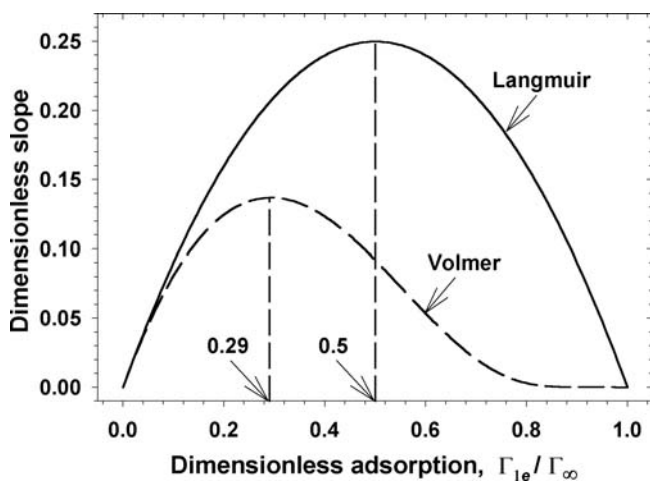


FIGURE 5.4 Plot of the dimensionless slope, \tilde{S}_l , vs. the dimensionless equilibrium surfactant adsorption, $\theta = \Gamma_{le} / \Gamma_{\infty}$, in accordance with Equations 5.82 and 5.83, corresponding to the cases of localized and nonlocalized adsorption.

maximum at $\theta \approx 0.29$. We recall that the Langmuir and Volmer isotherms correspond to *localized* and *nonlocalized* adsorption, respectively (see Section 5.2.1.1.2). Then Figure 5.4 shows that the symmetry/asymmetry of the plot \tilde{S}_l vs. θ provides a *test* for verifying whether the adsorption is localized or nonlocalized. (The practice shows that the fits of *equilibrium* surface tension isotherms do not provide such a test; theoretical isotherms corresponding to localized and nonlocalized adsorption are found to fit equally well surface tension data!)

From another viewpoint, the nonmonotonic behavior of $S_l(\theta)$ can be interpreted as follows. Equation 5.80 shows that $S_l \propto E_G \sqrt{\tau_{\sigma}}$; then the nonmonotonic behavior stems from the fact that E_G is an increasing function of c_1 , whereas τ_{σ} is a decreasing function of c_1 . This qualitative conclusion is valid also for the case of ionic surfactant, as demonstrated in the next section.

5.2.2.4 Generalization for Ionic Surfactants

In the case of ionic surfactants the dynamics of adsorption is more complicated because of the presence of a dynamic EDL. Indeed, the adsorption of surfactant at the interface creates surface charge, which is increasing in the course of the adsorption process. The charged interface repels the new-coming surfactant molecules, but attracts the conversely charged counterions (see Figure 5.1); some of them bind to the surfactant headgroups thus decreasing the surface charge density and favoring the adsorption of new surfactant molecules. The theoretical description of the overall adsorption process involves the (electro)diffusion equations for the surfactant ions, counterions, and coions, and the Poisson equation from electrodynamics. Different analytical and numerical approaches to the solution of this problem have been proposed.^{13,95-102} Below we describe an approach to the dynamics of ionic surfactant adsorption, which is simpler both as a concept and as a computer program realization, but agrees very well with the experiment.

Two timescales can be distinguished in the adsorption process of ionic species. The first timescale is characterized by the diffusion relaxation time of the EDL, $t_{edl} = 1 / (D_1 \kappa_c^2 l)$; see Equations 5.32 and 5.34 above. It accounts for the interplay of electrostatic interactions and diffusion. The second scale is provided by the characteristic time of the used experimental method, t_{exp} , that is, the minimum interfacial age that can be achieved with the given method; typically, $t_{exp} \geq 5 \times 10^{-3}$ s. For example, if the diffusivity is $D_1 = 5.5 \times 10^{-10}$ m²/s, for $l = 10^{-5}$ M and 10^{-2} M one calculates, correspondingly, $t_{edl} = 1.7 \times 10^{-5}$ and 1.7×10^{-8} s. We see that $\epsilon \equiv t_{edl} / t_{exp} \ll 1$ is a small parameter. The presence of such small parameter implies the existence of two characteristic length

scales: *inner* (in the EDL) $l_{in} \equiv (D_1 t_{edl})^{1/2}$ and *outer* (outside the EDL) $l_{out} \equiv (D_1 t_{exp})^{1/2}$. In fact, l_{in} characterizes the width of the layer in which the variation of the ionic concentrations is governed by the electric field, whereas l_{out} scales the width of the zone in which the concentrations of the species vary due to the diffusion. Next, we can apply the method of the matched inner and outer asymptotic expansions¹⁰³ to solve the problem. Without entering into mathematical details, here we outline the final results and the computational procedure, which is relatively simple.¹⁰⁴

In the outer zone, where the electrical field is zero we obtain a generalized version of the Hansen Equation 5.75 for all diffusing species:

$$c_{i,b} = c_{i\infty} - \frac{\tilde{\Gamma}_{i,e}}{\sqrt{\pi D_i t}} \quad (5.85)$$

where $c_{i,b}$ is the concentration of the respective ion at the inner boundary of the outer zone, D_i is diffusion coefficient, and $\tilde{\Gamma}_{i,e}$ is the total equilibrium adsorption of the respective species; see Equations 5.37 and 5.38. In Section 5.2.1.2.5 we specified the full set of equations that allow one to calculate all equilibrium parameters; supposedly the constants β , Γ_∞ , K_1 , and K_2 are determined from the best fit of experimental data — see the discussion related to Figure 5.2. (In the simpler case of nonionic surfactant the full set of equations reduces to a couple of corresponding adsorption and surface tension isotherms from Table 5.2, which enables us to calculate Γ_1 and σ for each given value of c_1 .) The computational procedure for the dynamic problem is the following:

1. We calculate $\tilde{\Gamma}_{i,e}$ using the full set of equations in Section 5.2.1.2.5.
2. Next, from Equation 5.85 we calculate $c_{i,b}(t)$ for a set of values of t in the experimental time interval.
3. Further, in the full set of equations in Section 5.2.1.2.5 we replace everywhere $c_{i\infty}$ with $c_{i,b}(t)$; then, for each value of t , we solve this system of equations to determine the functions $\Gamma_i(t)$, $\Phi_s(t)$, and $\sigma(t)$. In the long-time limit we can determine also $S_i = \partial\sigma/\partial t^{-1/2}$.

The justification of this procedure can be accomplished by means of the method of the matched asymptotic expansions.¹⁰⁴

Comparison of theory and experiment. To illustrate how the theory compares with the experiment, in Figure 5.5 we present five experimental curves for $\sigma(t)$ corresponding to five different surfactant concentrations, at fixed concentration of added electrolyte, 12 mM NaCl. The surfactant is sodium dodecyl-benzene-sulfonate (DDBS). (This specific sample was a technical product containing 82.6 wt% pure DDBS and 17.4 wt% Na_2SO_4 .) The dynamic surface tension $\sigma(t)$ was measured by means of the fast formed drop (FFD) technique.^{63,64} The method consists of a sudden formation of a drop at the orifice of a capillary by a quick breaking of a jet of surfactant solution, which flows out of the capillary. Thus, a fresh curved interface is formed at the capillary tip. The surfactant adsorbs at the immobile curved interface and, consequently, the surface tension and the pressure inside the drop decrease with time; the pressure is registered by means of a piezotransducer, whose electric output can be converted in terms of surface tension by using the Laplace equation of capillarity. In this way, the curves for $\sigma(t)$ in Figure 5.5 were obtained.¹⁰⁴ The capillary pressure was recorded every 0.1 s, which gives a large number of experimental points and provides good statistics. In addition, equilibrium surface tension isotherms have been obtained and processed as explained in Section 5.2.1.2.5 to determine the parameters β , Γ_∞ , K_1 , K_2 , etc. The van der Waals isotherm (Table 5.2) has been employed.

The long-time portions of the curves in Figure 5.5, plotted as σ vs. $t^{-1/2}$, comply very well with straight lines, whose slopes, S_i , are plotted in Figure 5.6a — the points. The theoretical curve for S_i is calculated using the procedure given after Equation 5.85. The curve is obtained using only the parameters of the equilibrium surface tension isotherm and the diffusion coefficients of the ionic

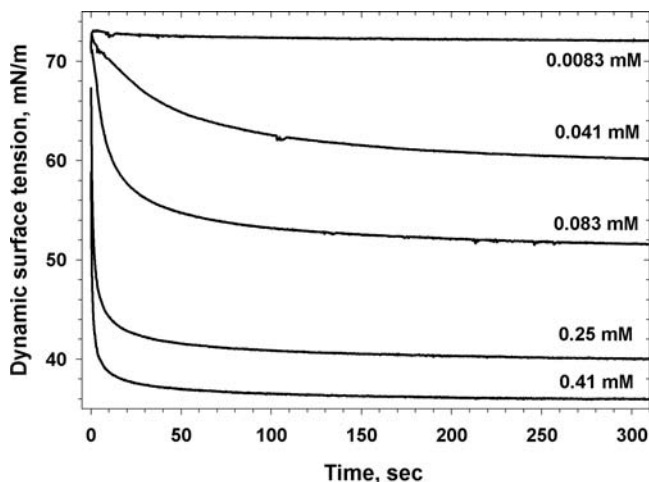


FIGURE 5.5 Experimental curves¹⁰⁴ for the relaxation of surface tension σ with time t for five fixed concentrations (denoted in the figure) of sodium dodecyl-benzene-sulfonate (DDBS). The solutions contain 12 mM added NaCl, and Na₂SO₄ whose concentration is 21 wt% that of DDBS.

species. We see that the agreement between theory and experiment is excellent. (No adjustable parameters have been used to fit the dynamic data.) The plot in Figure 5.6a exhibits a maximum, in agreement with our expectations (see Section 5.2.2.3).

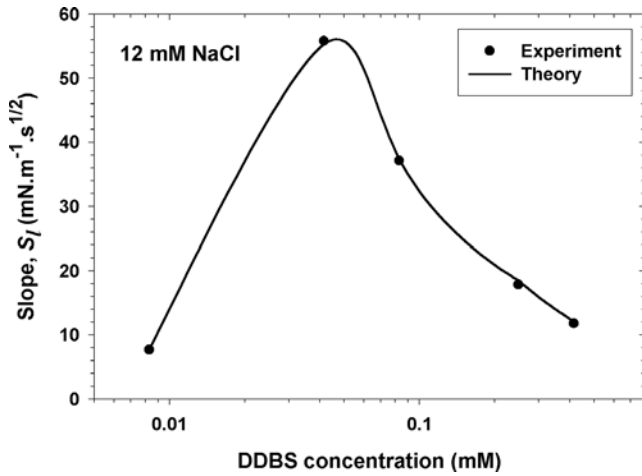
The comparison between theory and experiment could be carried out also in terms of the relaxation time of the surface tension, τ_σ . We can use the connection $\tau_\sigma = \pi (S_l/E_G)^2$, which follows from Equation 5.80. The Gibbs elasticity E_G is calculated from the van der Waals expression in Table 5.3. The results for τ_σ and E_G are shown in Figure 5.6b. We see the wide range of variation of the characteristic relaxation time τ_σ , which varies with more than four orders of magnitude in the investigated range of concentrations. Moreover, one sees that for the higher surfactant concentrations, the so-called long-time relaxation could be effectuated within 0.01 to 0.1 s. On the other hand, for the low surfactant concentrations the relaxation can be longer than 100 s. In part, this variation of the relaxation time t_σ with orders of magnitude is due to the strong variation of the surface elasticity E_G with the surfactant concentration; see the right-hand curve in Figure 5.6b.

5.2.2.5 Adsorption under Barrier Control

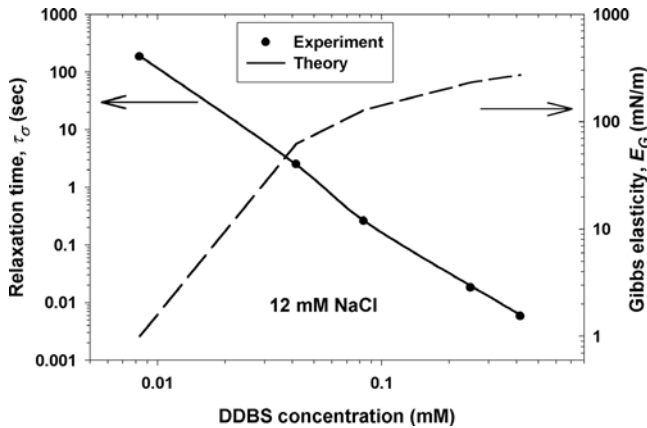
In general, adsorption is under barrier (kinetic, transfer) control when the stage of surfactant transfer from the subsurface to the surface is much slower than the diffusion stage because of some kinetic barrier. The latter can be due to steric hindrance, spatial reorientation, or conformational changes accompanying the adsorption of molecules, including destruction of the shells of oriented water molecules wrapping the surfactant hydrocarbon tail in water.¹⁰⁵ We will restrict our considerations to the case of pure barrier control, without double layer effects. In such case the surfactant concentration is uniform throughout the solution, $c_1 = \text{const.}$, and the increase of the adsorption $\Gamma_1(t)$ is solely determined by the transitions of surfactant molecules over the adsorption barrier, separating subsurface from surface:

$$\frac{d\Gamma_1}{dt} = Q \equiv r_{\text{ads}}(c_1, \Gamma_1) - r_{\text{des}}(\Gamma_1) \quad (5.86)$$

r_{ads} and r_{des} are the rates of surfactant adsorption and desorption. The concept of barrier-limited adsorption originates from the works of Bond and Puls¹⁰⁶ and Doss¹⁰⁷ and has been further developed



(a)



(b)

FIGURE 5.6 (a) Plot of the slope coefficient S_l vs. the surfactant (DDBS) concentration; the points are the values of S_l for the curves in Figure 5.5; the line is the theoretical curve obtained using the procedure described after Equation 5.85 (no adjustable parameters). (b) Plots of the relaxation time τ_σ and the Gibbs elasticity E_G vs. the DDBS concentration; E_G is computed from the equilibrium surface tension isotherm; $\tau_\sigma = \pi (S_l/E_G)^2$ is calculated using the above values of S_l .

by other authors.¹⁰⁸⁻¹¹⁵ Table 5.5 summarizes some expressions for the total rate of adsorption under barrier control, Q . The quantities K_{ads} and K_{des} in Table 5.5 are the rate constants of adsorption and desorption, respectively. Their ratio is equal to the equilibrium constant of adsorption:

$$K_{\text{ads}}/K_{\text{des}} = K \quad (5.87)$$

The parameters Γ_∞ and K are the same as in Tables 5.2 through 5.4. Setting $Q = 0$ (assuming equilibrium surface–subsurface), from each expression in Table 5.5 we deduce the respective equilibrium adsorption isotherm in Table 5.2. In addition, for $\beta = 0$ the expressions for Q related to the Frumkin and van der Waals model reduce, respectively, to the expressions for Q in the Langmuir and Volmer models. For $\Gamma_1 \ll \Gamma_\infty$ both the Frumkin and Langmuir expressions in Table 5.5 reduce to the Henry expression.

TABLE 5.5
Rate of Surfactant Adsorption for Different Kinetic Models

Type of Isotherm	Rate of Reversible Adsorption $Q = r_{\text{ads}}(c_1, \Gamma_1) - r_{\text{des}}(\Gamma_1)$
Henry	$Q = K_{\text{ads}} c_1 - K_{\text{des}} \Gamma_1 / \Gamma_{\infty}$
Freundlich	$Q = K_{\text{ads}} K^{m-1} c_1^m - K_{\text{des}} \Gamma_1 / \Gamma_{\infty}$
Langmuir	$Q = K_{\text{ads}} c_1 \left(1 - \frac{\Gamma_1}{\Gamma_{\infty}}\right) - K_{\text{des}} \Gamma_1 / \Gamma_{\infty}$
Frumkin	$Q = K_{\text{ads}} c_1 \left(1 - \frac{\Gamma_1}{\Gamma_{\infty}}\right) - K_{\text{des}} \frac{\Gamma_1}{\Gamma_{\infty}} \exp\left(-\frac{2\beta\Gamma_1}{kT}\right)$
Volmer	$Q = K_{\text{ads}} c_1 - K_{\text{des}} \frac{\Gamma_1}{\Gamma_{\infty} - \Gamma_1} \exp\left(\frac{\Gamma_1}{\Gamma_{\infty} - \Gamma_1}\right)$
van der Waals	$Q = K_{\text{ads}} c_1 - K_{\text{des}} \frac{\Gamma_1}{\Gamma_{\infty} - \Gamma_1} \exp\left(\frac{\Gamma_1}{\Gamma_{\infty} - \Gamma_1} - \frac{2\beta\Gamma_1}{kT}\right)$

Substituting Q from Table 5.5 into Equation 5.86, and integrating, we can derive explicit expressions for the relaxation of surfactant adsorption:

$$\frac{\sigma(t) - \sigma_e}{\sigma(0) - \sigma_e} \approx \frac{\Gamma_1(t) - \Gamma_{1,e}}{\Gamma_1(0) - \Gamma_{1,e}} = \exp\left(-\frac{t}{\tau_{\sigma}}\right) \quad (5.88)$$

Equation 5.88 holds for $\sigma(t)$ only in the case of small deviations from equilibrium, whereas there is not such a restriction concerning $\Gamma_1(t)$; the relaxation time in Equation 5.88 is given by the expressions:

$$\tau_{\sigma} = \left(K_{\text{des}} / \Gamma_{\infty}\right)^{-1} \quad (\text{Henry and Freundlich}) \quad (5.89)$$

$$\tau_{\sigma} = \left(\frac{K_{\text{des}}}{\Gamma_{\infty}} + \frac{K_{\text{ads}} c_1}{\Gamma_{\infty}}\right)^{-1} \quad (\text{Langmuir}) \quad (5.90)$$

Equation 5.88 predicts that the perturbation of surface tension, $\Delta\sigma(t) = \sigma(t) - \sigma_e$, relaxes exponentially. This is an important difference with the cases of adsorption under diffusion and electrodiffusion control, for which $\Delta\sigma(t) \propto 1/\sqrt{t}$; see Equations 5.70, 5.76, and 5.78. Thus, a test whether or not the adsorption occurs under purely barrier control is to plot data for $\ln[\Delta\sigma(t)]$ vs. t and to check if the plot complies with a straight line.

In the case of *ionic* surfactants the adsorption of surfactant ions is accompanied by binding of counterions. In addition, the concentrations of the ionic species vary across the EDL (even at equilibrium). These effects are taken into account in Equation 5.57, which can be used as an expression for Q in the case of Langmuirian barrier adsorption of an ionic surfactant.

In fact, a pure barrier regime of adsorption is not frequently observed. It is expected that the barrier becomes more important for substances of low surface activity and high concentration in the solution. Such adsorption regime was observed with propanol, pentanol, 1,6-hexanoic acid, etc.; see Reference 85 for details.

It may happen that the characteristic times of diffusion and transfer across the barrier are comparable. In such case we deal with *mixed* kinetic regime of adsorption. Insofar as the stages of diffusion and transfer are consecutive, the boundary conditions at the interface are

$$\frac{d\Gamma_1}{dt} = r_{\text{ads}}(c_1, \Gamma_1) - r_{\text{des}}(\Gamma_1) = D_1 \left(\frac{\partial c_1}{\partial t} \right)_{z=0} \quad (5.91)$$

The formal transition in Equation 5.91 from mixed to diffusion control of adsorption is not trivial and demands application of scaling and asymptotic expansions. The criterion for occurrence of adsorption under diffusion control (presence of equilibrium between subsurface and surface) is

$$\frac{a K_{\text{des}}}{D_1} \left(\frac{\partial \Gamma_1}{\partial c_1} \right)_e \gg 1 \quad (5.92)$$

where a is a characteristic thickness of the diffusion layer.

An important difference between the regimes of diffusion and barrier control is in the form of the respective initial conditions. In the case of large initial deformations, these are

$$\Gamma_1(0) = 0, \quad c_{1s}(0) = 0 \quad (\text{diffusion control}) \quad (5.93)$$

$$\Gamma_1(0) = 0, \quad c_{1s}(0) = c_{1\infty} \quad (\text{barrier control}) \quad (5.94)$$

Equation 5.93 reflects the fact that in the diffusion regime the surface is always assumed to be equilibrated with the subsurface. In particular, if $\Gamma_1 = 0$, then we must have $c_{1s} = 0$. In contrast, Equation 5.94 stems from the presence of barrier: for time intervals shorter than the characteristic time of transfer, the removal of the surfactant from the interface ($\Gamma_1 = 0$) cannot affect the subsurface layer (because of the barrier) and then $c_{1s}(0) = c_{1\infty}$. This purely theoretical consideration implies that the effect of barrier could show up at the short times of adsorption, whereas at the long times the adsorption will occur under diffusion control.¹¹⁶ The existence of barrier-affected adsorption regime at the short adsorption times could be confirmed or rejected by means of the fastest methods for measurement of dynamic surface tension.

5.3 CAPILLARY HYDROSTATICS AND THERMODYNAMICS

5.3.1 SHAPES OF FLUID INTERFACES

5.3.1.1 Laplace and Young Equations

A necessary condition for mechanical equilibrium of a fluid interface is the Laplace equation of capillarity¹¹⁷⁻¹²⁰

$$2H\sigma = \Delta P \quad (5.95)$$

Here H is the local mean curvature of the interface and ΔP is the local jump of the pressure across the interface. If $z = z(x, y)$ is the equation of the interface in Cartesian coordinates, then H can be expressed in the form:¹²⁰

$$2H = \nabla_s \cdot \left[\frac{\nabla_s z}{\left(1 + |\nabla_s z|^2\right)^{1/2}} \right] \quad (5.96)$$

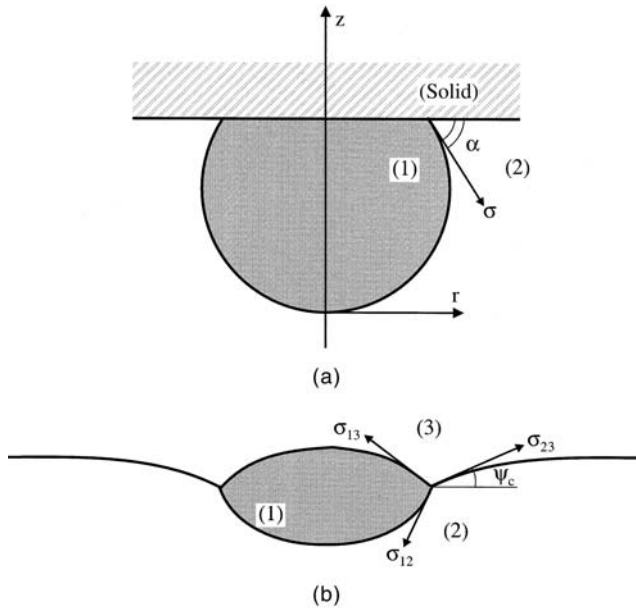


FIGURE 5.7 Sketch of fluid particle (1) attached to an interface. (a) Fluid particle attached to solid interface; α is the contact angle; σ is the interfacial tension of the boundary between the two fluid phases. (b) Fluid particle attached to a fluid interface; σ_{12} , σ_{13} , and σ_{23} are the interfacial tensions between the respective phases; ψ_c is the slope angle of the outer meniscus at the contact line.

where ∇_s is the gradient operator in the plane xy . More general expressions for H can be found in the literature on differential geometry.¹²⁰⁻¹²² Equation 5.95, along with Equation 5.96, represents a second-order partial differential equation that determines the shape of the fluid interface. The interface is bounded by a *three-phase contact line* at which the boundary conditions for the differential equation are formulated. The latter are the respective necessary conditions for mechanical equilibrium at the contact lines. When one of the three phases is solid (Figure 5.7a), the boundary condition takes the form of the Young¹²³ equation:

$$\sigma_{12} \cos \alpha = \sigma_{1s} - \sigma_{2s} \tag{5.97}$$

where α is the three-phase contact angle, σ_{12} is the tension of the interface between the fluid phases 1 and 2, whereas σ_{1s} and σ_{2s} are the tensions of the two fluid–solid interfaces. Insofar as the values of the three σ are determined by the intermolecular forces, the contact angle α is a material characteristic of a given three-phase system. However, when the solid is not smooth and chemically homogeneous, then the contact angle exhibits hysteresis; i.e., α has no defined equilibrium value.^{6,124} Contact angle hysteresis can be observed even with molecularly smooth and homogeneous interfaces under dynamic conditions.¹²⁵

When all the three neighboring phases are fluid, then the boundary condition takes the form of the Neumann¹²⁶ vectorial triangle:

$$\sigma_{12} \mathbf{v}_{12} + \sigma_{13} \mathbf{v}_{13} + \sigma_{23} \mathbf{v}_{23} = 0 \tag{5.98}$$

(see Figure 5.7b); here \mathbf{v}_{ik} is a unit vector, which is simultaneously normal to the contact line and tangential to the boundary between phases i and k . The Laplace, Young, and Neumann equations can be derived as conditions for minimum of the free energy of the system;^{35,120,127} the effect of the line tension can be also taken into account in Equations 5.97 and 5.98.¹²⁷

In the special case of spherical interface $H = 1/R$, with R the sphere radius, and Equation 5.95 takes its most popular form, $2\sigma/R = \Delta P$. In the case of axisymmetric meniscus (z axis of symmetry, Figure 5.7) the Laplace equation reduces to either of the following two equivalent forms:^{119,128}

$$\frac{1}{r} \frac{d}{dr} \left[\frac{rz'}{(1+z'^2)^{1/2}} \right] = \frac{\Delta P}{\sigma}, \quad z = z(r) \quad (5.99)$$

$$-\frac{r''}{(1+r'^2)^{3/2}} + \frac{1}{r(1+r'^2)^{1/2}} = \frac{\Delta P}{\sigma}, \quad r = r(z) \quad (5.100)$$

Two equivalent parametric forms of Laplace equation are often used for calculations:^{119,128}

$$\frac{d \sin \varphi}{dr} + \frac{\sin \varphi}{r} = \frac{\Delta P}{\sigma}, \quad \tan \varphi = \frac{dz}{dr} \quad (5.101)$$

or

$$\frac{d\varphi}{ds} = \frac{\Delta P}{\sigma} - \frac{\sin \varphi}{r}, \quad \frac{dr}{ds} = \cos \varphi, \quad \frac{dz}{ds} = \sin \varphi \quad (5.102)$$

Here, φ is the meniscus running slope angle and s is the arc length along the generatrix of the meniscus. Equation 5.102 is especially convenient for numerical integration, whereas Equation 5.101 may create numerical problems at the points with $\tan \varphi = \pm \infty$, like the particle equator in Figure 5.7a. A generalized form of Equation 5.101, with account for the interfacial (membrane) bending elastic modulus, k_c ,

$$\sigma \left(\frac{d \sin \varphi}{dr} + \frac{\sin \varphi}{r} \right) = \Delta P + \frac{k_c}{r} \cos \varphi \frac{d}{dr} \left\{ r \cos \varphi \frac{d}{dr} \left[\frac{1}{r} \frac{d}{dr} (r \sin \varphi) \right] \right\} \quad (5.103)$$

serves for description of the axisymmetric configurations of real and model cell membranes.^{35,129,130} The Laplace equation can be generalized to account also for the interfacial bending moment (spontaneous curvature), shear elasticity, etc.; for review see References 35 and 129. The latter effects are physically important for such systems or phenomena as capillary waves,¹³¹ lipid membranes,^{132,133} emulsions,¹³⁴ and microemulsions.¹³⁵

5.3.1.2 Solutions of Laplace Equations for Menisci of Different Geometry

Very often the capillary menisci have rotational symmetry. In general, there are three types of axially symmetric menisci corresponding to the three regions denoted in Figure 5.8: (1) meniscus meeting the axis of revolution, (2) meniscus decaying at infinity, and (3) meniscus confined between two cylinders, $0 < R_1 < r < R_2 < \infty$. These three cases are separately considered below.

5.3.1.2.1 Meniscus Meeting the Axis of Revolution

This includes the cases of a bubble/droplet under a plate (Figure 5.7a), the two surfaces of a floating lens (Figure 5.7b), and any kind of sessile or pendant droplets/bubbles. Such a meniscus is a part of a sphere when the effect of gravity is negligible, that is, when

$$\Delta \rho g b^2 / \sigma \ll 1 \quad (5.104)$$

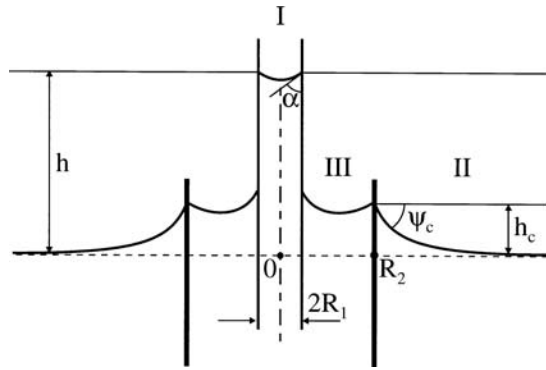


FIGURE 5.8 Capillary menisci formed around two coaxial cylinders of radii R_1 and R_2 . (I) Meniscus meeting the axis of revolution; (II) meniscus decaying at infinity; (III) meniscus confined between the two cylinders. h denotes the capillary raise of the liquid in the inner cylinder; h_c is the elevation of meniscus II at the contact line $r = R_2$.

Here g is the gravity acceleration, $\Delta\rho$ is the difference in the mass densities of the lower and the upper fluid, and b is a characteristic radius of the meniscus curvature. For example, if Equation 5.104 is satisfied with $b = R_1$ (see Figure 5.8), the raise, h , of the liquid in the capillary is determined by means of the equation⁶

$$h = (2\sigma \cos\alpha)/(\Delta\rho g R_1) \quad (5.105)$$

When the gravity effect is not negligible, the capillary pressure, ΔP , becomes dependent on the z -coordinate:

$$\Delta P = 2\sigma/b + \Delta\rho g z \quad (5.106)$$

Here b is the radius of curvature at the particle apex, where the two principal curvatures are equal (e.g., the bottom of the bubble in Figure 5.7a). Unfortunately, Equation 5.99, along with Equation 5.106, has no closed analytical solution. The meniscus shape can be exactly determined by numerical integration of Equation 5.102. Alternatively, various approximate expressions are available.^{128,136,137} For example, if the meniscus slope is small, $z'^2 \ll 1$, Equation 5.99 reduces to a linear differential equation of Bessel type, whose solution reads

$$z(r) = 2[I_0(qr) - 1]/(bq^2) \quad q \equiv (\Delta\rho g/\sigma)^{1/2} \quad (5.107)$$

where $I_0(x)$ is the modified Bessel function of the first kind and zeroth order.^{138,139} Equation 5.107 describes the shape of the lower surface of the lens in Figure 5.7b; similar expression can be derived also for the upper lens surface.

5.3.1.2.2 Meniscus Decaying at Infinity

Examples are the outer menisci in Figures 5.7b and 5.8. In this case the action of gravity cannot be neglected insofar as the gravity keeps the interface flat far from the contact line. The capillary pressure is

$$\Delta P = \Delta\rho g z \quad (5.108)$$

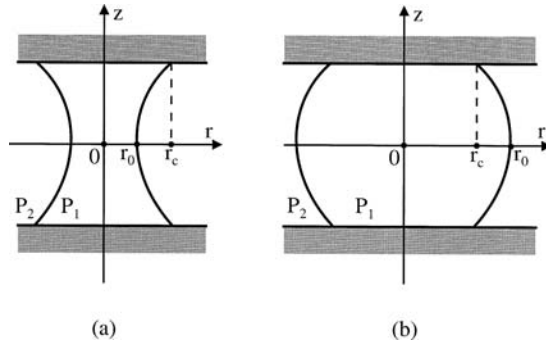


FIGURE 5.9 Concave (a) and convex (b) capillary bridges between two parallel plates. P_1 and P_2 denote the pressures inside and outside the capillary bridge, r_0 is the radius of its section with the midplane; r_c is the radius of the three-phase contact lines.

As mentioned above, Equation 5.99, along with Equation 5.108, has no closed analytical solution. On the other hand, the region far from the contact line has always small slope, $z'^2 \ll 1$. In this region Equation 5.99 can be linearized, and then in analogy with Equation 5.107 we derive

$$z(r) = A K_0(qr) \quad (z'^2 \ll 1) \quad (5.109)$$

where A is a constant of integration and $K_0(x)$ is the modified Bessel function of the second kind and zeroth order.^{138,139} The numerical integration of Equation 5.102 can be carried out by using the boundary condition¹²⁸ $z'/z = -qK_1(qr)/K_0(qr)$ for some appropriately fixed $r \gg q^{-1}$ (see Equation 5.109). Alternatively, approximate analytical solutions of the problem are available.^{128,137,140} In particular, Derjaguin¹⁴¹ has derived an asymptotic formula for the elevation of the contact line at the outer surface of a thin cylinder,

$$h_c = -R_1 \sin\psi_c \ln[qR_1\gamma_e (1 + \cos\psi_c)/4], \quad (qR_1)^2 \ll 1 \quad (5.110)$$

where R_1 is the radius of the contact line, ψ_c is the meniscus slope angle at the contact line (Figure 5.8), q is defined by Equation 5.107, and $\gamma_e = 1.781\,072\,418 \dots$ is the constant of Euler–Mascheroni.¹³⁹

5.3.1.2.3 Meniscus Confined between Two Cylinders ($0 < R_1 < r < R_2 < \infty$)

This is the case with the Plateau borders in real foams and emulsions, and with the model films in the Scheludko cell;^{142,143} such is the configuration of the capillary bridges (Figure 5.9a) and of the fluid particles pressed between two surfaces (Figure 5.9b). When the gravitational deformation of the meniscus cannot be neglected, the interfacial shape can be determined by numerical integration of Equation 5.102, or by iteration procedure.¹⁴⁴ When the meniscus deformation caused by gravity is negligible, analytical solution can be found as described below.

To determine the shape of the menisci depicted in Figures 5.9a and b, we integrate Equation 5.101 from r_0 to r to derive

$$\frac{dz}{dr} = \frac{k_1(r^2 - r_0^2) + r_0}{\pm[(r^2 - r_0^2)(r_1^2 - r^2)]^{1/2} |k_1|}, \quad k_1 \equiv \frac{P_1 - P_2}{2\sigma}, \quad r_1 \equiv \left| \frac{1 - k_1 r_0}{k_1} \right| \quad (5.111)$$

The pressures in phases 1 and 2, P_1 and P_2 , and r_0 are shown in Figure 5.9. Equation 5.111 describes curves, which after Plateau^{118,119,145-147} are called “nodoid” and “unduloid” (see Figure 5.10). The

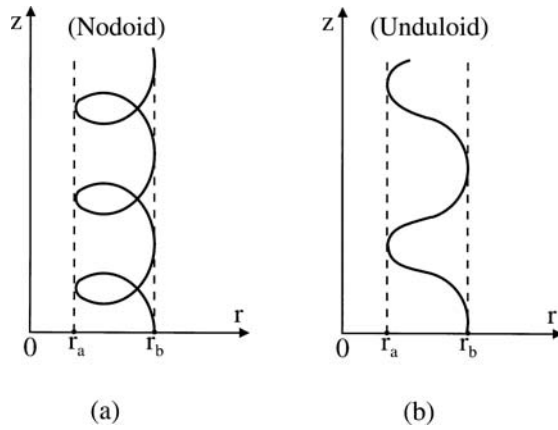


FIGURE 5.10 Typical shape of nodoid (a) and unduloid (b) Plateau curves. Note that the curves are confined between two cylinders of radii r_a and r_b .

nodoid (unlike the unduloid) has points with horizontal tangent, where $dz/dr = 0$. Then, with the help of Equation 5.111 we can deduce that the meniscus generatrix is a part of *nodoid* if $k_1 r_0 \in (-\infty, 0) \cup (1, +\infty)$, while the meniscus generatrix is a part of *unduloid* if $k_1 r_0 \in (0, 1)$.

In the special case, when $k_1 r_0 = 1$, the meniscus is spherical. In the other special case, $k_1 r_0 = 0$, the meniscus has the shape of *catenoid*, i.e.,

$$z = \pm r_0 \ln \left\{ r/r_0 + \sqrt{(r/r_0)^2 - 1} \right\}, \quad (k_1 = 0) \quad (5.112)$$

The meniscus has a “neck” (Figure 5.9a) when $k_1 r_0 \in (-\infty, 1/2)$; in particular, the generatrix is nodoid for $k_1 r_0 \in (-\infty, 0)$, catenoid for $k_1 r_0 = 0$, and unduloid for $k_1 r_0 \in (0, 1/2)$. For the configuration depicted in Figure 5.9a we have $r_1 > r_0$ (in Figure 5.10 $r_a = r_0$, $r_b = r_1$) and Equation 5.111 can be integrated to yield

$$z(r) = \pm \left\{ r_0 F(\phi_1, q_1) + r_1 \operatorname{sgn} k_1 \left[E(\phi_1, q_1) - \frac{1}{r r_1} \sqrt{(r^2 - r_0^2)(r_1^2 - r^2)} \right] \right\} \quad (r_0 \leq r \leq r_1) \quad (5.113)$$

where $\operatorname{sgn} x$ denotes the sign of x , $q_1 = (1 - r_0^2/r_1^2)^{1/2}$, $\sin \phi_1 = q_1^{-1} (1 - r_0^2/r^2)^{1/2}$; $F(\phi, q)$ and $E(\phi, q)$ are the standard symbols for elliptic integrals of the first and the second kind.^{138,139} A convenient method for computation of $F(\phi, q)$ and $E(\phi, q)$ is the method of the arithmetic-geometric mean (see Reference 138, chap. 17.6).

The meniscus has a “haunch” (Figure 5.9b) when $k_1 r_0 \in (1/2, +\infty)$; in particular, the generatrix is unduloid for $k_1 r_0 \in (1/2, 1)$, circumference for $k_1 r_0 = 1$, and nodoid for $k_1 r_0 \in (1, +\infty)$. For the configuration depicted in Figure 5.9b we have $r_0 > r_1$ (in Figure 5.10 $r_a = r_1$, $r_b = r_0$) and Equation 5.111 can be integrated to yield

$$z(r) = \mp \left[(r_0 - 1/k_1) F(\phi_2, q_2) - r_0 E(\phi_2, q_2) \right], \quad (r_1 \leq r \leq r_0) \quad (5.114)$$

where $q_2 = (1 - r_1^2/r_0^2)^{1/2}$, $\sin \phi_2 = q_2^{-1} (1 - r^2/r_0^2)^{1/2}$. Additional information about the shapes, stability, and nucleation of capillary bridges, and for the capillary-bridge forces between particles, can be found in chapter 11 of Reference 35.

5.3.1.3 Gibbs–Thomson Equation

The dependence of the capillary pressure on the interfacial curvature leads to a difference between the chemical potentials of the components in small droplets (or bubbles) and in the large bulk phase. This effect is the driving force of phenomena like nucleation^{148,149} and Ostwald ripening (see Section 5.3.1.4 below). Let us consider the general case of a multicomponent two-phase system; we denote the two phases by α and β . Let phase α be a liquid droplet of radius R . The two phases are supposed to coexist at equilibrium. Then we can derive^{4,5,150,151}

$$\left(\mu_i^\beta\right)_R - \left(\mu_i^\beta\right)_{R=\infty} = \left(\mu_i^\alpha\right)_R - \left(\mu_i^\alpha\right)_{R=\infty} = V_i^\alpha \frac{2\sigma}{R} \quad (5.115)$$

where μ is chemical potential, V_i is partial volume, and the superscripts denote phase and the subscripts denote component. Equation 5.115 is derived under the following assumptions. When β is a gaseous phase, it is assumed that the partial volume of each component in the gas is much larger than its partial volume in the liquid α ; this is fulfilled far enough from the critical point.¹⁵¹ When phase β is liquid, it is assumed that $P^\beta(R) = P^\beta(R = \infty)$, where P denotes pressure.

When phase β is an ideal gas, Equation 5.115 yields^{4,5,150,151}

$$\frac{P_i^\beta(R)}{P_i^\beta(\infty)} = \exp\left(\frac{2\sigma V_i^\alpha}{RkT}\right) \quad (5.116)$$

where $P_i^\beta(R)$ and $P_i^\beta(\infty)$ denote, respectively, the equilibrium vapor pressure of component i in the droplet of radius R and in a large liquid phase of the same composition. Equation 5.116 shows that the equilibrium vapor pressure of a droplet increases with the decrease of the droplet size. (For a bubble, instead of a droplet, R must be changed to $-R$ in the right-hand side of Equation 5.116 and the tendency becomes the opposite.) Equation 5.116 implies that in an aerosol of polydisperse droplets the larger droplets will grow and the smaller droplets will diminish to complete disappearance.

The small droplets are “protected” against disappearance when phase α contains a nonvolatile component. Then instead of Equation 5.116 we have

$$\frac{P_i^\beta(R)}{P_i^\beta(\infty)} = \frac{1 - X(R)}{1 - X(\infty)} \exp\left(\frac{2\sigma V_i^\alpha}{RkT}\right) \quad (5.117)$$

where X denotes the molar fraction of the nonvolatile component in phase α ; for $X(R) = X(\infty)$ Equation 5.117 reduces to Equation 5.116. Setting the left-hand side of Equation 5.117 equal to 1, we can determine the value $X(R)$ needed for a liquid droplet of radius R , surrounded by the gas phase β , to coexist at equilibrium with a large ($R = \infty$) liquid phase α of composition $X(\infty)$.

When both phases α and β are liquid, Equation 5.115 yields

$$\frac{X_i^\beta(R)}{X_i^\beta(\infty)} = \exp\left(\frac{2\sigma V_i^\alpha}{RkT}\right) \quad (5.118)$$

where $X_i^\beta(R)$ denotes the equilibrium molar fraction of component i in phase β coexisting with a droplet of radius R , and $X_i^\beta(\infty)$ denotes the value of $X_i^\beta(R)$ for $R \rightarrow \infty$, i.e., for phase β coexisting with a large phase α of the same composition as the droplet. In the case of an oil in water emulsion X_i^β can be the concentration of the oil dissolved in the water. In particular, Equation 5.118 predicts

that the large emulsion droplets will grow and the small droplets will diminish. This phenomenon is called Ostwald ripening (see the next section). If the droplets (phase α) contain a component that is insoluble in phase β , the small droplets will be protected against complete disappearance; a counterpart of Equation 5.117 can be derived:

$$\frac{X_i^\beta(R)}{X_i^\beta(\infty)} = \frac{1 - X(R)}{1 - X(\infty)} \exp\left(\frac{2\sigma V_i^\alpha}{RkT}\right) \quad (5.119)$$

where X denotes the equilibrium concentration in phase α of the component that is insoluble in phase β . Setting the left-hand side of Equation 5.119 equal to 1, we can determine the value $X(R)$ needed for an emulsion droplet of radius R , surrounded by the continuous phase β , to coexist at equilibrium with a large ($R = \infty$) liquid phase α of composition $X(\infty)$.

5.3.1.4 Kinetics of Ostwald Ripening in Emulsions

Ostwald ripening is observed when the substance of the emulsion droplets (we will call it component 1) exhibits at least minimal solubility in the continuous phase, β . As discussed above, the chemical potential of this substance in the larger droplets is lower than in the smaller droplets; see Equation 5.115. Then a diffusion transport of component 1 from the smaller toward the larger droplets will take place. Consequently, the size distribution of the droplets in the emulsion will change with time. The kinetic theory of Ostwald ripening was developed by Lifshitz and Slyozov,¹⁵² Wagner,¹⁵³ and further extended and applied by other authors.¹⁵⁴⁻¹⁵⁷ The basic equations of this theory are the following.

The volume of an emulsion droplet grows (or diminishes) due to the molecules of component 1 supplied (or carried away) by the diffusion flux across the continuous medium. The balance of component 1 can be presented in the form:¹⁵⁷

$$\frac{4\pi}{3} \frac{d}{dt} R^3(t) = 4\pi DRV_1 [c_m(t) - c_{\text{eq}}(R)] \quad (5.120)$$

where t is time, D is the diffusivity of component 1 in the continuous phase, V_1 is the volume per molecule of component 1, c_m is the number-volume concentration of component 1 in the continuous medium far away from the droplets surfaces, and $c_{\text{eq}}(R)$ is the respective equilibrium concentration of the same component for a droplet of radius R as predicted by the Gibbs–Thomson equation. Note that Equation 5.120 is rigorous only for a diluted emulsion, in which the interdroplet concentration levels off at a constant value, $c = c_m$, around the middle of the space between each two droplets. Some authors¹⁵⁵ add in the right-hand side of Equation 5.120 terms accounting for the convective mass transfer (in the case of moving droplets) and thermal contribution to the growth rate, as well.

Because the theory is usually applied to droplets of diameter not smaller than micrometer (which are observable by optical microscope), the Gibbs–Thomson equation, Equation 5.118, can be linearized to yield¹⁵⁷

$$c_{\text{eq}}(R) \approx c_\infty(1 + b/R), \quad b \equiv 2\sigma V_1/(kT) \quad (5.121)$$

with c_∞ the value of c_{eq} for a flat interface. With $\sigma = 50$ mN/m, $V_1 = 100 \text{ \AA}^3$, and $T = 25^\circ\text{C}$ we estimate $b = 2.5$ nm. The latter value justifies the linearization of the Gibbs–Thomson equation for droplets of micrometer size.

Let $f(R,t)$ be the size distribution function of the emulsion droplets such that $f(R,t) dR$ is the number of particles per unit volume in the size range from R to $(R + dR)$. The balance of the number of particles in the system reads

$$df dR = (j dt)|_R - (j dt)|_{R+dR}, \quad (j \equiv f dR/dt) \quad (5.122)$$

The term in the left-hand side of Equation 5.122 expresses the change of the number of droplets whose radius belongs to the interval $[R, R + dR]$ during a time period dt ; the two terms in the right-hand side represent the number of the incoming and outgoing droplets in the size interval $[R, R + dR]$ during time period dt . Dividing both sides of Equation 5.122 by $(dR dt)$ we obtain the so-called continuity equation in the space of sizes:¹⁵³⁻¹⁵⁷

$$\frac{\partial f}{\partial t} + \frac{\partial j}{\partial R} = 0 \quad (5.123)$$

One more equation is needed to determine c_m . In a closed system, this can be the total mass balance of component 1:

$$\frac{d}{dt} \left[c_m(t) + \frac{4\pi}{3} \int_0^\infty dR R^3 f(R,t) \right] = 0 \quad (5.124)$$

The first and the second terms in the brackets express the amount of component 1 contained in the continuous phase and in the droplets, respectively. This expression is appropriate for diluted emulsions when c_m is not negligible compared to the integral in the brackets.

Alternatively, in opened systems and in concentrated emulsions, we can use a mean field approximation based on Equation 5.121 to obtain the following equation for c_m :

$$c_m(t) = c_\infty \left[1 + \frac{b}{R_m(t)} \right], \quad R_m(t) \equiv \frac{\int_{R_0}^\infty dR R f(R,t)}{\int_{R_0}^\infty dR f(R,t)} \quad (5.125)$$

where R_0 is a lower limit of the experimental distribution, typically $R_0 \approx 1 \mu\text{m}$ as smaller droplets cannot be observed optically. The estimates show that the neglecting of the integrals over the interval $0 < R < R_0$ in Equation 5.125 does not significantly affect the value of R_m . We see that Equation 5.125 treats each emulsion droplet as surrounded by droplets of average radius R_m which provide a medium concentration c_m in accordance with the Gibbs–Thomson equation, Equation 5.121. From Equations 5.120 through 5.123 and 5.125 we can derive a simple expression for the flux j :

$$j(R,t) = Q \left(\frac{1}{RR_m} - \frac{1}{R^2} \right) f(R,t), \quad Q \equiv Dbc_\infty V_1 \quad (5.126)$$

In calculations we use the set of Equations 5.120, 5.123, and 5.124 or 5.125 to determine the distribution $f(R,t)$ at known distribution $f(R,0)$ at the initial moment $t = 0$. In other words, the theory predicts the evolution of the system at given initial state. From a computational viewpoint it is convenient to calculate $f(R,t)$ in a finite interval $R_0 \leq R < R_{\text{max}}$ (Figure 5.11). The problem can be

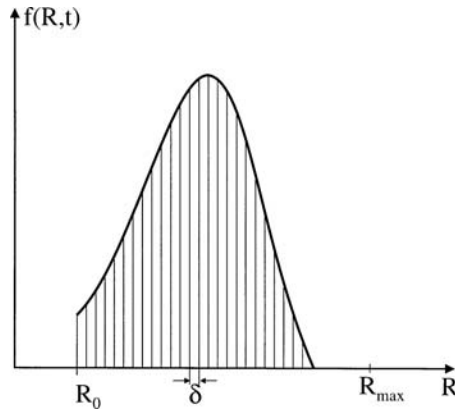


FIGURE 5.11 Sketch of the droplet size distribution function, $f(R,t)$ vs. the droplet radius R at a given moment t . δ is the length of the mesh used when solving the problem by discretization.

solved numerically by discretization: the interval $R_0 \leq R < R_{\max}$ is subdivided into small portions of length δ , the integrals are transformed into sums and the problem is reduced to solving a linear set of equations for the unknown functions $f_k(t) \equiv f(R_k, t)$, where $R_k = R_0 + k\delta$, $k = 1, 2, \dots$.

In practice, the emulsions are formed in the presence of surfactants. At concentrations above the critical micellization concentration (CMC) the swollen micelles can serve as carriers of oil between the emulsion droplets of different size. In other words, surfactant micelles can play the role of mediators of the Ostwald ripening. Micelle-mediated Ostwald ripening has been observed in solutions of nonionic surfactants.¹⁵⁸⁻¹⁶⁰ In contrast, it was found that the micelles do not mediate the Ostwald ripening in undecane-in-water emulsions at the presence of an *ionic* surfactant (SDS).¹⁶¹ It seems that the surface charge due to the adsorption of ionic surfactant (and the resulting double layer repulsion) prevents the contact of micelles with the oil drops, which is a necessary condition for micelle-mediated Ostwald ripening.

5.3.2 THIN LIQUID FILMS AND PLATEAU BORDERS

5.3.2.1 Membrane and Detailed Models of a Thin Liquid Film

Thin liquid films can be formed between two colliding emulsion droplets or between the bubbles in a foam. Formation of thin films accompanies the particle–particle and particle–wall interactions in colloids. From a *mathematical* viewpoint a film is thin when its thickness is much smaller than its lateral dimension. From a *physical* viewpoint a liquid film formed between two macroscopic phases is *thin* when the energy of interaction between the two phases across the film is not negligible. The specific forces causing the interactions in a thin liquid film are called *surface forces*. Repulsive surface forces stabilize thin films and dispersions, whereas attractive surface forces cause film rupture and coagulation. This section is devoted to the *macroscopic* (hydrostatic and thermodynamic) theory of thin films, while the *molecular* theory of surface forces is reviewed in Section 5.4 below.

In [Figure 5.12](#) a sketch of plane-parallel liquid film of thickness h is presented. The liquid in the film contacts with the bulk liquid in the *Plateau border*. The film is symmetric, i.e., it is formed between two *identical* fluid particles (drops, bubbles) of internal pressure P_0 . The more complex case of nonsymmetric and curved films is reviewed elsewhere.¹⁶²⁻¹⁶⁴

Two different, but supplementary, approaches (models) are used in the macroscopic description of a thin liquid film. The first of them, the “membrane approach,” treats the film as a membrane of zero thickness and one tension, γ , acting tangentially to the membrane (see the right-hand side of [Figure 5.12](#)). In the “detailed approach,” the film is modeled as a homogeneous liquid layer of

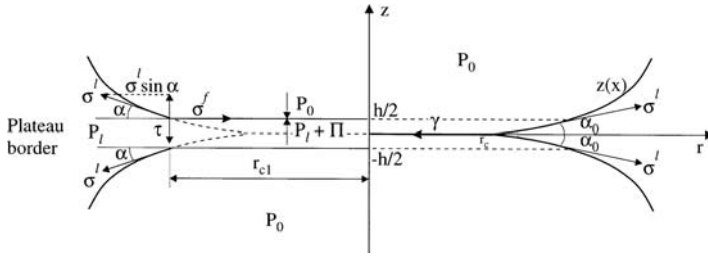


FIGURE 5.12 The detailed and membrane models of a thin liquid film (on the left- and right-hand side, respectively).

thickness h and surface tension σ^f . The pressure P_0 in the fluid particles is larger than the pressure, P_l , of the liquid in the Plateau border. The difference

$$P_c = P_0 - P_l \quad (5.127)$$

represents the capillary pressure of the liquid meniscus. By making the balance of the forces acting on a plate of unit width along the y -axis and height h placed normally to the film at $-h/2 < z < h/2$ (Figure 5.12) we derive the Rusanov¹⁶⁵ equation:

$$\gamma = 2\sigma^f + P_c h \quad (5.128)$$

Equation 5.128 expresses a condition for equivalence between the membrane and detailed models with respect to the lateral force. To derive the normal force balance we consider a parcel of unit area from the film surface in the detailed approach. Because the pressure in the outer phase P_0 is larger than the pressure inside the liquid, P_l , the mechanical equilibrium at the film surface is ensured by the action of an additional *disjoining* pressure, $\Pi(h)$, representing the surface force per unit area of the film surfaces¹⁶⁶

$$\Pi(h) = P_0 - P_l = P_c \quad (5.129)$$

(see Figure 5.12). Note that Equation 5.129 is satisfied only at equilibrium; at nonequilibrium conditions the viscous force can also contribute to the force balance per unit film area. In general, the disjoining pressure, Π , depends on the film thickness, h . A typical $\Pi(h)$ -isotherm is depicted in Figure 5.13 (for details see Section 5.4 below). We see that the equilibrium condition, $\Pi = P_c$, can be satisfied at three points shown in Figure 5.13. Point 1 corresponds to a film, which is stabilized by the double layer repulsion; sometimes such a film is called the “primary film” or “common black film.” Point 3 corresponds to unstable equilibrium and cannot be observed experimentally. Point 2 corresponds to a very thin film, which is stabilized by the short range repulsion; such a film is called the “secondary film” or “Newton black film.” Transitions from common to Newton black films are often observed with foam films.¹⁶⁷⁻¹⁷⁰ Note that $\Pi > 0$ means repulsion between the film surfaces, whereas $\Pi < 0$ corresponds to attraction.

5.3.2.2 Thermodynamics of Thin Liquid Films

In the framework of the membrane approach, the film can be treated as a single surface phase, whose Gibbs–Duhem equation reads:^{162,171}

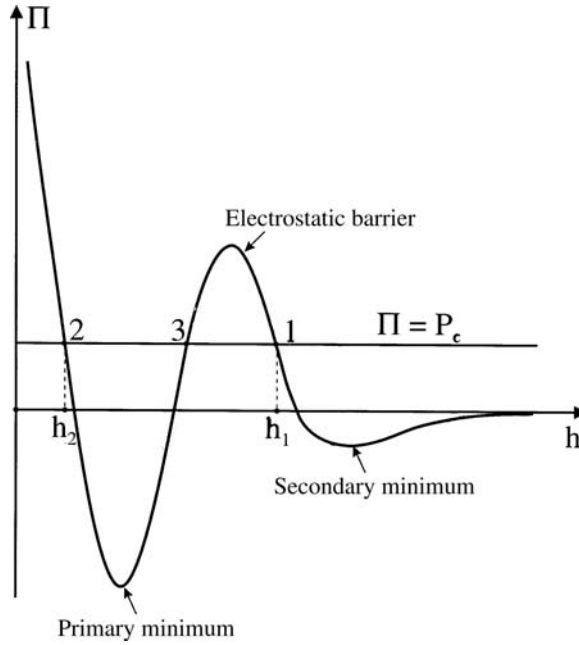


FIGURE 5.13 Sketch of a disjoining pressure isotherm of the DLVO type, Π vs. h . The intersection points of the $\Pi(h)$ -isotherm with the line $\Pi = P_c$ correspond to equilibrium films: $h = h_1$ (primary film), $h = h_2$ (secondary film). Point 3 corresponds to unstable equilibrium.

$$d\gamma = -s^f dT - \sum_{i=1}^k \Gamma_i d\mu_i \quad (5.130)$$

where γ is the film tension, T is temperature, s^f is excess entropy per unit area of the film, Γ_i and μ_i are the adsorption and the chemical potential of the i th component. The Gibbs–Duhem equations of the liquid phase (l) and the outer phase (o) read

$$dP_\chi = s_v^\chi dT + \sum_{i=1}^k n_i^\chi d\mu_i, \quad \chi = l, o \quad (5.131)$$

where s_v^χ and n_i^χ are entropy and number of molecules per unit volume, and P_χ is pressure ($\chi = l, o$). The combination of Equations 5.127 and 5.131 provides an expressions for dP_c . Let us multiply this expression by h and subtract the result from the Gibbs–Duhem equation of the film, Equation 5.130. The result reads

$$d\gamma = -\tilde{s} dT + h dP_c - \sum_{i=1}^k \tilde{\Gamma}_i d\mu_i \quad (5.132)$$

where

$$\tilde{s} = s^f + (s_v^o - s_v^l)h, \quad \tilde{\Gamma}_i = \Gamma_i + (n_i^o - n_i^l)h, \quad i = 1, \dots, k \quad (5.133)$$

An alternative derivation of the same equations is possible.^{172,173} Imagine two equidistant planes separated at a distance h . The volume confined between the two planes is thought to be filled with the bulk liquid phase (l). Taking surface excesses with respect to the bulk phases we can derive Equations 5.132 and 5.133 with \tilde{s} and $\tilde{\Gamma}_i$ being the excess surface entropy and adsorption ascribed to the surfaces of this liquid layer.^{172,173} A comparison between Equations 5.132 and 5.130 shows that there is one additional differential in Equation 5.132. It corresponds to one supplementary degree of freedom connected with the choice of the parameter h . To specify the model we need an additional equation to determine h . For example, let this equation be

$$\tilde{\Gamma}_1 = 0 \quad (5.134)$$

Equation 5.134 requires h to be the thickness of a liquid layer from phase (l), containing the same amount of component 1 as the real film. This thickness is called the thermodynamic thickness of the film.¹⁷³ It can be on the order of the real film thickness if component 1 is chosen in an appropriate way, say, the solvent in the film phase.

From Equations 5.129, 5.132, and 5.134 we obtain¹⁷²

$$d\gamma = -\tilde{s}dT + hd\Pi - \sum_{i=2}^k \tilde{\Gamma}_i d\mu_i \quad (5.135)$$

A corollary of Equation 5.135 is the Frumkin¹⁷⁴ equation:

$$\left(\frac{\partial \gamma}{\partial \Pi} \right)_{T, \mu_2, \dots, \mu_k} = h \quad (5.136)$$

Equation 5.136 predicts a rather weak dependence of the film tension γ on the disjoining pressure, Π , for equilibrium thin films (small h). By means of Equations 5.128 and 5.129, Equation 5.135 can be transformed to read¹⁷³

$$2d\sigma^f = -\tilde{s}dT - \Pi dh - \sum_{i=2}^k \tilde{\Gamma}_i d\mu_i \quad (5.137)$$

From Equation 5.137 we can derive the following useful relations:¹⁷²

$$2 \left(\frac{\partial \sigma^f}{\partial h} \right)_{T, \mu_2, \dots, \mu_k} = -\Pi \quad (5.138)$$

$$\sigma^f(h) = \sigma^l + \frac{1}{2} \int_h^\infty \Pi(h) dh \quad (5.139)$$

with σ^l the surface tension of the bulk liquid. Equation 5.139 allows calculation of the film surface tension when the disjoining pressure isotherm is known.

Note that the above thermodynamic equations are, in fact, corollaries from the Gibbs–Duhem equation of the membrane approach (Equation 5.130). There is an equivalent and complementary

approach, which treats the two film surfaces as separate surface phases with their own fundamental equations.^{165,175,176} Thus, for a flat symmetric film we postulate

$$dU^f = TdS^f + 2\sigma^f dA + \sum_{i=1}^k \mu_i dN_i^f - \Pi Adh \quad (5.140)$$

where A is area; U^f , S^f , and N_i^f are excess internal energy, entropy, and number of molecules ascribed to the film surfaces. Compared with the fundamental equation of a simple surface phase,⁵ Equation 5.140 contains an additional term, ΠAdh , which takes into account the dependence of the film surface energy on the film thickness. Equation 5.140 provides an alternative thermodynamic definition of disjoining pressure:

$$\Pi = -\frac{1}{A} \left(\frac{\partial U^f}{\partial h} \right) \quad (5.141)$$

5.3.2.3 The Transition Zone between Thin Film and Plateau Border

5.3.2.3.1 Macroscopic Description

The thin liquid films formed in foams or emulsions exist in a permanent contact with the bulk liquid in the Plateau border encircling the film. From a macroscopic viewpoint, the boundary between film and Plateau border is treated as a three-phase contact line: the line, at which the two surfaces of the Plateau border (the two concave menisci sketched in Figure 5.12) intersect at the plane of the film (see the right-hand side of Figure 5.12). The angle, α_0 , subtended between the two meniscus surfaces, represents the thin film contact angle. The force balance at each point of the contact line is given by Equation 5.98 with $\sigma_{12} = \gamma$ and $\sigma_{13} = \sigma_{23} = \sigma^l$. The effect of the line tension, κ , can be also taken into account. For example, in the case of a symmetric flat film with circular contact line, like those depicted in Figure 5.12, we can write¹⁷⁶

$$\gamma + \frac{\kappa}{r_c} = 2\sigma^l \cos \alpha_0 \quad (5.142)$$

where r_c is the radius of the contact line.

There are two film surfaces and two contact lines in the detailed approach (see the left-hand side of Figure 5.12). They can be treated thermodynamically as linear phases and a one-dimensional counterpart of Equation 5.140 can be postulated:¹⁷⁶

$$dU^L = TdS^L + 2\tilde{\kappa}dL + \sum_i \mu_i dN_i^L + \tau dh \quad (5.143)$$

Here U^L , S^L , and N_i^L are linear excesses, $\tilde{\kappa}$ is the line tension in the detailed approach, and

$$\tau = \frac{1}{L} \left(\frac{\partial U^L}{\partial h} \right) \quad (5.144)$$

is a one-dimensional counterpart of the disjoining pressure (see Equation 5.141). The quantity τ , called the *transversal tension*, takes into account the interaction between the two contact lines. The

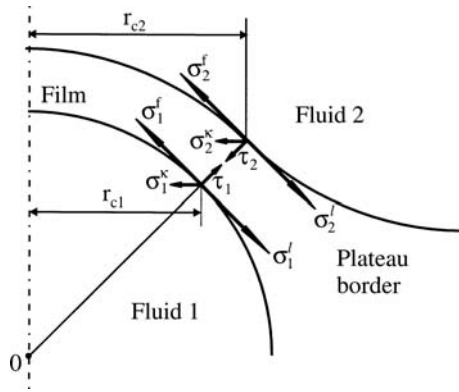


FIGURE 5.14 The force balance in each point of the two contact lines representing the boundary between a spherical film and the Plateau border (see Equation 5.145).

general force balance at each point of the contact line can be presented in the form of the following vectorial sum:¹⁶²

$$\sigma_i^f + \sigma_i^l + \sigma_i^k + \tau_i = \mathbf{0}, \quad i=1, 2 \quad (5.145)$$

The vectors taking part in Equation 5.145 are depicted in Figure 5.14, where $|\sigma_i^k| = \tilde{\kappa}_i / r_{ci}$. For the case of a flat symmetric film (Figure 5.12) the tangential and normal projections of Equation 5.145, with respect to the plane of the film, read

$$\sigma^f + \frac{\tilde{\kappa}}{r_{cl}} = \sigma^l \cos \alpha \quad (5.146)$$

$$\tau = \sigma^l \sin \alpha \quad (5.147)$$

Note that in general $\alpha \neq \alpha_0$ (see Figure 5.12). Besides, both α_0 and α can depend on the radius of the contact line due to line tension effects. In the case of straight contact line from Equations 5.139 and 5.146 we derive¹⁷³

$$\cos \alpha \Big|_{r_{cl}=\infty} = \frac{\sigma^f}{\sigma^l} = 1 + \frac{1}{2\sigma^l} \int_h^\infty \Pi(h) dh \quad (5.148)$$

Since $\cos \alpha \leq 1$, the surface tension of the film must be less than the bulk solution surface tension, $\sigma^f < \sigma^l$, and the integral term in Equation 5.148 must be negative in order for a nonzero contact angle to be formed. Hence, the contact angle, α , and the transversal tension, τ (see Equation 5.147), are integral effects of the long-range *attractive* surface forces acting in the transition zone between the film and Plateau border, where $h > h_1$ (see Figure 5.13).

In the case of a fluid particle attached to a surface (Figure 5.15) the integral of the pressure $P_l = P_0 - \Delta\rho g z$ over the particle surface equals the buoyancy force, F_b , which at equilibrium is counterbalanced by the disjoining-pressure and transversal-tension forces:^{162,177}

$$2\pi r_{cl} \tau = F_b + \pi r_{cl}^2 \Pi \quad (5.149)$$

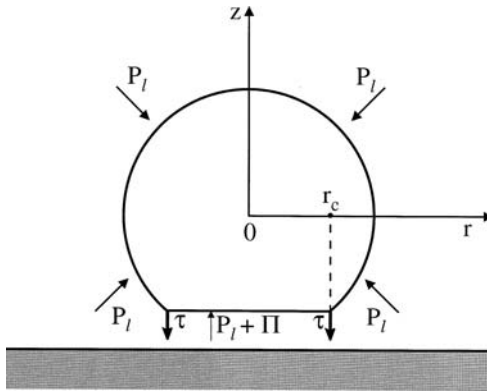


FIGURE 5.15 Sketch of the forces exerted on a fluid particle (bubble, drop, vesicle) attached to a solid surface: Π is the disjoining pressure, τ is the transversal tension, P_l is the pressure in the outer liquid phase.

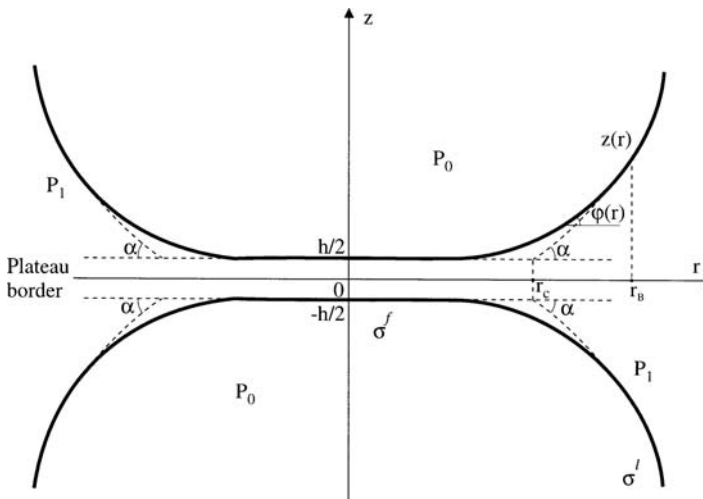


FIGURE 5.16 Liquid film between two attached fluid particles (bubbles, drops, vesicles). The solid lines represent the actual interfaces, whereas the dashed lines show the extrapolated interfaces in the transition zone between the film and the Plateau border.

F_b is negligible for bubbles of diameter smaller than $\sim 300 \mu\text{m}$. Then the forces due to τ and Π counterbalance each other. Hence, at equilibrium the role of the repulsive disjoining pressure is to keep the film thickness uniform, whereas the role of the attractive transversal tension is to keep the bubble (droplet) attached to the surface. In other words, the particle sticks to the surface at its contact line where the long-range attraction prevails (see Figure 5.13), whereas the repulsion predominates inside the film, where $\Pi = P_c > 0$. Note that this conclusion is valid not only for particle–wall attachment, but also for particle–particle interaction. For zero contact angle τ is also zero (Equation 5.147) and the particle will rebound from the surface (the other particle), unless some additional external force keeps it attached.

5.3.2.3.2 Micromechanical Description

From a microscopic viewpoint, the transition between the film surface and the meniscus is smooth, as depicted in Figure 5.16. As the film thickness increases across the transition zone, the disjoining pressure decreases and tends to zero at the Plateau border (see Figures 5.13 and 5.16). Respectively,

the surface tension varies from σ^f for the film to σ^l for the Plateau border.^{178,179} By using local force balance considerations, we can derive the equations governing the shape of the meniscus in the transition zone; in the case of axial symmetry (depicted in [Figure 5.16](#)), these equations read¹⁷⁹

$$\frac{d}{dr}(\sigma \sin \varphi) + \frac{1}{r} \sigma(r) \sin \varphi(r) = P_c - \Pi(h(r)) \quad (5.150)$$

$$-\frac{d}{dz}(\sigma \cos \varphi) + \frac{1}{r} \sigma(r) \sin \varphi(r) = P_c, \quad \tan \varphi(r) = \frac{dz}{dr} \quad (5.151)$$

where $\varphi(r)$ and $h(r) = 2z(r)$ are the running meniscus slope angle and thickness of the gap. Equations 5.150 and 5.151 allow calculation of the three unknown functions, $z(r)$, $\varphi(r)$, and $\sigma(r)$, provided that the disjoining pressure, $\Pi(h)$, is known from the microscopic theory. By eliminating P_c between Equations 5.150 and 5.151 we can derive¹⁷⁹

$$\frac{d\sigma}{dz} = -\Pi(h(r)) \cos \varphi(r) \quad (5.152)$$

This result shows that the hydrostatic equilibrium in the transition region is ensured by simultaneous variation of σ and Π . Equation 5.152 represents a generalization of Equation 5.138 for a film of uneven thickness and axial symmetry. Generalization of Equations 5.150 through 5.152 for the case of more complicated geometry is also available.^{162,163}

For the Plateau border we have $z \gg h$, $\Pi \rightarrow 0$, $\sigma \rightarrow \sigma^l = \text{const.}$, and both Equations 5.150 and 5.151 reduce to Equation 5.101 with $\Delta P = P_c$. The macroscopic contact angle, α , is defined as the angle at which the *extrapolated* meniscus, obeying Equation 5.101, meets the *extrapolated* film surface (see the dashed line in [Figure 5.16](#)). The real surface, shown by solid line in [Figure 5.16](#), differs from this *extrapolated* (idealized) profile, because of the interactions between the two film surfaces, which is taken into account in Equation 5.150, but not in Equation 5.101. To compensate for the difference between the real and idealized system, the line and transversal tensions are ascribed to the contact line in the macroscopic approach. In particular, the line tension makes up for the differences in surface tension and running slope angle:¹⁷⁹

$$\frac{\tilde{\kappa}}{r_c} = \int_0^{r_B} \left[\left(\frac{\sigma \sin^2 \varphi}{r \cos \varphi} \right)^{\text{real}} - \left(\frac{\sigma \sin^2 \varphi}{r \cos \varphi} \right)^{\text{idealized}} \right] dr \quad (5.153)$$

whereas τ compensates for the differences in surface forces (disjoining pressure):

$$\tau = \frac{1}{r_c} \int_0^{r_B} [(\Pi)^{\text{id}} - \Pi(r)] r dr \quad (5.154)$$

where

$$\begin{aligned} (\Pi)^{\text{id}} &= P_c & \text{for } 0 < r < r_c \\ (\Pi)^{\text{id}} &= 0 & \text{for } r > r_c \end{aligned}$$

The superscripts “real” and “idealized” in Equation 5.153 mean that the quantities in the respective parentheses must be calculated for the real and idealized meniscus profiles; the latter coincide for $r > r_B$ (Figure 5.16). Results for $\tilde{\kappa}$ and τ calculated by means of Equations 5.153 and 5.154 can be found in Reference 180.

In conclusion, it should be noted that the width of the transition region between a thin liquid film and Plateau border is usually very small¹⁷⁸ — below 1 μm . That is why the optical measurements of the meniscus profile give information about the thickness of the Plateau border in the region $r > r_B$ (Figure 5.16). Then, if the data are processed by means of the Laplace equation (Equation 5.101), one determines the contact angle, α , as discussed above. Despite that it is a purely macroscopic quantity, α characterizes the magnitude of the surface forces inside the thin liquid film, as implied by Equation 5.148. This has been pointed out by Derjaguin¹⁸¹ and Princen and Mason.¹⁸²

5.3.2.4 Methods for Measuring Thin Film Contact Angles

Prins¹⁸³ and Clint et al.¹⁸⁴ developed a method of contact angle measurement for macroscopic flat foam films formed in a glass frame in contact with a bulk liquid. They measured the jump in the force exerted on the film at the moment when the contact angle is formed. A similar experimental setup was used by Yamanaka¹⁸⁵ for measurement of the velocity of motion of the three-phase contact line.

An alternative method, which can be used in both equilibrium and dynamic measurements with vertical macroscopic films, was developed by Princen and Frankel.^{186,187} They determined the contact angle from the data for diffraction of a laser beam refracted by the Plateau border.

In the case of microscopic films, especially appropriate are the interferometric methods: light beams reflected or refracted from the liquid meniscus interfere and create fringes, which in turn give information about the shape of the liquid surfaces. The fringes are usually formed in the vicinity of the contact line, which provides a highly precise extrapolation procedure used to determine the contact angle (see Figure 5.16). We can distinguish several interference techniques depending on how the interference pattern is created. In the usual interferometry the fringes are due to interference of beams reflected from the upper and lower meniscus. This technique can be used for contact angle measurements with foam films,^{144,188-190} emulsion films,^{191,192} and adherent biological cells.¹³⁰ The method is applicable for not-too-large contact angles ($\alpha < 8^\circ$ to 10°); for larger meniscus slopes the region of fringes shrinks and the measurements are not possible.

The basic principle of differential interferometry consists of an artificial splitting of the original image into two equivalent and overlapping images (see Françon¹⁹³ or Beyer¹⁹⁴). Thus, interferometric measurements are possible with meniscus surfaces of larger slope. The differential interferometry in transmitted light was used by Zorin et al.^{195,196} to determine the contact angles of wetting and free liquid films. This method is applicable when the whole system under investigation is transparent to the light.

Differential interferometry in reflected light allows measurement of the shape of the upper reflecting surface. This method was used by Nikolov et al.^{177,197-199} to determine the contact angle, film and line tension of foam films formed at the top of small bubbles floating at the surface of ionic and nonionic surfactant solutions. An alternative method is the holographic interferometry applied by Picard et al.^{200,201} to study the properties of bilayer lipid membranes in solution. Film contact angles can be also determined from the Newton rings of liquid lenses, which spontaneously form in films from micellar surfactant solutions.¹⁴⁴

Contact angles can be also determined by measuring several geometric parameters characterizing the profile of the liquid meniscus and processing them by using the Laplace equation (Equation 5.101).^{202,203} The computer technique allows processing of many experimental points from meniscus profile and automatic digital image analysis.

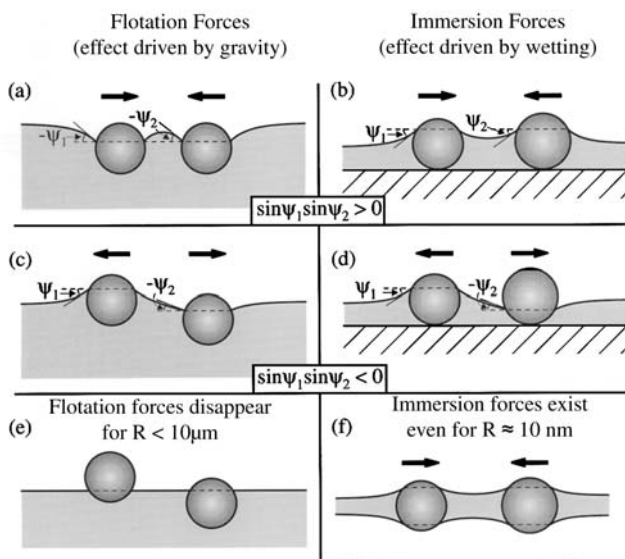


FIGURE 5.17 Flotation (a, c, e) and immersion (b, d, f) lateral capillary forces between two particles attached to fluid interface: (a) and (b) are two similar particles; (c) is a light and a heavy particle; (d) is a hydrophilic and a hydrophobic particle; (e) is small floating particles that do not deform the interface; (f) is small particles captured in a thin liquid film deforming the interfaces due to the wetting effects.

Contact angles of microscopic particles against another phase boundary can be determined interferometrically, by means of a film trapping technique (FTT).^{204,205} It consists of capturing of micrometer-sized particles, emulsion drops, and biological cells in thinning free foam films or wetting films. The interference pattern around the entrapped particles allows reconstruction of the meniscus shape, determination of the contact angles, and calculation of the particle-to-interface adhesion energy.^{204,205}

5.3.3 LATERAL CAPILLARY FORCES BETWEEN PARTICLES ATTACHED TO INTERFACES

5.3.3.1 Particle-Particle Interactions

The origin of the lateral capillary forces between particles captive at a fluid interface is the deformation of the interface, which is supposed to be flat in the absence of particles. The larger the interfacial deformation, the stronger the capillary interaction. It is known that two similar particles floating on a liquid interface attract each other²⁰⁶⁻²⁰⁸ (Figure 5.17a). This attraction appears because the liquid meniscus deforms in such a way that the gravitational potential energy of the two particles decreases when they approach each other. Hence, the origin of this force is the particle weight (including the Archimedes force).

A force of capillary attraction appears also when the particles (instead of being freely floating) are partially immersed in a liquid layer on a substrate²⁰⁹⁻²¹¹ (Figure 5.17b). The deformation of the liquid surface in this case is related to the wetting properties of the particle surface, i.e., to the position of the contact line and the magnitude of the contact angle, rather than to gravity.

To distinguish between the capillary forces in the case of floating particles and in the case of partially immersed particles on a substrate, the former are called lateral *flotation* forces and the latter, lateral *immersion* forces.^{208,211} These two kinds of force exhibit similar dependence on the interparticle separation but very different dependencies on the particle radius and the surface tension of the liquid (see References 35 and 212 for comprehensive reviews). The flotation and immersion forces can be both attractive (Figures 5.17a and b) and repulsive (Figures 5.17c and d). This is

determined by the signs of the meniscus slope angles ψ_1 and ψ_2 at the two contact lines: the capillary force is attractive when $\sin\psi_1 \sin\psi_2 > 0$ and repulsive when $\sin\psi_1 \sin\psi_2 < 0$. In the case of flotation forces $\psi > 0$ for *light* particles (including bubbles) and $\psi < 0$ for *heavy* particles. In the case of immersion forces between particles protruding from an aqueous layer $\psi > 0$ for *hydrophilic* particles and $\psi < 0$ for *hydrophobic* particles. When $\psi = 0$ there is no meniscus deformation and, hence, there is no capillary interaction between the particles. This can happen when the weight of the particles is too small to create significant surface deformation (Figure 5.17e). The immersion force appears not only between particles in wetting films (Figures 5.17b and d), but also in symmetric fluid films (Figure 5.17f). The theory provides the following asymptotic expression for calculating the lateral capillary force between two particles of radii R_1 and R_2 separated by a center-to-center distance L :^{35,207-212}

$$F = 2\pi\sigma Q_1 Q_2 q K_1(qL) \left[1 + O(q^2 R_k^2) \right] \quad r_k \ll L \quad (5.155)$$

where σ is the liquid–fluid interfacial tension, r_1 and r_2 are the radii of the two contact lines, and $Q_k = r_k \sin\psi_k$ ($k = 1, 2$) is the “capillary charge” of the particle;^{208,211} in addition

$$\begin{aligned} q^2 &= \Delta\rho g / \sigma && \text{(in thick film)} \\ q^2 &= (\Delta\rho q - \Pi') / \sigma && \text{(in thin films)} \end{aligned} \quad (5.156)$$

Here, $\Delta\rho$ is the difference between the mass densities of the two fluids, and Π' is the derivative of the disjoining pressure with respect to the film thickness; $K_1(x)$ is the modified Bessel function of the first order. The asymptotic form of Equation 5.155 for $qL \ll 1$ ($q^{-1} = 2.7$ mm for water),

$$F = 2\pi\sigma Q_1 Q_2 / L, \quad r_k \ll L \ll q^{-1} \quad (5.157)$$

looks like a two-dimensional analogue of Coulomb’s law, which explains the name capillary charge of Q_1 and Q_2 . Note that the immersion and flotation forces exhibit the same functional dependence on the interparticle distance; see Equations 5.155 and 5.157. On the other hand, their different physical origin results in different magnitudes of the capillary charges of these two kinds of capillary force. In this aspect they resemble the electrostatic and gravitational forces, which obey the same power law, but differ in the physical meaning and magnitude of the force constants (charges, masses). In the special case when $R_1 = R_2 = R$ and $r_k \ll L \ll q^{-1}$ we can derive^{211,212}

$$\begin{aligned} F &\propto (R^6 / \sigma) K_1(qL) && \text{for flotation force} \\ F &\propto \sigma R^2 K_1(qL) && \text{for immersion force} \end{aligned} \quad (5.158)$$

Hence, the flotation force decreases, while the immersion force increases, when the interfacial tension σ increases. Besides, the flotation force decreases much more strongly with the decrease of R than the immersion force. Thus, $F_{\text{flotation}}$ is negligible for $R < 10$ μm , whereas $F_{\text{immersion}}$ can be significant even when $R = 10$ nm. This is demonstrated in Figure 5.18 where the two types of capillary interaction are compared for a wide range of particle sizes. The values of the parameters used are particle mass density $\rho_p = 1.05$ g/cm³, surface tension $\sigma = 72$ mN/m, contact angle $\alpha = 30^\circ$, interparticle distance $L = 2R$, and thickness of the nondisturbed planar film $l_0 = R$. The drastic difference in the magnitudes of the two types of capillary forces is due to the different deformation of the water–air interface. The small floating particles are too light to create substantial deformation

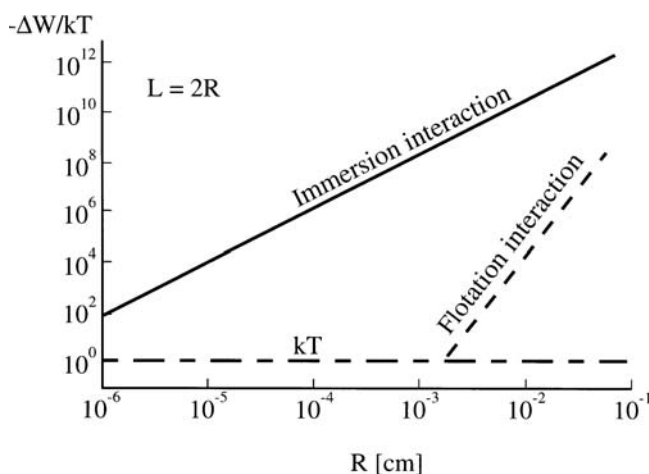


FIGURE 5.18 Plot of the capillary interaction energy in kT units, $\Delta W/kT$, vs. the radius, R , of two similar particles separated at a center-to-center distance $L = 2R$.

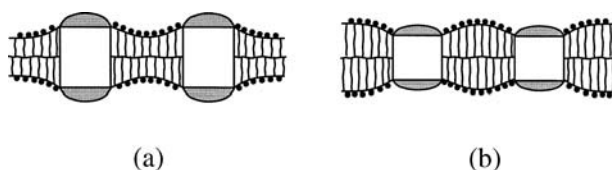


FIGURE 5.19 Inclusions (say, membrane proteins) in a lipid bilayer: the thickness of the inclusion can be greater (a) or smaller (b) than the thickness of the (nondisturbed) lipid bilayer. In both cases, the overlap of the deformations around the inclusions leads to an attraction between them (see References 35 and 133).

of the liquid surface, and the lateral capillary forces are negligible (Figure 5.17e). In the case of immersion forces the particles are restricted in the vertical direction by the solid substrate. Therefore, as the film becomes thinner, the liquid surface deformation increases, thus giving rise to a strong interparticle attraction.

As seen in Figure 5.18, the immersion force can be significant between particles whose radii are larger than few nanometers. It has been found to promote the growth of two-dimensional crystals from colloid particles,²¹³⁻²¹⁶ viruses, and globular proteins.²¹⁷⁻²²³ Such two-dimensional crystals have found various applications: for nanolithography,²²⁴ microcontact printing,²²⁵ as nanostructured materials in photo-electrochemical cells,²²⁶ for photocatalytic films,²²⁷ photo- and electro-luminescent semiconductor materials,²²⁸ as samples for electron microscopy of proteins and viruses,²²⁹ as immunosensors,²³⁰ etc. (for reviews see References 35 and 231).

In the case of interactions between inclusions in lipid bilayers (Figure 5.19) the elasticity of the bilayer interior must also be taken into account. The calculated energy of capillary interaction between integral membrane proteins turns out to be of the order of several kT .¹³³ Hence, this interaction can be a possible explanation of the observed aggregation of membrane proteins.^{133,232-234} The lateral capillary forces have been calculated also for the case of particles captured in a *spherical* (rather than planar) thin liquid film or vesicle.²³⁵

Lateral capillary forces between vertical cylinders or between spherical particles have been measured by means of sensitive electromechanical balance,²³⁶ piezotransducer balance,²³⁷ and torsion microbalance.²³⁸ Good agreement between theory and experiment has been established.^{237,238}

As already mentioned, the weight of micrometer-sized and sub-micrometer floating particles is not sufficient to deform the fluid interface and to bring about capillary force between the particles

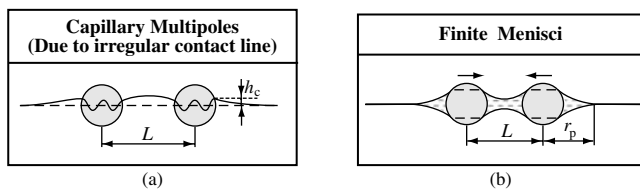


FIGURE 5.20 Special types of immersion capillary forces: (a) The contact line attachment to an irregular edge on the particle surface produces undulations in the surrounding fluid interface, which give rise to lateral capillary force between the particles. (b) When the size of particles entrapped in a liquid film is much greater than the nonperturbed film thickness, the meniscus surfaces meet at a finite distance, r_p ; in this case, the capillary interaction begins at $L \leq 2r_p$.

(Figure 5.17e). However, the situation changes if the contact line at the particle surface has *undulated* or *irregular* shape (Figure 5.20a). This may happen when the particle surface is rough, angular, or heterogeneous. In such cases, the contact line sticks to an edge or to the boundary between two domains of the heterogeneous surface. The undulated contact line induces undulations in the surrounding fluid interface.^{231,239-241} Let $z = \zeta(x, y)$ be the equation describing the interfacial shape around such isolated particle. Using polar coordinates (r, φ) in the xy plane, we can express the interfacial shape as a Fourier expansion:

$$\zeta(r, \varphi) = \sum_{m=1}^{\infty} r^{-m} (A_m \cos m\varphi + B_m \sin m\varphi) \quad (5.159)$$

where r is the distance from the particle center and A_m and B_m are coefficients. In analogy with electrostatics, Equation 5.159 can be interpreted as a multipole expansion: the terms with $m = 1, 2, 3, \dots$, play the role of capillary “dipoles,” “quadrupoles,” “hexapoles,” etc.^{231,240,241} The term with $m = 0$ (capillary “charge”) is missing since there is no axisymmetric contribution to the deformation (negligible particle weight). Moreover, the dipolar term with $m = 2$ is also absent because it is annihilated by a spontaneous rotation of the floating particle around a horizontal axis.²⁴⁰ Therefore, the leading term becomes the quadrupolar one, with $m = 2$. The interaction between capillary quadrupoles has been investigated theoretically.^{240,241} This interaction is nonmonotonic: attractive at long distances, but repulsive at short distances. Expressions for the rheological properties (surface dilatational and shear elasticity and yield stress) of Langmuir monolayers from angular particles have been derived.^{35,241} “Mesoscale” capillary multipoles have been experimentally realized by Bowden et al.,^{242,243} by appropriate hydrophobization or hydrophilization of the sides of floating plates.

At last, let us consider another type of capillary interactions — between particles surrounded by *finite* menisci. Such interactions appear when micrometer-sized or sub-micrometer particles are captured in a liquid film of much smaller thickness (Figure 5.20b).²⁴⁴⁻²⁴⁷ If such particles are approaching each other, the interaction begins when the menisci around the two particles overlap, $L < 2r_p$ in Figure 5.20b. The capillary force in this case is nonmonotonic: initially the attractive force increases with the increase of interparticle distance; then it reaches a maximum and further decays.²⁴⁷ In addition, there are hysteresis effects: the force is different on approach and separation at distances around $L = 2r_p$.²⁴⁷

5.3.3.2 Particle–Wall Interactions

The overlap of the meniscus around a floating particle with the meniscus on a vertical wall gives rise to a particle–wall interaction, which can be both repulsive and attractive. An example for a

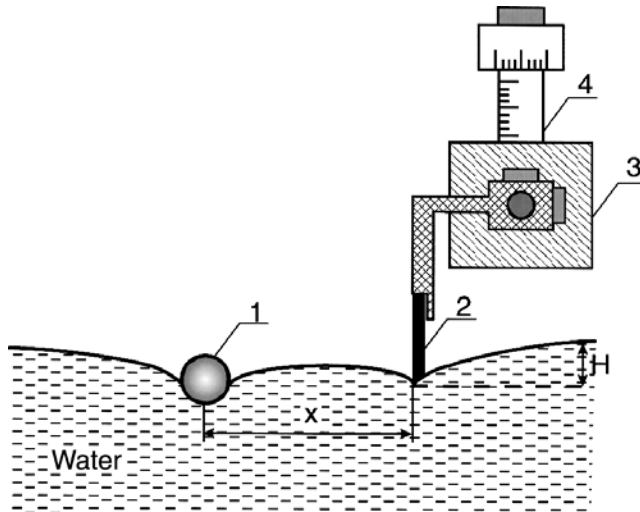


FIGURE 5.21 Experimental setup for studying the capillary interaction between a floating particle (1) and a vertical hydrophobic plate (2) separated at a distance, x . The edge of the plate is at a distance, H , lower than the level of the horizontal liquid surface far from the plate; (3) and (4) are micrometric table and screw (see References 249 and 250 for details).

controlled meniscus on the wall is shown in Figure 5.21, where the “wall” is a hydrophobic Teflon barrier whose position along the vertical can be precisely varied and adjusted.

Two types of boundary conditions at the wall are analyzed theoretically:^{35,248} fixed contact line (Figure 5.21) or, alternatively, fixed contact angle. In particular, the lateral capillary force exerted on the particle depicted in Figure 5.21 is given by the following asymptotic expression:^{35,248}

$$F = -\pi \sigma q \left[2 Q_2 H e^{-qx} + r_2 H e^{-qx} - 2 Q_2^2 K_1(qx) \right] \quad (5.160)$$

Here, Q_2 and r_2 are the particle capillary charge and contact line radius, H characterizes the position of the contact line on the wall with respect to the nondisturbed horizontal liquid surface (Figure 5.21); x is the particle–wall distance; q is defined by Equation 5.156 (thick films). The first term in the right-hand side of Equation 5.160 expresses the gravity force pushing the particle to slide down over the inclined meniscus on the wall; the second term originates from the pressure difference across the meniscus on the wall; the third term expresses the so-called capillary image force, that is, the particle is repelled by its mirror image with respect to the wall surface.^{35,248}

Static²⁴⁹ and dynamic²⁵⁰ measurements with particles near walls have been carried out. In the static measurements the equilibrium distance of the particle from the wall (the distance at which $F = 0$) has been measured and a good agreement with theory has been established.²⁴⁹

In the dynamic experiments²⁵⁰ knowing the capillary force F (from Equation 5.160), and measuring the particle velocity, \dot{x} , we can determine the drag force, F_d :

$$F_d = m\ddot{x} - F, \quad F_d \equiv 6\pi\eta R_2 f_d \dot{x} \quad (5.161)$$

where R_2 , m , and \ddot{x} are the particle radius, mass, and acceleration, η is the viscosity of the liquid, and f_d is the drag coefficient. If the particle were in the bulk liquid, f_d would be equal to 1 and F_d would be given by the Stokes formula. In general, f_d differs from unity because the particle is attached to the interface. The experiment²⁵⁰ gives f_d varying between 0.68 and 0.54 for particle contact angle varying from 49° to 82° ; the data are in good quantitative agreement with the

hydrodynamic theory of the drag coefficient.²⁵¹ In other words, the less the depth of particle immersion, the less the drag coefficient, as could be expected. However, if the floating particle is heavy enough, it deforms the surrounding liquid surface; the deformation travels together with the particle, thus increasing f_d several times.²⁵⁰ The addition of surfactant strongly increases f_d . The latter effect can be used to measure the surface viscosity of adsorption monolayers from low-molecular-weight surfactants,²⁵² which is not accessible to the standard methods for measurement of surface viscosity.

In the case of *protein* adsorption layers, the surface elasticity is so strong that the particle (Figure 5.21) is arrested in the adsorption film. Nevertheless, with heavier particles and at larger meniscus slopes, it is possible to break the protein adsorption layer. Based on such experiments, a method for determining surface elasticity and yield stress has been developed.²⁵³

5.4 SURFACE FORCES

5.4.1 DERJAGUIN APPROXIMATION

The excess surface free energy per unit area of a plane-parallel film of thickness h is^{14,254}

$$f(h) = \int_h^{\infty} \Pi(h) dh \quad (5.162)$$

where, as before, Π denotes disjoining pressure. Derjaguin²⁵⁵ derived an approximate formula, which expresses the energy of interaction between two spherical particles of radii R_1 and R_2 through the integral of $f(h)$:

$$U(h_0) = \frac{2\pi R_1 R_2}{R_1 + R_2} \int_{h_0}^{\infty} f(h) dh \quad (5.163)$$

Here h_0 is the shortest distance between the surfaces of the two particles (Figure 5.22). In the derivation of Equation 5.163 it is assumed that the interaction between two parcels from the particle surfaces, separated at the distance h , is approximately the same as that between two similar parcels in a plane-parallel film. This assumption is correct when the range of action of the surface forces and the distance h_0 are small compared to the curvature radii R_1 and R_2 . It has been established, both experimentally³⁴ and theoretically,²⁵⁶ that Equation 5.163 provides a good approximation in the range of its validity.

Equation 5.163 can be generalized for smooth surfaces of arbitrary shape (not necessarily spheres). For that purpose, the surfaces of the two particles are approximated with paraboloids in the vicinity of the point of closest approach ($h = h_0$). Let the principal curvatures at this point be c_1 and c'_1 for the first particle, and c_2 and c'_2 for the second particle. Then the generalization of Equation 5.163 reads²⁵⁴

$$U(h_0) = \frac{2\pi}{\sqrt{C}} \int_{h_0}^{\infty} f(h) dh \quad (5.164)$$

$$C \equiv c_1 c'_1 + c_2 c'_2 + (c_1 c_2 + c'_1 c'_2) \sin^2 \omega + (c_1 c'_2 + c'_1 c_2) \cos^2 \omega$$

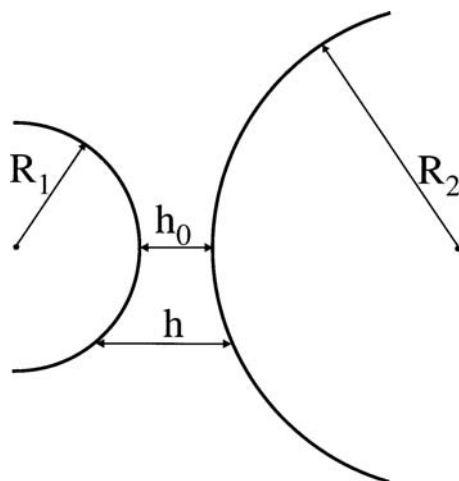


FIGURE 5.22 Two spherical particles of radii R_1 and R_2 ; the shortest and the running surface-to-surface distances are denoted by h_0 and h , respectively.

where ω is the angle subtended between the directions of the principal curvatures of the two approaching surfaces. For two spheres we have $c_1 = c'_1 = 1/R_1$, $c_2 = c'_2 = 1/R_2$, and Equation 5.164 reduces to Equation 5.163.

For two cylinders of radii r_1 and r_2 crossed at angle ω we have $c_1 = c_2 = 0$; $c'_1 = 1/r_1$, $c'_2 = 1/r_2$ and Equation 5.164 yields

$$U(h_0) = \frac{2\pi\sqrt{r_1 r_2}}{\sin\omega} \int_{h_0}^{\infty} f(h) dh \quad (5.165)$$

Equation 5.165 is often used in connection with the experiments with the surface force apparatus,^{34,257} in which the interacting surfaces are two crossed cylindrical mica sheets. The divergence in Equation 5.165 for $\omega = 0$ reflects the fact that the axes of the two infinitely long cylinders are parallel for $\omega = 0$ and thus the area of the interaction zone becomes infinite.

The main features of the Derjaguin approximation are the following: (1) It is applicable to any type of force law (attractive, repulsive, oscillatory), if the range of the forces is much smaller than the particles radii, and (2) it reduces the problem for interactions between particles to the simpler problem for interactions in plane-parallel films.

5.4.2 VAN DER WAALS SURFACE FORCES

The van der Waals interaction between molecules i and j obeys the law:

$$u_{ij}(r) = -\frac{\alpha_{ij}}{r^6} \quad (5.166)$$

where u_{ij} is the potential energy of interaction, r is the distance between the two molecules, and α_{ij} is a constant characterizing the interaction. In fact, the van der Waals forces represent an averaged dipole-dipole interaction, which is a superposition of three main terms: (1) orientation interaction: interaction between two permanent dipoles;²⁵⁸ (2) induction interaction: interaction between one permanent dipole and one induced dipole;²⁵⁹ (3) dispersion interaction: interaction between two induced dipoles.²⁶⁰ The theory yields³⁴

$$\alpha_{ij} = \frac{1}{(4\pi\epsilon_0)^2} \left[\frac{p_i^2 p_j^2}{3kT} + (p_i^2 \alpha_{oj} + p_j^2 \alpha_{oi}) + \frac{3 \alpha_{oi} \alpha_{oj} h_p v_i v_j}{2(v_i + v_j)} \right] \quad (5.167)$$

where p_i and α_{i0} are molecular dipole moment and electronic polarizability; h_p is the Planck constant; and v_i is the orbiting frequency of the electron in the Bohr atom.

For van der Waals interactions between molecules in a gas phase, the orientation interaction can yield from 0% (nonpolar molecules) up to 70% (molecules of large permanent dipole moment, like H₂O) of the value of α_{ij} ; the contribution of the induction interaction in α_{ij} is usually low, about 5 to 10%; the contribution of the dispersion interaction might be between 24% (water) and 100% (nonpolar hydrocarbons); for numerical data, see Reference 34.

According to the *microscopic* theory by Hamaker,²⁶¹ the van der Waals interaction between two macroscopic bodies can be found by integration of Equation 5.166 over all couples of molecules, followed by subtraction of the interaction energy at infinite separation between the bodies. The result depends on the geometry of the system. For a plane-parallel film from component 3 located between two semi-infinite phases composed from components 1 and 2, the van der Waals interaction energy per unit area and the respective disjoining pressure, stemming from Equation 5.166, are²⁶¹

$$f_{vw} = -\frac{A_H}{12\pi h^2}, \quad \Pi_{vw} = -\frac{\partial f_{vw}}{\partial h} = -\frac{A_H}{6\pi h^3} \quad (5.168)$$

where, as usual, h is the thickness of the film and A_H is the compound Hamaker constant:¹⁴

$$A_H = A_{33} + A_{12} - A_{13} - A_{23} \quad (A_{ij} = \pi^2 \rho_i \rho_j \alpha_{ij}, \quad i, j = 1, 2, 3) \quad (5.169)$$

A_{ij} is the Hamaker constant of components i and j ; ρ_i and ρ_j are the molecular number densities of phases i and j built up from components i and j , respectively. If A_{ii} and A_{jj} are known, we can calculate A_{ij} by using the Hamaker approximation

$$A_{ij} = (A_{ii} A_{jj})^{1/2} \quad (5.170)$$

In fact, Equation 5.170 is applicable to the dispersion contribution in the van der Waals interaction.³⁴

When components 1 and 2 are identical, A_H is positive (see Equation 5.169), therefore, the van der Waals interaction between identical bodies, in any medium, is always attractive. Besides, two dense bodies (even if nonidentical) will attract each other when placed in medium 3 of low density (gas, vacuum). When the phase in the middle (component 3) has intermediate Hamaker constant between those of bodies 1 and 2, A_H can be negative and the van der Waals disjoining pressure can be repulsive (positive). Such is the case of an aqueous film between mercury and gas.²⁶²

Lifshitz et al.^{263,264} developed an alternative approach to the calculation of the Hamaker constant A_H in condensed phases, called the *macroscopic* theory. The latter is not limited by the assumption for pairwise additivity of the van der Waals interaction (see also References 34, 254, and 265). The Lifshitz theory treats each phase as a continuous medium characterized by a given uniform dielectric permittivity, which is dependent on the frequency, ν , of the propagating electromagnetic waves. For the symmetric configuration of two identical phases “ i ” interacting across a medium “ j ,” the macroscopic theory provides the expression³⁴

$$A_H \equiv A_{ji} = A_{ji}^{(\nu=0)} + A_{ji}^{(\nu>0)} = \frac{3}{4} kT \left(\frac{\epsilon_i - \epsilon_j}{\epsilon_i + \epsilon_j} \right)^2 + \frac{3h_p \nu_e (n_i^2 - n_j^2)^2}{16\sqrt{2} (n_i^2 + n_j^2)^{3/2}} \quad (5.171)$$

where ϵ_i and ϵ_j are the dielectric constants of phases i and j ; n_i and n_j are the respective refractive indices for visible light; as usual, h_p is the Planck constant; ν_e is the main electronic absorption frequency, which is $\approx 3.0 \times 10^{15}$ Hz for water and most organic liquids.³⁴ The first term in the right-hand side of Equation 5.171, $A_{iji}^{(v=0)}$, is the so-called zero-frequency term, expressing the contribution of the orientation and induction interactions. Indeed, these two contributions to the van der Waals force represent electrostatic effects. Equation 5.171 shows that the zero-frequency term can never exceed $\frac{3}{4}kT \approx 3 \times 10^{-21}$ J. The last term in Equation 5.171, $A_{iji}^{(v>0)}$, accounts for the dispersion interaction. If the two phases, i and j , have comparable densities (as for emulsion systems, say, oil–water–oil), then $A_{iji}^{(v>0)}$ and $A_{iji}^{(v=0)}$ are comparable by magnitude. If one of the phases, i or j , has a low density (gas, vacuum), we obtain $A_{iji}^{(v>0)} \gg A_{iji}^{(v=0)}$. In the latter case, the Hamaker microscopic approach may give comparable $A_{iji}^{(v>0)}$ and $A_{iji}^{(v=0)}$ in contradiction to the Lifshitz macroscopic theory, which is more accurate for condensed phases.

A geometric configuration, which is important for disperse systems, is the case of two spheres of radii R_1 and R_2 interacting across a medium (component 3). Hamaker²⁶¹ has derived the following expression for the van der Waals interaction energy between two spheres:

$$U(h_0) = -\frac{A_H}{12} \left(\frac{y}{x^2 + xy + x} + \frac{y}{x^2 + xy + x + y} + 2 \ln \frac{x^2 + xy + x}{x^2 + xy + x + y} \right) \quad (5.172)$$

where

$$x = h_0/2R_1, \quad y = R_2/R_1 \leq 1 \quad (5.173)$$

and h_0 is the same as in Figure 5.22. For $x \ll 1$ Equation 5.172 reduces to

$$U(h_0) \approx -\frac{A_H}{12} \frac{y}{(1+y)x} = -\frac{2\pi R_1 R_2}{R_1 + R_2} \frac{A_H}{12\pi h_0} \quad (5.174)$$

Equation 5.174 can be also derived by combining Equation 5.168 with the Derjaguin approximation (Equation 5.163). It is worthwhile noting that the logarithmic term in Equation 5.172 can be neglected only if $x \ll 1$. For example, even when $x = 5 \times 10^{-3}$, the contribution of the logarithmic term amounts to about 10% of the result (for $y = 1$); consequently, for larger values of x this term must be retained.

Another geometric configuration, which corresponds to two colliding deformable emulsion droplets, is sketched in Figure 5.23. In this case the interaction energy is given by the expression²⁶⁶

$$U(h, r) = -\frac{A_H}{12} \left[\frac{3}{4} + \frac{R_s}{h} + 2 \ln \left(\frac{h}{R_s} \right) + \frac{r^2}{h^2} - \frac{2r^2}{R_s h} \right] \quad (h, r \ll R_s) \quad (5.175)$$

where h and r are the thickness and the radius of the flat film formed between the two deformed drops, respectively. R_s is the radius of the spherical part of the drop surface (see Figure 5.23). Equation 5.175 is a truncated series expansion; the exact formula, which is more voluminous, can be found in Reference 266. Expressions for U for other geometric configurations are also available.^{35,265}

The asymptotic behavior of the dispersion interaction at large intermolecular separations does not obey Equation 5.166; instead, $u_{ij} \propto 1/r^7$ due to the electromagnetic retardation effect established by Casimir and Polder.²⁶⁷ Various expressions have been proposed to account for this effect in the Hamaker constant.²⁶⁵

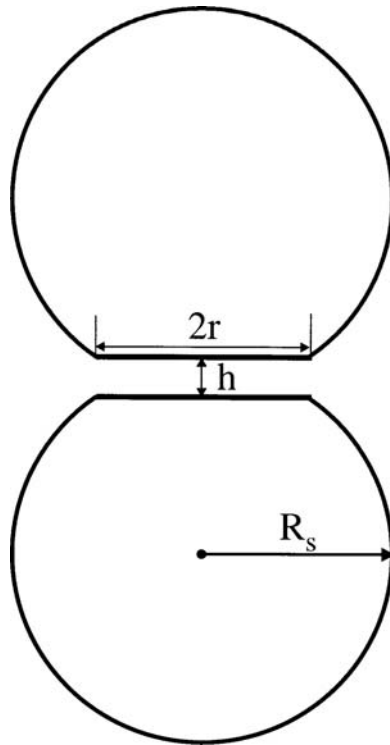


FIGURE 5.23 Thin film of radius r and thickness h formed between two attached fluid particles; the spherical part of the particle surface has radius R_s .

The orientation and induction interactions are electrostatic effects, so they are not subjected to electromagnetic retardation. Instead, they are subject to Debye screening due to the presence of electrolyte ions in the liquid phases. Thus, for the interaction across an electrolyte solution the screened Hamaker constant is given by the expression^{34,268}

$$A_H = A_0(2\kappa h)e^{-2\kappa h} + A_d \quad (5.176)$$

where A_0 denotes the contribution of orientation and induction interaction into the Hamaker constant and A_d is the contribution of the dispersion interaction; κ is the Debye screening parameter: $\kappa = \kappa_c I^{1/2}$ (see Equation 5.34).

5.4.3 ELECTROSTATIC SURFACE FORCES

5.4.3.1 Two Identically Charged Planes

First we consider the electrostatic (double layer) interaction between two identical charged plane parallel surfaces across a solution of symmetric $Z:Z$ electrolyte. The charge of a counterion (i.e., ion with charge opposite to that of the surface) is $-Ze$, whereas the charge of a coion is $+Ze$ ($Z = \pm 1, \pm 2, \dots$) with e the elementary charge. If the separation between the two planes is very large, the number concentration of both counterions and coions would be equal to its bulk value, n_0 , in the middle of the film. However, at finite separation, h , between the surfaces the two EDL overlap and the counterion and coion concentrations in the middle of the film, n_{10} and n_{20} , are no longer equal. Because the solution inside the film is supposed to be in electrochemical (Donnan) equilibrium with the bulk electrolyte solution of concentration n_0 , we can write²⁶⁹ $n_{10} n_{20} = n_0^2$ or, alternatively,

$$n_{10} = n_0/\sqrt{m}, \quad n_{20} = n_0\sqrt{m}, \quad m \equiv n_{20}/n_{10} \quad (5.177)$$

As pointed out by Langmuir,²⁷⁰ the electrostatic disjoining pressure, Π_{el} , can be identified with the excess osmotic pressure in the middle of the film:

$$\Pi_{el} = kT(n_{10} + n_{20} - 2n_0) = n_0 kT(m^{1/4} - m^{-1/4})^2 \quad (5.178)$$

Equation 5.178 demonstrates that for two identically charged surfaces Π_{el} is always positive, i.e., corresponds to repulsion between the surfaces. In general, we have $0 < m \leq 1$, because the coions are repelled from the film due to the interaction with the film surfaces. To find the exact dependence of Π_{el} on the film thickness, h , we solve the Poisson–Boltzmann equation for the distribution of the electrostatic potential inside the film. The solution provides the following connection between Π_{el} and h for symmetric electrolytes:^{254,271}

$$\Pi_{el} = 4n_0 kT \cot^2 \theta, \quad \kappa h = 2F(\varphi, \theta) \sin \theta \quad (5.179)$$

where $F(\varphi, \theta)$ is an elliptic integral of the first kind, and φ is related with θ as follows:

$$\cos \varphi = (\cot \theta) / \sinh(Z\Phi_s/2) \quad (\text{fixed surface potential } \Phi_s) \quad (5.180)$$

$$\tan \varphi = (\tan \theta) \sinh(Z\Phi_\infty/2) \quad (\text{fixed surface charge } \sigma_s) \quad (5.181)$$

$$\cosh(Z\Phi_\infty) = 1 + \frac{1}{2} \left(\frac{Ze\sigma_s}{\epsilon\epsilon_0 kT\kappa} \right)^2, \quad \Phi_s \equiv \frac{e\Psi_s}{kT} \quad (5.182)$$

Here, Φ_s is the dimensionless surface potential and Φ_∞ is the value of Φ_s for $h \rightarrow \infty$. Equation 5.179 expresses the dependence $\Pi_{el}(h)$ in a parametric form: $\Pi_{el}(\theta), h(\theta)$. Fixed surface potential or charge means that Φ_s or σ_s does not depend on the film thickness h . The latter is important to be specified when integrating $\Pi(h)$ or $f(h)$ (in accordance with Equations 5.162 to 5.165) to calculate the interaction energy.

In principle, it is possible for neither the surface potential nor the surface charge to be constant.²⁷² In such a case, a condition for *charge regulation* is applied, which in fact represents the condition for dynamic equilibrium of the counterion exchange between the Stern and diffuse parts of the EDL. As discussed in Section 5.2.1.2.3, the Stern layer itself can be considered as a Langmuirian adsorption layer of counterions. We can relate the maximum possible surface charge density (due to all surface ionizable groups) to Γ_1 in Equation 5.47: $\sigma_{\max} = Ze\Gamma_1$. Similarly, the effective surface charge density, σ_s , which is smaller by magnitude than σ_{\max} (because some ionizable groups are blocked by adsorbed counterions) can be expressed as $\sigma_s = Ze(\Gamma_1 - \Gamma_2)$. Then, with the help of Equation 5.44, the Stern isotherm (Equation 5.47) can be represented in the form:

$$\frac{\sigma_{\max} - \sigma_s}{\sigma_{\max}} = \left[1 + (K_2 I)^{-1} \exp(Z\Phi_s) \right]^{-1} \quad (5.183)$$

The product $Z\Phi_s$ is always positive. At high surface potential, $Z\Phi_s \rightarrow \infty$, from Equation 5.183 we obtain $\sigma_s \rightarrow \sigma_{\max}$, that is, no blocking of surface ionizable by adsorbed counterions.

When the film thickness is large enough ($\kappa h \geq 1$) the difference between the regimes of constant potential, constant charge, and charge regulation becomes negligible; i.e., the usage of each leads to the same results for $\Pi_{el}(h)$.¹⁴

When the dimensionless electrostatic potential in the middle of the film

$$\Phi_m = \frac{e}{kT} \Psi_m = -\frac{1}{2Z} \ln m \quad (5.184)$$

is small enough (the film thickness, h , is large enough), we can suppose that $\Phi_m \approx 2\Phi_1(h/2)$, where Φ_1 is the dimensionless electric potential at a distance $h/2$ from the surface (of the film) when the other surface is removed at infinity. Because

$$Z\Phi_1(h/2) = 4 e^{-\kappa h/4} \tanh(Z\Phi_s/4) \quad (5.185)$$

from Equations 5.178, 5.184, and 5.185 we obtain a useful asymptotic formula:²⁷³

$$\Pi_{el} \approx n_0 kT Z^2 \Phi_m^2 \approx 64 n_0 kT \left(\tanh \frac{Z\Phi_s}{4} \right)^2 e^{-\kappa h} \quad (5.186)$$

It is interesting to note that, when Φ_s is large enough, the hyperbolic tangent in Equation 5.186 is identically 1, and Π_{el} (as well as f_{el}) becomes independent of the surface potential (or charge). Equation 5.186 can be generalized for the case of 2:1 electrolyte (bivalent counterion) and 1:2 electrolyte (bivalent coion):²⁷⁴

$$\Pi_{el} = 432 n_{(2)} kT \left(\tanh \frac{v_{ij}}{4} \right)^2 e^{-\kappa h} \quad (5.187)$$

where $n_{(2)}$ is the concentration of the bivalent ions, the subscript “ $i;j$ ” takes value “2:1” or “1:2,” and

$$v_{2:1} = \ln \left[3 / (1 + 2e^{-\Phi_s}) \right], \quad v_{1:2} = \ln \left[(2e^{\Phi_s} + 1) / 3 \right] \quad (5.188)$$

5.4.3.2 Two Nonidentically Charged Planes

Contrary to the case of two identically charged surfaces, which always repel each other (see Equation 5.178), the electrostatic interaction between two plane-parallel surfaces of different potentials, Ψ_{s1} and Ψ_{s2} , can be either repulsive or attractive.^{254,275} Here, we will restrict our considerations to the case of low surface potentials, when the Poisson–Boltzmann equation can be linearized. Despite that it is not too general quantitatively, this case exhibits qualitatively all features of the electrostatic interaction between different surfaces.

If $\Psi_{s1} = \text{const.}$ and $\Psi_{s2} = \text{const.}$, then the disjoining pressure at constant surface potential reads²⁵⁴

$$\Pi_{el}^{\Psi} = \frac{\epsilon \epsilon_0 \kappa^2}{2\pi} \frac{2\Psi_{s1}\Psi_{s2} \cosh \kappa h - (\Psi_{s1}^2 + \Psi_{s2}^2)}{\sinh^2 \kappa h} \quad (5.189)$$

When the two surface potentials have opposite signs, i.e., when $\Psi_{s1}\Psi_{s2} < 0$, Π_{el}^{Ψ} is negative for all h and corresponds to electrostatic attraction (Figure 5.24a). This result could have been anticipated, as two charges of opposite sign attract each other. More interesting is the case when $\Psi_{s1}\Psi_{s2} > 0$,

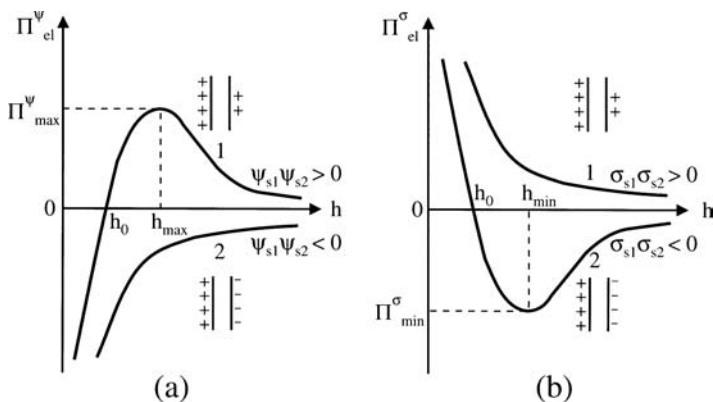


FIGURE 5.24 Electrostatic disjoining pressure at (a) fixed surface potential, Π_{el}^ψ , and (b) fixed surface charge density, Π_{el}^σ , both of them plotted vs. the film thickness h . ψ_{s1} and ψ_{s2} are the potentials of the two surfaces; σ_{s1} and σ_{s2} are the respective surface charge densities.

but $\psi_{s1} \neq \psi_{s2}$. In the latter case, the two surfaces repel each other for $h > h_0$, whereas they attract each other for $h < h_0$ (Figure 5.24a); h_0 is determined by the equation $\kappa h_0 = \ln(\psi_{s2} / \psi_{s1})$; $\psi_{s2} > \psi_{s1}$. Besides, the electrostatic repulsion has a maximum value of

$$\Pi_{el}^\psi(\max) = \frac{\epsilon\epsilon_0 \kappa^2}{2\pi} \psi_{s1}^2 \quad \text{at} \quad h_{\max} = \frac{1}{\kappa} \operatorname{arccosh} \frac{\psi_{s2}}{\psi_{s1}}, \quad \psi_{s2} > \psi_{s1} \quad (5.190)$$

A similar electrostatic disjoining pressure isotherm has been used to interpret the experimental data for aqueous films on mercury.²⁶² It is worthwhile noting that $\Pi_{el}^\psi(\max)$ depends only on ψ_{s1} ; i.e., the maximum repulsion is determined by the potential of the surface of lower charge.

If $\sigma_{s1} = \text{const.}$ and $\sigma_{s2} = \text{const.}$, then instead of Equation 5.189 we have²⁵⁴

$$\Pi_{el}^\sigma(h) = \frac{1}{2\epsilon\epsilon_0} \frac{2\sigma_{s1}\sigma_{s2} \cosh \kappa h + \sigma_{s1}^2 + \sigma_{s2}^2}{\sinh^2 \kappa h} \quad (5.191)$$

When $\sigma_1\sigma_2 > 0$, Equation 5.191 yields $\Pi_{el}^\sigma > 0$ for every h (see Figure 5.24b). However, when $\sigma_1\sigma_2 < 0$, Π_{el}^σ is repulsive for small thickness, $h < h_0$, and attractive for larger separations, $h > h_0$; h_0 is determined by the equation $\kappa h_0 = \ln(-\sigma_{s2} / \sigma_{s1})$; $|\sigma_{s2}| > |\sigma_{s1}|$. The electrostatic disjoining pressure in this case has a minimum value

$$\Pi_{el}^\sigma(\min) = \frac{1}{\epsilon\epsilon_0} \sigma_{s1} \sigma_{s2}, \quad \text{at} \quad h_{\min} = \frac{1}{\kappa} \operatorname{arccosh} \left(-\frac{\sigma_{s2}}{\sigma_{s1}} \right) \quad (5.192)$$

Finally, it should be noted that all curves depicted in Figure 5.24a and b decay exponentially at $h \rightarrow \infty$. An asymptotic expression for Z:Z electrolytes, which generalizes Equation 5.186, holds^{254,273}

$$\Pi_{el}(h) = 64 n_0 k T \gamma_1 \gamma_2 e^{-\kappa h}, \quad \gamma_k \equiv \tanh \left(\frac{Z e \psi_{sk}}{4 k T} \right), \quad k = 1, 2 \quad (5.193)$$

Equation 5.193 is valid for both low and high surface potentials, only if $\exp(-\kappa h) \ll 1$.

5.4.3.3 Two Charged Spheres

When the EDL are thin compared with the particle radii ($\kappa^{-1} \ll R_1, R_2$) and the gap between the particles is small ($h_0 \ll R_1, R_2$), we can use Equation 5.193 in conjunction with the Derjaguin approximation, Equations 5.162 and 5.163. The result for the energy of electrostatic interaction between two spheres reads

$$U_{\text{el}}(h_0) = \frac{128\pi R_1 R_2}{\kappa^2 (R_1 + R_2)} n_0 k T \gamma_1 \gamma_2 e^{-\kappa h} \quad (5.194)$$

Equation 5.194 is valid for any surface potentials ψ_{s1} and ψ_{s2} but only for $\exp(\kappa h) \gg 1$. Complementary expressions, which are valid for every $h \ll R_1, R_2$, but for small surface potentials can be derived by integrating Equations 5.189 and 5.191, instead of Equation 5.193. In this way, for $\psi_{s1} = \text{const.}$ and $\psi_{s2} = \text{const.}$, we can derive²⁷⁶

$$U_{\text{el}}^{\psi}(h_0) = \frac{\pi\epsilon\epsilon_0 R_1 R_2}{R_1 + R_2} \left[(\psi_{s1} + \psi_{s2})^2 \ln(1 + e^{-\kappa h_0}) + (\psi_{s1} - \psi_{s2})^2 \ln(1 - e^{-\kappa h_0}) \right] \quad (5.195)$$

or, alternatively, for $\sigma_{s1} = \text{const.}$ and $\sigma_{s2} = \text{const.}$ we obtain²⁷⁷

$$U_{\text{el}}^{\sigma}(h_0) = \frac{-\pi R_1 R_2}{\epsilon\epsilon_0 \kappa^2 (R_1 + R_2)} \left[(\sigma_{s1} + \sigma_{s2})^2 \ln(1 - e^{-\kappa h_0}) + (\sigma_{s1} - \sigma_{s2})^2 \ln(1 + e^{-\kappa h_0}) \right] \quad (5.196)$$

The range of validity of the different approximations involved in the derivations of Equations 5.194 to 5.196 is discussed in the book of Russel et al.²⁷⁸

As mentioned above, Equations 5.194 to 5.196 hold for $h_0 \ll R$. In the opposite case, when h_0 is comparable to or larger than the particle radius R , we can use the equation¹⁴

$$U_{\text{el}}(h_0) = \frac{4\pi\epsilon\epsilon_0 \psi_s^2 R^2}{2R + h_0} e^{-\kappa h_0} \quad (5.197)$$

stemming from the theory of Debye and Hückel²⁷⁹ for two identical particles. Equation 5.197 was derived by using the superposition approximation (valid for weak overlap of the two EDL) and the linearized Poisson–Boltzmann equation. A simple approximate formula, representing in fact interpolation between Equations 5.197 and 5.195 (the latter for $R_1 = R_2 = R$), has been derived by McCartney and Levine:²⁸⁰

$$U_{\text{el}}^{\psi}(h_0) = 4\pi\epsilon\epsilon_0 R \psi_s^2 \frac{R + h_0}{2R + h_0} \ln \left(1 + \frac{R e^{-\kappa h_0}}{R + h_0} \right) \quad (5.198)$$

Equation 5.198 has the advantage of giving a good approximation for every h_0 provided that the Poisson–Boltzmann equation can be linearized. Similar expressions for the energy of electrostatic interaction between two deformed droplets or bubbles (Figure 5.23) can be derived.²⁶⁶

5.4.4 DLVO THEORY

The first quantitative theory of interactions in thin liquid films and dispersions is the DLVO theory called after the names of the authors: Derjaguin and Landau²⁸¹ and Verwey and Overbeek.²⁷³ In

this theory, the total interaction is supposed to be a superposition of van der Waals and double layer interactions. In other words, the total disjoining pressure and the total interaction energy are presented in the form:

$$\Pi = \Pi_{\text{vw}} + \Pi_{\text{el}}, \quad U = U_{\text{vw}} + U_{\text{el}} \quad (5.199)$$

A typical curve, Π vs. h , exhibits a maximum representing a barrier against coagulation, and two minima, called primary and secondary minimum (see Figure 5.13); the U vs. h curve has a similar shape. The primary minimum appears if strong short-range repulsive forces (e.g., steric forces) are present. With small particles, the depth of the secondary minimum is usually small ($U_{\text{min}} < kT$). If the particles cannot overcome the barrier, coagulation (flocculation) does not take place, and the dispersion is stable because of electrostatic repulsion, which gives rise to the barrier. With larger colloidal particles ($R > 0.1 \mu\text{m}$) the secondary minimum could be deep enough to cause coagulation and even formation of ordered structures of particles.²⁸²

By addition of electrolyte or by decreasing the surface potential of the particles, we can suppress the electrostatic repulsion and thus decrease the height of the barrier. According to DLVO theory, the critical condition determining the onset of rapid coagulation is

$$U(h_{\text{max}}) = 0, \quad \left. \frac{dU}{dh} \right|_{h_{\text{max}}} = 0 \quad (5.200)$$

where $h = h_{\text{max}}$ denotes the position of the barrier.

By using Equation 5.174 for U_{vw} and Equation 5.194 for U_{el} we derive from Equations 5.199 and 5.200 the following criterion for the threshold of rapid coagulation of identical particles ($R_1 = R_2 = R$; $\gamma_1 = \gamma_2 = \gamma$):

$$\frac{\kappa^6}{n_0^2} = \left[\frac{768\pi}{A_H} kT e^{-1} \tanh^2 \left(\frac{Ze\psi_s}{4kT} \right) \right]^2 \quad (5.201)$$

For a $Z:Z$ electrolyte, substituting $\kappa^2 = (2Z^2e^2n_0)/(\epsilon_0\epsilon kT)$ into Equation 5.201, we obtain:

$$n_0(\text{critical}) \propto \frac{1}{Z^6} \tanh^4 \left(\frac{Ze\psi_s}{4kT} \right) \quad (5.202)$$

When ψ_s is high enough, the hyperbolic tangent equals 1 and Equation 5.202 yields $n_0(\text{critical}) \propto Z^{-6}$, which is, in fact, the empirical rule established earlier by Schultze²⁸³ and Hardy.²⁸⁴

5.4.5 NON-DLVO SURFACE FORCES

After 1980, a number of surface forces have been found that are not taken into account by conventional DLVO theory. They are considered separately below.

5.4.5.1 Ion Correlation Forces

As shown by Debye and Hückel,²⁷⁹ due to the strong electrostatic interaction between the ions in a solution, the positions of the ions are correlated in such a way that a counterion atmosphere appears around each ion, thus screening its Coulomb potential. The energy of formation of the counterion atmospheres contributes to the free energy of the system called correlation energy.²³

The correlation energy affects also a contribution to the osmotic pressure of the electrolyte solution, which can be presented in the form:²³

$$\Pi_{\text{osm}} = kT \sum_{i=1}^k n_i - \frac{kT \kappa^2}{24 \pi} \quad (5.203)$$

The first term in the right-hand side of the Equation 5.203 corresponds to an ideal solution, whereas the second term takes into account the effect of electrostatic interactions between the ions (the same effect is accounted for thermodynamically by the activity coefficient; see Equation 5.31).

The expression for Π_{el} in the DLVO theory (Equation 5.178) obviously corresponds to an ideal solution, with the contribution of the ionic correlations being neglected. Hence, in a more general theory, instead of Equation 5.199 we write:

$$\Pi = \Pi_{\text{vw}} + \Pi_{\text{el}} + \Pi_{\text{cor}} \quad (5.204)$$

where Π_{cor} is the contribution of the ionic correlations to the disjoining pressure. The theory of Π_{cor} takes into account the following effects: (1) the different ionic concentration (and hence the different Debye screening) in the film compared to that in the bulk solution; (2) the energy of deformation of the counterion atmosphere due to the image forces; (3) the energy of the long-range correlations between charge-density fluctuations in the two opposite EDL. For calculating Π_{cor} both numerical solutions^{285,286} and analytical expressions^{287,288} have been obtained. For example, in the case when the electrolyte is symmetric (Z:Z) and $\exp(-\kappa h) \ll 1$ we can use the asymptotic formula:²⁸⁷

$$\Pi_{\text{cor}} = \Pi_{\text{el}} \frac{Z^2 e^2 \kappa}{16 \pi \epsilon \epsilon_0 kT} (\ln 2 + 2I_C) + O(e^{-\kappa h}) \quad (5.205)$$

where Π_{el} is the conventional DLVO electrostatic disjoining pressure,

$$I_C = \frac{1}{2}(1+J) \ln 2 + \frac{2-2z^3+z}{2z(2z^2-1)^2} - \frac{1}{2}(1-J) \ln(z+z^2) - \frac{\sqrt{z^2-1}}{z} \left[1+J+4(2z^2-1)^{-3} \right] \arctan \sqrt{\frac{z-1}{z+1}}$$

$$J \equiv \frac{2z^2-3}{(2z^2-1)^3}, \quad z \equiv \left[1 + \left(\frac{e \sigma_s}{2 \epsilon \epsilon_0 kT \kappa} \right)^2 \right]^{1/2}$$

The results for the case of symmetric electrolytes are the following. Π_{cor} is negative and corresponds to attraction, which can be comparable by magnitude with Π_{vw} . In the case of 1:1 electrolyte Π_{cor} is usually a small correction to Π_{el} . In the case of 2:2 electrolyte, however, the situation can be quite different: the attractive forces, $\Pi_{\text{cor}} + \Pi_{\text{vw}}$, prevail over Π_{el} and the total disjoining pressure, Π , becomes negative. The effect of Π_{cor} is even larger in the presence of ions of higher valency. Thus, the ion-correlation attraction could be the explanation for the sign inversion of the second virial coefficient, β_2 , of micellar surfactant solutions (from $\beta_2 > 0$ to $\beta_2 < 0$, measured by light scattering) when the Na^+ ions are replaced by Al^{3+} ions at fixed total ionic strength (see figure 31 in Reference 289). Short-range net attractive ion-correlation forces have been measured

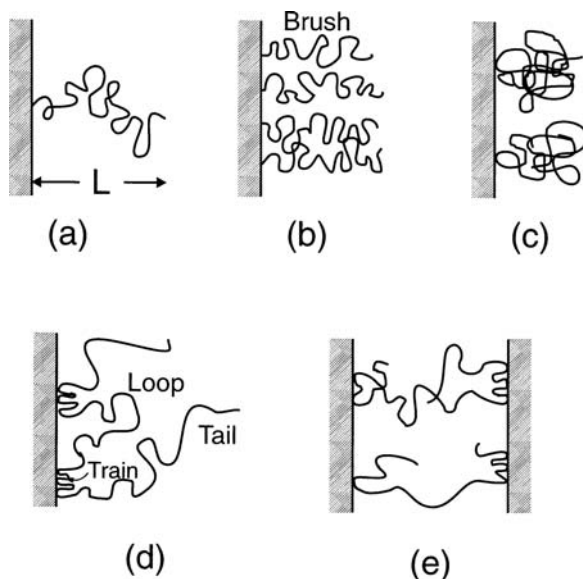


FIGURE 5.25 Polymeric chains adsorbed at an interface: (a) terminally anchored polymer chain of mean end-to-end distance L ; (b) a brush of anchored chains; (c) adsorbed (but not anchored) polymer coils; (d) configuration with a loop, trains, and tails; (e) bridging of two surfaces by adsorbed polymer chains.

by Marra^{290,291} and Kjellander et al.^{292,293} between highly charged anionic bilayer surfaces in CaCl_2 solutions. These forces are believed to be responsible for the strong adhesion of some surfaces (clay and bilayer membranes) in the presence of divalent counterions.^{34,292,294} On the other hand, Kohonen et al.²⁹⁵ measured a monotonic repulsion between two mica surfaces in $4.8 \times 10^{-3} M$ solution of MgSO_4 . Additional work is necessary to verify the theoretical predictions and to clarify the physical significance of the ion-correlation surface force.

Note that the theory predicts ion-correlation attraction not only across water films with overlapping EDL, but also across *oily* films intervening between two water phases. In the latter case, Π_{cor} is not zero because the ions belonging to the two outer double layers interact across the thin dielectric (oil) film. The theory for such a film²⁹⁶ predicts that Π_{cor} is negative (attractive) and strongly dependent on the dielectric permittivity of the oil film; Π_{cor} can be comparable by magnitude with Π_{vw} ; $\Pi_{\text{el}} = 0$ in this case.

5.4.5.2 Steric Interaction

5.4.5.2.1 Physical Background

The steric interaction between two surfaces appears when chain molecules, attached at some point(s) to a surface, dangle out into the solution (Figure 5.25). When two such surfaces approach each other, the following effects take place:^{34,297-299} (1) The entropy decreases due to the confining of the dangling chains, which results in a repulsive osmotic force known as *steric* or *overlap* repulsion. (2) In a poor solvent, the segments of the chain molecules attract each other; hence, the overlap of the two approaching layers of polymer molecules will be accompanied with some *intersegment attraction*; the latter can prevail for small overlap, however at the distance of larger overlap it becomes negligible compared with the osmotic repulsion. (3) Another effect, known as the *bridging attraction*, occurs when two opposite ends of the chain molecule can attach (adsorb) to the opposite approaching surfaces, thus forming a bridge between them (see Figure 5.25e).

Steric interaction can be observed in foam or emulsion films stabilized with nonionic surfactants or with various polymers, including proteins. The usual nonionic surfactants molecules are anchored

(grafted) to the liquid interface by their hydrophobic moieties. When the surface concentration of adsorbed molecules is high enough, the hydrophilic chains are called to form a brush (Figure 5.25b). The coils of macromolecules, such as proteins, can also adsorb at a liquid surface (Figure 5.25c). Sometimes, the configurations of the adsorbed polymers are very different from the statistical coil: loops, trains, and tails can be distinguished (Figure 5.25d).

The osmotic pressure of either dilute or concentrated polymer solutions can be expressed in the form:³⁰⁰

$$\frac{P_{\text{osm}}}{nkT} = \frac{1}{N} + \frac{1}{2}nv + \frac{1}{3}n^2w + \dots \quad (5.206)$$

Here N is the number of segments in the polymer chain, n is the number segment density, and v and w account for the pair and triplet interactions, respectively, between segments. In fact, v and w are counterparts of the second and third virial coefficients in the theory of imperfect gases;¹¹ v and w can be calculated if information about the polymer chain and the solvent is available:²⁷⁸

$$w^{1/2} = \bar{v}m/N_A, \quad v = w^{1/2}(1 - 2\chi) \quad (5.207)$$

where \bar{v} (m^3/kg) is the specific volume per segment, m (kg/mol) is the molecular weight per segment, N_A is the Avogadro number, and χ is the Flory parameter. The latter depends on both the temperature and the energy of solvent–segment interaction. Then, v can be zero (see Equation 5.207) for some special temperature, called the *theta temperature*. The solvent at the theta temperature is known as the *theta solvent* or *ideal solvent*. The theta temperature in polymer solutions is a counterpart of the Boil temperature in imperfect gases: this is the temperature at which the intermolecular (intersegment) attraction and repulsion are exactly counterbalanced. In a good solvent, however, the repulsion due mainly to the excluded volume effect dominates the attraction and $v > 0$. In contrast, in a poor solvent the intersegment attraction prevails, so $v < 0$.

5.4.5.2.2 Thickness of the Polymer Adsorption Layer

The steric interaction between two approaching surfaces appears when the film thickness becomes of the order of, or smaller than $2L$, where L is the mean-square end-to-end distance of the hydrophilic portion of the chain. If the chain were entirely extended, then L would be equal to Nl with l the length of a segment; however, due to the Brownian motion $L < Nl$. For an anchored chain, such as that depicted in Figure 5.25a, in a theta solvent, L can be estimated as:²⁷⁸

$$L \approx L_0 \equiv l\sqrt{N} \quad (5.208)$$

In a good solvent $L > L_0$, whereas in a poor solvent $L < L_0$. In addition, L depends on the surface concentration, Γ , of the adsorbed chains; i.e., L is different for an isolated molecule and for a brush (see Figures 5.25a and b). The mean field approach^{278,301} applied to polymer solutions provides the following equation for calculating L :

$$\tilde{L}^3 - \left(1 + \frac{1}{9}\tilde{\Gamma}^2\right)\tilde{L}^{-1} = \frac{1}{6}\tilde{v} \quad (5.209)$$

where \tilde{L} , $\tilde{\Gamma}$, and \tilde{v} are the dimensionless values of L , Γ , and v defined as follows:

$$\tilde{L} = L/(l\sqrt{N}), \quad \tilde{\Gamma} = \Gamma N \sqrt{w}/l, \quad \tilde{v} = v\Gamma N^{3/2}/l \quad (5.210)$$

For an isolated adsorbed molecule ($\tilde{\Gamma} = 0$) in an ideal solvent ($\tilde{\nu} = 0$), Equation 5.209 predicts $\tilde{L} = 1$, i.e., $L = L_0$.

5.4.5.2.3 Overlap of Adsorption Layers

We now consider the case of terminally anchored chains, like those depicted in Figure 5.25a and b. Dolan and Edwards³⁰² calculated the steric interaction free energy per unit area, f , as a function on the film thickness, h , in a theta solvent:

$$f(h) = \Gamma kT \left[\frac{\pi^2}{3} \frac{L_0^2}{h^2} - \ln \left(\frac{8\pi}{3} \frac{L_0^2}{h^2} \right) \right] \quad \text{for } h < L_0\sqrt{3} \quad (5.211)$$

$$f(h) = 4\Gamma kT \exp \left(-\frac{3h^2}{2L_0^2} \right) \quad \text{for } h > L_0\sqrt{3} \quad (5.212)$$

where L_0 is the end-to-end distance as defined by Equation 5.208. The boundary between the power-law regime ($f \propto 1/h^2$) and the exponential decay regime is at $h = L_0\sqrt{3} \approx 1.7 L_0$, with the latter slightly less than $2L_0$, which is the intuitively expected onset of the steric overlap. The first term in the right-hand side of Equation 5.211 comes from the osmotic repulsion between the brushes, which opposes the approach of the two surfaces; the second term is negative and accounts effectively for the decrease of the elastic energy of the initially extended chains when the thickness of each of the two brushes, pressed against each other, decreases.

In the case of good solvent, the disjoining pressure $\Pi = -df/dh$ can be calculated by means of Alexander–de Gennes theory as:^{303,304}

$$\Pi(h) = kT\Gamma^{3/2} \left[\left(\frac{2L_g}{h} \right)^{9/4} - \left(\frac{h}{2L_g} \right)^{3/4} \right] \quad \text{for } h < 2L_g, \quad L_g = N(\Gamma l^3)^{1/3} \quad (5.213)$$

where L_g is the thickness of a brush in a good solvent.³⁰⁵ The positive and the negative terms in the right-hand side of Equation 5.213 correspond to osmotic repulsion and elastic attraction. The validity of Alexander–de Gennes theory was experimentally confirmed by Taunton et al.,³⁰⁶ who measured the forces between two brush layers grafted on the surfaces of two crossed mica cylinders.

In the case of adsorbed molecules, like those in Figure 5.25c, which are not anchored to the surface, the measured surface forces depend significantly on the rate of approaching of the two surfaces.^{307,308} The latter effect can be attributed to the comparatively low rate of exchange of polymer between the adsorption layer and the bulk solution. This leads to a hysteresis of the surface force: different interaction on approach and separation of the two surfaces.³⁴ In addition, we can observe two regimes of steric repulsion: (1) weaker repulsion at larger separations due to the overlap of the tails (Figure 5.25d) and (2) stronger repulsion at smaller separations indicating overlap of the loops.³⁰⁹

5.4.5.3 Oscillatory Structural Forces

5.4.5.3.1 Origin of the Structural Forces

Oscillatory structural forces appear in two cases: (1) in thin films of pure solvent between two smooth *solid* surfaces; (2) in thin liquid films containing colloidal particles (including macromolecules and surfactant micelles). In the first case, the oscillatory forces are called the *solvation*

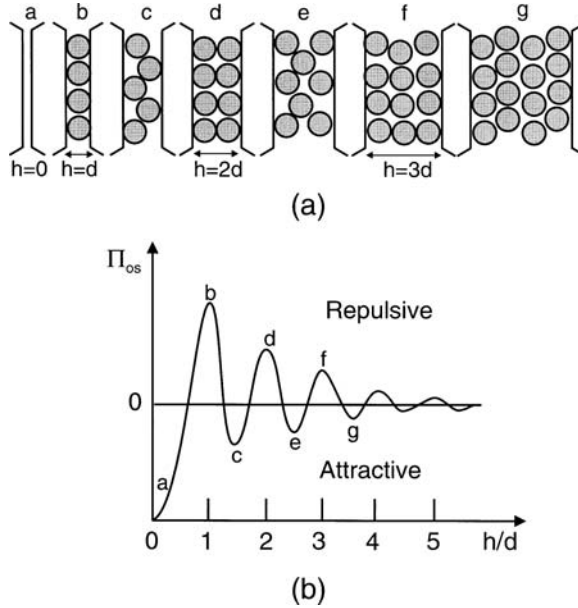


FIGURE 5.26 (a) Sketch of the consecutive stages of the thinning of a liquid film containing spherical particles; (b) plot of the related oscillatory structural component of disjoining pressure, Π_{os} , vs. the film thickness h (see Reference 34 for details).

forces.^{34,310} They are important for the short-range interactions between solid particles and dispersions. In the second case, the structural forces affect the stability of foam and emulsion films as well as the flocculation processes in various colloids. At higher particle concentrations, the structural forces stabilize the liquid films and colloids.³¹¹⁻³¹⁵ At lower particle concentrations, the structural forces degenerate into the so-called *depletion attraction*, which is found to destabilize various dispersions.^{316,317}

In all cases, the oscillatory structural forces appear when monodisperse spherical (in some cases ellipsoidal or cylindrical) particles are confined between the two surfaces of a thin film. Even one “hard wall” can induce ordering among the neighboring molecules. The oscillatory structural force is a result of overlap of the structured zones at two approaching surfaces.³¹⁸⁻³²¹ A simple connection between density distribution and structural force is given by the contact value theorem:^{34,321,322}

$$\Pi_{os}(h) = kT[n_s(h) - n_s(\infty)] \quad (5.214)$$

where Π_{os} is the disjoining pressure component due to the oscillatory structural forces, $n_s(h)$ is the particle number density in the subsurface layer as a function of the distance between the walls, h . Figure 5.26 illustrates the variation of n_s with h and the resulting disjoining pressure, Π_{os} . We see that in the limit of very small separations, as the last layer of particles is eventually squeezed out, $n_s \rightarrow 0$ and

$$\Pi_{os}(h) \rightarrow -kT n_s(\infty) \quad \text{for } h \rightarrow 0 \quad (5.215)$$

In other words, at small separations Π_{os} is negative (attractive). Equation 5.215 holds for both solvation forces and colloid structural forces. In the latter case, Equation 5.215 represents the osmotic pressure of the colloid particles and the resulting attractive force is known as the depletion force (see Section 5.4.5.3.3 below).

It is worthwhile noting that the wall can induce structuring in the neighboring fluid only if the magnitude of the surface roughness is negligible compared with the particle diameter, d . Indeed, when surface irregularities are present, the oscillations are smeared out and oscillatory structural force does not appear. If the film surfaces are fluid, the role of the surface roughness is played by the interfacial fluctuation capillary waves, whose amplitude (usually between 1 and 5 Å) is comparable to the diameter of the solvent molecules. That is the reason oscillatory solvation forces (due to structuring of solvent molecules) are observed only with liquid films, which are confined between smooth solid surfaces.³⁴ In order for structural forces to be observed in foam or emulsion films, the diameter of the colloidal particles must be much larger than the amplitude of the surface corrugations.³¹⁵

The period of the oscillations is, in fact, always about the particle diameter.^{34,315} In this aspect, the structural forces are appropriately called the “volume exclusion forces” by Henderson,³²³ who derived an explicit (although rather complex) formula for calculating these forces.

A semiempirical formula for the oscillatory structural component of disjoining pressure was proposed³²⁴

$$\begin{aligned}\Pi_{os}(h) &= P_0 \cos\left(\frac{2\pi h}{d_1}\right) \exp\left(\frac{d^3}{d_1^2 d_2} - \frac{h}{d_2}\right) \quad \text{for } h > d \\ &= -P_0 \quad \text{for } 0 < h < d\end{aligned}\tag{5.216}$$

where d is the diameter of the hard spheres, d_1 and d_2 are the period and the decay length of the oscillations which are related to the particle volume fraction, ϕ , as follows:³²⁴

$$\frac{d_1}{d} = \sqrt{\frac{2}{3}} + 0.237\Delta\phi + 0.633(\Delta\phi)^2; \quad \frac{d_2}{d} = \frac{0.4866}{\Delta\phi} - 0.420\tag{5.217}$$

Here $\Delta\phi = \phi_{\max} - \phi$ with $\phi_{\max} = \pi/(3\sqrt{2})$ the value of ϕ at close packing. P_0 is the particle osmotic pressure determined by means of the Carnahan–Starling formula³²⁵

$$P_0 = nkT \frac{1 + \phi + \phi^2 - \phi^3}{(1 - \phi)^3}, \quad n = \frac{6\phi}{\pi d^3}\tag{5.218}$$

where n is the particle number density. It is clear that for $h < d$, when the particles are expelled from the slit into the neighboring bulk suspension, Equation 5.216 describes the depletion attraction. On the other hand, for $h > d$ the structural disjoining pressure oscillates around P_0 as defined by Equation 5.218 in agreement with the finding of Kjellander and Sarman.³²⁶ The finite discontinuity of Π_{os} at $h = d$ is not surprising as, at this point, the interaction is switched over from the oscillatory to the depletion regime.

It is interesting to note that in an oscillatory regime the concentration dependence of Π_{os} is dominated by the decay length d_2 in the exponent (see Equations 5.216 and 5.217). Roughly speaking, for a given distance h , the oscillatory disjoining pressure Π_{os} increases five times when ϕ is increased 10%.³²⁴

The contribution of the oscillatory structural forces to the interaction free energy per unit area of the film can be obtained by integrating Π_{os} :

$$\begin{aligned}
 f_{os}(h) &= \int_h^{\infty} \Pi_{os}(h') dh' = F(h) && \text{for } h \geq d \\
 &= F(d) - P_0(d-h) && \text{for } 0 \leq h \leq d
 \end{aligned} \tag{5.219}$$

$$F(h) \equiv \frac{P_0 d_1 \exp\left[\left(d^3 / d_1^2 d_2\right) - (h / d_2)\right]}{4\pi^2 + (d_1 / d_2)^2} \left[\frac{d_1}{d_2} \cos\left(\frac{2\pi h}{d_1}\right) - 2\pi \sin\left(\frac{2\pi h}{d_2}\right) \right]$$

It should be noted that Equations 5.216 and 5.219 refer to hard spheres of diameter d . In practice, however, the interparticle potential can be “soft” because of the action of some long-range forces. If such is the case, we can obtain an estimation of the structural force by introducing an effective hard-core diameter:³¹⁴

$$d(T) = \left[\frac{3}{4\pi} \beta_2(T) \right]^{1/3} \tag{5.220}$$

where β_2 is the second virial coefficient in the virial expansion of the particle osmotic pressure: $P_{osm}/(nkT) = 1 + \beta_2 n/2 + \dots$. When the particles are ionic surfactant micelles (or other electrically charged particles), the diameter of the effective hard sphere can be approximated as $d \approx d_H + 2\kappa^{-1}$, where the Debye screening length, κ^{-1} , involves contributions from both the background electrolyte and the counterions dissociated from the micelles^{312,313,327,328}

$$\kappa^2 = \frac{e^2}{\epsilon_0 \epsilon K T} \left[2(CMC + I_a) + (C_s - CMC)\alpha_d \right] \tag{5.221}$$

Here, d_H is the micelle hydrodynamic diameter (usually measured by dynamic light scattering); as before, CMC stands for the critical micellization concentration, C_s is the total concentration of ionic surfactant; I_a is the ionic strength due to added inorganic electrolyte (if any), and α_d is the degree of ionization of the micelle surface ionizable groups (non-neutralized by bound counterions).

In [Figure 5.27](#) a curve calculated from Equation 5.216 is compared with the predictions of other studies. The dotted line is calculated by means of the Henderson theory.³²³ The theoretical curve calculated by Kjellander and Sarman³²⁶ for $\phi = 0.357$ and $h > 2$ by using the anisotropic Percus–Yeovick approximation is shown by the dashed line; the crosses represent grand canonical Monte Carlo simulation results due to Karlström.³²⁹ We proceed now with separate descriptions of solvation, depletion, and colloid structural forces.

5.4.5.3.2 Oscillatory Solvation Forces

When the role of hard spheres, like those depicted in [Figure 5.26](#), is played by the molecules of solvent, the resulting volume exclusion force is called the *oscillatory solvation force*, or sometimes when the solvent is water, the *oscillatory hydration force*.³⁴ The latter should be distinguished from the *monotonic* hydration force, which has a different physical origin and is considered separately in Section 5.4.5.4 below.

Measurement of the oscillatory solvation force became possible after the precise surface force apparatus had been constructed.³⁴ This apparatus allowed to measure the surface forces in thin

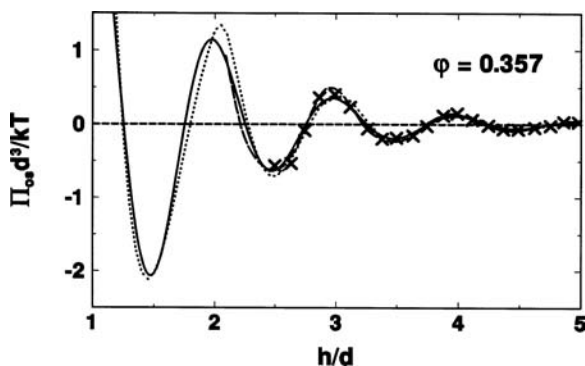


FIGURE 5.27 Dimensionless oscillatory disjoining pressure, $\Pi_{os} d^3/kT$, plotted vs. h/d . The solid curve calculated from Equation 5.216 is compared to the theories by Henderson³²³ (the dotted curve), Kjellander and Sarman³²⁶ (the dashed curve), and Karlström³²⁹ (the x points). (From Kralchevsky, P.A. and Denkov, N.D., *Chem. Phys Lett.*, 240, 385, 1995.)

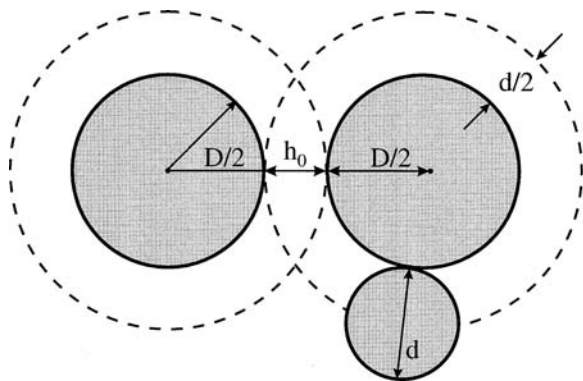


FIGURE 5.28 Overlap of the depletion zones around two particles of diameter D separated at a surface-to-surface distance h_0 ; the smaller particles have diameter d .

liquid films confined between mica (or modified mica) surfaces and in this way to check the validity of the DLVO theory down to thickness of about 5 \AA and even smaller. The experimental results with nonaqueous liquids of both spherical (CCl_4) or cylindrical (linear alkanes) molecules showed that at larger separations the DLVO theory is satisfied, whereas at separations on the order of several molecular diameters an oscillatory force is superimposed over the DLVO force law. In aqueous solutions, oscillatory forces were observed at higher electrolyte concentrations with periodicity of 0.22 to 0.26 nm, about the diameter of the water molecule.³⁴ As mentioned above, the oscillatory solvation forces can exist only between smooth solid surfaces.

5.4.5.3.3 Depletion Forces

Bondy³³⁰ observed coagulation of rubber latex in presence of polymer molecules in the disperse medium. Asakura and Oosawa³¹⁶ published a theory that attributed the observed interparticle attraction to the overlap of the depletion layers at the surfaces of two approaching colloidal particles (Figure 5.28). The centers of the smaller particles, of diameter, d , cannot approach the surface of a bigger particle (of diameter D) at a distance shorter than $d/2$, which is the thickness of the depletion layer. When the two depletion layers overlap (Figure 5.28), some volume between the large particles becomes inaccessible for the smaller particles. This gives rise to an osmotic pressure,

which tends to suck out the solvent between the bigger particles, thus forcing them against each other. The total depletion force experienced by one of the bigger particles is³¹⁶

$$F_{\text{dep}} = -kT n S(h_0) \quad (5.222)$$

where the effective depletion area is

$$\begin{aligned} S(h_0) &= \frac{\pi}{4} (2D + d + h_0)(d - h_0) & \text{for } 0 \leq h_0 \leq d \\ S(h_0) &= 0 & \text{for } d \leq h_0 \end{aligned} \quad (5.223)$$

Here, h_0 is the shortest distance between the surfaces of the larger particles, and n is the number density of the smaller particles. By integrating Equation 5.222 we can derive an expression for the depletion interaction energy between the two larger particles, $U_{\text{dep}}(h_0)$. For $D \gg d$ this expression reads:

$$U_{\text{dep}}(h_0)/kT \approx -\frac{3}{2} \phi \frac{D}{d^3} (d - h_0)^2 \quad 0 \leq h_0 \leq d \quad (5.224)$$

where $\phi = \pi n d^3/6$ is the volume fraction of the small particles. The maximum value of U_{dep} at $h_0 = 0$ is $U_{\text{dep}}(0)/kT \approx -3\phi D/(2d)$. For example, if $D/d = 50$ and $\phi = 0.1$, then $U_{\text{dep}}(0) = 7.5 kT$. This depletion attraction turns out to be large enough to cause flocculation in dispersions. de Hek and Vrij³¹⁷ studied systematically the flocculation of sterically stabilized silica suspensions in cyclohexane by polystyrene molecules. Patel and Russel³³¹ investigated the phase separation and rheology of aqueous polystyrene latex suspensions in the presence of polymer (Dextran T-500). The stability of dispersions is often determined by the competition between electrostatic repulsion and depletion attraction.³³² An interplay of steric repulsion and depletion attraction was studied theoretically by van Lent et al.³³³ for the case of polymer solution between two surfaces coated with anchored polymer layers. Joanny et al.³³⁴ and Russel et al.²⁷⁸ reexamined the theory of depletion interaction by taking into account the internal degrees of freedom of the polymer molecules; their analysis confirmed the earlier results of Asakura and Oosawa.³¹⁶

In the case of plane-parallel films the depletion component of disjoining pressure is

$$\begin{aligned} \Pi_{\text{dep}}(h) &= -n kT & h < d \\ \Pi_{\text{dep}}(h) &= 0 & h > d \end{aligned} \quad (5.225)$$

which is similar to Equation 5.215. This is not surprising because in both cases we are dealing with the excluded volume effect. Evans and Needham³³⁵ succeeded in measuring the depletion energy of two interacting bilayer surfaces in a concentrated Dextran solution; their results confirm the validity of Equation 5.225.

The depletion interaction is present always when a film is formed from micellar surfactant solution; the micelles play the role of the smaller particles. At higher micellar concentrations, the volume exclusion interaction becomes more complicated: it follows the oscillatory curve depicted in [Figure 5.26](#). In this case only, the first minimum (that at $h \rightarrow 0$) corresponds to the conventional depletion force.

5.4.5.3.4 Colloid Structural Forces

In the beginning of the 20th century, Johnnot³³⁶ and Perrin³³⁷ observed that soap films decrease their thickness by several stepwise transitions. The phenomenon was called *stratification*. Bruil and Lyklema³³⁸ and Friberg et al.³³⁹ studied systematically the effect of ionic surfactants and electrolytes on the occurrence of the stepwise transitions. Keuskamp and Lyklema³⁴⁰ anticipated that some oscillatory interaction between the film surfaces must be responsible for the observed phenomenon. Kruglyakov³⁴¹ and Kruglyakov and Rovin³⁴² reported the existence of stratification with emulsion films.

The experimental results obtained called for some theoretical interpretation. Some authors^{342,343} suggested that a possible explanation of the phenomenon can be the formation of lamella liquid-crystal structure inside the film. Such lamellar micelles are observed to form in surfactant solutions, but at concentrations much higher than those used in the experiments with stratifying films. The latter fact makes the lamella-liquid-crystal explanation problematic. Nikolov et al.^{311,312,344} observed stratification not only with micellar surfactant solutions but also with latex suspensions. The heights of the stepwise changes in the film thickness were approximately equal to the diameter of the spherical particles, contained in the foam film.^{311-315,345}

The experimental observations show that stratification is always observed when spherical colloidal particles are present in the film at a sufficiently high volume fraction; therefore, a realistic explanation can be that the stepwise transitions are manifestations of the oscillatory structural forces. The role of the “hard spheres” this time is played by the colloidal particles rather than by the solvent molecules. The mechanism of stratification was studied theoretically in Reference 346, where the appearance and expansion of black spots in the stratifying films were described as being a process of condensation of vacancies in a colloid crystal of ordered micelles within the film.

Two pronounced effects with stratifying films deserve to be mentioned. (1) The increase of electrolyte ionic strength, I_a , leads to smoother and faster thinning of the foam films from ionic surfactant solutions. When I_a becomes high enough, the stepwise transitions disappear.³¹² This can be explained by suppression of the oscillatory structural forces due to decrease of the effective micelle volume fraction because of shrinkage of the counterion atmospheres (see Equation 5.221). (2) In the case of nonionic surfactant micelles, an increase of temperature leads to a similar effect — disappearance of the stepwise character of the film thinning.³¹⁴ This can be attributed to the change of the intermicellar interaction from being repulsive to being attractive with an increase of temperature.³⁴⁷ The electrolyte and temperature dependence of the colloid structural forces provides a tool for the control of the stability of dispersions.

Oscillatory structural forces due to micelles³²⁸ and microemulsion droplets³⁴⁸ were directly measured by means of a surface force balance. The application of interference methods to free vertical stratifying films, containing 100-nm latex particles, showed that the particles form a colloid crystal structure of hexagonal packing inside the films.³⁴⁹ Structuring of latex particles, analogous to stratification, was observed also in wetting films.³⁵⁰ The measured contact angles of stratifying emulsion films, containing surfactant micelles, were found to agree well with Equation 5.219 (see also Equation 5.148).¹⁹² Theoretical modeling of the oscillatory force and the stepwise film thinning by means of the integral equations of statistical mechanics³⁵¹ and numerical simulations^{352,353} has been carried out.

5.4.5.4 Repulsive Hydration and Attractive Hydrophobic Forces

These two surface forces are observed in thin aqueous films. Their appearance is somehow connected with the unique properties of the water as solvent: small molecular size, large dipole moment, high dielectric constant, and formation of an extensive hydrogen bonding network.^{34,354}

5.4.5.4.1 Repulsive Hydration Forces

In their experiments with films from aqueous electrolyte solutions confined between two mica surfaces, Israelachvili et al.^{355,356} and Pashley^{357,358} examined the validity of the DLVO theory at

small film thickness. At electrolyte concentrations below 10^{-4} mol/l (KNO_3 or KCl), they observed the typical DLVO maximum (see Figure 5.13); however, at electrolyte concentrations higher than 10^{-3} mol/l they did not observe the expected DLVO maximum and primary minimum. Instead, a strong short-range repulsion was detected. Empirically, this force, called the hydration repulsion, appears to follow an exponential law:³⁴

$$f_{\text{hydr}}(h) = f_0 e^{-h/\lambda_0} \quad (5.226)$$

where the decay length $\lambda_0 \approx 0.6$ to 1.1 nm for 1:1 electrolytes and f_0 depends on the hydration of the surfaces but is usually about 3 to 30 mJ/m^2 .

The physical importance of the hydration force is that it stabilizes some dispersions preventing coagulation in the primary minimum. It is believed that the hydration force is connected with the binding of strongly hydrated ions at the interface. This is probably the explanation of the experimental results of Healy et al.,³⁵⁹ who found that even high electrolyte concentrations cannot cause coagulation of amphoteric latex particles due to binding of strongly hydrated Li^+ ions at the particle surfaces. If the Li^+ ions are replaced by weakly hydrated Cs^+ ions, the hydration repulsion becomes negligible, compared with the van der Waals attraction, and the particles coagulate as predicted by the DLVO theory. Hence, the hydration repulsion can be regulated by ion exchange.

For now, there is no generally accepted theory of the repulsive hydration forces. The first quantitative theory by Marčelja and Radič³⁶⁰ attributes the hydration repulsion to the water structuring in the vicinity of a surface, which leads to the appearance of a decaying polarization profile. This model was further developed by other authors.^{361,362} A different approach was proposed by Jönsson and Wennerström,³⁶³ who developed an explicit electrostatic model based on the image charge concept. Leikin and Kornyshev³⁶⁴ combined the main features of the solvent polarization³⁶⁰ and image charge³⁶³ models in a nonlocal electrostatic theory of the repulsion between electroneutral lipid bilayers. On the other hand, Israelachvili and Wennerström³⁶⁵ demonstrated that the short-range repulsion between lipid membranes may also be a manifestation of undulation, peristaltic, and protrusion forces, which are due to thermally excited fluctuations at the interfaces (see the next section).

In the case of charged surfaces, Henderson and Lozada-Cassou³⁶⁶ pointed out that the physical origin of the hydration repulsion can be attributed to the presence of a layer of lower dielectric constant, ϵ , in the vicinity of the interface. It was demonstrated that the DLVO theory complemented with such a layer correctly predicts the dependence of hydration repulsion on the electrolyte concentration. A further extension of this approach was given by Basu and Sharma,³⁶⁷ who incorporated the effect of the variation of ϵ in the theory of electrostatic disjoining pressure. Their model provides quantitative agreement with the experimental data at low electrolyte concentration and pH, and qualitative agreement at higher electrolyte concentration and pH.

A further development of the theory³⁶⁸ demonstrates that if the theory of Basu and Sharma³⁶⁷ is further extended by taking into account the finite size of the ions, then quantitative agreement between theory and experiment can be achieved for all electrolyte concentrations and pH. In summary, the hydration repulsion can be attributed to the interplay of the following two effects, which are neglected in the conventional DLVO theory.

The effect of the *dielectric saturation* is due to the presumed preferential alignment of the solvent dipoles near a charged surface. From the viewpoint of the macroscopic continuum theory, this effect is represented by a reduced dielectric permittivity, ϵ , in the vicinity of the interface.^{367,368} We can use the Booth³⁶⁹ formula to relate ϵ with the intensity of the electric field, $E = |d\psi/dx|$:

$$\epsilon(E) = n_r^2 + (\epsilon_b - n_r^2) \frac{3}{\beta E} \left(\coth \beta E - \frac{1}{\beta E} \right), \quad \beta \equiv \frac{5\mu(n_r^2 + 2)}{2kT} \quad (5.227)$$

where $n_p = 1.33$ is the refractive index of water, ϵ_b is the bulk dielectric constant (for $E = 0$), and $\mu = 1.85 \times 10^{-18}$ CGSE units is the dipole moment of water. Equation 5.227 is used by Basu and Sharma³⁶⁷ to calculate the hydration repulsion. However, it turns out that the finite size of the ions also gives a considerable contribution to the hydration repulsion.

The *volume excluded by the ions* becomes important in relatively thin films, insofar as the counterion concentration is markedly higher in the vicinity of a charged surface. This effect was taken into account³⁶⁸ by means of the Bikerman equation:^{370,371}

$$n_i(x) = \frac{1 - v \sum_k n_k(x)}{1 - v \sum_k n_{k0}} n_{i0} \exp U_i \quad (5.228)$$

Here, x is the distance to the charged surface; n_i and U_i are, respectively, the number density and the potential energy (in kT units) of the i th ion in the double electric layer; n_{i0} is the value of n_i in the bulk solution; the summation is carried out over all ionic species; v is the average excluded volume per counterion and can be theoretically estimated³⁶⁸ as equal to eight times the volume of the hydrated counterion.

The electrostatic boundary problem accounting for the effects of dielectric saturation and ionic excluded volume can be formulated as follows.³⁶⁸ The electric potential in the film, $\psi(x)$, satisfies the Poisson equation:

$$\epsilon_0 \frac{d}{dx} \left(\epsilon \frac{d\psi}{dx} \right) = -\rho(x) \quad (5.229)$$

where ϵ is given by Equation 5.227 and the surface charge density, $\rho(x)$, is determined from Equation 5.228:

$$\rho(x) = \frac{\sum_i Z_i e n_i^* \exp U_i}{1 + v \sum_i n_i^* \exp U_i}, \quad n_i^* \equiv \frac{n_{i0}}{1 + v \sum_k n_{k0}} \quad (5.230)$$

The potential energy U_i accounts for both the mean-field electrostatic energy and the energy of hydration³⁶⁷

$$U_i = -\frac{Z_i e \psi + W_i}{kT}, \quad W_i \equiv \frac{Z_i^2 e^2}{d_i} \left[\frac{1}{\epsilon(E)} - \frac{1}{\epsilon_b} \right] \quad (5.231)$$

where d_i is the diameter of the i th ion. The boundary condition of the charged surface reads:

$$\left. \frac{d\psi}{dx} \right|_{x=0} = -\frac{\sigma_s}{\epsilon_0 \epsilon_s}, \quad \epsilon_s \equiv \epsilon|_{x=0} \quad (5.232)$$

where σ_s is determined by the Stern isotherm, Equation 5.183. The boundary problem (Equations 5.229 to 5.232) can be solved numerically. Then, the total electrostatic disjoining pressure can be calculated by means of the expression³⁶⁸

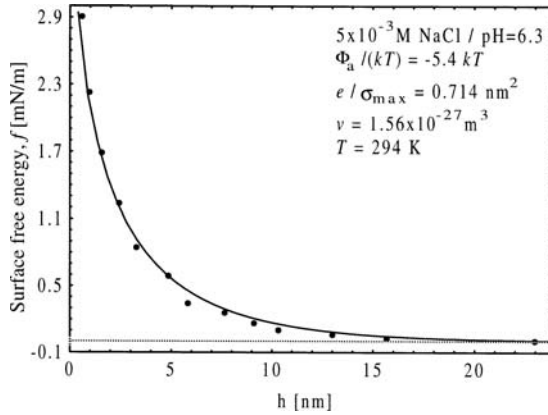


FIGURE 5.29 Comparison of theory³⁶⁸ with experimental data³⁵⁷ measured with solution of 5 mM NaCl at pH = 6.3 between mica surfaces: the total interaction free energy, $f = f_{vw} + f_{el} + f_{hr}$ is plotted against the film thickness h (see Equations 5.162 and 5.233). The solid line is the best fit calculated with adsorption energy $\Phi_a = -5.4 kT$ per Na^+ ion, and area per surface ionizable group 0.714 nm^2 .

$$\Pi_{el}^{tot} \equiv - \int_0^{\psi_m} \rho_m d\psi = \frac{kT}{v} \ln \left[\frac{1 + v \sum_k n_k^* \exp(-Z_i e \psi_m / kT)}{1 + v \sum_k n_k^*} \right] \quad (5.233)$$

where the subscript m denotes values of the respective variables at the midplane of the film. Finally, the non-DLVO hydration force can be determined as an excess over the conventional DLVO electrostatic disjoining pressure:

$$\Pi_{hr} \equiv \Pi_{el}^{tot} - \Pi_{el}^{DLVO} \quad (5.234)$$

where Π_{el}^{DLVO} is defined by Equation 5.178, which can be deduced from Equation 5.233 for $v \rightarrow 0$ and $\epsilon \equiv \epsilon_b$. Note that both the effect of $v \neq 0$ and $\epsilon \neq \epsilon_b$ lead to a larger value of ψ_m , which contributes to a positive (repulsive) Π_{hr} .

The theory³⁶⁸ based on Equations 5.227 to 5.234 gives an excellent numerical agreement with the experimental data of Pashley,^{357,358} Claesson et al.³⁷² and Horn et al.³⁷³ An illustration is given in Figure 5.29, where v is equal to eight times the volume of the hydrated Na^+ ion. In all cases, acceptable values of the adjustable parameters, σ_{max} and $\Phi_a = -\Delta\mu_2^{(0)}$ in the Stern isotherm are obtained (see Equations 5.49 and 5.183). It is interesting to note that in all investigated cases the effect of $v \neq 0$ gives about four times larger contribution in Π_{hr} compared to the effect of $\epsilon \neq \epsilon_b$.

5.4.5.4.2 Hydrophobic Attraction

Water does not spread spontaneously on hydrocarbons and the aqueous films on hydrocarbons are rather unstable.³⁷⁴ The cause for these effects is a strong attractive *hydrophobic* force, which is found to appear in aqueous films in contact with hydrophobic surfaces. The experiments showed that the nature of the hydrophobic surface force is different from the van der Waals and double layer interactions.³⁷⁵⁻³⁷⁹ It turns out that the hydrophobic interaction decays exponentially with the increase of the film thickness, h . The hydrophobic free energy per unit area of the film can be described by means of the equation:³⁴

$$f_{hydrophobic} = -2\gamma e^{-h/\lambda_0} \quad (5.235)$$

where typically $\gamma = 10$ to 50 mJ/m^2 , and $\lambda_0 = 1$ to 2 nm in the range $0 < h < 10 \text{ nm}$. Larger decay length, $\lambda_0 = 12$ to 16 nm , was reported by Christenson et al.³⁷⁹ for the range $20 < h < 90 \text{ nm}$. This amazingly long-range attraction entirely dominates the van der Waals forces. In particular, it can create rupture of foam films containing small oil droplets or larger hydrophobic surfaces. Ducker et al.³⁸⁰ measured the force between hydrophobic and hydrophilic silica particles and air bubbles by means of an atomic force microscope.

It was found experimentally that 1:1 and 2:2 electrolytes reduce considerably the long-range part of the hydrophobic attraction.^{378,379} The results suggest that this reduction is due to ion adsorption or ion exchange at the surfaces rather than to the presence of electrolyte in the solution itself. Therefore, the physical implication (which might seem trivial) is that the hydrophobic attraction across aqueous films can be suppressed by making the surfaces more hydrophilic. Besides, some special polar solutes are found to suppress the hydrophobic interaction at molecular level in the bulk solution, e.g., urea, $(\text{NH}_2)_2\text{CO}$, dissolved in water can cause proteins to unfold. The polar solutes are believed to destroy the hydrogen bond structuring in water; therefore, they are sometimes called chaotropic agents.³⁴

There is no generally accepted explanation of hydrophobic forces. Nevertheless, many authors agree that hydrogen bonding in water and other associated liquids is the main underlying factor.^{34,381} One possible qualitative picture of the hydrophobic interaction is the following. If there were no thermal motion, the water molecules would form an icelike tetrahedral network with four nearest neighbors per molecule (instead of 12 neighbors at close packing), since this configuration is favored by the hydrogen bond formation. However, due to the thermal motion a water molecule forms only about 3 to 3.5 transient hydrogen bonds with its neighbors in the liquid³⁸² with the lifetime of a hydrogen bond of about 10^{-11} s . When a water molecule is brought in contact with a nonhydrogen bonding molecule or surface, the number of its possible favorable configurations is decreased. This effect also reduces the number of advantageous configurations of the neighbors of the subsurface water molecules and some ordering propagates in the depth of the liquid. This ordering might be initiated by the orientation of the water dipoles at a water–air or water–hydrocarbon interface, with the oxygen atom oriented toward the hydrophobic phase.^{383–386} Such ordering in the vicinity of the hydrophobic wall is entropically unfavorable. When two hydrophobic surfaces approach each other, the entropically disfavored water is ejected into the bulk, thereby reducing the total free energy of the system. The resulting attraction can in principle explain the hydrophobic forces. However, the existing theory³⁸¹ is still far from a quantitative explanation for the experimental data.

Another hypothesis for the physical origin of the hydrophobic force considers a possible role of formation of gaseous capillary bridges between the two hydrophobic surfaces (see [Figure 5.9a](#)).^{34,387,388} In this case, the hydrophobic force would be a kind of capillary-bridge force (see chapter 11 in Reference 35). Such bridges could appear spontaneously, by nucleation (spontaneous dewetting), when the distance between the two surfaces becomes smaller than a certain threshold value, of the order of several hundred nanometers. Gaseous bridges could appear even if there is no dissolved gas in the water phase; the pressure inside a bridge can be as low as the equilibrium vapor pressure of water (23.8 mmHg at 25°C) owing to the high interfacial curvature of nodoid-shaped bridges (see Section 5.3.1.2.3 and Reference 35). A number of studies^{389–397} provide evidence in support of the capillary-bridge origin of the long-range hydrophobic surface force. In particular, the observation of “steps” in the experimental data was interpreted as an indication for separate acts of bridge nucleation.³⁹³

In summary, it is more likely that two different effects are called hydrophobic interaction: (1) the known molecular hydrophobic effect,^{34,398} which could bring about a relatively short-range attractive surface force,^{381,399} and (2) formation of capillary bridges-cavities between two hydrophobic surfaces.^{387–397} For now, there is sufficient evidence showing that both effects exist in reality, often in interplay with each other.

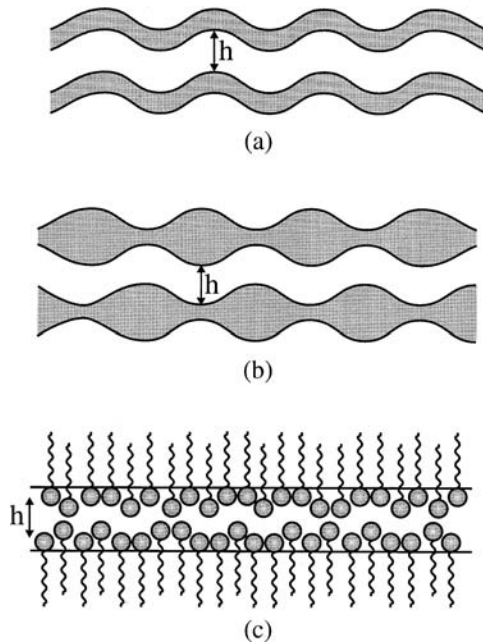


FIGURE 5.30 Surface forces due to configurational confinement of thermally excited modes into a narrow region of space between two approaching interfaces: (a) bending mode of membrane fluctuations giving rise to the undulation force; (b) squeezing mode of membrane fluctuations producing the peristaltic force; (c) fluctuating protrusion of adsorbed amphiphilic molecules engendering the protrusion surface force.

5.4.5.5 Fluctuation Wave Forces

All fluid interfaces, including lipid membranes and surfactant lamellas, are involved in a thermal fluctuation wave motion. The configurational confinement of such thermally excited modes within the narrow space between two approaching interfaces gives rise to short-range repulsive surface forces, which are considered below.

5.4.5.5.1 Undulation Forces

The undulation force arises from the configurational confinement related to the *bending mode* of deformation of two fluid bilayers. This mode consists in undulation of the bilayer at constant bilayer area and thickness (Figure 5.30a). Helfrich et al.^{400,401} established that two such bilayers, apart at a mean distance h , experience a repulsive disjoining pressure given by the expression:

$$\Pi_{\text{und}}(h) = \frac{3\pi^2 (kT)^2}{64 k_t h^3} \quad (5.236)$$

where k_t is the bending elastic modulus of the bilayer as a whole. The experiment⁴⁰² and the theory^{35,133} show that k_t is of the order of 10^{-19} J for lipid bilayers. The undulation force has been measured, and the dependence $\Pi_{\text{und}} \propto h^{-3}$ confirmed experimentally.⁴⁰³⁻⁴⁰⁵

5.4.5.5.2 Peristaltic Force

The peristaltic force³⁶⁵ originates from the configurational confinement related to the peristaltic (squeezing) mode of deformation of a fluid bilayer (Figure 5.30b). This mode of deformation consists in fluctuation of the bilayer thickness at a fixed position of the bilayer midsurface. The

peristaltic deformation is accompanied with extension of the bilayer surfaces. Israelachvili and Wennerström³⁶⁵ demonstrated that the peristaltic disjoining pressure is related to the stretching modulus, k_s , of the bilayer:

$$\Pi_{\text{per}}(h) \approx \frac{2(kT)^2}{\pi^2 k_s h^5} \quad (5.237)$$

The experiment⁴⁰⁶ gives values of k_s varying between 135 and 500 mN/m, depending on temperature and composition of the lipid membrane.

5.4.5.6 Protrusion Force

Because of the thermal motion, the protrusion of an amphiphilic molecule in an adsorption monolayer (or micelle) may fluctuate about the equilibrium position of the molecule (Figure 5.30c). In other words, the adsorbed molecules are involved in a discrete wave motion, which differs from the continuous modes of deformation considered above. Aniansson et al.^{407,408} analyzed the energy of protrusion in relation to the micelle kinetics. These authors assumed the energy of molecular protrusion to be of the form $u(z) = \alpha z$, where z is the distance out of the surface ($z > 0$) and determined $\alpha \approx 3 \times 10^{-11}$ J/m for single-chained surfactants. The average length of the Brownian protrusion of the amphiphilic molecules is on the order of $\lambda \equiv kT/\alpha$.³⁶⁵

By using a mean-field approach Israelachvili and Wennerström³⁶⁵ derived the following expression for the protrusion disjoining pressure, which appears when two protrusion zones overlap (Figure 5.30c):

$$\Pi_{\text{protr}}(h) = \frac{\Gamma kT}{\lambda} \frac{(h/\lambda) \exp(-h/\lambda)}{1 - (1 + h/\lambda) \exp(-h/\lambda)} \quad (5.238)$$

where λ is the characteristic protrusion length; $\lambda = 0.14$ nm at 25°C for surfactants with paraffin chain; Γ denotes the number of protrusion sites per unit area. Note that Π_{protr} decays exponentially for $h \gg \lambda$, but $\Pi_{\text{protr}} \propto h^{-1}$ for $h < \lambda$, i.e., Π_{protr} is divergent at $h \rightarrow 0$. The respective interaction free energy (per unit film area) is

$$f_{\text{protr}} = \int_h^\infty \Pi_{\text{protr}}(\hat{h}) d\hat{h} = -\Gamma kT \ln [1 - (1 - h/\lambda) \exp(-h/\lambda)] \quad (5.239)$$

Equation 5.238 was found to fit experimental data well for the disjoining pressure of liquid films stabilized by adsorbed protein molecules: bovine serum albumin (BSA).⁴⁰⁹ In that case, Γ was identified with the surface density of the loose secondary protein adsorption layer, while λ turned out to be about the size of the BSA molecule.⁴⁰⁹

5.5 HYDRODYNAMIC INTERACTIONS IN DISPERSIONS

5.5.1 BASIC EQUATIONS AND LUBRICATION APPROXIMATION

In addition to the surface forces (see Section 5.4 above), two colliding particles in a liquid medium also experience hydrodynamic interactions due to the viscous friction, which can be rather long range (operative even at distances above 100 nm). The hydrodynamic interaction among particles depends on both the type of fluid motion and the type of interfaces. The quantitative description

of this interaction is based on the classical laws of mass conservation and momentum balance for the bulk phases:⁴¹⁰⁻⁴¹⁵

$$\frac{\partial \rho}{\partial t} + \text{div}(\rho \mathbf{v}) = 0 \quad (5.240)$$

$$\frac{\partial}{\partial t}(\rho \mathbf{v}) + \text{div}(\rho \mathbf{v} \mathbf{v} - \mathbf{P} - \mathbf{P}_b) = 0 \quad (5.241)$$

where ρ is the mass density, \mathbf{v} is the local mass average velocity, \mathbf{P} is the hydrodynamic stress tensor; \mathbf{P}_b is the body-force tensor which accounts for the action of body forces such as gravity, electrostatic forces (the Maxwell tensor), etc. In a fluid at rest, and in the absence of body forces, the only contact force given by the hydrodynamic stress tensor is the scalar thermodynamic pressure, p , and \mathbf{P} can be written as $\mathbf{P} = -p\mathbf{I}$, where \mathbf{I} is the unit tensor in space. For a fluid in motion, the viscous forces become operative and

$$\mathbf{P} = -p\mathbf{I} + \mathbf{T} \quad (5.242)$$

where \mathbf{T} is the viscous stress tensor. From the definition of the stress tensor (Equation 5.242), it follows that the resultant hydrodynamic force, \mathbf{F} , exerted by the surrounding fluid on the particle surface, S , and the torque, \mathbf{M} , applied to it are given by the expressions^{410,412}

$$\mathbf{F} = \int_S \mathbf{P} \cdot \mathbf{n} \, dS, \quad \mathbf{M} = \int_S \mathbf{r}_0 \times \mathbf{P} \cdot \mathbf{n} \, dS \quad (5.243)$$

where \mathbf{r}_0 is the position vector of a point of S with respect to an arbitrarily chosen coordinate origin, and \mathbf{n} is the vector of the running unit normal to the surface S . In the presence of body forces, the total force, \mathbf{F}_{tot} , and torque, \mathbf{M}_{tot} , acting on the particle surface are

$$\mathbf{F}_{\text{tot}} = \mathbf{F} + \int_S \mathbf{P}_b \cdot \mathbf{n} \, dS, \quad \mathbf{M}_{\text{tot}} = \mathbf{M} + \int_S \mathbf{r}_0 \times \mathbf{P}_b \cdot \mathbf{n} \, dS \quad (5.244)$$

The dependence of the viscous stress on the velocity gradient in the fluid is a constitutive law, which is usually called the bulk rheological equation. The general linear relation between the viscous stress tensor, \mathbf{T} , and the rate of strain tensor,

$$\mathbf{D} = \frac{1}{2} [\nabla \mathbf{v} + (\nabla \mathbf{v})^T] \quad (5.245)$$

(the superscript T denotes conjugation) reads

$$\mathbf{T} = \zeta (\text{div } \mathbf{v}) \mathbf{I} + 2\eta \left[\mathbf{D} - \frac{1}{3} (\text{div } \mathbf{v}) \mathbf{I} \right] \quad (5.246)$$

The latter equation is usually referred as the Newtonian model or Newton's law of viscosity. In Equation 5.246, ζ is the dilatational bulk viscosity and η is the shear bulk viscosity. The usual liquids comply well with the Newtonian model. On the other hand, some concentrated macromolecular

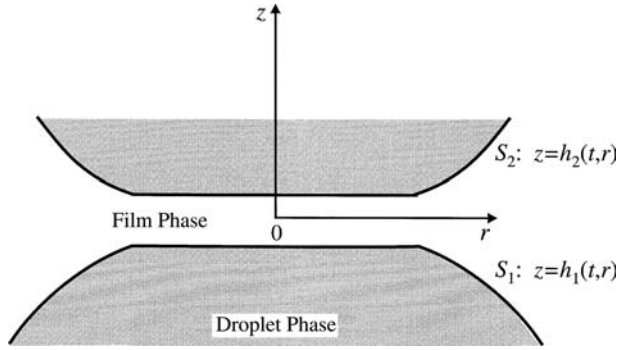


FIGURE 5.31 Sketch of a plane-parallel film formed between two identical fluid particles.

solutions, colloidal dispersions, gels, etc., may exhibit non-Newtonian behavior; their properties are considered in detail in some recent review articles and books.⁴¹⁵⁻⁴¹⁸ From Equations 5.241 and 5.246, we obtain the Navier–Stokes equation:^{419,420}

$$\rho \frac{d\mathbf{v}}{dt} = -\nabla p + \left(\zeta + \frac{1}{3}\eta \right) \nabla(\nabla \cdot \mathbf{v}) + \eta \nabla^2 \mathbf{v} + \mathbf{f}, \quad (\mathbf{f} \equiv \nabla \cdot \mathbf{P}_b) \quad (5.247)$$

for homogeneous Newtonian fluids, for which the dilatational and shear viscosities, ζ and η , do not depend on the spatial coordinates. In Equation 5.247, the material derivative d/dt can be presented as a sum of a local time derivative and a convective term:

$$\frac{d}{dt} = \frac{\partial}{\partial t} + (\mathbf{v} \cdot \nabla) \quad (5.248)$$

If the density, ρ , is constant, the equation of mass conservation (Equation 5.240) and the Navier–Stokes Equation 5.247 reduce to

$$\text{div } \mathbf{v} = 0, \quad \rho \frac{d\mathbf{v}}{dt} = -\nabla p + \eta \nabla^2 \mathbf{v} + \mathbf{f} \quad (5.249)$$

For low shear stresses in the dispersions, the characteristic velocity, V_z , of the relative particle motion is small enough for the Reynolds number, $\text{Re} = \rho V_z L / \eta$, to be a small parameter, where L is a characteristic length scale. In this case, the inertia terms in Equations 5.247 and 5.249 can be neglected. Then, the system of equations becomes linear and the different types of hydrodynamic motion become additive;^{278,421,422} e.g., the motion in the liquid flow can be presented as a superposition of elementary translation and rotational motions.

The basic equations can be further simplified in the framework of the lubrication approximation, which can be applied to the case when the Reynolds number is small and when the distances between the particle surfaces are much smaller than their radii of curvature (Figure 5.31).^{423,424} There are two ways to take into account the molecular interactions between the two particles across the liquid film intervening between them: (1) the body force approach; (2) the disjoining pressure approach. The former approach treats the molecular forces as components of the body force, \mathbf{f}

(Equation 5.247); consequently, they give contributions to the normal and tangential stress boundary conditions.^{425,426} In case (2), the molecular interactions are incorporated only in the normal stress boundary conditions at the particle surfaces. When the body force can be expressed as a gradient of potential, $\mathbf{f} = \nabla U$ (that is, $\mathbf{P}_b = U\mathbf{I}$), the two approaches are equivalent.⁴²⁷

If two particles are interacting across an electrolyte solution, the equations of continuity and the momentum balance, Equation 5.249, in lubrication approximation reads⁴²⁸

$$\nabla_{\parallel} \cdot \mathbf{v}_{\parallel} + \frac{\partial v_z}{\partial z} = 0, \quad \eta \frac{\partial^2 \mathbf{v}_{\parallel}}{\partial z^2} = \nabla_{\parallel} \cdot p + kT \sum_{i=1}^N z_i c_i \nabla_{\parallel} \Phi, \quad \frac{\partial p}{\partial z} + kT \sum_{i=1}^N z_i c_i \frac{\partial \Phi}{\partial z} = 0 \quad (5.250)$$

where \mathbf{v}_{\parallel} and ∇_{\parallel} are the projection of the velocity and the gradient operator on the plane xy ; the z axis is (approximately) perpendicular to the film surfaces S_1 and S_2 (see Figure 5.31); $c_i = c_i(r, z, t)$ is the ion concentration ($i = 1, 2, \dots, N$); Φ is the dimensionless electric potential (see Sections 5.2.1.2 and 5.2.2). It turns out that in lubrication approximation, the dependence of the ionic concentrations on the z coordinate comes through the electric potential $\Phi(r, z, t)$: we obtain a counterpart of the Boltzmann equation $c_i = c_{i,n}(r, z, t) \exp(-z_i \Phi)$, where $c_{i,n}$ refers to an imaginary situation of “switched off” electric charges ($\Phi \equiv 0$). The kinematic boundary condition for the film surfaces has the form:

$$\frac{\partial h_j}{\partial t} + \mathbf{u}_j \cdot \nabla_{\parallel} h_j = (v_z)_j \quad \text{at} \quad S_j \quad (j=1,2) \quad (5.251)$$

where \mathbf{u}_j is the velocity projection in the plane xy at the corresponding film surface, S_j , which is close to the interfacial velocity; $(v_z)_j$ is the z component of the velocity at the surface S_j . The general solution of Equations 5.250 and 5.251 could be written as

$$p = p_n + kT \sum_{i=1}^N (c_i - c_{i,n}) \quad (5.252)$$

$$\begin{aligned} \mathbf{v}_{\parallel} = & \frac{(z-h_1)(z-h_2)}{2\eta} \nabla_{\parallel} p_n + \frac{h_2-z}{h} \mathbf{u}_1 + \frac{z-h_1}{h} \mathbf{u}_2 \\ & + \frac{kTh^2}{4\eta} \sum_{i=1}^N \left[m_{2,i}(z) - \frac{h_2-z}{h} m_{2,i}(h_1) - \frac{z-h_1}{h} m_{2,i}(h_2) \right] \nabla_{\parallel} c_{i,n} \end{aligned} \quad (5.253)$$

Here $h = h_2 - h_1$ is the local film thickness; the meaning of $p_n(x, y, t)$ is analogous to that of $c_{i,n}(x, y, t)$; the functions, $m_{k,i}(z)$, account for the distribution of the i th ionic species in the EDL:

$$m_{0,i} \equiv \exp(-z_i \Phi) - 1, \quad m_{k,i}(z) \equiv \frac{2}{h} \int_0^z m_{k-1,i}(\hat{z}) d\hat{z} \quad (k = 1, 2, 3, i = 1, 2, \dots, N) \quad (5.254)$$

The equation determining the local thickness, h , of a film with fluid surfaces (or, alternatively, determining the pressure distribution at the surfaces of the gap between two solid particles of known shape) is

$$\frac{\partial h}{\partial t} + \nabla_{\parallel} \cdot \left[\frac{h}{2} (\mathbf{u}_1 + \mathbf{u}_2) \right] = \frac{1}{12\eta} \nabla_{\parallel} \cdot (h^3 \nabla_{\parallel} p) + \frac{kT}{8\eta} \nabla_{\parallel} \cdot \left\{ h^3 \sum_{i=1}^N [m_{2,i}(h_1) + m_{2,i}(h_2) - m_{3,i}(h_2) + m_{3,i}(h_1)] \nabla_{\parallel} c_{i,n} \right\} \quad (5.255)$$

The problem for the interactions upon central collisions of two axisymmetric particles (bubbles, droplets, or solid spheres) at small surface-to-surface distances was first solved by Reynolds⁴²³ and Taylor⁴²⁹ for solid surfaces and by Ivanov et al.^{430,431} for films of uneven thickness. Equation 5.255 is referred to as the general equation for films with deformable surfaces^{430,431} (see also the more recent reviews^{164,289,432}). The asymptotic analysis⁴³³⁻⁴³⁵ of the dependence of the drag and torque coefficient of a sphere, which is translating and rotating in the neighborhood of a solid plate, is also based on Equation 5.255 applied to the special case of stationary conditions.

Using Equation 5.244, we can obtain expressions for the components of the total force exerted on the particle surface, S , in the lubrication approximation:

$$F_{\text{tot},z} = \int_S \left[p_n + kT \sum_{i=1}^N (c_{is} - c_{i,n}) + \Pi_{\text{nel}} - p_{\infty} \right] dS \quad (5.256)$$

$$\mathbf{F}_{\text{tot},\parallel} = - \int_S \left(\eta \frac{\partial \mathbf{v}_{\parallel}}{\partial z} + \frac{2kT}{\kappa_c^2} \frac{\partial \Phi}{\partial z} \nabla_{\parallel} \Phi \right) dS \quad (5.257)$$

where p_{∞} is the pressure at infinity in the meniscus region (Figure 5.31) and $\Pi_{\text{nel}} \equiv \Pi - \Pi_{\text{el}}$ accounts for the contribution of non-electrostatic (non-double-layer) forces to the disjoining pressure (see Section 5.4). The normal and the lateral force resultants, F_z and \mathbf{F}_{\parallel} , are the hydrodynamic resistance and shear force, respectively.

5.5.2 INTERACTION BETWEEN PARTICLES OF TANGENTIALLY IMMOBILE SURFACES

The surfaces of fluid particles can be treated as tangentially immobile when they are covered by dense surfactant adsorption monolayers that can resist tangential stresses.^{164,289,432,436,437} In such a case, the bubbles or droplets behave as flexible balls with immobile surfaces. When the fluid particles are rather small (say, microemulsion droplets), they can behave like hard spheres; therefore, some relations considered below, which were originally derived for solid particles, can be also applied to fluid particles.

5.5.2.1 Taylor and Reynolds Equations, and Influence of the Particle Shape

In the case of two axisymmetric particles moving along the z axis toward each other with velocity $V_z = -dh/dt$ Equation 5.255 can be integrated, and from Equation 5.256 the resistance force can be calculated. The latter turns out to be proportional to the velocity and bulk viscosity and depends on the shape in a complex way. For particles with tangentially immobile surfaces and without surface electric charge ($\mathbf{u}_1 = \mathbf{u}_2 = 0$, $\Phi = 0$), Charles and Mason⁴³⁸ have derived

$$F_z = 6\pi\eta V_z \int_0^{\infty} \frac{r^3}{h^3} dr \quad (5.258)$$

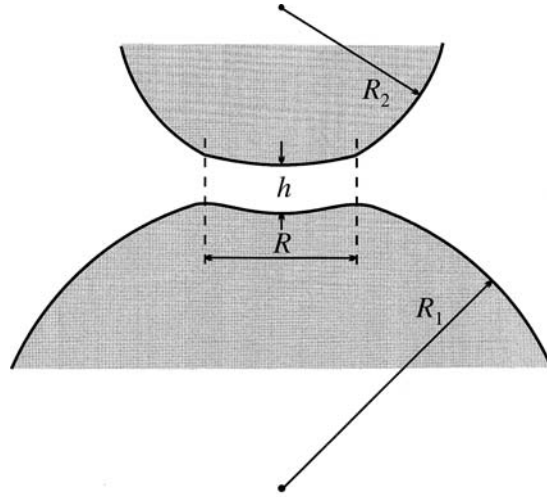


FIGURE 5.32 Sketch of a film between two nonidentical fluid particles of radii R_1 and R_2 . The film thickness and radius are denoted by h and R .

where r is the radial coordinate in a cylindrical coordinate system. In the case of two particles of different radii, R_1 and R_2 , film radius R , and uniform film thickness h (Figure 5.32), from Equation 5.258 the following expression can be derived:^{439,440}

$$F_z = \frac{3}{2} \pi \eta V_z \frac{R_*^2}{h} \left(1 + \frac{R^2}{h R_*} + \frac{R^4}{h^2 R_*^2} \right), \quad R_* \equiv 2R_1 R_2 / (R_1 + R_2) \quad (5.259)$$

This geometric configuration has proved to be very close to the real one in the presence of electrostatic disjoining pressure.¹⁸⁰ The Charles–Mason formula (Equation 5.258) and Equation 5.256 have been used to calculate the velocity of film thinning for a large number of cases, summarized by Hartland⁴⁴¹ in tables for more than 50 cases (two- and three-dimensional small drops, fully deformed large drops subjected to large forces, two-dimensional hexagonal drops, etc.).

Setting $R = 0$ in Equation 5.259, we can derive a generalized version of the Taylor formula⁴²⁹ for the velocity of approach of two nondeformable spheres under the action of an external (non-viscous) force, F_z .⁴⁴⁰

$$V_{Ta} = \frac{2hF_z}{3\pi\eta R_*^2} \quad (5.260)$$

When a solid sphere of radius R_c approaches a flat solid surface, we may use the Taylor formula with $R_* = 2R_c$ when the gap between the two surfaces is small compared to R_c .

In the case when two plane-parallel ellipsoidal disks of tangentially immobile surfaces are moving against each other under the action of an external force, $F_{tot,z}$, from Equations 5.255 and 5.256, we can derive the Reynolds equation⁴²³ for the velocity of film thinning:

$$V_{Re} = \frac{F_z h^3 (a^2 + b^2)}{3\pi\eta a^3 b^3} \quad (5.261)$$

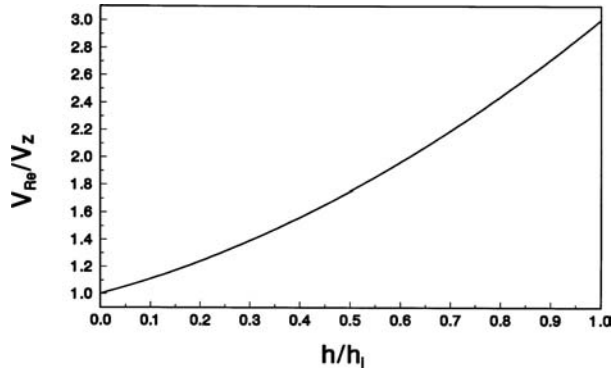


FIGURE 5.33 Plot of V_{Re}/V_z vs. h/h_i for two fluid particles (Equation 5.259) which are deformed because of the viscous friction in the transition zone between the film and the bulk phase (see Figure 5.32).

where a and b are the principal radii of curvature. If there is a contribution of the disjoining pressure, Π , the Reynolds equation for a flat axisymmetric film ($a = b = R$) between two fluid particles of capillary pressure P_c can be written in the form:¹⁴³

$$V_{Re} = \frac{2F_c h^3}{3\pi\eta R^4} = \frac{2(P_c - \Pi)h^3}{3\eta R^2} \quad (5.262)$$

From Equations 5.259 and 5.262 the ratio between the Reynolds velocity and the velocity of film thinning for a given force is obtained. In Figure 5.33, this ratio is plotted as a function of the film thickness, h , divided by inversion thickness, $h_i = R^2/R_c$.⁴³² We see that the influence of the viscous friction in the zone encircling the film (this influence is not accounted for in Equation 5.262) decreases the velocity of thinning about three times for the larger distances, whereas for the small distances this influence vanishes. From Equations 5.259 and 5.260, the ratio between the Taylor velocity (corresponding to nondeformable spheres) and the approaching velocity of two deformable particles can be calculated. The dependence of this ratio on the distance between the particles for different film radii is illustrated in Figure 5.34. We see that an increase of the film radius, R , and a decrease of the distance, h , lead to a decrease in the velocity. The existence of a film between the particles can decrease the velocity of particle approach, V_z , by several orders of magnitude.

5.5.2.2 Interactions among Nondeformable Particles at Large Distances

The hydrodynamic interaction between members of a group of small particles suspended in a viscous fluid has fundamental importance for the development of adequate models for calculating the particle collective diffusion coefficient and the effective viscosity of suspension.^{278,421,437,442,443} The Stokesian resistance is determined for a number of specific particle shapes under the condition that the particles are located so far apart that the hydrodynamic interactions can be ignored.⁴²¹ A general theory applicable to a single particle of arbitrary shape has been developed by Brenner.^{444,445} This method gives the first-order correction (with respect to the particle volume fraction) of the viscosity and diffusivity. Matrix relations between resistance and velocity for the pure translational and rotational motions of the members of a general multiparticle system involved in a linear shear flow are given by Brenner and O'Neill.⁴⁴⁶ In principle, from these relations we can further obtain the higher-order terms in the series expansion of the viscosity and diffusivity with respect to the powers of the particle volume fraction.

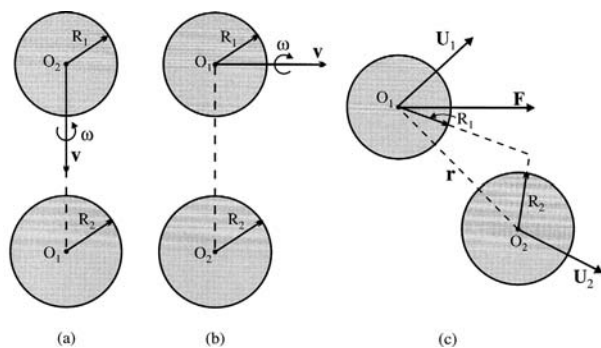


FIGURE 5.35 Types of hydrodynamic interactions between two spherical particles: (a) motion along and rotation around the line of centers; (b) motion along and rotation around an axis perpendicular to the line of centers; (c) the first particle moves under the action of an applied external force, F , whereas the second particle is subjected to the hydrodynamic disturbance created by the motion of the first particle.

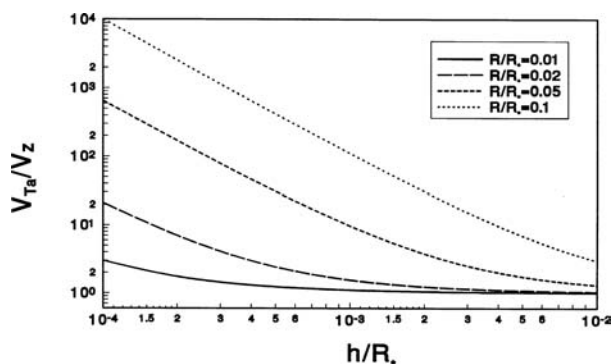


FIGURE 5.34 Plot of V_{Ta}/V_z vs. h/R_s for various values of the dimensionless film radius, R/R_s . V_{Ta} corresponds to two nondeformed (spherical) particles (Equation 5.260), whereas V_z is the velocity of approach of two deformed particles (Equation 5.259).

At present, the only multiparticle system for which exact values of the resistance tensors can be determined is that of two spheres. It turns out that all types of hydrodynamic flows related to the motion of two spherical particles (of radii R_1 and R_2) can be expressed as superpositions of the elementary processes depicted in Figure 5.35.^{278,412,421,422,447-456}

The first particle moves toward the second immobile particle and rotates around the line of centers (see Figure 5.35a). This is an axisymmetric rotation problem (a two-dimensional hydrodynamic problem) which was solved by Jeffery⁴⁴⁸ and Stimson and Jeffery⁴⁴⁹ for two identical spheres moving with equal velocities along their line of centers. Cooley and O'Neill^{450,451} calculated the forces for two nonidentical spheres moving with the same speed in the same direction or, alternatively, moving toward each other. A combination of these results permits evaluation of the total forces and torques acting on the particles.

The first particle then moves along an axis perpendicular to the center line and rotates around this axis, whereas the second particle is immobile; see Figure 5.35b (this is a typical three-dimensional hydrodynamic problem). The contribution of this asymmetric motion of the spheres to the resistance tensors was determined by Davis⁴⁵² and O'Neill and Majumdar.⁴⁵³

The first particle moves with linear velocity, \mathbf{U}_1 , under the action of an applied external force, \mathbf{F} , whereas the second particle is subjected to the hydrodynamic disturbances (created by the motion of the first particle) and moves with a linear velocity, \mathbf{U}_2 (see Figure 5.35c). As a rule, this is a three-dimensional hydrodynamic problem. For this case, Batchelor⁴⁵⁷ and Batchelor and Wen⁴⁵⁸ have derived the following expressions for the instantaneous translational velocities of the two particles in an otherwise quiescent and unbounded fluid:

$$\mathbf{U}_1 = \frac{\mathbf{F}}{6\pi\eta R_1} \cdot \left[A_{11}(r) \frac{\mathbf{r}\mathbf{r}}{r^2} + B_{11}(r) \left(\mathbf{I} - \frac{\mathbf{r}\mathbf{r}}{r^2} \right) \right] \quad (5.263)$$

$$\mathbf{U}_2 = \frac{\mathbf{F}}{6\pi\eta(R_1 + R_2)} \cdot \left[A_{12}(r) \frac{\mathbf{r}\mathbf{r}}{r^2} + B_{12}(r) \left(\mathbf{I} - \frac{\mathbf{r}\mathbf{r}}{r^2} \right) \right] \quad (5.264)$$

where \mathbf{r} is the vector connecting the particle centers and $r = |\mathbf{r}|$. Expressions for the mobility functions A_{ij} and B_{ij} ($i, j = 1, 2$) at large values of the dimensionless distance $s = 2r/(R_1 + R_2)$ and comparable particle radii $\lambda = R_2/R_1 = O(1)$ have been derived by Jeffrey and Onishi⁴⁵⁹ and Davis and Hill.⁴⁵⁶ The derived far-field expansions are

$$\begin{aligned} 1 - B_{11} &= \frac{68\lambda^5}{(1+\lambda)^6 s^6} + \frac{32\lambda^3(10 - 9\lambda^2 + 9\lambda^4)}{(1+\lambda)^8 s^8} + \frac{192\lambda^5(35 - 18\lambda^2 + 6\lambda^4)}{(1+\lambda)^{10} s^{10}} + O(s^{-12}) \\ B_{11} - A_{11} &= \frac{60\lambda^3}{(1+\lambda)^4 s^4} - \frac{60\lambda^3(8 - \lambda^2)}{(1+\lambda)^6 s^6} + \frac{32\lambda^3(20 - 123\lambda^2 + 9\lambda^4)}{(1+\lambda)^8 s^8} \\ &\quad + \frac{64\lambda^2(175 + 1500\lambda - 426\lambda^2 + 18\lambda^4)}{(1+\lambda)^{10} s^{10}} + O(s^{-12}) \\ A_{11} - \frac{2A_{12}}{1+\lambda} &= 1 - \frac{3}{(1+\lambda)s} + \frac{4(1+\lambda^2)}{(1+\lambda)^3 s^3} - \frac{60\lambda^3}{(1+\lambda)^4 s^4} + \frac{32\lambda^3(15 - 4\lambda^2)}{(1+\lambda)^6 s^6} - \frac{2400\lambda^3}{(1+\lambda)^7 s^7} \\ &\quad - \frac{192\lambda^3(5 - 22\lambda^2 + 3\lambda^4)}{(1+\lambda)^8 s^8} + \frac{1920\lambda^3(1+\lambda^2)}{(1+\lambda)^9 s^9} - \frac{256\lambda^5(70 - 375\lambda - 120\lambda^2 + 9\lambda^3)}{(1+\lambda)^{10} s^{10}} \\ &\quad - \frac{1536\lambda^3(10 - 151\lambda^2 + 10\lambda^4)}{(1+\lambda)^{11} s^{11}} + O(s^{-12}) \\ B_{11} - \frac{2B_{12}}{1+\lambda} &= 1 - \frac{3}{2(1+\lambda)s} - \frac{2(1+\lambda^2)}{(1+\lambda)^3 s^3} - \frac{68\lambda^5}{(1+\lambda)^6 s^6} - \frac{32\lambda^3(10 - 9\lambda^2 + 9\lambda^4)}{(1+\lambda)^8 s^8} \\ &\quad - \frac{192\lambda^5(35 - 18\lambda^2 + 6\lambda^4)}{(1+\lambda)^{10} s^{10}} - \frac{16\lambda^3(560 - 553\lambda^2 + 560\lambda^4)}{(1+\lambda)^{11} s^{11}} + O(s^{-12}) \end{aligned} \quad (5.265)$$

In the case of a small heavy sphere falling through a suspension of large particles (fixed in space), we have $\lambda \gg 1$; the respective expansions, corresponding to Equation 5.265, were obtained by Fuentes et al.⁴⁶⁰ In the opposite case, when $\lambda \ll 1$, the suspension of small background spheres will reduce the mean velocity of a large heavy particle (as compared with its Stokes velocity⁴⁶¹) because the suspension behaves as an effective fluid of larger viscosity as predicted by the Einstein viscosity formula.^{457,460}

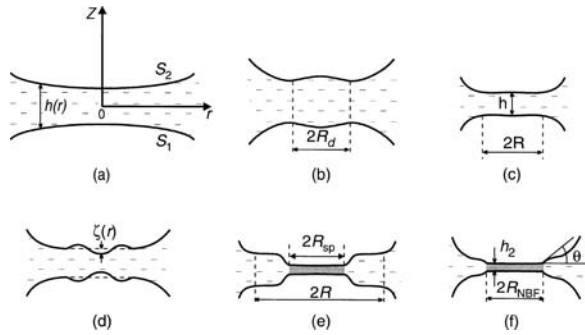


FIGURE 5.36 Main stages of formation and evolution of a thin liquid film between two bubbles or drops: (a) mutual approach of slightly deformed surfaces; (b) at a given separation, the curvature at the center inverts its sign and a dimple arises; (c) the dimple disappears, and eventually an almost plane-parallel film forms; (d) due to thermal fluctuations or other disturbances the film either ruptures or transforms into a thinner Newton black film (e), which expands until reaching the final equilibrium state (f).

5.5.2.3 Stages of Thinning of a Liquid Film

Experimental and theoretical investigations^{162,170,289,432,437,462,463} show that during the approach of two fluid colloidal particles, a flat liquid film can appear between their closest regions (see Figure 5.23). The hydrodynamic interactions as well as the buoyancy, the Brownian, electrostatic, van der Waals, and steric forces and other interactions can be involved in film formation.^{134,180,439,464,465} The formation and the evolution of a foam or emulsion film usually follows the stages shown in Figure 5.36.

Under the action of an outer driving force, the fluid particles approach each other. The hydrodynamic interaction is stronger at the front zones and leads to a weak deformation of the interfaces in this front region. In this case, the usual hydrodynamic capillary number, $Ca = \eta V_z / \sigma$, which is a small parameter for nondeformable surfaces, should be modified to read $Ca = \eta V_z R_s / \sigma h$, where the distance, h , between the interfaces is taken into account. The shape of the gap between two drops for different characteristic times was calculated numerically by many authors.^{465–485} Experimental investigation of these effects for symmetric and asymmetric drainage of foam films were carried out by Joye et al.^{474,475} In some special cases, the deformation of the fluid particle can be very fast: for example, the bursting of a small air bubble at an air–water interface is accompanied by a complex motion resulting in the production of a high-speed liquid jet (see Boulton-Stone and Blake⁴⁸⁵).

When a certain small separation, h_i , the inversion thickness, is reached, the sign of the curvature in the contact of the fluid particles (drops, bubbles) changes. A concave lens-shaped formation called a *dimple* is formed (see Frankel and Mysels⁴⁸⁶). This stage is also observed for asymmetric films.⁴⁷⁵ A number of theoretical studies have described the development of a dimple at the initial stage of film thinning.^{465–485} The inversion thickness can be calculated from a simple equation in which the van der Waals interaction is explicitly taken into account (see Section 5.4.2)^{164,431,465}

$$h_i = \frac{F_z(\sigma_1 + \sigma_2)}{4\pi\sigma_1\sigma_2} \left(1 - \frac{A_H R_s}{12F_z h_i} \right) \quad (5.266)$$

where σ_1 and σ_2 are the interfacial tensions of the phase boundaries S_1 and S_2 ; in this case F_z is the external force (of nonviscous and non-van der Waals origin) experienced by the approaching particles; A_H is the Hamaker constant. In the case, when the van der Waals force is negligible, Equation 5.266 reduces to $h_i = F_z(\sigma_1 + \sigma_2) / (4\pi\sigma_1\sigma_2)$.^{164,431} Danov et al.⁴³⁹ have shown that in the

case of Brownian flocculation of identical small droplets, h_i obeys the following transcendental equation:

$$h_i = \frac{kT}{2\pi\sigma z_i} \left\{ \int_0^{z_i} \left(\frac{z_i}{z} \right)^2 \frac{\gamma(z)}{\gamma(z_i)} \exp \left[\frac{U(z) - U(z_i)}{kT} \right] \frac{dz}{z_i} \right\}^{-1} \quad (5.267)$$

where kT is the thermal energy; $\gamma(z) = F_z/V_z$ is the hydrodynamic resistance given by Equation 5.259; U is the potential energy due to the surface forces (see Equation 5.164); and z is the distance between the droplet mass centers. These authors pointed out that with an increase of droplet size the role of the Brownian force in the film formation decreases, but for micrometer-sized liquid droplets the Brownian force is still by several orders of magnitude greater than the buoyancy force due to gravity. If the driving force is large enough, so that it is able to overcome the energy barrier created by the electrostatic repulsion and/or the increase of the surface area during the droplet deformation, then film with a dimple will be formed. On the contrary, at low electrolyte concentration (i.e., strong electrostatic repulsion) such a dimple might not appear. Parallel experiments⁴⁸⁷ on the formation and thinning of emulsion films of macroscopic and microscopic areas, prepared in the Scheludko cell¹⁴³ and in a miniaturized cell, show that the patterns and the timescales of the film evolution in these two cases are significantly different. There is no dimple formation in the case of thin liquid films of small diameters.⁴⁸⁷

In the case of predominant van der Waals attraction, instead of a dimple, a reverse bell-shaped deformation, called a *pimple*, appears and the film quickly ruptures.^{465,472,481,484} The thickness, h_p , at which the pimple appears can be calculated from the relationship:⁴⁶⁵

$$h_p = \left(\frac{A_H R_*}{12 F_z} \right)^{1/2} \quad (5.268)$$

The pimple formation thickness depends significantly on the radius, R_* . If a drop of tangentially immobile surfaces and radius R_d is driven by the buoyancy force, then we have

$$F_z = \frac{4}{3} \pi R_d^3 \Delta\rho g \quad (5.269)$$

where $\Delta\rho$ is the density difference, and g is the gravity acceleration. For the collision of this drop with another immobile one, we have $h_p^2 = A_H / (16\pi \Delta\rho g R_d^2)$. We see that h_p is inversely proportional to the drop radius. For typical values of the Hamaker constant $A_H = 4 \times 10^{-20}$ J, density difference $\Delta\rho = 0.12 \times 10^3$ g/cm³, and $R_d = 10$ μ m, the thickness of pimple formation is $h_p = 82.3$ nm. Note that this thickness is quite large. The pimple formation can be interpreted as the onset of instability without fluctuations (stability analysis of the film intervening between the drops has been carried out elsewhere⁵²).

As already mentioned, if the van der Waals force (or other attractive force) is not predominant, first a dimple forms in the thinning liquid films. Usually the dimple exists for a short period of time; initially it grows, but as a result of the swift outflow of liquid it decreases and eventually disappears. The resulting plane-parallel film thins at almost constant radius R . When the electrostatic repulsion is strong, a thicker primary film forms (see point 1 in Figure 5.13). From the viewpoint of conventional DLVO theory, this film must be metastable. Indeed, the experiments with microscopic foam films, stabilized with sodium octyl sulfate or sodium dodecyl sulfate in the presence of different amount of electrolyte,⁴⁸⁸ show that a black spot may suddenly form and a transition to

secondary (Newton black) film may occur (see point 2 in [Figure 5.13](#)). The rate of thinning depends not only on the capillary pressure (the driving force) but also very strongly on the surfactant concentration (for details, see Section 5.5.3.2 below).

The appearance of a secondary film (or film rupture, if the secondary film is not stable) is preceded by corrugation of the film surfaces due to thermally excited fluctuations or outer disturbances. When the derivative of the disjoining pressure, $\partial\Pi/\partial h$, is positive, the amplitude of the fluctuations (ζ in [Figure 5.36d](#)) spontaneously grows. As already mentioned, the instability leads to rupture of the film or to formation of black spots. The theory of film stability was developed by de Vries,⁴⁸⁹ Vrij,⁴⁹⁰ Felderhof,⁴²⁵ Sche and Fijnaut,⁴²⁶ Ivanov et al.,⁴⁹¹ Gumerman and Homsy,⁴⁹² Malhotra and Wasan,⁴⁹³ Maldarelli and Jain,⁴²⁷ and Valkovska et al.⁴⁹⁴ On the basis of the lubrication approximation for tangentially immobile surfaces, Ivanov et al.⁴⁹¹ and Valkovska et al.⁴⁹⁴ derived a general expression for the critical film thickness, h_{cr} , by using long-waves stability analysis:

$$h_{cr} = h_{tr} \left(\frac{\sigma h_{tr}^2}{kT} \right)^{1/4} \exp \left(- \frac{k_{cr}^2 R^2}{32 h_{cr}^3} \int_{h_{cr}}^{h_{tr}} \frac{h^3 \Pi'}{P_c - \Pi} dh \right) \quad (5.270)$$

where k_{cr} is the wave number of the critical wave defined as

$$k_{cr}^2 = \frac{1}{\sigma} \int_{h_{cr}}^{h_{tr}} \frac{h^3 \Pi'}{P_c - \Pi} dh \bigg/ \int_{h_{cr}}^{h_{tr}} \frac{h^6}{P_c - \Pi} dh \quad (5.271)$$

In Equation 5.271, h_{tr} is the so-called transitional thickness^{490,491,494} at which the increase of free energy due to the increased film area and the decrease of free energy due to the van der Waals interaction in the thinner part ([Figure 5.36d](#)) compensate for each other. At h_{tr} the most rapidly growing fluctuation (the critical wave) becomes unstable. The transitional thickness obeys the following equation:^{491,494}

$$\frac{24 h_{cr}^3 [P_c - \Pi(h_{tr})]}{R^2 k_{cr}^2 h_{tr}^4} + \frac{\sigma k_{cr}^2 h_{tr}^3}{2 h_{cr}^3} = \Pi'(h_{tr}) \quad (5.272)$$

[Figures 5.37](#) and [5.38](#) show the critical thicknesses of rupture, h_{cr} , for foam and emulsion films, respectively, plotted vs. the film radius.⁴⁹⁵ In both cases the film phase is the aqueous phase, which contains $4.3 \times 10^{-4} M$ SDS + added NaCl. The emulsion film is formed between two toluene drops. Curve 1 is the prediction of a simpler theory, which identifies the critical thickness with the transitional one.⁴⁹³ Curve 2 is the theoretical prediction of Equations 5.270 to 5.272 (no adjustable parameters); in Equation 5.171 for the Hamaker constant the electromagnetic retardation effect has also been taken into account.²⁷⁸ In addition, [Figure 5.39](#) shows the experimental dependence of the critical thickness vs. the concentration of surfactant (dodecanol) for aniline films. [Figures 5.37](#) to [5.39](#) demonstrate that when the film area increases and/or the electrolyte concentration decreases the critical film thickness becomes larger.

The surface corrugations do not necessarily lead to film rupture. Instead, black spots (secondary films of very low thickness; h_2 in [Figure 5.13](#)) can be formed. The typical thickness of plane-parallel films at stage c ([Figure 5.36c](#)) is about 200 nm, while the characteristic thickness h_2 of the Newton black film ([Figure 5.36e](#) and [f](#)) is about 5 to 10 nm. The black spots either coalesce or grow in diameter, forming an equilibrium secondary (Newton black) film with a thickness h_2 and radius R_{sp} . These spots grow until they cover the whole film area.

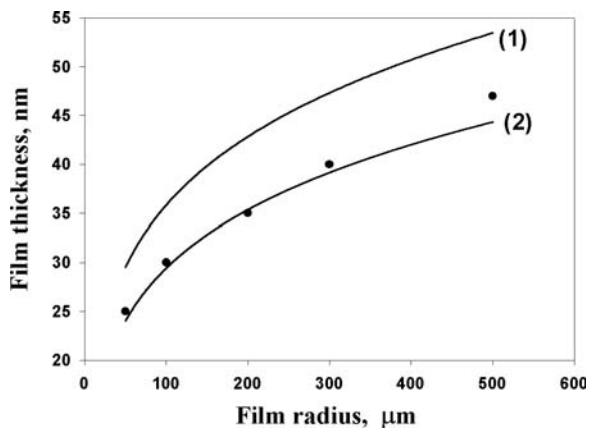


FIGURE 5.37 Dependence of the critical thickness, h_{cr} , on the radius, R , of foam films. The experimental points are data from Reference 495; the films are formed from a solution of $4.3 \times 10^{-4} M$ SDS + $0.25 M$ NaCl. Curve 1 is the prediction of the simplified theory,⁴⁹³ whereas Curve 2 is calculated using Equations 5.270 to 5.272; no adjustable parameters.

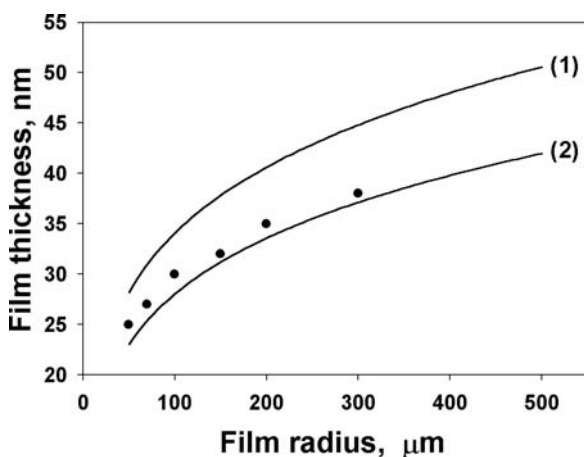


FIGURE 5.38 Critical thickness, h_{cr} , vs. radius, R , of emulsion films, toluene/water/toluene. The experimental points are data from Reference 495; the films are formed from a solution of $4.3 \times 10^{-4} M$ SDS + $0.1 M$ NaCl. Curve 1 is the prediction of the simplified theory,⁴⁹³ whereas Curve 2 is calculated using Equations 5.270 to 5.272; no adjustable parameters.

After the entire film area is occupied by the Newton black film, the film radius increases until it reaches its equilibrium value, $R = R_{\text{NBF}}$ (Figure 5.36f). Finally, the equilibrium contact angle is established. For more details about this last stage of film thinning, see part IV.C of Reference 164.

5.5.2.4 Dependence of Emulsion Stability on the Droplet Size

Experimental data^{497,498} show that the emulsion stability correlates well with the lifetime of separate thin emulsion films or of drops coalescing with their homophase. To simplify the treatment we will consider here the lifetime of a single drop pressed against its homophase under the action of gravity. To define the *lifetime* (or drainage time) τ , we assume that in the initial and final moments the film has some known thicknesses h_m and h_f :

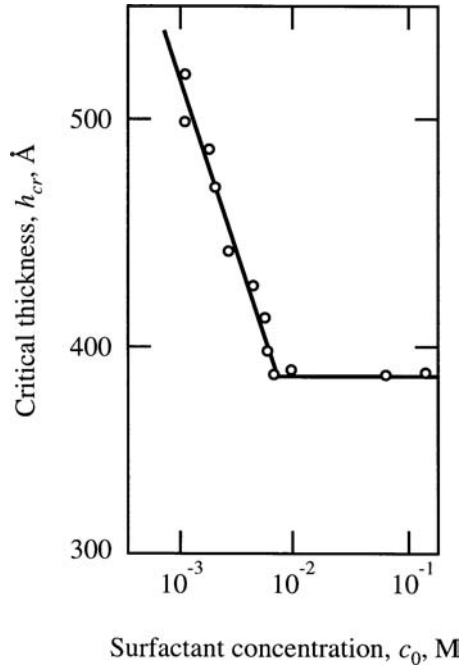


FIGURE 5.39 Dependence of the critical thickness, h_{cr} , of aniline films on the concentration of dodecanol, c_0 . (Modified from Ivanov, I.B., *Pure Appl. Chem.*, 52, 1241, 1980.)

$$\tau = \int_{h_f}^{h_{in}} \frac{dh}{V_z} = \frac{3\pi\eta R_*^2}{2F_z} \left[\ln\left(\frac{h_{in}}{h_f}\right) + \frac{R^2}{h_f R_*} \left(1 - \frac{h_f}{h_{in}}\right) + \frac{R^4}{2h_f^2 R_*^2} \left(1 - \frac{h_f^2}{h_{in}^2}\right) \right] \quad (5.273)$$

The final thickness, h_f , may coincide with the critical thickness of film rupture. Equation 5.273 is derived for tangentially immobile interfaces from Equation 5.259 at a fixed driving force (no disjoining pressure).

In the case of gravity-driven coalescence of a droplet with its homophase, the driving force is given by Equation 5.269 and the mean drop radius is $R_* = 2R_d$. Then, from Equations 5.269 and 5.273 we can deduce the droplet lifetime in the so-called Taylor regime, corresponding to nondeformed droplets ($R = 0$):

$$\tau_{Ta} = \frac{6\pi\eta R_d^2}{F_z} \ln\left(\frac{h_{in}}{h_f}\right) = \frac{9\eta}{2gR_d\Delta\rho} \ln\left(\frac{h_{in}}{h_f}\right) \quad (5.274)$$

We see that τ_{Ta} depends logarithmically on the ratio of the initial and final thickness. Moreover, in the Taylor regime the lifetime, τ , decreases with the increase of the driving force, F_z , and the drop radius, R_d . The latter fact is confirmed by the experimental data of Dickinson et al.⁴⁹⁹ (Figure 5.40).

In the case of deformed drops ($R \neq 0$), the drainage time, τ , is determined by Equation 5.273, and in such a case the fluid particles approach each other in the Reynolds regime.^{432,496} The dependence of τ on R_d in Equation 5.273 is very complex, because the driving force, F_z , and the film radius, R , depend on R_d . The film radius can be estimated from the balance of the driving and capillary force:^{432,496}

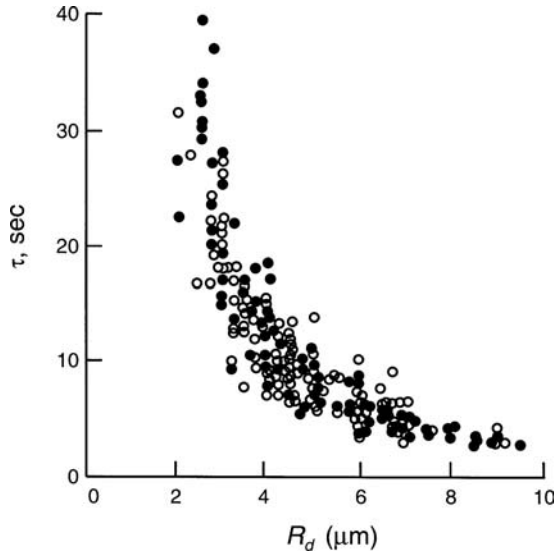


FIGURE 5.40 Experimental data of Dickinson et al.⁴⁹⁹ for the lifetime, τ , of drops vs. their radius, R_d . The oil drops are pressed against their homophase by the buoyancy force. (From Dickinson, E. et al., *J. Chem. Soc. Faraday Trans.*, 84, 871, 1988.)

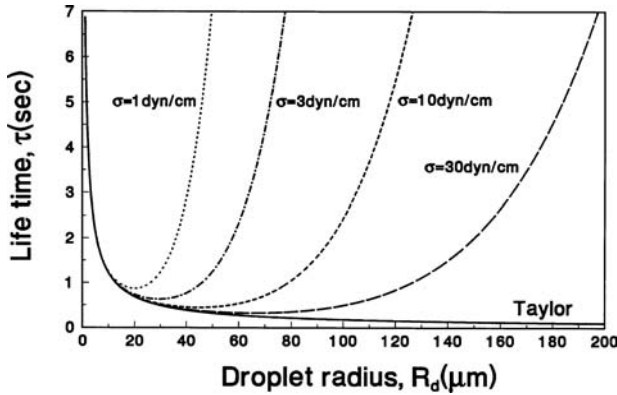


FIGURE 5.41 Calculated lifetime, τ , of drops approaching a fluid interface in Taylor regime (the solid line) and in Reynolds regime (the other lines) as a function of the droplet radius, R_d .

$$R^2 = \frac{F_z R_d}{2\pi\sigma} \tag{5.275}$$

In this regime, the lifetime, τ , increases with an increase of the driving force, F_z . This is exactly the opposite trend compared to results for the Taylor regime (see Equation 5.274). The result can be rationalized in view of Reynolds equation (Equation 5.262). In the numerator of this equation, $F_z \propto R_d^3$, whereas in the denominator $R^4 \propto R_d^8$ (see Equation 5.275); as a result, the drainage rate becomes proportional to R_d^{-5} , i.e., V_z decreases as the droplet radius increases.

The numerical results from Equations 5.273 to 5.275 for the lifetime or drainage time, τ , vs. the droplet radius, R_d , are plotted in Figure 5.41 for parameter values typical for emulsion systems: $\Delta\rho = 0.2 \text{ g/cm}^3$, $\eta = 1 \text{ cP}$, $h_f = 5 \text{ nm}$, and $h_{in} = R_d/10$. The various curves in Figure 5.41 correspond

to different values of the surface tension, σ , shown in the figure. The left branches of the curves correspond to the Taylor regime (nondeformed droplets), whereas the right branches correspond to the Reynolds regime (formation of film between the droplets). In particular, the data shown in Figure 5.40 correspond to the left branch (Figure 5.41); in addition, the data also comply with the right branch.⁴³² The presence of a deep minimum on the τ vs. R_d curve was first pointed out by Ivanov.^{500,501} The theoretical dependencies in Figure 5.41 agree well with experimental data⁵⁰² for the lifetime of oil droplets pressed by the buoyancy force against a large oil–water interface in a system containing protein: BSA.

5.5.3 EFFECT OF SURFACE MOBILITY

The hydrodynamic interactions between fluid particles (drops, bubbles) suspended in a liquid medium depend on the interfacial mobility. In the presence of surfactants, the bulk fluid motion near an interface disturbs the homogeneity of the surfactant adsorption monolayer. The ensuing surface tension gradients act to restore the homogeneous equilibrium state of the monolayer. The resulting transfer of adsorbed surfactant molecules from the regions of lower surface tension toward the regions of higher surface tension constitutes the Marangoni effect. The analogous effect, for which the surface tension gradient is caused by a temperature gradient, is known as the Marangoni effect of thermocapillarity. In addition, the interfaces possess specific surface rheological properties (surface elasticity and dilatational and shear surface viscosities), which give rise to the so-called Boussinesq effect (see below).⁵⁰³

5.5.3.1 Diffusive and Convective Fluxes at an Interface — Marangoni Effect

To take into account the influence of surfactant adsorption, Equations 5.240 and 5.241 are to be complemented with transport equations for each of the species ($k = 1, 2, \dots, N$) in the bulk phases^{410,413,436,437}

$$\frac{\partial c_k}{\partial t} + \text{div}(c_k \mathbf{v} + \mathbf{j}_k) = r_k \quad (k = 1, 2, \dots, N) \quad (5.276)$$

where c_k and \mathbf{j}_k are bulk concentration and flux, respectively, of the k th species — note that \mathbf{j}_k includes the molecular diffusive flux, the flux driven by external forces (e.g., electrodiffusion^{428,436,437}), and the thermodiffusion flux⁴³⁶ — and r_k is the rate of production due to chemical reactions, including surfactant micellization or micelle decay. The surface mass-balance equation for the adsorption, Γ_k , has the form:^{428,436,437}

$$\frac{\partial \Gamma_k}{\partial t} + \nabla_s \cdot (\Gamma_k \mathbf{v}_s + \mathbf{j}_k^s) = r_k^s + \mathbf{n} \cdot \langle \mathbf{j}_k \rangle \quad (5.277)$$

where \mathbf{n} is the unit normal to the interface directed from phase 1 to phase 2; $\langle \rangle$ denotes the difference between the values of a given physical quantity at the two sides of the interface; ∇_s is the surface gradient operator;⁵⁰⁴ \mathbf{v}_s is the local material surface velocity; \mathbf{j}_k^s is the two-dimensional flux of the k th component along the interface; and r_k^s accounts for the rate of production of the k th component due to interfacial chemical reactions and could include conformational changes of adsorbed proteins. Equation 5.277 provides a boundary condition for the normally resolved flux, \mathbf{j}_k . From another viewpoint, Equation 5.277 represents a two-dimensional analogue of Equation 5.276. The interfacial flux, \mathbf{j}_k^s , can also contain contributions from the interfacial molecular diffusion, electrodiffusion, and thermodiffusion. A simple derivation of the time-dependent convective-diffusion equation for surfactant transport along a deforming interface is given by Brenner

and Leal,⁵⁰⁵⁻⁵⁰⁸ Davis et al.,⁴⁴³ and Stone.⁵⁰⁹ If the molecules are charged, the bulk and surfaces electrodiffusion fluxes can be expressed in the form:^{428,510,511}

$$\mathbf{j}_k = -D_k(\nabla c_k + z_k c_k \nabla \Phi), \quad \mathbf{j}_k^s = -D_k^s(\nabla_s \Gamma_k + z_k \Gamma_k \nabla_s \Phi) \quad (5.278)$$

for the bulk and interfacial phase. Here, D_k and D_k^s are the bulk and surface collective diffusion coefficients, respectively, which are connected with the diffusion coefficients of individual molecules, $D_{k,0}$ and $D_{k,0}^s$, through the relationship⁵¹¹

$$D_k = \frac{D_{k,0}}{kT} \frac{K_b(\phi_k)}{(1-\phi_k)} \frac{\partial \mu_k}{\partial \ln \phi_k}, \quad D_k^s = \frac{D_{k,0}^s}{kT} K_s(\Gamma_k) \frac{\partial \mu_k^s}{\partial \ln \Gamma_k} \quad (5.279)$$

where μ_k and μ_k^s are the bulk and surface chemical potentials, respectively. The dimensionless bulk friction coefficient, K_b , accounts for the change in the hydrodynamic friction between the fluid and the particles (created by the hydrodynamic interactions between the particles). The dimensionless surface mobility coefficient, K_s , accounts for the variation of the friction of a molecule in the adsorption layer. Feng⁵¹² has determined the surface diffusion coefficient, the dilatational elasticity, and the viscosity of a surfactant adsorption layer by theoretical analysis of experimental data. Stebe and Maldarelli^{513,514} studied theoretically the surface diffusion driven by large adsorption gradients. The determination of bulk and surface diffusion coefficients from experimental data for the drainage of nitrobenzene films stabilized by different concentrations of dodecanol was reported.⁵¹⁰

Note that the adsorption isotherms, relating the surface concentration, Γ_k , with the subsurface value of the bulk concentration, c_k (see Section 5.2.2.1 above), or the respective kinetic Equation 5.86 for adsorption under barrier control (see Section 5.2.2.5), should also be employed in the computations based on Equations 5.276 to 5.279 in order for a complete set of equations to be obtained.

Another boundary condition is the equation of the interfacial momentum balance:^{414,432,437}

$$\nabla_s \cdot \boldsymbol{\sigma} = \mathbf{n} \cdot \langle \mathbf{P} + \mathbf{P}_b \rangle \quad (5.280)$$

where $\boldsymbol{\sigma}$ is the interfacial stress tensor, which is a two-dimensional counterpart of the bulk stress tensor, \mathbf{P} . Moreover, a two-dimensional analogue of Equations 5.242, 5.245, and 5.246, called the Boussinesq–Scriven constitutive law, can be postulated for a fluid interface:^{164,437,503,515-519}

$$\boldsymbol{\sigma} = \sigma_a \mathbf{I}_s + (\eta_{dl} - \eta_{sh})(\nabla_s \cdot \mathbf{v}_s) \mathbf{I}_s + \eta_{sh} [(\nabla_s \mathbf{v}_s) \cdot \mathbf{I}_s + \mathbf{I}_s \cdot (\nabla_s \mathbf{v}_s)^T] \quad (5.281)$$

where η_{dl} and η_{sh} are the interfacial dilatational and shear viscosities, respectively; \mathbf{I}_s is the unit surface idemfactor;⁵⁰⁴ and, as usual, σ_a is the scalar adsorption part of the surface tension (see Section 5.2.1.2.2). In view of the term $\sigma_a \mathbf{I}_s$ in Equation 5.281, the Marangoni effects are hidden in the left-hand side of the boundary condition (Equation 5.280) through the surface gradient of σ_a :

$$\nabla_s \sigma_a = - \sum_{k=1}^N \frac{E_k}{\Gamma_k} \nabla_s \Gamma_k - \frac{E_T}{T} \nabla_s T, \quad E_k = - \left(\frac{\partial \sigma_a}{\partial \ln \Gamma_k} \right)_{T, \Gamma_{j \neq k}}, \quad E_T = - \left(\frac{\partial \sigma_a}{\partial \ln T} \right)_{\Gamma_k} \quad (5.282)$$

where E_k is the Gibbs elasticity for the k th surfactant species (see Equation 5.6) and E_T represents the thermal analogue of the Gibbs elasticity. The thermocapillary migration of liquid drops or bubbles and the influence of E_T on their motion are investigated in a number of works.⁵²⁰⁻⁵²²

In fact, Equation 5.281 describes an interface as a two-dimensional Newtonian fluid. On the other hand, a number of non-Newtonian interfacial rheological models have been described in the literature.⁵²³⁻⁵²⁶ Tambe and Sharma⁵²⁷ modeled the hydrodynamics of thin liquid films bounded by viscoelastic interfaces, which obey a generalized Maxwell model for the interfacial stress tensor. These authors^{528,529} also presented a constitutive equation to describe the rheological properties of fluid interfaces containing colloidal particles. A new constitutive equation for the total stress was proposed by Horozov et al.⁵³⁰ and Danov et al.⁵³¹ who applied a local approach to the interfacial dilatation of adsorption layers.

When the temperature is not constant, the bulk heat transfer equation complements the system and involves Equations 5.240, 5.241, and 5.276. The heat transfer equation is a special case of the energy balance equation. It should be noted that more than 20 various forms of the overall differential energy balance for multicomponent systems are available in the literature.^{410,413} The corresponding boundary condition can be obtained as an interfacial energy balance.^{437,519} Based on the derivation of the bulk⁵³² and interfacial^{531,533} entropy inequalities (using the Onsager theory), various constitutive equations for the thermodynamic mass, heat, and stress fluxes have been obtained.

5.5.3.2 Fluid Particles and Films of Tangentially Mobile Surfaces

When the surface of an emulsion droplet is mobile, it can transmit the motion of the outer fluid to the fluid within the droplet. This leads to a special pattern of the fluid flow and affects the dissipation of energy in the system. The problem concerning the approach of two nondeformed (spherical) drops or bubbles of pure phases has been investigated by many authors.^{432,459,460,466,467,534-539} A number of solutions, generalizing the Taylor equation (Equation 5.260), have been obtained. For example, the velocity of central approach, V_z , of two spherical drops in pure liquid is related to the hydrodynamic resistance force, F_z , by means of a Padé-type expression derived by Davis et al.⁴⁶⁶

$$V_z = \frac{2hF_z}{3\pi\eta R_*^2} \frac{1 + 1.711\xi + 0.461\xi^2}{1 + 0.402\xi}, \quad \xi = \frac{\eta}{\eta_d} \sqrt{\frac{R_*}{2h}} \quad (5.283)$$

where h is the closest surface-to-surface distance between the two drops, and η_d is the viscosity of the disperse phase (the liquid in the droplets). In the limiting case of solid particles, we have $\eta_d \rightarrow \infty$, and Equation 5.283 reduces to the Taylor equation (Equation 5.260). Note that in the case of close approach of two drops ($\xi \gg 1$), the velocity V_z is proportional to \sqrt{h} . This implies that the two drops can come into contact ($h = 0$) in a finite period of time ($\tau < \infty$) under the action of a given force, F_z , because the integral in Equation 5.273 is convergent for $h_f = 0$. This is in contrast to the case of immobile interfaces ($\xi \ll 1$), when $V_z \propto h$ and $\tau \rightarrow \infty$ for $h_f \rightarrow 0$.

In the other limiting case, that of two nondeformed gas bubbles ($\eta_d \rightarrow 0$) in pure liquid, Equation 5.283 cannot be used; instead, V_z can be calculated from the expression due to Beshkov et al.⁵³⁹

$$V_z = \frac{F_z}{2\pi\eta R_d \ln(R_d/h)} \quad (5.284)$$

Note that in this case $V_z \propto (\ln h)^{-1}$, and the integral in Equation 5.273 is convergent for $h_f \rightarrow 0$. In other words, the theory predicts that the lifetime, τ , of a doublet of two colliding spherical bubbles in pure liquid is finite. Of course, the real lifetime of a doublet of bubbles or drops is affected by the surface forces for $h < 100$ nm, which should be accounted for in F_z and which may lead to the formation of thin film in the zone of contact.^{134,266}

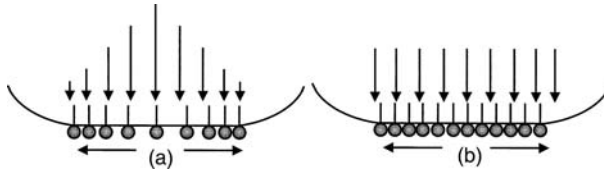


FIGURE 5.42 Damping of convection-driven surface tension gradients by influx of surfactant from the drop interior. (a) Since the mass transport is proportional to the perturbation, the larger the perturbation, the stronger the flux tending to eliminate it. (b) Uniform surfactant distribution is finally reached.

Let us proceed with the case of deformed fluid particles (Figure 5.23). A number of theoretical studies⁵⁴⁰⁻⁵⁴³ have been devoted to the thinning of plane-parallel liquid films of pure liquid phases (no surfactant additives). Ivanov and Traykov⁵⁴² derived the following exact expressions for the velocity of thinning of an emulsion film:

$$V_z = \left(\frac{32 \Delta P^2}{\rho_d \eta_d R^4} \right)^{1/3} h^{5/3}, \quad \frac{V_z}{V_{Re}} = \frac{1}{\epsilon_e}, \quad \epsilon_e \equiv \left(\frac{\rho_d \eta_d h^4 F_z}{108 \pi \eta^3 R^4} \right)^{1/3} \quad (5.285)$$

where ρ_d is the density of the disperse phase, V_{Re} is the Reynolds velocity defined by Equation 5.262, and ϵ_e is the so-called emulsion parameter. Substituting typical parameter values in Equations 5.283 and 5.285 we can check that at a given constant force the velocity of thinning of an emulsion film is smaller than the velocity of approach of two nondeformed droplets and much larger than V_{Re} . It is interesting to note that the velocity of thinning as predicted by Equation 5.285 does not depend on the viscosity of the continuous phase, η , and its dependence on the drop viscosity, η_d , is rather weak. There are experimental observations confirming this prediction (see Reference 32, p. 381).

The presence of surfactant adsorption monolayers decreases the mobility of the droplet (bubble) surfaces. This is due to the Marangoni effect (see Equation 5.282). From a general viewpoint, we may expect that the interfacial mobility will decrease with the increase of surfactant concentration until eventually the interfaces become immobile at high surfactant concentrations (see Section 5.5.2, above); therefore, a pronounced effect of surfactant concentration on the velocity of film drainage should be expected. This effect really exists (see Equation 5.286, below), but in the case of emulsions it is present only when the surfactant is predominantly soluble in the continuous phase.

Traykov and Ivanov⁵⁴³ established (both theoretically and experimentally) the interesting effect that when the surfactant is dissolved in the disperse phase (that is, in the emulsion droplets), the droplets approach each other just as in the case of pure liquid phases, i.e., Equation 5.285, holds. Qualitatively, this effect can be attributed to the fact that the convection-driven surface tension gradients are rapidly damped by the influx of surfactant from the drop interior; in this way, the Marangoni effect is suppressed. Indeed, during the film drainage the surfactant is carried away toward the film border, and a nonequilibrium distribution, depicted in Figure 5.42a appears. Because, however, the mass transport is proportional to the perturbation, the larger the deviation from equilibrium, the stronger the flux tending to eliminate the perturbation (the surfactant flux is denoted by thick arrows in Figure 5.42b). In this way, any surface concentration gradient (and the related Marangoni effect) disappears. The emulsion films in this case behave as if surfactant is absent.

In the opposite case, when the surfactant is soluble in the continuous phase, the Marangoni effect becomes operative and the rate of film thinning becomes dependent on the surface (Gibbs) elasticity (see Equation 5.282). Moreover, the convection-driven local depletion of the surfactant monolayers in the central area of the film surfaces gives rise to fluxes of bulk and surface diffusion of surfactant molecules. The exact solution of the problem^{428,430,462,510,511,543} gives the following expression for the rate of thinning of symmetric planar films (of both foam and emulsion type):

$$\frac{V_z}{V_{Re}} = 1 + \frac{1}{\varepsilon_e + \varepsilon_f}, \quad \frac{1}{\varepsilon_f} = \frac{6\eta D_s}{hE_G} + \frac{3\eta D}{\Gamma(\partial\sigma/\partial c)} \quad (5.286)$$

where, as usual, D and D_s are the bulk and interfacial collective diffusion coefficients (see Equation 5.279); E_G is the Gibbs elasticity; and ε_f is the so-called foam parameter.⁴⁹⁶ In the special case of foam film, one substitutes $\varepsilon_e = 0$ in Equation 5.286. Note that the diffusive surfactant transport, which tends to restore the uniform adsorption monolayers, damps the surface tension gradients (which oppose the film drainage) and thus accelerates the film thinning. However, at large surfactant concentrations, the surface elasticity, E_G , prevails, ε_f increases, and, consequently, the thinning rate decreases down to the Reynolds velocity, $V_z \rightarrow V_{Re}$ (see Equation 5.286). Similar expressions for the rate of film thinning, which are appropriate for various ranges of values of the interfacial parameters, can be found in the literature.^{164,431,432,477,544,545} A table describing the typical ranges of variation of the interfacial properties (Γ , E_G , D , D_s , $\partial\sigma/\partial c$, etc.) for emulsion and foam systems can be found in Reference 164, table 2 therein. For $h < 100$ nm, the influence of the disjoining pressure should be taken into account (see Equation 5.262). In some studies,^{164,440,527,546-549} the effect of the interfacial viscosity on the rate of thinning and the lifetime of plane-parallel films is investigated; this effect is found to decrease when the film thickness, h , becomes smaller and/or the film radius, R , becomes larger.

Note that Equation 5.286 does not hold in the limiting case of foam films ($\varepsilon_e = 0$) at low surfactant concentration, $\varepsilon_f \rightarrow 0$. The following expression is available for this special case:⁴⁹⁶

$$V_z/V_{Re} = (1 + 1/\varepsilon_f) / \left[1 + 4h^2 / (3R^2\varepsilon_f) \right] \quad (5.287)$$

The merit of this equation is that it gives as limiting cases both V_z/V_{Re} for foam films without surfactant, $\varepsilon_f \rightarrow 0$, and Equation 5.286 with $\varepsilon_e = 0$ (note that in the framework of the lubrication approximation, used to derive Equation 5.286, the terms $\propto h^2/R^2$ are being neglected). Equation 5.287 has also some shortcomings, which are discussed in Reference 496.

Another case, which is not described by the above equations, is the approach of two nondeformed (spherical) bubbles in the presence of surfactant. The velocity of approach in this case can be described by means of the expression:^{431,440,501,511}

$$\frac{V_z}{V_{Ta}} = \frac{h_s}{2h} \left\{ \left[\frac{h(1+b)}{h_s} + 1 \right] \ln \left[\frac{h_s}{h(1+b)} + 1 \right] - 1 \right\}^{-1} \quad (5.288)$$

where the parameters b and h_s account for the influence of bulk and surface diffusivity of surfactants, respectively. From Equation 5.279 these parameters are calculated to be⁵¹¹

$$b \equiv \frac{3\eta c D_0 K_b(\phi)}{kT\Gamma^2(1-\phi)}, \quad h_s \equiv \frac{6\eta D_0^s K_s(\Gamma)}{kT\Gamma} \quad (5.289)$$

A generalization of Equation 5.288 to the more complicated case of two nondeformed (spherical) emulsion droplets which account for the influence of surface viscosity has been published in Reference 440.

Returning to the parameter values, we note that usually $\varepsilon_e \ll \varepsilon_f$ and $\varepsilon_e \ll 1$. Then, comparing the expressions for V_z/V_{Re} as given by Equations 5.285 and 5.286, we conclude that the rate of thinning is much greater when the surfactant is dissolved in the droplets (the disperse phase) in comparison with the case when the surfactant is dissolved in the continuous phase. This prediction

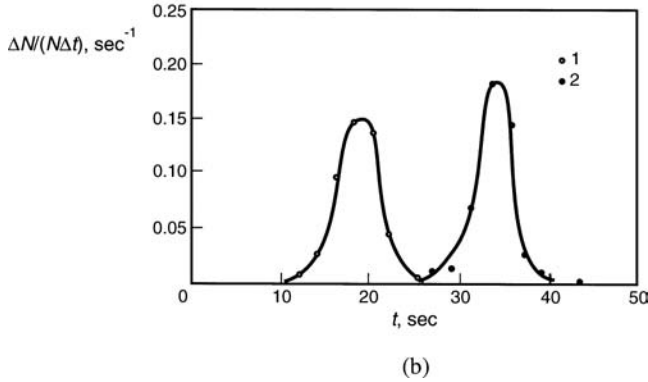
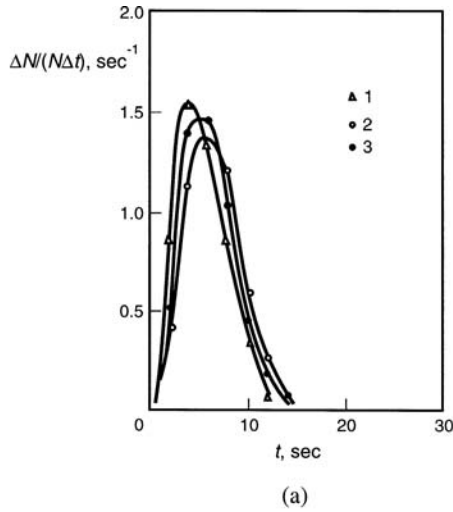


FIGURE 5.43 Histograms for the lifetimes of emulsion films: $\Delta N/N$ is the relative number of films that have ruptured during a time interval $\Delta t = 0.4$ s. (a) Surfactant in the drops: benzene films between water drops containing surfactant sodium octylsulfonate of concentration (1) 0 M, (2) 10^{-4} M, and (3) 2×10^{-3} M. (b) Surfactant in the film: (1) benzene film with 0.1 M of lauryl alcohol dissolved in the film, (2) water film with 2×10^{-3} M of sodium octylsulfonate inside. (From Traykov, T.T. and Ivanov, I.B., *Int. J. Multiphase Flow*, 3, 471, 1977.)

of the theory was verified experimentally by measuring the number of films that rupture during a given period of time,⁵⁵⁰ as well as the rate of thinning. When the surfactant was dissolved in the drop phase, the average lifetime was the same for all surfactant concentrations (Figure 5.43a), in agreement with Equation 5.285. For the emulsion film with the same, but inverted, liquid phases (the former continuous phase becomes disperse phase, and vice versa), i.e., the surfactant is in the film phase, the average lifetime is about 70 times longer — compare curve 3 in Figure 5.43a with curve 2 in Figure 5.43b. The theoretical conclusions have been also checked and proved in experimental measurements with nitroethane droplets dispersed in an aqueous solution of the cationic surfactant hexadecyl trimethyl ammonium chloride (HTAC).⁴⁹⁸

5.5.3.3 Bancroft Rule for Emulsions

There have been numerous attempts to formulate simple rules connecting the emulsion stability with the surfactant properties. Historically, the first was the Bancroft rule,⁵⁵¹ which states that “to

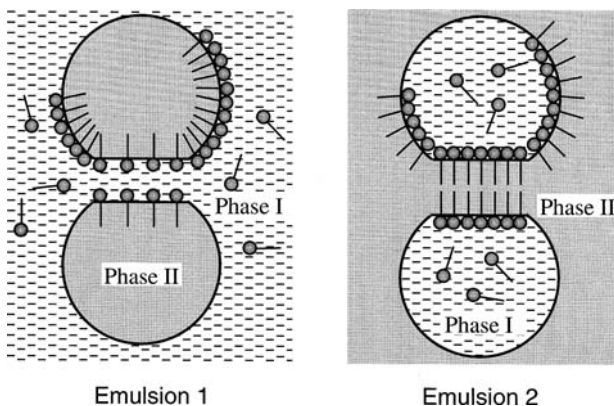


FIGURE 5.44 The two possible types of emulsions obtained just after the homogenization; the surfactant is soluble in Phase I.

have a stable emulsion the surfactant must be soluble in the continuous phase.” A more sophisticated criterion was proposed by Griffin⁵⁵² who introduced the concept of hydrophilic-lipophilic balance (HLB). As far as emulsification is concerned, surfactants with an HLB number in the range of 3 to 6 must form water in oil (W/O) emulsions, whereas those with HLB numbers from 8 to 18 are expected to form oil in water (O/W) emulsions. Different formulae for calculating the HLB numbers are available; for example, the Davies expression⁵⁵³ reads

$$\text{HLB} = 7 + (\text{hydrophilic group number}) - 0.475n_c \quad (5.290)$$

where n_c is the number of $-\text{CH}_2-$ groups in the lipophilic part of the molecule. Shinoda and Friberg⁵⁵⁴ proved that the HLB number is not a property of the surfactant molecules only, but also depends strongly on the temperature (for nonionic surfactants), on the type and concentration of added electrolytes, on the type of oil phase, etc. They proposed using the phase inversion temperature (PIT) instead of HLB for characterization of the emulsion stability.

Davis⁵⁵⁵ summarized the concepts about HLB, PIT, and Winsor’s ternary phase diagrams for the case of microemulsions and reported topologically ordered models connected with the Helfrich membrane bending energy. Because the curvature of surfactant lamellas plays a major role in determining the patterns of phase behavior in microemulsions, it is important to reveal how the optimal microemulsion state is affected by the surface forces determining the curvature energy.^{163,556,557} It is hoped that lattice models^{558,559} and membrane curvature models^{560,561} will lead to predictive formulae for the microemulsion design.

Ivanov et al.^{496,500,501,562} have proposed a semiquantitative theoretical approach that provides a straightforward explanation of the Bancroft rule for emulsions. This approach is based on the idea of Davies and Rideal³² that both types of emulsions are formed during the homogenization process, but only the one with lower coalescence rate survives. If the initial drop concentration for both emulsions is the same, the coalescence rates for the two emulsions — $(\text{Rate})_1$ for emulsion 1 and $(\text{Rate})_2$ for emulsion 2 (Figure 5.44) — will be proportional to the respective coalescence rate constants, $k_{c,1}$ and $k_{c,2}$ (see Section 5.6, below), and inversely proportional to the film lifetimes, τ_1 and τ_2 :

$$\frac{(\text{Rate})_1}{(\text{Rate})_2} \approx \frac{k_{c,1}}{k_{c,2}} \approx \frac{\tau_2}{\tau_1} \approx \frac{V_1}{V_2} \quad (5.291)$$

Here V_1 and V_2 denote the respective velocities of film thinning. After some estimates based on Equations 5.262, 5.273, 5.285, and 5.286, we can express the ratio in Equation 5.291 in the form:

$$\frac{(\text{Rate})_1}{(\text{Rate})_2} \approx (486\rho_d D_s^3)^{1/3} \left(\frac{h_{cr,1}^3}{h_{cr,2}^2} \right)^{1/3} \left(\frac{\eta_d}{R^2} \right)^{1/3} \frac{P_c - \Pi_1}{E_G (P_c - \Pi_2)^{2/3}} \quad (5.292)$$

where $h_{cr,1}$ and $h_{cr,2}$ denote the critical thickness of film rupture for the two emulsions in Figure 5.44. Many conclusions can be drawn, regarding the type of emulsion to be formed:

1. If the disjoining pressures, Π_1 and Π_2 , are zero, the ratio in Equation 5.292 will be very small. Hence, emulsion 1 (surfactant soluble in the continuous phase) will coalesce much more slowly and it will survive. This underlines the crucial importance of the surfactant location (which is connected with its solubility), thus providing a theoretical foundation for Bancroft's rule. The emulsion behavior in this case will be controlled almost entirely by the hydrodynamic factors (kinetic stability).
2. The disjoining pressure, Π , plays an important role. It can substantially change and even reverse the behavior of the system if it is comparable by magnitude with the capillary pressure, P_c . For example, if $(P_c - \Pi_2) \rightarrow 0$ at a finite value of $P_c - \Pi_1$ (which may happen, for example, for an O/W emulsion with oil soluble surfactant), the ratio in Equation 5.292 may become much larger than unity, which means that emulsion 2 will become thermodynamically stable. In some cases the stabilizing disjoining pressure is large enough for emulsions with a very high volume fraction of the disperse phase (above 95% in some cases) to be formed.⁵⁶³
3. The Gibbs elasticity, E_G , favors the formation of emulsion 1, because it slows the film thinning. On the other hand, increased surface diffusivity, D_s , decreases this effect, because it helps the interfacial tension gradients to relax, thus facilitating the formation of emulsion 2.
4. The film radius, R , increases and the capillary pressure, P_c , decreases with the drop radius, R_d . Therefore, larger drops will tend to form emulsion 1, although the effect is not very pronounced.
5. The difference in critical thicknesses of the two emulsions only slightly affects the rate ratio in Equation 5.292, although the value of h_{cr} itself is important.
6. The viscosity of the continuous phase, η , has no effect on the rate ratio, which depends only slightly on the viscosity of the drop phase, η_d . This is in agreement with the experimental observations (see Reference 32).
7. The interfacial tension, σ , affects the rate ratio directly only through the capillary pressure, $P_c = 2\sigma/R_d$. The electrolyte primarily affects the electrostatic disjoining pressure, Π , which decreases as the salt content increases, thus destabilizing the O/W emulsion. It can also influence the stability by changing the surfactant adsorption (including the case of nonionic surfactants).
8. The temperature strongly affects the solubility and surface activity of nonionic surfactants.³ It is well known that at higher temperature nonionic surfactants become more oil soluble, which favors the W/O emulsion. Thus, solubility may change the type of emulsion formed at the PIT. The surface activity has numerous implications; the most important is the change of the Gibbs elasticity, E_G , and the interfacial tension, σ .
9. Surface active additives (cosurfactants, demulsifiers, etc.), such as fatty alcohols in the case of ionic surfactants, may affect the emulsifier partitioning between the phases and its adsorption, thereby changing the Gibbs elasticity and the interfacial tension. The surface-active additive may also change the surface charge (mainly by increasing the

spacing among the emulsifier ionic headgroups), thus decreasing the repulsive electrostatic disjoining pressure and favoring the W/O emulsion. Polymeric surfactants and adsorbed proteins increase the steric repulsion between the film surfaces. They may favor either O/W or W/O emulsions, depending on their conformation at the interface and their surface activity.

10. The interfacial bending moment, B_0 , can also affect the type of the emulsion, although this is not directly visible from Equation 5.292. (Note that $B_0 = -4k_c H_0$, where H_0 is the so-called spontaneous curvature and k_c is the interfacial curvature elastic modulus.¹²⁹ Typically, B_0 is of the order of 5×10^{-11} N.) Usually, for O/W emulsions, B_0 opposes the flattening of the droplet surfaces in the zone of collision (Figure 5.23), but for W/O emulsions favors the flattening.¹³⁴ This effect might be quantified by the expression for the curvature contribution in the energy of droplet–droplet interaction:¹³⁴

$$W_c = -2\pi R^2 B_0 / R_d, \quad (R/R_d)^2 \ll 1 \quad (5.293)$$

It turns out that $W_c > 0$ for the droplet collisions in an O/W emulsion, while $W_c < 0$ for a W/O emulsion.¹³⁴ Consequently, the interfacial bending moment stabilizes the O/W emulsions but destabilizes the W/O ones. There is supporting experimental evidence⁵⁶⁴ for microemulsions, i.e., for droplets of rather small size. Moreover, the effect of the bending moment can be important even for micrometer-sized droplets.¹³⁴ This is because the bent area increases faster ($R^2 \propto R_d^2$) than the bending energy per unit area decreases ($W_c/R^2 \propto 1/R_d$) when the droplet radius, R_d , increases (see Equation 5.293).

For micrometer-sized emulsion droplets the capillary pressure can be so high that a film may not appear between the drops. In such a case, instead of Equation 5.292, we can use analogous expression for nondeformed (spherical) drops.⁵⁶⁵

5.5.3.4 Demulsification

It has been known for a long time³² that one way to destroy an emulsion is to add a surfactant, which is soluble in the drop phase — this method is termed *chemical demulsification*. To understand the underlying process, let us consider two colliding emulsion droplets with film formed in the zone of collision (see Figures 5.23 and 5.45). As discussed above, when the liquid is flowing out of the film, the viscous drag exerted on the film surfaces (from the side of the film interior) carries away the adsorbed emulsifier toward the film periphery. Thus, a nonuniform surface distribution of the emulsifier (shown in Figure 5.45a by empty circles) is established. If demulsifier (the closed circles in Figure 5.45b) is present in the drop phase, it will occupy the interfacial area freed by the emulsifier. The result will be a saturation of the adsorption layer, as shown in Figure 5.45b. If the demulsifier is sufficiently surface active, its molecules will be able to decrease substantially, and even to eliminate completely, the interfacial tension gradients, thus changing the emulsion to type 2 (see Figure 5.44 and Section 5.5.3.2, above). This leads to a strong increase in the rate of film thinning, rapid drop coalescence, and emulsion destruction.^{500,501} The above mechanism suggests that the demulsifier has to possess the following properties:

1. It must be soluble in the drop phase or in both phases, but in the latter case its solubility in the drop phase must be much higher.
2. Its diffusivity and concentration must be large enough to provide a sufficiently large demulsifier flux toward the surfaces and thus eliminate the gradients of the interfacial tension.
3. Its surface activity must be comparable and even higher than that of the emulsifier; otherwise, even though it may adsorb, it will not be able to suppress the interfacial tension gradients.

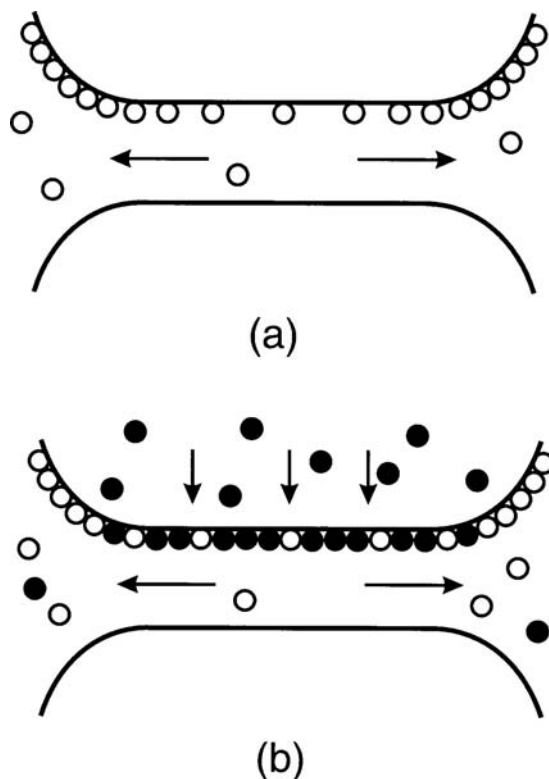


FIGURE 5.45 (a) Nonuniform surface distribution of an emulsifier due to drag from the draining film. (b) Suppression of the surface tension gradients by a demulsifier added in the drop phase.

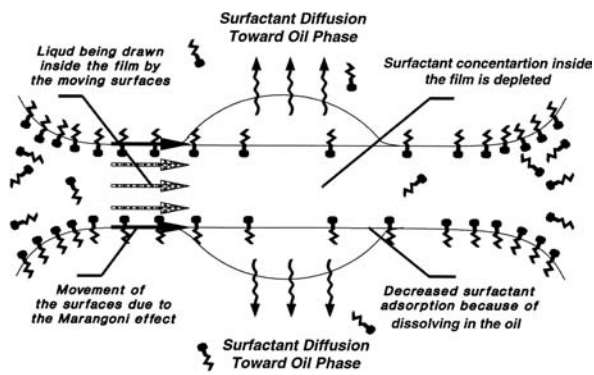
In regard to defoaming, various mechanisms are possible, which are discussed in Section 5.7, below.

5.5.4 INTERACTIONS IN NONPREEQUILIBRATED EMULSIONS

The common nonionic surfactants are often soluble in both water and oil phases. In the practice of emulsion preparation, the surfactant (the emulsifier) is initially dissolved in one of the liquid phases and then the emulsion is prepared by homogenization. In such a case, the initial distribution of the surfactant between the two phases of the emulsion is not in equilibrium; therefore, surfactant diffusion fluxes appear across the surfaces of the emulsion droplets. The process of surfactant redistribution usually lasts from many hours to several days, until finally equilibrium distribution is established. The diffusion fluxes across the interfaces, directed either from the continuous phase toward the droplets or the reverse, are found to stabilize both thin films and emulsions. In particular, even films, which are thermodynamically unstable, may exist several days because of the diffusive surfactant transfer; however, they rupture immediately after the diffusive equilibrium has been established. Experimentally, this effect manifests itself in phenomena called *cyclic dimpling*⁵⁶⁶ and *osmotic swelling*.⁵⁶⁷ These two phenomena, as well as the equilibration of two phases across a film,^{568,569} are described and interpreted below.

5.5.4.1 Surfactant Transfer from Continuous to Disperse Phase (Cyclic Dimpling)

The phenomenon of cyclic dimpling was first observed^{501,566} with xylene films intervening between two water droplets in the presence of the nonionic emulsifier Tween 20 or Tween 80 (initially



(a)



(b)

FIGURE 5.46 Spontaneous cyclic dimpling caused by surfactant diffusion from the aqueous film toward the two adjacent oil phases. (a) Schematic presentation of the process. (b) Photograph of a large dimple just before flowing out; the interference fringes in reflected light allow determination of the dimple shape.

dissolved in water but also soluble in oil). The same phenomenon also has been observed with other emulsion systems.

After the formation of such an emulsion film, it thins down to an equilibrium thickness (approximately 100 nm), determined by the electrostatic repulsion between the interfaces. As soon as the film reaches this thickness, a dimple spontaneously forms in the film center and starts growing (Figure 5.46a). When the dimple becomes bigger and approaches the film periphery, a channel forms connecting the dimple with the aqueous phase outside the film (Figure 5.46b). Then, the water contained in the dimple flows out leaving an almost plane-parallel film behind. Just afterward, a new dimple starts to grow and the process repeats again. The period of this cyclic dimpling remains approximately constant for many cycles and could be from a couple of minutes up to more than 10 min. It was established that this process is driven by the depletion of the surfactant concentration on the film surfaces due to the dissolving of surfactant in the adjacent drop phases. The depletion triggers a surface convection flux along the two film surfaces and a bulk diffusion flux in the film interior. Both fluxes are directed toward the center of the film. The surface convection causes a tangential movement of the film surfaces; the latter drag along a convective influx of solution in the film, which feeds the dimple. Thus, the cyclic dimpling appears to be a process leading to stabilization of the emulsion films and emulsions due to the influx of additional liquid in the region between the droplets, which prevents them from a closer approach, and eventually, from coalescence.

Combining the general equation of films with deformable interfaces (Equation 5.255), the mass balance (Equations 5.276 and 5.277), and the boundary condition for the interfacial stresses (Equation 5.281), we can derive⁵⁷⁰

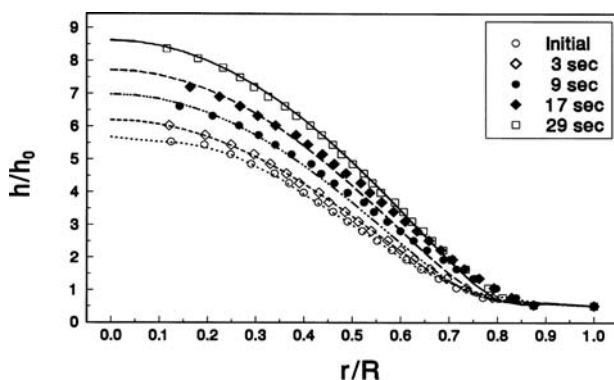


FIGURE 5.47 Comparison between the theory of cyclic dimpling (the lines) and the experimental data (the points) for the dimple shape, $h(r)$, determined from the interference fringes (see Figure 5.46b); emulsifier is anionic surfactant sodium nonylphenol polyoxyethylene-25 sulfate and the oil phase is styrene.

$$\frac{\partial h}{\partial t} + \frac{1}{3\eta r} \frac{\partial}{\partial r} \left\{ rh^3 \frac{\partial}{\partial r} \left[\frac{\sigma}{r} \frac{\partial}{\partial r} \left(r \frac{\partial h}{\partial r} \right) + \Pi(h) \right] \right\} = \frac{1}{2r} \frac{\partial}{\partial r} \left(\frac{jhr^2}{\Gamma} \right) \quad (5.294)$$

where j is the diffusion flux in the drop phase, and, as usual, r is radial coordinate, $h(r,t)$ is the film thickness, σ is surface tension, Γ is adsorption, and Π is disjoining pressure. The comparison between the numerical calculations based on Equation 5.294 and the experimental data for the cyclic dimpling with the anionic surfactant sodium nonylphenol polyoxyethylene-25 sulfate show a very good agreement (Figure 5.47). The experimental points are obtained from the interference fringes (see Figure 5.46). The shape in the initial moment, $t = 0$, serves as an initial condition for determining $h(r,t)$ by solving Equation 5.294. The curves for $t = 3, 9, 17,$ and 29 s represent theoretical predictions. The scaling parameters along the h and r axes in Figure 5.47 are $h_0 = 350$ nm and $R = 320$ μ m, with the latter the film radius; the only adjustable parameter is the diffusion flux, j .

5.5.4.2 Surfactant Transfer from Disperse to Continuous Phase (Osmotic Swelling)

Velev et al.⁴⁹⁸ reported that emulsion films, formed from preequilibrated phases containing the nonionic surfactant Tween and 0.1 M NaCl, spontaneously thin to Newton black films (thickness ≈ 10 nm) and then rupture. However, when the nonionic surfactant Tween 20 or Tween 60 is initially dissolved in the xylene drops and the film is formed from the nonpreequilibrated phases, no black film formation and rupture are observed.^{501,567} Instead, the films have a thickness above 100 nm, and we observe formation of channels of larger thickness connecting the film periphery with the film center (Figure 5.48). We may observe that the liquid is circulating along the channels for a period from several hours to several days. The phenomenon continues until the redistribution of the surfactant between the phases is accomplished. This phenomenon occurs only when the background surfactant concentration in the continuous (the aqueous) phase is not lower than the CMC. These observations can be interpreted in the following way.

Because the surfactant concentration in the oil phase (the disperse phase) is higher than the equilibrium concentration, surfactant molecules cross the oil–water interface toward the aqueous phase. Thus, surfactant accumulates within the film, because the bulk diffusion throughout the film is not fast enough to transport promptly the excess surfactant into the Plateau border. As the background surfactant concentration in the aqueous phase is not less than CMC, the excess surfactant present in the film is packed in the form of micelles (denoted by black dots in Figure 5.48a). This decreases the chemical potential of the surfactant inside the film. Nevertheless,

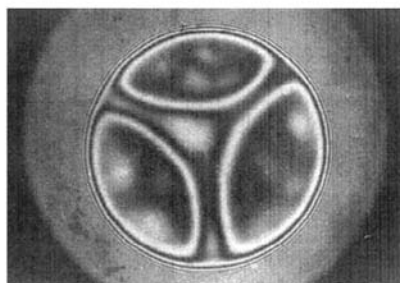
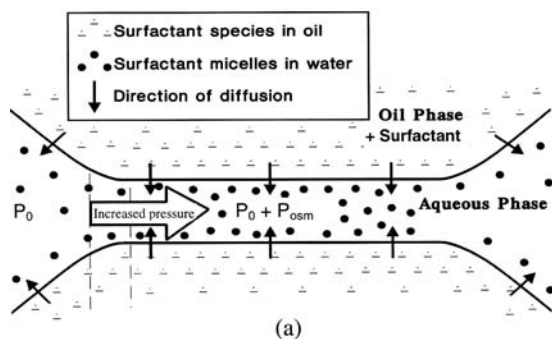


FIGURE 5.48 Osmotic swelling of an aqueous film formed between two oil droplets. (a) The surfactant dissolved in the oil is transferred by diffusion toward the film, where it forms micelles, the osmotic effects of which increase the local pressure. (b) Photograph of a typical pattern from a circular film with channels.

the film is subjected to osmotic swelling because of the increased concentration of micelles within. The excess osmotic pressure

$$P_{\text{osm}} = kT C_{\text{mic}} \geq P_c \quad (5.295)$$

counterbalances the outer capillary pressure and arrests further thinning of the film. Moreover, the excess osmotic pressure in the film gives rise to a convective outflow of solution: this is the physical origin of the observed channels (Figure 5.48b).

Experimental data^{501,567} show that the occurrence of the above phenomenon is the same for initial surfactant concentration in the water varying from 1 up to 500 times the CMC, if only some amount of surfactant is also initially dissolved also in the oil. This fact implies that the value of the surfactant chemical potential inside the oil phase is much greater than that in the aqueous phase, with the latter closer to its value at the CMC in the investigated range of concentrations.

5.5.4.3 Equilibration of Two Droplets across a Thin Film

In the last two sections, we considered mass transfer from the film toward the droplets and the reverse, from droplets toward the film. In both cases, the diffusion fluxes lead to stabilization of the film. Here we consider the third possible case corresponding to mass transfer from the first droplet toward the second one across the film between them. In contrast with the former two cases, in the last case the mass transfer is found to destabilize the films. Experimentally, the diffusion transfer of alcohols, acetic acid, and acetone was studied.^{571,572} The observed destabilization of the films can be attributed to the appearance of Marangoni instability,⁵⁶⁸ which manifests itself through the growth of capillary waves at the interfaces, which eventually can lead to film rupture.

The Marangoni instabilities can appear not only in thin films, but also in the simpler case of a single interface. In this case, the Marangoni instability may bring about spontaneous emulsification. This effect has been theoretically investigated by Sternling and Scriven,⁵⁷³ whose work stimulated numerous theoretical and experimental studies on spontaneous emulsification. Lin and Brenner⁵⁷⁴ examined the role of the heat and mass transfer in an attempt to check the hypothesis of Holly⁵⁷⁵ that the Marangoni instability can cause the rupture of tear films. Their analysis was extended by Castillo and Velarde,⁵⁷⁶ who accounted for the tight coupling of the heat and mass transfer and showed that it drastically reduces the threshold for Marangoni convection. Instability driven by diffusion flux of dissolved oil molecules across an asymmetric liquid film (oil–water–air film) has been theoretically investigated.⁵⁶⁹ It was found that even small decrements of the water–air surface tension, caused by the adsorbed oil, are sufficient to trigger the instability.

5.5.5 HYDRODYNAMIC INTERACTION OF A PARTICLE WITH AN INTERFACE

There are various cases of particle–interface interactions, which require separate theoretical treatment. The simpler case is the hydrodynamic interaction of a solid particle with a solid interface. Other cases are the interactions of fluid particles (of tangentially mobile or immobile interfaces) with a solid surface; in these cases, the hydrodynamic interaction is accompanied by deformation of the particle. On the other hand, the colloidal particles (both solid and fluid) may hydrodynamically interact with a fluid interface, which thereby undergoes a deformation. In the case of fluid interfaces, the effects of surfactant adsorption, surface diffusivity, and viscosity affect the hydrodynamic interactions. A special class of problems concerns particles attached to an interface, which are moving throughout the interface. Another class of problems is related to the case when colloidal particles are confined in a restricted space within a narrow cylindrical channel or between two parallel interfaces (solid and/or fluid); in the latter case, the particles interact simultaneously with both film surfaces.

The theoretical contributions are limited to the case of low Reynolds number^{421,422,496,577–579} (mostly for creeping flows, see Section 5.5.1), avoiding the difficulties arising from the nonlinearity of the equations governing the fluid motion at higher velocities. Indeed, for low Reynolds numbers, the term $\mathbf{v} \cdot \nabla \mathbf{v}$ in the Navier–Stokes equation (see Equations 5.247 to 5.249) is negligible, and we may apply the method of superposition to solve the resulting linear set of equations. This means that we may first solve the simpler problems about the particle elementary motions: (1) particle translation (without rotation) in an otherwise immobile liquid, (2) particle rotation (without translation) in an otherwise immobile liquid, and (3) streamlining of an immobile particle by a Couette or Poiseuille flow. Once the problems about the elementary motions have been solved, we may obtain the linear and angular velocity of the real particle motion combining the elementary flows. The principle of combination is based on the fact that for low Reynolds numbers the particle acceleration is negligible, and the net force and torque exerted on the particle must be zero. In other words, the hydrodynamic drag forces and torques originating from the particle translation and rotation are counterbalanced by those originating from the streamlining:

$$\mathbf{F}_{\text{translation}} + \mathbf{F}_{\text{rotation}} + \mathbf{F}_{\text{streamlining}} = \mathbf{0}, \quad \mathbf{M}_{\text{translation}} + \mathbf{M}_{\text{rotation}} + \mathbf{M}_{\text{streamlining}} = \mathbf{0} \quad (5.296)$$

That is the reason we will now consider expressions for \mathbf{F} and \mathbf{M} for various types of elementary motions.

5.5.5.1 Particle of Immobile Surface Interacting with a Solid Wall

The force and torque exerted on a solid particle were obtained in the form of a power series with respect to R_d/l , where R_d is the particle radius and l is the distance from the center of the particle to the wall. Lorentz⁵⁸⁰ derived an asymptotic expression for the motion of a sphere along the normal

to a planar wall with an accuracy of up to R_d/l . Faxen⁵⁸¹ developed the method of reflection for a sphere moving between two parallel planes in a viscous fluid. Using this method, Wakiya⁵⁸² considered the cases of motion in flow of Couette and Poiseuille; however, the method employed by him cannot be applied to small distances to the wall.⁴⁴² The next important step was taken by Dean and O'Neill⁵⁸³ and O'Neill,⁵⁸⁴ who found an exact solution for the force and the torque acting on a spherical particle moving tangentially to a planar wall at an arbitrary distance from the wall. The limiting case of small distances between the particle and the wall was examined by several authors.^{433-435,585} Instead of an exact solution of the problem, the authors derived asymptotic formulae for the force and torque. Keh and Tseng⁵⁸⁶ presented a combined analytical-numerical study for the slow motion of an arbitrary axisymmetric body along its axis of revolution, with the latter normal to a planar surface. The inertial migration of a small solid sphere in a Poiseuille flow was calculated by Schonberg and Hinch⁵⁸⁷ for the case when the Reynolds number for the channel is of the order of unity.

Below we present expressions for the forces and torques for some of the elementary motions. In all cases we assume that the Reynolds number is small, the coordinate plane xy is parallel to the planar wall and h is the shortest surface-to-surface distance from the particle to the wall.

First, we consider the case of a pure translational motion: a solid spherical particle of radius R_d that translates along the y axis with a linear velocity U and angular velocity $\omega \equiv 0$ in an otherwise quiescent fluid. In spite of the fact that the particle does not rotate, it experiences a torque, \mathbf{M} , directed along the x axis, due to friction with the viscous fluid. The respective asymptotic expressions⁴³³⁻⁴³⁵ for the components of the drag force, \mathbf{F} , and torque, \mathbf{M} , read

$$F_x = 0, \quad F_y = -6\pi\eta UR_d f_y, \quad M_x = -8\pi\eta UR_d^2 m_x, \quad M_y = 0 \quad (5.297)$$

$$f_y = \left(\frac{8}{15} + \frac{16}{375} \frac{h}{R_d} \right) \ln \left(\frac{2R_d}{h} \right) + 0.58461 + O \left(\frac{h}{R_d} \right) \quad (5.298)$$

$$m_x = \left(\frac{1}{10} + \frac{43}{250} \frac{h}{R_d} \right) \ln \left(\frac{2R_d}{h} \right) - 0.26227 + O \left(\frac{h}{R_d} \right) \quad (5.299)$$

where f_y and m_x are dimensionless drag force and torque coefficients, respectively.

Second, we consider the case of pure rotation: a solid spherical particle of radius R_d is situated at a surface-to-surface distance, h , from a planar wall and rotates with angular velocity, ω , around the x axis in an otherwise quiescent fluid. The corresponding force and torque resultants are⁴³³⁻⁴³⁵

$$F_x = 0, \quad F_y = -6\pi\eta \omega R_d^2 f_y, \quad M_x = -8\pi\eta \omega R_d^3 m_x, \quad M_y = 0 \quad (5.300)$$

$$f_y = \frac{2}{15} \ln \left(\frac{R_d}{h} \right) - 0.2526 + O \left(\frac{h}{R_d} \right), \quad m_x = \frac{2}{5} \ln \left(\frac{R_d}{h} \right) + 0.3817 + O \left(\frac{h}{R_d} \right) \quad (5.301)$$

From Equations 5.297 to 5.301, it follows that the force and the torque depend weakly (logarithmically) on the distance, h , as compared to the Taylor or Reynolds laws (Equations 5.260 and 5.261).

As discussed in Sections 5.5.2.1 and 5.5.3.2, a fluid particle in the presence of high surfactant concentration can be treated as a deformable particle of tangentially immobile surfaces. Such a particle deforms when pressed against a solid wall (see the inset in Figure 5.49). To describe the drag due to the film intervening between the deformed particle and the wall, we may use the

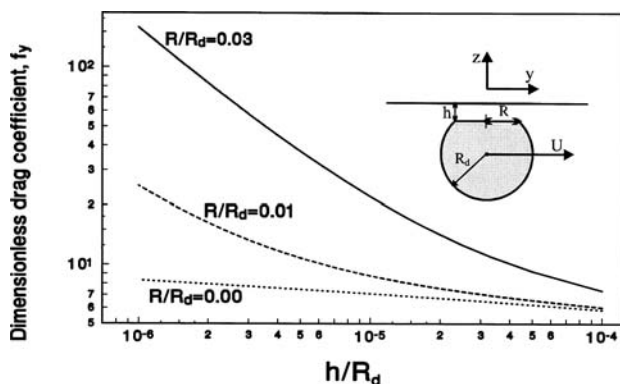


FIGURE 5.49 Deformed fluid particle (the inset) moving tangentially to an immobile solid surface: plot of the dimensionless drag coefficient, f_y , vs. the dimensionless film thickness, h/R_d , for three values of the dimensionless film radius, R/R_d (see Equation 5.303).

expression derived by Reynolds⁴²³ for the drag force exerted on a planar solid ellipsoidal disk, which is parallel to a solid wall and is moving along the y axis at a distance h from the wall:

$$F_x = 0, \quad F_y = -\pi\eta U \frac{h}{ab} \quad (5.302)$$

Here, a and b are the semiaxes of the ellipse; for a circular disk (or film), we have $a = b = R$. By combining Equations 5.297 and 5.298 with Equation 5.302, we can derive an expression for the net drag force experienced by the deformed particle (the inset in Figure 5.49) when it moves along the y axis with a linear velocity U :

$$F_y = -6\pi\eta UR_d f_y, \quad f_y = \frac{R^2}{6hR_d} + \left(\frac{8}{15} + \frac{16}{375} \frac{h}{R_d} \right) \ln \left(\frac{2R_d}{h} \right) + 0.58461 + O \left(\frac{h}{R_d} \right) \quad (5.303)$$

Here, as usual, h and R denote the film thickness and radius, and R_d is the curvature radius of the spherical part of the particle surface. The dependence of the dimensionless drag coefficient, f_y , on the distance h for different values of the ratio R/R_d is illustrated in Figure 5.49. The increase of R/R_d and the decrease of h/R_d may lead to an increase of the drag force, f_y , by an order of magnitude. That is the reason the film between a deformed particle and a wall can be responsible for the major part of the energy dissipation. Moreover, the formation of doublets and flocks of droplets separated by liquid films seems to be of major importance for the rheological behavior of emulsions.

5.5.5.2 Fluid Particles of Mobile Surfaces

Let us start with the case of pure phases, when surfactant is missing and the fluid–liquid interfaces are mobile. Under these conditions, the interaction of an emulsion droplet with a planar solid wall was investigated by Ryskin and Leal,⁵⁸⁸ and numerical solutions were obtained. A new formulation of the same problem was proposed by Liron and Barta.⁵⁸⁹ The case of a small droplet moving in the restricted space between two parallel solid surfaces was solved by Shapira and Haber.^{590,591} These authors used the Lorentz reflection method to obtain analytical solutions for the drag force and the shape of a small droplet moving in Couette flow or with constant translational velocity.

The more complicated case, corresponding to a viscous fluid particle approaching the boundary between two pure fluid phases (all interfaces deformable), was investigated by Yang and Leal,^{592,593} who succeeded in obtaining analytical results.

Next, we proceed with the case when surfactant is present and the Marangoni effect becomes operative. Classical experiments carried out by Lebedev⁵⁹⁴ and Silvey⁵⁹⁵ show that the measured velocity of sedimentation, U , of small fluid droplets in a viscous liquid (pure liquid phases assumed) does not obey the Hadamar⁵⁹⁶ and Rybczynski⁵⁹⁷ equation:

$$F = 2\pi\eta UR_d \frac{3\eta_d + 2\eta}{\eta_d + \eta} \quad (5.304)$$

where F is the drag force. The limiting case $\eta_d \rightarrow 0$ corresponds to bubbles, whereas in the other limit, $\eta_d \rightarrow \infty$, Equation 5.304 describes solid particles. Note that Equation 5.304 is derived for the motion of a spherical fluid particle (drop or bubble) of viscosity η_d in a liquid of viscosity η in the absence of any surfactant. The explanation of the contradiction between theory and experiment^{594,595} turned out to be very simple: even liquids that are pure from the viewpoint of the spectral analysis may contain some surface-active impurities, whose bulk concentration might be vanishingly low, but which can provide a dense adsorption layer at the restricted area of the fluid particle surface. Then, the effects of Gibbs elasticity and interfacial viscosity substantially affect the drag coefficient of the fluid particle. The role of the latter two effects was investigated by Levich,⁴³⁶ Edwards et al.,⁴³⁷ and He et al.⁵⁹⁸ for the motion of an emulsion droplet covered with a monolayer of nonsoluble surfactant (adsorption and/or desorption not present). These authors used the Boussinesq–Scriven constitutive law of a viscous fluid interface (Equation 5.281), and established that only the dilatational interfacial viscosity, η_{dl} , but not the shear interfacial viscosity, η_{sh} , influences the drag force. If the surfactant is soluble in both phases and the process of adsorption is diffusion controlled (see Section 5.2.2.1) the generalization of Equation 5.304 is

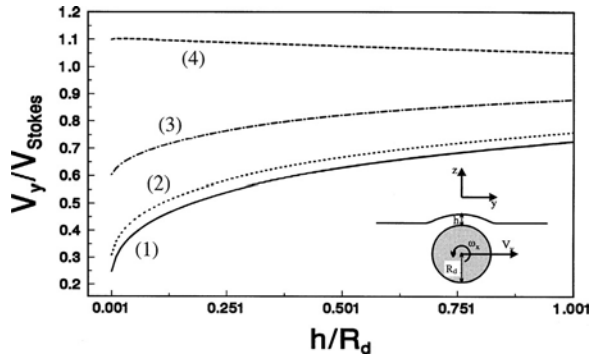
$$F = 2\pi\eta UR_d \left[3 - \left(1 + \frac{\eta_d}{\eta} + \frac{2\eta_{dl}}{\eta R_d} + \frac{R_d E_G}{3\eta D_s} \frac{2}{2 + 2\frac{R_d D}{h_a D_s} + \frac{R_d D_d}{h_{d,a} D_s}} \right)^{-1} \right] \quad (5.305)$$

where D_d is the surfactant diffusion coefficient in the drop phase; c and c_d are the concentrations of surfactant in the continuous and drop phases, respectively; $h_a = \partial\Gamma/\partial c$ and $h_{d,a} = \partial\Gamma/\partial c_d$ are the slopes of adsorption isotherms with respect to the surfactant concentration. In the limiting case without surfactant Equation 5.305 is reduced to the Hadamar⁵⁹⁶ and Rybczynski⁵⁹⁷ equation (Equation 5.304).

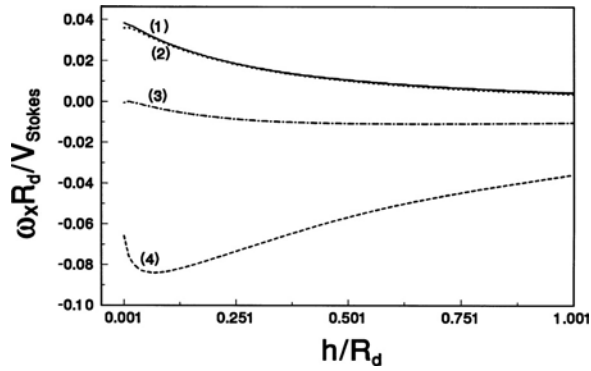
Danov et al.^{251,599-602} investigated theoretically the hydrodynamic interaction of a fluid particle with a fluid interface in the presence of surfactant. The numerical results of these authors reveal that there is a strong influence of both shear and dilatational interfacial viscosities on the motion of the fluid particle when the particle–interface distance, h , is approximately equal to or smaller than the particle radius, R_d . For example, in the presence of an external force acting parallel to the interface (along the y axis), the stationary motion of the spherical particle close to the viscous interface is a superposition of a translation along the y axis with velocity V_y and a rotation (around the x axis) with an angular velocity, ω_x (see the inset in Figure 5.50a). The numerical results of Danov et al.^{601,602} for V_y and ω_x normalized by the Stokes velocity, $V_{\text{Stokes}} = F/(6\pi\eta R_d)$, are plotted in Figures 5.50a and 5.50b vs. h/R_d for four different types of interfaces: (1) solid particle and solid wall (see Equations 5.297 to 5.299); (2) fluid particle and fluid interface for $K = E = 100$; (3) the same system as (2) but for $K = E = 10$; and (4) the same system as (2) but for $K = E = 1$, where

$$K \equiv \eta_{dl}/(\eta R_d), \quad E \equiv \eta_{sh}/(\eta R_d) \quad (5.306)$$

(For the definition of the interfacial viscosities, η_{dl} and η_{sh} , see Equation 5.281.) As seen in Figure 5.50a, the velocity of the sphere, V_y , is less than V_{Stokes} for the solid (1) and the highly viscous



(a)



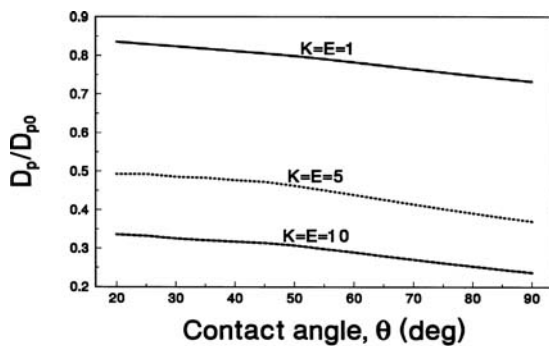
(b)

FIGURE 5.50 Spherical particle moving tangentially to a viscous interface: plots of the stationary dimensionless linear (V_y/V_{Stokes}) (a) and angular ($\omega_x R_d/V_{\text{Stokes}}$) (b) velocities vs. the dimensionless thickness, h/R_d . The curves corresponds to various surface viscosities: (1) $K = E = \infty$ (solid surfaces); (2) $K = E = 100$; (3) $K = E = 10$, and (4) $K = E = 1$ (see Equation 5.306).

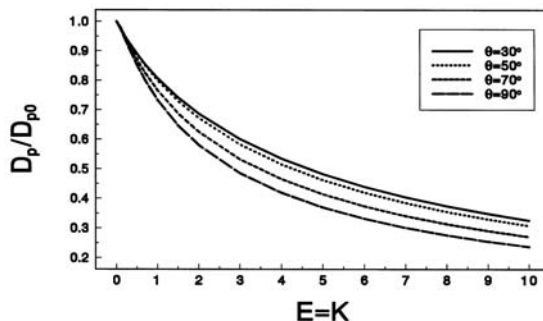
(2) interfaces, and V_y noticeably decreases when the distance h decreases. However, in case (4), corresponding to low surface viscosities, the effect is quite different: V_y/V_{Stokes} is greater than unity (the sphere moves faster near the interface than in the bulk), and its dependence on h is rather weak. The result about the angular velocity, ω_x , is also intriguing (Figure 5.50b). The stationary rotation of a sphere close to a solid (1) or highly viscous (2) interface is in the positive direction, i.e., $\omega_x > 0$. For the intermediate interfacial viscosity (3), the sphere practically does not rotate, whereas, for the interfaces of low viscosity (4), the drop rotates in the opposite direction, i.e., $\omega_x < 0$. The inversion of the sign of ω_x is due to the fact that the friction of the particle with the bulk fluid below it (see the inset in Figure 5.50a) becomes stronger than the friction with the interface above the particle.

Finally, we consider the case of a solid particle attached to a liquid–fluid interface. This configuration is depicted in Figure 5.17e; note that the position of the particle along the normal to the interface is determined by the value of the three-phase contact angle. Stoops and Leal⁶⁰³ investigated the case when such an attached particle is subjected to a flow directed normally to the interface. These authors determined the critical capillary number, beyond which the captured particle is removed from the interface by the flow.

Danov et al.²⁵¹ examined the case of an attached particle moving along a liquid–gas interface under the action of an applied force directed tangentially to the interface. The effect of the contact



(a)



(b)

FIGURE 5.51 Effect of adsorbed surfactant on the surface diffusivity, D_p , of a Brownian particle attached to a fluid interface: (a) plot of D_p/D_{p0} vs. particle contact angle, θ , for various surface viscosities (see Equation 5.306); (b) plot of D_p/D_{p0} vs. the dimensionless surface viscosity, $K = E$, for various θ .

angle (the depth of immersion), as well as the effect of adsorbed surfactant on the drag force, were investigated. These authors also calculated the surface diffusion coefficient of a Brownian particle attached to the liquid surface. Let D_p and D_{p0} be the particle surface diffusion coefficient in the presence and in the absence of surfactant, respectively. In Figure 5.51a, we plot the results for D_p/D_{p0} vs. the solid–liquid–gas contact angle, θ , for three different values of the parameters K and E characterizing the surface viscosities (see Equation 5.306): (1) $K = E = 1$, (2) $K = E = 5$, and (3) $K = E = 10$. The relatively small slope of the curves in Figure 5.51a indicates that D_p/D_{p0} depends less significantly on the contact angle, θ , than on the surface viscosity characterized by K and E . Note, however, that D_{p0} itself depends markedly on θ : the absolute value of D_{p0} is smaller for the smaller values of θ (for deeper immersion of the particle in the liquid phase). Figure 5.51b presents the calculated dependence of D_p/D_{p0} on the surface viscosity characterized by K and E ($K = E$ is used in the calculations) for various fixed values of the contact angle, θ . Apparently, the particle mobility decreases faster for the smaller values of K and then tends to zero insofar as the fluid surface “solidifies” for the higher values of the surface viscosities. The experimental data from measurements of the drag coefficient of spherical particles attached to fluid interfaces²⁵⁰ showed very good agreement with the predictions of the theory.²⁵¹

The role of surface viscosity and elasticity on the motion of a solid particle trapped in a thin film, at an interface, or at a membrane of a spherical vesicle has been recently investigated in References 604 and 605. The theoretical results^{604,605} have been applied to process the experimental data for the drag coefficient of polystyrene latex particles moving throughout the membrane of a giant lipid vesicle.^{606–612} Thus, the interfacial viscosity of membranes has been determined.

5.5.6 BULK RHEOLOGY OF DISPERSIONS

The description of the general rheological behavior of colloidal dispersions requires information regarding the drag forces and torques experienced by the individual particles.^{278,613,614} In dilute systems, the hydrodynamic interactions between the particles can be neglected and their motion can be treated independently. In contrast, when the particle concentration is higher, the effect of hydrodynamic interactions between a spherical particle and an interface on the drag force and torque acquires considerable importance. The viscosity and the collective diffusion coefficient of colloidal dispersions can be strongly affected also by long-range surface forces, like the electrostatic double layer force; see Section 5.9.2.4 below.

Long ago Einstein⁶¹⁵ obtained a formula for the diffusion coefficient for solid spheres in the dilute limit:

$$D = kT/(6\pi\eta_m R_p) \quad (5.307)$$

where R_p is the particle radius and η_m is the viscosity of the liquid medium. This relation was later generalized by Kubo⁶¹⁶ for cases when the hydrodynamic resistance becomes important. The further development in this field is reviewed by Davis.⁵⁷⁷

The particle–particle interactions lead to a dependence of the viscosity, η , of a colloidal dispersion on the particle volume fraction, ϕ . Einstein⁶¹⁷ showed that for a suspension of spherical particles in the dilute limit:

$$\eta = \eta_m [1 + 2.5\phi + O(\phi^2)] \quad (5.308)$$

Later Taylor⁶¹⁸ generalized Equation 5.308 for emulsion systems taking into account the viscous dissipation of energy due to the flow inside the droplets. Oldroyd⁶¹⁹ took into account the effect of surface viscosity and generalized the theory of Taylor⁶¹⁸ to diluted monodisperse emulsions whose droplets have viscous interfaces. Taylor,⁶²⁰ Fröhlich and Sack,⁶²¹ and Oldroyd⁶²² applied asymptotic analysis to derive the next term in Equation 5.308 with respect to the capillary number. Thus, the effect of droplet interfacial tension was included. This generalization may be important at high shear rates. Another important generalization is the derivation of appropriate expressions for the viscosity of suspensions containing particles with different shapes.^{421,422} A third direction of generalization of Equation 5.308 is to calculate the next term in the series with respect to the volume fraction, ϕ . Batchelor⁶²³ took into account the long-range hydrodynamic interaction between the particles to derive:

$$\eta = \eta_m [1 + 2.5\phi + 6.2\phi^2 + O(\phi^3)] \quad (5.309)$$

From a mathematical viewpoint, Equation 5.309 is an exact result; however, from a physical viewpoint, Equation 5.309 is not entirely adequate to the real dispersions, as only the long-range hydrodynamic interactions are operative in colloids. A number of empirical expressions have been proposed in which the coefficient multiplying ϕ^2 varies between 5 and 15.⁶²⁴ The development of new powerful numerical methods during the last 5 years helped for a better understanding of the rheology of emulsions.⁶²⁵⁻⁶³³ The simple shear and Brownian flow of dispersions of elastic capsules, rough spheres, and liquid droplets were studied in References 626, 630, 632, and 633. The effect of insoluble surfactants and the drop deformation on the hydrodynamic interactions and on the rheology of dilute emulsions are the subject of investigation in References 627, 629, and 631. Loewenberg and Hinch^{625,628} discussed the basic ideas of the numerical simulations of concentrated emulsion flows. These works are aimed at giving a theoretical interpretation of various experimental results for dilute and concentrated dispersions. When the Peclet number is not small, the convective

term in the diffusion equation (Equations 5.276 and 5.277) cannot be neglected and the respective problem has no analytical solution. Thus, a complex numerical investigation has to be applied.^{634,635}

The formulae of Einstein,^{615,617} Taylor,⁶¹⁸ and Oldroyd⁶¹⁹ have been generalized for dilute emulsions of mobile surfaces with account for the Gibbs elasticity and the bulk and surface diffusion and viscosity.⁶³⁶

$$\frac{\eta}{\eta_m} = 1 + \left(1 + \frac{3}{2} \langle \varepsilon_m \rangle\right) \phi + O(\phi^2), \quad \langle \varepsilon_m \rangle \equiv \frac{\sum R_d^3 \varepsilon_m}{\sum R_d^3} \quad (5.310)$$

where $\langle \varepsilon_m \rangle$ is the average value of the interfacial mobility parameter, ε_m , for all droplets in the control volume. The mobility parameter of individual drops, ε_m , and the effective surfactant diffusion coefficient, D_{eff} , are⁶³⁶

$$\varepsilon_m \equiv \left[\frac{\eta_d}{\eta_m} + \frac{2}{5} \left(\frac{R_d E_G}{2\eta_m D_{\text{eff}}} + \frac{3\eta_{\text{dl}} + 2\eta_{\text{sh}}}{R_d \eta_m} \right) \right] \bigg/ \left[1 + \frac{\eta_d}{\eta_m} + \frac{2}{5} \left(\frac{R_d E_G}{2\eta_m D_{\text{eff}}} + \frac{3\eta_{\text{dl}} + 2\eta_{\text{sh}}}{R_d \eta_m} \right) \right] \quad (5.311)$$

$$D_{\text{eff}} \equiv D_s + \frac{R_d D}{2h_a} + \frac{R_d D_d}{3h_{d,a}} \quad (5.312)$$

(see Equation 5.305 and below). If the droplet size distribution in the emulsion, and the interfacial rheological parameters are known, then the average value $\langle \varepsilon_m \rangle$ can be estimated. For monodisperse emulsions the average value, $\langle \varepsilon_m \rangle$, and the interfacial mobility parameter, ε_m , are equal. In the special case of completely mobile interfaces, that is, $R_d E_G / (\eta_m D_{\text{eff}}) \rightarrow 0$ and $(3\eta_{\text{dl}} + 2\eta_{\text{sh}}) / (R_d \eta_m) \rightarrow 0$, the mobility parameter, ε_m , does not depend on the droplet size, and from Equation 5.311 and 312 the Taylor⁶¹⁸ formula is obtained. It is important to note that the Taylor formula takes into account only the bulk properties of the phases (characterized by η_d / η_m); in such a case ε_m is independent of R_d and the Taylor equation is applicable also to polydisperse emulsions. If only the Marangoni effect is neglected ($E_G \rightarrow 0$), then Equations 5.311 and 5.312 become equivalent to the Oldroyd⁶¹⁹ formula, which is originally derived only for monodisperse emulsions.

For higher values of the particle volume fraction, the rheological behavior of the colloidal dispersions becomes rather complex. We will consider qualitatively the observed phenomena, and next we will review available semiempirical expressions.

For a simple shear (Couette) flow, the relation between the applied stress, τ , and the resulting shear rate, $\dot{\gamma}$, can be expressed in the form:

$$\tau = \eta \dot{\gamma} \quad (5.313)$$

(For example, when a liquid is sheared between two plates parallel to the xy plane, we have $\dot{\gamma} = \partial v_x / \partial z$.) A typical plot of $\dot{\gamma}$ vs. τ is shown in Figure 5.52a. For low and high shear rates, we observe Newtonian behavior ($\eta = \text{const.}$), whereas in the intermediate region a transition from the lower shear rate viscosity, η_0 , to the higher shear rate viscosity, η_∞ , takes place. This is also visualized in Figure 5.52b, where the viscosity of the colloidal dispersion, η is plotted vs. the shear rate, $\dot{\gamma}$; note that in the intermediate zone η has a minimum.⁴¹⁵

Note also that both η_0 and η_∞ depend on the particle volume fraction, ϕ . de Kruijff et al.⁶²⁴ proposed the semiempirical expansions:

$$\frac{\eta_0}{\eta_m} = 1 + 2.5\phi + (4 \pm 2)\phi^2 + (42 \pm 10)\phi^3 + \dots \quad (5.314)$$

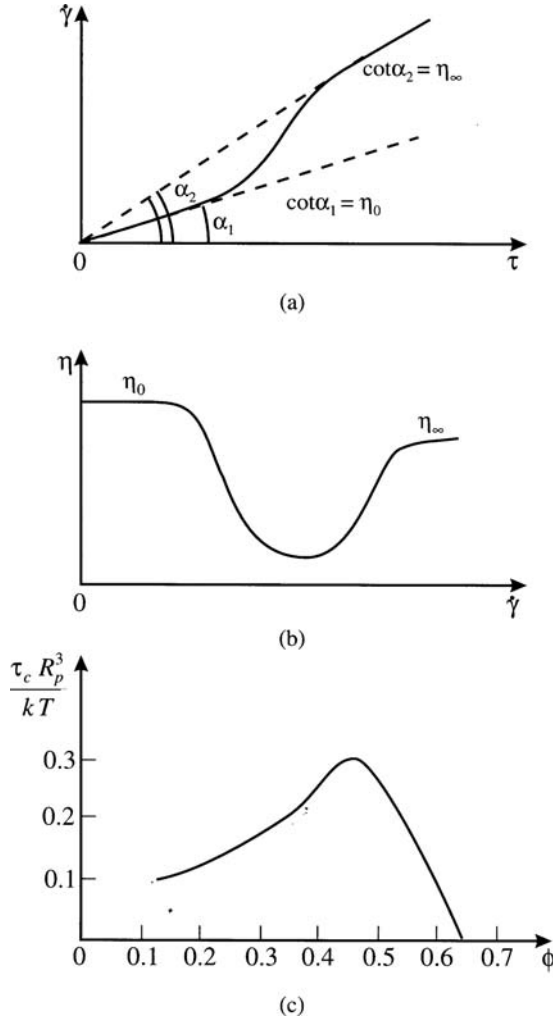


FIGURE 5.52 Qualitative presentation of basic relations in rheology of suspensions: (a) rate of strain, $\dot{\gamma}$, vs. applied stress, τ , (see Equation 5.313); (b) average viscosity of a suspension, η , vs. rate of strain, $\dot{\gamma}$; (c) dimensionless parameter τ_c (Equation 5.317) vs. particle volume fraction ϕ .

$$\frac{\eta_\infty}{\eta_m} = 1 + 2.5\phi + (4 \pm 2)\phi^2 + (25 \pm 7)\phi^3 + \dots \quad (5.315)$$

as well as two empirical expressions that can be used in the whole range of values of ϕ :

$$\frac{\eta_0}{\eta_m} = \left(1 - \frac{\phi}{0.63}\right)^{-2}, \quad \frac{\eta_\infty}{\eta_m} = \left(1 - \frac{\phi}{0.71}\right)^{-2} \quad (5.316)$$

In regard to the dependence of η on the shear stress, τ , Russel et al.²⁷⁸ reported that for the intermediate values of τ , corresponding to non-Newtonian behavior (Figure 5.52a and b), the experimental data correlate reasonably well with the expression:

TABLE 5.6
Maximum Packing Volume Fraction, ϕ_{\max} ,
for Various Arrangements
of Monodisperse Spheres

Arrangement	ϕ_{\max}
Simple cubic	0.52
Minimum thermodynamically stable configuration	0.548
Hexagonally packed sheets just touching	0.605
Random close packing	0.637
Body-centered cubic packing	0.68
Face-centered cubic/hexagonal close packed	0.74

$$\frac{\eta - \eta_{\infty}}{\eta - \eta_0} = \frac{1}{1 + (\tau / \tau_c)^n} \quad (5.317)$$

with $1 \leq n \leq 2$, where τ_c is the value of τ for which $\eta = (\eta_0 + \eta_{\infty})/2$. In its own turn, τ_c depends on the particle volume fraction ϕ (see Figure 5.52c). We see that τ_c increases with the volume fraction, ϕ , in dilute dispersions then passes through a maximum and finally decreases to zero; note that $\tau_c \rightarrow 0$ corresponds to $\eta_0 \rightarrow \infty$. The peak at $\phi \approx 0.5$ is the only indication that the hard-sphere disorder–order transition either occurs or is rheologically significant in these systems.²⁷⁸

The restoring force for a dispersion to return to a random, isotropic situation at rest is either Brownian (thermal fluctuations) or osmotic.⁶³⁷ The former is most important for submicrometer particles and the latter for larger particles. Changing the flow conditions changes the structure, and this leads to thixotropic effects, which are especially strong in flocculated systems.

Krieger and Dougherty⁶³⁸ applied the theory of corresponding states to obtain the following expression for the viscosity of hard-sphere dispersions:

$$\frac{\eta}{\eta_m} = \left(1 - \frac{\phi}{\phi_{\max}} \right)^{-[\eta]\phi_{\max}} \quad (5.318)$$

where $[\eta]$ is the dimensionless intrinsic viscosity, which has a theoretical value of 2.5 for monodisperse rigid spheres, and ϕ_{\max} is the maximum packing volume fraction for which the viscosity η diverges. The value of ϕ_{\max} depends on the type of packing of the particles⁴¹⁵ (Table 5.6). The maximum packing fraction, ϕ_{\max} , is very sensitive to particle-size distribution and particle shape.⁶³⁹ Broader particle-size distributions have greater values of ϕ_{\max} . On the other hand, nonspherical particles lead to poorer space-filling and hence lower ϕ_{\max} . Table 5.7 presents the values of $[\eta]$ and ϕ_{\max} obtained by fitting the results of a number of experiments on dispersions of asymmetric particles using Equation 5.318. The trend of $[\eta]$ to increase and of ϕ_{\max} to decrease with increasing asymmetry is clearly seen, but the product, $[\eta]\phi_{\max}$, is almost constant; $[\eta]\phi_{\max}$ is about 2 for spheres and about 1.4 for fibers. This fact can be utilized to estimate the viscosity of a wide variety of dispersions.

A number of rheological experiments with foams and emulsions are summarized in the reviews by Prud'home and Khan⁶⁴⁰ and Tadros.⁶⁴¹ These experiments demonstrate the influence of films between the droplets (or bubbles) on the shear viscosity of the dispersion as a whole. Unfortunately, there is no consistent theoretical explanation of this effect accounting for the different hydrodynamic resistance of the films between the deformed fluid particles as compared to the nondeformed

TABLE 5.7
Values of $[\eta]$ and ϕ_{\max} for a Number of Dispersions Obtained
by Fitting Experimental Data by Means of Equation 5.318

System	$[\eta]$	ϕ_{\max}	$[\eta]\phi_{\max}$	Ref.
Spheres (submicron)	2.7	0.71	1.92	de Kruif et al. ⁶²⁴
Spheres (40 μm)	3.28	0.61	2.00	Giesekus ⁶⁵¹
Ground gypsum	3.25	0.69	2.24	Turian and Yuan ⁶⁵²
Titanium dioxide	5.0	0.55	2.75	Turian and Yuan ⁶⁵²
Glass rods (30 \times 700 μm)	9.25	0.268	2.48	Clarke ⁶⁵³
Quartz grains (53 to 76 μm)	5.8	0.371	2.15	Clarke ⁶⁵³
Glass fibers:				
Axial ratio 7	3.8	0.374	1.42	Giesekus ⁶⁵¹
Axial ratio 14	5.03	0.26	1.31	Giesekus ⁶⁵¹
Axial ratio 21	6.0	0.233	1.40	Giesekus ⁶⁵¹

spherical particles (see Sections 5.5.2 and 5.5.3). In the case of emulsions and foams, the deformed droplets or bubbles have a polyhedral shape, and maximum packing fraction can be $\phi_{\max} \approx 0.9$ and even higher. For this case, a special geometric rheological theory has been developed.^{437,642,643}

Wessel and Ball⁶⁴⁴ and Kanai et al.⁶⁴⁵ studied in detail the effects of shear rate on the fractal structure of flocculated emulsion drops. They showed that the size of the flocs usually decreases with the increase of the shear stress; often the flocs are split to single particles at high shear rates. As a result, the viscosity decreases rapidly with the increase of the shear rate.

Interesting effects are observed when a dispersion contains both larger and smaller particles; the latter are usually polymer coils, spherical or cylindrical surfactant micelles, or microemulsion droplets. The presence of the smaller particles may induce clustering of the larger particles due to the depletion attraction (see Section 5.4.5.3.3, above); such effects are described in the works on surfactant-flocculated and polymer-flocculated emulsions.⁶⁴⁶⁻⁶⁴⁹ Other effects can be observed in dispersions representing mixtures of liquid and solid particles. Yuhua et al.⁶⁵⁰ have established that if the size of the solid particles is larger than three times the size of the emulsion drops, the emulsion can be treated as a continuous medium (of its own average viscosity), in which the solid particles are dispersed; such treatment is not possible when the solid particles are smaller.

5.6 KINETICS OF COAGULATION

There are three scenarios for the occurrence of a two-particle collision in a dispersion depending on the type of particle–particle interactions. (1) If the repulsive forces are predominant, the two colliding particles will rebound and the colloidal dispersion will be stable. (2) When at a given separation the attractive and repulsive forces counterbalance each other (the film formed upon particle collision is stable), aggregates or flocs of attached particles can appear. (3) When the particles are fluid and the attractive interaction across the film is predominant, the film is unstable and ruptures; this leads to coalescence of the drops in emulsions or of the bubbles in foams.

To a great extent, the occurrence of coagulation is determined by the energy, U , of particle–particle interaction. U is related to the disjoining pressure, Π , by means of Equations 5.162 and 5.163. Qualitatively, the curves Π vs. h (see Figure 5.13) and U vs. h are similar. The coagulation is called fast or slow depending on whether the electrostatic barrier (see Figure 5.13) is less than kT or much higher than kT . In addition, the coagulation is termed *reversible* or *irreversible* depending on whether the depth of the primary minimum (see Figure 5.13) is comparable with kT or much greater than kT .

Three types of driving forces can lead to coagulation. (1) The body forces, such as gravity and centrifugal force, cause sedimentation of the heavier particles in suspensions or creaming of the

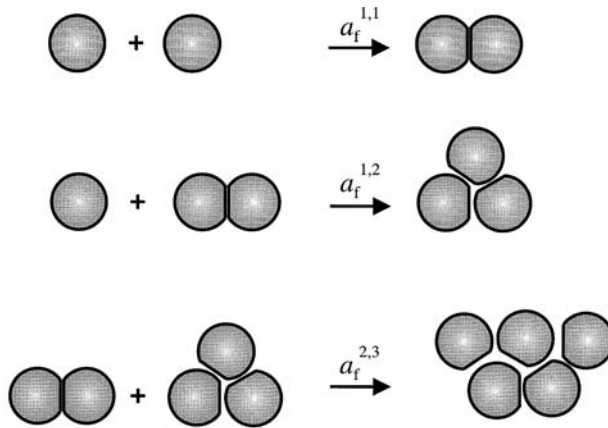


FIGURE 5.53 Elementary acts of flocculation according to the von Smoluchowski scheme; $a_f^{i,j}$ ($i, j = 1, 2, 3, \dots$) are rate constants of flocculation.

lighter droplets in emulsions. (2) For the particles that are smaller than about $1 \mu\text{m}$, the Brownian stochastic force dominates the body forces, and the Brownian collision of two particles becomes a prerequisite for their attachment and coagulation. (3) The temperature gradient in fluid dispersions causes termocapillary migration of the particles driven by the Marangoni effect. The particles moving with different velocities can collide and form aggregates.

5.6.1 IRREVERSIBLE COAGULATION

The kinetic theory of fast irreversible coagulation was developed by von Smoluchowski.^{654,655} Later the theory was extended to the case of slow and reversible coagulation. In any case of coagulation (flocculation), the general set of kinetic equations reads

$$\frac{dn_k}{dt} = \frac{1}{2} \sum_{i=1}^{k-1} a_f^{i,k-1} n_i n_{k-i} - n_k \sum_{i=1}^{\infty} a_f^{k,i} n_i + q_k \quad (k = 1, 2, \dots) \quad (5.319)$$

Here, t is time; n_1 denotes the number of single particles per unit volume; n_k is the number of aggregates of k particles ($k = 2, 3, \dots$) per unit volume; $a_f^{i,j}$ ($i, j = 1, 2, 3, \dots$) are rate constants of flocculation (coagulation; see Figure 5.53); q_k denotes the flux of aggregates of size k which are products of other processes, different from the flocculation itself (say, the reverse process of aggregate disassembly or the droplet coalescence in emulsions; see Equations 5.331 and 5.335 below). In the special case of irreversible coagulation without coalescence, we have $q_k \equiv 0$. The first term in the right-hand side of Equation 5.319 is the rate of formation of k aggregates by the merging of two smaller aggregates, whereas the second term expresses the rate of loss of k aggregates due to their incorporation into larger aggregates. The total concentration of aggregates (as kinetically independent units), n , and the total concentration of the constituent particles (including those in aggregated form), n_{tot} , can be expressed as

$$n = \sum_{k=1}^{\infty} n_k, \quad n_{\text{tot}} = \sum_{k=1}^{\infty} k n_k \quad (5.320)$$

The rate constants can be expressed in the form:

$$a_f^{i,j} = 4\pi D_{i,j}^{(0)} (R_i + R_j) E_{i,j} \quad (5.321)$$

where $D_{i,j}^{(0)}$ is the relative diffusion coefficients for two flocks of radii R_i and R_j and aggregation number i and j , respectively; $E_{i,j}$ is the so-called collision efficiency.^{470,656} Below we give expressions for $D_{i,j}^{(0)}$ and $E_{i,j}$ appropriate for various physical situations.

The Einstein approach (see Equation 5.307), combined with the Rybczynski-Hadamard equation (Equation 5.304) leads to the following expression for the relative diffusivity of two isolated Brownian droplets:

$$D_{i,j}^{(0)} = \frac{kT}{2\pi\eta} \frac{\eta_d + \eta}{3\eta_d + 2\eta} \left(\frac{1}{R_i} + \frac{1}{R_j} \right) \text{ (perikinetic coagulation)} \quad (5.322)$$

The limiting case $\eta_d \rightarrow 0$ corresponds to two bubbles, whereas in the other limit ($\eta_d \rightarrow \infty$) Equation 5.322 describes two solid particles or two fluid particles of tangentially immobile surfaces.

When the particle relative motion is driven by a body force or by the thermocapillary migration (rather than by self-diffusion), Equation 5.322 is no longer valid. Instead, in Equation 5.321 we have to formally substitute the following expression for $D_{i,j}^{(0)}$ (see Rogers and Davis⁶⁵⁷):

$$D_{i,j}^{(0)} = \frac{1}{4} (R_i + R_j) |\mathbf{v}_i - \mathbf{v}_j| \text{ (orthokinetic coagulation)} \quad (5.323)$$

Here \mathbf{v}_j denotes the velocity of a flock of aggregation number j . Physically, Equation 5.323 accounts for the fact that some particle (usually a larger one) moves faster than the remaining particles and can “capture” them upon collision. This type of coagulation is called *orthokinetic* to distinguish it from the self-diffusion-driven perikinetic coagulation described by Equation 5.322. In the case of gravity-driven flocculation, we can identify \mathbf{v}_j with the velocity U in Equation 5.304, where F is to be set equal to the gravitational force exerted on the particle; for a solid particle or a fluid particle of tangentially immobile surface, this yields $\mathbf{v}_j = 2g\Delta\rho R_j^2/(9\eta)$ with g the acceleration due to gravity and $\Delta\rho$ the density difference between the two phases.

In the case of orthokinetic coagulation of liquid drops driven by the thermocapillary migration, the particle velocity \mathbf{v}_j is given by the expression (see Young et al.⁶⁵⁸):

$$\mathbf{v}_j = \frac{2R_j E_T \lambda}{(3\eta_d + 2\eta)(\lambda_d + 2\lambda)} \nabla(\ln T) \text{ (thermocapillary velocity)} \quad (5.324)$$

where the thermal conductivity of the continuous and disperse phases are denoted by λ and λ_d , respectively. The interfacial thermal elasticity, E_T , is defined by Equation 5.282.

The collision efficiency, $E_{i,j}$, in Equation 5.321 accounts for the interactions (of both hydrodynamic and intermolecular origin) between two colliding particles. The inverse of $E_{i,j}$ is often called the *stability ratio* or the *Fuchs factor*⁶⁵⁹ and can be expressed in the following general form:^{14,470}

$$W_{i,j} = \frac{1}{E_{i,j}} = 2 \int_0^\infty \frac{\beta(s)}{(s+2)^2} \exp\left[\frac{U_{i,j}(s)}{kT}\right] ds, \quad s \equiv \frac{2h}{R_i + R_j} \quad (5.325a)$$

$$\beta \equiv \left(2\pi\eta R_* \frac{3\eta_d + 2\eta}{\eta_d + \eta} \right)^{-1} \frac{F_z}{V_z}$$

where, as usual, h is the closest surface-to-surface distance between the two particles; R_* is defined by Equation 5.259; $U_{ij}(s)$ is the energy of (nonhydrodynamic) interactions between the particles (see Section 5.4 above); $\beta(s)$ accounts for the hydrodynamic interactions; and F_z/V_z is the particle friction coefficient. Thus, $\beta \rightarrow 1$ for $s \rightarrow \infty$, insofar as for large separations the particles obey the Rybczynski–Hadamard equation (Equation 5.304). In the opposite limit, $s \ll 1$, i.e., close approach of the two particles, F_z/V_z can be calculated from Equation 5.260, 283, 284, or 288, depending on the specific case. In particular, for $s \ll 1$, we have $\beta \propto 1/s$ for two solid particles (or fluid particles of tangentially immobile surfaces), $\beta \propto s^{-1/2}$ for two liquid droplets, and $\beta \propto \ln s$ for two gas bubbles. We see that for two solid particles ($\beta \propto 1/s$), the integral in Equation 5.325a may be divergent. To overcome this problem, one usually accepts that for the smallest separations U_{ij} is dominated by the van der Waals interaction, as given by Equation 5.174, i.e., $U_{ij} \rightarrow -\infty$, and, consequently, the integrand in Equation 5.325a tends to zero for $s \rightarrow 0$.

Note that the value of W_{ij} is determined mainly by the values of the integrand in the vicinity of the electrostatic maximum (barrier) of U_{ij} (see Figure 5.13), insofar as U_{ij} enters Equation 5.325a as an exponent. By using the method of the saddle point, Derjaguin¹⁴ estimated the integral in Equation 5.325a:

$$W_{ij} \equiv \frac{1}{E_{ij}} \approx \left[\frac{8\pi kT}{-U''_{ij}(s_m)} \right]^{1/2} \frac{\beta(s_m)}{(s_m + 2)^2} \exp \left[\frac{U_{ij}(s_m)}{kT} \right] \quad (5.325b)$$

where s_m denotes the value of s corresponding to the maximum. We see that the larger the barrier, $U_{ij}(s_m)$, the smaller the collision efficiency, E_{ij} , and the slower the coagulation.

Note also that for imaginary particles, which experience neither long-range surface forces ($U_{ij} = 0$) nor hydrodynamic interactions ($\beta = 1$), Equation 5.325a yields a collision efficiency $E_{ij} = 1$ and Equation 5.321 reduces to the von Smoluchowski^{654,655} expression for the rate constant of the fast irreversible coagulation. In this particular case, Equation 5.319 represents an infinite set of nonlinear differential equation. If all flocculation rate constants are the same and equal to a_f , the problem has a unique exact solution:^{654,655}

$$n = \frac{n_0}{1 + a_f n_0 t / 2}, \quad n_k = n_0 \frac{(a_f n_0 t / 2)^{k-1}}{(1 + a_f n_0 t / 2)^{k+1}} \quad (k = 1, 2, \dots) \quad (5.326)$$

It is supposed that the total average concentration of the constituent particles (in both singlet and aggregated form), n_{tot} , does not change and is equal to the initial number of particles, n_0 . Unlike n_{tot} , the concentration of the aggregates, n , decreases with time, while their size increases. Differentiating Equation 5.326 we obtain:

$$\frac{dn}{dt} = -\frac{a_f}{2} n^2, \quad \frac{d\bar{V}}{dt} = \frac{a_f}{2} \phi_0, \quad \bar{V} \equiv \frac{\phi_0}{n} \quad (5.327)$$

where \bar{V} is the average volume per aggregate and ϕ_0 is the initial volume fraction of the constituent particles. Combining Equations 5.321 and 5.327, we obtain the following result for perikinetic (Brownian) coagulation:

$$\frac{\bar{V}}{V_0} = 1 + \frac{t}{t_{\text{Br}}}, \quad t_{\text{Br}} = \frac{R_0^2}{3\phi_0 D_0 E_0} \quad (5.328)$$

where $V_0 = 4\pi R_0^3/3$ is the volume of a constituent particle, t_{Br} is the characteristic time of the coagulation process in this case, E_0 is an average collision efficiency, and D_0 is an average diffusion coefficient.

In contrast, \bar{V} is not a linear function of time for orthokinetic coagulation. When the flocculation is driven by a body force, i.e., in case of sedimentation or centrifugation, we obtain:⁶⁵⁶

$$\frac{\bar{V}}{V_0} = \left(1 - \frac{t}{3t_{bf}}\right)^{-3}, \quad t_{bf} = \frac{2R_0}{3\phi_0 v_{bf} E_0} \quad (5.329)$$

where t_{bf} is the characteristic time in this case and v_{bf} is an average velocity of aggregate motion. As discussed above, when the body force is gravitational, we have $v_{bf} = 2g\Delta\rho R_0^2/(9\eta)$.

When the orthokinetic coagulation is driven by the thermocapillary migration, the counterpart of Equation 5.329 reads⁶⁵⁶

$$\frac{\bar{V}}{V_0} = \exp\left(\frac{t}{t_{tm}}\right), \quad t_{tm} = \frac{2R_0}{3\phi_0 v_{tm} E_0} \quad (5.330)$$

where v_{tm} is an average velocity of thermocapillary migration and t_{tm} is the respective characteristic time. Note that $D_0 \propto R_0^{-1}$, $v_{bf} \propto R_0^2$ and $v_{tm} \propto R_0$ (see Equations 5.307 and 5.324). Then, from Equations 5.328 to 5.330, it follows that the three different characteristic times exhibit different dependencies on particle radius: $t_{Br} \propto R_0^3$, $t_{bf} \propto R_0^{-1}$, while t_{tm} is independent of R_0 . Thus, the Brownian coagulation is faster for the smaller particles, the body force-induced coagulation is more rapid for the larger particles, whereas the thermocapillary driven coagulation is not so sensitive to the particle size.⁶⁶⁰

The von Smoluchowski scheme based on Equations 5.326 and 5.327 has found numerous applications.²⁷⁸ An example for biochemical application is the study^{661,662} of the kinetics of flocculation of latex particles caused by human gamma globulin in the presence of specific “key-lock” interactions. The infinite set of von Smoluchowski equations (Equation 5.319) was solved by Bak and Heilmann⁶⁶³ in the particular case when the aggregates cannot grow larger than a given size; an explicit analytical solution was obtained by these authors.

5.6.2 REVERSIBLE COAGULATION

In the case of reversible coagulation, the flocs can disaggregate because the primary minimum (Figure 5.13) is not deep enough.¹⁴ For example, an aggregate composed of $i + j$ particles can be split on two aggregates containing i and j particles. We denote the rate constant of this reverse process by $a_r^{i,j}$ (Figure 5.54a). It is assumed that both the straight process of flocculation (Figure 5.53) and the reverse process (Figure 5.54a) take place. The kinetics of aggregation in this more general case is described by the von Smoluchowski set of equations, Equation 5.319, where we have to substitute:

$$q_1 = \sum_{i=1}^{\infty} a_r^{1,i} n_{i+1}, \quad q_k = \sum_{i=1}^{\infty} a_r^{k,i} n_{i+k} - \frac{1}{2} n_k \sum_{i=1}^{k-1} a_r^{i,k-i} \quad (k = 2, 3, \dots) \quad (5.331)$$

In Equation 5.331 q_k equals the rate of formation of k aggregates in the process of disassembly of larger aggregates minus the rate of decay of the k aggregates. As before, the total number of constituent particles, n_{tot} , does not change. However, the total number of the aggregates, n , can either increase or decrease depending on whether the straight or the reverse process prevails.

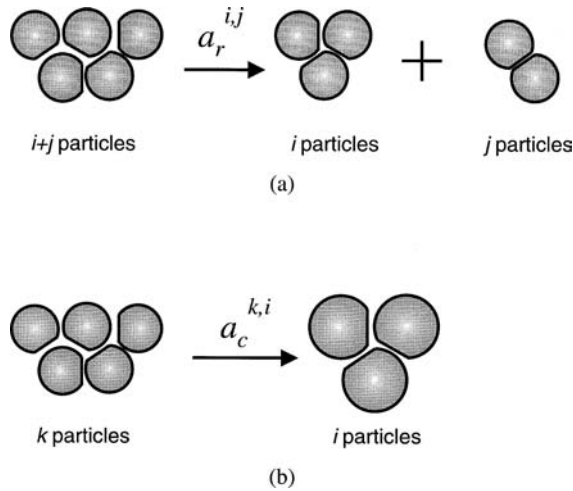


FIGURE 5.54 Elementary acts of aggregate splitting (a) and droplet coalescence within an aggregate (b); $a_r^{i,j}$ and $a_c^{k,i}$ ($i, j, k = 1, 2, 3, \dots$) are the rate constants of the respective processes.

Summing up all equations in 5.319 and using Equation 5.331, we derive the following equation for n :

$$\frac{dn}{dt} = \frac{1}{2} \sum_{i=1}^{\infty} \sum_{j=1}^{\infty} (a_r^{i,j} n_{i+j} - a_f^{i,j} n_i n_j) \quad (5.332)$$

Martinov and Muller⁶⁶⁴ reported a general expression for the rate constants of the reverse process:

$$a_r^{i,j} = \frac{D_{i,j}^{(0)} E_{i,j}}{Z_{i,j}} \frac{1}{(R_i + R_j)^2} \quad (5.333)$$

where $Z_{i,j}$ is the so-called irreversible factor, which can be presented in the form

$$Z_{i,j} = \frac{1}{8} \int_{U_{i,j} < 0} (s+2)^2 \exp\left[-\frac{U_{i,j}(s)}{kT}\right] ds \quad (5.334)$$

The integration in Equation 5.334 is carried out over the region around the primary minimum, where $U_{i,j}$ takes negative values (see Figure 5.13). In other words, $Z_{i,j}$ is determined by the values of $U_{i,j}$ in the region of the primary minimum, whereas $E_{i,j}$ is determined by the values of $U_{i,j}$ in the region of the electrostatic maximum (see Equations 5.325b and 5.334). When the minimum is deeper, $Z_{i,j}$ is larger and the rate constant in Equation 5.333 is smaller. In addition, as seen from Equations 5.325b and 5.333, the increase of the height of the barrier also decreases the rate of the reverse process. The physical interpretation of this fact is that to detach from an aggregate a particle has first to go out from the well and then to “jump” over the barrier (Figure 5.13).

To illustrate the effect of the reverse process on the rate of flocculation, we solved numerically the set of Equations 5.319, 5.331, and 5.332. To simplify the problem, we used the following assumptions: (1) the von Smoluchowski assumption that all rate constants of the straight process are equal to a_f ; (2) aggregates containing more than M particles cannot decay; (3) all rate constants

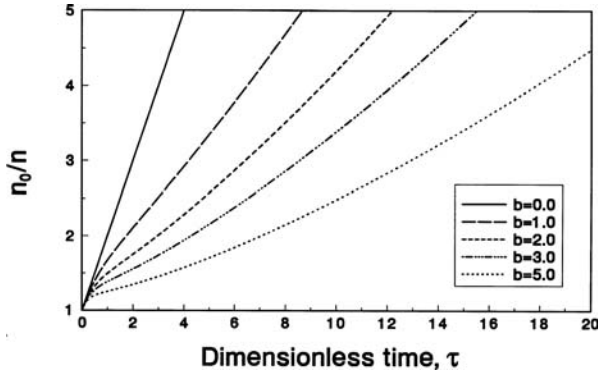


FIGURE 5.55 Reversible coagulation: theoretical plot of the inverse dimensionless aggregate concentration, n_0/n , vs. the dimensionless time, $\tau = a_p n_0 t/2$, in the case of $M = 4$ and various values of the dimensionless ratio, $b = 2a_r/(n_0 a_f)$, of the rate constants of the reverse and straight process, a_r and a_f .

of the reverse process are equal to a_r ; and (4) at the initial moment, only single constituent particles of concentration n_0 are available. In Figure 5.55, we plot the calculated curves of n_0/n vs. the dimensionless time, $\tau = a_p n_0 t/2$, for a fixed value, $M = 4$, and various values of the ratio of the rate constants of the straight and the reverse process, $b = 2a_r/(n_0 a_f)$. Note that n is defined by Equation 5.320. We see that in an initial time interval all curves in Figure 5.55 touch the von Smoluchowski distribution (corresponding to $b = 0$), but after this period we observe a reduction in the rate of flocculation which is larger for the curves with larger values of b (larger rate constants of the reverse process). These S-shaped curves are typical for the case of reversible coagulation, which is also confirmed by the experiment.^{14,665}

5.6.3 KINETICS OF SIMULTANEOUS FLOCCULATION AND COALESCENCE IN EMULSIONS

When coalescence is present, in addition to the flocculation, the total number of constituent drops, n_{tot} (see Equation 5.320), does change, in contrast to the case of pure flocculation considered above.³² Hartland and Gakis⁶⁶⁶ and Hartland and Vohra⁶⁶⁷ were the first to develop a model of coalescence that relates the lifetime of single films to the rate of phase separation in emulsions of fairly large drops (approximately 1 mm) in the absence of surfactant. Their analysis was further extended by Lobo et al.⁶⁶⁸ to quantify the process of coalescence within an already creamed or settled emulsion (or foam) containing drops of size less than 100 μm ; these authors also took into account the effect of surfactants, which are commonly used as emulsifiers. Danov et al.⁶⁶⁹ generalized the von Smoluchowski scheme to account for the fact that the droplets within the flocs can coalesce to give larger droplets, as illustrated in Figure 5.54b. In this case, in the right-hand side of Equation 5.319 we have to substitute⁶⁶⁹

$$q_1 = \sum_{i=2}^{\infty} a_c^{i,1} n_i, \quad q_k = \sum_{i=k+1}^{\infty} a_c^{i,k} n_i - n_k \sum_{i=1}^{k-1} a_c^{k,i} \quad (k = 2, 3, \dots) \quad (5.335)$$

where $a_c^{k,i}$ is the rate constant of transformation (by coalescence) of an aggregate containing k droplets into an aggregate containing i droplets (see Figure 5.54b). The newly formed aggregate is further involved in the flocculation scheme, which thus accounts for the fact that the flocculation and coalescence processes are interdependent. In this scheme, the total coalescence rate, $a_{c,\text{tot}}^i$, and the total number of droplets, n_{tot} , obeys the following equations:⁶⁶⁹

$$\frac{dn_{\text{tot}}}{dt} = - \sum_{i=2}^{\infty} a_{c,\text{tot}}^i n_i, \quad a_{c,\text{tot}}^i = \sum_{k=1}^{i-1} (i-k) a_c^{i,k} \quad (i = 2, 3, \dots) \quad (5.336)$$

To determine the rate constants of coalescence, $a_c^{k,i}$, Danov et al.⁴³⁹ examined the effects of droplet interactions and Brownian motion on the coalescence rate in dilute emulsions of micrometer- and submicrometer-sized droplets. The processes of film formation, thinning, and rupture were included as consecutive stages in the scheme of coalescence. Expressions for the interaction energy due to the various DLVO and non-DLVO surface forces between two deformed droplets were obtained²⁶⁶ (see also Section 5.4 above).

Average models for the total number of droplets are also available.^{670,671} The average model of van den Tempel⁶⁷⁰ assumes linear structure of the aggregates. The coalescence rate is supposed to be proportional to the number of contacts within an aggregate. To simplify the problem, van den Tempel has used several assumptions; one of them is that the concentration of the single droplets, n_1 , obeys the von Smoluchowski distribution (Equation 5.326) for $k = 1$. The average model of Borwankar et al.⁶⁷¹ is similar to that of van den Tempel but is physically more adequate. The assumptions used by the latter authors⁶⁷¹ make their solution more applicable to cases in which the flocculation (rather than the coalescence) is slow and is the rate determining stage. This is confirmed by the curves shown in Figure 5.56 which are calculated for the same rate of coalescence, but for three different rates of flocculation. For relatively high rates of flocculation (Figure 5.56a), the predictions of the three theories differ. For the intermediate rates of flocculation (Figure 5.56b), the prediction of the model by Borwankar et al.⁶⁷¹ is close to that of the more detailed model by Danov et al.⁶⁶⁹ For very low values of the flocculation rate constant, a_f , for which the coalescence is not the rate-determining stage, all three theories⁶⁶⁹⁻⁶⁷¹ give numerically close results (Figure 5.56c). (For more details about the coupling of coalescence and flocculation in dilute oil in water emulsions see the recent review, Reference 672.)

5.7 MECHANISMS OF ANTIFOAMING

In Sections 5.4 to 5.6 we considered the main interparticle forces that govern the stability of colloidal systems and some of the mechanisms that result in destabilization of suspensions and emulsions (coagulation, demulsification). In various technologies (such as pulp and paper production, drug manufacturing, textile dyeing, crude oil processing, and many others) very voluminous and stable foams can appear, which impede the normal technological process and are, therefore, rather undesired. In these cases, various oils and oil–solid mixtures are introduced as additives to the foaming media for an efficient foam control.⁶⁷³ Such oils and oil–silica mixtures are commonly termed antifoams or defoamers.⁶⁷³⁻⁶⁷⁷ Antifoams are used in consumer products as well (e.g., in washing powders and antidyspepsia drugs). Sometimes, oils are introduced in surfactant solutions for other reasons and the observed foam destabilization effect is undesired — a typical example is the use of silicone oils as hair conditioners in shampoos.^{678,679} The mechanisms responsible for the foam destruction effect of oil-based antifoams are still not entirely understood and are the subject of intensive studies.

A typical antifoam consists of an oil (polydimethylsiloxane or hydrocarbon), dispersed hydrophobic solid particles (e.g., hydrophobized silica), or a mixture of both.⁶⁷⁴ The oil–solid mixtures are often called antifoam *compounds*. The weight concentration of the solid particles in compounds is around several percent (typically between 2 and 8). A strong synergistic effect between the oil and the solid particles is observed in the compounds — in most cases, the latter are much more efficient than either of their individual components, if taken separately.^{674,675} The compounds are used at a concentration below 0.1 wt%, whereas the oils are used at higher concentrations (up to several percent) due to their lower antifoam efficiency. The antifoams are usually preemulsified in the form of oil drops or mixed oil–solid globules of micrometer size.

A detailed discussion on many aspects of the mechanisms of antifoaming can be found in review articles by Garrett,⁶⁷⁴ Wasan and Christiano,⁶⁷⁶ as well as in the books by Exerowa and Kruglyakov⁶⁷⁵ and Kralchevsky and Nagayama.⁶⁷⁷ In the present section, we compare the mechanisms of foam destruction by oils and oil–silica compounds. The discussion is based on results

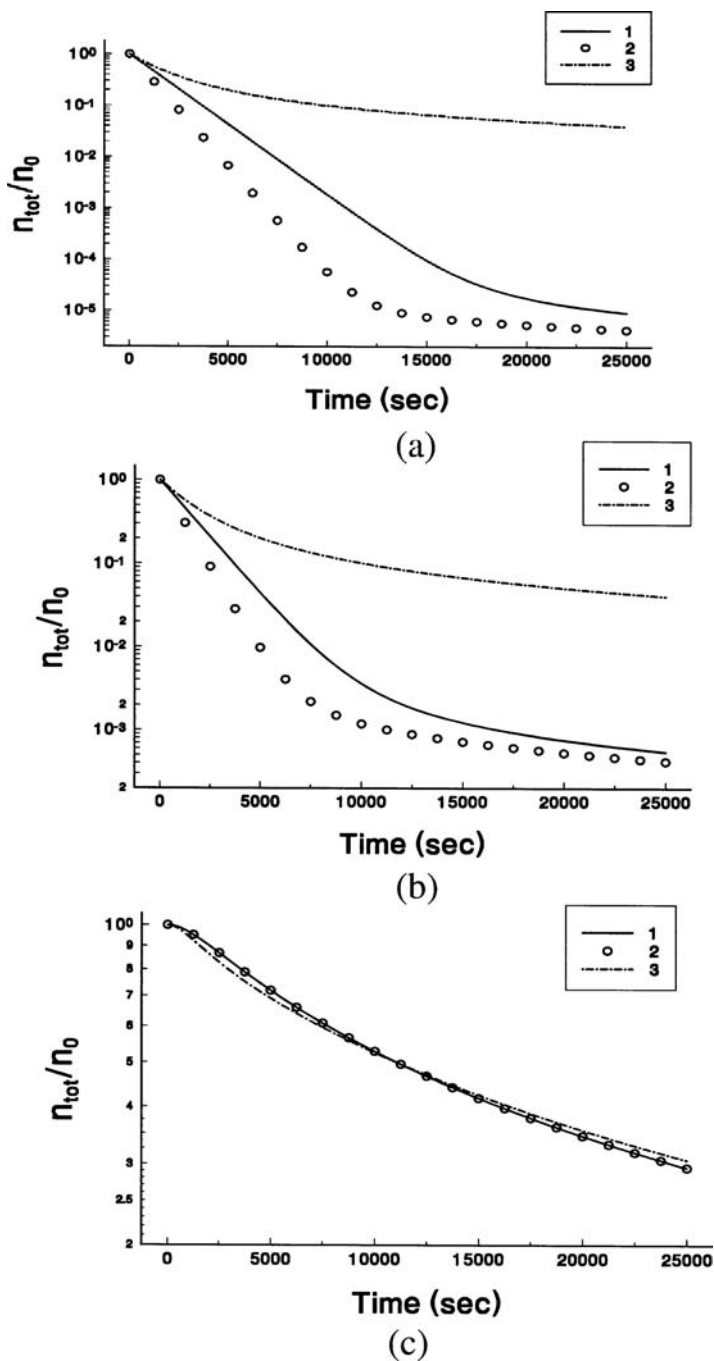


FIGURE 5.56 Relative change in the total number of drops, n_{tot} , vs. time, t ; initial number of primary drops $n_0 = 10^{12} \text{ cm}^{-3}$; coalescence rate constant $k_c^{2,1} = 10^{-3}/\text{s}$. Curve 1: numerical solution of Equation 5.336. Curve 2: output of the model of Borwankar et al.⁶⁷¹ Curve 3: output of the model of van den Tempel.⁶⁷⁰ The values of the flocculation rate constant are (a) $a_f = 10^{-11} \text{ cm}^3/\text{s}$; (b) $a_f = 10^{-13} \text{ cm}^3/\text{s}$; (c) $a_f = 10^{-16} \text{ cm}^3/\text{s}$.

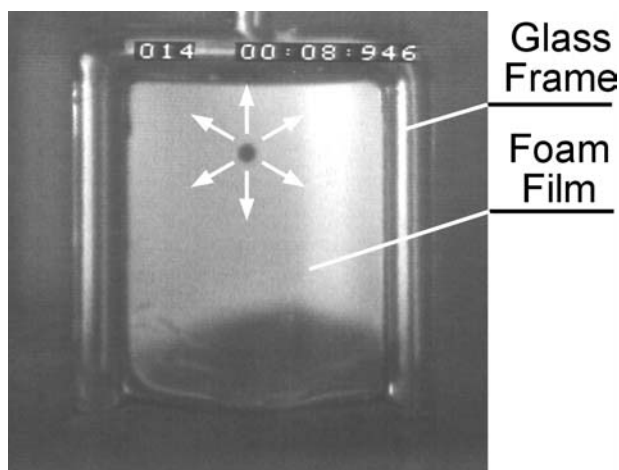


FIGURE 5.57 Image of a large foam film in the moment of its rupture by pre-emulsified globules of an antifoam compound (4.2 wt% of hydrophobic silica dispersed in silicone oil). The film is formed on a rectangular glass frame, which is rapidly withdrawn from 10 mM solution of the anionic surfactant dioctyl sulfosuccinate (hereafter denoted for brevity as AOT). We see a hole (the black circle in the upper part of the film) which, in reality, rapidly expands with time. The film ruptures 0.5 s after its formation at a thickness of about several micrometers. The image is taken by a high-speed video camera as explained in Reference 681.

obtained during the last several years (some of them are still unpublished), so that the aim of the section is to complement the aforementioned reviews.

5.7.1 LOCATION OF ANTIFOAM ACTION — FAST AND SLOW ANTIFOAMS

An important question about the mechanism of foam destruction is which is the structural element (foam film or Plateau border) actually destroyed by the antifoam globules. This question has practical importance, because the diameter of the globules in the commercial antifoams should fit the typical size of the structural element to be destroyed — the film thickness or the cross section of the Plateau border (PB), respectively.⁶⁷⁸ Most researchers consider that the antifoam globules rupture the foam films,^{674,675} whereas Koczko et al.⁶⁸⁰ suggest that the antifoam globules first escape from the foam films into the neighboring PB and become trapped there; only afterward, the globules are assumed to destroy the PB and the neighboring foam films.

Direct microscopic observations by a high-speed video camera showed that the foam destruction by typical antifoam compounds (comprising silicone oil and silica) occurred through rupture of the foam lamellae.^{681,682} Experiments with small (millimeter-sized) and large (centimeter-sized) foam films showed that the compounds induced the formation of a hole in the foam films at the early stages of the film thinning process (Figure 5.57). This is possible because the foam films stabilized by low molecular mass surfactants thin rapidly, within several seconds, down to a thickness of 1 μm to several micrometers which is comparable to the diameter of the antifoam globules.⁶⁸¹ As a result, the foam films rupture within several seconds after their formation. Accordingly, the foam produced from such solutions disappear completely for less than 10 s in a standard shake test.⁶⁸¹ For this reason, the antifoams that are able to break the foam films are termed *the fast antifoams*.⁶⁸³ Experiments with several ionic and nonionic surfactants have confirmed that the observed foam film destruction is rather typical for mixed oil–silica antifoams.^{681–685}

On the other hand, similar experimental methods showed^{678,679,686,687} that the foam destruction occurred in a different manner when pure oils (without silica particles) were used as antifoams. The oil drops were seen to leave the foam films (without rupture) during the film thinning process. The

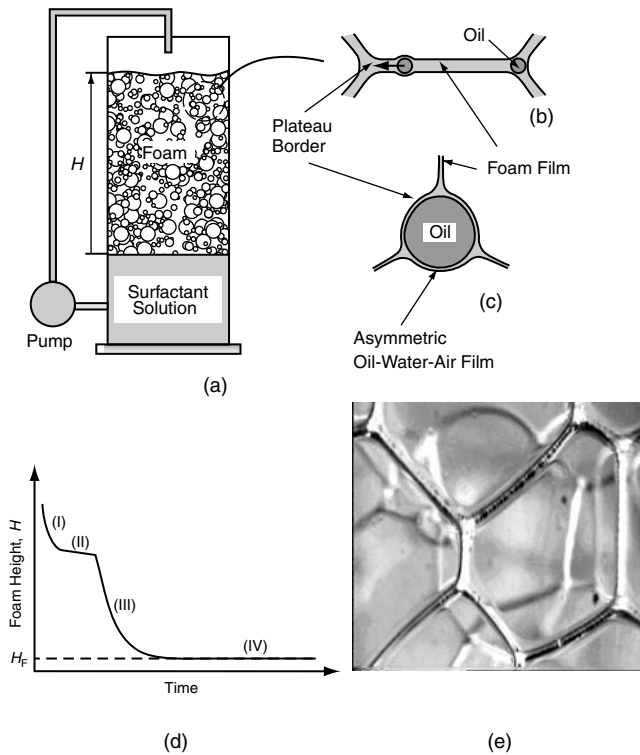


FIGURE 5.58 Foam destruction by oil drops (slow antifoams).^{678,679,698} (a, b) The oil drops are rapidly expelled from the foam films into the neighboring PBs soon after the foam is formed. (c) The drops are strongly compressed in the narrowing PBs and asymmetric oil–water–air films are formed. The drop entry and foam destruction occur when the compressing pressure exceeds a certain critical value, which depends on the particular system. (d) Schematic presentation of the main stages of foam evolution in the presence of oil drops — (I) drainage of liquid from the foam without bubble coalescence; (II) stable foam due to the insufficient compression of the oil drops; (III) foam destruction as a result of drop entry in the PBs; (IV) long-living residual foam with final height H_F ; (e) Photograph of real foam cells with many oil drops trapped in the PBs (the drops are visualized by the wavy profile of the PBs).

antifoam drops were accumulated in the PBs and remained trapped there for a certain period of time,^{678,679} as presumed by Koczó et al.⁶⁸⁰ The slow process of water drainage from the foam led to a gradual narrowing of the PBs and the oil drops became strongly compressed with time. When the compressing capillary pressure exceeded some critical value, the oil drops entered the walls of the PB, inducing its destruction and the rupture of the neighboring foam films (Figure 5.58).⁶⁷⁸ A much longer time was needed for foam destruction in this case — typically, more than several minutes. That is why these antifoams were termed the *slow antifoams*.⁶⁸³ Furthermore, a residual foam of well-defined height, which remained stable for many hours, was observed in such systems.

These studies show that the foam destruction may occur through rupture of either the foam films or the PBs, depending on the particular system. Further experiments have shown that the main factor determining the position of foam destruction, and whether a given antifoam behaves as fast or slow, is the magnitude of the so-called entry barrier (see Section 5.7.3, below).

5.7.2 BRIDGING-STRETCHING MECHANISM

As mentioned above, microscopic observations by a high-speed video camera were made⁶⁸¹ to clarify the detailed mechanism of foam film rupture by mixed antifoams. They showed that when an antifoam globule connected (bridged) the surfaces of a foam film, an unstable oil bridge was formed, which stretched with time due to uncompensated capillary pressures at the oil–air and oil–water interfaces, and eventually ruptured the entire foam film (Figure 5.59). The term *bridging-stretching* was suggested^{681,688} to describe this mechanism. The bridging-stretching mechanism explains why the typical antifoam compounds contain a high excess of oil — the antifoam globules should be able to deform for effectuation of the bridge stretching and rupture.

The stability of oil bridges in foam films was studied theoretically by Garrett^{674,689} on the basis of the theory of capillarity. The analysis showed that a necessary condition for having an unstable bridge is that the bridging coefficient:

$$B = \sigma_{AW}^2 + \sigma_{OW}^2 - \sigma_{OA}^2 \quad (5.337)$$

should be positive. Here, σ is interfacial tension and the subscripts AW, OW, and OA denote the air–water, oil–water, and oil–air interfaces, respectively. A more refined capillary model⁶⁸⁸ showed that oil bridges, formed from oil drops of diameter comparable to or smaller than the film thickness, might be metastable even at positive values of B . Therefore, the size of the oil bridges should be above a certain critical value (which depends on the film thickness and the interfacial tensions) for having an unstable oil bridge. This theoretical result was invoked to explain the reduced stability of the foam films in the presence of a spread oil layer (for details see Reference 688).

5.7.3 ROLE OF THE ENTRY BARRIER

Any mechanism of foam destruction by preemulsified antifoam globules requires an entry of these globules at the surface of the foam film or the PB (e.g., Figures 5.58 and 5.59). The entry event depends on two major factors. (1) The equilibrium position of an oil drop (lens) on the air–water interface, which is determined by the values of the interfacial tensions σ_{AW} , σ_{OW} , and σ_{OA} ; see Figure 5.7. (2) The repulsive forces (e.g., of electrostatic origin), which stabilize the asymmetric oil–water–air film, formed when an antifoam globule approaches the foam film surface; the barrier created by these forces should be overcome for the globule entry to occur.^{674,676,680,690-694}

A theoretical analysis shows (see, e.g., Reference 674) that if the so-called entry coefficient:

$$E = \sigma_{AW} + \sigma_{OW} + \sigma_{OA} \quad (5.338)$$

is negative (as it is the case with some oils and surfactant solutions), the oil drops do not have a stable equilibrium position at the surface and spontaneously submerge into the surfactant solution. Such oils are inactive as antifoams because no oil bridges can be formed (factor 1 is decisive). One of the main reasons to use silicone oils in various antifoam formulations is that these oils usually have positive values of B and E coefficients in the solutions of most conventional (hydrocarbon-based) surfactants.^{674,695} Besides, it was theoretically shown that a positive value of B necessarily corresponds to a positive value of E (the reverse is not always true).^{677,696}

The experiments show, however, that many oils with positive B and E coefficients might have low antifoam efficiency.^{678,679,686,687} In these cases, the stability of the asymmetric oil–water–air films is very high, and the formation of unstable oil bridges becomes impossible for kinetic reasons (factor 2 is decisive). The repulsive interaction that should be overcome for effectuation of the antifoam globules entry on the solution surface is usually termed the *entry barrier*. A recently

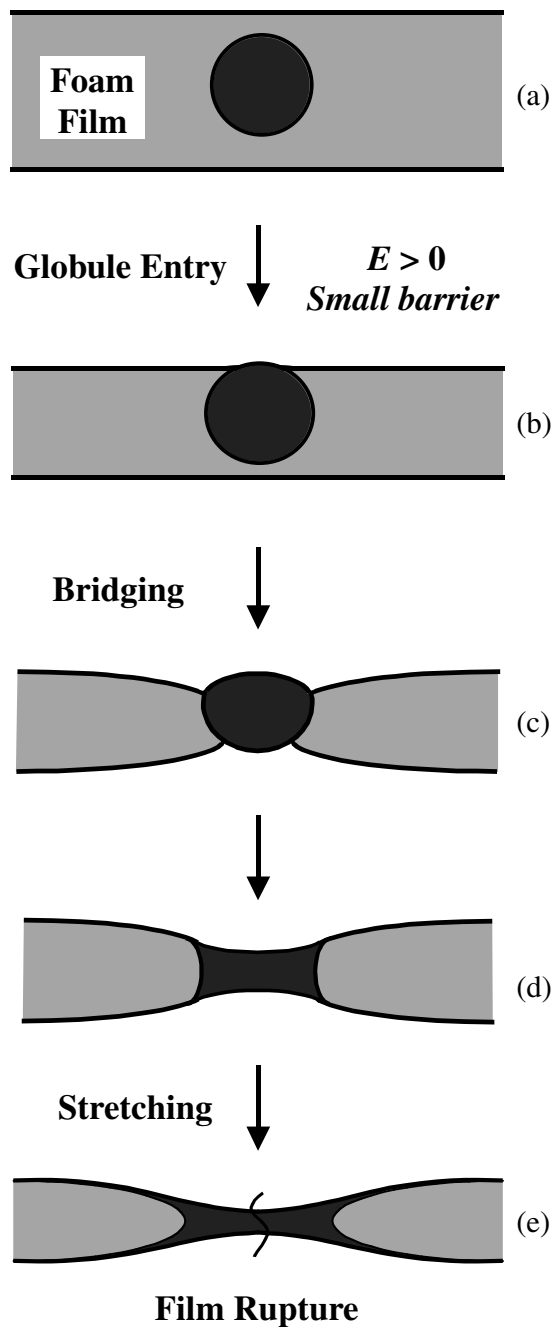


FIGURE 5.59 Schematic presentation of the bridging-stretching mechanism of foam film rupture by antifoam globules.^{681,688} After an oil bridge is formed (a–c), it stretches due to uncompensated capillary pressures at the oil–water and oil–air interfaces (c–e). Finally, the bridge ruptures in its thinnest central region (the vertical wavy line in e). The globule entry is possible only if the entry coefficient, $E > 0$, and the entry barrier is low (see Section 5.7.3).

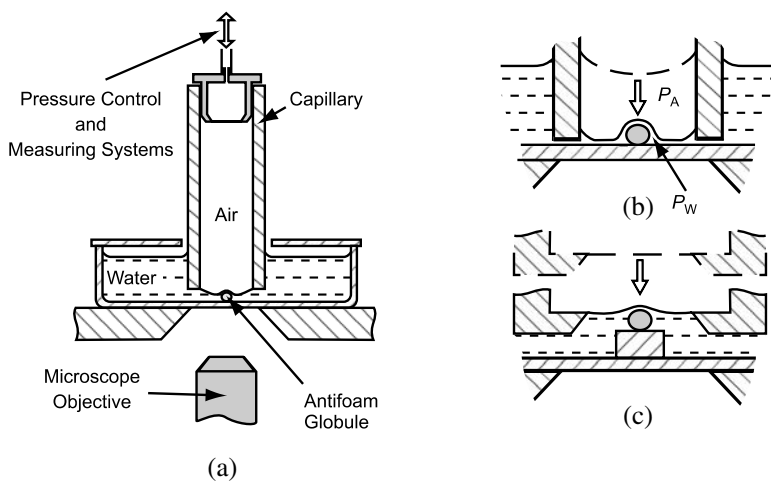


FIGURE 5.60 Scheme of the experimental setup and the basic principle of the film trapping technique, FTT.⁶⁹⁷ (a) Vertical capillary, partially immersed in surfactant solution containing antifoam globules, is held close to the bottom of the experimental vessel. (b) The air pressure inside the capillary, P_A , is increased and the convex air–water meniscus in the capillary is pressed against the glass substrate. Some of the antifoam globules remain trapped in the formed glass–water–air film and are compressed by the meniscus. At a given critical capillary pressure, $P_C^{CR} = P_A - P_W$, the asymmetric film formed between the antifoam globule and the solution surface ruptures and an event of globule entry is observed by an optical microscope. (c) Another modification called “gentle FTT” is used for measuring entry barriers lower than 20 Pa — an initially flat meniscus is formed, which allows the trapping of antifoam globules at a virtually zero capillary pressure.

developed film trapping technique (FTT)^{687,697,698} allowed a precise quantification of the entry barrier with actual micrometer-sized antifoam globules, and a number of important results have been obtained. The principle of the FTT and some of the main conclusions, drawn from the results obtained by this technique, are briefly discussed below.

5.7.3.1 Film Trapping Technique

The principle and the experimental setup of the FTT are illustrated in Figure 5.60.^{687,697,698} Briefly, a vertical glass capillary is positioned at a small distance above the flat bottom of a glass vessel. The lower end of the capillary is immersed in the working surfactant solution which contains dispersed antifoam globules. The capillary is connected to a pressure control system which allows us to vary and to measure the air pressure in the capillary, P_A . When P_A increases, the air–water meniscus in the capillary is pushed against the glass substrate and a wetting film (glass–water–air) is formed, which traps some of the antifoam globules. The setup allows us to determine the capillary pressure of the air–water meniscus around the trapped drops, $P_C = P_A - P_W$, where P_W is the pressure in the aqueous film (for details, see References 697 and 698). The experiments show that the trapped antifoam globules enter (pierce) the surface of the wetting film at a given, critical capillary pressure, P_C^{CR} . Therefore, the equipment allows us to measure P_C^{CR} as a function of various parameters, such as the types of oil and surfactant, concentration of solid particles in the compound, size of the antifoam globules, etc. A larger value of P_C^{CR} corresponds to a higher entry barrier (more difficult drop entry), and vice versa. For compounds with very low entry barriers, a special version of the FTT was developed⁶⁹⁷ (gentle FTT), see Figure 5.60c. Experiments in the presence and absence of a pre-spread oil layer can be performed, which allows evaluation of the effect of oil spreading on the entry barrier.

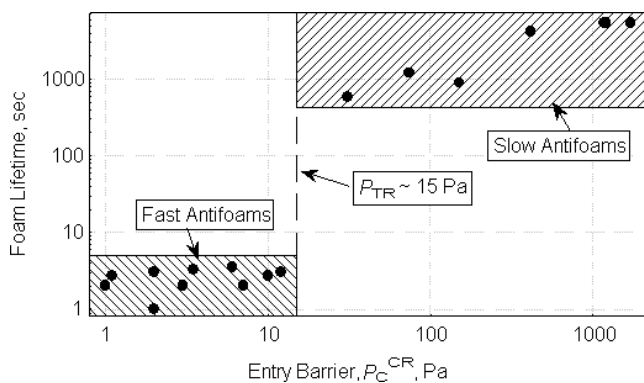


FIGURE 5.61 Correlation between the entry barrier, P_C^{CR} , and the foam lifetime measured for various surfactant-antifoam systems: The experimental data (solid circles) fall into two distinct regions: systems in which the foam is destroyed in less than 5 s (fast antifoams) and $P_C^{\text{CR}} < 15$ Pa; and systems for which the defoaming time is longer than 8 min (slow antifoams) and $P_C^{\text{CR}} > 20$ Pa. The composition of the various systems is given in Reference 698.

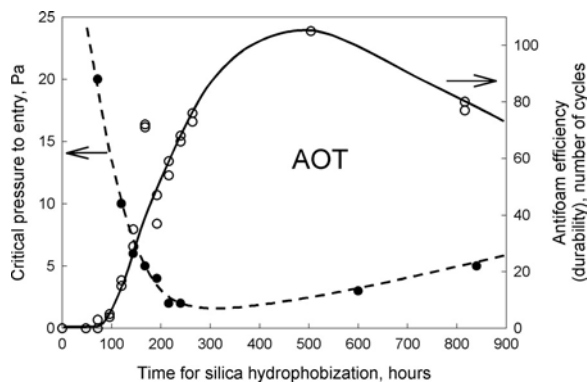
5.7.3.2 Critical Entry Pressure for Foam Film Rupture

Experiments with a large set of systems (various oils, compounds, and surfactants) showed^{683,698} that there is a well-defined threshold value, $P_{\text{TR}} \approx 15$ Pa, which separates the fast (foam film breaking) from the slow (PB breaking) antifoams. Some of the results from these experiments are summarized in Figure 5.61, where the relationship between the foam lifetime and the entry barrier, P_C^{CR} , is shown. We see from this figure that all experimental points fall into two distinct regions: (1) Systems in which the foam is destroyed for less than 10 s, i.e., these correspond to fast antifoams; for them $P_C^{\text{CR}} < 15$ Pa. (2) Systems for which the defoaming time is longer than 5 min (slow antifoams); for them $P_C^{\text{CR}} > 20$ Pa. Therefore, the magnitude of the entry barrier is of crucial importance for the timescale of foam destruction by oil-based antifoams. Another relation of P_C^{CR} with the antifoam activity (more precisely, with the height of the residual foam, H_{r} in the presence of oil drops; see Figure 5.58d) was discussed in References 678 and 698.

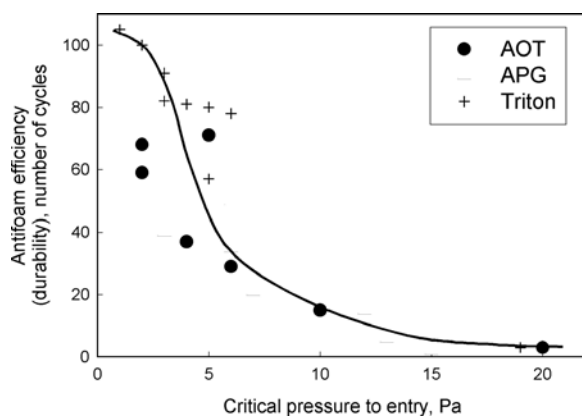
Note that at high surfactant concentrations, only oil–solid compounds have been observed to behave as fast antifoams, whereas both oils and compounds could behave as slow antifoams depending on the magnitude of the entry barrier (at low surfactant concentrations, the pure oils could also act as fast antifoams). In all experiments it was found that the hydrophobic solid particles reduce the entry barrier by one to two orders of magnitude, but sometimes P_C^{CR} remains higher than the threshold value, P_{TR} , and the compound is unable to break the foam films. In the latter cases, the compound globules are expelled into the neighboring PB during the process of foam film drainage. These results confirm the idea of Garrett⁶⁷⁴ that the main role of the solid particles in the antifoam compounds is to reduce the entry barrier of the globules.

5.7.3.3 Optimal Hydrophobicity of Solid Particles

Some authors accept^{695,699} that the use of more hydrophobic solid particles results in more active antifoam compounds. In a recent study,⁶⁸⁵ this idea was experimentally tested by applying the following procedure for a gradual increase of silica hydrophobicity: initially hydrophilic silica particles were mixed with silicone oil at a room temperature, and this mixture was stored under mild stirring for a long period of time. Under these conditions, the adsorption of silicone oil on the silica surface is a slow process that takes weeks before the final, most hydrophobic state of the particles is reached. The antifoam efficiency of the compound was tested every day, and the results obtained with various systems unambiguously showed the presence of a well-pronounced, optimal silica hydrophobicity corresponding to highest antifoam efficiency.



(a)



(b)

FIGURE 5.62 (a) Critical pressure for globule entry, P_C^{CR} (full circles), and efficiency (empty circles) of a silicone oil–silica compound in 10 mM AOT solution, as functions of the time of silica hydrophobization. (b) The dependence of the compound efficiency on P_C^{CR} for solutions of three different surfactants: 10 mM anionic AOT, 0.6 mM nonionic APG, and 1 mM nonionic Triton X-100. (Adapted from Marinova et al., *Langmuir*, 18, 3399, 2002.)

The antifoam efficiency in these experiments was evaluated⁶⁸⁵ by an automatic shake test. Briefly, 100 ml of the foaming solution was placed in a standard 250 ml glass bottle and 0.01% of the compound was introduced into this sample. The bottle was then mechanically agitated in a series of consecutive shake cycles. After each cycle of agitation for 10 s, the solution remained quiescent for another 60 s and the defoaming time was measured (defined as the time for appearance of a clean water–air interface without bubbles). Afterward, a new shaking cycle was performed and this procedure was repeated until the defoaming time exceeded 60 s in three consecutive cycles — this was considered the moment of compound exhaustion (see Section 5.7.4 and Figure 5.64 below for further explanations). A larger number of cycles before compound exhaustion corresponds to better antifoam durability (efficiency), and vice versa.

The observed maximum (see the illustrative result presented in Figure 5.62a) was explained⁶⁸⁵ as a result of two requirements that stem from the main role of the silica particles, namely, to assist the globule entry by rupturing the asymmetric oil–water–air films (Figure 5.63). The first requirement, formulated by Garrett,⁶⁷⁴ is that the particles should be sufficiently hydrophobic to be dewetted by the oil–water and air–water interfaces (otherwise, the solid particles would stabilize, rather than destabilize the asymmetric film). The other requirement⁶⁸⁵ is that the particles should protrude

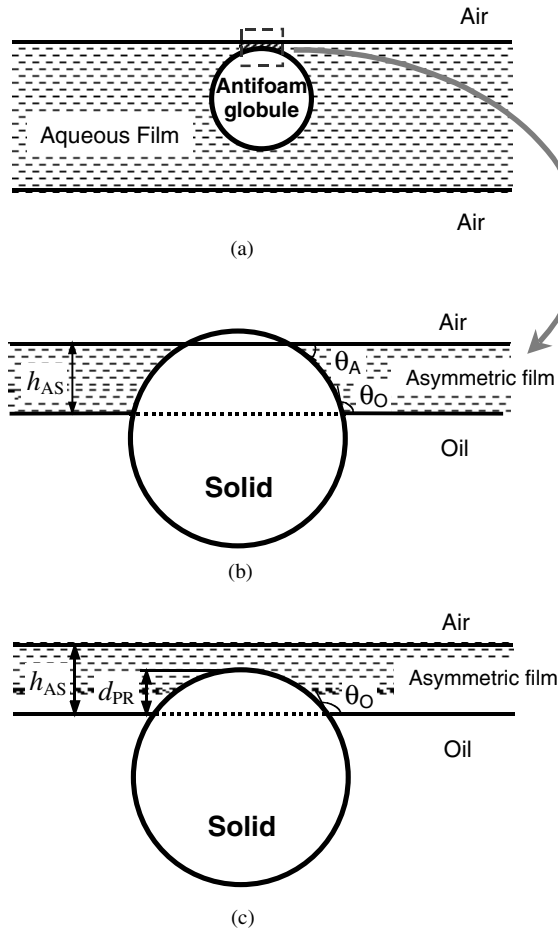


FIGURE 5.63 Schematic explanation of the optimal hydrophobicity of the solid particles in oil–solid antifoam compounds. (a) When an antifoam globule approaches the foam film surface, an asymmetric oil–water–air film of thickness h_{AS} forms. (b) The zone of contact in an enlarged scale. If the protrusion depth, d_{PR} , of the solid particle is larger than h_{AS} , the particle should be sufficiently hydrophobic ($\theta_A + \theta_O > 180^\circ$) to pierce the air–water interface and induce a film rupture; however, if the particle is insufficiently hydrophobic ($\theta_A + \theta_O < 180^\circ$), it would stabilize the film.⁶⁷⁴ (c) On the other side, if the solid particle is overhydrophobized, then $d_{PR} < h_{AS}$ and the particle is again unable to pierce the asymmetric film.⁶⁸⁵

sufficiently deep into the aqueous phase to bridge the surfaces of the asymmetric oil–water–air film, and it is better satisfied by more hydrophilic particles. Therefore, an optimal hydrophobicity is expected, at which both requirements are balanced, the entry barrier is low, and the antifoam is most active. Indeed, a straightforward correlation between the antifoam efficiency and the magnitude of the entry barrier, P_C^{CR} , was observed in the studied systems (Figure 5.62b). For spherical particles, the optimal hydrophobicity was expressed as a most favorable three-phase contact angle solid–water–oil:⁶⁸⁵

$$\cos \theta_O \approx h_{AS} / R_P - 1 \quad (5.339)$$

where h_{AS} is the thickness of the asymmetric oil–water–air film, and R_P is the particle radius (Figure 5.63). This angle corresponds to the condition $h_{AS} = d_{PR}$, where $d_{PR} = R_P(1 + \cos \theta_O)$ is the equilibrium protrusion depth of the solid particle into the aqueous phase.

TABLE 5.8
Entry Barriers, P_C^{CR} , of Different Antifoams
in Surfactant Solutions in the Presence and
Absence of a Pre-spread Layer of Oil,
from Which the Antifoam Is Prepared

Antifoam	Surfactant	Spread Layer	P_C^{CR} , Pa
Dodecane	2.6 mM SDDBS	No	96 ± 5
		Yes	48 ± 5
Hexadecane	2.6 mM SDDBS	No	80 ± 5
		Yes	400 ± 10
Silicone oil	10 mM AOT	No	28 ± 1
		Yes	19 ± 2
Compound 1	10 mM AOT	No	8 ± 1
		Yes	3 ± 2
Compound 2	10 mM AOT	No	20 ± 5
		Yes	4 ± 1
Compound 1	1 mM Triton X-100	No	30 ± 1
		Yes	5 ± 2
Compound 2	1 mM Triton X-100	No	22 ± 1
		Yes	7 ± 1

SDDBS and AOT denote the anionic surfactants sodium dodecylbenzenesulfonate and sodium dioctyl-sulfosuccinate, respectively. Triton X-100 is the nonionic surfactant nonylphenol deca(ethylene-glycolether). Compound 1 is a mixture of silicone oil and hydrophobized silica; Compound 2 is an emulsion of Compound 1, which contains also solid particles of Span 60. Data from References 684 and 687.

5.7.3.4 Role of the Pre-spread Oil Layer

It has been known for many years^{674,700,701} that some correlation exists between the spreading behavior of the oils and their antifoam activity. The value of the spreading coefficient:

$$S = \sigma_{AW} - \sigma_{OW} - \sigma_{OA} \quad (5.340)$$

which characterizes the mode of spreading of the oil on the surface of the solution, and the rate of oil spreading have been often considered important factors for antifoam activity. However, as shown by Garrett et al.,⁷⁰² the oil spreading is not a necessary condition for having an active antifoam, and many studies^{678,679,686} have confirmed that the correlation is not always present.

The effect of the spread oil on the entry barriers of various oils and oil-silica compounds was studied by the FTT.^{683,684,687} The experimental results showed that the presence of a pre-spread oil layer on the surface of the solution reduces by several times the entry barrier for mixed oil-silica compounds (Table 5.8). Furthermore, it was found⁶⁸⁴ that the entry barrier in many systems is below the threshold value $P_{TR} \approx 15$ Pa (which separates the fast from slow antifoams, see Figure 5.61), only in the presence of a pre-spread layer of oil. In other words, these antifoams behave as fast ones only because the oil spreads rapidly on the solution surface during foaming, reducing in this way the entry barrier below P_{TR} . The results for the entry barrier of oil drops (without silica) also showed a moderate reduction of the entry barrier by a pre-spread oil in most systems.^{684,687} However,

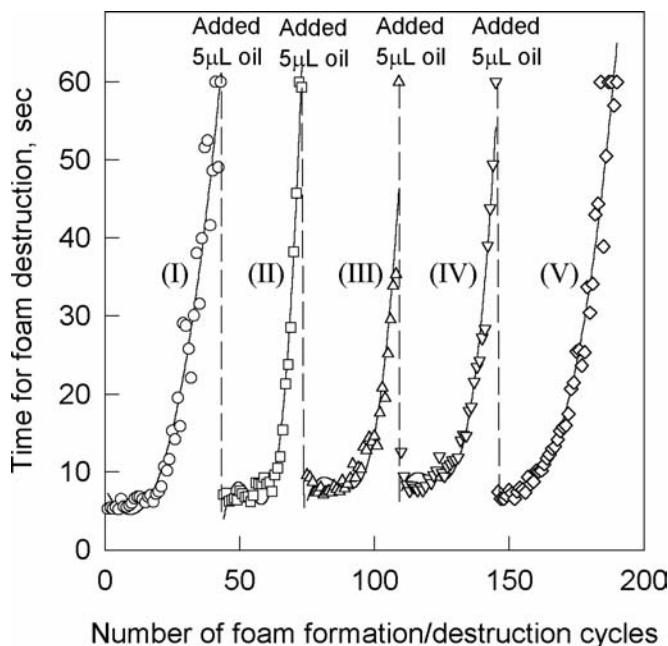


FIGURE 5.64 Consecutive cycles of exhaustion and reactivation of mixed oil–silica compound in 10 mM solution of the anionic surfactant sodium dioctyl-sulfosuccinate (AOT). An initially active antifoam (defoaming time ≈ 5 s) gradually loses its activity with the number of foam formation/destruction cycles in a standard shake test.⁷⁰³ The introduction of silicone oil results in a perfect restoration of the antifoam activity. Five exhaustion curves (indicated by roman numbers; the symbols indicate the experimentally measured defoaming time) and the corresponding four reactivation events (the vertical dashed lines) are shown. (Adapted from Denkov et al., *Langmuir*, 16, 2525, 2000.)

at least in one of the studied systems (hexadecane drops in solutions of the anionic surfactant sodium dodecylbenzenesulfonate; see Table 5.8) a significant increase of the entry barrier upon oil spreading was observed.⁶⁸⁷ The entry barrier of the oils in surfactant solutions above their critical micelle concentration (CMC) is higher than P_{TR} both in the presence and absence of spread oil, which explains why the pure oils behave as slow antifoams at typical surfactant concentrations.

We can conclude from the results shown in Table 5.8 that there is a well-pronounced synergistic effect between the solid particles present in compounds and the spread oil. Most of the studied fast antifoams have sufficiently low entry barriers exclusively as a result of the combined action of the solid particles and the spread oil layer.⁶⁸⁴

As mentioned in Section 5.7.2, the spread layer of oil has another important role as well. The spread oil is able to feed the oil bridges, formed in foam films, by a mechanism explained in Reference 688 — as a result, larger and less stable oil bridges are formed.

5.7.4 MECHANISMS OF COMPOUND EXHAUSTION AND REACTIVATION

The process of antifoam exhaustion (deactivation) is illustrated in Figure 5.64 — the time for foam destruction in a standard shake test is shown as a function of the number of the shaking cycle (see Section 5.7.3.3 for the used shake test).⁷⁰³ Shorter defoaming time means more active antifoam, and vice versa. As seen from Figure 5.64, the initial high activity of the antifoam deteriorates with the foaming cycles and the defoaming time becomes longer than 60 s after 45 cycles — the antifoam has been exhausted. This process is very undesirable from a practical viewpoint, and more durable antifoams (able to sustain a larger number of foam destruction cycles) are sought by the manufacturers.

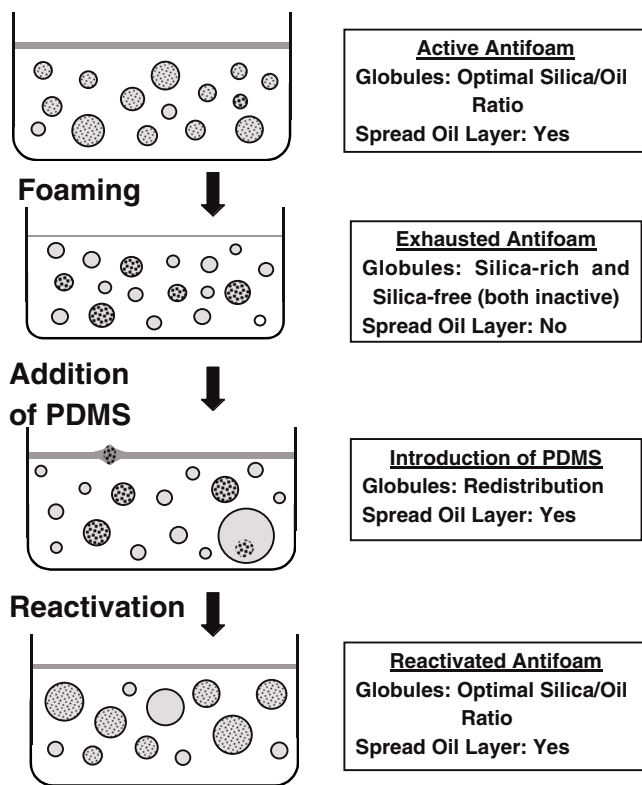


FIGURE 5.65 Schematic presentation of the processes of antifoam exhaustion and reactivation of emulsified oil–silica antifoam compound.

Interestingly, the addition of a new portion of oil (without silica particles) leads to a complete restoration of the antifoam activity (Figure 5.64). Note that the oil itself has a very weak antifoam activity in the absence of silica. Therefore, the antifoam reactivation certainly involves the solid particles that have been introduced with the first portion of mixed antifoam. The subsequent foaming cycles lead to a second exhaustion series, and such consecutive periods of exhaustion/reactivation can be repeated several times.

Systematic experiments⁷⁰³ with solutions of the anionic surfactant sodium dioctylsulfosuccinate (AOT) showed that the exhaustion of mixed silica–silicone oil antifoams is due to two closely interrelated processes: (1) partial segregation of the oil and silica into two distinct, inactive populations of antifoam globules, silica-free and silica-enriched; (2) disappearance of the spread oil layer from the solution surface (Figure 5.65). The oil drops deprived of silica, which appear in process 1, are unable to enter the air–water interface and to destroy the foam lamellae, because the entry barrier is too high for them. On the other hand, the antifoam globules enriched in silica trap some oil, which is not available for spreading on the solution surface. As a result, the spread oil layer gradually disappears from the solution surface (process 2) due to oil emulsification in the moment of foam film rupture. Ultimately, both types of globules, silica-enriched and silica-free, become unable to destroy the foam films, and the antifoam transforms into an exhausted state. Accordingly, the reactivation process is due to (1) restoration of the spread oil layer and (2) rearrangement of the solid particles from the exhausted antifoam with the fresh oil into new antifoam globules having optimal silica concentration. No correlation between the size of the antifoam globules and their activity was established in these experiments, which showed that the reduction of the globule size (which is often considered as the main factor in the antifoam exhaustion) was

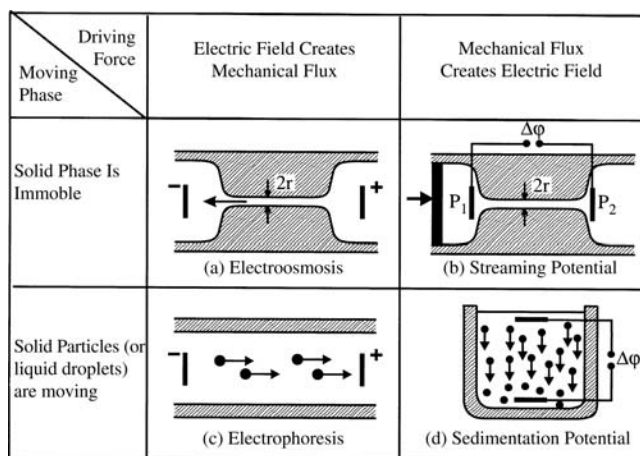


FIGURE 5.66 The four basic electrokinetic phenomena. (a) Electroosmotic liquid flow through a capillary (of charged walls) appears when an electric potential difference is applied. (b) Streaming electric potential appears when a pressure drop drives the liquid to flow through the capillary. (c) Electrophoretic motion of charged particles is observed in an external electric field. (d) Sedimentation potential is established when charged particles are moving under the action of gravity.

a second-order effect in the studied systems. Similar conclusions were drawn from experiments with nonionic surfactants as well.⁶⁸²

In conclusion, progress has been achieved during the last several years in revealing the mechanisms of foam destruction by oil-based antifoams. This progress has been greatly facilitated by the various methods for direct microscopic observations of the foams and foam films (including some of the foam destruction events), and by the implementation of the film trapping technique for a direct measurement of the entry barriers of the antifoam globules.

5.8 ELECTROKINETIC PHENOMENA IN COLLOIDS

The term *electrokinetic phenomena* refers to several processes that appear when a charged surface (or colloidal particle) is set in a relative motion with respect to the adjacent liquid phase. Classically, four types of electrokinetic phenomena are distinguished: electroosmosis, streaming potential, electrophoresis, and sedimentation potential (Figure 5.66). These are discussed in Sections 5.8.2 to 5.8.6. At present, the electrical conductivity (at constant electrical field) and the dielectric response (at alternating electrical field) of the disperse systems are often considered together with the electrokinetic phenomena, because the theoretical approaches and the governing equations are similar (Section 5.8.7). Experimental methods based on all these phenomena are widely used for characterization of the electrical surface potential in dispersions. A comprehensive presentation of the topic until the end of 1980s can be found in review articles⁷⁰⁴⁻⁷¹⁴ and monographs.⁷¹⁵⁻⁷¹⁷ The recent development of the area is reviewed in the collective monograph, Reference 718. The major experimental techniques are described in chapter 4 of Reference 716 and chapters 8 to 14 in Reference 718. Recently, a substantial interest has been raised by the apparent discrepancy between the results obtained by different electrokinetic methods for one and the same system. This problem is discussed in Section 5.8.8. Finally, the electrokinetic properties of air–water and oil–water interfaces are briefly described in Section 5.8.9.

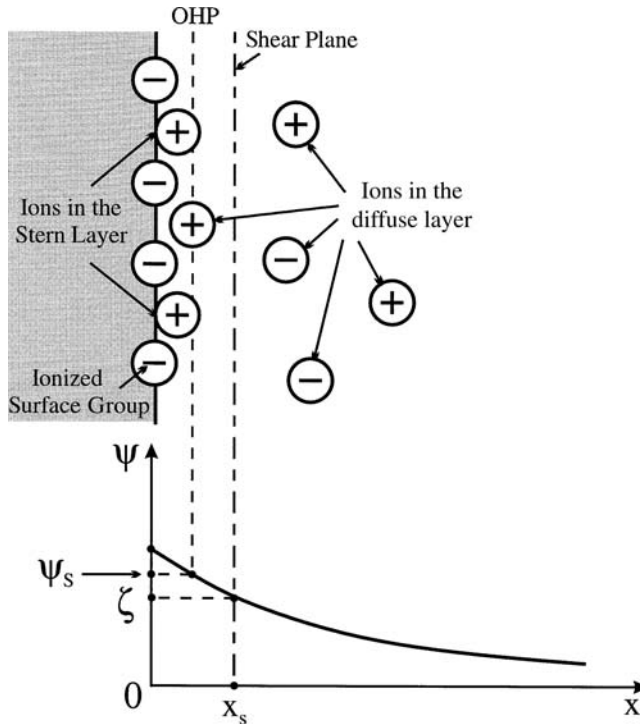


FIGURE 5.67 Schematic presentation of the structure of the EDL. The surface charge is created by ionized surface groups and/or by ions tightly adsorbed in the Stern layer. The plane of closest approach of the ions from the diffuse part of the EDL is called the outer Helmholtz plane (OHP). The electric potential in the OHP plane is referred to as the surface potential, ψ_s , in the text. The shear plane, $x = x_s$, separates the hydrodynamically immobile liquid that moves together with the surface, $x < x_s$, from the mobile liquid, $x > x_s$, which has nonzero relative velocity with respect to the surface. Note that the ions in the immobile part of the EDL can move with respect to the surface under an applied electric field, which gives rise to the anomalous surface conductivity (see Section 5.8.8).

5.8.1 POTENTIAL DISTRIBUTION AT A PLANAR INTERFACE AND AROUND A SPHERE

When a dielectric phase (solid or fluid) is placed in contact with polar liquid, such as water, the interface becomes charged due to either specific adsorption of ions initially dissolved in the polar liquid, or dissociation of surface ionizable groups.^{14,34,717} The final result of these two processes is the formation of an electric double layer (EDL) (Figure 5.67), which may contain three types of ions:

1. Ions attached to the surface by chemical bond are those parts of the ionized groups which remain bound after the dissociation process.
2. Ions bound by very strong Coulomb attraction (after partial loss of molecules from the ion solvating shell) or by some other noncovalent specific, short-range attraction build up the so-called Stern layer.
3. Ions that are involved in more or less free Brownian motion present the diffuse part of the EDL.

The ions from groups (1) and (2), considered together, determine the effective surface charge density, σ_s , which must be balanced by an excess of counterions in the diffuse layer (equal in

magnitude and opposite in sign). The distribution of electrical potential in the diffuse layer is usually rather accurately described by the Poisson–Boltzmann equation:

$$\nabla^2 \psi = -\frac{e}{\epsilon \epsilon_0} \sum_j Z_j n_{b,j} \exp\left[-\frac{e Z_j \psi}{kT}\right] \quad (5.341)$$

where ψ is the local (average) value of the electrical potential; e is the elementary charge; ϵ is the relative dielectric permittivity of the liquid; ϵ_0 is the electrical permittivity *in vacuo*; and Z_j and $n_{b,j}$ are the number of charges and the bulk number concentration, respectively, of ion j . The model of the EDL based on Equation 5.341 is called in the literature Gouy–Chapman or Gouy–Stern model. For symmetric ($Z:Z$) electrolyte, the Poisson–Boltzmann equation can be written in the form:

$$\nabla^2 \psi = \frac{2eZn_0}{\epsilon \epsilon_0} \sinh\left(\frac{eZ\psi}{kT}\right) \quad (5.342)$$

where n_0 is the bulk electrolyte number concentration. For a flat interface (see Figure 5.67), Equation 5.342 has an exact analytical solution:^{34,278,717}

$$\psi(x) = \frac{2kT}{eZ} \ln\left[\frac{1 + \gamma_s \exp(-\kappa x)}{1 - \gamma_s \exp(-\kappa x)}\right] \quad (5.343)$$

where

$$\gamma_s \equiv \tanh\left(\frac{Ze\psi_s}{4kT}\right), \quad \kappa \equiv \left(\frac{2e^2 Z^2 n_0}{\epsilon \epsilon_0 kT}\right)^{1/2}$$

and ψ_s is the electrical potential at the surface of closest approach of the ions from the diffuse layer to the interface. This surface is called the *outer Helmholtz plane* and ψ_s is called the *surface potential*. The surface charge and potential are interrelated by the expression:

$$\sigma_s = -\epsilon \epsilon_0 \left(\frac{d\psi}{dx}\right)_{x=0} = (8\epsilon \epsilon_0 kT n_0)^{1/2} \sinh\left(\frac{eZ\psi_s}{2kT}\right) \quad (5.344)$$

which is a direct corollary^{14,34} from Equation 5.342 and the condition for overall electroneutrality of the interface.

If the surface potential is small, we can expand in series the logarithm in the right-hand side of Equation 5.343 and derive the Debye–Hückel equation:

$$\psi(x) = \psi_s \exp(-\kappa x), \quad \frac{Ze\psi_s}{kT} < 1 \quad (5.345a)$$

On the other hand, the potential always decays exponentially far from the interface ($\kappa x \gg 1$) at an arbitrary magnitude of ψ_s (see Equation 5.343):

$$\psi(x) = \frac{4kT}{eZ} \gamma_s \exp(-\kappa x), \quad \kappa x \gg 1 \quad (5.345b)$$

The potential distribution around a spherical particle can be found from the Poisson–Boltzmann equation (Equation 5.341), which in this case reads

$$\frac{1}{r^2} \frac{d}{dr} \left(r^2 \frac{d\Psi}{dr} \right) = -\frac{e}{\varepsilon \varepsilon_0} \sum_j Z_j n_{b,j} \exp \left[-\frac{e Z_j \Psi(r)}{kT} \right] \quad (5.346)$$

The respective boundary conditions are

$$\Psi(r = R) = \Psi_s, \quad \Psi(r \rightarrow \infty) = 0$$

Equation 5.346 has an analytical solution only in the case of small surface potential:

$$\Psi(r) = \Psi_s \frac{R \exp[-\kappa(r-R)]}{r}, \quad \frac{Ze\Psi_s}{kT} < 1 \quad (5.347)$$

In this case, the surface charge density is a linear function of Ψ_s :

$$\sigma_s = \frac{\varepsilon \varepsilon_0 (1 + \kappa R)}{R} \Psi_s, \quad \frac{Ze\Psi_s}{kT} < 1 \quad (5.348)$$

For a large surface potential, Ψ_s , the potential distribution can be found by numerical integration of the Poisson–Boltzmann equation. Far from the sphere surface, the potential always obeys the law:

$$\Psi(r) = \Psi_s^* \frac{R \exp[-\kappa(r-R)]}{r}, \quad \kappa(r-R) \gg 1 \quad (5.349)$$

where $\Psi_s^*(\kappa R, \Psi_s)$ is an effective potential, which can be found by numerical solution of the Poisson–Boltzmann equation. By using the method of matched asymptotic expansions, Chew and Sen⁷¹⁹ obtained for a thin EDL ($\kappa R > 1$):

$$\Psi_s^* = \frac{4kT}{Ze} \left(\gamma_s + \frac{\gamma_s^3}{2\kappa R} \right) \quad (5.350)$$

A useful relationship between Ψ_s and s_s for a sphere was proposed by Loeb et al.:⁷²⁰

$$\sigma_s = \frac{\varepsilon \varepsilon_0 \kappa kT}{Ze} \left[2 \sinh \left(\frac{Ze\Psi_s}{2kT} \right) + \frac{4}{\kappa R} \tanh \left(\frac{Ze\Psi_s}{4kT} \right) \right] \quad (5.351)$$

and was theoretically justified by other authors.^{718,721-724} Equation 5.351 coincides with the exact numerical results within an accuracy of a few percent for $\kappa R > 0.5$ and arbitrary surface potential.^{716,720} A general approach for derivation of approximate (but accurate) expressions relating Ψ_s and σ_s , including for systems containing nonsymmetric electrolytes, has been proposed by Ohshima.^{724,725}

5.8.2 ELECTROOSMOSIS

When an electrical field of intensity E is applied in parallel to a charged flat interface, the excess of counterions in the diffuse layer gives rise to a body force exerted on the liquid. The liquid starts moving with local velocity varying from zero in the plane of shear ($x = x_s$) to some maximal value,

V_{EO} , at a large distance from the wall (see Figure 5.67). The magnitude of this electroosmotic velocity was calculated by von Smoluchowski⁷²⁶ under the assumptions that: (1) the ion distribution in the diffuse layer obeys the Poisson–Boltzmann equation, (2) at each point the electrical force is balanced by the viscous friction, and (3) the liquid viscosity in the diffuse layer is equal to that of the bulk liquid, η . The final result reads⁷²⁶

$$V_{\text{EO}} = -\frac{\varepsilon \varepsilon_0 \zeta}{\eta} E \quad (5.352)$$

where ζ is the electrical potential in the shear plane, i.e., $\zeta \equiv \psi(x = x_s)$. The quantity

$$\mu_{\text{EO}} = \frac{V_{\text{EO}}}{E} = -\frac{\varepsilon \varepsilon_0 \zeta}{\eta} \quad (5.353)$$

is called *electroosmotic mobility*. The von Smoluchowski consideration is also applicable to capillaries of a radius much larger than the Debye screening length, κ^{-1} . Therefore, by measuring the liquid flow through a capillary, like that shown in Figure 5.66, we can determine the ζ potential of the capillary surface. It is usually acceptable⁷¹⁶ to measure the liquid flux (volume displaced per unit time), J_{EO} , along with the electric current transported by the liquid, I_{EO} :

$$J_{\text{EO}} = \pi r^2 V_{\text{EO}} \quad \text{and} \quad I_{\text{EO}} = \pi r^2 \chi_b E \quad (5.354)$$

where r is the capillary radius and χ_b is the bulk conductivity of the liquid. The ratio

$$\left| J_{\text{EO}} / I_{\text{EO}} \right| = \left| V_{\text{EO}} / \chi_b E \right| = \frac{\varepsilon \varepsilon_0 \zeta}{\eta \chi_b} \quad (5.355)$$

does not depend on the capillary radius and can be used to determine ζ . Quite often, however, the high concentration of ions in the double electric layer leads to a much higher conductivity in the surface region, compared to that in the bulk electrolyte solution. To account for this effect Bikerman⁷²⁷ introduced the term *specific surface conductivity*, χ_s , which presents an excess quantity over the bulk conductivity. Then, Equation 5.354 is modified to read

$$I_{\text{EO}} = (\pi r^2 \chi_b + 2 \pi r \chi_s) E \quad (5.356)$$

and Equation 5.355 acquires the form:

$$\left| J_{\text{EO}} / I_{\text{EO}} \right| = \frac{\varepsilon \varepsilon_0 \zeta}{\eta (\chi_b + 2 \chi_s / r)} \quad (5.357)$$

Alternatively, instead of measuring the electroosmotic liquid flux at zero pressure difference across the capillary, we can determine⁷¹⁶ ζ by measuring the counterpressure, ΔP_{EO} , necessary to completely stop the net liquid transport through the capillary:

$$\Delta P_{\text{EO}} = \frac{8 \varepsilon \varepsilon_0 \zeta}{\pi r^4 (\chi_b + 2 \chi_s / r)} I_{\text{EO}} \quad (5.358)$$

Bikerman⁷²⁷ obtained the following expression for χ_s in the case of a symmetric (Z:Z) electrolyte, under the assumption that the surface conductivity is due only to the ions located in the movable part of the diffuse layer:

$$\chi_s = \frac{2Z^2 e^2 n_0}{kT \kappa} \left\{ D^+ \left[\exp\left(-\frac{Ze\zeta}{2kT}\right) - 1 \right] \left(1 + \frac{3m^+}{Z^2} \right) + D^- \left[\exp\left(\frac{Ze\zeta}{2kT}\right) - 1 \right] \left(1 + \frac{3m^-}{Z^2} \right) \right\} \quad (5.359)$$

where D^\pm are ion diffusion coefficients, while m^\pm are dimensionless ion mobilities, defined as

$$m^\pm = \frac{2}{3} \left(\frac{kT}{e} \right)^2 \frac{\epsilon \epsilon_0}{\eta} \frac{Z^2}{D^\pm} = \frac{2\epsilon \epsilon_0 N_A kT}{3\eta} \frac{Z^2}{\Lambda^0} = 12.84 \times 10^{-4} \left(\frac{Z^2}{\Lambda^0} \right) \quad \text{at } 25^\circ \text{ C in water} \quad (5.360)$$

Λ^0 ($\text{m}^2/\Omega/\text{mol}$) is the limiting molar conductivity of ions at infinite dilution. The typical values of χ_s are around $10^{-9}/\Omega$. For comparison, the bulk conductivity, χ_b , is given by

$$\chi_b = \frac{e^2}{kT} \sum D_j Z_j^2 n_{b,j} \quad (5.361)$$

and can vary within a wide range (note that χ_s and χ_b have different dimensions).

Equation 5.357 shows that for determination of ζ and χ_s , we need measurements with several capillaries made of the same material, but with different radii. The effect of the surface conductivity can be neglected when the criterion:

$$\frac{2\chi_s}{\chi_b r} \sim \frac{\exp\left(\frac{Ze\psi_s}{2kT}\right)}{\kappa r} \ll 1 \quad (5.362)$$

is satisfied.^{716,717,728} In other words, the surface conductivity is negligible at low surface potential and high ionic strength. Besides, Equation 5.355 can be applied^{716,728,729} also to electroosmotic flow in porous plugs or membranes if (1) the typical pore size is much larger than κ^{-1} , (2) the effects of the surface conductivity, χ_s , are negligible, and (3) the flow is laminar.

This consideration can be extended to include capillaries of radii comparable to κ^{-1} and the cases when the potential distribution cannot be approximated using the results for a planar wall.^{707,716}

The so-called plane interface technique⁷³⁰⁻⁷³² is a modification of the electroosmotic method, in which submicrometer particles are used as probes to visualize the osmotic velocity profile close to an interface. The method allowed precise determination of the ζ potential at mica, quartz, sapphire, and fused-silica surfaces as a function of pH.^{731,732} The attempt^{730,732,733} to apply the plane interface technique to the air–water interface, however, gave ambiguous results, probably due to the interfacial fluidity.

5.8.3 STREAMING POTENTIAL

If a pressure drop, $\Delta P = P_1 - P_2$, is imposed at the ends of a capillary, like such as shown in [Figure 5.66](#), the liquid starts moving through the capillary.^{716,723} The charges in the mobile part of the double layer at the capillary wall are thus forced to move toward the end of the capillary. As a result, a streaming current, I_{ST} , appears, which leads to the accumulation of excess charge at the capillary end. This excess charge gives rise to an electric potential difference between the ends of the capillary, called *streaming potential*, E_{ST} . On its own, the streaming potential causes a current

flow, I_C , in a direction opposite to I_{ST} . Finally, a steady state is established when $|I_C| = |I_{ST}|$ and the net electric current across the capillary becomes zero. We can directly measure E_{ST} by probe electrodes, and the following relationship is used to determine the ζ potential of the capillary walls:⁷¹⁶

$$\frac{E_{ST}}{\Delta P} = \frac{\varepsilon \varepsilon_0 \zeta}{\eta(\chi_b + 2\chi_s/r)} \quad (5.363)$$

Alternatively, instead of measuring E_{ST} , we can measure the streaming current, I_{ST} , by using the appropriate electrical circuit:⁷¹⁶

$$I_{ST} = -\frac{\varepsilon \varepsilon_0}{\eta} \frac{\pi r^2}{L} \Delta P \zeta \quad (5.364)$$

Here, L denotes the length of the capillary. An important advantage of the streaming current measurement is that the surface conductivity does not matter for the calculation (see Equation 5.364), and experimental determination of χ_s is not necessary. Similar experiments were performed by Scales et al.⁷³⁴ to determine the ζ potential of mica surface.

Equations 5.363 and 5.364 are valid only if the capillary radius is much larger than the thickness of the diffuse layer. A number of modifications were suggested in the literature to extend the theoretical consideration to narrower capillaries and porous plugs (see, for example, the review article by Dukhin and Derjaguin⁷⁰⁷ and the book of Hunter⁷¹⁶). Measurements of the streaming potential, streaming current, and electrical conductance of plugs made of latex particles were performed and analyzed by van den Hoven and Bijsterbosch.⁷³⁵

5.8.4 ELECTROPHORESIS

The movement of a charged colloidal particle in an external electrical field is called *electrophoretic motion* and the respective phenomenon is electrophoresis. The electrophoretic velocity in the two limiting cases, of a thin and thick EDL around a spherical particle, can be calculated by von Smoluchowski⁷³⁶ and Hückel⁷³⁷ formulas:

$$V_{EL} = \frac{\varepsilon \varepsilon_0 \zeta}{\eta} E, \quad \kappa R \gg 1 \quad (\text{von Smoluchowski}) \quad (5.365)$$

$$V_{EL} = \frac{2}{3} \frac{\varepsilon \varepsilon_0 \zeta}{\eta} E, \quad \kappa R \ll 1 \quad (\text{Hückel}) \quad (5.366)$$

It is important to note that Equation 5.365 is valid for particles of arbitrary shape and size, if the following requirement is fulfilled: the dimensions of the particle and the local radii of curvature of the particle surface are much larger than the Debye screening length.

The problem for spherical particles at arbitrary κR was solved by Henry⁷³⁸ who obtained:

$$\mu_{EL} = \frac{V_{EL}}{E} = \frac{2}{3} \frac{\varepsilon \varepsilon_0 \zeta}{\eta} f_1(\kappa R) = \frac{Q}{6\pi\eta R(1+\kappa R)} f_1(\kappa R) \quad (\text{Henry}) \quad (5.367)$$

where μ_{EL} is the particle electrophoretic mobility, Q is the particle charge, and $f_1(\kappa R)$ is a correction factor given by:

$$\begin{aligned}
f_1(\kappa R) &= \frac{3}{2} - \frac{9}{2}(\kappa R)^{-1} + \frac{75}{2}(\kappa R)^{-2} - 330(\kappa R)^{-3}, \quad \kappa R > 1 \\
f_1(\kappa R) &= 1 + \frac{1}{16}(\kappa R)^2 - \frac{5}{48}(\kappa R)^3 - \frac{1}{96}[(\kappa R)^4 - (\kappa R)^5] \\
&\quad + \left[\frac{1}{8}(\kappa R)^4 - \frac{1}{96}(\kappa R)^6 \right] \exp(\kappa R) E_1(\kappa R), \quad \kappa R < 1
\end{aligned} \tag{5.368}$$

and

$$E_1(x) \equiv \int_1^{\infty} e^{-sx} \frac{ds}{s}$$

is an integral exponent of the first order. The limiting values, $f_1(\kappa R \rightarrow \infty) = 3/2$ and $f_1(\kappa R \rightarrow 0) = 1$, reduce the Henry equation to the equations of von Smoluchowski and Hückel, respectively. The effect of the surface conductivity, χ_s , can be phenomenologically included in this approach, as shown by Henry.⁷³⁹ Also, if the material of the particle has finite electrical conductivity, χ_p , its electrophoretic mobility is given by⁷³⁸

$$\mu_{\text{EL}} = \frac{2}{3} \frac{\varepsilon \varepsilon_0 \zeta}{\eta} f_2(\kappa R, \chi_p / \chi_b) \tag{5.369}$$

where

$$f_2(\kappa R, \chi_p / \chi_b) = 1 + 2 \frac{(\chi_b - \chi_p)}{(2\chi_b + \chi_p)} [f_1(\kappa R) - 1] \tag{5.370}$$

It was shown,^{707,708,715} however, that the approach of Henry is strictly valid only for small values of the ζ potential, $Z e \zeta / k T < 1$, because it neglects the relaxation and the retardation effects, connected with distortion of the counterion atmosphere around the moving particle. Solutions of the problem for not-too-high ζ potentials were suggested by Overbeek⁷⁴⁰ and Booth.⁷⁴¹ The mobility of a spherical, nonconducting particle of arbitrary ζ potential and arbitrary κR was rigorously calculated by Wiersema et al.⁷⁴² and by O'Brien and White.⁷⁴³ In [Figure 5.68](#), the results of O'Brien and White⁷⁴³ for the particle mobility as a function of the ζ potential at different values of κR are represented. One interesting conclusion from these calculations is that the mobility has a maximum for $\kappa R > 3$; i.e., a given value of μ_{EL} may result from two different values of ζ . The maximum in these curves appears at $\zeta \sim 150$ mV. The numerical algorithm of O'Brien and White⁷⁴³ is sufficiently rapid to allow application to individual sets of experimental data.

Explicit approximate expressions were suggested by several authors. For a thin EDL, Dukhin and Derjaguin⁷⁰⁷ derived a formula, which was additionally simplified (without loss of accuracy) by O'Brien and Hunter:⁷⁴⁴

$$\mu_{\text{EL}} = \frac{\varepsilon \varepsilon_0}{\eta} \zeta - 4 \frac{\varepsilon \varepsilon_0 k T}{e} \left\{ \frac{\frac{\tilde{\zeta}}{2} - \frac{\ln 2}{Z} \left[1 - \exp(-Z \tilde{\zeta}) \right]}{2 + \frac{\kappa R}{M} \exp(-Z \tilde{\zeta} / 2)} \right\}, \quad \kappa R \gg 1 \tag{5.371}$$

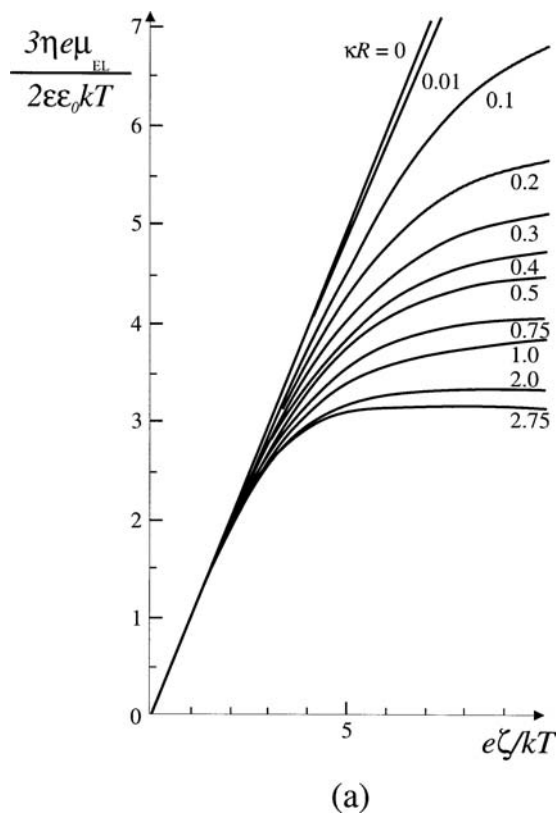


FIGURE 5.68 The dimensionless electrophoretic mobility of spherical particles vs. the dimensionless ζ potential for various values of κR : (a) κR varies between 0 and 2.75; (b) κR varies between 3 and infinity. (From O'Brien, R.W. and White, L.R., *J. Chem. Soc. Faraday Trans.*, 2, 74, 1607, 1978.)

where $\tilde{\zeta} \equiv e\zeta/kT$ is the dimensionless ζ potential, $\tilde{M} = (1 + 3m/Z^2)$, and m is the dimensionless mobility of the ions (see Equation 5.360). Equation 5.371 was derived assuming equal valency and mobility of the counterions and coions. The comparison with the exact numerical calculations showed that Equation 5.371 is rather accurate for $\kappa R > 30$ and arbitrary ζ potential. Another explicit formula of high accuracy (less than 1% for arbitrary ζ potential) and wider range of application ($\kappa R > 10$) was suggested by Ohshima et al.⁷⁴⁵

For low values of the ζ potential, Ohshima⁷⁴⁶ suggested an approximate expression for the Henry function (Equations 5.367 and 5.368), which has a relative error of less than 1% for arbitrary values of κR :

$$\mu_{EL} = \frac{2}{3} \frac{\epsilon \epsilon_0 \zeta}{\eta} \left(1 + \frac{1}{2 \left\{ 1 + 2.5 / [\kappa R (1 + 2e^{-\kappa R})] \right\}^3} \right) \quad (5.372)$$

Recently, Ohshima⁷⁴⁷ derived an extension of Equation 5.372, which is accurate for $\tilde{\zeta} < 3$ at arbitrary values of κR .

The electrophoretic mobility of particles having a cylindrical or ellipsoidal shape was studied theoretically by Stigter,⁷⁴⁸ van der Drift et al.,⁷⁴⁹ and Ohshima.⁷⁵⁰ The polyelectrolytes⁷⁵¹⁻⁷⁵³ and the spherical particles covered by a layer of polymer^{754,755} (or of polyelectrolyte) are two other types of systems that have been matters of great interest. In a recent series of papers Ohshima and

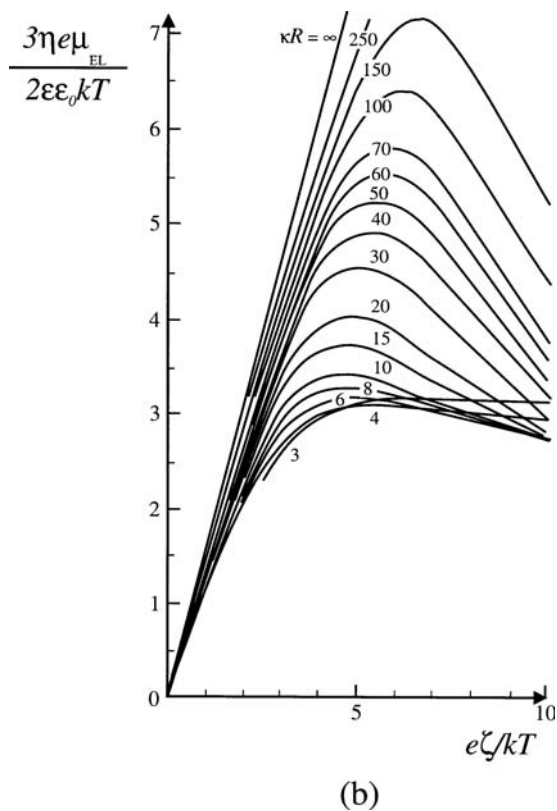


FIGURE 5.68 (CONTINUED)

Kondo⁷⁵⁶⁻⁷⁵⁸ derived a general analytical formula for the case of a hard particle, covered by a layer of polyelectrolyte. In the corresponding limiting cases, the general expression reduces to the known expressions for a hard spherical particle, a platelike particle covered by a polyelectrolyte layer, or a charged porous sphere.^{756,757}

Churaev and Nikologorskaja⁷⁵⁹ performed measurements of the electrophoretic mobility and the diffusion coefficient of silica particles before and after adsorption of polyethylenoxides. They found that the experimental data can be explained only by assuming that the adsorbed polymer layer not only shifts the shear plane apart from the particle surface (thus increasing the hydrodynamic radius of the particles) but also substantially reduces the particle surface potential. According to the authors⁷⁵⁹ the decrease in the surface charge could be due to the lower dielectric permittivity in the adsorption layer compared to that of water. It is rather possible that a similar effect played a role in the experiments of Furusawa et al.,⁷⁶⁰ who showed that the adsorption of hydroxylpropylcellulose on latex particles may completely shield their charge (the particle ζ potential becomes zero). As the adsorption layer was shown to be very stable in a wide range of pH and electrolyte concentrations, such particles can be used as a reference sample for electrophoretic measurements. These particles exactly follow the electroosmotic liquid flow in the cell and, hence, represent a convenient probe sample for the plane interface technique mentioned in Section 5.8.2.

The effect of the interparticle interactions on the electrophoretic mobility in concentrated dispersions was theoretically studied by Levine and Neale.⁷⁶¹ They used a cell model with two alternative boundary conditions at the cell boundary to describe the hydrodynamic flow: the free surface model of Happel⁷⁶² and the zero vorticity model of Kuwabara.⁷⁶³ The results⁷⁶¹ suggested that the zero vorticity model is more appropriate, because it represents in a more correct way the

limit to low particle concentration. Experiments at very low electrolyte concentrations, when the electrostatic interactions between the particles are very strong, were performed by Deggelmann et al.⁷⁶⁴ They observed a strong increase in the electrophoretic mobility at lower ionic strength (when the electrostatic interaction is stronger and the particles form a liquid-like structure) which was in apparent contradiction to the predictions of the Levine and Neale theory.⁷⁶¹ One possible explanation of this surprising result could be that the decrease of the ionic strength leads to a simultaneous increase in the surface potential,³⁴ and this effect prevails over the increased interparticle interactions. Further development of the electrokinetic theory for concentrated dispersions was presented by Kozak and Davis⁷⁶⁵ and by Ohshima.^{757,766}

Another interesting experimental study of concentrated suspensions of human erythrocytes was performed by Zukoski and Saville.⁷⁶⁷ Although volume fractions as high as 75% were employed, the electrophoretic mobility changed by the factor $(1 - \phi)$ in the whole concentration range, which was simply explained by the backflow of liquid necessary to conserve the suspension volume. The electrostatic and hydrodynamic particle–particle interactions apparently canceled each other in these experiments. Note that the electrolyte concentration was relatively high and, contrary to the experiments of Deggelmann et al.,⁷⁶⁴ the EDL were thin in comparison with the particle size.

Recent progress was achieved in the theoretical description of the electrophoretic mobility of spherical particles in oscillating electrical field⁷⁶⁸ (so-called dynamic mobility); see also Section 5.8.7.2. General equations at an arbitrary frequency, ζ potential, and κR , as well as analytical formulas for low ζ potentials, were derived by Mangelsdorf and White.⁷⁶⁸ Theory and experiment⁷⁶⁹ demonstrated rather strong frequency dependence of the electrophoretic response of the particles in the hertz and kilohertz regions. A general theoretical expressions, along with explicit approximate formulae, for the dynamic electrophoretic mobility of spheres and cylinders were derived by Ohshima.^{757,770,771} The electrophoretic measurements in oscillating fields are stimulated also by the fact that the undesirable effect of the electroosmotic flow in the experimental cell, created by the charge at the cell walls, is strongly suppressed in this type of equipment.^{769,772}

Another important recent development is the construction of equipment capable of measuring the mobility of nanometer-sized particles, such as micelles and protein molecules. The different mobility of proteins in polymer gels is widely used for their separation and identification,⁷⁷³ but this method is not suitable for the physicochemical study of proteins, because the interactions of the protein molecules with the polymer gel matrix could be rather specific. For a long time the electrophoretic mobility of proteins in a free solution was studied by the “moving boundary method” of Tiselius,⁷⁷⁴ since electrophoretic equipment based on dynamic light scattering (Section 5.9.2.1) is limited to particles of a size between approximately 50 nm and 10 μm . The method of Tiselius is not so easy and, in principle, it is not very suitable for micellar solutions, because a boundary between solutions of different concentrations must be formed. Imae et al.^{775,777–780} described an improved version of electrophoretic light scattering equipment applicable to particles of a diameter as small as several nanometers. The feasibility of this equipment was demonstrated⁷⁷⁶ by measuring the electrophoretic mobility of micelles of sodium dodecylsulfate (SDS) and of mixed micelles of SDS with nonionic surfactants. The electrokinetic properties of micelles are discussed in the recent review by Imae.⁷⁸⁰ This experimental advance is accompanied by progress in the theoretical analysis of the electrophoretic mobility of nonspherical and nonuniformly charged particles (such as proteins) with some spatial charge distribution on the particle surface.^{781–784} One quite interesting conclusion from the work of Yoon⁷⁸⁴ was that Henry’s formula, Equations 5.367 and 5.368, is correct for spherical particles of arbitrary charge distribution (with Q the net particle charge in this case), provided that the electrical potential is low and can be described by the linearized Poisson–Boltzmann equation.

More details about the method of electrophoretic mobility measurement by means of dynamic light scattering are given in Section 5.9.2.1.

5.8.5 SEDIMENTATION POTENTIAL

When a charged particle is sedimenting under the action of gravity (Figure 5.66d) the ions in the EDL are not obliged to follow the particle motion. Instead, a continuous flow of ions enters the lower half of the particle diffuse layer and leaves its upper half. The net effect is a spatial separation of the negative and positive charges, which creates the sedimentation potential of intensity, E_{SED} . At a steady state, the electrical current caused by the particle motion must be counterbalanced by an equal-in-magnitude (but opposite-in-direction) current created by E_{SED} . The potential, E_{SED} , can be directly measured by means of electrode probes placed at two different levels in the suspension of settling particles. von Smoluchowski⁷⁸⁵ derived the following equation connecting E_{SED} and the ζ potential of spherical nonconducting particles:

$$E_{\text{SED}} = \frac{\varepsilon \varepsilon_0}{\eta} \frac{F_g \rho_p}{\chi_b} \quad \text{at } \kappa R \gg 1 \quad (5.373)$$

where $F_g = gV_p(d_p - d_g)$ is the gravity force (with subtracted Archimedes' force) acting on a particle; ρ_p is the particle number concentration; g is gravity acceleration; V_p is the particle volume; d_p is the particle mass density; and d_g is the mass density of the disperse medium. Generalization of the theoretical consideration to arbitrary values of κR was given by Booth.⁷⁸⁶ The theory was later refined by Ohshima et al.,⁷⁸⁷ who performed exact numerical calculations and proposed explicit formulas for the cases of not-too-high surface potential and for thin EDL. The effect of particle concentration was considered by Levine et al.,⁷⁸⁸ who used a cell model to account for the hydrodynamic interaction between the particles. The theory of Levine et al.⁷⁸⁸ is restricted to thin double layers ($\kappa R > 10$) and low surface potentials.

5.8.6 ELECTROKINETIC PHENOMENA AND ONZAGER RECIPROCAL RELATIONS

All electrokinetic phenomena include the coupled action of an electrical force (with the respective electrical current) and a hydrodynamic force (with the respective hydrodynamic flux). Therefore, we can apply the general approach of the linear thermodynamics of irreversible processes to write^{789,790}

$$\begin{aligned} J_1 &= \alpha_{11} F_1 + \alpha_{12} F_2 \\ J_2 &= \alpha_{21} F_1 + \alpha_{22} F_2 \end{aligned} \quad (5.374)$$

where F_j ($j = 1, 2$) are the forces, J_j are coupled fluxes, and α_{ij} are phenomenological coefficients. According to the Onsager reciprocal relations, α_{12} must be equal to α_{21} , i.e., the following relationships must be satisfied (see Equation 5.374):

$$\left(\frac{J_1}{F_2} \right)_{F_1=0} = \left(\frac{J_2}{F_1} \right)_{F_2=0} \quad (5.375)$$

Other relations, which directly follow from the assumption $\alpha_{12} = \alpha_{21}$ are

$$\left(\frac{J_1}{F_2} \right)_{J_2=0} = \left(\frac{J_2}{F_1} \right)_{J_1=0} ; \quad \left(\frac{J_1}{J_2} \right)_{F_1=0} = - \left(\frac{F_2}{F_1} \right)_{J_2=0} ; \quad \left(\frac{J_1}{J_2} \right)_{F_2=0} = - \left(\frac{F_2}{F_1} \right)_{J_1=0} \quad (5.376)$$

In the cases of the immobile solid phase (electroosmosis and streaming potential; see Figures 5.66a and 5.66b), we can identify^{789,790}

$$\begin{aligned} J_1 &\equiv J_w; & F_1 &\equiv \Delta P \\ J_2 &\equiv I; & F_2 &\equiv E \end{aligned} \quad (5.377)$$

where J_w is the water flux and I is the current. Then, the counterpart of Equation 5.375 reads

$$\left(\frac{J_w}{E}\right)_{\Delta P=0} = \left(\frac{I}{\Delta P}\right)_{E=0} \quad (5.378)$$

Equation 5.378 connects the phenomenological coefficients appearing in electroosmosis (the left-hand side) with those in streaming potential experiments (the right-hand side). We must note that Equation 5.378 is valid even if the surface conductivity is important or when the double layers are not thin with respect to the capillary diameter. Furthermore, this type of relationship is valid even for electrokinetic experiments with porous plugs and membranes with pores of nonuniform size and shape. The respective counterparts of the other relations (Equation 5.376) are

$$\left(\frac{I}{\Delta P}\right)_{J_w=0} = \left(\frac{J_w}{E}\right)_{I=0}; \quad \left(\frac{I}{J_w}\right)_{E=0} = -\left(\frac{\Delta P}{E}\right)_{J_w=0}; \quad \left(\frac{I}{J_w}\right)_{\Delta P=0} = -\left(\frac{\Delta P}{E}\right)_{I=0} \quad (5.379)$$

In the case of mobile charged particles (electrophoresis and sedimentation potential; Figure 5.66c and 5.66d), we should identify J_1 as the flux of particles, J_p , and F_1 as the gravity force, F_g . Then, the Onsager relations read

$$\left(\frac{J_p}{E}\right)_{F_g=0} = \left(\frac{I}{F_g}\right)_{E=0}; \quad \left(\frac{I}{F_g}\right)_{J_p=0} = \left(\frac{J_p}{E}\right)_{I=0} \quad (5.380a)$$

$$\left(\frac{I}{J_p}\right)_{E=0} = -\left(\frac{F_g}{E}\right)_{J_p=0}; \quad \left(\frac{I}{J_p}\right)_{F_g=0} = -\left(\frac{F_g}{E}\right)_{I=0} \quad (5.380b)$$

Again, Equations 5.379 and 5.380 are valid even for concentrated dispersions when strong electrostatic and hydrodynamic interactions between the particles may take place.

We can verify that all explicit expressions given in Sections 5.8.2 through 5.8.5 satisfy the Onsager relations.

5.8.7 ELECTRIC CONDUCTIVITY AND DIELECTRIC RESPONSE OF DISPERSIONS

5.8.7.1 Electric Conductivity

Here we consider briefly the conductivity, χ , of dispersions subjected to a constant electric field of intensity, E . The behavior of dispersions in alternating fields is considered in Section 5.8.7.2.

Charged particles influence the net conductivity in several ways: (1) the presence of particles having dielectric constant and conductivity different from those of the medium affects the local electrical field and the conditions for ion transport (e.g., nonconducting particles act as obstacles to the electromigrating ions and polarize the incident electric field); (2) the increased ionic concentration in the diffuse ion

cloud surrounding the particles leads to higher local conductivity; and (3) the migrating charged particles may also contribute to the total electric current.

Effect (1) was analyzed by Maxwell,⁷⁹¹ who derived the following expression for the conductivity of diluted suspension of uncharged particles:

$$\chi = \chi_b \left(\frac{1 - 2\Omega\phi}{1 + \Omega\phi} \right), \quad \Omega = \frac{\chi_b - \chi_p}{2\chi_b + \chi_p} \quad (5.381)$$

where χ_p is the conductivity of the particles, χ_b is the conductivity of the medium, and ϕ is the particle volume fraction. As shown by Maxwell, this result includes an important contribution from the polarization of the field by the particles. Fricke⁷⁹² modified the Maxwell approach to consider particles of oblate or prolate spheroidal shape and obtained the formula:

$$\chi = \chi_b \left(\frac{1 - X\Omega\phi}{1 + \Omega\phi} \right), \quad \Omega = \frac{\chi_b - \chi_p}{X\chi_b + \chi_p} \quad (5.382)$$

where the X factor depends on the particle conductivity and shape. Because the theory of Fricke⁷⁹² assumes random orientation of the particles, it is strictly valid only for diluted suspensions of non-interacting particles and a not-too-high intensity of the electrical field. These expressions were used by Zukoski and Saville⁷⁶⁷ to interpret the conductivity data from human erythrocyte suspensions at high ionic strength and relatively low surface potential where the effect of the surface conductivity is negligible (see Equation 5.362).

The contribution of the particle surface conductivity (effect (2)) for a thin EDL can be accounted for phenomenologically in a similar way, and the final result for nonconducting particles reads^{707,793}

$$\chi = \chi_b \left[1 - \frac{3}{2}\phi \left(1 - \frac{3\chi_s}{\chi_b R + \chi_s} \right) \right], \quad \kappa R \gg 1 \quad (5.383)$$

Numerical procedures for calculating the conductivity of dispersions without restriction to double layer thickness were developed by O'Brien.^{794,795} A formula for thin EDL, explicitly accounting for the ion mobility, is given by Ohshima et al.⁷⁹⁶

As discussed by Dukhin and Derjaguin,⁷⁰⁷ the electrophoretic migration of the particles (effect (3)) is negligible if the measurements are performed under conditions such that the particles cannot release their charges on the electrodes.

5.8.7.2 Dispersions in Alternating Electrical Field

As mentioned in Section 5.8.4, the electrical field, in general, polarizes the EDL around a charged particle. This means that the spherical symmetry of the ion cloud breaks down, and the additional force appearing between the charged particle and the distorted ion atmosphere must be taken into account for proper description of the particle dynamics. If the external field is suddenly switched off, some finite period of time is needed for restoration of the spherically symmetric configuration. This time can be estimated^{278,715,797} from the ion diffusivity and from the characteristic path length, l ; the ions should travel:

$$\tau_{\text{REL}} \sim \frac{l^2}{D_{\text{SI}}} \approx \frac{(R + \kappa^{-1})^2}{D_{\text{SI}}} = \frac{(1 + \kappa R)^2}{\kappa^2 D_{\text{SI}}} \quad (5.384)$$

where $D_{SI} \approx 10^{-9} \text{ m}^2/\text{s}$ is the ion diffusion coefficient. If the particles are subjected to an oscillatory field of frequency, ω , much higher than τ_{REL}^{-1} , the ion clouds will have no time to respond, and the system will behave as though containing particles with nonpolarizable double layers. On the other hand, at a low frequency, $\omega \ll \tau_{REL}^{-1}$, the ion clouds will polarize, exactly following the temporal changes of the applied field. At intermediate frequencies, $\omega \sim \tau_{REL}^{-1}$, the EDL will follow the field variations with some delay, and the dielectric constant of the colloidal dispersion, ϵ , will show a strong dependence on ω . The numerical estimate (see Equation 5.384) shows that τ_{REL} is typically of the order of 10^{-3} s and the characteristic frequency, ω_{REL} , falls in the kilohertz range. For thin EDL, there is an additional relaxation time, τ_κ , connected with the ion transport across the double layer^{715,797,798} (i.e., in a radial direction with respect to the particle surface). Because the diffusion path in this case is $l \sim \kappa^{-1}$, the relaxation time is⁷⁹⁸

$$\tau_\kappa \sim \kappa^{-2}/D_{SI} \quad (5.385)$$

Therefore, τ_κ is inversely proportional to the electrolyte concentration, and the corresponding characteristic frequency, ω_κ , is typically in the megahertz range.

The polarizability of the individual molecules is also frequency dependent, but the characteristic values are of the order of $10^{11}/\text{s}$ and $10^{15}/\text{s}$ for the rotational and electronic polarization, respectively.³⁴ Therefore, in the typical frequency domain for investigation of dispersions ($1/\text{s} \leq \omega \leq 10^8/\text{s}$) the polarizability, ϵ_p , of the material building up the particles is frequency independent. On the other hand, the disperse medium (which is usually an electrolyte solution) has a dielectric permittivity, ϵ_b , for which the frequency dependence can be described by the Debye–Falkenhagen theory.⁷⁹⁹ Besides, the characteristic relaxation time of the bulk electrolyte solutions is also given by Equation 5.385.⁷⁹⁹

The typical experiment for determination of the dielectric response of a suspension consists^{278,715,797} of measuring the magnitude and phase-lag of the current, $I_c(t)$, passing through the suspension under an applied, oscillating electrical field, $E(t) = E_0 \cos(\omega t)$. The current, in turn, contains two components — one connected with the free charges and another connected with the polarization. Use of the complex presentation of the applied field is widely accepted:^{278,715}

$$E(t) = \text{Re}\{E_0 \exp(i\omega t)\} \quad (5.386)$$

where $\text{Re}\{f\}$ means that the real part of the complex function, f , is considered. Very often the $\text{Re}\{x\}$ sign is not explicitly stated, but is understood. This formalism, using complex functions, is rather convenient because the magnitude and the phase-lag of the current both can be described by one quantity — the complex conductivity, χ^* :

$$I_c(t) = \text{Re}\{\chi^* E_0 \exp(i\omega t)\} \quad (5.387)$$

The physical meaning of the real and of the imaginary parts of χ^* is the following.⁷¹⁵ $\text{Re}\{\chi^*\}$ is proportional to the dissipated energy in the system — the heat produced per period of the field oscillation is equal to $1/2 E_0^2 \text{Re}\{\chi^*\}$. On the other hand, the phase-lag of the current (with respect to the applied field) is characterized by the phase angle,

$$\varphi = \arctan \left[\frac{\text{Im}\{\chi^*\}}{\text{Re}\{\chi^*\}} \right]$$

The complex conductivity, χ^* , of a dispersion is usually defined as²⁷⁸

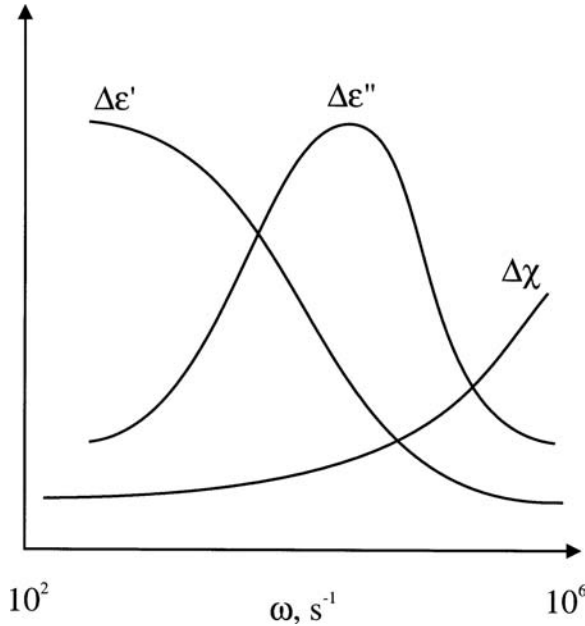


FIGURE 5.69 Schematic presentation of the electric conductivity, $\Delta\chi$, the real part, $\Delta\epsilon'$, and the imaginary part, $\Delta\epsilon''$, of the dielectric permittivity increments of dispersion as functions of the frequency of the electric field, ω . For definitions of $\Delta\chi$, $\Delta\epsilon'$, and $\Delta\epsilon''$, see Equation 5.390.

$$\chi^*(\omega, \phi) = \chi(\omega, \phi) - i\omega\epsilon_0\epsilon'(\omega, \phi) \quad (5.388)$$

where χ is the real part of χ^* and ϵ' is the “loss-free” part of the dielectric response. Alternatively, we can define²⁷⁸

$$\chi^*(\omega, \phi) = \chi(0, \phi) + \omega\epsilon_0\epsilon''(\omega, \phi) - i\omega\epsilon_0\epsilon'(\omega, \phi) \quad (5.389)$$

where the frequency dependence of the real part of χ^* was totally assigned to the imaginary part of the dielectric constant. Both conventions are used in the literature,²⁷⁸ and we should note that in the first case the dielectric constant of the suspension is a real number ($\epsilon = \epsilon'$, $\epsilon'' = 0$), whereas in the second case ϵ is considered a complex number ($\epsilon = \epsilon' + i\epsilon''$). Also, since the effect of the particles is of primary interest, we consider the changes of these quantities with respect to the properties of the disperse medium:²⁷⁸

$$\Delta\chi(\omega, \phi) \equiv \frac{\chi(\omega, \phi) - \chi(\omega, 0)}{\chi(\omega, 0)\phi}; \quad \Delta\epsilon'(\omega, \phi) \equiv \frac{\epsilon'(\omega, \phi) - \epsilon'(\omega, 0)}{\phi} \quad (5.390)$$

$$\Delta\epsilon'' \equiv \frac{\chi(\omega, \phi) - \chi(0, \phi)}{\omega\epsilon_0\phi}$$

In Figure 5.69 the typical frequency dependencies of $\Delta\chi$, $\Delta\epsilon'$, and $\Delta\epsilon''$ in the kilohertz range are schematically represented (a number of real experimental plots are given in the books by Dukhin and Shilov⁷¹⁵ and Russel et al.²⁷⁸). As shown in the figure, the value of ϵ'' goes through a maximum, which corresponds to a maximal dissipation of energy in the suspension. The values of χ and ϵ' are, respectively, monotonously decreasing and increasing with the frequency. In general, the

experiments show that the magnitude of $\Delta\epsilon'$ increases with the values of κR and the ζ potential. The magnitude of $\Delta\chi$ also increases with the ζ potential but decreases with κR . The magnitude of $\Delta\epsilon''$ increases with the ζ potential. In dilute dispersions, none of the three quantities depends on the particle concentration in the framework of the experimental accuracy, as would be expected. The theory of the dielectric response in this low-frequency range was mostly developed by Dukhin and colleagues,⁷¹⁵ and analytical formulas are available for thin EDL⁷¹⁵ or low surface potential.⁷¹⁰

During the last decade the dielectric response of dispersions in the megahertz range was extensively studied. O'Brien⁷⁹⁸ presented the complex conductivity of a dilute dispersion in the form (see Equation 5.381):

$$\chi^* = (\chi_b + i\omega\epsilon_0\epsilon_b) \frac{(1 - 2\Omega\phi)}{(1 + \Omega\phi)} \quad (5.391)$$

where the complex function $\Omega(\chi_b, \chi_s, \epsilon_b, \epsilon_p, \omega)$ is given by the expression:

$$\Omega \equiv \frac{\chi_b - 2\chi_s/R + i\omega\epsilon_0(\epsilon_b - \epsilon_p)}{2(\chi_b + \chi_s/R) + i\omega\epsilon_0(2\epsilon_b + \epsilon_p)} \quad (5.392)$$

Here, ϵ_p is the relative dielectric permittivity of the particle substance. As shown by O'Brien,⁷⁹⁸ at high frequency ($\omega \gg D\kappa^2 \sim \chi_b/\epsilon_0\epsilon_b$), Equation 5.392 reduces to the result for uncharged particles, $\Omega = (\epsilon_b - \epsilon_p)/(2\epsilon_b + \epsilon_p)$. At low frequency ($\omega \ll \chi_b/\epsilon_0\epsilon_b$), Equation 5.392 coincides with the high-frequency limit of the formula derived by Hinch.⁸⁰⁰

$$\Omega = \frac{1}{2} - \frac{3}{2} \beta / [2 + \beta(1 + \delta)] \quad (5.393)$$

where

$$\beta = \frac{2}{\kappa R} \left(1 + 3 \frac{m}{Z^2} \right) \exp\left(\frac{eZ\zeta}{2kT} \right) \quad (5.394)$$

$$\delta = \left[1 + (i\omega R^2/D_{SI})^{1/2} \right] / \left[1 + (i\omega R^2/D_{SI})^{1/2} + \frac{1}{2} i\omega R^2/D_{SI} \right] \quad (5.395)$$

The high-frequency limit of Equation 5.393 is $\Omega = (1 - \beta)/(2 + \beta)$, which, as stated above, is identical to the low-frequency limit of Equation 5.392 because $\chi_s/\chi_b R = \beta/2$.⁷⁹⁸ We can conclude that the combination of Equations 5.391 through 5.393 covers the whole range of frequencies that are of interest.⁷⁹⁸

This approach was further extended by O'Brien⁷⁹⁸ to include the cases of concentrated dispersion of randomly packed spheres and porous plugs. A comparison with experimental data on Pyrex plugs revealed very good agreement in the frequency range from 10^3 to 10^7 /s. Midmore et al.⁸⁰¹ measured the dielectric response of concentrated latex suspensions (ϕ was varied between 0.1 and 0.5) in the range between 1 and 10 MHz and also found that the data can be well reproduced by the cell type of theoretical model. However, the estimated ζ potential from the conductivity measurements was considerably larger than the value determined by electrophoretic measurement (this issue will be discussed in the following section). Equipment and procedures for performing calibration and measurement of the dielectric response of dispersions are described in References

801 through 803. A large set of numerical results for various values of the particle ζ potential and the ionic strength of the disperse medium were presented by Grosse et al.⁸⁰⁴

We now briefly describe the technique of colloid vibration potential (CVP) for determination of the particle ζ potential. In this type of experiment, an ultrasonic wave is introduced into the suspension, thus leading to oscillatory motion of the particles. Because of the difference in the mass densities of the particles and the surrounding fluid, the ion cloud does not follow the particle motion (similar to the case of particle sedimentation), and spatial separation of the positive and negative charges appears. The corresponding electrical potential is called the *colloid vibration potential* and can be measured by two probe electrodes separated by distance $\lambda/2$ in the direction of the ultrasound propagation (λ is the sound wavelength). The theory for diluted suspensions was developed by Enderby⁸⁰⁵ and Booth and Enderby⁸⁰⁶ and further extended to concentrated systems by Marlow et al.⁸⁰⁷ The connection between the colloid vibration potential, E_{CVP} and the particle ζ potential is^{807,808}

$$E_{\text{CVP}} = \frac{2 P_0 \phi}{\chi_b} \frac{(d_p - d_b)}{d_b} \frac{\epsilon_b \epsilon_0}{\eta} \zeta f_2(\kappa R, \phi) \quad (5.396)$$

where P_0 is the amplitude of the sound pressure, and d_p and d_b are the mass densities of the particles and medium, respectively. The function $f_2(\kappa R, \phi)$ accounts for the particle–particle interactions; for diluted systems, $f_2(\kappa R, \phi \rightarrow 0) = 1$, and for thin EDL $f_2(\kappa R \gg 1, \phi) = (1 - \phi)$.

The experiments performed by several research groups⁸⁰⁷⁻⁸⁰⁹ showed good agreement of theoretical predictions with the experimental data. This is rather encouraging and a little surprising result, keeping in mind that the experiments with simple electrolytes (where a similar effect called “ionic vibration potential” exists⁸¹⁰) produced data that are often not well explained⁸⁰⁹ by the corresponding theory.⁸¹⁰ The CVP technique can be applied to concentrated dispersions.

O’Brien⁸¹¹ showed that the CVP is related through the Onzager relations to the so-called electrokinetic sonic amplitude (ESA). The latter appears when an alternating electric field is applied to a suspension of charged particles. The ensuing oscillatory motion of the particles creates a macroscopic acoustic wave, whose amplitude and phase lag can be experimentally measured and used for characterization of the dispersed particles. The method allows determination of the size and ζ potential of the particles in a concentrated dispersion without need of dilution.⁸¹²⁻⁸¹⁸ In general, the problem consists of two stages: first, the dynamic electrophoretic mobility is determined from the CVP or ESA data, and second, the particle ζ potential is calculated from the dynamic mobility by using various theoretical models. The effect of surface conductivity on the analysis of the ESA and CVP data was recently considered by Dukhin et al.⁸¹⁷ and by Löbbus et al.⁸¹⁸ The CVP and ESA are often termed *electroacoustic phenomena* in the literature.

5.8.8 ANOMALOUS SURFACE CONDUCTANCE AND DATA INTERPRETATION

Theoretical interpretation of the measured electrokinetic quantities is always based on a number of explicit and implicit assumptions. Because the meaning of the obtained data depends on the adequacy of the theory used for their interpretation, the underlying assumptions are often questioned and discussed in the literature.^{705,707,716,819} In this section, we briefly discuss the current evaluation of the importance of some effects that are not taken into account in the conventional theory.

All the consideration up to now implies that the dielectric permittivity and the viscosity in the EDL (at least for $x \geq x_s$; see Figure 5.67) are equal to those of the bulk disperse medium. A more refined approach^{793,819} shows that for thin double layers the formulae, stemming from the von Smoluchowski theory, may remain unaltered if the “real” ζ potential ($\zeta = \psi(x_s)$) is replaced by the quantity⁷⁹³

$$\zeta_{\text{obs}} = \frac{\eta_b}{\varepsilon_b} \int_0^{\infty} \frac{\varepsilon(x)}{\eta(x)} \frac{d\psi}{dx} dx = \frac{\eta_b}{\varepsilon_b} \int_0^{\zeta} \frac{\varepsilon(\psi)}{\eta(\psi)} d\psi \quad (5.397)$$

where $\varepsilon(x)$ and $\eta(x)$ account for local variations of the dielectric constant and viscosity in the double layer, while ε_b and η_b are the respective values in the bulk medium. Hunter⁸¹⁹ analyzed a number of theoretical and experimental results and concluded that this effect is “small under most conditions.” Recently, Chan and Horn⁸²⁰ and Israelachvili⁸²¹ performed dynamic experiments using the surface force apparatus and showed that the water viscosity is practically constant down to distances one to two molecular diameters from a smooth mica surface. Their experiments also demonstrated that the shear plane at a smooth surface is shifted no more than one to two molecular layers apart from the surface. Therefore, we may expect that for smooth surfaces the ζ potential should be very close to the surface potential, ψ_s , at least for not-too-high electrolyte concentrations and surface potentials.

The case of a rough solid surface is much more complicated,^{707,793} because the surface roughness affects not only the position of the shear plane, but also the surface charge density distribution and the surface conductivity. Therefore, a general approach to rough surfaces is missing and we should choose between several simple models (see below) to mimic as close as possible the real surface.

Another very important issue in this respect is the way to account for the surface conductivity. The formula of Bikerman⁷²⁷ (Equation 5.359), the correction factor to the electrophoretic mobility of Henry⁷³⁸ (Equation 5.368), and the formula of O’Brien and Hunter⁷⁴⁴ (Equation 5.371), quoted above are derived under the assumption that only the ions in the movable part ($x \geq x_s$; Figure 5.67) of the EDL contribute to the surface conductivity, χ_s . Moreover, the ions in the EDL are taken to have the same mobility as that in the bulk electrolyte solution. A variety of experimental data^{707,715,793,822-827} suggest, however, that the ions behind the shear plane ($x < x_s$) and even those adsorbed in the Stern layer may contribute to χ_s . The term *anomalous surface conductance* was coined for this phenomenon. Such an effect can be taken into account theoretically, but new parameters (such as the ion mobility in the Stern layer) must be included in the consideration. Hence, the interpretation of data by these more complex models usually requires the application of two or more electrokinetic techniques which provide complementary information.^{803,828} Dukhin and van de Ven⁸²⁸ specify three major (and relatively simple) types of models as being most suitable for data interpretation. These models differ in the way they consider the surface conductivity and the connection between ψ_s and ζ :

- Model 1 ($\zeta = \psi_s$ and $\chi_s = \chi_s^{\text{EDL}}$): This is the simplest possible model accounting for the surface conductivity, because it assumes that an immobile part of the diffuse layer is absent. As a result, $x_s = 0$, $\zeta = \psi_s$, and χ_s is due only to ions in the diffuse layer.
- Model 2 ($\zeta \neq \psi_s$, $\chi_s = \chi_s^{\text{EDL}}$): In this model two parts of the diffuse layer (hydrodynamically mobile and immobile, respectively) are distinguished. The surface conductivity is taken to include contributions from the ions in the whole diffuse layer, including the hydrodynamically immobile part. The mobility of the ions in the diffuse layer is considered to be the same as that in the bulk, while the mobility of the ions in the Stern layer is set equal to zero. The Gouy–Chapman theory, e.g., Equation 5.343, is used to connect the values of ζ and ψ_s . Therefore, the value of x_s is an important parameter in this model. According to Dukhin and van de Ven,⁸²⁸ this model is most suitable for particles with a rough surface or for a surface covered with a layer of nonionic surfactants or polymers.^{822,823,825}
- Model 3 ($\zeta = \psi_s$, $\chi_s = \chi_s^{\text{EDL}} + \chi_s^{\text{Stern}}$): As in model 1, it is assumed that the whole diffuse part of the EDL is hydrodynamically mobile. In addition, the ions in the Stern layer are allowed to move in an external electrical field and to contribute to χ_s . This model seems to be appropriate for the description of electrophoresis of biological cells (if glycocalyx on the cell surface is not present) and particles covered by ionic surfactants.⁸²⁴

Theoretical descriptions of the electrokinetic phenomena in the framework of these three models were developed in the literature and reviewed by Dukhin and van de Ven.⁸²⁸ The effect of particle polydispersity on the data interpretation by the different models was analyzed in the same study.⁸²⁸

The interest in anomalous surface conductance has been high during the last several years^{795,817,818,822-823} as a result of the finding that most of the studied latex samples have shown electrokinetic properties that cannot be described by conventional theory. In particular, the electric potential determined by electrophoresis was substantially lower than that measured in dielectric studies.^{795,801,823-826} Also, the electrophoretic ζ potential, calculated from the conventional theory, showed a maximum as a function of the electrolyte concentration, while we should expect a gradual decrease.^{803,829} Several hypotheses^{825,826} were discussed in the literature to explain this discrepancy, most of them connected with the anomalous surface conductance of the latex particles. According to the "hairy model,"^{826,827} the particle surface is covered by a layer of flexible polymer chains, which are extended into the solution at a distance, which depends on the electrolyte concentration. Since the position of the shear plane, x_s , is to be close to the outer boundary of this polymer layer, the thickness of the immobile hydrodynamic layer (and the corresponding anomalous surface conductance created by the ions in the immobile layer) appears to be strongly dependent on the ionic strength. This hypothesis found some experimental confirmation in experiments⁸²⁷ with latex particles, preheated for a certain period of time at a temperature above the glass transition temperature of the polymer. As shown by Rosen and Saville,⁸²⁷ the electrokinetic properties of the preheated latexes become much closer to those expected from the classical theory. On the other hand, Shubin et al.⁸⁰³ made systematic measurements to distinguish which type of ions are responsible for the anomalous conductance of the latex particles, those in the diffuse part or those in the Stern layer. The authors⁸⁰³ concluded that their data can be interpreted only by assuming ion transport in the Stern layer. Recent theoretical analysis of Saville⁸³³ showed that the presence of a thin permeable (hairy) polymer layer on the surface of colloid particles indeed has an important effect on their electrophoretic mobility, while the suspension conductivity might be very slightly affected.

Experiments⁸³⁰⁻⁸³² made in different laboratories suggest that the importance of the discussed effect depends strongly on the type of particles used. Gittings and Saville⁸³¹ and Russel et al.⁸³⁰ found latex samples (commercial and laboratory-made ones) for which the electrokinetic properties can be well described by the classical theory, without need to invoke the anomalous surface conductance. These observations were complemented by the results of Bastos-Gonzalez et al.,⁸³² who performed heat treatment of polystyrene latexes with different surface groups. The experiments by several methods showed⁸³² that the surface of the sulfate and aldehyde latexes changed upon heating, while the sulfonate and carboxyl latexes did not show a detectable change of their properties. Better understanding of the electrokinetic properties of latex particles is of significant importance, because the latexes are widely used^{278,717} as model systems for quantitative investigation of a variety of colloidal phenomena, and their reliable characterization is needed for these tasks.

5.8.9 ELECTROKINETIC PROPERTIES OF AIR–WATER AND OIL–WATER INTERFACES

The experimental methods based on electrokinetic phenomena (and especially electrophoresis) have found very widespread application for routine characterization of electrical surface properties of solid particles, liquid droplets, porous media, synthetic membranes, etc. A systematic presentation of the main results obtained on different types of systems is given in chapters 6 to 8 of Reference 716, and in chapters 8 to 33 of Reference 718. A glance at the books^{278,715-718} and review articles⁷⁰⁴⁻⁷¹⁴ in the field, however, shows that the properties of air–water and oil–water interfaces are either not considered at all or only briefly mentioned. This fact is surprising, as a number of studies⁸³⁴⁻⁸⁴³ (the first performed more than 70 years ago) have convincingly demonstrated a substantial negative ζ potential at bare (without any surfactant) air–water and oil–water interfaces. This spontaneous charging cannot be explained in a trivial way — it requires the specific preferential adsorption of some kind of ion, because from a purely electrostatic viewpoint the approach of an ion to the

interface of water and a nonpolar fluid is unfavorable because of the image forces.³⁴ Measurements of the electrophoretic mobility of air bubbles and oil droplets demonstrated a strong pH dependence of their ζ potential: it is almost zero at a pH of around 3 and goes down to -120 mV at a pH ~ 11 . Therefore, two main hypotheses, connected with the dissociation-association equilibrium of water ($\text{H}_2\text{O} = \text{H}^+ + \text{OH}^-$) were suggested in the literature to explain the phenomenon: (1) specific adsorption of HO^- ions in the boundary layer of water molecules, and (2) negative adsorption, i.e., depletion of H^+ ions in the boundary layer.

Marinova et al.⁸⁴² performed a series of systematic measurements of the electrophoretic mobility of oil in water emulsion droplets to check these (and some other) possible hypotheses. Analysis of the obtained results leads to the conclusion that the charges originate from hydroxyl ions, which specifically adsorb at the oil–water interface. The pH dependence of the surface charge was interpreted by using Stern’s adsorption isotherm, yielding the value of $\sim 25 kT$ for the specific adsorption energy per HO^- ion. Although some speculations about the underlying mechanism were presented^{841,842} the molecular picture behind this value is rather obscured. We may expect that the computer methods for studying the molecular structuring and dynamics at interfaces (including hydrogen bond effects) will be very helpful in revealing the physical origin of the surface charge. Dunstan and Saville⁸⁴¹ suggested the idea that the specific adsorption of ions, responsible for the charging of hydrophobic surfaces, may be connected with the anomalous electrokinetic behavior of latex particles, as discussed in the previous section.

The air–water and oil–water interfaces, covered with adsorption layers of nonionic surfactants, are also negatively charged at neutral pH, which has an important impact on the stability of foams and emulsions.^{462,835,842,844–846} Again, a strong pH dependence of the ζ potential is established: the higher the pH, the larger in magnitude the ζ potential. The effect of the adsorbing nonionic surfactants on the magnitudes of the surface potential of air–water interfaces was analyzed in detail in Reference 846. The electrokinetic properties of fluid interfaces in the presence of cationic or anionic surfactants are more understandable (at least qualitatively): the interfaces are positively or negatively charged, respectively. In the presence of an adsorbed protein layer, the interfacial electric potential is usually close to that of the protein molecules at the pH of the disperse medium. In this way, the surface charge may change from negative to positive around the isoelectric point of the protein.

5.9 OPTICAL PROPERTIES OF DISPERSIONS AND MICELLAR SOLUTIONS

The light scattering methods for studying colloidal systems can be classified in two wide groups: static light scattering (SLS) and dynamic light scattering (DLS). The latter is often called quasi-elastic light scattering (QELS) or photon correlation spectroscopy (PCS). In SLS methods, the averaged-over-time intensity of the scattered light is measured as a function of the particle concentration and/or scattering angle. In DLS methods, the time fluctuations of the scattered light are measured. The light scattering methods possess a number of advantages, which make them particularly suitable for investigation of colloid systems. In general, these methods are noninvasive; applicable to very small and unstable (when dried) particles, such as surfactant micelles and lipid vesicles; suitable for characterization of particle size and shape, as well as of interparticle interactions; and relatively fast, not requiring very expensive equipment. The theoretical basis of light scattering methods is outlined in Sections 5.9.1 and 5.9.2. The main applications of the methods to surfactant solutions and colloidal dispersions are summarized in Section 5.9.3.

5.9.1 STATIC LIGHT SCATTERING

A comprehensive presentation of the SLS theory can be found in the monographs by Van de Hulst⁸⁴⁷ and Kerker.⁸⁴⁸ The basic concepts are discussed in the textbooks by Hiemenz and Rajagopalan⁸⁴⁹ and Lyklema;⁸⁵⁰ a collection of the classical papers on this topic is reprinted in Reference 851.

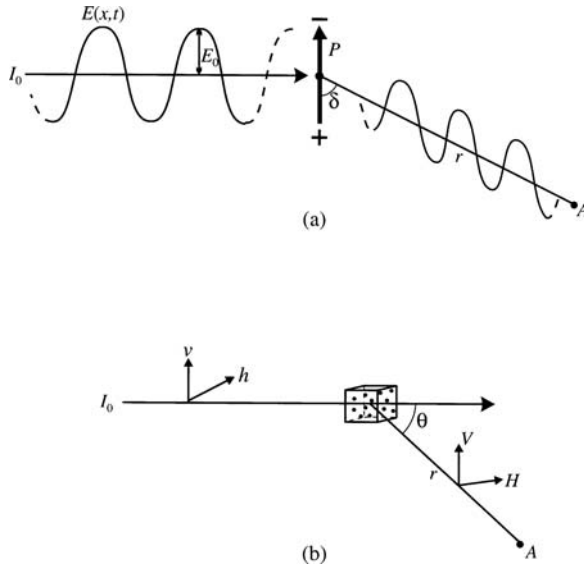


FIGURE 5.70 Geometry of the light scattering experiment. (a) Plane polarized monochromatic beam of intensity I_0 induces the variable dipole, p , which emits an electromagnetic wave (scattered light); the detector is at point A. (b) The incident beam can be vertically polarized, horizontally polarized, or nonpolarized with respect to the scattering plane. Angle δ is formed between the directions of the dipole and the scattered beam, while the angle θ is between the directions of the incident and scattered beams. The axes (v,h) and (V,H) denote the vertical and horizontal directions for the incident and scattered beam, respectively.

5.9.1.1 Rayleigh Scattering

The scattering of light from colloidal particles of dimensions much smaller than the light wavelength (e.g., surfactant micelles) can be analyzed in the framework of the Rayleigh theory,⁸⁵² which was originally developed for light scattering from gases. A beam of monochromatic, polarized light can be described by the amplitude of its electrical vector (see Figure 5.70).

$$E = E_0 \cos 2\pi \left(vt - \frac{x}{\lambda} \right) \quad (5.398)$$

Here, x is the coordinate in direction of the incident beam, t is time, and v and λ are the frequency and the wavelength of the light, respectively. The light induces a variable dipole in the particle:

$$p = \alpha E = \alpha E_0 \cos 2\pi \left(vt - \frac{x}{\lambda} \right) \quad (5.399)$$

where α is the excess particle polarizability (i.e., the difference between the polarizability of the particle and the polarizability of the same volume of the medium). The induced dipole creates an electromagnetic field of the same frequency (scattered light) with an intensity (energy flux per unit area perpendicular to the scattered beam) averaged over time of⁸⁴⁹

$$\langle I_s \rangle_t = \frac{16\pi^4}{\lambda_0^4 r^2} \left(\frac{\alpha}{4\pi\epsilon_0} \right)^2 \langle I_0 \rangle_t \sin^2 \delta, \quad \langle I_0 \rangle_t = \frac{c\epsilon_0}{2} E_0^2 \approx 1.328 \times 10^{-3} E_0^2 \text{ W/m}^2 \quad (5.400)$$

where the brackets denote time averaging, δ is the angle between the direction of the induced dipole and the direction of the scattered beam, $\langle I_0 \rangle_t$ is the intensity of the incident beam, λ_0 is the light wavelength *in vacuo*, r is the distance between the scattering dipole and the detector, c is the speed of light, and ϵ_0 is the dielectric permittivity of the *vacuo*. For vertically polarized light, $\delta = \pi/2$, while for horizontally polarized light $\delta = (\pi/2 - \theta)$; θ is the scattering angle (see Figure 5.70). Nonpolarized light can be formally considered as the superposition of one vertically polarized and one horizontally polarized beam of equal intensity. In the Rayleigh theory,⁸⁵² the scatterers are considered to be independent of each other, and the total intensity of the scattered light from a suspension of number concentration ρ is proportional to the number of particles observed by the detector, N ($N = \rho V_S$; V_S is the scattering volume). To characterize the light scattering with a quantity independent from the geometry of the equipment, we usually consider the reduced intensity of the scattered light called Rayleigh ratio:

$$R(\theta) \equiv \frac{\langle I_s \rangle_t}{\langle I_0 \rangle_t} \frac{r^2}{V_S} = \frac{16\pi^4}{\lambda_0^4} \left(\frac{\alpha}{4\pi\epsilon_0} \right)^2 \rho P(\theta) \quad (5.401)$$

where the factor $P(\theta)$ depends on the polarization of the incident beam. In the case of small particles (of dimensions much smaller than λ):

$$P_v(\theta) = 1, \quad P_h(\theta) = \cos^2 \theta, \quad P_u(\theta) = \frac{1}{2}(1 + \cos^2 \theta) \quad (5.402)$$

where the subscripts v , h , and u denote vertically polarized, horizontally polarized, or nonpolarized incident beam, respectively. In the more general case, $P(\theta)$ also depends on the size and shape of the scattering particles (see below); hence, it is sometimes called the scattering form factor of the particles. By using the continuum theory of dielectric polarization, we can express the excess polarizability of a spherical particle of radius R and refractive index n_p , which is immersed in a medium of refractive index, n_m , by means of the Lorenz–Lorentz equation:³⁴

$$\left(\frac{\alpha}{4\pi\epsilon_0} \right) = n_m^2 \left(\frac{n_p^2 - n_m^2}{n_p^2 + 2n_m^2} \right) R^3 \quad (5.403)$$

Because in many cases n_p and R are not known and the particles may have a nonspherical shape, another way for deducing the excess particle polarizability is used: α is expressed through the change of the refractive index of the suspension, n , with the particle concentration:⁸⁵³

$$\alpha = \frac{\epsilon_0(n^2 - n_m^2)}{\rho} \approx 2\epsilon_0 n_m \left(\frac{dn}{d\rho} \right) = 2\epsilon_0 n_m \frac{M}{N_A} \left(\frac{dn}{dc} \right) \quad (5.404)$$

Here M is the mass of a particle, c is the particle mass concentration ($c = \rho M/N_A$ and N_A is the Avogadro number). The quantity (dn/dc) presents the refractive index gradient of the suspension and is measured by refractometer of high sensitivity. Combining Equations 5.401 and 5.404, we can derive the following expression for the Rayleigh ratio of a suspension of independent scatterers:

$$R_j(\theta) \equiv c K M P_j(\theta), \quad K \equiv \frac{4\pi^2 n_0^2}{\lambda_0^4 N_A} \left(\frac{dn}{dc} \right)^2, \quad \text{and} \quad j = v, h, u \quad (5.405)$$

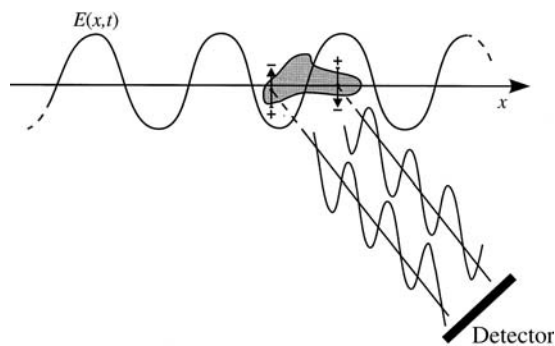


FIGURE 5.71 The Rayleigh–Debye–Gans⁸⁵⁷⁻⁸⁵⁹ theory is based on the assumptions that (1) the incident beam propagates without being affected by the particles, and (2) the scattered light, received by the detector, is a superposition of the beams emitted from the induced dipoles in the different parts of the particle.

which (in principle) allows us to determine the particle mass, M , from the intensity of the scattered light. Equation 5.405 has several important limitations: (1) the particle dimensions must be much smaller compared to the light wavelength, (2) the particle concentration must be very low to avoid interparticle interactions and the interference of light beams scattered by different particles, and (3) the particles do not absorb light (the suspension is colorless).

5.9.1.2 Rayleigh–Debye–Gans Theory

The radiation of a particle, comparable in size to the light wavelength, leads to induction of dipoles in different parts of the particle that are not in phase (Figure 5.71). The net scattered light received by the detector is a result of the interference of the beams scattered from the different points of the particle. In this case, the function $P(\theta)$ depends on the particle size and shape. If the particles have an anisodiametrical shape, $P(\theta)$ could depend on their orientation as well. Typical examples are rodlike particles that are preferentially oriented along a given direction by an electric⁸⁵⁴⁻⁸⁵⁶ or hydrodynamic field. In most systems, however, the particles are randomly oriented, and averaging over all possible orientations is performed to calculate $P(\theta)$.

A rather general approach for determination of the function $P(\theta)$ was proposed by Rayleigh⁸⁵⁷ and further developed by Debye⁸⁵⁸ and Gans.⁸⁵⁹ The main assumption in the Rayleigh–Debye–Gans (RDG) theory is that the incident beam that excites the electrical dipoles in the particle is not influenced (in either magnitude or phase) by the presence of the particle. This requirement is better satisfied by smaller particles with a refractive index close to that of the disperse medium. The respective quantitative criterion reads

$$\frac{4\pi l}{\lambda} |n_p - n_m| \ll 1 \quad (5.406)$$

where l is a length of the order of the size of the particle (l coincides with the radius for spheres). For such “soft” scatterers, the phase difference of the waves created by the induced dipoles in different parts of the particle (considered to be independent in the RDG theory) can be calculated by geometric consideration.

Because the scattered waves propagating in a forward direction, $\theta = 0^\circ$, are all in phase (positive interference), the intensity of the scattered light is maximal in this direction and $P(0) = 1$. Comparison with Equation 5.405 shows that $R(0) = cKM$; hence, we can define

$$P_j(\theta) \equiv R_j(\theta)/R(0), \quad j = v, h, u \quad (5.407)$$

The general expression for the scattering form factor of randomly oriented particles and vertically polarized light reads⁸⁵⁸

$$P_v(\theta) = \frac{1}{N^2} \sum_{i=1}^N \sum_{j=1}^N \frac{\sin(q r_{ij})}{q r_{ij}} \quad (5.408)$$

where $q = (4\pi n/\lambda_0)\sin(\theta/2)$ is the magnitude of the scattering vector, and r_{ij} is the distance between the i th and j th scattering subunit. The double sum is taken over all subunits of total number N . The particle scattering factor was calculated for typical particle shapes (Table 5.9; see table 8.5 in Reference 848).

Once $P_v(\theta)$ is known, we can calculate $P_h(\theta)$ and $P_u(\theta)$ through the relationships (see Equation 5.402):

$$P_h(\theta) = P_v(\theta)\cos^2\theta, \quad P_u(\theta) = \frac{1}{2}P_v(\theta)(1 + \cos^2\theta) \quad (5.409)$$

The expansion in series of $\sin(qr_{ij})$ in the right-hand side of Equation 5.408 leads to a fairly simple and general result:⁸⁶⁰

$$\lim_{\theta \rightarrow 0} P_v(\theta) \approx 1 - \left[\frac{q^2}{3!N^2} \right] \sum_{i=1}^N \sum_{j=1}^N r_{ij}^2 = 1 - \frac{q^2 \langle R_g^2 \rangle}{3} \quad (5.410)$$

where $\langle R_g^2 \rangle^{1/2}$ is the radius of gyration for a particle that is arbitrary in shape and size. This result shows that the initial part of the function $P(\theta)$, corresponding to small scattering angles, enables one to determine the radius of gyration, no matter what the particle shape. For that purpose, the experimentally measured intensity of the scattered light is represented in the form (see Equation 5.405):

$$\frac{Kc}{R_v(\theta)} = [MP_v(\theta)]^{-1} = \frac{1}{M} \left[1 + \frac{16}{3} \frac{\pi^2}{\lambda^2} \langle R_g^2 \rangle \sin^2(\theta/2) + O(q^4) \right] \quad (5.411)$$

and $Kc/R_v(\theta)$ is plotted vs. $\sin^2(\theta/2)$. For a nonpolarized or horizontally polarized primary beam, $R_v(\theta)$, in the left-hand side of Equation 5.411 is to be replaced by $2R_u(\theta)/(1 + \cos^2\theta)$ or $R_h(\theta)/\cos^2\theta$, respectively.

The radii of gyration for a sphere of radius R_s , for a thin rodlike particle of length L , for a Gaussian coil containing N segments of length l , and for a thin disk of radius R_d are given by^{847,849,861}

$$\langle R_g^2 \rangle = \frac{3}{5} R_s^2 \quad (\text{sphere}) \quad (5.412a)$$

$$\langle R_g^2 \rangle = \frac{1}{12} L^2 \quad (\text{rodlike particle}) \quad (5.412b)$$

$$\langle R_g^2 \rangle = \frac{1}{6} N l^2 \quad (\text{Gaussian coil}) \quad (5.412c)$$

$$\langle R_g^2 \rangle = \frac{1}{2} R_d^2 \quad (\text{thin disk}) \quad (5.412d)$$

TABLE 5.9

Scattering Function, $P_v(q)$, Single Particle Translational Diffusion Coefficient, D_0 , and Single Particle Rotational Diffusion Coefficient, Θ , for Particles of Different Shape

Shape of the Particle	$P_v(q), D_0, \Theta$	Ref.
1. Homogeneous sphere of radius R	$P_v(q) = \left[\frac{3}{\tilde{R}^3} (\sin \tilde{R} - \tilde{R} \cos \tilde{R}) \right]$ $D_0 = \frac{kT}{6\pi\eta R}; \quad \Theta = \frac{kT}{8\pi\eta R^3}$	857
2. Ellipsoid with semiaxes (R, R, pR)	$P_v(q) = \int_0^{\frac{\pi}{2}} \left[\frac{3}{\tilde{R}^3} (\sin \tilde{R} - \tilde{R} \cos \tilde{R}) \right]^2 \left(\tilde{R} \sqrt{\cos^2 \theta + p^2 \sin^2 \theta} \right) \cos \theta d\theta$ $D_0 = \frac{kT}{6\pi\eta R} \left[\frac{3}{4} p\beta + \frac{1}{8} p\alpha_{\parallel} + \frac{1}{4} \frac{\alpha_{\perp}}{p} \right]$ $\Theta = \frac{3kT}{16\pi p R^3 \eta} \frac{(p^2 \alpha_{\parallel} + \alpha_{\perp})}{(p^2 + 1)}$ $\alpha_{\parallel} = \frac{2(p^2 \beta - 1)}{p^2 - 1}; \quad \alpha_{\perp} = \frac{p^2(1 - \beta)}{p^2 - 1}$ $\beta = \frac{\cosh^{-1} p}{p(p^2 - 1)^{1/2}} \quad \text{for } p > 1 \text{ (prolate ellipsoid)}$ $\beta = \frac{\cos^{-1} p}{p(1 - p^2)^{1/2}} \quad \text{for } p < 1 \text{ (oblate ellipsoid)}$	860, 862 863, see also 864
3. Thin rodlike particle of length L and diameter d	$P_v(q) = \frac{2}{qL} \int_0^{qL} \frac{\sin u}{u} du - \left[\frac{2 \sin(qL/2)}{qL} \right]^2$ $D_0 = \frac{kT}{3\pi\eta L} \ln(L/d)$ $\Theta = \frac{3kT}{\pi\eta L^3} [\ln(2L/d) - 0.5]$	865, see also 866, 867 863, see also 864, 868, 869
4. Thin disk of radius R	$P_v(q) = \frac{2}{\tilde{R}^2} \left[1 - \frac{J_1(2\tilde{R})}{\tilde{R}} \right]$ $D_0 = \frac{kT}{12\eta R}; \quad \Theta = \frac{3kT}{32\eta R^3}$	870, 871 863
5. Gaussian coil of contour length L and persistent length, l_p . If the coil is considered to contain N segments of length l , then $L = Nl$ and $l = 2l_p$	$P_v(q) = \frac{2}{z^2} [\exp(-z) + z - 1]; \quad z = q^2 \langle R_g^2 \rangle$ $\langle R_g^2 \rangle = \frac{1}{3} Ll_p = \frac{1}{6} Nl^2$ $D = \frac{kT}{3\pi\eta L} \left[1.303 (L/l_p)^{1/2} \right]$ $\Theta = \frac{kT}{1.013\eta L^3} (L/l_p)^{3/2}$	872 873

Note: $\tilde{R} \equiv qR$, where $q = 4\pi n \lambda_0^{-1} \sin(\theta/2)$ is the magnitude of the scattering vector; η is shear viscosity of the medium and kT is thermal energy; $J_1(x)$ is the Bessel function of the first kind.

The radius of gyration for a wormlike chain of length L , persistent length l_p , and diameter d was found to be⁸⁶¹

$$\langle R_g^2 \rangle = L^2 \left\{ \frac{1}{3} \tilde{l}_p - \tilde{l}_p^2 + 2 \tilde{l}_p^4 \left[\tilde{l}_p^{-1} - 1 + \exp\left(-\frac{1}{\tilde{l}_p}\right) \right] \right\} + \frac{d^2}{8} \quad (\text{wormlike chain}) \quad (5.413)$$

where $\tilde{l}_p = l_p / L$. For a random coil ($\tilde{l}_p \ll 1$, $l_p = l/2$, $L = Nl$, and $d \ll L$), Equation 5.413 reduces to Equation 5.412c. In the other limiting case of $\tilde{l}_p \gg 1$, Equation 5.413 reduces to the result for a cylinder of length L and diameter d :

$$\langle R_g^2 \rangle = \frac{1}{12} L^2 + \frac{1}{8} d^2 \quad (\text{cylinder}) \quad (5.414)$$

This consideration can be further generalized to account for the interaction between the particles (see Section 5.9.1.4, below).

5.9.1.3 Theory of Mie

If the condition in Equation 5.406 is violated, the RDG theory is not valid. A solution of the scattering problem for particles arbitrary in size has been found only for several particular shapes. Mie⁸⁷⁴ succeeded in finding a complete general solution of the Maxwell equations for a sphere in a periodic electromagnetic field. The refractive indices of the sphere, n_p , and of the medium, n_m , are considered to be complex numbers (i.e., the theory is applicable to light-absorbing substances, including metals):

$$n_j^2(\omega) = \epsilon_j(\omega) - i \frac{4\pi\chi_j(\omega)}{\omega} \quad \text{or} \quad n_j(\omega) = \tilde{n}_j(\omega) - ik_j(\omega); \quad j = p \text{ or } m \quad (5.415)$$

Here, $\epsilon_j(\omega)$ and $\chi_j(\omega)$ are the dielectric permittivity and the electrical conductivity, respectively, for a given circular frequency, ω , of the field, while \tilde{n}_j and k_j are the real and the imaginary parts, respectively, of the refractive index.

As shown by Mie⁸⁷⁴ and Debye,⁸⁷⁵ the electromagnetic field of the light scattered by a sphere can be presented as an infinite series over associated Legendre polynomials, $P_n^l(\cos\theta)$, multiplied by spherical Bessel functions, $h_n^{(2)}(2\pi r/\lambda)$. The coefficients in this series must be determined from the boundary conditions and afterward can be used to calculate the angular dependence of the amplitude and polarization of the scattered field. Different boundary conditions were imposed in the case of conducting or dielectric materials of the sphere and of the medium.

The numerical calculation of the complete problem presents a formidable task, and a number of practical recommendations for appropriate simplifications are given in the specialized literature.⁸⁴⁷⁻⁸⁴⁹ Typically, the final result of such calculations is presented in terms of the efficiency factors for absorption and scattering, Q_{abs} and Q_{sca} . The magnitudes of Q_{abs} and Q_{sca} depend on λ , \tilde{n} , k , θ , and the particle size. For nonabsorbing particles ($k_p = 0$), $Q_{\text{abs}} = 0$; for nonscattering particles ($\tilde{n}_p = \tilde{n}_m$), $Q_{\text{sca}} = 0$. The efficiency factors can be directly related to the absorbance and turbidity of the suspension (see Section 5.9.1.7). A similar approach was used to investigate the scattering from coated spheres; long circular, elliptic, and parabolic cylinders; flat disks; spheroids; and others (see References 847, 848, and 876).

The theory of Mie⁸⁷⁴ is used also in the laser diffraction method for particle size analysis.⁸⁷⁷ In this method, the light scattered by the particles is collected over a range of angles (usually between 1° and 20°) in the forward direction. The corresponding experimental setup is usually

referred to as Fourier optics. The method is applied to relatively large particles (typically between 0.3 and 600 μm) when the scattered light in a forward direction (projected on a screen) presents a combination of concentric fringes. The angular intensity distribution of the scattered light is analyzed to deduce the particle size distribution. For particles of diameter above several micrometers, the diffraction pattern is usually interpreted by simpler approximate theories, like that of the Fraunhofer diffraction.⁸⁷⁷

5.9.1.4 Interacting Particles

5.9.1.4.1 Fluctuation Theory of Static Light Scattering

All previous discussion has been based on the assumption that the scatterers are independent; however, in most cases this assumption is not justified. A general approach for calculating $R(\theta)$ for a suspension of small interacting particles was proposed by Einstein.⁸⁷⁸ He related the fluctuations in the polarizability of suspension with the fluctuations of the particle concentration. The final result reads

$$R_j(\theta) = \frac{4\pi^2 n_m^2 \left(\frac{dn}{dc}\right)^2}{\lambda_0^4 N_A} c P_j(\theta) \left[\frac{\partial(\Pi / N_A kT)}{\partial c} \right]^{-1} \quad j = v, u, h \quad (5.416)$$

where $\Pi(c)$ is the osmotic pressure of the suspension. For a low particle concentration, the osmotic pressure is expanded in series with respect to the particle concentration:

$$\frac{\Pi}{N_A kT} = A_1 c + A_2 c^2 + A_3 c^3 + \dots \quad j = v, u, h \quad (5.417)$$

where A_j are virial coefficients ($A_1 = 1/M$). Then, the relationship between c and $R(\theta)$ can be rewritten in the form:⁸⁷⁹

$$\frac{Kc}{R_j(\theta)} P_j(\theta) = \frac{1}{M} + 2A_2 c + \dots \quad j = v, u, h \quad (5.418)$$

where $P_j(\theta)$ is given by Equation 5.402, depending on the polarization of the incident light. As seen from this expression, the particle mass can be determined by measuring $R(\theta)$ at several concentrations and extrapolating the result toward $c = 0$. The intercept of the obtained straight line (at small concentrations) is equal to $1/M$, while the slope provides the second osmotic virial coefficient, A_2 , which is a measure of the interparticle interactions.

The system of large interacting particles requires a modification of the Einstein approach, because we should account for correlations in the position of the scattering subunits within a given particle, along with correlations in the positions of different particles. If the condition in Equation 5.406 is satisfied, we can decompose these correlations into two different terms to obtain⁸⁸⁰

$$R_j(\theta) = K_1 \rho P_j(\theta) S(\rho, q); \quad K_1 = \frac{4\pi^2 n_m^2 \left(\frac{dn}{d\rho}\right)^2}{\lambda_0^4 N_A} \quad j = v, u, h \quad (5.419)$$

where the particle form factor $P_j(\theta)$ is the same as for noninteracting particles, while the structure factor $S(\rho, q)$, accounts for the interactions. By definition, the static structure factor is

$$S(\rho, q) = 1 + \rho \int_0^{\infty} 4\pi r^2 [g(r) - 1] \frac{\sin qr}{qr} dr \quad (5.420)$$

where $g(r)$ is the pair radial distribution function.

For small particles, $g(r)$ is substantially different from unity only at interparticle distances $r \ll q^{-1}$. Then, the structure factor is equal to the inverse osmotic compressibility of the suspension:⁸⁸⁰

$$S(\rho, q) \approx 1 + \rho \int_0^{\infty} 4\pi r^2 [g(r) - 1] \equiv \left[\frac{\partial(\Pi/kT)}{\partial \rho} \right]_T^{-1} \quad (5.421)$$

and Equation 5.419 reduces to the Einstein expression, Equation 5.416, with ρ (instead of c) used as a measure of the particle concentration — note that Equation 5.416 does not depend on the particular choice of the concentration definition.

5.9.1.4.2 Zimm-Plot (Method of Double Extrapolation)

The substitution of Equation 5.410 in Equation 5.418 suggests a graphical procedure for interpretation of light scattering data from suspensions of large interacting particles of arbitrary shape. Keeping the leading terms we obtain:

$$\frac{Kc}{R_v(\theta)} = \frac{1}{M} \left[1 + \frac{16}{3} \left(\frac{\pi n}{\lambda_0} \right)^2 \sin^2(\theta/2) \langle R_g^2 \rangle \right] + 2A_2 c + \dots \quad (5.422)$$

Based on this formula, Zimm⁸⁸¹ suggested plotting $Kc/R_v(\theta)$ against $[\sin^2(\theta/2) + bc]$, where b is an arbitrary constant usually chosen to satisfy the condition $bc_{\max} \sim 1$. This method requires measurements at different concentrations and scattering angles. The data are presented as a grid of points (Figure 5.72), which allows extrapolation (1) to zero angle for each used concentration, and (2) to zero concentration for each scattering angle. Finally, the extrapolated points for zero concentration (at different angles) are extrapolated to zero angle, and the points for zero angle (at different concentrations) are extrapolated to zero concentration. In the ideal case, the two extrapolated curves must cut the ordinate $Kc/R_v(\theta)$ at the same point, which is the inverse mass of the particle. Respectively, the initial slope of the curve $c = 0$ provides the square radius of gyration, $\langle R_g^2 \rangle$, while the initial slope of the curve $\theta = 0$ gives the second osmotic virial coefficient, A_2 .

For nonpolarized or horizontally polarized incident beams, $R_v(\theta)$ in Equation 5.422 is to be replaced by $2R_u(\theta)/(1 + \cos^2\theta)$ or $R_h(\theta)/\cos^2\theta$, respectively.

5.9.1.4.3 Interpretation of the Second Osmotic Virial Coefficient

Generally speaking, positive values of A_2 mean net repulsion between the particles, while negative values of A_2 correspond to attraction. For more detailed analysis of the values of the second osmotic virial coefficient, the use of other definitions of the particle concentration is more convenient. The common virial expansion¹¹

$$\frac{\Pi}{kT} = \rho + \frac{1}{2}\beta_2\rho^2 + \dots \quad (5.423)$$

defines another second virial coefficient, β_2 , which has the dimensions of volume and is widely used in statistical thermodynamics. The coefficients, A_2 and β_2 , are interconnected through the relationship:

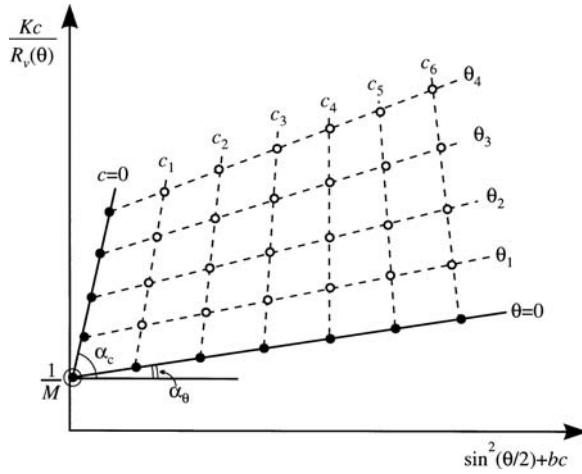


FIGURE 5.72 Schematic presentation of the Zimm plot⁸⁸¹ (method of double extrapolation). The data from measurements at several concentrations (c_1 to c_6) and scattering angles (θ_1 to θ_4) are presented by empty circles. Then, extrapolation to $c = 0$ for each angle and to $\theta = 0$ for each concentration is numerically performed (see the black dots). Both lines, $c = 0$ and $\theta = 0$, should meet the ordinate at the point M^{-1} , where M is the particle mass. The slope angle of the line $c = 0$ is equal to $\alpha_c = \tan^{-1} \left[\frac{(4\pi n / \lambda_0)^2 \langle R_g^2 \rangle}{3M} \right]$, while the slope angle of the line $\theta = 0$ is equal to $\alpha_\theta = \tan^{-1} (2A_2)$.

$$\beta_2 = 2 \frac{M^2}{N_A} A_2 \quad (5.424)$$

For the central interaction between the particles, we can rigorously show that^{11,880}

$$\beta_2 = \int_0^\infty [1 - g(r)] 4\pi r^2 dr = \int_0^\infty \left[1 - \exp\left(-\frac{W(r)}{kT}\right) \right] 4\pi r^2 dr \quad (5.425)$$

where r is the distance between the centers of mass of the particles, and $W(r)$ is the pair interaction energy. More general expressions for β_2 in the case of anisodiametrical particles are also available.^{11,880} The usage of β_2 is convenient when the experimental results about the particle interactions must be compared to theoretical calculations. For hard spheres, β_2 is equal to $8V_p$, where V_p is the particle volume. This fact was used by some authors to define so-called effective volume of the particle through the measured second virial coefficient:^{314,324}

$$V_{\text{EFF}} = \frac{1}{8} \beta_2 = \frac{1}{4} \frac{A_2 M^2}{N_A}; \quad A_2, \beta_2 > 0 \quad (5.426)$$

Note that V_{EFF} could be substantially different from the actual particle volume, V_p , if long-range interactions between the particles are present. The counterpart of Equation 5.422 in terms of ρ and β_2 reads

$$\frac{K_1 \rho}{R_v(\theta)} = \left[1 + \frac{16}{3} \left(\frac{\pi n}{\lambda_0} \right)^2 \sin^2(\theta/2) \langle R_g^2 \rangle \right] + \beta_2 \rho + \dots; \quad K_1 = \frac{4\pi^2 n_m^2}{\lambda_0^4} \left(\frac{dn}{d\rho} \right)^2 \quad (5.427)$$

In the case of microemulsions and suspensions of spherical particles, it is usually more convenient to use the volume fraction, ϕ , of the dispersed particles as a measure of their concentration.⁸⁸²⁻⁸⁸⁷ By using the fact that $\phi = \rho V_p$, we can obtain the virial expansion:

$$\frac{\Pi}{kT} = B_1 \phi + B_2 \phi^2 + \dots; \quad B_1 = \frac{1}{V_p} \quad \text{and} \quad B_2 = \frac{\beta_2}{2 V_p^2} \quad (5.428)$$

The light scattering data can be interpreted by using the equation:

$$\frac{K_2 \phi}{R_v(\theta)} = \frac{1}{V_p} \left[1 + \frac{16}{3} \left(\frac{\pi n}{\lambda_0} \right)^2 \sin^2(\theta/2) \langle R_g^2 \rangle \right] + 2 B_2 V_p \phi; \quad K_2 = \frac{4 \pi^2 n_m^2}{\lambda_0^4} \left(\frac{dn}{d\phi} \right)^2 \quad (5.429)$$

Therefore, the double extrapolation procedure in these variables provides the real volume of the particles, V_p . The quantity $2B_2V_p$ is dimensionless and often denoted in the literature as λ_v (see Section 5.9.2.4, below). For hard spheres, $\lambda_v = 8$.

5.9.1.5 Depolarization of Scattered Light

The polarization of the incident beam is denoted by subscripts v , h , or u for vertically polarized, horizontally polarized, or nonpolarized light, respectively. Generally, the Rayleigh constant can be considered to consist of two components, R^V and R^H , corresponding to the vertical and horizontal directions of the electrical field of the scattered light (Figure 5.70). Therefore, we can define six quantities: R_v^V , R_h^V , R_u^V , R_v^H , R_h^H , and R_u^H , the values of which provide information about the size, shape, and anisotropy of the scattering particles.⁸⁸⁸⁻⁸⁹⁰ Depending on the polarization of the incident light, it is accepted to define three depolarization coefficients:

$$\begin{aligned} \Delta_v &= \frac{R_v^H}{R_v^V}, \quad \Delta_h = \frac{R_h^H}{R_h^V} \\ \Delta_u &= \frac{R_u^H}{R_u^V} = \frac{R_v^H + R_h^H}{R_v^V + R_h^V} = \frac{1 + \Delta_h}{1 + \Delta_v} \end{aligned} \quad (5.430)$$

Usually, Δ_v , Δ_h , and Δ_u refer to a scattering angle $\theta = 90^\circ$ and small concentrations, $c \rightarrow 0$ (the scattering from the solvent is subtracted). The values of Δ_v , Δ_h , and Δ_u can be used to determine the type of the suspended particles (Table 5.10). Note that the inherent particle anisotropy is reflected in the value of Δ_v , while Δ_u contains a contribution from the particle size as well.

We can define the so-called optical anisotropy of the particles

$$\delta^2 = \frac{(\alpha_1 - \alpha_2)^2 + (\alpha_2 - \alpha_3)^2 + (\alpha_3 - \alpha_1)^2}{(\alpha_1 + \alpha_2 + \alpha_3)^2} \quad (5.431)$$

where α_1 , α_2 , and α_3 are the polarizabilities of the particle along its three main axes. As shown by Cabannes⁸⁸⁸ for particles arbitrary in size:

$$\delta^2 = \frac{10 \Delta_u}{6 - 7 \Delta_u} \quad (5.432)$$

TABLE 5.10
Depolarization Coefficients of Different
Types of Particles^{888,889}

Particles	Δ_v	Δ_h	Δ_u
Small, isotropic	0	Not defined	0
Small, anisotropic	$(0 \div 1)$	1	$(0 \div 1)$
Large, isotropic	0	∞	$(0 \div 1)$
Large, anisotropic	$(0 \div 1)$	1	$(0 \div 1)$

In the particular case of small particles and $\theta = 90^\circ$, we have:

$$P_v(90^\circ) = \frac{3+3\Delta_v}{3-4\Delta_v}; \quad R_v(90^\circ) = c K M \frac{3+3\Delta_v}{3-4\Delta_v} \quad (5.433a)$$

$$P_u(90^\circ) = \frac{6+6\Delta_u}{6-7\Delta_u}; \quad R_u(90^\circ) = \frac{1}{2} c K M \frac{6+6\Delta_u}{6-7\Delta_u} \quad (5.433b)$$

Comparison of Equations 5.402, 5.405, and 5.433b shows that in the case of small anisotropic particles, we have an additional multiplier

$$\left(\frac{6+6\Delta_u}{6-7\Delta_u} \right)$$

called the *Cabannes' factor*. Therefore, the correct determination of the particle mass in such systems requires measurements of both $R(90^\circ)$ and $\Delta(90^\circ)$.

5.9.1.6 Polydisperse Samples

The light scattering methods provide statistically averaged quantities when applied to polydisperse samples (e.g., micellar or polymer solutions). The case of independent scatterers can be rigorously treated^{862,881} by using the mass distribution function of the particles, $f(M)$. By definition, $dm = f(M)dM$ is the mass of particles in the range between M and $(M + dM)$, scaled by the total particle mass. As shown by Zimm,⁸⁸¹ the scattering law in such a system can be presented similarly to the case of monodisperse particles (see Equation 5.405):

$$\left[\frac{Kc}{R_j(\theta)} \right]^{-1} = \int_0^\infty f(M) M P_j(\theta, M) dM = \langle M \rangle_m \langle P_j(\theta) \rangle_m \quad j = u, v, h \quad (5.434)$$

where c is the total particle concentration, while the averaged molecular mass, $\langle M \rangle_m$, and form factor, $\langle P(\theta) \rangle_m$, are defined as

$$\langle M \rangle_m = \int_0^\infty M f(M) dM, \quad \langle P_j(\theta) \rangle_m = \frac{1}{\langle M \rangle_m} \int_0^\infty f(M) M P_j(\theta, M) dM \quad (5.435)$$

For small scattering angles, $P_v(\theta, M) \rightarrow 1 - 1/3 q^2 \langle R_g^2(M) \rangle$, where $\langle R_g^2(M) \rangle$ is the squared radius of gyration of particles having mass M . Substituting this expression in Equation 5.434, we obtain⁸⁸¹

$$\left[\frac{Kc}{R_v(\theta)} \right]_{\theta \rightarrow 0}^{-1} = \langle M \rangle_m \left(1 - \frac{1}{3} q^2 \int_0^{\infty} f(M) \langle R_g^2(M) \rangle M dM \right) \quad (5.436)$$

This expression can be used as a starting point for analysis of the scattered light intensity by polydisperse samples. If the shape of the particles is known (that is, $\langle R_g^2(M) \rangle$ is a known function; see Equation 5.412), we can determine two parameters characterizing the distribution $f(M)$ (e.g., its mean value and standard deviation) from the experimentally measured intercept and slope of the line, $[cK/R_v(\theta)]^{-1}$ vs. q^2 . For small particles, $P(\theta \rightarrow 0, M) \approx 1$ and

$$\left[\frac{Kc}{R(\theta)} \right] \approx 1/\langle M \rangle_m \quad (5.437)$$

Therefore, in this case, we can determine the mass averaged particle mass (Equation 5.435).

5.9.1.7 Turbidimetry

Instead of measuring the intensity of the scattered light at a given angle, θ , we can measure the extinction of the incident beam propagating through the suspension.^{853,879} The method is called *turbidimetry* and was widely used in the past, because the necessary equipment was essentially the same as that for measuring the absorption of light by colored solutions. Usually, nonpolarized light is used in these experiments; hence, the following consideration corresponds to nonpolarized incident beams.

The turbidity, τ [m^{-1}], of a suspension is defined through a counterpart of the Beer–Lambert equation:^{848,849}

$$I(x) = I_0 \exp(-\tau x) \quad (5.438)$$

On the other hand, the turbidity can be calculated by integrating the scattered light in all directions and dividing by the intensity of the incident beam:

$$\tau = \int_{\theta=0}^{\pi} \int_{\varphi=0}^{2\pi} \frac{\langle I_s(\theta) \rangle_t}{\langle I_0 \rangle_t} r^2 \sin \theta d\theta d\varphi = 2\pi \int_0^{\pi} R_u(\theta) \sin \theta d\theta \quad (5.439)$$

For suspension of noninteracting scatterers, it is convenient to introduce so-called dissipation factor, Q :

$$Q = \frac{3}{8} \int_0^{\pi} P_v(\theta) (1 + \cos^2 \theta) \sin \theta d\theta \quad (5.440)$$

Also, for noninteracting particles, we have (see Equations 5.402 and 5.407):

$$R_u(\theta) \equiv R_u(0) P_u(\theta) = R_u(0) P_v(\theta) \left(\frac{1 + \cos^2 \theta}{2} \right) \quad (5.441)$$

Therefore, τ can be expressed as

$$\tau = \frac{8\pi}{3} Q R_u(0) = \frac{16\pi}{3} Q \frac{R_u(90^\circ)}{P_v(90^\circ)} = \frac{8\pi}{3} Q c K M \quad (5.442)$$

Note that for small particles $P_v(\theta) = 1$, $Q = 1$, and $\tau = (8\pi/3)cKM$. This simpler case can be generalized to suspensions of interacting particles and the final result reads⁸⁷⁹

$$\tau = \frac{\frac{8}{3}\pi K c}{\frac{1}{M} + 2A_2 c} \quad (5.443)$$

Therefore, for small particles, Kc/τ is a linear function of c in the low concentration range, and the intercept and slope of the straight line allow us to calculate M and A_2 , respectively.

The above consideration was for particles not absorbing light. If particles do absorb light, we must use the Mie theory (Section 5.9.1.3). Equation 5.438 is modified to read⁸⁴⁷⁻⁸⁴⁹

$$I(x) = I_0 \exp[-(\xi + \tau)x] \quad (5.444)$$

and the absorbance, ξ , and the turbidity, τ , of a suspension containing spherical particles of radius R are determined from:

$$\xi = \pi R^2 \rho Q_{\text{abs}} \quad \text{and} \quad \tau = \pi R^2 \rho Q_{\text{sca}} \quad (5.445)$$

where Q_{abs} and Q_{sca} must be numerically calculated as mentioned in Section 5.9.1.3.

5.9.2 DYNAMIC LIGHT SCATTERING

We represent here only the basic methods and equations used for dynamic light scattering (DLS) data analysis. Detailed description of the subject can be found in the available monographs.⁸⁹¹⁻⁸⁹⁷

5.9.2.1 DLS by Monodisperse, Noninteracting Spherical Particles

In the DLS methods, the time fluctuations of the intensity of the scattered light, $I_s(t)$, are analyzed. These fluctuations are caused by the translational and rotational Brownian motion of the particles, which leads to perpetual variation of the particle configuration with the resulting change in the interference pattern of the scattered light. The time course of the detector signal, which is proportional to $I_s(t)$, can be analyzed by two different devices.

5.9.2.1.1 Spectrum Analyzer

This equipment is used when the intensity of the scattered light is high and an analog output from the photomultiplier tube (the detector) is available. The power spectrum, $P(q, \omega)$, of the output signal is extracted. For example, in the case of translational diffusion of monodisperse spherical particles:

$$P^{(2)}(q, \omega) = \frac{2 q^2 D / \pi}{\omega^2 + (2 q^2 D)^2} + \delta(\omega) \quad (5.446)$$

where D is the translational diffusion coefficient of the particles and $\delta(x)$ is the Dirac-delta function. According to Equation 5.446, the power spectrum is Lorentzian, centered at $\omega = 0$ with a half-width equal to $2q^2D$. From the value of D , we can calculate the hydrodynamic radius of the particle, R_h , by means of the Stokes–Einstein formula:

$$R_h = \frac{kT}{6\pi\eta D} \quad (5.447)$$

where η is the shear viscosity of the disperse medium.

5.9.2.1.2 Correlator

This type of instrument is aimed at calculating the autocorrelation function of the intensity of the scattered light, defined as

$$g^{(2)}(q, \tau) \equiv \frac{1}{\langle I_s \rangle_t^2} \lim_{T \rightarrow \infty} \frac{1}{2T} \int_{-T}^T I_s(t) I_s(t + \tau) dt = \langle I_s(t) I_s(t + \tau) \rangle_t / \langle I_s \rangle_t^2 \quad (5.448)$$

An important advantage of the correlators is that they are capable of working even with very low intensities of the scattered light, when each photon is separately counted by the detector. From a theoretical viewpoint, $P^{(2)}(q, \omega)$ and $g^{(2)}(q, \tau)$ provide essentially the same information, because for a stationary random process (as in the case with diffusion) these two quantities are Fourier transforms of each other (Wiener–Khinchine theorem):⁸⁸⁰

$$g^{(2)}(q, \tau) = \int_{-\infty}^{+\infty} P^{(2)}(\omega) \cos(\omega \tau) d\omega \quad (5.449a)$$

$$P^{(2)}(q, \omega) = \frac{1}{2\pi} \int_{-\infty}^{+\infty} g^{(2)}(\tau) \cos(\omega \tau) d\tau \quad (5.449b)$$

Therefore, $g^{(2)}(q, \tau)$ can be calculated if $P^{(2)}(q, \omega)$ is experimentally determined, and vice versa. In the particular case of translational diffusion of monodisperse spherical particles (see Equation 5.446),

$$g^{(2)}(q, \tau) = \int_{-\infty}^{+\infty} \left[\delta(\omega) + \frac{2q^2 D/\pi}{\omega^2 + (2q^2 D)^2} \right] \cos(\omega \tau) d\omega = 1 + \exp(-2q^2 D \tau) \quad (5.450)$$

In reality, the experiment provides the function:

$$G^{(2)}(q, \tau) = 1 + F \exp(-2q^2 D \tau) \quad (5.451)$$

where the factor F accounts for the spatial coherence of the scattering volume and depends on the aperture of the detector. If the detector radius is $\sim \lambda r/b$ (r is the distance between the scattering volume and the detector, b is the radius of the scattering volume, and $\lambda^2 r^2 / \pi b^2$ is the coherence area),⁸⁹⁸ F is close to unity. For a larger radius of the detector, F would be orders of magnitude smaller, and the signal/noise ratio will be also small.

Equations 5.446 and 5.450 are applicable in the so-called homodyne method (or self-beating method), where only scattered light is received by the detector.⁸⁹¹⁻⁸⁹⁶ In some cases, it is also desirable to capture by the detector a part of the incident beam that has not undergone the scattering process. This method is called *heterodyne* (or method of the local oscillator) and sometimes provides information that is not accessible by the homodyne method.⁸⁹² It can be shown that if the intensity of the scattered beam is much lower than that of the detected nonscattered (incident) beam, the detector measures the autocorrelation function of the electrical field of the scattered light, defined as

$$g^{(1)}(q, \tau) \equiv \langle E_s^*(t) E_s(t + \tau) \rangle / \langle I_s \rangle_t \quad (5.452)$$

where $E_s(t)$ is the intensity of the electrical field of the light and the asterisk indicates complex conjugation. The counterparts of Equations 5.446 and 5.450 in the heterodyne method read

$$P^{(1)}(q, \omega) = \frac{q^2 D / \pi}{\omega^2 + (q^2 D)^2} \quad (5.453a)$$

$$g^{(1)}(q, \tau) = \exp(-q^2 D \tau) \quad (5.453b)$$

In this case, the Wiener–Khinchine theorem, Equation 5.449, is also valid if $g^{(2)}(q, \tau)$ is replaced by $g^{(1)}(q, \tau)$ and $P^{(2)}(q, \omega)$ by $P^{(1)}(q, \omega)$. In addition, for the diffusion process, $g^{(1)}(q, \tau)$ and $g^{(2)}(q, \tau)$ are interrelated by the Siegert equation:

$$g^{(2)}(q, \tau) = 1 + |g^{(1)}(q, \tau)|^2 \quad (5.454)$$

If charged particles are placed in an external, constant electrical field (e.g., in electrophoretic equipment), they acquire a drift velocity, \mathbf{V}_{EL} , which is superimposed upon the diffusion. The respective power spectrum in the heterodyne method is⁸⁹⁹

$$P^{(1)}(q, \omega) = \frac{1}{2} \left[\frac{q^2 D / \pi}{(\omega + \mathbf{q} \cdot \mathbf{V}_{EL})^2 + (q^2 D)^2} + \frac{q^2 D / \pi}{(\omega - \mathbf{q} \cdot \mathbf{V}_{EL})^2 + (q^2 D)^2} \right] \quad (5.455a)$$

where \mathbf{q} is the scattering vector equal to the difference between the scattered and incident wavevectors

$$\left(|\mathbf{q}| = \frac{4\pi n}{\lambda_0} \sin(\theta/2) \right)$$

Therefore, the power spectrum is a sum of two Lorentzians which are shifted in frequency, but their half-width remains determined by the translational diffusion coefficient. The autocorrelation function in this case is

$$g^{(1)}(q, \tau) = \exp(-q^2 D \tau) \cos[\mathbf{q} \cdot \mathbf{V}_{EL} \tau] \quad (5.455b)$$

Equations 5.455a and 5.455b show that, in principle, from one experiment we can simultaneously determine D and V_{EL} . In practice, a series of experiments at different intensities of the

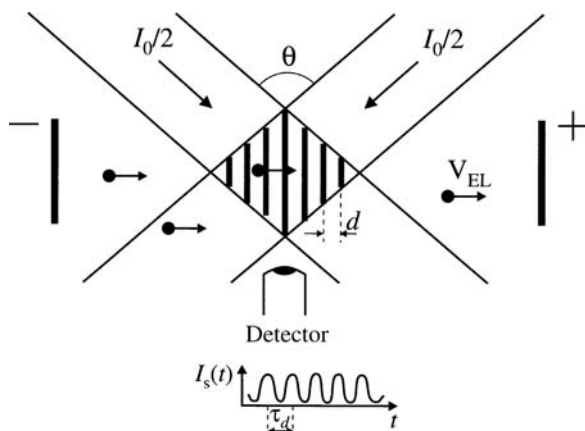


FIGURE 5.73 The method of crossed beams for measurement of particle drift velocity, V_{EL} . The incident laser beam of intensity I_0 is split into two coherent beams by using an optical prism (not shown in the figure). Then, the two beams meet each other in the scattering volume and form an interference pattern. The distance between the bright planes of this pattern is $d = \lambda_0/[2n \sin(\theta/2)]$. The particles, moving under the action of applied electrical potential, give rise to pulses of scattered light when passing through the bright planes. The time interval, τ_d , between two consecutive pulses, created by a given particle, is $\tau_d = d/V_{EL}$. Since d is known and τ_d is measured from the autocorrelation function of the scattered light, we can calculate the drift velocity, V_{EL} .

external field, E , are performed, and the linear function V_{EL} vs. E is plotted. The slope of the resulting line gives the electrophoretic mobility, $\mu \equiv V_{EL}/E$. In a similar way the velocity of aerodynamic fluxes can be studied by using tracer particles (laser doppler anemometry).⁹⁰⁰

The scattering geometry used in most of the commercial equipment for measuring the electrophoretic mobility of particles⁹⁰¹ is shown schematically in Figure 5.73. The incident laser beam is split into two parts of equal intensity, which are afterward crossed in the scattering volume. At the crossing point a pattern of consecutive dark and bright interference planes is formed, due to the mutual coherence of the beams. Therefore, when the particle (driven by the external electrical field) crosses the bright planes, it scatters light which is received by the detector as a sequence of pulses. The time interval between the two pulses of light scattered by one and the same particle, depends on the distance between the interference planes (determined by the geometry of the crossing beams) and on the particle velocity. The corresponding autocorrelation function of the intensity of the scattered light is a damped cosine function, the period of which allows calculation of the particle drift velocity and electrophoretic mobility. A modification⁹⁰¹ of the equipment allows measurement of relatively low mobilities with high precision, which is particularly important for nonaqueous dispersions.

5.9.2.2 DLS by Polydisperse, Noninteracting Spherical Particles

For polydisperse samples of noninteracting particles, the autocorrelation function (or the power spectrum) presents a superposition of the respective functions of the individual species, weighted by the intensities of light scattered by them. Several procedures have been employed to analyze the signal from polydisperse samples. The most straightforward procedure⁹⁰² is the method of cumulants, in which the log of the measured correlation function is expanded in series:

$$\ln [g^{(1)}(q, \tau)] = \sum_{n=1}^{\infty} K_n(q) \frac{(-\tau)^n}{n!} \quad (5.456)$$

The first cumulant

$$K_1(q) = \lim_{\tau \rightarrow 0} \frac{d \ln g^{(i)}(q, \tau)}{d \tau}$$

defines an effective diffusion coefficient:

$$D_{\text{EFF}} = \frac{K_1(q)}{q^2} \quad (5.457)$$

For noninteracting particles, D_{EFF} presents the so-called z -average diffusion coefficient, $\langle D \rangle_z$:

$$D_{\text{EFF}} = \langle D \rangle_z \equiv \frac{\int_0^{\infty} f(M) M P(q, M) D(M) dM}{\int_0^{\infty} f(M) M P(q, M) dM} \quad (5.458)$$

The second cumulant

$$K_2(q) = \lim_{\tau \rightarrow 0} \frac{d^2 \ln g^{(i)}(q, \tau)}{d \tau^2}$$

provides information about the polydispersity of the sample:

$$\frac{K_2(q)}{q^4} = \langle D^2 \rangle_z - \langle D \rangle_z^2 \quad (5.459)$$

The higher-order cumulants, K_3 and K_4 , are measures of the distribution asymmetry and flatness, respectively. It is usually difficult to determine K_3 and K_4 reliably.

The mean hydrodynamic radius, calculated from D_{EFF} , is given by:

$$\langle R_h \rangle = \frac{kT}{6 \pi \eta \langle D \rangle_z} = \frac{\int_0^{\infty} f(M) M P(q, M) dM}{\int_0^{\infty} f(M) M P(q, M) R_h^{-1}(M) dM} \quad (5.460)$$

The main advantage of the cumulant method is that it does not require any assumption about the particular shape of the size distribution. The main drawback of this method is that a variety of rather different distributions may have similar values of K_1 and K_2 . Therefore, we cannot obtain reliable information about the size distribution only from DLS data. The cumulant method is most suitable when the size distribution is known to be monomodal and relatively narrow.

For polymodal or wide distributions the histogram method⁹⁰³⁻⁹¹¹ (or the exponential sampling method) is more representative. In this method, the particle size distribution is presented by a finite number of discrete sizes, each of them an adjustable fraction of the total concentration. Then, the

correlation function is calculated and compared with the measured one. The relative amplitude of each size class is varied to give the best agreement between the calculated and the experimental functions. Although conceptually simple, the histogram method is not straightforward, because a given correlation function can be described by an infinite variety of particle distributions (ill-posed mathematical problem). To overcome this difficulty, we must invoke independent criteria to restrict the population of possible solutions and to choose “the most reasonable” one. Several procedures were proposed and realized as computer programs; the most widely used of them are CONTIN,^{894,904} non-negative least squares (NNLS),⁹⁰⁵ singular value analysis,⁹⁰⁷ maximum entropy,⁹¹⁰ regularization technique,⁹¹¹ and several others.^{906,908,909} For more thorough and reliable results, multiangle measurements and combined analysis of the data from SLS and DLS on the basis of Mie theory are recommended.

5.9.2.3 DLS by Nonspherical Particles

In diluted suspensions, translation and rotation of the particles can be considered as statistically independent. Then, the correlation function of the scattered light can be presented as composed of two parts⁹¹² — phase autocorrelation function, $C_\phi(q, \tau)$, accounting for the translational diffusion, and amplitude autocorrelation function, $C_B(\tau)$, determined by the particle rotation:

$$g^{(1)}(q, \tau) = C_B(\tau) C_\phi(q, \tau) \quad (5.461)$$

where, by definition,

$$C_B(\tau) \equiv \langle B^*(0)B(\tau) \rangle_t / \langle B(0)^2 \rangle_t \quad (5.462)$$

$B(t)$ is the scattering amplitude of a particle, which depends on the particle polarizability at given orientation. $B(t)$ changes with time due to reorientation of the particle. If the scatterers are spherical, $B(t)$ is constant and $C_B(\tau) = 1$. Note that $C_B(\tau)$ does not depend on the scattering angle and can be calculated if the polarizability tensor and the rotational diffusion tensor of the particles are known. The calculation of $C_\phi(q, \tau)$ requires averaging of the translational diffusion tensor of the particle over all possible orientations to obtain the averaged translational diffusion coefficient.

The polarizability of cylindrically symmetric particles (rod-shaped or ellipsoidal particles) can be characterized by isotropic (α) and anisotropic (β) parts of the polarizability tensors:⁸⁹²

$$\alpha \equiv \frac{1}{3} (\alpha_{\parallel} + 2\alpha_{\perp}), \quad \beta \equiv (\alpha_{\parallel} - \alpha_{\perp}) \quad (5.463)$$

where α_{\parallel} and α_{\perp} are the polarizabilities in the parallel and perpendicular direction, respectively, to the symmetry axis. The autocorrelation function for small, monodisperse, cylindrically symmetric particles has the form:⁸⁹²

$$g_v^{(1)V}(q, \tau) = \alpha^2 \exp(-q^2 D \tau) + \frac{4}{45} \beta^2 \exp[-(q^2 D + 6\Theta)\tau] \quad (5.464)$$

where Θ is the rotational diffusion coefficient; the subscript v and the superscript V denote vertically polarized incident and scattered beams, respectively. As $g_v^{(1)V}$ consists of two exponents (the second is difficult to determine precisely, because it is weaker in magnitude and decays more rapidly compared to the first), it is preferable to perform measurements also in depolarized light.^{892,912}

$$g_v^{(1)H}(q, \tau) = \frac{\beta^2}{15} \exp \left[-(q^2 D + 6\Theta) \tau \right] \quad (5.465)$$

which presents one exponent depending on both, D and Θ .

For long rodlike particles, the autocorrelation function is a sum of exponentials⁸⁹³

$$g_v^{(1)V}(\tau) = \sum_{l=0, l \text{ even}}^{\infty} B_l \exp \left\{ -[q^2 D + l(l+1)\Theta] \tau \right\} \quad (5.466)$$

The amplitude coefficients B_l are defined through spherical Bessel functions and can be calculated if the particle length is specified. The extraction of the value of Θ from the experimentally obtained correlation function obeying Equation 5.466 is a formidable task, which makes it very difficult to deduce reliably results for large particles from only DLS. In such systems, the electrooptical methods⁸⁵⁴⁻⁸⁵⁶ are more accurate for measurement of Θ .

If a homodyne method is used, the measured autocorrelation function $g^{(2)}(q, \tau)$ can be interpreted by using the Siegert relation, Equation 5.454. The translational and rotational diffusion coefficients for several specific shapes of the particles are given in Table 5.9. The respective power spectrum functions can be calculated by using the Fourier transform, Equation 5.449b.

5.9.2.4 Effect of the Particle Interactions

The diffusion coefficient of the particles in suspension depends on concentration of particles due to the interparticle interactions.⁹¹³⁻⁹²⁰ Furthermore, we should distinguish the self-diffusion (or tracer diffusion) coefficient, D_S , from the collective diffusion (or mutual diffusion) coefficient, D_C . The self-diffusion coefficient accounts for the motion of a given particle and can be formally defined as an autocorrelation function of the particle velocity:^{880,913}

$$D_S = \frac{1}{3} \int_0^{\infty} \langle \mathbf{V}(0) \cdot \mathbf{V}(\tau) \rangle d\tau \quad (5.467)$$

where the brackets denote the averaging over the stochastic particle motion. The mean-square displacement, $\langle \Delta r^2(t) \rangle$, of a given particle is given by⁹¹³

$$\langle \Delta r^2(t) \rangle = 6 D_S t; \quad \text{for } t \gg \tau_{Br} \equiv M/6\pi\eta R_h \quad (5.468)$$

where τ_{Br} is the characteristic time of the Brownian motion of a particle of mass M and hydrodynamic radius, R_h . The collective diffusion coefficient is a collective property of the suspension and characterizes the evolution of small concentration gradients in the linear approximation (Fick's law):⁹¹³

$$\frac{\partial \rho}{\partial t} = -D_C \Delta \rho \quad (5.469)$$

Hence, D_C is the quantity determined in conventional, gradient diffusion measurements. For non-interacting particles (very diluted suspension) $D_S = D_C$.

As discussed above, DLS experiment provides the autocorrelation function $g^{(1)}(q, \tau)$ or some other quantity that contains equivalent information ($g^{(2)}(q, \tau)$ or $P(q, \omega)$). Similar to the case of noninteracting particles, we can define an effective diffusion coefficient:

$$D_{\text{EFF}}(q, \rho) \equiv K_1/q^2 \quad (5.470)$$

where $K_1(q, \rho)$ is the first cumulant of the autocorrelation function. It was shown^{913,917} that the low- q limit of D_{EFF} coincides with D_C :

$$D_C(\rho) = \lim_{q \rightarrow 0} [D_{\text{EFF}}(q, \rho)]; \quad q R_h < 1 \quad (5.471)$$

while the high- q limit of $D_{\text{EFF}}(q, \rho)$ provides the so-called short-time self-diffusion coefficient:⁹¹³

$$D_S^S(\rho) = D_{\text{EFF}}(q, \rho); \quad \text{for } q R_h \gg 1 \quad (5.472)$$

More general expressions for $D_{\text{EFF}}(q, \rho)$ at intermediate values of q are also available,^{894,897,917-922} in terms of the static structure factor, $S(q, \rho)$, and the so-called dynamic structure factor, $F(q, \rho, \tau)$:⁹¹³

$$D_{\text{EFF}}(q, \rho) = -\frac{1}{S(q, \rho)} \lim_{\tau \rightarrow 0} \left[\frac{\partial F(q, \rho, \tau)/q^2}{\partial \tau} \right]_{q, \rho} \equiv \frac{H(q, \rho)}{S(q, \rho)} \quad (5.473)$$

By definition, the dynamic structure factor accounts for the correlations between the positions of the particles at different moments of time:⁹¹³

$$F(q, \rho, \tau) \equiv \frac{1}{N} \sum_{k=1}^N \sum_{j=1}^N \left\langle \exp\left\{i\mathbf{q} \cdot [\mathbf{r}_k(0) - \mathbf{r}_j(\tau)]\right\} \right\rangle \quad (5.474)$$

where \mathbf{q} is the scattering vector, and $\mathbf{r}_k(t)$ is the position of particle k in the moment t . Both functions, $F(q, \rho, \tau)$ and $H(q, \rho)$, include contributions from hydrodynamic interactions between the particles. Note that $F(q, \rho, \tau = 0) \equiv S(q, \rho)$, while for noninteracting Brownian particles:^{892,913}

$$F(q, \tau) = \langle \exp[-i\mathbf{q} \cdot \Delta \mathbf{r}(\tau)] \rangle = \exp(-q^2 D_0 \tau) \quad (5.475)$$

where D_0 is the diffusion coefficient at negligible interparticle interactions.

An important consequence of Equations 5.471, 5.473, 5.474, and 5.421 can be derived at the low- q limit:⁹¹³

$$D_C(\rho) = \frac{(\partial \Pi / \partial \rho)}{f(\rho)} \quad (5.476)$$

where $(\partial \Pi / \partial \rho)$ is the osmotic compressibility, and $f(\rho) = H^{-1}(q = 0, \rho)$ is the friction (drag) coefficient of the particles in the suspension. Equation 5.476 represents the generalized Stokes–Einstein relation. Equations 5.471 and 5.472 show that we can determine (at least in principle) $D_C(\rho)$ and $D_S^S(\rho)$ by measuring the first cumulant, $K_1(q, \rho)$, at different scattering angles. On the other hand, D_S and D_C can be calculated in numerical experiments performed by Monte Carlo or Brownian dynamics methods.^{923,924}

As shown by Batchelor⁹¹⁴ and Felderhof,⁹¹⁶ to the first order in the volume fraction, ϕ , the diffusion coefficients, D_C and D_S^S , can be presented as

$$D_C = D_0 [1 + \lambda_C \Phi] \quad (5.477)$$

$$D_S^S = D_0 [1 + \lambda_A \Phi] \quad (5.478)$$

where D_0 is the diffusion coefficient at infinite dilution, while λ_C and λ_A are coefficients that depend on the interparticle interactions (including the hydrodynamic ones). Felderhof⁹¹⁶ succeeded in presenting λ_C as a sum of several terms, each of them an explicit integral over the pair distribution function, $g(r)$ (see also References 921 and 925):

$$\lambda_C = \lambda_V + \lambda_O + \lambda_A + \lambda_S + \lambda_D \quad (5.479)$$

$$\lambda_V = 3 \int_0^\infty dx [1 - g(x)] x^2 \quad (5.480a)$$

$$\lambda_O = -3 \int_0^\infty dx [1 - g(x)] x \quad (5.480b)$$

$$\begin{aligned} \lambda_A = \frac{3}{2} \int_0^\infty dx & \left[-2.5x^{-4} + 2.25x^{-6} + 5.3334x^{-8} - 61.42x^{-10} \right. \\ & - 94.24x^{-12} + 134.58x^{-14} - 248.46x^{-16} \\ & \left. - 1587.4x^{-18} + 727.2x^{-20} + O(x^{-22}) \right] g(x) x^2 \end{aligned} \quad (5.480c)$$

$$\begin{aligned} \lambda_S = \int_0^\infty dx & \left[18.75x^{-7} - 7.5x^{-9} - 89.39x^{-11} + 215.5x^{-13} + 843.8x^{-15} \right. \\ & \left. + 435.9x^{-17} + 4164x^{-19} + O(x^{-21}) \right] g(x) x^2 \end{aligned} \quad (5.480d)$$

$$\lambda_D = 1 \quad (5.480e)$$

where $x = r/R$, and R is the particle radius. Comparison of Equation 5.480a with Equation 5.425 shows that λ_V presents another definition of the second osmotic virial coefficient:

$$\lambda_V = \frac{\beta_2}{V_p} = 2 B_2 V_p = \frac{2M^2}{N_A V_p} A_2 \quad (5.481)$$

λ_O stems from the far-field (Oseen) hydrodynamic interaction, while λ_A , λ_S , and λ_D account for the near-field hydrodynamics.⁹¹⁶

Note that Equations 5.480a, 5.480b, and 5.480e are exact, while in Equations 5.480c and 5.480d the terms up to x^{-20} in a series expansion are taken into account. For hard spheres, we can calculate⁹²⁶

$\lambda_V^{\text{HS}} = 8$, $\lambda_O^{\text{HS}} = -6$, $\lambda_A^{\text{HS}} = -1.831$, $\lambda_S^{\text{HS}} = 0.285$, and $\lambda_C^{\text{HS}} = 1.454$. DLS experiments⁹²⁷ with suspension of sterically stabilized silica particles in organic solvents (used as a model of hard sphere dispersion) gave $\lambda_C^{\text{HS}} = 1.4 \pm 0.2$, which is in a good agreement with the theoretical value. A numerical algorithm for calculation of the next terms in the expansions in Equations 5.480c and 5.480d was developed,⁹²⁵ but usually the first several terms (up to x^7) are enough to calculate precisely λ_A and λ_C . λ_k ($k = V, O, A, S, C$) were calculated for simple functions modeling the pair interaction energy (sticky potential, square-well potential, etc.), and some of the results are shown in Table 5.11.

The important case of charged particles, interacting through electrostatic and van der Waals forces was analyzed by several authors.^{922,929-933} It was shown^{921,929} that the contribution of the near-field terms (λ_A , λ_S , and λ_D) is negligible for electrostatically repelling particles when the collective diffusivity is concerned. For weakly charged particles (low surface potential and small size), explicit formulae for the coefficients were obtained⁹²⁹ (see Table 5.11). For strongly charged particles and in the cases when the van der Waals attraction is operative, we need numerical procedures to calculate λ_k .^{921,929} This approach allows us to determine the particle charge (or electrical potential) from the measured values of λ_V (by SLS) or λ_C (by DLS) if the particle size and the ionic strength are known.^{929,930}

At low ionic strength ($\kappa R \sim 1$), other effects connected with the finite diffusivity of the small ions in the EDL surrounding the particle are present.^{929,934,935} The noninstantaneous diffusion of the small ions (with respect to the Brownian motion of the colloid particle) could lead to detectable reduction of the single particle diffusion coefficient, D_0 , from the value predicted by the Stokes–Einstein relation, Equation 5.447. For spherical particles, the relative decrease in the value of D_0 is largest at $\kappa R \approx 1$ and could be around 10 to 15%. As shown in the normal-mode theory,⁹¹⁹ the finite diffusivity of the small ions also affects the concentration dependence of the collective diffusion coefficient of the particles. Belloni et al.⁹³¹ obtained an explicit expression for the contribution of the small ions in λ_C :

$$\Delta\lambda_{\text{SI}} = \frac{Z^2 L_B}{R} \frac{1}{(1 + \kappa R)^2} \frac{3}{(\kappa R)^2} \frac{D_0}{D_{\text{SI}}} \quad (5.482)$$

where Z is the number of charges per particle, $L_B = e^2/(4\pi\epsilon_0\epsilon kT)$ is the Bjerrum length, and D_{SI} is the diffusion coefficient of the small ions. The ratio of $\Delta\lambda_{\text{SI}}$ and the electrostatic part in λ (see Table 5.11):

$$\frac{\Delta\lambda_{\text{SI}}}{\lambda_C^{\text{EL}}} = \frac{1}{(1 + \kappa R)} \frac{D_0}{D_{\text{SI}}} \approx \frac{1}{(1 + \kappa R)} \frac{R_{\text{SI}}}{R} \quad (5.483)$$

shows⁹²⁹ that the relative contribution of the small ions is above 10% only when the particles are small ($R \leq 4$ nm) and at a not very high ionic strength ($\kappa R \sim 1$). This could be the case with protein molecules and charged spherical micelles. Otherwise, the effect of the finite diffusivity of the small ions is negligible in comparison with the effect of the direct particle–particle electrostatic interaction.

5.9.2.5 Concentrated Dispersions: Photon Cross-Correlation Techniques, Fiber-Optics DLS, and Diffusing Wave Spectroscopy

A major drawback of the conventional DLS experiment is that the dispersion must be transparent for the light beam. For micrometer-sized particles, this requires concentrations below 10^{-5} vol %. Often the concentration of the samples is higher and their dilution for investigation is not desirable. The autocorrelation function of multiply scattered light is difficult to interpret and to extract

TABLE 5.11

Expressions for the Correction Factors, λ_v , λ_o , λ_c , and λ_A , for Different Types of Interaction between Spherical Particles

Type of Interaction	λ_v	λ_o	λ_c	λ_A	Ref.
1. Hard spheres					
$W(r) = \begin{cases} 0 & ; \quad r \geq 2R \\ +\infty & ; \quad r < 2R \end{cases}$					
a. Nonslip boundary condition	+8.00	-6.00	+1.454	-1.8315	926
b. Perfect slip boundary condition	+8.00	-4.00	+3.511	-0.562	
2. Sticky hard spheres					
$g(r) = \begin{cases} 1; & r > 2R \\ 1 + \frac{R}{6\tau}; & r = 2R \\ 0; & r < 2R \end{cases}$	+8 - (2/τ)	-6 + (1/τ)	1.454 - (1.125/τ)	1.8315 - (0.295/τ)	928
τ-stickiness parameter					
3. Weakly charged particles					
$W(r) = \begin{cases} \frac{(Ze)^2 \exp[\kappa(2R-r)]}{4\pi\epsilon_0\epsilon r(1+\kappa R)^2}; & r \geq 2R \\ +\infty; & r < 2R \end{cases}$	$8 + \frac{Z^2 L_B (1+2\kappa R)}{R (1+\kappa R)^2} \frac{3}{(\kappa R)^2}$	$-6 - \frac{Z^2 L_B}{R} \frac{1}{(1+\kappa R)^2} \frac{3}{\kappa R}$	$1.45 + \frac{Z^2 L_B}{R} \frac{1}{(1+\kappa R)} \frac{3}{(\kappa R)^2}$	$-1.83 + \frac{Z^2 L_B \exp(2\kappa R)}{R (1+\kappa R)^2} \times \left[\frac{15}{6} E_3(2\kappa R) - \frac{27}{18} E_5(2\kappa R) \right]$	929

Note: Z is the number of charges per particle, $L_B = e^2/(4\pi\epsilon_0\epsilon kT)$ is the Bjerrum length, $E_n(x) \equiv \int_0^\infty \frac{e^{-xt}}{t^n} dt$ ($n = 1, 2, 3, \dots$) is integral exponent function.

subsequent information about the particle size. Several powerful techniques have been proposed aimed at overcoming this problem and extending the application of DLS to more concentrated suspensions.

One obvious way to reduce the contribution of the multiple light scattering is to use a very thin sample cell of an optical path length below 100 μm .^{936,937} Alternatively, Phillies^{938,939} suggested using a more complex optical system comprising two laser beams and two detectors focused in the same sample volume and having exactly the same scattering vector (in direction and magnitude). The signals from the two detectors are cross-correlated by using a photon correlator. It has been shown⁹³⁸⁻⁹⁴¹ that the signals from the two detectors are correlated only for the light that is scattered once (single scattering), whereas the contributions from double and higher-order multiple scattering are uncorrelated. Therefore, when the signals from the two detectors (single + multiple scattering) are cross-correlated, only the signal corresponding to single scattering from the particles gives a contribution into the time dependence of the cross-correlation function. As a result, we obtain a time correlation function from turbid samples, which is similar to those obtained from transparent samples and can be interpreted in the same way. Several other cross-correlation schemes were suggested by Schätzel⁹⁴¹ and some of them have found realization in practice.⁹⁴¹⁻⁹⁴⁵ In two-color dynamic light scattering (TCDLS),⁹⁴¹⁻⁹⁴⁴ two laser beams of different colors are used and the angles between the incident beams and the detectors (all in the same plane) are chosen in such a way as to define equal scattering vectors. In three-dimensional light scattering (3DDLS)^{941,945} two incident beams of the same wavelength enter the sample from slightly above and slightly below the average scattering plane. The two detectors are also placed above and below the average scattering plane, respectively, so that the third dimension is used to achieve equal scattering vectors in the 3DDLS method. Both techniques have proved to suppress efficiently the multiple scattering in concentrated latex dispersions (see, e.g., the recent review by Pusey⁹⁴²). Furthermore, it was shown⁹⁴⁵ that the same cross-correlation techniques can be used to eliminate the multiple scattering in SLS experiments. These techniques can be applied to turbid samples, for which the contribution of the single light scattering is a detectable fraction (>1%) of the total intensity of the scattered light.

Two different techniques have been developed for studying even more concentrated (opaque) colloidal dispersions. The fiber-optic DLS or fiber-optical quasi-elastic light scattering (FOQELS) was proposed by Tanaka and Benedek⁹⁴⁶ and has undergone substantial development during the last years.⁹⁴⁷⁻⁹⁵¹ In this method, an optical fiber is applied to guide the incident beam toward the suspension and to collect the scattered light. Because the same fiber is used for particle illumination and for collecting the scattered light, the optical path is the shortest possible, and the contribution of the multiple scattering is enormously reduced. The main problem with the first versions of FOQELS equipment was that the detected signal presented a superposition of homodyne and heterodyne components, the second created by the light reflected from the front face of the optical fiber.⁹⁵² The relative contribution of the homodyne component increased with the particle concentration and this led to ambiguity in data interpretation. Several improvements were proposed⁹⁵³⁻⁹⁵⁵ to avoid the detection of this backward reflected light. A schematic of the version developed by Wiese and Horn⁹⁵⁴ is shown in Figure 5.74. The laser beam 1 enters the fiber-optic Y-coupler and illuminates the particles through fiber 2, which is submerged in the dispersion. The backscattered light re-enters optical fiber 2 and through fiber 3 reaches the detector. The front face of the optical fiber is inclined at an angle of 10° with respect to the optical axis, to reduce the intensity of the backreflected beam, which otherwise would act as a local oscillator. With this equipment, very concentrated dispersions (up to 40%) can be studied.⁹⁵⁴ Another type of miniaturized fiber probe, comprising two optical fibers (one for illumination, and the other for receiving the scattered light), was proposed for *in situ* process control by Dhadwal et al.⁹⁵⁵ The use of single-mode fibers (whose core diameter is of the order of the light wavelength) is another innovation that facilitates the data interpretation in FOQELS experiments.^{954,955} In the last years, the fiber-optic DLS transformed into a useful tool for studying concentrated particle dispersions.

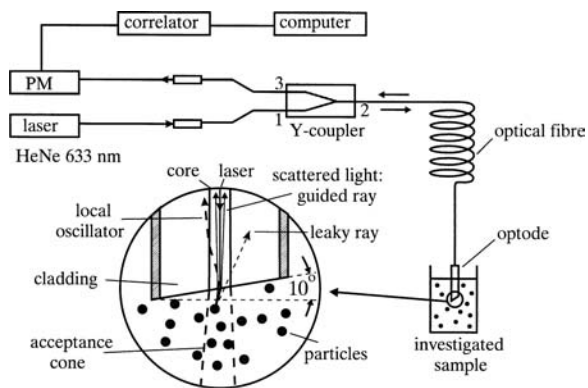


FIGURE 5.74 Schematics of experimental setup for fiber-optic DLS. Laser beam 1 illuminates the particles through the Y-coupler and fiber 2, which is submerged in the dispersion. The backscattered light reenters fiber 2, and through fiber 3 it reaches the detector. The front face of fiber 2 is cut at 10° with respect to the optical axis (the inset) to reduce the intensity of the backreflected beam, which otherwise would act as a local oscillator reaching the detector. (Modified from Wiese, H. and Horn, D., *J. Chem. Phys.*, 94, 6429, 1991.)

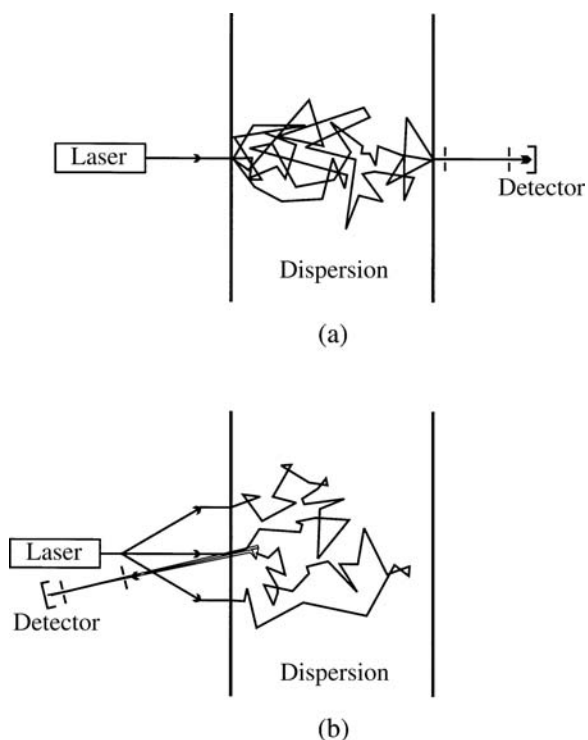


FIGURE 5.75 Diffusion wave spectroscopy (DWS). The light reaches the detector after multiple acts of scattering from dispersed particles. The optical path of the light in the dispersion is modeled as a result of random diffusion motion. Forward (a) or backward (b) scattered light can be analyzed.

The diffusing wave spectroscopy⁹⁵⁶⁻⁹⁵⁹ (DWS) is another useful technique for studying the dynamics of opaque dispersions. The key feature of the DWS experiment is the measurement of the autocorrelation function $g^{(2)}(\tau)$ of a light that has undergone multiple scattering. Both configurations, forward scattering and backward scattering, were studied (see Figure 5.75). To derive a

theoretical expression for $g^{(2)}(\tau)$, the transport of light in the concentrated dispersion is considered^{958,959} as a diffusion process (this explains the term “diffusion wave spectroscopy”). The path of each photon in the dispersion is modeled by random, multiple scattering from a sequence of particles. The attenuation of the temporal light correlation due to the Brownian motion of the particles is calculated for each light path. The contributions of all paths are then summed (by using an appropriate averaging procedure) to calculate the autocorrelation function. Therefore, it is essential to have many scattering events for each photon before its detection by the photomultiplier. In this multiple scattering regime, the characteristic time is determined by the cumulative effect of many particles and is much shorter, compared to the single scattering regime.⁹⁵⁹ Thus, the timescale in this experiment is much faster, and the particle motion is studied over length scales much smaller than λ . The experimental equipment for DWS is practically the same as that for conventional DLS. The main difficulties with the method arise when the autocorrelation function must be interpreted to extract information about the particle dynamics. The method was applied⁹⁵⁹⁻⁹⁷⁰ to several complex colloidal systems (liquid-like concentrated dispersions, colloidal crystals, foams, emulsions, particles in porous media and under shear) and many nontrivial results have been obtained.

5.9.3 APPLICATION OF LIGHT SCATTERING METHODS TO COLLOIDAL SYSTEMS

The aim of this section is to illustrate the most typical applications of light scattering methods to dispersions and micellar surfactant solutions.

5.9.3.1 Surfactant Solutions

5.9.3.1.1 Critical Micellar Concentration, Aggregation Number, Second Virial Coefficient

The application of light scattering methods for investigating micellar solutions started with the studies of Debye.⁹⁷¹ He showed that from measurements of the turbidity as a function of the surfactant concentration we can determine the critical micellar concentration (CMC), the micellar mass (and the corresponding aggregation number, v_a), and the second osmotic virial coefficient, A_2 . For larger micelles, additional information about the micellar size and shape was obtained.⁹⁷² Later, numerous studies provided valuable information about CMC, v_a , and A_2 for a variety of nonionic and ionic surfactants.⁹⁷³⁻⁹⁷⁸ Currently, SLS is a routine method for determination of these quantities. Nevertheless, the information obtained by SLS from micellar solutions must be handled with some care,⁹⁷⁹⁻⁹⁸¹ because one of the main assumptions of the SLS theory (i.e., that the properties of the micelles, v_a and A_2 , remain constant with the micellar concentration) was shown to be not entirely fulfilled for these systems. This is particularly important for more concentrated surfactant solutions, where transitions in micellar size and shape may take place.

5.9.3.1.2 Diffusion Coefficient, Size, Shape, and Polydispersity of Micelles

DLS has the advantage that valuable information about the micellar diffusion coefficient,⁹⁸² D , and hydrodynamic radius, R_h , could be obtained at fixed surfactant concentration. Moreover, the effect of intermicellar interactions is less pronounced for the values of D and R_h , than the values measured by SLS. The combination of SLS and DLS allows determination of the size, shape, and polydispersity of micelles. Such systematic studies^{930,982,983} were performed for sodium dodecylsulfate micelles at large ionic strength (0.15 to 0.6 M NaCl) and variable temperature (10 to 85°C) to reveal the transition from small spherical to large rod-shaped micelles. A comparison of $\langle R_g \rangle$ (determined by SLS) with R_h (determined by DLS) was used to verify the rodlike shape of micelles. More refined analyses⁹⁸⁴⁻⁹⁸⁶ included the effects of the micellar polydispersity and flexibility of the rodlike micelles. The persistent length of the SDS rods was determined⁹⁸² to be ~ 70 nm; of cetylpyridinium bromide rods,^{987,988} ~ 25 to 40 nm; of hexadecyltrimethylammonium salicylate,⁹⁸⁹ ~ 100 to 150 nm; of sodium dodecyl dioxyethylenesulfate,⁹⁹⁰ ~ 165 to 190 nm. Such studies provide data that are used as a test of the thermodynamic theories of the growth of rodlike micelles.⁹⁹¹

5.9.3.1.3 Intermicellar Interactions

The concentration dependencies of $R(\theta)$ and D_{EFF} were used^{930,992-994} to investigate the interactions between SDS micelles at different electrolyte concentrations. Corti and Degiorgio⁹³⁰ interpreted the measured values of A_2 and λ_C by using a model accounting for the electrostatic repulsion and van der Waals attraction between the micelles. In this way, the Hamaker constant and the micellar charge were determined. The assumption that the micelles do not change in size and shape in the studied range of electrolyte concentrations was questioned later by Mazer.⁹⁸² Indeed, Corti and Degiorgio⁹³⁰ and Dorshow et al.⁹⁹² needed a rather large value of the Hamaker constant to describe the attraction between the micelles. Several other studies^{932,993,994} were directed to determine the micellar charge and its variation with the electrolyte concentration; however, some of them were based on approximated formulae for the electrostatic interaction energy between the micelles, assuming low electrical surface potential. The typical surface potential of SDS micelles is⁹⁹⁵ ~60 to 70 mV, and more complex and rigorous approaches^{921,996} must be used to describe correctly the electrostatic interaction. The accumulated light scattering data suggest that very often the observed concentration dependencies present a result of the combined action of intermicellar interactions and changes of the micellar size and shape. Mazer⁹⁸² concludes that for SDS micelles the intermicellar interactions prevail only at low and moderate electrolyte concentrations ($\leq 0.2 M$ NaCl).

A combination of SLS and DLS methods was used⁹⁹⁷ to investigate the behavior of nonionic micellar solutions in the vicinity of their cloud point. It had been known for many years that at a high temperature the micellar solutions of polyoxyethylene-alkyl ether surfactants (C_nEO_m) separate into two isotropic phases. The solutions become opalescent with the approach of the cloud point, and several different explanations of this phenomenon were proposed. Corti and Degiorgio⁹⁹⁷ measured the temperature dependence of D_{EFF} and $\langle I_S \rangle$, and found that they can be described as a result of critical phase separation, connected with intermicellar attraction and long-range fluctuations in the local micellar concentration. Far from the cloud point, the micelles of nonionic surfactants with a large number of ethoxy-groups ($m \sim 30$) may behave as hard spheres.³²⁴

5.9.3.1.4 Microemulsions

Microemulsions are another type of system that has been intensively studied by light scattering methods.^{882-887,998-1001} Vrij and co-workers^{882,998} used SLS to determine the volume of water in oil microemulsion droplets and the second osmotic virial coefficient. Two interesting conclusions from their studies were drawn:⁹⁹⁸ (1) the van der Waals forces between the water cores of the droplets (if considered to be nondeformable spheres) are too weak to explain the observed strong attraction, and (2) the minimal distance between the centers of mass of two droplets upon collision is smaller than the droplet diameter. Similar observations were made by other authors and were explained by using several different models. Calje et al.⁹⁹⁸ and Lemaire et al.⁹⁹⁹ assumed that the aforementioned effects were due to mutual overlap of the surfactant monolayers covering the droplets. Denkov et al.⁸⁸⁶ argued that the droplets may deform upon collision and showed that the attraction between deformable droplets is stronger compared with that between hard spheres of the same Hamaker constant. Auvrey¹⁰⁰² and Fletcher et al.^{1003,1004} attributed the observed effects to the coalescence (fusion) of some fraction of the droplets. The droplet fusion also could be connected to the observed^{1005,1006} sharp increase of the electric conductivity of water in oil microemulsions at a given threshold value of the droplet volume fraction (percolation model) and to the observed¹⁰⁰⁷ exchange of water-soluble fluorescent probes between droplets. The presence of droplet aggregates was demonstrated^{1008,1009} by electrooptic birefringence, and their lifetime was estimated in some cases. Although a number of other experimental methods were invoked to analyze the structure and dynamics of microemulsions, the nature of the interdroplet interactions is by no means well understood.⁸⁸⁷ A critical behavior of microemulsions was observed¹⁰¹⁰ at certain conditions.

Light scattering methods (often in combination with other experimental methods) are widely used for the investigation of complex surfactant systems such as mixed micelles,^{1011,1012} block

copolymer micelles,^{1013,1014} iridescent lamellar phases,^{1015,1016} complexes between micelles and polymers,¹⁰¹⁷⁻¹⁰²⁰ aggregates of biosurfactants¹⁰²¹⁻¹⁰²³ (micelles and vesicles), and many others.

The scattering of light from interfaces^{1024,1025} and thin liquid films^{1026,1027} provides other possibilities for studying surfactant systems. Light scattering from interfaces covered with surfactant monolayers allowed investigation of the interfacial tension and of the rheological properties of the monolayers. Such measurements were successfully applied¹⁰²⁴ for measurement of ultra-low interfacial tension, as well as the bending constant of surfactant monolayers in microemulsion systems. SLS and DLS from liquid films were used^{1026,1027} for measurement of the interaction forces between the film surfaces as a function of the film thickness.

5.9.3.2 Dispersions

5.9.3.2.1 Size, Shape, and Polydispersity of Particles

The classical application of SLS to dispersions is for determination of the particle size, shape, and polydispersity.^{847,848} Earlier studies were restricted to diluted samples of noninteracting particles with size comparable to the light wavelength. Substantial progress has been achieved during the last decades in the application of light scattering methods to more difficult samples. The invention of DLS allowed the precise determination of particle size in the nanometer range. On the other side, the application of the laser diffraction method^{877,1028} extended the upper limit of measurable particle size to several hundred micrometers. A variety of theoretical procedures has been proposed⁹⁰³⁻⁹¹¹ to solve the inverse scattering problem and to determine more reliably the particle size distribution from light scattering data. Several theoretical approaches were developed to handle data from SLS¹⁰²⁹⁻¹⁰³¹ and DLS^{956-961,1032} experiments on concentrated samples, where the multiple scattering is substantial. Alternatively, the cross-correlation techniques⁹³⁸⁻⁹⁴⁵ and fiber-optic probes were applied⁹⁴⁸⁻⁹⁵⁵ to avoid the multiple scattering in concentrated suspensions. A new types of theories, based on extensive computer calculations, emerged in the 1970s for description of the light scattering from large arbitrary-shaped particles — the extended boundary condition method^{1033,1034} (EBCM) and the coupled dipole method^{1035,1036} (CDM). All these new directions are rapidly developing and they substantially enlarge the area of application of light scattering methods.

5.9.3.2.2 Static and Dynamic Structure Factors

SLS and DLS experiments have played a very important role for a deeper understanding of the structure and dynamics of suspensions containing strongly interacting particles.^{913,1037-1051} A number of theoretical approaches, based on modern statistical theories, were proposed for calculation of the static and dynamic structure factors of monodisperse^{913,922,917-919} and polydisperse suspensions.¹⁰⁵²⁻¹⁰⁵⁴ The hydrodynamic and electrostatic interactions between charged particles have been subjects of particular interest. The experimentally attainable quantities, such as pair distribution function and effective diffusion coefficients, were used as test probes for the rapidly developing theories. The importance of different factors (particle and electrolyte concentrations, particle charge, etc.) for the phase transitions in suspensions have been systematically investigated. The liquid-like and colloidal crystal states were found to have distinct features, which can be quantitatively studied by light scattering experiments. An excellent review of this topic is given by Pusey and Tough.⁹¹³

The kinetics of crystallization of colloidal suspensions at high particle concentration and/or low ionic strength is another phenomenon that has been the subject of intensive experimental studies.^{1045-1051,1055,1056} The timescale of the crystallization process in suspensions is much slower (compared to that in atomic liquids), which makes it available for direct measurement by light scattering methods. The induction time, the crystallization rate, and the structure and size distribution of the growing crystallites have been studied as functions of different factors. The structure of the colloid crystals is conventionally studied by Bragg diffraction^{1039,1045} or Kossel lines analysis.¹⁰⁴⁷⁻¹⁰⁴⁹

Substantial interest has been raised in the problem of the structure and dynamics of suspensions in shear hydrodynamic fields.¹⁰⁵⁷⁻¹⁰⁶⁵ The experiments showed that both shear-induced melting and shear-induced ordering can be observed at different particle volume fractions and shear rates. The nonequilibrium microstructure of the suspension under shear can be investigated in these experiments and compared with the predictions from analytical theories and computer simulations.

5.9.3.2.3 Kinetics of Coagulation and Structure of the Formed Aggregates

During the last decade, substantial progress has been achieved in our understanding of coagulation phenomenon (see also Section 5.6). Light scattering, electron microscopy, and other experimental methods,^{1066,1067} in combination with extensive numerical experiments and theoretical work,¹⁰⁶⁸⁻¹⁰⁷⁰ revealed that the aggregates formed upon the coagulation of colloidal particles have a fractal-type structure;¹⁰⁷¹ i.e., they exhibit size-scale invariance. The fractal dimension of the aggregates (which is a measure of their compactness) depends on the specific regime of aggregation. Two limiting regimes of colloid aggregation can be distinguished: diffusion-limited aggregation (DLA), which corresponds to barrierless (rapid) coagulation, and reaction-limited aggregation (RLA), in which the repulsive barrier in the pair interaction energy is around several kT (slow coagulation). In DLA, the coagulation rate is limited solely by the time between the collisions of the particles due to the diffusion. In RLA, a large number of collisions is required before two particles can stick together, which leads to much slower aggregation rate. Computer simulations and analytical theories¹⁰⁷² predict that for DLA the clusters formed have a fractal dimension $d_f \approx 1.8$ and the average mass of the aggregates must be a linear function of time,¹⁰⁷³ $\langle M \rangle \propto t$ (see, e.g., Equation 5.328). In contrast, for RLA^{1074,1075} $d_f \approx 2.1$ and $\langle M \rangle \propto \exp(k_a t)$,¹⁰⁷⁶ where the aggregation constant k_a depends on the sticking probability and the time between collisions. The size distribution of the formed aggregates is also different in the two regimes.¹⁰⁷⁷ All these theoretical predictions were verified¹⁰⁷⁸⁻¹⁰⁸⁰ by SLS and DLS methods on colloid particles of different material (silica, polystyrene, gold, hematite). The results about the size distribution of the aggregates were scaled¹⁰⁷⁸ on a single master curve, whose shape was found to be independent of the regime of aggregation and the material of the particles. The fractal approach and the light scattering techniques have found also a wide application for analysis of the protein aggregation and the early stages of protein crystallization.¹⁰⁸¹⁻¹⁰⁸⁵

ACKNOWLEDGMENT

The authors are indebted to Miss M. Paraskova for typing the text and drawing the figures.

REFERENCES

1. Jungermann, E., *Cationic Surfactants*, Marcel Dekker, New York, 1970.
2. Lucassen-Reynders, E.H., *Anionic Surfactants — Physical Chemistry of Surfactant Action*, Marcel Dekker, New York, 1981.
3. Schick, M.J., *Nonionic Surfactants: Physical Chemistry*, Marcel Dekker, New York, 1986.
4. Gibbs, J.W., *The Scientific Papers of J.W. Gibbs*, Vol. 1, Dover, New York, 1961.
5. Ono, S. and Kondo, S., Molecular theory of surface tension in liquids, in *Handbuch der Physik*, Vol. 10, Flügge, S., Ed., Springer, Berlin, 1960.
6. Adamson, A.W. and Gast, A.P., *Physical Chemistry of Surfaces*, 6th ed., Wiley, New York, 1997.
7. Freundlich, H., *Colloid and Capillary Chemistry*, Methuen, London, 1926.
8. Langmuir, I., *J. Am. Chem. Soc.*, 40, 1361, 1918.
9. Volmer, M., *Z. Phys. Chem.*, 115, 253, 1925.
10. Frumkin, A., *Z. Phys. Chem.*, 116, 466, 1925.
11. Hill, T.L., *An Introduction to Statistical Thermodynamics*, Addison-Wesley, Reading, MA, 1962.
12. Lucassen-Reynders, E.H., *J. Phys. Chem.*, 70, 1777, 1966.

13. Borwankar, R.P. and Wasan, D.T., *Chem. Eng. Sci.*, 43, 1323, 1988.
14. Derjaguin, B.V., *Theory of Stability of Colloids and Thin Liquid Films*, Plenum Press, Consultants Bureau, New York, 1989.
15. Shchukin, E.D., Pertsov, A.V., and Amelina, E.A., *Colloid Chemistry*, Moscow University Press, Moscow, 1982 [Russian]; Elsevier, 2001 [English].
16. Zeldowitch, J., *Acta Physicochim.* (USSR), 1, 961, 1934.
17. Halsey, G. and Taylor, H.S., *J. Chem. Phys.*, 15, 624, 1947.
18. Gurkov, T.G., Kralchevsky, P.A., and Nagayama, K., *Colloid Polym. Sci.*, 274, 227, 1996.
19. Butler, J.A.V., *Proc. R. Soc. Ser. A*, 135, 348, 1932.
20. Fainerman, V.B. and Miller, R., *Langmuir*, 12, 6011, 1996.
21. Vaughn, M.W. and Slattery, J.C., *J. Colloid Interface Sci.*, 195, 1, 1997.
22. Makievski, A.V. et al., *J. Phys. Chem. B*, 102, 417, 1998.
23. Landau, L.D. and Lifshitz, E.M., *Statistical Physics*, Part 1, Pergamon, Oxford, 1980.
24. Hachisu, S., *J. Colloid Interface Sci.*, 33, 445, 1970.
25. Kalinin, V.V. and Radke, C.J., *Colloids Surf. A*, 114, 337, 1996.
26. Warszyński, P. et al., *J. Chyst. Chem., B*, 102, 10948, 1998.
27. Kralchevsky, P.A. et al., *Langmuir*, 15, 2351, 1999.
28. Prosser, A.J. and Frances, E.I., *Colloids Surf. A*, 178, 1, 2001.
29. Kirkwood, J.G. and Oppenheim, I., *Chemical Thermodynamics*, McGraw-Hill, New York, 1961.
30. Robinson, R.A. and Stokes, R.H., *Electrolyte Solutions*, Butterworths, London, 1959.
31. Gouy, G., *J. Phys. Radium*, 9, 457, 1910.
32. Davies, J. and Rideal, E., *Interfacial Phenomena*, Academic Press, New York, 1963.
33. Grahame, D.C., *Chem. Rev.*, 41, 441, 1947.
34. Israelachvili, J.N., *Intermolecular and Surface Forces*, Academic Press, London, 1992.
35. Kralchevsky, P.A. and Nagayama, K., *Particles at Fluid Interfaces and Membranes*, Elsevier, Amsterdam, 2001.
36. Matijević, E. and Pethica, B.A., *Trans. Faraday Soc.*, 54, 1382, 1958.
37. van Voorst Vader, F., *Trans. Faraday Soc.*, 56, 1067, 1960.
38. Tajima, K., *Bul. Chem. Soc. Jpn.*, 44, 1767, 1971.
39. Stern, O., *Z. Elektrochem.*, 30, 508, 1924.
40. Tajima, K., Muramatsu, M., and Sasaki, T., *Bul. Chem. Soc. Jpn.*, 43, 1991, 1970.
41. Tajima, K., *Bul. Chem. Soc. Jpn.*, 43, 3063, 1970.
42. Danov, K.D. et al., manuscript in preparation.
43. Cross, A.W. and Jayson, G.G., *J. Colloid Interface Sci.*, 162, 45, 1994.
44. Johnson, S.B. et al., *Langmuir*, 11, 2367, 1995.
45. Alargova, R.G. et al., *Langmuir*, 13, 5544, 1997.
46. Rathman, J.F. and Scamehorn, J.F., *J. Phys. Chem.*, 88, 5807, 1984.
47. Berr, S.S. et al., *J. Phys. Chem.*, 90, 6492, 1986.
48. Rosen, M.J., *Surfactants and Interfacial Phenomena*, Wiley, New York, 1989.
49. Clint, J., *Surfactant Aggregation*, Chapman & Hall, London, 1992.
50. Alargova, R.G. et al., *Langmuir*, 14, 4036, 1998.
51. Dimov, N.K. et al., *J. Colloid Interface Sci.*, 2002, in press.
52. Valkovska, D.S., Danov, K.D., and Ivanov, I.B., *Colloids Surf. A*, 175, 179, 2000.
53. Danov, K.D., Kralchevsky, P.A., and Ivanov, I.B., in *Encyclopedic Handbook of Emulsion Technology*, Sjöblom, J., Ed., Marcel Dekker, New York, 2001, chap. 26.
54. Dukhin, S.S., Kretzschmar, G., and Miller, R., *Dynamics of Adsorption at Liquid Interfaces*, Elsevier, Amsterdam, 1995.
55. Eastoe, J. and Dalton, J.S., *Adv. Colloid Interface Sci.*, 85, 103, 2000.
56. Lord Rayleigh, *Proc. R. Soc. London*, 29, 71, 1879.
57. Bohr, N., *Philos. Trans. R. Soc. London, A*, 209, 281, 1909.
58. Defay, R. and Pétré, G., Dynamic surface tension, in *Surface and Colloid Science*, Vol. 3, Matijević, E., Ed., Wiley, New York, 1971, p. 27.
59. Miller, R. and Kretzschmar, G., *Adv. Colloid Interface Sci.*, 37, 97, 1991.
60. Wantke, K.-D., Lunkenheimer, K., and Hempt, C., *J. Colloid Interface Sci.*, 159, 28, 1993.
61. Chang, C.-H. and Franses, E.I., *J. Colloid Interface Sci.*, 164, 107, 1994.

62. Johnson, D.O. and Stebe, K.J., *J. Colloid Interface Sci.*, 182, 525, 1996.
63. Horozov, T. and Arnaudov, L., *J. Colloid Interface Sci.*, 219, 99, 1999.
64. Horozov, T. and Arnaudov, L., *J. Colloid Interface Sci.*, 222, 146, 2000.
65. van den Tempel, M. and Lucassen-Reynders, E.H., *Adv. Colloid Interface Sci.*, 18, 281, 1983.
66. Langevin, D., *Colloids Surf.*, 43, 121, 1990.
67. Lemaire, C. and Langevin, D., *Colloids Surf.*, 65, 101, 1992.
68. Grigorev, D.O., Krotov, V.V., and Noskov, B.A., *Colloid J.*, 56, 562, 1994.
69. Mysels, K.J., *Colloids Surf.*, 43, 241, 1990.
70. Kralchevsky, P.A., Radkov, Y.S., and Denkov, N.D., *J. Colloid Interface Sci.*, 161, 361, 1993.
71. Fainerman, V.B., Miller, R., and Joos, P., *Colloid Polym. Sci.*, 272, 731, 1994.
72. Fainerman, V.B. and Miller, R., *J. Colloid Interface Sci.*, 176, 118, 1995.
73. Horozov, T.S. et al., *Colloids Surf. A*, 113, 117, 1996.
74. Mishchuk, N.A. et al., *Colloids Surf. A*, 192, 157, 2001.
75. van den Bogaert, R. and Joos, P., *J. Phys. Chem.*, 83, 17, 1979.
76. Möbius, D. and Miller, R., Eds., *Drops and Bubbles in Interfacial Research*, Elsevier, Amsterdam, 1998.
77. Jho, C. and Burke, R., *J. Colloid Interface Sci.*, 95, 61, 1983.
78. Joos, P. and van Hunsel, J., *Colloid Polym. Sci.*, 267, 1026, 1989.
79. Fainerman, V.B. and Miller, R., *Colloids Surf. A*, 97, 255, 1995.
80. Miller, R., Bree, M., and Fainerman, V.B., *Colloids Surf. A*, 142, 237, 1998.
81. Senkel, O., Miller, R., and Fainerman, V.B., *Colloids Surf. A*, 143, 517, 1998.
82. Bain, C.D., Manning-Benson, S., and Darton, R.C., *J. Colloid Interface Sci.*, 229, 247, 2000.
83. Rotenberg, Y., Boruvka, L., and Neumann, A.W., *J. Colloid Interface Sci.*, 37, 169, 1983.
84. Makievski, A.V. et al., *J. Phys. Chem.*, 103, 9557, 1999.
85. Joos, P., *Dynamic Surface Phenomena*, VSP BV, AH Zeist, the Netherlands, 1999.
86. Ward, A.F.H. and Tordai, L., *J. Chem. Phys.*, 14, 453, 1946.
87. Miller, R., *Colloid Polym. Sci.*, 259, 375, 1981.
88. McCoy, B.J., *Colloid Polym. Sci.*, 261, 535, 1983.
89. Hansen, R.S., *J. Chem Phys.*, 64, 637, 1960.
90. Filippov, L.K., *J. Colloid Interface Sci.*, 164, 471, 1994.
91. Daniel, R. and Berg, J.C., *J. Colloid Interface Sci.*, 237, 294, 2001.
92. Sutherland, K.L., *Aust. J. Sci. Res.*, A5, 683, 1952.
93. Abramowitz, M. and Stegun, I.A., *Handbook of Mathematical Functions*, Dover, New York, 1965.
94. Korn, G.A. and Korn, T.M., *Mathematical Handbook*, McGraw-Hill, New York, 1968.
95. Danov, K.D. et al., *Langmuir*, 16, 2942, 2000.
96. Dukhin, S.S., Miller, R., and Kretzschmar, G., *Colloid Polym. Sci.*, 261, 335, 1983.
97. Dukhin, S.S. and Miller, R., *Colloid Polym. Sci.*, 272, 548, 1994.
98. MacLeod, C. and Radke, C.J., *Langmuir*, 10, 3555, 1994.
99. Vlahovska, P.M., et al., *J. Colloid Interface Sci.*, 192, 194, 1997.
100. Danov, K.D. et al., *Colloids Surf. A*, 156, 389, 1999.
101. Diamant, H. and Andelman, D., *J. Phys. Chem.*, 100, 13732, 1996.
102. Diamant, H., Ariel, G., and Andelman, D., *Colloids Surf. A*, 183–185, 259, 2001.
103. Nayfeh, A.H., *Perturbation Methods*, Wiley, New York, 1973.
104. Danov, K.D. et al., manuscript in preparation.
105. Durbut, P., Surface activity, in *Handbook of Detergents*, Part A, Broze, G., Ed., Marcel Dekker, New York, 1999, chap. 3.
106. Bond, W.N. and Puls, H.O., *Philos. Mag.*, 24, 864, 1937.
107. Doss, K.S.G., *Koll. Z.*, 84, 138, 1938.
108. Blair, C.M., *J. Chem. Phys.*, 16, 113, 1948.
109. Ward, A.F.H., *Surface Chemistry*, Butterworths, London, 1949.
110. Dervichian, D.G., *Koll. Z.*, 146, 96, 1956.
111. Hansen, R.S. and Wallace, T., *J. Phys. Chem.*, 63, 1085, 1959.
112. Baret, J.F., *J. Phys. Chem.*, 72, 2755, 1968.
113. Baret, J.F., *J. Chem. Phys.*, 65, 895, 1968.
114. Baret, J.F., *J. Colloid Interface Sci.*, 30, 1, 1969.

115. Borwankar, R.P. and Wasan, D.T., *Chem. Eng. Sci.*, 38, 1637, 1983.
116. Dong, C. et al., *Langmuir*, 16, 4573, 2000.
117. Laplace, P.S., *Traité de mécanique céleste*, Suppléments au Livre X, 1805, 1806.
118. Bakker, G., Kapillartät und Oberflächenspannung, in *Handbuch der Experimentalphysik*, Vol. 6, Akademische Verlagsgesellschaft, Leipzig, 1928.
119. Princen, H.M., The equilibrium shape of interfaces, drops, and bubbles, in *Surface and Colloid Science*, Vol. 2, Matijević, E., Ed., Wiley, New York, 1969, p. 1.
120. Finn, R., *Equilibrium Capillary Surfaces*, Springer-Verlag, New York, 1986.
121. Weatherburn, C.E., *Differential Geometry in Three Dimensions*, Cambridge University Press, Cambridge, 1930.
122. McConnell, A.J., *Application of Tensor Analysis*, Dover, New York, 1957.
123. Young, T., *Philos. Trans. R. Soc. London*, 95, 55, 1805.
124. Jonson, R.E. and Dettre, R.H., Wettability and contact angles, in *Surface and Colloid Science*, Vol. 2, Matijević, E., Ed., Wiley, New York, 1969, 85.
125. Starov, V.M., *Adv. Colloid Interface Sci.*, 39, 147, 1992.
126. Neumann, F., *Vorlesungen über die Theorie der Capillarität*, B.G. Teubner, Leipzig, 1894.
127. Ivanov, I.B., Kralchevsky, P.A., and Nikolov, A.D., *J. Colloid Interface Sci.*, 112, 97, 1986.
128. Hartland, S. and Hartley, R.W., *Axisymmetric Fluid-Liquid Interfaces*, Elsevier, Amsterdam, 1976.
129. Kralchevsky, P.A., Eriksson, J.C., and Ljunggren, S., *Adv. Colloid Interface Sci.*, 48, 19, 1994.
130. Tachev, K.D. et al., *Colloids Surf. B*, 19, 61, 2000.
131. Meunier, J. and Lee, L.T., *Langmuir*, 7, 1855, 1991.
132. Dan, N., Pincus, P., and Safran, S.A., *Langmuir*, 9, 2768, 1993.
133. Kralchevsky, P.A. et al., *J. Chem. Soc. Faraday Trans.*, 91, 3415, 1995.
134. Petsev, D.N., Denkov, N.D., and Kralchevsky, P.A., *J. Colloid Interface Sci.*, 176, 201, 1995.
135. De Gennes, P.G. and Taupin, C., *J. Phys. Chem.*, 86, 2294, 1982.
136. Concus, P., *J. Fluid Mech.*, 34, 481, 1968.
137. Kralchevsky, P.A., Ivanov, I.B., and Nikolov, A.D., *J. Colloid Interface Sci.*, 112, 108, 1986.
138. Abramowitz, M. and Stegun, I.A., *Handbook of Mathematical Functions*, Dover, New York, 1965.
139. Janke, E., Emde, F., and Lösch, F., *Tables of Higher Functions*, McGraw-Hill, New York, 1960.
140. Lo, L.L., *J. Fluid Mech.*, 132, 65, 1983.
141. Derjaguin, B.V., *Dokl. Akad. Nauk U.S.S.R.*, 51, 517, 1946.
142. Scheludko, A., *Proc. K. Ned. Akad. Wet.*, B65, 87, 1962.
143. Scheludko, A., *Adv. Colloid Interface Sci.*, 1, 391, 1967.
144. Dimitrov, A.S. et al., *Colloids Surf.*, 47, 299, 1990.
145. Plateau, J., Experimental and theoretical researches on the figures of equilibrium of a liquid mass withdrawn from the action of gravity, in *The Annual Report of the Smithsonian Institution*, Washington, D.C., 1863, pp. 207–285.
146. Plateau, J., The figures of equilibrium of a liquid mass, in *The Annual Report of the Smithsonian Institution*, Washington, D.C., 1864, pp. 338–369.
147. Plateau, J., *Statique Expérimentale et Théoretique des Liquides Soumis aux Seules Forces Moléculaires*, Gauthier-Villars, Paris, 1873.
148. Zettlemoyer, A.C., *Nucleation*, Marcel Dekker, New York, 1969.
149. Abraham, E.F., *Homogeneous Nucleation Theory*, Academic Press, New York, 1974.
150. Thomson, W. (Lord Kelvin), *Proc. R. Soc.*, 9, 225, 1858; *Philos. Mag.*, 17, 61, 1859.
151. Lupis, C.H.P., *Chemical Thermodynamics of Materials*, North-Holland, New York, 1983.
152. Lifshitz, I.M. and Slyozov, V.V., *Zh. Exp. Teor. Fiz.*, 35, 479, 1958 [in Russian].
153. Wagner, C., *Z. Electrochem.*, 35, 581, 1961.
154. Kahlweit, M., *Faraday Discuss. Chem. Soc.*, 61, 48, 1976.
155. Parbhakar, K., Lewandowski, J., and Dao, L.H., *J. Colloid Interface Sci.*, 174, 142, 1995.
156. Kabalnov, A.S., Pertzov, A.V., and Shchukin, E.D., *Colloids Surf.*, 24, 19, 1987.
157. Kabalnov, A.S. and Shchukin, E.D., *Adv. Colloid Interface Sci.*, 38, 69, 1992.
158. McClements, D.J. et al., *Food Hydrocolloids*, 6, 415, 1992.
159. Weiss, J., Coupland, J.N., and McClements, D.J., *J. Phys. Chem.*, 100, 1066, 1996.
160. Weiss, J., Cancelliere, C., and McClements, D.J., *Langmuir*, 16, 6833, 2000.
161. Kabalnov, A.S., *Langmuir*, 10, 680, 1994.

162. Ivanov, I.B. and Kralchevsky, P.A., Mechanics and thermodynamics of curved thin liquid films, in *Thin Liquid Films*, Ivanov, I.B., Ed., Marcel Dekker, New York, 1988, p. 49.
163. Kralchevsky, P.A. and Ivanov, I.B., *J. Colloid Interface Sci.*, 137, 234, 1990.
164. Kralchevsky, P.A., Danov, K.D., and Ivanov, I.B., Thin liquid film physics, in *Foams: Theory, Measurements and Applications*, Prud'homme, R.K., Ed., Marcel Dekker, New York, 1995, p. 1.
165. Rusanov, A.I., *Phase Equilibria and Surface Phenomena*, Khimia, Leningrad, 1967 [Russian]; *Phasengleichgewichte und Grenzflächenerscheinungen*, Akademie Verlag, Berlin, 1978 [German].
166. Derjaguin, B.V. and Kussakov, M.M., *Acta Physicochem. U.S.S.R.*, 10, 153, 1939.
167. Exerowa, D. and Scheludko, A., *Bull. Inst. Chim. Phys. Bulg. Acad. Sci.*, 4, 175, 1964.
168. Mysels, K.J., *J. Phys. Chem.*, 68, 3441, 1964.
169. Exerowa, D., *Commun. Dept. Chem. Bulg. Acad. Sci.*, 11, 739, 1978.
170. Kruglyakov, P.M., Equilibrium properties of free films and stability of foams and emulsions, in *Thin Liquid Films*, Ivanov, I.B., Ed., Marcel Dekker, New York, 1988, p. 767.
171. Martynov, G.A. and Derjaguin, B.V., *Kolloidn. Zh.*, 24, 480, 1962.
172. Toshev, B.V. and Ivanov, I.B., *Colloid Polym. Sci.*, 253, 558, 1975.
173. Ivanov, I.B. and Toshev, B.V., *Colloid Polym. Sci.*, 253, 593, 1975.
174. Frumkin, A., *Zh. Phys. Khim. U.S.S.R.*, 12, 337, 1938.
175. de Feijter, J.A., Thermodynamics of thin liquid films, in *Thin Liquid Films*, Ivanov, I.B., Ed., Marcel Dekker, New York, 1988, p. 1.
176. Kralchevsky, P.A. and Ivanov, I.B., *Chem. Phys. Lett.*, 121, 111, 1985.
177. Nikolov, A.D. et al., *AIChE Symp. Ser.*, 252, Vol. 82, 82, 1986.
178. de Feijter, J.A. and Vrij, A., *J. Electroanal. Chem.*, 47, 9, 1972.
179. Kralchevsky, P.A. and Ivanov, I.B., *Chem. Phys. Lett.*, 121, 116, 1985.
180. Denkov, N.D., Petsev, D.N., and Danov, K.D., *J. Colloid Interface Sci.*, 176, 189, 1995.
181. Derjaguin, B.V., *Acta Physicochim. U.S.S.R.*, 12, 181, 1940.
182. Princen, H.M. and Mason, S.G., *J. Colloid Sci.*, 20, 156, 1965.
183. Prins, A., *J. Colloid Interface Sci.*, 29, 177, 1969.
184. Clint, J.H. et al., *Nature (London)*, 223, 291, 1969.
185. Yamanaka, T., *Bull. Chem. Soc. Jpn.*, 48, 1755, 1975.
186. Princen, H.M., *J. Phys. Chem.*, 72, 3342, 1968.
187. Princen, H.M. and Frankel, S., *J. Colloid Interface Sci.*, 35, 186, 1971.
188. Scheludko, A., Radoev, B., and Kolarov, T., *Trans. Faraday Soc.*, 64, 2213, 1968.
189. Haydon, D.A. and Taylor, J.L., *Nature (London)*, 217, 739, 1968.
190. Kolarov, T. and Zorin, Z.M., *Kolloidn. Zh.*, 42, 899, 1980.
191. Kruglyakov, P.M. and Rovin, Yu.G., *Physical Chemistry of Black Hydrocarbon Films*, Nauka, Moscow, 1978 [in Russian].
192. Marinova, K.G. et al., *Langmuir*, 14, 2011, 1998.
193. Françon, M., *Progress in Microscopy*, Pergamon Press, London, 1961.
194. Beyer, H., *Theorie und Praxis der Interferenzmicroscopie*, Akademische Verlagsgesellschaft, Leipzig, 1974.
195. Zorin, Z.M., *Kolloidn. Zh.*, 39, 1158, 1977.
196. Zorin, Z. et al., in *Surface Forces and Liquid Interfaces*, Derjaguin, B.V., Ed., Nauka, Moscow, 1983, p. 200 [in Russian].
197. Nikolov, A.D., Kralchevsky, P.A., and Ivanov, I.B., *J. Colloid Interface Sci.*, 112, 122, 1986.
198. Lobo, L.A. et al., *Langmuir*, 6, 995, 1990.
199. Dimitrov, A.S. et al., *J. Colloid Interface Sci.*, 151, 462, 1992.
200. Picard, G., Schneider, J.E., and Fendler, J.H., *J. Phys. Chem.*, 94, 510, 1990.
201. Picard, G., Denicourt, N., and Fendler, J.H., *J. Phys. Chem.*, 95, 3705, 1991.
202. Skinner, F.K., Rotenberg, Y., and Neumann, A.W., *J. Colloid Interface Sci.*, 130, 25, 1989.
203. Dimitrov, A.S. et al., *J. Colloid Interface Sci.*, 145, 279, 1991.
204. Hadjiiski, A. et al., *Langmuir*, 12, 6665, 1996.
205. Ivanov, I.B. et al., *Biophys. J.*, 75, 545, 1998.
206. Nicolson, M.M., *Proc. Camb. Philos. Soc.*, 45, 288, 1949.
207. Chan, D.Y.C., Henry, J.D., and White, L.R., *J. Colloid Interface Sci.*, 79, 410, 1981.

208. Paunov, V.N. et al., *J. Colloid Interface Sci.*, 157, 100, 1993.
209. Kralchevsky, P.A. et al., *J. Colloid Interface Sci.*, 151, 79, 1992.
210. Kralchevsky, P.A. et al., *J. Colloid Interface Sci.*, 155, 420, 1993.
211. Kralchevsky, P.A. and Nagayama, K., *Langmuir*, 10, 23, 1994.
212. Kralchevsky, P.A. and Nagayama, K., *Adv. Colloid Interface Sci.*, 85, 145, 2000.
213. Denkov, N.D. et al., *Langmuir*, 8, 3183, 1992.
214. Dimitrov, A.S. et al., *Langmuir*, 10, 432, 1994.
215. Sasaki, M. and Hane, K., *J. Appl. Phys.*, 80, 5427, 1996.
216. Du, H. et al., *Mater. Chem. Phys.*, 51, 277, 1977.
217. Price, W.C., Williams, R.C., and Wyckoff, R.W.G., *Science*, 102, 277, 1945.
218. Cosslett, V.E. and Markham, R., *Nature* (London), 161, 250, 1948.
219. Horne, R.W. and Pasquali-Ronchetti, I., *J. Ultrastruct. Res.*, 47, 361, 1974.
220. Harris, J.R., *Micron Microsc. Acta*, 22, 341, 1991.
221. Yoshimura, H. et al., *Ultramicroscopy*, 32, 265, 1990.
222. Yamaki, M., Higo, J., and Nagayama, K., *Langmuir*, 11, 2975, 1995.
223. Nagayama, K., *Colloids Surf. A*, 109, 363, 1996.
224. Burmeister, F. et al., *Adv. Mater.*, 10, 495, 1998.
225. Xia, Y. et al., *Langmuir*, 12, 4033, 1996.
226. Lindström, H. et al., *J. Phys. Chem.*, 100, 3084, 1996.
227. Matsushita, S., Miwa, T., and Fujishima, A., *Langmuir*, 13, 2582, 1997.
228. Murray, C.B., Kagan, C.R., and Bawendi, M.G., *Science*, 270, 1335, 1995.
229. Jap, B.K. et al., *Ultramicroscopy*, 46, 45, 1992.
230. De Rossi, D., Ahluwalia, A., and Mulè, M., *IEEE Eng. Med. Biol.*, 13, 103, 1994.
231. Kralchevsky, P.A. and Denkov, N.D., *Curr. Opinion Colloid Interface Sci.*, 6, 383, 2001.
232. Gil, T. et al., *Biochim. Biophys. Acta*, 1376, 245, 1998.
233. Mansfield, S.L., Gotch, A.J., and Harms, G.S., *J. Phys. Chem. B*, 103, 2262, 1999.
234. Fisher, L.R. and Malloy A.R., *Annu. Rep. Prog. Chem.*, Sect. C, 95, 373, 1999.
235. Kralchevsky, P.A., Paunov, V.N., and Nagayama, K., *J. Fluid Mech.*, 299, 105, 1995.
236. Camoin, C. et al., *Europhys. Lett.*, 3, 449, 1987.
237. Velev, O.D. et al., *Langmuir*, 9, 3702, 1993.
238. Dushkin, C.D. et al., *Phys. Rev. Lett.*, 75, 3454, 1995.
239. Lucassen, J., *Colloids Surf.*, 65, 131, 1992.
240. Stamou, D., Duschl, C., and Johannsmann, D., *Phys. Rev. E*, 62, 5263, 2000.
241. Kralchevsky, P.A., Denkov, N.D., and Danov, K.D., *Langmuir*, 17, 7694, 2001.
242. Bowden, N. et al., *Science*, 276, 233, 1997.
243. Bowden, N. et al., *J. Am. Chem. Soc.*, 121, 5373, 1999.
244. Velikov, K.P., Durst, F., and Velev, O.D., *Langmuir*, 14, 1148, 1998.
245. Sur, J. and Pak, H.K., *J. Korean Phys. Soc.*, 38, 582, 2001.
246. Danov, K.D. et al., in *Studies in Surface Science and Catalysis*, Vol. 132, Iwasawa, Y., Oyama, N., and Kunieda, H., Eds., Elsevier, Amsterdam, 2001, p. 519.
247. Danov, K.D., Pouligny, B., and Kralchevsky, P.A., *Langmuir*, 17, 6599, 2001.
248. Kralchevsky, P.A. et al., *J. Colloid Interface Sci.*, 167, 47, 1994.
249. Velev, O.D. et al., *J. Colloid Interface Sci.*, 167, 66, 1994.
250. Petkov, J.T. et al., *J. Colloid Interface Sci.*, 172, 147, 1995.
251. Danov, K.D. et al., *J. Colloid Interface Sci.*, 175, 36, 1995.
252. Petkov, J.T. et al., *Langmuir*, 12, 2650, 1996.
253. Petkov, J.T., Gurkov, T.D., and Campbell, B.E., *Langmuir*, 17, 4556, 2001.
254. Derjaguin, B.V., Churaev, N.V., and Muller, V.M., *Surface Forces*, Plenum Press, Consultants Bureau, New York, 1987.
255. Derjaguin, B.V., *Kolloid Z.*, 69, 155, 1934.
256. Attard, P. and Parker, J.L., *J. Phys. Chem.*, 96, 5086, 1992.
257. Tabor, D. and Winterton, R.H.S., *Nature* (London), 219, 1120, 1968.
258. Keesom, W.H., *Proc. Amst.*, 15, 850, 1913.
259. Debye, P., *Physik*, 2, 178, 1920.
260. London, F., *Z. Physics*, 63, 245, 1930.

261. Hamaker, H.C., *Physics*, 4, 1058, 1937.
262. Usui, S., Sasaki, H., and Hasegawa, F., *Colloids Surf.*, 18, 53, 1986.
263. Lifshitz, E.M., *Soviet Phys. JETP* (Engl. Transl.), 2, 73, 1956.
264. Dzyaloshinskii, I.E., Lifshitz, E.M., and Pitaevskii, L.P., *Adv. Phys.*, 10, 165, 1961.
265. Nir, S. and Vassilieff, C.S., Van der Waals interactions in thin films, in *Thin Liquid Films*, Ivanov, I.B., Ed., Marcel Dekker, New York, 1988, p. 207.
266. Danov, K.D. et al., *J. Chem. Phys.*, 99, 7179, 1993.
267. Casimir, H.R. and Polder, D., *Phys. Rev.*, 73, 360, 1948.
268. Mahanty, J. and Ninham, B.W., *Dispersion Forces*, Academic Press, New York, 1976.
269. Moelwyn-Hughes, E.A., *Physical Chemistry*, Pergamon Press, London, 1961, chap. 21.
270. Langmuir, I., *J. Chem. Phys.*, 6, 873, 1938.
271. Tenchov, B.G. and Brankov, J.G., *J. Colloid Interface Sci.*, 109, 172, 1986.
272. Vassilieff, C.S. et al., *J. Colloid Interface Sci.*, 93, 8, 1983.
273. Verwey, E.J.W. and Overbeek, J.Th.G., *The Theory of Stability of Lyophobic Colloids*, Elsevier, Amsterdam, 1948.
274. Muller, V.M., *Kolloidn. Zh.*, 38, 704, 1976.
275. McCormack, D., Carnie, S.L., and Chan, D.Y.C., *J. Colloid Interface Sci.*, 169, 177, 1995.
276. Hogg, R., Healy, T.W., and Fuerstenau, D.W., *Trans. Faraday Soc.*, 62, 1638, 1966.
277. Usui, S., *J. Colloid Interface Sci.*, 44, 107, 1973.
278. Russel, W.B., Saville, D.A., and Schowalter, W.R., *Colloidal Dispersions*, Cambridge University Press, Cambridge, 1989.
279. Debye, P. and Hückel, E., *Z. Phys.*, 24, 185, 1923.
280. McCartney, L.N. and Levine, S., *J. Colloid Interface Sci.*, 30, 345, 1969.
281. Derjaguin, B.V. and Landau, L.D., *Acta Physicochim. U.S.S.R.*, 14, 633, 1941.
282. Efremov, I.F., Periodic colloidal structures, in *Colloid and Surface Science*, Vol. 8, Matijević, E., Ed., Wiley, New York, 1976, p. 85.
283. Schultze, H., *J. Prakt. Chem.*, 25, 431, 1882.
284. Hardy, W.B., *Proc. R. Soc. London*, 66, 110, 1900.
285. Guldbrand, L. et al., *J. Chem. Phys.*, 80, 2221, 1984.
286. Kjellander, R. and Marčelja, S., *J. Phys. Chem.*, 90, 1230, 1986.
287. Attard, P., Mitchell, D.J., and Ninham, B.W., *J. Chem. Phys.*, 89, 4358, 1988.
288. Kralchevsky, P.A. and Paunov, V.N., *Colloids Surf.*, 64, 245, 1992.
289. Danov, K.D., Kralchevsky, P.A., and Ivanov, I.B., in *Handbook of Detergents, Part A: Properties*, Broze, G., Ed., Marcel Dekker, New York, 1999, p. 303.
290. Marra, J., *J. Phys. Chem.*, 90, 2145, 1986.
291. Marra, J., *Biophys. J.*, 50, 815, 1986.
292. Kjellander, R. et al., *J. Phys. Chem.*, 92, 6489, 1988.
293. Kjellander, R. et al., *J. Chem. Phys.*, 92, 4399, 1990.
294. Khan, A., Jönsson, B., and Wennerström, H., *J. Phys. Chem.*, 89, 5180, 1985.
295. Kohonen, M.M., Karaman, M.E., and Pashley, R.M., *Langmuir*, 16, 5749, 2000.
296. Paunov, V.N. and Kralchevsky, P.A., *Colloids Surf.*, 64, 265, 1992.
297. Tadros, Th.F., Steric interactions in thin liquid films, in *Thin Liquid Films*, Ivanov, I.B., Ed., Marcel Dekker, New York, 1988, p. 331.
298. Patel, S.S. and Tirlé, M., *Annu. Rev. Phys. Chem.*, 40, 597, 1989.
299. Ploehn, H.J. and Russel, W.B., *Adv. Chem. Eng.*, 15, 137, 1990.
300. de Gennes, P.G., *Scaling Concepts in Polymer Physics*, Cornell University Press, Ithaca, NY, 1979, chap. 3.
301. Dolan, A.K. and Edwards, S.F., *Proc. R. Soc. London*, A337, 509, 1974.
302. Dolan, A.K. and Edwards, S.F., *Proc. R. Soc. London*, A343, 627, 1975.
303. de Gennes, P.G., *C.R. Acad. Sci. (Paris)*, 300, 839, 1985.
304. de Gennes, P.G., *Adv. Colloid Interface Sci.*, 27, 189, 1987.
305. Alexander, S.J., *Physique*, 38, 983, 1977.
306. Taunton, H.J. et al., *Macromolecules*, 23, 571, 1990.
307. Klein, J. and Luckham, P., *Nature (London)*, 300, 429, 1982; *Macromolecules*, 17, 1041, 1984.
308. Luckham, P.F. and Klein, J., *J. Chem. Soc. Faraday Trans.*, 86, 1363, 1990.

309. Sonntag, H. et al., *Adv. Colloid Interface Sci.*, 16, 381, 1982.
310. Horn, R.G. and Israelachvili, J.N., *Chem. Phys. Lett.*, 71, 192, 1980.
311. Nikolov, A.D. et al., Ordered structures in thinning micellar foam and latex films, in *Ordering and Organisation in Ionic Solutions*, Ise, N. and Sogami, I., Eds., World Scientific, Singapore, 1988.
312. Nikolov, A.D. and Wasan, D.T., *J. Colloid Interface Sci.*, 133, 1, 1989.
313. Nikolov, A.D. et al., *J. Colloid Interface Sci.*, 133, 13, 1989.
314. Nikolov, A.D. et al., *Prog. Colloid Polym. Sci.*, 82, 87, 1990.
315. Wasan, D.T. et al., *Colloids Surf.*, 67, 139, 1992.
316. Asakura, S. and Oosawa, F., *J. Chem. Phys.*, 22, 1255, 1954; *J. Polym. Sci.*, 33, 183, 1958.
317. de Hek, H. and Vrij, A., *J. Colloid Interface Sci.*, 84, 409, 1981.
318. Snook, I.K. and van Megen, W., *J. Chem. Phys.*, 72, 2907, 1980.
319. Kjellander, R. and Marčelja, S., *Chem Phys Lett.*, 120, 393, 1985.
320. Tarazona, P. and Vicente, L., *Mol. Phys.*, 56, 557, 1985.
321. Evans, R., and Parry, A.O., *J. Phys. Condens. Matter*, 2, SA15, 1990.
322. Henderson, J.R., *Mol. Phys.*, 59, 89, 1986.
323. Henderson, D., *J. Colloid Interface Sci.*, 121, 486, 1988.
324. Kralchevsky, P.A. and Denkov, N.D. *Chem. Phys. Lett.*, 240, 385, 1995; *Prog. Colloid Polym. Sci.*, 98, 18, 1995.
325. Carnahan, N.F. and Starling, K.E., *J. Chem. Phys.*, 51, 635, 1969.
326. Kjellander, R. and Sarman, S., *Chem. Phys. Lett.*, 149, 102, 1988.
327. Beresford-Smith, B. and Chan, D.Y.C., *Chem. Phys. Lett.*, 92, 474, 1982.
328. Richetti, P. and Kékicheff, P., *Phys. Rev. Lett.*, 68, 1951, 1992.
329. Karlström, G., *Chem. Scripta*, 25, 89, 1985.
330. Bondy, C., *Trans. Faraday Soc.*, 35, 1093, 1939.
331. Patel, P.D. and Russel, W.B., *J. Colloid Interface Sci.*, 131, 192, 1989.
332. Aronson, M.P., *Langmuir*, 5, 494, 1989.
333. van Lent, B. et al., *J. Colloid Interface Sci.*, 137, 380, 1990.
334. Joanny, J.F., Leibler, L., and de Gennes, P.G., *J. Polym. Sci.*, 17, 1073, 1979.
335. Evans, E. and Needham, D., *Macromolecules*, 21, 1822, 1988.
336. Johnnot, E.S., *Philos. Mag.*, 70, 1339, 1906.
337. Perrin, R.E., *Ann. Phys.*, 10, 160, 1918.
338. Bruil, H.G. and Lyklema, J., *Nature (London)*, 233, 19, 1971.
339. Friberg, S., Linden, St.E., and Saito, H., *Nature (London)*, 251, 494, 1974.
340. Keuskamp, J.W. and Lyklema, J., *ACS Symp. Ser.*, 8, 191, 1975.
341. Kruglyakov, P.M., *Kolloidn. Zh.*, 36, 160, 1974.
342. Kruglyakov, P.M. and Rovin, Yu.G., *Physical Chemistry of Black Hydrocarbon Films*, Nauka, Moscow, 1978 [in Russian].
343. Manev, E., Sazdanova, S.V., and Wasan, D.T., *J. Dispersion Sci. Technol.*, 5, 111, 1984.
344. Basheva, E.S. et al., in *Surfactants in Solution*, Vol. 12, Mittal, K.L., and Shah, D.O., Eds., Plenum Press, New York, 1991, p. 467.
345. Bergeron, V. and Radke, C.J., *Langmuir*, 8, 3020, 1992.
346. Kralchevsky, P.A. et al., *Langmuir*, 6, 1180, 1990.
347. Claesson, P.M. et al., *J. Chem. Soc. Faraday Trans. I*, 82, 2735, 1986.
348. Parker, J.L., Richetti, P., and Kékicheff, P., *Phys. Rev. Lett.*, 68, 1955, 1992.
349. Basheva, E.S., Danov, K.D., and Kralchevsky, P.A., *Langmuir*, 13, 4342, 1997.
350. Dushkin, C.D. et al., *Langmuir*, 9, 3695, 1993.
351. Pollard, M.L. and Radke, C.J., *J. Chem. Phys.*, 101, 6979, 1994.
352. Chu, X.L., Nikolov, A.D., and Wasan, D.T., *Langmuir*, 10, 4403, 1994.
353. Chu, X.L., Nikolov, A.D., and Wasan, D.T., *J. Chem. Phys.*, 103, 6653, 1995.
354. Stanley, H.E. and Teixeira, J., *J. Chem. Phys.*, 73, 3404, 1980.
355. Israelachvili, J.N. and Adams, G.E., *J. Chem. Soc. Faraday Trans. 1*, 74, 975, 1978.
356. Israelachvili, J.N. and Pashley, R.M., *Nature (London)*, 300, 341, 1982.
357. Pashley, R.M., *J. Colloid Interface Sci.*, 80, 153, 1981.
358. Pashley, R.M., *J. Colloid Interface Sci.*, 83, 531, 1981.
359. Healy, T.W. et al., *Faraday Discuss. Chem. Soc.*, 65, 156, 1978.

360. Marčelja, S. and Radič, N., *Chem. Phys Lett.*, 42, 129, 1976.
361. Schibi, D. and Ruckenstein, E., *Chem. Phys Lett.*, 95, 435, 1983.
362. Attard, P. and Batchelor, M.T., *Chem. Phys. Lett.*, 149, 206, 1988.
363. Jönsson, B. and Wennerström, H., *J. Chem. Soc. Faraday Trans. 2*, 79, 19, 1983.
364. Leikin, S. and Kornyshev, A.A., *J. Chem. Phys.*, 92, 6890, 1990.
365. Israelachvili, J.N. and Wennerström, H., *J. Phys. Chem.*, 96, 520, 1992.
366. Henderson, D. and Lozada-Cassou, M., *J. Colloid Interface Sci.*, 114, 180, 1986; *J. Colloid Interface Sci.*, 162, 508, 1994.
367. Basu, S. and Sharma, M.M., *J. Colloid Interface Sci.*, 165, 355, 1994.
368. Paunov, V.N. et al., *J. Colloid Interface Sci.*, 182, 239, 1996.
369. Booth, F., *J. Chem. Phys.*, 19, 391, 1951.
370. Bikerman, J.J., *Philos. Mag.*, 33, 384, 1942.
371. Rowlinson, J.S., Development of theories of inhomogeneous fluids, in *Fundamentals of Inhomogeneous Fluids*, Henderson, D., Ed., Marcel Dekker, New York, 1992.
372. Claesson, P., Carmona-Ribeiro, A.M., and Kurihara, K., *J. Phys. Chem.*, 93, 917, 1989.
373. Horn, R.G., Smith, D.T., and Haller, W., *Chem. Phys. Lett.*, 162, 404, 1989.
374. Tchaliowska, S. et al., *Langmuir*, 6, 1533, 1990.
375. Pashley, R.M. et al., *Science*, 229, 1088, 1985.
376. Rabinovich, Y.I. and Derjaguin, B.V., *Colloids Surf.*, 30, 243, 1988.
377. Parker, J.L., Cho, D.L., and Claesson, P.M., *J. Phys. Chem.*, 93, 6121, 1989.
378. Christenson, H.K. et al., *J. Phys. Chem.*, 93, 1472, 1989.
379. Christenson, H.K. et al., *J. Phys. Chem.*, 94, 8004, 1990.
380. Ducker, W.A., Xu, Z., and Israelachvili, J.N., *Langmuir*, 10, 3279, 1994.
381. Eriksson J.C., Ljunggren, S., and Claesson, P.M., *J. Chem. Soc. Faraday Trans. 2*, 85, 163, 1989.
382. Joesten, M.D. and Schaad, L.J., *Hydrogen Bonding*, Marcel Dekker, New York, 1974.
383. Stillinger, F.H. and Ben-Naim, A., *J. Chem. Phys.*, 47, 4431, 1967.
384. Conway, B.E., *Adv. Colloid Interface Sci.*, 8, 91, 1977.
385. Kuzmin, V.L. and Rusanov, A.I., *Kolloidn. Zh.*, 39, 455, 1977.
386. Dubrovich, N.A., *Kolloidn. Zh.*, 57, 275, 1995.
387. Christenson, H.K. and Claesson, P.M., *Science*, 239, 390, 1988.
388. Parker, J.L., Claesson, P.M., and Attard, P., *J. Phys. Chem.*, 98, 8468, 1994.
389. Carambassis, A. et al., *Phys. Rev. Lett.*, 80, 5357, 1998.
390. Mahnke, J. et al., *Phys. Chem. Chem. Phys.*, 1, 2793, 1999.
391. Considine, R.F., Hayes, R.A., and Horn, R.G., *Langmuir*, 15, 1657, 1999.
392. Considine, R.F. and Drummond, C., *Langmuir*, 16, 631, 2000.
393. Attard, P., *Langmuir*, 16, 4455, 2000.
394. Yakubov, G.E., Butt, H.-J., and Vinogradova, O., *J. Phys. Chem. B*, 104, 3407, 2000.
395. Ederth, T., *J. Phys Chem. B*, 104, 9704, 2000.
396. Ishida, N. et al., *Langmuir*, 16, 5681, 2000.
397. Ishida, N. et al., *Langmuir*, 16, 6377, 2000.
398. Tanford, C., *The Hydrophobic Effect*, Wiley, New York, 1980.
399. Leckband, D.E. et al., *Science*, 255, 1419, 1992.
400. Helfrich, W., *Z. Naturforsch.*, 33a, 305, 1978.
401. Servuss, R.M. and Helfrich, W., *J. Phys. (France)*, 50, 809, 1989.
402. Fernandez-Puente, L. et al., *Europhys. Lett.*, 28, 181, 1994.
403. Safinya, C.R. et al., *Phys. Rev. Lett.*, 57, 2718, 1986.
404. McIntosh, T.J., Magid, A.D., and Simon, S.A., *Biochemistry*, 28, 7904, 1989.
405. Abillon, O. and Perez, E., *J. Phys. (France)*, 51, 2543, 1990.
406. Evans, E.A. and Skalak, R., *Mechanics and Thermodynamics of Biomembranes*, CRC Press, Boca Raton, FL, 1980.
407. Aniansson, G.A.E. et al., *J. Phys. Chem.*, 80, 905, 1976.
408. Aniansson, G.A.E., *J. Phys. Chem.*, 82, 2805, 1978.
409. Dimitrova, T.D. et al., *Langmuir*, 17, 8069, 2001.
410. Bird, R.B., Stewart, W.E., and Lightfoot, E.N., *Transport Phenomena*, Wiley, New York, 1960.
411. Germain, P., *Mécanique des Milieux Continus*, Masson et Cie, Paris, 1962.

412. Batchelor, G.K., *An Introduction of Fluid Mechanics*, Cambridge University Press, London, 1967.
413. Slattery, J.C., *Momentum, Energy, and Mass Transfer in Continua*, R.E. Krieger, Huntington, NY, 1978.
414. Landau, L.D. and Lifshitz, E.M., *Fluid Mechanics*, Pergamon Press, Oxford, 1984.
415. Barnes, H.A., Hutton, J.F., and Walters, K., *An Introduction to Rheology*, Elsevier, Amsterdam, 1989.
416. Walters, K., Overview of macroscopic viscoelastic flow, in *Viscoelasticity and Rheology*, Lodge, A.S., Renardy, M., and Nohel, J.A., Eds., Academic Press, London, 1985, p. 47.
417. Boger, D.V., *Annu. Rev. Fluid Mech.*, 19, 157, 1987.
418. Barnes, H.A., *J. Rheol.*, 33, 329, 1989.
419. Navier, M., *Mém. Acad. Sci.*, 6, 389, 1827.
420. Stokes, G.G., *Trans. Cambr. Philos. Soc.*, 8, 287, 1845.
421. Happel, J. and Brenner, H., *Low Reynolds Number Hydrodynamics with Special Applications to Particulate Media*, Prentice-Hall, Englewood Cliffs, NJ, 1965.
422. Kim, S. and Karrila, S.J., *Microhydrodynamics: Principles and Selected Applications*, Butterworth-Heinemann, Boston, 1991.
423. Reynolds, O., *Philos. Trans. R. Soc. London*, A177, 157, 1886.
424. Lamb, H., *Hydrodynamics*, Cambridge University Press, London, 1963.
425. Felderhof, B.U., *J. Chem. Phys.*, 49, 44, 1968.
426. Sche, S. and Fijnaut, H.M., *Surface Sci.*, 76, 186, 1976.
427. Maldarelli, Ch. and Jain, R.K., The hydrodynamic stability of thin films, in *Thin Liquid Films*, Ivanov, I.B., Ed., Marcel Dekker, New York, 1988, p. 497.
428. Valkovska, D.S. and Danov, K.D., *J. Colloid Interface Sci.*, 241, 400, 2001.
429. Taylor, P., *Proc. R. Soc. London*, A108, 11, 1924.
430. Dimitrov, D.S. and Ivanov, I.B., *J. Colloid Interface Sci.*, 64, 97, 1978.
431. Ivanov, I.B. et al., *Chem. Eng. Sci.*, 40, 137, 1985.
432. Ivanov, I.B. and Dimitrov, D.S., Thin film drainage, in *Thin Liquid Films*, Ivanov, I.B., Ed., Marcel Dekker, New York, 1988, p. 379.
433. O'Neill, M.E. and Stewartson, K., *J. Fluid Mech.*, 27, 705, 1967.
434. Goldman, A.J., Cox, R.G., and Brenner, H., *Chem. Eng. Sci.*, 22, 637, 1967.
435. Goldman, A.J., Cox, R.G., and Brenner, H., *Chem. Eng. Sci.*, 22, 653, 1967.
436. Levich, V.G., *Physicochemical Hydrodynamics*, Prentice-Hall, Englewood Cliffs, NJ, 1962.
437. Edwards, D.A., Brenner, H., and Wasan, D.T., *Interfacial Transport Processes and Rheology*, Butterworth-Heinemann, Boston, 1991.
438. Charles, G.E. and Mason, S.G., *J. Colloid Sci.*, 15, 236, 1960.
439. Danov, K.D. et al., *Langmuir*, 9, 1731, 1993.
440. Danov, K.D., Valkovska, D.S., and Ivanov, I.B., *J. Colloid Interface Sci.*, 211, 291, 1999.
441. Hartland, S., Coalescence in dense-packed dispersions, in *Thin Liquid Films*, Ivanov, I.B., Ed., Marcel Dekker, New York, 1988, p. 663.
442. Hetsroni, G., Ed., *Handbook of Multiphase System*, Hemisphere Publishing, New York, 1982, pp. 1–96.
443. Davis, A.M.J., Kezirian, M.T., and Brenner, H., *J. Colloid Interface Sci.*, 165, 129, 1994.
444. Brenner, H., *Chem. Eng. Sci.*, 18, 1, 1963.
445. Brenner, H., *Chem. Eng. Sci.*, 19, 599, 1964; *Chem. Eng. Sci.*, 19, 631, 1964.
446. Brenner, H. and O'Neill, M.E., *Chem. Eng. Sci.*, 27, 1421, 1972.
447. Van de Ven, T.G.M., *Colloidal Hydrodynamics*, Academic Press, London, 1988.
448. Jeffery, G.B., *Proc. Lond. Math. Soc.*, 14, 327, 1915.
449. Stimson, M. and Jeffery, G.B., *Proc. R. Soc. London*, A111, 110, 1926.
450. Cooley, M.D.A. and O'Neill, M.E., *Mathematika*, 16, 37, 1969.
451. Cooley, M.D.A. and O'Neill, M.E., *Proc. Cambridge Philos. Soc.*, 66, 407, 1969.
452. Davis, M.H., *Chem. Eng. Sci.*, 24, 1769, 1969.
453. O'Neill, M.E. and Majumdar, S.R., *Z. Angew. Math. Phys.*, 21, 164, 1970; *Z. Angew. Math. Phys.*, 21, 180, 1970.
454. Davis, M.H., *Two Unequal Spheres in a Slow Linear Shear Flow*, Rept. NCAR-TN/STR-64, National Center for Atmospheric Research, Boulder, CO, 1971.
455. Batchelor, G.K., *J. Fluid Mech.*, 74, 1, 1976.
456. Davis, R.H. and Hill, N.A., *J. Fluid Mech.*, 236, 513, 1992.

457. Batchelor, G.K., *J. Fluid Mech.*, 119, 379, 1982.
458. Batchelor, G.K. and Wen, C.-S., *J. Fluid Mech.*, 124, 495, 1982.
459. Jeffrey, D.J. and Onishi, Y., *J. Fluid Mech.*, 139, 261, 1984.
460. Fuentes, Y.O., Kim, S., and Jeffrey, D.J., *Phys. Fluids*, 31, 2445, 1988; *Phys. Fluids*, A1, 61, 1989.
461. Stokes, G.G., *Trans. Cambridge Philos. Soc.*, 1, 104, 1851.
462. Exerowa, D. and Kruglyakov, P.M., *Foam and Foam Films: Theory, Experiment, Application*, Elsevier, New York, 1998.
463. Ivanov, I.B. et al., *Proceedings of the International Conference on Colloid Surface Science*, Wolfram, E., Ed., Akademia Kiado, Budapest, 1975, p. 583.
464. Denkov, N.D., Petsev, D.N., and Danov, K.D., *Phys. Rev. Lett.*, 71, 3226, 1993.
465. Valkovska, D.S., Danov, K.D., and Ivanov, I.B., *Colloid Surf. A*, 156, 547, 1999.
466. Davis, R.H., Schonberg, J.A., and Rallison, J.M., *Phys. Fluids*, A1, 77, 1989.
467. Chi, B.K. and Leal, L.G., *J. Fluid Mech.*, 201, 123, 1989.
468. Ascoli, E.P., Dandy, D.S., and Leal, L.G., *J. Fluid Mech.*, 213, 287, 1990.
469. Yiantsios, S.G. and Davis, R.H., *J. Fluid Mech.*, 217, 547, 1990.
470. Zhang, X. and Davis, R.H., *J. Fluid Mech.*, 230, 479, 1991.
471. Chesters, A.K., *Trans. Inst. Chem. Eng. A*, 69, 259, 1991.
472. Yiantsios, S.G. and Davis, R.H., *J. Colloid Interface Sci.*, 144, 412, 1991.
473. Yiantsios, S.G. and Higgins, B.G., *J. Colloid Interface Sci.*, 147, 341, 1991.
474. Joye, J.-L., Hirasaki, G.J., and Miller, C.A., *Langmuir*, 8, 3083, 1992.
475. Joye, J.-L., Hirasaki, G.J., and Miller, C.A., *Langmuir*, 10, 3174, 1994.
476. Abid, S. and Chesters, A.K., *Int. J. Multiphase Flow*, 20, 613, 1994.
477. Li, D., *J. Colloid Interface Sci.*, 163, 108, 1994.
478. Saboni, A., Gourdon, C., and Chesters, A.K., *J. Colloid Interface Sci.*, 175, 27, 1995.
479. Rother, M.A., Zinchenko, A.Z., and Davis, R.H., *J. Fluid Mech.*, 346, 117, 1997.
480. Singh, G., Miller, C.A., and Hirasaki, G.J., *J. Colloid Interface Sci.*, 187, 334, 1997.
481. Cristini, V., Blawdziewicz, J., and Loewenberg, M., *J. Fluid Mech.*, 366, 259, 1998.
482. Bazhlekov, I.B., Chesters, A.K., and van de Vosse, F.N., *Int. J. Multiphase Flow*, 26, 445, 2000.
483. Bazhlekov, I.B., van de Vosse, F.N., and Chesters, A.K., *J. Non-Newtonian Fluid Mech.*, 93, 181, 2000.
484. Chesters, A.K. and Bazhlekov, I.B., *J. Colloid Interface Sci.*, 230, 229–243, 2000.
485. Boulton-Stone, J.M. and Blake, J.R., *J. Fluid Mech.*, 254, 437, 1993.
486. Frankel, S. and Mysels, K., *J. Phys. Chem.*, 66, 190, 1962.
487. Velev, O.D. et al., *J. Colloid Interface Sci.*, 175, 68, 1995.
488. Exerowa, D., Nikolov, A., and Zacharieva, M., *J. Colloid Interface Sci.*, 81, 419, 1981.
489. de Vries, A.J., *Rec. Trav. Chim. Pays-Bas. Belg.*, 77, 441, 1958.
490. Vrij, A., *Discuss. Faraday Soc.*, 42, 23, 1966.
491. Ivanov, I.B. et al., *Trans. Faraday Soc.*, 66, 1262, 1970.
492. Gumerman, R.J. and Homsey, G.M., *Chem. Eng. Commun.*, 2, 27, 1975.
493. Malhotra, A.K. and Wasan, D.T., *Chem. Eng. Commun.*, 48 35, 1986.
494. Valkovska, D.S., Danov, K.D., and Ivanov, I.B., *Adv. Colloid Interface Sci.*, 96, 101–129, 2002.
495. Manev, E.D., Sazdanova, S.V., and Wasan, D.T., *J. Colloid Interface Sci.*, 97, 591, 1984.
496. Ivanov, I.B., *Pure Appl. Chem.*, 52, 1241, 1980.
497. Aveyard, R. et al., *Prog. Colloid Polym. Sci.*, 89, 114, 1992.
498. Velev, O.D. et al., *Colloids Surf. A*, 83, 43, 1994.
499. Dickinson, E., Murray, B.S., and Stainsby, G., *J. Chem. Soc. Faraday Trans.*, 84, 871, 1988.
500. Ivanov, I.B., Lectures at INTEVEP, Petroleos de Venezuela, Caracas, June 1995.
501. Ivanov, I.B. and Kralchevsky, P.A., *Colloid Surf. A*, 128, 155, 1997.
502. Basheva, E.S. et al., *Langmuir*, 15, 6764, 1999.
503. Boussinesq, M.J., *Ann. Chim. Phys.*, 29, 349, 1913; *Ann. Chim. Phys.*, 29, 357, 1913.
504. Aris, R., *Vectors, Tensors, and the Basic Equations of Fluid Mechanics*, Prentice-Hall, Englewood Cliffs, NJ, 1962.
505. Brenner, H. and Leal, L.G., *J. Colloid Interface Sci.*, 62, 238, 1977.
506. Brenner, H. and Leal, L.G., *J. Colloid Interface Sci.*, 65, 191, 1978.
507. Brenner, H. and Leal, L.G., *AIChE J.*, 24, 246, 1978.
508. Brenner, H. and Leal, L.G., *J. Colloid Interface Sci.*, 88, 136, 1982.

509. Stone, H.A., *Phys. Fluids*, A2, 111, 1990.
510. Valkovska, D.S. and Danov, K.D., *J. Colloid Interface Sci.*, 223, 314, 2000.
511. Stoyanov, S.D. and Denkov, N.D., *Langmuir*, 17, 1150, 2001.
512. Feng, S.-S., *J. Colloid Interface Sci.*, 160, 449, 1993.
513. Stebe, K.J. and Maldarelli, Ch., *Phys. Fluids*, A3, 3, 1991.
514. Stebe, K.J. and Maldarelli, Ch., *J. Colloid Interface Sci.*, 163, 177, 1994.
515. Scriven, L.E., *Chem. Eng. Sci.*, 12, 98, 1960.
516. Scriven, L.E. and Sternling, C.V., *J. Fluid Mech.*, 19, 321, 1964.
517. Slattery, J.C., *Chem. Eng. Sci.*, 19, 379, 1964; *Chem. Eng. Sci.*, 19, 453, 1964.
518. Slattery, J.C., *I&EC Fundam.*, 6, 108, 1967.
519. Slattery, J.C., *Interfacial Transport Phenomena*, Springer-Verlag, New York, 1990.
520. Barton, K.D. and Subramanian, R.S., *J. Colloid Interface Sci.*, 133, 214, 1989.
521. Feuillebois, F., *J. Colloid Interface Sci.*, 131, 267, 1989.
522. Merritt, R.M. and Subramanian, R.S., *J. Colloid Interface Sci.*, 131, 514, 1989.
523. Mannheimer, R.J. and Schechter, R.S., *J. Colloid Interface Sci.*, 12, 98, 1969.
524. Pintar, A.J., Israel, A.B., and Wasan, D.T., *J. Colloid Interface Sci.*, 37, 52, 1971.
525. Gardner, J.W. and Schechter, R.S., *Colloid Interface Sci.*, 4, 98, 1976.
526. Li, D. and Slattery, J.C., *J. Colloid Interface Sci.*, 125, 190, 1988.
527. Tambe, D.E. and Sharma, M.M., *J. Colloid Interface Sci.*, 147, 137, 1991.
528. Tambe, D.E. and Sharma, M.M., *J. Colloid Interface Sci.*, 157, 244, 1993.
529. Tambe, D.E. and Sharma, M.M., *J. Colloid Interface Sci.*, 162, 1, 1994.
530. Horozov, T. et al., A local approach in interfacial rheology: theory and experiment, in *First World Congress on Emulsion*, Paris, 1993, 3–20, 137.
531. Danov, K.D., Ivanov, I.B., and Kralchevsky, P.A., Interfacial rheology and emulsion stability, in *Second World Congress on Emulsion*, Paris, 1997, 2–2, 152.
532. de Groot, S.R. and Mazur, P., *Non-equilibrium Thermodynamics*, Interscience, New York, 1962.
533. Moeckel, G.P., *Arch. Rat. Mech. Anal.*, 57, 255, 1975.
534. Rushton, E. and Davies, G.A., *Appl. Sci. Res.*, 28, 37, 1973.
535. Haber, S., Hetsroni, G., and Solan, A., *Int. J. Multiphase Flow*, 1, 57, 1973.
536. Reed, L.D. and Morrison, F.A., *Int. J. Multiphase Flow*, 1, 573, 1974.
537. Hetsroni, G. and Haber, S., *Int. J. Multiphase Flow*, 4, 1, 1978.
538. Morrison, F.A. and Reed, L.D., *Int. J. Multiphase Flow*, 4, 433, 1978.
539. Beshkov, V.N., Radoev, B.P., and Ivanov, I.B., *Int. J. Multiphase Flow*, 4, 563, 1978.
540. Murdoch, P.G. and Leng, D.E., *Chem. Eng. Sci.*, 26, 1881, 1971.
541. Reed, X.B., Riolo, E., and Hartland, S., *Int. J. Multiphase Flow*, 1, 411, 1974; *Int. J. Multiphase Flow*, 1, 437, 1974.
542. Ivanov, I.B. and Traykov, T.T., *Int. J. Multiphase Flow*, 2, 397, 1976.
543. Traykov, T.T. and Ivanov, I.B., *Int. J. Multiphase Flow*, 3, 471, 1977.
544. Lu, C.-Y.D. and Cates, M.E., *Langmuir*, 11, 4225, 1995.
545. Jeelani, S.A.K. and Hartland, S., *J. Colloid Interface Sci.*, 164, 296, 1994.
546. Zapryanov, Z. et al., *Int. J. Multiphase Flow*, 9, 105, 1983.
547. Malhotra, A.K. and Wasan, D.T., *Chem. Eng. Commun.*, 55, 95, 1987.
548. Malhotra, A.K. and Wasan, D.T., Interfacial rheological properties of adsorbed surfactant films with applications to emulsion and foam stability, in *Thin Liquid Films*, Ivanov, I.B., Ed., Marcel Dekker, New York, 1988, p. 829.
549. Singh, G., Hirasaki, G.J., and Miller, C.A., *J. Colloid Interface Sci.*, 184, 92, 1996.
550. Traykov, T.T., Manev, E.D., and Ivanov, I.B., *Int. J. Multiphase Flow*, 3, 485, 1977.
551. Bancroft, W.D., *J. Phys. Chem.*, 17, 514, 1913.
552. Griffin, J., *Soc. Cosmet. Chem.*, 5, 4, 1954.
553. Davies, J.T., in *Proceedings of the 2nd International Congress on Surface Activity*, Vol. 1, Butterworths, London, 1957, p. 426.
554. Shinoda, K. and Friberg, S., *Emulsion and Solubilization*, Wiley, New York, 1986.
555. Davis, H.T., Factors determining emulsion type: HLB and beyond, in *Proc. First World Congress on Emulsion*, 19–22 Oct., Paris, 1993, p. 69.

556. Israelachvili, J., The history, applications and science of emulsion, in *Proc. First World Congress on Emulsion*, 19–22 Oct., Paris, 1993, p. 53.
557. Kralchevsky, P.A., *J. Colloid Interface Sci.*, 137, 217, 1990.
558. Gompper, G. and Schick, M., *Phys. Rev.*, B41, 9148, 1990.
559. Lerczak, J., Schick, M., and Gompper, G., *Phys. Rev.*, 46, 985, 1992.
560. Andelman, D. et al., *J. Chem. Phys.*, 87, 7229, 1987.
561. Chandra, P. and Safran, S., *Europhys. Lett.*, 17, 691, 1992.
562. Danov, K.D. et al., Bancroft rule and hydrodynamic stability of thin films and emulsions, in *Proc. First World Congress on Emulsion*, 19–22 Oct., Paris, 1993, p. 125.
563. Kunieda, H. et al., *Colloids Surf.*, 47, 35, 1990.
564. Koper, G.J.M. et al., *J. Phys. Chem.*, 99, 13291, 1995.
565. Ivanov, I.B., Danov, K.D., and Kralchevsky, P.A., *Colloids Surf. A*, 152, 161, 1999.
566. Velev, O.D., Gurkov, T.D., and Borwankar, R.P., *J. Colloid Interface Sci.*, 159, 497, 1993.
567. Velev, O.D. et al., *Phys. Rev. Lett.*, 75, 264, 1995.
568. Danov, K. et al., Marginal stability of emulsion thin film, in *Proceedings of the Conference of Synergetics, Order and Chaos*, Velarde, M., Ed., World Scientific, Singapore, 1988, p. 178.
569. Valkovska, D.S. et al., *Langmuir*, 16, 8892, 2000.
570. Danov, K.D. et al., *J. Colloid Interface Sci.*, 188, 313, 1997
571. Ivanov, I.B., Chakarova, S.K., and Dimitrova, B.I., *Colloids Surf.*, 22, 311, 1987.
572. Dimitrova, B.I., Ivanov, I.B., and Nakache, E., *J. Dispersion Sci. Technol.*, 9, 321, 1988.
573. Sternlng, C.V. and Scriven, L.E., *AIChE J.*, 5, 514, 1959.
574. Lin, S.P. and Brenner, H.J., *J. Colloid Interface Sci.*, 85, 59, 1982.
575. Holly, F.J., in *Wetting, Spreading and Adhesion*, Padday, J.F., Ed., Academic Press, New York, 1978, p. 439.
576. Castillo, J.L. and Velarde, M.G., *J. Colloid Interface Sci.*, 108, 264, 1985.
577. Davis, R.H., *Adv. Colloid Interface Sci.*, 43, 17, 1993.
578. Uijttewaall, W.S.J., Nijhof, E.-J., and Heethaar, R.M., *Phys. Fluids*, A5, 819, 1993.
579. Zapryanov, Z. and Tabakova, S., *Dynamics of Bubbles, Drops and Rigid Particles*, Kluwer Academic, London, 1999.
580. Lorentz, H.A., *Abh. Theoret. Phys.*, 1, 23, 1906.
581. Faxen, H., *Arkiv. Mat. Astron. Fys.*, 17, 27, 1923.
582. Wakiya, S., *J. Phys. Soc. Jpn.*, 12, 1130, 1957.
583. Dean, W.R. and O'Neill, M.E., *Mathematika*, 10, 13, 1963.
584. O'Neill, M.E., *Mathematika*, 11, 67, 1964.
585. Cooley, M.D.A. and O'Neill, M.E., *J. Inst. Math. Appl.*, 4, 163, 1968.
586. Keh, H.J. and Tseng, C.H., *Int. J. Multiphase Flow*, 1, 185, 1994.
587. Schonberg, J. and Hinch, E.J., *J. Fluid Mech.*, 203, 517, 1989.
588. Ryskin, G. and Leal, L.G., *J. Fluid Mech.*, 148, 1, 1984; *J. Fluid Mech.*, 148, 19, 1984; *J. Fluid Mech.*, 148, 37, 1984.
589. Liron, N. and Barta, E., *J. Fluid Mech.*, 238, 579, 1992.
590. Shapira, M. and Haber, S., *Int. J. Multiphase Flow*, 14, 483, 1988.
591. Shapira, M. and Haber, S., *Int. J. Multiphase Flow*, 16, 305, 1990.
592. Yang, S.-M. and Leal, L.G., *J. Fluid Mech.*, 149, 275, 1984.
593. Yang, S.-M. and Leal, L.G., *Int. J. Multiphase Flow*, 16, 597, 1990.
594. Lebedev, A.A., *Zh. Russ. Fiz. Khim.*, 48, 1916.
595. Silvey, A., *Phys. Rev.*, 7, 106, 1916.
596. Hadamar, J.S., *C. R. Acad. Sci. (Paris)*, 152, 1735, 1911.
597. Rybczynski, W., *Bull. Int. Acad. Sci. Cracovie*, A, 1911.
598. He, Z., Dagan, Z., and Maldarelli, Ch., *J. Fluid Mech.*, 222, 1, 1991.
599. Danov, K.D. et al., *Chem. Eng. Sci.*, 50, 263, 1995.
600. Danov, K.D. et al., *Chem. Eng. Sci.*, 50, 2943, 1995.
601. Danov, K.D. et al., *Int. J. Multiphase Flow*, 21, 1169, 1995.
602. Danov, K.D. et al., *Chem. Eng. Sci.*, 53, 3413, 1998.
603. Stoos, J.A. and Leal, L.G., *J. Fluid Mech.*, 217, 263, 1990.

604. Danov, K.D., Dimova, R.I., and Pouligny, B., *Phys. Fluids*, 12, 2711, 2000.
605. Dimova, R.I. et al., *J. Colloid Interface Sci.*, 226, 35, 2000.
606. Angelova, M.I. and Pouligny, B., *Pure Appl. Optics*, 2, 261, 1993.
607. Pouligny, B., Martinot-Lagarde, G., and Angelova, M.I., *Prog. Colloid Polym. Sci.*, 98, 280, 1995.
608. Dietrich, C., Angelova, M., and Pouligny, B., *J. Phys. II France*, 7, 1651, 1997.
609. Velikov, K. et al., *Europhys. Lett.*, 40(4), 405, 1997.
610. Velikov, K. et al., *Colloids Surf. A*, 149, 245, 1999.
611. Dimova, R. et al., *Eur. Phys. J. B*, 12, 589, 1999.
612. Danov, K.D. et al., in *Studies in Surface Science and Catalysis*, Vol. 132, Elsevier, Amsterdam, 2001.
613. Hunter, R.J., *Foundation of Colloid Science*, Vol. 1, Clarendon Press, Oxford, 1987.
614. Hunter, R.J., *Foundation of Colloid Science*, Vol. 2, Clarendon Press, Oxford, 1989.
615. Einstein, A., *Ann. Phys.*, 19, 289, 1906.
616. Kubo, R., *Rep. Prog. Phys.*, 29, 255, 1966.
617. Einstein, A., *Ann. Phys.*, 34, 591, 1911.
618. Taylor, G.I., *Proc. R. Soc. A*, 138, 41, 1932.
619. Oldroyd, J.G., *Proc. R. Soc. A*, 232, 567, 1955.
620. Taylor, G.I., *Proc. R. Soc. A*, 146, 501, 1934.
621. Fröhlich, H. and Sack, R., *Proc. R. Soc. A*, 185, 415, 1946.
622. Oldroyd, J.G., *Proc. R. Soc. A*, 218, 122, 1953.
623. Batchelor, G.K., *J. Fluid Mech.*, 83, 97, 1977.
624. de Kruijff, C.G. et al., *J. Chem. Phys.*, 83, 4717, 1985.
625. Loewenberg, M. and Hinch, E.J., *J. Fluid Mech.*, 321, 395, 1996.
626. Da Cunha, F.R. and Hinch, E.J., *J. Fluid Mech.*, 309, 211, 1996.
627. Li, X. and Pozrikidis, C., *J. Fluid Mech.*, 341, 165, 1997.
628. Loewenberg, M., *J. Fluids Eng.*, 120, 824, 1998.
629. Blawdziewicz, J., Vajnryb, E., and Loewenberg, M., *J. Fluid Mech.*, 395, 29, 1999.
630. Ramirez, J.A. et al., *Chem. Eng. Sci.*, 54, 149, 1999.
631. Blawdziewicz, J., Vlahovska, P., and Loewenberg, M., *Physica A*, 276, 50, 2000.
632. Breyannis, G. and Pozrikidis, C., *Theor. Comp. Fluid Dynam.*, 13, 327, 2000.
633. Li, X. and Pozrikidis, C., *Int. J. Multiphase Flow*, 26, 1247, 2000.
634. Rednikov, A.Y., Ryazantsev, Y.S., and Velarde, M.G., *Phys. Fluids*, 6, 451, 1994.
635. Velarde, M.G., *Philos. Trans. R. Soc., Math. Phys. Eng. Sci.*, 356, 829, 1998.
636. Danov, K.D., *J. Colloid Interface Sci.*, 235, 144, 2001.
637. Barnes, H.A., Rheology of emulsions — a review, in *Proc. First World Congress on Emulsion*, 19–22 Oct., Paris, 1993, p. 267.
638. Krieger, L.M. and Dougherty, T.J., *Trans. Soc. Rheol.*, 3, 137, 1959.
639. Wakeman, R., *Powder Tech.*, 11, 297, 1975.
640. Prud'home, R.K. and Khan, S.A., Experimental results on foam rheology, in *Foams: Theory, Measurements, and Applications*, Prud'home, R.K. and Khan, S.A., Eds., Marcel Dekker, New York, 1996, p. 217.
641. Tadros, T.F., Fundamental principles of emulsion rheology and their applications, in *Proc. First World Congress on Emulsion*, 19–22 Oct., Paris, 1993, p. 237.
642. Pal, R., Bhattacharya, S.N., and Rhodes, E., *Can. J. Chem. Eng.*, 64, 3, 1986.
643. Edwards, D.A. and Wasan, D.T., Foam rheology: the theory and role of interfacial rheological properties, in *Foams: Theory, Measurements, and Applications*, Prud'home, R.K. and Khan, S.A., Eds., Marcel Dekker, New York, 1996, p. 189.
644. Wessel, R. and Ball, R.C., *Phys. Rev.*, A46, 3009, 1992.
645. Kanai, H. et al., *Rheol. Acta*, 31, 333, 1992.
646. Pal, R., *Chem. Eng. Commun.*, 98, 211, 1990.
647. Pal, R., *Colloids Surf. A*, 71, 173, 1993.
648. Prins, A., Liquid flow in foams as affected by rheological surface properties: a contribution to a better understanding of the foaming behaviour of liquids, in *Hydrodynamics of Dispersed Media*, Hulin, J.P. et al., Eds., Elsevier/North-Holland, Amsterdam, 1990, p. 5.
649. Babak, V.G., *Colloids Surf. A*, 85, 279, 1994.
650. Yuhua, Y., Pal, R., and Masliyah, J., *Chem Eng. Sci.*, 46, 985, 1991.

651. Giesekus, H., Disperse systems: dependence of rheological properties on the type of flow with implications for food rheology, in *Physical Properties of Foods*, Jowitt, R. et al., Eds., Applied Science London, 1983, chap. 13.
652. Turian, R. and Yuan, T.-F., *AIChE J.*, 23, 232, 1977.
653. Clarke, B., *Trans. Inst. Chem. Eng.*, 45, 251, 1967.
654. von Smoluchowski, M., *Phys. Z.*, 17, 557, 1916.
655. von Smoluchowski, M., *Z. Phys. Chem.*, 92, 129, 1917.
656. Wang, H. and Davis, R.H., *J. Colloid Interface Sci.*, 159, 108, 1993.
657. Rogers, J.R. and Davis, R.H., *Mettal. Trans.*, A21, 59, 1990.
658. Young, N.O., Goldstein, J.S., and Block, M.J., *J. Fluid Mech.*, 6, 350, 1959.
659. Fuchs, N.A., *Z. Phys.*, 89, 736, 1934.
660. Friedlander, S.K., *Smoke, Dust and Haze: Fundamentals of Aerosol Behaviour*, Wiley-Interscience, New York, 1977.
661. Singer, J.M. et al., *J. Colloid Interface Sci.*, 45, 608, 1973.
662. Leckband, D.E. et al., *Biochemistry*, 33, 4611, 1994.
663. Bak, T.A. and Heilmann, O., *J. Phys. A Math. Gen.*, 24, 4889, 1991.
664. Martinov, G.A. and Muller, V.M., in *Research in Surface Forces*, Vol. 4, Plenum Press, Consultants Bureau, New York, 1975, p. 3.
665. Elminyawi, I.M., Gangopadhyay, S., and Sorensen, C.M., *J. Colloid Interface Sci.*, 144, 315, 1991.
666. Hartland, S. and Gakis, N., *Proc. R. Soc. London*, A369, 137, 1979.
667. Hartland, S. and Vohra, D.K., *J. Colloid Interface Sci.*, 77, 295, 1980.
668. Lobo, L., Ivanov, I.B., and Wasan, D.T., *AIChE J.*, 39, 322, 1993.
669. Danov, K.D. et al., *J. Colloid Interface Sci.*, 167, 8, 1994.
670. van den Tempel, M., *Recueil*, 72, 433, 1953.
671. Borwankar, R.P., Lobo, L.A., and Wasan, D.T., *Colloid Surf.*, 69, 135, 1992.
672. Dukhin, S., Sæther, Ø., and Sjöblom, J., Coupling of coalescence and flocculation in dilute O/W emulsions, in *Encyclopedic Handbook of Emulsion Technology*, Sjöblom, J., Ed., Marcel Dekker, New York, 2001, p. 71.
673. Garrett, P.R., Ed., *Defoaming: Theory and Industrial Applications*, Marcel Dekker, New York, 1993.
674. Garrett, P.R., The mode of action of antifoams, in *Defoaming: Theory and Industrial Applications*, Marcel Dekker, New York, 1993, chap. 1.
675. Exerowa, D. and Kruglyakov, P.M., *Foams and Foam Films*, Elsevier, Amsterdam, 1998, chap. 9.
676. Wasan, D.T. and Christiano, S.P., in *Handbook of Surface and Colloid Chemistry*, Birdi, K.S., Ed., CRC Press, Boca Raton, FL, 1997, p. 179.
677. Kralchevsky, P.A. and Nagayama, K., *Particles at Fluid Interfaces and Membranes*, Studies in Interface Science, Vol. 10, Elsevier, Amsterdam, 2001, chap. 14.
678. Basheva, E.S. et al., *Langmuir*, 16, 1000, 2000.
679. Basheva, E.S. et al., *Langmuir*, 17, 969, 2001.
680. Koczo, K., Koczona, J.K., and Wasan, D.T., *J. Colloid Interface Sci.*, 166, 225, 1994.
681. Denkov, N.D., Cooper, P. and Martin, J.-Y., *Langmuir*, 15, 8514, 1999.
682. Marinova, K. and Denkov, N.D., *Langmuir*, 17, 2426, 2001.
683. Denkov, N.D. and Marinova, K., Antifoaming action of oils, in *Proceedings of the 3rd EuroConference on Foams, Emulsions and Applications*, Zitha, P., Banhart, J., and Verbist, G., Eds., MIT, Bremen, 2000, p. 199.
684. Denkov, N.D., Tcholakova, S., Marinova, K., and Hadjiiski, A., Role of oil spreading for the efficiency of mixed oil–solid antifoams, *Langmuir*, 2002, in press.
685. Marinova, K.M. et al., Optimal hydrophobicity of silica in mixed oil–silica antifoams, *Langmuir*, 18, 3399, 2002.
686. Arnaudov, L. et al., *Langmuir*, 17, 6999, 2001.
687. Hadjiiski, A. et al., *Langmuir*, 17, 7011, 2001.
688. Denkov, N.D., *Langmuir*, 15, 8530, 1999.
689. Garrett, P.R., *J. Colloid Interface Sci.*, 76, 587, 1980.
690. Kulkarni, R.D., Goddard, E.D., and Kanner, B., *J. Colloid Interface Sci.*, 59, 468, 1977.
691. Kruglyakov, P.M., in *Thin Liquid Films: Fundamentals and Applications*, Ivanov, I.B., Ed., Surfactant Science Series, Vol. 29, Marcel Dekker, New York, 1988, chap. 11.

692. Bergeron, V., Fagan, M.E., and Radke C., *Langmuir*, 9, 1704, 1993.
693. Bergeron, V. et al., *Colloids Surf. A: Physicochem. Eng. Asp.*, 122, 103, 1997.
694. Koczo, K., Lloyd, L., and Wasan, D.T., *J. Colloid Interface Sci.*, 150, 492, 1992.
695. Kulkarni, R.D., Goddard, E.D., and Chandar, P., in *Foams: Theory, Measurements, and Applications*, Prud'homme, R.K. and Khan, S.A., Eds., Surfactant Science Series, Vol. 57, Marcel Dekker, New York, 1996, chap. 14.
696. Aveyard, R. et al., *J. Chem. Soc. Faraday Trans.*, 89, 4313, 1993.
697. Hadjiiski, A. et al., *Langmuir*, 18, 127, 2002.
698. Hadjiiski, A. et al., Role of entry barriers in the foam destruction by oil drops, *Proceedings of the 13th Symposium on Surfactants in Solution*, Mittal, K.L., Moudgil, B., and Shah, D., Eds., Marcel Dekker, New York, 2002, in press.
699. Lichtman, I.A., Sinka, J.V., and Evans, D.W., *Assoc. Mex. Tec. Ind. Celul. Pap. (Bol.)*, 15, 2632, 1975.
700. Ross, S., *J. Phys. Colloid Chem.*, 54, 429, 1950.
701. Jha, B.K., Christiano, S.P., and Shah, D.O., *Langmuir*, 16, 9947, 2000.
702. Garrett, P.R., Davis, J., and Rendall, H.M., *Colloids Surf. A Physicochem. Eng. Asp.*, 85, 159, 1994.
703. Denkov N.D. et al., *Langmuir*, 16, 2515, 2000.
704. Overbeek, J.Th.G., *Adv. Colloid Sci.*, 3, 97, 1950.
705. Overbeek, J.Th.G., in *Colloid Science*, Vol. 1, Kruyt, H.R., Ed., Elsevier, Amsterdam, 1952, p. 197.
706. Overbeek, J.Th.G. and Wiersema, P.H., in *Electrophoresis*, Vol. 2, Bier, M., Ed., Academic Press, New York, 1967, chap. 1.
707. Dukhin, S.S. and Derjaguin, B.V., in *Surface and Colloid Science*, Vol. 7, Matijević, E., Ed., John Wiley, New York, 1974, chap. 3.
708. Derjaguin, B.V., Dukhin, S.S., and Shilov, V.N., *Adv. Colloid Interface Sci.*, 13, 141 and 153, 1980.
709. Uzgiris, E., *Adv. Colloid Interface Sci.*, 14, 75, 1981.
710. Saville, D.A., *Adv. Colloid Interface Sci.*, 16, 267, 1982.
711. O'Brien, R.W., *Adv. Colloid Interface Sci.*, 16, 281, 1982.
712. Mandel, M. and Odjik, T., *Annu. Rev. Phys. Chem.*, 35, 75, 1984.
713. Dukhin, S.S., *Adv. Colloid Interface Sci.*, 44, 1, 1993.
714. Dukhin, A.S. and Goetz, P.J., *Adv. Colloid Interface Sci.*, 92, 73, 2001.
715. Dukhin, S.S. and Shilov, V.N., *Dielectric Phenomena and the Double Layer in Disperse Systems and Polyelectrolytes*, Wiley, New York, 1974.
716. Hunter, R.J., *Zeta Potential in Colloid Science*, Academic Press, New York, 1981.
717. Hunter, R.J., *Foundations of Colloid Science*, Vol. 2, Clarendon Press, Oxford, 1989, chaps. 6 and 13.
718. Ohshima, H. and Furusawa, K., Eds., *Electrical Phenomena at Interfaces: Fundamentals, Measurements, and Applications*, 2nd ed., Marcel Dekker, New York, 1998.
719. Chew, W.C. and Sen, P.N., *J. Chem. Phys.*, 77, 2042, 1982.
720. Loeb, A.L., Wiersema, P.H., and Overbeek, J.Th.G., *The Electric Double Layer around a Spherical Colloidal Particle*, MIT Press, Cambridge, MA, 1961.
721. Dukhin, S.S., Semenikhin, N.M., and Shapinskaia, L.M., *Dokl. Akad. Nauk S.S.S.R.*, 193, 385, 1970.
722. Stokes, A.N., *J. Chem. Phys.*, 65, 261, 1976.
723. Ohshima, H., Healy, T.W., and White L.R., *J. Colloid Interface Sci.*, 90, 17, 1982.
724. Ohshima, H., Electrical double layer, in *Electrical Phenomena at Interfaces: Fundamentals, Measurements, and Applications*, 2nd ed., Ohshima, H. and Furusawa, K., Eds., Marcel Dekker, New York, 1998, chap. 1.
725. Ohshima, H., *J. Colloid Interface Sci.*, 171, 525, 1995.
726. von Smoluchowski, M., in *Handbuch der Elektrizität und des Magnetismus*, Vol. 2, Barth, Leipzig, 1921, 366.
727. Bikerman, J.J., *Trans. Faraday Soc.*, 36, 154, 1940.
728. O'Brien, R.W., *J. Colloid Interface Sci.*, 110, 477, 1986.
729. Bowen, W.R. and Jacobs, P.M., *J. Colloid Interface Sci.*, 111, 223, 1986.
730. Sasaki, H. et al., *J. Colloid Interface Sci.*, 142, 266, 1991.
731. Nishimura, S. et al., *J. Colloid Interface Sci.*, 152, 359, 1992.
732. Furusawa, K., Sasaki, H., and Nashima, T., Electro-osmosis and streaming potential measurements, in *Electrical Phenomena at Interfaces: Fundamentals, Measurements, and Applications*, 2nd ed., Ohshima, H. and Furusawa, K., Eds., Marcel Dekker, New York, 1998, chap. 9.

733. Usui, S., Imamura, Y., and Sasaki, H., *J. Colloid Interface Sci.*, 118, 335, 1987.
734. Scales, P.J., Healy, T.W., and Evans, D.F., *J. Colloid Interface Sci.*, 124, 391, 1988; Scales, P.J., Grieser, F., and Healy, T.W., *Langmuir*, 6, 582, 1989.
735. van den Hoven, Th.J.J. and Bijsterbosch, B.H., *Colloids Surf.*, 22, 187, 1987.
736. von Smoluchowski, M., *Z. Phys. Chem.*, 92, 129, 1918.
737. Hückel, E., *Phys. Z.*, 25, 204, 1924.
738. Henry, D.C., *Proc. R. Soc. London*, A133, 106, 1931.
739. Henry, D.C., *Trans. Faraday Soc.*, 44, 1021, 1948.
740. Overbeek, J.Th.G., *Kolloid Beih.*, 54, 287 and 364, 1943.
741. Booth, F., *Proc R. Soc. London*, A203, 514, 1950.
742. Wiersema, P.H., Loeb, A.L., and Overbeek, J.Th.G., *J. Colloid Interface Sci.*, 22, 78, 1966.
743. O'Brien, R.W. and White, L.R., *J. Chem. Soc. Faraday Trans.*, 2, 74, 1607, 1978.
744. O'Brien, R.W. and Hunter, R.J., *Can. J. Chem.*, 59, 1878, 1981.
745. Ohshima, H. et al., *J. Chem. Soc. Faraday Trans.*, 2, 79, 1613, 1983; 80, 1299 and 1643, 1984.
746. Ohshima, H., *J. Colloid Interface Sci.*, 168, 269, 1994.
747. Ohshima, H., *J. Colloid Interface Sci.*, 239, 587, 2001.
748. Stigter, D., *J. Phys. Chem.*, 82, 1417 and 1424, 1978.
749. van der Drift, W.P.J.T., de Keizer, A., and Overbeek, J.Th.G., *J. Colloid Interface Sci.*, 71, 67 and 79, 1979.
750. Ohshima, H., *J. Colloid Interface Sci.*, 180, 299, 1996.
751. Hermans, J.J., *J. Polym. Sci.*, 18, 527, 1955.
752. Overbeek, J.Th.G. and Stigter, D., *Rec. Trav. Chim.*, 75, 543, 1956.
753. Imai, N. and Iwasa, K., *Israel J. Chem.*, 11, 223, 1973.
754. Koopal, L.K. and Lyklema, J., *Discuss. Faraday Soc.*, 59, 230, 1975; *J. Electroanal. Chem.*, 100, 895, 1979.
755. Brooks, D.E. and Seaman, G.V.F., *J. Colloid Interface Sci.*, 43, 670, 1973; 43, 687, 1973; 43, 700, 1973; 43, 714, 1973.
756. Ohshima, H. and Kondo, T., *J. Colloid Interface Sci.*, 116, 305, 1987; 135, 443, 1990; 163, 474, 1994.
757. Ohshima, H., Interfacial electrokinetic phenomena, in *Electrical Phenomena at Interfaces: Fundamentals, Measurements, and Applications*, 2nd ed., Ohshima, H. and Furusawa, K., Eds., Marcel Dekker, New York, 1998, chap. 2.
758. Ohshima, H., *J. Colloid Interface Sci.*, 233, 142, 2001.
759. Churaev, N.V. and Nikologorskaja, E.A., *Colloids Surf.*, 59, 71, 1991.
760. Furusawa, K., Chen, Q., and Tabori, N., *J. Colloid Interface Sci.*, 137, 456, 1990.
761. Levine, S. and Neale, G.H., *J. Colloid Interface Sci.*, 47, 520, 1974; *J. Colloid Interface Sci.*, 49, 332, 1974.
762. Happel, J., *Am. Inst. Chem. Eng. J.*, 4, 197, 1958.
763. Kuwabara, S., *J. Phys. Soc. Jpn.*, 14, 527, 1959.
764. Deggelmann, M. et al., *J. Colloid Interface Sci.*, 143, 318, 1991.
765. Kozak, M.W. and Davis, E.J., *J. Colloid Interface Sci.*, 127, 497, 1989; 129, 166, 1989.
766. Ohshima, H., *J. Colloid Interface Sci.*, 188, 481, 1997.
767. Zukoski, C.F. and Saville, D.A., *J. Colloid Interface Sci.*, 115, 422, 1987.
768. Mangelsdorf, C.S. and White, L.R., *J. Chem. Soc. Faraday Trans.*, 88, 3567, 1992; *J. Colloid Interface Sci.*, 160, 275, 1993.
769. Gaigalas, A.K., Woo, S., and Hubbard, J.B., *J. Colloid Interface Sci.*, 136, 213, 1990.
770. Ohshima, H., *J. Colloid Interface Sci.*, 179, 431, 1996.
771. Ohshima, H., *J. Colloid Interface Sci.*, 185, 131, 1997.
772. Schätzel, K. et al., *J. Colloid Interface Sci.*, 143, 287, 1991.
773. Abramson, H.A., Moyer, L.S., and Gorin, M.H., *Electrophoresis of Proteins*, Reinhold, New York, 1942.
774. Tiselius, A., *Trans. Faraday Soc.*, 33, 524, 1937.
775. Imai, T., Otani, W., and Oka, K., *J. Phys. Chem.*, 94, 853, 1990.
776. Kameyama, K. and Takagi, T., *J. Colloid Interface Sci.*, 140, 517, 1990.
777. Imai, T., *J. Phys. Chem.*, 94, 5953, 1990.
778. Imai, T. and Kohsaka T., *J. Phys. Chem.*, 96, 10030, 1992.

779. Imai, T. and Hayashi, N., *Langmuir*, 9, 3385, 1993.
780. Imae, T., Electrostatic and electrokinetic properties of micelles, in *Electrical Phenomena at Interfaces: Fundamentals, Measurements, and Applications*, 2nd ed., Ohshima, H. and Furusawa, K., Eds., Marcel Dekker, New York, 1998, chap. 28.
781. Anderson, J.L., *J. Colloid Interface Sci.*, 105, 45, 1985.
782. Fair, M.C. and Anderson, J.L., *J. Colloid Interface Sci.*, 127, 388, 1989.
783. Yoon, B.J. and Kim, S., *J. Colloid Interface Sci.*, 128, 275, 1989.
784. Yoon, B.J., *J. Colloid Interface Sci.*, 142, 575, 1991.
785. von Smoluchowski, M., *Bull. Akad. Sci. Cracovie Sci. Math. Nat.*, 1, 182, 1903.
786. Booth, F., *J. Chem. Phys.*, 22, 1956, 1954.
787. Ohshima, H. et al., *J. Chem. Soc. Faraday Trans. 2*, 80, 1299, 1984.
788. Levine, S., Neale, G., and Epstein, N., *J. Colloid Interface Sci.*, 57, 424, 1976.
789. Mazur, P. and Overbeek, J.Th.G., *Rec. Trav. Chim.*, 70, 83, 1951.
790. De Groot, S.R., Mazur, P., and Overbeek, J.Th.G., *J. Chem. Phys.*, 20, 1825, 1952.
791. Maxwell, J.C., *Electricity and Magnetism*, Oxford University Press (Clarendon), London, 1873.
792. Fricke, H., *Phys. Rev.*, 24, 575, 1924; 26, 682, 1925.
793. Dukhin, S.S., *Electroconductivity and Electrokinetic Properties of Disperse Systems*, Naukova Dumka, Kiev, 1975, chap. 2 [in Russian].
794. O'Brien, R.W., *J. Colloid Interface Sci.*, 81, 234, 1981.
795. O'Brien, R.W. and Perrins, W.T., *J. Colloid Interface Sci.*, 99, 20, 1984; 110, 447, 1986.
796. Ohshima, H., Healy, T.W., and White, L.R., *J. Chem. Soc. Faraday Trans.*, 2, 79, 1613, 1983.
797. De Lacey, E.H.B. and White, L.R., *J. Chem. Soc. Faraday Trans.*, 2, 77, 2007, 1981.
798. O'Brien, R.W., *J. Colloid Interface Sci.*, 113, 81, 1986.
799. Debye, P. and Falkenhagen, H., *Phys. Z.*, 29, 121 and 401, 1928.
800. Hinch, E.J., *J. Chem. Soc. Faraday Trans. 2*, 80, 535, 1984.
801. Midmore, B.R., Hunter, R.J., and O'Brien, R.W., *J. Colloid Interface Sci.*, 120, 210, 1987; 123, 486, 1988.
802. Myers, D.F. and Saville, D.A., *J. Colloid Interface Sci.*, 131, 448, 1989.
803. Shubin, V.E., Hunter, R.J., and O'Brien, R.W., *J. Colloid Interface Sci.*, 159, 174, 1993.
804. Grosse, C. et al., *J. Colloid Interface Sci.*, 242, 75, 2001.
805. Enderby, J.A., *Proc. Phys. Soc.*, A207, 321, 1951.
806. Booth, F. and Enderby, J.A., *Proc. Phys. Soc.*, A208, 351, 1952.
807. Marlow, B.J., Fairhurst, D., and Pendse, H.P., *Langmuir*, 4, 611, 1988.
808. Hozumi, Y. and Furusawa, K., *Colloid Polym. Sci.*, 268, 469, 1990.
809. Durand Vidal, S. et al., *Prog. Colloid Polym. Sci.*, 98, 184, 1995.
810. Debye, P., *J. Chem. Phys.*, 1, 13, 1933.
811. O'Brien, R.W., *J. Fluid Mech.*, 190, 71, 1988.
812. Rider, P.F. and O'Brien, R.W., *J. Fluid Mech.*, 257, 607, 1993.
813. Takeda, S. et al., Dynamic electrophoresis, in *Electrical Phenomena at Interfaces: Fundamentals, Measurements, and Applications*, 2nd ed., Ohshima, H. and Furusawa, K., Eds., Marcel Dekker, New York, 1998, chap. 13.
814. Gibb, S.E. and Hunter, R.J., *J. Colloid Interface Sci.*, 224, 99, 2000.
815. Kong, L., Beattie, J.K., and Hunter, R.J., *J. Colloid Interface Sci.*, 238, 70, 2001.
816. Rasmusson, M., *J. Colloid Interface Sci.*, 240, 432, 2001.
817. Dukhin, A.S. et al., *Langmuir*, 16, 2615, 2000.
818. Löbbus, M. et al., *J. Colloid Interface Sci.*, 229, 174, 2000.
819. Hunter, R.J., *J. Colloid Interface Sci.*, 22, 231, 1966.
820. Chan, D.Y.C. and Horn, R.G., *J. Chem. Phys.*, 83, 5311, 1985.
821. Israelachvili, J.N., *J. Colloid Interface Sci.*, 110, 263, 1986.
822. Dukhin, S.S. and Semnikhin, M.M., *Kolloidn. Zh.*, 32, 360, 1978.
823. Fridrikhsberg, D.A. et al., *Kolloidn. Zh.*, 48, 967, 1986.
824. Zukoski, C.F. and Saville, D.A., *J. Colloid Interface Sci.*, 114, 32, 1986.
825. Midmore, B.R. and Hunter, R.J., *J. Colloid Interface Sci.*, 122, 521, 1988; Midmore, B.R., Diggins, D., and Hunter, R.J., *J. Colloid Interface Sci.*, 129, 153, 1989.
826. Van der Put, A.G. and Bijsterbosch, B.H., *J. Colloid Interface Sci.*, 75, 512, 1980; 92, 499, 1983.

827. Rosen, L.A. and Saville, D.A., *J. Colloid Interface Sci.*, 144, 82, 1990; 149, 2, 1992.
828. Dukhin, A.S. and van de Ven, T.G.M., *J. Colloid Interface Sci.*, 165, 9, 1994.
829. Meijer, A.E.J., van Megen, W.J., and Lyklema, J., *J. Colloid Interface Sci.*, 66, 99, 1978.
830. Russel, A.S. et al., *Langmuir*, 11, 1553, 1995.
831. Gittings, M.R. and Saville, D.A., *Langmuir*, 11, 798, 1995.
832. Bastos-Gonzalez, D., Hidalgo-Alvarez, R., and de las Nieves, F.J., *J. Colloid Interface Sci.*, 177, 372, 1996.
833. Saville, D.A., *J. Colloid Interface Sci.*, 222, 137, 2000.
834. Alty, T., *Proc. R. Soc.*, A106, 315, 1924.
835. Usui, S., Sasaki, H., and Matsukawa, H., *J. Colloid Interface Sci.*, 65, 36, 1978; *J. Colloid Interface Sci.*, 81, 80, 1981.
836. McShea, J.A. and Callaghan, I.C., *Colloid Polym. Sci.*, 261, 757, 1983.
837. Yoon, R.-H. and Jordan, J.L., *J. Colloid Interface Sci.*, 113, 430, 1986.
838. Graciaa, A. et al., *J. Colloid Interface Sci.*, 172, 131, 1995.
839. Dickinson, W., *Trans. Faraday Soc.*, 37, 140, 1941.
840. Taylor, A.J. and Wood, F.W., *Trans. Faraday Soc.*, 53, 523, 1957.
841. Dunstan, D.E. and Saville, D.A., *J. Chem. Soc. Faraday Trans.*, 88, 2031, 1992; 89, 527, 1993; *J. Colloid Interface Sci.*, 166, 472, 1994.
842. Marinova, K.G. et al., *Langmuir*, 12, 2045, 1996.
843. Graciaa, A. et al., *J. Colloid Interface Sci.*, 172, 131, 1995.
844. Exerowa, D., *Colloid Polym. Sci.*, 257, 1089, 1979.
845. Waltermo, A. et al., *J. Dispersion Sci. Technol.*, 15, 273, 1994.
846. Karraker, K.A. and Radke, C.J., *Adv. Colloid Interface Sci.*, 96, 231, 2002.
847. Van de Hulst, H.C., *Light Scattering by Small Particles*, Wiley, New York, 1957; 2nd ed., Dover, New York, 1981.
848. Kerker, M., *The Scattering of Light and Other Electromagnetic Radiation*, Academic Press, New York, 1969.
849. Hiemenz, P.C. and Rajagopalan, R., *Principles of Colloid and Surface Chemistry*, 3rd ed., Marcel Dekker, New York, 1997, chap. 5.
850. Lyklema, J., *Fundamentals of Interface and Colloid Science*, Vol. 1, Academic Press, New York, 1991, chap. 7.
851. McIntyre, D. and Gornick, F., Eds., *Light Scattering from Dilute Polymer Solutions*, Gordon & Breach, New York, 1964.
852. Rayleigh, L., *Philos. Mag.*, 41, 107, 1871; 41, 274, 1871; 41, 447, 1871.
853. Debye, P., *J. Appl. Phys.*, 15, 338, 1944.
854. O'Konski, C.T., Ed., *Molecular Electrooptics*, Marcel Dekker, New York, 1976.
855. Jennings, B.R., Ed., *Electro-optics and Dielectrics of Macromolecules and Colloids*, Plenum Press, New York, 1979.
856. Stoilov, S.P., *Colloid Electrooptics: Theory, Techniques and Applications*, Academic Press, New York, 1991.
857. Rayleigh, L., *Proc. R. Soc.*, A84, 25, 1910; A90, 219, 1914; A94, 296, 1918.
858. Debye, P., *Ann. Phys.*, 46, 809, 1915.
859. Gans, R., *Ann. Phys.*, 65, 97, 1921; 67, 353, 1923; 76, 29, 1925.
860. Guinier, A., *Ann. Phys. (France)*, 12, 161, 1939.
861. Yamakawa, H., *Modern Theory of Polymer Solutions*, Harper & Row, New York, 1971.
862. Shull, C.C. and Roess, L.C., *J. Appl. Phys.*, 18, 295, 1947.
863. Brenner, H., *Int. J. Multiphase Flow*, 1, 195, 1974.
864. Zero, K. and Pecora, R., in *Dynamic Light Scattering*, Pecora, R., Ed., Plenum Press, New York, 1985, chap. 3.
865. Neugebauer, T., *Ann. Phys.*, 42, 509, 1942.
866. Saito, N. and Ikeda, Y., *J. Phys. Soc. Jpn.*, 6, 305, 1951.
867. Fournet, G. and Guinier, A., *J. Phys. Radium*, 11, 516, 1950.
868. Riseman, J. and Kirkwood, J.G., *J. Chem. Phys.*, 18, 512, 1950.
869. Broersma, S., *J. Chem. Phys.*, 32, 1626, 1960; 32, 1632, 1960.
870. Kratky, O. and Porod, G., *J. Colloid Sci.*, 4, 35, 1949.

871. Becher, P., *J. Phys. Chem.*, 63, 1213, 1959.
872. Debye, P., Technical Report No 637 to Rubber Reserve Company, Washington, April 9, 1945.
873. Hearst, J.E., *J. Chem. Phys.*, 38, 1062, 1963.
874. Mie, G., *Ann. Phys.*, 25, 377, 1908.
875. Debye, P., *Ann. Phys.*, 30, 755, 1909.
876. Asano, S. and Yamamoto, G., *Appl. Opt.*, 14, 29, 1975; 18, 712, 1979.
877. Glatter, O., Sieberer, J., and Schnablegger, H., *Part. Part. Syst. Charact.*, 8, 274, 1991.
878. Einstein, A., *Ann. Phys.*, 33, 1275, 1910.
879. Debye, P., *J. Phys. Colloid Chem.*, 51, 18, 1947.
880. McQuarrie, D.A., *Statistical Mechanics*, Harper & Row, New York, 1976.
881. Zimm, B.H., *J. Chem. Phys.*, 16, 1093, 1948; 16, 1099, 1948.
882. Agterof, W.G.M., van Zomeren, J.A.J., and Vrij, A., *Chem. Phys. Lett.*, 43, 363, 1976.
883. Cazabat, A.M. and Langevin, D., *J. Chem. Phys.*, 74, 3148, 1981.
884. Brunetti, S. et al., *J. Phys. Chem.*, 87, 1028, 1983.
885. Baker, R.C. et al., *J. Colloid Interface Sci.*, 100, 332, 1984.
886. Denkov, N.D. et al., *J. Colloid Interface Sci.*, 143, 157, 1991.
887. Koper, G.J.M. et al., *J. Phys. Chem.*, 99, 13 291, 1995.
888. Cabannes, P., *La Diffusion Moleculaire de la Lumiere*, Presses Universitaires de France, Paris, 1929.
889. Utiyama, H., in *Light Scattering from Polymer Solutions*, Huglin, M.B., Ed., Academic Press, New York, 1972, chap. 4.
890. Eskin, B.E., *Light Scattering from Polymer Solutions*, Nauka, Leningrad, 1986, chap. 1 [in Russian].
891. Chu, B., *Laser Light Scattering: Basic Principles and Practice*, 2nd ed., Academic Press, New York, 1991.
892. Berne, B.J. and Pecora, R., *Dynamic Light Scattering with Applications to Chemistry, Biology and Physics*, Wiley, New York, 1976.
893. Pecora, R., Ed., *Dynamic Light Scattering: Applications of Photon Correlation Spectroscopy*, Plenum Press, New York, 1985.
894. Schmitz, K.S., *An Introduction to Dynamic Light Scattering by Macromolecules*, Academic Press, New York, 1990.
895. Brown, W., Ed., *Dynamic Light Scattering: The Method and Some Applications*, Clarendon Press, Oxford, 1993.
896. Brown, W., Ed., *Light Scattering: Principles and Development*, Clarendon Press, Oxford, 1996.
897. Dhont, J.K.G., *An Introduction to Dynamics of Colloids*, Elsevier, Amsterdam, 1996.
898. Jakeman, E., Oliver, C.J., and Pike, E.R., *J. Phys A*, 3, L 45, 1970.
899. Ware, B.R., *Adv. Colloid Interface Sci.*, 4, 1, 1974.
900. Durst, F., Melling, A., and Whitelaw, J.H., *Principles and Practice of Laser Doppler Anemometry*, 2nd ed., Academic Press, New York, 1981.
901. Miller, J.F., Schatzel, K., and Vincent, B., *J. Colloid Interface Sci.*, 143, 532, 1991.
902. Koppel, D.E., *J. Chem. Phys.*, 57, 4814, 1972.
903. Gulari, E., Gulari, E., Tsunashima, Y., and Chu, B., *J. Chem. Phys.*, 70, 3965, 1979.
904. Provencher, S.W., *Comput. Phys. Commun.*, 27, 213, 1982.
905. Morrison, I.D. et al., *Langmuir*, 4, 496, 1985.
906. Bertero, M., Boccacci, C. De Mol, and Pike, E.R., in *Optical Particle Sizing, Theory and Practice*, Gousbet, G. and Greban, G., Eds., Plenum Press, New York, 1988.
907. Finsy, R. et al., *J. Chem. Phys.*, 91, 7374, 1989.
908. Nicolai, T. et al., *Macromolecules*, 23, 1165, 1990.
909. Nicolai, T. et al., *Macromolecules*, 23, 5088, 1990.
910. Bryan, R.K., *Eur. Biophys. J.*, 18, 165, 1990; Landowski, J. and Bryan, R.K., *Macromolecules*, 24, 6364, 1991.
911. Schnablegger, H. and Glatter, O., *Appl. Opt.*, 30, 4889, 1991.
912. Pecora, R., *J. Chem. Phys.*, 49, 1036, 1968.
913. Pusey, P.N. and Tough, R.J.A., in *Dynamic Light Scattering*, Pecora, R., Ed., Plenum Press, New York, 1985, chap. 4.
914. Batchelor, G.K., *J. Fluid Mech.*, 52, 245, 1972; 74, 1, 1976.
915. Felderhof, B.U., *Physica*, 89A, 373, 1977.

916. Felderhof, B.U., *J. Phys. A Math. Gen.*, 11, 929, 1978.
917. Ackerson, B.J., *J. Chem. Phys.*, 64, 242, 1976; 69, 684, 1978.
918. Hess, W. and Klein, R., *Adv. Physics*, 32, 173, 1983.
919. Schurr, J.M., *Chem. Phys.*, 111, 55, 1987.
920. Russel, W.B. and Glendinning, A.B., *J. Chem. Phys.*, 74, 948, 1981.
921. Denkov, N.D. and Petsev, D.N., *Physica A*, 183, 462, 1992.
922. Nägele, G., *Phys. Rep.*, 272, 215, 1996.
923. Hirtzel, C.S. and Rajagopalan, R., in *Micellar Solutions and Microemulsions: Structure, Dynamics and Statistical Thermodynamics*, Springer-Verlag, New York, 1990, chap. 7.
924. Gaylor, K.J. et al., in *Light Scattering in Liquids and Macromolecular Solutions*, Degiorgio, V., Corti, M., and Giglio, M., Eds., Plenum Press, New York, 1980.
925. Jones, R.B. and Schimtz, R., *Physica A*, 149, 373, 1988.
926. Cichocki, B. and Felderhof, B.U., *J. Chem. Phys.*, 89, 1049 and 3705, 1988.
927. Kops-Werkhoven, M.M. and Fijnaut, H.M., *J. Chem. Phys.*, 74, 1618, 1981.
928. Cichocki, B. and Felderhof, B.U., *J. Chem. Phys.*, 93, 4427, 1990; 94, 563, 1991.
929. Petsev, D.N. and Denkov, N.D., *J. Colloid Interface Sci.*, 149, 329, 1992; Petsev, D.N., Denkov, N.D., and Nagayama, K., *Chem. Phys.*, 175, 265, 1993.
930. Corti, M. and Degiorgio, V., *J. Phys. Chem.*, 85, 711, 1981.
931. Belloni, L., Drifford, M., and Turq, P., *J. Phys. Lett.*, 46, L207, 1985; 46, L1183, 1985.
932. Drifford, M. et al., *J. Colloid Interface Sci.*, 105, 587, 1985.
933. Nagele, G., Mandl, B., and Klein, R., *Prog. Colloid Polym. Sci.*, 98, 117, 1995.
934. Ohshima, H. et al., *J. Chem. Soc. Faraday Trans. 2*, 80, 1299, 1984.
935. Schumacher, G.A. and van de Ven, T.G.M., *Faraday Discuss. Chem. Soc.*, 83, 75, 1987; *J. Chem. Soc. Faraday Trans.*, 87, 971, 1991.
936. Bauer, D.R., *J. Phys. Chem.*, 84, 1592, 1980.
937. Cummins, P.G. and Staples, E.J., *J. Phys. E*, 14, 1171, 1981.
938. Phillies, G.D.J., *J. Chem. Phys.*, 74, 260, 1981.
939. Phillies, G.D.J., *Phys. Rev. A*, 24, 1939, 1981.
940. Dhont, J.K.G. and de Kruif, C.G., *J. Chem. Phys.*, 79, 1658, 1983.
941. Schätzel, K., *J. Modern Opt.*, 38, 1849, 1991.
942. Pusey, P.N., *Curr. Opinion Colloid Interface Sci.*, 4, 177, 1999.
943. Drewel, M., Ahrens, J., and Schatzel, K., in *Proc. 2nd International Congress on Particle Sizing*, Arizona University Press, Tucson, AZ, 1990.
944. Segré, P.N. et al., *J. Modern Opt.*, 42, 1929, 1995.
945. Aberle, L.B. et al., *Appl. Optics*, 37, 6511, 1998.
946. Tanaka, T. and Benedek, G.B., *Appl. Opt.*, 14, 189, 1975.
947. Sorensen, C.M., Mockler, R.C., and O'Sullivan, W.J., *Phys. Rev. A*, 14, 1520, 1976; 17, 2030, 1978.
948. Dhadwal, H.S. and Ross, D.A., *J. Colloid Interface Sci.*, 76, 478, 1980.
949. Auweter, H. and Horn, D., *J. Colloid Interface Sci.*, 105, 399, 1985; *J. Phys. D*, 22, 1257, 1989.
950. Thomas, J.C. and Tjin, S.C., *J. Colloid Interface Sci.*, 129, 15, 1989.
951. MacFayden, A.J. and Jennings, B.R., *Opt. Laser Technol.*, 22, 715, 1990.
952. Thomas, J.C., *Langmuir*, 5, 1350, 1989.
953. Meeran, P.V. et al., *J. Colloid Interface Sci.*, 160, 117, 1993.
954. Wiese, H. and Horn, D., *J. Chem. Phys.*, 94, 6429, 1991.
955. Dhadwal, H.S., Ansari, R.R., and Meyer, W.V., *Rev. Sci. Instrum.*, 62, 2963, 1991.
956. Maret, G. and Wolf, P.E., *Z. Phys. B*, 65, 409, 1987.
957. Rosenbluch, M. et al., *Phys. Rev. Lett.*, 58, 2754, 1987; 60, 1130, 1988.
958. Pine, D.J. et al., *Phys. Rev. Lett.*, 60, 1134, 1988.
959. Pine, D.J. et al., in *Scattering and Localization of Classical Waves in Random Media*, Sheng, P., Ed., World Scientific, Singapore, 1989.
960. Golubentsev, A.A., *Sov. Phys. JETP*, 59, 26, 1984.
961. Stephen, M.J., *Phys. Rev. B*, 37, 1, 1988.
962. Durian, D.J., Weitz, D.A., and Pine, D.J., *Science*, 252, 686, 1991.
963. Sanyal, S. et al., *Phys. Rev. Lett.*, 72, 2963, 1994.
964. Liu, A.J. et al., *Phys. Rev. Lett.*, 76, 3017, 1996.

965. Mason, T.G., Hu, G., and Weitz, D.A., *J. Opt. Soc. Am. A*, 14, 139, 1997.
966. Durian, D.J., *Phys. Rev. E*, 55, 1739, 1997.
967. Durian, D.J., *Curr. Opinion Colloid Interface Sci.*, 2, 615, 1997.
968. Hebraud, P. et al., *Phys. Rev. Lett.*, 78, 4657, 1997.
969. Maret, G., *Curr. Opinion Colloid Interface Sci.*, 2, 251, 1997.
970. Gisler, T. and Weitz, D.A., *Curr. Opinion Colloid Interface Sci.*, 3, 586, 1998.
971. Debye, P., *Ann. N.Y. Acad. Sci.*, 51, 575, 1949.
972. Debye, P. and Anacker, E.W., *J. Phys. Colloid Chem.*, 55, 644, 1959.
973. Mysels, K.J. and Princen, L.H., *J. Phys. Chem.*, 63, 1696, 1959.
974. Huisman, H.F., *Proc. Kon. Ned. Akad. Wet.*, B67, 367, 1964; B67, 376, 1964; B67, 388, 1964; B67, 407, 1964.
975. Vrij, A. and Overbeek, J.Th.G., *J. Colloid Sci.*, 17, 570, 1962.
976. Becher, P., in *Nonionic Surfactants*, Schick, M.J., Ed., Marcel Dekker, New York, 1967, chap. 15.
977. Hall, D.J. and Tiddy, G.J.T., in *Anionic Surfactants: Physical Chemistry of Surfactant Action*, Lucasen-Reynders, E.H., Ed., Marcel Dekker, New York, 1981, chap. 2.
978. Eicke, H.-F., *Topics Current Chem.*, 87, 85, 1980.
979. Mukerjee, P., *J. Phys. Chem.*, 76, 565, 1972.
980. Israelachvili, J.N., Mitchell, D.J., and Ninham, B.W., *J. Chem. Soc., Faraday Trans.*, 2, 72, 1525, 1976.
981. Ruckenstein, E. and Nagarajan, R., *J. Colloid Interface Sci.*, 57, 388, 1976; 91, 500, 1983.
982. Mazer, N.A., in *Dynamic Light Scattering*, Pecora, R., Ed., Plenum Press, New York, 1985, chap. 8.
983. Mazer, N.A., Benedek, G.B., and Carey, M.C., *J. Phys. Chem.*, 80, 1075, 1976.
984. Briggs, J., Nicoli, D.F., and Ciccolello, R., *Chem. Phys. Lett.*, 73, 149, 1980.
985. Mishic, J.R. and Fisch, M.R., *J. Chem. Phys.*, 92, 3222, 1990.
986. Schillen, K., Brown, W., and Johnsen, R.M., *Macromolecules*, 27, 4825, 1994.
987. Porte, G., Appell, J., and Poggi, Y., *J. Phys. Chem.*, 84, 3105, 1980.
988. Appell, J. and Porte, G., *J. Colloid Interface Sci.*, 81, 85, 1981.
989. Imae, T., *J. Phys. Chem.*, 94, 5953, 1990.
990. Alargova, R. et al., *Langmuir*, 11, 1530, 1995.
991. Alargova, R.G. et al., *Langmuir*, 14, 4036, 1998.
992. Dorshow, R. et al., *J. Phys. Chem.*, 86, 2388, 1982; 87, 1409, 1983.
993. Missel, P.J. et al., *J. Phys. Chem.*, 84, 1044, 1980.
994. Rohde, A. and Sackman, E., *J. Colloid Interface Sci.*, 78, 330, 1980.
995. Hartland, G.V., Grieser, F., and White, L.R., *J. Chem. Soc. Faraday Trans.*, 1, 83, 591, 1987; Dunstan, D.E. and White, L.R., *J. Colloid Interface Sci.*, 134, 147, 1990.
996. Ortega, F. et al., *J. Phys. Chem.*, 94, 501, 1990.
997. Corti, M. and Degiorgio, V., *Phys. Rev. Lett.*, 45, 1045, 1980; *J. Phys. Chem.*, 85, 1442, 1981.
998. Calje, A., Agterof, W., and Vrij, A., in *Micellization, Solubilization and Microemulsions*, Mittal, K., Ed., Plenum Press, New York, 1977.
999. Lemaire, B., Bothorel, P., and Roux, D., *J. Phys. Chem.*, 87, 1023, 1983.
1000. Cazabat, A.M., Langevin, D., and Pouchelon, A., *J. Colloid Interface Sci.*, 73, 1, 1980.
1001. Hou, M.J., Kim, M., and Shah, D.O., *J. Colloid Interface Sci.*, 123, 398, 1988.
1002. Auvrey, L., *J. Phys. Chem. (Paris)*, 46, 163, 1985.
1003. Fletcher, P.D.I., Howe, A.M., and Robinson, B.H., *J. Chem. Soc. Faraday Trans.*, 1, 83, 985, 1987.
1004. Fletcher, P.D.I. and Holzwarth, J.F., *J. Phys. Chem.*, 95, 2550, 1991.
1005. Lagues, M., Ober, R., and Taupin, C., *J. Phys. Lett.*, 39, 487, 1978.
1006. Lagourette, B. et al., *Nature (London)*, 281, 60, 1979.
1007. Eicke, H.-F., Shepherd, J.C.W., and Steineman, A., *J. Colloid Interface Sci.*, 56, 168, 1976.
1008. Guering, P. and Cazabat, A.M., *J. Phys. Lett.*, 44, 601, 1983.
1009. Guering, P., Cazabat, A.M., and Paillette, M., *Europhys. Lett.*, 2, 953, 1986.
1010. Dorshow, R.B. and Nicoli, D.F., in *Measurement of Suspended Particles by QELS*, Dahneke, B.E., Ed., Wiley, New York, 1983, p. 529.
1011. Guering, P., Nilsson, P.-G., and Lindman, B., *J. Colloid Interface Sci.*, 105, 41, 1985.
1012. Kato, T., Takeuchi, H., and Seimiya, T., *J. Colloid Interface Sci.*, 140, 253, 1990.
1013. Tuzar, Z. and Kratochvil, P., in *Surface and Colloid Science*, Vol. 15, Matijević, E., Ed., Plenum Press, New York, 1993, chap. 1.

1014. Cogan, K.A. and Gast, A.P., *Macromolecules*, 23, 745, 1990; Chu, B., *Langmuir*, 11, 414, 1995.
1015. Satoh, N. and Tsujii, K., *J. Phys. Chem.*, 91, 6629, 1987.
1016. Thunig, C., Hoffmann, H., and Platz, G., *Prog. Colloid Polym. Sci.*, 79, 297, 1989; 83, 167, 1990.
1017. McDonald, J.A. and Rennie, A.R., *Prog. Colloid Polym. Sci.*, 98, 75, 1995.
1018. Goddard, E.D. and Ananthapadmanabhan, K.P., Eds., *The Interactions of Surfactants with Polymers and Proteins*, CRC Press, Boca Raton, FL, 1993.
1019. Bahadur, P., Dubin, P., and Rao, Y.K., *Langmuir*, 11, 1951, 1995; Li, Y. et al., *Macromolecules*, 28, 3098, 1995.
1020. Hayakawa, K. and Kwak, J.C.T., in *Cationic Surfactants: Physical Chemistry*, Rubingh, D.N. and Holland, P.M., Eds., Marcel Dekker, New York, 1991, chap. 5.
1021. Corti, M. and Canti, L., *Adv. Colloid Interface Sci.*, 32, 151, 1990.
1022. Bloomfield, V.A., in *Dynamic Light Scattering*, Pecora, R., Ed., Plenum Press, New York, 1985, chap. 10.
1023. Egelhaaf, S.U., Pedersen, J.S., and Schurtenberger, P., *Prog. Colloid Polym. Sci.*, 98, 224, 1995.
1024. Langevin, D., Ed., *Light Scattering by Liquid Surfaces and Complementary Techniques*, Marcel Dekker, New York, 1992.
1025. Earnshaw, J.C. and McCoo, E., *Langmuir*, 11, 1087, 1995.
1026. Vrij, A., Joosten, J.G.H., and Fijnaut, H.M., *Adv. Chem. Phys.*, 48, 329, 1981.
1027. Joosten, J.G.H., in *Thin Liquid Films*, Ivanov, I.B., Ed., Marcel Dekker, New York, 1988, chap. 9.
1028. Hirleman, E.D., *Part. Part. Syst. Charact.*, 4, 128, 1987.
1029. van de Hulst, H.C., *Multiple Light Scattering*, Academic Press, New York, 1980.
1030. Penders, M.G.H.M. and Vrij, A., *J. Chem. Phys.*, 93, 3704, 1990.
1031. Apfel, U., Hörner, K.D., and Ballauff, M., *Langmuir*, 11, 3401, 1995.
1032. Bryant, G. and Thomas, J.C., *Langmuir*, 11, 2480, 1995.
1033. Barber, P.W., Yeh, C., and Wang, D.-S., *Appl. Opt.*, 14, 2864, 1975; 17, 797, 1978; 18, 1190, 1979.
1034. Quirantes, A. and Delgado, A.V., *Prog. Colloid Polym. Sci.*, 98, 145, 1995.
1035. Purcell, E.M. and Pennypacker, C.R., *Astrophys. J.*, 186, 705, 1973.
1036. Buitenhuis, J., Dhont, J.K.G., and Lekkerkerker, H.N.W., *J. Colloid Interface Sci.*, 162, 19, 1994.
1037. Schaefer, D.W., *J. Chem. Phys.*, 66, 3980, 1977.
1038. Finsy, R. et al., *J. Chem. Phys.*, 82, 3812, 1985.
1039. Clark, N.A., Hurd, A.J., and Ackerson, B.J., *Nature (London)*, 281, 57, 1979.
1040. Pieranski, P., *Contemp. Phys.*, 24, 25, 1983.
1041. Pusey, P.N., *Philos. Trans. R. Soc. London*, A293, 429, 1979.
1042. van Megen, W., Pusey, P.N., and Bartlett, P., *Phase Transitions*, 21, 207, 1990.
1043. Piazza, R. and Degiorgio, V., *Physica A*, 182, 576, 1982.
1044. Degiorgio, V. et al., *J. Chem. Soc. Faraday Trans*, 87, 431, 1991.
1045. Dhont, J.K.G., Smits, K., and Lekkerkerker, H.N.M., *J. Colloid Interface Sci.*, 152, 386, 1992.
1046. Hiltner, P.A. and Krieger, I.M., *J. Phys. Chem.*, 73, 2386, 1969.
1047. Yoshiyama, T., Sogami, I., and Ise, N., *Phys. Rev. Lett.*, 53, 2153, 1984.
1048. Sogami, I. and Yoshiyama, T., *Phase Transitions*, 21, 171, 1990.
1049. Monovoukas, Y. and Gast, A.P., *Phase Transitions*, 21, 183, 1990.
1050. Bartsch, E., *Curr. Opinion Colloid Interface Sci.*, 3, 577, 1998.
1051. Van Megen, W. et al., *Phys. Rev. E*, 58, 6073, 1998.
1052. D'Aguzzo, B. and Klein, R., *J. Chem. Soc. Faraday Trans.*, 87, 379, 1991.
1053. Krause, R. et al., *Physica A*, 178, 241, 1991.
1054. Wagner, N.J. et al., *J. Chem. Phys.*, 95, 494, 1991.
1055. Pusey, P.N. and van Megen, W., *Nature (London)*, 320, 340, 1986.
1056. Härtl, W., Klemp, R., and Versmold, H., *Phase Transitions*, 21, 229, 1990.
1057. Harland, J.L. and van Megen, W., *Phys. Rev. E*, 55, 3054, 1997.
1058. Russel, W.B. et al., *Langmuir*, 13, 3871, 1997.
1059. Palberg, T., *Curr. Opinion Colloid Interface Sci.*, 2, 607, 1997.
1060. Hoffman, R.L., *J. Colloid Interface Sci.*, 46, 491, 1974.
1061. Bossis, G., Brady, J.F., and Mathis, C., *J. Colloid Interface Sci.*, 126, 1 and 16, 1988.
1062. Wagner, N.J. and Russel, W.B., *Phys. Fluids*, A2, 491, 1990.
1063. Ackerson, B.J. and Clark, N.A., *Physica A*, 118, 221, 1983; *Phys. Rev. A*, 30, 906, 1984.

1064. Ackerson, B.J. and Pusey, P.N., *Phys. Rev. Lett.*, 61, 1033, 1988.
1065. Ackerson, B.J., *Physica A*, 174, 15, 1991.
1066. Weitz, D.A. and Oliveria, M., *Phys. Rev. Lett.*, 52, 1433, 1984.
1067. Weitz, D.A. et al., *Phys. Rev. Lett.*, 53, 1651, 1984; *Phys. Rev. Lett.*, 54, 1416, 1985; 57, 2037, 1986.
1068. Meakin, P., in *Phase Transitions*, Vol. 12, Domb, C. and Lebowitz, J.L., Eds., Academic Press, New York, 1988.
1069. Weitz, D.A., Lin, M.Y., and Huang, J.S., in *Physics of Complex and Supramolecular Fluids*, Safran, S.A., and Clark, N.A., Eds., Wiley-Interscience, New York, 1987.
1070. Kolb, M., *Phys. Rev. Lett.*, 53, 1654, 1984.
1071. Mandelbrot, B.B., *The Fractal Geometry of Nature*, Freeman, New York, 1983.
1072. Meakin, P., *Phys. Rev. Lett.*, 51, 1119, 1983.
1073. Van Dongen, G.J. and Ernst, M.H., *Phys. Rev. Lett.*, 54, 1396, 1985.
1074. Brown, W.D. and Ball, R.C., *J. Phys. A*, 18, L517, 1985.
1075. Schaeffer, D.W. et al., *Phys. Rev. Lett.*, 52, 2371, 1984.
1076. Ball, R.C. et al., *Phys. Rev. Lett.*, 58, 274, 1987.
1077. Meakin, P., Vicsek, T., and Family, F., *Phys. Rev. B*, 31, 564, 1985.
1078. Lin, M.Y. et al., in *Fractals in the Natural Sciences*, Fleischmann, M., Tildesley, D.J., and Ball, R.C., Eds., Princeton University Press, Princeton, NJ, 1989.
1079. Amal, R., Raper, J.A., and Waite, T.D., *J. Colloid Interface Sci.*, 140, 158, 1990.
1080. Odriozola, G. et al., *J. Colloid Interface Sci.*, 240, 90, 2001.
1081. Georgialis, Y. and Saenger, W., *Adv. Colloid Interface Sci.*, 46, 165, 1993.
1082. Georgialis, Y. et al., *J. Crystal Growth*, 126, 245, 1993.
1083. Eberstein, W., Georgialis, Y., and Saenger, W., *J. Crystal Growth*, 143, 71, 1994.
1084. Muschol, M. and Rosenberger, F., *J. Chem Phys.*, 103, 10424, 1995.
1085. Nikolai, T., Urban, C., and Schurtenberger, S., *J. Colloid Interface Sci.*, 240, 419, 2001.

6 Solubilization in Aqueous Surfactant Systems

Harald Høiland and Anne Marit Blokhus

CONTENTS

- 6.1 Introduction
 - 6.1.1 Partitioning Equilibria
 - 6.2 Experimental Methods
 - 6.2.1 Solubility
 - 6.2.1.1 Total Solubility
 - 6.2.1.2 Vapor Pressure
 - 6.2.2 Physical Properties of the Surfactant
 - 6.2.2.1 Changes in the Critical Micelle Concentration
 - 6.2.2.2 Changes in the Krafft Point
 - 6.2.3 Spectroscopic Methods
 - 6.2.3.1 Ultraviolet Spectroscopy
 - 6.2.3.2 Fluorescence
 - 6.2.3.3 Nuclear Magnetic Resonance Methods
 - 6.2.4 Separation Methods
 - 6.2.4.1 Chromatographic Methods
 - 6.2.4.2 Ultrafiltration
 - 6.2.5 Thermodynamic Data
 - 6.3 Results
 - 6.3.1 Partition Coefficients
 - 6.3.1.1 Partition Coefficients of Alcohols
 - 6.3.1.2 Partition Coefficients of Gases, Aliphatic Hydrocarbons, and Aromatic Hydrocarbons
 - 6.3.1.3 Partition Coefficients of Phenols, Naphthols, Amines, Amides, and Aldehydes
 - 6.3.2 Activity Coefficients
 - 6.3.3 Energetics of Solubilization
 - 6.3.4 Model Calculations
 - 6.3.5 Partial Molar Volumes and Compressibilities
 - 6.3.6 Solubilization Sites and Structural Effects
 - 6.3.7 Solubilization in Mixed Micelles
 - 6.4 List of Abbreviations
 - 6.4.1 Anionic Surfactants
 - 6.4.2 Cationic Surfactants
- References

6.1 INTRODUCTION

One of the most important properties of aqueous micellar solutions is their ability to enhance the solubility of otherwise sparingly soluble substances. This seems to have been acknowledged as far back as 1846 when, according to McBain and Hutchinson,¹ Persoz observed increased solubility in soap solutions.

The process of enhanced solubility in micellar solutions is normally referred to as solubilization, or in the words of McBain *solubilization* is the term given “to a particular mode of bringing into solution substances that are otherwise insoluble in a given medium.”¹ Similar definitions were proposed later, with the only significant change that solubilization includes increased solubility caused by the presence of micelles. Over the years a considerable amount of empirical information relating to solubilization has been published. The early studies have been reviewed by McBain,² Klevens,³ McBain and Hutchinson,¹ and by Elworthy et al.⁴ Later developments have been described in several reviews, the most comprehensive is the book edited by Christian and Scamehorn.⁵

At least three components are present in systems where solubilization takes place, i.e., the solvent, the micelle-forming amphiphile, and the component that is solubilized. In this chapter we only deal with aqueous systems. The micelle-forming amphiphile is termed *surfactant* here, and the third component is termed the *solute*. Of course, the micelles can be composed of a mixture of surfactants and several solutes can be added. However, we concentrate on micelles of one surfactant with one solute added, although a short review of mixed micelles is given.

The surfactants can be anionic, cationic, zwitterionic, or nonionic depending on the hydrophilic headgroup. The important characteristic of micelles is that the hydrocarbon chains constitute the inner part of the micelle. Here the concentration of water is low or negligible, and the concentration of ionic headgroups in this region is also negligible.⁶⁻⁸ The inner hydrocarbon region thus consists of randomly oriented hydrocarbon chains forming a liquid-like region.^{9,10} The ionic headgroups, counterions, water, and parts of the hydrocarbon chain are positioned in a thin layer surrounding the micelle.^{11,12}

The geometric form of the micelles depends on the concentration of the surfactant and on additives. In the absence of additives the micelles are spherical for concentrations ranging from the critical micelle concentration (cmc) to at least ten times the cmc.^{6,13,14} At higher surfactant concentrations or with additives (added salt is the most efficient) rodlike or prolate micelles will form.^{6,15} At high surfactant concentration or with large amounts of additive, the micellar phase becomes unstable, and other phases will be present. In most cases a hexagonal phase or a lamellar phase will be the phases in equilibrium with the aqueous micellar phase.^{16,17}

The solubilizing power of micelles is associated with the hydrocarbon core, and it is thus not surprising that apolar molecules like *n*-alkanes generally appear to solubilize in the core region of the micelles although simple geometry shows that parts of the solubilized molecule will be close to the headgroup region.¹⁸ The volume and the aggregation number of the spherical micelles will normally increase by the solubilization process.¹⁹⁻²²

The solubilization of polar molecules, such as alcohols, in aqueous surfactant systems is quite complex, as demonstrated by the water–potassium decanoate–octanol system, which is well characterized. The entire phase diagram has been mapped.^{23,24} However, keeping confined to the aqueous micellar phase, polar solutes are generally found to solubilize in the micelles with the polar group anchored in the headgroup region. If the hydrocarbon chain of the polar compound is sufficiently long, it will presumably extend to the micellar core.^{6,25-28} However, it appears likely that the number of polar solutes anchored in the headgroup region is limited; Lianos and Zana²⁹ suggest about 2.4. From solubility measurements it has been observed that the amount of alcohol solubilized per amphiphile molecule can be significantly larger, in some cases more than five alcohol molecules per amphiphile in the micelle.²⁹⁻³¹ In these cases there is some evidence suggesting that the alcohol molecules will penetrate deeper into the micelle.^{31,32}

Concerning aromatic solutes there is less agreement about the solubilization process. Data have been presented suggesting that, for example, benzene, is located in the micellar interior, in the palisade layer, or near the micellar surface, or indeed in all these locations.³³⁻³⁸

It is also known that additives may change the size and shape of micelles.³⁹⁻⁴¹ At a certain point, as the surfactant or additive concentrations change, ionic micelles may change shape from spherical or nearly spherical to rodlike or other elongated forms. This may also affect the solubilization of the additive. It appears that alkane solubilization increases as the micelles become large, rodlike aggregates, whereas for polar additives like alcohols the solubilization decreases.⁴²⁻⁴⁵

6.1.1 PARTITIONING EQUILIBRIA

The solubilization process seems to be well understood on a qualitative basis. Quantitatively, however, there appears to be less agreement. First, in reporting the extent of solubilization different authors may use different definitions and concentration units, as we discuss later. Second, for a three-component system both the concentrations of the surfactant and the solute can be varied. This means that we rarely find data that are directly comparable due to variation in concentrations. Often solubilization is reported as single points along the concentration profiles of surfactant and solute. In some cases the method of measurement sets the limits.

The simplest thermodynamic model for solubilization is the pseudophase or phase separation model. The micelles are treated as a separate phase consisting of surfactant and the solubilized molecules. Solubilization is regarded as a simple distribution or equilibrium of the solute between the aqueous and the micellar phases, i.e.,

$$\mu_{A,\text{aq}} = \mu_{A,\text{mic}} \quad (6.1)$$

This equilibrium or partitioning of a solute between micelles and the aqueous surroundings has not been uniformly described in the literature. We speak of distribution coefficient or constant, partition coefficient or constant, or equilibrium constant to describe equilibria that are the same qualitatively speaking. However, the definition of the above-mentioned coefficients or constants varies. In this chapter we refer to the process as a partitioning of a molecule between micelles and the aqueous surroundings, and we term it the *partition coefficient* regardless of the concentration units used to define it.

By using the mole fraction scale, the partition coefficient can thus be defined as

$$K_x = X_{\text{mic}}/X_{\text{aq}} \quad (6.2)$$

Here X_{mic} represents the mole fraction of the solute in the micellar pseudophase, X_{aq} the mole fraction of solute in the surrounding aqueous phase, and the activity coefficients have been neglected.⁴⁶⁻⁴⁸ Other concentration units have been used in calculating the partition coefficient from Equation 6.1, for example, the molarity scale. However, this requires knowledge of the molar volumes in the micellar state,⁴⁹⁻⁵¹ and is thus less rational than mole fractions.

The mass action model describes micelle formation as an equilibrium process. The micellar aggregation number becomes an important parameter. The solubilization process can be treated as a stepwise addition of solute molecules to the micelles.⁵²⁻⁵⁵ However, the partition coefficient based on this model requires the aggregation number, which makes it difficult to use in practice. There are several methods of simplification. One is to define the partition coefficient as:^{56,57}

$$K_s = C_{\text{mic}}/C_{s,\text{mic}} C_{\text{aq}} \quad (6.3)$$

where C_{mic} , C_{aq} , and $C_{s,\text{mic}}$ are molar concentrations of the solute in the micelles, in the aqueous surroundings, and of the surfactant in the micelles, respectively. All the molarities have been defined

with respect to the total volume of the solution. This definition is in better accordance with the mass action model, but it is nevertheless simple to convert K_x into K_s , and vice versa, because

$$K_s = X_{\text{mic}} / (1 - X_{\text{mic}}) C_{\text{aq}} \quad (6.4)$$

This is related to X_{aq} of Equation 6.2 by

$$X_{\text{aq}} = C_{\text{aq}} / (55.5 + C_{\text{aq}}) \quad (6.5)$$

Roux et al.^{58,59} combined the use of a mass action model for the surfactant and a pseudophase model for the solute, arriving at a slightly complicated expression for the partition coefficient. In the terms of Roux et al.

$$-\ln K_D = \ln(\beta m_3 / X_{B'}) + X_{B'} - 1 \quad (6.6)$$

The partition coefficient K_D will, for an ideal system, be defined as before, Equation 6.2. β is the fraction of solute in the aqueous phase, m_3 the molality of the solute, and $X_{B'}$ the mole fraction of solute molecules in the micellar phase.

DeLisi et al.⁶⁰⁻⁶² used the opposite approach, in the sense that the pseudophase model was used for the surfactant and the mass action model for the solute. This means that the partition coefficient is defined as in Equation 6.2.

The models of Roux et al. and of DeLisi et al. have been developed, as discussed later, to model thermodynamic data, in particular partial molar quantities.

Yet another definition often used by Mahmoud et al.⁶³ is

$$K_c = X_{\text{mic}} / C_{\text{aq}} \quad (6.7)$$

This is also easily converted into K_x or K_s as:

$$K_c = K_s (1 - X_{\text{mic}}) = K_x X_{\text{aq}} / C_{\text{aq}} \quad (6.8)$$

K_x , K_s , and K_c are all partition coefficients, and in this chapter we mostly use K_x , thus recalculating data from K_s or K_c .

In this chapter the main aim is to present partition coefficients for solutes in aqueous surfactant systems, having carried out a critical evaluation of the data. We concentrate on polar solutes. Energetics of solubilization and solubilization sites in the micelles are also discussed.

6.2 EXPERIMENTAL METHODS

Many different experimental methods have been used to determine the partition coefficient of solutes. In this chapter it is not possible to present all the different methods, but we try to give a representative selection of the most-used methods. The methods have been classified into the following main groups: (1) solubility, (2) properties of the surfactants, (3) spectroscopic methods, (4) separation methods, (5) thermodynamic functions.

Most of these methods rely on using the pseudophase approach, and, as will be evident from the description of the methods, they normally determine the fraction of solute in the micellar phase, α , defined as

$$\alpha = n_{\text{mic}} / n_{\text{tot}} \quad (6.9)$$

where n_{mic} is the number of moles of solute in the micelle and n_{tot} is the total number of moles of solute. The relation between α and the partition coefficient K_x is as follows:

$$K_x = 55.5\alpha / [(1 - \alpha)(\alpha m_{\text{tot}} + m_{\text{s,mic}})] \quad (6.10)$$

where $m_{\text{s,mic}}$ and m_{tot} are the molal concentration of surfactant in the micellar state and the total molal concentration of solute, respectively. In all equations above, activity coefficients have been neglected.

6.2.1 SOLUBILITY

6.2.1.1 Total Solubility

Classically, the partition coefficients have been obtained from total solubility measurements, which are based on the ability of micellar solutions to enhance the solubility of compounds that are otherwise insoluble or sparingly soluble in water. The solubility limit for the solute at different surfactant contents is detected experimentally by, for example, turbidity or density measurements.

The solubility of gases has basically been studied by this method. The data have recently been reviewed by King.⁶⁴

Based on the standard definition of the partition coefficient, Equation 6.2, the following expression can be derived for the correlation between the total solubility of the solute and the surfactant concentration:⁴⁷

$$m_{\text{tot}} = \frac{K_x M_{\text{H}_2\text{O}} m_{\text{aq}}}{1 - K_x M_{\text{H}_2\text{O}} m_{\text{aq}}} (m_{\text{s,tot}} - m_{\text{s,cmc}}) + m_{\text{aq}} \quad (6.11)$$

Equation 6.11 suggests linearity between the total solubility of the solute and the surfactant micellar concentration. Experiments have shown that the solubility of a solute does indeed increase linearly with the surfactant content, but only as long as the surfactant concentration is fairly low.^{29,65-67} Typically, deviations from linearity occur at surfactant concentrations between 0.05 and 0.1 *m*. As long as Equation 6.9 is obeyed, the partition coefficient can be obtained from the slope of the linear plot.

The method is accurate, but the result is limited to low surfactant concentrations (the linear part) and solute concentrations at saturation. It should also be noted that the stability of a phase depends on the properties of the precipitating phase as well. For water–surfactant–alcohol systems the precipitating phases may be an alcohol-rich phase (L_2) or a lamellar phase (D),¹⁶ and the data indicate that the linear part where Equation 6.9 is fulfilled coincides with the part where the precipitating phase is the alcohol-rich L_2 phase.^{31,68}

6.2.1.2 Vapor Pressure

For a volatile solute, the vapor pressure can be measured. This can be done as a function of the solute concentration at constant surfactant concentration. The activity of the solute is P/P^0 where P^0 is the vapor pressure of the pure solute. Two sets of data are required, the activity (or vapor pressure) of the solute in water and the activity (or vapor pressure) of the solute in aqueous surfactant solution. The horizontal distance between these two curves is a direct measure of the solubilized solute. The experimental techniques used for this purpose are headspace chromatography as used by Hayase and Hayano⁶⁹ and Spink and Colgan,⁷⁰ or the final equilibrium pressure over a solution containing a known quantity of volatile liquid can be measured. The latter method has been developed by Tucker and Christian.^{71,72} This method has the added advantage of providing an easy

way to calculate activity coefficients of the solute in the micellar state. A detailed account of the method and its merits has recently been made by Tucker.⁷³ From these data, plots based on Henry's law can be constructed, and at any given partial pressure of the solute the difference between the concentration of solute in the surfactant solution and the concentration of solute in the pure aqueous solution give the solute concentration in the micellar aggregates. The partition coefficient of the solute is thereby easily calculated. By this method the partition coefficient can be found as a function of both surfactant and solute concentration. However, to obey Henry's law most work has been performed at low solute concentrations.

6.2.2 PHYSICAL PROPERTIES OF THE SURFACTANT

6.2.2.1 Changes in the Critical Micelle Concentration

Addition of a solute will normally decrease the cmc. This decrease in the cmc can be correlated with the partition coefficient through the following relation proposed by Shirahama and Kashiwabara:⁷⁴

$$-\frac{d \ln \text{cmc}}{dX_{\text{aq}}} = \theta K_x \quad (6.12)$$

where θ is a coefficient that has been referred to as the ISA (interaction of surfactant and additive) coefficient by Hayase and Hayano.⁷⁵ Different approaches have been used to interpret θ physically, leading to expressions where θ is related to the degree of counterion dissociation of the micelles upon addition of solute.^{76,77} Treiner⁷⁸ has focused on the initial slope of the variation of the cmc with concentration of solute and derived the following relation:

$$\log \frac{\text{cmc}_w}{\text{cmc}_{w,s}} = K_M m_{\text{tot}} \quad (6.13)$$

cmc_w and $\text{cmc}_{w,s}$ is in water and in presence of solute at molality, m_{tot} , and K_M is a constant given by

$$K_M = \frac{1}{2} \left\{ k_s^N + \frac{K_x \times 55.5}{2.303} \right\} \quad (6.14)$$

The partition coefficient, K_x , can easily be calculated from this expression if the Setchenov salting constant k_s^N is known.

The decrease in the cmc induced by the solute is easily detected by conductivity measurements from which the counterion dissociation degree can also be calculated. These methods, however, depend either on the estimation of θ or on determination of the Setchenov constant (below the cmc). In some cases the Setchenov constant has been found experimentally; in other cases it has been calculated empirically.

6.2.2.2 Changes in the Krafft Point

By treating the Krafft point as the melting point of the hydrated solid surfactant, the partition coefficient of the solute can be calculated from its effect on the Krafft point.⁷⁹ Simple thermodynamic considerations lead to the following relationship at low mole fractions of solute in the micellar phase:

$$-\Delta T = \frac{K_x R T_0^2}{55.5 \Delta H_{\text{fus}}} m_{\text{tot}} \quad (6.15)$$

where $-\Delta T = T - T_0$ is the Krafft point depression. The subscript zero denotes the absence of solute, ΔH_{fus} is the enthalpy of fusion of the surfactant (hydrated solid to micellar state). Equation 6.15 suggests a linear plot of ΔT vs. m_{tot} from which the partition coefficient, K_x , can be calculated. The Krafft point depression can be determined by observing the disappearance of turbidity during heating detected, for example, by ultraviolet (UV) measurements.

6.2.3 SPECTROSCOPIC METHODS

6.2.3.1 Ultraviolet Spectroscopy

The method is based on the observation that chromophore-containing solutes undergo significant shifts in their UV spectra upon solubilization in micelles.⁸⁰ The experimentally determined molar absorbance of a solute at a given wavelength in a micellar solution, E , will be an average value of the molar absorbance of the molecules in the micellar and the aqueous phase.

$$E = \alpha E_{\text{mic}} + (1 - \alpha) E_{\text{aq}} \quad (6.16)$$

When the condition $c_{s,\text{mic}} \gg c_{\text{mic}}$ is fulfilled, the partition coefficient K_x will be related to the molar absorbances in the following way:

$$\frac{E_{\text{aq}}}{E - E_{\text{aq}}} = A + \frac{55.56A}{K_x} \frac{1}{(c_{s,\text{tot}} - c_{s,\text{cmc}})} \quad (6.17)$$

where $A = E_{\text{aq}} (E_{\text{aq}} - E_{\text{mic}})^{-1}$. The partition coefficient is obtained by plotting the left-hand side of Equation 6.17 against $(c_{s,\text{tot}} - c_{s,\text{cmc}})^{-1}$ provided that the plots are described by straight lines. The method is non-disturbing, but restricted to chromophore-containing solutes and also dependent on an appropriate change in the absorbance between the aqueous and the solubilized state.

6.2.3.2 Fluorescence

The description given here is confined to the method developed by Abuin and Lissi⁸¹ demonstrating the use of fluorescence as a method for determining partition coefficients for solutes that are not by themselves fluorescent. The method is based on the observation that an additive changes the characteristics of the fluorescence of a micelle-incorporated probe such as pyrene. It is assumed that the fluorescence intensity of micelle-incorporated pyrene is determined only by the mole fraction of solute in the micellar pseudophase. The probe fluorescence intensity ratio I/I_0 in the absence and presence of a solute is measured as a function of the solute concentration at different surfactant concentrations. From plots of the intensity ratio vs. the solute concentration at different surfactant concentrations we obtain a set of additive concentrations c_{tot} that corresponds to the same I/I_0 value and thereby the same X_{mic} and K_x . C_{tot} is related to the concentration of micellized surfactant, $c_{s,\text{mic}}$, through the following equation:

$$\frac{C_{\text{tot}} \times 18}{(1000 - \Psi_{\text{mic}})} = \frac{X_{\text{mic}}}{K_x} + \frac{X_{\text{mic}}}{(1 - X_{\text{mic}})} \frac{C_{s,\text{mic}} \times 18}{(1000 - \Psi_{\text{mic}})} \quad (6.18)$$

where Ψ_{mic} is the volume of micellar pseudophase in a liter of solution. The partition coefficient K_x and X_{mic} can thus be evaluated from a plot of the left-hand side of Equation 6.18 vs. $C_{s,\text{mic}} \times 18 / (1000 - \Psi_{\text{mic}})^{-1}$. By this method the partition coefficient can be found at different mole fractions of the solute in the micellar pseudophase.

6.2.3.3 Nuclear Magnetic Resonance Methods

Basically two nuclear magnetic resonance (NMR) techniques can be used to determine the partition coefficient. The first is based on the Fourier transform NMR pulsed-gradient spin echo (FT-PGSE) self-diffusion technique,⁸² the other by the NMR paramagnetic relaxation technique.⁵⁰ In both techniques the fraction of solute in the micelle, α , is determined and K_x can thus be calculated through Equation 6.10.

In the self-diffusion experiments α is obtained through the following relation:

$$\alpha = \frac{D_{\text{free}} - D_{\text{obs}}}{D_{\text{free}} - D_{\text{mic}}} \quad (6.19)$$

where D_{free} and D_{mic} are the self-diffusion coefficients of the solute in the aqueous and the micellar phase, respectively. D_{free} can be obtained from the diffusion coefficient of the solute in water (in the absence of micelles). For solutes that are too insoluble to measure by NMR, the self-diffusion coefficient must be estimated. However, D_{free} must be corrected for possible micellar obstruction effects. D_{mic} can be taken as equal to the micellar self-diffusion coefficient. This can be taken as the self-diffusion coefficient of the surfactant if the surfactant concentration is well above the cmc (negligible surfactant monomer concentration). Alternatively, the micellar diffusion coefficient can be obtained by monitoring the self-diffusion coefficient of a very hydrophobic solute such as tetramethylsilane (TMS), which can be regarded as completely solubilized in the micellar phase.

The NMR paramagnetic relaxation method is based on the difference in the relaxation rates of the solute in aqueous and micellar solutions, in the presence and absence of a small concentration of paramagnetic ions. With the assumption that the paramagnetic ions have no influence on the relaxation rate for the solute in the micellar phase, the fraction of the solute in the micellar phase, α , can be calculated as follows:

$$\alpha = 1 - \frac{R_{\text{obs}}^p - R_{\text{obs}}}{R_{\text{aq}}^p - R_{\text{aq}}} \quad (6.20)$$

R_{obs}^p and R_{obs} are the observed spin-lattice relaxation rates of the solubilized species, with and without paramagnetic ions added, respectively, and R_{aq}^p and R_{aq} are the corresponding quantities in the aqueous phase.

Both methods have the advantage that they can be used for almost any surfactant–solute system, and they are not limited to any specific concentration range. However, at low concentrations the NMR signal may be too weak to detect, and for the self-diffusion method, the correction for micellar obstruction effects is not clear. In one paper, Stilbs⁸² makes a correction of about 9%; in another it is noted that it is doubtful if the micelles really represent an obstacle, and no correction term is employed.⁸³ The paramagnetic method has a disadvantage of introducing a salt to the system, which could, in principle, affect the equilibria. However, Gao et al.⁵⁰ have made a thorough investigation, concluding that this effect is negligible.

6.2.4 SEPARATION METHODS

6.2.4.1 Chromatographic Methods

Armstrong and Nome⁸⁴ have shown that chromatographic methods such as high-pressure liquid chromatography (HPLC) and thin layer chromatography (TLC)⁸⁵ can be used for determination of partition coefficients. The aqueous micellar solutions are used as the mobile phase. When the concentration of micelles in the mobile phase is increased, the retention and capacity factors of

many solutes decrease dramatically. As a result of this, the partition coefficients can be obtained from the following equation from HPLC retention data:

$$\frac{V_s}{V_e - V_m} = \frac{\bar{V}_m(K_{mw} - 1)}{K_{sw}} C_{s,\text{mic}} + \frac{1}{K_{sw}} \quad (6.21)$$

where V_s is the volume of the stationary phase, V_m is the volume of the mobile phase, and V_e is the elution volume of the solute, \bar{V}_m is the partial molar volume of the surfactant in the micelle, K_{sw} is the partition coefficient of a solute between the micellar and the stationary phase, and K_{mw} is the partition coefficient of a solute between the micellar and aqueous phases. This is related to K_x in the following manner: $K_x = K_{mw} \times \bar{V}_m \times 55.5$. By plotting $V_s/(V_e - V_m)$, which is the measured quantity, as a function of the micellar surfactant concentration we should obtain a straight line. The partition coefficient can be found from the ratio of the slope and the intercept.

In TLC, Equation 6.22 is expressed in terms of the retardation factor, R_f . A plot of $R_f/(1 - R_f)$ vs. $C_{s,\text{mic}}$ should give a straight line and the partition coefficient can be found from the slope/intercept ratio in the same way as for HPLC.

These methods cannot be used for solutes that bind strongly to the stationary phase, and there might also be a problem with the binding of the surfactant to the stationary phase in TLC.

6.2.4.2 Ultrafiltration

The method is based on the ability of certain membranes to retain large molecules or aggregates, for example, micelles. A small part of the micellar solution is passed through the membrane, and the concentration of solute is determined in the filtrand and filtrate solutions. The partition coefficient of the solute can thus be calculated from the fraction of micellar-associated solute, which is given by the following relation:⁸⁶

$$\alpha = (c_{\text{filtrand}} - c_{\text{filtrate}})/c_{\text{filtrand}} \quad (6.22)$$

This method can in principle be used at any concentration of solute and surfactant. Problems may, however, arise from the adsorption of surfactant or solute to the membrane.

6.2.5 THERMODYNAMIC DATA

The approach to the thermodynamics of solubilization in micellar solutions is based on the determination of a given partial molar property of the solute (volume, enthalpy, heat capacity, compressibility) as a function of the surfactant content. The simplest approach is to use the pseudophase model. The partial molar quantity, Y , will thus be an average value of Y in the micellar and aqueous phases, as described by

$$Y = \alpha Y_{\text{mic}} + (1 - \alpha) Y_{\text{aq}} \quad (6.23)$$

Y_{aq} will normally be known from measurements in pure water. However, there are still two unknown quantities and only one equation. This is normally overcome by measuring at several surfactant concentrations, and fitting the data to a model. Equation 6.23 should preferably be used at infinite solubilize dilution.

The addition of solute will also influence the cmc of the surfactant, which in turn means that a correction is needed for the overall partial molar quantity, Y . This has been taken into account in the models proposed by Roux et al.⁵⁸ and DeLisi et al.⁶⁰ The models have been applied to different thermodynamic properties, mostly volumes and heat capacities, and for different surfactant–solute systems.

TABLE 6.1
A Comparison of Reported Distribution Coefficients
of Pentanol in Aqueous Solutions of SDS at 298.15 K
(with emphasis on the surfactant concentration and
pentanol concentration of measurement)

Method	SDS Conc.	C ₅ OH Conc	K _x	Ref.
Total solubility	cmc-0.05	High	190	47
NMR relaxation	0.17	Low	378	87
NMR self-diffusion	0.17–0.88	Low	560	82, 88
Electron spin echo	0.1		604	89
Molar volume	0.03	Infinite dilution	624	90
Krafft point	0.012	0–0.015	718	91
Vapor pressure	0.04	0–0.01	722	69, 75
Fluorescence	0.02–0.05	Infinite dilution	750	92
Variation of cmc	cmc	Low	776	93
Gas chromatography	0.06	< 0.2	790	94
	0.05	< 0.2	820	95
Pulse radiolysis	cmc-0.2	0.1	833	96
Enthalpies	0.05	< 0.03	850	97
Molar volume	cmc-0.25	Infinite dilution	927	62, 98
	cmc-0.4	Infinite dilution	944	61
Molar compressibility	0.05–0.2	Infinite dilution	725	181
Emf counterions	cmc-0.05	< 0.05	1030	99
Enthalpies			1166	101
	cmc-0.3	Infinite dilution	1180	102
Volumes	cmc-0.4	0.02	1232	59

6.3 RESULTS

6.3.1 PARTITION COEFFICIENTS

The experimental techniques vary in the sense that some will determine the partition coefficients directly and some will determine the fraction of solute solubilized in the micellar phase. The data are easily converted if the surfactant and solute concentrations are given.

However, as will be apparent from the data presented, there are large discrepancies in the partition coefficients presented. If we take one of the most-studied systems, sodium dodecyl sulfate (SDS) and 1-pentanol, the data are given in Table 6.1. The mole fraction scale, Equation 6.1, has been used in Table 6.1, and data originally given in other units have been recalculated. As can be seen, several experimental techniques have been used, but practically all investigations have been carried out at low concentrations of SDS, less than 0.25 *M* and in most cases below 0.05 *M*. Most investigations have also been at low pentanol concentrations; in many cases, the data have been extrapolated to infinite dilution.

The table clearly shows large discrepancies between the various sets of data. If we, for the time being, exclude partition coefficient measured from total solubilities, the partition coefficients varies between 378 and 1232, which is far outside the expected errors associated with experiments or the models used to derive them. The average value can be calculated as 830 ± 230 . Some systematic discrepancies seem to be present. The NMR data provide the low values whereas the thermodynamic methods yield higher values. The NMR methods rely on the use of D₂O instead of H₂O as solvent,

but it is not clear what possible effect could be associated with the change of solvent. The partition coefficients based on thermodynamic data, partial molar volumes, enthalpies, and heat capacities represent the other extreme. Exceptions are the partial molar volume data of Manabe et al.⁹⁰ and the partial molar compressibility data of Høiland et al.¹⁸² It is not possible to explain these differences and thus reach a firm conclusion on which partition coefficients to recommend.

Initially, the vapor pressure measurements appear to be the most direct, but even here some assumptions are needed. The amount of alcohol in the micellar phase needs to be determined. To do this the difference in vapor pressure between a pure aqueous and a micellar solution is measured.^{69,73} If the ions of the surfactant salts out alcohol, the vapor pressure of pure water is not the correct comparison, and this could lead to lower partition coefficients.⁵⁹ Thermodynamic data are well suited for model calculations, and both the models of DeLisi et al.^{60,102} and Héту et al.⁵⁹ fit the data well. Although in reasonable internal agreement, the partition coefficients calculated from partial molar volumes differ from those calculated from enthalpies; the first is 927 or 944, the latter 1166.^{61,62,98,100}

Treiner¹⁰³ has reviewed the method of calculating partition coefficients based on changes in the cmc as alcohol (or other solutes) is added. It is concluded that this method is a well-suited approach. It is worth noting that this method results in a partition coefficient that agrees well with vapor pressure measurements.

It is also worth noting that the discrepancies between the various methods is less if the surfactant is dodecyltrimethylammonium bromid ($C_{12}Br$). Although there have been fewer investigations of this system, the average value of six thermodynamic investigations is 580 ± 90 ,^{94,104-109} the average of two using the cmc method is 605,^{93,208} and even the NMR methods are in reasonable agreement — the average of three investigations is 560.^{50,110}

Table 6.2 provides detailed data for solubilization in cationic surfactants, and it is apparent from the table that there are large discrepancies in the K_x data for several systems.

6.3.1.1 Partition Coefficients of Alcohols

The partition coefficients of alcohols in cationic and anionic surfactant solutions are given in Tables 6.2 and 6.3. For the cationic surfactants all the data are given to illustrate the variation; in some cases a critical review of the data has been carried out, resulting in a quoted “probable value.” For the anionic surfactants, recommended values are given based on consideration of the systematic differences described above and the average of all data. For many of the systems only one set of measurements has been carried out, and for these systems the values have been taken as given in the original paper. With the exception of data from total solubilities, the measurements have been carried out at low alcohol concentrations or the values have been extrapolated to infinite dilution. This means that the values quoted in Tables 6.2 and 6.3 can be regarded as values at infinite alcohol dilution.

One point that was not focused on in the discussion of the partition coefficients of pentanol in SDS given above, is the possible variation with concentration. It is conceivable that the distribution coefficients vary with both solute and surfactant concentration. If we look first at the variation with surfactant concentration, values based on thermodynamic data are the most abundant. The calculation of partition coefficients from thermodynamic data do in most cases assume that they are independent of the surfactant concentration, and this assumption seems to be confirmed by the experimental data. It thus seems reasonable to conclude that the distribution coefficient is independent of surfactant concentration, at least over a moderate range and at low alcohol contents. Thus, the data in Tables 6.2 and 6.3 are valid at any surfactant concentration, at least up to about 0.3 M .

When the alcohol content varies at constant surfactant concentration, things change. The large discrepancies between data at low alcohol content and the data from total solubility experiments immediately suggest that the distribution coefficient varies significantly with respect to alcohol

TABLE 6.2
Partition Coefficients of Alcohols and Diols in
Aqueous Cationic Surfactant Systems at 298.15 K^a

Alcohol	Surfactant	K_x^o	Ref.
Methanol	C ₁₂ Br	10	108
Ethanol	C ₁₂ Br	30	93, 108
1-Propanol	C ₁₂ Br	68	93
	C ₁₂ Br	55	178
	C ₁₂ Br	100	108
	C ₁₂ Br	46	87
	Probable C ₁₂ Br	67 ± 14	
	C ₁₄ Br	37	178
	C ₁₆ Br	30	178
2-Propanol	C ₁₂ Br	54	93
	C ₁₂ Br	39	178
	C ₁₄ Br	26	178
	C ₁₆ Br	21	178
1-Butanol	C ₁₂ Br	190	93,181
	C ₁₂ Br	262	178
	C ₁₂ Br	144 ± 32	87, 169
	C ₁₂ Br	222	108
	C ₁₂ Br	212	208
	Probable C ₁₂ Br	206 ± 20	
	C ₁₄ Br	181	178
	C ₁₄ Br	50	65
	C ₁₄ Br	230	181
	C ₁₄ Br	216	208
	Probable C ₁₄ Br	210 ± 20	
	C ₁₆ Br	161	178
	C ₁₆ Br	99	179
	C ₁₆ Br	320	180
	C ₁₆ Br	(55)	135
	C ₁₆ Br	360	181
	C ₁₆ Br	227	208
Probable C ₁₆ Br	300 ± 70		
<i>t</i> -Butanol	C ₁₄ Cl	214	103
	CPC	1160	42
	C ₁₂ Br	90	93
	C ₁₂ Br	81	178
	C ₁₂ Br	222	167
	C ₁₄ Br	61	178
	C ₁₆ Br	53	178
1-Pentanol	C ₁₂ Br	575	93
	C ₁₂ Br	578	83
	C ₁₂ Br	586	104
	C ₁₂ Br	544	105
	C ₁₂ Br	722	108
	C ₁₂ Br	500	106
	C ₁₂ Br	610	106
	C ₁₂ Br	401	87

TABLE 6.2 (continued)
Partition Coefficients of Alcohols and Diols in
Aqueous Cationic Surfactant Systems at 298.15 K^a

Alcohol	Surfactant	K_x^o	Ref.
	C ₁₂ Br	536	50
	C ₁₂ Br	480	181
	C ₁₂ Br	642	208
	Probable C ₁₂ Br	560 ± 50	
	C ₁₄ Br	(180)	65
	C ₁₄ Br	722	106
	C ₁₄ Br	725 (160)	182
	C ₁₄ Br	630	181
	C ₁₄ Br	725	208
	Probable C ₁₄ Br	720 ± 20	
	C ₁₄ Cl	692	103
	C ₁₄ Cl	828	112
	C ₁₄ BzCl	525	103
	C ₁₄ BzCl	450	112
	C ₁₆ Br	550	180
	C ₁₆ Br	833	106
	C ₁₆ Br	(205)	135
	C ₁₆ Br	822	112
	C ₁₆ Br	920	181
	C ₁₆ Br	809	208
	Probable C ₁₆ Br	820 ± 50	
	C ₁₆ PCl	1132	112
	C ₁₆ BzCl	922	112
	C ₁₆ PCl	2840	42
	C ₁₆ PCl	1133	112
1-Hexanol	C ₁₂ Br	1778	93
	C ₁₂ Br	1007	87
	C ₁₂ Br	1887	108
	C ₁₂ Br	1480	181
	C ₁₂ Br	2319	178
	C ₁₂ Br	1828	208
	Probable C ₁₂ Br	1850 ± 250	
	C ₁₄ Br	1792	178
	C ₁₄ Br	(550)	65
	C ₁₄ Br	2150 (740)	182
	C ₁₄ Br	1800	181
	C ₁₄ Br	2415	208
	Probable C ₁₄ Br	2200 ± 200	
	C ₁₆ Br	1453	178
	C ₁₆ Br	1500	180
	C ₁₆ Br	(777)	30
	C ₁₆ Br	1558	179
	C ₁₆ Br	(566)	135
	C ₁₆ Br	3100	181
	C ₁₆ Br	2990	208
	Probable C ₁₆ Br	3000 ± 300	
	C ₁₄ Cl	2138	103
2-Hexanol	C ₁₄ Br	1170 (330)	182

TABLE 6.2 (continued)
Partition Coefficients of Alcohols and Diols in
Aqueous Cationic Surfactant Systems at 298.15 K^a

Alcohol	Surfactant	K_x^o	Ref.
Cyclohexanol	C ₁₂ Br	743	178
	C ₁₄ Br	492	178
	C ₁₆ Br	344	178
	C ₁₆ Br	385	127
1-Heptanol	C ₁₂ Br	3996	108
	C ₁₂ Br	4400	181
	C ₁₄ Br	7100	181
	C ₁₆ Br	4400	180
	C ₁₆ Br	7900	181
1-Octanol	C ₁₂ Br	9782	178
	C ₁₂ Br	3957	87
	C ₁₄ Br	8808	178
	C ₁₆ Br	7551	178
	C ₁₆ Br	13900	179
1-Decanol	C ₁₂ Br	83315	178
	C ₁₄ Br	75932	178
	C ₁₆ Br	107760	178
	C ₁₆ Br	59328	179
	C ₁₆ Br	468	93
Benzyl alcohol	C ₁₂ Br	592	83
	C ₁₂ Br	473	50
	C ₁₂ Br	411	87
	C ₁₆ Br	405	127
	C ₁₆ Br	1041	179
	C ₁₄ Cl	832	103
	C ₁₄ BzCl	832	103
	C ₁₆ Br	1420	179
2-Phenylethanol	C ₁₆ Br	3374	179
3-Phenylpropanol	C ₁₆ Br	142	185
1,2-Hexanediol	C ₁₂ Br	28	185
1,6-Hexanediol	C ₁₂ Br		

^a Data in parenthesis are from solubility measurements.

concentration. Indeed, this has been shown by Abuin and Lissi,⁸¹ Perez-Villard et al.,¹¹¹ and Morgan et al.¹¹² We should therefore be careful when comparing data at different alcohol concentrations. In fact, some of the discrepancies in the data as demonstrated above could be due to measurements at different alcohol contents, although it is not easy to make a thorough investigation of this effect based on the information available.

It is also of considerable interest to look at concentration dependence from another angle by focusing on the fraction of alcohol solubilized by the micelles. If the distribution coefficient does not vary with surfactant concentration, it is obvious that the fraction of alcohol solubilized does, as demonstrated by Equation 6.8. Here, it is rearranged taking into account that the alcohol is at infinite dilution:

$$\alpha = m_{s,\text{mic}} K_x / (m_{s,\text{mic}} K_x + 55.5) \quad (6.24)$$

TABLE 6.3
Partition Coefficients of Alcohols and Alkanediols in Aqueous Anionic Surfactant Systems at 298.15 K

Alcohol	Surfactant	K_x^o	K_x	Ref.
Methanol	SDS	19		93
Ethanol	SDS	51		93
	LiFOS	76		67
1-Propanol	SDS	105 ± 15		50, 82, 87, 89, 93, 98, 100
	LiDS	110		67
	LiFOS	158		67
2-Propanol	SDS	72		93
2-Methylpropanol	SDS	450		
1-Butanol	C ₇ COOK	112		168
	C ₉ COOK	174		168
	C ₁₁ COOK	151		168
	C ₁₃ COOK	158		168
	SDS	325 ± 50	51	59, 61, 62, 69, 79, 82, 87, 93, 98–100, 109, 169–172, 181
	LiDS	302	42	67
	LiFOS	363	40	67
	NaPFO	355		48
	KPFO	219		48
	NaDCh	53		113
2-Butanol	SDS	175		82, 183
<i>t</i> -Butanol	SDS	256		93
2-Methylbutanol	SDS	240		183
3-Methylbutanol	SDS	760		
3,3-Dimethyl-2-butanol	SDS	1070		
1-Pentanol	C ₇ COOK	200		168
	C ₉ COONa	782		175
	C ₉ COOK	355		168
	C ₁₀ COONa	720		175
	C ₁₁ COOK	676		168
	C ₁₃ COOK	776		168
	NaOS	716		175
	SDS	780 ± 50	190	47, 59, 61, 62, 69, 79, 82, 87, 89, 90, 92–94, 97–101, 110, 129, 149, 170–172, 181
	LiDS	794	212	67, 141
	LiFOS	912	200	67
	NaPFO	692		48
	KPFO	467		48
	NaDC	122		113
2-Pentanol	SDS	500		82, 183
3-Pentanol	SDS	420		82, 183
1-Hexanol	C ₇ COOK	831		168
	C ₉ COOK	1023		168
	C ₉ COONa	1010	455	30, 225
	C ₁₁ COOK	1047		168
	C ₁₃ COOK	1290		168

TABLE 6.3 (continued)
Partition Coefficients of Alcohols and Alkanediols in Aqueous Anionic Surfactant Systems at 298.15 K

Alcohol	Surfactant	K_x^o	K_x	Ref.
	SDS	2300 ± 150	750	30, 59, 69, 79, 81, 82, 87, 89, 90, 93, 98–100, 170–172, 181
	LiDS	1820	758	67, 141
	LiFOS	1513	526	67
	NaPFO	1550	320	67
	KPFO	1020	240	67
	NaDC	510		113
2-Hexanol	SDS	1500		182, 183
3-Hexanol	SDS	2160		100
Cyclohexanol	SDS	1030		182, 183
2-Methylcyclohexanol	SDS	1000		183
4-Methylcyclohexanol	SDS	2800		183
1-Heptanol	C ₇ COOK	1905		168
	C ₉ COOK	3388		168
	C ₁₁ COOK	3090		168
	C ₁₃ COOK	4073		168
	SDS	5500 ± 500	2650	58, 69, 70, 79, 82, 90, 93, 98, 100, 129, 170–172, 177, 181
	NaPFO			67
	KPFO	3250		67
		2150		
	NaCh	2100		70, 113
	NaDCh	3100		70
2-Heptanol	SDS	4060	1500	177, 183
3-Heptanol	SDS	2970	1010	177, 183
4-Heptanol	SDS	2820	930	177, 183
1-Octanol	C ₇ COOK	5128		168
	C ₉ COOK	6310		168
	C ₁₁ COOK	10700		168
	C ₁₃ COOK	12900		168
	SDS	17000	4500	47, 82, 87, 90, 173
2-Octanol	SDS	9400		183
1-Nonanol	C ₇ COOK	12500		168
	C ₉ COOK	22000		168
	C ₁₁ COOK	25100		168
	C ₁₃ COOK	33100		168
1-Decanol	SDS	25700		
Benzyl alcohol	SDS	440 ± 40	173	50, 82, 87, 93, 110, 135, 174, 177
	KPFO	234		48
Phenylmethanol	SDS	562		130
Phenylethanol	SDS	1050		130
2-Phenylethanol	SDS	890		176
3-Phenylpropanol	SDS	1880		130, 176
	NaDCh	554		184

TABLE 6.3 (continued)
Partition Coefficients of Alcohols and Alkanediols in Aqueous Anionic Surfactant Systems at 298.15 K

Alcohol	Surfactant	K_x^o	K_x	Ref.
Phenylbutanol	SDS	4250		130
	NaDCh	1150		184
Phenylpentanol	SDS	10500		130
	NaDCh	4030		184
Phenylhexanol	SDS	24500		130
	NaDCh	15400		184
Trifluoroethanol	LiDS	69		67
	LiFOS	105		67
Pentafluoropropanol	LiDS	250		67
	LiFOS	590		67
Heptafluorobutanol	LiDS	910		67
	LiFOS	1780		67
Nonafluoropentanol	LiDS	1900		67
	LiFOS	4790		67
Perfluorobutanol	NaPFO	1900		48
	KPFO	1350		48
1,3-Propanediol	SDS	28		176
1,4-Butanediol	SDS	42		176
1,2-Hexanediol	SDS	178		185
1,6-Hexanediol	SDS	240		176
		48		185
2,5-Hexanediol	SDS	162		176
1,8-Octanediol	SDS		311	177
1,9-Nonanediol	SDS		743	177
1,10-Decanediol	SDS	9120	3800	176, 177

K_x^o is at infinite alcohol dilution, and K_x is at the solubility limit.

Experimentally Spink and Colgan¹¹³ have shown how α varies for heptanol in SDS and sodium cholate and deoxycholate. Figure 6.1 shows the variation of α with the surfactant concentration using heptanol as an example. The solid line is the fraction of heptanol solubilized as calculated from Equation 6.24 using the K_x value given in Table 6.2. This can be compared with α values determined experimentally as given by Spink and Colgan^{70,113} and Stilbs.⁸² These data are at sufficiently low alcohol concentration to make the comparison. The agreement is excellent. The fraction solubilized varies considerably at low surfactant concentrations, whereas above approximately 0.25 M SDS there is little change.

The other possibility is keeping the surfactant concentration constant and varying the alcohol content. By inspecting Tables 6.2 and 6.3 it can be seen that the K_x values at the solubility limit of the alcohol are much lower than those at low alcohol content. Figure 6.2 shows data for 1-butanol in 0.22 M SDS, where NMR-FT-PGSE data are available. These have been compared to the data by Perez-Villard et al.¹¹¹ and the values calculated by Rao and Ruckenstein¹¹⁴ using a molecular thermodynamic model. The agreement is good, particularly bearing in mind that the data of Perez-Villard et al.¹¹¹ will be at SDS concentrations close to the cmc. The model of Rao and Ruckenstein seems to overestimate the partition coefficient at low alcohol concentrations, but still shows the correct trend.

Lee et al.¹¹⁵⁻¹¹⁷ have shown how the partition coefficient changes with the solute content for cationic surfactant. They find that it can be described by the following equation:

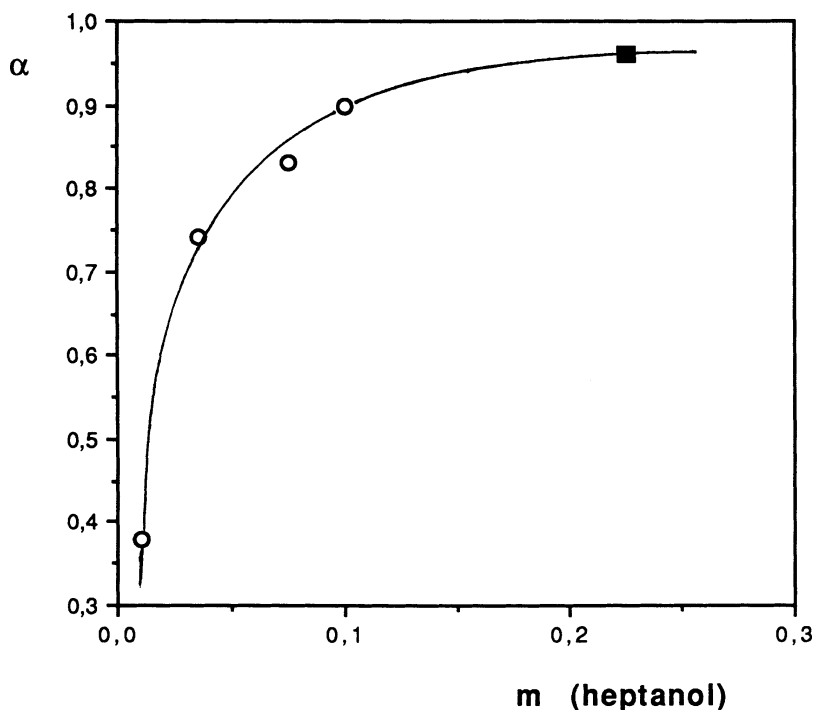


FIGURE 6.1 The fraction of alcohol in the micellar pseudophase, α , as a function of the total heptanol content. The solid line is according to Equation 6.24, \circ from Spink and Colgan¹¹³ and \blacksquare from Stilbs.⁸²

$$K_x = K_x^o(1 - BX_{mic})^2 \quad (6.25)$$

where K_x^o is the partition coefficient at infinite dilution (with respect to the solute) and B is a constant. For butanol in SDS the data shown in Figure 6.2 fit Equation 6.25 very well with a B value of 0.756. For the other alcohols, 1-pentanol to 1-heptanol, only two points on the K_x vs. X_{mic} curve are available, at infinite dilution and at saturation. However, we could still calculate B of Equation 6.25, but it is of limited value, particularly as the data of Abuin and Lissi⁸¹ on the solubilization of hexanol and heptanol in SDS at 293 K do not follow Equation 6.25. Their K_x values at low alcohol concentrations and at saturation, 2300 and 790 for hexanol, are in excellent agreement with the data presented in Table 6.2. However, as X_{mic} increases, they find that the distribution coefficient remains constant up to about $X_{mic} = 0.5$, where it decreases rapidly, reaching a new constant value at around $X_{mic} = 0.65$.

6.3.1.2 Partition Coefficients of Gases, Aliphatic Hydrocarbons, and Aromatic Hydrocarbons

Partition coefficients of gases and hydrocarbons are presented in Tables 6.4 and 6.5. The partition coefficients of gases have mainly been determined from solubilities. Most of the data were obtained by King and co-workers, and King has also reviewed the data available.⁶⁴ It was previously demonstrated that the partition coefficient of alcohols at the solubility limit was significantly lower than at infinite alcohol dilution. For the gases and hydrocarbons, however, the solubility is very low, even in surfactant solutions; typically, the mole fraction at the solubility limit is of the order 10^{-4} to 10^{-3} , whereas for the alcohols it is of the order 10^{-1} . Initially, we might thus expect that the variation of partition coefficients with total hydrocarbon concentration would be of minor importance, and that values at the solubility limit and at infinite dilution could be compared. However,

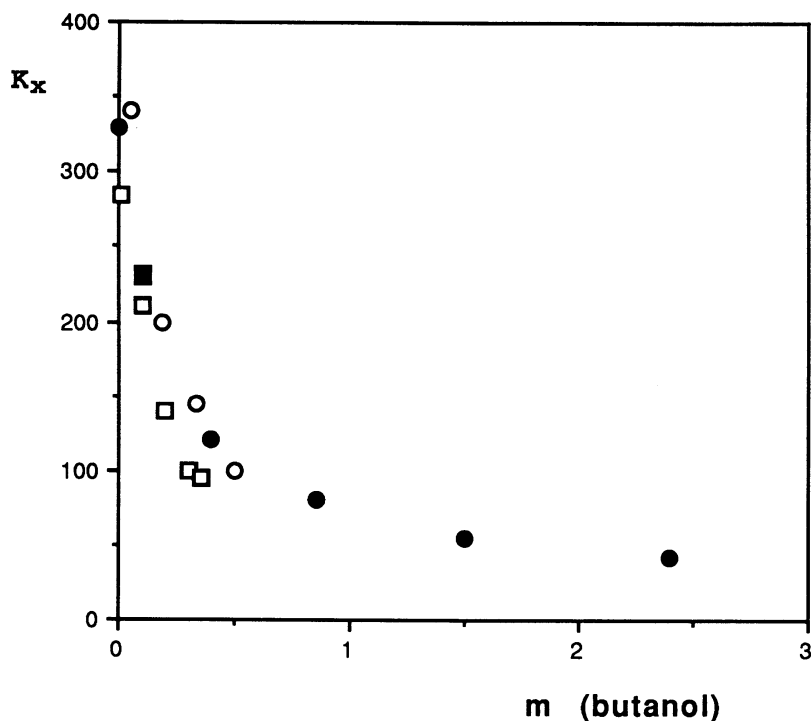


FIGURE 6.2 The variation of the partition coefficient of butanol in SDS as a function of the butanol content: ○ from Rao and Ruckenstein¹¹⁴ (calculated values), □ from Perez-Villard et al.,¹¹¹ ■ from Stilbs,⁸² and ● from Høiland et al.¹⁸²

Christian and co-workers⁴² have shown that the partition coefficients for hydrocarbons vary with the total hydrocarbon concentration. For example, the K_x values of cyclohexane in C_{16} PCI and SDS change from 23,800 to 30,000, and from 14,800 to 20,100, respectively, as the hydrocarbon content increases from infinite dilution to the solubility limit. This variation of partition coefficients with solubilize concentration is opposite to that observed for alcohols. According to Dunaway et al.²¹⁴ this supports the idea that hydrocarbons are solubilized in the micellar interior. The incorporation of hydrocarbon in the micellar interior probably expands the hydrocarbon part of the micelle, providing a more favorable environment for further solubilization.

The gases and hydrocarbons seem to present a more regular feature than the alcohols in the sense that the micellar solubilities and hence the partition coefficients increase in a regular way with the boiling point of the solubilize,¹⁸⁷ which, as pointed out by King, is consistent with a picture where the dispersion forces are the dominant mode of interaction. The partition coefficients of these compounds also seem to increase with increasing length of the surfactant, but are relatively unaffected by the headgroup of the surfactant or the counterion. In comparison, the alcohols do not show the same kind of regularity.

The main features of gas and alkane solubilization suggest that they are solubilized in a hydrocarbon-like environment, with the amount solubilized dependent on the volume of hydrocarbon available, and they are only moderately influenced by the environment outside the micellar core.

The partition coefficients of aromatic hydrocarbons and derivatives are presented in [Table 6.5](#). If we compare data with aliphatic hydrocarbons containing the same number of carbon atoms, the partition coefficients of the aromatic compounds are significantly lower, as expected from their respective solubilities in water. It also appears that the partitioning of aromatic compounds is more dependent on the surfactant headgroup than the aliphatic, but data are scarce and few comparisons can be made.

TABLE 6.4
Partition Coefficients of Gases, Aliphatic
Hydrocarbons, and Halocarbons in Aqueous
Surfactant Solutions at 298.15 K

Solubilizate	Surfactant	K_x	Ref.	
Oxygen (O ₂)	NaOS	31	186	
	NaDeS	35	186	
	SDS	44	187	
	Na-1-HS	17	188	
	LiPFO	74	189	
	NaPFO	78	188	
	C ₁₂ Br	31	190	
	C ₁₆ Br	52	187, 190	
Carbon dioxide (CO ₂)	SDS	15	191	
	Na-1-HS	7	191	
	NaPFO	23	191	
	C ₁₆ Br	24	191	
Argon	SDS	44	187	
	Na-1-HS	16	188	
	NaPFO	67	188	
	LiPFDe	83	189	
	C ₁₂ Br	28	190	
	C ₁₆ Br	58	187, 190	
Methane	C ₇ COONa	39	30, 192	
	NaHS	27	186	
	SDS	74	187	
	Na-1-HS	39	188	
	NaPFO	74	188	
	LiPFDe	90	189	
	C ₁₂ Br	67	190	
	C ₁₆ Br	113	190	
	Ethane	C ₇ COONa	121	18, 193
		NaHS	106	186
NaOS		200	186	
NaDeS		276	186	
SDS		326	186, 187	
Na-1-HS		132	188	
LiPFO		185	189	
NaPFO		179	188	
LiPFDe		238	189	
C ₁₂ Br		235	190	
C ₁₆ Br		456	190	
Propane		C ₇ COONa	362	193
		NaHS	282	186
		NaOS	527	194
	SDS	1190	186, 194	
	Na-1-HS	373	188	
	LiPFO	494	189	
	NaPFO	542	188	
	LiPFDe	769	189	
	C ₁₂ Br	770	190	
	C ₁₆ Br	1760	190	

TABLE 6.4 (continued)
Partition Coefficients of Gases, Aliphatic
Hydrocarbons, and Halocarbons in Aqueous
Surfactant Solutions at 298.15 K

Solubilizate	Surfactant	K_x	Ref.
Butane	C ₇ COONa	784	193
	SDS	6025	193, 195
Pentane	SDS	16400	193, 195
	C ₁₆ PCI	40200	93
Hexane	SDS	18200	195
	SDS	32400	94
	C ₁₆ PCI	2.4×10^5	28
Cyclohexane	SDS	3100	176, 195
	C ₁₆ Br	23700	195
Heptane	SDS	1.0×10^6	196
Dichloromethane	SDS	195	195, 197
	C ₁₂ Br	280	93
	C ₁₆ Br	320	197
Trichloromethane	SDS	630	195, 197
Chloroform	SDS	580	63, 93, 197
	C ₁₂ Br	460	93
	C ₁₆ Br	1440	197
Tetrafluoromethane	SDS	132	190
Tetrachloromethane	SDS	2750	93, 190, 195
	C ₁₆ Br	5500	197
Iodoethane	SDS	1220	93
Halothane	SDS	600	93
	C ₁₂ Br	525	93
1-Bromobutane	C ₁₂ Br	1150	93
1-Iodobutane	SDS	6500	198
	C ₁₆ Br	25000	199

6.3.1.3 Partition Coefficients of Phenols, Naphthols, Amines, Amides, and Aldehydes

The partition coefficients of phenols and naphthols are given in Table 6.6 and Table 6.7 gives the same data for amines, amides, and aldehydes. Only for a few of these compounds do we find more than one set of data, and as noted above, in cases where there is more than one investigation, the K_x values do not necessarily agree very well. In these cases the K_x values quoted in Tables 6.6 and 6.7 are based on a comparison of the given values and the experimental method used, and a “best” value is obtained.

6.3.2 ACTIVITY COEFFICIENTS

In developing distribution coefficients the activity coefficients of the solute in the micelle and in the aqueous environment have been neglected. The large decrease in K_x observed as the alcohol content increases toward saturation indicates that the activity coefficients deviate significantly from unity as the alcohol content increases.

Vapor pressure studies are well suited for extracting information about activity coefficients, and it is thus not surprising that most information stems from such work.

TABLE 6.5
Partition Coefficients of Aromatic Hydrocarbons and
Derivatives in Aqueous Surfactant Solutions at 298.15 K

Solubilizate	Surfactant	K_x	Ref.
Benzene	SDS	1100 ± 100	52, 83, 167, 176, 195, 200–205
	C ₁₂ Br	1500	83, 93
	C ₁₆ Br	2200	63, 200, 203, 206
	C ₁₆ PCI	2200	207
Toluene	SDS	2900 ± 100	83, 195, 200–204
	C ₁₂ Br	2200	93
	C ₁₆ Br	6200	200, 203, 206
	C ₁₆ PCI		
Nitrobenzene	SDS	1220	200, 203, 204
	C ₁₂ Br	1380	203
	C ₁₆ Br	2200	200, 203, 206
Chlorobenzene	SDS	3900	200
	C ₁₂ Br	3600	93
	C ₁₆ Br	7200	200, 206
1,2-Dichlorobenzene	SDS	7750	195
Bromobenzene	C ₁₆ Br	11000	203, 206
Ethylbenzene	SDS	15200	203
<i>p</i> -Xylene	SDS	11100	52, 195, 201, 203, 205
Naphthalene	SDS	6500	195
	SDS	19600	52, 200, 201
	C ₁₆ Br	83300	52
1-Methylnaphthalene	SDS	64500	52, 203
Anthracene	SDS	3.7×10^5	52, 195, 203
	C ₁₆ Br	2.4×10^6	52
Phenanthrene	SDS	4.0×10^5	52
Pyrene	SDS	1.5×10^6	52

Christian et al.^{43,118} base their measurements on the pure component as the standard state. They define the activity coefficient of the organic solute as

$$a = \gamma X_{\text{mic}} \quad (6.26)$$

The activity coefficient is defined as the relative volatility of the solute in the micelle, compared to the volatility of the solute in an ideal solution at the same mole fraction, i.e., p_s/p_s^o , where p_s is the partial pressure above the micellar solution and p_s^o the partial pressure above the pure solute.

The result is three different patterns. Simple alkanes, represented by hexane in hexadecylpyridinium chloride, exhibit an activity coefficient that gradually decreases from about 5 to about 3.2 at the solubility limit, which for this system is rather low. For benzene we observe a different trend. The activity coefficient increases from about 1.15 to about 1.5, apparently going through a maximum at X_{mic} around 0.5. Compared with hexane the activity coefficient of benzene does not vary much with composition. The activity coefficients of pentanol and phenols are less than unity at low solute contents. Typically, the values are around 0.1 at infinite dilution, increasing gradually toward unity as the mole fraction increases. For pentanol, unity is practically reached around the solubility limit. This is as required by the reciprocal relationship between the distribution coefficient and the activity coefficient.

TABLE 6.6
Partition Coefficients of Phenols and Naphthols in Aqueous
Solutions of Surfactants at 298.15 K

Solubilizate	Surfactant	K_x	Ref.
Phenol	SDS	580 ± 50	86, 130, 167, 195, 200–205, 211
	KPFO	135	48
	C_{12} Br	515	203
	C_{16} Br	1200	179
	C_{16} PCl	3600	28, 115, 207
2-Methylphenol	SDS	1220	195
3-Methylphenol	SDS	1380	195
4-Methylphenol	SDS	1380	195
	C_{16} Br	4610	86
	SDS	2700	86, 195
4-Ethylphenol	C_{16} Br	43000	86
	C_{16} PCl	29800	28
	SDS	15000	86
4-Propylphenol	C_{16} Br	77700	86
	SDS	21000	86
4-t-Butylphenol	C_{16} Br	94400	86
	SDS	58000	86
4-t-Pentylphenol	C_{16} Br	2.4×10^5	86
	SDS	3310	195
2,3-Dimethylphenol	SDS	3630	195
2,4-Dimethylphenol	SDS	3630	195
2,5-Dimethylphenol	SDS	3630	195
2,6-Dimethylphenol	SDS	3310	195
3,5-Dimethylphenol	SDS	3630	195
2,4,5-Trimethylphenol	SDS	7080	195
2,3,5,6-Tetramethylphenol	SDS	15500	195
	SDS	930	195, 202
4-Fluorophenol	C_{16} PCl	7000	28
	C_{16} PCl	26000	115
2-Chlorophenol	C_{16} PCl	29800	115
3-Chlorophenol	SDS	1950	195, 202, 212
	C_{16} PCl	44100	28, 115
4-Chlorophenol	SDS	2700	202
	C_{16} PCl	46200	28
4-Bromophenol	SDS	3500	195, 202
4-Iodophenol	C_{16} PCl	1.2×10^5	115
2,3-Dichlorophenol	C_{16} PCl	1.7×10^5	115
2,4-Dichlorophenol	C_{16} PCl	1.1×10^5	115
2,5-Dichlorophenol	C_{16} PCl	43100	115
2,6-Dichlorophenol	C_{16} PCl	1.8×10^5	115
3,4-Dichlorophenol	SDS	5250	195
3,5-Dichlorophenol	SDS	15800	195
2,3,5-Trichlorophenol	SDS	47900	195
2,3,4,5-Tetrachlorophenol	SDS	1000	195, 203, 204
	C_{12} Br	1150	203
	C_{16} PCl	13000	115
4-Cyanophenol	SDS	850	195
	C_{16} PCl	5050	28
4-Methoxyphenol	SDS	850	195

TABLE 6.6 (continued)
Partition Coefficients of Phenols and Naphthols in Aqueous Solutions of Surfactants at 298.15 K

Solubilizate	Surfactant	K_x	Ref.
	C ₁₆ PCI	3900	28
4-Ethoxyphenol	SDS	1580	195
1-Naphthol	SDS	5800	200
	SDS	10200	195
2-Naphthol	SDS	5700	203
	SDS	13300	200
	C ₁₂ Br	6650	203
<i>o</i> -Cresol	SDS	1160	209
	C ₁₆ PCI	10300	213
<i>m</i> -Cresol	SDS	1220	209
	C ₁₆ PCI	10600	213
<i>p</i> -Cresol	SDS	1300	86, 202, 209, 210
	C ₁₂ Br	9500	86
	C ₁₆ PCI	12400	28, 207, 213

6.3.3 ENERGETICS OF SOLUBILIZATION

The standard Gibbs energy of solubilization can be determined from distribution coefficients by the usual relation, $\Delta G_t^o = -RT \ln K$, where K is the partition coefficient. Actually it may be more precise to refer to this quantity as the Gibbs energy of transfer, because the process involves a transfer of a third component from the aqueous phase to the micellar pseudophase. We therefore use this term here. It should be noted that the value obtained for ΔG_t^o depends on the standard state chosen. From a statistical mechanical standpoint, Ben-Naim¹¹⁹ has argued that the molarity scale is preferable for calculating standard Gibbs energies of transfer. However, Kauzman,¹²⁰ Gurney,¹²¹ and also Tanford¹²² prefer the mole fraction standard state. Sepulveda et al.¹²³ also preferred to use the mole fraction scale in their derivation of the thermodynamics of transfer from water to the micellar phase, and we do the same, i.e.,

$$\Delta G_t^o = -RT \ln K_x \quad (6.27)$$

It appears that for each surfactant system, ΔG_t^o is a linear function of the number of carbon atoms of the solubilizate; see, for example, the work by DeLisi and co-workers who have studied alcohol solubilization in SDS, dodecyltrimethylammonium bromide, and dodecyltrimethylamine oxide.^{100,108,124} In this work we prefer to plot ΔG_t^o as a function of the number of CH₂ groups of the solubilizate. Tables 6.2 through 6.6 contain K_x data for several homologous series in anionic, cationic, and nonionic surfactants, and on this basis the following relationship has been tested:

$$\Delta G_t^o = A + B n\text{CH}_2 \quad (6.28)$$

This means that for 1-alcohols, CH₃-(CH₂)_{*n*}-CH₂OH, the A parameter ($n = 0$) is in principle the ΔG_t^o value of ethanol, and for hydrocarbons the A value is ΔG_t^o of ethane. Values of the A and B parameters for the various systems are presented in Table 6.8. Basically all systems fit Equation 6.28 well, and it also turns out that the B parameter is surprisingly constant for nearly all systems. Exceptions are phenylalcohols in sodium deoxycholate micelles and primary alcohols in lithium perfluoro-octane-sulfonate. The average value of the B parameter for all other systems is -2.48 ± 0.06 kJ/mol

TABLE 6.7
Partition Coefficients of Amines, Amides, Aldehydes,
Ketones, and Ethers in Aqueous Surfactant Solutions
at 298.15 K

Solubilizate	Surfactant	K_x	Ref.
Diethylamine	C ₁₂ Br	90	93
Triethylamine	C ₁₂ Br	610	93
Benzylamine	C ₁₂ Br	500	93
Aniline	SDS	400	86, 195, 217
	C ₁₂ Br	710	217
	C ₁₆ Br	1220	86
	C ₁₆ PCl	1880	28
4-Methylaniline	SDS	1100	195
	C ₁₆ PCl	2900	28
4-Ethylaniline	C ₁₆ PCl	7500	28
4-Isopropylaniline	C ₁₆ PCl	15300	28
4-Chloroaniline	C ₁₆ PCl	9900	28
4-Bromoaniline	C ₁₆ PCl	16800	28
4-Cyanoaniline	C ₁₆ PCl	2500	28
4-Methoxyaniline	C ₁₆ PCl	880	28
4-Trifluoromethylaniline	C ₁₆ PCl	27800	28
<i>p</i> -Toluidine	SDS	1060	86
	C ₁₆ Br	2350	86
Butyraldehyde	C ₁₂ Br	130	93
Benzaldehyde	C ₁₂ Br	720	93
	C ₁₆ Br	830	206
	C ₁₆ Br	1330	203
Acetone	SDS	50	218
2-Butanone	SDS	117	82
	C ₁₂ Br	50	93
2-Pentanone	SDS	350	83
	C ₁₂ Br	145	83
2-Hexanone	SDS	950	82
2-Heptanone	SDS	2670	82
Cyclohexanone	C ₁₂ Br	200	93
Acetophenone	SDS	1850	201, 203, 205
	C ₁₂ Br	1050	93
	C ₁₆ Br	1250	203, 206
Propiophenone	SDS	1500	203, 219
	C ₁₆ Br	2700	203
Benzophenone	SDS	25000	219
Diethyl ether	C ₁₂ Br	78	93
Tetrahydrofuran	C ₁₂ Br	50	93
Dioxane	SDS	72	83
	C ₁₂ Br	44	83,93
Propionamide	SDS	175	195
Butanamide	SDS	269	195
Pentanamide	SDS	550	195

(K_x measured on the mole fraction scale). This can be compared to earlier published values. Wishnia¹²⁵ found -3.23 kJ/mol for the transfer of the gaseous alkanes, DeLisi and Milioto¹⁰² quote -2.4 kJ/mol based on their data, and Høiland et al.¹²⁶ -2.78 kJ/mol as an average value for the transfer of the alcohols

TABLE 6.8
Parameters of the Equation $\Delta G_i^o = A + Bn_{\text{CH}_2}$
for the Transfer of Solubilizates from Water
to the Micellar Pseudophase (mole fraction scale)

Solubilizates	Surfactant	A	B
1-Propanol/1-heptanol	C ₉ COOK	7.58	2.44
	C ₁₁ COOK	7.84	2.47
	SDS	9.17	2.48
	C ₁₂ Br	8.08	2.50
	C ₁₄ Br	8.91	2.39
	C ₁₆ Br	9.17	2.38
	LiFOS	10.30	2.17
2-Butanol/2-hexanol	SDS	7.94	2.49
3-Pentanol/3-hexanol	SDS	7.64	2.42
Propane/hexane	SDS	16.12	2.50
ω -Phenylpropane/ ω -phenylhexane	SDS	16.51	2.13
Propanone/hexanone	SDS	6.73	2.56
Fluorinated alcohols	LiDS	11.39	2.52

pentanol to decanol in several surfactants. However, the present number is based on the largest number of data by far and is probably as good as can be expected.

It is not surprising that the B parameter of Equation 6.28 is constant as it is primarily the Gibbs energy of transfer for a CH_2 group from water to the hydrocarbon part of a micelle. It also makes sense that the systems where the B parameter is significantly different from this value are the phenylalcohols, where the large phenyl group presumably affects the ΔG_i^o values of at least the nearest CH_2 groups, and the surfactant system lithium perfluoro-octanesulfonate, where the micellar interior contains fluorine.

If we look at the values of ΔG_i^o as such, it appears that the ΔG_i^o values for the cationic surfactant dodecyltrimethylammonium bromide are more positive than for the anionic SDS, having the same hydrocarbon chain length. DeLisi and Milioto¹⁰² interpreted this difference suggesting that the anionic micelles have a larger affinity toward the alcohol OH^- group than do cationic micelles. The nonionic surfactant, dodecyltrimethylamine oxide, exhibited ΔG_i^o values practically equal to those of the dodecyltrimethylammonium bromide, and thus its affinity toward the alcohol OH^- group should be about the same. However, from Tables 6.2 and 6.3 it is possible to plot ΔG_i^o values of alcohols solubilized by other surfactants as well. Figure 6.3 shows ΔG_i^o values of alcohols for SDS, potassium dodecanoate, and dodecyltrimethylammonium bromide. The data are presented on the mole fraction scale. On the scale of Figure 6.3 it seems that all points fall on the same curve. Closer inspection reveals that the data for the cationic surfactant fall between the two anionic ones. It is thus doubtful that there is any straightforward distinction between anionic and cationic surfactants as far as affinity toward OH^- groups is concerned.

The enthalpies of transfer can be determined from calorimetric measurements or by measuring the distribution coefficient as a function of temperature and carrying out the differentiation:

$$\Delta H_i^o = -T^2 \left(\frac{\partial (\Delta G_i^o / T)}{\partial T} \right) \quad (6.29)$$

However, the latter method may not be entirely satisfactory because the temperature may also influence the micellar pseudophase. The calorimetric data of DeLisi and Milioto¹⁰⁰ and Aveyard and Lawrence,¹²⁸ have also been plotted in Figure 6.3. ΔH_i^o data based on Equation 6.29 have also been included. The data of Hayase et al.¹²⁹ are at low alcohol concentration and those of Høiland

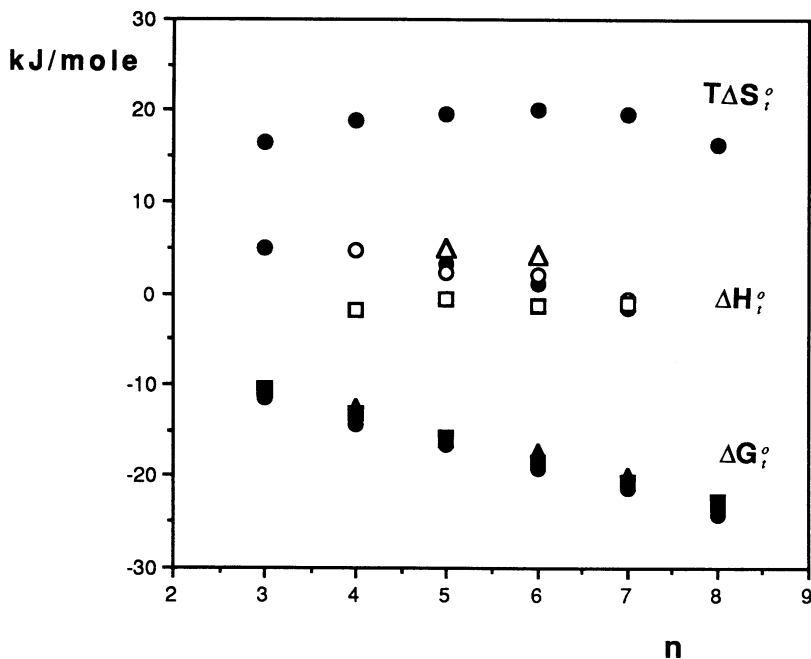


FIGURE 6.3 Transfer functions for alcohols from water to micelles at 298.15 K. $\Delta G_i^o = -RT \ln K_x$: ● SDS, ▲ = C₁₂Cook, ■ = C₁₂Br. $T\Delta S_i^o$ and ΔH_i^o are for aqueous SDS. ● From DeLisi and Milioto,¹⁰⁰ □ from Hayase et al.,¹²⁹ ○ from Aveyard and Lawrence,¹²⁸ and △ from Høiland et al.⁴⁷

et al.⁴⁷ are at saturation. The agreement between the various sets of data is not very good, particularly as the data of Hayase et al.¹²⁹ give negative values for ΔH_i^o . However, the use of Equation 6.29 can be questioned, and the variation of K_x with temperature can be small compared with the error in K_x . The other sets of data are at least in reasonable agreement, showing that the solubilization process is endothermic for the lower alcohol homologues, apparently becoming exothermic for heptanol.

The entropies of transfer are positive at 298.15 K. Neither the enthalpy nor the entropy of transfer appears to be a linear function of the number of carbon atoms. The methylene group contribution is not constant, but depends on the alcohol chain length. DeLisi and Milioto¹⁰² have tried to explain this by taking the size of the solute into consideration. The solubilization of additives in the micelles thus involves a micellar rearrangement to accommodate the alkyl chain. In principle, short-chain alcohols, mostly accommodated in the palisade layer, need less rearrangement of the micelle than the longer-chain alcohols that will require a cavity suitable to accommodate part of the alkyl chain.

The energetics of transfer for secondary alcohols are not very different from the primary alcohols.¹⁰² For the lower homologues, propanol and butanol, the differences on ΔG_i^o , ΔH_i^o , and $T\Delta S_i^o$ are basically within the experimental error. However, for the longer-chain alcohols it appears that ΔG_i^o is less negative for the secondary alcohols, whereas the ΔH_i^o and $T\Delta S_i^o$ values are more positive.

It is generally accepted that the hydrophobicity of alcohols is enhanced when the hydrogenated alkyl chain is fluorinated. Only a few such systems have been studied,¹⁰² but it appears that ΔG_i^o is more negative for the fluorinated alcohols, whereas the enthalpies and entropies of transfer are more positive. The effect on $T\Delta S_i^o$ is larger than that on ΔH_i^o . It thus seems that the difference between the hydrogenated and fluorinated alcohols largely stems from a more pronounced hydrophobic effect of the fluorinated chain in the aqueous phase, and is not an effect of a larger affinity toward the micelles.

Spink and Colgan¹¹³ have tried to analyze the transfer of aliphatic groups from water to alkanes or from water to micelles by using data on alkane transfer by Amidon and Anik,¹³¹ Nichols et al.,¹³² and Wishnia.¹²⁵ It appears that the enthalpy of transfer is negative for the methyl group and positive for the methylene group. There appears to be only a small entropy contribution from the methylene group, but a significant and negative contribution from the methyl group. The driving force for solubilization thus seems to be an entropic effect for the methyl group and a smaller, enthalpic effect for the methylene group.

6.3.4 MODEL CALCULATIONS

A well-used method for calculating thermodynamic quantities is based on group additivity. From Table 6.8 it is clear that each CH₂ group contributes by -2.48 kJ/mol to the Gibbs energy of transfer, or by a value of $\ln K_x = 1.00$. This provides a basis for calculating group contributions to the partition coefficient. The group contribution of a CH₂ group appears to be rather independent of the surfactant involved in the micelle formation. This seems reasonable as it is generally assumed that the CH₂ groups reside in the micellar interior, which is similar to fluid hydrocarbon practically irrespective of surfactant type. The same is probably true for the CH₃ group whereas the other group contributions most likely depend on the surfactant, particularly the headgroup. However, it is obvious from the data in Tables 6.3 through 6.7 that group additivity is of limited accuracy for estimating K_x values. If we take the OH- group, it is apparent that it will take on different values according to position, as 1-, 2-, and 3-alcohols exhibit different K_x values. Nevertheless, Treiner¹⁰³ has already calculated group contributions for various groups related to the surfactant micelles of dodecyltrimethylammonium bromide, C₁₂Br, not taking the more subtle differences into account. Fair estimates of K_x can be obtained by using these numbers. However, it may be more interesting to look at the trends as far as the group contributions go. Treiner finds the following:¹⁰³

- The ether group, secondary and tertiary amines, has group contributions that are negative; i.e., they oppose solubilization by micelles.
- Hydroxyl, ester, and ketone groups have group contributions close to zero, but still on the negative side.
- Aldehyde, nitrile, and halogenated groups exhibit positive group contributions (of about the same order of magnitude as the methylene group).

Another approach has been to correlate water-micelle partitioning with water-octanol partitioning. Treiner and Mannebach⁹³ showed that this works for water-SDS partitioning provided that outliers are excluded; in this instance it means that aliphatic and aromatic hydrocarbons and haloalkanes had to be omitted from the scheme. Valsaraj and Thibodeaux¹⁹⁵ made a thorough study of comparing K (or $\log K$) values of water-SDS with the water-octanol system. The following correlation functions have been found by using the data given (the partition coefficients are based on the molar scale):

$$\log K_m = 0.32 + 0.827 \log K_{\text{oct}} \quad (6.30a)$$

$$\log K_m = 0.740 + 0.693 \log K_{\text{oct}} (\pm 0.38) \quad (6.30b)$$

$$\log K_m = 0.326 + 0.826 \log K_{\text{oct}} (\pm 0.29) \quad (6.30c)$$

The first equation (6.30a) is the correlation function given by Valsaraj and Thibodeaux,¹⁹⁵ the second is a recalculation made by Abraham et al.²¹⁵ using all the solutes listed by Valsaraj and Thibodeaux (Valsaraj and Thibodeaux only used 57 of 63 listed solubilizates), and the third is the same correlation but obtained by Abraham et al. by excluding aliphatic amides and lactames. In any case

the standard deviation is quite high. Garrone et al.²¹⁶ did the same comparison for the solubilization of monosubstituted benzoic acids, obtaining a standard deviation of ± 0.12 on the same scale as above. However, by including the molar refraction of the solubilize, R , and making a best fit, the standard deviation was reduced to ± 0.05 and the equation read:

$$\log K_m = 1.35 + 0.405 \log K_{\text{oct}} + 0.306 R \quad (6.31)$$

However, it may not be too difficult to fit an equation of the type given in Equation 6.31 to a limited amount of data, or a homologous series. It is considerably more difficult to adapt a single equation to all kinds of solubilizates.

Abraham²²⁰ developed what is termed a general solvation equation. The main idea behind the model involves the creation of a cavity in the solvent, incorporation of the solvent in the cavity, and turning on solute–solvent interactions. These interactions require a relevant solute parameter, and the ones chosen were R_2 the excess molar refraction, π_2^H the solute dipolarity/polarizability, a_2^H and β_2^H the hydrogen-bond acidity and basicity, respectively, and V_x a characteristic volume.²²¹ Applying this general equation to 132 solutes in aqueous SDS, Abraham et al.²¹⁵ obtained the following equation for the partition coefficient:

$$\log K_x = 1.201 + 0.542 R_2 - 0.400 \pi_2^H - 0.133 \Sigma a_2^H - 1.580 \Sigma \beta_2^H + 2.793 V_x \quad (6.32)$$

The standard deviation of $\log K_x$ is 0.171, which is quite high. For example, for 1-pentanol in SDS the predicted K_x is 603 ± 250 . Nevertheless, it is a good fit taking into account the number of solubilizates covered by a single equation and the fact that the K_x differ considerably for the various investigations. If, for example, we compare this result with the experimental results given in Table 6.1, it is well within the experimental variance.

Quina et al.²²² have used the same general solvation equation on solubilizates in SDS, $C_{12}\text{Br}$, $C_{16}\text{Br}$, and the nonionic Brij-35 surfactant. In SDS they do not attempt to fit as many solubilizates as Abraham et al., using 66 solubilizates for SDS, 39 for $C_{12}\text{Br}$, and 42 for $C_{16}\text{Br}$. The equations read

$$\begin{aligned} \text{SDS: } \log K_x &= 1.12 + 0.32 R_2 - 0.57 \pi_2^H - 0.08 \Sigma a_2^H \\ &\quad - 1.84 \Sigma \beta_2^H + 3.25 V_x (\pm 0.13) \end{aligned} \quad (6.33a)$$

$$\begin{aligned} C_{12}\text{Br: } \log K_x &= 0.87 + 0.57 R_2 - 0.40 \pi_2^H + 0.28 \Sigma a_2^H \\ &\quad - 1.82 \Sigma \beta_2^H + 2.98 V_x (\pm 0.16) \end{aligned} \quad (6.33b)$$

$$\begin{aligned} C_{16}\text{Br: } \log K_x &= 0.98 + 0.76 R_2 - 0.32 \pi_2^H + 1.02 \Sigma a_2^H \\ &\quad - 3.78 \Sigma \beta_2^H + 3.57 V_x (\pm 0.19) \end{aligned} \quad (6.33c)$$

In a later paper Abraham et al.²²³ fitted 46 solubilizates in hexadecylpyridinium chloride, $C_{16}\text{PCL}$, obtaining the following result:

$$\begin{aligned} C_{16}\text{PCL: } \log K_x &= 1.31 + 0.973 R_2 - 0.736 \pi_2^H + 0.769 \Sigma a_2^H \\ &\quad - 2.84 \Sigma \beta_2^H + 3.386 V_x (\pm 0.147) \end{aligned} \quad (6.33d)$$

TABLE 6.9
Partition Coefficients Calculated from
(a) Equation 6.32, (b) Equation 6.33, and
(c) Recommended Experimental Values
at 298.15 K

Solubilizate	SDS ^a	SDS ^b	SDS ^c	C ₁₂ Br ^b	C ₁₂ Br ^c
Cyclohexane	4850	8160	3500	3360	
Cyclohexanol	720	710	1000	465	743
1-Hexanol	1500	2150	2300	1190	1850
2-Hexanone	805	620	950	440	
Phenol	775	615	580	806	515
Hexylamine	1330	1890		675	
Benzene	1250	1400		780	

Even if the standard deviation is given in each case, it may still be illustrative to calculate a few partition coefficients based on these equations. The result is shown in Table 6.9. The agreement is good, but not excellent, although when experimental values of, for example, benzene in SDS vary between 400¹⁷⁶ and 1410⁸³ (Abraham et al.²¹⁵ used 890 as input), it is not easy to evaluate whether the larger discrepancies are due to the model equation or to unreliable K_x data, or simply, the problem concerning K_x data presented in the literature is the lack of a standard state.

The advantage of the Abraham model equation is that it is general and the parameters are related to physicochemical properties. The obvious point taken from all equations is that the volume term dominates and increased volume increases the partition coefficient. Contributions to this term are the energy needed to create a cavity of the right size and the interaction forces that will appear when a solubilizate is introduced into the cavity. In comparing SDS and C₁₆PCI Abraham et al.²²³ use the scaled particle theory and find that the major factor for K_x as it is larger in C₁₆PCI than in SDS is increased general dispersion interactions between the solubilizate and the micelles. Comparison with water–alcohol partitioning indicates that SDS micelles are as hydrophobic as water-saturated isobutanol and C₁₆PCI as hydrophobic as water-saturated pentanol.

For the cationic surfactants studied, the excess molar refraction and solute hydrogen-bond acidity contribute positively to K_x , although the effect is small. Solubilizate dipolarity exhibits a weakly negative contribution to K_x and the solubilizate hydrogen-bond basicity a significant negative contribution to K_x .

6.3.5 PARTIAL MOLAR VOLUMES AND COMPRESSIBILITIES

Partial molar volumes and compressibilities of solutes at infinite dilution have proved valuable as a tool for studying water–solute interactions in aqueous solution, and a number of systems have been investigated.²²⁴ It has therefore been of interest to determine these quantities for solubilizates in the micellar state. By using Equation 6.23 these quantities can be obtained.

Table 6.10 shows that the partial molar volumes and particularly the isentropic partial molar compressibilities at infinite dilution are significantly higher in the micellar environment than in water. As far as the partial molar volume is concerned, the increment per CH₂ group is reasonably constant. The values are 15.9 cm³/mol in water and 16.8 cm³/mol in the micelles. This can be compared to a CH₂ group value of 16.1 in octane and 16.2 in heptane^{98,226} and 16.8 for the molar volume of pure alcohols. It means that as far as the volume of a CH₂ group in the micelle is concerned, pure alcohol is the best comparison.

The partial molar volume consists of a fairly large intrinsic contribution and a contribution due to solute–solvent interactions. The intrinsic part becomes zero or close to zero when partial molar

TABLE 6.10
Partial Molar Volumes and Isentropic Partial Molar
Compressibilities of Alcohols at Infinite Dilution
in Aqueous Surfactant Solutions at 298.15 K
(volumes in cm³/mol, compressibilities in
cm³/mol/bar)

Alcohol	Solvent	V_2	$K_2 \times 10^4$	Ref
Methanol	Water	38.2		224
	SDS	38.8		98
Ethanol	Water	55.1		224
	SDS	56.1		98
1-Propanol	Water	70.7	6.2	224
	Alkane	83.3		98
	C ₉ COONa	73.3	65.5	225
	SDS	72.8		98
	C ₁₂ Br	73.7		105
2-Propanol	Water	71.9		224
	SDS	73.9		59
	C ₁₂ Br	73.6		105
1-Butanol	Water	86.6	4.6	224
	Octane	99.8		98
	C ₉ COONa	90.0	74.5	225
	SDS	89.0	51.7	59, 98, 182
	C ₁₂ Br	91.2		105
1-Pentanol	Water	102.7	2.4	224
	Octane	115.8		98
	Heptane	114.5	136	226
	C ₉ COONa	107.0	86.6	225
	SDS	105.3	67.5	98, 182
	C ₁₀ Br	107.4		106
	C ₁₂ Br	107.5	67.2	105, 106
	C ₁₄ Br	107.7	70.1	105
		106.1	70.3	182
	C ₁₆ Br	108.0	75.7	105
	C ₁₀ Cl	106.7		104
	C ₁₂ Cl	106.5		104
	C ₁₄ Cl	107.3		104
C ₁₆ Cl	107.5		104	
1-Hexanol	Water	118.7	0.5	224
	C ₉ COONa	123.8	94.7	225
	SDS	122.2	81.4	105, 182
	C ₁₂ Br	124.0		105
	C ₁₄ Br	123.4	84.8	182
2-Hexanol	Water	118.5	-1.2	224
	SDS	121.2	69.0	182
	C ₁₄ Br	123.2	77.8	182
3-Hexanol	Water	117.1	2.8	224
	SDS	119.6	66.5	182
1-Heptanol	Water	133.4	0.9	224
	C ₇ COONa	140.9	106.6	225
	C ₉ COONa	140.8	105.0	225
	C ₁₁ COONa	139.5	100.0	225
	SDS	139.5	92.0	226

TABLE 6.10 (continued)
Partial Molar Volumes and Isentropic Partial Molar Compressibilities of Alcohols at Infinite Dilution in Aqueous Surfactant Solutions at 298.15 K (volumes in cm³/mol, compressibilities in cm³/mol/bar)

Alcohol	Solvent	V_2	$K_2 \times 10^4$	Ref
2-Heptanol	Water	134.3	0.6	224
	SDS	139.0	88.5	226
3-Heptanol	Water	133.4	-4.4	224
	SDS	137.3	78.0	226
4-Heptanol	Water	132.6	-3.7	224
	SDS	137.5	79.5	226
1-Octanol	C ₇ COONa	157.7	116.6	225
	C ₉ COONa	157.2	112.5	225
	C ₁₁ COONa	156.6	109.3	225
	SDS	157.5		226
1-Nonanol	C ₇ COONa	175.0	122.9	225
	C ₉ COONa	174.3	121.3	225
	C ₁₁ COONa	173.3	120.4	225
	SDS	174.7		226
1-Decanol	C ₇ COONa	191.8	131.1	225
	C ₉ COONa	191.2	129.2	225
	C ₁₁ COONa	189.8	129.1	225
	SDS	191.7		226

compressibilities are studied. Therefore, this quantity is often more sensitive than the volume. If we look at partial molar compressibilities of alcohols in water, additivity of group values is not working very well. Because the hydration layer is part of a structured solvent, it is not possible to single out group contributions to any degree of accuracy. It is the total compressibility of the hydration layer that counts, although on average it appears that there is a slight negative contribution of adding CH₂ groups. In a less structured environment, as in pure alcohols, group contributions seem to work better, the average contribution for each CH₂ group in the series butanol to decanol is $(7.9 \pm 0.3) \times 10^{-4}$ cm³/mol/bar. Solubilized in the micelles, the group additivity scheme also works reasonably well, with the CH₂ contribution $(8.5 \pm 1.5) \times 10^{-4}$ cm³/mol/bar for butanol to decanol in sodium decanoate, the only micellar system that has been studied for all these alcohols. The closest match is once more a comparison with pure alcohols, suggesting that polar interactions are important when alcohols solubilize in the micelles. For alkanes in sodium decanoate micelles the CH₂ group contribution is $(10.7 \pm 0.5) \times 10^{-4}$ cm³/mol/bar for heptane to decane.

If we look at the absolute values of partial molar volumes and compressibilities of alcohols solubilized in micelles, it appears that for the lower alcohols, up to heptanol, volumes and compressibilities exhibit lower values in SDS than in carboxylates. It also appears that the partial molar compressibilities of these alcohols are higher than the molar compressibility of the pure alcohols when solubilized in the carboxylate micelles and lower when solubilized in SDS.

In cationic micelles the partial molar compressibility is generally slightly higher than for the anionic ones. There are two possible explanations for the differences in partial molar compressibility for an alcohol in the various micellar systems. It is possible that the micellar structure is slightly different and that it is easier to compress a carboxylate micelle around an alcohol molecule than it is for a dodecylsulfate micelle. However, the partial molar compressibility of a surfactant molecule

is higher in SDS than in carboxylate micelles and this suggests another explanation. It is generally assumed that a single alcohol molecule is solubilized with the polar group at the micellar surface, which means that the hydroxyl group and the first few CH_2 groups are in an aqueous or partly aqueous environment. This environment is likely to depend on the surfactant headgroup, and compressibilities will vary accordingly.

6.3.6 SOLUBILIZATION SITES AND STRUCTURAL EFFECTS

A neutral molecule solubilized in the micelle can be located in several positions or microenvironments. As early as the 1930s it was suggested by Lawrence¹³³ that the site of a solubilized molecule would be dependent on the hydrophobic/hydrophilic composition of the solubilize. Two extremes are easily identified:^{29,134} the core of the micelle providing a hydrocarbon-like microenvironment, and the palisade layer providing an aqueous or water-rich interfacial environment. It seems logical to assume, then, that nonpolar solutes like alkanes would prefer the micellar core and that polar molecules would be anchored at the surface. However, this is an oversimplification; available data tend to contradict it. First, the solubility of alkanes in micelles is significantly lower than expected if compared to solubility in hydrocarbon solvents.^{51,125} Second, the size of a micelle is normally such that part of the solute would be close to the surface at any time. Sepulveda et al.⁵¹ state that for SDS micelles at least half of the solute will be within 4 to 5 Å of the surface. We should also consider the timescale of the experiments, as the timescale for intramicellar migration is short. The rate constants of entry and exit of molecules to and from micelles is of the order 10^{-6} and 10^{-9} /s.^{135,136}

Benzene appears to be the most-studied solute with respect to solubilization sites. Mukerjee and Cardinal¹³⁴ found, from UV measurements, that the average environment of the solubilized benzene was polar. Simon et al.¹³⁷ criticized these measurements and from data on partition coefficients it was argued that benzene was located in a nonpolar environment. The same was found by Hirose and Sepulveda⁸⁶ by inspecting the Gibbs energy of transfer. However, earlier NMR studies by Eriksson and Gillberg¹³⁸ indicated that above a solute mole fraction of 0.45 the core was a significant environment. Matsuo et al.¹³⁹ seemed to confirm this conclusion, finding that benzene solubilizes in the micellar core above a benzene-to-surfactant molar ratio of 0.6. Jobe et al.³⁶ concluded from ultrasonic vibration measurements that benzene prefers the micellar surface at low content, but that the core becomes important at higher contents.

For polar solutes, like *n*-alcohols, it is generally assumed that they reside at the micellar surface.^{139,140} Experiments seem to confirm that the alcohol intercalates between the surfactant monomers with the polar group anchored at the micellar surface.^{76,78,81,141,142} However, Figure 6.4 shows a plot of the relative electrical conductivity and the isentropic compressibility of 1-hexanol in a 0.075 M solution of SDS at 298.15 K. The data have been taken from Reference 31. Recent data on alcohols in SDS and C_{14}Br show the same general trend.¹⁸² The conductivity increases linearly with the hexanol content up to a certain point. If hexanol is solubilized with the polar group at the micellar surface, the surface charge density is expected to decrease, discharging associated counterions. The result is an increased electrical conductivity,¹⁴³⁻¹⁴⁵ as observed. The compressibility also increases linearly up to about the same point. This increase must be an effect of the solubilization process as 1-hexanol is more compressible in a hydrocarbon-like environment than it is in water.¹⁴⁶ However, at a certain alcohol content, there is an abrupt change of the slope for both quantities. The compressibility exhibits a more pronounced increase with added alcohol, suggesting either that suddenly a larger fraction of the alcohol becomes solubilized or that the added alcohol becomes solubilized in an environment that is more hydrocarbon-like than before. The conductivity remains practically constant above this point, or decreases slightly, suggesting that the micellar surface charge density remains constant, which means that the added alcohol no longer is accommodated at the micellar surface. It is also worth noting that the alcohol-to-surfactant ratio of the micelle at the point where the slopes change in Figure 6.4 is about 2.1. Lianos and Zana²⁹ have argued from geometric considerations that about 2.5 alcohol molecules per surfactant

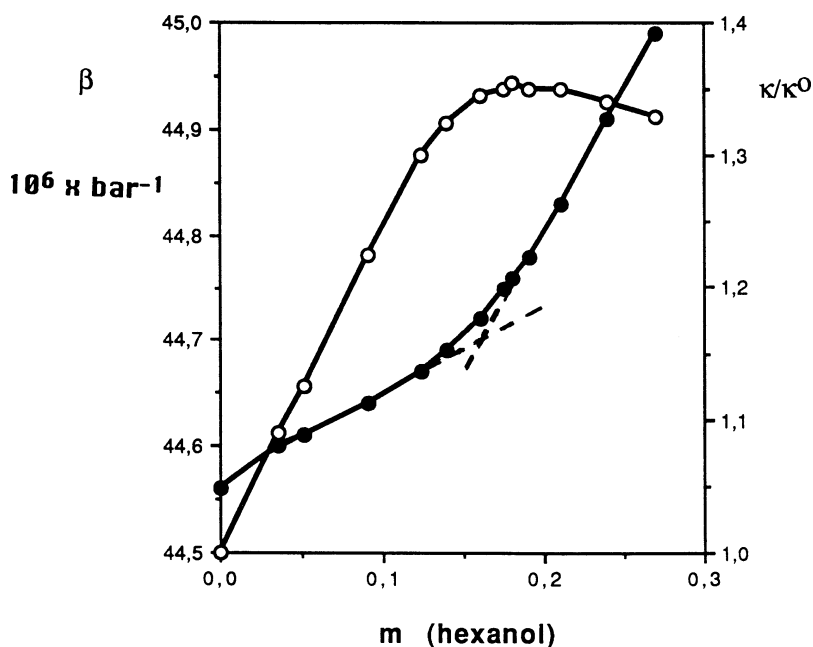


FIGURE 6.4 The isentropic compressibility (β), \circ , and the relative conductivity (K/K^b), \bullet , of the water-SDS-hexanol system as a function of the hexanol content.

molecule can be accommodated at the micellar surface. It thus appears that alcohols, like benzene, are basically located at the micellar surface at low concentrations, but can be solubilized in the core, or certainly in a more hydrocarbon-like microenvironment, at higher concentrations. This trend seems to be general for medium-chain alcohols, pentanol to octanol, in surfactant solutions.¹⁴⁷ However, for this to happen the surfactant concentration must also be rather low, below about 0.15 M for the SDS-hexanol system.³¹ Wan-Badhi et al.²²⁷ have noticed the same irregular behavior from ultrasonic relaxation studies of 1-hexanol in C₁₆Br solutions. However, they suggest that it may be due to concentration fluctuations that affect the ultrasonic relaxation, as it appears as one approaches the phase boundary. From their data the break in the curve occurs approximately at a hexanol concentration of 0.09 M in 0.05 M C₁₆Br, which is only about halfway to the solubility limit of about 0.2 M. Although we cannot exclude their explanation, it seems that the change in ultrasonic relaxation observed, which roughly coincides with observations from the conductivity and speed of sound measurements described above, occurs at concentrations that are significantly below the phase boundary.

At higher surfactant concentrations the ratio of alcohol to surfactant molecules does not exceed 2 at the phase boundary, and it appears that the alcohols promote structural changes of the micelles, for example from spherical to rodlike or ellipsoidal structures. This structural change is dependent both on the surfactant concentration and on the amount of solute, which is apparent from the study carried out by Backlund and co-workers^{228,229} who mapped the whole L1-phase of the SDS-1-hexanol and C₁₆Br-1-hexanol systems demonstrating regions in the phase diagram relating to spherical micelles, spherical swollen micelles, and rodlike micelles.

The self-association of surfactant molecules can qualitatively be understood as a balance between electrostatic and hydrophobic forces. The formation of different amphiphile structures can be explained simplistically by a geometric packing parameter $N_s = v/al$ providing a measure of the hydrophilic-lipophilic balance.^{230,231} In the packing parameter, v is the volume of the hydrocarbon chain, a is the headgroup area, and l is the chain length, which is close to the fully extended molecular length of the chain. From this geometric consideration, it turns out that N_s is about $1/3$

for spherical micelles, about $\frac{1}{2}$ for cylindrical micelles, and about 1 for planar bilayers. The sphere-to-rod transition observed by addition of inorganic salt to surfactant solutions^{6,15} is thus explained by the reduction in the electrostatic repulsion between the headgroups of the surfactant leading to an decrease in a , and thereby an increase in the packing parameter. Polar solutes like medium- to long-chain 1-alcohols, which are primarily solubilized in the palisade layer of the surfactant micelle, reduce the electrostatic repulsion between the charged surfactant headgroups and increase the effective hydrocarbon volume, also resulting in a sphere-to-rod transition. In accordance, it is observed that the more hydrophobic the alcohol, the more efficient it is in promoting this sphere-to-rod transition.^{19,232,233} Aromatic hydrocarbons are generally thought to solubilize at or near the hydrocarbon–water interface through interaction with the positively charged headgroup of cationic micelles, and thereby induce growth and formation of rodlike micelles.^{19,234,235} Aliphatic hydrocarbons, on the other hand, as they are solubilized in the micellar core, retard the transition and simply produce swelling of the spherical micelles.^{19,21,236} Further, the addition of alkanes to solutions of rodlike micelles shows that these are replaced by smaller spherical micelles; i.e., alkanes induce rod-to-sphere transition.^{237,238} A similar effect has been observed at high concentrations of 1-alcohols or benzene in cationic surfactants.^{143,232,234} Initially, the solubilization takes place in the palisade layer promoting sphere-to-rod transition, but upon further addition the solute also resides in the micellar core with the transition from rodlike to spherical swollen micelles the result.

6.3.7 SOLUBILIZATION IN MIXED MICELLES

The term *mixed micelle* means a micelle composed of two (or more) surfactant components, with each surfactant component able to form micelles on its own. As far as we are aware, only two-component mixed micelles have been studied. Nishikido¹⁴⁸ has recently reviewed most of the work done.

Treiner et al.^{95,149} have described the partitioning of a solute between a mixed micellar pseudophase and the aqueous surroundings by the equation:

$$\ln K_{x,m} = X_m \ln K_{x,1} + (1 - X_m) \ln K_{x,2} + X_m(1 - X_m)B \quad (6.34)$$

where $K_{x,m}$ is the partition coefficient of the solute in the mixed micellar solution, $K_{x,1}$ and $K_{x,2}$ are the partition coefficients in the single surfactant solution, and x_m is the mixed micellar mole fraction. B is an empirical parameter. The deviation from ideality, for the cmc, can be derived from the regular solution theory.¹⁵⁰⁻¹⁵² The monomer concentration of binary mixed micellar systems, C_m , can be expressed as

$$C_m = X_m C_1 \gamma_1 + X_m C_2 \gamma_2 \quad (6.35)$$

C_1 and C_2 are the cmc of the pure surfactants, respectively, and γ_1 and γ_2 the activity coefficients, which according to regular solution theory can be calculated from $\gamma_2 = \exp(\beta X_1^2)$. The coefficient β represents an interaction parameter that is equal to B of Equation 6.34 provided that regular solution theory can be applied. Treiner et al.¹⁵³ have shown that this is not the case, but that there is a correlation between the two parameters.

For most systems β and hence B are negative. This means that a negative deviation from ideality is expected, as seen from Equation 6.34. The main exception, exhibiting positive B values, seems to be systems where one of the surfactants contains perfluoro groups. Negative B values imply a negative deviation from ideality, or a negative synergistic effect of the mixed micelle on solubilization.

For alkanes, such as cyclohexane, hexane, and decane, it appears that the partition coefficient increases in mixed surfactant systems, contrary to what was expected from Equation 6.34.¹⁵⁴⁻¹⁵⁶ For polar solutes such as alcohols,¹⁵⁵⁻¹⁵⁸ the dye yellow OB,¹⁵⁹⁻¹⁶² and barbiturates,^{158,162} it appears that a negative synergistic effect is present as expected. However, there are some exceptions. First,

positive synergistic effects have been observed for yellow OB in $M(C_{12}SO_4)_2/C_{12}E_m$ systems where M is zinc, manganese, copper, or magnesium.¹⁶¹ It has been argued^{149,163} that for such systems the definition of a solubilization concentration is difficult as the whole nonionic surfactant does not participate in the solubilization process, as well as that the apparent increased solubilization may be dependent on the method of calculation. Yellow OB also show a positive synergistic effect in the system octylbenzenesulfonate/ $C_{12}E_9$ ¹⁵⁹ as a result of a reduction of the surface micellar charge decreasing the micellar constraint. This explanation has been criticized by Treiner et al.,¹⁵³ who offer a specific stacking effect induced by the benzene rings of the micellar octylbenzenesulfonate as an alternative.

However, by far the most notable exceptions are 1-pentanol and benzylalcohol in benzyldimethyltetradecyl-ammonium chloride ($C_{14}BzCl$) and trimethyltetradecyl-ammonium chloride ($C_{14}Cl$). When the partition coefficient of benzylalcohol was plotted vs. the micellar composition, at first the normal negative synergistic effect was observed. However, at intermediate mole fractions the partition coefficient started increasing, reaching a distinct maximum at a mole fraction of about 0.3 $C_{14}Cl$.¹⁶⁴ For 1-pentanol a sharp maximum was observed at a $C_{14}Cl$ mole fraction of about 0.1.¹⁶⁵ This maximum disappears when salt is added (0.05 mol/dm³ NaCl) or when the surfactant chain length of one of the benzyl-containing surfactants is increased to $C_{16}BzCl$.¹⁶⁶ Solubilization of 1-pentanol in the system $C_{16}BzCl/C_{16}PCl$ (hexadecylpyridinium chloride) showed a negative synergistic effect, but the initial decrease was very sudden and the partition coefficient remained practically constant between mole fractions 0.1 to 0.9, which does not conform with Equation 6.30.¹⁶⁶ It was suggested that if the interactions between the two surfactants are weak, addition of a solute that interacts more strongly with one of them could change the mixed micellar structure; however, the authors admit that any interpretation is speculative. Distinct synergistic effects of solubilization are of great practical interest. We may envisage that by carefully choosing surfactant systems, selective separation methods could be developed. Morgan et al.¹¹² therefore used their headspace gas chromatography to study the same systems, specifically looking for the reported synergistic effects and found no evidence whatever of a positive synergistic effect. The data of pentanol are quite similar to data on 1-hexanol; a gradual change in the partition coefficient with micellar composition is observed for all systems. The strong antis synergistic effect observed for 1-pentanol in $C_{16}BzCl/C_{16}PCl$ is also absent in their studies. It is not possible to explain these different results. Two different experimental methods have been used, calorimetry and headspace chromatography, and this could lead to different results,⁴⁹ although the discrepancies observed for these systems seem to go beyond this rather simple explanation.

6.4 LIST OF ABBREVIATIONS

6.4.1 ANIONIC SURFACTANTS

C_7COOK	potassium octanoate
C_9COOK	potassium decanoate
$C_{11}COOK$	potassium dodecanoate
$C_{13}COOK$	potassium tetradecanoate
C_7COONa	sodium octanoate
C_9COONa	sodium decanoate
$C_{10}COONa$	sodium undecanoate
LiDS	lithium dodecyl sulfate
LiFOS	lithium perfluoro-octanesulfonate
KPFO	potassium perfluoro-octanoate

NaOS	sodium octyl sulfate
NaPFO	sodium perfluoro-octanoate
NaCh	sodium cholate
NaDCh	sodium deoxycholate
SDS	sodium dodecyl sulfate

6.4.2 CATIONIC SURFACTANTS

C ₁₂ Br	trimethyldodecylammonium bromide
C ₁₄ Br	trimethyltetradecylammonium bromide
C ₁₆ Br	trimethylhexadecylammonium bromide
C ₁₄ Cl	trimethyltetradecylammonium chloride
C ₁₄ BzCl	benzyltrimethyltetradecylammonium chloride
C ₁₆ PCl	hexadecylpyridinium chloride

REFERENCES

1. McBain, M.E.L. and Hutchinson, E., *Solubilization and Related Phenomena*, Academic Press, New York, 1955.
2. McBain, J.W, *Adv. Colloid Sci.*, 1, 99, 1942.
3. Klevens, H.B., *Chem. Rev.*, 47, 1 1950.
4. Elworthy, P.H., Florence, A.T. and Macfarlane, C.B., *Solubilization by Surface-Active Agents and Its Application in Chemistry and the Biological Sciences*, Chapman & Hall, London, 1968.
5. Christian, S.D. and Scamehorn, J.F., Eds., *Solubilization in Surfactant Aggregates*, Marcel Dekker, New York, 1995.
6. Lindman, B. and Wennerström, H., *Top. Curr. Chem.*, 87, 1, 1980.
7. Grieser, F. and Drummond, C.J., *J. Phys. Chem.*, 92, 5580, 1988.
8. Kalyasundaram, K. and Thomas, J.K., *J. Phys. Chem.*, 80, 1462, 1976.
9. Zana, R., in *Surfactant Solutions New Methods of Investigation*, Zana, R. Ed., Marcel Dekker, New York, 1987.
10. Wennerström, H. et al., *J. Am. Chem. Soc.*, 101, 6860, 1979.
11. Hayter, J.B. and Penfold, J., *J. Colloid Interface Sci.*, 261, 1022, 1983.
12. Berr, S.S. et al., *J. Phys. Chem.*, 90, 6492, 1986.
13. Aamodt, M., Landgren, M., and Jönsson, B., *J. Phys. Chem.*, 96, 945, 1992.
14. Fisher, L.R. and Oakenful, D.G., *Chem. Soc. Rev.*, 6, 25, 1977.
15. Wennerström, H. and Lindman, B., *Phys. Rep.*, 52, 1, 1979.
16. Ekwall, P., Mandell, L., and Fontell, K., *Mol. Cryst. Liq.*, 8, 157, 1969.
17. Ekwall, P., *Adv. Liq. Cryst.*, 1, 1 1975.
18. Karaborni, S. et al., *Langmuir*, 9, 1175, 1993.
19. Lindemuth, P.M. and Bertrand, G.L., *J. Phys. Chem.*, 97, 7769, 1993.
20. Almgren, M. and Swarup, S., *J. Phys. Chem.*, 86, 4212, 1983
21. Malliaris, A., *J. Phys. Chem.*, 91, 6511, 1987.
22. Abe, M. et al., *Colloids Surf.*, 67, 37, 1992.
23. Ekwall, P., Mandell, L., and Fontell, K., *J. Colloid Interface Sci.*, 31, 508, 1969.
24. Jönsson, B., Landgren, M., and Olofsson, G., in *Solubilization in Surfactant Aggregates*, Christian, S.D and Scamehorn, J.F., Eds., Marcel Dekker, New York, 1995.
25. Rosen, M.J., *Surfactants and Interfacial Phenomena*, John Wiley & Sons, New York, 1989.
26. Shinoda, K., *Principles of Solution and Solubility*, Marcel Dekker, New York, 1978.
27. Szajdzinski-Pietek, E. et al., *J. Colloid Interface Sci.*, 110, 514, 1986.
28. Lee, B.-H. et al., *J. Phys. Chem.*, 95, 360, 1991.
29. Lianos, P. and Zana, R., *J. Colloid Interface Sci.*, 101, 587, 1984.
30. Høiland, H. et al., *J. Colloid Interface Sci.*, 107, 576, 1985.
31. Backlund, S. et al., *Acta Chem. Scand.*, A40, 241, 1986.

32. Høiland, H. and Blokhuis, A.M., in *The Structure, Dynamics and Equilibrium Properties of Colloidal Systems*, Bloor, D.M. and Wyn-Jones, E., Eds., Kluwer, Amsterdam, 1990.
33. Rehfeldt, S.J., *J. Phys. Chem.*, 74, 117, 1966.
34. Fendler, J.H. and Patterson, L.K., *J. Phys. Chem.*, 75, 3907, 1971.
35. Mukerjee, P. and Cardinal, J.R., *J. Phys. Chem.*, 82, 1620, 1978.
36. Jobe, D.J., Reinsborough, V.C., and White, P.J., *Can. J. Chem.*, 60, 279, 1982.
37. Nagarajan, R., Chaiko, M.A., and Ruckenstein, E., *J. Phys. Chem.*, 88, 2916, 1984.
38. Heindl, A., Strnad, J., and Kohler, H.-H., *J. Phys. Chem.*, 97, 742, 1993.
39. Reiss-Husson, F. and Luzzatti, V.J. *Colloid Interface Sci.*, 21, 534, 1966.
40. Porte, G. et al., *J. Phys. Chem.*, 88, 5713, 1984.
41. Høiland, H., Veggeland, K., and Backlund, S., in *Surfactants in Solution*, Vol. 4, Mittal, K.L. and Bothorel, P., Eds., Plenum, New York, 1987, 309.
42. Smith, G.A. et al., *J. Colloid Interface Sci.*, 130, 254, 1989.
43. Christian, S.D. et al., *J. Colloid Interface Sci.*, 113, 439, 1986.
44. Abuin, E.B., Valenzuela, E., and Lissi, E.A., *J. Colloid Interface Sci.*, 101, 401, 1984.
45. Valenzuela, E., Abuin, E., and Lissi, E.A., *J. Colloid Interface Sci.*, 102, 46, 1984.
46. Goto, A. and Endo, F.J. *Colloid Interface Sci.*, 66, 26, 1978.
47. Høiland, H., Ljosland, E., and Backlund, S., *J. Colloid Interface Sci.*, 101, 467, 1984.
48. Treiner, C. and Chattopadhyay, A.K., *J. Colloid Interface Sci.*, 109, 101, 1986.
49. DeLisi, R., Genova, C., and Liveri, V.T., *J. Colloid Interface Sci.*, 95, 428, 1983.
50. Gao, Z., Wasylishen, R.E., and Kwak, J.C.T., *J. Phys. Chem.*, 93, 2190, 1989.
51. Sepulveda, L., Lissi, E., and Quina, F., *Adv. Colloid Interface Sci.*, 25, 1, 1986.
52. Almgren, M., Grieser, F., and Thomas, J.K., *J. Am. Chem. Soc.*, 101, 279, 1979.
53. Moroi, Y., Sato, K., and Matuura, R., *J. Phys. Chem.*, 86, 2463, 1982.
54. Moroi, Y., Noma, H., and Matuura, R., *J. Phys. Chem.*, 87, 872, 1983.
55. Tachiya, M., *J. Chem. Phys. Lett.*, 33, 289, 1975.
56. Christian, S.D., Tucker, E.E., and Lane, E.H., *J. Colloid Interface Sci.*, 84, 423, 1981.
57. Gamboa, C. and Olea, A.F., *Langmuir*, 9, 2066, 1993.
58. Roux, A.H. et al., *J. Solution Chem.*, 13, 1, 1984.
59. Héту, D., Roux, A.H., and Desnoyers, J.E., *J. Solution Chem.*, 16, 529, 1987.
60. DeLisi, R. and Liveri, V.T., *Gazz. Chim. Ital.*, 113, 371, 1983.
61. DeLisi, R. et al., *J. Solution Chem.*, 13, 121, 1984.
62. DeLisi, R. et al., *J. Solution Chem.*, 15, 23, 1986.
63. Mahmoud, F.Z. et al., *J. Colloid Interface Sci.*, 131, 96, 1989.
64. King, A.D., Jr., in *Solubilization in Surfactant Aggregates*, Christian, S.D. and Scamehorn, J.F., Eds., Marcel Dekker, New York, 1995, 35.
65. Zana, R. et al., *J. Colloid Interface Sci.*, 80, 208, 1981.
66. Høiland, H., Blokhuis, A.M., and Backlund, S., *J. Colloid Interface Sci.*, 125, 741, 1988.
67. Muto, Y. et al., *J. Colloid Interface Sci.*, 113, 165, 1989.
68. Høiland, H., Blokhuis, A.M., and Backlund, S., *J. Colloid Interface Sci.*, 125, 741, 1988.
69. Hayase, K. and Hayano, S., *Bull. Chem. Soc. Jpn.*, 50, 83, 1977.
70. Spink, C.H. and Colgan, S., *J. Colloid Interface Sci.*, 97, 41, 1984.
71. Tucker, E.E. and Christian, S.D., *J. Chem. Thermodyn.*, 11, 1137, 1979.
72. Tucker, E.E. and Christian, S.D., *J. Phys. Chem.*, 83, 426, 1979.
73. Tucker, E.E., in *Solubilization in Surfactant Aggregates*, Christian, S.D. and Scamehorn, J.F., Eds., Marcel Dekker, New York, 1995, 429.
74. Shirahama, K. and Kashiwabara, T., *J. Colloid Interface Sci.*, 36, 65, 1971.
75. Hayase, K. and Hayano, H., *J. Colloid Interface Sci.*, 63, 446, 1978.
76. Manabe, M., Koda, M., and Shirahama, K., *J. Colloid Interface Sci.*, 77, 189, 1980.
77. Abu-Hamdiyyah, M. and Kumari, K., *J. Phys. Chem.*, 94, 6445, 1990.
78. Treiner, C., *J. Colloid Interface Sci.*, 90, 444, 1982.
79. Kaneshina, S., Kamaya, H., and Ueda, I., *J. Colloid Interface Sci.*, 83, 589, 1981.
80. Mukerjee, P. and Ko, J.-S., *J. Phys. Chem.*, 96, 6090, 1992.
81. Abuin, E.B. and Lissi, E.A., *J. Colloid Interface Sci.*, 95, 198, 1983.
82. Stilbs, P., *J. Colloid Interface Sci.*, 87, 385, 1982.

83. Stilbs, P., *J. Colloid Interface Sci.*, 94, 463, 1983.
84. Armstrong, D.W. and Nome, F., *Anal. Chem.*, 53, 1662, 1981.
85. Armstrong, D.W. and Stine, G.Y., *J. Am. Chem. Soc.*, 105, 2962, 1983.
86. Hirose, C. and Sepúlveda, L., *J. Phys. Chem.*, 85, 3689, 1981.
87. Gao, Z. et al., *Colloids Surf.*, 45, 269, 1990.
88. Carlfors, J. and Stilbs, P., *J. Colloid Interface Sci.*, 104, 489, 1985.
89. Baglioni, P. and Kevan, L., *J. Phys. Chem.*, 91, 1516, 1987.
90. Manabe, M., Shirahama, K., and Koda, M., *Bull. Chem. Soc. Jpn.*, 49, 2904, 1976.
91. Kaneshina, S., Kamaya, H., and Ueda, I., *J. Colloid Interface Sci.*, 83, 589, 1981.
92. Hartland, G.V., Grieser, F., and White, L.R., *J. Chem. Soc. Faraday Trans. I*, 83, 591, 1978.
93. Treiner, C. and Mannebach, M.-H., *J. Colloid Interface Sci.*, 118, 217, 1989.
94. Treiner, C. et al., *J. Solution Chem.*, 18, 217, 1989.
95. Treiner, C., Bocquet, J.F., and Pommier, C., *J. Phys. Chem.*, 90, 3052, 1986.
96. Almgren, M., Grieser, F., and Thomas, J.K., *J. Chem. Soc. Faraday Trans. I*, 75, 1674, 1979.
97. Bury, R. and Treiner, C., *J. Solution Chem.*, 18, 499, 1989.
98. DeLisi, R. et al., *J. Solution Chem.*, 15, 623, 1986.
99. Manabe, M. et al., *Langmuir*, 6, 1596, 1990.
100. DeLisi, R. and Milioto, S., *J. Solution Chem.*, 17, 245, 1988.
101. Nguyen, D., Venable, R.L., and Bertrand, G.L., *Colloids Surf.*, 65, 231, 1992.
102. DeLisi, R. and Milioto, S., in *Solubilization in Surfactant Aggregates*, Christian, S.D. and Scamehorn, J.F., Eds, Marcel Dekker, New York, 1995, 59.
103. Treiner, C., in *Solubilization in Surfactant Aggregates*, Christian, S.D. and Scamehorn, J.F., Eds, Marcel Dekker, New York, 1995, 383.
104. DeLisi, R., Fiscaro, E., and Milioto, S., *J. Solution Chem.*, 18, 403, 1989.
105. DeLisi, R., Milioto, S., and Verrall, R.E., *J. Solution Chem.*, 19, 97, 1990.
106. DeLisi, R., Milioto, S., and Triolo, R., *J. Solution Chem.*, 17, 673, 1988.
107. DeLisi, R. et al., *J. Solution Chem.*, 16, 373, 1987.
108. DeLisi, R., Milioto, S., and Turco-Liveri, V., *J. Colloid Interface Sci.*, 117, 64, 1987.
109. DeLisi, R. and Milioto, S., *J. Solution Chem.*, 16, 767, 1987.
110. Stilbs, P., *J. Colloid Interface Sci.*, 89, 547, 1982.
111. Perez-Villard, V. et al., *Colloid Polym. Sci.*, 268, 965, 1990.
112. Morgan, M.E. et al., *Langmuir*, 10, 2170, 1994.
113. Spink, C.H. and Colgan, S., *J. Phys. Chem.*, 87, 888, 1983.
114. Rao, I.V. and Ruckenstein, E., *J. Colloid Interface Sci.*, 113, 375, 1986.
115. Lee, B.-H. et al., *Langmuir*, 6, 230, 1990.
116. Lee, B.-H. et al., *J. Phys. Chem.*, 95, 360, 1991.
117. Lee, B.-H. et al., *Langmuir*, 7, 1332, 1991.
118. Tucker, E.E. and Christian, S.D., *Faraday Symp. Chem. Soc.*, 17, 11, 1982.
119. Ben-Naim, A., *J. Phys. Chem.*, 82, 792, 1978.
120. Kauzman, W., *Adv. Protein Chem.*, 14, 1, 1959.
121. Gurney, R.W., *Ionic Processes in Solution*, McGraw-Hill, New York, 1962.
122. Tanford, C., *The Hydrophobic Effect*, John Wiley & Sons, New York, 1973.
123. Sepulveda, L., Lissi, E., and Quina, F., *Adv. Colloid Interface Sci.*, 25, 1, 1986.
124. Milioto, S., Romancino, D., and DeLisi, R., *J. Solution Chem.*, 16, 943, 1987.
125. Wishnia, A., *J. Phys. Chem.*, 67, 2079, 1963.
126. Høiland, H. et al., in *Surfactants in Solution*, Vol. 2, Mittal, K.L. and Lindman, B., Eds., Plenum, New York, 1984, 949.
127. Treiner, C., Chattopadhyay, A.K., and Bury, R., *J. Colloid Interface Sci.*, 104, 569, 1985.
128. Aveyard, R. and Lawrence, A.S.C., *Trans. Faraday Soc.*, 60, 2265, 1964.
129. Hayase, K., Hayano, S., and Tsubota, H., *J. Colloid Interface Sci.*, 101, 336, 1984.
130. Kawamura, H. et al., *J. Phys. Chem.*, 93, 5536, 1989.
131. Amidon, G.L. and Anik, S.T., *J. Phys. Chem.*, 84, 970, 1980.
132. Nichols, N. et al., *J. Chem. Thermodyn.*, 8, 1081, 1976.
133. Lawrence, A.S.C., *Trans. Faraday Soc.*, 33, 815, 1937.
134. Mukerjee, P. and Cardinal, J.R., *J. Phys. Chem.*, 82, 8156, 1978.

135. Gettings, J. et al., *J. Chem. Soc. Faraday II*, 74, 1957, 1978.
136. Selwyn, J.C. and Scaiano, J.C., *Can. J. Chem.*, 59, 663, 1981.
137. Simon, S.A., McDaniel, R.V., and McIntosh, T.J., *J. Phys. Chem.*, 86, 1449, 1982.
138. Eriksson, J.C. and Gillberg, G., *Acta Chem. Scand.*, 17, 1478, 1963.
139. Matsuo, T., Yudato, K., and Nagamura, T., *J. Colloid Interface Sci.*, 83, 354, 1981.
140. Mukerjee, P., Cardinal, I.R., and Desai, N.R., in *Micellization, Solubilization and Microemulsions*, Vol. 1, Mittal, K.L., Ed., Plenum Press, New York, 1977.
141. Lianos, P. and Zana, R., *Chem. Phys. Lett.*, 72, 171, 1980.
142. Lianos, P. et al., *J. Phys. Chem.*, 86, 1019, 1982.
143. Tominaga, T., Stem, T.B., and Evans, D.F., *Bull. Chem. Soc. Jpn.*, 53, 795, 1980.
144. Lawrence, A.S.C. and Pearson, J.T., *Trans. Faraday Soc.*, 63, 495, 1967.
145. Backlund, S. and Rundt, K., *Acta Chem. Scand.*, A34, 433, 1980.
146. Høiland, H., *J. Solution Chem.*, 6, 291, 1977.
147. Backlund, S. et al., *Prog. Colloid Interface Sci.*, 74, 93, 1987.
148. Nishikido, N., in *Solubilization in Surfactant Aggregates*, Christian, S.D. and Scamehorn, J.F., Eds., Marcel Dekker, New York, 1995, 143.
149. Treiner, C., Khodja, A.A., and Fromon, M., *Langmuir*, 3, 729, 1987.
150. Rubingh, D.N., in *Solution Chemistry of Surfactants*, Mittal, K.L., Ed., Plenum Press, New York, 1979, 337.
151. Clint, J.H., *J. Chem. Soc.*, 71, 1327, 1975.
152. Bourrel, M., Bernard, D., and Graciaa, A., *Tenside Deterg.*, 21, 311, 1986.
153. Treiner, C., Nortz, M., and Vaution, C., *Langmuir*, 6, 1211, 1990.
154. Carrion Fite, F.J., *Tenside Deterg.*, 22, 5, 1985.
155. Ngyen, C.M., Rathman, J.F., and Scamehorn, J.F., *J. Colloid Interface Sci.*, 112, 438, 1986.
156. Zhu, B.Y. and Rosen, M.J., *J. Colloid Interface Sci.*, 99, 438, 1984.
157. Holland, P.M. and Rubingh, D.N., *J. Phys. Chem.*, 87, 1984, 1983.
158. Treiner, C. et al., *Colloids Surf.*, 14, 285, 1985.
159. Tokinawa, F. and Tsujii, K., *Bull. Chem. Soc. Jpn.*, 46, 1338, 1973.
160. Nishikido, N., *J. Colloid Interface Sci.*, 60, 242, 1971.
161. Muto, Y. et al., *J. Colloid Interface Sci.*, 124, 632, 1988.
162. Rosen, M.J. and Hua, X.Y., *J. Colloid Interface Sci.*, 86, 164, 1982.
163. Barry, B.W. and El Eina, D.D., *J. Pharm. Sci.*, 28, 210, 1976.
164. Bury, R., Souhalia, E., and Treiner, C., *J. Phys. Chem.*, 95, 3824, 1991.
165. Bury, R. et al., *Anal. Chim. Acta*, 251, 69, 1991.
166. Makayassi, A., Bury, R., and Treiner, C., *Langmuir*, 10, 1359, 1994.
167. Causi, S., DeLisi, R., and Milioto, S., *J. Solution Chem.*, 19, 995, 1990.
168. Shinoda, K., *J. Phys. Chem.*, 58, 1136, 1954.
169. Marangoni, D.G. and Kwak, J.C.T., *Langmuir*, 7, 2083, 1991.
170. Manabe, M. et al., *Bull. Chem. Soc. Jpn.*, 61, 1551, 1988.
171. Manabe, M. and Koda, K., *Bull. Chem. Soc. Jpn.*, 51, 1599, 1978.
172. Hayase, K. and Hayano, S., *Bull. Chem. Soc. Jpn.*, 51, 933, 1978.
173. Leaist, D.G., *J. Solution Chem.*, 20, 175, 1990.
174. Treiner, C., *J. Colloid Interface Sci.*, 93, 33, 1983.
175. Héту, D. et al., *Langmuir*, 10, 4039, 1994.
176. Abu-Hamdiyya, M. and El-Danab, C., *J. Phys. Chem.*, 87, 5443, 1983.
177. Blokhus, A.M., Høiland, H., and Backlund, S., *J. Colloid Interface Sci.* 114, 9, 1986.
178. Abu-Hamdiyyah, M. and Kumari, K., *J. Phys. Chem.*, 94, 2518, 1990.
179. Abu-Hamdiyyah, M., *J. Phys. Chem.*, 90, 1345, 1986.
180. Miyashita, Y. and Hayano, S., *J. Colloid Sci.*, 86, 344, 1982.
181. Eda, Y., Takisawa, N., and Shirahama, K., *Langmuir*, 12, 325, 1996.
182. Høiland, H. et al., *Colloids Surf.*, A183–185, 651, 2001.
183. Eda, Y., Takisawa, N., and Shirahama, K., *Langmuir*, 13, 2432, 1997.
184. Kawamura, H. et al., *J. Solution Chem.*, 20, 817, 1991.
185. Kennedy, C.A. et al., *Colloid. Polym. Sci.*, 279, 1, 2001.
186. Bolden, P.L., Hoskins, J.C. and King, A.D., Jr., *J. Colloid Interface Sci.*, 91, 454, 1983.

187. Matheson, I.B.C. and King, A.D., Jr., *J. Colloid Interface Sci.*, 66, 464, 1978.
188. Prapaitrakul, W. and King, A.D., Jr., *J. Colloid Interface Sci.*, 112, 387, 1986.
189. Prapaitrakul, W. and King, A.D., Jr., *J. Colloid Interface Sci.*, 118, 224, 1987.
190. Prapaitrakul, W. and King, A.D., Jr., *J. Colloid Interface Sci.*, 106, 186, 1985.
191. Ownby, D.W., Prapaitrakul, W., and King, A.D., Jr., *J. Colloid Interface Sci.*, 125, 526, 1988.
192. Prapaitrakul, W., Shwikat, A., and King, A.D., Jr., *J. Colloid Interface Sci.*, 115, 443, 1987.
193. Ben-Naim, A. and Wilf, J., *J. Solution Chem.*, 12, 671, 1983.
194. Ownby, D.W. and King, A.D., Jr., *J. Colloid Interface Sci.*, 101, 271, 1984.
195. Valsaraj, K.T. and Thibodeaux, L.J., *Sep. Sci. Technol.*, 25, 369, 1990.
196. Høiland, H., Ljosland, E., and Backlund, S., *J. Colloid Interface Sci.*, 101, 467, 1984.
197. Valsaraj, K.T. et al., *Water Res.*, 22, 1173, 1988.
198. Löfroth, J.E. and Almgren, M., *J. Phys. Chem.*, 86, 1636, 1982.
199. Cuccovia, I.M. et al., *J. Am. Chem. Soc.*, 104, 4544, 1982.
200. Marina, M.L., Vera, S., and Rodriguez, A.R. *Chromatographia*, 28, 379, 1989.
201. Tomasella, F.P. and Cline-Love, L.J., *Anal. Chem.*, 62, 1315, 1990.
202. Pelizetti, E. and Pramauro, E., *Anal. Chim. Acta*, 169, 1, 1985.
203. Foley, J.P., *Anal. Chim. Acta*, 231, 237, 1990.
204. Yarmchuk, P. et al., *Anal. Chem.*, 54, 2233, 1982.
205. Katsuha, S. and Saito, K., *Chem. Lett.*, 349, 1994.
206. Lavine, B.K., White, A.J., and Han, J.H., *J. Chromatogr.*, 542, 29, 1991.
207. Smith, G.A. et al., *Langmuir*, 3, 598, 1987.
208. Attwood, D. et al., *Colloid Polym. Sci.*, 272, 584, 1994.
209. Terabe, S. et al., *J. Chromatogr. Sci.*, 27, 653, 1989.
210. Smith, S.C. and Khaledi, M.G., *J. Chromatogr.*, 632, 177, 1993.
211. Yang, X. and Matthews, M.A., *J. Colloid Interface Sci.*, 229, 53, 2000.
212. Pelizzi, E. and Pramauro, E., *J. Phys. Chem.*, 88, 990, 1984.
213. Bhat, S.N. et al., *Ind. Eng. Chem. Res.*, 26, 1217, 1987.
214. Dunaway, C.S., Christian, S.D., and Scamehorn, J.F., in *Solubilization in Surfactant Aggregates*, Christian, S.D. and Scamehorn, J.F., Eds., Marcel Dekker, New York, 1995, 3.
215. Abraham, M.H. et al., *J. Chem. Soc. Perkin Trans.*, 2, 887, 1995.
216. Garrone, A. et al., *Quant. Struct. Act. Relat.*, 11, 171, 1992.
217. Leilèvre, J., Millot, F., and Gaboriaud, R., *J. Chim. Phys.*, 87, 1663, 1990.
218. Leigh, J. and Scaiano, J.C., *J. Am. Chem. Soc.*, 105, 5652, 1983.
219. Scaiano, J.C. and Selwyn, J.C., *Can. J. Chem.*, 59, 2368, 1981.
220. Abraham, M.H., *Chem. Soc. Rev.*, 22, 73, 1993.
221. Abraham, M.H. and McGowan, J.C., *Chromatographia*, 23, 243, 1987.
222. Quina, F.H., Alonso, E.O., and Farah, J.P.S., *J. Phys. Chem.*, 99, 11708, 1995.
223. Abraham, M.H. et al., *J. Chem. Soc. Perkin Trans.*, 2, 19, 1997.
224. Høiland, H., in *Thermodynamic Data for Biochemistry and Biotechnology*, Hinz, H.-J., Ed., Springer Verlag, Berlin, 1986.
225. Vikingstad, E., *J. Colloid Interface Sci.*, 72, 75, 1979 (values recalculated by present author using Equation 6.23).
226. Høiland, H. and Blokhuis, A.M., Unpublished results.
227. Wan-Badhi, W., Bloor, D.M., and Wynne-Jones, E., *Langmuir*, 10, 2219, 1994.
228. Backlund, S. et al., *Acta Chem. Scand.*, A40, 241, 1986.
229. Vikholm, I. et al., *J. Colloid Interface Sci.*, 116, 582, 1987.
230. Israelachvili, J.N., Mitchell, D.J., and Ninham, B., *J. Chem. Soc. Faraday Trans. II*, 72, 1525, 1976.
231. Mitchell, D.J. and Ninham, B.W., *J. Chem. Soc. Faraday Trans. II*, 77, 601, 1981.
232. KabidurDin, Kumar, S., Kirti, Goyal, P.S., *Langmuir*, 12, 1490, 1996.
233. Ljosland, E. et al., *Prog. Colloid Polym. Sci.*, 70, 34, 1985.
234. Eriksson, J.C. et al., in *Solution Behaviour of Surfactants*, Mittal, K.L. and Fendler, E.J., Eds., Plenum Press, New York, 907, 1982.
235. Heindl, A. Strnad, J., and Kohler, H.-H., *J. Phys. Chem.*, 97, 742, 1993.
236. Clarke, D.E. and Hall, D.G., *Colloid Polymer Sci.*, 252, 153, 1974.
237. Nilsson, S., Blokhuis, A.M., and Saure, A., *Langmuir*, 14, 6028, 1998.
238. Hoffman, H. and Ulbricht, W.J., *J. Colloid Interface Sci.*, 129, 388, 1989.

7 Colloid Systems and Interfaces — Stability of Dispersions through Polymer and Surfactant Adsorption

P. Somasundaran, B. Markovic, X. Yu, and S. Krishnakumar

CONTENTS

- 7.1 Introduction
- 7.2 Colloidal Forces
 - 7.2.1 van der Waals Force
 - 7.2.2 Hydrophobic Force
 - 7.2.3 Steric and Bridging Forces
 - 7.2.4 Hydration and Solvation Forces
 - 7.2.4.1 Capillary Condensation Forces
 - 7.2.5 Interacting Double Layers
 - 7.2.6 Summation of Various Forces
 - 7.2.7 Kinetics of Aggregation
- 7.3 Experimental Assessment of Dispersion Stability
 - 7.3.1 Sedimentation Methods
 - 7.3.2 Rheological methods
- 7.4 Dispersion in the Absence of Dispersing Agents
- 7.5 Adsorption and Its Effect on Dispersion
 - 7.5.1 Factors Affecting Adsorption
 - 7.5.2 Surfactant Adsorption and Its Effect on Dispersion Properties
 - 7.5.2.1 In Aqueous Media
 - 7.5.2.1.1 Ionic Surfactants
 - 7.5.2.1.2 Nonionic Surfactants
 - 7.5.2.1.3 Flocculation by Phase Separation
 - 7.5.2.2 In Organic Media
 - 7.5.2.2.1 Oxide Surfaces
 - 7.5.2.2.2 Hydrophobic Surfaces (Graphite)
 - 7.5.2.2.3 Effect of Water on Dispersion Stability of Alumina
 - 7.5.2.2.4 Electron Spin Resonance Studies on Water-Induced Flocculation
 - 7.5.3 Adsorption of Polymers and Its Effect on Dispersion Properties
 - 7.5.3.1 Theoretical Considerations on Polymer Adsorption
 - 7.5.3.2 Basic Concepts of Adsorbed Polymer Conformations
 - 7.5.3.3 Mechanisms of Flocculation by Adsorbed Polymers

- 7.5.3.3.1 Bridging
- 7.5.3.3.2 Simple Charge Neutralization and Charge Patch Neutralization
- 7.5.3.4 Role of Polymer Conformation in Flocculation and Stabilization
- 7.5.3.5 Stability of Dispersion in the Presence of Polymers
 - 7.5.3.5.1 Fluorescence Spectroscopy for Polymer Conformation and Association Measurement
 - 7.5.3.5.2 Electron Spin Resonance Spectroscopy for the Study of Adsorbed Polymer and Surfactant Layers
 - 7.5.3.5.3 Effect of Adsorbed Polymer Conformation on Dispersion Characteristics
 - 7.5.3.5.4 Dual Polymer System for Enhanced Flocculation
 - 7.5.3.5.5 Flocculation with Ultralow Polymer Dosage
 - 7.5.3.5.6 Stabilization of Aqueous and Nonaqueous Suspensions with a Hydrophobically Modified Polymer

7.6 Summary

[Acknowledgments](#)

[References](#)

7.1 INTRODUCTION

Dispersions in both aqueous and nonaqueous media are used in many products including paints, dyestuffs, pigments, printing inks, papers, adhesives, cosmetics, detergents, ceramics, and pharmaceutical and pesticidal formulations. Use of coagulants to clarify drinking water was practiced in ancient China and Egypt. Mineral and environmental engineers have applied the concepts of colloid science to help them utilize and preserve enormous resources, which would otherwise be waste material.¹ Today, ceramic products ranging from building bricks to expensive china to rocket parts are made from clay–water sols by applying principles of colloid science.² The wide use of colloid science in the areas of cosmetics and detergents has added many products into our daily life.³ Knowledge of human life either written on paper or stored on film or disk has depended on the application of colloidal science in papermaking and development of new magnetic and electronic materials. High-quality ceramics are also very important as substrates for electronic devices and are used in the preparation of capacitors, ferrites, and piezoelectrics.⁴ The initial excitement of the discovery of the high temperature superconducting oxide phases has been considerably dampened by the inability to process them into mechanically strong and durable products. The main reason for the structural failure of ceramic materials is the presence of flaws in the material, which facilitates initiation and propagation of cracks. These flaws are introduced into the material during the powder processing stage, and hence the future of ceramics, to a great extent, will depend on the control of the state of dispersion of the powder prior to firing.⁵ Agglomerates and inhomogeneities in the dispersion result in poor packing, grain growth porosity, and other defects. Good initial dispersion of ceramic powders in liquids is essential for production of high-quality ceramics. The similarity between some biological systems and colloid dispersions, such as blood and proteins and polyelectrolytes,⁶ has made colloid science more attractive to the scientific community. The successful applications of colloidal concepts in biological system include encapsulation, controlled drug release, and prevention or promotion of cell adhesion.⁷

A colloidal system is composed of one or more dispersed phases and a continuous medium. Colloids are present as dispersed systems, characterized by slow diffusion and slow (often negligible) sedimentation under normal gravity, which sets the size of the colloidal particles to the range of 1 nm to 1 μ m. Systems in which a significant fraction of particles is in a size range that is larger than the colloidal range are termed *suspensions*.

TABLE 7.1
Summary of Forces Between Two Identical Particles in Aqueous Media

Force	Nature	Source
Electrical double layer	Repulsive	Structure of surfaces and adsorption of ions
van der Waals	Usually attractive	Universal presence
Steric interaction	Repulsive	Induced by adsorbed species
Hydration/solvation interaction	Attractive/repulsive	Hydration or solvation of adsorbent and adsorbate
Polymeric bridging	Attractive	Induced by adsorbed long-chain polymer
Hydrophobic interaction	Attractive	Intrinsic or induced by adsorption

Some colloidal systems such as polymer solutions and surfactant solutions containing micelles are thermodynamically stable and form spontaneously. These types of colloids are called lyophilic colloids. However, most systems encountered contain lyophobic colloids (particles insoluble in the solvent). In the preparation of such lyophobic colloidal dispersions, the presence of a stabilizing substance is essential. Because van der Waals forces usually tend to lead to agglomeration (flocculation) of the particles, stability of such colloids requires that the particles repel one another, either by carrying a net electrostatic charge or by being coated with an adsorbed layer of large molecules compatible with the solvent.

In this chapter, the theories as well as the experimental justification for the mechanism of stabilization and destabilization of colloidal dispersions are outlined. Interacting forces between colloidal particles are analyzed and an overview of experimental methods for assessing the dispersion and relevant properties is given. The stabilization and flocculation of dispersions in the presence of surfactants and polymers is discussed in the last two sections.

7.2 COLLOIDAL FORCES

Colloidal systems are composed of one or more dispersed phases and a continuous medium. In the processing of dispersions, aggregates or agglomerates in the dry state are broken into smaller particles in the dispersion medium. Total energy of the system increases due to the increase in surface energy resulting from the increase in the surface area and possible changes in the structure and composition of the surface. The nature and the magnitude of the surface energy are determined by the physicochemical properties of the particles and the solvent since the particles will have a tendency to undergo aggregation to reduce the surface energy. A colloidal dispersion is not a thermodynamically stable system.

Colloidal particles in a dispersion medium are always subjected to Brownian motion with frequent collisions between them. Stability and other characteristics of dispersion are thus determined by the nature of the interactions between the particles during such collisions. When attractive forces dominate, the particles will aggregate and the dispersion may destabilize. When repulsive forces dominate, the system will remain in a dispersed state.

Generally, there are six important types of particle–particle interaction forces that can exist in a dispersion as summarized in Table 7.1.

7.2.1 VAN DER WAALS FORCE

London explained the van der Waals forces (the universal attractive forces) acting between all atoms, molecules, ions, etc. on the basis of wave mechanics. These short-range forces result from the interaction between temporary dipoles on some molecules and induced dipoles on the neighboring molecules, and a quantum mechanical effect leading to attraction between nonpolar molecules. Most of the interpretations of London–van der Waals forces in the past have been based on

the Hamaker approach,⁸ which involves pairwise addition of the microscopic forces acting between two bodies. The attractive energy between two atoms varies inversely as the sixth power of the distance separating them and is given by

$$V_A = -\frac{\beta}{l^6} \quad (7.1)$$

where β is the London constant, which depends on the properties of the specific atoms.

In the case of dispersion, these forces are due to spontaneous electric and magnetic polarizations giving rise to a fluctuating electromagnetic field within the dispersed solid and the medium separating the particles. The interaction energy between two identical spheres of radius R at a distance H between their centers remains the same for a constant ratio of R to H . Calling H/R as S , the interaction energy is given as

$$V_A = \frac{-A}{6} \left[\frac{2}{S^2 - 4} + \frac{2}{S^2} + \ln \frac{S^2 - 4}{S^2} \right] \quad (7.2)$$

For the simplest case, the net attractive force between two particles at small separation distance after neglecting the retardation correction is given as

$$V = \frac{-AR}{12l} \quad (7.3)$$

where $l = H - 2R$ and A is the combined Hamaker constant. The Hamaker constant can be estimated theoretically by calculating certain molecular constants from optical data. For a system of solid 1 dispersed in a medium 2, the combined Hamaker constant can be expressed as

$$A = A_{11} + A_{22} - 2A_{12} \quad (7.4)$$

As an approximation, $A_{12} = (A_{11}A_{22})^{1/2}$, so that

$$A = \left[A_{11}^{1/2} - A_{22}^{1/2} \right]^2 \quad (7.5)$$

7.2.2 HYDROPHOBIC FORCE

Hydrophobic interactions may exist naturally or be induced by the adsorbed hydrophobic species. Polar solvent molecules squeezed between two hydrophobic surfaces have reduced freedom to form structures in certain directions, because contact with the particle surfaces is essentially avoided. The hydrophobic surfaces therefore have a preference to associate with each other. It is found that hydrophobic interactions extend over a much longer range than the van der Waals force.⁹ Graphite and coal are a few of the solids possessing natural hydrophobicity, and their aggregation is observed in polar solvents. More often, surface hydrophobicity of the solid particles can be induced by the adsorption of surfactants.

Hydrophobic forces were first measured experimentally by Israelachvili and Pashley¹⁰ with mica surfaces in equilibrium with cetyltrimethylammonium bromide solution. The hydrophobic force was found to decay exponentially in the range of 0 to 10 nm. van Oss¹¹ described the rate of decay with distance in terms of interaction energy as

$$\Delta G_l = \pi R \lambda \Delta G_{l_0} \exp\left[\frac{(l_0 - l)}{\lambda}\right] \quad (7.6)$$

where λ is the correlation length of the molecules of the liquid medium, ΔG is the interaction energy at the distance of l_0 , the minimum equilibrium distance. In aqueous solutions, $\lambda \approx 0.6$, three times the water molecule dimension, which may be attributed to the fact that the water molecules tend to occur in clusters of three or more molecules resulting from hydrogen bonding with each other.

Although the real origin of the hydrophobic force still remains a mystery, its effect on dispersion stability has long been recognized. Somasundaran et al.¹² reported a clear relationship between the stability and the surfactant adsorption density as well as the chain length of the adsorbed surfactants.

7.2.3 STERIC AND BRIDGING FORCES

Steric forces arise from the overlap of the adsorbed layers and can be repulsive or attractive in nature depending on whether or not the outermost layers on the particles prefer to be in contact with the solvent. If the solvent power of the medium for the exposed portions of the exterior layer, for example, those of an adsorbed polymer layer, is satisfactory, they will be compatible with the medium and the suspension will remain stable.^{13,14} On the other hand, if the solvent power for the adsorbed layer is minimal, there will be a tendency for the exposed portions of the adsorbed layer on one particle to interpenetrate into those of a layer on another particle and thereby promote aggregation.

Interpenetration and aggregation is possible only if the net change in Gibbs free energy due to the interpenetration of the polymer chains is negative. The Gibbs free energy change is considered in such cases to be determined essentially by the change in entropy due to the release of solvent molecules and due to the decrease in randomness of the polymer chain and by the enthalpy of desolvation of the polymer chains. For flocculation to occur according to this mechanism, the increase in entropy due to the release of solvent molecules should outweigh the loss of entropy due to the interpenetration of polymer chains and increase in enthalpy of desolvation. It is clear that the desolvation characteristics of the adsorbed polymer species and the dependence of it on solution properties such as temperature and ionic strength will be important in determining aggregation by this mechanism. Ottewill and Walker⁵⁸ derived an equation for the energy change due to an overlap of the adsorbed layers by using Flory's liquid lattice model for polymer solutions.^{13,55}

$$V_{\text{steric}}(a) = \frac{4\pi kTC_v^2}{3v_1^2\rho_2^2}(\psi_1 - \kappa_1)(\delta - a)^2(3R + 2\delta + a/2) \quad (7.7)$$

where

C_v = concentration of material in the adsorbed layer

v_1 = molecular volume of solvent molecules

ρ_2 = density of the adsorbate

Ψ_1, κ_1 = entropy and enthalpy parameters of mixing proposed by Flory

δ = adsorbed layer thickness

R = particle radius

a = distance separating the surfaces of two approaching particles

Steric repulsion can be explained in the following manner. When two particles with adsorbed long-chain molecules approach each other, the entropy per adsorbed molecule decreases, causing desorption and a concomitant increase in the interfacial energy. This means that additional work has to be input to bring the particles together, which manifests itself as a repulsive force.

A long-chain adsorbate with several active sites on it can induce aggregation by attaching itself to two or more particles. Polymers can provide such bridging between particles, particularly under conditions where particles are not totally coated by the polymeric species. If particles are already

fully covered with polymers, bridging can take place only if there is either detachment of some portion of the polymer already on a particle to provide sites for attachment of polymer fractions adsorbed on other particles or polymer–polymer bonding itself. It has been suggested that maximum flocculation occurs when the fraction of particle surface covered by polymer molecules is close to 0.5. Note that this hypothesis has not, however, been experimentally proved. As indicated earlier, bridging should be possible even when particles are fully covered if some detachment and reattachment of the adsorbed polymer is possible. Adsorption of polymers is in general found to be irreversible, that is, except in the occasional case of polymers with functional groups that form covalent bonds with the surface species, only due to the cumulative effect of adsorption of a single polymer molecule on several sites. Detachment and reattachment of portions of such a polymer should, however, be possible and such a process should facilitate bridging. This has been shown to be so by allowing polymers to be displaced from the surface by adding competing agents into the system. Thus, polyacrylamide can be desorbed from clay by adding phosphates into the solution. Absence of bridging might be interpreted to suggest the presence of strong repulsive steric interactions between dangling portions of the adsorbed polymer chains.

For steric stabilization and bridging flocculation by adsorbed polymers, there is still no satisfactory quantitative theory. This is because any theory for those processes must be couched in terms of one or the other of the theories of polymer solution thermodynamics, which are at best semi-quantitative. Also, to calculate the distance dependence of the steric interaction, it is necessary to predict the conformation of close-packed polymer molecules. In fact, except in θ solvents, it is very difficult to predict the polymer conformation in solution.¹³ Despite these difficulties, some progress has been made in developing pragmatic models capable of predicting the distance dependence of the steric and bridging interactions.

7.2.4 HYDRATION AND SOLVATION FORCES

Recent work on the measurement of forces acting between surfaces on liquids has revealed the existence of some powerful short-range forces that have their origin on the packing ordering of molecules at the interface.^{15,16} These include hydration and solvation interactions and also effects due to phase changes in the interlayer between two surfaces in close proximity. The DLVO theory is based on the continuum theory — both the interacting bodies and the medium are characterized by their dielectric properties, which do not change with surface separation. However, this is not valid for small separation distances where due to molecular ordering the properties are quite different from in the bulk. At these small separation distances forces due to phase separation or phase transitions in the liquid film between the surfaces, including capillary condensation and cavitation and forces due to surface-induced solvent structures come into play and can contribute significantly to the stability of dispersions. The repulsion between the particles is due to the necessity for ions to lose their bound water to allow the approach to continue and this is thermodynamically unfavorable. However, the hydration effect can result in significantly enhanced attraction between two hydrophobic particles.

The presence of an isolated surface induces ordering (layering) of the adjacent molecules of the fluid in contact with it, and this gives rise to a density profile with an oscillatory nature. The magnitude of the oscillation decays with distance from the surface and for the two surfaces at a sufficiently large separation the density profile from either surface has decayed to the bulk value at the midplane. As the surfaces are brought close together, there is an overlap of the density profiles. There is an enhancement of ordering at separation distances close to an integral number of layers or molecular diameters, and this is energetically favorable. At intermediate distances the density profiles overlap destructively and will cause a free energy maximum. The result is a free energy curve that oscillates between repulsive maxima and attractive minima as the surface separation is varied. Surface roughness smears out the ordering and removes this oscillatory force. Similarly, solvent penetration into an adsorbed layer removes these short-range forces. In force

measurements of mica surface immersed in organic solvents, it was found that the adsorption of small quantities of water on the surfaces removed the oscillatory forces, probably by disturbing the molecular ordering of the solvent. The important aspect of these repulsive structural forces is that at distances below 30 Å they can exceed van der Waals forces and electrical double layer forces.

7.2.4.1 Capillary Condensation Forces¹⁷

Phase changes can occur at the interface of solids and liquid mixtures. As mentioned earlier, a surface excess of a second species will cause a disruption of the molecular ordering and a reduction of the free energy maxima and minima arising from packing constraints. In the case of water on the surface of mica in a nonpolar solvent due to the low contact angle of water on mica it will form an annulus around the contact area of two such surfaces. This is analogous to capillary condensation from the vapor phase. The thermodynamically stable state for two surfaces in close proximity in a nonpolar liquid containing water is with a bridge of water connecting the two surfaces. The water bridge should be stable when the surface separation is less than or equal to twice the Kelvin radius. The net effect of this spontaneous capillary condensation occurring at separation distances lower than about 10 Å is to provide a very strong attractive force as well as large adhesion between the surfaces. The adhesion at contact reflects the interfacial tension of the water–nonpolar liquid interface and is an order of magnitude larger than expected either from van der Waals or solvation forces.

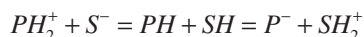
7.2.5 INTERACTING DOUBLE LAYERS

Most substances acquire surface electrical charges when brought in contact with a polar medium, resulting from one or more of the following:

1. Preferential dissolution and solvation of surface species followed by dissociation of some of these species
2. Lattice imperfection on solid surfaces
3. Adsorption of ions or impurities at the solid–liquid interface

The surface charge influences the spatial distribution of ions or molecules in the surrounding solution, attracting ions of opposite charge but repelling ions of similar charge from the surface. Along with the thermal motion, this leads to the formation of the diffused electrical double layer, which consists of the charged surface, neutralizing counterions, and, farther from the surface, coions distributed in a diffuse manner¹⁸ (Figure 7.1).

In the absence of any significant ionization in low-dielectric-constant media, the other three mechanisms are highly improbable. In the absence of any adsorbable surfactants, the dissociation of surface groups appears to be the most general mechanism and the ion responsible for the charge transfer between solvent and particle is the proton. The direction of protonic transfer depends on the relative basicity or acidity of solvent and particle. If the solid surface is represented by PH and the solution by SH , the sign of the surface charge due to proton acceptance or donation is governed by the relative proton donating/proton accepting capacity of the surface and the solution:



In cases where the particle charge is the result of adsorption of ionic surfactants, its sign depends on the adsorbability of the surfactant cation and anion. The most probable mechanism as elucidated by Fowkes and Pugh²⁰ is the adsorption of the surfactant as an ion pair (neutral molecule) followed by a proton exchange reaction the direction of which depends on the relative acidity/basicity of the surfactant and the surface. The final step in the charge generation process is the dissociation

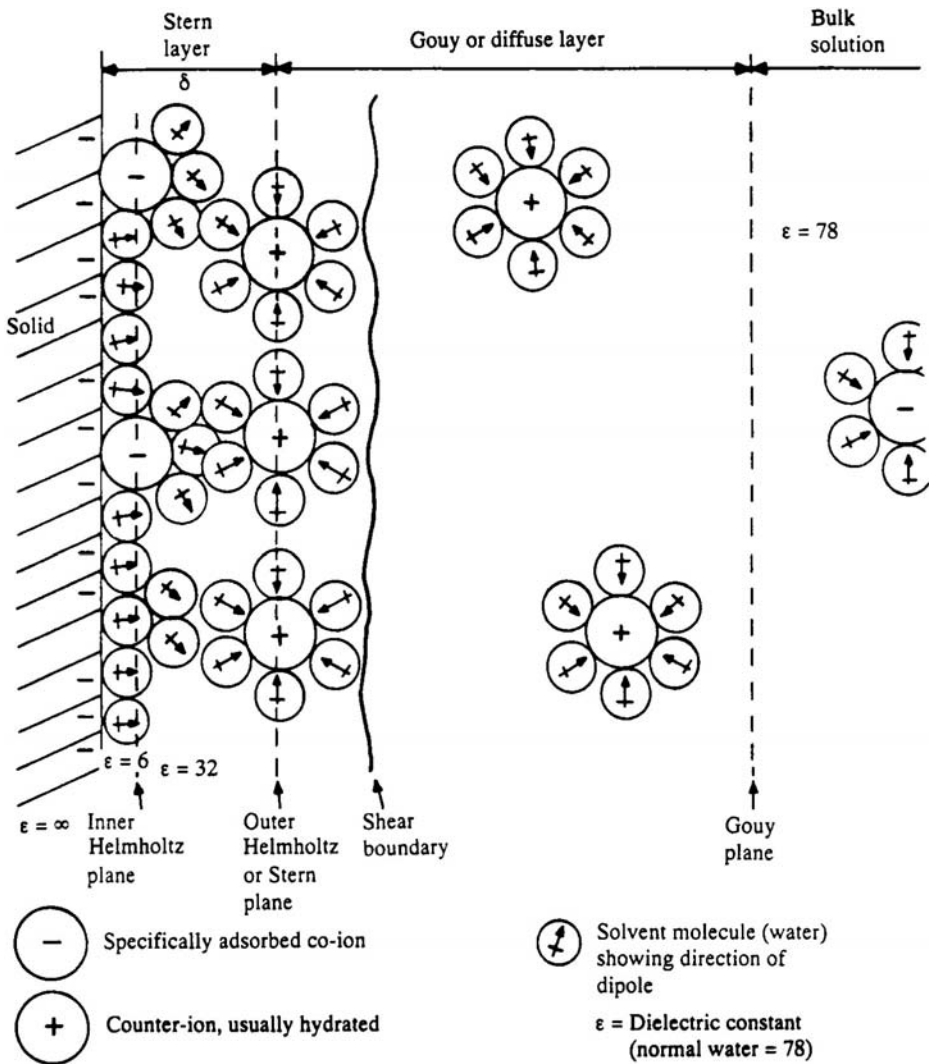


FIGURE 7.1 Schematic representation of the electrical double layer in the vicinity of the solid–liquid interface. (From Williams, R.A., in *Colloid and Surface Engineering: Applications in the Process Industries*, Butterworth-Heinemann, Oxford, 1992. With permission.)

of the desorption of the protonated/deprotonated surfactant species leaving a net charge at the interface. **Figure 7.2** depicts this process schematically.

Despite the difficulties in quantitative treatment, there exist theoretical models based on the classical treatment initiated by Gouy, Chapman, Debye, and Hückel and later modified by Stern and Grahame. As shown in **Figure 7.3**, a reasonable representation of the potential distribution by the Poisson–Boltzmann equation can be given as

$$\frac{d^2\Psi}{dl^2} = -\frac{e}{\epsilon} \sum_i z_i n_{i_0} \exp\left(\frac{z_i e \Psi}{kT}\right) \quad (7.8)$$

where Ψ is the potential at a distance l from the surface, ϵ is the permittivity of the medium ($\epsilon = \epsilon_0 \epsilon_r$), n_{i_0} is the bulk concentration of ions of charge z_i , e is the electronic unit charge, k is the Boltzmann constant, and T is the absolute temperature.

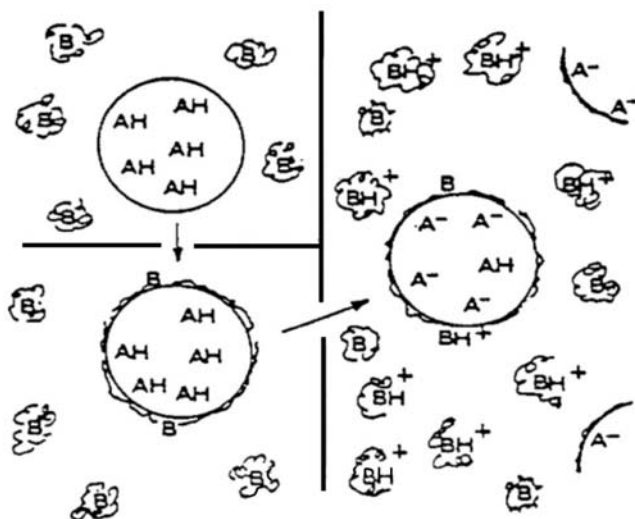


FIGURE 7.2 Schematic representation of the origin of surface charge in nonaqueous media. (From Fowkes, F.M. and Pugh R.J., *ACS Symposium Series*, 240, 331, 1984. With permission.)

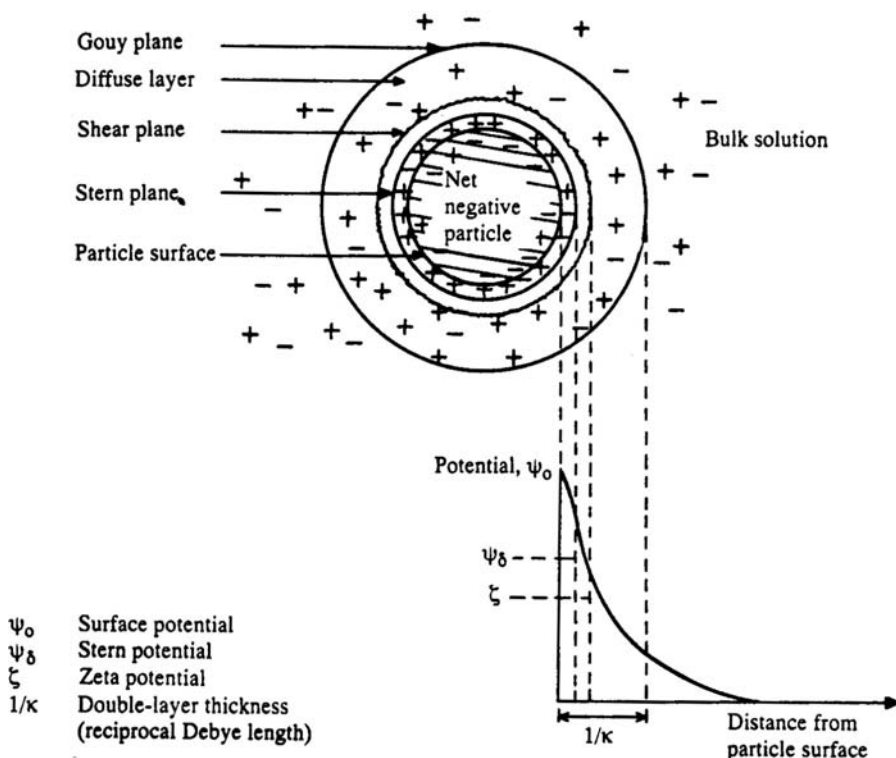


FIGURE 7.3 Distribution of electrical potential in the double layer region surrounding a charged particle showing the position of zeta potential and the reciprocal Debye length. (From Williams, R.A., in *Colloid and Surface Engineering: Applications in the Process Industries*, Butterworth-Heinemann, Oxford, 1992. With permission.)

For low charge density, $z_i e \Psi / kT < 1$, an explicit solution of the above equation can be written in the form:

$$\Psi(l) = \Psi_\delta \exp(-\kappa l) \quad (7.9)$$

where κ is known as the reciprocal Debye length with $1/\kappa$ often referred to as the double layer thickness, which can be calculated from

$$\kappa = \left(\frac{1000 e^2 N_A}{ekT} \sum z_i^2 M_i \right)^{1/2} \quad (7.10)$$

where N_A is Avogadro's constant and Z_i and M_i are the valency and molar concentration of the ion, respectively.

The nature and the thickness of the electrical double layer are important because the interaction between charged particles is governed by the overlap of their diffuse layers. Unfortunately, it is impossible to measure directly the Stern potential Ψ_δ . Instead, the zeta potential, ζ , which is the potential at the shear plane close to the Stern plane, can be experimentally measured and is often used as a measure of the surface potential.

For most simple situations, the repulsive interaction energy between two identical charged particles of equal radius R and zeta potential ζ at a distance of separation l can be given by

$$V_e = 0.5\pi\epsilon R \zeta^2 \ln[1 + \exp(-\kappa l)] \quad (7.11)$$

Although derived based on the low surface charge density, Equation 7.11 has been found to be valid for situations where the zeta potential is as high as 50 mV.

7.2.6 SUMMATION OF VARIOUS FORCES

The DLVO theory, which has been used with success to explain stabilization mainly in aqueous systems, states that the overall interaction energy is the sum of the electrostatic and van der Waals forces. However, this has been extended now to include the steric forces as well. The total interaction energy can be expressed as

$$V_T = V_{\text{elec}} + V_A + V_{\text{steric}} \quad (7.12)$$

Figure 7.4 shows the total interaction energy as a function of particle separation and displays a maximum, called the energy barrier.¹⁹ For suspensions to be destabilized, the particles must have enough energy to surmount this barrier during collisions. In the absence of electrostatic interactions the particles can get trapped in the secondary minimum and form loose aggregates that can usually be redispersed easily. The electrostatic forces, however, cause the disappearance of the secondary minimum and increase the barrier to the primary minimum thereby decreasing the probability of aggregation. Thus, a combination of electrostatic and steric forces is necessary for effective stabilization.²⁰ In systems stabilized solely by electrostatic forces, an energy barrier of about 30 kT is desirable with a Debye length $1/\kappa$ of not more than 1000 Å.

For systems stabilized solely by electrostatic repulsion, a decrease in the energy barrier will lead to rapid coagulation. The energy barrier can be decreased by the addition of counterions that can specifically adsorb and alter the surface charge or cause double layer compression. The critical coagulation concentration for different ions depends on the valency of the ions as formulated by

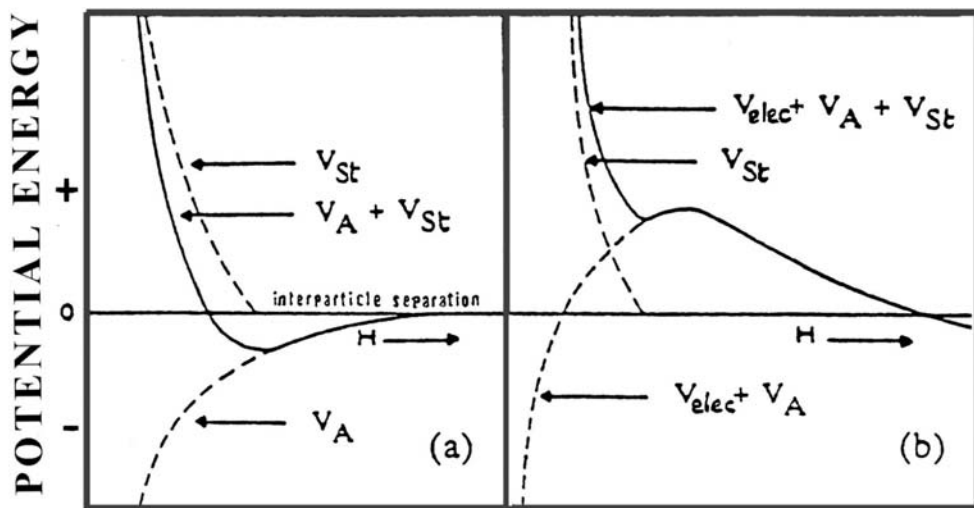


FIGURE 7.4 Diagram representing the variation of total interaction energy between particles with separation distance. (From Fowkes, F.M. and Pugh R.J., *ACS Symposium Series*, 240, 331, 1984. With permission.)

Schultze and Hardy. Typically, c_c , the critical coagulation concentration, is proportional to z^2 , where z is the valency of the ion.

Adsorbed layers of surfactants and polymers can affect stability in the following manner. If they are charged, they can produce, increase, or decrease the electrostatic repulsion. In case of polymer or long-chain molecules, steric repulsion occurs when the adsorbed layers start to penetrate. The adsorbed layer has a Hamaker constant different from that of the particle, and hence the van der Waals interactions are altered.

7.2.7 KINETICS OF AGGREGATION

The rate of aggregation will depend essentially on probability of collision between particles, probability of attachment during such collisions, and probability of their detachment from the aggregates subsequently. While the probability of collision will depend on the Brownian motion determined essentially by the temperature of the system and on fluid flow motions determined by the viscosity of the fluid medium and external stirring, probabilities of adhesion and detachment are dependent on the type of physicochemical interactions between the particles and, to some extent, on velocity gradients in the medium.

Both Brownian and velocity gradient aggregations are described by von Smoluchowski treatment, which relates the rate of aggregation to the radius of the particle and the total number of particles in the system in the following manner. Aggregation due to Brownian motion, known as perikinetic aggregation, leads to a decrease in the number of particles governed by the following second-order equation if every collision is successful in creating an adhesion:

$$\frac{dN_t}{dt} = -8\pi Dr N_t^2 \quad (7.13)$$

where N_t is the total number of particle at time t , D is the diffusion coefficient for the particle, and r is the radius of the particle. The integrated form of Equation 7.13 is

$$N_t = \frac{N_0}{1 + 8\pi Dr N_0 t} \quad (7.14)$$

This derivation takes into account formation of only doublets. In reality, primary particles can also aggregate with multiplets. Solution for all particle aggregates containing i particles is given as

$$\sum_{i=1}^{\infty} N_i = \frac{N_0}{1 + 4\pi D r N_0 t} \quad (7.15)$$

Slow stirring can indeed promote aggregation. Such aggregation under the influence of velocity gradient is known as orthokinetic aggregation. The rate of orthokinetic aggregation is given by

$$-\frac{dN_t}{dt} = \frac{16Gr^3}{3} \sum_{k=1}^p N_k^2 k \quad (7.16)$$

G is velocity gradient, N_k is number of k particles per unit volume, k is particles formed by aggregation of two particles, p is particle of limiting size in shear gradient G . As mentioned earlier, the above formulations assume that every collision is fruitful. In reality, only a fraction of the collisions might be effective and as a result the aggregation might be slow. The magnitude of this fraction is dependent on the nature of interactions between particles and, to some extent, viscous properties of the liquid film between the particles. If V is the total energy of interaction between particles of radii r_i and r_j when they are separated by a distance d , the fraction of effective collisions, α , according to Fuchs is given by the following expression:

$$\frac{1}{\alpha} = 2 \int_2^{\infty} \exp\left(\frac{V}{kT}\right) \frac{dS}{S^2} \quad (7.17)$$

where k is the Boltzmann constant and S is equal to $2d/(r_i + r_j)$. As an example, for maximum V equal to 5, 15 and 25 kT, α is 2.5×10^{-2} , 10^{-5} , and 10^{-9} , respectively.

The interactions between particles that are important in determining α are made up of London–van der Waals attractive forces (V_a); electrical double layer forces (V_e) which can be attractive or repulsive in nature; bridging forces (V_b), which are always attractive; and steric forces (V_s), which arise from the overlap of adsorbed layers. Steric forces can be repulsive or attractive depending on the solubility properties of the adsorbed layer.

7.3 EXPERIMENTAL ASSESSMENT OF DISPERSION STABILITY

Stability in colloidal dispersions is defined as resistance to molecular or chemical disturbance, and the distance the system is removed from a reference condition may be used as a measure of stability. The stability can be analyzed from both energetic and kinetic standpoints. The kinetic approach uses the stability ratio, W , as a measure of the stability. W is defined as the ratio of the rate of flocculation in the absence of any energy barrier to that when there is an energy barrier due to adsorbed surfactant or polymer. These processes are referred to as rapid and slow flocculation with rate constants k_T and k_s , respectively, such that $W = k_T/k_s$. The stability of colloidal suspensions can be evaluated using various techniques. In practice, two methods are mainly used: sedimentation and rheology measurements.

7.3.1 SEDIMENTATION METHODS

This is a relatively simple method in which a series of tubes containing the dispersion in a homogeneous state are arranged. The settling rate is estimated by monitoring the rate of descent

of the upper interface with time and gives information on the stability of the dispersion. A high value of settling rate corresponds to an unstable dispersion, and vice versa, as flocculated particles settle more rapidly than deflocculated particles except in concentrated systems where hindered settling occurs. Sedimentation volumes can typically be measured after a settling rate determination after allowing the samples to settle for a considerably long time. Sediment volumes provide valuable information on the nature of the flocs. For example, flocculated particles form soft and loosely packed sediments and have large sediment volumes and are easily redispersed in most cases. However, stable suspensions will form compact sediments of smaller volume that are not easy to redisperse. Techniques such as visual observation, light scattering, and absorbance measurements with a spectrophotometer are generally used to study sedimentation rates. Two other useful parameters can be measured from these tests that yield further qualitative information on the nature of the dispersion/flocculation. Percent weight settled is estimated by removing a fixed volume of the dispersion after a fixed amount of time and calculating the amount of solids settled in that time. In many applications, particularly when the liquid needs to be recycled, clarity of the supernatant is an important factor. Therefore, the turbidity or light transmittance of supernatant after flocculation is also sometimes monitored as a criterion for suspension stability. This parameter is dependent on the particle size distribution (the same is valid for settling rate determination). This is very useful especially in the case of polymers and reflects the efficiency of fine particle capture by the flocculating agent. Advanced imaging techniques such as computerized axial tomography (CAT) scans can also be used to gain information on the structure of suspension and flocs.²¹

7.3.2 RHEOLOGICAL METHODS

These methods are widely used to assess dispersion stability and can give very useful information on the particle–particle interactions with the dispersion medium. These measurements, however, give indirect information about the stability of dispersions and must be used in conjunction with sedimentation tests for maximum benefit.

Additional tests to determine wettability of the surfaces include flotation and two-phase separation. In flotation the particles after treatment with the surface modifier are introduced into a stream of bubbles and the amount of solids floated out in a fixed period of time is taken as a measure of the hydrophobicity of the particles. A modification of the flotation technique is the bubble pickup, in which single bubbles are generated in a controlled manner and contacted with the dispersed particles. The weight of particles thus removed by a fixed number of bubbles is taken as a measure of the hydrophobicity.

In the two-phase separation test, a known amount of the dispersion is introduced into a separatory funnel consisting of two immiscible phases (one aqueous and the other organic). The particles are shaken thoroughly and then allowed to separate into the two phases. The two phases are then separated and the amounts of solids in each of them determined, yielding a partition coefficient reflective of the wettability of the particle surface.

7.4 DISPERSION IN THE ABSENCE OF DISPERSING AGENTS

Figure 7.5 shows the settling behavior of bare alumina particles in solvents of varying polarity.²² It can be observed that with an increase in solvent polarity the dispersion stability displays a maximum, which corresponds to a minimum in the normalized settling rate; the normalization is done to account for differences in the density and the viscosity of the solvents. The normalized settling rate equals the observed settling rate times the solvent viscosity/(particle density minus the solvent density). The maximum stability in this case is observed in moderately polar solvents ($20 < \epsilon < 45$). Bare particles suspended in a liquid medium are in constant Brownian motion and can flocculate rapidly on collision if the V_a term is larger than about 15 kT. Stabilization can usually be achieved by decreasing the van der Waals attractive forces. The potential energy due to the van

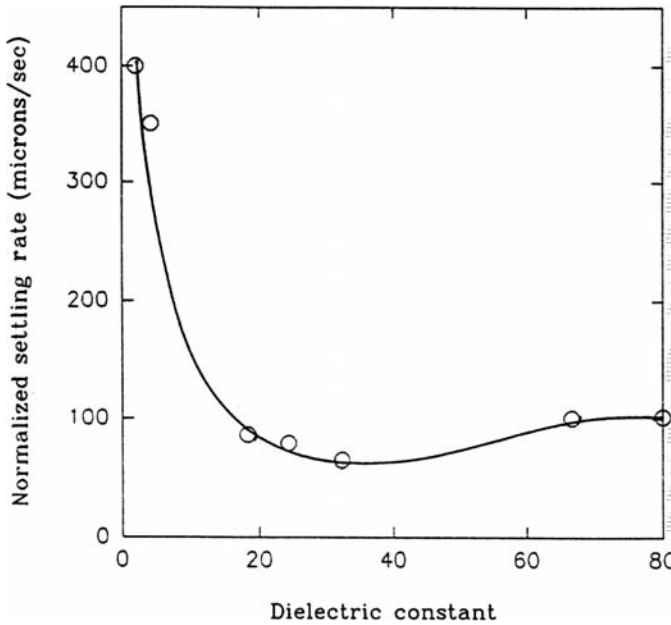


FIGURE 7.5 Stability of alumina particles in solvents of different polarities. (From Krishnakumar, S. and Somasundaran, P., *Colloids Surf.*, 117, 37, 1996. With permission.)

der Waals interaction can be calculated approximately for two spherical particles suspended in a liquid medium using the following equation:

$$V_a = -A_{S/L/S}(a/12H_0) \quad \text{for } H_0 \ll a \quad (7.18)$$

where $A_{S/L/S}$ is the combined Hamaker constant for the solid in the liquid and can be estimated from the equation:

$$A_{S/L/S} = A_S + A_L - 2(A_S A_L)^{1/2} \quad (7.19)$$

where A_S and A_L are the Hamaker constants of the respective solids and liquids in vacuum.

$$A_S(kT) = 113.7 \frac{(\epsilon - 1)^2}{(\epsilon + 1)^{3/2} (\epsilon + 2)^{1/2}} \quad (7.20)$$

The A values for ceramic substrates and liquids can also be estimated from Equation 7.20, where ϵ is the static dielectric constant of the material being considered. A value of $\epsilon_s = 9.3$ is assumed for alumina based on reported measurements²³ and A_{al} is estimated as 70.5 kT from Equation 7.20. Similar calculations have been performed for the different liquids considered here, and the results are shown in Table 7.2. For a given set of particles, the $A_{S/L/S}$ value is directly proportional to the van der Waals attractive energy. It can be seen from the values shown in Table 7.2 that the dispersion behavior as predicted by changes in the van der Waals interaction is similar to the observed behavior. This suggests that the primary cause for the observed changes in stability with solvent polarity is the change in the attractive interaction. Figure 7.6 depicts the variation of the attractive potential

TABLE 7.2
Hamaker Constant and Dispersion Stability
for Alumina in Different Solvents

Solvent	Dielectric Constant	A_L (kJ)	A_{SLS} (kJ)	Observed Behavior
Cyclohexane	2.02	11.2	25.5	Poor
Chloroform	4.3	40.4	4.3	Poor
2-Butanol	10.8	85.7	0.8	Good
Isopropanol	18.3	89	1.1	Good
Ethanol	24.3	94.6	1.9	Good
Methanol	32.4	99	2.5	Good
Methanol/water (40%)	66.7	106.3	3.8	Good-Poor
Water	80	107.5	3.9	Good-Poor

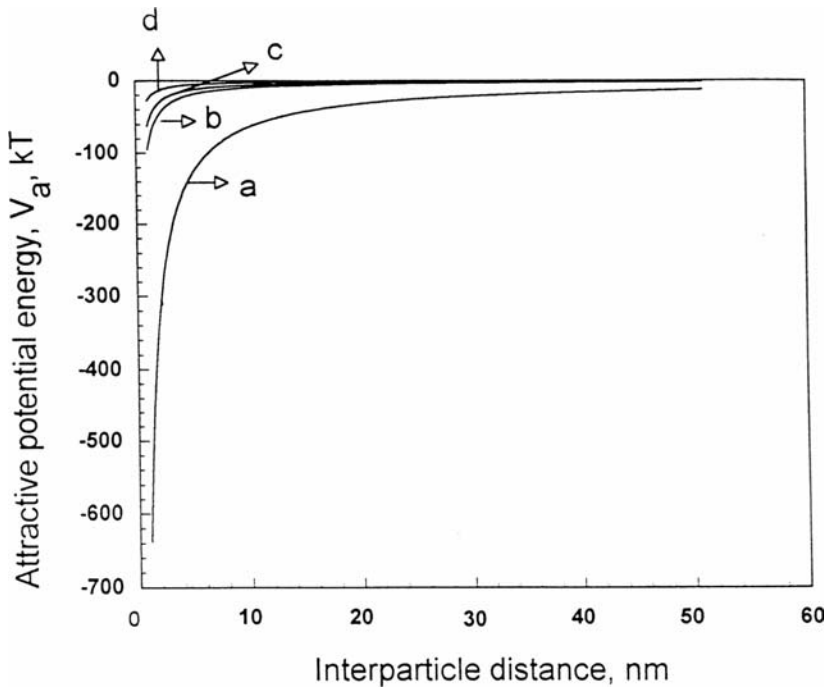


FIGURE 7.6 Variation of attractive potential between particles as a function of separation distance for (a) cyclohexane, (b) water, (c) ethanol, and (d) isopropanol. (From Krishnakumar, S. and Somasundaran, P., *Colloids Surf.*, 117, 37, 1996. With permission.)

(Equation 7.20) with interparticle distance for these bare alumina particles in different liquids. It can be seen that at low interparticle separations the attractive energy is maximum for cyclohexane ($A_{SLS} = 25.5$ kJ) and minimum for isopropanol ($A_{SLS} = 1.1$ kJ). However, be aware that in polar liquids, alumina is also capable of developing significant amount of surface charge, which can enhance the dispersion stability by contributing to the electrostatic repulsion term.

7.5 ADSORPTION AND ITS EFFECT ON DISPERSION

Adsorption of molecules on solids from solution is important in controlling a variety of interfacial processes, such as mineral flotation and other solid–liquid separation processes, flocculation/dispersion, blood clotting, and micellar flooding of oil wells. Adsorption results from energetically favorable interactions between the solid adsorbate and the solute species. Adsorption of surfactants on minerals from aqueous or organic solutions is often a complex process, as it can be influenced by all components of the system: solid, solvent, and solute. Several interactions such as electrostatic attraction, covalent bonding, hydrogen bonding or nonpolar interactions between the adsorbate and the adsorbent species, and lateral interaction between the adsorbed species, as well as their desorption, can contribute to the adsorption process.

Adsorption can be considered a process of selective partitioning of the adsorbent species to the interface in preference to the bulk and is the result of interactions of such species with the surface species on the solid. The interactions responsible for adsorption can be either physical or chemical in nature. Therefore, adsorption can be broadly classified into two categories — physical adsorption (or physisorption) and chemical adsorption (or chemisorption) — depending on the nature of the forces involved.²⁴ Physical adsorption is usually weak and reversible and involves small energy changes. The van der Waals forces and electrostatic forces are primarily responsible for physical adsorption, which is also characterized by a high rate of adsorption and formation of multilayers.²⁵ Chemical adsorption occurs through covalent bonding between the adsorbate and the surface species on the solid. Chemical adsorption normally involves an activation stage and is characterized by relatively higher energy changes and a low rate of adsorption. The adsorption is usually strong and irreversible and is limited to a monolayer. A distinction between physical and chemical adsorption can usually be made from the temperature dependence of the adsorption process. In the case of physical adsorption, the adsorption generally decreases with increasing temperature while in the case of chemisorption it increases. However, it must be noted that the distinction between physical and chemical adsorption is an arbitrary one and in many cases an intermediate or combined character of adsorption is encountered. In some cases, like adsorption of gases on metal surfaces, physisorption may take place initially and may be followed by adsorbent–adsorbate reactions, resulting in chemisorption.²⁶

The adsorption density, which is the amount of adsorbate removed from the solution to the interface, can be mathematically expressed as²⁷

$$\Gamma_i = 2rC \exp\left(\frac{-\Delta G_{\text{ads}}^o}{RT}\right) \quad (7.21)$$

where Γ_i is the adsorption density in the plane δ , which is at the distance of closest approach of counterions to the surface, r is the effective radius of the adsorbed ions, C is the bulk concentration of the adsorbate in mol/ml, R is the gas constant, T is the absolute temperature, and ΔG_{ads}^o is the standard free energy of adsorption. In practice, however, the adsorption density is measured as depletion of the adsorbate from the solution as shown in the following equation:

$$\Gamma = (C_f - C_i) \frac{V}{W} \quad (7.22)$$

where Γ is the adsorption density in mol/g, C_f and C_i are the initial and final concentration of the adsorbate in mol/l, V is the volume of solution in liters, and W is the weight of the adsorbent in grams.

The net driving force for adsorption ΔG^o can be considered to be the sum of a number of contributing forces:

$$\Delta G_{\text{ads}}^o = \Delta G_{\text{elec}}^o + \Delta G_{\text{chem}}^o + \Delta G_{c-c}^o + \Delta G_{c-s}^o + \Delta G_H^o + \Delta G_{\text{H}_2\text{O}}^o + \dots \quad (7.23)$$

where ΔG_{elec}^o is the electrostatic interaction term, ΔG_{chem}^o is the chemical term due to covalent bonding, ΔG_{c-c}^o is the lateral interaction term owing to the cohesive chain–chain interaction among adsorbed long-chain surfactant species, ΔG_{c-s}^o is due to interaction between hydrocarbon chains and hydrophobic sites on the solid, ΔG_H^o is the hydrogen bonding term, and $\Delta G_{\text{H}_2\text{O}}^o$ is the solvation or desolvation term owing to hydration of the adsorbate or any other species from the interface during adsorption. For each surfactant–solid–solvent system, several of the above terms can be significant, depending on the mineral and the surfactant type, surfactant concentration, background electrolyte, and solvent temperature. For nonmetallic minerals, electrostatic attraction and lateral interaction effects are considered to be the major factors determining adsorption whereas for salt-type minerals, such as calcite, and sulfides, such as galena, the chemical term often becomes significant. In organic liquids the electrostatic forces are minimal and adsorption depends on the hydrophobic and hydrophilic interactions among the constituents.

7.5.1 FACTORS AFFECTING ADSORPTION

There are several factors controlling adsorption that also influence the mechanisms governing the adsorption process. These have been reviewed by Parfitt and Rochester²⁵ and are briefly discussed here.

- *Nature of the surface:* The physical characteristics of the solid (surface area, porosity, etc.) determine the area available for adsorption while the chemical nature of the surface determines the reactivity of the surface toward a given solute. The heterogeneity and the presence of adsorbed impurities can also affect the adsorption process.
- *Chemical structure of the solute and its interactions with the solvent:* The structure (hydrocarbon chain length, branching, nature and location of polar functional groups) of the solute and its interactions with the solvent (solubility, complexation, micellization) have a marked effect on its adsorption. For example, it is well known from Traube's rule that for aqueous surfactant solutions the surface activity and hence the adsorption at the liquid–air interface increases with an increase in the chain length of the solute molecule. The solutes of interest, surfactants, are also capable of forming association structures in solution (micelles or reverse micelles depending on the solvent), which is a measure of their solvophobicity.
- *Nature of the solvent:* The solvent can influence the adsorption by interacting with the surface and/or the solute, thereby weakening the interaction between the solute and the surface. The chemical nature of the solvent and its polarity are important properties in question.
- *Nature of the interactions between the surface and the adsorbed solute:* The structure and orientation of the adsorbed layer depend on the relative strength of the interaction between the surfactant and the surface and the surfactant association behavior in the bulk solution. An example of such an interaction in aqueous systems is the electrostatic interaction between the charged surface sites and the charged surfactant molecules.
- *Temperature:* Temperature can affect adsorption by altering the properties of the solute, surface, solvent as well as their mutual interactions. Usually physical adsorption that is weak decreases with an increase in temperature probably because of increased solubility of the solute. The effect of temperature on chemisorption depends on the nature of the chemical reaction taking place at the surface. Chemisorption usually increases within a temperature range, above which it decreases.

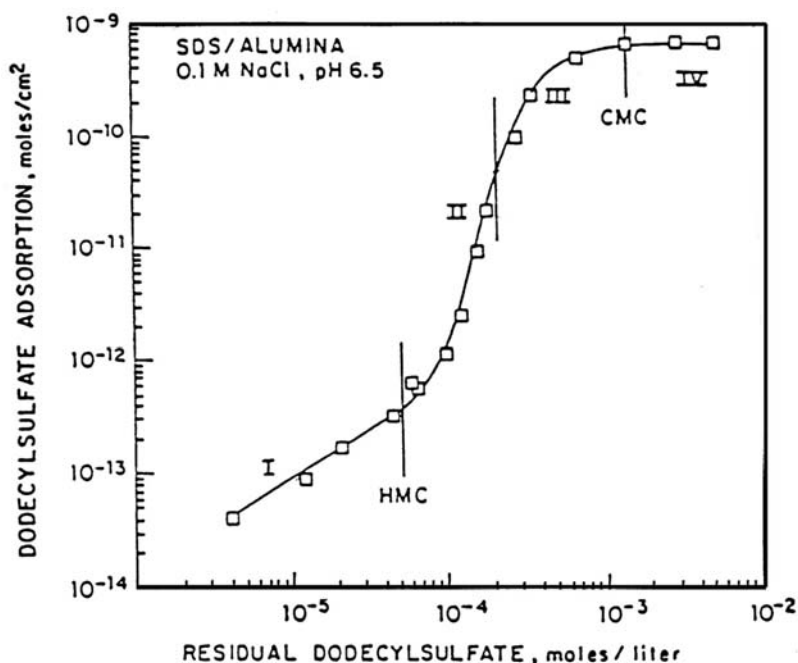


FIGURE 7.7 Adsorption isotherm of SDS on alumina at pH 6.5. (From Somasundaran, P. and Fuerstenau, D.W., *J. Phys. Chem.*, 70, 90, 1966. With permission.)

7.5.2 SURFACTANT ADSORPTION AND ITS EFFECT ON DISPERSION PROPERTIES

7.5.2.1 In Aqueous Media

Dispersion properties can be modified by adsorption of surfactants at the solid–liquid interface. Surfactant adsorption can alter the dispersion properties by changing the van der Waals attraction, electrostatic repulsion, and the steric forces between the particles as discussed earlier. The extent of the modification depends on the adsorption density (surface coverage), packing and orientation of molecules at the interface, and the nature of charges on the molecule. Therefore, it is important to first discuss the adsorption process itself in terms of the dominant mechanisms and possible orientations.

7.5.2.1.1 Ionic Surfactants

A typical adsorption isotherm of charged surfactants on oppositely charged surfaces is shown in Figure 7.7,²⁸ where the adsorption of negatively charged sodium dodecylsulfate (SDS) on positively charged alumina is shown. This isotherm is characterized by four regions, attributed to four different dominant mechanisms operative in each region. Mechanisms involved in these regions may be viewed as follows:

- Region I has a slope of unity under constant ionic strength conditions and is characterized by the existence of electrostatic interactions between the ionic surfactant and the oppositely charged solid surface.
- Region II is marked by a conspicuous increase in adsorption, which is attributed to the onset of surfactant aggregation at the surface through lateral interaction between hydrocarbon chains. This phenomenon is referred to as hemimicelle formation.^{23,29} Such colloidal aggregates formed on the surface are referred to as *solloids* (surface colloids). In the case of simple ionic surfactants, such aggregates have also been called hemimicelles, admicelles, and surfactant self-assemblies.³⁰

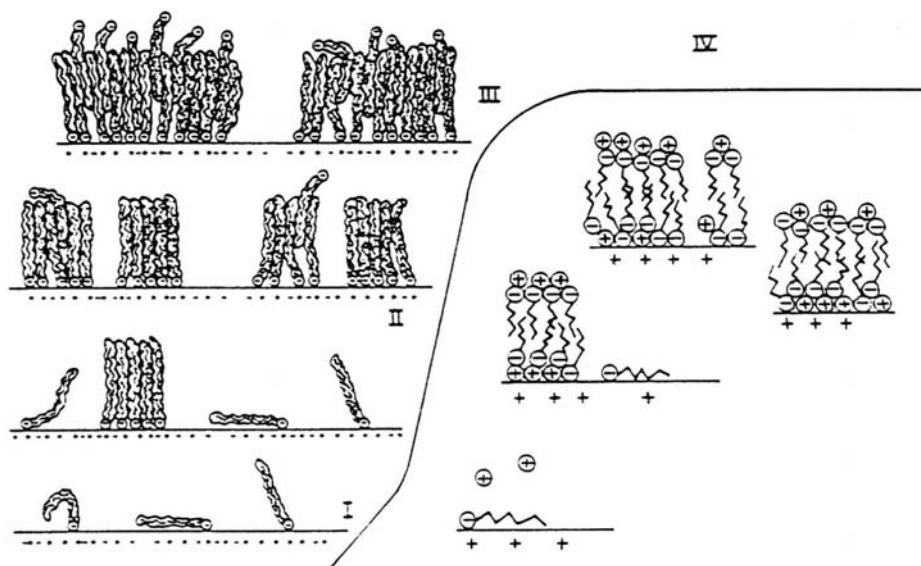


FIGURE 7.8 Schematic representation of the correlation of surface charge and the growth of surface aggregates. (From Somasundaran, P. and Fuerstenau, D.W., *J. Phys. Chem.*, 70, 90, 1966. With permission.)

- Region III shows a marked decrease in the slope of the isotherm, and this is ascribed to the increasing electrostatic hindrance to the surfactant adsorption following interfacial charge reversal caused by the adsorption of the charged species in Region III and beyond; both the adsorbent species and the adsorbate are similarly charged.
- Region IV and the plateau in it correspond to the maximum surface coverage as determined by micelle formation in the bulk or monolayer coverage, whichever is attained at the lowest surfactant concentration; further increase in surfactant concentration does not alter the adsorption density. A schematic representation of adsorption by lateral interactions is given in Figure 7.8.

Figure 7.9 shows the variation in electrophoretic mobility of alumina as a function of the dodecyl sulfonate concentration. It can be seen that the electrophoretic mobility changes sign and then increases with surfactant concentration. This suggests that the dispersions should be electrostatically stabilized at high surfactant concentrations. However, measurements of particle hydrophobicity by bubble pickup showed an initial increase in particle hydrophobicity followed by a decrease at higher surfactant loadings.³¹ This can be explained by examining Figure 7.8, where the surface is shown to be rendered hydrophilic at higher surfactant concentrations by adsorption of a second layer of surfactant with reverse orientation. Also the particles continue to aggregate even after the system has undergone charge reversal, and this is attributed to the fact that it may be possible for the partially covered surfaces to be bridged by the adsorbed surfactant species.

7.5.2.1.2 Nonionic Surfactants

The adsorption of ethoxylated alcohol on silica³² displays an isotherm similar to that for SDS on alumina (Figure 7.10). However, the absence of electrostatic repulsion between the adsorbed nonionic species results in an exceedingly high slope for the hemimicellar region. Adsorption of these surfactants was found to depend on the degree of ethoxylation as well as the alkyl chain length³³ (Figures 7.11 and 7.12). At constant chain length, the extent of adsorption at low concentrations was found to be greater for surfactants with a higher degree of ethoxylation. However, the plateau adsorption is higher for the surfactants with a lower degree of ethoxylation. A linear relationship is obtained when the parking area at plateau adsorption is plotted against the ethoxylation

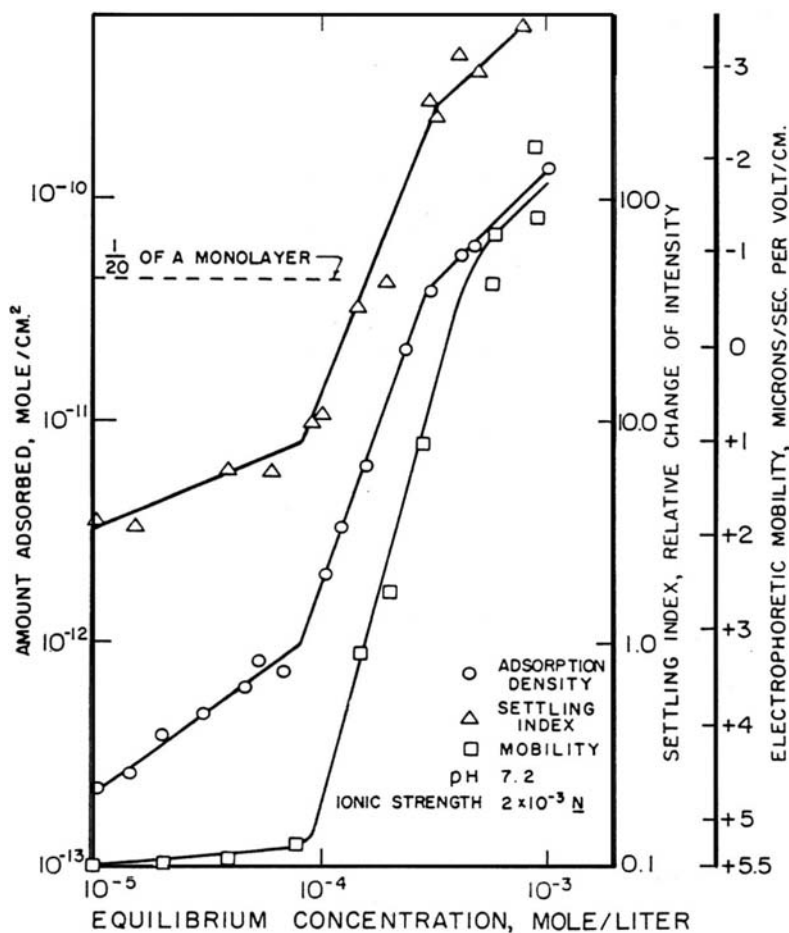


FIGURE 7.9 Variation in the electrophoretic mobility of alumina particles with SDS concentration. (From Somasundaran, P. and Fuerstenau, D.W., *J. Phys. Chem.*, 70, 90, 1966. With permission.)

number. This yields a parking area per $-\text{OCH}_2\text{CH}_2$ segment of 9.2 \AA^2 , suggesting direct adsorption of the ethylene oxide (EO) chains on the silica surface. On the other hand, the alkyl chain length only affects the onset of plateau adsorption, which is in line with the decrease in critical micelle concentration (CMC) with increase in hydrocarbon chain length. Based on these observations, hydrogen bonding is proposed to be the initial driving force for adsorption and the higher uptake of surfactants with higher EO number, at low concentrations is clearly due to the cumulative hydrogen bonding interactions of the EO chains with the hydroxylated silica surface. However, at higher concentrations hydrophobic chain-chain interactions become more significant, as evidenced by the progressive increase in slope of the adsorption isotherm with decrease in EO number (the smaller the EO number, the lesser is the steric hindrance due to the ethoxyl groups, which promotes chain-chain interaction).

The effect of adsorption density and surfactant structure on the hydrophobicity of silica is shown in Figure 7.13.³³ In the absence on any adsorbed surfactant, silica is hydrophilic and its hydrophobicity increases with increase in the adsorption of C_8EO_{10} . In the case of the higher ethoxyl chain length, C_8EO_{40} , the hydrophobicity decreases at higher surface coverages and the original surface coverage is restored when plateau adsorption is reached. The observed changes in hydrophobicity are explained in terms of conformational changes of the hydrocarbon chains of the adsorbed surfactant molecules at the silica-liquid interface. At low adsorption densities the hydrocarbon

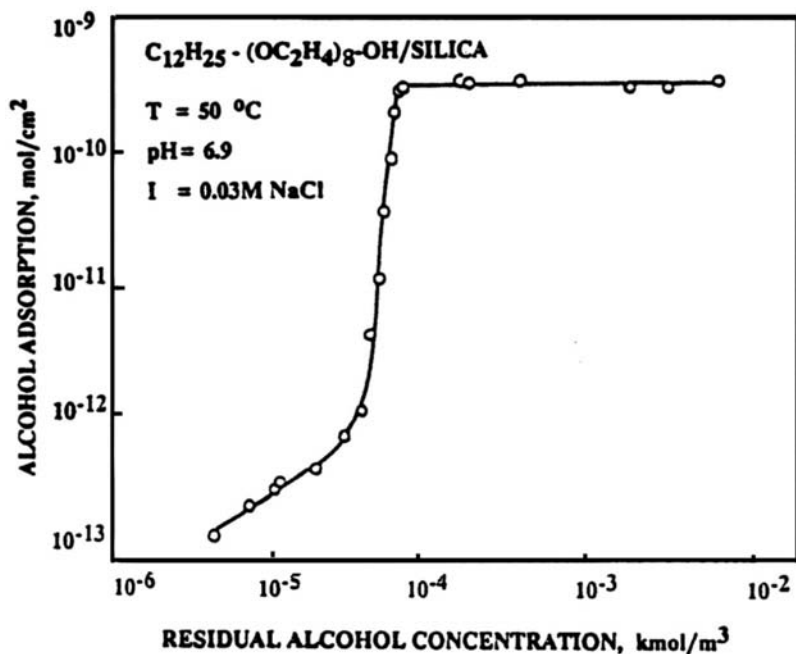


FIGURE 7.10 Adsorption isotherm of alkylaryl ethoxylated alcohol ($C_{12}EO_8$) on silica. (From Fu, E., *Doctoral Thesis*, Columbia University, New York, 1987. With permission.)

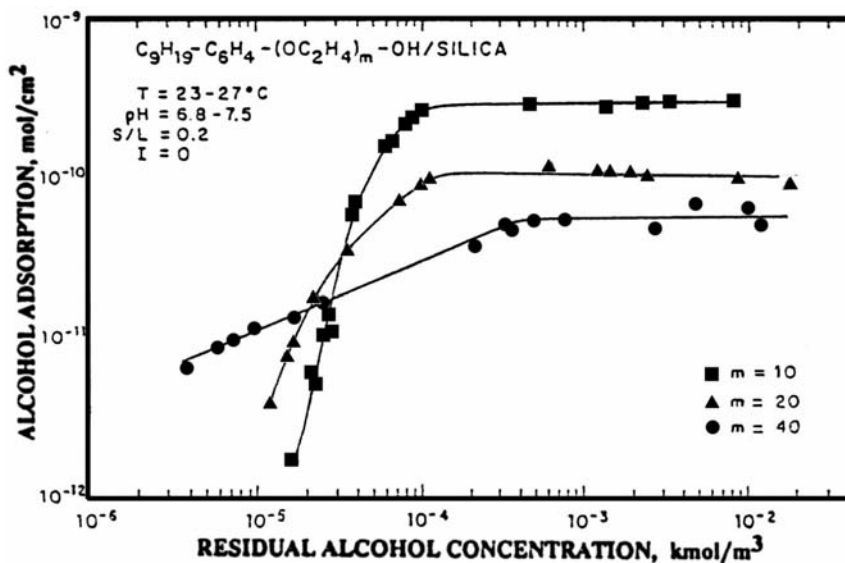


FIGURE 7.11 Adsorption isotherms of nonylphenoxyethoxylated alcohols on silica. (From Somasundaran, P., Snell, E. and Xu, Q., *J. Colloid Interface Sci.*, 144(1), 159, 1991. With permission.)

chains are most likely lying flat on the surface providing maximum coverage with hydrocarbon chains and thereby rendering the surface hydrophobic. As adsorption density increases, however, the flatly adsorbed hydrocarbon chains will be pushed out by the adsorbing EO chains and hence the surface coverage by the hydrocarbon chains is reduced. This explains the decrease in hydrophobicity

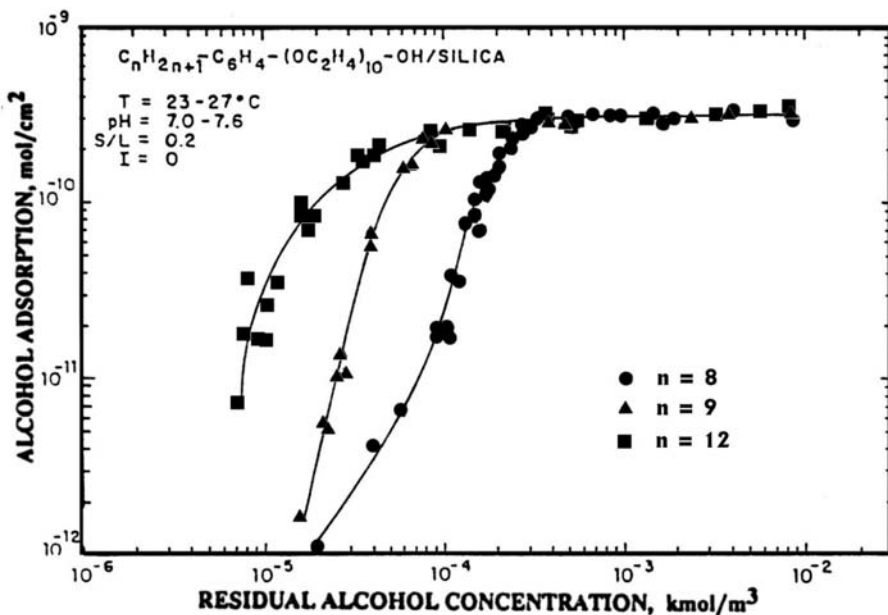


FIGURE 7.12 Adsorption isotherms of EO₁₀ alcohols of different chain lengths on silica. (From Somasundaran, P., Snell, E. and Xu, Q., *J. Colloid Interface Sci.*, 144(1), 159, 1991. With permission.)

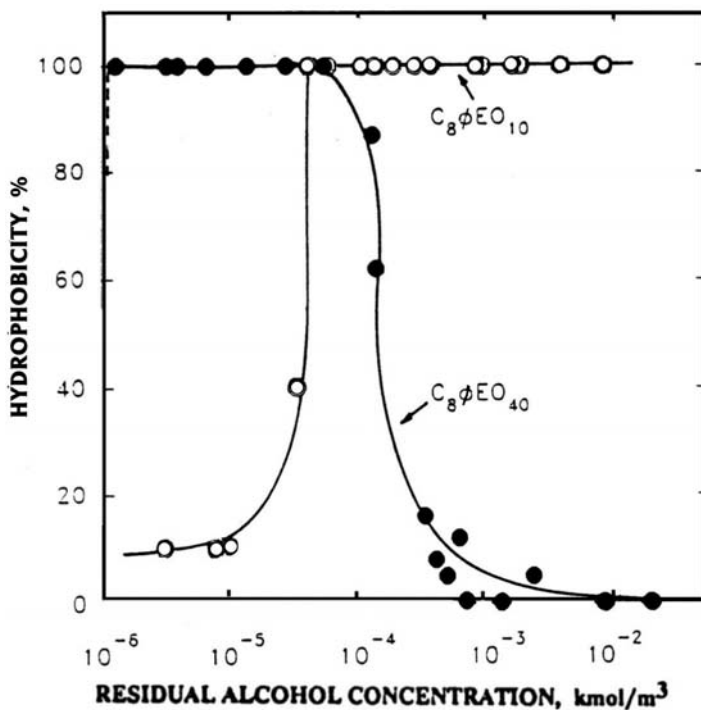


FIGURE 7.13 Change in hydrophobicity of silica upon adsorption on nonionic surfactants. (From Somasundaran, P., Snell, E. and Xu, Q., *J. Colloid Interface Sci.*, 144(1), 159, 1991. With permission.)

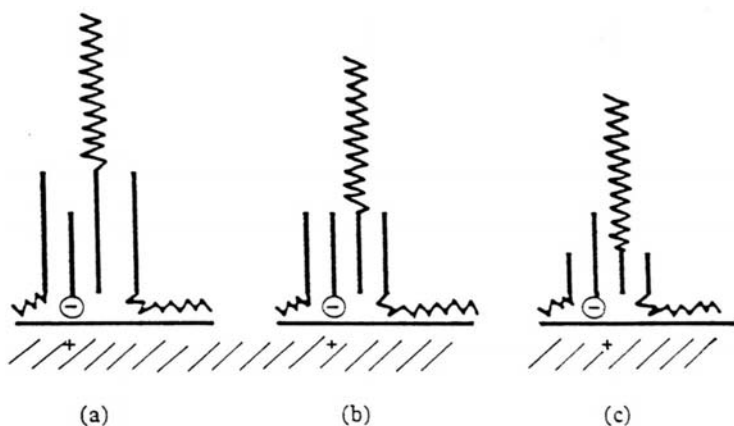


FIGURE 7.14 Schematic representation of the adsorption mechanisms for SDS/ $C_{12}EO_8$ mixtures on kaolinite. (From Xu, Q. and Somasundaran, P., *Miner. Metal. Processing*, 9, 29, 1992. With permission.)

at higher adsorption for C_8EO_{40} ; at plateau adsorption, the surface is covered least by hydrocarbon chains, and hence the hydrophilicity of silica is restored. The possibility that bilayer adsorption is responsible for restoration of hydrophilicity is precluded in this case because no surface aggregation occurs due to steric hindrance. However, for C_8EO_{10} , the higher adsorption density and the higher aggregation at the interface (which causes hydrophobic patches on the surface) will offset the effect of any conformational changes in the hydrocarbon chains and leads to maximum hydrophobicity at plateau adsorption. In the case of surfactant mixtures, for example, both SDS and $C_{12}EO_8$ adsorb on kaolinite by themselves. Adsorption of $C_{12}EO_8$ on kaolinite is influenced by the presence of anionic SDS. The plateau adsorption in all cases is higher from its mixtures of SDS than in its absence.³⁴ These higher plateau adsorption values are due to additional adsorption of $C_{12}EO_8$ with reverse orientation. At low concentrations the chain–chain interactions between the adjacently adsorbed SDS and $C_{12}EO_8$ molecules will provide additional energy gain for the adsorption process. These hydrophobic interactions at the interface will result in the formation of the hydrophobic microdomains into which the hydrocarbon chains of additional $C_{12}EO_8$ molecules can become incorporated as a second layer. This is schematically shown in Figure 7.14.³⁴ The evolution of such an adsorbed layer clearly changes the wetting behavior of the particle surface as indicated by the skin flotation tests. This shows a sharp decrease in the flotation of kaolinite with increase in the adsorption of the nonionic surfactant. Mixed surfactant adsorption also causes stabilization in these dispersions. The settling rate is dramatically reduced in this case without significant alterations in zeta potential. The observed stability is attributed to the reversed adsorption layer, with the protruding EO chains providing steric repulsion to the approaching particles.

7.5.2.1.3 Flocculation by Phase Separation

Phase separation of polymers and surfactants has been demonstrated as a means to control solid–liquid dispersion. It has been shown that partially water-miscible surface active solvents, *N*-alkyl-2-pyrrolidone, can effectively control the stability of graphite aqueous dispersion.³⁵ As shown in Figure 7.15, graphite particles that are dispersed via electrostatic repulsion can be successfully flocculated by octyl pyrrolidone. Extremely rapid flocculation occurs at 2.0 wt% octyl pyrrolidone. Further increase in pyrrolidone concentration decreases the settling rate, suggesting that the graphite particles are restabilized. The other significant finding is that, at optimum pyrrolidone concentration, all the graphite particles form a single large floc, and the volume of the sediment shows that the graphite is packed very closely.

This flocculation is proposed to be due to strong adsorption at the solid–liquid interface (particle surface) due to the phase separation forming regions or patches rich in pyrrolidone. It is known

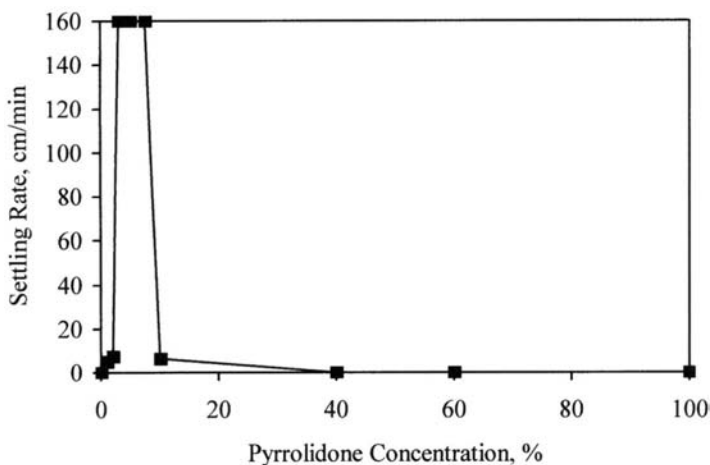


FIGURE 7.15 Flocculation of graphite with octyl pyrrolidone.

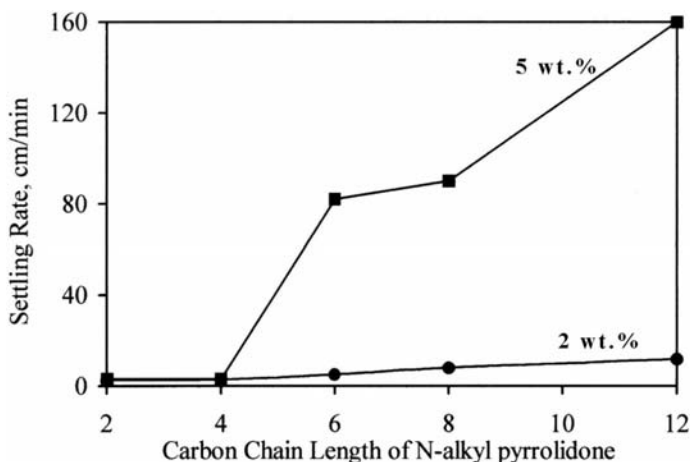


FIGURE 7.16 Effect of alkyl chain length on flocculation of graphite with pyrrolidone.

that longer-chain *N*-alkyl-2-pyrrolidones exhibit lower consolute temperature (LCT). Once when a sufficient amount of pyrrolidone is adsorbed at the solid–liquid interface, the conditions for phase separation can be satisfied. Consecutively, particles aggregate to minimize the total free energy, resulting in the strong flocculation (Figure 7.16).

The phase separation flocculation depends strongly on the temperature. Excellent flocculation occurred when the concentration exceeded the maximum miscibility at temperatures higher than the LCT. The flocculation was reversible and the particles were restabilized at temperatures below the LCT. Chain length of the alkyl group has a similar effect: the longer the alkyl chain, the lower the concentration at which phase separation occurs. Such an effect is clearly illustrated in Figure 7.17.

7.5.2.2 In Organic Media

Adsorption of surfactants from nonaqueous media has been widely employed to disperse hydrophilic solids in organic liquids. The main goal of most of these applications is to achieve uniform

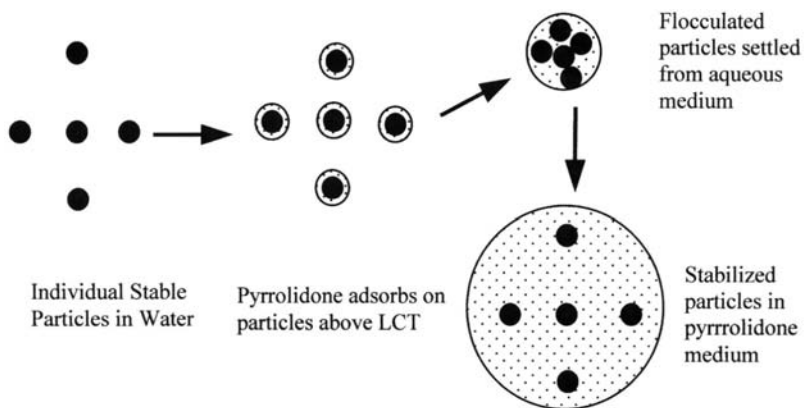


FIGURE 7.17 Schematic representation of hypothesized phase separation flocculation mechanism.

and complete coverage of the surface with the surfactant. For a majority of systems involving adsorption in nonpolar media, a maximum monolayer coverage has been observed. Adsorption from organic solutions usually involves physical forces and can be described by the following exchange process:



where A_{sol} and B_{sol} are the adsorbate and solvent molecules in solution and A_{surf} and B_{surf} are the respective molecules on the surface. The adsorption process according to the above scheme can usually be described by the Langmuir adsorption isotherm:

$$\Gamma_A = \frac{K_{\text{ads}} X_{A,s}}{1 + K_{\text{ads}} X_{A,s}} \quad (7.25)$$

where Γ_A is the surface concentration, X_A is the mole fraction of the adsorbate in solution, and K_{ads} is the equilibrium constant for the adsorption. Several other modified Langmuirian equations have been proposed for measured adsorption data taking into account heterogeneities of the adsorbent.^{36,37}

In nonpolar media due to the low ionization of the solute species, electrostatic attractive or repulsive forces can be ruled out as a major mechanism for adsorption. However, polar interactions have to be considered especially when polar surfaces such as oxides are involved. Recent work has shown acid–base interactions between the surface species and the solute molecules to be responsible for adsorption in nonaqueous media. Fowkes³⁸ has suggested that the interaction between a solid surface and an uncharged adsorbate can be divided into two parts, dispersive interactions and polar interactions. The dispersive interactions are due to the fluctuating dipole moments created by the movement of electrons in any atom or molecule and thus occur between all atoms and molecules. Polar interactions refer to specific interactions between hydrophilic surface groups and functional groups in the adsorbate molecules.

7.5.2.2.1 Oxide Surfaces

Figure 7.18 shows the adsorption isotherms of aerosol OT (AOT) on alumina and silica from cyclohexane.³⁹ It can be seen that the anionic surfactant has a greater affinity for the basic oxide than for the acidic oxide. The situation is reversed in the case of the adsorption of the cationic surfactant dimethyl dodecylamine (DDA). DDA adsorbs more on acidic silica than on alumina (Figure 7.19). Calculations based on a plateau adsorption value of about 3×10^{-6} mol/m² on alumina

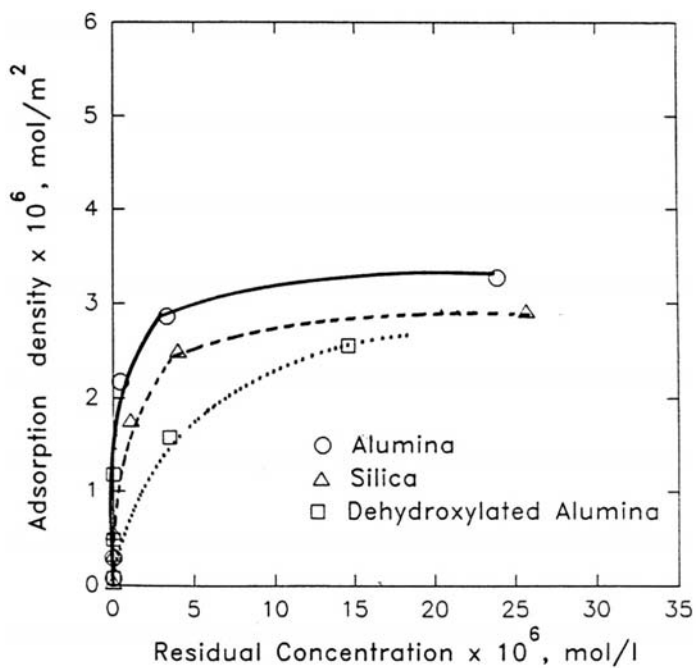


FIGURE 7.18 Adsorption isotherm of AOT on different solids from cyclohexane. (From Krishnakumar, S. and Somasundaran, P., *Langmuir*, 10, 2786, 1994. With permission.)

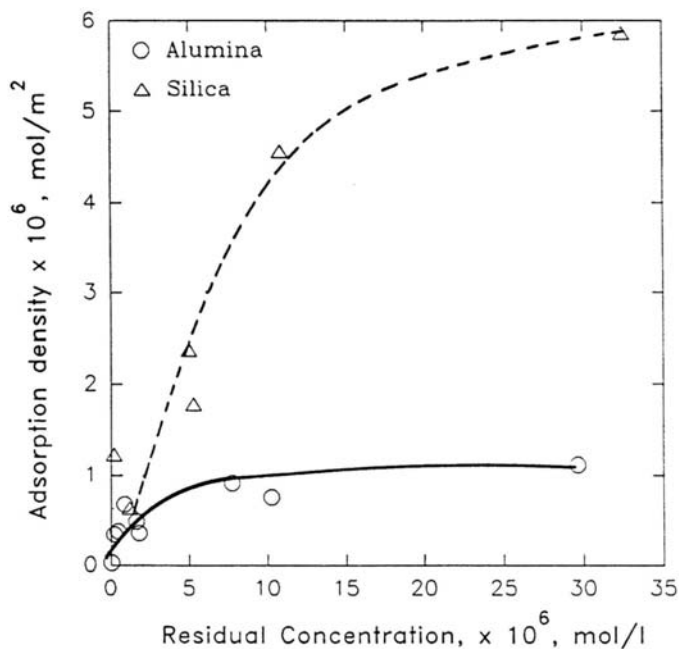


FIGURE 7.19 Adsorption isotherm of cationic DDA on different solids. (From Krishnakumar, S. and Somasundaran, P., *Langmuir*, 10, 2786, 1994. With permission.)

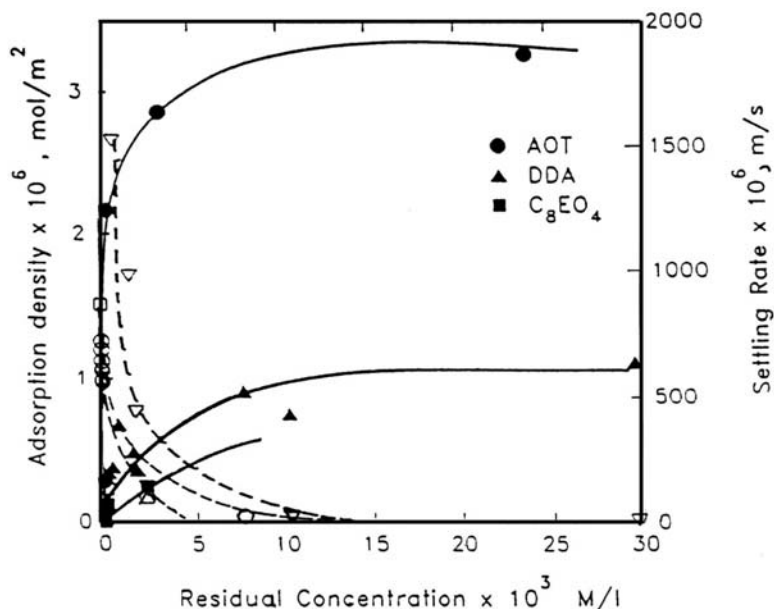


FIGURE 7.20 Settling rate variation of alumina suspensions upon adsorption of different surfactants in organic media.

give a parking area of about 0.55 nm^2 for the AOT molecule. This is in good agreement with the published values for AOT parking areas at the water–xylene and water–isooctane interfaces, suggesting that it adsorbs at the alumina–cyclohexane interface as a monolayer in an orientation perpendicular to the adsorbent with the hydrocarbon chain extending into the solution. Similar calculations based on the plateau adsorption for the cationic surfactant give a parking area of 1.6 nm^2 per molecule, which is much less than the area occupied by a flatly adsorbing DDA molecule ($\sim 4 \text{ nm}^2$), suggesting that this also adsorbs perpendicular to the adsorbent. Figure 7.18 also shows the adsorption of AOT on dehydroxylated alumina. Dehydroxylation, in this case, is achieved by heating the alumina at 900°C for 48 h and verified by observing the disappearance of the OH vibration bands at 3800 cm^{-1} from the infrared spectrum of the alumina sample. Dehydroxylation increases the acidity of the surface and hence reduces the adsorption of the anionic AOT. It is clear from these results that AOT adsorbs through interactions with the hydroxyl groups on the oxide surface. These results also suggest that for a given surfactant the relative acidity of the oxide surface is one of the major factors that determine the extent of interaction. Because both anionic and cationic surfactants adsorb on alumina and silica, can be inferred that electrostatic forces do not play a major role in this adsorption.

Figure 7.20 shows the settling rates of alumina suspensions as a function of surfactant adsorption.⁴¹ It can be observed that the suspensions are stabilized by the adsorption of the anionic, cationic, and nonionic surfactants (although to different extent) and the maximum stability corresponds to the onset of the plateau in the adsorption isotherm. The adsorption, as discussed earlier, takes place with the polar group of the surfactant interacting with the surface hydroxyls and the hydrocarbon tails of the amphipathic surfactant molecules sticking out into the solvent phase. Thus, the stability produced by surfactant adsorption can be attributed to a hydrophobic modification of the surface that disperses well in the nonpolar liquids.

7.5.2.2.2 Hydrophobic Surfaces (Graphite)

The adsorption isotherm of AOT on graphite from cyclohexane follows a very interesting pattern, as shown in Figure 7.21.⁴² The adsorption increases sharply in the initial part, suggesting high

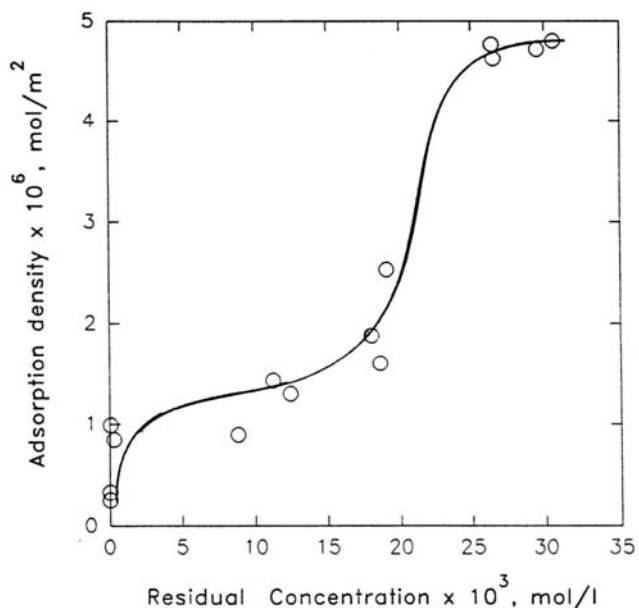


FIGURE 7.21 Adsorption isotherm of AOT on graphite from cyclohexane. (From Krishnakumar, S. and Somasundaran, P., *Colloids Surf.*, 117, 227, 1996. With permission.)

affinity of the surfactant for the solid at low concentrations. The adsorption then appears to reach a plateau and calculations based on apparent monolayer coverage at this level yield a parking area of approximately $1.03 \text{ nm}^2/\text{AOT molecule}$. This molecular parking area corresponds to an AOT molecule adsorbing flatly at the solid–liquid interface. At higher AOT concentrations, above 10^{-2} mol/dm^3 , there is a further sharp increase in the adsorbed amount and this reaches to about five times the initial plateau value at about $3 \times 10^{-2} \text{ mol/dm}^3$. It is interesting to note that this sharp increase occurs above the CMC of AOT ($1 \times 10^{-3} \text{ mol/dm}^3$), although it does not coincide with the onset of micellization.

The settling behavior of these dispersions as a function of the adsorbed AOT amount is also very interesting (Figure 7.22). Settling rate rises sharply first and then decreases as sharply, suggesting restabilization. At low surface coverages the polar headgroup of the flatly adsorbing AOT is exposed to the solvent with which it is not compatible. In such a case the AOT molecules, as shown in Figure 7.23a, can form interparticle aggregates that would effectively create a polar microdomain to shield the headgroups from the solvent. Such an interparticle aggregation can account for the increased settling rate. As the AOT concentration is increased, the adsorbed molecules are proposed to form aggregates at the interface, as shown in Figure 7.23b. This leads to the sharp increase in the adsorption density as well as the decrease in settling rate due to the disappearance of the interparticle aggregation observed at low surface coverages. Formation of such reverse hemimicelle-like aggregates at the interface have been reported earlier for the adsorption of 1-decanol on graphitized carbon black from nonpolar solvents.⁴³

7.5.2.2.3 Effect of Water on Dispersion Stability of Alumina

Figure 7.24 shows the effect of water on the stability of alumina suspensions that have been dispersed in cyclohexane by the adsorption of a monolayer of AOT.⁴¹ As the water content in the system increases, the suspension goes through a series of flocculated, stabilized, and flocculated stages. In an extremely dry state the dispersions flocculate rapidly, and the addition of trace amounts of water stabilizes the suspensions quite significantly. Thereafter, the suspensions remain stable over a range of water concentrations and then flocculate very rapidly at higher water concentrations.

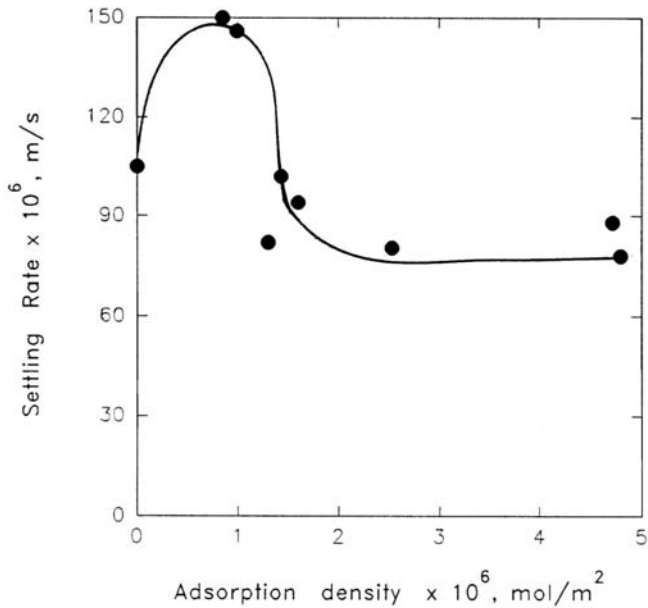


FIGURE 7.22 Variation in settling rate of graphite suspensions in cyclohexane as a function of AOT adsorption density. (From Krishnakumar, S. and Somasundaran, P., *Colloids Surf.*, 117, 227, 1996. With permission.)

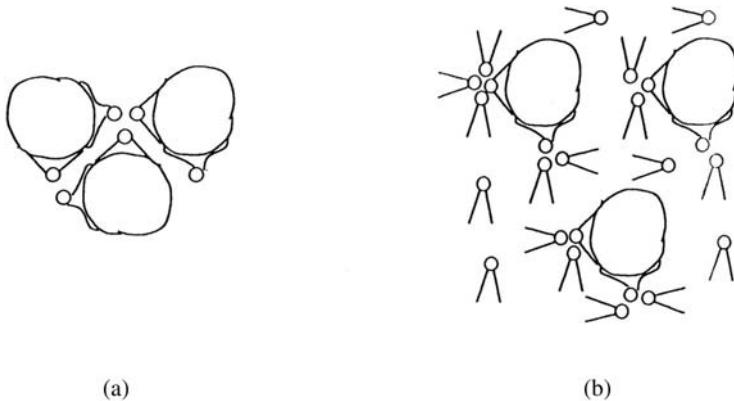


FIGURE 7.23 Schematic representation of adsorption of AOT on graphite at low (a) and high (b) concentrations. (From Krishnakumar, S. and Somasundaran, P., *Colloids Surf.*, 117, 227, 1996. With permission.)

The concentration of water at which the suspension reflocculates correlates well with the solubility of water in the bulk solution. Surface charge measurements made using the electrokinetic sonic amplitude system (ESA) (Figure 7.25) shows clearly that addition of trace amounts of water induces a significant amount of charge at the surface.⁴¹ This observation along with that of the drastic increase of conductivity of the dispersions (also shown in Figure 7.25) upon small additions of water leads to the conclusion that the stabilization in this case is due to the water-induced ionization of the adsorbed surfactant layer and resultant electrostatic repulsion among the particles. At higher water concentrations there is a slight decrease in the surface charge as measured by the ESA. But this decrease in surface charge cannot fully explain the massive flocculation observed in this case. From the water adsorption isotherm also shown in Figure 7.24 it can be seen that the water

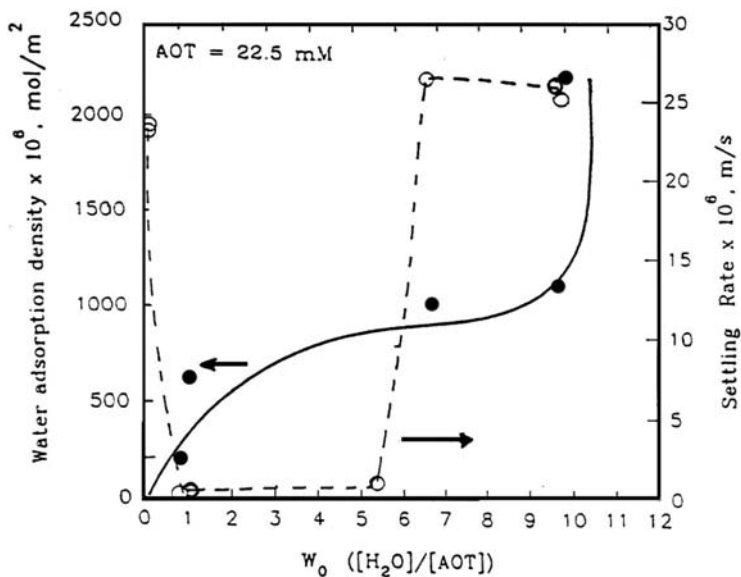


FIGURE 7.24 Effect of water on the alumina suspension stability and the corresponding adsorption of water.

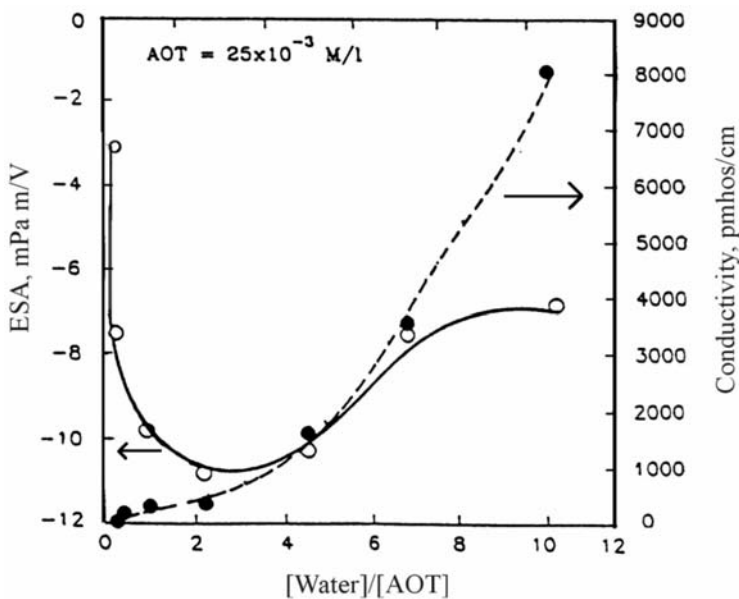


FIGURE 7.25 ESA and conductivity of alumina suspensions with adsorbed AOT as a function of water concentration.

adsorption increases sharply close to the onset of the flocculation. We further investigated this behavior using electron spin resonance spectroscopy.

7.5.2.2.4 Electron Spin Resonance Studies on Water-Induced Flocculation

In these studies the spectral response of 7-doxy stearic acid which is co-adsorbed along with the surfactant was monitored as a function of water adsorption.⁴¹ 7-doxy stearic acid adsorbed on the

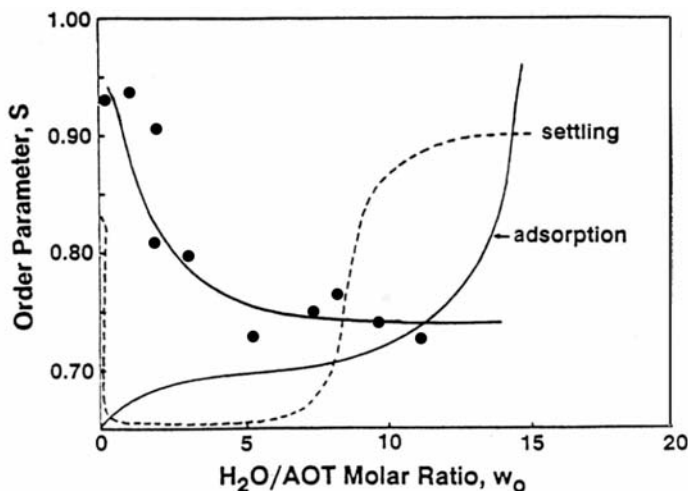


FIGURE 7.26 Effect of water on the order parameter, S , calculated from the ESR spectra of 7-doxyl stearic acid co-adsorbed with AOT at the alumina–cyclohexane interface.

alumina surface gives a characteristic anisotropic spectrum that can be quantified using the order parameter, which can be calculated from the spectral characteristics. The order parameter varies between $S = 1$ (highly ordered, restricted) and $S = 0$ (highly random and mobile) and reflects the state of the environment in which the probe resides. The order parameter calculated in this case decreases with increase in water concentration and levels off at approximately the same water concentration corresponding to the onset of flocculation (Figure 7.26). These results indicate that there is a change in the structure of the adsorbed layer with the surfactant layer becoming more fluid and mobile as water adsorbs at the interface. This opens up the possibility for the water layers on different particles to penetrate across the surfactant layers and bridge the particles together during collisions, thereby causing massive flocculation as observed.

7.5.3 ADSORPTION OF POLYMERS AND ITS EFFECT ON DISPERSION PROPERTIES

7.5.3.1 Theoretical Considerations on Polymer Adsorption

To understand the behavior of polymers at interfaces, it is essential to gain a clear picture of their behavior in solution first. Modern polymer solution studies were pioneered by Flory.^{13,44} Since then, there has been considerable effort to elucidate solution behavior of polymers and many models have been proposed. The theoretical treatment of polymer adsorption characteristics and conformation characteristics received considerable attention, mainly because of the significant applications.

One parameter that is commonly used to specify the dimension of a linear polymer molecule is the *root-mean-square (rms) end-to-end length*. The simplest, and also the most primitive, model for a polymer molecule is the *random flight chain*, also termed the *freely jointed chain*. In this model, the bonds are represented by volumeless lines in space, and there are no restrictions on the valency angles or on the rotations about the bonds. The rms end-to-end length, $\langle h^2 \rangle_0^{1/2}$, can be represented as

$$\langle h^2 \rangle_0^{1/2} = lN^{1/2} \quad (7.26)$$

where l is the *step length* and N the number of steps.

TABLE 7.3
Some Scaling Law Prediction
in the Semidilute Regime

Property	Scaling Law	
	Good Solvent	θ Solvent
$c^* \sim$	$N^{-4/5}$	$N^{-1/2}$
$R_g^2 \sim$	$Nc^{-1/4}$	N
$\xi \sim$	$c^{-3/4}$	c^{-1}
$(\Pi/T) \sim$	$c^{9/4}$	c^3

Note: c = polymer concentration; c^* = the polymer concentration at which the total volume of the chain just fills the available volume, whose value must be comparable to that in polymer coil; ξ = the *correlation length* or *average mesh size*, which represents the mean distance between intersections of the trajectories of the polymer chains; Π = osmotic pressure.

The random flight chain has the simplest mathematical properties, but, unfortunately, also has the smallest degree of structural similarity to real polymers. A more complex model considering the fixed valency angle (τ) and the restrictions of free rotation has been proposed:

$$\langle h^2 \rangle^{1/2} = lN^{1/2} \left\{ \frac{1 - \cos \tau}{1 + \cos \tau} \right\}^{1/2} \delta_f \quad (7.27)$$

where δ_f is the steric factor, which clearly also is a measure of the flexibility of the polymer chain (usually $1.5 \leq \delta_f \leq 2.5$). For the carbon backbone polymers used most often, $\cos \tau = -1/3$ and $\delta_f \sim 2.0$; therefore the $\langle h^2 \rangle / \langle h^2 \rangle_0$ equals to 8.

Other parameters used as a measure for the dimension of a polymer molecule include *rms radius of gyration* (R_g), *average span* ($\langle S_x \rangle$), the maximum extension averaged in all direction), and *Hollingsworth radius* ($\langle R_{\text{Holl}} \rangle$), the radius of the smallest sphere that contains all the segments of a chain). Their relationships, for a random coiled polymer chain, can be summarized as

$$R_g : \langle S_x \rangle : \langle h^2 \rangle^{1/2} : \langle R_{\text{Holl}} \rangle = \left(\frac{1}{6} \right)^{1/2} : 0.92 : 1.00 : 1.14 \quad (7.28)$$

As discussed by de Gennes,⁴⁵ scaling law focuses attention on the exponents and refrains from the determination of any prefactory constants, which are usually much more difficult to determine. Some predictions of scaling law theory for polymers of high molecular weight in both good solvents and θ solvents in the semidilute regime are summarized in Table 7.3.

The structure of adsorbed polymer layers on specific substrates from given solvents is less understood than the properties of polymer solution. It has, for many years, been derived by the self-consist theory where each chain has an average potential with a short-range part and a long-range repulsive part proportional to the concentration profile.⁴⁶⁻⁴⁸ de Gennes⁴⁹ constructed from scaling laws a completely different scheme that provided a better insight into the polymer adsorbed layers despite the fact that it does not predict the numerical parameters of any governing formula. The two techniques (self-consist field and scaling) complement each other and have provided considerable useful information for understanding the polymer behavior at interfaces.

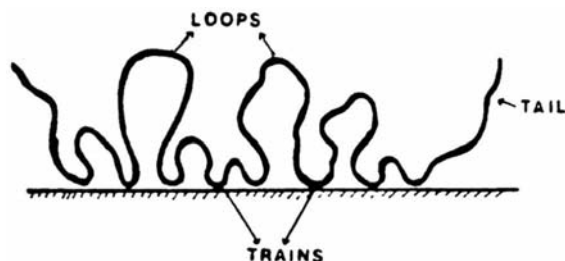


FIGURE 7.27 Schematic representation of an adsorbed polymer chain at the solid–liquid interface. (From Sato, T. and Ruch, R., in *Steric Stabilization of Colloidal Dispersion by Polymer Adsorption*, Marcel Dekker, New York, 1980. With permission.)

Compared to most cases addressed by the above researchers, the behavior of polyelectrolytes are more complex. One of the most prominent differences is the occurrence of long-range electrostatic interactions, whereas in the case of uncharged polymers only nearest-neighbor interactions play a role. Because of the wide application of polyelectrolytes, some attempts have been made to describe the adsorption of polyelectrolytes. Most theories have been developed by incorporating the electrostatic free energy into the models for uncharged polymers.⁵⁰

7.5.3.2 Basic Concepts of Adsorbed Polymer Conformations

The process of polymer adsorption is quite different in many aspects from that of small molecules; the latter has been studied extensively in the past. These differences in their adsorption characteristics arise in turn from the obvious flexibility of the larger polymer molecules, so that in addition to the usual adsorption factors considered, such as the adsorbate–adsorbent, adsorbate–solvent, and adsorbent–solvent interactions, a major aspect to be understood is the conformation of polymer molecules at the interface and its role in dispersion. Polymers have a large number of functional groups, each of which can potentially adsorb at the surface, whereas smaller molecules are mostly monofunctional.

The importance of adsorbed polymer conformation at interfaces was first recognized by Jenkel and Rumbach in 1951.⁵¹ A model of adsorbed polymer conformation was proposed based on the observation that amount of polymer adsorbed per unit area of the surface corresponds to a layer more than ten molecules thick. In that model, not all the segments of a polymer are in contact with the surface. As schematically shown in [Figure 7.27](#), those segments that are in direct contact with the surface are termed *trains*; those between and extending into solution are termed *loops*; the free ends of the polymer extending into solution are termed *tails*. Sato and Ruch⁵² classified the possible conformations for most situations into the six types shown in [Figure 7.28](#).

7.5.3.3 Mechanisms of Flocculation by Adsorbed Polymers

As mentioned earlier, polymers can exert a dramatic influence on colloidal stability. However, the description of particle interactions in the presence of polymers is complex, and even a qualitative estimation of conditions for attraction or repulsion has yet to be developed. Three theories have been proposed to explain flocculation of charged particles by oppositely charged polyelectrolytes: bridging, simple charge neutralization, and charge patch neutralization.

7.5.3.3.1 Bridging

The original bridging mechanism was proposed by Ruehrwein and Ward⁵³ in 1952 and later advanced by La Mer and co-workers.^{54,55} Bridging is considered to be a consequence of the adsorption of the segments of individual polymer molecules on the surfaces of more than one

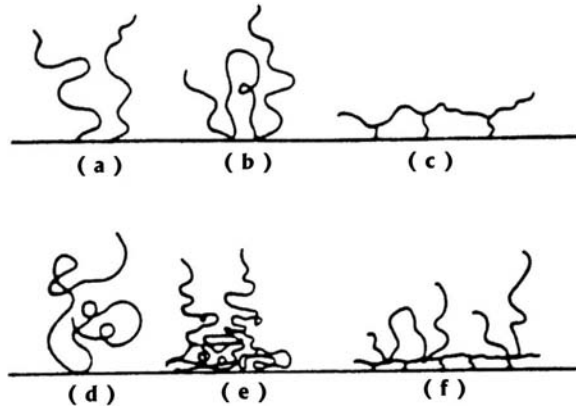


FIGURE 7.28 Conformation of adsorbed polymer: (a) single point attachment, (b) loop adsorption, (c) flat multiple site attachment, (d) random coil, (e) nonuniform segment distribution, and (f) multilayer. (From Sato, T. and Ruch, R., in *Steric Stabilization of Colloidal Dispersion by Polymer Adsorption*, Marcel Dekker, New York, 1980. With permission.)

particle. Such bridging links the particles together into loose aggregates. This mechanism has been validated by many works:⁵⁶

1. Polymers produce large, stronger, and better settling flocs than simple electrolytes.
2. The effectiveness of a polymer of a given type increases with molecular weight.
3. Linear polymer is more effective than branched polymers of comparable molecular weight and chemical structure.
4. At high concentrations, polymeric flocculants restabilize the particles.
5. Highly charged particles are flocculated by like-charged polymers only after their electrostatic potential has been sufficiently reduced by the addition of electrolyte.

When two particles with preadsorbed polymer approach each other, the free energy diminishes or rises depending on the surface coverage (θ) and the nature of the polymer.⁵⁷ Because of adsorption of additional segments, there can be a free energy contribution, ΔG_{ads} , which is proportional to the additional segments adsorbed and related to the affinity between polymer and solid surface, χ_s . Adsorption occurs only if there are unoccupied sites on the particle surface so that additional adsorption is unlikely at high coverages, $\theta \sim 1$. In most cases, ΔG_{ads} is <0 indicating an attractive contribution. It is also possible to have an entropic contribution, ΔG_{con} , due to the restriction of the number of available conformations if adsorbed polymer layers overlap. This contribution is always repulsive. Another contribution may exist from the free energy of mixing, ΔG_{mix} , due to the interaction between segments and solvents as determined by the Flory–Huggins parameter χ . Upon overlap, the number of those interactions increases. In good solvents ($\chi < 0$), $\Delta G_{\text{mix}} > 0$, and repulsion occurs between the segments, e.g., steric hindrance; in poor solvents, $\Delta G_{\text{mix}} < 0$ and segment attraction prevails, e.g., hydrophobic flocculation. The overall effect is determined by the sum of these contributions. Unfortunately, these effects are often interdependent, which makes their quantitative description extremely difficult.

Ottewill and Walker⁵⁸ derived an equation for the energy change for the overlap of adsorbed layers by using the Flory’s liquid lattice theory for polymer solutions:

$$V_r = \frac{4\pi kTc}{3vp[\phi - K][\delta - H/2]^2 [3r + 2\delta + H/2]} \quad (7.29)$$

where c is the concentration of material in the adsorbed layer, v is the molecular volume of the solvent, p is the density of the adsorbate, ϕ and K are the entropy and enthalpy of mixing respectively, proposed by Flory, δ is the adsorbed layer thickness, H is the closest distance of approach, and r is the particle radius.

La Mer^{59,60} and others⁶¹ have related the bridging efficiency factor to the fractional surface coverage of polymers (θ). The original La Mer model and subsequently modified models can be generally described as

$$E = f\theta(1 - \theta) \quad (7.30)$$

where E is the bridging efficiency factor and f is the constant ($1 < f < 2$).

From Equation 7.30, it is clear that E will have a maximum when θ is 0.5, corresponding to 50% particle surface coverage with polymer. However, in the practice, optimum polymer dosages are often found at much lower θ value.

Other than “classical bridging,” for which a polymer chain must adsorb on more than two particles, Somasundaran et al.¹² postulated that bridging may occur between two particles by two separate adsorbed polymer molecules. Similar to the hydrophobic interaction, when surface-active polymers adsorb on particles via terminal-hydrophilic groups with hydrophobic groups extending into the bulk solution, bridging may occur through lateral interactions between the hydrophobic groups extending from particles to reduce the surface energy of the hydrophobic groups.

7.5.3.3.2 Simple Charge Neutralization and Charge Patch Neutralization

Oppositely charged polyelectrolytes reduce the particle surface charge density such that particles may approach each other sufficiently closely so that the attractive van der Waals force becomes effective. Flocculation caused by this mechanism should not be sensitive to the molecular weight of the polymer.

Gregory⁶² proposed another flocculation mechanism, *charge patch neutralization*. There is no need for a one-to-one correspondence between charges on the surface and the adsorbed polymer. If the charge density of a polymer in its adsorbed state is higher than that of the surface, then patches of positively and negatively charged sites will appear on the particles. Thus, although the particles may have overall neutrality or even excess charge of the same sign, there exists the possibility of aggregation due to the attraction of oppositely charged patches on different particles.

Charge neutralization (simple and/or patch) is often the mechanism for flocculation by low molecular-weight polyelectrolytes.

7.5.3.4 Role of Polymer Conformation in Flocculation and Stabilization

Bridging can occur only if the extent of adsorbed polymer chain from the particle surface into medium is greater than the minimum particle approach distance over which the interparticle repulsion acts. This distance is of the order of the sum of the thickness of the electrostatic double layers of the approaching particles. The spatial extension of polymer molecules depends not only on molecular weights of the polymer but also, significantly, on the conformation of the adsorbed polymer molecules. To meet the requirement of bridging, we can either reduce the thickness of electrostatic double layers or use polymers of high molecular weight and extended conformation. An increase in ionic strength reduces the thickness of the double layers; however, the extension of the polyelectrolyte is reduced at the same time because of the potential screening effect.

Apparently, polymer conformation plays an important role in flocculation caused predominantly by bridging. This effect of polymer conformation on the dispersion properties has been confirmed by many observations where significantly different dispersion behavior is obtained with identical adsorption density and electrostatic property. There have been substantial efforts both theoretically and experimentally to develop relationships between the stability and the polymer conformation

and guidelines for the optimum conformation to achieve desired dispersion properties. Despite these efforts, the progress is meager mainly because of the absence of reliable techniques and the complexity of systems. Tjipangandjara and Somasundaran^{63,64} showed conformation of adsorbed polyacrylic acid to have a significant effect on the stability of alumina dispersions. An experiment involving manipulation of polymer conformation in solution and at interface by shifting pH up and down was designed with polymer conformation monitored by pyrene fluorescence emission technique. They found that the conformation of adsorbed polymer can be altered by changing the solution conditions, and depending on the adsorption density and direction of pH shift, significant enhancement in flocculation or stabilization can be obtained.

Another important effect that is critical but often ignored is the timescale involved in flocculation processes. The kinetics of polymer diffusion to interface, adsorption, conformation, and reconformation and particle collision are quite different for different particle–polymer–solvent systems.⁶⁵ The polymer diffusion and particle collision rate can be controlled by the intensity and the time of agitation applied. Unfortunately, there is very little information on the rate at which adsorbed polymer chains attain their equilibrium conformation. The only information available is that of polymer adsorption on a flat surface.⁶⁶ A two-step process was observed, in which the polymer first adsorbs and then undergoes a very slow reconformation, which may take hours. This information is not very useful for the flocculation of suspensions. Optimum flocculation is usually obtained at a much lower surface coverage instead of the saturation condition used in the above study. Nevertheless, of importance is the relative rate of the reconformation process compared to the particle collision, whether particles collide before or after an equilibrium conformation state of the adsorbed polymers is achieved. This effect is manifested in the case of concentrated suspensions in which there is a high particle collision rate. In most practical polymeric flocculations, it is very unlikely that equilibrium conformation is achieved.

7.5.3.5 Stability of Dispersion in the Presence of Polymers

Besides the electrostatic forces, the suspension stability in the presence of polymers and surfactants is controlled by several other forces.⁶⁷ In the case of flocculation, a bridging theory by adsorbed polymers and surfactants is an accepted mechanism in addition to charge neutralization. On the other hand, in the case of suspension stabilization, steric interactions by adsorbed polymer and/or surfactant layer on particle surfaces become dominant.⁶⁸ In addition to adsorption density of the dispersant, conformation and orientation of the polymers and surfactants adsorbed on the particles will play a major role in controlling the suspension stability.⁵⁵ However, the conformation requirements for flocculation or dispersion are not known mainly because of the complex nature of adsorption and the lack of reliable techniques to monitor conformation *in situ*. Techniques used normally to determine the polymer adsorbed layer thickness (e.g., ellipsometry, viscometry, etc.) do not give sufficient information and, more important, cannot work *in situ*. In contrast, fluorescence and electron spin resonance spectroscopy techniques are powerful tools for probing *in situ* the microstructure orientation and conformation of adsorbed polymer and surfactant layers.⁶⁹ These techniques, used along with classical ones to determine suspension properties such as settling rate, supernatant turbidity, zeta potential, and adsorption density, can provide required information for developing predictive capabilities on the conformation criteria and schemes to manipulate the stability of suspensions.

7.5.3.5.1 Fluorescence Spectroscopy for Polymer Conformation and Association Measurement

Pyrene has been used widely as a photophysical probe because of its long fluorescence lifetime and great tendency for excimer formation. Emission characteristics of pyrene molecules depend on the nature of the solvent. The ratio of relative intensities of the I_{st} (373 nm) and III_{rd} (383 nm) peaks, I_{III}/I_{I} , in a pyrene emission spectrum decreases as the polarity of the solvent increases. This

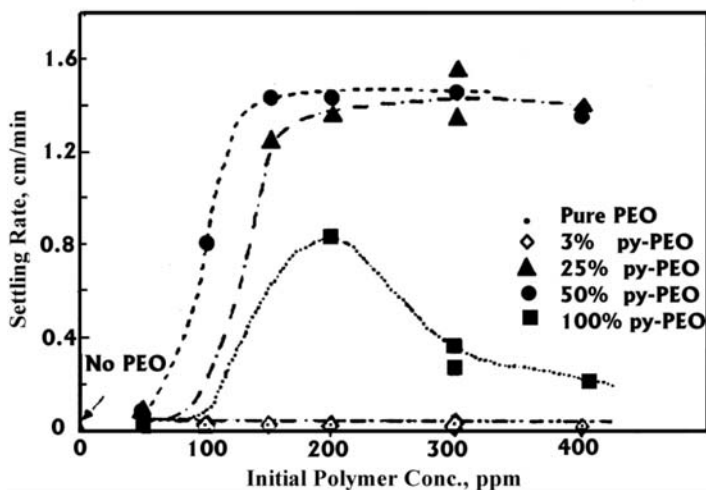


FIGURE 7.29 Settling rate of silica suspensions (5% vol.) with pyrene-labeled and unlabeled PEO. (From Campbell, A. and Somasundaran, P., *J. Colloid Interface Sci.*, 229, 257, 2000. With permission.)

ratio has been used to estimate polarities of solvents as well as surfactant micelles and aggregates in aqueous solutions.⁷⁰ Here, we show the use of pyrene fluorescence spectroscopy for determination of the association of hydrophobically modified polymers in bulk solution as well as at the solid–liquid interface. This type of polymers has been developed recently to increase the viscosity and the elasticity of solutions because they undergo interesting intra- and intermolecular associations.⁷¹ We have found the use of hydrophobically modified polymers for controlling the stability of polar and nonpolar suspensions to be promising because of their unique structure, which can provide either flocculation by intermolecular aggregation or stabilization by steric hindrance, depending on the orientation at the solid–liquid interface, which is dependent on the nature of the particles and the extent of adsorption.⁷²

Excimer fluorescence of pyrene attached to synthetic polymer chains can be used to study polymer conformation in solution and on particle surfaces. In this case, fluorescence spectroscopy involves the measurement of the emission intensity of monomer (I_m observed at 375 nm) and excimer (I_e at 480 nm). The ratio of I_e to I_m is related to coiling/stretching behavior of a labeled polymer and we have called it the coiling index.⁷³ In the absence of intermolecular interactions (the polymer concentration used is usually below this limit), a high value of I_e/I_m can be considered the result of a coiled conformation whereas a low value is associated with a stretched conformation.

In a recent study, the necessity for understanding the effects that molecular probes (e.g., pyrene) can have on colloidal system has been clearly illustrated.⁷⁴ Mixtures of pyrene-labeled and unlabeled polyethylene oxide (PEO) were adsorbed on silica and the properties of the resulting suspension were monitored. Settling rate results (Figure 7.29) clearly demonstrated that pyrene-labeled PEO has a marked effect on the flocculation of silica suspension. It has been shown that even relatively small amounts of labeled polymer, when mixed with unlabeled polymer, can dramatically affect the behavior of their mixtures. On the other hand, it has also been shown that when labeled polymer was used in sufficiently low amounts (<3%), the mixture behavior does not differ from that due to the unlabeled polymer. These findings once again underscore the fact that while certain measurement techniques are invaluable for investigating colloidal phenomena, potential effects caused by introduction of various molecular probes into the system should always be noted.

Recent developments of some new high-performance composite materials, cosmetics, paints, and microelectronic components require a better understanding and manipulation of the colloidal interactions in nonpolar media.^{5,75} However, unlike in the previous cases, pyrene cannot be used

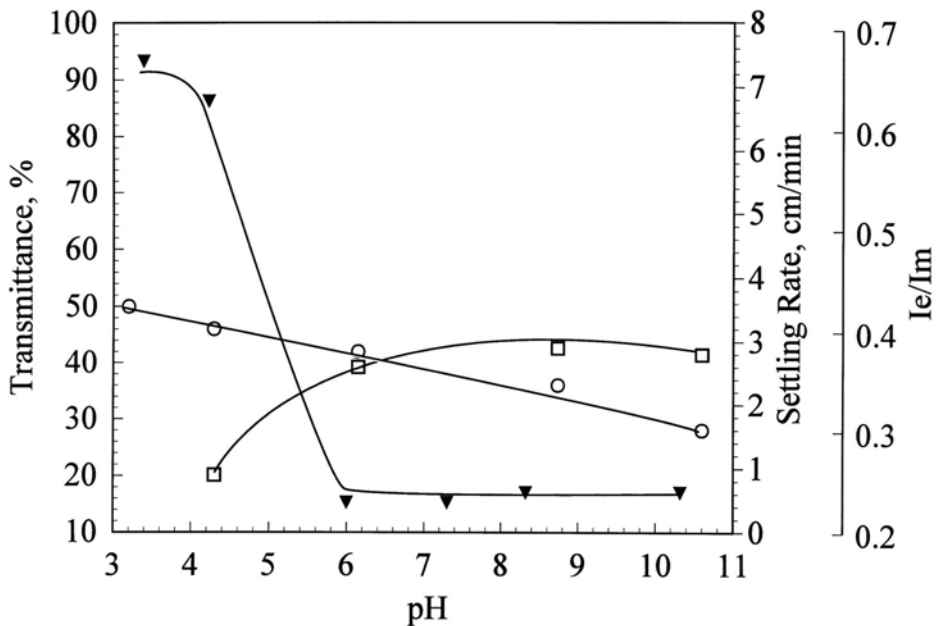


FIGURE 7.30 Flocculation of alumina particles with PAA (20 ppm); □, settling rate; ○, transmittance; ▼, coiling index (I_e/I_m). (From Tjipangandjara, K.F. et al., *Colloids Surf.*, 44, 229, 1990. With permission.)

as a probe for studying aggregation in apolar media. Because of its own hydrophobicity, it will stay in the hydrophobic bulk environment. Therefore, a less hydrophobic fluorescence probe, 7-dimethyl amino 4-methylcoumarin (Coumarin 311) was chosen for the study of the alumina–toluene interface. It has been reported that the wavelength of the Coumarin 311 emission maximum shifts from 391 to 471 nm when the solvent is changed from hexane to water.⁵ Polarity of an unknown environment can then be estimated by monitoring the position of the emission maximum.

7.5.3.5.2 Electron Spin Resonance Spectroscopy for the Study of Adsorbed Polymer and Surfactant Layers

Electron spin resonance spectroscopy (ESR), also known as electron paramagnetic resonance (EPR), is based on the property that an unpaired electron placed in a magnetic field shows a typical resonance energy absorption spectrum sensitive to its environment. Recently, this technique, which was primarily developed for biological studies of membrane properties, has been adapted for the study of adsorbed polymer/surfactant layers.⁷⁶ The mobility of the ESR probe (stable free radical incorporated into the polymer or surfactant molecule) depends of orientation of the surfactant or polymer and the viscosity of the local environment around the probe.

7.5.3.5.3 Effect of Adsorbed Polymer Conformation on Dispersion Characteristics

In a study of dispersion characteristics of alumina suspension with polyacrylic acid ($M_w = 88,000$) the polymer conformation at the alumina–water interface was determined as a function of pH using pyrene-labeled polymer along with settling rate and transmittance (Figure 7.30).⁷⁷ It can be seen that the polymer is coiled (high I_e/I_m) at low pH and that the stretched polymer results in better flocculation in terms of increasing settling rate and larger floc size (observed by CAT scan) but poor flocculation in terms of the supernatant clarity. Apparently, the stretched polymer at high pH provides better interparticle bridging while the electrostatic attraction between oppositely charged polymer molecules and alumina particles causes better capture of fine particles yielding a clear supernatant at low pH values.

The above experiments were conducted under “fixed” pH conditions: pH was preadjusted and both polymer and alumina particles were conditioned at the same pH before mixing. To investigate the effect of adsorbed polymer conformational changes on flocculation performance, polyacrylic acid was adsorbed at pH 4 and the pH of the suspension was then shifted to 10, and vice versa. Enhanced flocculation was observed in terms of both the settling rate and the supernatant clarity (Figure 7.31a), when pH was shifted up from 4. In contrast, when the pH was shifted down from 10, the settling rate was similar to that observed under the fixed pH conditions (Figure 7.31b). A maximum in the supernatant transmittance was observed at pH 7, the value which corresponds to the isoelectric point of alumina with adsorbed polymer. The direction of pH shift (low to high or reverse) governs the polymer conformational changes: coiled polymer adsorbed on the alumina surface at low pH stretches out when the pH is raised, but the initially stretched polymer does not coil when the pH is lowered.

Changes in polymer conformation at the alumina–water interface are schematically shown in Figure 7.32.⁷⁷ When the polymer is initially adsorbed at low pH in coiled conformation, it stretches out because of increasing electrostatic repulsion caused by the ionization of the carboxyl groups and the charge reversal of alumina particles (Figure 7.32, a to c). In this case some of the polymer chains are dangling into the solution providing interparticle bridging. In the reverse case, when pH was shifted from 10 to 4 (Figure 7.32, d to f), the stretched polymer that initially adsorbs on the particle surface through hydrogen bonding and retains the same conformation throughout the change in pH.

For significant improvement in supernatant clarity obtained in the scheme when the pH was shifted rather than fixed, the following two-step flocculation mechanism is proposed:

1. At low pH, the polymer chain captures all alumina particles into small flocs;
2. When pH is shifted up, the stretched polymer bridges these small flocs to create much larger aggregates that settle rapidly, but that retain the smallest particles, as well.

7.5.3.5.4 Dual Polymer System for Enhanced Flocculation

Combined use of two or more polymers to enhance desired suspension property (flocculation or stabilization) is not an unknown procedure.^{12,78} In some systems, it is possible to achieve the synergistic effect of two different polymers when one (usually of low molecular weight) can adsorb strongly onto the particle surface while the other (of much higher molecular weight) can provide interparticle bridging. Some authors have reported such synergism for the combination of low-molecular-weight cationic and high-molecular-weight anionic polymers.^{79,80} Most studies on double flocculants, however, have been empirical, and the mechanisms are not well developed.

Flocculation of alumina suspensions obtained by the sequential addition of polystyrene sulfonate ($M_w = 4600$) and cationic polyacrylamide ($M_w = 4,000,000$) at pH 4.5 is compared in Figure 7.33 with that obtained using single polymers. While the anionic polystyrene sulfonate had only a minor effect, cationic polyacrylamide did not produce any flocculation. However, when used together, both polymers adsorb completely. This coadsorption is attributed to the interaction of complexes between cationic polyacrylamide and the polystyrene sulfonate at the solid–liquid interface.⁸¹ The mechanism of the superior flocculation obtained with the dual polymer system is illustrated schematically in Figure 7.34. The anionic polystyrene sulfonate adsorbs on alumina surface and acts as an anionic “anchor” for the adsorption of the long-chain cationic polymer, which ultimately provides interparticle bridging and excellent flocculation.

Similar behavior was observed in a study of the other dual-polymer flocculation system.⁸² A combination of a polyacrylic acid (PAA, $M_w = 10,000$) and a high-molecular-weight cationic copolymer of acrylamide and quarternary acrylate salt (Percol™, Allied Colloids) was investigated for flocculating aqueous alumina suspensions. Although the turbidity of the supernatant was found to decrease somewhat when only PAA was used (Figure 7.35), suggesting some flocculation, neither

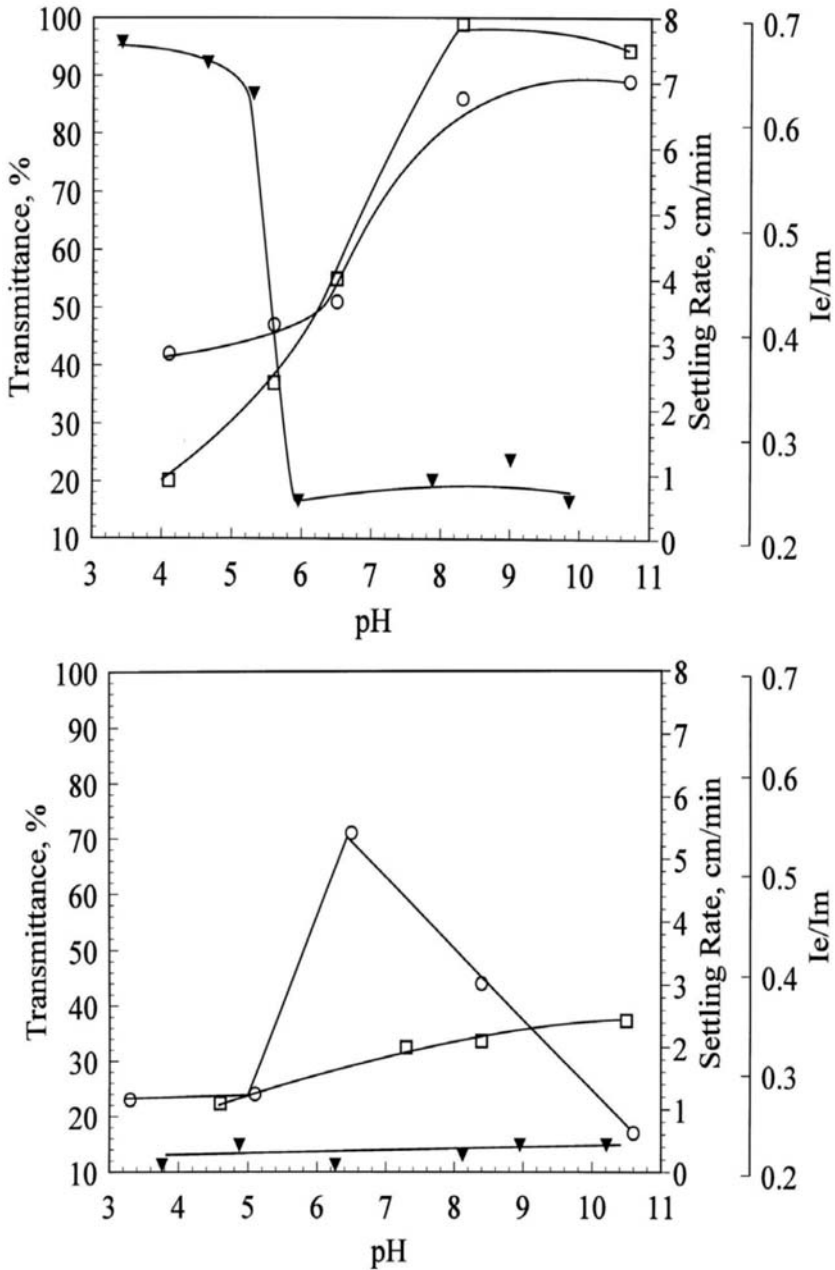


FIGURE 7.31 Flocculation of alumina particles with PAA (20 ppm) under shifting pH conditions: (top) initial pH = 4; (bottom) initial pH = 10. \square , settling rate; \circ , transmittance; \blacktriangledown , coiling index (I_e/I_m). (From Tjipangandjara, K.F. et al., *Colloids Surf.*, 44, 229, 1990. With permission.)

the polymer molecular weight nor the charge effects (pH = 8, close to the isoelectric point of alumina) were sufficient for strong bridging or charge neutralization. The addition of only Percol has caused even lesser flocculation due to negligible interactions between the positively charged polymer and the slightly positively charged alumina surface.

When both PAA and Percol were added to the suspension, flocculation was found to improve markedly (Figure 7.35). In addition, it can be seen that sequential addition of the two polymers

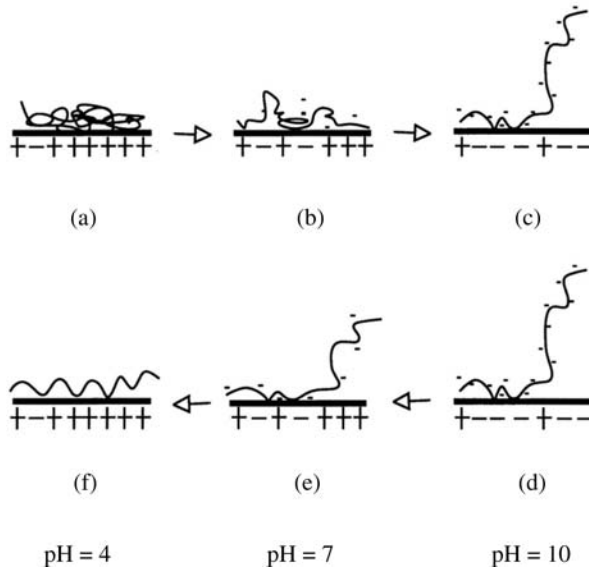


FIGURE 7.32 Schematic representation of the variation of polymer conformation at the solid-liquid interface. (From Tjipangdjara, K.F. et al., *Colloids Surf.*, 44, 229, 1990. With permission.)

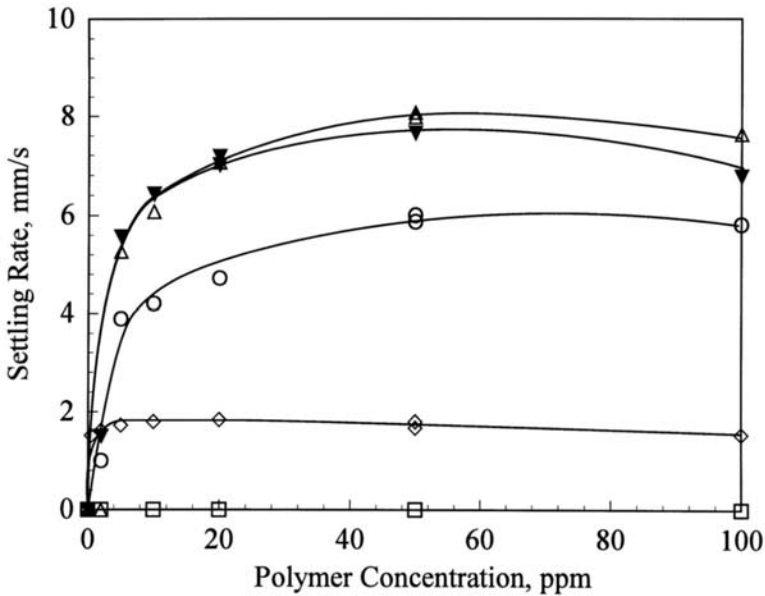


FIGURE 7.33 Flocculation response of alumina suspension with dual polymer systems. \square , C-PAM alone; \diamond , PSS alone; \circ , PSS and C-PAM; \triangle , C-PAM after PSS; \blacktriangledown , PSS after C-PAM. (From Yu, X. and Somasundaran, P., *Colloids Surf.*, 81, 17, 1993. With permission.)

(PAA first, then Percol) produces better flocculation that coaddition (polymers premixed). These findings again confirm the previously proposed mechanism (Figure 7.34) in which the low-molecular-weight polymer provides particle surface charge neutralization and formation of smaller primary flocs. Consecutively, the high-molecular-weight polymer of the opposite charge can successfully bridge the neutralized particles and primary flocs, causing maximum flocculation.

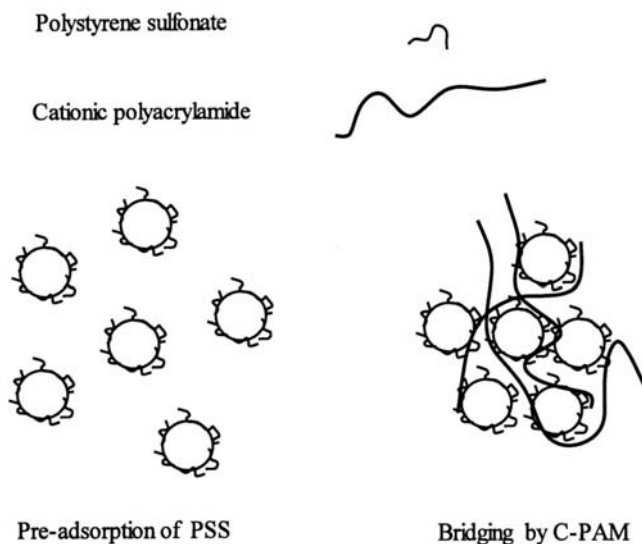


FIGURE 7.34 Schematic model for flocculation with dual polymer system. (From Yu, X. and Somasundaran, P., *Colloids Surf.*, 81, 17, 1993. With permission.)

7.5.3.5.5 Flocculation with Ultralow Polymer Dosage

As mentioned earlier, typical polymer dosage used for flocculation of oxide minerals is of the order of several parts per million (ppm). Some recent results, surprisingly, show that a relatively low molecular weight polymer (PAA, $M_w = 50,000$), generally considered to be a dispersant, can flocculate aqueous alumina suspensions at ultralow dosages of parts per billion (ppb) effectively.⁸³ This unexpected result (Figure 7.36) has been attributed to specific interactions, namely, hydrogen bonding between surface $-OH$ groups and PAA. Although these interactions do not effectively change the overall charge of alumina particles (see zeta potential in Figure 7.36), they can compensate for the charges on microdomains occupied by the polymer and cause particle aggregation based on the charge patch neutralization model.⁶⁰

Addition of a surfactant can further enhance the flocculation at the ultralow polymer dosage regime. As shown in Figure 7.37, the addition of anionic surfactant (SDS) significantly improves the flocculation at very low polymer concentrations.⁸⁴ At higher polymer levels, the surfactant addition has no effect on flocculation. This is probably due to a significant fraction of adsorption sites already occupied by polymer, making them unavailable for adsorption of the surfactant molecules.

7.5.3.5.6 Stabilization of Aqueous and Nonaqueous Suspensions with a Hydrophobically Modified Polymer

The interest in hydrophobically modified polymers (containing both hydrophilic and hydrophobic groups along polymer backbone) has increased recently due to their possible use in many different applications including stabilization of both aqueous and nonaqueous suspensions. A study using DAPRAL GE 202 (polymer with comblike structure: hydrophobic and hydrophilic chains and carboxyl groups along the backbone) has shown some unusual performance.⁸⁵ The effect of DAPRAL on the stability of aqueous alumina suspensions is shown in Figure 7.38 along with the zeta potential change and adsorption isotherm. The drastic effect of the polymer addition on suspension stability cannot be attributed to electrostatic forces: suspension stability remains unchanged to a polymer concentration of 150 ppm, while most of the zeta potential change takes place in that region. Subsequently, the stability of the suspension increases markedly with further increase in the DAPRAL concentration, whereas there is only a minor change in the zeta potential.

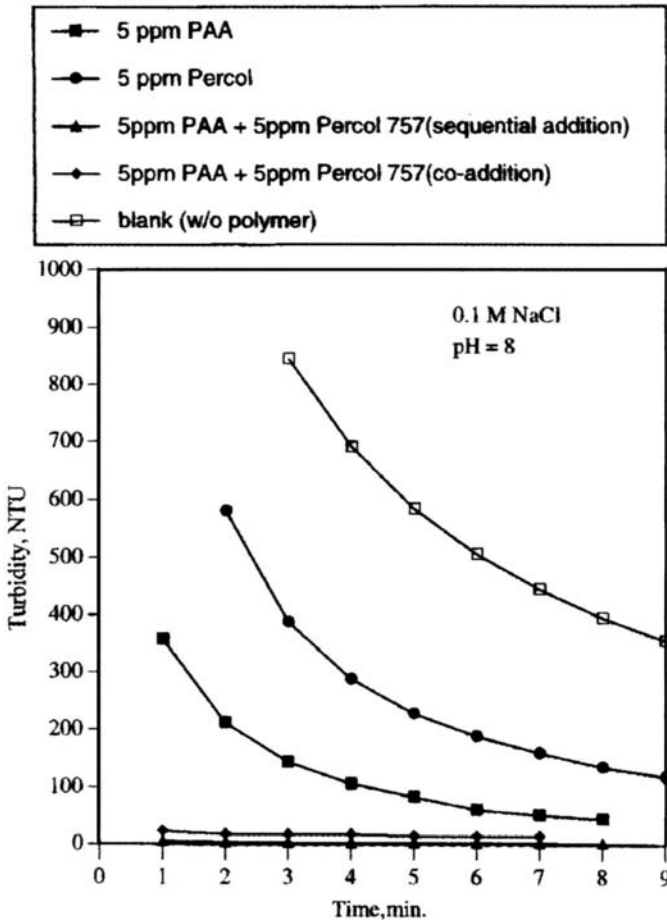


FIGURE 7.35 Enhanced flocculation with dual polymer system: PAA and Percol. (From Fan, A. et al., *Colloids Surf. A*, 162, 141, 2000. With permission.)

The same polymer, DAPRAL, with both hydrophobic and hydrophilic groups, can be also used for stabilizing nonaqueous suspensions. The results obtained for the settling rate of alumina in toluene as a function of DAPRAL concentration are given in Figure 7.39. The polymer adsorption is proposed to be primarily through the interaction between surface hydroxyl groups and the hydrophilic (EO) polymer side chains with the hydrophobic side chains exposed toward bulk solution causing suspension stabilization. This possibility was investigated by using 7-dimethyl amino 4-methylcoumarin as a fluorescence probe to detect the polymer orientation on the particles. Correlation of the observed shift of maximum wavelength (Figure 7.39) with suspension stability suggests the increase in the hydrophobicity of the alumina surface; this supports the mechanism proposed above for the observed stability of the alumina suspension.

7.6 SUMMARY

Colloidal particles are subjected to a number of attractive and repulsive forces and the stability of dispersions depends on the interplay of these various forces. The van der Waals attractive forces between particles have their origin in the electron wave fluctuations and are usually effective at close ranges. Electrical double layer interactions stem from the presence of ionized species at the interface and are effective at distances proportional to the double layer thickness for the given

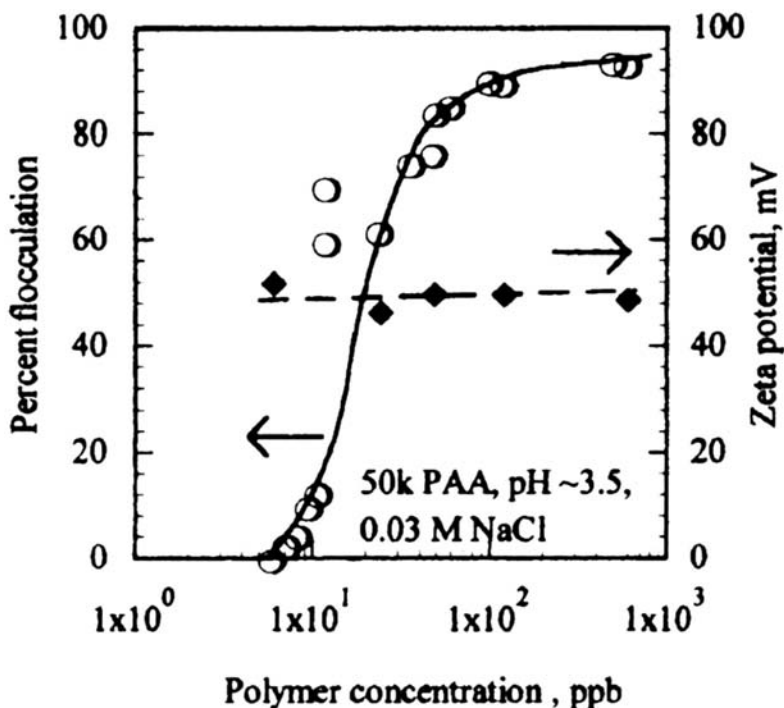


FIGURE 7.36 Flocculation and zeta potential of alumina particles as a function of polymer concentration. (From Das, K.K. and Somasundaran, P., *Colloids Surf. A*, 182, 25, 2001. With permission.)

system. In aqueous systems, this is usually of the order of 100 \AA at an ionic strength of 10^{-3} mol/l . In nonaqueous systems, this is very large as the potential decays only very slowly from the surface. Another dominant force, steric force, depends on the nature and size of the adsorbed species, but is typically short range. Other forces such as solvation, hydration, and capillary forces occur due to structural ordering at the interface and are active at separation distances on the order of 4 nm.

These forces and hence the stability of the dispersions can be altered/controlled by the adsorption of ions, surfactants, or polymers at the solid–liquid interface. Adsorption of surfactants and polymers at the solid–liquid interface depends on the nature of the surfactant or polymer, the solvent, and the substrate. Ionic surfactants adsorbing on oppositely charged surfaces exhibit a typical four-region isotherm. Such adsorption can alter the dispersion stability mainly by changing the double layer interaction, which depends on the extent of adsorption. Thus, it is seen that alumina suspensions are destabilized by the adsorption of SDS when the zeta potential is reduced to zero. At higher concentrations, bilayered surfactant adsorption can occur with changes in wettability and flocculation of the particles by altering the hydrophobic interactions.

Nonionic surfactants adsorb primarily through hydration or hydrogen bond interactions and this depends on the hydration characteristics of the substrate. These surfactants can also affect the double layer forces due to charge screening effects. Nonionic surfactants affect the dispersion stability mainly by altering the van der Waals interaction and the hydrophobic forces, which in turn depend on the nature and orientation of the adsorbed surfactant layer. The adsorption of nonionic surfactants can be greatly enhanced by the presence of ionic surfactants, and vice versa. Experiments have shown that nonionic and ionic surfactants when used in mixtures can be forced to adsorb on substrates on which they do not show much adsorption by themselves. The synergistic effect of these mixtures on adsorption is hypothesized to be due to the reduction in charge repulsion causing better packing of the ionic surfactants, whereas for nonionic surfactants the increase in adsorption is due to their solubilization in the hydrophobic microdomains formed by the ionic surfactants.

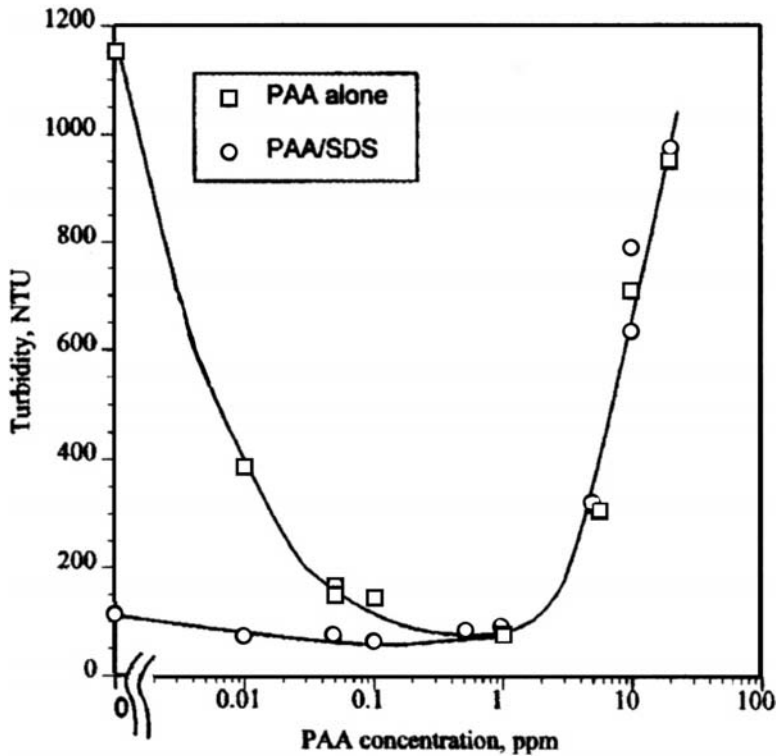


FIGURE 7.37 Turbidity of alumina suspension as a function of polymer concentration with and without surfactant (SDS, 1.25×10^{-3} mol/dm³). (From Fan, A. et al., *Colloids Surf. A*, 146, 397, 1999. With permission.)

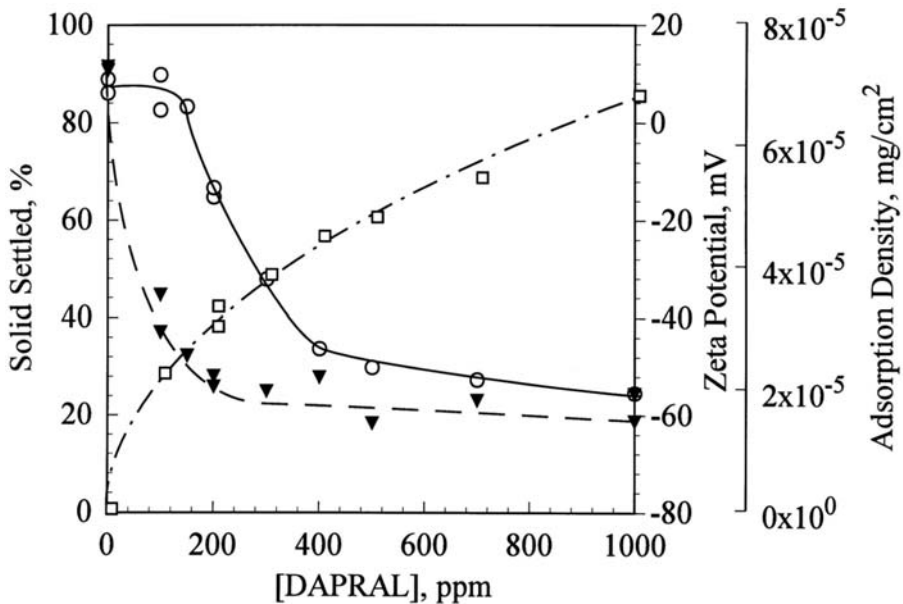


FIGURE 7.38 Adsorption of DAPRAL on alumina and its effect on stability and zeta potential. PH = 8; $S/L = 2.5\%$; \square , adsorption; \blacktriangledown , zeta potential; \circ , settling rate. (From Somasundaran, P. and Yu, X., *Adv. Colloid Interface Sci.*, 53, 33, 1994. With permission.)

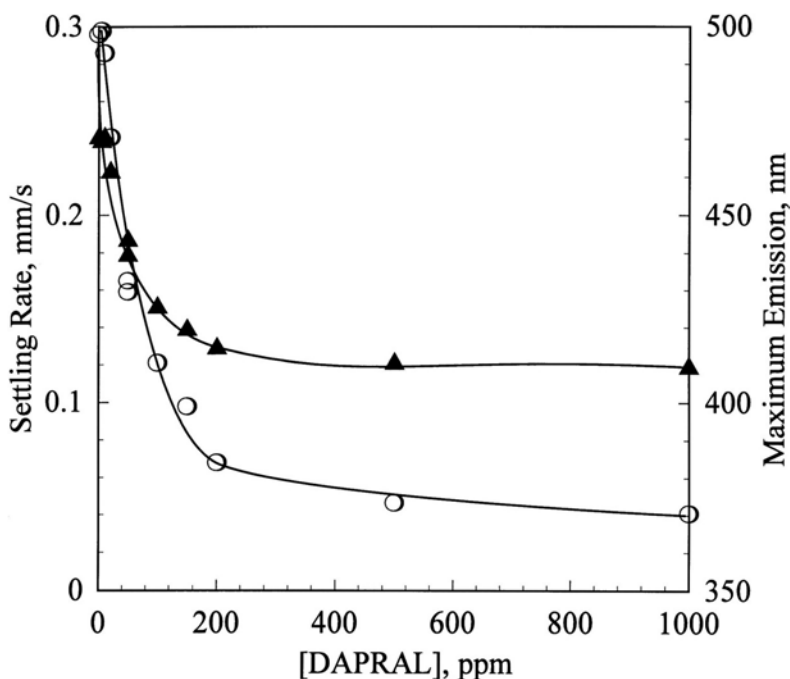


FIGURE 7.39 Effect of DAPRAL on stability and hydrophobicity of alumina in toluene. ▲, emission wavelength; ○, settling rate. (From Somasundaran, P. and Yu, X., *Adv. Colloid Interface Sci.*, 53, 33, 1994. With permission.)

These mixed systems give rise to interesting adsorbed layer structures that can be manipulated for desired dispersion properties.

In organic media, adsorption of surfactants depends on the relative acid–base characteristics of the solute, solvent, and substrate. Adsorption of ionic surfactants on oxide surfaces proceeds to a monolayer, and there is no evidence of lateral interaction between the adsorbed molecules. Such uniform adsorption imparts stability to the dispersion mainly by reducing the van der Waals attractive forces. However, on hydrophobic surfaces, interactions are possible among the polar groups of the adsorbed molecules leading to the formation of reverse solloids and a concomitant increase in adsorption density somewhat resembling solloid formation in aqueous media. This leads to a decrease in dispersion stability. The presence of water markedly affects the suspension stability in nonaqueous media. When present in trace amounts, it induces ionization in the adsorbed layer and imparts electrostatic stability to the dispersion, whereas at high concentrations it promotes capillary condensation between the particles leading to flocculation.

Adsorption of polymeric dispersants and flocculants in aqueous media is controlled by the polymer charge, molecular weight, solvent, solution conditions (pH, ionic strength), and porosity of the substrate. However, the adsorbed polymer layer structure is very different from that of the surfactants. A polymer can have various configurations at the interface and the adsorbed layer can be thought of as a fuzzy polymer layer with trains, loops, and tails. Polymer adsorption affects dispersion stability by altering the electrostatic forces (in the case of polyelectrolytes) and mainly the steric forces, which are in this case significant as the adsorbed layer thickness is large for polymers. Flocculation by polymers is mainly by charge neutralization and bridging, which depends on the relative size of the polymer chain and the particle and more importantly on the conformational state of the adsorbed polymer. Also, it is clear that reorientation of the polymer molecules at the interface can take place in response to changes in the environmental conditions such as pH and this can produce drastic alternations. Interactions between different polymers can also influence

dispersion behavior. Thus, the use of two polymers in sequence is very effective as it can control the kinetics of aggregation and the floc structure. It has been clearly established that dispersion stability can be manipulated through control of polymer structure and its conformation at the solid-liquid interface.

ACKNOWLEDGMENTS

The authors acknowledge the financial support of the Industry/University Cooperative Research Center (IUCRC) for Advanced Studies in Novel Surfactants at Columbia University (National Science Foundation Grant EEC-98-04168), the Engineering Research Center (ERC) for Particle Science and Technology at the University of Florida (National Science Foundation Grant EEC-94-02989), and the Industrial Partners of the IUCRC and ERC.

REFERENCES

1. Somasundaran, P., Wang, Y.H.C., and Acar, S., in *Future Trends in Polymer Science and Technology*, Technomic, 1987, 134.
2. Evans, A.G. and Langdon, T.G., *Prog. Mater. Sci.*, 21, 174, 1976.
3. Remz, H.M., *Cosmetics Toiletries*, 103, 70, 1988.
4. Novotny, V., *Colloids Surf.*, 24, 361, 1987.
5. Blier, A., in *Ultrastructure Processing of Ceramics, Glasses and Composites*, L.L. Hench and D.R. Ulrich, Eds., John Wiley & Sons, New York, 1984, 391.
6. Goldsmith, H. and Mason, S.G., *Biorheology*, 12, 181, 1975.
7. Max, B., *Interfacial Phenomena in Biological Systems*, Surfactant Science Series, Vol. 39, Marcel Dekker, New York, 1991.
8. Hamaker, H.C., *Rec. Trav. Chim.*, 55, 63, 1936.
9. Pashley, R.M. et al., *Science*, 229, 1088, 1985.
10. Israelachvili, J.N. and Pashley, R.M., *J. Colloid Interface Sci.*, 98, 500, 1984.
11. van Oss, C.J., in *Interaction Forces in Aqueous Media*, Marcel Dekker, New York, 1994.
12. Somasundaran, P., Healey, T.W., and Fuerstenau, D.W., *J. Colloid Interface Sci.*, 22, 599, 1966.
13. Flory, P.J., in *Statistical Mechanics of Chain Molecules*, Wiley Interscience, New York, 1969.
14. Yoon, R-H. and Ravishankar, S.A., *J. Colloid Interface Sci.*, 166, 215, 1994.
15. Horn, R. and Israelachvili, J., *J. Phys. Chem.*, 75, 1400, 1981.
16. Christenson, H.K., *J. Dispersion Sci. Technol.*, 9, 171, 1988.
17. Christenson, H.K., *J. Colloid and Interface Sci.*, 104, 234, 1985.
18. Williams, R.A., in *Colloid and Surface Engineering: Applications in the Process Industries*, Colloid and Surface Engineering Series, Butterworth-Heinemann, Oxford, 1992, 3.
19. Lyklema, J., *Adv. Colloid Interface Sci.*, 2, 65, 1968.
20. Fowkes, F.M. and Pugh R.J., in *Polymer Adsorption and Dispersion Stability*, ACS Symposium Series, Vol. 240, 331, 1984.
21. Somasundaran, P., Huang, Y.-B., and Gryte, C.C., *Powder Tech.*, 53, 73, 1987.
22. Krishnakumar, S. and Somasundaran, P., *Colloids Surf.*, 117, 37, 1996.
23. Young, K.F. and Frederikse, H.P.R., *J. Phys. Chem. Ref. Data*, 2, 313, 1973.
24. Adamson, A.W., *Physical Chemistry of Surfaces*, 4th ed., John Wiley & Sons, New York, 1982.
25. Parfitt, G.D. and Rochester, C.H., in *Adsorption from Solution at the Solid/Liquid Interface*, G.D. Parfitt and C.H. Rochester, Eds., Academic Press, New York, 1983, 3.
26. Zangwill, A., in *Physics at Surfaces*, Cambridge University Press, New York, 1988, chap. 14.
27. Goddard, E.D. and Somasundaran, P., *Croatica Chem. Acta*, 48, 451, 1976.
28. Somasundaran, P. and Fuerstenau, D.W., *J. Phys. Chem.*, 70, 90, 1966.
29. Gaudin, A.M. and Fuerstenau, D.W., *Min. Eng.*, 7, 66, 1955.
30. Somasundaran, P. and Kunjappu, J.T., *Colloids Surf.*, 37, 245, 1989.
31. Somasundaran, P., Chandar, P., and Chari, K., *Colloids Surf.*, 8, 121, 1983.
32. Fu, E., *Doctoral Thesis*, Columbia University, New York, 1987.

33. Somasundaran, P., Snell, E. and Xu, Q., *J. Colloid Interface Sci.*, 144(1), 159, 1991.
34. Xu, Q. and Somasundaran, P., *Miner. Metal. Processing*, 9, 29, 1992.
35. Somasundaran, P. et al., *US patent*, 6051143, 2000.
36. Marczewska, A.W. and Jaroniec, M., *Montash Chem.*, 114, 711, 1983.
37. Marczewska, A.W. and Jaroniec, M., in *Surface and Colloid Science*, E. Matijević, Ed., Vol 14, Plenum Press, New York, 1987, 301.
38. Fowkes, F.M., in *Chemistry and Physics at Interfaces*, American Chemical Society, Washington, D.C., 1965, 1.
39. Krishnakumar, S. and Somasundaran, P., *Langmuir*, 10, 2786, 1994.
40. Maitra, A.N. and Eicke, H.F., *J. Phys. Chem.*, 85, 2687, 1981.
41. Krishnakumar, S., Somasundaran, P., and Yu, X., in *Proceedings of First International Forum on Particle Technology*, AIChE, Denver, 1994, 213.
42. Krishnakumar, S. and Somasundaran, P., *Colloids Surf.*, 117, 227, 1996.
43. Gu, T. and Zhu, B-Y., *Colloids Surf.*, 46, 81, 1990.
44. Flory, P.J., *Principles of Polymer Chemistry*, Cornell University Press, Ithaca, NY, 1953.
45. de Gennes, P.G., in *Scaling Concepts in Polymer Physics*, Cornell University Press, Ithaca, 1979.
46. Jones, J.S. and Richmond, P., *Faraday Trans. II*, 80, 865, 1980.
47. Scheutjens, J. and Fleer, G., in *The Effect of Polymers on Dispersion Properties*, Th. Tadros, Ed., Academic Press, London, 1982, 42.
48. Kawaguchi, M. and Takahashi, A., *Adv. Colloid Interface Sci.*, 37, 219, 1992.
49. de Gennes, P.G., *Macromolecules*, 14, 1637, 1987; 15, 1062, 1982.
50. Scheutjens, J. and Fleer, G., *J. Phys. Chem.*, 83, 1619, 1979; 84, 178, 1980.
51. Jenkel, E. and Rumbach, R., *Z. Elektrochem.*, 55, 612, 1951.
52. Sato, T. and Ruch, R., in *Stabilization of Colloidal Dispersion by Polymer Adsorption*, Marcel Dekker, New York, 1980, 3.
53. Ruehrwein, R.A. and Ward, E.W., *Soil Sci.*, 73, 485, 1952.
54. La Mer, V.K. and Healey, T.W., *Rev. Pure Appl. Chem.*, 13, 112, 1963.
55. La Mer, V.K., *J. Colloid Sci.*, 19, 291, 1964.
56. Slater, R.W. and Kitchener, J.A., *Discuss. Faraday Soc.*, 42, 267, 1966.
57. Lyklema, J., in *Flocculation, Sedimentation and Consolidation*, B. Moudgil and P. Somasundaran, Eds., Engineering Foundation, New York, 1985.
58. Ottewill, R.H. and Walker, T., *Kolloid Z.Z. Polym.*, 224, 330, 1967.
59. Healy, T.W. and La Mer, V.K., *J. Phys. Chem.*, 66, 1835, 1962.
60. Smellie, R.H. and La Mer, V.K., *J. Colloid Sci.*, 23, 589, 1958.
61. van der Ven, T.G.H., *J. Colloid Interface Sci.*, 82(1), 290, 1981.
62. Gregory, J., *J. Colloid Interface Sci.*, 42, 448, 1973.
63. Tjipangandjara, K.F. and Somasundaran, P., *Colloids Surf.*, 55, 245, 1991.
64. Tjipangandjara, K.F. and Somasundaran, P., *Adv. Powder Technol.*, 3 (2), 119, 1992.
65. Gregory, J. and Sheihin, I., *Br. Polym. J.*, 6, 47, 1974.
66. Grant, W.H., Smith, L.E., and Stromberg, R.R., *Faraday Disc. Chem. Soc.*, 59, 209, 1975.
67. Faust, S.D. and Aly, M.O., in *Chemistry of Water Treatment*, Butterworths, Boston, 1983.
68. Sato, T. and Ruch, R., Steric stabilization, in *Steric Stabilization of Colloidal Dispersion by Polymer Adsorption*, Marcel Dekker, New York, 1986.
69. Chandar, P., Doctoral thesis, Columbia University, New York, 1986.
70. Dong, D.C. and Winnik, M.A., *Can. J. Chem.*, 62, 2560, 1984.
71. Sivadasan, K. and Somasundaran, P., *Colloids Surf.*, 49, 229, 1990.
72. Maltesh, C. et al., *Langmuir*, 8, 1511, 1992.
73. Chandar, P. et al., *Langmuir*, 3, 298, 1987.
74. Campbell, A. and Somasundaran, P., *J. Colloid Interface Sci.*, 229, 257, 2000.
75. McKay, R.B., in *Interfacial Phenomena in Apolar Media*, Marcel Dekker, New York, 1987, 361.
76. Moudgil, B. and Somasundaran, P., in *Flocculation, Sedimentation and Consolidation*, AIChE, New York, 1987.
77. Tjipangandjara, K.F. et al., *Colloids Surf.*, 44, 229, 1990.
78. Shimabayashi, S., Nishino, K., and Nakagaki, M., *Colloids Surf.*, 63, 121, 1992.
79. Britt, K.W., Dillon, A.G., and Evans, L.A., *Tappi*, 60, 102, 1977.

8 Controlled Synthesis and Processing of Ceramic Oxides — A Molecular Approach

Jarl B. Rosenholm and Mika Lindén

CONTENTS

- 8.1 Introduction
- 8.2 Chemical Equilibrium Properties — The Macroscopic Scales
 - 8.2.1 Thermodynamics of Electrolyte–Ion Equilibria
 - 8.2.2 Precipitation–Dissolution Equilibria
 - 8.2.3 Anion Solvation Equilibria
 - 8.2.4 Cation Solvation Equilibria
 - 8.2.5 Complexation Reactions — Conditional Constants
 - 8.2.6 Ion Association and Hydration
 - 8.2.7 Summary
- 8.3 Atomic Equilibrium Properties — The Microscopic Scales
 - 8.3.1 The Partial Charge Model
 - 8.3.2 Condensed Species
 - 8.3.3 Complexation by Anionic Species
 - 8.3.4 Summary
- 8.4 Mixed Solvent and Nonaquatic Systems
 - 8.4.1 Organic Precursors in Aqueous Solvents
 - 8.4.2 Mixed Solvent Systems
 - 8.4.3 Inorganic Precursors in Nonaqueous Solvents
 - 8.4.4 Summary
- 8.5 Nucleation and Growth of Sol Particles
 - 8.5.1 Supersaturation of Associating and Nonassociating Ions
 - 8.5.2 Thermodynamic Description of the Nucleation and Growth
 - 8.5.3 Kinetics of Hydrolysis, Association, and Polymerization
 - 8.5.4 Summary
- 8.6 Peptization of Sols
 - 8.6.1 Electrostatic Stabilization of Sols
 - 8.6.2 Specific Binding and Surface Precipitation of Ions and Ligands
 - 8.6.3 Specific Binding of Ligands and Surface Modifiers
 - 8.6.4 Summary

- 8.7 **Controlled Gelation of Sols**
 - 8.7.1 **Mechanism of Formation of S+I- Mesophases, General**
 - 8.7.2 **Influence of Additives on CTA+-Silicate Mesophase Formation as Studied by in Situ SAXS**
 - 8.7.2.1 **No Additive**
 - 8.7.2.2 **n-Alcohols**
 - 8.7.2.3 **n-Amines**
 - 8.7.2.4 **Long-Chain Carboxylates**
 - 8.7.2.5 **Hydrocarbons**
 - 8.7.3 **Summary**
- 8.8 **List of Abbreviations**
 - 8.8.1 **Alphabetical symbols**
 - 8.8.2 **Greek Symbols**

References

8.1 INTRODUCTION

Sol-gel processing of ceramic oxides is understood in a number of ways by different scientific communities. For inorganic chemists, sol-gel synthesis is merely a synthesis route of particles whose structure is of key interest. Minor attention is paid to the intermediates leading to the formation of the particles. On the other hand, for analytical chemists the interest is directed to the complexes formed during the hydrolysis and condensation of mostly metal cations in aqueous solutions. For colloid chemists, who define the sol as a suspension of particles of colloidal dimensions (1 nm to 1 μ m), the aim is to investigate the conditions for the stabilization (or aggregation) of the sol. Recently, special attention has been paid to particles that have particular optical, electrical, and chemical properties. These nanoparticles are special in that they possess a larger fraction of atoms/molecules in the surface layer than in the bulk and fall within the 1 to 10 (-50) nm range. Sol manufacture then simply means the processing of nanosized particles without reference to the details of the synthesis route or the intermediates.

Gel formation is for most communities just as ill-defined. The most straightforward definition is provided by colloid science. Gel formation is due to the sol instabilization by physicochemical means producing a flocculated, loose network of particles extending macroscopically over the system under investigation. This should be carefully distinguished from a strong (dense) coagulated sediment. For particles with sizes lying beyond the colloidal range, the corresponding, generally used expression is aggregated loose particle ensemble and agglomerated dense (often rounded) particle cluster. The distinction is important, as quite different physicochemical conditions determine the state of these systems.

To describe the sol-gel manufacturing of ceramic oxides in a heuristic way we need to encompass the entire chain from the synthesis occurring in (most often aqueous) solutions of the elements, over the kinetically determined formation of the intermediates, to the creation of the particles. The precursor particle sols may then be processed further, forming the monoliths, gels, fibers, or sheets. In this chapter all these steps (due to the limited space allocated) are discussed and illustrated with only a few pertinent examples. The focus is on aqueous processes, but they are related to templated systems and organic solutions. Special emphasis is placed on the possibility of predicting the outcome of the synthesis through knowledge of the key parameters controlling the synthesis and the pertinent reference data needed for such analysis. Moreover, the reference scales used when producing the data available in the literature are correlated to some extent and the dependency on the physicochemical conditions is also touched upon. As indicated in the chapter title, the discussion is taken to a molecular level and limited to ionic and amorphous solids.

8.2 CHEMICAL EQUILIBRIUM PROPERTIES — THE MACROSCOPIC SCALES

In this chapter the synthesis performed in aqueous solutions is considered, first, on a thermodynamic, macroscopic scale and later on a microscopic level using atomic properties of the elements to explain or to predict the processes occurring.

8.2.1 THERMODYNAMICS OF ELECTROLYTE-ION EQUILIBRIA

It is customary to select the letters representing the species under study with reference to the properties focused on. Consequently, for an acid–base reaction A(cid) and B(ase) are useful, but for a reaction between ionic species A(nion) and C(ation) may be more illustrative. If specific attention is paid to the reaction with metal cations, then M(etal) is frequently used instead of C(ation). For the simplest case, we may thus write



This notation is somewhat confusing, because the anion (A^-) is a base (electron donor) in the Lewis sense. However, as shown later the base anion was in most cases originally a cation (A^{z+}), which upon hydrolysis reacts to anion species (A^-). We therefore maintain the notation indicated. Moreover, the equilibrium is reached for species consisting of a number of, e.g., anions and cations:



where v denotes the stoichiometric constants and z the valency (charge number) of the ions. The multiion expression chosen is important when considering reactions leading to particle formation (see below). The equilibrium constant for the reaction (8.2) is written in the usual way as

$$K_{eq}(A_{v_A} M_{v_M}) = a_{A_{v_A} M_{v_M}} / a_A^{v_A} a_M^{v_M} \quad (8.3)$$

As charge neutrality has to be obeyed, the partial reactions



have to fulfill the charge conservation condition $|z(-)v_A| = |z(+)v_M|$. If expressed with the concentration (molarity) scale the basic thermodynamic properties of the salt are

$$a_{A_{v_A} M_{v_M}} = a_{\pm}^v = a_A^{v_A} a_M^{v_M} \quad (8.5)$$

where $v = v_A + v_M$ and a is the activity of the species.¹ The mean activity can be expressed in terms of the (mean) activity coefficient and concentration as

$$a_{\pm}^v = y_{\pm}^v c_{\pm}^v = (y_A^{vA} c_A^{vA})(y_M^{vM} c_M^{vM}) \quad (8.6)$$

Thus,¹

$$y_{\pm}^v = y_A^{vA} y_M^{vM} \Leftrightarrow y_{\pm} = (y_A^{vA} y_M^{vM})^{1/v} \quad (8.7a)$$

$$c_{\pm}^v = c_A^{vA} c_M^{vM} = (v_A^{vA} v_M^{vM}) c^v \Leftrightarrow c_{\pm} = (v_A^{vA} v_M^{vM})^{1/v} c \quad (8.7b)$$

since $c_i = v_i c$. We can thus write for the activity of the salt

$$a_{\pm}^v = (v_A^{vA} v_M^{vM})(c y_{\pm})^v = (Q c y_{\pm})^v \quad (8.8)$$

where $Q = (v_A^{vA} v_M^{vM})^{1/v}$ is given as tabulated values in Table 8.1.

TABLE 8.1
The $Q (= (v_A^{vA} v_M^{vM})^{1/v})$ Factor
for Various Types of Salts

z-	z+					
	1+	2+	3+	4+	5+	6+
1-	1.0000	1.5874	2.2795	3.0314	3.8236	4.6450
2-	1.5874	1.0000	2.5509	1.5874	3.8483	2.2795
3-	2.2795	2.5508	1.0000	3.5360	4.1284	1.5874
4-	3.0314	1.5874	3.5360	1.0000	4.5279	2.5509
5-	3.8236	3.8483	4.1284	4.5279	1.0000	5.5228
6-	4.6450	2.2795	1.5874	2.5509	5.5228	1.0000

Note the smaller diagonal (and some other symmetric salt) Q values due to the different number of ions in the salt necessary to satisfy the charge conservation requirement. If we choose $\sum_i v_i = \sum_i z_i$ for the symmetric salts, the diagonal values would be 1.0000, 2.0000, 3.0000, 4.0000, 5.0000, and 6.0000, respectively.

Equation 8.2 obviously defines the general thermodynamic condition for the crystallization of solids. The equilibrium constant provides the key to calculate the standard molar Gibbs free energy for the process:

$$\Delta G_m^0 = -RT \ln K_{eq} (A_{vA} M_{vM}) \quad (8.9)$$

where R is the gas constant and T the absolute temperature.

From the temperature dependency, the entropy may be evaluated and the enthalpy may finally be calculated using the Gibbs–Helmholtz equation.

It should be noted, however, that the equilibrium between the ion species and the salt is usually thermodynamically referred to dilute solutions, i.e., sufficiently dilute that the ions do not experience other ions. Therefore, it is customary to replace the activity by the concentration. At higher concentrations the approximation $a \approx c$ is not acceptable and the change in activity should be corrected for via the activity coefficient. The tabulated equilibrium constants are, however, almost always based on concentrations and not on activities. Then, the contribution of all ions to the interaction has to be accounted for which is done by introducing the ionic strength:

$$I = \frac{1}{2} \sum_i c_i z_i^2 = \frac{1}{2} c \sum_i \nu_i z_i^2 = k c \quad (8.10)$$

for which the charge conservation condition $|z(-)\nu_A| = |z(+)\nu_M|$ must apply. The ionic strength can be rationalized by a constant $k = \frac{1}{2} \sum_i \nu_i z_i^2$ for all types of salts. In Table 8.2 the k is given as the coordinate of the multivalent anion and cation.

TABLE 8.2
The Ionic Strength Defined as $I = kc$ (where the $k = \frac{1}{2} \sum_i \nu_i z_i^2$ is read as the intersection value of the valency of the anion (A^{z-}) and cation (M^{z+}), respectively)

z^-	z^+					
	1+	2+	3+	4+	5+	6+
1-	1	3	6	10	15	21
2-	3	4	15	12	35	24
3-	6	15	9	42	60	27
4-	10	12	42	16	90	60
5-	15	35	60	90	25	165
6-	21	24	27	60	165	36

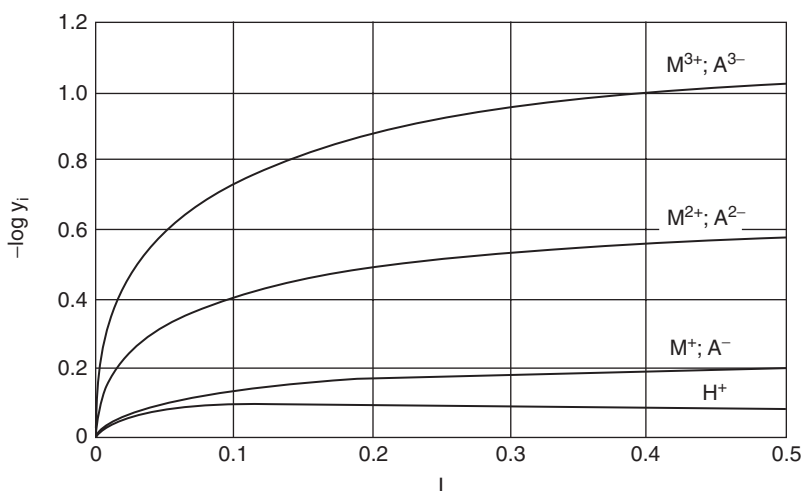


FIGURE 8.1 The relationship between the activity coefficient ($-\log y_i$) and the ionic strength for aqueous solutions of mono-, di-, and trivalent ions. (From Ringbom, A., *Complexation in Analytical Chemistry*, Wiley Interscience, New York, 1963, 24. With permission.)

For example, the ionic strength of a fully dissociated A_2M_3 salt, which at a concentration c dissociates into $2A^{3-}$ and $3M^{2+}$ ions is $15c$. Note the much lower diagonal (and some other symmetric salt) k values, which are due to the different number of ions in the salt necessary to satisfy the charge conservation requirement. If we choose $\sum_i \nu_i = \sum_i z_i$ for the symmetric salts, the diagonal values would be 1, 8, 27, 64, 125, and 216, respectively. Schematically, the contribution of the ionic strength is presented in Figure 8.1.³

It is obvious that the activity coefficients give a strong contribution at $0 < I < 0.1$. For the most dilute region, the activity constant can be corrected with, e.g., the Debye–Hückel limiting law, which for aqueous solutions at 25°C states:^{4,5}

$$-\log y_{\pm} = 0.51 |z(-)z(+)| \left[\sqrt{I} / (1 + \sqrt{I}) \right] \approx 0.51 |z(-)z(+)| \sqrt{I} \quad (8.11)$$

where the absolute value of $|z(-)z(+)|$ is for symmetric electrolytes and single ions expressed as z^2 . For 1:1 electrolytes $|z(-)z(+)| \sqrt{I} \approx \sqrt{c}$. The approximate expression is accurate to 0.01 mol/dm³, but the extended form has been used approximatively to 0.1 mol/dm³. For ionic strengths of 0.001, 0.01, and 0.1 the bracket becomes 0.03, 0.09, and 0.24, respectively. However, when $|z(-)z(+)| \geq 4$, large deviations may be found already at 0.01 mol/dm³. Other extended variants of the Debye–Hückel limiting law apply for wider concentration ranges.² In dilute solutions both the concentrations and the ionic strength may favorably be expressed in terms of pc and pI ($p = -\log$), respectively, in accordance with the acidity (pH).

The single ion activity coefficient in Figure 8.1 for each ion participating in the equilibrium may be used to correct graphically each concentration (Equation 8.10) to its activity. The change in y_i expressed with concentrations is dramatically reduced at higher ionic strengths. It is only for ions with high charges (valencies) where a considerable change can be found. In particular, the constancy of the proton should be noted, which indicates that only a minor error is introduced if the concentration instead of the activity of the proton is used to define the pH. For the tabulation of chemical equilibrium data the ionic strength at which K_{eq} has been determined should clearly be specified.

The definition of the limit for dilute solutions is obviously important for the proper use of available chemical data. Moreover, as this property is also of particular importance for the sol–gel process discussed later it deserves further analysis. In the Debye–Hückel ionic-cloud model, the influence of dissolved ions on a particular central ion is evaluated by comparing the mean distance between ions to the dimension of the ion cloud surrounding it. The latter is evaluated by the so-called Debye (or Debye–Hückel reciprocal) length ($1/\kappa$), which may be approximatively written for aqueous solutions at 25°C as⁶

$$1/\kappa = \left[(\epsilon_r \epsilon_0 RT / (2F^2 I)) \right]^{1/2} \approx 9.6223 * 10^{-9} (kc)^{1/2} \quad (8.12)$$

where F is the Faraday constant, ϵ_r the relative dielectric constant, ϵ_0 the permittivity of vacuum, R the gas constant, and T the absolute temperature. The k parameter in parenthesis is for aqueous solutions at 298 K and is given in Table 8.2. As discussed later the Debye length is in the nanometer range for most electrolyte solutions more dilute than 0.1 mol/dm³. The Debye lengths for a range of salts are given in Tables 8.3 and 8.4.

The numerical values in Table 8.3 hold for all odd decade concentrations (e.g., $c = 10^{-1}$, 10^{-3} , 10^{-5} , etc. mol/dm³). However, for $c = 10^{-1}$ (= 0.1) mol/dm³ the given Debye length has to be divided by 10 and for $c = 10^{-5}$ mol/dm³ the Debye length has to be multiplied by 10, etc.

Accordingly, the numerical values of Table 8.4 hold for all even decade concentrations (e.g., $c = 1$, 10^{-2} , 10^{-4} , etc. mol/dm³). However, for $c = 1.0$ mol/dm³ the given Debye length has to be divided by 10 and for $c = 10^{-4}$ mol/dm³ the Debye length has to be multiplied by 10, etc.

If $1/\kappa$ is larger than the mean distance between ions ($= (1/2 N_A c)^{1/3}$), 1:1 electrolyte the long-range Coulombic interactions dominate the interaction and the Debye–Hückel ion cloud is said to be fine grained.⁷ If $1/\kappa$ is smaller than the mean distance between ions the ion cloud is said to be coarse grained while the nearest ion is not within the Debye–Hückel cloud. Then non-Coulombic interactions of a neighboring ion to the central ion contribute to the overall interaction.⁷ It is found that

TABLE 8.3
The Approximative Debye Length for 0.001 mol/dm³ Electrolyte Solutions in nm Defined in Equation 8.12 (read as the intersection value of the valency of the anion, A^{z-}, and cation, M^{z+}, respectively)

z-	z+					
	1+	2+	3+	4+	5+	6+
1-	9.622	5.556	3.928	3.043	2.484	2.100
2-	5.556	4.811	2.484	2.778	1.626	1.964
3-	3.928	2.484	3.207	1.485	1.242	1.852
4-	3.043	2.778	1.485	2.406	1.014	1.242
5-	2.484	1.626	1.242	1.014	1.924	0.749
6-	2.100	1.964	1.852	1.242	0.749	1.604

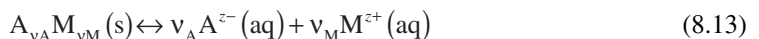
TABLE 8.4
The Approximative Debye Length for 0.01 mol/dm³ Electrolyte Solutions in nm Defined in Equation 8.12 (read as the intersection value of the valency of the anion, A^{z-}, and cation, M^{z+}, respectively)

z-	z+					
	1+	2+	3+	4+	5+	6+
1-	3.043	1.757	1.242	0.962	0.786	0.664
2-	1.757	1.521	0.786	0.879	0.514	0.621
3-	1.242	0.786	1.014	0.470	0.393	0.586
4-	0.962	0.879	0.470	0.761	0.321	0.393
5-	0.786	0.514	0.393	0.321	0.609	0.237
6-	0.664	0.621	0.586	0.393	0.237	0.507

0.001 mol/dm³ may be taken as the limit above which the simple ion interaction for 1:1 electrolytes ceases to apply.

8.2.2 PRECIPITATION–DISSOLUTION EQUILIBRIA

The precipitation of solids is for the sake of thermodynamic clarity tabulated as solubility product constants in the literature. The relevant equilibrium is the reverse of the process (Equation 8.2), i.e., the dissolution of a solid to an equilibrated saturated solution:



where (s) denotes the solid phase and (aq) the saturated aqueous phase. As the solid phase is taken as the standard state ($a_{A_{v_A}M_{v_M}} = 1$), we may write

$$K_{\text{sp}}(A_{\text{vA}}M_{\text{vM}}) = a_{A(\text{aq})}^{\text{vA}} a_{M(\text{aq})}^{\text{vM}} \quad (8.14)$$

It is furthermore postulated that the saturated solution in equilibrium with the sparingly soluble solid is sufficiently dilute to be considered ideal, and we may thus set the activity coefficients $y_A = y_M \approx 1$, giving

$$K_{\text{sp}}(A_{\text{vA}}M_{\text{vM}}) \approx c_{A(\text{aq})}^{\text{vA}} c_{M(\text{aq})}^{\text{vM}} = (Qc_{(\text{aq})})^{\text{v}} \quad (8.15)$$

where Q was given in Table 8.1. To clearly distinguish from the other equilibria present in the aqueous solutions it is useful to denote the negative logarithm of the solubility product constant pS to conform with the pH concept. The standard state chosen for the solubility product is in accord with the other solvent scales that refer to dilute solutions.

The solubility product constant may be determined by direct measurements or calculated from the standard Gibbs free energies of formation (ΔG_f°) of the species involved at their standard states. For the reaction scheme (Equation 8.13) the Gibbs free energy change is:⁸

$$\Delta G_m^\circ = v_A \Delta G_f^\circ(A^{z-}, \text{aq}) + v_M \Delta G_f^\circ(M^{z+}, \text{aq}) - \Delta G_f^\circ(A_{\text{vA}}M_{\text{vM}}, s) \quad (8.16)$$

The solubility product constant is then calculated in accordance with Equation 8.9 as

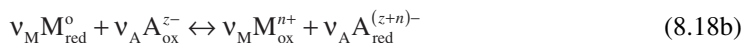
$$\text{pS} = -\log K_{\text{sp}}(A^{\text{vA}}, M^{\text{vM}}) = -\log(a_{A(\text{aq})}^{\text{vA}} a_{M(\text{aq})}^{\text{vM}}) = -\text{v} \log a_{\pm} \quad (8.17)$$

The simple notation used above is based on sparingly soluble salts in solution. The straightforward presentation may be obscured if the ions are solvated, which is discussed below. In Figure 8.2 the solubility of a range of salts is plotted as a function of pH.⁹

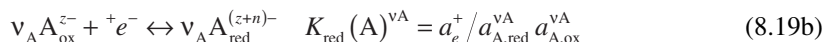
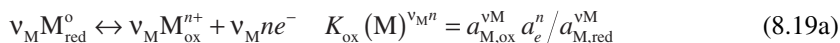
The partial reactions (Equation 8.4) may also be used to account for the reduction–oxidation (red-ox) processes frequently occurring in the solutions. Assuming a greater power for M to reduce A, we may write for the transfer of n electrons the general red-ox reaction:



where the charge neutrality $|v_M(z+n)(+)| = |v_A(z+n)(-)|$ must prevail. However, the red-ox reactions must be related to the reduction of the substances to their neutral elements (Scheme 8.4b). If we assume that the cation is oxidized from pure metal ($n = z(+)$),



We may write the partial reactions as oxidation and reduction reactions, respectively:



The greater the $K_{\text{red}}(M)$, the greater is the power of M_{red}^0 to reduce A_{ox} in Scheme 8.18. For the overall reaction the equilibrium constant is

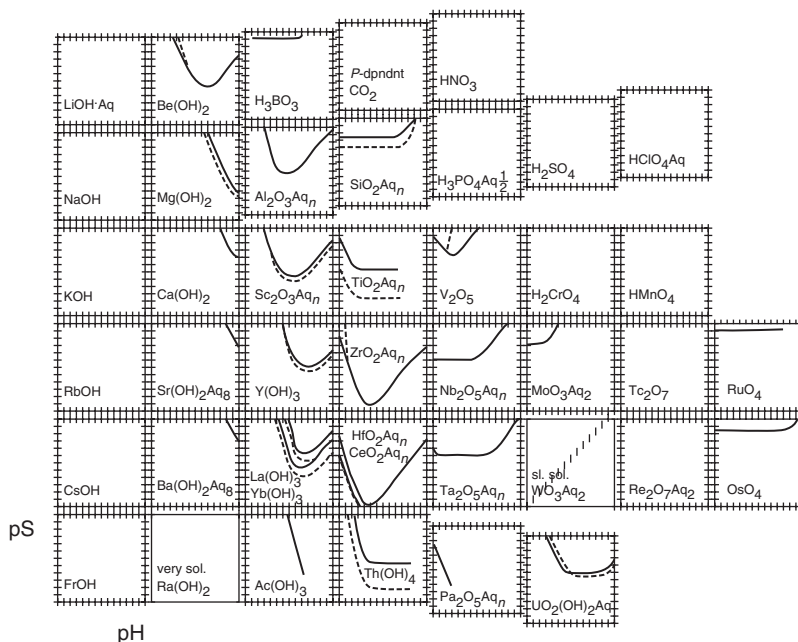


FIGURE 8.2 The solubility of metal oxides and hydroxides ($-\log S_m$) as a function of pH at or near 25°C in 1.0 mol/dm³ aqueous solutions assuming noble gas ions. The pS ranges from 12 to 0 and pH from 0 to 14. The solid curve represents initial equilibria and the dashed curve represents aged solution equilibria. (From Rich, R.L., *J. Chem. Ed.*, 62, 44, 1985. With permission of the American Chemical Society.)

$$K_{ro} = a_{M,ox}^{vM} a_{A,red}^{vA} / a_{M,red}^{vM} a_{A,ox}^{vA} = K_{red} (A)^{vA} / K_{red} (M)^{vM} \quad (8.20)$$

provided that $v_{m,n} = v_{A,n}$.

The standard molar Gibbs free energy for the red-ox process is defined in the traditional way as

$$\Delta G_m^\theta = G_m - G_m^\theta = -RT \ln K_{ro} \quad (8.21)$$

The standard electrode potentials (electromotoric forces, EMK, E_{red}^θ for different reduction reactions are tabulated in most textbooks on physical chemistry.^{2,5}

$$\Delta E_{red} = E_{red} - E_{red}^\theta + (RT/F) \ln(a_{M,ox}/a_{M,red}) \quad (8.22)$$

The potential is given as the difference between the potential of the element and that of the solution. A positive E value indicates that the reduction reaction is spontaneous. Noble metals have positive E values, whereas the opposite is true for (non-noble) metals, such as Na and K, which have negative E values. In the latter case the Gibbs free energy becomes negative and the reaction proceeds spontaneously. The relationships between ΔG_m^θ and $\Delta E_{(v)}^\theta$ are given by the equality

$$\Delta G_m^\theta = -RT \ln K_{ro} = -n\Delta E^\theta F \quad (8.23a)$$

$$\log K_{ro} = (zEF/2.3RT) = 16.92n\Delta E^\theta \quad (8.23b)$$

at 25°C when the potential is given in volts. The mean activity coefficient of the dissolved salt may thus be related to the electrochemical potential with reference to the pure element.

Written in logarithmic form, Scheme 8.19a (when $v_M = 1$) gives

$$pe = -\log a_e = (1/n) \left[-\log K_{\text{red}}(M) + \log \left(a_{M,\text{red}} / a_{M,\text{ox}} \right) \right] \quad (8.24)$$

Moreover, it is defined that $(1/n)[- \log K_{\text{red}}(M)] = pe_o$ and therefore we obtain

$$pe = pe_o + \left[\log \left(a_{M,\text{ox}} / a_{M,\text{red}} \right) \right] \quad (8.25)$$

This scale provides a reversed measure of the reducing power of the solutions in the same way as pH is the reversed scale of acidity. The smaller the pe, the more strongly reducing the solution. We thus obtain

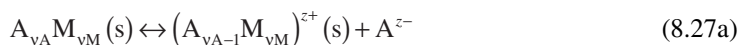
$$pe = 16.92E \quad (8.26)$$

at 25°C when E is given in volts.

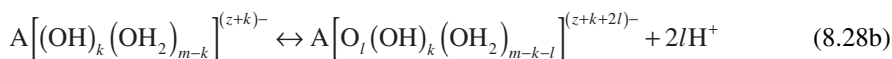
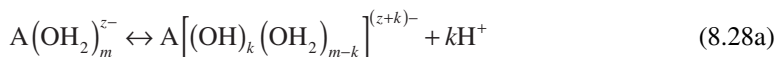
The pe expression is thus chosen to conform with the pH principles. However, the relationship between the red-ox state of the hydrated elements and the pH is usually given as E–pH relationships. In the Pourbaix diagrams¹⁰ presented in [Figure 8.3](#) it is assumed that $(a_{M,\text{ox}}/a_{M,\text{red}}) = 1$.

8.2.3 ANION SOLVATION EQUILIBRIA

Anion solvation leads to reactions with the solvent molecules producing a variety of anions possibly with reversed charge. This influences the pH for the aqueous solution of the hydrolyzed ions (see below). The pH concept is, however, traditionally only dealt with for the ions of the (IVB–) VB–VIIB groups producing what is called acids, although it is well known that metal cations are also acidic when dissolved in water. We may think of the acids as formed through the dissolution and hydrolysis of the acidic (anionic) element:



where m is the coordination number of the anion. The Brønsted acidity is due to the release of protons from the aquo complex formed:



where the ion species and their equilibrium constants are identified with their deprotonation constants k and l . The involvement of water in the deprotonation is omitted for clarity. The partial equilibrium constants for the deprotonation steps may then be combined to give the equilibrium constant for the formation of the acid:

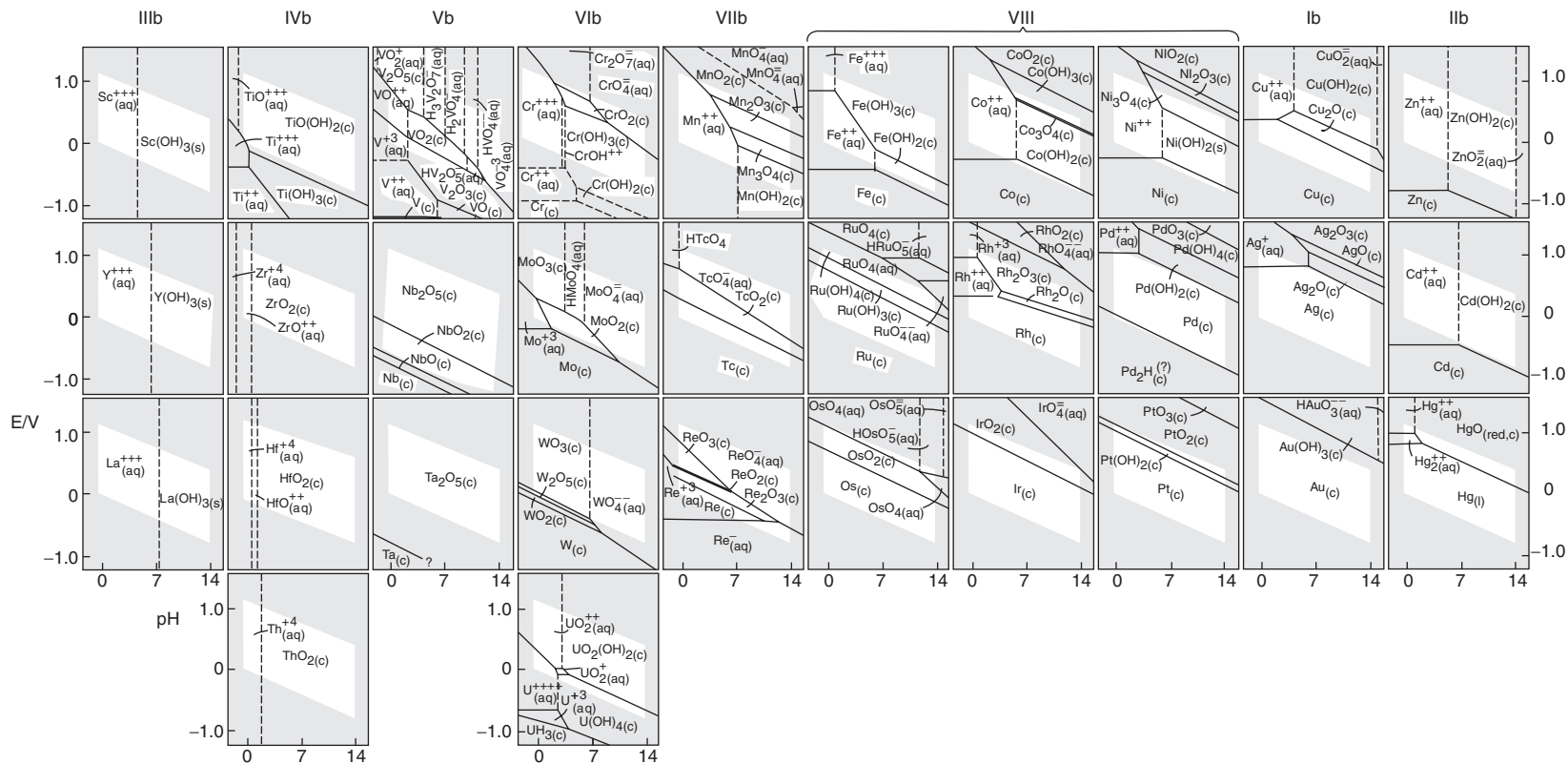
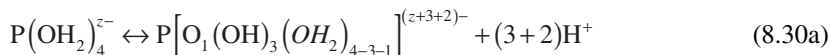


FIGURE 8.3 The dependency of the metal ion speciation on the standard electrode potential (E) and pH (Pourbaix diagram). (From Campbell, J.A., *Chemical Systems*, W.H. Freeman, San Francisco, 1970, 1020–1021. With permission.)

$$\left. \begin{aligned} K_k &= a_{Ak} a_H^k / a_{Aw} \\ K_l &= a_{Akl} a_H^{2l} / a_{Ak} \end{aligned} \right\} K_{kl} = K_k * K_l = a_{Akl} a_H^{k+2l} / a_{Aw} \quad (8.29)$$

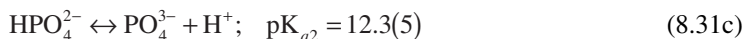
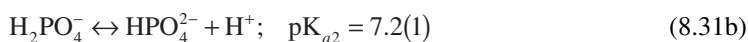
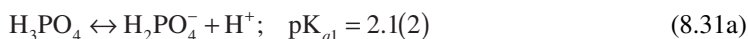
where a_{Aw} denotes the activity of the aquo complex. These steps are not referred to in the textbooks when introducing an acid. For example, we assume that $A = P$ (phosphorus), $m = 4$, $k = 3$, and $l = 1$. We then obtain phosphoric acid (reaction in one step):



Obviously, the (cationic) phosphorus must be given an oxidation state of +5 (instead of E⁻) in order for the phosphoric acid to be neutral:



Thus, as discussed above, the acid element is originally a Lewis base (cation)! The neutral phosphorus acid ($P[O_1(OH)_3]^0 = H_3PO_4$) may then stepwise release the protons as a function of the pH to produce the anionic species expected:



This procedure of expressing the acids as oxo-hydroxo complexes of water is in full agreement with the corresponding reactions occurring with, e.g., the transition metal cations in aqueous solutions. [Table 8.5](#) provides the dissociation constants for acids expressed in this unconventional way.¹⁰

In the table the pK_a for $CO(OH)_2$ is corrected (from the value given in parenthesis) for the influence of the partial pressure. Some of the pK_a values are estimated. However, from the tabulation it is fully clear that the deprotonation is very much predominated by the degree of oxolation of the core acid (cat)ion. The oxidation state and the degree of hydroxylation has only a second-hand effect on the protonation strength. It is well known that the first deprotonation can for inorganic acids be described as⁴

$$pK_a = 7 - 5l \quad (8.32a)$$

where l = the number of oxo ligands in the acid (Scheme 8.28b). For the series $Cl(OH)$, $ClO(OH)$, $ClO_2(OH)$, and $ClO_3(OH)$ we would then expect the pK_a values to be 7, 2, -3, and -8, respectively. They are not far from the values listed. For some acids it is important to know the real number of oxygen atoms bound directly to the core atom to choose a correct l number. For example, phosphorous acid can vary with an increasing number of hydrogen atoms bound directly to P. The protons do not change either the l number or the pK_a value. The empirical formula for the second and third dissociation step is⁴

$$pK_a = 7 - 5(l + 2z) \quad (8.32b)$$

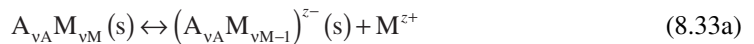
TABLE 8.5
The First Dissociation Constant of Acids in Aqueous Solution at 25°C
(arranged according to the degree of oxolation)

$z = 1$		$z = 3$		$z = 5$		$z = 7$	
Cl(OH)	7.4	ClO(OH)	2.0	ClO ₂ (OH)	-1	ClO ₃ (OH)	-7
Br(OH)	8.6	IO(OH)	1.6	IO ₂ (OH)	0.8	IO ₃ (OH)	1.6
I(OH)	10.2						
$z = 3$		$z = 4$		$z = 6$			
As(OH) ₃	9.4	SO(OH) ₂	1.9	SO ₂ (OH) ₂	<0		
Sb(OH) ₃	11.0	SeO(OH) ₂	2.5	SeO ₂ (OH) ₂	<0		
		TeO(OH) ₂	2.2	TeO ₂ (OH) ₂	<0		
$z = 4$		$z = 3$		$z = 5$			
Si(OH) ₄	9.9	NO(OH)	3.3	NO ₂ (OH)	-1.4		
Ge(OH) ₄	8.6						
$z = 3$		$z = 5$					
B(OH) ₃	9.3	PO(OH) ₃	2.1				
		AsO(OH) ₃	2.3				
		$z = 4$					
		CO(OH) ₂	3.9 (6.4)				

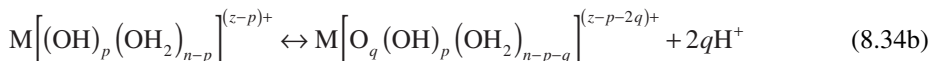
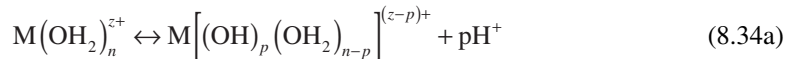
where z = charge (valency). For the series PO(OH)₃, PO₂(OH)₂⁻, PO₃(OH)₂²⁻ the expected pK_a value is ($l = 1, z = 0$) 2, ($l = 2, z = -1$) 7, and ($l = 3, z = -2$) 12, respectively. Each deprotonation step enhances the pK_a by about 5 pH units. This trend holds also for the negative oxidation states represented by the hydride acids in aqueous solutions. For di- or oligo-nuclear acids the correlation is not so straightforward. It should also be noted that these pK_a values must be corrected for the ionic strength. For example, for a 0.1 mol/dm³ acetic acid solution, the pK_a = 4.76 is expected to change to 4.64. We will return to this analysis when discussing the atomic properties of the acids and hydrolyzed metal cations.

8.2.4 CATION SOLVATION EQUILIBRIA

It is now time to relate the solubility of ion species with the acidity of the solution. In the same way as for the anion (Equation 8.27) we may write for the cation



where n is the coordination number of the cation. The acidity is due to the release of protons from the aquo complex formed:

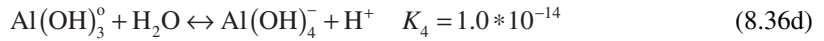
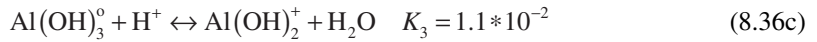
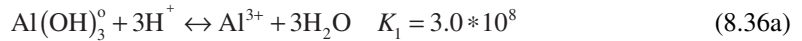


where the involvement of water in the deprotonation is omitted for clarity. Although the hydrolyzed species are presented for consistency as cations, it is obvious that when the deprotonation proceeds anionic species may also form. As will be shown later this holds true especially for the oxalated species. The partial equilibrium constants for the deprotonation steps may then be combined to give the equilibrium constant for the formation of the acid:

$$\left. \begin{aligned} K_p &= a_{M_p} a_{H^+}^p / a_{M_w} \\ K_l &= a_{A_{pq}} a_{H^+}^{2q} / a_{M_p} \end{aligned} \right\} K_{pq} = K_p * K_q = a_{M_{pq}} a_{H^+}^{p+2q} / a_{M_w} \quad (8.35)$$

where the ion species and their equilibrium constants are identified with their deprotonation constants p and q .

We may as an example take the hydrolysis reactions of aluminum as total reactions from $Al(OH)_3^0$ (Gibbsite) at an ionic strength of 0.011. The solubility of Gibbsite has been found to be determined by the following equilibria:^{11,12}



The other mononuclear and oligomeric ion species as well as the contribution from the $Al(OH)_3^0$ complex can be neglected. The total aluminum content in solution may thus be calculated from the concentration of the ion species indicated:

$$[Al]_{tot} = [Al^{3+}] + [Al(OH)^{2+}] + [Al(OH)_2^+] + [Al(OH)_3^0] + [Al(OH)_4^-] \quad (8.37)$$

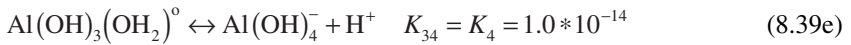
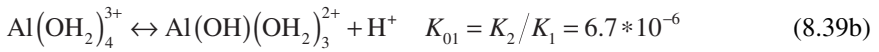
Inserting the equilibrium constants, we obtain the pH dependency of the solubility when the ionic strength is 0.011 as:^{11,12}

$$[Al]_{tot} = 3.0 * 10^8 [H^+]^3 + 2.0 * 10^3 [H^+]^2 + 1.1 * 10^{-2} [H^+] + 1.0 * 10^{-14} [H^+]^{-1} \quad (8.38)$$

The fit was found to be accurate within 3% despite that a large number of other species contribute a minor amount to the equilibrium. The equilibria may be used to describe the deprotonation steps of the hydrated aluminum ion. However, to be correct a coordination number of 4 or 6 should be chosen for the Al^{3+} ions. Despite that the sixfold coordination seems to be more realistic for aqueous solutions whereas four is typical for structural aluminum (in solids), we assume for clarity a coordination number of four. Then, we obtain the following reactions for the hydrated aluminum ion:

TABLE 8.6
The Experimental Activity Products and the
Corresponding Standard Gibbs Free Energy
of Formation of Al(OH)₃⁰ and the Hydroxoions
of Aluminum

Activity Products	1.3 * 10 ⁸	1.3 * 10 ³	9.5 * 10 ⁻³	8.9 * 10 ⁻¹⁵
$\Delta G_f^\circ/\text{kJ/mol}$	-1154.8	-698.3	-905.8	-1311.7



where the equilibrium constants are identified by the protonation step in question. The $\text{p}K_a$ value reported for the six coordinated aquo ion ($\text{Al}(\text{OH}_2)_6^{3+}$) is 5.0, which agrees closely with the equilibrium constant ($\text{p}K_a = 5.2$, Equation 8.39b) for the four-coordinated ion assumed here. Multiplying the concentration of the ion species with their activity coefficients we may calculate the solubility product (Equation 8.17) and the standard Gibbs free energy (Equation 8.16). Combined with the Gibbs free energy of formation of the Al^{3+} ion (-489.40 kJ/mol) and water (236.77 kJ/mol) we may calculate the standard Gibbs free energy for $\text{Al}(\text{OH})_3^0$ and the ion species (Equations 8.14 and 8.15; Table 8.6).^{11,12}

The values reported by different authors vary to some degree as a result of the experimental conditions (concentration, ionic strength, temperature, etc.) and the sensitivity of the detection methods used. For a 1 mol/kg ion concentration, the species listed in Figure 8.4 were found to contribute to the solubility equilibrium.¹³ It is obvious that the ionic strength influences the solubility to a great extent, as shown by the species distribution of aluminum in Figure 8.5.¹³ The pH dependency of the solubility clearly varies also for elements in the same group (Figure 8.6).¹⁴

For silica the corresponding equilibrium is much simpler, as the solubility remains at a constant level under acidic conditions. However, the solubility is much larger than for the metal oxides (see Figure 8.2). The solubility is illustrated in Figure 8.7.¹⁵

The solubility in the acidic–neutral range may be described by the Cherkinskii equation:¹⁵

$$\text{pc}_{\text{Si}} = -\log c_{\text{Si}} = 2.44 + 0.053\text{pH} \quad (8.40)$$

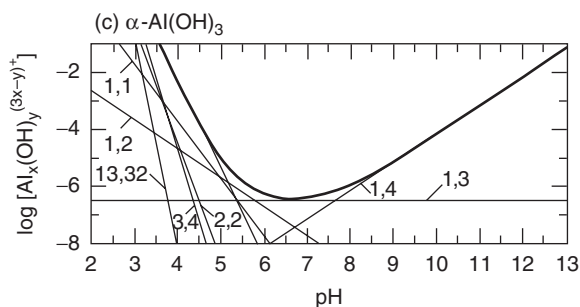


FIGURE 8.4 The relative concentration of different aluminum (III) hydroxide species as a function of pH at 25°C in 1.0 mol/dm³ aqueous solutions. The bold line represents the solubility limit. (From Baes, C.F. and Mesmer, R.E., *The Hydrolysis of Cations*, John Wiley & Sons, New York, 1976. With permission.)

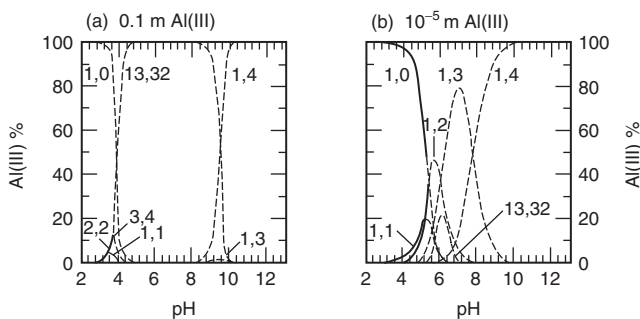


FIGURE 8.5 The relative concentration of different aluminum (III) hydroxide species as a function of pH at 25°C in 10⁻¹ (a) and 10⁻⁵ (b) mol/dm³ aqueous solutions. (From Baes, C.F. and Mesmer, R.E., *The Hydrolysis of Cations*, John Wiley & Sons, New York, 1976. With permission.)

The reason for the enhanced solubility of metal cations (e.g., Al³⁺) at low pH is their weaker M–O bond, which sensitizes it for acidic attack. In alkaline solutions the silica structure is disintegrated due to the formation of different soluble anionic silica species. In Figure 8.8 the strength of the M–O bond is plotted as a function of the ion potential ($\psi = z/r$).¹⁶ Note the exceptional bond strength of Si–O and Al–O, which are the most abundant elements.

The solubility of the cations is closely related to their hydration enthalpies. It has been found that it is possible to correlate the hydration enthalpies of cations with the inverse of their “effective hydration radii” (r_{eff} in nm). Thus, by adding 0.085 nm (\approx radius of the oxygen atom in water) to the Pauling crystal radius, the following expression¹⁷ is obtained:

$$\Delta H = -6987 \left(z^2 / r_{\text{eff}} \right) \text{ kJ/mol} \quad (8.41)$$

For anions, a linear plot is obtained by adding 0.01 nm to the Pauling crystal radius.

The ionic hydration energies (enthalpies and Gibbs free energies) of metals are consequently roughly a linear function of the square of the oxidation state divided by the effective ion radius (z^2/r_{eff} , Figure 8.9).¹⁷ It may be added that ΔH_{hyd} and ΔG_{hyd} , respectively, of the individual alkali halide ion pairs form two linear branches with a maximum at CsI (KBr).

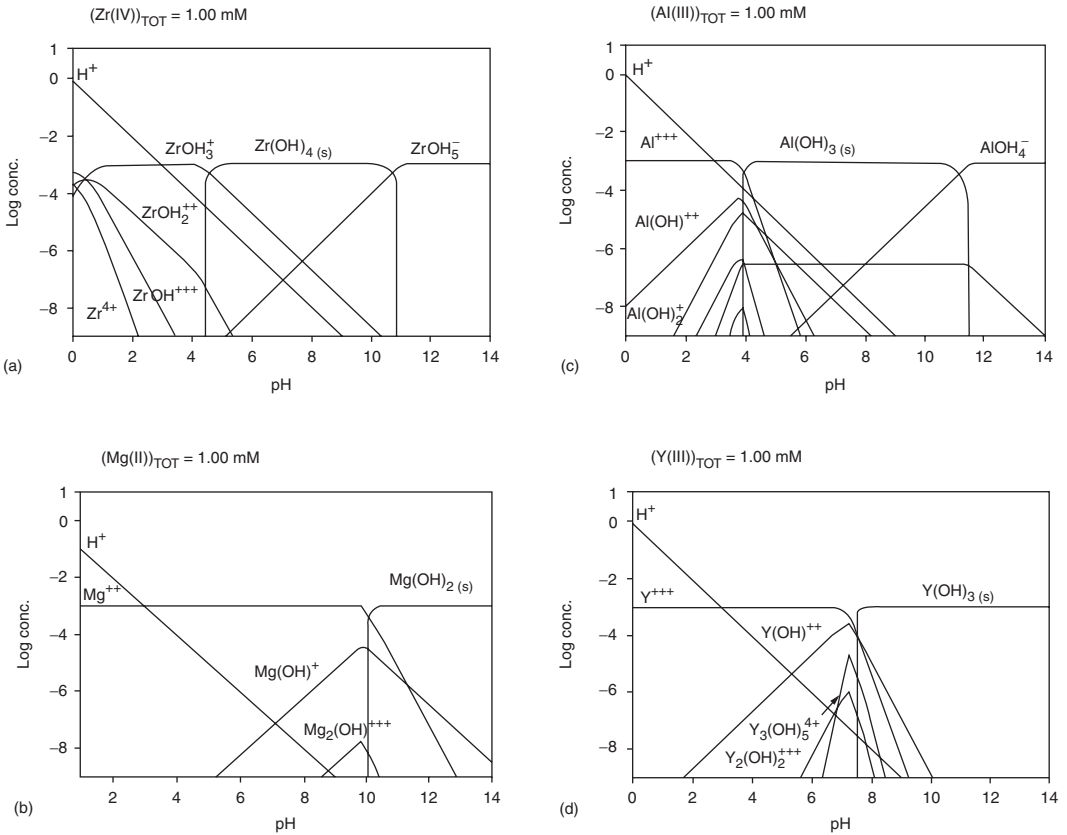


FIGURE 8.6 The relative concentration of different zirconium, aluminum, magnesium, and yttrium hydroxide species as a function of pH at 25°C in 1.0 mol/dm³ aqueous solutions. (From Bergström, L., in *Surface and Colloid Chemistry in Advanced Ceramics Processing*, R.J. Pugh and L. Bergström, Eds., Marcel Dekker, New York, 1994, 100–101. With permission.)

8.2.5 COMPLEXATION REACTIONS — CONDITIONAL CONSTANTS

So far, only the reactions with the solvent assumed to be water have been considered. However, in practical situations other components are usually simultaneously present in the solutions, including impurities, reaction products, and cosolvents. We thus need a simple method to present the equilibrium of interest. One approach to resolve this problem is the use of conditional constants originally introduced by Schwarzenbach as apparent constants and developed further by Ringbom and Kolthoff.³ For a simple reaction between an L(igand) and a M(et al) ion, the ML complex is formed:



where the equilibrium constant K_{ML} is also denoted the stability constant for the complex. However, if all the other side reactions M and L participates in are accounted for, we can express the conditional stability constant as

$$K_{ML'} = c_{ML} / c_M' c_L' \quad (8.43)$$

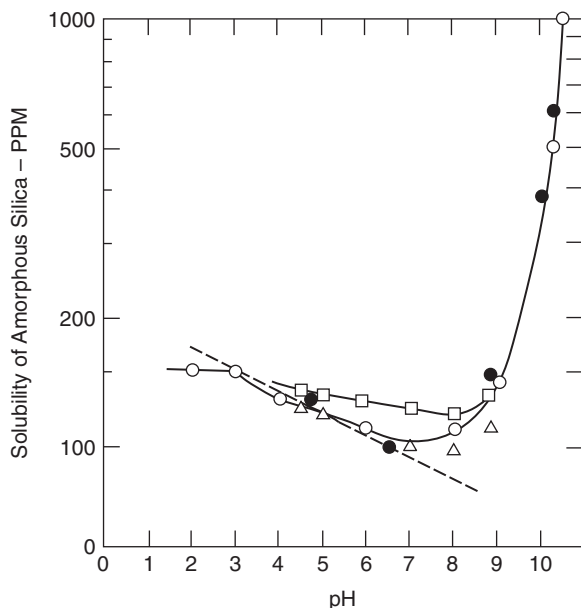


FIGURE 8.7 The solubility of amorphous silica as a function of pH: O 12°C, ● 19°C, Δ 20°C and □ 30°C. (From Iler, R.K., *The Chemistry of Silica*, John Wiley & Sons, New York, 1979, 42. With permission.)

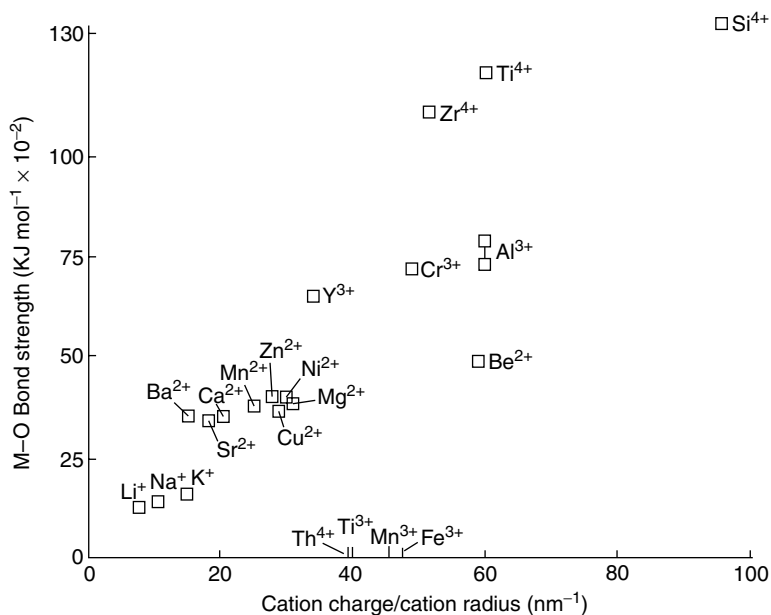


FIGURE 8.8 The strength of the metal–oxygen bond related to the metal cation ion potential (charge/radius). The average values refer to the gas–solid transition at 18°C. (From Terry, B., *Hydrometallurgy*, 10, 135, 1983. With permission of Elsevier Science.)

where, e.g., c'_M denotes the sum of all concentrations of the different M-containing species present which have not reacted with L. The reverse holds obviously for c'_L . Frequently, it is specially indicated whether both the M and L or only one of their side reactions is considered by placing

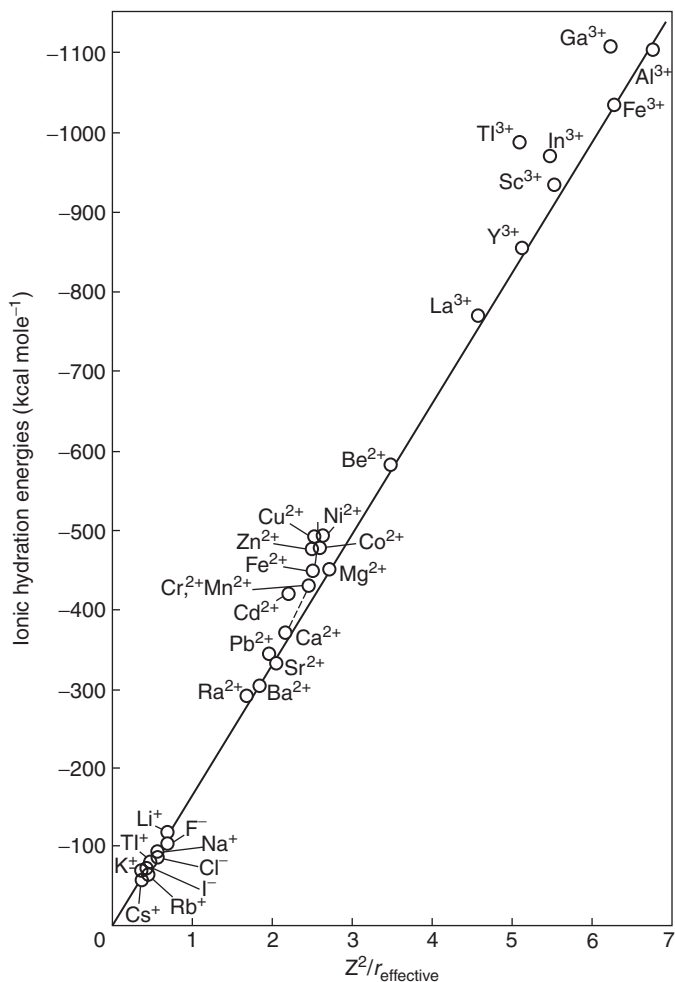


FIGURE 8.9 The ion hydration energy plotted as a function of the square of the valency divided by the effective radius of the cation. (From Phillips, C.S.G. and Williams, R.J.P., *Inorganic Chemistry*, Oxford University Press, New York, 1965, 162. With permission.)

the prime on those reactants, e.g., $K_{ML'}$. Of course, the conditional constants will be dependent on the physicochemical reaction conditions. The conditional constant may be related to the stability constant with the so-called α coefficients:³

$$K_{ML'} = K_{ML} / \alpha_M \alpha_L \Leftrightarrow \alpha_M = c_{M'} / c_M \quad \text{and} \quad \alpha_L = c_L / c_{L'} \quad (8.44)$$

The α coefficients may thus be considered a measure of the degree of side reactions. If no side reactions occur, $\alpha = 1$. Obviously, the α coefficients must be functions of the equilibrium constants, e.g.,

$$\alpha_{M(A)} = 1 + c_A K_{MA} + c_A^2 K_{MA2} + \dots \quad (8.45a)$$

$$\alpha_{L(B)} = 1 + c_B K_{BL} + c_B^2 K_{B2L} + \dots \quad (8.45b)$$

Clearly, e.g., the $\alpha_{M(A)}$ corrects the stability constant for side reactions between M and A. The terms on the right-hand side thus represent the concentrations of the disturbing complexes expressed terms of c_M and c_L , respectively. The stability constants and the α coefficients have been tabulated for a wide range of complexes.

It should be noted that the conditional constants may also be used for neutralization reactions, red-ox reactions, and precipitation reactions. This treatment provides a rational approach to the interference of specifically interacting (multivalent) ions and ligands on the purely ionic interaction and complexation reactions (e.g., hydrolysis) of interest. It is, however, clear from Equation 8.45 that the disturbing action of ligands and competing metal cations is reduced upon dilution.

8.2.6 ION ASSOCIATION AND HYDRATION

It is of general interest to find ways to determine and to interpret the mean activity coefficient of electrolyte solutions. The reason is that this coefficient should indicate the degree of deviation from ideality. When considering the synthesis of particles from solution the deviation is most probably due to clustering of the ions prior to precipitation. Recently, pure empirical fitting of the mean activity coefficient to the degree of association (β) has provided interesting results. It was found that most electrolytes for which data are available for concentrations extending to very concentrated solutions are represented by two regions. For dilute solutions, the data may be represented by the degree of dissociation ($= 1 - \beta$):¹⁸

$$\ln y_{\pm} = s \ln(1 - \beta) \quad (8.46)$$

where s is a regression constant. It may be claimed that since the specific conductivity is related to the transport properties of the ions, the degree of ionization may favorably be expressed by the ratio of the molar conductivity to the limiting molar conductivity at infinite dilution: $\beta = [(\Lambda^{\infty} - \Lambda)/\Lambda^{\infty}]$. An association that reduces the activity is then expected to sensitively influence the molar conductivity. For dilute solutions we may write (Equation 8.46)

$$\ln a_{\pm} = \ln(Qc y_{\pm}) = \ln(Qc) + s \ln[(\Lambda^{\infty} - \Lambda)/\Lambda^{\infty}] \quad (8.47)$$

For concentrated solutions ($c_{\text{cell}} > 1 \text{ mol/dm}^3$) the data follow the empirical relationship:¹⁸

$$\ln y_{\pm} = -t \ln(1 - \beta) - u \quad (8.48a)$$

where t and u are regression constants. Equation 8.48a may be rewritten by substituting $u = t \ln v$, where v is a (regression) constant:¹⁸

$$\ln y_{\pm} = -t \ln \alpha - t \ln v = -t \ln[v(1 - \beta)] \quad (8.48b)$$

Equations 8.46 and 8.48a are not functions of concentration or ionic strength. These equations provide linear fits at least up to 10 mol/dm^3 . However, in the intermediate range (0.1 to 1.0 mol/dm^3) there is a curved section interlinking the two linear branches (Figure 8.10).¹⁸

In particular, the analytical concentration seems alone to be a parameter quite unsuitable for this purpose. Moreover, the relationship of the mean activity coefficient to the degree of association is exponential. Although a premature conclusion, it may be supposed that fractal aggregation (to particles) may be related to the mean activity coefficient.

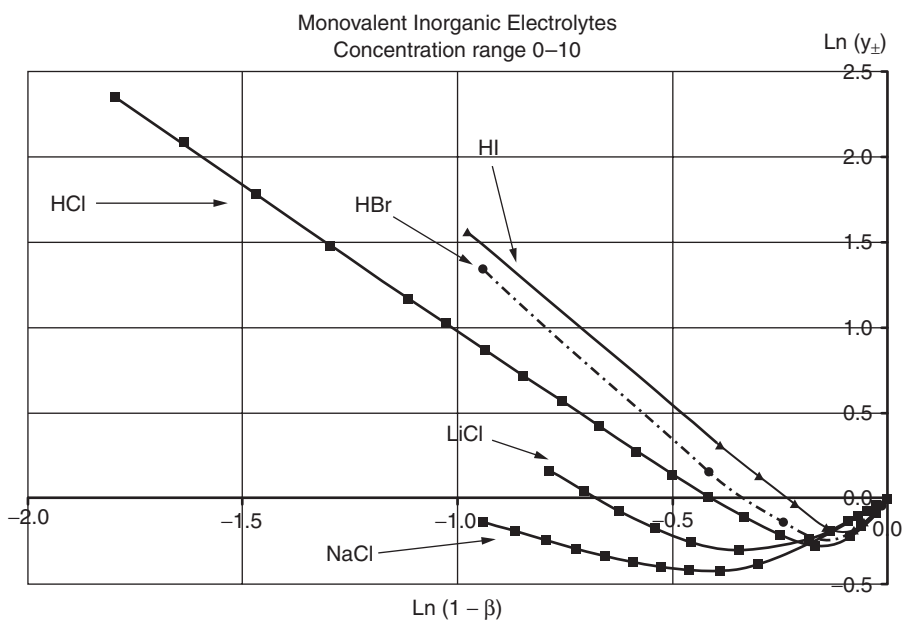
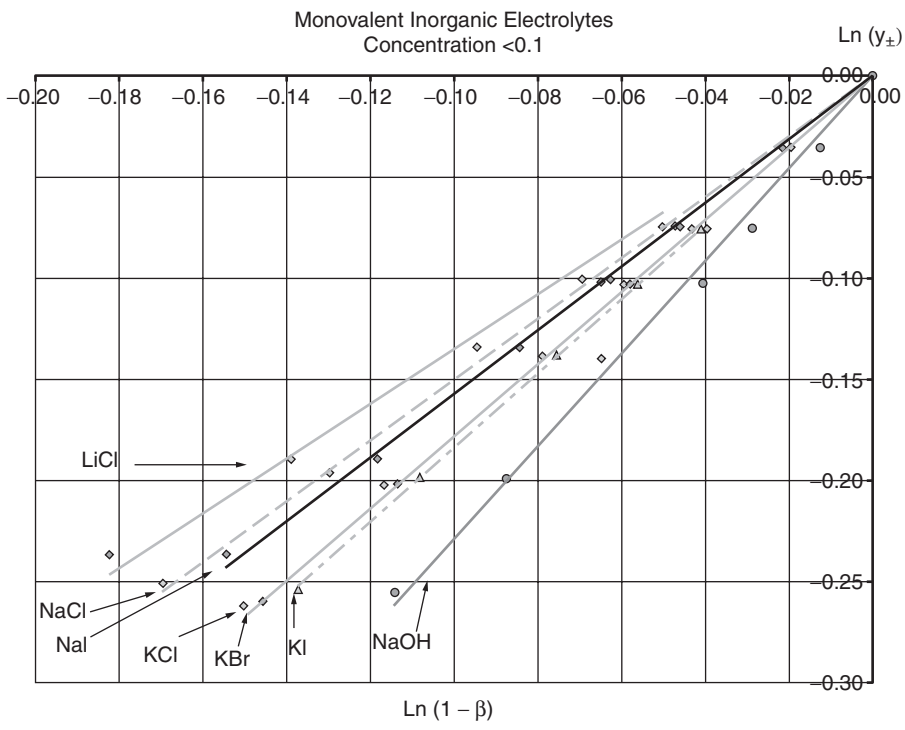


FIGURE 8.10 The mean activity coefficient ($-\ln y_{\pm}$) plotted as a function of the degree of dissociation $\ln(1 - \beta)$, β = degree of association, for a range of 1:1 salts. (Courtesy of T. Hurme.)

It should be noted, however, that β , as it is due to the association of a multiion salt (Equation 8.13), is a complex function of the mean activity coefficient and the concentration of the ionic species. Consider a salt that dissociates according to Scheme 8.13. Because of hydrolysis and condensation, or some other causes, a number of the ions associate to an aggregate with some ligands. Assuming $f > g$,

$$gM^{z+} + fL^{z-} \leftrightarrow M_g L_f^{(gz(+)fz(-))+} \quad (8.49)$$

where $g \neq \nu_M$ and $f \neq \nu_A$ relative to Scheme 8.13, but L could equal A . If a fraction β of the cations form the aggregate, we find the following equilibrium concentrations:¹

$$\text{Cations: } c_M = \nu_M c \rightarrow c_{gM} = (1 - \beta) \nu_M c \quad (8.50a)$$

$$\text{Anions: } c_A = \nu_A c \rightarrow c_{fV} = \left[\nu_A - \beta (f \nu_M / g) \right] c \quad (8.50b)$$

$$\text{Aggregate: } c_{gf} - \left[\beta (\nu_M / g) \right] c \quad (8.50c)$$

Note that the idea of complete vs. partial dissociation is adopted here.

These give the relationship between the mean activity coefficient of the salt ($y_{\pm,AM}$) and the aggregate ($y_{\pm,gf}$):

$$y_{\pm,AM}^V = (1 - \beta)^{\nu_M} \left[1 - \beta (f \nu_M / g \nu_A) \right]^{\nu_A} y_{\pm,gf}^V \quad (8.51a)$$

The complex function becomes considerably simpler if the aggregate is electrically neutral, i.e., $f \nu_M = g \nu_A$. Under such conditions,

$$y_{\pm,AM} = (1 - \beta) y_{\pm,gf} \quad (8.51b)$$

An even simpler case occurs when $g = \nu_M$ and $f = \nu_A$, i.e., the aggregate is identical with the salt. Then, these relationships may be used to correct the mean activity coefficient for the incomplete dissociation.

The momentary association of simple ions is a well-known phenomenon that has been treated in a number of ways. For example, the ion association constant of Bjerrum has received much experimental support. However, the association of simple electrolytes is considered to be short-lived and has been included in the Debye–Hückel electrostatic theory as correction constants to the concentration. On the contrary, the hydration of the ions may be long-lived. This may be accounted for by considering additionally the ionic interaction:⁷

1. The work done when the number of *water* molecules is reduced because they are captured in the hydration spheres of the ions.
2. The work done when the *ions* are covered with the water sheet.

With these corrections, the Debye–Hückel relation takes the form:⁷

$$-\log y_{\pm,exp} = \left\{ \left[A \sqrt{c} \right] / \left[RT (1 + B a \sqrt{c}) \right] \right\} + (2.3 n_h / n) \log a_w - 2.3 \log \left[(n_w + n) / (n_w - n_h + n) \right] \quad (8.52)$$

where n is the amount of 1:1 electrolyte hydrated by n_h water molecules in n_w of water, A ($= 0.51$, 25°C) and B ($= 0.3291 \times 10^8$, 25°C) are the Debye–Hückel constants, and a is the radius of the salts taken as the sum of the ion radii. As seen, the Coulombic interaction is corrected for the change in water activity and the change of ion concentration. Upon the concentration increase the $a_w < 1$ and in general $n_h > n$ (more than one hydration water per ion), the correction terms may equal and subsequently reverse the concentration dependence given by the Coulombic interaction.

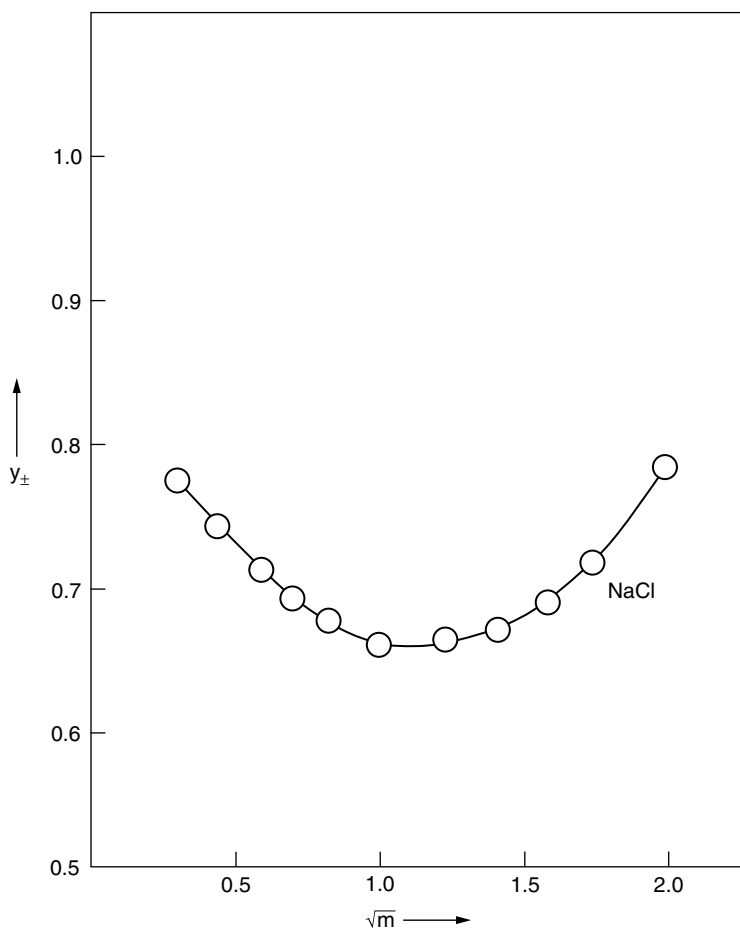


FIGURE 8.11 The mean activity coefficient of NaCl calculated from Equation 8.52: $a = 0.397$, $n_h = 3.5$, plotted through the experimental points as a function of the square root of the molality. (From Bockris, J.O.M. and Reddy, A.K., *Modern Electrochemistry*, Vol. 1, Plenum Press, New York, 1974. With permission.)

All the quantities a , n_h , and a_w have to be known to test this equation against experimental data. Assuming that a_w is known from independent measurements, a and n_h have been evaluated from a fit to the experimental data (Figure 8.11).⁷

As seen, the fit is quite good and is found to produce a and n_h values that are in reasonable accord with experimental values up to 5 mol/kg. For the simple 1:1 salt indicated, the hydration may be split in hydration numbers of the ions. The model has, however, the drawback that the \sqrt{c} model is fundamentally restricted to concentrations lower than 1 mol/kg.

The difference between the simple and the complex salts lies in the capability of the ions to deprotonate the water molecules associated with them. For simple ions this is not probable. The hydrolyzed and deprotonated metal cations form multinuclear complexes through oxolation–olation reactions discussed below. These reactions are dependent, not only on the pH, but also on the total metal concentration. By using the conditional constant approach this is illustrated as the dependency of $\log \alpha(\text{Fe}(\text{OH}))$ plotted as a function of the pH for a range of concentrations of Fe^{3+} ions in Figure 8.12.³

The curves are plotted for simplicity using the following equation:

$$\alpha_{\text{Fe}(\text{OH})} = (c'_{\text{Fe}}/c_{\text{Fe}}) = \left\{ [\text{Fe}^{3+}] + [\text{Fe}(\text{OH})^{2+}] + [\text{Fe}(\text{OH})_2^+] + 2[\text{Fe}_2(\text{OH})_2^{4+}] \right\} / [\text{Fe}^{3+}] \quad (8.53a)$$

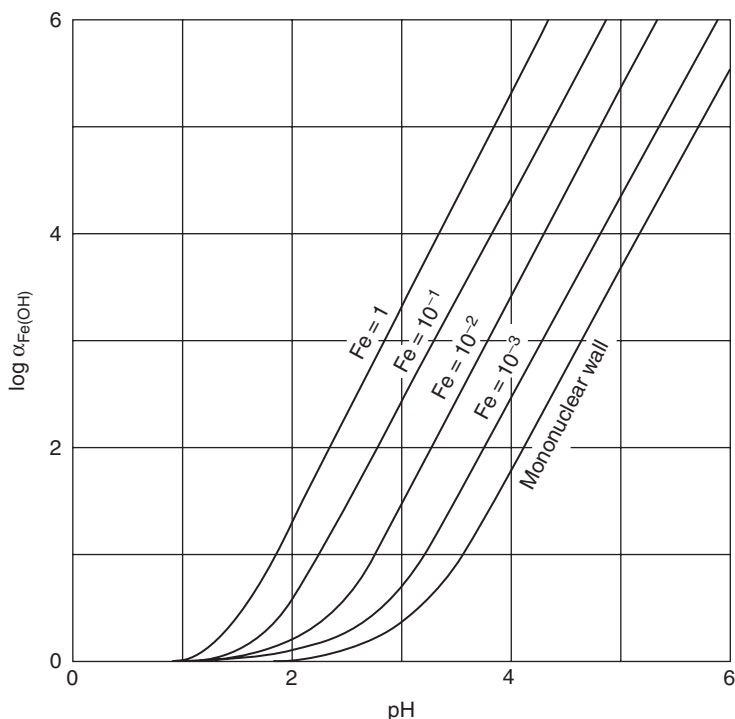


FIGURE 8.12 The degree of side reactions ($\log \alpha$) for $\text{Fe}(\text{OH})_i$ plotted against the pH for various values of c_{Fe} . (From Ringbom, A., *Complexation in Analytical Chemistry*, Wiley Interscience, New York, 1963, 47. With permission.)

Inserting the equilibrium constants, we obtain

$$\alpha_{\text{Fe}(\text{OH})} = 1 + [\text{OH}^-] * 10^{11.0} + [\text{OH}^-]^2 * 10^{21.7} + 2[\text{OH}^-]^2 [\text{Fe}^{3+}] * 10^{25.1} \quad (8.53b)$$

It is obvious that only the last term representing a binuclear complex is dependent on the Fe concentration, and this term gives a contribution only if $[\text{Fe}] > 10^{-3.7}$ representing the mononuclear wall in Figure 8.12. Obviously, condensation-mediated complexes may form only at concentrations exceeding the mononuclear wall. These kinds of calculations thus provide an easy way to evaluate the presence of multinuclear species in solutions. It should, however, be noted that the formation of multinuclear complexes is slow. Thus, to reach equilibrium the reactions should be performed at elevated temperatures (see, however, the discussion of phase equilibria below).

8.2.7 SUMMARY

To conclude, the interrelated parameters shown in Figure 8.13 influence the dissolution (pS, Equation 8.13) or, in reverse, the precipitation of salts (Equation 8.2) where M(etal) and A(nion) is considered as reacting specifically. The nonspecific ions, on the other hand, are thought to be contributing only to the Coulombic interaction given by the I (onic strength) and the Debye length ($1/\kappa$).

The proton activity is defined as Brønsted acidity and the acidity scale is related to the deprotonation of an acid to an anion. The pH scale is normalized through the convention that the dissociation constant for the hydronium ion (K_{HW}) is set equal to unity where $K_{\text{W}} = 1.0 * 10^{-14}$ at 25°C. The pH of a solution is usually measured by determining the potential of a cell in which a

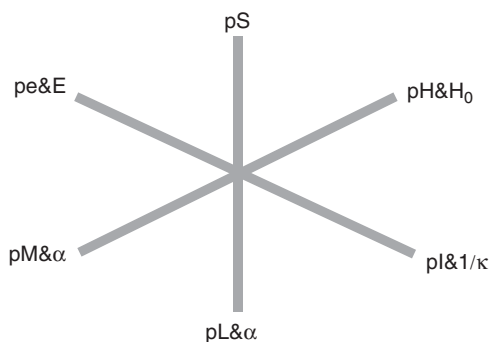


FIGURE 8.13 The type of ion species present in electrolyte solutions is simultaneously dependent on a range of parameters such as the solubility (pS), red-ox state (pe&E), the acidity (pH&H₀), the ionic strength (pI&1/κ), the presence of specifically binding cations (pM&α), and other ligands (pL&α).

hydrogen electrode is one component. In practice, pH is measured with a glass electrode that has a potential proportional to pH. As mentioned, however, the pH should be corrected for an enhanced ionic strength,³⁻⁵ e.g., by employing Equation 8.11.

The normal pH concept introduced above is restricted to dilute solutions. The pH scale may also be expanded by accounting for the changes in the activity coefficients of the acid and the conjugated base. The Hammett acidity function for solutions is related, e.g., to Equations 8.30 and 8.31 for the first deprotonation step in the following way:^{19,20}

$$H_o = -\log a_H + \log(y_{HA}/y_A) = pH + \log(y_{HA}/y_A) = pK_a - \log(c_{HA}/c_A) \quad (8.54a)$$

The Hammett acidity function is thus related to the pH as

$$pH = H_o - \log(y_{HA}/y_A) \quad (8.54b)$$

The Hammett basicity function is defined in the same way as

$$H_o = -\log a_H + \log(y_{HB}/y_B) = pH + \log(y_{HB}/y_B) = pK_a - \log(c_{HB}/c_B) \quad (8.55)$$

The specificity of the ions has so far been discussed from the chemical equilibria point of view. It can, however, be predicted to some extent from atomic properties, which will be presented in the next section.

8.3 ATOMIC EQUILIBRIUM PROPERTIES — THE MICROSCOPIC SCALES

In the previous section it was shown that the properties of metal ions may be related to the ratio of their charge over the ion radius. However, depending on the property to be correlated, the $\phi = z^2/r$ (hydration potential), $\psi_{ion} = z/r$ (ionic potential), or $\sigma_{ion} = z/r^2$ (ion charge density) may be used to linearize the relationship. It seems thus possible to use easily available properties for the prediction of the behavior of the metal ions. As shown, the valency provides less predictivity for the elements forming acids, but rather the degree of oxolation. In this chapter we present the very promising partial charge model (PCM) developed by Livage and Henry for the prediction of the oxo-hydroxo complexes formed. Finally, an attempt is made to relate these reactions with the oxolation and olation processes occurring in aqueous systems.

8.3.1 THE PARTIAL CHARGE MODEL

The PCM provides a surprisingly simple and straightforward method to predict the metal cation hydration and subsequent deprotonation. It is based on the electronegativity concept of Pauling and the principle of electronegativity equalization by Sanderson: When two or more atoms initially different in electronegativity combine, they adjust to the same electronegativity (χ_M) of the metal. It has been shown that the electronegativity corresponds to the electronic chemical potential and further according to Mulliken to the ionization energy (I_e) and affinity (A_e) of the electron:²¹

$$\chi_M = \mu_e = \frac{1}{2} (I_e + A_e) \quad (8.56)$$

A large difference in the electronegativity between the metal and the ligand produces electrovalent bonds. A small difference produces covalent bonds. An estimate of the percentage of ionic bonding ($\%$)_{ib} over covalency between atoms A and B is given by⁴

$$(\%)_{ib} = 16|\chi_A^0 - \chi_B^0| + 3.5|\chi_A^0 - \chi_B^0|^2 \quad (8.57)$$

When $|\chi_A^0 - \chi_B^0| \approx 2.1$, there is about 50% contribution of ionic bonding. For the transition metals the electronegativity has been found to follow the equation:²²

$$\chi_M = 0.22d + 4.6 \log z(+) - 0.7 \quad (8.58a)$$

where d is the number of d electrons and $z(+)$ is the valency (ion charge). The equation holds for octahedral complexes. For tetrahedral complexes the electronegativity is²²

$$\chi_M(\text{Tetrahedral}) = \chi_M(\text{octahedral}) + 0.25 \quad (8.58b)$$

It is assumed that the electronegativity of an atom changes linearly with its charge:²³

$$\chi_i = \chi_i^0 = \eta_i \delta_i \quad (8.59)$$

where χ_i^0 is the electronegativity of the neutral atom, η_i corresponds to its hardness according to the Pearson model, and δ_i is the partial charge of the atom. Following Sanderson it was proposed:²¹

$$\eta_i = 1.36\sqrt{\chi_i^0} = \frac{1}{2}(I_e - A_e) \quad (8.60)$$

where the relationship according to Mulliken is also indicated. The total charge (z) of a given chemical species is equal to the sum of the partial charges of all individual atoms:

$$z = \sum_i \delta_i \quad (8.61)$$

We may now rewrite Equation 8.59 in terms of the mean electronegativity:^{24,25}

$$\langle \chi_i \rangle = \left[\sum_i \sqrt{\chi_i^0} + 1.36z \right] / \left[\sum_i \left(1/\sqrt{\chi_i^0} \right) \right] \quad (8.62)$$

where the mean electronegativity for a diatomic molecule is taken as the geometric average of the neutral atoms: $\langle \chi_{ij} \rangle = (\chi_i^0 \chi_j^0)^{1/2}$. Then the partial charge takes the form:

$$\delta_i = (\langle \chi_i \rangle - \chi_i^0) / (1.36 \sqrt{\chi_i^0}) = \sigma_i (\langle \chi_i \rangle - \chi_i^0) \quad (8.63)$$

where $\sigma_i = 1/\eta_i$ corresponds to the so-called softness of the atoms.

Considering the coordination of n water molecules to the metal described in Scheme 8.33b and the deprotonation equilibrium Equation 8.34a the reaction proceeds as long as $\delta(\text{OH})$ remains positive and stops when $\delta(\text{OH}) = 0$. Charge conservation leads then to the stable aquo-hydroxo cationic metal ion $M[(\text{OH})_p(\text{OH}_2)_{n-p}]^{(z-p)+}$ to²³

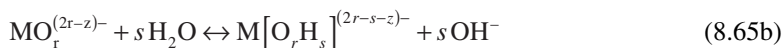
$$p = \left\{ [z - n\delta(\text{OH}) - \delta(\text{M})] / [1 - \delta(\text{H}_2\text{O})] \right\} \quad (8.64a)$$

The mean electronegativity is given by $\langle \chi \rangle = \chi(\text{OH}) = 2.71$. The partial charges $\delta(\text{H}_2\text{O})$ and $\delta(\text{M})$ can be calculated from Equation 8.63, leading to

$$p = 1.45z - 0.45n - \left\{ 1.07 [2.71 - \chi^0(\text{M})] / [\sqrt{\chi^0(\text{M})}] \right\} \quad (8.64b)$$

Consequently, the degree of hydroxylation can be easily calculated provided that the oxidation state and the coordination number of the cation are known. This formula holds for very acidic (low pH) solutions only.

The metal ions with a high valency may induce a more extensive deprotonation producing oxo-hydroxo-aquo species indicated in Scheme 8.34b. However, rather than discussing the reaction as a deprotonation of aquo complexes, it is customary to relate the oxo species to the degree of uptake of hydroxyl ions (reverse of reaction 8.65b) in alkaline solutions:



where $\text{M}[\text{O}_r\text{H}_s]^{(2r-s-z)-}$ equals the nonaquatic oxo-hydroxo species $\text{M}[\text{O}_{r-s}(\text{OH})_s]^{(2r-s-z)-}$. The deprotonation continues as long as $\delta(\text{H})$ remains negative and stops when $\delta(\text{H}) = 0$. In addition to being directly related to the Lux–Flood exchange of oxo ions (pO scale), it may also be related to the disintegration of a metal oxide. According to Scheme 8.33a written without charges,



This disintegration is followed by the reverse of Scheme 8.65a producing hydrated ionic species. If the corresponding charges were introduced and $v_M = 1$ the stoichiometric constant for oxygen would be $v_0 = z/2$ as the valency for the oxo ion is always -2 .

Charge conservation leads for the stable oxo-hydroxo cationic metal ion $\text{M}[\text{O}_r\text{H}_s]^{(2r-s-z)-} = \text{M}[\text{O}_{r-s}(\text{OH})_s]^{(2r-s-z)-}$ to²⁴

$$s = [2r - z + r\delta(\text{O}) - \delta(\text{M})] \quad (8.67a)$$

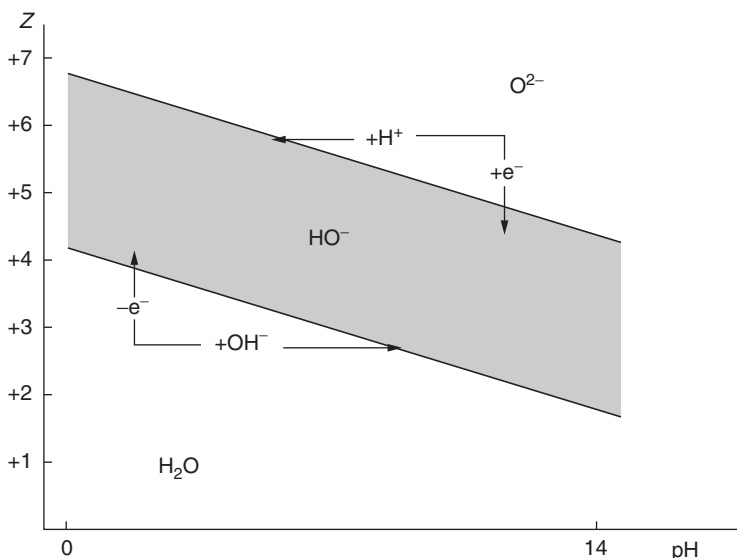


FIGURE 8.14 Charge vs. pH diagram indicating the aquo, hydroxo, and oxo domains for the hydrolyzed cations. The possible initiation mechanisms for condensation reactions are indicated. (From Jolivet, J.-P., *Metal Oxide Chemistry and Synthesis*, John Wiley & Sons, Chichester, U.K., 2000, 34. With permission.)

Obviously, the relation to the aquo-hydroxo-oxo complex is $q = r - s$ and $p = s$ leading to $r = p + q$ and since $z < (p + 2q)$ the complex is in fact an anion. The mean electronegativity is given by $\langle \chi \rangle = \chi^0(\text{H}) = 2.1$. For water $\chi(\text{H}_2\text{O}) = 2.491$, while $\delta(\text{H}) = +0.20$ and $\delta(\text{O}) = -0.40$. The degree of hydroxylation is thus obtained as²³

$$s = 1.45r - z + \left\{ 0.74 \left[2.1 - \chi^0(\text{M}) \right] / \left[\sqrt{\chi^0(\text{M})} \right] \right\} \quad (8.67b)$$

These types of anionic species may be found only in dilute aqueous solutions at high pH. For the hydroxo-aquo species of mean electronegativity $\langle \chi \rangle_p$ the deprotonation goes on until it equals the mean electronegativity of water $\langle \chi \rangle_w$.

$$\langle \chi \rangle_p = \langle \chi \rangle_w = 2.732 - 0.035 \text{ pH} \quad (8.68)$$

The hydrolysis ratio h (protons removed from an aquo ion) of the aquo species $\text{M}[(\text{OH}_2)_n]^{z+}$ can then be easily calculated at any pH value from²⁴

$$h = \left\{ \left[z - n\delta(\text{O}) - 2n\delta(\text{H}) - \delta(\text{M}) \right] / \left[1 - \delta(\text{H}) \right] \right\} \quad (8.69)$$

where the partial charges for each element is given by Equation 8.63:

$$\delta_i = \left(\langle \chi \rangle_w - \chi_i^0 \right) / \left(1.36 \sqrt{\chi_i^0} \right) \quad (8.70)$$

These relations apply for any metal cation in aqueous solution. Obviously, the hydrolysis ratio of a given precursor depends mainly on both the oxidation state of the cation ($z+$) and the pH of the solution. A valency–pH diagram may then be drawn (Figure 8.14) where three domains are separated by two lines represented by $h = 1$ and $h = 2\delta - 1$, respectively, originally drawn by Jorgensen.²⁵⁻²⁷

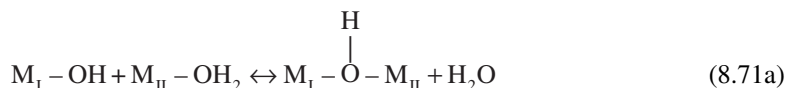
Condensation of mononuclear species in aqueous solutions becomes possible only if hydroxyl groups are present in the precursor, i.e., if the species are located between the lines. This region

can be reached by adding base to low-valence metal ion solutions or acid to high-valence metal ion solutions. As discussed above it can also be reached via red-ox reactions.

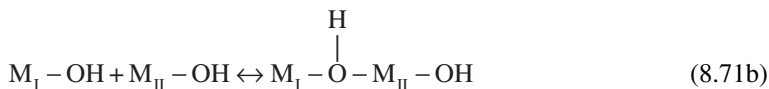
8.3.2 CONDENSED SPECIES

Precipitation occurs in aqueous solutions at pH_{PZC} , i.e., when the surface charge density equals zero. Condensation of the cationic species $\text{M}[(\text{OH})_p(\text{OH}_2)_{n-p}]^{(z-p)+}$ occurs when the pH is increased (adding OH^-) to the pH_{PZC} , which is reached when $p = z$. Condensation of the anionic species $\text{M}[\text{O}_r\text{H}_s]^{(2r-s-z)-} = \text{M}[\text{O}_{r-s}(\text{OH})_s]^{(2r-s-z)-}$ is obtained by lowering the pH (adding H^+) to the pH_{PZC} , which is reached when $s = 2r - z$. In both cases, the rough formula of the precursor for condensation corresponds to the neutral species $\text{M}[\text{O}_r\text{H}_{2r-z}]^0$.

Condensation occurs through olation or oxolation. In the olation a oxygen bridge is formed between the metal ions. When the coordination is fulfilled, the condensation reaction (olation) proceeds as an nucleophilic substitution:²⁶



with an increase in the coordination number of M_{II} . When the coordination need remains unsatisfied, the olation proceeds as a nucleophilic addition reaction:²⁶



In both cases, the condensation process is formally considered to start with the nucleophilic addition of a OH group onto a metal ion. In both cases the reacting species are OH groups. This means that condensation does not occur as long as stable hydroxylated precursors are not formed in aqueous solutions, i.e., only if $\chi(\text{MO}_{z/2}) < \chi(\text{OH})$. Oxolation indicates that the metals become joined with an oxo-bridge:²⁶



This reaction also starts with a nucleophilic addition of $-\text{OH}$, but is followed by a 1,3-proton transfer to liberate water. The elements in the periodic table can then be subdivided in three classes of basic aquo-ions and acidic oxy-ions.²³⁻²⁵

Class I: $\chi^0(\text{M}) < \chi^0(\text{H})$. Charge transfer goes toward the hydrogen atom which loses its acidic character. No condensation is observed. Aqueous hydroxo species behave like Brønsted bases:



In these cases the M–O bond is strongly ionic, which applies also for its oxide. This critical electronegativity is, however, very low and only low-valence large cations such as alkaline earth cations behave in this way. The critical electronegativity for the basic dissociation is denoted $\chi^*(\text{B})$.

Class II: $\chi^*(\text{B}) < \chi^0(\text{M}) < \chi^*(\text{O})$, where the latter defines the critical electronegativity when only olation and no oxolation occurs. The M–OH bond remains stable in an aqueous medium. These cations are expected to condense only through olation leading to precipitated $[\text{MO}_2]^0$ species.

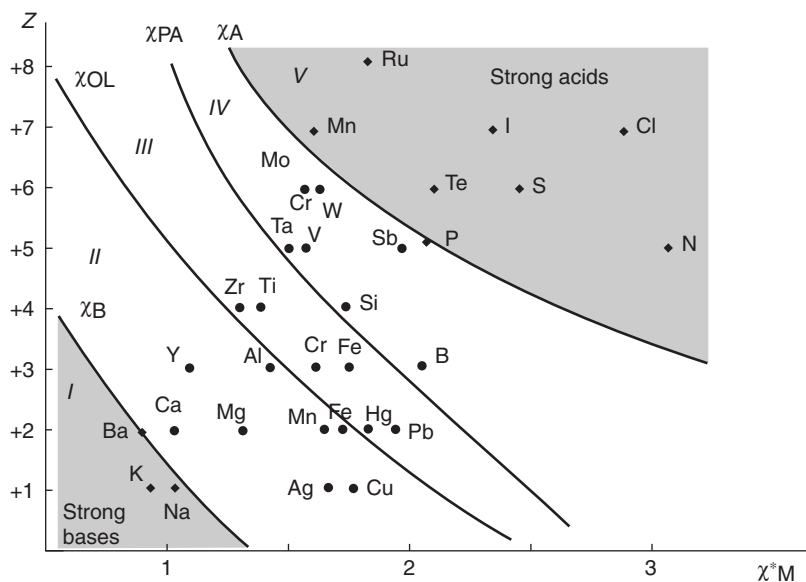


FIGURE 8.15 Charge vs. critical electronegativity diagram showing five classes of behavior for the zero-charge $M[O_xH_{2x-z}]^0$ species of the metal cation (M^{z+}). In domains I and V, the species remain monomeric and soluble. In domain II the species condense by olation only, and in domain IV solely by oxolation. Both latter condensation processes may be simultaneous in domain III. (From Jolivet, J.-P., *Metal Oxide Chemistry and Synthesis*, John Wiley & Sons, Chichester, U.K., 2000, 35. With permission.)

Class III: $\chi^*(O) < \chi^*(M) < \chi^*(OH)$. The M–OH bond remains stable in an aqueous medium. Within this range both olation and oxolation are expected to occur leading to hydrous oxide $M[(O_{z/2}(OH_2)_{x-1}]^0$ precipitation.

Class IV: $\chi^*(OH) < \chi^*(M) < \chi^*(A)$, where $\chi^*(OH)$ the nucleophilicity of the OH group. The M–OH bond remains stable in an aqueous medium. These cations are expected to condense only through oxolation leading to molecular polyacids.

Class V: $\chi^*(M) > \chi^*(H)$, M is more electronegative than hydrogen. No condensation is observed. Aqueous hydroxo species thus behave like Brønsted acids:



In these cases the M–O bond has a covalent character, which is true also for its oxide. As discussed, this applies for very electronegative elements at the upper right of the periodic table (P^V , S^{VI} , Cl^{VII}). As shown, however, this refers to the neutral oxo-hydroxo species. The Brønsted acidity also applies with highly charged d metal cations such as Mn^{VII} . The critical electronegativity for the acidic dissociation is denoted $\chi^*(A)$.

These classes are illustrated in Figure 8.15 as the dependency of the valency on the electronegativity of the metal cation.²⁵⁻²⁷

The precipitation is usually achieved when approaching the pH_{PZC} . Because the electronegativity for Classes III–V is intermediate in character (amphoteric) they correspond to network formers producing stable oligomers and extended networks also in the dry state.

8.3.3 COMPLEXATION BY ANIONIC SPECIES

Although it is obvious that anions do react in the same way as metal cations with water, the anions are treated merely as monoprotonated species that may either compete with the water (HX) or with the hydroxyl ions (monodentate anion X^-) in the coordination sphere. The electronegativity can be

calculated for the complexed precursor ($\langle \chi \rangle_p$) as done previously for the anion ($\chi(X)$) and its protonated form ($\chi(HX)$), respectively. Equalization of the mean electronegativity for the metal precursor ($\langle \chi \rangle_p$) with the electronegativities of the basic ($\chi(X)$) and acidic ($\chi(HX)$) forms of the acid ligand leads to the following electronegativity range ($\chi(HX) \geq \langle \chi \rangle_p \geq \chi(X)$) where complexation is expected to occur. Outside this range, complexed species are not stable.

The above analysis can be easily generalized to multivalent species of the form H_tX . Complexation occurs if ($\chi(H_tX) \geq \langle \chi \rangle_p \geq \chi(X)$), while outside this range the complexes cannot be stable. Within this domain, two classes may be distinguished:^{24,25}

Class i: ($\chi(H_tX) \geq \langle \chi \rangle_p \geq \chi(H_{t-1}X)$). In this range anions can act as network formers. They are tightly bonded in the coordination sphere of the metal. Upon precipitation of a solid phase, a basic salt structure forms.

Class ii: ($\chi(H_{t-1}X) \geq \langle \chi \rangle_p \geq \chi(X)$). In this range anions are still bonded to the metal, but elimination is still possible through ionic dissociation of a partly protonated acid form ($H_uX^{(t-u)-}$, where $0 < u < t$). Therefore, despite complexation of solute precursors, anions can be removed during the precipitation reaction leading to an oxide network free of anions. This analysis shows that multivalent anions can be used to monitor the size, shape, and morphology of oxide particles, while monovalent anions cannot be used for such a purpose.

Because the hydrolysis ratio was found to increase with pH (Equation 8.69), the electronegativity range where complexation is expected to occur must also depend on pH. To compute such pH ranges it is necessary to equalize the mean electronegativity of the complexed precursor ($\langle \chi \rangle_p$) with $\langle \chi \rangle_u = \chi[(H_uX)^{(t-u)-}]$, the mean electronegativity of the u -protonated form ($0 < u < t$) of the X^{t-} anion. By applying charge conservation, a critical hydrolysis ratio (h^*) may be found, which can be converted into a critical pH_u^* through Equation 8.69. It provides a quantitative guide to predict whether complexation occurs as a function of pH. A computation for Al^{3+} with $z = 3$, $n = 6$, and $\chi^0(Al) = 1.47$ is presented in Figure 8.16 where $\langle \chi \rangle_u$ is plotted as a function of pH_u^* for $0 < u < 4$.²⁵ It is assumed that anions form bidentate complexes in the inner coordination sphere.

It is obvious that three ranges can be distinguished:^{24,25}

Range 1: Ionic dissociation occurs if $pH > pH_0^*$. Anions cannot stay within the coordination sphere of the metal as its aqueous precursors are not sufficiently electronegative to polarize their electronic clouds.

Range 2: Hydrolysis occurs if $pH < pH_t^*$ as the aqueous metal precursors are now too electronegative. Protons are therefore preferentially fixed on the anion rather than hydroxo groups, leading to the hydrolysis of the latter.

Range 3: Complexation is expected if $pH_t^* < pH < pH_0^*$. This range depends on the valency of the anion. It becomes larger when s increases. Within such a range an optimum pH for complexation pH_v can be defined according to

$$pH_v = \frac{1}{2} (pH_t^* + pH_0^*) \quad (8.74)$$

8.3.4 SUMMARY

It should be noted that due care has to be taken when using electronegativities for the modeling of chemical reactions because it is dependent on the type of bonds formed (e.g., sp hybridizations). Consequently, any theory not correcting for this contribution must be considered an estimation. The PCM presented is therefore a semiquantitative model. Moreover, Livage and Henry clearly state that the PCM does not yet include the contributions of metal concentration (and pS), coprecipitation with other metals (pM scale), ionic strength (pI scale), red-ox processes (pe/E scale), temperature, and pressure. However, the model is surprisingly capable of giving a first estimate of the complexation of metal cations with aquatic ligands.

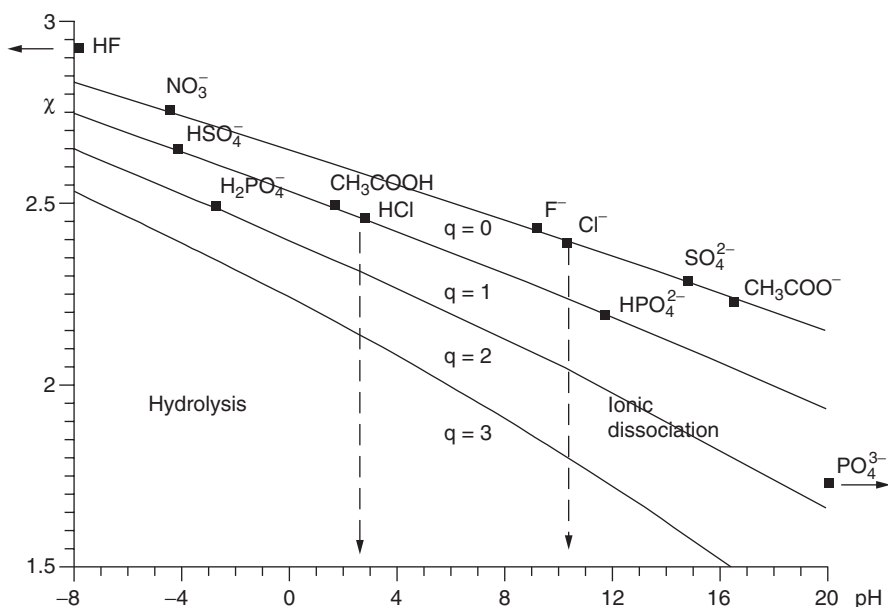


FIGURE 8.16 Electronegativity vs. pH diagram for the complexation of Al^{3+} by monodentate anions as a function of the number of anions other than the hydroxyl in the coordination sphere. For example, the acidity range for complexation by chloride ions is determined by the $\chi(\text{Cl}^-)$ and $\chi(\text{HCl})$ values. (From Jolivet, J.-P., *Metal Oxide Chemistry and Synthesis*, John Wiley & Sons, Chichester, U.K., 2000, 206. With permission.)

8.4 MIXED SOLVENT AND NONAQUATIC SYSTEMS

In previous sections the complications have been kept to a minimum by using simple salts where, e.g., the steric hindrance of the ligand molecule has been neglected and the competition between solvent molecules for the metal cation was unimportant. However, in a very large number of applications alkoxy precursors are used, which upon hydrolysis produce not only the hydrolysis products discussed previously, but also a mixed solvent. It has been shown that mixed solvents may be used to control the hydrolysis and to induce special properties to the particle.²⁶ Chelating agents may be used to control the particle form or to quench the entire condensation reaction. A special class of additives, i.e., surfactants and polymers, are used as sol stabilizers and/or templates for the gel formed.²⁸ Finally, fully anhydrous solvents may be used to control the condensation kinetics through a slow release of water.²⁹ In this section a short survey is presented on some of the special properties introduced when using such systems for the preparation of precursors to sols and gels. However, the basic concepts for the analysis and control of the key reactions have been dealt with to some depth in the previous sections.

8.4.1 ORGANIC PRECURSORS IN AQUEOUS SOLVENTS

Three important reactions may occur in aqueous alkoxy $\text{M}(\text{OR})_n$ solutions (simplified denotation is used).

1. They hydrolyze liberating an alcohol to be mixed with water forming a hydroxo complex:



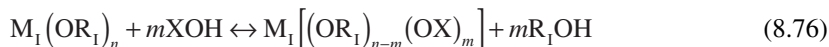
2. They condense with the hydroxo complex, again liberating alcohol to the solvent:



3. They exchange the alkoxy group with the alcohol in the mixed solvent:



The overall reaction may proceed as follows:²³



where X = H, M_{II}, or R_{II}, respectively. The entire process depends on the charge distribution or rather the electronegativities of the species formed. It requires three successive conditions: $\delta(M) > 0$, $\delta(OR) < \delta(H)$, and $\delta(ROH) > 0$. If one of these conditions fails the corresponding step becomes a limiting step for the overall reaction.

According to the PCM the softness of the alkoxy group, A (C_nO_mH_p) is given by²³

$$\sigma_A = \left\{ \left[\left(n / \sqrt{\chi_C^0} \right) + \left(m / \sqrt{\chi_O^0} \right) + \left(p / \sqrt{\chi_H^0} \right) \right] / 1.36 \right\} \quad (8.77)$$

The mean electronegativity of the alkoxy group is

$$\langle \chi \rangle_A = \left\{ \left[\left(n / \sqrt{\chi_C^0} \right) + \left(m / \sqrt{\chi_O^0} \right) + \left(p / \sqrt{\chi_H^0} \right) \right] / 1.36 \sigma_A \right\} \quad (8.78)$$

The partial charge can then be computed as

$$\delta_A = \sigma_A (\langle \chi \rangle - \langle \chi \rangle_A) \quad (8.79)$$

For the hydrolysis reaction the positive charge $\delta(M)$ decreases when the number of carbon atoms in the alkyl chain increases. The sensitivity toward hydrolysis should then decrease, in agreement with experimental observations. This is particularly valid for the most typical alkoxides (R = Me, Et, i-Pr).

For the condensation reactions it was found that the conditions ($\delta(M) > 0$, $\delta(OH) < 0$, and $\delta(H) < 0$) are generally fulfilled for cations of sufficient charge. However, $\delta(ROH) > 0$ while $\delta(H_2O) < 0$, which means that the condensation of hydrolyzed alkoxides will proceed via the elimination of alcohol molecules rather than water molecules.

An example of the influence of the alkoxy groups is provided in the classic work by Stöber et al.³⁰ They found the following for TROS (RO = alkoxy group) in ethanol:

- The reaction rates increased according to OMe > OEt > OPr > OPe.
- The particle sizes grew according to OPe > OPr > OEt > OMe.

For the exchange process of alcohols mixed with water the same conditions apply. It was found that although the mean electronegativity of the complex ($\langle \chi \rangle$) remains the same, the protonated group having a larger (positive) partial charge ($\delta(ROH)$) will be removed. The same groups will also be removed upon further hydrolysis with water.

The exchange of alkoxy groups with the solvent is apparent from the parallel sequence found by Stöber et al.³⁰ for TEOS that

- The reaction rates increased according to MeOH > EtOH > PrOH > BuOH.
- The particle sizes grew according to BuOH > PrOH > EtOH > MeOH.
- The particle size distribution grew according to BuOH > PrOH > EtOH > MeOH.

The rate of hydrolysis is at minimum when $\text{pH} \approx 7$ and the rate of condensation is at minimum when $\text{pH} \approx 4$.²⁶ Drawing parabolas through these minima provides the relative rate of hydrolysis and condensation. As a generalization it may be stated that at $\text{pH} < 5$ to 6 the hydrolysis dominates over condensation and at $\text{pH} > 5$ to 6 the reverse is true. Consequently, if complete hydrolysis is the aim, the pH should be kept at about 4 for some time before initiating the condensation by adjusting the acidity to $\text{pH} < 4$ or $\text{pH} > 4$. However, the rate of condensation is dependent on the concentration and is diminishing with dilution shifting the parabola downward. This also influences the relative contribution of hydrolysis and condensation. It is thus not surprising that the condensation is the slowest in the neutral pH range. In acidic solutions the extensive hydrolysis and condensation leads to rapid formation of gel structures. In alkaline solutions the condensation is rapid, but the enhanced charging and dissolution of silica species enables rearrangement to occur producing more dense particulate structures, as shown in [Figure 8.17](#).¹⁵

The particle size distribution appeared for the larger alcohols as a bimodality when the particles reached a critical size that was characteristic for the system. As shown in [Figure 8.18](#) the particle size reached a maximum only for a certain composition of H₂O, TEOS, EtOH, and NH₃.³⁰

The PCM model can, as shown, also be used to describe the effect of other anions, surfactants, or chelates, e.g., with fatty acid templates. If $\delta(\text{RH}) < 0$ (e.g., for an acetate group), it will remain in the gel produced and must be removed by pyrolysis, extraction, or some other means. We shall return to this matter when discussing the use of templates in the sol–gel processing of porous particles and gels.

8.4.2 MIXED SOLVENT SYSTEMS

The example presented above provides a straightforward indication of why mixed solvents may influence the hydrolysis of cations. The solvent molecules that are capable of acting as ligands to the metal cation, e.g., due to proton exchange, have of course the most dramatic and specific effects.²³

On the other hand, dipolar solvent molecules may also compete with the aquo ligands in the coordination sphere of the metal cation, e.g., in the nonprotonated acid form (HX). Adduct formation in the absence of proton exchange or ion association (e.g., in nonaqueous solvents) is denoted as an Lewis acid–base interaction. The adduct formation may be described and evaluated by using the Hammett function introduced previously (Equations 8.54 and 8.55) according to^{19,20}



$$H_o = \log a_A \log(y_{AB}/y_B) = \text{p}K_{\text{eq}} + \log(c_{AB}/c_B) \quad (8.80b)$$

where a_A is the activity of the Lewis acid (electron pair acceptor, e.g., a metal cation) and $a_B = y_B c_B$ is the activity of the Lewis base (electron pair donor). Experimentally the counterpair of the acid or base to be investigated may be chosen to facilitate the detection of the stoichiometric or equivalence point. The Hammett function may be experimentally determined by the use of indicators as one of the acid or base pair.

A very illustrative example of the influence the mixed solvent water–methanol has on the precipitation of Gibbsite (Al(OH)₃) is found in the patent of Wilhelmy.³¹ As shown in [Figure 8.19](#), the particle shape is dramatically influenced by pH (c_{NaOH}) and by the relative amount of methanol.

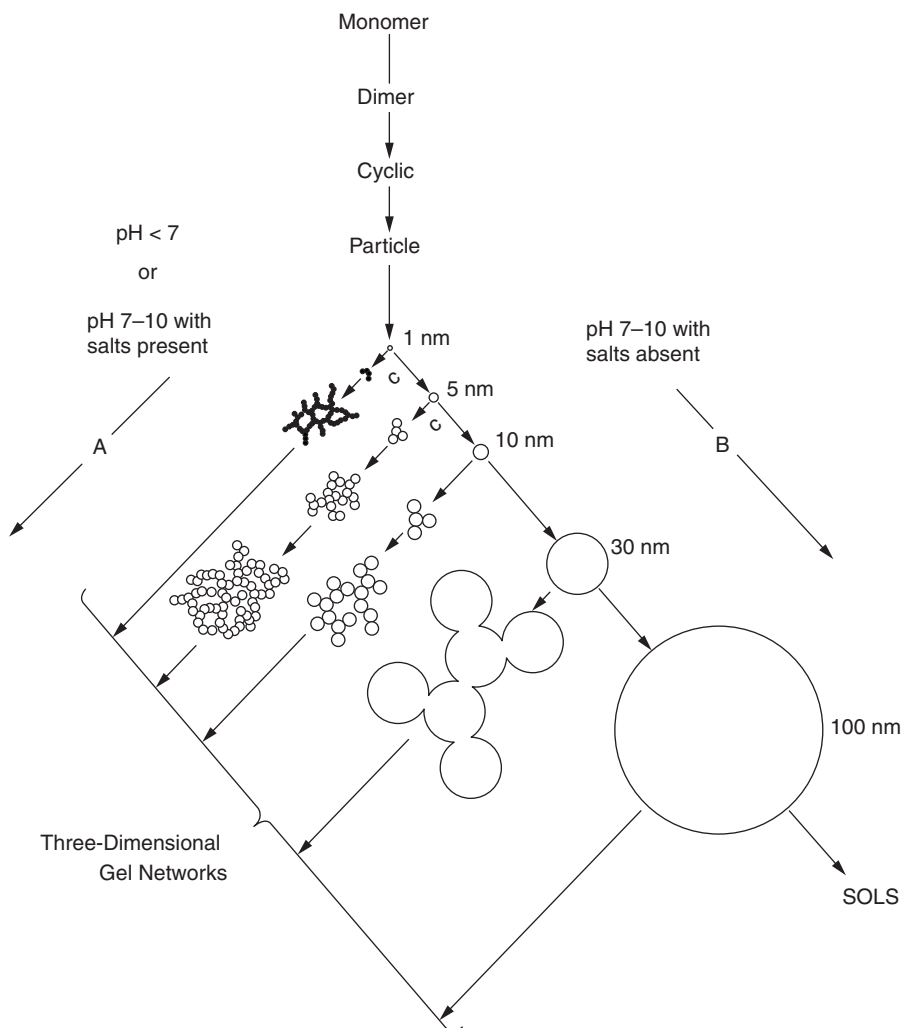


FIGURE 8.17 The polymerization routes of silica in acidic and alkaline solutions. In acidic solutions the polymeric species aggregate and form three-dimensional networks. In alkaline solutions the sufficient solubility produces particulate sols. (From Iler, R.K., *The Chemistry of Silica*, John Wiley & Sons, New York, 1979, 174. With permission.)

Mixed solvents may also have a purely dielectric and dispersive interaction with the metal species, which may lead to an salting-out or salting-in effect of the ions. These effects will be discussed to some extent when the stabilization of the sols are considered.

8.4.3 INORGANIC PRECURSORS IN NONAQUEOUS SOLVENTS

Particles have been synthesized in the following organic media:

- Organic liquids to influence the solubility and hydrolysis of the ions
- Reverse micelles as an confined reaction media for nanoparticles
- Water/oil (W/O) emulsions as an confined media for microparticles

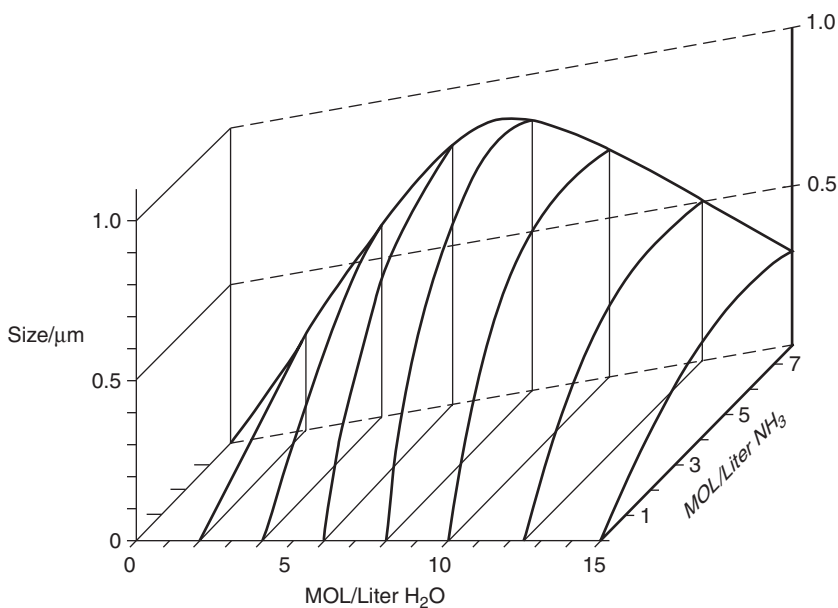


FIGURE 8.18 The dependency of the size of silica particles on the degree of dilution and the concentration of ammonia in 0.28 mol/dm^3 aqueous ethanol solutions. (From Stöber, W. et al., *J. Colloid Interface Sci.*, 26, 64, 1968. With permission.)

When surface active agents are considered, a further complication may be encountered. Because of their surface active nature, the surfactants not only enrich at the surfaces, but also form extended structures themselves. At low concentrations, the surfactants remain as dissolved monomers or associate to oligomers. However, when the critical micellization concentration (cmc) is surpassed, a cooperative association is activated to micelles (1 to 10 nm) consisting typically of some 50 to 100 monomers. At still higher concentrations, or in the presence of cosurfactants (alcohols, amines, fatty acids, etc.), liquid crystalline phases may separate. These phases have an infinite order on the x-ray scale, but may remain as powders on the NMR (nuclear magnetic resonance) scale. When the lamellar liquid crystalline phase is in equilibrium with the liquid micellar phase the conditions are optimal for emulsions to form. The interface of the emulsion droplets (1 to 100 μm) are stabilized by the lamellar liquid crystal. Both the micelles and the emulsions may be of the oil in water (o/w) or water in oil (w/o) type. Obviously, substances that otherwise are insoluble in the dispersion medium may be solubilized in the micelles or emulsified in the emulsions. For a more thorough analysis, the reader is directed to pertinent references in the literature.⁶

*Liquid extraction*²⁹ relates to the chelation by surfactants or their oligomers, thus rendering the substance soluble in the extraction medium ($w \rightarrow o$ or $o \rightarrow w$). Liquid extraction may be used to extract, e.g., HCl, which forms during the hydrolysis of metal chlorides mixed into a chlorinated hydrocarbon liquid. The extraction is mediated with a complex forming agent, such as an primary, secondary, or tertiary amine. As a result, the originally extremely acidic aqueous phase is rendered more neutral, which leads to the hydrolysis and condensation of the metal ion complexes. The efficiency of extraction is expressed with partition coefficients. The organic solvent may also be used to host a donor that releases water in a delayed and controlled way, thus controlling the rate of hydrolysis.

*Reversed micelles*³² stabilize a nanometer-sized aqueous environment within the surfactant aggregate, which is dispersed in a fully nonhydrous or a semipolar solvent. In this micellar core environment we may dissolve metal salt solutions that react to the extent of the available reactants.

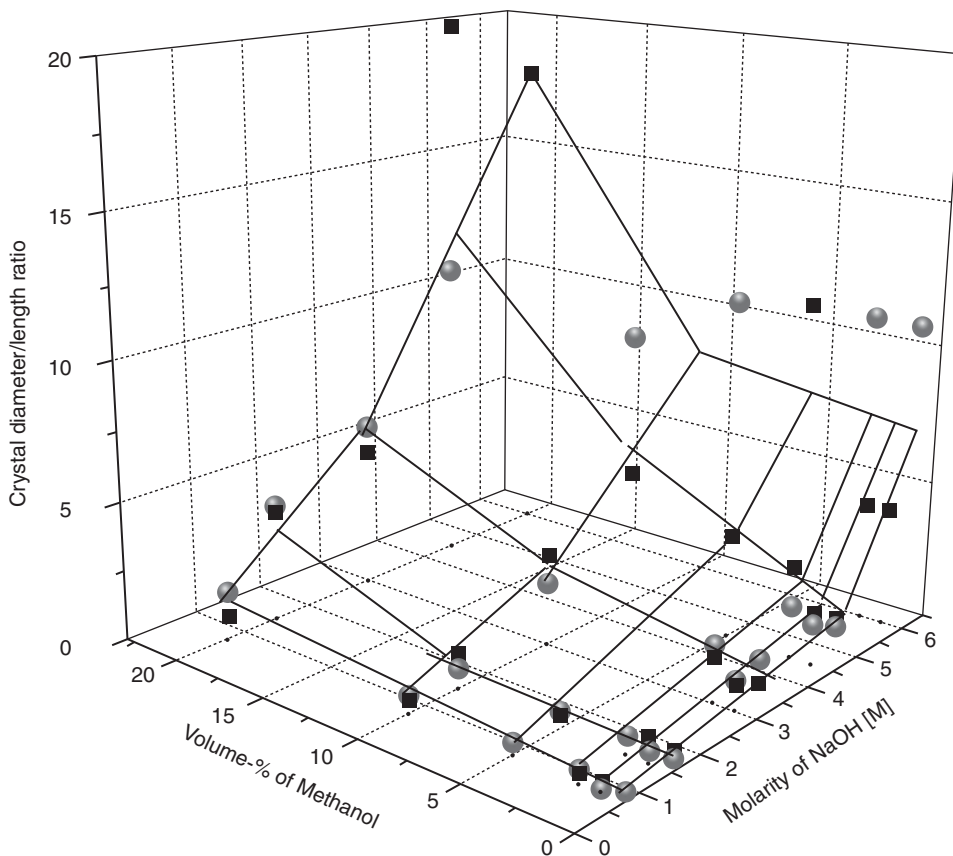


FIGURE 8.19 The dependency of the shape of aluminum hydroxide particles on the relative amount of NaOH and methanol at 75°C ($C(\text{Al})/C(\text{NaOH}) = 0.6$ (●), 0.7 (■)). (Redrawn from Wihelmy, R.B., U.S. Patent, 4,822,593, 1989.)

At the same time the aggregates stabilize the nanoparticles formed in the solution. However, the aggregates may be destabilized lyotropically (ionic surfactants) or termally (nonionic surfactants), which releases the aggregates. The main problem is to find suitable surfactant systems that remain stable with solubilized concentrated electrolyte solutions and with the released reaction products. Frequently, substantial phase separations may occur.

Water/oil (W/O) emulsions are thermodynamically unstable aggregates. Similar to the reversed surfactant systems, the electrolyte solutions are encapsulated but in this case merely mechanically. However, the stability can usually be controlled from seconds (destabilization) to months (stabilization). The size of the emulsion droplets and the stability are sensitively dependent on the physicochemical processing conditions. The emulsion systems are best characterized by phase diagrams.

The surfactant systems may also be used as liquid crystals or polymer stabilized rigid gels to control the long-term stability. In all these cases the surfactants remain in the structure and have to be removed by extraction or pyrolysis.

8.4.4 SUMMARY

The influence of any functional organic component on the system is obviously complex. It may only change the physicochemical state of the solvent or associate to colloidal structures themselves. More specifically, surfactants may compete with the ligands in the coordination sphere of the

multivalent ions and thus act as chelating agents. The chelation may be followed by association of the surfactants. The extended structures formed may act as templates directing the growth of the inorganic matrix; template chemistry is discussed later.

8.5 NUCLEATION AND GROWTH OF SOL PARTICLES

The basic steps leading to the formation of nuclei have been discussed in terms of the association and condensation of metal species. The state of the complexes is dependent on the metal ion concentration (pc_{MI}), the acidity of the solution (pH) the ionic strength (pI), the presence of competing noncomplexing ligands ($pL = pc_L$) and competing specifically interacting (complexing) metal ions ($pM = pc_{MI}$), and the occurrence of red-ox reactions (pe). All these simultaneously influence the solubility (pS) and reprecipitation of metal complexes and should be monitored during the synthesis, e.g., by using conditional constants. However, a prediction of the reactions occurring is provided by the PCM for dilute solutions. In this section we discuss the options available for the nucleation and growth of particles.

8.5.1 SUPERSATURATION OF ASSOCIATING AND NONASSOCIATING IONS

The basic criterion for the formation of polymeric precursors (embryo) and nanosized nuclei is a sufficient multivalent ion concentration or the production of a supersaturation of nonassociation metal oxides. However, it seems that the kinetics of the reaction is determined by the formation of oligomeric precursors characterized as critical clusters consisting of some 100 to 1000 monomers. The final particle size will depend sensitively on the relative speed of nucleation and growth. A great dispersion degree is achieved when the nucleation is fast and the growth is slow. The growth of the particles will depend on the following conditions, among others:

- The temperature (the rate of condensation is enhanced at higher temperatures)
- The proximity of the charge neutralization point (pH_{PZC})
- The concentration of the reactants and ligands
- The viscosity of the solution (determines the diffusion speed of the reactants)
- The amount of reactive or adsorbing impurities
- The structure of the reactants (i.e., the steric hindrance of the reactions)
- The stability of the sol formed (i.e., the aggregation of the particles)

Thus, in dilute solutions ($c_M < 10^{-4}$ to 10^{-3} mol/dm³) the formation of nuclei may be fast, but the particle growth is slow.³³ For $2 < pc_M < 1$ mol/dm³ both processes are fast and precipitates form rapidly. When the concentration supersedes 2 to 3 mol/dm³, the high viscosity of the solution may restrict the diffusion of reactants to the surface. As a result a large number of very small particles may form. The options provided by the organic systems discussed above should, however, be kept in mind.

8.5.2 THERMODYNAMIC DESCRIPTION OF THE NUCLEATION AND GROWTH

The classical way to describe the conditions needed for the formation of a nucleus is to relate it to supersaturation, i.e., the concentration of the metal cation and possible ligands. This approach is particularly relevant for nonassociating metal complexes. The different process stages are schematically illustrated in [Figure 8.20](#).^{25,33,34}

To relate the necessary parameters, we introduce them in the equation for Gibbs free energy (G):

$$G = U + PV - TS + \mu n + \sigma A \quad (8.81)$$

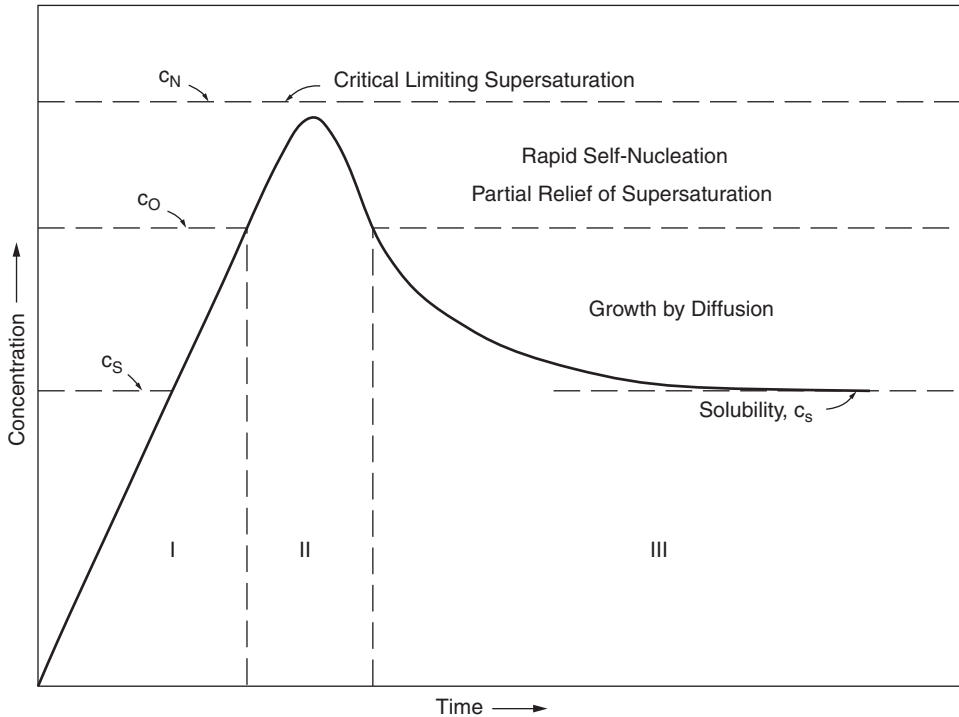


FIGURE 8.20 Schematic representation of the dependency of nucleation and growth on the degree of supersaturation. In the concentration range (c_N – c_0 , range II), both nucleation and growth occur, while only growth occur in the concentration range (c_0 – c_s , range III). (From La Mer, V.K. and Dinegar, R.H., *J. Am. Chem. Soc.*, 72, 4847, 1950. With permission.)

where U = internal energy, P = pressure, V = volume, μ = chemical potential, n = amount of substance (number of moles, but a one-component system is initially assumed), σ = surface energy, and A = surface area. Differentiation gives

$$dG = dU + VdP + PdV - SdT - Td + nd\mu + \mu dn + Ad\sigma + \sigma dA \quad (8.82)$$

For a reversible system for which the heat exchange may be written, $dQ = TdS$, we find

$$dU = TdS - PdV - \mu dn - \sigma dA \quad (8.83)$$

the two latter terms being identified as non-PV work.

Inserted into the differential equation for Gibbs free energy, we find

$$dG = VdP - SdT + nd\mu + Ad\sigma \quad (8.84)$$

At equilibrium ($dG = 0$) for which the temperature ($dT = 0$) and pressure ($dP = 0$) is constant we find for the surface excess, Γ :

$$\Gamma = (n/A) = -(d\sigma/d\mu) = -(1/RT)(d\sigma/d\ln a) \approx -(1/RT)(d\sigma/d\ln c) \quad (8.85)$$

where R = the gas constant. This is the Gibbs adsorption equation relating the amount of substance dissolved in the solution with the excess of substance adsorbed to the surface or interface. For a

curved surface at constant external pressure the contribution of the curvature to the total energy may be evaluated in the following way:⁶

$$dG = V \int dP = V\Delta P \quad (8.86)$$

where the integration was done from the pressure on the planar surface (P_o) to the enhanced pressure over the curved surface ($P_o + \Delta P$). To evaluate the ΔP term, we reconsider the Gibbs differential assuming no chemical ($d\mu = 0$) or surface work ($d\sigma = 0$) to be done at constant temperature ($dT = 0$). To find an useful expression, Hiemenz⁶ suggested an unconventional derivation by adding the σdA work of expansion to the Gibbs free energy:

$$dG = VdP + \sigma dA \quad (8.87)$$

A test for exact differentials (order of differentiation unimportant) shows that⁶

$$\partial/\partial A [(\partial G/\partial P)_A]_P = \partial/\partial P [(\partial G/\partial A)_P]_A \quad \text{or} \quad (\partial V/\partial A)_P = (\partial \sigma/\partial P)_A \quad (8.88)$$

For a first approximation we write for a sphere $(\partial V/\partial A)_P = [(\partial V/\partial r)(\partial r/\partial A)]_P = (4\pi r^2/8\pi r) = r/2$. Introducing this result into Equation 8.86, we obtain

$$\int d\sigma = \frac{1}{2}r \int dP \Leftrightarrow \Delta\sigma = \frac{1}{2}r\Delta P \quad (8.89)$$

Assuming that the initial state is $\sigma = 0$ and $P = P_o$ and the final state is σ and $P_o + \Delta P$, we obtain the Laplace pressure for the spherical shape (bubble, droplet, particle):

$$\Delta P = 2\sigma/r \quad (8.90)$$

Correspondingly, the activity of the substance increases as a function of the curvature:

$$dG = nd\mu = nRT(\ln a_r - \ln a_o) = nRT \ln(a_r/a_o) \quad (8.91)$$

The dissolution of a salt was discussed previously and for 1 mol ($n = 1$) of a complex salt in equilibrium with its saturated solution, we may write (Equation 8.14)

$$dG = vRT \ln(a_{\pm,r}/a_{\pm,o}) = vRT \ln(Q_r c_r y_{\pm,r}/Q_o c_o y_{\pm,o}) \approx vRT \ln(c_r/c_o) \quad (8.92)$$

where a_{\pm} is the mean activity of the salt (see Equations 8.5 through 8.8). For a multivalent salt the omission of Q and y_{\pm} may prove to be too rough. The surface energy term may also be integrated from the initial to the final state providing the surface work relating to defect energies, $A\Delta\sigma$. Inserted into the differentiated Gibbs Equation 8.84, we find

$$dG = 2\sigma V/r - SdT + vRT \ln(a_{\pm,r}/a_{\pm,o}) + A\Delta\sigma \quad (8.93)$$

At equilibrium ($dG = 0$) and for constant temperature ($dT = 0$). Replacing $V = M/\rho$ and $A\Delta\sigma$ for a sphere, we find

$$vRT \ln(a_{\pm,o}/a_{\pm,r}) = 2\sigma V/r + A\Delta\sigma = (2\sigma/r + 3\Delta\sigma/r)M/\rho \quad (8.94)$$

which represents the dissolution spherical particles given by the Kelvin equation. The precipitation is thus related to the curvature of the particles (proportional to V) formed and the surface energy work (proportional to A) done. The same expressions may be derived for any particle shape provided that the area of each unit is known. Then $A_p = \sum_i A_i$ and $A_p\sigma_p = \sum_i A_i\sigma_i$. Equation 8.94 is usually derived by focusing solely on the change in energy upon bending the interface. We then assume that the surface energy for the last term remains constant ($d\sigma = 0$) and it is thus neglected.⁶

The *rate of nucleation* has, as a function of curvature, been successfully linearly correlated with the degree of relative supersaturation according to Equation 8.94:

$$vRT \ln\left[\left(\frac{1}{2}c_r \sum_i v_{i,r} z_i^2\right) / \left(\frac{1}{2}c_o \sum_i v_{i,o} z_i^2\right)\right] \approx vRT \ln(c_r/c_o) \quad (8.95a)$$

where v is the total number of ions dissolved from one salt molecule. The nucleation rate can according to Figure 8.20 be written in a similar way:

$$\text{rate of nucleation} \approx vRT \left[(c_N - c_S) / c_S \right] \quad (8.95b)$$

The number of nuclei thus increases with an enhanced degree of supersaturation and a decreasing solubility of the precipitate (c_S). It is therefore advisable to precipitate slowly in dilute and heated solutions to diminish $(c_N - c_S)$ and to reduce the rate of nucleation. A low c_N may be achieved through reactions producing a slow release of reagents. If the supersaturated solution remains stable, seeding with foreign or equal crystals may be needed.

The growth rate of the nuclei has been correlated both with the degree of supersaturation and the diffusional transport of ions to the surface. For the dissolution of the sparingly soluble salt $A_{vA}M_{vM}$ (Process 8.13) it has been found that the growth rate of the nuclei may be expressed as³⁵

$$\text{growth rate} \approx (K_N^{1/v} - K_S^{1/v})^2 \quad (8.96)$$

where K is the solubility product ($K_{sp} = (Qc)^v$, Equation 8.15) of the electrolyte salt at supersaturation (N) and at saturation (S), respectively (Figure 8.20). The growth of sparingly soluble electrolyte crystals in aqueous solutions thus generally follows a parabolic rate law where the rate $\approx (c_N - c_S)^2$.

Transport properties are studied off equilibrium, thus investigating the irreversible or the steady-state process. The flux (J) may be considered the time-dependent change of any nondifferentiated state variable (X) in the Gibbs free energy function (Equation 8.84) divided by the cross sectional area through which the flow occurs. The flow is induced by the gradient of the conjugated differentiated state variable (Y). The flux J is thus defined as

$$J = (dX/dt)/A_\phi = -k(dY/dl) \quad (8.97)$$

where A_ϕ = the cross sectional area the flow crosses, and k is a conductivity (inverse of the resistance). The fluxes can be simultaneously coupled, but are considered separate in this context. For the transport of molecules in the absence of repulsive forces we have the Fick's first law, which states

$$J_c = (dn/dt)/A_\phi = -D_c (dc/dl) = -(D_c c/RT)(d\mu/dl) \quad (8.98)$$

where D_c is the diffusion coefficient. As seen, the equation basically describes the time-dependent flow of matter that is induced by the gradient of the chemical potential. For a sphere, the growth and transport of substance occur radially (in the r direction) and thus

$$J_c = (dn/dt)v/vA_\phi = (d(nv)/dt)/vA_\phi = -D_c (dc/dr) \quad (8.99)$$

where v denotes the molar volume of the solid. For a spherical particle $A_\phi = 4\pi N_p r^2$ (N_p = number of particles). Since $nv = 4\pi N_p r^3/3$, then $nv/A_\phi = r/3$ and

$$(dr/dt) = -3D_c v (dc/dr) \approx -3D_c v ((c_N - c_S)/r) \quad (8.100)$$

where c_N = concentration of the supersaturated solution and c_S = concentration of the equilibrium saturated solution. Instead of the radius we may choose a diffusive layer thickness ($r \rightarrow \delta$). A thorough mixing of the solution ensures that δ remains small.

The radial growth rate can also be related to the homogeneity of the process. The following relative growth rates for particles has been established³⁶ (consult Reference 25 for size distributions):

- For bimodal particles ($r_2 < r_1$) the proportional growth is $dr_1/r_1 = (r_1/r_2) dr_2/r_2$.
- For polynuclear growth ($dr/dt = k$, $dr_2/dr_1 = 1$) the growth is $dr_1/r_1 = (r_2/r_1) dr_2/r_2$.
- For diffusive growth ($dr_2/dr_1 = r_2^3/r_1^3$) the growth is $dr_1/r_1 = (r_2/r_1)^2 dr_2/r_2$.

It should be noted that the time dependency of the nucleation and the particle growth may be related to any kinetic rate law, since $(dn/dt) = [(dN_m/dt)/N_A]$, where N_m = number of molecules per particle and N_A = Avogadro's number. Usually the second-order rate law is chosen, although a very large number of molecules form the nuclei. Obviously, a very large number of ions associate continuously to clusters, but most of them disintegrate instantly. However, some of them manage to form clusters that are larger than a critical size. The rate law given by the kinetic molecular theory then contain a Boltzmann factor proportional to the cluster volume ($4\pi r^3/3$) and a frequency factor proportional to the surface area of the cluster ($4\pi r^2$).^{36,37} The basic proportionalities given above remain, but because this theory is not in direct relationship with the thermodynamic considerations discussed above, it will not be treated further in this context.

The reactions occurring for multivalent metal cations occur over many condensation steps and may not obey the kinetic rules outlined above. Silicate polymerization is known to depend on the presence of oligomeric ion species.^{26,38,39} Gibbsite (formally $\text{Al}(\text{OH})_3$) is known not to precipitate sufficiently rapidly from supersaturated solutions, but needs seeding for particle growth.⁴⁰⁻⁴³ Moreover, depending on the temperature and the composition of the solution, different solid species may form. This is illustrated in [Figure 8.21](#).⁴³

As shown, $\text{Al}(\text{OH})_3$ precipitates at moderate temperatures (60°C), but as the temperature is raised to 368 K (95°C) Boehmite (formally $\text{AlO}(\text{OH})$) begins to precipitate from solutions rich in Na_2O (dissolved NaOH) and Al_2O_3 (dissolved $\text{Al}(\text{OH})_3$). At 423 K (150°C) only Boehmite precipitates, but at 623 K (350°C) both Boehmite and alumina may precipitate. Depending on the reaction conditions, the $\text{Al}(\text{OH})_3$ precipitates as Gibbsite or Bayerite, respectively. In [Figure 8.22](#) the compositions of the industrial extraction and precipitation of Gibbsite are illustrated.⁴³

The precipitation from dilute solutions is delicately dependent on the physicochemical conditions, especially the pH and pI as well as the precipitation time. Impurities frequently enhance the solubility, but may cause a delay of the precipitation; see ligand reaction (Equation 8.42).

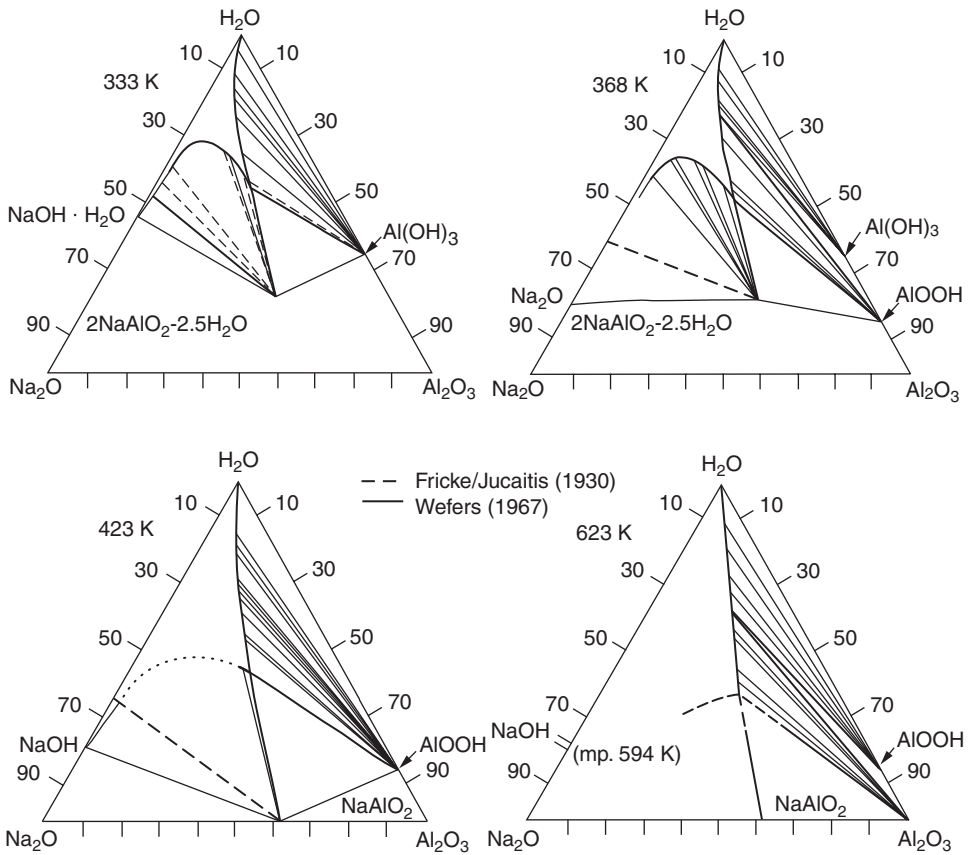


FIGURE 8.21 Phase diagram for the system $\text{Na}_2\text{O}-\text{Al}_2\text{O}_3-\text{H}_2\text{O}$ at four different temperatures. The precipitation of Gibbsite, Bayerite, Boehmite, and alumina from supersaturated aqueous solutions is dependent on the temperature. (From Wefers, K. and Misra, C., Report 19, Alcoa Laboratories, 1987, 44. With permission.)

It is quite typical that the first crystal form is not the most stable, but that it recrystallizes with time to a more stable crystal form. This introduces three unresolved questions concerning the structure of the so-called primary particles:

1. It seems probable that all primary particles are in fact clusters of condensed crystallites of 2 to 10 nm size, cemented together with an amorphous porous gel. Although much larger in size (100 to 500 nm) the primary particles may dissolve according to the crystallite size (Equation 8.94).
2. The minimum size of a colloidal particle has been arbitrarily chosen to be 10 nm to ensure that a sufficient number of constituent atoms/molecules may be considered to have the bulk material properties. The surface layer is typically amorphous, but may recrystallize (slowly) to the final bulk material. The surface chemistry outlined above thus relates to the amorphous surface layer, but not to the actual (recrystallized) surface of the bulk solid phase.
3. Nanoparticles must thus be considered to be either crystallites alone or the cementitious polymeric gel formed. In the former case the surface chemistry is well characterized if it is not covered by the gel. However, in the latter case the surface chemistry of the gel is rather obscure.

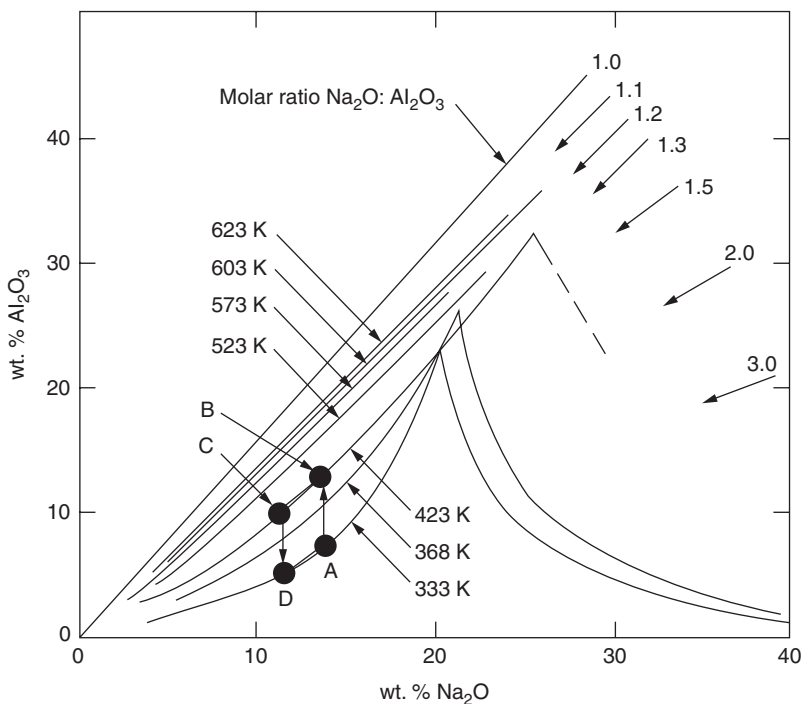


FIGURE 8.22 The variation in concentration of the extraction upon heating (A → B), dilution (B → C), supersaturation and precipitation upon cooling (C → D) of the Bayer process is indicated in the rectangular phase diagram of the $\text{Na}_2\text{O}-\text{Al}_2\text{O}_3-\text{H}_2\text{O}$ system. Evaporation of the spent liquor brings the concentration back to A (D → A). Note the variation of the extension of the aqueous phase as a function of temperature. (From Wefers, K. and Misra, C., Report 19, Alcoa Laboratories, 1987, 45. With permission.)

The primary particles may be illustrated as formed from coacervates of the crystallites, probably interlinked by dissolved polymeric species. Critical nucleus sizes for crystallization from aqueous solutions extend from the stable oligomeric species to polymers of 100 to 1000 ions/molecules. During the condensation, the shape of the crystallites is induced on the particulate structures formed (Figure 8.23).^{26,44}

This phenomenon is known for surfactant liquid crystals, where the macroscopic shape can be induced by external forces. Thus, if an external orienting force is exerted on the crystallite coacervates and a sufficient time is allowed for the crystallization to be completed, a macroscopic homogeneous crystal may form. Otherwise, even the primary particles are expected to be heterogeneous.

It should be kept in mind that crystallization is facilitated if the constituent ions are of the same size. As discussed the hydration potential ($\phi = z^2/r_{\text{eff}}$, Equation 8.41) was linearly related to the hydration enthalpy and energy. Because the primary hydration shell may be considered a part of the effective radius of the particle, it may be assumed that both the charge of the ion and the attracted hydration sheet influences the crystallization. For multivalent ions the energy gain in a crystal is maximized if a noble gas configuration is maintained during charging. A larger valency increases the bonding energy considerably. For transition metals the cost of ionization is much less critical.

8.5.3 KINETICS OF HYDROLYSIS, ASSOCIATION, AND POLYMERIZATION

The kinetic stability of the aquo complexes may be considered one important factor for hydrolysis and condensation. In Figure 8.24 the stability is characterized as the dissociation constant for one water molecule from the saturated aquo complex.^{26,45}

	Coacervates	Tactoids	Crystalloids	Flocks
Rods				
Plates				
Spheres				

FIGURE 8.23 Particles are formed from coacervates of crystallites that condense over tactoids and crystalloids to particulate flocs. Upon aging the flocs condense to dense agglomerates, but maintain the shape of the original crystallites. (From Heller, W., in *Polymer Colloids II*, R.M. Fitch, Ed., Plenum Press, New York, 1980. With permission of Elsevier Science.)

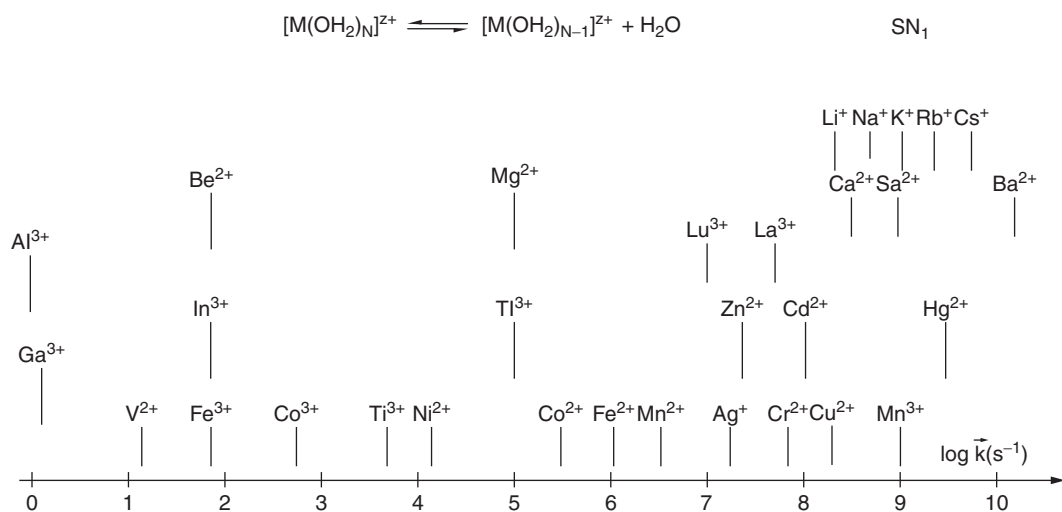


FIGURE 8.24 The kinetic lability of the aquo complexes of metal cations illustrated as the dissociation constant of the first water molecule from the saturated aquo complex. (From Livage, J. et al., *Prog. Solid State Chem.*, 18, 265, 1988. With permission.)

It is clear that the stability is related to the nucleophilicity of the metal cation (see Figure 8.9). However, as illustrated by the PCM model, the condensation reactions are much more complex.

The precipitation of Gibbsite is quite intriguing because of the exceedingly slow crystallization from caustic concentrated aluminate solutions and deserves additional attention. As discussed previously, the type of aluminum complexes are numerous and they change dramatically with pH (Figure 8.4) and pI (Figure 8.5). Al^{3+} has been found to exist as a free ion only at $\text{pH} < 3$. Moreover, from the discussion of the phase behavior of Gibbsite it is obvious that the temperature (and pressure) also influences the distribution of the Al species. However, both theoretical considerations and experimental evidence suggest that either ionic $\text{Al}(\text{OH})_4^-$ or the neutral $\text{Al}(\text{OH})_3\text{OH}_2$ is the dominant species in solution.⁴⁰⁻⁴² Hem and co-workers^{11,12} have thoroughly analyzed the equilibrium distribution of free, polymeric and crystalline Al species in dilute (4.5×10^{-4} mol/dm³) aqueous solutions of dissolved Gibbsite at a constant ionic strength (10^{-2} mol/dm³). It was found that the free Al species reached equilibrium within 23 h which decreased rapidly with the amount of NaOH. The approach to equilibrium could be followed as a change in pH (see Equations 8.37 and 8.38). The time-dependent distribution of the polymeric species and the nuclei was sensitively dependent on the $n(\text{NaOH})/n(\text{Al}(\text{OH})_3)$ ratio, the speed of alkali addition, and the mixing time.

Three different reaction periods could be discerned:^{11,12}

- First, there was a linear increase in the amount of polymeric species over the first hour, and the amount increased, the more slowly the alkali was added. This indicates a first-order time dependency. After 4 days the polymers begin to condense to nuclei, reducing the initial rate as only a few reach the critical nucleus size.
- Second, during the period of 40 to 120 days another linear, first-order reaction is observed. It was concluded using SEM (scanning electron microscopy) pictures that within this period the polymeric species reach the sizes of nuclei.
- Finally, after 120 days the reaction rate was again reduced. Simultaneously, the methods used for characterization became too insensitive for the detection of the free and polymeric species. The probable reason is the consumption of these species during the growth of the nuclei.

Taking the most important Al species into account (Equations 8.37 and 8.38) and the (hexagonal) crystal form of the Gibbsite particle, Hem¹² could calculate the surface energy of the crystal planes. The surface energy was evaluated by taking the derivative of the energy function corresponding to Equation 8.94 with respect to the 001-side length of the particle. The area and the volume, respectively, were defined by the hexagonal surface plane and the edges defined by the thickness of the Gibbsite particle. Because the first and second derivative of the energy function with respect to the 001-side length was found to be positive, it was claimed that the extreme point was a minimum. Setting the first derivative to zero, Hem calculated the surface energies for the face and edge of the crystal.

The surface can be visualized as built up by cubic units where each side represents an interaction site.^{35,46} This allows the surface to be represented by inhomogenities, such as kinks, steps, vacancies, and ad atoms. The sites by which an adsorbed atom can simultaneously be bonded with can be maximally five for the vacancy, four for the kink, two for the step, and one for the ad atom. Obviously, the molecular adsorption energy is a function of the surface roughness, here represented by ξ :⁴⁶

$$\xi = n_s \varepsilon / kT = n_s / kT \left[\frac{1}{2} (\Phi_{LL} + \Phi_{SS}) - \Phi_{SL} \right] \quad (8.101)$$

where n_s = number of surface bonds formed upon adsorption, ε = potential energy balance per bond, and Φ = the type of potential energy assigned for each bond. The surface charge has been found to influence the adsorption and subsequently the reaction rate. The contribution from the surface

potential can thus be included in the Φ expressions. As seen, the potential energy balance corresponds to the molecular adhesion work upon adsorption, i.e., it is an effective molecular surface energy. It has been found that the surface roughness enhances the growth rate; i.e., the inhomogeneities may be considered surface nuclei, which induces surface precipitation.

8.5.4 SUMMARY

The thermodynamic approach is a straightforward way to interlink the solution properties to the formation of a solid surface during the precipitation of particles. However, the idealized process is obscured by the reality: The particles form within a diffuse coacervate through slow crystallization of typically 2 to 10 nm crystallites. Kinetically the process is determined by the stabilization of critical oligomeric species, but a number of subsequent polymerization processes follow, all of which have different rates. The precipitating particles are mostly heterogeneous. It thus seems that no simple model can be designed for the entire oligomerization–polymerization–crystallization–precipitation process. On the contrary, each process stage must be modeled separately.

8.6 PEPTIZATION OF SOLS

Preparation of the primary oligomeric clusters has been discussed in terms of the association of the ions in electrolyte solutions or condensation-mediated ion clustering. Dependent on the electrolyte concentration and the physicochemical state (P, T, pS, pH, pI, pc_L , pc_M , pe) of the system, the ions associate to polymeric species or then the ion clusters may reach the critical size that enables them to grow to primary particles of some 100 nm in size. As discussed, they are probably a coagulate of cemented crystallites of 1 to 10 nm size. However, to be useful for further processing, these must be stabilized to sols, i.e., to a stable dispersion of particles of colloidal (10 to 1000 nm) size.

There are basically two approaches for the stabilization:^{6,14,25}

- Electrostatic stabilization
- Steric stabilization

As indicated above, some ions may dissolve from the ionic crystals formed (Equations 8.27a and 8.33a). Most frequently, it is the more extensively solvated metal cations that dissolve (Equation 8.33a), but they are in some cases replaced by cations of lower charge (cation exchange). This leads to an excess of negative charges at the surface. If the anion is an oxide, then the surface oxygens are known to become hydrolyzed and are at low pH capable of forming protonated cationic ($>O-H_2^+$) surface groups. At high pH these surface groups are deprotonated to anionic ($>O^-$) surface groups. Both the effective amount of dissolved cations and the degree of dissociation of the surface hydroxyl (and other Brønsted active) groups determine the surface charge of the particles. Depending on the way the charge is regulated, either the metal cations or the protons are then denoted potential determining ions. If the cation concentration (pc_M) is varied, the cations are potential determining, but if the pH (pc_H) is varied, the protons are potential determining.



However, the cations may also be involved in hydration and hydrolysis equilibria as a function of pH (Equations 8.33 and 8.34), which alters their charges and affinities for the surface groups. The surface hydroxyl groups may, of course, be involved in the competition of the ligand sites in

the coordination sphere of the cation. Moreover, depending on the deprotonation degree, the cation assumes a large number of different charges. Both the charge and the chemical affinity for the surface groups or free surface sites may lead to the adsorption or reprecipitation of the dissolved metal cation clusters, which was shown to depend on the surface roughness. These reactions and adsorption can, of course, occur for foreign cations as well. It is then rightfully claimed that the particles in solution are overextended pH regions, covered with a reprecipitated surface gel layer that has properties different from the naked particle surface.⁴¹ This equals the situation found for the crystallites and primary particles discussed in the previous section.

Because of the heterogeneous surface properties, different cleaning procedures have been suggested for the removal of the surface gel layer and to bring the dissolution of cations into equilibrium with the indifferent support electrolyte (for which there is no specific chemical adsorption). The surface is, however, quite rich in energy and it is not surprising to find many of the cleaning solution components (mostly ions) adsorbing instead. Additionally, the successive extraction leads to a gradient surface poor in native metal cations. Rather, it is characterized by stable but unnatural (pristine) surface properties.^{6,33,47}

8.6.1 ELECTROSTATIC STABILIZATION OF SOLS

The electrostatic properties of particles can be described by two key parameters, the surface charge density and the kinetic surface potential. The surface charge density (σ_o) corresponds to the potential at the particle surface (ψ_o). This charge regulates the interaction of dissolved ions with the surface and the effective charge is dependent on the degree of adsorbed counterions to the surface. In this section we discuss the relative effect of simple ions (no deprotonation and no condensation of aquo ligands) on sol stability when the pH is varied.

The purely charge controlled stabilization of sols has been successfully described by the Deryagin–Landau–Veerwey–Overbeek (DLVO) theory. The potential energy (Φ) of the particles is determined by adding the repulsive (positive Coulomb) energy to the attractive (negative van der Waals) energy. For large particles, i.e., assuming a planar contact surface, the DLVO theory states that^{6,14,25,33,48}

$$\Phi = 64c\kappa^{-1} RT\gamma_o^2 \exp(-\kappa d) - A_H/12\pi d^2 \quad (8.103)$$

where c = concentration of ions (number of ions per unit volume/ N_A) near the surface, κ^{-1} = Debye length (Equation 8.9, Tables 8.3 and 8.4), γ = complex ratio of the surface potential given by the Gouy–Chapman theory,⁶ A_H = the Hamaker constant (this material constant is dependent on the particle shape), and d = distance between the surfaces of two approaching particles. For low surface potentials, $\gamma_o \approx ze\psi_o/4\kappa T$ (Debye–Hückel approximation). Typically, the attractive energy predominates at very short distances (0 to 5 nm) whereas the repulsive energy extends to longer distances (0 to 10 nm). If the ion cloud is sufficiently extensive around the particles to create a repulsive barrier, the attachment of the particles is kinetically hindered (Figure 8.25) and the sol is stable.

However, if the ionic strength is enhanced, the thickness of the electrolyte cushion is rendered thinner. A larger fraction of particles may then collide per unit time, leading to a coagulation of the particles to a dense sediment. For a 0.1-mol/dm³ 1:1 electrolyte solution, the repulsive electrostatic barrier (Tables 8.3 and 8.4) may be considered to be effectively removed and the particle coagulation is controlled by diffusion alone. Sometimes a balance is reached at intermediate distances (3 to 5 nm), which is characterized by a weak negative minimum. Then, the particles form a loose flocculated structure that is easily redispersed. To a great extent the association kinetics follows the same principles as for the ions discussed above, but at a slower rate.^{6,25,33,48}

As mentioned, the surface charge can be determined by potentiometric, Coulometric, or conductometric titration of protons or metal cations to the surface at a constant ionic strength. Most

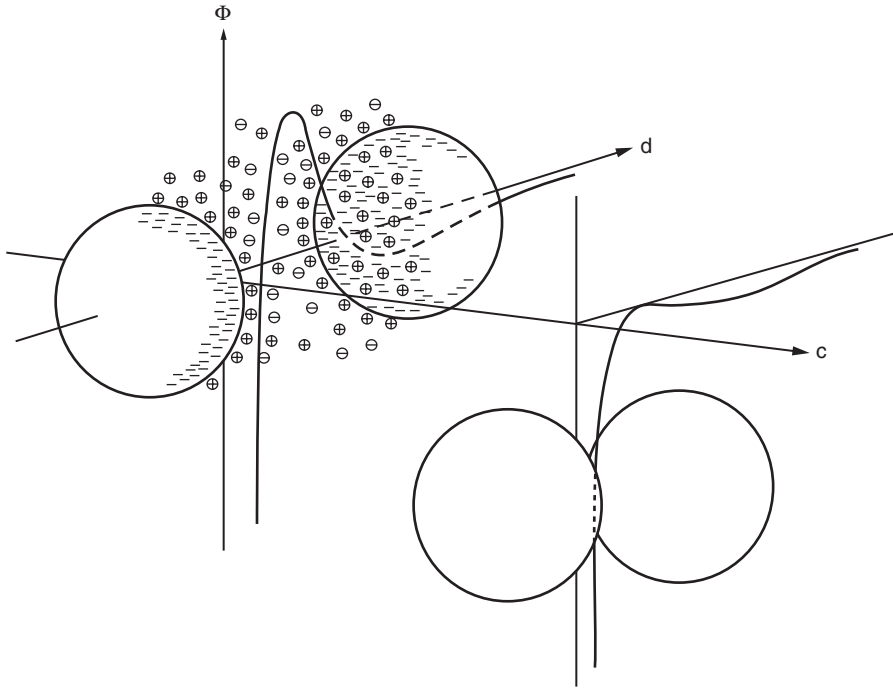


FIGURE 8.25 The stability of a sol (a suspension of colloidal particles) may be evaluated from the balance of repulsive (electrostatic) interaction forces and attractive (dispersive) interaction forces, e.g., by applying the DLVO theory (Equation 8.103). If a potential energy barrier exists the system is stable (left). If the barrier is removed, the coagulation of the particles is controlled by diffusion alone. (Courtesy of Jean Le Bell.)

frequently, the titration is done as a function of pH, and then the surface charge density is determined by

$$\sigma_o = F(\Gamma_{H^+} - \Gamma_{OH^-}) = \left(\frac{F}{wA_{sp}}\right)(n_{H^+}^s - n_{OH^-}^s) \quad (8.104)$$

where $\Gamma = n_i^s / A = n_i^s / wA_{sp}$ (subscript s relates to surface sites). The point at which $\sigma_o = 0$ is denoted the point of zero charge (pH_{PZC}). As discussed above, this is the pH where the condensation reactions occur most readily due to the absence of an electrostatic barrier upon approach. Note the very unusual σ_o for SiO_2 , which is zero in the range $2 < pH < 6$ (Figure 8.26).⁴⁷

Recalling the reaction schemes (Equation 8.102) representing the surface proton exchange, we find the following equilibrium constants:⁴⁸

$$K_a^s(\text{acid}) = a_{MOH}^s a_H^s / a_{MOH2}^s \approx c_{MOH}^s c_H^s / c_{MOH2}^s \quad (8.105a)$$

$$K_a^s(\text{base}) = a_{MO}^2 a_H^s / a_{MOH}^s \approx c_{MO}^s c_H^s / c_{MOH}^s \quad (8.105b)$$

However, in these cases the proton exchange occurs at the surface of the particle(s) and this must be related to the concentration (or activity) of the protons in the equilibrium solution. This may be done by applying the Boltzmann equation, which states

$$c_H = c_H^s \exp - (e\Psi_o / kT) \quad (8.106)$$

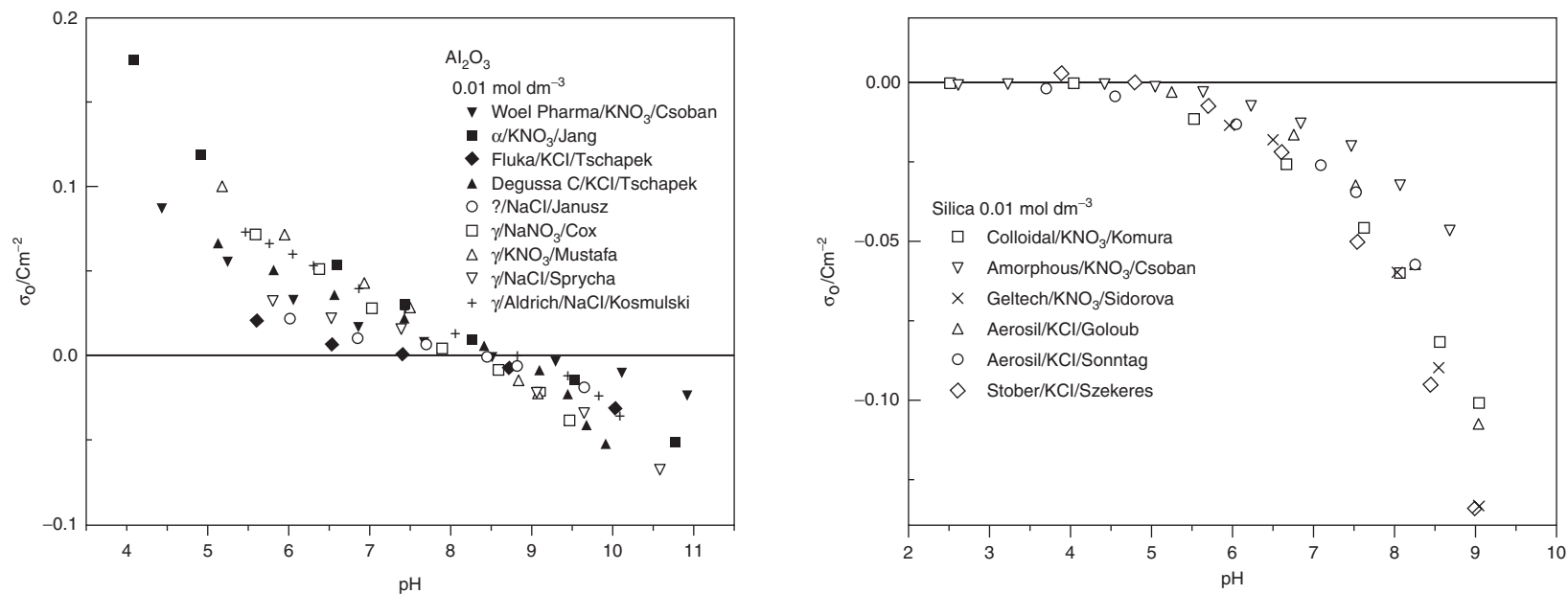


FIGURE 8.26 The surface charge density for aqueous 0.01 mol/dm³ electrolyte sols of alumina and silica as a function of pH. (From Kosmulski, M., *Chemical Properties of Material Surfaces*, Surface Science Services, 102, A.T. Hubbard, Ed., Marcel Dekker, New York, 2001, 224. With permission.)

Now the surface charge density may also be written in terms of the fraction of charged surface hydroxyls:

$$\sigma_o = eN_{\text{site}} \left[\frac{(c_{\text{MOH2}}^s - c_{\text{MO}}^s)}{(c_{\text{MOH}}^s + c_{\text{MOH2}}^s + c_{\text{MO}}^s)} \right] \quad (8.107a)$$

where the number of surface sites, $N_{\text{site}} = [(V/N_A)(c_{\text{MOH2}}^s + c_{\text{MO}}^s + c_{\text{MOH}}^s)]$. Inserting the equilibrium constants, we obtain⁴⁸

$$\begin{aligned} \sigma_o = eN_{\text{site}} & \left\{ \left[\left(\frac{c_H}{K_a^s} (a) \right) \exp - (e\psi_o/kT) - \left(\frac{K_a^s (b)}{c_H} \right) \exp (e\psi_o/kT) \right] \right. \\ & \left. \div \left[1 + \left(\frac{c_H}{K_a^s} (a) \right) \exp - (e\psi_o/kT) + \left(\frac{K_a^s (b)}{c_H} \right) \exp (e\psi_o/kT) \right] \right\} \end{aligned} \quad (8.107b)$$

The surface charge density can thus be related to the pK_a^s values for the surface protons in the same way as done in solutions. According to the Nernst equation, the surface potential can be related to the pH_{PZC} as

$$\psi_o = 2.3RT/F (\text{pH}_{\text{PZC}} - \text{pH}) \quad (8.108)$$

The Hammett function may also be used for the determination of the acidity of surface sites. For solids dispersed in nonaqueous liquids, Walling defined the acid strength as the ability of the surface sites to convert an adsorbed neutral base into its conjugate acid:^{19,20}

$$\begin{aligned} H_o &= -\log a_H^s + \log (y_{\text{HB}}^s / y_B^s) = \text{pH}^s + \log (y_{\text{HB}}^s / y_B^s) \\ &= \text{pK}_a^s - \log (c_{\text{HB}}^s / c_B^s) \end{aligned} \quad (8.109)$$

where the pH^s stands for the surface acidity. The reaction proceeds as a proton transfer from the surface to the adsorbate. Similarly, for solids the basic surface site strength is defined as the ability to convert an adsorbed neutral acid into its conjugated base. This means that the adsorbate donates a proton to the surface:^{19,20}

$$\begin{aligned} H_o &= -\log a_H^s + \log (y_{\text{HA}}^s / y_A^s) = \text{pH}^s + \log (y_{\text{HA}}^s / y_A^s) \\ &= \text{pK}_a^s - \log (c_{\text{HA}}^s / c_A^s) \end{aligned} \quad (8.110)$$

In both cases the equivalence point coincides with the equilibrium $c_{\text{HB}}^s = c_B^s$ and $c_{\text{HA}}^s = c_A^s$, respectively. There are a number of standard indicators with a range of pK_a values used in organic solvents for this purpose. Their color change thus matches the equivalence point. However, the pK_a values used are determined in aqueous solutions as a function of pH.

The kinetic potential is usually denoted as the zeta (ζ) potential and it is determined from the electrophoretic mobility of the extremely dilute particles in an electric field. More recently, the use of electrokinetic sonic amplitude (ESA), acoustosizer (AZR), or colloid (or ultrasonic) vibration potential (CVP) has become available for the determination of the ζ potential in rather concentrated particle suspensions. Again the ζ potential may be measured as a function of either the metal concentration or the pH. In the latter case the point where the mobility ceases is denoted the isoelectric point (pH_{IEP} [Figure 8.27](#)).⁴⁷ It correlates particularly well with the stability of the sol,

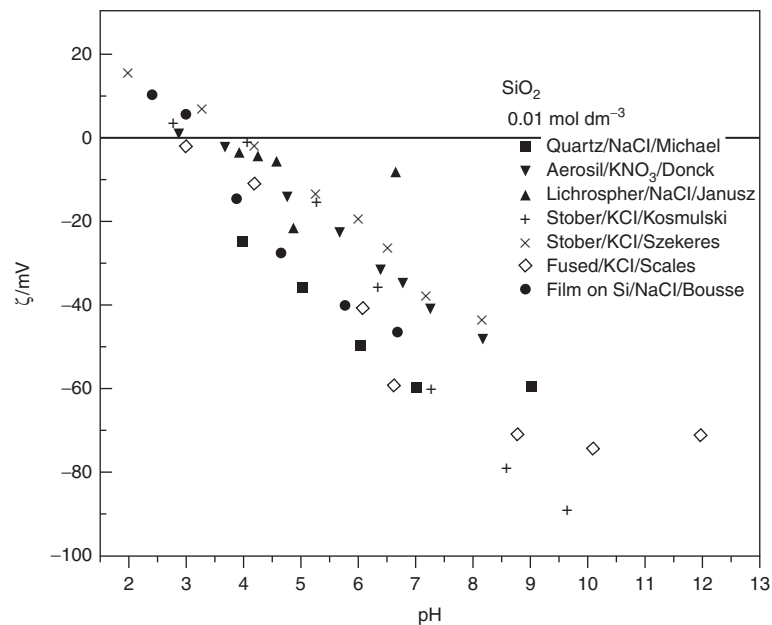
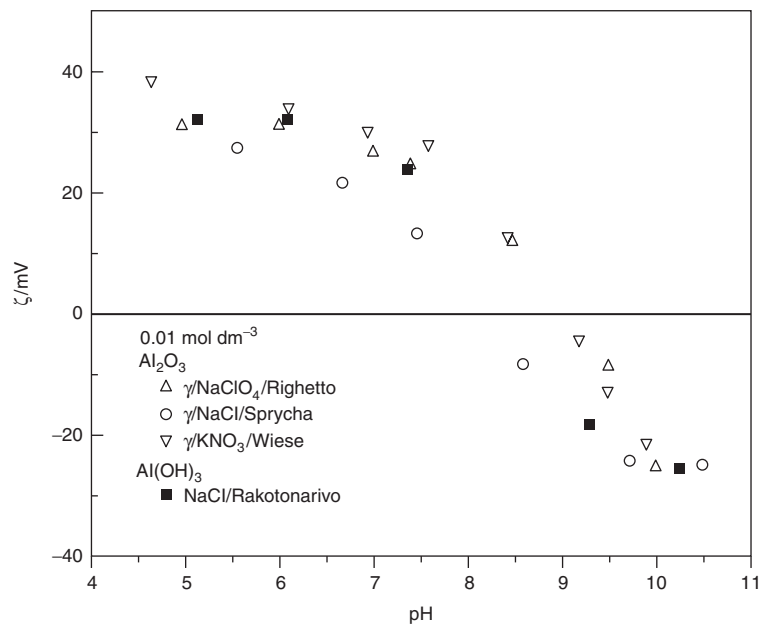


FIGURE 8.27 The effective surface charge (ζ potential) for aqueous 0.01 mol/dm³ electrolyte sols of alumina and silica as a function of pH. (From Kosmulski, M., *Chemical Properties of Material Surfaces*, Surface Science Services, 102, A.T. Hubbard, Ed., Marcel Dekker, New York, 2001, 250. With permission.)

TABLE 8.7
The pH Ranges for Charge Reversal
for Some Ceramic Oxides at 25°C

Valency	Oxide	pH Range
$z = +1$	$M_2O, M(OH)$	$10 < \text{pH} < 14$
$z = +2$	$MO, M(OH)_2$	$8 < \text{pH} < 12$
$z = +3$	$M_2O_3, MO(OH)$	$6 > \text{pH} < 10$
	$M(OH)_3, (M_3O_4)$	
$z = +4$	$MO_2, M(OH)_4$	$4 < \text{pH} < 8$
		$2 < \text{pH} < 6$
$z = +5$	M_2O_5	$1 < \text{pH} < 5$
$z = +6$	MO_3	$0 < \text{pH} < 4$

as it represents the effective charge of the particles. It may be visualized as the surface charge screened by the ion cloud surrounding the particle. The thickness of the layer indicates the efficiency of the screening and is given by the Debye length ($1/\kappa$, Equation 8.12, Tables 8.3 and 8.4).

As discussed above, the particles may assume a wide variety of surface properties depending on how they are manufactured and conditioned (e.g., washed). Moreover, the surface is hydrolyzed to an extent that is also dependent on the conditioning of the powder (e.g., heat treatment). There is thus a very large scatter of the points of zero charge and the iso-electric points found for ceramic oxides. Instead of offering a specified selection of assumedly best values for each crystal form and degree of hydroxylation of the lattice and surface, pH ranges for the charge reversal are provided in Table 8.7.⁴⁷

Although the ranges indicated are wide, it is obvious that they follow a certain pattern. It seems that the $z = +4$ oxides may be characterized by two subgroups, one following the sequence of $+1 < z < +4$ and the other the sequence $+4 < z < +6$. The $z = +4$ oxides were shown in aqueous solutions to be capable of forming both aquo-hydroxo and hydroxo-oxo complexes as a function of pH. The lower charged metals formed predominantly aquo-hydroxo complexes while the higher-charged metals formed predominantly hydroxo-oxo complexes as a function of pH (see Figure 8.14). The critical pH values seem to roughly coincide with the $\text{p}K_a$ of their acids in aqueous solutions. It thus seems that the PCM theory is also related to the charge properties of the metal oxides. The electronegativity of the metal oxide may be averaged according to:⁴⁷

$$\langle \chi \rangle (M_{\text{VM}}O_{\text{VO}}) = [\chi_{\text{M}}^{\text{VM}} \chi_{\text{O}}^{\text{VO}}]^{1/(\text{VM}+\text{VO})} \quad (8.111)$$

where χ_{M} and χ_{O} are the electronegativities of the metal and oxygen, respectively. The point of zero charge may now be described as a linear function of the electronegativity:⁴⁷

$$\text{pH}_{\text{PZC}} = a - b \langle \chi \rangle (M_{\text{VM}}O_{\text{VO}}) \quad (8.112a)$$

where a (= 57.3 to 61.4) and b (= 8.48 to 9.25) are regression coefficients and χ is given in volts. A slightly different form has also been suggested:⁴⁷

$$\text{pH}_{\text{PZC}} = 14.43 - 0.58(1 + 2z)\chi_{\text{Mz}} \quad (8.112b)$$

where z is the charge of the metal cation and χ_{Mz} the electronegativity at that particular oxidation state. The pH_{PZC} has also been linearly correlated to, e.g., the effective ion potential ($\psi = z/r$)_{eff}, the

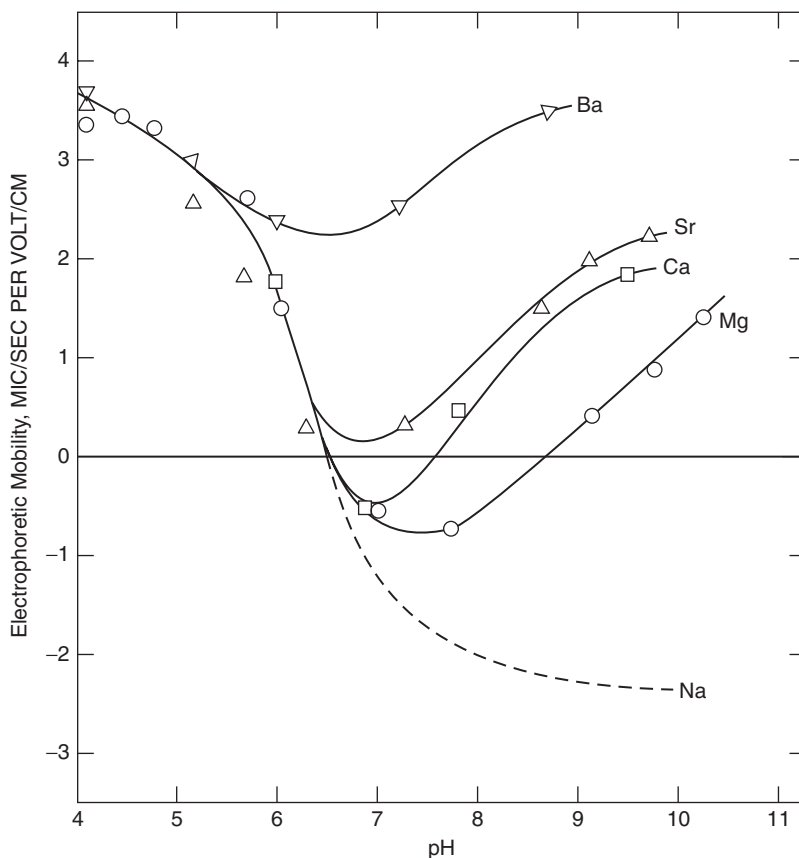


FIGURE 8.28 The electrophoretic mobility of titania (rutile) particles in aqueous solutions of 0.33×10^{-3} mol/dm³ nitrate solutions of different mono- and divalent cations as a function of pH. (From Fuerstenau, D.W. et al., in *Adsorption from Aqueous Solutions*, Vol. 3, P.W. Tewari, Ed., Plenum Press, New York, 1981, 112. With permission.)

effective ion charge density ($\sigma = z/r^2$)_{eff}, and the coordination number. The corrections refer to crystal field stabilization energy of the metal cation that is a nonelectrostatic contribution to the energy of hydration of the cation.

8.6.2 SPECIFIC BINDING AND SURFACE PRECIPITATION OF IONS AND LIGANDS

As shown in [Figure 8.24](#), the collective influence of the added simple (indifferent) ions is that they enhance the screening of the surface charge. At the end, the effective surface charge is reduced to zero and the particles are diffusively coagulated. For multivalent ions the simple balance between repulsive (Coulomb) and attractive (van der Waals) forces is rendered more complicated because of the enhanced solvolytic activity of the cations. From [Figures 8.4](#) to [8.6](#) it is obvious that the cations form a wide range of ionic species that bear high cationic and anionic charges. This means that the formal charge may vary considerably and even become opposite, which influences the electrostatic adsorption. The charge reversal from positive to negative, which is expected for the particles at enhanced pH, may thus be initiated or then the positive charge may even be enforced. This is due to the specific excess adsorption of cations to the positive surface aided by the chemical contribution to the overall energy balance ([Figure 8.28](#)).⁴⁹

From an electrostatic point of view, the specific adsorption of cations is explained as an inhibition of the proton adsorption and an induced hydroxyl ion adsorption. For the original proton

equilibrium ($\Gamma_{H^+} = \Gamma_{OH^-}$) to be restored, a higher proton concentration in the bulk is required, which is observed as a shift of the pH_{PZC} to lower values. The opposite occurs for the isoelectric point (pH_{IEP}). The specific adsorption is thus sensitively detected as an enlarged difference between pH_{PZC} and pH_{IEP} . The contribution of the specific adsorption of cations and anions, respectively, to the surface charge density may be described as

$$\sigma_o = F(\Gamma_{H^+} + z(+)\Gamma_{z^+} - \Gamma_{OH^-}) \quad (8.113a)$$

$$\sigma_o = F(\Gamma_{H^+} - \Gamma_{OH^-} - z(-)\Gamma_{z^-}) \quad (8.113b)$$

The simple surface hydration and proton exchange enables the metal cation complexes also to adsorb due to ligand exchange. Equally with the solvent association and condensation processes this adsorption may lead to the formation of extended gel structures and surface precipitation. However, as the surface site distribution and surface potential influence these processes, the physicochemical conditions (pS, pH, pI, pe) where they occur do not match those for the solution species.⁵⁰

Figure 8.29 illustrates the relationship between the charge reversal and the formation of a surface gel resulting in precipitation of divalent cations when the pH is increased. Three pH regions can be discerned. In the most acidic solutions the divalent metal cations are not expected to produce any deprotonated hydroxy complexes (see Figure 8.14) and thus their specific effect is rather small. (Note, however, Ba^{2+} in Figure 8.28.) The pH dependency then resembles that of indifferent ions. At extremely high pH the metal hydroxide precipitates and coats the particle. Consequently, the charge properties correspond to the metal hydroxide and not to the particle. An incomplete coating is reflected as a shift of the pH_{IEP} (Figure 8.28) toward lower pH values. In the intermediate pH range, where a charge reversal is observed, a gel formation is initiated at the surface through condensation reactions much in the same way as for high-valency cations in aqueous solutions. This occurs at a pH well below the bulk precipitation. It may be considered an overlapping phenomenon consisting of the normal charge screening and the surface precipitation, respectively. For high-valency cations the surface precipitation processes may be considerably more complex, but equal in nature.

8.6.3 SPECIFIC BINDING OF LIGANDS AND SURFACE MODIFIERS

It is well known that the sols are reprecipitated (coagulated to stable sol) after synthesis mainly with mineral acids and surfactants, depending on whether aqueous, mixed, or nonhydrous solvents are used.²⁹ The ligand adsorption to the surface groups occurs thus in much the same way as the adsorption of cation complexes discussed above. The ligand adsorption in the presence of other competing reagents may thus be organized with conditional constants, while the probability of adsorption may be evaluated with the PCM model. In both cases tabulated reference data are extensively published and easily available.

To evaluate the adsorption of chelates and organic ligands, such as surfactants, a simple adsorption isotherm model may be used. The perhaps most straightforward model has been developed by Langmuir. Assuming that the surface is basic and the adsorbate is acidic in the Brønsted or the Lewis sense, we obtain for the displacement of the solvent liquid (L) molecules by the adsorbate (A):⁵¹

$$K_{ads} = a_A^s a_L / a_A a_L^s \quad (8.114)$$

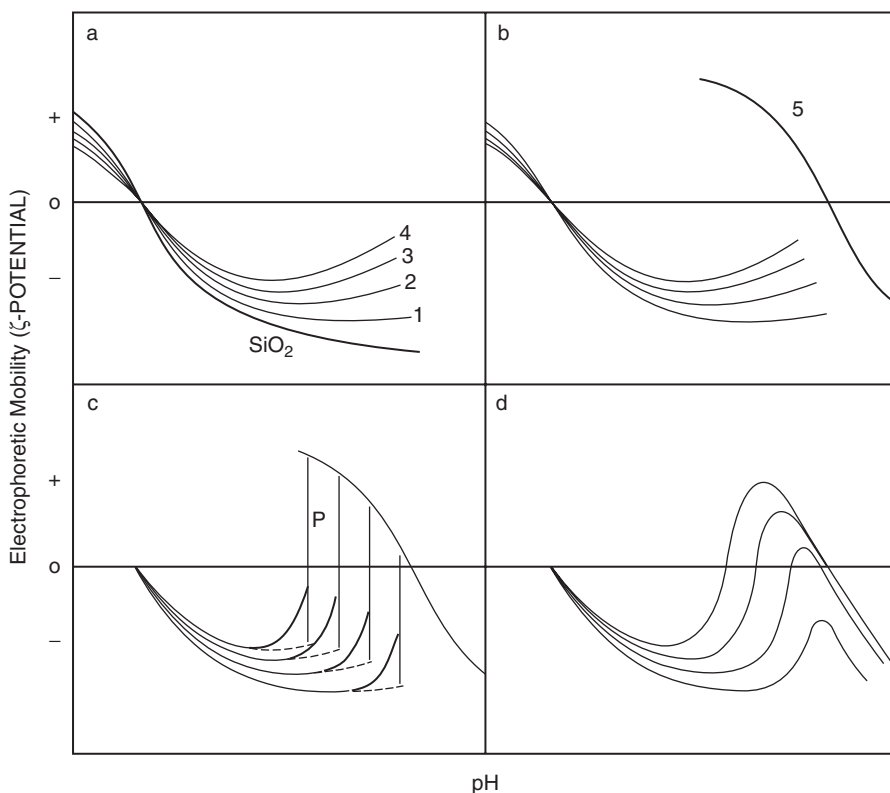


FIGURE 8.29 A schematic presentation of the dependency of the electrophoretic mobility (ζ potential) on pH when the divalent cations precipitate as metal hydroxides on the particle surface at high pH. (a) Normal behavior for increasing electrolyte concentration. (b) Metal hydroxide (5) form at high pH. (c-d) Depending on the electrolyte concentration the second crossover point moves to lower pH due to enhanced surface precipitation. (From James, R.O. and Healy, T.W., *J. Colloid Interface Sci.*, 40, 61, 1972. With permission of Harcourt Inc.)

If the surface sites are located sufficiently far apart the adsorbed molecules may be considered to behave ideally and the activities can be replaced by mole fractions ($x_L^s = 1 - x_A^s$). Maintaining the concentration scale for the bulk solution we may rewrite Equation 8.114 in the following form:

$$K_{\text{ads}} = x_A^s c_L / (1 - x_A^s) c_A \quad (8.115)$$

where the equilibrium constant is expressed consistently in ratios of the amount of the components. The fraction of sites occupied is obtained by further rewriting the equation in the form:

$$x_A^s = (n_A^s / n_m^s) = c_A K_{\text{ads}} / (c_L + c_A K_{\text{ads}}) \quad (8.116)$$

where n_m^s = saturated adsorption (total number of sites) and c_i = equilibrium concentration. To find the plot by which the adsorption data are expected to be linearized we invert the equation and multiply it by $c_A w$:^{6,51}

$$c_A / (n_A^s / w) = c_L / [K_{\text{ads}} / (n_m^s / w)] + c_A / (n_m^s / w) = a + b c_A \quad (8.117)$$

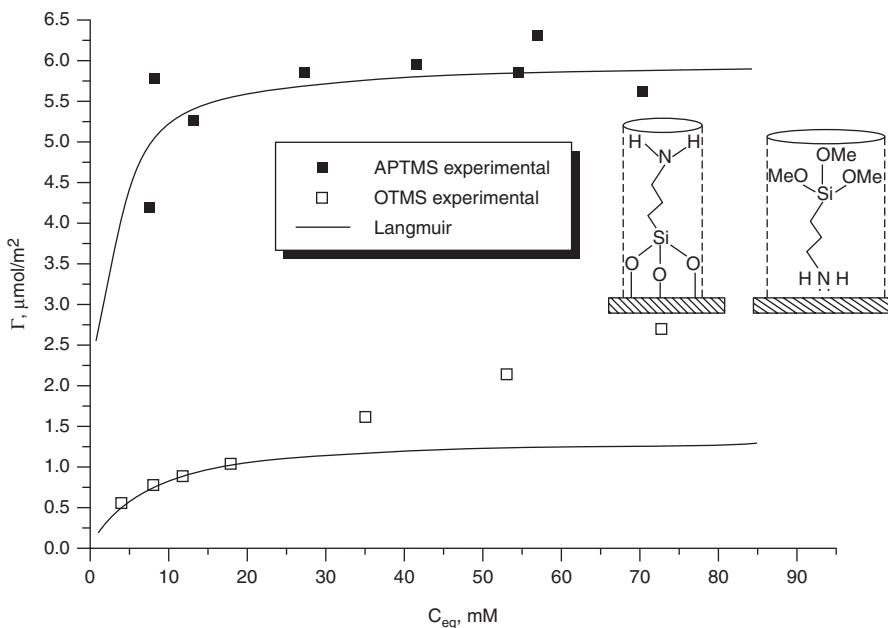


FIGURE 8.30 The fit of the Langmuir isotherm to the experimental surface excess of APTMS and OTMS silanes determined for aqueous solutions at 25°C. (From Eklund, T. et al., in *Silanes and Other Coupling Agents*, Vol. 2, K.L. Mittal, Ed., VSP BV, Zeist, 2000, 63. With permission.)

where w = weight (mass) of the solid particles. A plot of $c_A/(n_m^s/w)$ against c_A should provide a straight line for which the intercept a and the slope b gives the $K_{\text{ads}} = b/a$. It can also be used to determine the surface area if the cross sectional area of the molecule or ion is known (a_o), since $A_{\text{sp}} = N_A a_o / b = N_A n_m^s / w$. The number of sites is obviously: $N_A n_m^s = A_{\text{sp}} w / a_o$. A fit of Equation 8.117 to the adsorption data of two silanes onto porous silica particles is presented in Figure 8.30.⁵²

The same equation has also been used to quantify the amount of specifically adsorbed cations. For both Lewis and Brønsted acids and bases this adsorption isotherm relates to the Hammett function (Equations 8.80, 8.109, and 8.110).

8.6.4 SUMMARY

The same factors that determine the reactions in aqueous solutions self-evidently also occur at the particle surfaces in equilibrium with the solution. The benefit of recognizing this fact is that the same tabulations of critical properties may be used to predict the surface reactions. The sol particles may be considered to represent a rigidized macrocluster of ion species. It should, however, be kept in mind that corrections have to be made for the adsorption against an ion cloud and against a surface potential. Both the surface charge and the site distribution at the surface (the surface morphology) influence the gel formation and the surface precipitation as well. The specific adsorption may, of course, be used for surface modification of the particle surfaces.

A particularly interesting example on the interplay between the proton exchange for the surface hydroxyls and the adsorption or desorption of solution species is provided by silica. As mentioned above, it is known that the hydrolysis of silica species is minimal at $6 < \text{pH} < 7$. It is therefore expected that the number of $>\text{SiOH}_2^+$ groups (Equation 8.102a) increases when the pH scale descends and the number of $>\text{SiO}^-$ groups (Equation 8.102b) increases when the pH scale ascends. Moreover, it is expected that the stability of silica sols would be the least at $6 < \text{pH} < 7$. As shown in Figure 8.31 this is exactly what is observed.^{15,26}

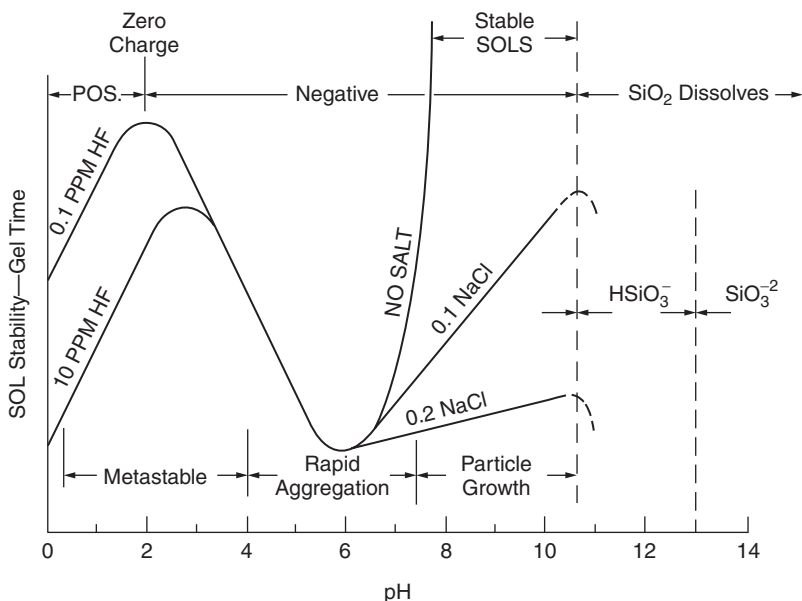


FIGURE 8.31 The sol stability and gel time of silica may be divided into three regions: At extremely acidic conditions the Si–O bond is ruptured producing condensed aggregates. In very alkaline solutions, there is a sufficient charge and solubility to ensure a rearrangement to dense particulate structures. In the neutral range a rapid aggregation occurs due to a low surface charge density. (From Iler, R.K., *The Chemistry of Silica*, John Wiley & Sons, New York, 1979, 367. With permission.)

In alkaline solutions in the range $6 < \text{pH} < 10$, it is known that the surface charge is sufficient to keep the particles stable. However, the screening of the surface charges with electrolyte (e.g., NaCl) destabilizes the sol as expected. Under extremely alkaline conditions ($\text{pH} > 10$) the dissolved silica produces negatively charged species indicated in Figure 8.31 by the dissociation steps of silicic acid. Because the solubility is enhanced in this range (Equation 8.40), the ionic strength grows and the sol is coagulated in the absence of added salt. The alkaline branch is thus in full accord with the expectations of the DLVO model (Equation 8.103).

However, the behavior of silica sols in acidic solutions is quite intriguing. It has been extensively documented that the surface charge density indicates that a zero surface charge persists at least in the range of $6 < \text{pH} < 2$ (see Figure 8.26).⁴⁷ As discussed above, precipitation would be expected to occur over this entire pH_{pzc} range! On the other hand, the effective surface charge (ζ potential) changes almost linearly over a wide pH range ($2 < \text{pH} < 10$, Figure 8.27) reaching the pH_{IEP} at around 2.⁴⁷ The pH_{IEP} seems to shift to slightly higher values when the ionic strength increases. There is clearly a contradiction between the surface charging expected from the hydrolysis experiments and the surface charge density measured. The successive change of the negative ζ potential does, however, agree with the hydrolysis expected in alkaline solutions, but not with the point of maximum precipitation (see Figure 8.31) at $\text{pH} \approx 6$.

The explanation for the obscure behavior observed in acidic media must be sought in the interplay between the dissolved silica and the particle surface. In alkaline solutions, the enhanced charging is evidently due to the overlapping of the surface deprotonation equilibrium and the disintegration of the silica surface. This is observed as a rapid enhancement of the surface charge density and a continuous enhancement of the ζ potential. However, in acidic solutions the condensation reaction is most probably activated at $\text{pH} < 6$ initiating a competition with the proton adsorption equilibrium. As a result, the surface hydroxyls react with the dissolved silica instead of

recharging due to an increasing number of positive $>\text{SiOH}_2^+$ groups. The exchange is observed as a tremendous buffering capacity for a number of siliceous minerals (4 to 6 pH units) peaking around $6 \geq \text{pH} \geq 4$. The buffering is activated in minutes and continues for extended periods. The adsorbed and condensed neutral species carry no charge ($\sigma_o = 0$). The remaining effective ζ potential must then be due to charged adsorbed species that have not reacted with the surface hydroxyls. The apparent $\text{pH}_{\text{IEP}} \approx 2$ is therefore merely due to the adsorbed surface gel layer providing an efficient steric hindrance for coagulation (gelation). The much lower solubility of the metal oxides seems to prevent this effect.

The influence of the cations and anions has been discussed separately with the solution properties and reactions in the main focus. It has, however, been known over 100 years that anions play a crucial role for the stabilization and coagulation of colloids.⁵³ More recently, the contribution of anions on the stabilization of particles, biocolloids, and bubbles has received renewed attention.^{54,55} In these papers, it has been pointed out that there exists a collaborative interaction between cations and anions upon adsorption of one of the complexes from solution. At high concentrations this effect renders the simple indifferent ions specific and selective to each other.⁵⁵ It is also seen as a dependency on the acid–base pair chosen for the regulation of the pH. This effect certainly needs to be added as an extension to (correction of) the DLVO theory.⁵⁶ However, as shown in this paper, it is just as probable that the anion and cation collaborate during the adsorption and formation of gels and precipitates at the surface. The presence of such mixed phases has been confirmed experimentally, e.g., during the formation of hydroxoapatite in silica gel layers.⁵⁷

The contribution of the solid content is frequently forgotten when evaluating the stability of the sols. However, because a number of ions dependent on pH and ionic strength are kinetically bound to the particle surface, the interrelationship between the Debye length and the particle load may be investigated. The example provided is a monodisperse latex sol of 100 nm particle size (Figure 8.32).⁵⁸

As seen, four areas can be separated from each other. At extended Debye lengths (low ionic strengths) the sol remains in a crystalline-like arrangement to quite high particle volume fractions. The higher the volume fraction, the smaller must the Debye length be to maintain the Bragg crystal order. Obviously, this region may be characterized by the sol particles filling the entire sample volume, which reduces the freedom of movement of the particles. At higher electrolyte concentrations, the diminishing Debye length provides free space in the sol and the particle arrangement becomes random. Between these two Debye length–particle volume fraction areas, there is a narrow region of coexistence. Here the highly arranged (iridescent in light) and the disordered (dark in light) phases may be observed as phase-separated in the same sample holder. This shows that it is the effective radius of the particles that determines the packing. Observe that the bending of the narrow coexistence range occurs at extreme dilution (10^{-5} to 10^{-4} mol/dm³), at the limit of dilute electrolyte solutions (10^{-3} to 10^{-2} mol/dm³) and at the limit of concentrated electrolyte solutions (10^{-1} mol/dm³). They are all critical in some sense when applying different models to electrolyte solutions and sols.^{6,14,25,33,48,55}

In particular, it should be noted that above the 10^{-1} mol/dm³ limit specific interactions are observed that are typical for hard core systems.⁵⁵ Toward higher particle packing densities a phase transition is indicated by two perpendicular lines that traverse the volume fraction axis at about 0.50 and 0.55. The lower volume fraction has been shown to coincide with the freezing of noninteracting colloids and the latter border with colloid crystal formation in the apparent absence of any attraction forces.^{59,60} All in all, three colloid sol states emerge as a function of the effective packing: a well-ordered Bragg crystal state dependent on the electrolyte expanded effective radius, a disordered sol state, and either a disordered (low Φ_p) or ordered (high Φ_p) sol state characterized by hard core particle interactions. Of particular interest is the possibility of producing coexisting ordered and disordered phases in the same sample holder.⁵⁸

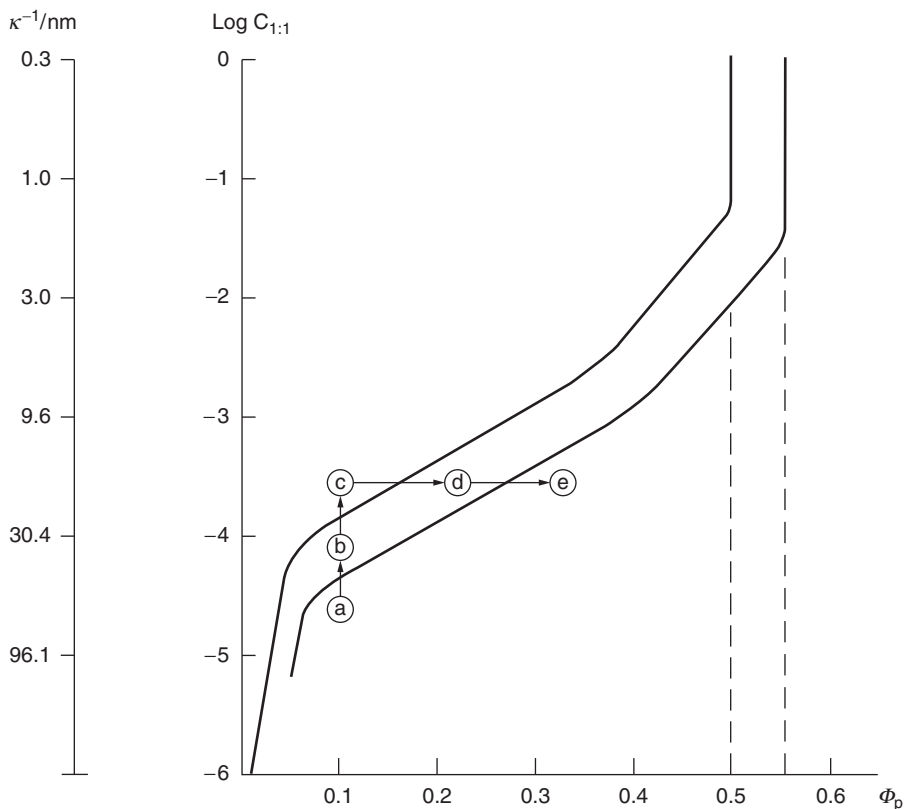


FIGURE 8.32 The sol stability is dependent both on the electrolyte concentration and on the dry content of the particles. As illustrated for monodisperse 100 nm latex particles at 25°C an ordered (iridescent) crystal particle lattice forms at low electrolyte concentrations over a wide range of volume fractions. At higher electrolyte concentrations an irregular particle order persists. However, at intermediate concentrations both ordered and disordered particle phases may coexist. Thus, the iridescent latex sol may be “melted” over the coexistence range by increasing the salt concentration (a → b → c) and be refrozen by increasing the particle content (c → d → e). Above 0.1 mol/dm³ the ion “cushion” around the particles is effectively removed and the sol may be described as a hard core particle system producing the properties found when increasing the volume fraction of particles above 0.5. (From Rosenholm, J.B. et al., in *Ceramic Interfaces*, R.St.C. Smart and J. Nowotny, Eds., IOM London, 1998, 451. With permission.)

8.7 CONTROLLED GELATION OF SOLS

As discussed in the previous sections, inorganic complexes in solution are of different size and charge depending on the degree of hydrolysis, deprotonation, and condensation. These factors depend on a variety of factors, including solution pH, concentration, aging time, temperature, and physicochemical properties of the inorganic species. These ionic species range from essentially monomeric ions to polyions, i.e., inorganic polyelectrolytes, which may undergo a variety of reactions with other species present in solution instead of condensing into an inorganic bulk structure. It is to be expected that the strength of these ligand interactions will depend on the size, structure, and charge of the inorganic oligomeric species. The interactions between inorganic species and surface active agents have attracted a lot of interest during the last decade after the pioneering work of scientists from the Mobil Oil Company.^{61,62} It was unambiguously shown that supramolecular surfactant aggregates can be used as structure-directing agents for the preparation of

inorganic–surfactant composite structures with tunable mesoscopic order resembling the structure of liquid crystalline surfactant phases. Formation of silicate and aluminosilicate gels in the presence of surfactants with subsequent calcination is used to obtain mesoporous materials with uniform channels in the size range 2 to 20 nm, thus filling the gap between mesoporous materials obtained from pillaring of layered silicates and mesoporous gels. In most cases, cationic quaternary ammonium surfactants have been used as complexing ligands together with silicate under alkaline conditions where the silicate is negatively charged. However, mesoscopically ordered silica can also be synthesized under acidic conditions using cationic surfactants.^{63,64} Furthermore, a wide variety of other structure-directing agents, such as aliphatic amines,⁶⁵ ethoxy-based neutral surfactants,⁶⁶ block-copolymers of the ABC type,⁶⁷ preformed liquid crystals,⁶⁸ etc., have also been successfully applied. Here, the pH and the temperature are adjusted to optimize the inorganic–organic interactions. Therefore, electrostatic and covalent interactions, hydrogen bonding, and van der Waals interactions can all be used as driving forces for the assembly of the organic and the inorganic constituents. The same synthesis strategy has also been used in the preparation of a wide variety of nonsiliceous materials. Several excellent reviews^{69–77} covering different aspects of the synthesis and properties of these materials have appeared recently, and the interested reader is referred to these and the references therein for a more general overview of the different synthesis routes applied and the vast potential application areas for these materials. The focus here is on silicates as the vast majority of the published mechanistic studies concern the formation of silicate–surfactant mesophases under basic conditions. However, the applicability of the results presented can be extended also to nonsiliceous material synthesis. In the following, the inorganic–surfactant mesophase formation is discussed in more detail with special emphasis on *in situ* studies. The second part of this section concerns the use of mixed surfactant systems to control the mesoscopic phase behavior as studied mainly by *in situ* small-angle x-ray scattering (SAXS).

8.7.1 MECHANISM OF FORMATION OF S⁺I⁻ MESOPHASES, GENERAL

A lot of work has been devoted to the investigation of the mechanism of formation of cationic surfactant–anionic silicate composites synthesized under alkaline conditions, often denoted the S⁺I⁻ route. The kinetic nature of inorganic–surfactant systems calls for the use of *in situ* techniques to study their formation. *In situ* SAXS and XRD,^{78–82} cryo-TEM,⁸³ (²⁹Si, ¹⁴N, ⁸¹Br, ²H, or ¹³C)-NMR,^{84–87} fluorescence probing,^{88,89} FT-IR spectroscopy,^{90,91} and electron spin resonance measurements^{92–95} have yielded valuable information on the different stages involved in the formation process. There is now some agreement in that the formation, at least in the case when surfactants carry an opposite charge with respect to the inorganic species present in solution, involves (1) hydrolysis of the silicate precursor, (2) condensation of silicate units leading to oligomeric/polymeric silica, (3) the binding of surfactant to oligomeric/polymeric inorganic species paralleled by a cooperative self-assembly into a mesoscopically ordered inorganic–surfactant phase concentrated in surfactant and in silicate polyions, and a dilute phase. The phase separation process increases the local concentration of inorganic species facilitating further condensation into a rigid framework. While early stages of the mesostructure formation is determined mainly by the surfactant properties, subsequent structural phase transformations to lower-energy configurations may be induced as changes in the charge density of the silicate occurs upon condensation.²⁸ Furthermore, some of the surfactant may also be expelled from the composite structure during the course of condensation due to charge-matching constraints.⁹⁶ Therefore, the interplay between organic–organic, inorganic–organic, and inorganic–inorganic interactions is of utmost importance in forming the final material.

The early stages of the process are very similar to those occurring in corresponding systems of mixtures of oppositely charged organic polyelectrolyte and surfactant.⁹⁷ Organic polyelectrolyte–surfactant systems are much easier to investigate, however, because of the absence of further polymerization reactions, which enables studies to be carried out under equilibrium conditions. It

has been shown, for example, that the amount of surfactant bound to the polyelectrolyte as well as the degree of cooperativity of the supramolecular assembly both increase with increasing degree of polymerization of the polyelectrolyte. Furthermore, it is also well known that the extent of polyelectrolyte–surfactant interactions increases with increasing alkyl chain length of the surfactant. Both features are observed also in the case of inorganic polyions and oppositely charged surfactants, stressing the similarity between the systems. However, despite the kinetic nature of inorganic–surfactant systems, a lot of information concerning polyelectrolyte–surfactant interactions can be gained through detailed studies on the initial stages of mesophase formation in these systems. Realizing that the formed polyelectrolyte–surfactant complex possesses surfactant properties, at least at moderate degrees of polymerization, opens up possibilities to utilize the availability and chemical diversity of inorganic polyelectrolytes and subsequently transfer, at least qualitative, knowledge to corresponding organic polyelectrolyte–surfactant systems, decreasing the need for extensive, time-consuming precursor synthesis work.

Despite that the silicate–surfactant mesophase formation resembles the phase separation normally observed in surfactant–polyelectrolyte systems, it is interesting to note that it is still possible to make qualitative predictions about the influence of inorganic–surfactant phase behavior based on models developed for dilute surfactant systems. The packing parameter concept^{98,99} is based on a geometric model that relates the geometry of the individual surfactant molecule to the shape of the supramolecular aggregate structures most likely to form. N_s is defined as

$$N_s = v/la_o \quad (8.118)$$

where v is the volume, l is the effective length of the hydrophobic portion, and a_o is the effective area of the hydrophilic headgroup of the surfactant. For N_s values of 0.33, 0.5, and 1 spherical, rodlike, and lamellar geometries, respectively, are expected to form. For example, Huo and co-workers¹⁰⁰ demonstrated that the packing parameter concept could be used to qualitatively describe the phase behavior observed for silica–gemini surfactant composites as a function of the structure of the gemini surfactant. Another approach to vary the N_s value is to introduce another semipolar or apolar additive to the surfactant solution, which is solubilized by the supramolecular surfactant aggregate. The influence of the solubilized additive on the N_s value will depend on the locus of solubilization within the aggregate, which in turn is determined by the polarity of the additive. The effectiveness of a particular additive is in turn governed by the partition of the additive between the bulk liquid and the micelle. This latter means of influencing the value of the packing parameter is discussed in the next section.

8.7.2 INFLUENCE OF ADDITIVES ON CTA⁺–SILICATE MESOPHASE FORMATION AS STUDIED BY *IN SITU* SAXS

The large number of synthesis routes applied in the synthesis of hexagonally ordered silicate–surfactant composites, differing in pH, silicate precursor, synthesis temperature, reactant concentrations, etc., makes it difficult to clearly attribute observed differences in kinetics, phase formation, etc., to single parameters. To be able to make it easier for the reader to follow the discussion, we limit ourselves to one synthesis route, which results in a hexagonally ordered surfactant–silicate material in the absence of additives.¹⁰¹ The fast, highly reproducible, room-temperature synthesis is most suitable for *in situ* studies. The synthesis composition is the same in all cases described below, with a molar composition of 157/3/0.15/1 H₂O/NH₃/C₁₆TAB/TEOS, respectively, apart from the fact that different semipolar or apolar additives are added. This makes it easier to attribute the observed effects more specifically to changes in the organic–organic and organic–inorganic interactions, respectively. The setup used for the *in situ* studies is schematically shown in [Figure 8.33](#).

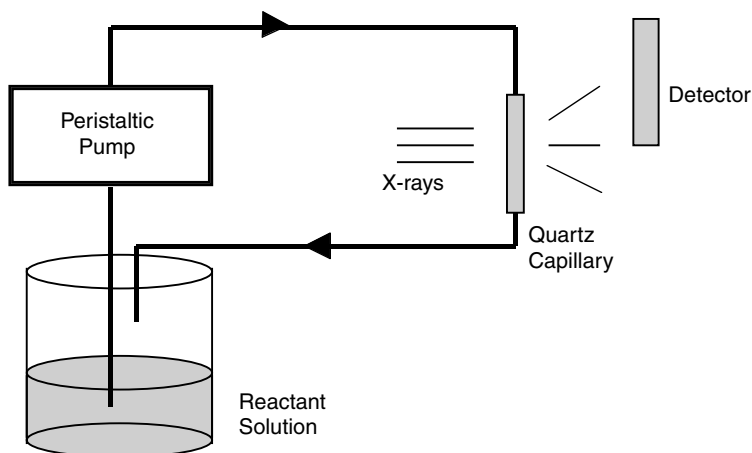


FIGURE 8.33 Schematic representation of the experimental setup used for *in situ* synchrotron SAXS measurements on the formation of mesoscopically ordered silicate–surfactant mesophases. The reactant solution is pumped through a thin quartz capillary and a diffractogram is recorded every 300 ms. The reaction is initiated by emulsifying a macroscopically phase-separated system of tetraethoxysilane and an aqueous phase, respectively. See text for details.

8.7.2.1 No Additive

An example of a time-resolved x-ray diffractogram measured *in situ* during the formation of a two-dimensional, hexagonally ordered silicate–CTAB material is shown in Figure 8.34.¹⁰² The formation of the surfactant–silicate mesophase occurs within 80 s after mixing the reagents, as shown by the appearance of a low-angle Bragg reflection. Two other reflections, which could be indexed assuming a hexagonal unit cell, appears shortly after. The reflections shift to higher angles, i.e., lower *d*-spacings with time; in other words, the mesophase contracts with time. The contraction of the mesophase is accompanied by an increase in the intensity ratio of the (110) vs. the (200) reflection, I_{110}/I_{200} . The intensity of the diffuse scattering indicative of the presence of micelles decreases gradually as the intensity of the Bragg peaks increased. Based on these results we may conclude the following: the observed contraction of the mesophase is a result of interaggregate condensation in the formed mesophase. Furthermore, it may also partly originate from the fact that some TEOS is initially solubilized inside the supramolecular aggregates, which contract upon release of hydrolyzed species. The intra-aggregate condensation is also responsible for the observed I_{110}/I_{200} ratio, since this effect originates from the increase in the density of the inorganic walls upon silicate condensation.^{96,103,104} The rate-limiting step in this particular synthesis is the hydrolysis of TEOS, as silicate condensation occurs readily at the synthesis pH of 10.7. The formation of the hexagonal phase is not preceded by the formation of other mesophase(s) in this particular case, as has been observed for other synthesis compositions.

8.7.2.2 *n*-Alcohols

Short-chain fatty alcohols ($n_c \geq 4$) have been used extensively together with ionic surfactants to stabilize microemulsions and emulsions, i.e., aggregates of lower interfacial curvature. These are accumulated in the palisade layer of the surfactant aggregates and are therefore referred to as cosurfactants. Using a mixture of fatty alcohol (butanol to octanol) and CTAB as structure-directing agents in the synthesis of mesoscopically ordered silica also induces a gradual transition from the hexagonal phase to the lamellar phase, through a two-phase region where both phases coexist, with increasing alcohol/CTAB ratio.¹⁰² As expected, the transition occurs at lower fatty alcohol/CTAB molar ratios with increasing chain length of the alcohol, reflecting the increase in the fraction of

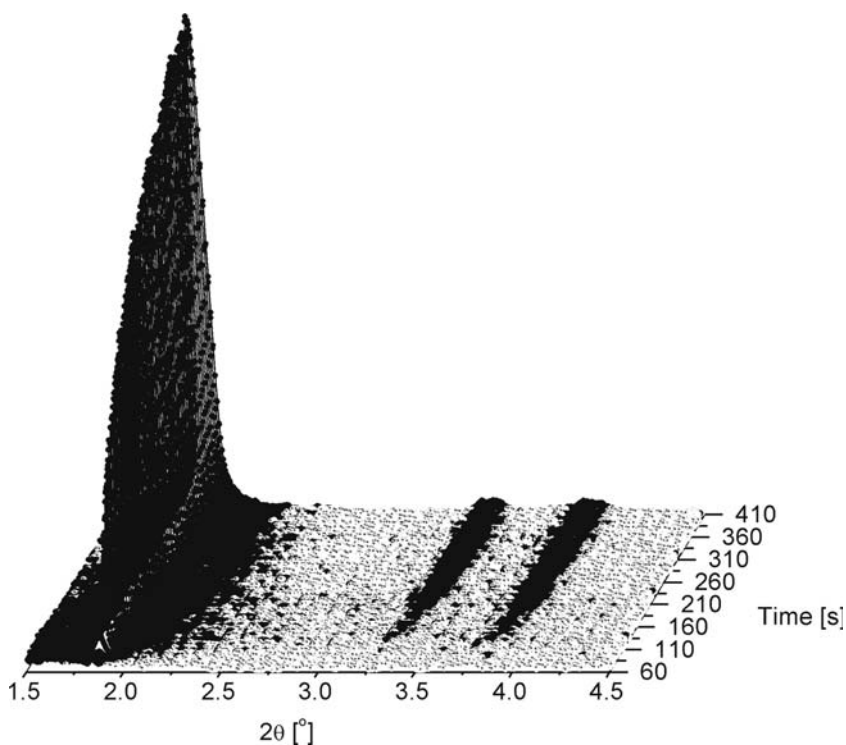


FIGURE 8.34 Development of the *in situ* XRD pattern as a function of time during the formation of a hexagonal silicate-surfactant mesophase in the system TEOS-water-CTAB-ammonia. (From Ågren, P. et al., *Langmuir*, 16, 8809, 2000. With permission of the American Chemical Society.)

alcohol being solubilized by the surfactant aggregate. Although alcohols are known to have a profound influence on the hydrolysis-condensation kinetics as well as on the aqueous solubility of silica, the alcohol/water ratio is low enough in the present case to exclude such effects from the discussion. Interestingly, the *d*-spacing of both the hexagonal and the lamellar phase also increases with increasing fatty alcohol chain length as also observed for some polar arenes. *In situ* SAXS measurements reveal that the silicate-CTAB hexagonal mesophase actually solubilizes a fair amount of alcohol after it has formed, as shown in Figure 8.35. This may point toward two possible reasons for the observed increase in the *d*-spacing upon addition of alcohol. First, the oligomeric silicate-surfactant complexes serving as building units for the hexagonal mesophase possess strong surfactant properties and have the possibility of solubilizing more alcohol than the CTAB micelles in themselves. Second, the CTAB packing density is determined by the charge density of the silicate oligomers and may be low enough to allow alcohol molecules to fill in the gap between the bound CTA⁺ ions. The latter conclusion is supported by the fact that a fair amount of arene may be postsolubilized into the dried, as-made surfactant-silicate hexagonal mesophase.¹⁰⁵ The *in situ* SAXS investigations also stressed the strongly kinetic nature of the mesophase formation. Depending on the butanol or hexanol/CTAB ratio, two coexisting hexagonal phases (see Figure 8.35) and occasionally even an additional lamellar phase could be resolved, before a one-phase lamellar region was reached upon further addition of *n*-alcohol. The phase having the highest interfacial curvature is the last to appear and this phase closely resembles the hexagonal phase obtained in the absence of cosurfactant. Such three-phase regions do not appear in the standard phase diagrams of CTAB/alcohol/water systems and are against the phase rule if at thermodynamic equilibrium. However, the ongoing hydrolysis and condensation reactions together with the parallel precipitation of silicate-surfactant complexes result in a strongly time-dependent effective reactant concentrations

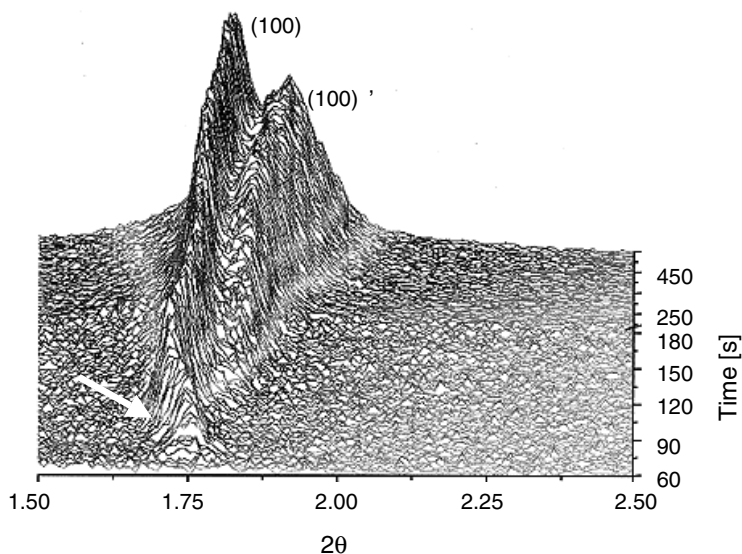


FIGURE 8.35 Development of the *in situ* XRD pattern as a function of reaction time during the formation of a hexagonal silicate-surfactant mesophase in the system TEOS-water-CTAB-ammonia-hexanol. The hexanol/CTAB molar ratio equals 0.45. Only the (100) reflections of the two hexagonal phases are displayed. The arrow highlights the uptake of hexanol after the formation of the mesophase. (From Ågren, P. et al., *J. Phys. Chem. B*, 103, 5943, 1999. With permission of the American Chemical Society.)

as well as silicate speciation. The alcohol/CTAB ratio may change with time, as will probably also the Si/CTAB ratio. However, it is interesting to note that these changes lead to the formation of distinct, highly ordered phases and not to a gradual change in the d -spacing with time.

8.7.2.3 *n*-Amines

Aliphatic amines have a pK_a value around 10.7, which means that they are partly protonated under the ammonia-catalyzed synthesis conditions discussed here with a $pH \approx 11$. The protonation will increase the water solubility of the amines compared to that of an alcohol of similar chain length. Furthermore, the amines may interact more strongly with silicate ions compared to alcohol. However, both the degree of protonation and the aqueous solubility will decrease with increasing chain length of the amine, as the degree of protonation of the amine will probably decrease when solubilized in CTAB micelles due to the positive interfacial potential of the micelles. Therefore, the influence of the fatty amine on the CTAB-silicate mesophase evolution should resemble that of fatty alcohols with increasing chain length. This has been observed in practice. Addition of octylamine to CTAB-silicate synthesis also leads to a transition to the lamellar phase through a hexagonal-lamellar phase coexistence region, suggesting that the octylamine is solubilized as a cosurfactant in the palisade layer of the CTAB portion of the composite structure and therefore lead to an increase in the effective packing parameter. Again, *in situ* SAXS measurements reveal the existence of an intermediate region where two hexagonal phases coexist, separated by only 0.1 nm in d -spacing.¹⁰⁶ The d -spacing of the hexagonal phase increases with increasing octylamine/CTAB molar ratio as also observed for the fatty alcohols. The addition of butylamine, on the other hand, leads to a completely different effect. Instead of leading to an increase in the effective packing parameter the opposite is observed; the hexagonal phase is retained, but the d -spacing continuously decreases with increasing butylamine/CTAB ratio, as shown in [Figure 8.36](#). The d -spacing vs. time plot also seems to indicate that in this case there are two steps involved in

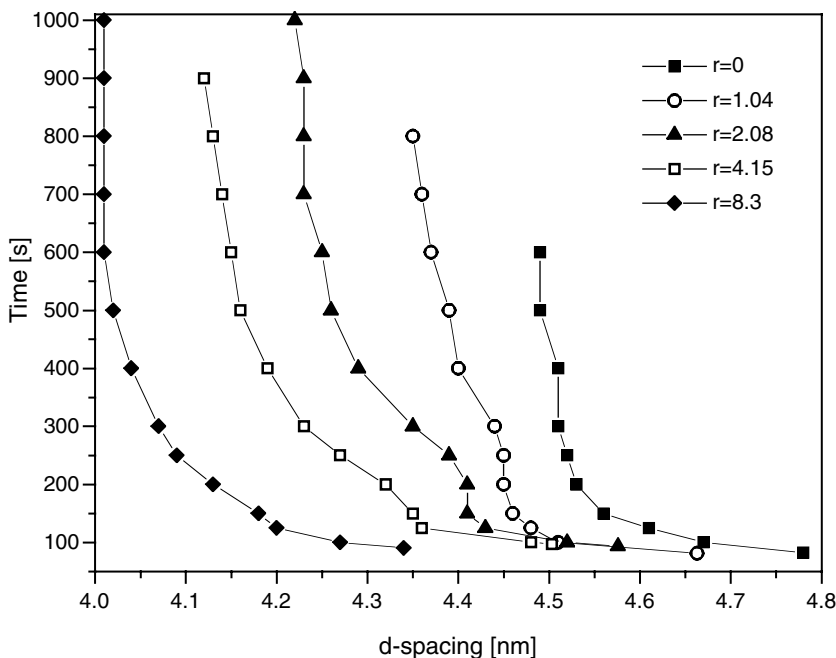


FIGURE 8.36 The d -spacing of the hexagonal phase formed in the system TEOS–water–CTAB–ammonia–butylamine as a function of time for different butylamine/CTAB molar ratios, r . (From Ågren, P. et al., *Langmuir*, 16, 8809, 2000. With permission of the American Chemical Society.)

the organization of the hexagonal mesophase; an initial fast shrinkage by approximately 0.2 nm during the few seconds, which is virtually independent of the butylamine/CTAB molar ratio, and a subsequent contraction, which is more pronounced the higher the butylamine/CTAB molar ratio. Butylamine will preferentially not be solubilized in the CTAB micelles but will remain in the bulk, due to its high water solubility. It is therefore free to hydrogen-bond to the oligomeric silicate and therefore to compete with the CTA⁺ ions for potential binding sites, acting as a complexing ligand. This will lead to a decrease in the number of CTA⁺ ions incorporated in the silicate–surfactant mesophase and therefore to a decrease in the hydrocarbon volume in the organic portion of the composite, which in the end controls the diameter of the pores. The latter step in the contraction process may be related to the expulsion of some of the amine from the mesophase as a result of silicate condensation. As expected, hexylamine shows an intermediate behavior and behaves like butylamine at low hexylamine/CTAB ratios while a transition to the lamellar phase is observed at higher hexylamine/CTAB ratios as for octylamine. It is interesting to note, however, that in effect the interfacial curvature first decreases and then increases with increasing hexylamine/CTAB ratio, which normally is not observed in pure surfactant systems. It is clear that the balance between the two effects, solubilization into the CTAB micelles and adsorption to the silicate in the bulk, is governed by the hydrophobicity of the amine, i.e., the hydrocarbon chain length. This is also manifested in the amine/CTAB ratios needed for inducing the decrease in the d -spacing and the transition to the lamellar phase, respectively, which decreases with increasing chain length. This is in nice agreement with what is known about both surfactant adsorption to interfaces and extent of solubilization in micelles, both of which are enhanced with increasing chain length of the surfactant. It should be noted, however, that it is not necessary that the amine be protonated for the adsorption to occur; a similar decrease in the d -spacing of the hexagonal phase is observed upon addition of benzylamine and aniline, with pK_a values of 9.3 and 4.6, respectively, although the decrease in the d -spacing is much more pronounced in the presence of butylamine and benzylamine compared to aniline.¹⁰⁷

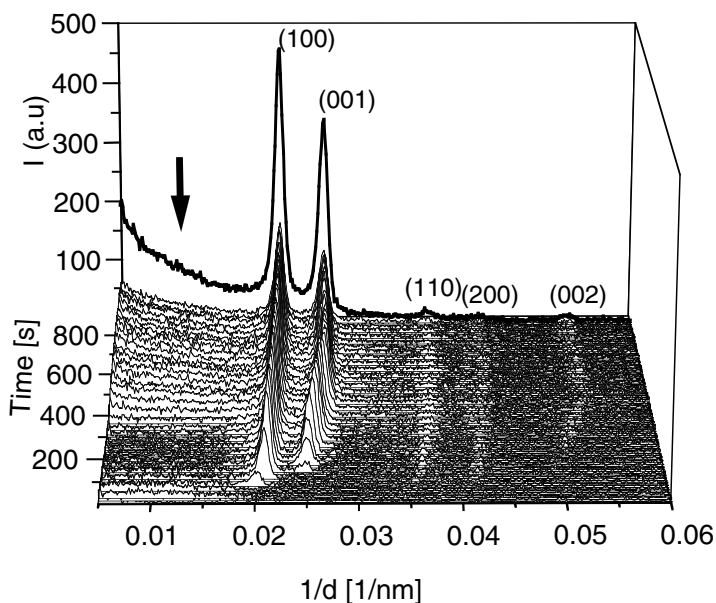


FIGURE 8.37 Development of the *in situ* XRD pattern as a function of reaction time during the formation of coexisting hexagonal and lamellar silicate–surfactant mesophases in the system TEOS–water–CTAB–ammonia–decanoate. The decanoate/CTAB molar ratio equals 0.35. The arrow highlights the highly diffuse scattering in the low-angle region originating from the formation of small particles. (From Lind, A. et al., *Langmuir*, 18, 1380, 2002. With permission of the American Chemical Society.)

8.7.2.4 Long-Chain Carboxylates

Mixtures of oppositely charged surfactants have been studied extensively, due to their industrial importance as emulsifiers and rheology modifiers. It is well known, for example, that these cationic/anionic surfactant mixtures readily form extended, wormlike micelles in solution already at low concentrations due to their lower interfacial charge density. Furthermore, the formation of anionic–cationic ion pairs is commonly observed in these systems. It is therefore to be expected that addition of an anionic surfactant to the CTAB–silicate system should result in pronounced changes in the mesoscopic phase behavior and mainly result in the formation of phases with lower interfacial curvature. This is what is observed, and addition of octanoate, decanoate, and dodecanoate, respectively, has been shown to induce a hexagonal-to-lamellar phase transition in carboxylate–CTAB–silicate systems.¹⁰⁸ The transition occurs at lower fatty carboxylate/CTAB ratios with increasing chain length of the carboxylate anion, as expected. The *d*-spacing of both the hexagonal and the lamellar phase increases with increasing chain length of the anionic surfactant. In these respects, the anionic–cationic surfactant mixtures behave like mixtures of nonionic and cationic surfactants. However, *in situ* SAXS measurements reveal an important difference between the two cases. There is a pronounced increase in the diffuse scattering region at short reaction times in the presence of decanoate when the hydrophobic TEOS is used as the silica source, as shown in Figure 8.37. The diffuse scattering goes through a minimum and then increases again. This can be understood based on a better initial solubilization of TEOS inside emulsion droplets stabilized by the cationic–anionic surfactant mixture compared to that of CTAB alone. This can be seen as a more pronounced shrinkage of the initially formed hexagonal phase as the TEOS hydrolyzed upon contact with water leaves the surfactant portion of the mesophase. The better initial TEOS dispersion leads to an increase in the number of nuclei, which in turn results in the formation of smaller particles accounting for the increase in the intensity of the diffuse scattering at longer reaction times. Therefore, it seems that while a large portion of any fatty alcohol is solubilized by

the silicate–surfactant mesophase after its formation, the decanoate forms ion pairs with the CTA⁺ ions and they behave like one kinetic unit throughout the synthesis.

8.7.2.5 Hydrocarbons

Solubilization of hydrophobic additives within the core of the supramolecular assembly has been widely used to increase the pore size of mesoporous silicas up to 10 nm. Trimethylbenzene (TMB) has been the most widely used additive, although aliphatic hydrocarbons have been used as well. CTAB micelles in themselves cannot solubilize such large amounts of hydrocarbon inside their core in the absence of cosurfactant, due to the preferred high curvature of the charged micelles. Therefore, it seems more than plausible that the surfactant–oligomeric complexes serving as building units for the mesophase are surfactants in themselves as already discussed. However, it has also been shown that the swelling of the hexagonal mesophase is crucially dependent on the time at which the swelling agent is added to the synthesis and that the swelling effect decreases if the swelling agent is added at a later stage.^{62,63} This effect is because the silicate framework becomes rigid with increasing degree of inter- and intra-aggregate condensation. *In situ* SAXS measurements on the solubilization of toluene and hexane, respectively, by hexagonally ordered CTAB–silicate mesophases reveal several important aspects of the solubilization process.¹⁰⁹ When toluene is used as the swelling agent, the long-range order of the hexagonal phase is maintained throughout the synthesis. Furthermore, a large portion of the toluene is incorporated into the surfactant–silicate mesophase after it has formed, as revealed by the pronounced swelling of the hexagonal phase long after its formation, as shown in [Figure 8.38](#). The situation changes quite remarkably when hexane is used as the swelling agent. Almost no change in the *d*-spacing of the ordered hexagonal phase is observed after it appears in the diffractogram. However, it is accompanied by a poorly ordered phase with higher *d*-spacing. Upon increasing the hexane–CTAB ratio the poorly ordered phase starts to dominate, leading to a loss of periodicity in the composite. This phase is kinetically stabilized during the synthesis, and the *d*-spacing of this phase can be increased by increasing the stirring rate. We attribute these differences to the different availabilities of toluene and hexane, respectively, during the synthesis. There is not enough CTAB in the system for a micellar transport mechanism to be in effect during the development of the surfactant–silicate mesophase, which is the reason the transport of the swelling agent must be controlled by the solubility of the hydrocarbon in the continuous phase. The higher water solubility of toluene compared to hexane ($7 \cdot 10^{-4} M$ and $7 \cdot 2 \cdot 10^{-3} m$, respectively) together with the possibility for toluene to be solubilized both in the palisade layer and the core of the surfactant assembly leads to a faster incorporation of toluene into the developing composite structure. The solubility of both swelling agents is further increased due to the released ethanol originating from the hydrolysis of the TEOS. If toluene is added at a later stage, another interesting effect was observed apart from the already discussed lower degree of swelling. If the toluene was added just after the first signs of the development of mesoscopic order in the system, three coexisting hexagonal phases are clearly resolvable in the diffractogram. Again, a time-dependent change in the toluene/CTAB ratio during the synthesis and/or a change in the silicate speciation is supposed to account for this effect, as in the case of *n*-alcohol added to the synthesis. However, it is very interesting to note that distinctive phases rather than a loss of order are observed.

8.7.3 SUMMARY

In this chapter we have tried to show how a rational addition of “neutral” additives or ligands complexing with either the inorganic or organic reactants, respectively, can be used to control the mesoscopic phase behavior of inorganic–surfactant composites. The focus has been on siliceous materials, but the approach is applicable also to the synthesis of nonsiliceous materials. The discussion has been merely qualitative in nature, due to the partial lack of accurate experimental

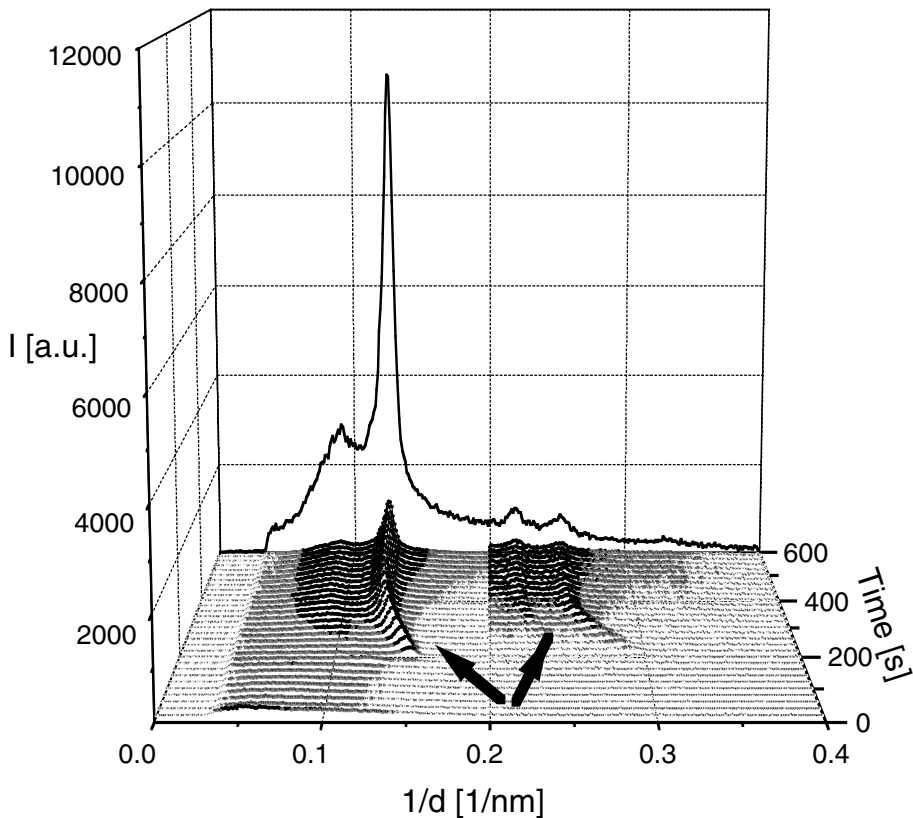


FIGURE 8.38 Development of the *in situ* XRD pattern as a function of reaction time during the formation of coexisting hexagonal and lamellar silicate–surfactant mesophases in the system TEOS–water–CTAB–ammonia–toluene. The toluene/CTAB molar ratio equals 23.2. The arrow highlights the pronounced swelling of the hexagonal phase after its formation due to the solubilization of toluene. (From Lindén, M. et al., *Langmuir*, 16, 5831, 2000. With permission of the American Chemical Society.)

means of gaining chemical information on these rapidly evolving systems. However, recent developments in the area of *in situ* mass spectrometry,¹¹⁰ for example, promise to allow accurate data to be collected, which could shed some new light on the events occurring on the molecular level during the formation of these materials, especially concerning the role of the time-dependent speciation of inorganic polyions in controlling phase behavior.

8.8 LIST OF ABBREVIATIONS

8.8.1 ALPHABETICAL SYMBOLS

A	anion	<i>a</i>	activity
A	acid	<i>b</i>	constant
A	surface area	<i>c</i>	concentration
A _H	Hamaker constant	<i>d</i>	distance
B	base	<i>f</i>	stoichiometric constant
C	cation	<i>g</i>	stoichiometric constant
D _C	diffusion coefficient	<i>h</i>	hydrolysis ratio
E	standard electrode potential	<i>i</i>	species indication
F	Faraday constant	<i>k</i>	constant

G	Gibbs free energy	<i>k</i>	hydroxo number (anions)
H ₀	Hammett function	<i>l</i>	oxo number (anions)
<i>I</i>	ionic strength	<i>m</i>	coordination number (anions)
<i>J</i>	flux	<i>n</i>	coordination number (cations)
<i>K</i>	equilibrium constant	<i>n</i>	number of electrons/bonds
L	ligand	<i>n</i>	amount of substance
M	metal cation, Molar mass	<i>p</i>	hydroxo number (cations)
N _A	Avogadro's number	<i>q</i>	oxo number (cations)
<i>P</i>	pressure	<i>r</i>	oxo number (cations)
<i>Q</i>	stoichiometric factor	<i>s</i>	hydroxo number (cation)
<i>R</i>	gas constant	<i>s</i>	regression constant
<i>S</i>	solubility product	<i>t</i>	regression constant
<i>S</i>	entropy	<i>t</i>	proton number (acid)
<i>T</i>	temperature (K)	<i>u</i>	regression constant
<i>U</i>	internal energy	<i>u</i>	proton number (acid)
<i>V</i>	volume	<i>v</i>	regression constant
<i>X</i>	state variable	<i>w</i>	mass (weight) of substance
<i>Y</i>	state variable	<i>y</i>	activity coefficient (concentrations)
		<i>z</i>	charge number (valency)

8.8.2 GREEK SYMBOLS

α	degree of side reactions
β	degree of association
Γ	surface excess
δ	partial charge of atoms
ϵ	dielectric constant ($\epsilon_0\epsilon_r$)
ϵ	potential energy
ζ	effective surface charge
η	hardness of atoms
κ^{-1}	Debye length
μ	chemical potential
ν	stoichiometric constant
ξ	surface roughness
π	3.14
ρ	density
σ	softness of atoms ($1/\eta$)
σ_0	surface charge density
Φ	potential energy
χ	electronegativity
Υ	complex ratio of surface potential
Ψ_0	surface potential

REFERENCES

1. Robinson, R.A. and Stokes, R.H., *Electrolyte Solutions*, 2nd ed., Butterworths, London, 1959.
2. Atkins, P. and de Paula, J., *Atkins' Physical Chemistry*, 7th ed., Oxford University Press, Oxford, 2002.
3. Ringbom, A., *Complexation in Analytical Chemistry*, Wiley Interscience, New York, 1963.
4. Hägg, G., *Allmän och organisk kemi*, Almqvist & Wiksell, Uppsala, Sweden, 1966.
5. Daniels, F. and Alberty, R.A., *Physical Chemistry*, 3rd ed., Wiley International, New York, 1966.

6. Hiemenz, P.C., *Principles of Colloid and Surface Chemistry*, 2nd ed., Marcel Dekker, Inc., New York, 1986.
7. Bockris, J.O.M. and Reddy, A.K., *Modern Electrochemistry*, Vol. 1, Plenum Press, New York, 1974.
8. Lide, D.R. and Frederikse, H.P.R., Eds., *CRC Handbook of Chemistry and Physics*, 77th ed., CRC Press, Boca Raton, FL, 1996.
9. Rich, R.L., Periodicity in the acid-base behavior of oxides and hydroxides, *J. Chem. Ed.*, 62, 44, 1985.
10. Campbell, J.A., *Chemical Systems*, W.H. Freeman, San Francisco, 1970.
11. Hem, J.D. and Roberson, C.E., Form and stability of aluminium hydroxide complexes in dilute solutions, in *Chemistry of Aluminium in Natural Water*, Geol. Survey Water-Supply, 1827-A, 1-55, U.S. Government Printing Office, Washington, D.C., 1967.
12. Smith, R.W. and Hem, J.D., Effect of aging on aluminium hydroxide complexes in dilute aqueous solutions, in *Chemistry of Aluminium in Natural Water*, Geol. Survey Water-Supply, 1827-D, 1-51, U.S. Government Printing Office, Washington, D.C., 1967.
13. Baes, C.F. and Mesmer, R.E., *The Hydrolysis of Cations*, John Wiley & Sons, New York, 1976.
14. Bergström, L., Surface characterization of ceramic powders, in *Surface and Colloid Chemistry in Advanced Ceramics Processing*, R.J. Pugh and L. Bergström, Eds., Surface Science Series, 51, Marcel Dekker, New York, 1994.
15. Iler, R.K., *The Chemistry of Silica*, John Wiley & Sons, New York, 1979.
16. Terry, B., The acid decomposition of silicate minerals, Part I. Reactivities and modes of dissolution of silicates, *Hydrometallurgy*, 10, 135, 1983.
17. Phillips, C.S.G. and Williams, R.J.P., *Inorganic Chemistry*, Oxford University Press, New York, 1965.
18. Hurme, T., Ultrafiltration of Acid Sulphite Spent Liquor to Produce Carbohydrates, Thesis, Åbo Akademi University, Finland, 1998, appendix.
19. Rochester, C., *Acidity Functions*, Academic Press, London, 1970.
20. Tanabe, K., *Solid Acid and Bases*, Academic Press, New York, 1970.
21. Jensen, W.B., The Lewis acid-base concepts: recent results and prospects for the future, in *Acid-Base Interactions*, K.L. Mittal and H.R. Anderson, Eds., Vol. 3, VSP, Utrecht, the Netherlands, 1991.
22. Karlsson, K., *Silikatkemi, glas eldfasta material*, Åbo Akademi University, Finland, 1985.
23. Livage, J. and Henry, M., A predictive model for inorganic polymerization reactions, in *Ultrastructure Processing of Advanced Ceramics*, J.D. Mackenzie and D.R. Ulrich, Eds., John Wiley & Sons, New York, 1988, 183.
24. Henry, M., Jolivet, J.-P., and Livage, J., Aqueous chemistry of metal cations: hydrolysis, condensation and complexation, *Struct. Bonding*, 77, 154, 1992.
25. Jolivet, J.-P., *Metal Oxide Chemistry and Synthesis*, John Wiley & Sons, Chichester, U.K., 2000.
26. Brinker, C.J. and Scherer, G.W., *Sol-Gel Science*, Academic Press, London, 1990.
27. Jorgensen, C.K., *Inorganic Complexes*, Academic Press, London, 1963.
28. Monnier, A. et al., Cooperative formation of inorganic-organic interfaces in the synthesis of silicate mesostructures, *Science*, 261, 1299, 1993.
29. Woodhead, J.L. and Segal, D.L., Sol-gel processing, *Chem. Br.*, April, 310, 1984.
30. Stöber, W., Fink, A., and Bohn, E., Controlled growth of monodisperse silica spheres in the micron size range, *J. Colloid Interface Sci.*, 26, 62, 1968.
31. Wilhelmy, R.B., Control of Form of Crystal Precipitation of Aluminium Hydroxide Using Cosolvents and Varying Caustic Concentration, U.S. Patent 4,822,593, 1989.
32. Friberg, S.E., Yang, C.-C., and Sjöblom, J., Amphiphilic association structures and the microemulsion/gel method for ceramics: influence on original phase regions by hydrolysis and condensation of silicon tetraethoxide, *Langmuir*, 8, 372, 1992.
33. Shaw, D.J., *Introduction to Colloid and Surface Chemistry*, 4th ed., Butterworth-Heinemann, Oxford, 1992, 1-20.
34. La Mer, V.K. and Dinegar, R.H., Theory, production and mechanism of formation of monodispersed sols, *J. Am. Chem. Soc.*, 72, 4847, 1950.
35. Nielsen, A.E., Theory of electrolyte crystal growth, the parabolic law, *Pure Appl. Chem.*, 53, 2025, 1981.
36. Pierre, A.C., Sol-gel processing of ceramic powders, *Cer. Bull.*, 70, 1281, 1991.
37. Schüth, F. et al., Techniques for analyzing the early stages of crystallization reactions, *Solid State Sci.*, 3, 801, 2001.

38. Schüth, F., Nucleation and crystallization of solids from solution, *Curr. Opinion, Solid State Mater. Sci.*, 5, 389, 2001.
39. Glasser, L.S.D., Sodium silicates, *Chem. Br.*, January, 33, 1982.
40. Smart, R.St.C. et al., Nucleation and precipitation mechanisms in precursors to colloidal alumina, in *Ceramic Interfaces*, R.St.C. Smart and J. Nowotny, Eds., 483, IOM, London, 1998.
41. Gerson, A.R., The role of fuzzy interfaces in the nucleation, growth and agglomeration of aluminium hydroxide in concentrated caustic solutions, in *Prog. Cryst. Growth Mater. Characterization*, in press, 2001.
42. Sillanpää, A.J. et al., A computational study of aluminium hydroxide solvation, *J. Phys. Chem.*, A105, 10111, 2001.
43. Wefers, K. and Misra, C., Oxides and Hydroxides of Aluminium, Report 19, Alcoa Laboratories, 1987.
44. Heller, W., in *Polymer Colloids II*, R.M. Fitch, Ed., Plenum Press, New York, 1980.
45. Livage, J., Henry, M. and Sanchez, C., Sol-gel chemistry of transition metal oxides, in *Prog. Solid State Chem.*, 18, 259, 1988.
46. Bourne, J.R., The influence of solvent on crystal growth kinetics, *AIChE Symp. Ser.*, 76, 59, 1980.
47. Kosmulski, M., *Chemical Properties of Material Surfaces*, Surface Science Services, 102, A.T. Hubbard, Ed., Marcel Dekker, New York, 2001.
48. Hunter, R.J., *Foundations of Colloid Science*, Vol. 1, Clarendon Press, Oxford, 1989, chap. 6.
49. Fuerstenau, D.W., Manmohan, D., and Raghavan, S., The adsorption of alkaline-earth metal ions at the rutile/aqueous solution interface, in *Adsorption from Aqueous Solutions*, Vol. 3, P.W. Tewari, Ed., Plenum Press, New York, 1981, 93.
50. James, R.O. and Healy, T.W., Adsorption of hydrolyzable metal ions at the oxide-water interface, I. Co(II) adsorption on SiO₂ and TiO₂ as model systems, *J. Colloid Interface Sci.*, 40, 42, 1972.
51. Bäckman, J., Eklund, T., and Rosenholm, J.B., Acid-base characterization of porous silica particles, in *Acid-Base Interactions*, Vol. 2, K.L. Mittal, Ed., VSP BV, Zeist, 2000, 465.
52. Eklund, T. et al., Investigation of the adsorption of mono- and bifunctional silanes from toluene onto porous silica particles and from aqueous solutions onto E-glass fibers, in *Silanes and Other Coupling Agents*, Vol. 2, K.L. Mittal, Ed., VSP BV, Zeist, 2000, 55.
53. Collins, K.D. and Washabaugh, The Hofmeister effect and the behaviour of water at interfaces, *Q. Rev. Biophys.*, 18, 323, 1985.
54. Craig, V.S.J., Ninham, B.W., and Pashley, R.M., The effect of electrolytes on bubble coalescence in water, *J. Phys. Chem.*, 97, 10192, 1993.
55. Kosmulski, M. and Rosenholm, J.B., Electroacoustic study of adsorption of ions on anatase and zirconia from very concentrated electrolytes, *J. Phys. Chem.*, 100, 11681, 1996.
56. Ninham, B.W., On progress in forces since the DLVO theory, *Adv. Colloid Interface Sci.*, 83, 1, 1999.
57. Jokinen, M., Bioceramics by the Sol-Gel Method: Processing and Properties of Monoliths, Films and Fibres, Thesis, Åbo Akademi University, Finland, 1999.
58. Rosenholm, J.B. et al., Colloidal properties related to the ceramic particles and the sintered body, in *Ceramic Interfaces*, R.St.C. Smart and J. Nowotny, Eds., IOM London, 433, 1998.
59. Pusey, P.N. and van Mengen, W., Phase behaviour of concentrated suspensions of nearly hard colloidal spheres, *Nature (London)*, 320, 340, 1986.
60. Van Mengen, W. and Underwood, S.M., Change in crystallization mechanism at the glass transition of colloidal spheres, *Nature (London)*, 362, 616, 1993.
61. Kresge, C.T. et al., Ordered mesoporous molecular sieves synthesized by a liquid-crystal template mechanism, *Nature (London)*, 359, 710, 1992.
62. Beck, J.S. et al., A new family of mesoporous molecular sieves prepared with liquid crystal templates, *J. Am. Chem. Soc.*, 114, 10834, 1992.
63. Huo, Q. et al., Organization of organic molecules with inorganic molecular species into nanocomposite biphasic arrays, *Chem. Mater.*, 6, 1176, 1994.
64. Huo, Q., Margoese, D.I., Ciesla, U., Feng, P., Gier, T.E., Sieger, P., Leon, R., Petroff, P.M., Schüth, F., and Stucky, G.D., Generalized synthesis of periodic surfactant/inorganic composite materials, *Nature (London)*, 368, 317, 1994.
65. Tanev, P.T. and Pinnavaia, T.J., A neutral templating route to mesoporous molecular sieves, *Science*, 267, 865, 1995.

66. Bagshaw, S.A., Prouzet, E., and Pinnavaia, T.J., Templating of mesoporous molecular sieves by nonionic polyethylene oxide surfactants, *Science*, 269, 1242, 1995.
67. Templin, M. et al., Organically modified aluminosilicate mesostructures from block copolymer phases, *Science*, 278, 1795, 1997.
68. Attard, G.S., Glyde, J.C., and Göltner, C.G., Liquid-crystalline phases as templates for the synthesis of mesoporous silica, *Nature (London)*, 378, 366, 1995.
69. Dabbs, D.M. and Aksay, I.A., Self-assembled ceramic products by complex fluid templation, *Annu. Rev. Phys. Chem.*, 51, 61, 2000.
70. Stein, A., Melde, B.J., and Schroden, R.C., Hybrid inorganic-organic mesoporous silicates — nanoscopic reactors coming of age, *Adv. Mater.*, 12, 1403, 2000.
71. Selvam, P., Bhatia, S.K., and Sonwane, C.G., Recent advances in processing and characterization of periodic mesoporous MCM-41 silicate molecular sieves, *Ind. Eng. Chem. Res.*, 40, 3237, 2001.
72. Antonietti, M., Surfactants for novel templating applications, *Curr. Opinion Colloid Interface Sci.*, 6, 244, 2001.
73. Sayari, A. and Hamoudi, S., Periodic mesoporous silica-based organic-inorganic nanocomposite materials, *Chem. Mater.*, 13, 3151, 2001.
74. Schüth, F., Non-siliceous mesostructured and mesoporous materials, *Chem. Mater.*, 13, 3184, 2001.
75. Lindén, M. et al., Recent advances in nano- and macroscale control of hexagonal, mesoporous materials, *J. Porous Mater.*, 5, 177, 1998.
76. Corma, A., From microporous to mesoporous molecular sieve materials and their use in catalysis, *Chem. Rev.*, 97, 2373, 1997.
77. Ying, J.Y., Mehnert, C.P., and Wong, M.S., Synthesis and applications of supramolecular-templated mesoporous materials, *Angew. Chem. Int. Ed.*, 38, 56, 1999.
78. O'Brien, S. et al., Formation of silica-surfactant mesophases studied by real-time *in situ* x-ray powder diffraction, *J. Chem. Soc. Chem. Commun.*, 2423, 1995.
79. Matjiasic, A. et al., Room temperature synthesis of silicate mesoporous materials. An *in-situ* study of the lamellar to hexagonal phase transition, *J. Chem. Soc. Chem. Commun.*, 1123, 1996.
80. Lindén, M., Schunk, S.A., and Schüth, F., The initial stages of formation of MCM-41 studied by *in-situ* XRD, *Angew. Chem. Int. Ed.*, 37, 82, 1998.
81. O'Brien, S. et al., Time-resolved *in situ* x-ray powder diffraction study of the formation of mesoporous silicates, *Chem. Mater.*, 11, 1822, 1999.
82. Rathousky, J. et al., Time-resolved *in situ* x-ray diffraction study of MCM-41 structure formation from homogeneous environment, *Phys. Chem. Chem. Phys.*, 1, 3053, 1999.
83. Regev, O., Nucleation events during the synthesis of mesoporous materials using liquid crystalline templating, *Langmuir*, 12, 4940, 1996.
84. Steele, A., Carr, S.W., and Anderson, M.W., ¹⁴N NMR study of surfactant mesophases in the synthesis of mesoporous silicates, *J. Chem. Soc., Chem. Commun.*, 1571, 1994.
85. Firouzi, A. et al., Cooperative organization of inorganic-surfactant biomimetic assemblies, *Science*, 267, 1138, 1995.
86. Firouzi, A. et al., Alkaline lyotropic silicate-surfactant liquid crystals, *J. Am. Chem. Soc.*, 118, 3596, 1997.
87. Wang, L.-Q., Exarhos, G.J., and Liu, J., Nuclear magnetic resonance — characterization of self-assembled nanostructured materials, *Adv. Mater.*, 11, 1331, 1999.
88. Zana, R. et al., Fluorescence probing investigations of the mechanism of formation of organized mesoporous silica, *Langmuir*, 15, 2603, 1999.
89. Fräsch, J. et al., *In situ* investigations on cetyltrimethylammonium surfactant/silicate systems: precursors of organized mesoporous MCM-41-type siliceous materials, *Langmuir*, 16, 9049, 2000.
90. Calabro, D.C., Valyocsik, E.W., and Ryan, F.X., *In situ* ATR/FTIR study of mesoporous silicate syntheses, *Microporous Mater.*, 7, 243, 1996.
91. Zholobenko, V.L. et al., Synthesis of MCM-41 materials: an *in situ* FTIR study, *Microporous Mater.*, 11, 83, 1996.
92. Zhang, J., Luz, Z., and Goldfarb, D.J., EPR studies of the formation mechanism of the mesoporous materials MCM-41 and MCM-50, *J. Phys. Chem. B*, 101, 7087, 1997.
93. Galarneau, A. et al., Kinetics of formation of micelle-templated silica mesophases monitored by electron paramagnetic resonance, *J. Colloid Interface Sci.*, 201, 105, 1998.

94. Zhang, J. and Goldfarb, D., *In situ* investigations of the formation mechanism of mesoporous materials via the dynamics and ordering of spin-probes — pH and Si/surfactant effect, *Microporous Mesoporous Mater.*, 48, 143, 2001.
95. Ottaviani, M.F. et al., EPR investigations on the formation of micelle-templated silica, *Microporous Mesoporous Mater.*, 44, 1, 2001.
96. Lindén, M. et al., Phase behavior and wall formation in Zr(SO₄)₂/CTABr and TiOSO₄/CTABr mesophases, *Chem. Mater.*, 11, 3002, 1999.
97. Göltner, C. and Antonietti, M., Mesoporous materials by templating of liquid crystalline phases, *Adv. Mater.*, 9, 431, 1997.
98. Israelachvili, J.N., Mitchell, D.J., and Ninham, B.W., Theory of self-assembly of hydrocarbon amphiphiles into micelles and bilayers, *J. Chem. Soc. Faraday Trans. 2*, 72, 1525, 1976.
99. Israelachvili, J.N., Mitchell, D.J., and Ninham, B.W., *Biochim. Biophys. Acta*, 470, 185, 1977.
100. Huo, Q. et al., Mesostructure design with gemini surfactants: supercage formation in a three-dimensional hexagonal array, *Science*, 268, 1324, 1995.
101. Grün, M., Lauer, I., and Unger, K., *Adv. Mater.*, 9, 254, 1997.
102. Ågren, P. et al., Kinetics of cosurfactant–surfactant–silicate phase behavior. 1. Short chain alcohols, *J. Phys. Chem. B*, 103, 5943, 1999.
103. Edler, K.J. et al., Diffuse wall structure and narrow mesopores in highly crystalline MCM-41 materials studied by x-ray diffraction, *J. Chem. Soc. Faraday Trans.*, 93, 199, 1997.
104. Impéror-Clerc, M., Davidson, P., and Davidson, A., Existence of a microporous corona around the mesopores of silica-based SBA-15 materials templated by triblock copolymers, *J. Am. Chem. Soc.*, 122, 11925, 2000.
105. Denoyel, R. and Sabio Rey, E., Solubilization in confined surfactant mesophases, *Langmuir*, 14, 7321, 1998.
106. Ågren, P. et al., Kinetics of cosurfactant–surfactant–silicate phase behavior. 2. Short-chain amines, *Langmuir*, 16, 8809, 2000.
107. Lind, A. et al., Solubilization of benzene derivatives in silicate-surfactant systems, *Colloids Interfaces A*, 183, 415, 2001.
108. Lind, A. et al., Controlled oil solubilization by silicate-catanionic surfactant mesophases as studied by *in situ* and *ex situ* XRD, *Langmuir*, 18, 1380, 2002.
109. Lindén, M. et al., Solubilization of oil in silicate-surfactant mesostructures, *Langmuir*, 16, 5831, 2000.
110. Bussian, P. et al., Speciation in solution: analysis of silicate oligomers using ESI-MS, *Angew. Chem. Int. Ed.*, 112, 4065, 2000.

9 Solubilization in Surfactant Systems

Clarence A. Miller

CONTENTS

- 9.1 Introduction
- 9.2 A Simple Model of Solubilization
- 9.3 Experimental Measurements of Solubilization
- 9.4 Solubilization in Microemulsions
- 9.5 Theories of Solubilization in Micellar Solutions
- 9.6 Rates of Solubilization
 - 9.6.1 Solubilization of Pure Oils by Micellar Solutions
 - 9.6.2 Solubilization of Mixed Oils by Micellar Solutions
 - 9.6.3 Solubilization by Microemulsions
- 9.7 Solubilization by Intermediate Phase Formation
 - 9.7.1 General Remarks and Techniques
 - 9.7.2 Results

Acknowledgment

References

9.1 INTRODUCTION

One reason that surfactants are useful in a wide variety of applications is that, under suitable conditions, their aqueous solutions are able to dissolve substantial amounts of compounds that have very low solubilities in water. Similarly, surfactants can greatly increase the solubility of water and other polar compounds in hydrocarbons and other liquids of low polarity. This phenomenon, which involves incorporation of the solute by aggregates of surfactant molecules, is known as solubilization. It occurs not only for small surfactant aggregates such as (nearly) spherical micelles but also for larger aggregates such as microemulsion drops, vesicles, and cylindrical and platelike micelles. Lyotropic liquid crystals containing regular arrays of surfactant aggregates are also effective media for solubilization.

In this chapter some experimental results and theories of solubilization are reviewed. In accordance with the author's interests and space limitations, the selection of topics is not comprehensive and emphasizes microemulsions and dynamic processes involving solubilization to a greater extent than does a recent collection of review articles on solubilization.¹ Earlier extensive discussions of solubilization have been given by McBain and Hutchinson,² Elworthy et al.,³ and Mackay.⁴

Surfactant molecules by definition have polar groups such as ions or ethylene oxide chains and nonpolar groups such as hydrocarbon or fluorocarbon chains. When they are added to water, aggregation normally occurs at fairly low concentrations to minimize the area of contact between the nonpolar groups and water. For low temperatures and molecules with long, straight hydrocarbon chains, separation into a crystalline solid phase and a dilute aqueous solution of molecularly

dissolved surfactant is found. However, above a temperature known as the Krafft point, which depends on surfactant structure, the chains become more flexible and do not pack into regular, crystalline structures. Instead, dilute solutions of rather hydrophilic surfactants form small aggregates or micelles containing perhaps 50 to 100 molecules in which the polar groups are on the surface and thus exposed to water while the nonpolar groups make up the interior and are largely shielded from water. The behavior of chains inside micelles is similar to that in liquid hydrocarbons although their freedom of motion is restricted somewhat by their attachment to the polar groups at the micelle surface. For most surfactants micelle formation begins rather abruptly over a narrow concentration range, and it is useful to speak of a critical micelle concentration (CMC).

More lipophilic surfactants form larger, nonspherical micelles, vesicles, or lyotropic liquid crystalline phases at rather low concentrations in water. For example, at temperatures above those where the chains form crystalline structures, phospholipids and other surfactants with two relatively long hydrocarbon chains typically form the lamellar liquid crystalline phase consisting of many parallel surfactant bilayers separated by water layers. The hydrocarbon interiors of the bilayers are rather fluid as in micelles. Of course, in this case a true phase separation occurs beginning at a definite surfactant concentration.

In the next section a simple model is described that provides some understanding of the essentials of solubilization. Then some measurement techniques, experimental results, and theories of equilibrium solubilization are presented for micelles and microemulsions. Finally, dynamic phenomena such as solubilization rates and solubilization by intermediate phases formed after the solute contacts a surfactant solution are discussed.

9.2 A SIMPLE MODEL OF SOLUBILIZATION

We begin with a relatively simple model, which was suggested some years ago by Mukerjee⁵ and which provides considerable insight on solubilization of small amounts of solutes in spherical micelles. Suppose that an aqueous micellar solution has reached its solubilization limit and is in equilibrium with an excess liquid phase of a pure hydrocarbon or some other compound of low polarity. Equating the chemical potentials μ_b° and μ_m of the solute in the bulk organic phase and in the micelles, we have

$$\mu_b^\circ = \mu_m = \mu_m^\circ + RT \ln x_m \quad (9.1)$$

where x_m is the mole fraction of the solute in the micelles and where ideal mixing in the micelles has been assumed. If we assume that we can treat the surface of a spherical micelle like an interface between bulk fluids, the pressure in the nonpolar interior of the spherical micelle is higher than that in the surrounding water by an amount $(2\gamma/r)$, where γ is the interfacial tension and r the micelle radius. Since μ_m° must be evaluated at this higher pressure, we have

$$\mu_m^\circ = \mu_b^\circ + (2\gamma v/r) \quad (9.2)$$

where v is the molar volume of the solute. Also, pressure in the bulk oil phase has been taken equal to that in the water, a reasonable assumption here because the radii of curvature of the oil–water interface greatly exceed the micelle radius r , which is only some 1 to 3 nm. Substituting this expression into Equation 9.1, we obtain

$$x_m = \exp\left[-(2\gamma v/rRT)\right] \quad (9.3)$$

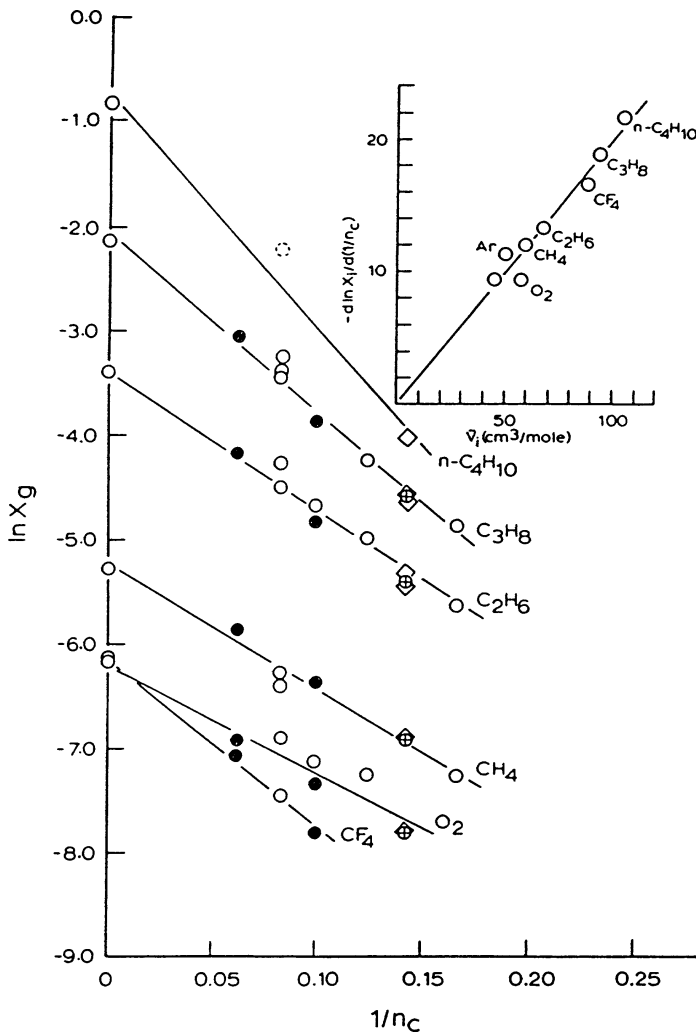


FIGURE 9.1 Logarithm of gas solubilities as a function of the reciprocal carbon chain length ($1/n_c$) of the surfactant. Symbols: \circ = sodium alkyl sulfates (and n -heptane at $(1/n_c) = 0$); \bullet = alkyltrimethyl ammonium bromides; \diamond = sodium octanoate; \oplus = sodium 1-heptane sulfonate; \odot = SDS/0.1 M NaCl. *Inset:* Slopes of straight lines in main figure as a function of gas molar volume. (From King, A.D., in *Solubilization in Surfactant Aggregates*, Christian, S.D. and Scamehorn, J.F., Eds., Marcel Dekker, New York, 1995. With permission.)

King⁶ has shown that the dependence predicted by this model of x_m on both v and surfactant chain length, which determines r , is in quantitative agreement with experimental data for pure gases of low molecular weight solubilized in ionic surfactant micelles. The gases include oxygen and argon as well as light hydrocarbons (Figure 9.1). The value of interfacial tension γ required to fit the data was about 28 mN/m. He also found that the same value of γ could fit data obtained by solute vapor pressure measurements above micellar solutions (see Reference 7) having cyclohexane, n -pentane, and n -hexane solubilized in similar micelles at ambient temperature where these solutes would be liquids. Data obtained by McBain and Richards⁸ on solubilization of longer-chain hydrocarbons in potassium laurate are reasonably consistent with the dependence on molar volume predicted by the above equation for straight-chain and branched hydrocarbons with six to ten carbon

atoms as well as for cyclohexane and simple aromatics such as benzene, toluene, and ethylbenzene. For longer-chain aliphatic compounds solubilization is very low, and the data are not sufficiently accurate to make the comparison. However, with sodium oleate as the surfactant the observed dependence of solubilization on solute molar volume⁸ is not well described by this simple model even for straight-chain hydrocarbons.

According to Equation 9.3, solubilization should increase with decreasing interfacial tension γ between the micelles and water. It is known that interfacial tension decreases as a surfactant's hydrophilic and lipophilic properties become more nearly balanced, for example, as salinity or hardness of the aqueous phase increases in the case of ionic surfactants. Solubilization increases under these conditions as well, so that the predicted trend is in qualitative agreement with experimental data.

Equation 9.3 is satisfactory only when micelles are small and spherical and solubilization is relatively low. While the above derivation can apply either to nonpolar species solubilized in the micelle interior or to amphiphilic species such as alcohols that basically form mixed micelles with the surfactant, caution should be used in the latter case. The reason is that alcohols less hydrophilic than the surfactant can cause the micelles to become rodlike, thus violating the assumption of spherical micelles employed in the analysis.

The above analysis can be extended in various ways to provide insight, although not necessarily useful quantitative predictions, for other situations. For example, long, cylindrical micelles can be considered, in which case the factor of 2 disappears from Equation 9.3. Indeed, surfactant bilayers can also be considered⁹ if we include a surface energy term in writing the free energy change ΔF for transferring δn moles of solute from the bulk oil phase into a bilayer of fixed half-thickness d as

$$\Delta F = \left[-\mu_b^o + \mu_m^o + RT \ln x_m + \gamma (\partial A / \partial n) \right] \delta n \quad (9.4)$$

where A is bilayer area and n is the number of moles of solubilized solute. Since r is infinite, $\mu_m^o = \mu_b^o$, according to Equation 9.2. Moreover, $(\partial A / \partial n) = (v/d)$. Hence, setting $\Delta F = 0$ yields Equation 9.3 without the factor of 2 and with r replaced by d .

Another possible extension is to consider an excess oil phase which is a mixture of two or more species. Provided that mixing within the micelle can still be considered ideal and that activity coefficients for all species in the bulk oil mixture are known, an expression for x_{mi} for each solute is readily obtained. Micelles formed from surfactant mixtures can be treated provided that micelle composition is known or can be calculated from theories of mixed micelles such as regular solution theory¹⁰ and that solubilization is low enough not to affect micelle shape or composition. Finally, nonideal mixing in the micelles can be included if some model for the nonideality is available as well as data for evaluating the relevant parameters. Perhaps the simplest scheme for incorporating nonideality with nonpolar solutes is to use volume fractions instead of mole fractions in the spirit of Flory–Huggins theory.

9.3 EXPERIMENTAL MEASUREMENTS OF SOLUBILIZATION

One quantity of interest is that discussed in the preceding section, i.e., the maximum possible solubilization of a solute by a micellar solution, which occurs when it is in equilibrium with a bulk phase of the solute. Data may be presented as the mole fraction x_m of solute in the micelle as in the above equations. More commonly, however, we find a plot of the moles of solute dissolved in the micellar solution as a function of surfactant concentration. Above the CMC such a plot usually exhibits a straight line whose slope is the moles of solute solubilized per mole of surfactant in the micelles (see Figure 9.2). Below the CMC the amount solubilized is usually constant and equal to the solute solubility in water.

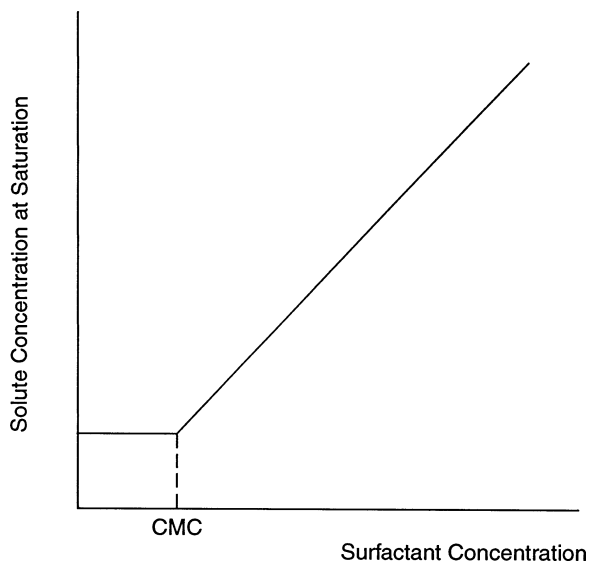


FIGURE 9.2 Typical variation of solubilization with surfactant concentration.

The maximum solubilization may be determined by measuring the turbidity of a micellar solution while adding successive increments of bulk liquid (or solid) solute. When each increment is first injected, turbidity increases because the drops of solute scatter light. If complete solubilization occurs, turbidity returns to its initial low value. If not, the solubilization limit has been reached. Caution is necessary in using this technique because many hours may be required for each increment to be solubilized as the solubilization limit is approached. When dealing with certain liquid solutes such as aromatics and amphiphilic compounds added to solutions of nonionic surfactants, one must be careful that the solute concentration where the solution becomes turbid is a true solubilization limit with an excess solute phase and not a cloud point with all the solute incorporated into micelles but with an excess water phase.

For volatile solutes the micellar solution may be allowed to reach equilibrium with a bulk solute phase with which it is not in direct contact, mass transfer between them occurring through an intervening vapor phase. An apparatus where several surfactant solutions having different concentrations may be equilibrated simultaneously in this way with a single drop of bulk solute has been described by Moroi et al.¹¹ When equilibrium is reached, the individual surfactant solutions are analyzed for solute content. An alternative method involving vapor pressure measurements is to add increments of solute to a micellar solution until the solute partial pressure above the solution reaches its known vapor pressure.⁷

Sometimes we may be chiefly interested in how much solute is solubilized in the micelles and how much is simply dissolved in water at concentrations below the solubilization limit. Several methods for determining this partitioning have been described. For example, measurement of solute self-diffusion coefficients using NMR techniques provides this information because micelles are much larger than dissolved solute molecules and therefore diffuse much more slowly.¹² So does the nuclear magnetic resonance (NMR) paramagnetic relaxation technique in which a small amount of a suitable paramagnetic ion added to the surfactant solution significantly increases the spin-lattice relaxation rate of the molecularly dissolved solute but not of the solubilized solute.¹³ Solute vapor pressure measurements above a micellar solution yield values of solute activity that can be used to calculate the partitioning.⁷ Yet another technique involves determining the effect of small amounts of solute on the CMC as measured, for example, by conductivity methods for ionic surfactants (see Reference 14, which also provides an extensive list of partition coefficients determined in this way).

9.4 SOLUBILIZATION IN MICROEMULSIONS

The above discussion applies to situations where solubilization is rather limited, i.e., x_m below — usually well below — 0.5. However, when the hydrophilic and lipophilic properties of a surfactant are nearly balanced, solubilization of nonpolar solutes can be much greater. In this case solubilization significantly affects the shape and/or size of the surfactant micelles or other aggregates, and the resulting phase is usually called a microemulsion. Although the term *microemulsion* normally refers to thermodynamically stable isotropic liquids containing substantial amounts of both oil and water, there is no widely accepted degree of solubilization at which a “micellar solution” becomes a “microemulsion.” Microemulsions were discovered and studied by Hoar and Schulman some 60 years ago,¹⁵ but they have been investigated extensively only during the past three decades, owing initially to their possible application in increasing petroleum recovery from underground formations and later to other possible applications as well as their intriguing phase behavior and microstructure, which are of inherent fundamental interest.

A general pattern of microemulsion phase behavior exists for systems containing comparable amounts of water and a pure hydrocarbon or hydrocarbon mixture together with a few percent surfactant. For somewhat hydrophilic conditions, the surfactant films tend to bend in such a way as to form a water-continuous phase, and an oil in water microemulsion coexists with excess oil. Drops in the microemulsion are spherical with diameters of order 10 nm. Both drop size and solubilization expressed as (V_o/V_s) , the ratio of oil to surfactant volume in the microemulsion, increase as the system becomes less hydrophilic. At the same time interfacial tension between the microemulsion and oil phases γ_{mo} decreases. Just the opposite occurs for somewhat lipophilic conditions. That is, a water in oil microemulsion coexists with excess water with drop size and solubilization of water (V_w/V_s) increasing and interfacial tension γ_{mw} decreasing as the system becomes less lipophilic. When the hydrophilic and lipophilic properties of the surfactant films are nearly balanced, a bicontinuous microemulsion phase coexists with both excess oil and excess water. For a balanced film (V_o/V_s) and (V_w/V_s) in the microemulsion are nearly equal, as are γ_{mo} and γ_{mw} . The former typically have values between 2 and 10, whereas the latter are of order 10^{-4} to 10^{-2} mN/m. The above trends in solubilization and interfacial tension are summarized in Figure 9.3. As Huh¹⁶ has pointed out, the product $(V_o/V_s)^2\gamma_{mo}$ at balanced or “optimal” conditions has a nearly constant value. Thus, interfacial tension decreases as solubilization increases. Even away from optimal conditions, solubilization and interfacial tension are strongly correlated,¹⁷ as shown in Figure 9.4. If surfactant concentration is increased at optimal conditions, transition occurs at some concentration from the three-phase region mentioned above to a single-phase microemulsion region.

Various changes can cause the system to shift from hydrophilic to lipophilic conditions and thus undergo the phase changes described above. Winsor¹⁸ observed the basic pattern of phase behavior and recognized that it was related to the hydrophilic and lipophilic properties of the surfactant. Shinoda and Friberg¹⁹ conducted extensive studies of nonionic surfactant systems where an increase in temperature makes the surfactant films less hydrophilic. Several groups investigated anionic surfactant systems of interest in enhanced oil recovery where increases in salinity or divalent cation concentration produce more lipophilic conditions but increases in temperature generally cause small shifts in the opposite direction (see References 17, 20, and 21). Anton et al.^{22,23} studied microemulsions made with cationic surfactants and anionic–cationic mixtures. Kahlweit et al.²⁴ investigated a wide range of both ionic and nonionic surfactants.

In this connection, it should be noted that typical single-chain ionic surfactants are too hydrophilic to form balanced microemulsions under most conditions of interest, and we must either add a lipophilic cosurfactant such as pentanol or hexanol or use a double-chain ionic surfactant instead. Of course, cosurfactants can also be used with nonionic surfactants. It should be recognized that the size and shape of aggregates in a microemulsion are influenced by cosurfactant incorporated into the surfactant films but not by that dissolved in oil and water, whether in the microemulsion itself or in coexisting excess phases. The same is true for nonionic surfactants themselves, which

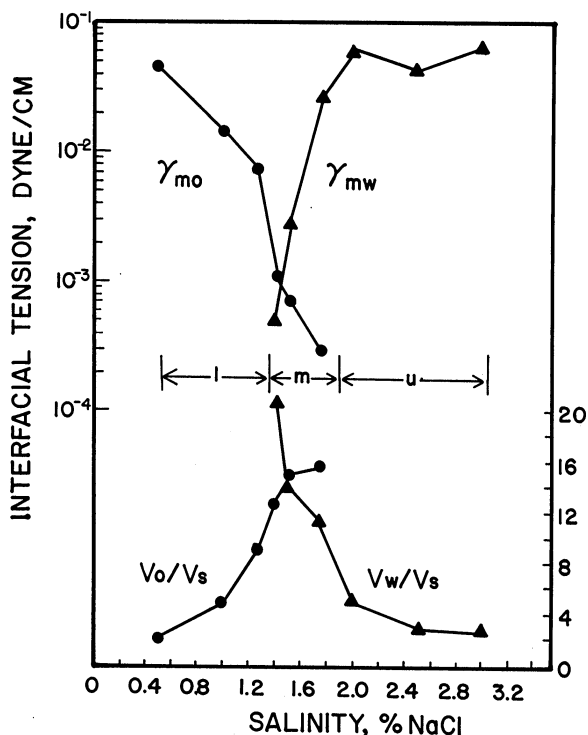


FIGURE 9.3 Interfacial tensions and solubilization parameters for microemulsions in a system containing a synthetic petroleum sulfonate, an alcohol cosurfactant, a mixture of refined oils, and NaCl brine. (From Reed, R.L. and Healy, R.N., in *Improved Oil Recovery by Surfactant and Polymer Flooding*, Shah, D.O. and Schechter, R.S., Eds., Academic Press, New York, 1977. With permission.)

have appreciable solubilities in hydrocarbons. As a result, the temperatures required to yield optimal conditions for surfactant–cosurfactant mixtures and even for commercial nonionic surfactants, which are mixtures of species having a range of ethylene oxide chain lengths, depend on the overall concentrations of surfactant and cosurfactant in the system and on the relative amounts of oil and water present.

Other factors that can influence microemulsion phase behavior are pH, which affects the charge of the film when the surfactant has an acidic or basic group, pressure, and the molar volume of the hydrocarbon making up the oil phase. Oils with large molar volumes penetrate surfactant films to a lesser extent and hence are less effective in bending the film toward a water in oil configuration than are oils with small molar volumes. Accordingly, increasing oil chain length shifts the system and phase behavior toward more hydrophilic conditions.

Solubilization at optimal conditions can be increased and interfacial tension decreased by, for example, increasing both hydrocarbon and ethylene oxide chain lengths of a nonionic surfactant. However, as optimal solubilization increases, the temperature range over which the microemulsion coexists with both oil and water decreases, and interfacial tension variation with temperature becomes more rapid; i.e., the system becomes more sensitive to small changes in temperature. For ionic surfactants an analogous increase in optimal solubilization can be achieved by increasing hydrocarbon chain length of the surfactant and decreasing salinity. Here, too, the higher solubilization is accompanied by an increase in system sensitivity. Adding a short-chain alcohol such as isobutanol, which has little effect on the balance of hydrophilic and lipophilic properties, decreases optimal solubilization and increases interfacial tension. However, it can prevent formation of the lamellar liquid crystalline phase for surfactants having long, straight hydrocarbon chains. The

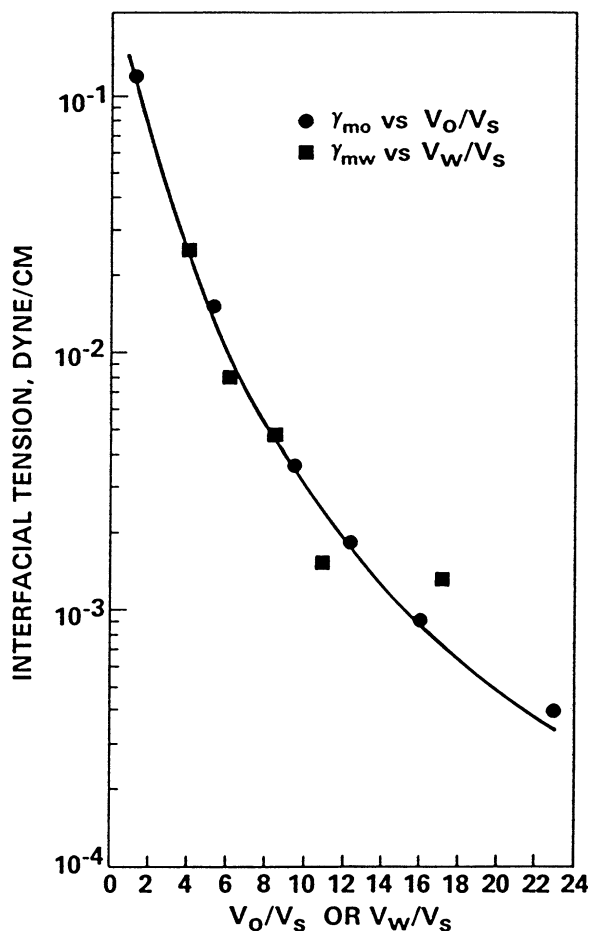


FIGURE 9.4 Correlation of interfacial tension with solubilization parameter for the same system as in Figure 9.3. (From Reed, R.L. and Healy, R.N., in *Improved Oil Recovery by Surfactant and Polymer Flooding*, Shah, D.O. and Schechter, R.S., Eds., Academic Press, New York, 1977. With permission.)

lamellar phase normally has less ability to solubilize hydrocarbon than does a bicontinuous microemulsion.²⁵ It can also have a higher viscosity although rather dilute lamellar phases with relatively low viscosities are frequently found in nearly balanced systems.²⁶

The general pattern of microemulsion phase behavior described above is seen when the amounts of water and hydrocarbon present are comparable. However, a hydrocarbon-free mixture of surfactant and water (or brine) near optimal conditions is typically not a simple micellar solution but either the lamellar liquid crystalline phase or a dispersion of this phase in water.²⁶ Starting with such a mixture and adding hydrocarbon, we sometimes find that the system passes through several multiphase regions before reaching the microemulsion/oil/water equilibrium characteristic of optimal conditions.²⁶

Ruckenstein and Chi²⁷ presented a thermodynamic treatment of a microemulsion consisting of fixed amounts of oil, water, and surfactant. The analysis yielded an optimum droplet diameter, demonstrated that the entropy of dispersion made an important contribution to microemulsion free energy, and confirmed that a very low interfacial tension of the droplets was required for thermodynamic stability. Indeed, to a first approximation, we can often estimate droplet size by taking the area per surfactant molecule as that for which interfacial tension would be zero.

For a microemulsion in equilibrium with excess dispersed phase, e.g., an oil in water microemulsion in equilibrium with excess oil, the bending properties of the surfactant films covering the droplets must also be considered, and droplet radius is typically not far from the “natural” radius the film would assume at an isolated oil–water interface. Miller and Neogi²⁸ and Mukherjee et al.²⁹ analyzed this case using concepts based on Hill’s thermodynamics of small systems³⁰ and explicitly including bending effects. Their equations for equilibrium are given by

$$-4\pi rN[\gamma + (2H/r)] + (\partial G_{md}/\partial r)_{T,p,n_d,n_c,n_s} = 0 \quad (9.5)$$

$$8\pi rN[\gamma - (H/r)] + (\partial G_{md}/\partial r)_{T,p,N,n_c,n_s} = 0 \quad (9.6)$$

where N is the number of droplets of radius r in a unit volume of microemulsion, γ the interfacial tension of the droplets, and H the “bending stress” of the surfactant films of the droplets, basically the change with curvature of the free energy of a film occupying a unit area. Also G_{md} is the contribution to the microemulsion free energy per unit volume resulting from the entropy of dispersion and the energy of interaction among droplets. For example, in a simple case we could use the well-known Carnahan–Starling equation based on a hard sphere model:³¹

$$G_{md} = NkT \left\{ \ln \phi - 1 + \phi \left[(4 - 3\phi)/(1 - \phi)^2 \right] + \ln(3V_c/4\pi r^3) \right\} \quad (9.7)$$

where ϕ is the volume fraction of droplets in the microemulsion and V_c is the volume of a molecule of the continuous phase of the microemulsion.

The partial derivative in Equation 9.5 is taken at constant temperature, pressure, and number of moles per unit volume n_c , n_d , and n_s of continuous phase, dispersed phase, and surfactant in the microemulsion. However, the number of droplets N may vary. This equation applies even when no excess phase is present and would be used to find the equilibrium droplet radius in that case. In Equation 9.6, the partial derivative is taken at constant N but with variable n_d . It is applicable only when excess disperse phase is present. Using both these equations, the above authors found that with a given amount of surfactant present, more droplets of smaller size are predicted than would be expected based on the pertinent natural radius. That is, solubilization with an excess of the dispersed phase is somewhat less than if droplets assumed their natural radius. In this case the energy required to bend the film beyond its natural radius is offset by the decrease in free energy associated with the increased entropy of the more numerous droplets.

It is also possible for a microemulsion containing spherical droplets to separate into a more concentrated microemulsion and excess continuous phase, e.g., an oil in water microemulsion in equilibrium with excess water, provided that attractive interaction among the droplets is sufficiently large. In other words, a microemulsion can have a limited capability to solubilize its continuous phase as well as its disperse phase. Interfacial tension between the phases should be very low as both are continuous in the same component. Such a phase separation is similar to that which takes place at the cloud point of nonionic surfactants. A simple theory of how it could occur for microemulsions was proposed by Miller et al.³² If excess continuous phase separates in this way and, at the same time, there is more disperse phase present than can be solubilized, the microemulsion can coexist with both oil and water phases. Although this situation of three-phase coexistence involving a microemulsion containing droplets probably exists at some compositions in some systems, in most situations the microemulsion in a three-phase region is bicontinuous (see below). The above discussion emphasizes the early theoretical work on microemulsions with droplets, but numerous papers (e.g., References 33 through 38) have appeared extending and improving the simple theory, describing methods for calculating bending properties of surfactant films, etc.

Based on data such as those showing a gradual decrease in electrical conductivity of microemulsions near optimal conditions as they became more lipophilic, Scriven³⁹ suggested that both oil and water were continuous under these conditions, in contrast to microemulsions far from optimal conditions, which were either oil continuous or water continuous. Several years later the bicontinuous structure was observed using a special electron microscopy technique in which the microemulsion is vitrified, i.e., cooled so fast that it freezes without crystallization of ice.⁴⁰

Several theories of bicontinuous microemulsions have been developed based on distribution of oil and water among cells, e.g., those arranged in a regular cubic array, with the surfactant located at those cell boundaries where oil and water are in contact.⁴¹⁻⁴⁴ A key objective of these theories is to predict the cell size and hence the amounts of oil and water solubilized when both phases are present in excess. The cell size is considered representative of the average dimension of the irregular and constantly fluctuating oil and water regions in an actual microemulsion. The main conclusion of this work is that cell size is comparable to the “persistence length” of the film, i.e., the length below which the film begins to offer substantial resistance to bending. More recently both electron microscopy experiments and theory have indicated that the bicontinuous microstructure may consist of branching cylindrical segments under some conditions.^{45,46}

9.5 THEORIES OF SOLUBILIZATION IN MICELLAR SOLUTIONS

As indicated previously, the “Laplace pressure” model is useful in understanding certain aspects of how surfactant and solute properties influence solubilization in small spherical micelles, and its predictions agree quantitatively with experimental data in some cases. It is closely related to the model of microemulsion with spherical droplets discussed in the preceding section. Because the latter model considers droplets large enough to have a core containing only solute, it contains no term to account for mixing of surfactant and solute. If ideal mixing within the micelle is included in the model, Equation 9.6 becomes

$$8\pi rN[\gamma - (H/r)] + (4\pi RTNr^2/v)\ln x_m + (\partial G_{md}/\partial r)_{T,p,N,n_c,n_s} = 0 \quad (9.8)$$

If bending effects and the term in G_{md} are neglected, Equation 9.8 simplifies to Equation 9.3. Note that in the derivation of Equation 9.3 it was implicitly assumed that the number density of micelles N and their radius r were already known for the solute-free case and that they remained unchanged during solubilization. That is, an expression such as Equation 9.5 had already been invoked.

Thus, we can generalize the previous Laplace pressure derivation by solving Equations 9.5 and 9.8 simultaneously. Nevertheless, the model is still phenomenological in nature and involves assumptions such as ideal mixing in the micelle and requires that parameters such as the bending stress be known. Accordingly, a more detailed description is desirable that takes a molecular view of micelle structure and explicitly accounts for such factors as electrical interaction among surfactant ions at the surface of a micelle and interaction among hydrocarbon chains within the micelle. Several efforts to develop such improved models have been made.

Nagarajan and Ruckenstein⁴⁷ have summarized their model of micelle formation and solubilization in micellar solutions developed in several previous papers. It includes contributions to the free energy of aggregation from (1) transfer of the hydrocarbon chains of the surfactants from water into the micelle, (2) conformations of the hydrocarbon chains inside the micelle, (3) formation of the micelle–water interface, (4) interaction among headgroups (including either electrical interaction for ionic surfactants or interaction among ethylene oxide chains for nonionic surfactants), (5) mixing of solutes with surfactants, and (6) mixing of the micelles and the aqueous solvent. Solubilization of nonpolar solutes can affect items (2), (3), (5), and (6), the last if the number, size, or shape of

the micelles is significantly changed. Spherical, cylindrical, and platelike micelles or aggregates are considered. However, aggregate diameter is not limited by the length of the surfactant tails; i.e., microemulsion drops are permitted if enough solubilization occurs for them to form. Surfactant tails are modeled as flexible chains that are placed on an appropriate lattice with one end of the chain at the micelle surface. When a nonpolar material is solubilized, the micelle interior is treated as a uniform solution of the tails in the solubilize. The free energy of the micelle–water surface is obtained by surface solution theory, considering the micelle interior to be a mixture of tails and solubilize. The free energy of mixing (item 5) is calculated using a Flory–Huggins approach.

With appropriate values of the various parameters, this model yielded predictions in good agreement with experiment on such phenomena as the amounts of various pure hydrocarbons solubilized in micelles of sodium dodecyl sulfate SDS as well as the amounts of benzene and *n*-hexane solubilized in the same micelles from various mixtures of the two hydrocarbons. It was also able to predict transformation of rodlike micelles to spherical microemulsion droplets as a result of hydrocarbon solubilization, an effect that has been observed experimentally.⁴⁸ In the absence of hydrocarbon, films of these surfactants can attain their preferred curvatures only by forming cylindrical micelles, as micelle radius is limited to the extended length of a surfactant molecule. However, when considerable hydrocarbon is present, this constraint no longer applies, and spherical microemulsion droplets can grow until the preferred curvature is reached.

A related model of micelle formation and solubilization has been developed by Jönsson and others in Lund. A relatively brief summary has been published,⁴⁹ but the original papers referenced there should be consulted for the detailed equations. The initial emphasis was on solubilization of amphiphilic solutes such as alcohols by solutions of ionic surfactants because a major objective was to model not only the micellar solution region but also the liquid crystalline regions of ternary phase diagrams for ionic surfactant–alcohol–water systems. Significant progress toward this objective has been achieved. Recently, a two-region model of a micelle has been included in this theory, which can handle nonpolar solutes because it considers that the solute can be distributed between the micellar surface region and an interior or “core” region.

Computer simulations offer the prospect of understanding how solubilization takes place on a molecular scale. At present, models of surfactant and solute molecules are relatively simple to allow molecular dynamics simulations for several thousand molecules to be carried out over time intervals of interest using computers currently available. Karaborni et al.,⁵⁰ for example, modeled a surfactant molecule as a straight chain of lipophilic segments, the hydrocarbon tail, joined to a small cluster of hydrophilic segments, the headgroup. An oil molecule was a chain of lipophilic segments, and a water molecule a single hydrophilic segment. Interaction between like segments was described by a Lennard–Jones potential with a cutoff distance, while that between unlike segments included only excluded volume effects.

The simulations they reported⁵⁰ were for a system of 501 surfactant molecules having a five-segment tail and a four-segment head; 852 oil molecules, half with two segments and half with three; and about 25,000 water molecules. The starting configuration was an oil drop, 23 micelles, and some surfactant monomers, and the simulations were carried out over some 1.6 million time steps. They found, as expected, that surfactant adsorbed at the surface of the (initially bare) oil drop and that the shorter-chain oil was preferentially solubilized. Of interest are their results regarding the amount of solubilization resulting from collisions of micelles with the oil drop and the amount resulting from dissolution of individual molecules in the aqueous phase with later incorporation into micelles. The latter process was more important for the shorter-chain oil, the former for the longer-chain oil. Some of the micelles became larger and incorporated more surfactant molecules as they solubilized substantial amounts of oil.

Nelson et al.⁵¹ used Monte Carlo techniques and were able to obtain the equilibrium shape of micelles with various amounts of solubilized oil. However, their surfactant and oil molecules had fewer segments than those in the work just described.

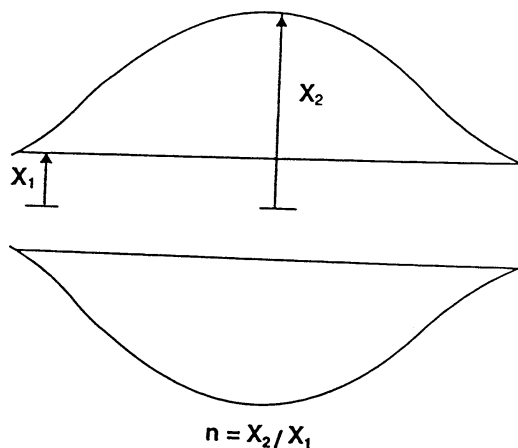


FIGURE 9.5 Schematic diagram of drop-on-fiber technique for measuring solubilization rates. Fiber radius X_1 and drop radius X_2 , which varies with time, are needed to calculate the rate of solubilization.

9.6 RATES OF SOLUBILIZATION

9.6.1 SOLUBILIZATION OF PURE OILS BY MICELLAR SOLUTIONS

In many situations, for example, removal of oily soils during cleaning processes, both the amount and the rate of solubilization are important. However, considerably less is known about the rates than about the equilibrium conditions.

Much of the information available on rates of solubilization of liquid hydrocarbons into aqueous micellar solutions has been obtained by the drop-on-fiber technique developed by Carroll.⁵² Basically, key dimensions of a drop attached to a fiber and having a constant nonzero contact angle are measured as a function of time and the results used to calculate the time dependence of drop volume V and surface area A (Figure 9.5). Ward⁵³ has reviewed the individual and joint studies that he and Carroll made using this technique with ionic and nonionic surfactants and their mixtures. Basically, they found that $[-A^{-1}(dV/dt)]$, the solubilization rate per unit area, was constant for a given drop and independent of initial drop size for fixed compositions of the oil and surfactant solution. This result implies that the rate is controlled by processes occurring at the oil–water interface and not by diffusion in the surfactant solution. The rate was also found to be proportional to surfactant concentration, which indicated that it was controlled by the rate of “adsorption” of surfactant from micelles. Moreover, the rate increased with increasing temperature for nonionic surfactants, with the increase especially rapid as the cloud point temperature of the surfactant was approached. Finally, as molecular weight (and volume) of the hydrocarbon increased, the rate of solubilization decreased as might be expected since, as indicated above, the equilibrium solubilization capacity for hydrocarbons of surfactant solutions decreases with increasing molecular volume.

Chen et al.⁵⁴ investigated solubilization of individual triolein drops, typically 50 to 100 μm in diameter, injected into rectangular glass cells, which were approximately 400 μm in thickness and contained nonionic surfactant solution (Figure 9.6). They used videomicroscopy to measure drop diameters as a function of time and thereby determine solubilization rates. No observable triolein solubilization occurred at 35°C for a 2 wt% solution of the pure nonionic surfactant C_{14}E_6 , which has a cloud point of 40°C. For other surfactants they found, as did Carroll and Ward for hydrocarbons, that solubilization rates were independent of drop size and proportional to surfactant concentration. Table 9.1 shows some of their results along with corresponding results for n -hexadecane for comparison. For 2 wt% C_{12}E_6 with 0.1 wt% added n -dodecanol, which has a cloud point of 39°C, the solubilization rate of triolein at 30°C was 0.01 $\mu\text{m}^3/\mu\text{m}^2\text{min}$. In contrast, the same solution

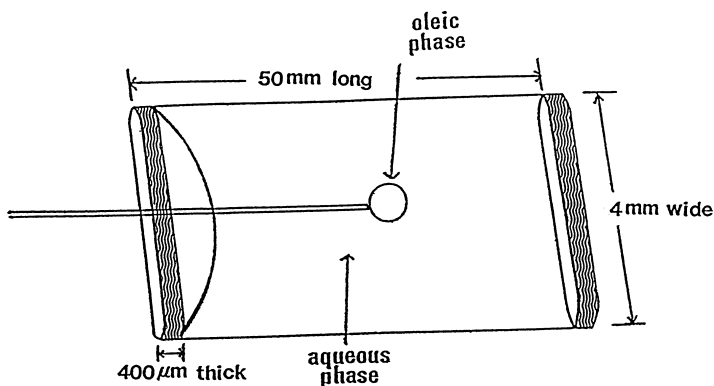


FIGURE 9.6 Schematic illustration of contacting experiment in which a small oil drop is injected into an aqueous surfactant solution to measure solubilization rate.

TABLE 9.1
Solubilization of Triolein and *n*-Hexadecane at 30°C⁵⁴

Surfactant	Triolein Equilibrium Solubilization Ratio (mass)	Triolein Solubilization Rate ($\mu\text{m}/\text{min}$)	Hexadecane Equilibrium Solubilization Ratio (mass)	Hexadecane Solubilization Rate ($\mu\text{m}/\text{min}$)
2 wt% Tergitol 15-S-7	0.24–0.30	0.09	0.69–0.75	0.58
Same + 0.15 wt% <i>n</i> -hexanol	0.40–0.46	0.20	0.95–1.0	1.19
2 wt% C ₁₂ E ₆ + 0.1 wt% <i>n</i> -dodecanol	0.15–0.20	0.01	0.68–0.75	0.67
2 wt% C ₁₂ E ₆ + 0.3 wt% <i>n</i> -hexanol	0.25–0.30	0.03–0.05	0.82–0.91	0.96

solubilized *n*-hexadecane at $0.67 \mu\text{m}^3/\mu\text{m}^2\text{min}$. When 0.3 wt% *n*-hexanol was used instead of *n*-dodecanol, the cloud point remained the same, but the solubilization rate of triolein increased more than threefold. Finally, when the commercial secondary alcohol ethoxylate Tergitol 15-S-7, which has a cloud point of 37°C, was used without alcohol, the rate of triolein solubilization at 30°C was even greater — $0.09 \mu\text{m}^3/\mu\text{m}^2\text{min}$. Percentage changes in the solubilization rate of *n*-hexadecane were much smaller. Tergitol 15-S-7 is a mixture of species with the alcohol group located at various positions along a chain of approximately 15 carbon atoms and with an average ethylene oxide number of 7.

Table 9.1 also shows that while *n*-hexadecane solubilization rates for different surfactants are, for the most part, roughly proportional to the corresponding equilibrium solubilization capacities, the same is not true for triolein. In addition, the ratio of solubilization rates of triolein and *n*-hexadecane for a given surfactant solution is much smaller than that of the respective solubilization capacities. All these results indicate that triolein is much more difficult to solubilize than *n*-hexadecane, probably because it is a larger and less flexible molecule. As micelles are continually being adsorbed and emitted at the oil–water interface, it seems reasonable that triolein would be more difficult to incorporate into emitted micelles, especially those formed from surfactants that all have straight hydrocarbon tails of the same length. Adding an alcohol with a different chain length or using a surfactant such as Tergitol 15-S-7, which is mixture of species with different tail configurations, should make packing in the micelle interior more disordered and facilitate triolein solubilization, in agreement with the experimental results.

For solutions of typical ionic surfactants with no added salts the studies of Carroll and Ward showed that solubilization rates were much smaller than those for nonionic surfactants, presumably because the surfactant ions adsorbed at the oil–water interface repelled the micelles of like charge in the solution. Indeed, Bolsman et al.⁵⁵ found no measurable solubilization of *n*-hexadecane into solutions of a pure benzene sulfonate and a commercial xylene sulfonate. They injected small oil drops into the surfactant solutions and observed whether the resulting turbidity disappeared over time due to solubilization. Similarly, Kabalnov⁵⁶ found from Ostwald ripening experiments that the rate of solubilization of undecane into solutions of pure SDS was independent of surfactant concentration and about the same as the rate in the absence of surfactant. That is, the hydrocarbon presumably left the bulk oil phase in this system by dissolving in virtually micelle-free water near the interface. In similar experiments Taylor⁵⁷ and Soma and Papadopoulos⁵⁸ observed a small increase in the solubilization rate of decane with increasing SDS concentration. De Smet et al.,⁵⁹ who used sodium dodecyl benzene sulfonate, which does not hydrolyze, found, like Kabalnov, a minimal effect of surfactant concentration.

Cussler, Evans, and co-workers^{60,61} used the rotating disk technique with radioactively tagged solutes to measure the solubilization rates of pure, solid fatty acids and a solid monoglyceride by several surfactant solutions. The advantage of this technique is that the velocity distribution is known and can be controlled by varying the speed of disk rotation. Temperatures were below the “penetration temperatures” of the systems where surfactant entering the crystalline solids causes melting of the regular chain arrangement, thereby transforming it to a lamellar liquid crystal, which can swell in the form of myelinic figures. Kabin et al.⁶² also used a rotating disk to study solubilization rates of abietic acid in solutions of several pure nonionic surfactants at 24°C.

An effort was made to use the same technique for liquid solutes⁶³ by trapping the liquid in a porous membrane having the shape of a disk. Ward⁵³ also reported results of some experiments with liquid oils using this method.

As indicated above, both Carroll and Ward with the drop-on-fiber technique and Chen et al. with the oil drop technique concluded that the constant solubilization rate per unit area they observed implied that the rate was controlled by processes occurring at the interface such as “adsorption” of surfactant from micelles in the aqueous solution and “desorption” of oil-containing micelles. If the process had been limited by the rate of diffusion in the stagnant aqueous solution with local equilibrium at the interface, the solubilization rate per unit area would have increased with decreasing drop size. Details of the adsorption and desorption processes are not clear. Carroll proposed that the dissociation of micelles when very near the interface might be a key step in the adsorption process as has sometimes been assumed in interpreting data on dynamic surface tension.⁶⁴ However, as data on micelle dissociation rates are not available for the nonionic surfactant systems he studied, the validity of this mechanism cannot be assessed at present. Moreover, if we assume that the oil-to-surfactant ratio in emitted micelles is approximately equal to the equilibrium solubilization ratio, the data shown in Table 9.1 suggest that the adsorption rates of surfactant from the same micellar solution are different for triolein and *n*-hexadecane drops. If so, factors other than micelle dissociation rate have significant effects on the adsorption rate.

Shaeiwitz et al.⁶¹ concluded from analysis of their data for solid solutes that at high speeds of disk rotation where mass transfer would be very fast, micelle desorption would be the rate-limiting step. However, at the actual speeds used in their experiments mass transfer of the desorbed micelles to the bulk solution was also important. For liquid solutes the results of Huang et al.⁶³ indicated that adsorption, not desorption, was the rate-limiting step, the same as later found by Carroll and Ward and Chen et al.

McClements and Dungan⁶⁵ reported, based on light scattering measurements, that the Sauter or surface-volume mean diameter of drops in a dilute emulsion of *n*-hexadecane in water remained constant while the number of drops decreased with time during solubilization of the hydrocarbon into a 2 wt% solution of Tween 20 (sorbitan monolaurate). Weiss et al.⁶⁶ found similar results for the same surfactant with *n*-tetradecane and *n*-octadecane. This result, which seems surprising in

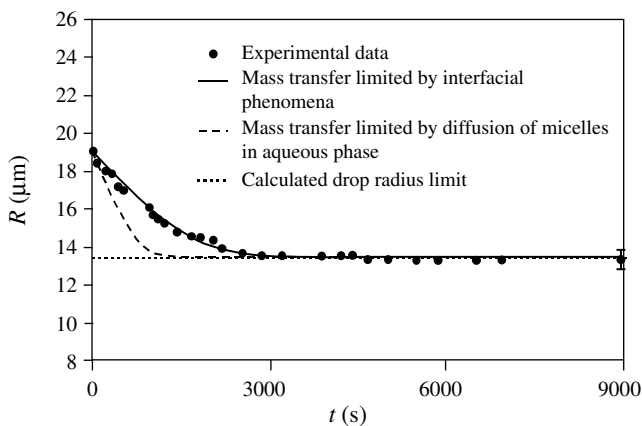


FIGURE 9.7 Variation of radius with time for a drop initially containing 80 mol% *n*-decane and 20 mol% squalane following injection into a 2.5 wt% solution of $C_{12}E_8$ at 23°C. The solid and dashed curves represent theoretical predictions based on interfacially controlled and diffusion-controlled mass transfer, respectively. (From Peña, A.A. and Miller, C.A., *J. Colloid Interface Sci.*, 244, 154, 2001. With permission.)

view of the decrease in size over time seen for the individual drops being solubilized, can be explained if polydispersity is taken into account.⁶⁷ Basically, the contribution of smaller drops to the Sauter mean diameter is minimal. Because the percentage change in diameters of the larger drops is much smaller than the volume change, the Sauter mean diameter is nearly constant. Calculating the change in interfacial area over time using the constant drop size result, McClements and Dungan were able to explain their data on solubilization rates by a model having a constant interfacial mass transfer coefficient. For constant drop size the same result is obtained if the rate is controlled by interfacial phenomena, bulk diffusion, or by some combination of the two.

9.6.2 SOLUBILIZATION OF MIXED OILS BY MICELLAR SOLUTIONS

The components of oil mixtures usually dissolve at different (and varying) rates in aqueous surfactant solutions, behavior which is relevant in applications such as separations, controlled drug delivery, and emulsion stability. A classic example is the work of Higuchi and Misra,⁶⁸ who noted many years ago that the timescale for coarsening of drops in a dilute emulsion of carbon tetrachloride in water stabilized by the ionic surfactant Aerosol OT (AOT) could be increased significantly by adding tiny amounts of *n*-hexadecane or Nujol. Although their theory based on diffusion-controlled mass transport exhibited only qualitative agreement with experiment, their results established the well-known practice of adding a component preferentially soluble in the dispersed phase of an emulsion as a way to retard Ostwald ripening.

It seems that the role of micelles was first considered by Goldberg et al.,^{69,70} who studied transport of micelle-solubilized drugs from the aqueous environment to an oil phase dispersed as drops. They measured mass transfer rates in two systems where solubility of the oil in the aqueous phase was negligible. Their model included partitioning between the bulk aqueous phase and micelles and both diffusional and interfacial resistances to mass transfer. Agreement with experimental data was best when interfacial resistance to mass transfer was limiting.

More recently, Peña and Miller⁷¹ investigated solubilization rates of mixtures of *n*-decane and squalane into 2.5 wt% solutions of pure $C_{12}E_8$ at 23°C using the oil drop method described above. They first measured the rate of solubilization of pure decane, confirming that the rate was controlled by interfacial phenomena as in Carroll's work, and demonstrated that pure squalane was not solubilized to any significant extent under these conditions. Next they measured solubilization rates of decane from various mixtures of the two hydrocarbons. Figure 9.7 shows results from one of these experiments together with predictions of a model based on assuming that the rate of decane

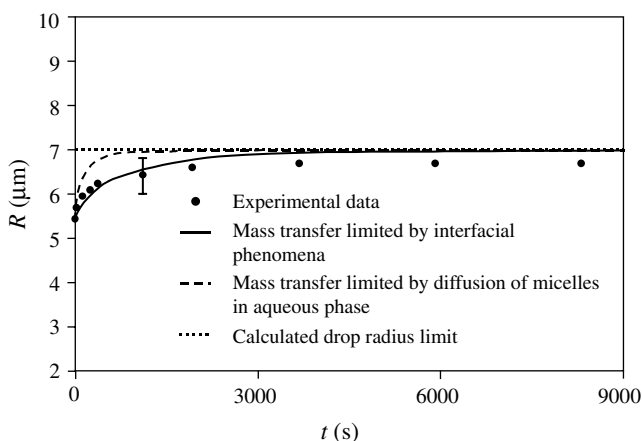


FIGURE 9.8 Variation of radius with time for a drop initially containing 100 mol% squalane following injection into a 2.5 wt% solution of $C_{12}E_8$ at 22°C containing solubilized *n*-decane at half its equilibrium value. Solid and dashed curves have the same meaning as in Figure 9.7. (From Peña, A.A. and Miller, C.A., *J. Colloid Interface Sci.*, 244, 154, 2001. With permission.)

solubilization at any time during the experiment was limited by interfacial phenomena and proportional to its mole fraction in the drop. The limiting value of drop radius in Figure 9.7 agrees with that expected for complete solubilization of the decane; i.e., it is equal to the radius of a drop containing all the squalane present initially.

A key aspect of their model is the following expression for the rate of change in drop volume V with time:

$$\left(\frac{dV}{dt}\right) = 4\pi a^2 k c_s (\theta_B - \theta_I) \quad (9.9)$$

Here a is the drop radius, k a specific solubilization rate determined experimentally, c_s the concentration of surfactant in micelles, and θ_B and θ_I the ratios of concentrations of the soluble species in the bulk and at the interface to the equilibrium solubilization capacity c_∞ at c_s . This equation for interfacially controlled transport is the counterpart to the well-known von Smoluchowski equation for diffusion-controlled transport:

$$\left(\frac{dV}{dt}\right) = 4\pi a D \nu c_\infty (\theta_B - \theta_I) \quad (9.10)$$

where D is the diffusivity and ν the molar volume of the soluble species.

They also performed experiments in which squalane drops were injected into 2.5 wt% solutions of $C_{12}E_8$ partially saturated with decane. Results of an experiment of this type are shown in Figure 9.8 along with predictions of the same model. Good agreement is obtained.

The analysis was extended to predict mean drop size evolution for mixed emulsions consisting initially of some drops of pure decane and some of pure squalane.⁷¹ Its predictions based on interfacially controlled transport were in better agreement with the experimental results of Binks et al.⁷² than were those of the authors' model, which was based on diffusion-controlled transport.

Selective solubilization can also occur in mixtures of polar and nonpolar oils. Using their oil drop method described previously, Chen et al.⁷³ measured solubilization rates of mixtures of triolein and oleic acid in solutions of pure nonionic surfactants. As Figure 9.9 shows for a drop initially containing 85/15 triolein/oleic acid by weight injected into 2 wt% Tergitol 15-S-7 at 35°C, they observed that the solubilization process consisted of two stages. In the first stage, the drop radius

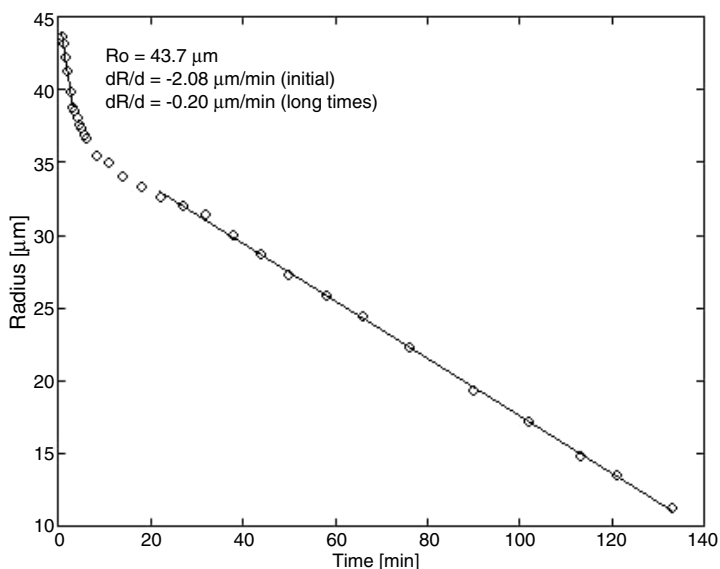


FIGURE 9.9 Variation with time of radius of drop containing 85/15 triolein/oleic acid (by weight) injected into 2 wt% Tergitol 15-S-7 at 35°C.

decreased rapidly accompanied by vigorous spontaneous convection, whereas in the second stage the slope of the plot of radius as a function of time, which is equal to the solubilization rate per unit area, had a constant value an order of magnitude smaller than the initial rate. The final rate was approximately equal to that of pure triolein in the same surfactant solution. They interpreted these results as indicating that virtually all the oleic acid was solubilized along with some triolein during the initial rapid solubilization stage. With this assumption and the measured decrease of 46% in drop volume during the first 5 min, they found that about twice as much triolein as oleic acid (by volume) was solubilized during this stage. The initial solubilization rate and ratio of triolein to oleic acid solubilized during the first stage were about the same for drops containing 80/20 and 75/25 triolein/oleic acid. When even more oleic acid was present initially, the lamellar liquid crystal could be seen forming at the drop surface. The initial solubilization rate was approximately proportional to surfactant concentration for a given drop composition but did not vary significantly with temperature between 29 and 35°C. However, the rate in the second stage was sensitive to temperature as expected from the earlier experiments for pure triolein.⁵⁴

Initial rapid solubilization was also seen for triolein/oleic acid mixtures in 2 wt% solutions of the pure linear alcohol ethoxylate $C_{12}E_6$ at 35°C. Here, too, about twice as much triolein as oleic acid was solubilized during this stage. However, no significant amount of triolein was solubilized thereafter as would be expected from the previous study of pure triolein.⁵⁴ Finally, to confirm that this behavior was not limited to oils containing triolein, Chen et al.⁷³ showed that initial rapid solubilization occurred for a drop containing 88/12 *n*-hexadecane/oleic acid by weight injected into 2 wt% $C_{12}E_8$ at 25°C.

For the system of Figure 9.9 interfacial tension as measured by the spinning drop technique fell during the first few minutes of the experiment to 0.05 mN/m, remained there for about half an hour, then increased over a period of 2 h to 0.2 to 0.3 mN/m, not far below the value of 0.4 mN/m obtained at long times for pure triolein with the same surfactant solution. This behavior indicates that the surfactant film at the interface between the drop and surfactant solution shifted from lipophilic to hydrophilic conditions as oleic acid was solubilized, the minimum in tension occurring at the balanced condition (see Figure 9.3). Support for this interpretation was obtained by repeating

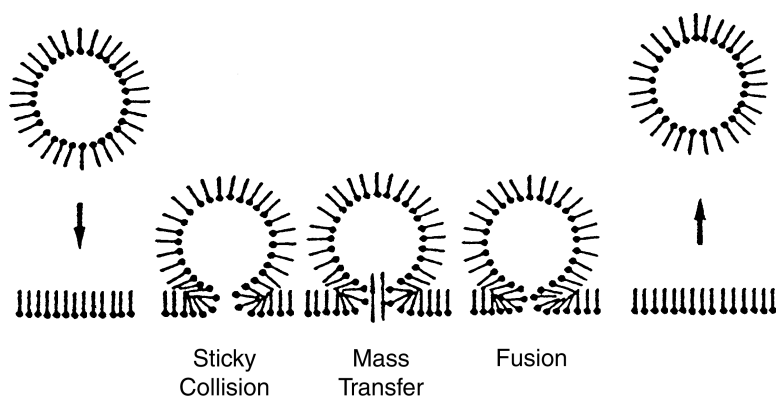


FIGURE 9.10 Schematic diagram illustrating proposed mechanism of solubilization involving temporary fusion of microemulsion drops with interface. (From Plucinski, P. and Nitsch, W., *J. Phys. Chem.*, 97, 8983, 1993. With permission.)

the experiment of Figure 9.9 with the surfactant solution buffered to pH 10. Although Marangoni flow and some spontaneous emulsification were observed, there was no rapid initial solubilization stage because oleic acid at the interface was ionized almost immediately after drop injection, so that the surfactant film at the interface was hydrophilic during the entire experiment. After a very rapid transient, interfacial tension rose to 1 to 2 mN/m and remained there throughout the experiment. The higher tension than at neutral pH is expected when the more hydrophilic soap is present.

9.6.3 SOLUBILIZATION BY MICROEMULSIONS

Tondre and Zana⁷⁴ used the stopped-flow method to study rates of mixing of oil with oil in water microemulsions and of water with water in oil microemulsions in the water/*n*-dodecane/SDS/1-pentanol system. They found that mixing was much slower in the former case, apparently owing to electrostatic repulsion between the microemulsion droplets and drops of *n*-dodecane. Plucinski and co-workers⁷⁵⁻⁷⁷ measured initial mass transfer rates between an aqueous phase and a water in oil microemulsion containing the double-chain anionic surfactant AOT. They used a cell in which both phases were stirred and employed various metal cations and an amino acid as solutes. Since the amino acid was taken into the surfactant film as a cation, electrostatic effects had a major influence on the solubilization process in their experiments including the relative rates of solubilization of different cations present in the aqueous phase. The authors concluded that mass transfer was controlled by an interfacial process that involved adsorption of a microemulsion droplet at the bulk oil–water interface, transport of solute between the droplet and the aqueous solution through the neck where they were joined, and sealing off of the neck and subsequent emission of the droplet into the microemulsion phase (Figure 9.10). Solubilization rates by the microemulsion were found to increase when short-chain alcohols were added as cosurfactants to increase interfacial flexibility and when the initial diameter of the microemulsion droplets was less than the equilibrium value that occurs when an excess water phase is present. In the latter case microemulsion droplets grew due to osmotic effects when they were adsorbed at the interface with the aqueous phase, thereby increasing solubilization of the dissolved solutes.

Wen and Papadopoulos⁷⁸ used videomicroscopy to measure the rate of shrinkage of a single drop of pure water immersed in a surfactant-containing oil phase, which itself was in contact with an aqueous solution of NaCl. They found that the solubilization rate of water was controlled by phenomena at the drop interface, suggesting that transport in multiple emulsions is limited by interfacial effects, not diffusion.

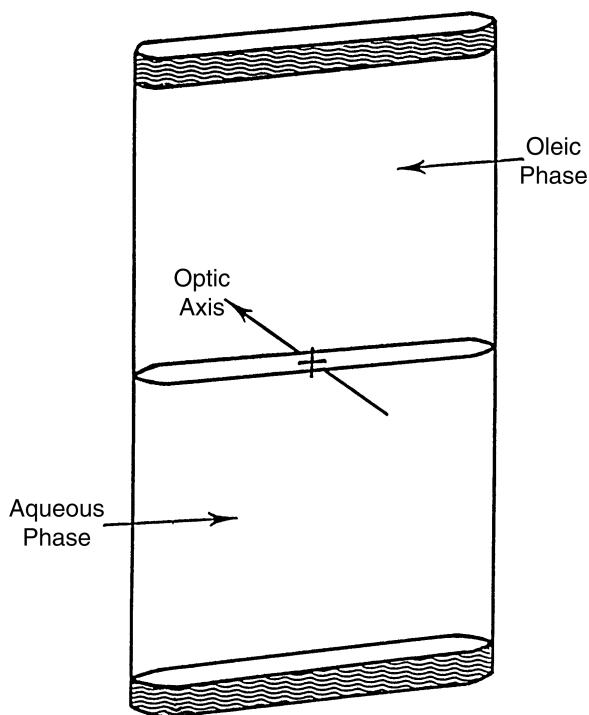


FIGURE 9.11 Rectangular glass capillary cell used in vertical-stage contacting experiments.

9.7 SOLUBILIZATION BY INTERMEDIATE PHASE FORMATION

9.7.1 GENERAL REMARKS AND TECHNIQUES

In the preceding sections solubilization of compounds brought into contact with micellar solutions or microemulsions was considered. However, owing to diffusion and the complex phase behavior of oil–water–surfactant systems, more interesting phenomena sometimes occur. In particular, new phases may develop at the interface upon contact of an oil with a surfactant solution, either initially or at a subsequent time. These intermediate phases, often microemulsions or liquid crystals, may themselves be capable of solubilizing considerable oil, indeed more than the initial surfactant solution. This behavior is significant in some cleaning processes and in other potential applications of surfactants such as their use for recovery of organic liquid contaminants from groundwater aquifers and for enhanced oil recovery.

Videomicroscopy has been the method used to observe intermediate phase formation. Two different techniques have been developed for contacting the oil and surfactant solution. In the vertical cell technique^{79,80} (Figure 9.11) half of a glass cell of rectangular cross section is filled with the aqueous phase using capillary action and that end of the cell is then sealed with a resin cured by ultraviolet light. The cell is subsequently placed in a thermal stage on a microscope, especially built for these experiments, whose stage is vertical. The oil phase is then carefully injected from above using a syringe, with care taken to minimize mixing at the oil–water interface. In recent work cells 400 μm in thickness have been used, which permit insertion of a thin hypodermic needle for the injection step. Intermediate phases that form at the surface of contact are readily observed, and their thicknesses can be measured as a function of time.

Except at long times not of interest here, this configuration is basically that of two semi-infinite phases brought into contact. Accordingly, provided that convection is absent, diffusion coefficients

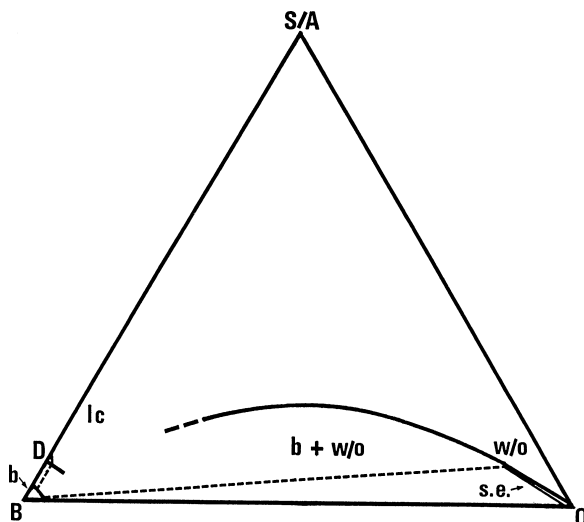


FIGURE 9.12 High-salinity diffusion path for contact of composition D with oil (O) indicating an intermediate brine phase (b) and spontaneous emulsification in the oil phase (s.e.). lc and w/o denote the lamellar liquid crystalline phase and a water in oil microemulsion, respectively. S/A denotes the surfactant/alcohol mixture in this pseudoternary diagram. (From Raney, K.H. and Miller, C.A., *AIChE J.*, 33, 1791, 1987. With permission.)

are constant, and local equilibrium prevails at all interfaces, the behavior can be analyzed using a similarity transform to solve the diffusion equations (see Reference 81). Because the local composition as given by this solution depends on the variable $(x/t^{1/2})$, where x is the distance from the initial surface of contact and t is the time, and because this variable always ranges between very large negative and very large positive values and is constant at all interfaces, the set of compositions in the system is the same at all times and can be plotted on the phase diagram. Such a plot is known as a “diffusion path” and is especially useful for ternary systems. It reveals not only which intermediate phases form, if any, but also whether spontaneous emulsification can be expected. Emulsification results when some of the predicted compositions within a phase are supersaturated, i.e., lie inside a two-phase region, as was initially shown by Ruschak and Miller,⁸¹ who were able to explain quantitatively the conditions for spontaneous emulsification in several oil–water–alcohol systems.

Complete information on phase behavior including tie-lines and on diffusion coefficients is rarely available for oil–water–surfactant systems. Nevertheless, Raney and Miller⁸² used plausible phase diagrams for an anionic surfactant–NaCl brine–hydrocarbon system as a function of salinity to calculate diffusion paths that exhibited intermediate phase formation and spontaneous emulsification in agreement with experimental observations made using the vertical cell technique. For example, Figure 9.12 shows a diffusion path for a surfactant–alcohol–brine mixture of composition D in contact with oil for a case when initial salinity is high. An intermediate brine phase is predicted as well as spontaneous emulsification in the oil phase, both of which were, in fact, observed.

A qualitative picture of the diffusion path sufficient to indicate the number and types of intermediate phases that form can frequently be inferred from knowledge of the location of various single-phase and multiphase regions on the equilibrium phase diagram without having detailed information on tie-line compositions and without actually solving the governing equations. This procedure was used in interpreting the experiments in water–hydrocarbon–nonionic surfactant systems discussed below.

In the second technique a syringe is used to inject individual drops of oil into a similar glass cell that has been filled with the surfactant solution and placed in a thermal stage resting on a

conventional (horizontal) microscope stage⁸³ (see Figure 9.6). The advantage of this procedure is that the oil volume is small in comparison with that of the surfactant solution as occurs in many applications, with the result that composition of the oil phase varies with time. Thus, while the vertical cell technique is most useful for situations when intermediate phase formation begins immediately upon contact, the oil drop technique is best suited for situations where oil composition must change before the intermediate phase can develop. Changes in the diameter of the drop can be monitored over time, and the time of initial formation and the manner and rate of growth of intermediate phases can be observed.

In the absence of convection the behavior can often be analyzed using a quasi-steady-state solution to the diffusion equations because the time required for diffusion to produce equilibration in the drop, which is of order a^2/D with a the drop radius (typically 25 to 50 μm) and D the diffusivity, is normally much less than the time of the experiment (several minutes). This quasi-steady-state approach predicts that drop composition is uniform but varies with time and that the time required for intermediate phase formation to begin for given drop and solution compositions is proportional to the square of the initial drop radius.^{83,84} Results obtained using the oil drop technique that are consistent with these predictions are discussed below.

9.7.2 RESULTS

Mixtures containing 1 wt% of the pure nonionic surfactant C_{12}E_5 in water were contacted with pure *n*-hexadecane and *n*-tetradecane at various temperatures between 25 and 60°C using the vertical cell technique.⁷⁹ Similar experiments were performed with C_{12}E_4 and *n*-hexadecane between about 15 and 40°C.⁸⁵ In both cases the temperature ranged from well below to well above the phase inversion temperature (PIT) of the system, i.e., the temperature where hydrophilic and lipophilic properties of the surfactant are balanced and a middle phase microemulsion forms (analogous to the optimal salinity for ionic surfactants mentioned above). The different intermediate phases that were seen at different temperatures and the occurrence of spontaneous emulsification in some but not all of the experiments could be understood in terms of known aspects of the phase behavior, e.g., published phase diagrams for the C_{12}E_5 –water–*n*-tetradecane system,⁸⁶ and diffusion path theory. That is, plausible diffusion paths could be found that showed the observed intermediate phases and/or spontaneous emulsification for each temperature.

Of particular interest is that the contacting experiments showed formation of an intermediate microemulsion phase from temperatures near the surfactant cloud point to those just above the PIT (Figure 9.13). Near the PIT, the lamellar liquid crystal appeared as a second intermediate phase for situations where it was not already present in the initial surfactant–water mixture. It is well known, as discussed above, that the capability of microemulsions to solubilize oil increases with increasing temperature for nonionic surfactants in the temperature range of interest here. Because the location of the microemulsion–oil interface could be determined as a function of time from videotapes of the experiments, it was possible to calculate the rates of solubilization of hydrocarbon by the surfactant-rich L_1 phase above the cloud point. As shown in Figure 9.11, the rates increased rapidly with temperature.⁸⁷ Below the surfactant cloud point where no intermediate phase formed, solubilization rates were much lower and not accurately measurable using this technique. Presumably, they were of the same order of magnitude as those found in similar systems by Carroll using the drop-on-fiber technique discussed above.

This behavior involving solubilization by an intermediate microemulsion phase could also be related to detergency. Separate experiments with the same pure surfactants and radioactively tagged hydrocarbons demonstrated that hydrocarbon removal from polyester/cotton fabric was maximized near the PIT.^{85,87} Under these conditions the soil is apparently solubilized rapidly into the intermediate microemulsion phase, which then is readily dispersed into the washing bath by agitation owing to its ultralow interfacial tension with the aqueous phase. Below the PIT, less oil can be solubilized by a given amount of surfactant and, as shown in Figure 9.14, the rate of solubilization



FIGURE 9.13 Video frame showing intermediate phases 4 min after contact in $C_{12}E_5$ -water-*n*-tetradecane water system at 45°C near the PIT. (From Benton, W.J. et al., *J. Colloid Interface Sci.*, 110, 363, 1986. With permission.)

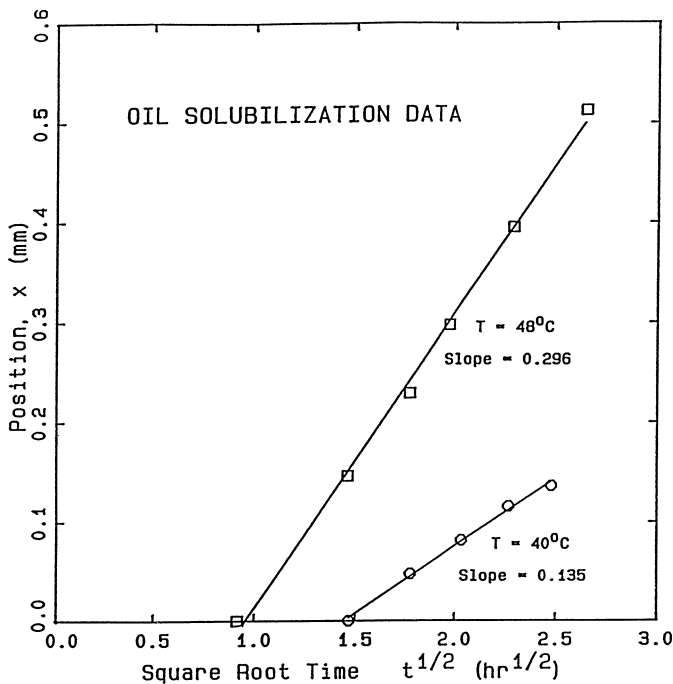


FIGURE 9.14 Time variation at two temperatures of position of oil interface following contact of the L_1 phase with oil for the $C_{12}E_5$ -water-*n*-tetradecane system. (From Miller, C.A. and Raney, K.H., *Colloids Surf. A*, 74, 169, 1993. With permission.)

is slower. Above the PIT the surfactant partitions preferentially into the oil, causing the oil phase to take up water and actually increase in volume. Vigorous spontaneous emulsification of water in the oil phase is also observed.^{79,85} It is worth emphasizing that the PIT depends on both the surfactant

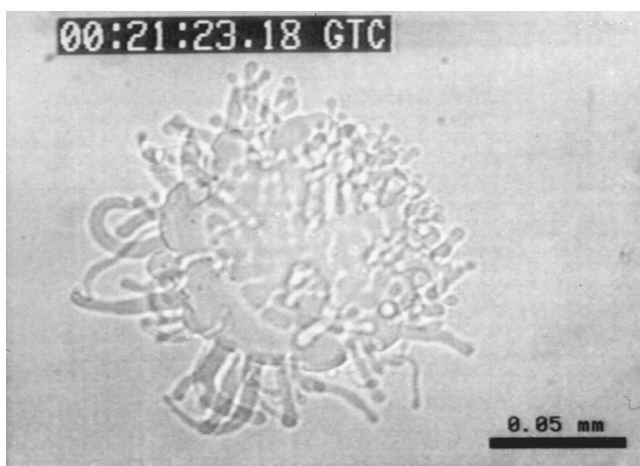


FIGURE 9.15 Video frame showing intermediate lamellar phase forming as myelinic figures about 21 min after injection of a drop containing 85/15 *n*-hexadecane/oleyl alcohol into a solution containing 0.05 wt% $C_{12}E_8$ at 50°C. (From Lim, J.C. and Miller, C.A., *Langmuir*, 7, 2021, 1991. With permission.)

and oil compositions. For *n*-hexadecane, which is frequently used as a model soil to represent mineral oils, the surfactant–water mixture in the washing bath near the PIT is a dispersion of the lamellar liquid crystalline phase in water for these surfactants.

As indicated previously, the oil drop technique is most useful when an intermediate phase forms only after drop composition has changed during the course of the experiment owing to diffusion of surfactant and water into the drop and/or to diffusion of the initial components of the drop into the surfactant solution at different rates. One interesting set of experiments involved solutions of pure nonionic surfactants below their cloud points and drops that were mixtures of *n*-decane and oleyl alcohol.⁸³ Addition of this rather lipophilic alcohol produces a significant reduction in the PIT. Figure 9.15 is a video frame showing formation of an intermediate lamellar liquid crystalline phase as “myelinic figures,” i.e., filaments with concentric bilayers, some 20 min after a drop containing 85% *n*-hexadecane and 15% oleyl alcohol was injected into a solution containing 0.05 wt% $C_{12}E_8$ at 50°C. Under these conditions the initial drop composition corresponds to a situation slightly above the PIT. However, as surfactant diffuses in, the drop becomes more hydrophilic, solubilizes more water, and increases in volume. According to the quasi-steady-state approximation, drop composition moves along the coexistence curve as indicated by the arrows in the schematic phase diagram of Figure 9.16 until it reaches point *F*. Because *EF* is the limiting tie-line of the L_1 – L_2 region, another phase must form as more surfactant enters the drop having composition *F*. For these systems this additional phase is the lamellar liquid crystal, as shown in Figure 9.16. Because its microstructure is anisotropic, it grows in the form of the myelinic figures seen in Figure 9.15.

The quasi-steady-state analysis⁸³ predicts that the time t_1 from the start of the experiment until the lamellar phase starts to develop is given by

$$t_1 = ka_o^2/Dw_s \quad (9.11)$$

where *K* is a parameter depending only on the shape of the coexistence curve and the position of point *F*, a_o is the initial drop radius, *D* the diffusivity of the surfactant in the aqueous solution, and w_s the surfactant concentration in the bulk aqueous phase. Experiments confirmed the predicted dependence on a_o and w_s and yielded a reasonable value for *D* when *K* was evaluated from experimental information on phase behavior.⁸³

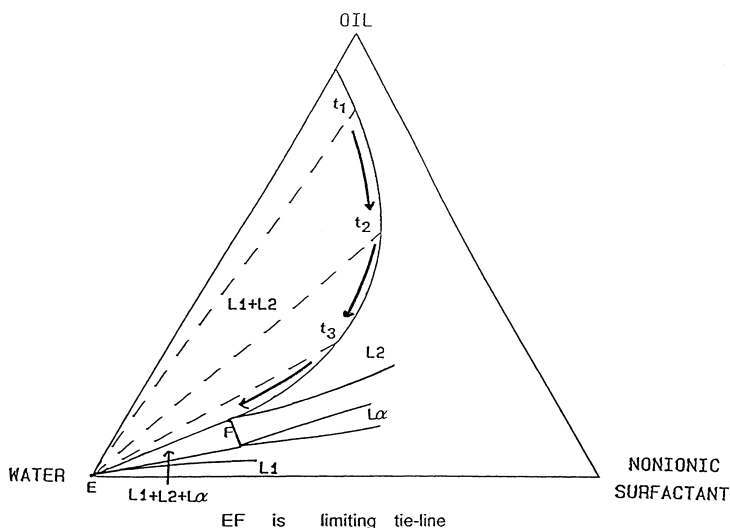


FIGURE 9.16 Schematic phase diagram illustrating variation in drop composition with time during contacting experiment.

For the various pure nonionic surfactants studied, it was found that whenever swelling and development of an intermediate lamellar phase were seen as in Figure 9.15, i.e., whenever the system was initially above the PIT, the quasi-steady-state model based on diffusion control was applicable. Moreover, washing experiments for the same conditions showed good removal of the soil from polyester/cotton fabric.⁸⁸ However, when the system was initially below the PIT, no intermediate phase was seen, and the drop was very slowly solubilized into the surfactant solution, presumably at a rate governed by interfacial phenomena as in the solubilization experiments described previously. It is likely that myelinic figures containing substantial amounts of hydrocarbon such as those shown in Figure 9.15 are rather fluid and are readily broken off and dispersed into the washing bath by the agitation that occurs during a washing process.

Similar experiments were carried out in which drops that were mixtures of *n*-decane and various alcohols were injected into dilute solutions of a zwitterionic (amine oxide) surfactant. Here, too, the lamellar phase was the first intermediate phase observed when the system was initially above the PIT. However, with alcohols of intermediate chain length such as *n*-heptanol, it formed more rapidly than with oleyl alcohol, and the many, small myelinic figures that developed broke up quickly into tiny droplets in a process resembling an explosion.^{89,90} The high speed of the inversion to hydrophilic conditions was caused by diffusion of *n*-heptanol into the aqueous phase, which is faster than diffusion of surfactant into the drop. The alcohol also made the lamellar phase more fluid and thereby promoted the rapid breakup of myelinic figures into droplets. Further loss of alcohol caused both the lamellar phase and the remaining microemulsion to become supersaturated in oil, which produced spontaneous emulsification of oil.

ACKNOWLEDGMENT

A. A. Peña read the entire manuscript and made useful suggestions, especially in the section dealing with solubilization rates.

REFERENCES

1. Christian, S.D. and Scamehorn, J.F., Eds., *Solubilization in Surfactant Aggregates*, Marcel Dekker, New York, 1995.
2. McBain, M.E.L. and Hutchinson, E., *Solubilization and Related Phenomena*, Academic Press, New York, 1955.
3. Elworthy, P.H., Florence, A.T., and Macfarlane, C.B., *Solubilization by Surface-Active Agents*, Chapman & Hall, London, 1968.
4. Mackay, R.A., Solubilization, in *Nonionic Surfactants*, Schick, M.J., Ed., Marcel Dekker, New York, 1987, chap. 6.
5. Mukerjee, P., Odd-even alternation in chain length variation of micellar properties — evidence of some solid-like character of micellar core, *Kolloid Z. Z. Polym.*, 236, 76, 1970.
6. King, A.D., Solubilization of gases, in *Solubilization in Surfactant Aggregates*, Christian, S.D. and Scamehorn, J.F., Eds., Marcel Dekker, New York, 1995, chap. 2.
7. Tucker, E.E., Vapor pressure studies of solubilization, in *Solubilization in Surfactant Aggregates*, Christian, S.D. and Scamehorn, J.F., Eds., Marcel Dekker, New York, 1995, chap. 13.
8. McBain, J.W. and Richards, P.H., Solubilization of inorganic liquids by detergents, *Ind. Eng. Chem.*, 38, 642, 1946.
9. Zourab, S.M. and Miller, C.A., Equilibrium and dynamic behavior for systems containing nonionic surfactants, *n*-hexadecane, triolein, and oleyl alcohol, *Colloids Surf. A*, 95, 173, 1995.
10. Holland, P., Nonideal mixed monolayer model, in *Phenomena in Mixed Surfactant Systems*, Scamehorn, J.F., Ed., ACS Symposium Series #311, American Chemical Society, Washington, D.C., 1986, chap. 8.
11. Moroi, Y. et al., Solubilization of benzene, naphthalene, anthracene, and pyrene in 1-dodecanesulfonic acid micelles, *J. Phys. Chem.*, 99, 2372, 1995.
12. Stilbs, P., Solubilization, as studied by nuclear spin relaxation and NMR-based self-diffusion techniques, in *Solubilization in Surfactant Aggregates*, Christian, S.D. and Scamehorn, J.F., Eds., Marcel Dekker, New York, 1995, chap. 11.
13. Gao, Z., Wasylishen, R.E., and Kwak, J.C.T., An NMR paramagnetic relaxation method to determine distribution coefficients of solubilization in micellar systems, *J. Phys. Chem.*, 93, 2190, 1989.
14. Treiner, C., The partitioning of neutral solutes between micelles and water as deduced from critical micelle concentration determinations, in *Solubilization in Surfactant Aggregates*, Christian, S.D. and Scamehorn, J.F., Eds., Marcel Dekker, New York, 1995, chap. 12.
15. Hoar, T.P. and Schulman, J.H., Transparent water in oil dispersions — the oleopathic hydromicelle, *Nature (London)*, 152, 102, 1943.
16. Huh, C., Interfacial tensions and solubilizing ability of a microemulsion phase that coexists with oil and brine, *J. Colloid Interface Sci.*, 71, 408, 1979.
17. Reed, R.L. and Healy, R.N., Some physicochemical aspects of microemulsion flooding: a review, in *Improved Oil Recovery by Surfactant and Polymer Flooding*, Shah, D.O. and Schechter, R.S., Eds., Academic Press, New York, 1977, 383.
18. Winsor, P.A., *Solvent Properties of Amphiphilic Compounds*, Butterworth, London, 1954.
19. Shinoda, K. and Friberg, S., *Emulsions and Solubilization*, John Wiley & Sons, New York, 1986.
20. Bourrel, M. and Schechter, R.S., *Microemulsions and Related Systems*, Marcel Dekker, New York, 1988.
21. Miller, C.A. and Qutubuddin, S., Enhanced oil recovery with microemulsions, in *Interfacial Phenomena in Apolar Media*, Eicke, H.-F. and Parfitt, G.D., Eds., Marcel Dekker, New York, 1987, chap. 4.
22. Anton, R.E., Garces, N., and Yajure, A., A correlation for three-phase behavior of cationic surfactant-oil-water systems, *J. Dispersion Sci. Technol.*, 18, 539, 1997.
23. Anton, R.E. et al., Surfactant-oil-water systems near the affinity inversion. IX: Optimum formulation and phase behavior of mixed anionic-cationic systems, *J. Dispersion Sci. Technol.*, 14, 401, 1993.
24. Kahlweit, M. et al., General patterns of phase behavior of mixtures of water, nonpolar solvent, amphiphiles, and electrolytes, 1,2, *Langmuir*, 4, 499, 1988; 5, 305, 1989.
25. Hackett, J.L. and Miller, C.A., Microemulsion to liquid crystal transition in two anionic surfactant systems, *SPE Res. Eng.*, 3, 791, 1988.

26. Miller, C.A., Ghosh, O., and Benton, W.J., Behavior of dilute lamellar liquid-crystalline phases, *Colloids Surf.*, 19, 197, 1986.
27. Ruckenstein, E. and Chi, J.C., Stability of microemulsions, *J. Chem. Soc. Faraday Trans. II*, 71, 1690, 1975.
28. Miller, C.A. and Neogi, P., Thermodynamics of microemulsions: combined effects of dispersion entropy of drops and bending energy of surfactant films, *AIChE J.*, 26, 212, 1980.
29. Mukherjee, S., Miller, C.A., and Fort, T., Jr., Theory of drop size and phase continuity in microemulsions. I. Bending effects with uncharged surfactants, *J. Colloid Interface Sci.*, 91, 223, 1983.
30. Hill, T.L., *Thermodynamics of Small Systems*, Vol. 1, W.A. Benjamin, New York, 1964.
31. Carnahan, N.F. and Starling, K.E., Equation of state for nonattracting rigid spheres, *J. Chem. Phys.*, 51, 635, 1969.
32. Miller, C.A. et al., Ultralow interfacial tensions and their relation to phase separation in micellar solutions, *J. Colloid Interface Sci.*, 68, 221, 1977.
33. Huh, C., Equilibrium of a microemulsion that coexists with oil or brine, *Soc. Petrol. Eng. J.*, 23, 829, 1982.
34. Mitchell, D.J. and Ninham, B.W., Micelles, vesicles, and microemulsions, *J. Chem. Soc. Faraday Trans. II*, 77, 601, 1981.
35. Ruckenstein, E., An explanation for the unusual phase behavior of microemulsions, *Chem. Phys. Lett.*, 98, 573, 1983.
36. Safran, S.A. and Turkevich, L.A., Phase diagrams for microemulsions, *Phys. Rev. Lett.*, 50, 1930, 1983.
37. Overbeek, J.T.G., Theoretical estimates of droplet sizes and size distributions in microemulsions, *Prog. Colloid Polym. Sci.*, 83, 1, 1990.
38. Jeng, J.-F. and Miller, C.A., Theory of microemulsions with spherical drops. I. Phase diagrams and interfacial tensions in gravity-free systems, *Colloids Surf.*, 28, 247, 1987.
39. Scriven, L.E., Equilibrium bicontinuous structures, in *Micelles, Solubilization, and Microemulsions*, Vol. 2, Mittal, K.L., Ed., Plenum Press, New York, 1977, 877.
40. Jahn, W. and Strey, R., Microstructure of microemulsions by freeze fracture electron microscopy, *J. Phys. Chem.*, 92, 2294, 1988.
41. Talmon, Y. and Prager, S., Statistical thermodynamics of phase equilibria in microemulsions, *J. Chem. Phys.*, 69, 2984, 1978.
42. Jouffroy, J., Levinson, P., and de Gennes, P., Phase equilibria involving microemulsions, *J. Phys.*, 43, 1241, 1982.
43. Widom, B., A model microemulsion, *J. Chem. Phys.*, 81, 1030, 1984.
44. Andelman, D. et al., Structure and phase equilibria of microemulsions, *J. Chem. Phys.*, 87, 7229, 1987.
45. Bernheim-Grosswasser, A. et al., Direct observation of phase separation in microemulsion networks, *Langmuir*, 15, 5448, 1999.
46. Tlustý, T. and Safran, S.A., Microemulsion networks: the onset of bicontinuity, *J. Phys. Condens. Matter*, 12, A253, 2000.
47. Nagarajan, R. and Ruckenstein, E., Theory of surfactant self-assembly: a predictive molecular thermodynamic approach, *Langmuir*, 7, 2934, 1991.
48. Hoffmann, H.H. and Ulbricht, W., Transition of rodlike to globular micelles by the solubilization of additives, *J. Colloid Interface Sci.*, 129, 388, 1989.
49. Jönsson, B., Landgren, M., and Olofsson, G., Solubilization of uncharged molecules in ionic micellar solutions: toward an understanding at the molecular level, in *Solubilization in Surfactant Aggregates*, Christian, S.D. and Scamehorn, J.F., Eds., Marcel Dekker, New York, 1995, chap. 4.
50. Karaborni, S., van Os, N.M., Esselink, K., and Hilbers, P.A.J., Molecular dynamics simulations of oil solubilization in surfactant solutions, *Langmuir*, 9, 1175, 1993.
51. Nelson, P.H., Hatton, T.A., and Rutledge, G., Asymmetric growth in molecules containing oil, *J. Chem. Phys.*, 110, 9673, 1999.
52. Carroll, B.J., The accurate measurement of contact angle, phase contact areas, drop volume, and Laplace excess pressure in drop-on-fiber systems, *J. Colloid Interface Sci.*, 57, 488, 1976.
53. Ward, A.J.I., Kinetics of solubilization in surfactant-based systems, in *Solubilization in Surfactant Aggregates*, Christian, S.D. and Scamehorn, J.F., Eds., Marcel Dekker, New York, 1995, chap. 7.
54. Chen, B.H., Miller, C.A., and Garrett, P.R., Rates of solubilization into nonionic surfactant solutions, *Colloids Surf. A*, 128, 129, 1997.

55. Bolsman, T.A.B.M., Veltmatt, F.T.G., and van Os, N.M., The effect of surfactant structure on the rate of oil solubilization into aqueous surfactant solutions, *J. Am. Oil Chem. Soc.*, 65, 280, 1988.
56. Kabalnov, A.S., Can micelles mediate mass transfer between oil droplets? *Langmuir*, 10, 680, 1994.
57. Taylor, P., Ostwald ripening in emulsions, *Colloids Surf. A*, 99, 175, 1995.
58. Soma, J. and Papadopoulos, K.D., Ostwald ripening in sodium dodecyl sulfate-stabilized decane-in-water emulsions, *J. Colloid Interface Sci.*, 181, 225, 1996.
59. De Smet, Y., Deriemaeker, L., and Finsy, R., Ostwald ripening of alkane emulsions in the presence of surfactant micelles, *Langmuir*, 15, 6745, 1999.
60. Chan, A., Evans, D.F., and Cussler, E.L., Explaining solubilization kinetics, *AICHE J.*, 22, 1006, 1976.
61. Shaeiwitz, J.A. et al., The mechanism of solubilization in detergent solutions, *J. Colloid Interface Sci.*, 84, 47, 1981.
62. Kabin, J.A. et al., Removal of organic films from rotating disks using aqueous solutions of nonionic surfactants: effect of surfactant molecular structure, *J. Colloid Interface Sci.*, 206, 102, 1998.
63. Huang, C., Evans, D.F., and Cussler, E.L., Linoleic acid solubilization with a spinning liquid disk, *J. Colloid Interface Sci.*, 82, 499, 1981.
64. Danov, K.D., Adsorption from micellar surfactant solutions: nonlinear theory and experiment, *J. Colloid Interface Sci.*, 183, 223, 1996.
65. McClements, D.J. and Dungan, S.R., Light scattering study of solubilization of emulsion droplets by nonionic surfactant solutions, *Colloids Surf. A*, 104, 127, 1995.
66. Weiss, J. et al., Influence of molecular structure of hydrocarbon emulsion droplets on their solubilization in nonionic surfactant micelles, *Colloids Surf. A*, 121, 53, 1997.
67. Peña, A.A. and Miller, C.A., *Ind. Eng. Chem. Res.*, in press.
68. Higuchi, W.I. and Misra, J., Physical degradation of emulsions via the molecular diffusion route and the possible prevention thereof, *J. Pharm. Sci.*, 51, 459, 1962.
69. Goldberg, A.H. et al., Mechanisms of interphase transport. I. Theoretical considerations of diffusion and interfacial barriers in transport of solubilized systems, *J. Pharm. Sci.*, 56, 1432, 1967.
70. Goldberg, A.H. et al., Mechanisms of interphase transport. II. Theoretical considerations and experimental evaluation of interfacially controlled transport in solubilized systems, *J. Pharm. Sci.*, 58, 1341, 1969.
71. Peña, A.A. and Miller, C.A., Kinetics of compositional ripening in emulsions stabilized by nonionic surfactants, *J. Colloid Interface Sci.*, 244, 154, 2001.
72. Binks, B.P. et al., Kinetics of swelling of oil in water emulsions, *Langmuir*, 14, 5402, 1998.
73. Chen, B.H., Miller, C.A., and Garrett, P.R., Rates of solubilization of triolein/fatty acid mixtures by nonionic surfactant solutions, *Langmuir*, 14, 31, 1998.
74. Tondre, C. and Zana, R., Rate of dissolution of *n*-alkanes and water in microemulsions of water/sodium dodecyl sulfate(1/3) + 1-pentanol(2/3)/*n*-dodecane in rapid mixing experiments, *J. Dispersion Sci. Technol.*, 1, 179, 1980.
75. Plucinski, P. and Nitsch, W., Kinetics of interfacial phenylalanine solubilization in a liquid/liquid microemulsion system, *J. Phys. Chem.*, 97, 8983, 1993.
76. Plucinski, P. and Nitsch, W., Mechanism of mass transfer between aqueous phase and water in oil microemulsion, *Langmuir*, 10, 371, 1994.
77. Plucinski, P. and Reitmeir, J., The influence of cosurfactants on the solubilization of phenylalanine in water in oil microemulsion, *Colloids Surf. A*, 97, 157, 1995.
78. Wen, L. and Papadopoulos, K.D., Effects of surfactants on water transport in $W_1/O/W_2$ emulsions, *Langmuir*, 16, 7612, 2000.
79. Benton, W.J., Raney, K.H., and Miller, C.A., Enhanced videomicroscopy of phase transitions and diffusional phenomena in oil-water-nonionic surfactant systems, *J. Colloid Interface Sci.*, 110, 363, 1986.
80. Mori, F. et al., Phase behavior, dynamic contacting, and detergency in systems containing triolein and nonionic surfactants, *Colloids Surf.*, 40, 323, 1989.
81. Ruschak, K.J. and Miller, C.A., Spontaneous emulsification in ternary systems with mass transfer, *Ind. Eng. Chem. Fundam.*, 11, 534, 1972.
82. Raney, K.H. and Miller, C.A., Diffusion path analysis of dynamic behavior of oil-water-surfactant systems, *AICHE J.*, 33, 1791, 1987.

10 Cohesion Energy Parameters Applied to Surface Phenomena

Charles M. Hansen

CONTENTS

- 10.1 [Introduction](#)
 - 10.2 [Theory](#)
 - 10.3 [Solubility Parameter Calculations](#)
 - 10.4 [Computer Techniques](#)
 - 10.5 [Water](#)
 - 10.6 [Entropy Considerations](#)
 - 10.7 [Applications of Cohesion Parameters to Surface Phenomena](#)
 - 10.8 [Controlled Adsorption \(Self-Assembly\)](#)
 - 10.9 [Conclusion](#)
- [References](#)

10.1 INTRODUCTION

Cohesion energy parameters have been used for many purposes since Hildebrand and Scott wrote their pioneering books.^{1,2} Cohesion energy parameters, initially called solubility parameters, have been successfully used in the coatings industry to predict solubility for over 30 years. The pioneering work of Hildebrand and Scott in the 1950s^{1,2} was quickly taken up by Burrell³ with considerable success. Some problems still remained. Many of these, including simultaneously accounting for both permanent dipole interactions and hydrogen bonding, were overcome by the division of the Hildebrand solubility parameter itself into three parts by Hansen.⁴⁻⁷ This division is theoretically justified and its necessity has been verified in practice in thousands of situations. These deal primarily, but not exclusively, with predicting solubility, i.e., affinities between solvents and a polymer or binder.

The ability to find hundreds (or thousands) of mixtures of nonsolvents that will predictably dissolve materials in question is particularly convincing of the need for the division of cohesion energy parameters into at least three parts. Such mixtures of nonsolvents have been systematically found for such varied materials as cholesterol, cellulose nitrate, polystyrene, epoxies, etc.

With this predictive capability, it is not surprising that cohesion energy parameters have also been used to interpret surface phenomena. Examples are included below.

10.2 THEORY

The total cohesion energy itself, E , can be divided into parts. The three parts used by Hansen are those attributable to nonpolar interactions, E_D , permanent dipole–permanent dipole interactions, E_p ,

and hydrogen bonding (electron interchange) interactions, E_H . The nonpolar interactions are common to all atoms, while the polar and hydrogen bonding interactions involve molecules that orient with respect to each other.

$$E = E_D + E_p + E_H \quad (10.1)$$

It has been possible to divide the total cohesion energy in this manner for a large number of materials including gases, solvents, polymers, pigments, surfaces, biological materials, etc.⁸⁻¹¹ The term cohesion energy parameters is now used interchangeably with solubility parameters because these parameters reflect energy relations and affinities in general.

Application of cohesion energy parameters to interpreting surface phenomena requires additional caution. Steric hindrance and molecular orientation effects become very significant. The difference between the local cohesion energy parameter for one end of a molecule compared with the local cohesion parameter at the other end is often very large. For surface active agents it is customary to say that the one end is hydrophilic and the other end is very hydrophobic. For smaller molecules this difference from one end of the molecule to the other end may not affect interpretation of solubility phenomena, but can affect surface phenomena, for example.

Dividing Equation 10.1 by the molar volume, V , gives

$$E/V = E_D/V + E_p/V + E_H/V \quad (10.2)$$

and

$$\delta^2 = \delta_D^2 + \delta_p^2 + \delta_H^2 \quad (10.3)$$

δ is the Hildebrand solubility parameter^{1,2} and δ_D , δ_p , and δ_H are called Hansen parameters. These are the square roots of the cohesion energy densities for the respective energy types. The units are $\text{MPa}^{1/2}$. The values in these units are numerically 2.046 times larger than those in $(\text{cal}/\text{cm}^3)^{1/2}$.

10.3 SOLUBILITY PARAMETER CALCULATIONS

The latent heat of vaporization of common liquids can usually be found in handbooks at the normal boiling point. Their total cohesion energy (energy of vaporization) is then found by subtracting RT from this. R is the universal gas constant and T is the absolute temperature. This cohesive energy quantitatively accounts for the breakage of all the bonds that make a liquid a liquid. The cohesion energy must be found or estimated at 25°C to calculate the cohesive energy density parameters at this reference temperature. The molar volume of the solvent is also required. The nonpolar cohesion energy can usually be calculated by methods described in the literature.^{8,11-14} This involves determining the cohesion energy for look-alike hydrocarbon counterparts called homomorphs and/or generalized correlations based on the critical temperature and molecular volume. The polar parameter can be found with the help of the dipole moment when this is available. When it is not, group contributions are usually used. The hydrogen bonding parameter has been found as the remaining energy after the others were determined wherever possible according to Equation 10.1. Group contributions are frequently more reliable than this procedure, which involves subtracting large numbers from each other. These procedures are described in more detail elsewhere.^{8,11-14}

The Hansen characterization is usually considered a sphere. The cohesion energy parameters of those liquids where affinities are highest are located within the sphere. The center of the sphere has the values of the δ_{DP} , δ_{PP} , and δ_{HP} parameters, taken as characteristic for the solute. The magnitude of the radius of the sphere, R , is determined by the type of interaction being correlated.

This will be smallest for true solubility, larger for swelling to, say, 25%, and still larger for swelling to, say, 3%.

The boundary of the spherical characterization is based on the requirement that the “good” solvents have a distance from the center of the sphere, RA , less than R . RA is given by the relation:

$$(RA)^2 = 4(\delta_{DP} - \delta_{DS})^2 + (\delta_{PP} - \delta_{PS})^2 + (\delta_{HP} - \delta_{HS})^2 \quad (10.4)$$

The subscripts P and S are used with these parameters to indicate solute and solvent, respectively.

A convenient single parameter to describe solvent quality is the RED number. This is defined as the distance RA divided by the radius of the sphere, R .

$$RED = RA/R \quad (10.5)$$

When the RED number is less than 1.0, high affinity is predicted. Progressively higher RED numbers indicate increasingly lower affinities. Computer printouts can be easily scanned for numbers greater than or less than 1.0 or organized in increasing RED number. This facilitates substitution of a solvent whose parameters are entered as the center of a fictitious sphere with radius 1.0. The most likely candidates as substitutes will be at the top of the list.

It has been shown in chapter 2 of Reference 11 that the RED number relates to the Flory interaction parameter χ_{12} .¹⁵ There is a major difference in that χ_{12} does not account for hydrogen bonding, and must therefore be considered lacking in this respect. For strictly nonpolar systems:

$$\chi_{12}/\chi_c = (RA/R)^2 = (RED)^2 \quad (10.6)$$

χ_c is the so-called critical value, which becomes 0.5 for a polymer of infinite molecular weight. This equation cannot be used for polar or hydrogen-bonded systems, it is only given to show how the two approaches would otherwise relate to each other.

It has been shown in chapter 2 of Reference 11 that the δ_D , δ_P and δ_H parameters, which are frequently called Hansen solubility parameters (HSP) relate to the corresponding states theory of polymer solutions developed by Prigogine and co-workers¹⁶ and extended by Patterson.¹⁷ The constant, 4, in Equation 10.5 is also found in the leading term of the Prigogine approach for the same purpose; it differentiates molecular interactions from atomic interactions. More detail is given in chapter 2 of Reference 11. It might be noted, however, that the HSP approach is also based on a corresponding states calculation of the δ_D parameter with 25°C as a reference temperature. The correspondence between HSP and the Prigogine–Patterson approach is most clearly seen by dividing Equation 10.4 by the quantity 4. This should also be done when trying to relate the HSP approach to any of the other previous theories of polymer solution thermodynamics.

Hildebrand and Scott^{1,2} used the geometric mean rule to describe the interaction between molecules of two unlike species to arrive at the total solubility parameter. Strictly speaking, this was valid for nonpolar type molecules only. The fact that Equation 10.4 has produced hundreds of satisfactory correlations of solubility, swelling, permeation, surface phenomena, etc., confirms that the geometric mean rule is likewise applicable to molecules engaging in permanent dipole–permanent dipole and hydrogen bonding interactions as well.

The cohesion energy parameters for mixtures are usually averaged using the volume fraction times the cohesion energy parameters for the respective solvents present. This approach must be used with caution for surface applications.

Experience has shown that the RED number combined with a solvent molecular size parameter, such as the molar volume, frequently provides all the technical information required to evaluate solvent quality. The original Hildebrand theory predicted that larger solvent molecules are inherently poorer solvents than smaller counterparts with the same cohesion energy parameter. Molecular size

is of major significance for dissolving polymers with very high molecular weights and crystalline materials, and in determining the rate of permeation, such as for protective clothing^{18,19} and viable human skin.²⁰ Smaller molecular species with very close matches in cohesion energy parameters with the materials in question are required before solution and/or very rapid permeation takes place.

Solvent selection, as such, requires not only knowledge of solution behavior, but also of environmental regulations, solvent viscosity, flash point, odor, etc. Most major solvent suppliers and many larger companies have computer programs to help find optimum solvents. Cohesion energy parameter calculations based on the equations above are central in programs dealing with solvent selection.¹¹

10.4 COMPUTER TECHNIQUES

Computer techniques are readily applied to cohesion energy parameter calculations. Solubility, swelling, contact angle, wetting tensions, or other data that are generated by contact with a large number of different liquids can be computer-processed to arrive at the cohesive energy density parameters of the material in question. The example in [Table 10.1](#) is for the solubility of cholesterol at a concentration of 0.5 g/5 ml in the solvents in the list. Good solvents are those dissolving at least this much and are indicated in the SOL column with a "1." Bad solvents dissolve less than this and are indicated with a "0." The program optimizes a "sphere" with the least error for nondissolving solvents inside the sphere (0*) and dissolving solvents outside the sphere (1*). "Errors" are indicated by the * in [Table 10.2](#), and can be attributed to molecular size of the solvents in many cases, as discussed above. When this becomes a problem, corrections are possible by organizing the printout in molar volume order, for example, and seeing how the data can be processed further taking this into consideration. Solvent quality is indicated in the RED column using Equation 10.5 above.

Computer techniques are not always necessary, and simple two-dimensional plots using δ_p and δ_H can often be used to solve practical problems. The nonpolar cohesion energy parameter cannot be neglected in every case, but, for example, when comparing noncyclic solvents in practical situations, it is found that their nonpolar parameters will be rather close regardless of structure. Cyclic solvents, and those containing atoms significantly larger than carbon, such as chlorine, bromine, metals, etc., will have higher nonpolar parameters. The cohesion energy parameter for aliphatic hydrocarbon solvents, i.e., the nonpolar parameter, increases only slightly with increased chain length, a trend that is also found for polymers.

10.5 WATER

Mixtures with water are often nonideal, and the behavior of water itself is not always easy to interpret. This has, of course, caused problems with predicting the behavior of water. An example of a problem caused by nonideal mixtures with water is the interpretation of cohesion energy parameters for materials such as the dye Rhodamin FB (C.I. Basic Violet 10).^{8,22} The nonideality of mixtures of solvent and water led to a very nonspherical (noncircular) cohesion energy parameter plot. This characterization improves drastically when the data points for pure solvents only are considered. A computer analysis based on the pure solvent data confirms that a good spherical characterization of Rhodamin FB is possible. This is confirmed in [Table 10.2](#). See also the discussion in chapter 11 of Reference 11.

The fact of considerable irregularity in the "spherical" plot in Reference 18 has been used in the past to indicate severe problems with the spherical characterization. This particular problem really concerns the nonideality of water mixtures, coupled with a reluctance to allow the spherical characterization to encompass a much higher energy region than would allow the liquid state. Because of its tendency to nonideal behavior, the use of data for water or its mixtures is not suggested in these characterizations. If such data are used, this should be done with caution.

TABLE 10.1A
Calculated Solubility Sphere for Cholesterol Solubility — RED Order
(see Equation 10.5)

No.	Solvent	δ_D	δ_P	δ_H	Solubility	RED	V
96	1,4-Dioxane	19.0	1.8	7.4	1	0.284	85.7
229	Trichloroethylene	18.0	3.1	5.3	1	0.502	90.2
44	Chloroform	17.8	3.1	5.7	1	0.507	80.7
162	Methylene dichloride	18.2	6.3	6.1	1	0.517	63.9
17	Benzyl alcohol	18.4	6.3	13.7	1	0.543	103.6
48	Cyclohexanol	17.4	4.1	13.5	1	0.586	106.0
61	<i>o</i> -Dichlorobenzene	19.2	6.3	3.3	1	0.590	112.8
120	Ethylene dichloride	19.0	7.4	4.1	1	0.600	79.4
222	Tetrahydrofuran	16.8	5.7	8.0	1	0.626	81.7
177	Nitrobenzene	20.0	8.6	4.1	1	0.627	102.7
41	Chlorobenzene	19.0	4.3	2.0	1	0.639	102.1
6	Acetophenone	19.6	8.6	3.7	1	0.658	117.4
13	Benzene	18.4	0.0	2.0	1	0.704	89.4
225	Toluene	18.0	1.4	2.0	1	0.709	106.8
123	Ethylene glycol monobutyl ether	16.0	5.1	12.3	1	0.758	131.6
30	Butyl acetate	15.8	3.7	6.3	1	0.774	132.5
106	Ethyl acetate	15.8	5.3	7.2	1	0.777	98.5
40	Carbon tetrachloride	17.8	0.0	0.6	1	0.841	97.1
56	Diacetone alcohol	15.8	8.2	10.8	1	0.854	124.2
172	Methyl-2-pyrrolidone	18.0	12.3	7.2	1	0.863	96.5
28	1-Butanol	16.0	5.7	15.8	1	0.894	91.5
124	Ethylene glycol monoethyl ether	16.2	9.2	14.3	1	0.924	97.8
167	Methyl isobutyl ketone	15.3	6.1	4.1	1	0.949	125.8
82	Diethyl ether	14.5	2.9	5.1	1	0.997	104.8
90	Dimethylformamide	17.4	13.7	11.3	1	0.999	77.0
4	Acetone	15.5	10.4	7.0	0	1.003	74.0
126	Ethylene glycol monomethyl ether	16.2	9.2	16.4	0	1.006	79.1
181	2-Nitropropane	16.2	12.1	4.1	0	1.080	86.9
94	Dimethyl sulfoxide	18.4	16.4	10.2	0	1.127	71.3
37	γ -Butyrolactone	19.0	16.6	7.4	0	1.129	76.8
140	Hexane	14.9	0.0	0.0	0	1.170	131.6
104	Ethanol	15.8	8.8	19.4	0	1.179	58.5
204	Propylene carbonate	20.0	18.0	4.1	0	1.279	85.0
178	Nitroethane	16.0	15.5	4.5	0	1.286	71.5
75	Diethylene glycol	16.6	12.0	20.7	0	1.304	94.9
205	Propylene glycol	16.8	9.4	23.3	0	1.348	73.6
105	Ethanolamine	17.0	15.5	21.2	0	1.478	59.8
179	Nitromethane	15.8	18.8	5.1	0	1.504	54.3
153	Methanol	15.1	12.3	22.3	0	1.525	40.7
121	Ethylene glycol	17.0	11.0	26.0	0	1.565	55.8
131	Formamide	17.2	26.2	19.0	0	2.071	39.8

Note: $\delta_D = 20.4$; $\delta_P = 2.8$; $\delta_H = 9.4$; $R = 12.6$; $FIT = 1.000$; and $NO = 41$.

Water can be considered as possessing duality. One way to consider the energy properties of water is to use the usual cohesion energy parameters based on the energy of evaporation. This is presumably considering water as single molecules. If we correlate the solubility of water in different solvents at 1%, a different set of parameters for associated water evolves.¹⁰ This correlation suggests

TABLE 10.1B
Calculated Solubility Sphere for Cholesterol Solubility — Alphabetical Order

No.	Solvent	δ_D	δ_P	δ_H	Solubility	RED	V
4	Acetone	15.5	10.4	7.0	0	1.003	74.0
6	Acetophenone	19.6	8.6	3.7	1	0.658	117.4
13	Benzene	18.4	0.0	2.0	1	0.704	89.4
17	Benzyl alcohol	18.4	6.3	13.7	1	0.543	103.6
28	1-Butanol	16.0	5.7	15.8	1	0.894	91.5
30	Butyl acetate	15.8	3.7	6.3	1	0.774	132.5
37	γ -Butyrolactone	19.0	16.6	7.4	0	1.129	76.8
40	Carbon tetrachloride	17.8	0.0	0.6	1	0.841	97.1
41	Chlorobenzene	19.0	4.3	2.0	1	0.639	102.1
44	Chloroform	17.8	3.1	5.7	1	0.507	80.7
48	Cyclohexanol	17.4	4.1	13.5	1	0.586	106.0
56	Diacetone alcohol	15.8	8.2	10.8	1	0.854	124.2
61	<i>o</i> -Dichlorobenzene	19.2	6.3	3.3	1	0.590	112.8
75	Diethylene glycol	16.6	12.0	20.7	1	1.304	94.9
82	Diethyl ether	14.5	2.9	5.1	1	0.997	77.0
90	Dimethylformamide	17.4	13.7	11.3	1	0.999	77.0
94	Dimethyl sulfoxide	18.4	16.4	10.2	0	1.127	71.3
96	1,4-Dioxane	19.0	1.8	7.4	1	0.284	85.7
104	Ethanol	15.8	8.8	19.4	0	1.179	58.5
105	Ethanolamine	17.0	15.5	21.2	0	1.478	59.8
106	Ethyl acetate	15.8	5.3	7.2	1	0.777	98.5
120	Ethylene dichloride	19.0	7.4	4.1	1	0.600	79.4
121	Ethylene glycol	17.0	11.0	26.0	0	1.565	55.8
123	Ethylene glycol monobutyl ether	16.0	5.1	12.3	1	0.758	131.6
124	Ethylene glycol monoethyl ether	16.2	9.2	14.3	1	0.924	97.8
126	Ethylene glycol monomethyl ether	16.2	9.2	16.4	0	1.006	79.1
131	Formamide	17.2	26.2	19.0	0	2.071	39.8
140	Hexane	14.9	0.0	0.0	0	1.170	131.6
153	Methanol	15.1	12.3	22.3	0	1.525	40.7
162	Methylene dichloride	18.2	6.2	6.1	1	0.517	63.9
167	Methyl isobutyl ketone	15.3	6.1	4.1	1	0.949	125.8
172	Methyl-2-pyrrolidone	18.0	12.3	7.2	1	0.863	96.5
177	Nitrobenzene	20.0	8.6	4.1	1	0.627	102.7
178	Nitroethane	16.0	15.5	4.5	0	1.286	71.5
179	Nitromethane	15.8	18.8	5.1	0	1.504	54.3
181	2-Nitropropane	16.2	12.1	4.1	0	1.080	86.9
204	Propylene carbonate	20.0	18.0	4.1	0	1.279	85.0
205	Propylene glycol	16.8	9.4	23.3	0	1.348	73.6
222	Tetrahydrofuran	16.8	5.7	8.0	1	0.626	81.7
225	Toluene	18.0	1.4	2.0	1	0.709	106.8
229	Trichloroethylene	18.0	3.1	5.3	1	0.502	90.2

Note: $\delta_D = 20.4$; $\delta_P = 2.8$; $\delta_H = 9.4$; $R = 12.6$; FIT = 1.000; and NO = 41.

that about six water molecules on the average are associated at room temperature and reduce the hydrogen bonding parameter from 42.3 MPa^{1/2} for the single molecules to 16.5 MPa^{1/2} when solubility in a bulk liquid phase is concerned. A correlation has also been reported in chapter 1 of Reference 11 for the total miscibility of water using data points for 167 liquids. The δ_D , δ_P , δ_H , and R values found were 18.1, 17.1, 16.9, and 13.0. More research is clearly needed in this area. The differences in the correlations necessarily reflect some aspect of structure in the systems concerned.

TABLE 10.2
Calculated Solubility Sphere for Rhodamin FB

No.	Solvent	δ_D	δ_P	δ_H	Solubility	RED	V
4	Acetone	15.5	10.4	7.0	0	1.125	74.0
13	Benzene	18.4	0.0	2.0	0	1.991	89.4
28	1-Butanol	16.0	5.7	15.8	0*	0.999	91.5
30	Butyl acetate	15.8	3.7	6.3	0	1.517	132.5
37	γ -Butyrolactone	19.0	16.6	7.4	0*	0.988	76.8
47	Cyclohexane	16.8	0.0	0.2	0	2.076	108.7
56	Diacetone alcohol	15.8	8.2	10.8	1*	1.001	124.2
75	Diethylene glycol	16.6	12.0	20.7	1	0.486	94.9
80	Diethylene glycol monomethyl ether	16.2	7.8	12.6	1	0.934	118.0
81	Diethylenetriamine	16.7	13.3	14.3	1	0.487	108.0
90	Dimethylformamide	17.4	13.7	11.3	1	0.677	77.0
94	Dimethyl sulfoxide	18.4	16.4	10.2	1	0.741	71.3
98	Dipropylene glycol	16.5	10.6	17.7	1	0.570	130.9
104	Ethanol	15.8	8.8	19.4	1	0.732	58.5
121	Ethylene glycol	17.0	11.0	26.0	1	0.815	55.8
126	Ethylene glycol monoethyl ether	16.2	9.2	16.4	1	0.707	79.1
129	2-Ethyl hexanol	15.9	3.3	11.8	0	1.294	156.6
136	Glycerol	17.4	12.1	29.3	1	0.996	73.3
153	Methanol	15.1	12.3	22.3	1	0.589	40.7
165	Methylisoamyl ketone	16.0	5.7	4.1	0	1.530	142.8
172	Methyl-2-pyrrolidone	18.0	12.3	7.2	1*	1.042	96.5
193	1-Pentanol	15.9	4.5	13.9	0	1.138	108.6
199	1-Propanol	16.0	6.8	17.4	0*	0.889	75.2
205	Propylene glycol	16.8	9.4	23.3	1	0.772	73.6
222	Tetrahydrofuran	16.8	5.7	8.0	0	1.295	81.7
225	Toluene	18.0	1.4	2.0	0	1.902	106.8
229	Trichloroethylene	18.0	3.1	5.3	0	1.615	90.2
244	Water	15.5	16.0	42.3	0	1.965	18.0

Note: $\delta_D = 16.7$; $\delta_P = 17.5$; $\delta_H = 18.5$; $R = 12.2$; $FIT = 0.930$; $NO = 28$.

Source: Data from Riedel, G., *Farbe Lack*, 82(4), 281–287, 1976.

10.6 ENTROPY CONSIDERATIONS

The Hansen characterization is usually considered a sphere, even although it is really a modified spheroid. The constant 4 in Equation 10.4 modifies the spheroid to a “sphere.” The cohesion energy parameters of those liquids where affinities are highest are located within the sphere. The center of the sphere has the values of the δ_{DP} , δ_{PP} , and δ_{HP} parameters, taken as characteristic for the solute. This may not be quite true because of entropy effects. The radius of the sphere, R , reflects the condition where the free energy change, ΔG^M , for the process being considered is zero. This is discussed here in terms of the mixing process, for which reason the superscript M is used. The entropy effects, $T\Delta S^M$ and enthalpy effects, ΔH^M , are in balance. Thus, on the sphere surface

$$\Delta G^M = \Delta H^M - T\Delta S^M = 0 \quad (10.7)$$

and

$$\Delta H^M = T\Delta S^M \quad (10.8)$$

The boundary of the spherical characterization is based on the requirement that the good solvents have a distance from the center of the sphere, RA , less than R . RA is given by Equation 10.4. The constant 4 in this equation was first suggested by Skaarup in Hansen⁶ and has been confirmed by a large number of experiments. As stated above, without the constant 4, the characterization is a spheroid, which is less convenient to work with in practice, especially in terms of plotting data. At the same time the constant 4 is also found in the leading term in the Prigogine corresponding states theory of polymer solutions.^{11,16,17}

The reason for the constant 4 is that materials with polar and hydrogen bonding components are oriented on a molecular scale, whereas the atomic dispersion effects are more general and do not reflect directional orientation over longer periods of time. The entropy changes on mixing can generally be expected to be larger in the more oriented systems, thus favoring solution in these according to Equations 10.4, 10.7, or 10.8. This allows a greater difference in cohesion energy parameters since ΔH^M is directly proportional to this difference in the Hildebrand theory. The constant 4 accounts for this greater ease of solution, i.e., greater entropy change potentially found in the molecularly oriented solvents compared with those where this is not the case. The constant 4 indicates solute–solvent differences in the polar and hydrogen bonding parameters may be as large as twice those in the dispersion parameters with solution still a possibility.

10.7 APPLICATIONS OF COHESION PARAMETERS TO SURFACE PHENOMENA

Because interfacial free energy and adhesion properties result from intermolecular forces, they are closely related to cohesion parameters, and the idea has been well explored.⁸ The author has been particularly influenced by the early experiments where the suspension of fine particles in pigment powders was used to characterize 25 organic and inorganic pigment surfaces.⁷ Figures 10.1 through 10.3, taken from Reference 7 and retaining the numbering scheme therein (or in References 4 to 6), show one of these early correlations for an Isol Benzidine Yellow pigment. It can be seen that there were apparent chemical reactions rather than physical interactions with some of the solvents, a factor that must always be kept in mind for acids and amines, in particular. This technique for characterizing the surfaces of pigments, powders, and related materials has been practiced with success over the years. We can use variations in sedimentation rates in different solvents where the material does not suspend for very long times in given solvents. This is a somewhat more involved procedure requiring normalizing for solvent viscosities and the density difference between solvent and sedimenting material. This approach has also been used with success, however. Chapter 5 of Reference 11 is devoted to the details of characterizing pigments, fillers, and fibers by this approach. It must be warned, however, that the success of such a characterization depends very much on the intensity of the surface (treatment) of a given particulate material. Surfaces with less quantity of treatment gave much poorer correlations than those with more extensive treatment. Surface adsorption correlations based on sedimentation rates for untreated particulate surfaces often appeared to resemble the correlation for complete miscibility in water reported above. As the degree of treatment increases, the intensity of its effect increases. At the same time the energy quality (HSP) of the ultimate surface at high treatment becomes more apparent. There are intensive effects with such surfaces as well as qualitative effects. When the intensity is lacking, it can be difficult both to characterize the surface and to use the given material in practice. There are several problems with the acid–base approach to surface characterization in view of this. We do not gain the full advantage of quantitative polar and hydrogen bonding evaluations, and the “intensity” of the given surface quality will not necessarily be discerned either. In one case it was possible to correlate zeta potential data for blanc fixe where an acid–base interpretation was not possible.¹¹

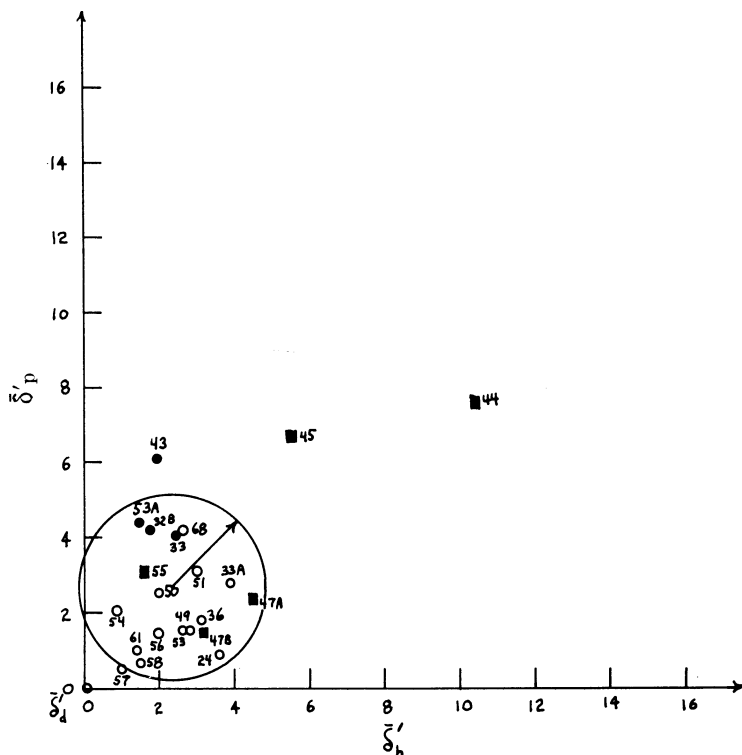


FIGURE 10.1 The volume of suspension for a pigment (Isol Benzidine Yellow, GA-PR, 9500). Primes are used to distinguish surface properties. (○) = long time suspension; (●) = suspension for shorter times; (■) = reaction.

The correlation of surface free energy with cohesion energy parameters by Beerbower in Hansen¹⁴ appears to crown many earlier correlations of Hildebrand solubility parameters with surface free energy.⁸ This equation is

$$\gamma = 0.0715 V^{1/3} \left[\delta_D^2 + 0.632 (\delta_P^2 + \delta_H^2) \right] \quad (10.9)$$

This correlation was also supported by independent calculations relating to the structure of the liquids in the surface which yielded essentially the same constant 0.0715. It is noteworthy that the polar and hydrogen bonding parameters are weighted with the same coefficient. This is the same situation as for correlating the solubility, swelling, etc., data as discussed above.

Beerbower has reported many other correlations of surface phenomena with cohesion energy parameters in Reference 23. Examples include the work of adhesion on mercury, frictional properties of polyethylene untreated and treated for 2 and 5 min with $H_2S_2O_7$, the Joffé effect (effect of liquid immersion on fracture strength of soda-lime glass) and the Rehbinder effect (crushing strength of Al_2O_3 granules under various liquids).

Hansen and Wallström⁹ picked up on Hansen's earlier work^{24,25} and showed that the cohesion energy parameters for liquids that spontaneously spread on surfaces allow plotting of regions of spontaneous spreading using δ_p vs. δ_H . Such a plot is given in Figure 10.4 for an epoxy coating. This type of data is easily generated by simply applying droplets of the different liquids on the surface in question, and observing whether or not they spontaneously spread. The numbers assigned

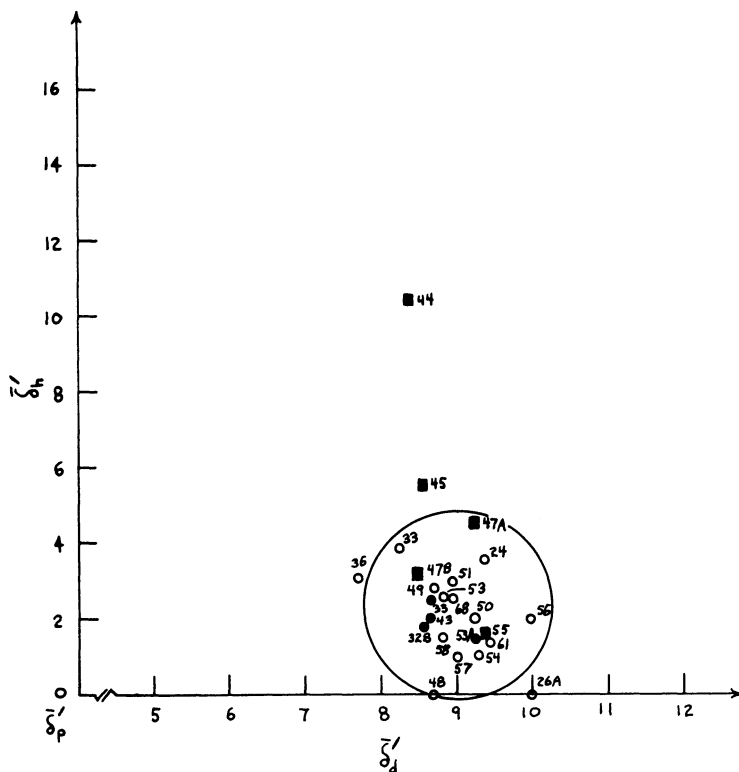


FIGURE 10.2 The volume of suspension for a pigment. Primes are used to distinguish surface properties. (○) = long time suspension; (●) = suspension for shorter times; (■) = reaction.

to the solvents in Figures 10.4 to 10.6 are those used in the original source. An additional feature shown on this plot is that a region can also be plotted using a wetting tension experiment. This larger region is determined by intentionally spreading the droplets of those liquids that do not spontaneously spread. The film thus generated will either hold as a film or break up/retract. This ability to plot two regions for surfaces for the spontaneous spreading and lack of film retraction, respectively, seems to be general.

Surface characterization by simple observation of the behavior of many liquids, as reported in Figure 10.4, provides information not available in any other way. This type of characterization appears necessary if one requires that two different surfaces fully match each other energetically to ensure optimum adhesion, for example. Matching of the critical surface tensions does not ensure a full energetic match. Matching critical surface tensions only ensures that a given liquid behaves identically on the two different surfaces in question. The behavior of this single liquid is furthermore dependent on the liquid series used to establish the point. Matching the spontaneous spreading behavior in a large number of liquids, as shown in Figure 10.4, ensures that the critical surface tension will be essentially the same for the two surfaces for any liquid series used to determine it.

There is a certain duality reflected by these plots. A cohesion energy plot of the solubility or swelling of an epoxy would not encompass, for example, hexane. This solvent will not swell or attack an epoxy film if adhesion is to be enhanced using the technique of improved “bite” by an active solvent. The spontaneous spreading plot for this same material will encompass hexane because the low surface tension of hexane dictates that it will spontaneously spread over the higher-energy epoxy film. This can cause the center of the spheres derived from spreading data for different liquids to be located in negative space, which, of course, is not a realistic situation. More research is required to appreciate fully the usefulness of these plots. There is a particular question regarding

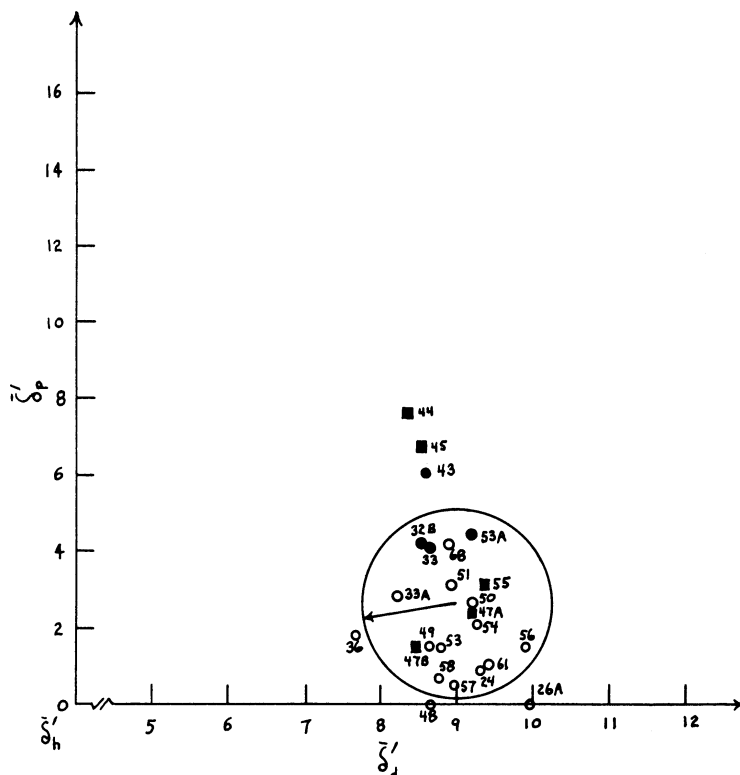


FIGURE 10.3 The volume of suspension for a pigment. Primes are used to distinguish surface properties. (○) = long time suspension; (●) = suspension for shorter times; (■) = reaction.

which single solvent best represents the cohesion energy coordinates for the surface in question. This is discussed in the following.

Hansen and Wallström⁹ proceeded to compare a Zisman critical tension plot with a similar approach where the cosine of the contact angle was plotted against the difference in cohesion energy parameters between the substrate and the liquids used for the testing. Such a comparison is given in [Figures 10.5 and 10.6](#)⁹ for a polyethylene substrate. It can be seen that the two approaches in essence arrive at a characteristic energy value. This may be expressed in units of surface energy or in units of bulk energy (cohesion energy parameters). Liquids having energies below this will spontaneously spread. The energy of the liquids can be expressed with either a surface free energy or with cohesion energy parameters. In any case this is just a single point on the boundary of a plot of the type shown in [Figure 10.4](#). The same liquids can be located on [Figure 10.4](#), and show that an attempt has been made to coordinate the solubility parameters and the surface tensions of the test liquids. The solvents in question are 1-glycerine, 2-ethylene glycol, 3-1,3-butanediol, and 7-ethylene glycol monoethyl ether acetate. A comparison of this situation with bulk energy considerations is given in the next paragraph.

Who would determine the solubility parameter for a polymer by the following method? One makes up a series of liquids with different, known solubility parameters and determines the degree of swelling of the polymer in question in those liquids that do not fully dissolve it. One subsequently determines the solubility parameter of the polymer by extrapolating the degree of swelling to infinity. This corresponds to total solution. This extrapolation can be done by plotting $1/(\text{degree of swelling})$ vs. solvent composition (solubility parameter). We now focus attention on that fictitious liquid from this extrapolation, which just dissolves the polymer. It is therefore on the boundary of the solubility characterization. However, we assume that there is no better solvent than this anyway,

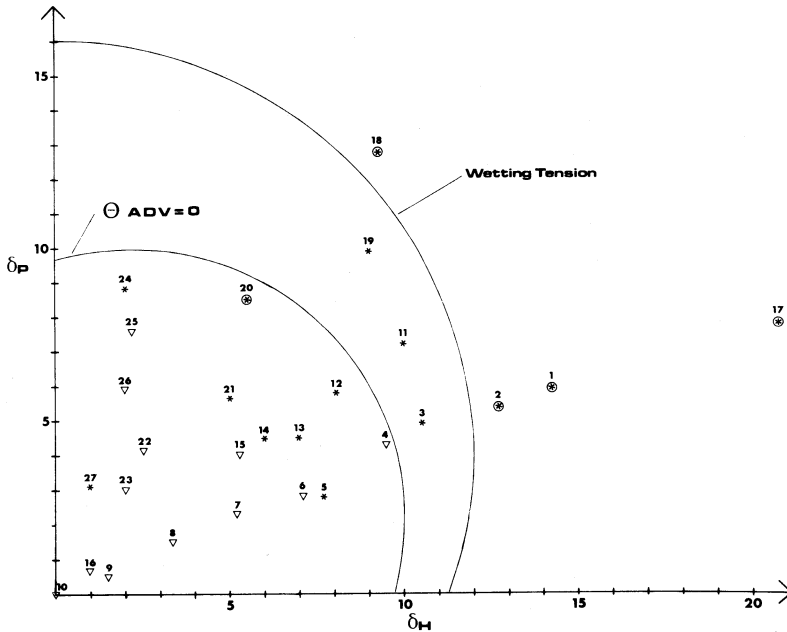


FIGURE 10.4 Cohesive energy plot of contact angle and wetting tension data for an epoxy coating. (From Hansen, C.M. and Wallström, E., *J. Adhes.* (<http://www.tandf.co.uk>), 15, 275–286, 1983. With permission.)

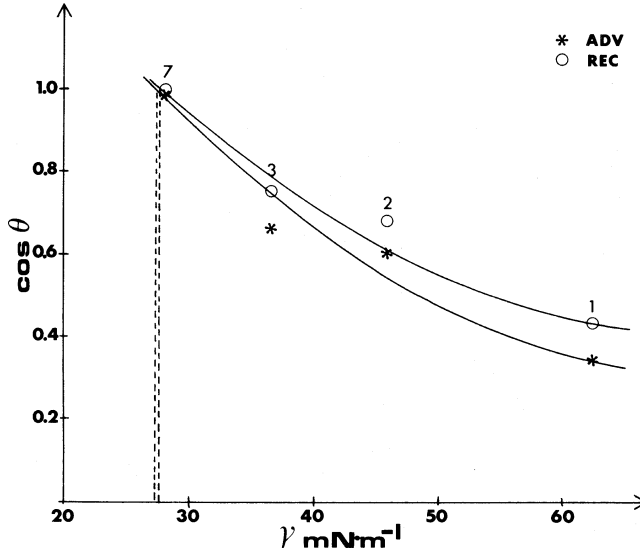


FIGURE 10.5 $\cos(\theta)$ vs. surface tension for a low-density polyethylene substrate. (From Hansen, C.M. and Wallström, E., *J. Adhes.*, (<http://www.tandf.co.uk>), 15, 275–286, 1983. With permission.)

and consequently assign the polymer solubility parameters corresponding to those of the boundary solvent. This is exactly what we do when the critical surface tension is measured. It is to be hoped that this method is never used to determine solubility parameters for polymers, and that this simple example sheds some light on the true meaning of the critical surface tension.

A recent development in the coatings industry is the planned separation of a liquid coating, which is applied as a single coat, into primer and topcoat layers comparable to the result obtained

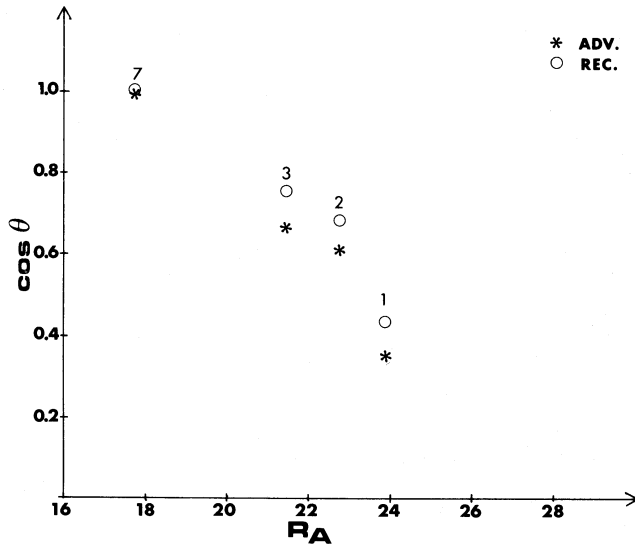


FIGURE 10.6 $\cos(\theta)$ vs. energy difference, R_A , for a low-density polyethylene substrate. (From Hansen, C.M. and Wallström, E., *J. Adhes.*, (<http://www.tandf.co.uk>), 15, 275–286, 1983. With permission.)

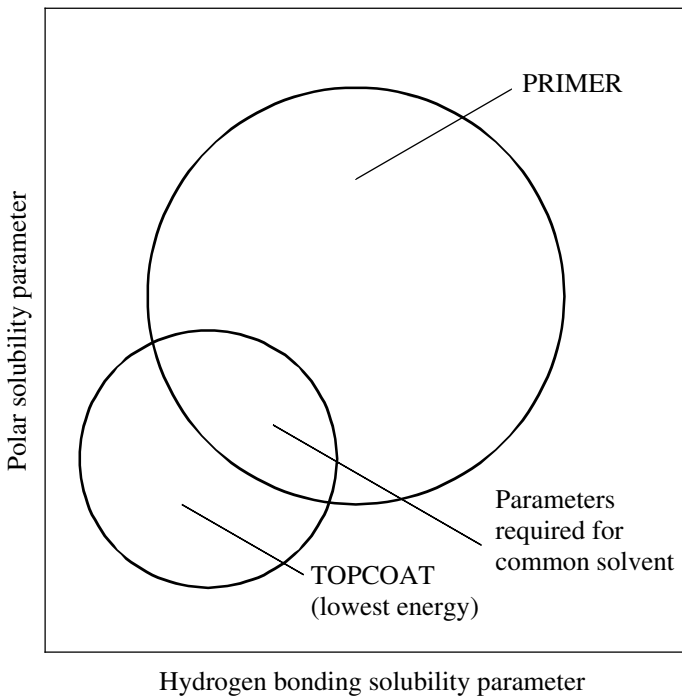


FIGURE 10.7 Schematic drawing for designing self-stratifying coatings.

with a two-coat system applied one coat at a time. These self-stratifying coatings can be designed using cohesion energy parameters.^{26,27} Figure 10.7 shows the principles involved for selecting the solvent that can make these work. The polymer with cohesion energy parameters nearest the origin will be the topcoat, as it has the lower (surface or cohesion) energy of the two. A solvent is required that dissolves both polymers, so it will be located in the common region to the spheres portrayed.

Mutual solubility of two polymers is promoted when the solvent favors the polymer that is most difficult to dissolve.²⁸ This is usually the one with the higher molecular weight. It is clear that selection of the optimum solvent for this process of designed generation of an interface is aided by systematic use of cohesion energy parameters.

10.8 CONTROLLED ADSORPTION (SELF-ASSEMBLY)

Significant tasks for formulators are to control the surface and interfacial energies of products, especially if these coatings are water reducible. This is required to allow substrate wetting, to maintain stable dispersions, and to provide/ensure adequate and durable adhesion to given substrates. Guidelines for courses of action are frequently available when cohesion energy parameters are referred to. Some guides are discussed in the following.

It is a well-known fact that a small percentage of acid groups (or alcohol groups) on a polymer chain will promote adhesion and adsorption to many surfaces. The cohesion energy parameter of an isolated acid group is high. We can consider the cohesion energy properties of formic acid as an isolated part of a polymer chain. The polar cohesion energy parameter of an acid group is not so high. It would seem logical to systematically use acid groups for adsorption to high energy surfaces and to make certain that the cohesion energy parameters for the solvent and bulk of the product are much lower, such that isolated acid groups would not be dissolved. This would provide an anchor that the product itself will not be able to remove. If, on the other hand, the solvent were too good for the anchor, it can be presumed an acid group may be too readily dissolved off the surface, or at least take part in a dynamic equilibrium of adsorption and desorption. Absorbed/adsorbed water can sometimes interfere with such anchors at high-energy surfaces.

The reverse of the above thinking is systematically used by those designing associative thickeners and by nature itself with hydrophobic bonding in proteins, for example. Certain segments of given molecules have such low cohesive energy parameters that they are no longer soluble in the media, which is usually aqueous, and they either seek out their own kind (associate), or perhaps adsorb on or penetrate into a low-energy surface where cohesion energy parameters suitably match. The positive effects of associative thickeners can be counteracted by the presence of solvents preferentially locating where the hydrophobic bonding is to occur. The hydrophobic bonds lose strength, or may even be dissolved away.

The helical structure of proteins is determined by hydrogen bonding. The cohesion energy parameters representative of these bonds are somewhat higher than levels that allow solution in water. As long as a protein has a helical structure, it is not truly and completely soluble in water. The cohesion energy parameters of aqueous solvent can be increased such that they approach the values characteristic of the hydrogen bonding in the proteins. This can be done by additions of urea, for example. When enough urea has been added, the cohesion energy parameters of the new aqueous solvent are such that the hydrogen-bonded protein is truly dissolved. The initially dispersed protein was oriented and had a given structure/surface. After addition of sufficient urea it becomes fully dissolved/denatured and the surface structure it once had no longer exists in the same way. This is another example of the dissolving of hydrogen-bonded species with a solvent having the appropriate cohesive energy parameters.

A related example of changing polymer structure is that found when an initially hydrophobic polymer, such as cellulose, is contacted with water. In a short time it has a hydrophilic surface. This is also evidenced by noting how water initially pearls up on the floor of a forest or on peat moss. Given a short time, the pearled drop disappears into the bulk of the material. This type of behavior has been seen in many polymer films in practice. After sufficiently long immersion in water, a once hydrophobic surface becomes hydrophilic. These are thought to be examples of how materials and parts of materials seek out regions with energy similarity to themselves. The materials, or segments of them, must clearly be able to move to do this. The regions they seek have cohesion energy parameters more similar to their own than the regions they leave. Surface phenomena of

this type are controlled by a balance between exclusion from a given environment with unfavorable cohesion parameters and some extent of attraction to another location in the system where the cohesion energy parameters are more favorable. Analytical confirmation of the rotation of cellulose polymer chains in changing environments has not been demonstrated experimentally, so this must be considered a theory for the present.

A challenge to the creative mind is to derive new uses for high-energy groups that are not particularly water soluble/water sensitive. The division of the cohesion energy into at least three parts allows these considerations to be made in a reasonably quantitative manner. We can choose nitro groups or perhaps groups containing phosphorus as examples of species characterized by high polar cohesion energy parameters and low or moderate hydrogen bonding parameters. The total cohesion energy parameters for ethanol and nitromethane are very close, 26.1 and 25.1 MPa^{1/2}, respectively. Ethanol is soluble in water; nitromethane is not. Ethanol has a relatively high hydrogen bonding parameter (19.4 MPa^{1/2}) compared with nitromethane (5.1 MPa^{1/2}). This makes all the difference. Would not the nitro group be a suitable anchor analogous to the discussion concerning acid groups above? And it would not be hydrophilic with the inherent problems of water sensitivity associated with high hydrogen bonding parameters.

A final example is an extension of this kind of analysis. The question can be raised where the hydrophobic end of a given surfactant will tend to preferentially reside? An aliphatic end group would have lower affinity for polystyrene, for example, than an aromatic one. Octane will not dissolve polystyrene whereas toluene will. This is reflected by their cohesion energy parameters. This same reasoning applies to other polymers. A surfactant with a fluorinated end will not dissolve in many polymers where a hydrocarbon end will. The cohesion energy parameters characteristic of fluorocarbons are too low. Although these examples are obvious to those skilled in the science of surfaces, they point to the possibility of quantifying affinities of surface active materials in terms of the cohesion energy parameters of their respective end groups. Those familiar with cohesion energy parameters can already discern differences that may improve the chances of success.

Additional examples of controlled adsorption are given in Reference 11, where the cohesion energy parameters for over 860 chemicals are given. There are also over 450 correlations for solubility, swelling, adsorption, chemical resistance, barrier properties, etc.

10.9 CONCLUSION

Hansen solubility parameters can be used to characterize surfaces. A special technique using relative sedimentation rates in a large number of different liquids allows characterization of particulate surfaces such as pigments, fillers, and fibers. The spontaneous spreading and wetting tension tests can be used to characterize coatings, substrates, and the like. These results together with all of the other characterizations possible (solubility, swelling, permeation rate, chemical resistance, etc.) confirm that the division of the cohesion energy into (at least) three parts quantitatively accounting for nonpolar, permanent dipole–permanent dipole, and hydrogen bonding interactions is basically correct. The fact of agreement in principle with the Prigogine corresponding states theory of polymer solutions lends further credence to this. No other approach to predict polymer solubility quantitatively accounts for hydrogen bonding. The permanent dipole–permanent dipole and hydrogen bonding interactions therefore necessarily follow the geometric mean rule for predicting interactions between unlike molecules to allow this.

REFERENCES

1. Hildebrand, J. and Scott, R.L., *The Solubility of Nonelectrolytes*, 3rd ed., Reinhold, New York, 1950.
2. Hildebrand, J. and Scott, R.L., *Regular Solutions*, Prentice-Hall, Englewood Cliffs, NJ, 1962.

3. Burrell, H., Solubility parameters for film formers, *Off. Dig.*, 27(369), 726–758, 1972; Burrell, H., A solvent formulating chart, *Off. Dig.*, 29(394), 1159–1173, 1957; Burrell, H., The use of the solubility parameter concept in the United States, *VI Federation d'Associations de Techniciens des Industries des Peintures, Vernis, Emaux et Encres d'Imprimerie de l'Europe Continentale, Congress Book*, 1962, 21–30.
4. Hansen, C.M., The three dimensional solubility parameter-key to paint component affinities I, *J. Paint Technol.*, 39(505), 104–117, 1967.
5. Hansen, C.M., The three dimensional solubility parameter — key to paint component affinities II, *J. Paint Technol.*, 39(511), 505–510, 1967.
6. Hansen, C.M. and Skaarup, K., The three dimensional solubility parameter — key to paint component affinities III, *J. Paint Technol.*, 39(511), 511–514, 1967.
7. Hansen, C.M., *The Three Dimensional Solubility Parameter and Solvent Diffusion Coefficient*, Doctoral dissertation, Danish Technical Press, Copenhagen, 1967.
8. Barton, A.F.M., *Handbook of Solubility Parameters and Other Cohesion Parameters*, CRC Press, Boca Raton, FL, 1983; Barton, A.F.M., *Handbook of Polymer-Liquid Interaction Parameters and Solubility Parameters*, CRC Press, Boca Raton, FL, 1990.
9. Hansen, C.M. and Wallström, E., On the use of cohesion parameters to characterize surfaces, *J. Adhes.*, 15, 275–286, 1983.
10. Hansen, C.M., The affinities of organic solvents in biological systems, *J. Am. Ind. Hyg. Assoc.*, 49(6), 301–308, 1988.
11. Hansen, C.M., *Hansen Solubility Parameters: A User's Handbook*, CRC Press, Boca Raton, FL, 1999.
12. Blanks, R.F. and Prausnitz, J.M., Thermodynamics of polymer solubility in polar and nonpolar systems, *Ind. Eng. Chem. Fund.*, 3(1), 1–8, 1964.
13. Hansen, C.M., Solubility parameters, in *Paint Testing Manual*, J.V. Koleske, Ed., American Society for Testing and Materials, Philadelphia, 1995, 383–404.
14. Hansen, C.M. and Beerbower, A., Solubility parameters, in *Kirk-Othmer Encyclopedia of Chemical Technology*, Suppl. Vol., 2nd ed., A. Standen, Ed., Wiley Interscience, New York, 1971, 889–910.
15. Flory, P.J., Thermodynamics of polymer solutions, *Discuss. Faraday Soc.*, 49, 7–29, 1970.
16. Prigogine, I. (with the collaboration of A. Bellemans and A. Mathot), *The Molecular Theory of Solutions*, North-Holland, Amsterdam, 1957, chap. 16 and 17.
17. Patterson, D., Role of free volume changes in polymer solution thermodynamics, *J. Polym. Sci. C*, 16, 3379–3389, 1968.
18. Hansen, C.M. and Hansen, K.M., Solubility parameter prediction of the barrier properties of chemical protective clothing, in *Performance of Protective Clothing: Second Symposium*, ASTM STP 989, S.Z. Mansdorf, R. Sager, and A.P. Nielsen, Eds., American Society for Testing and Materials, Philadelphia, 1988, 197–208.
19. Hansen, C.M., Billing, C.B., Jr., and Bentz, A.P., Selection and use of molecular parameters to predict permeation through fluoropolymer-based protective clothing materials, in *The Performance of Protective Clothing*, Vol. 4, ASTM STP 1133, J.P. McBriarty and N.W. Henry, Eds., American Society for Testing and Materials, Philadelphia, 1992, 894–907.
20. Ursin, C. et al., A comparative study of the permeation of 13 commonly used solvents through viable human skin *in vitro*, including a rough screening of the chemical effect on the proliferative ability of the epidermal cells, *Am. Ind. Hyg. Assoc. J.*, 56, 651–660, 1995.
21. Anonymous, *Chemical and Engineering News*, October 18, 1993, 40–61.
22. Riedel, G., Löslichkeit von Farbstoffen in Organischen Lösungsmitteln, *Farbe Lack*, 82(4), 281–287, 1976.
23. Beerbower, A., Boundary Lubrication — Scientific and Technical Applications Forecast, AD747336, Office of the Chief of Research and Development, Department of the Army, Washington, D.C., 1972.
24. Hansen, C.M., Characterization of surfaces by spreading liquids, *J. Paint Technol.*, 42(550), 660–664, 1970.
25. Hansen, C.M., Surface dewetting and coatings performance, *J. Paint Technol.*, 44(570), 57–60, 1972.
26. Misev, T.A., Thermodynamic analysis of phase separation in self-stratifying coatings — solubility parameters approach, *J. Coatings Technol.*, 63(795), 23–28, 1991.
27. Carr, C., Benjamin, S., and Wallbridge, D.J., Fluorinated resins in self-stratifying coatings, *Eur. Coatings J.*, 4, 262–266, 1995.
28. Hansen, C.M., On application of the three dimensional solubility parameter to the prediction of mutual solubility and compatibility, *Farg Lack*, 13(6), 132–138, 1967.

11 Self-Assembly of Monodispersed Spherical Colloids into Complex Structures

Yunan Xia, Byron Gates, Yadong Yin, and Yugang Sun

CONTENTS

- 11.1 [Introduction](#)
- 11.2 [Self-Assembly and Monodispersed Spherical Colloids](#)
- 11.3 [Well-Defined Aggregates of Spherical Colloids](#)
 - 11.3.1 [Template-Assisted Self-Assembly](#)
 - 11.3.2 [Mechanism for the TASA Process](#)
 - 11.3.3 [Control over the Self-Assembled Structures](#)
 - 11.3.4 [Hybrid Aggregates of Spherical Colloids](#)
- 11.4 [Opaline Lattices of Spherical Colloids](#)
 - 11.4.1 [Crystallization by Confined Self-Assembly](#)
 - 11.4.2 [Control over the Thickness of Opaline Lattices](#)
 - 11.4.3 [Control over the Density and Structure of Defects](#)
 - 11.4.4 [Control over the Crystal Orientation of Opaline Lattices](#)
 - 11.4.5 [Inverse Opals: Crystalline Lattices of Interconnected Air Balls](#)
- 11.5 [Hierarchical Self-Assembly of Colloidal Particles](#)
- 11.6 [Concluding Remarks](#)
- [Acknowledgments](#)
- [References](#)

11.1 INTRODUCTION

Colloidal particles are small objects with at least one characteristic dimension in the range of 1 nm to 1 μm .¹ This range of size is a manifestation of the importance of Brownian motion²—the endless translational diffusion resulting from the incompletely averaged-out bombardment that each particle receives from the molecules of a dispersion medium. In broad terms, colloidal particles can be considered giant molecules and can be treated, to a certain degree, according to the theories of statistical mechanics.³ Since the pioneering work by Ostwald and Graham more than 140 years ago, colloids have been extensively studied in the context of chemistry, materials science, biology, condensed matter physics, applied optics, and fluid dynamics.⁴ The importance of colloids can also be appreciated from their ubiquitous presence in a variety of commercial products such as foods, drinks, inks, paints, toners, coatings, papers, cosmetics, photographic films, rheological fluids, and magnetic recording media.¹⁻⁵

The production of colloidal particles as monodispersed samples that are uniform in shape, size, composition, and surface properties has been a major goal of colloid science since the beginning of the 20th century. Many advances in this field were spurred by the elaboration of synthetic methods capable of generating monodispersed colloids in relatively large quantities.⁶ Thanks to many years of continuous efforts, a variety of colloids can now be synthesized as truly monodispersed samples in which the shape and size of the particles and the net charges that are chemically fixed on their surfaces are all identical to within a few percent.⁷ Spherical colloids, in particular, have been the most successful and best-established examples of monodispersed systems. Driven by the minimization of interfacial energy, the spherical shape may represent the simplest form that a colloidal particle can easily adopt during the nucleation or growth process. A number of chemical approaches have been developed to generate spherical colloids from a range of different materials such as organic polymers and inorganic materials.⁶⁻⁸ It has also been possible to achieve good control over the properties of spherical colloids by changing their intrinsic parameters, such as diameters, chemical compositions, bulk substructures, crystallinities (polycrystalline vs. amorphous), and surface functional groups (thus the density and polarity of surface charges and interfacial free energy).⁹

Studies on spherical colloids have enriched our understanding on the interactions between colloidal particles,¹⁰ as well as their hydrodynamics in various types of dispersion media.¹¹ On the other hand, spherical colloids may also represent a class of ideal building blocks that could be readily self-assembled into three-dimensionally ordered lattices such as colloidal crystals or synthetic opals.¹²⁻¹⁵ The ability to crystallize spherical colloids into spatially periodic structures has allowed us to obtain interesting and often useful functionality not only from the constituent material of the colloidal particles, but also from the long-range order exhibited by these periodic lattices.¹⁶⁻¹⁸ The beautiful, iridescent colors of opals, for example, are caused by the long-range ordered lattice of silica colloids that are colorless by themselves.¹⁹ As a matter of fact, studies on the optical properties of these materials have now evolved into a new and active field of research that is often referred to as photonic crystals or photonic bandgap (PBG) structures.²⁰

This chapter gives a brief introduction to current research activities that center on the self-assembly of colloidal particles. Our aim is to illustrate how colloidal particles can be employed as building blocks to effectively generate certain types of complex structures that are difficult or impossible to fabricate using other approaches. We begin this chapter with a brief description of self-assembly and monodispersed colloids. We then discuss three self-assembly strategies in detail in the following sections:

1. Organization of monodispersed spherical colloids into complex aggregates with well-controlled sizes, shapes, and internal structures by combining physical templating and attractive capillary forces
2. Crystallization of monodispersed spherical colloids into long-range ordered lattices (opals and inverse opals) using confined self-assembly
3. Hierarchical self-assembly that involves colloidal particles with sizes on two different scales

We conclude with some personal perspectives on the directions future research in this area might take.

11.2 SELF-ASSEMBLY AND MONODISPersed SPHERICAL COLLOIDS

Self-assembly is the spontaneous organization of predesigned building blocks (molecules or objects) into stable aggregates through noncovalent interactions.²¹ The capability and feasibility of self-assembly in generating complex and diverse structures is especially evident in biological systems, including cells, lipid bilayers, the DNA duplex, and the tertiary and quaternary structure of proteins.²²

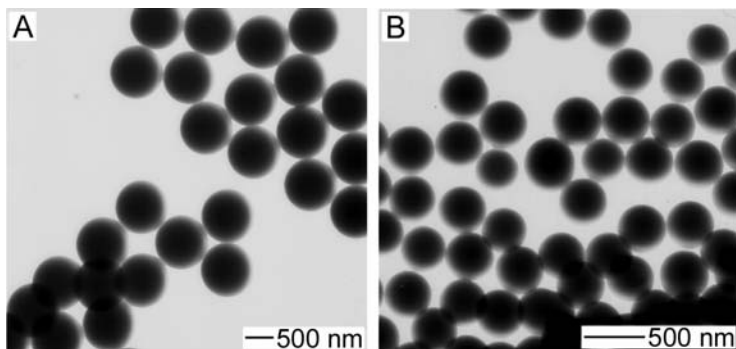


FIGURE 11.1 TEM images of two examples of spherical colloids that can be readily synthesized as monodispersed samples in large quantities: (A) silica spheres (~500 nm in diameter); (B) polystyrene beads (~300 nm in diameter). Both samples can also be commercially obtained from vendors such as Duke Scientific and Polysciences.

Based on these biological examples, chemists have developed various strategies of self-assembly to produce two- and three-dimensional structures with dimensions ranging from molecular, through nanoscopic and mesoscopic, to macroscopic scales.²³⁻²⁶ Interactions that have been extensively exploited for forming self-assembled structures include capillary forces, hydrogen bonds, metal-ligand coordination bonds, electrostatic interactions, hydrophobic interactions, receptor-ligand interactions, as well as DNA duplex formation.²⁷

Self-assembly has been actively explored as an effective approach to complex structures with nanometer- to millimeter-scale dimensions that are difficult (or impossible) to generate using traditional techniques. The key idea of a self-assembly process is that the final structure is close to or at a thermodynamic equilibrium; it thus tends to form spontaneously, and to reject defects. Self-assembly usually provides routes to structures possessing greater order than can be reached in non-self-assembling structures. In general, the final product is predetermined by the characteristics of the building blocks: the information that determines the final structure is often coded in the structures and properties (for example, shapes and surface functionalities) of the initial subunits. Studies in self-assembly have often proceeded through three steps: (1) design of building blocks with desired functionalities; (2) preparation of these building blocks in the laboratory; and (3) characterization of the self-assembled structures. In all these studies, it is highly desired to have the ability to modify the properties of the building blocks systematically in an effort to understand the rules of self-assembly and make predictions about the self-assembled structures.

Monodispersed spherical colloids provide a class of building blocks well-suited for use with self-assembly processes. Thanks to many years of continuous efforts, a rich variety of chemical methods are now available for producing spherical colloids as monodispersed samples, in large quantities, and with diameters precisely controlled in the range of a few nanometers to several hundred micrometers.⁶⁻⁹ The best-established and most commonly used methods are “controlled precipitation” for inorganic oxides and “emulsion polymerization” for organic polymers. By using these two methods, inorganic oxides such as amorphous silica can be readily prepared as uniform spheres with diameters ranging from tens of nanometers to ~1 μm ; polymer latexes of 20 nm to 100 μm in diameter can also be readily produced as uniform beads. Figure 11.1 shows transmission electron microscopy (TEM) images of two such colloidal samples: silica spheres of ~500 nm in diameter and polystyrene beads of ~300 nm in diameter. Such monodispersed spherical colloids can also be commercially obtained in relatively large quantities from a number of companies, although the diversity of materials might be limited.¹⁷ The major products of these companies are based on silica colloids or polystyrene latexes, and are usually supplied as stabilized suspensions (>1 wt.%) in either water or organic solvents. The polarity and density of surface charges can both

be specified when orders are placed. All these commercial products can be directly used without further purification or separation.

It is also feasible to control the surface properties of spherical colloids. For silica colloids synthesized using the Stöber method,²⁸ their surface is often terminated in the silanol group ($-\text{Si}-\text{OH}$), which can ionize to generate a negatively charged interface at pH values higher than 7.⁹ When potassium persulfate is used as the water-soluble radical initiator, the surface of polymer latexes prepared through emulsion polymerization is often terminated in the negatively charged sulfate group.⁸ Other acidic (e.g., $-\text{COOH}$) and basic (e.g., $-\text{NH}_2$) groups can also be introduced into the surface layer by mixing appropriate compounds with the monomer. The polarity of these surface groups can be controlled by adjusting the pH value of dispersion medium. In some cases, both positively and negatively charged functional groups can be placed on the same colloidal particle. At a particular pH, the negative and positive charges on the surfaces of these colloidal particles can be balanced to yield amphoteric or zwitterionic colloidal systems. In addition, the interfacial properties of spherical colloids can be modified in a controllable way by forming self-assembled monolayers (SAMs) with appropriate terminal groups.²⁹⁻³¹

The interfacial properties of spherical colloids can be further modified by coating them with thin shells of a different chemical composition. It has been demonstrated that the structure, size, and composition of these hybrid particles could be alternated in a controllable way to tailor their optical, electrical, thermal, mechanical, electrooptical, magnetic, and catalytic properties over a broad range.³²⁻³⁵ Such a modification is also useful in tuning the interactions between colloidal spheres, and stabilizing the dispersion of these spheres in a particular solvent. A large number of methods have been successfully demonstrated for coating spherical colloids with thin shells of the desired material. Most of these methods involved the use of a controlled adsorption and/or reaction (e.g., precipitation, grafted polymerization, and sol-gel condensation) on the surfaces of spherical colloids.³⁶ Although these methods are straightforward to work with, they often have difficulty in controlling the homogeneity and thickness of the coating. Two elegant approaches have recently been demonstrated by several groups, which allowed for the formation of uniform and dense coatings on spherical colloids. In the first approach, the surfaces of spherical colloids (e.g., gold or silver nanoparticles) were grafted with an appropriate primer that could greatly enhance the coupling (and thus deposition) of silica precursors to these surfaces.^{37,38} In the second method, electrostatic attractive adsorption of polyelectrolytes and charged objects was used to build (in a layer-by-layer fashion) a shell with well-controlled thickness around the template — spherical colloids whose surfaces had been appropriately derivatized with charged functional groups.^{39,40} This method has been successfully applied to a variety of spherical colloids and coating materials. Subsequent removal of the core templates yielded hollow spheres made of the coating material. The availability of core-shell colloidal particles provides another route to increase the complexity of structures formed through self-assembly.

11.3 WELL-DEFINED AGGREGATES OF SPHERICAL COLLOIDS

A number of methods have recently been demonstrated or reexamined for assembling colloidal particles into discrete aggregates. For example, Velev et al.⁴¹ have exploited the surface confinement provided by liquid droplets to organize polystyrene beads into spherical objects. Huck et al.⁴² further extended the capability of this approach to assemble microfabricated hexagonal rings into spherical, weblike structures. Tien et al.⁴³ also used patterns of self-assembled monolayers to direct the deposition and self-organization of charged colloids in the designated regions of a solid substrate. This strategy was later employed by Aizenberg et al.⁴⁴ and Chen et al.⁴⁵ to organize spherical colloids into discrete aggregates supported on flat substrates. Although these attempts have demonstrated the feasibility of using templates to assemble colloidal particles into discrete aggregates with specific geometric shapes, their ability to control the size, shape, and internal structure of the resultant

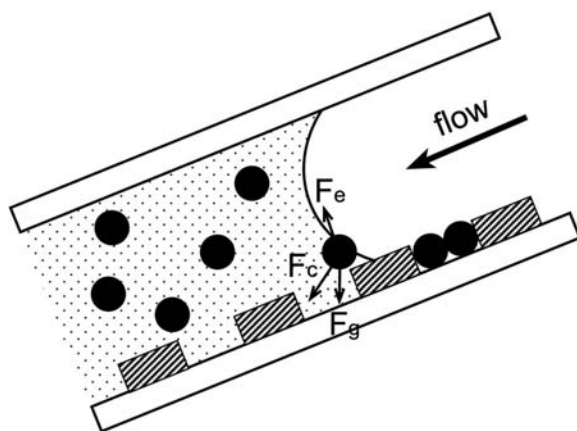


FIGURE 11.2 A cross sectional view of the fluidic cell that can be used to assemble spherical colloids into well-defined aggregates. In this illustration, dimers are formed in the two-dimensional array of cylindrical holes that serve as physical templates. This schematic also illustrates the possible forces that may be exerted on the colloidal particle located in the region next to the rear edge of the liquid slug: the gravitational force (F_g), the capillary force (F_c) as a result of liquid meniscus, and the electrostatic force (F_e). Depending on the signs of charges on the surfaces of particles and bottom substrate, there might exist a repulsive or attractive electrostatic force between their surfaces.

assemblies still need to be demonstrated or greatly improved. To this end, we have recently introduced the use of surface relief structures as the physical templates to assemble spherical colloids into uniform aggregates characterized by a well-controlled size, shape, and structure.⁴⁶ This approach is now referred to as TASA, for template-assisted self-assembly.⁴⁷ The capability and feasibility of this approach have been fully demonstrated by generating a rich variety of polygonal and polyhedral aggregates from spherical colloids that are very difficult (or impossible) to fabricate using other methods.⁴⁶⁻⁵¹ Because it is relatively easy and straightforward to change the shape and dimensions of the templates using conventional microlithographic techniques, this new approach provides an effective route to colloidal aggregates with a range of diverse and complex architectures.

11.3.1 TEMPLATE-ASSISTED SELF-ASSEMBLY

The key step in a TASA process is the dewetting of a liquid slug of colloidal suspension confined within a fluidic cell. Figure 11.2 shows the schematic illustration of such a fluidic cell that is often constructed by sandwiching a square-shaped frame of Mylar thin film between two solid substrates.⁵² The surface of the bottom substrate is patterned with an array of relief templates (e.g., holes or trenches) using conventional microlithographic techniques. When the liquid slug slowly dewets through this cell, the capillary force exerted on its rear edge pushes the spherical colloids into the physical templates. The maximum number of particles that can be retained in each template and the structural arrangement among them are determined by the dimensional ratio between the template and the spherical colloids. As a result, this self-assembly procedure always gives the quantitative formation of colloidal aggregates with a prespecified size, shape, and internal structure. If necessary, the spherical colloids within each template hole can be fused together into a permanent piece by heating the entire system at temperatures slightly higher than the glass transition temperature of the colloidal material. In this case, the surfaces of colloids in physical contact are welded together due to the viscoelastic deformation of spherical colloids.^{53,54} The welded aggregates of spherical colloids can be subsequently released from the templates by sonicating the sample in a deionized water bath.

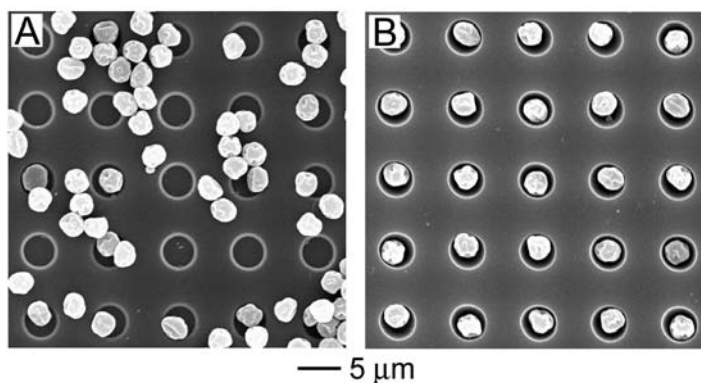


FIGURE 11.3 The SEM images of two TASA samples that were generated using polystyrene beads terminated in the amine group. The pH value of the colloidal dispersion was (A) 6.5 and (B) 8.5, respectively. The strong attraction between polymer beads and the template surface for sample A made it difficult to move the particles across the surface using capillary force alone. As a result, it was impossible to control the TASA process to generate aggregates with well-defined structures. We were able to obtain well-defined assemblies when this attractive interaction was switched to a repulsive one by increasing the pH value of the dispersion medium from 6.5 to 8.5. The irregular shape of these colloidal particles was intrinsic to this commercially obtained sample, not due to any deformation caused by the TASA process.

As illustrated in [Figure 11.2](#), the efficiency of a TASA process is determined by the balanced interplay of three forces: the capillary force (F_c) associated with the meniscus of the liquid slug; the gravitational force (F_g) due to a difference in density between the colloids and the dispersion medium; and the electrostatic interaction (F_e) between charged colloids and the substrate surface. In addition, Brownian motion may also play a significant role for colloidal particles of less than 1 μm in diameter. For colloidal particles made of organic polymers, the gravitational force could be neglected because the densities of polymers are often very close to that of water ($\sim 1.0 \text{ g/cm}^3$). For electrostatic interaction, a slightly repulsive force (as illustrated in [Figure 11.2](#)) is required to ensure that no particle will randomly stick to the substrate, including both recessed and raised regions of the surface. In this case, the colloidal particles can be somewhat levitated from the template surface by a certain distance when the colloidal suspension dewets through the fluidic cell. As a result, the capillary force (F_c) created by the liquid meniscus will be able to move the colloidal particles across the surface of the bottom substrate unless they are physically trapped by the template holes.

In practice, we can obtain repulsive interactions between colloidal particles and the bottom substrate by appropriately modifying their surfaces and/or by adjusting the pH value of the dispersion medium. For example, the surfaces of polymer beads prepared through an emulsion polymerization process are often terminated in the negatively charged sulfate ($-\text{SO}_4$) group, when potassium persulfate is used as the water-soluble initiator.⁸ For as-synthesized silica spheres, their surfaces are often terminated in the silanol group ($-\text{Si}-\text{OH}$), which can dissociate to give a negatively charged interface at pH values ≥ 6 .⁹ In these two cases, we have to treat the surface of bottom substrate with oxygen plasma to make its interface negatively charged at pH values ≥ 6 . Under these conditions, there will exist a repulsive interaction between the negatively charged template surface and the polymer beads (or silica spheres) involved in the TASA process.

We further demonstrated the importance of this repulsive electrostatic interaction by using colloidal particles whose surface were terminated in the amine group ($-\text{NH}_2$). For this system, we could control the sign of interaction between the colloidal particles and template surface by changing the pH value of dispersion medium. [Figure 11.3](#) shows the scanning electron microscopy (SEM) images of two samples that were prepared from colloidal dispersions with their pH values adjusted to 6.5 and 8.5, respectively. At pH = 6.5, there existed an attractive interaction between the positively

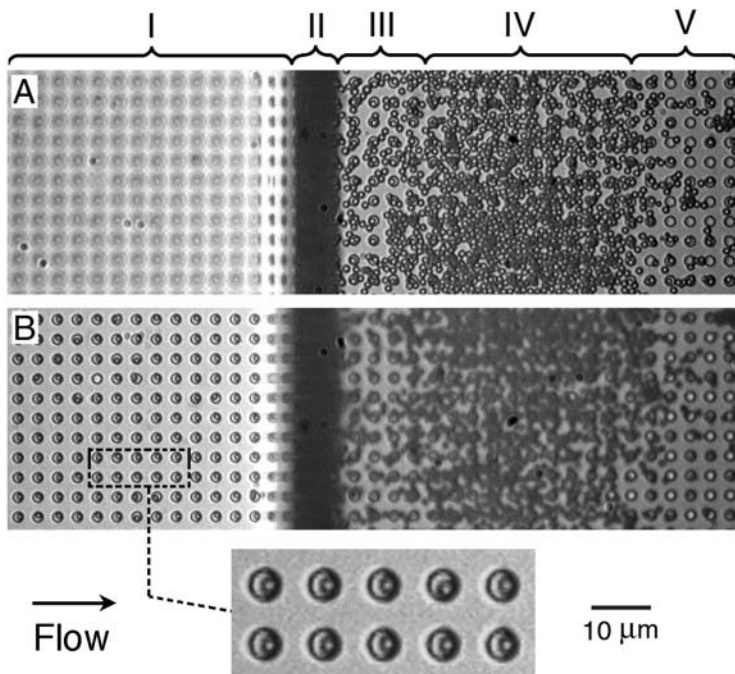


FIGURE 11.4 Optical microscopy images showing the self-assembly of 3.1- μm polystyrene beads in a two-dimensional array cylindrical holes that were 5 and 2.3 μm in diameter and depth, respectively. The arrow indicates the flow direction. The dark line (region II) in the middle of the image represents the rear edge of the liquid slug. The sample was focused on the liquid-filled (A) and dewetted (B) region of the fluidic cell.

charged polymer beads ($-\text{NH}_3^+$) and the negatively charged template surface. This attraction was sufficiently strong that it was impossible to move these colloidal particles across the template surface. These colloids tended to be randomly deposited on the entire surface of the template during the dewetting process. At $\text{pH} = 8.5$, this attractive interaction was significantly weakened (or even switched to a slightly repulsive one), and the capillary force was able to push one polymer bead into each template hole and form a well-defined assembly.

11.3.2 MECHANISM FOR THE TASA PROCESS

As illustrated in [Figure 11.2](#), the capillary force (F_c) created by the meniscus at the rear edge of the liquid slug plays the most important role in determining the success of a TASA process. This force has to be sufficiently strong to beat the Brownian motion and thus push colloidal particles into the template holes. When the colloidal dispersion flows across the fluidic cell, the capillary force also has to be strong enough to clean up the top surface of the template holes. As a result, the colloidal particles will only be trapped in the template holes, not on the raised regions of the template substrate. We have followed the entire dewetting process using an optical microscope in an effort to gain some deep insights into the mechanism involved in a TASA process.

Figure 11.4 shows two optical micrographs that were captured during the *in situ* observation of a TASA process. In this case, the diameters of the polystyrene beads and the cylindrical holes were 3.1 and 5 μm , respectively. Only one polystyrene bead could be possibly retained in each hole. The influence of gravitational force was minimized by maintaining the flow direction of liquid slug (indicated by an arrow) in the horizontal direction. The dark line (region II) in the middle of each image represented the rear edge of the liquid slug. In region I, only the template holes were filled by colloidal particles and water. In regions III to V, the entire cell was still filled with the

colloidal dispersion. Because of a large difference in the refractive index between water and air, it was impossible to focus simultaneously on both sides of the cell across the dark line. Figure 11.4A shows an optical image where the liquid side (regions III to V) was in focus. Because polystyrene beads that were not restrained by the template holes were pushed to move along with the liquid at a certain speed in the direction indicated by the arrow, they were most concentrated in region IV rather than region III. The density of colloidal particles in region V was probably similar to that of the original dispersion. In region III, almost every hole had been occupied by one polymer bead, while only a few template holes in region V were filled by the polymer beads. Different from region I, the polymer beads physically trapped by templates in regions III and V were randomly positioned in the holes. Figure 11.4B gives the image where region I was in focus. It can be clearly seen that almost every hole had one polymer bead physically trapped within it while the top surface of the template was essentially free of particles. This observation indicates that all the beads not trapped by the templates were rolled across by the capillary force exerted through the meniscus of the liquid slug. Note that almost all the polymer beads trapped in the holes had been positioned at equivalent sites to yield a regular two-dimensional array of beads (see the inset at the bottom of Figure 11.4). Because there was still water in each template hole, we believe that such a spatial ordering was largely driven by the capillary force (along the direction indicated by the arrow) caused by the rear edge of the liquid slug and the force induced by the shear flow.⁵⁵

This *in situ* observation also provides an intuitive insight regarding the efficiency of a TASA process. The colloidal particles in the liquid slug always have a certain probability to be trapped by the template holes as a result of sedimentation. When their concentration is not sufficiently high, only a small portion of the template holes can be filled through this mechanism (as seen in region V). As their concentration becomes sufficiently high, the majority of the holes will be completely occupied by colloidal particles (as seen in regions III and IV), even before the rear edge of the liquid slug has passed through these regions. The capillary force has a dual function in this process: (1) serving as a scavenger to clean up the top surface of the template once the liquid has dewetted from region I and (2) increasing the concentration of colloidal particles in regions III and IV by moving untrapped particles from region I to these two regions. This hypothesis was further supported by another observation: in most cases, very few template holes in the dewetted region were occupied by colloidal particles when the dewetting process just started. After the edge of the liquid slug had moved forward for a certain distance and enough colloidal particles had been concentrated in regions II to IV, the holes could be filled with colloidal particles at a yield approaching 100%. This *in situ* study also indicates that we can easily obtain perfect arrays of colloidal aggregates as long as the colloidal particles have reached a high enough concentration.

11.3.3 CONTROL OVER THE SELF-ASSEMBLED STRUCTURES

There are a number of ways to control the size, shape, and structure of aggregates self-assembled from spherical colloids. In our initial demonstrations, we have focused on templates with cylindrical cross sections because we happen to have such photomasks in our laboratory.⁴⁶ Even with these simple templates, we were able to obtain a range of polygonal and polyhedral aggregates. In these cases, the number of spherical colloids retained in each cylindrical hole and thereby the structural arrangement among these colloids are controlled by the ratios between the dimensions (diameter D and depth H) of holes and the diameter (d) of the spherical colloids. By simply varying these ratios, we have been able to obtain a range of uniform aggregates having well-defined polygonal or polyhedral architectures. Figure 11.5 shows the SEM images of several examples of polygonal aggregates that were assembled by templating polystyrene beads against two-dimensional arrays of cylindrical holes. These holes were fabricated in thin films of photoresist with dimensions of $D = 2 \mu\text{m}$ and $H = 1 \mu\text{m}$. By reducing the diameter of polystyrene beads from 1.0 to 0.6 μm , we could obtain uniform aggregates of colloidal particles in the form of dimers, trimers, pentagons, and hexagons.⁴⁷ The overall yield of the prespecified aggregates as calculated from the geometric

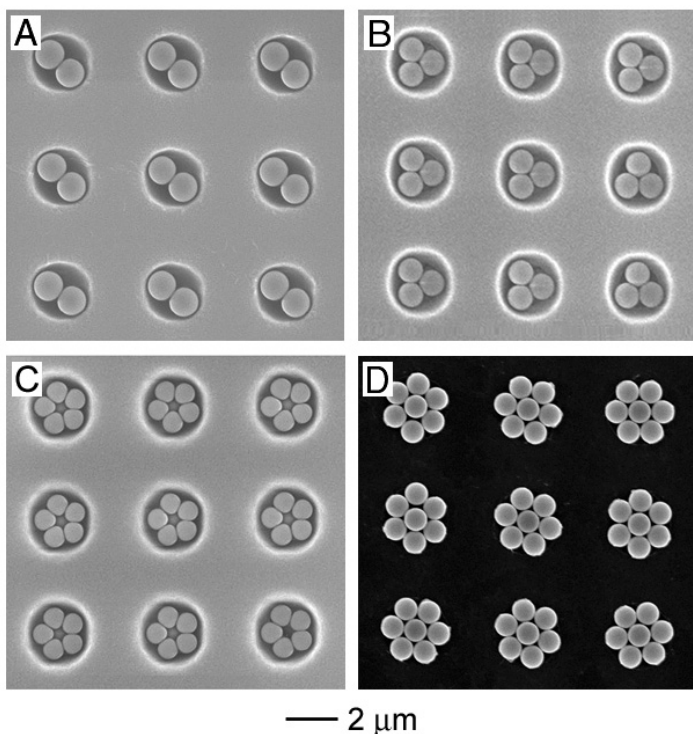


FIGURE 11.5 The SEM images of several typical examples of polygonal aggregates that were formed through self-assembly by templating polystyrene beads against two-dimensional arrays of cylindrical holes: (A) dimers of 1.0- μm beads, (B) trimers of 0.9- μm beads, (C) pentagons of 0.7- μm beads, and (D) hexagons of 0.6- μm beads. The cylindrical holes used in all these experiments were $\sim 2\ \mu\text{m}$ in diameter and $\sim 1\ \mu\text{m}$ in depth. The photoresist pattern still remained on the substrate for samples A to C, and had been removed for sample D.

parameters of the template and the polymer beads were usually higher than $\sim 90\%$. Common defects were aggregates containing fewer polymer beads than expected. This kind of defect could be eliminated by varying the concentration of the colloidal dispersion and/or by flowing a moderately dilute ($< 0.1\%$) colloidal dispersion through the fluidic cell more than once. By optimizing these parameters, we were able to generate defect-free arrays of colloidal aggregates as large as several square millimeters in area and contained more than 10^5 elements. At the current stage of development, this number is mainly restricted by the areas of test patterns on our photomasks. We believe that the self-assembly process, itself, should be extendable to substrates as large as tens of square centimeters in area. In other experiments, it was also demonstrated that the depth of template holes could be increased to generate multilayered structures (such as polyhedral aggregates) from spherical colloids.

We have also fully exploited templates other than cylindrical holes to fabricate aggregates of spherical colloids with more complex structures. [Figure 11.6A](#) shows the SEM image of a two-dimensional array of triangular aggregates that were assembled by templating against a two-dimensional array of prism-shaped holes. [Figure 11.6B](#) shows the SEM image of a two-dimensional array of bent trimers that were assembled in two interconnected cylindrical holes. The use of templates with noncylindrical cross sections has also made it possible to control the spatial orientation of the aggregates in the plane of the two-dimensional assembly. [Figures 11.6C and D](#) display chainlike aggregates that were assembled by templating against straight trenches patterned in thin films of photoresist. In these two cases, the length of aggregates was solely determined by the longitudinal dimension of the trenches, and the internal structure (linear vs. zigzag) was defined by the relative ratio between the lateral dimension of templates and the diameter of spherical

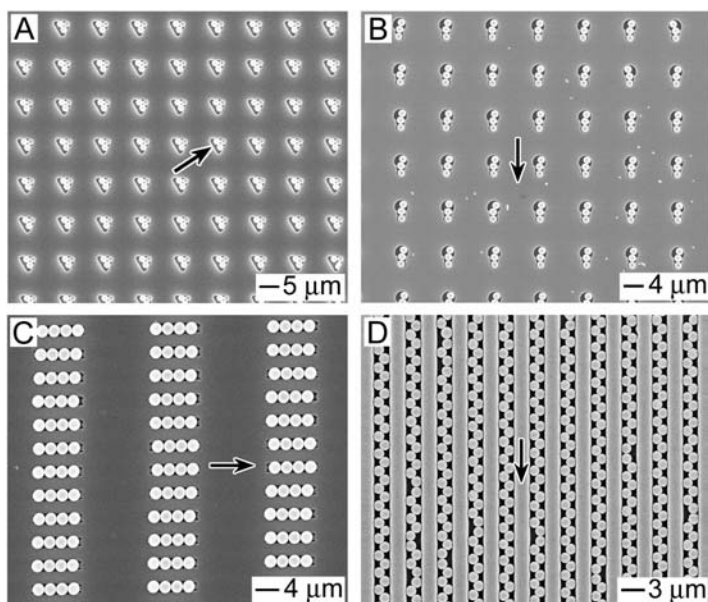


FIGURE 11.6 The SEM images of two-dimensional arrays of colloidal aggregates that were assembled under the confinement of templates other than cylindrical holes. The arrow indicates the flow direction for the liquid slug. (A) Triangular templates of 5 μm in edge length, and 1.75- μm silica spheres; (B) templates composed of two connected cylindrical holes of 2 and 3 μm in diameter, and 1.75- μm silica spheres; (C) rectangular templates with lateral dimensions of 8 $\mu\text{m} \times 2 \mu\text{m}$, and 2- μm polystyrene beads; and (D) trenches of 2.0 μm in width and 2 cm in length, and 1.3- μm polymer beads. Note that the use of noncircular patterns as the templates also allowed one to control the spatial orientation of the colloidal aggregate in the plane of the substrate.

colloids. Again, it was possible to achieve a preferential orientation (in the plane of the self-assembled structures) for these aggregates by using templates with noncircular cross sections. These experiments clearly demonstrated that the TASA process has the ability to assemble spherical colloids into complex aggregates on solid supports that are characterized by both positional and orientational orders.

11.3.4 HYBRID AGGREGATES OF SPHERICAL COLLOIDS

The structural complexity of colloidal aggregates can be further increased by sequentially dewetting dispersions of different colloids through the same fluidic cell.^{47,48} The success of this approach depends on the ability to precisely control the dimensional ratio between the template and the spherical colloids to ensure that only a well-controlled number of particles are added to the template in each step. Figure 11.7A shows the SEM image of such a sample that contains an array of hybrid dimers assembled from 1.6- μm silica colloids and 2.8- μm polystyrene beads. In this demonstration, the 2.8- μm polymer beads were first delivered (using TASA) into the array of cylindrical holes ($D = 5.0 \mu\text{m}$, $H = 2.5 \mu\text{m}$) patterned in a thin film of photoresist. The polymer bead in each cylindrical hole was in physical contact with the wall as a result of the shear force (due to the liquid flow) and the attractive capillary force generated during solvent evaporation.⁵⁵ The position of each polymer bead in the cylindrical hole could be fixed by heating the sample to a temperature slightly higher than the glass transition temperature (T_g) of the polymer for a few minutes. This substrate containing a two-dimensional array of polymer beads on its surface was then used in another step of TASA to add one more particle of smaller size into the remaining space of each cylindrical hole. In principle, it is possible to keep adding more particles with a decreasing size to

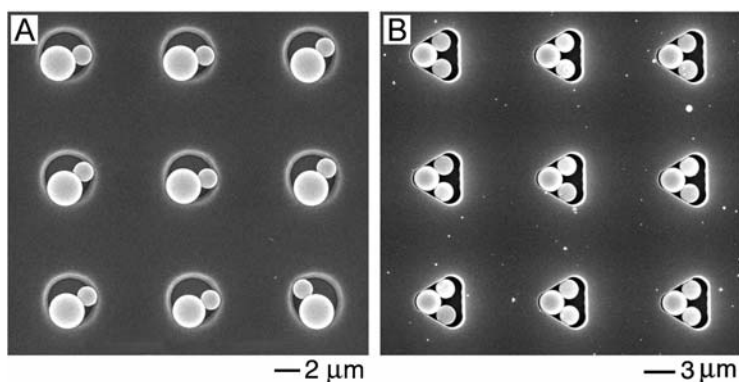


FIGURE 11.7 (A) The SEM image of a two-dimensional array of hybrid dimers self-assembled from 2.8- μm polystyrene beads and 1.6- μm silica spheres. The different spherical colloids were added to each template hole through two steps of TASA. (B) The SEM image of a two-dimensional array of H_2O -shaped aggregates that were generated using two-step assembly from polystyrene and silica spheres of 2.5 and 1.8 μm in diameter, respectively.

a colloidal aggregate to form more complex hierarchical structures. Besides their difference in size, the colloidal particles involved in various steps of TASA could also be different in chemical composition, as well as in surface or bulk properties.

Figure 11.7B shows the SEM image of another array of hybrid aggregates that were assembled from 2.5- μm polystyrene beads and 1.8- μm silica colloids. By choosing prism-shaped holes as the templates, it has been possible to form H_2O -shaped aggregates by adding one polystyrene bead and two silica spheres into each template hole through two separate steps of TASA. Again, colloidal particles in each hole maintained physical contacts due to the attractive capillary force created during solvent evaporation. Once formed, the colloidal particles in each aggregate could be permanently welded into a single unit by heating the sample to a temperature slightly higher than the glass transition temperature of the polymer. Afterward, these aggregates could be released into a liquid medium by dissolving the photoresist film in isopropanol under sonication. It was found that the yield of this multistep TASA process strongly depended on the difference between the diameters of spherical colloids used in each step. A yield as high as $\sim 90\%$ has been obtained when the diameters of these colloidal spheres were relatively close to each other (when their difference in size was within 20%). These hybrid aggregates are expected to find uses as the building blocks in other self-assembly processes to generate periodic structures with higher complexities.⁵⁶ Even for the self-assembly strategy itself, it might be useful and extendable to other systems that involve colloidal particles made of soft materials (e.g., cells and vesicles).⁵⁷

11.4 OPALINE LATTICES OF SPHERICAL COLLOIDS

A large number of different approaches have been demonstrated for crystallizing spherical colloids into three-dimensionally periodic structures (or opaline lattices).¹¹⁻¹⁸ Several of them are, in particular, useful in generating opaline lattices over relatively large areas and with well-controlled structures. For example, sedimentation in a gravitational field provides a simple and effective method for generating closely packed structures from spherical colloids with sizes larger than ~ 500 nm.⁵⁸⁻⁶⁰ The method based on repulsive electrostatic interactions can organize highly charged colloids into body-centered-cubic (bcc) or face-centered-cubic (fcc) crystals with thickness up to several hundred layers.¹⁵ The approach based on attractive capillary forces (as a result of solvent evaporation) has been used in a layer-by-layer fashion to fabricate three-dimensional opaline lattices as thick as 50 layers.⁶⁰⁻⁶⁴ As we are limited by space, here we concentrate on the confined self-assembly

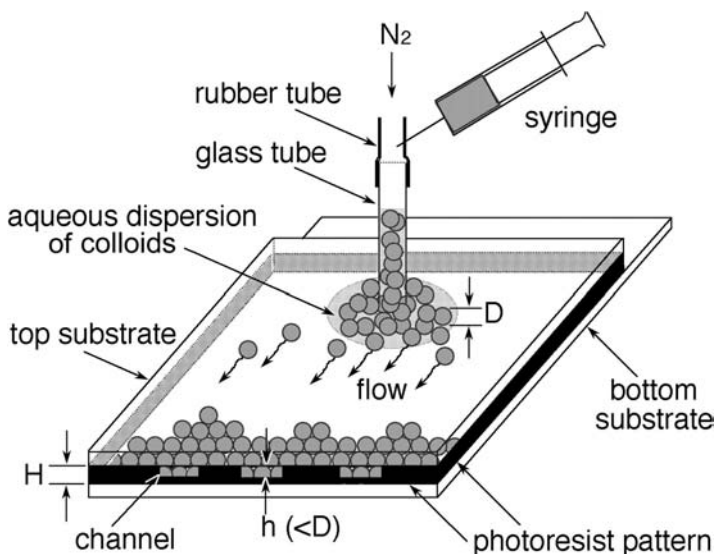


FIGURE 11.8 A schematic illustration of the experimental procedure used for the confined self-assembly of spherical colloids into a three-dimensional opaline lattice.

(CSA) method mainly developed by our research group.⁶⁵⁻⁷⁰ In this method, physical confinement and shear flow are combined in a unique way to assemble spherical colloids (regardless of their size, composition, or surface properties) into large opaline lattices (over several square centimeters in area) with thickness ranging from a monolayer up to several hundred layers. The opaline lattice formed using this method exhibit a cubic-close-packed structure, with its (111) planes parallel to the surfaces of solid substrates used to construct the microfluidic cell.

11.4.1 CRYSTALLIZATION BY CONFINED SELF-ASSEMBLY

Monodispersed spherical colloids often organize themselves into long-range ordered lattices when they are subjected to a physical confinement.⁷¹⁻⁷³ Highly charged spherical colloids, for example, spontaneously order into a bcc or fcc structure when they are confined between two substrates and their volume fraction has reached a value $>50\%$.^{15,74} We have recently extended this approach to assemble spherical colloids into three-dimensional opaline lattices by combining physical confinement and hydrodynamic shear flow.⁶⁵⁻⁷⁰ In this new approach, spherical colloids (regardless of surface and bulk properties) with diameters in the range of 50 nm to 1 μm were injected into a specially designed microfluidic cell (Figure 11.8) and subsequently concentrated and crystallized into a highly ordered lattice. Continuous sonication was the key to the success of this approach: the vibration caused by sonication can place each spherical colloid at the lattice point corresponding to a thermodynamic minimum. We have demonstrated the capability and feasibility of this approach by assembling polystyrene beads or silica spheres into opaline lattices over areas as large as several square centimeters.

The microfluidic cell shown in Figure 11.8 could be fabricated using either photolithographic or nonphotolithographic methods. For example, we could construct such a cell by sandwiching a square frame of photoresist film between two glass slides tightened with binder clips. In this case, the photoresist film was spin-coated on the bottom substrate and exposed to ultraviolet (UV) light for ~ 67 s through a mask patterned with the square frame ($\sim 2 \times 2$ cm^2 in area, with a line width of ~ 50 μm). This same photoresist film was then exposed to UV light for an additional ~ 5 s through another mask covered with a test pattern of parallel lines (500 μm in width and separated by 100 μm). These two masks were aligned such that the lines on the second mask overlapped with

at least one of the sides of the square frame. After developing, a square frame of photoresist was formed on the surface of the bottom substrate; at least one side of the frame had an array of shallow trenches in its surface that could let the solvent flow through while keeping the colloidal particles in the cell. More recently, we extended the designs of fluidic cells to systems forgoing the requirement of cleanroom facilities. A number of convenient methods that rapidly generate fluidic cells were demonstrated by sandwiching a square frame of Mylar film between two glass substrates and tightening with binder clips.⁵²

After an aqueous dispersion of monodispersed spherical colloids was injected into the cell, a positive pressure was applied through the glass tube to force the solvent (water) to flow through the channels. The beads were accumulated at the bottom of the cell, and crystallized into a three-dimensional opaline lattice under continuous sonication. So far, we have successfully applied this approach to assemble monodispersed colloids (both polystyrene beads and silica spheres) into ccp lattices over areas of several square centimeters. This method is relatively fast: opaline lattices of a few square centimeters in area could be routinely obtained within several days. This method is also remarkable for its flexibility; it could be directly employed to crystallize spherical colloids of various materials with diameters between 200 nm and 10 μm into three-dimensional opaline lattices. In addition, this procedure could be easily modified to crystallize spherical colloids with diameters as small as 50 nm.⁶⁷

11.4.2 CONTROL OVER THE THICKNESS OF OPALINE LATTICES

The successful application of three-dimensional opaline lattices as photonic crystals requires a good control over the thickness for these spatially ordered lattices. For example, the midgap rejection ratio of an opaline lattice can be continuously tuned from 0 to 20 dB by simply controlling the thickness of this lattice in the propagation direction of incident light.⁷⁵ For opaline lattices assembled within microfluidic cells, the number of (111) planes normal to the glass substrates is determined by the ratio between the thickness of cell (H) and the diameter of spherical colloids (D) (see Figure 11.8). By changing either parameter, the total number of layers of the opaline lattice could be continuously changed from 1 to more than 200.⁶⁶ More specifically, the thickness of a microfluidic cell could be controlled from ~ 0.5 to 20 μm by using different photoresists, photoresist thinners, or multiple steps of spin-coating. For opaline lattices with thicknesses between 20 and 100 μm , we had to switch to alternative materials, such as Mylar thin films (Fralock, Canoga, CA).⁵²

Figure 11.9 shows the SEM images of several typical examples of opaline lattices assembled from monodispersed spherical colloids, and characterized by different thicknesses. Figure 11.9A shows the SEM image of 1.05- μm polystyrene beads assembled in a microfluidic cell 1.2 μm thick. In this case, only a monolayer could be formed. Self-assembly of 480-nm polystyrene beads in a cell of the same thickness could give a bilayer (Figure 11.9B). Opaline lattices of spherical colloids assembled in cells with thicker spacers also maintain the demonstrated long-range order, with its (111) planes oriented parallel to the glass substrates. Figure 11.9C and D show the cross sections of two opaline lattices assembled from 480-nm and 230-nm polystyrene beads in 12- μm -thick microfluidic cells. The number of (111) planes for these two opaline lattices was ~ 25 and ~ 60 , respectively. These two SEM images also illustrate the uniformity and well-controlled number of (111) layers for these opaline lattices. Such a three-dimensional opaline lattice can reject a very narrow wavelength interval of light with the middle position determined by the Bragg equation and the intensity determined by the number of (111) planes.

11.4.3 CONTROL OVER THE DENSITY AND STRUCTURE OF DEFECTS

Defects seem to be inevitable in all three-dimensional opaline lattices of spherical colloids because a thermodynamic equilibrium is seldom accomplished in the self-assembly process. The presence of defects could have a profound influence on the structure and thus photonic band gap properties

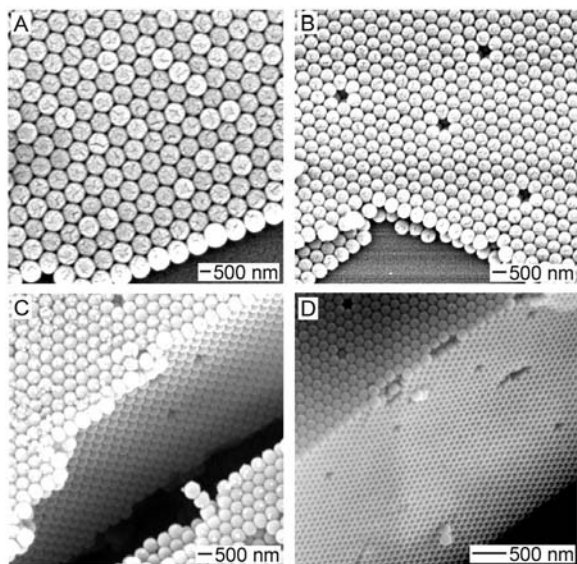


FIGURE 11.9 SEM images of several opaline lattices that were fabricated by assembling (A) 1.05- μm polystyrene beads in a 1.2- μm thick cell; (B) 0.48- μm polystyrene beads in a 1.2- μm thick cell; (C) 0.48- μm polystyrene beads in a 1.2- μm thick cell; and (D) 230-nm polystyrene beads in a 12- μm thick cell.

of these opaline lattices. It was predicted that approximately a 2% deviation in periodicity could destroy the complete photonic band gap of an inverse opaline structure.⁷⁶ On the other hand, the application of colloidal crystals could also be greatly enhanced by doping them with smaller or larger colloids to generate defect states in their photonic band structures.⁷⁷⁻⁷⁹ For example, the formation of a well-defined defect inside a three-dimensional opaline lattice might allow the propagation of photons at a specific frequency within the otherwise forbidden band gap. The frequency of this allowed mode can be conveniently controlled by varying the structure and dimension of this defect. As a result, it is of great importance to understand quantitatively the influence of defect structure and density on the photonic band gap properties of opaline lattices.

We have extended the capability of confined self-assembly to prepare three-dimensional opaline lattices of spherical colloids with well-controlled defects by doping these lattices with known amounts of smaller colloids.⁸⁰ As discussed in a number of studies,⁸¹⁻⁸⁶ the introduction of spherical colloids with different sizes into the otherwise monodispersed sample of spherical colloids may lead to disordering and phase segregation in the crystallization process. Unlike doping a semiconductor, which is often carried out by the diffusion of acceptor or donor atoms into the host lattice that has already been formed in advance, colloids of different sizes (potential defect sites) have to be added to the dispersion of host colloids before an opaline lattice is constructed from these colloids. For example, we could choose 230-nm polystyrene beads to construct the host lattice, and introduce 155-nm polystyrene beads as the dopant to generate defects. These dopants had to be added into the aqueous dispersion of 230-nm polystyrene beads before they were organized into three-dimensional opaline lattices. A major advantage of this approach was the ability to control precisely the density of defects in an opaline lattice of spherical colloids. In addition to the particular dopant described here, other types of dopants (e.g., colloids with a larger size than the host and colloids made of other materials) can also be easily incorporated into the three-dimensional opaline lattices.

The correlation between doping level and defect structure has been studied by characterizing the dried opaline samples with SEM. [Figure 11.10](#) shows the SEM images of three opaline lattices that had been doped with different levels of small dopants. [Figure 11.10A](#) and [B](#) show the (111) planes and cross-sectional view of an opaline lattice of 230-nm polystyrene beads that had been doped with 1.4% 155-nm polystyrene beads. The arrows highlight a few dopant colloids, which

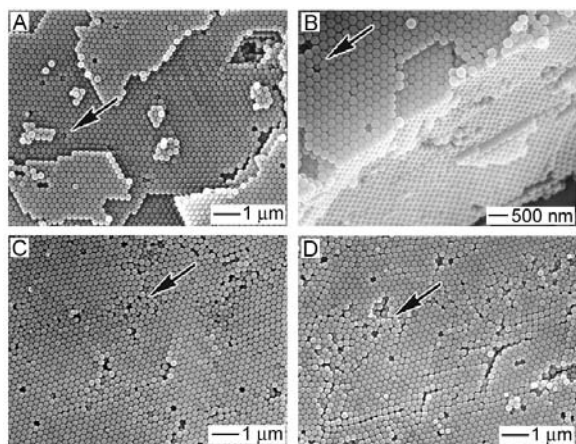


FIGURE 11.10 The SEM images of three opaline lattices assembled from aqueous dispersions of 230-nm polystyrene beads that had been doped with different levels of 155-nm polystyrene beads. (A, B) The (111) planes and cross-sectional view of an opaline lattice with a doping level of $\sim 1.4\%$. Doping at such a low percentage only generated some point defects (such as those indicated by the arrows) in this three-dimensional lattice, which still exhibited a long-range order in all three dimensions. (C, D) The (111) planes of two other opaline lattices with doping levels of $\sim 9.1\%$ and $\sim 17\%$, respectively. As indicated by arrows, the 155-nm polymer beads tended to segregate into isolated, relatively small domains at such high levels of doping, and these lattices became disordered over the long-range scale.

mainly existed as point defects in this three-dimensional lattice. At such a low level of doping, the crystallinity or long-range order was essentially preserved in this three-dimensional lattice. For samples doped with higher levels of small colloids, point defects could still be observed and new types of defects started to appear, which seemed to have a more profound influence on the long-range order for these three-dimensional lattices. Figure 11.10C shows the top view of an opaline lattice of 230-nm polystyrene beads that had been doped with 9.1% 155-nm polystyrene beads. In addition to point defects, dislocations were also observed in this assembled lattice with slight variance in the domain orientation across each dislocation point. The dopants also tended to segregate from the host colloids into isolated, relatively smaller domains within the three-dimensional host lattice. Further increases in the doping level up to 17% were accompanied with a higher density of dislocations, and much smaller domain sizes or significant deterioration in crystallinity for the host lattice (Figure 11.10D). This SEM analysis also reveals the importance of monodispersity in achieving long-range order in an opaline lattice self-assembled from spherical colloids. When the concentration of the dopant reached a certain level, a phase segregation occurred, which may lead to the formation of opaline lattices with relatively small domain sizes. In accordance, the attenuation (or rejection ratio) of the band gap was also decreased monotonically as the doping level was increased.⁸⁰

11.4.4 CONTROL OVER THE CRYSTAL ORIENTATION OF OPALINE LATTICES

When grown on the surface of a flat substrate, the opaline lattice of spherical colloids often has its (111) planes oriented parallel to the surface of this substrate. To generate opaline lattices with other orientations, we must use substrates whose surfaces are patterned with appropriate arrays of relief structures.⁸⁷⁻⁹⁰ For example, we have recently demonstrated that it was possible to fabricate (100)-oriented opaline lattices by employing a square array of cylindrical holes as the template to control the spatial orientation (Figure 11.11A). The dimensions of these cylindrical holes had to be selected such that a square planar tetramer of the spherical colloids could be formed in each cylindrical hole during the nucleation process. These tetramers could then serve as seeds to define

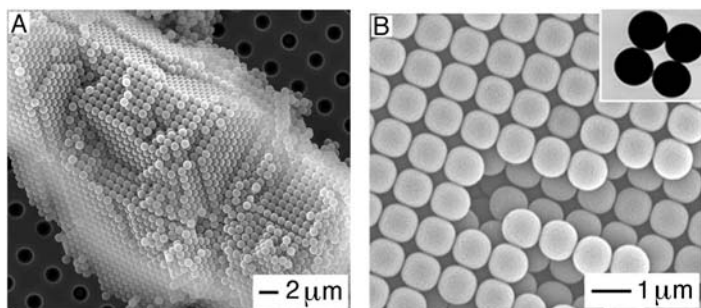


FIGURE 11.11 (A) The SEM image of a three-dimensional opaline lattice of 1- μm polystyrene beads that was fabricated by templating against a two-dimensional array of cylindrical holes that were 2 μm in diameter, 1.2 μm in depth, and separated by 2 μm . Directed by the relief structures on the substrate, the (100) planes, rather than (111), of this three-dimensional opaline lattice had been oriented parallel to the surface of the solid substrate. (B) An opaline lattice that was crystallized from an aqueous dispersion of spherical polymer beads that had been doped with $\sim 1\%$ of their square tetramers. The inset shows the TEM image of one such tetramer. Note that the presence of these square templates had resulted in the formation of a three-dimensional opaline lattice that bears a symmetry similar to that of the square tetramer.

and direct the growth of the opaline lattice in the direction perpendicular to the substrate. When the separation between adjacent cylindrical holes matched the center-to-center distance between the spherical colloids in the close-packed lattice, an unusual opaline lattice (Figure 11.11A) would be generated, in which the (100) planes, rather than the (111), were oriented parallel to the surface of the solid substrate.

In another demonstration, we found that the small aggregates formed via the TASA process were immediately useful as templates to generate three-dimensional lattices of spherical colloids with symmetries or orientations other than those commonly observed for the spherical systems on flat substrates.⁴⁶ For example, when 1% of the square-shaped, tetramer aggregates was mixed with spherical colloids, they were able to direct the spherical colloids into an opaline lattice with its (100) planes oriented parallel to the surface of a flat substrate (Figure 11.11B). In this case, the three-dimensional opaline lattice tended to develop a symmetry similar to the added aggregates during the crystallization process. This ability to control the orientation of an opaline lattice provides another way to change the photonic properties of a colloidal crystal.

11.4.5 INVERSE OPALS: CRYSTALLINE LATTICES OF INTERCONNECTED AIR BALLS

Synthesis by templating against opaline lattices provides a convenient and versatile method for generating macroporous materials with highly ordered structures. After an opaline lattice of spherical colloids has been dried, the void spaces ($\sim 26\%$ in volume) among the colloids can be easily infiltrated with a liquid precursor through capillary action.⁹¹ Subsequent solidification or precipitation of the precursor and removal of the template colloids gives a three-dimensional porous structure. These porous materials are referred to as “inverse opals” or “inverted opals” because they have a long-range ordered three-dimensional open framework complementary to that of an opaline lattice.⁹²⁻¹⁰² An inverse opal can also be considered a periodic lattice of uniform air balls interconnected to each other by small circular “windows.” The volume fraction of solid material in an inverse opal can be easily controlled by changing the concentration of the precursor solution or the number of infiltration steps. The fidelity of this templating method is mainly determined by van der Waals interactions, the wetting of the colloidal surfaces by the precursor solution, kinetic factors such as the filling of void spaces within the template lattice, and the volume shrinkage of precursor associated with the solidification process.

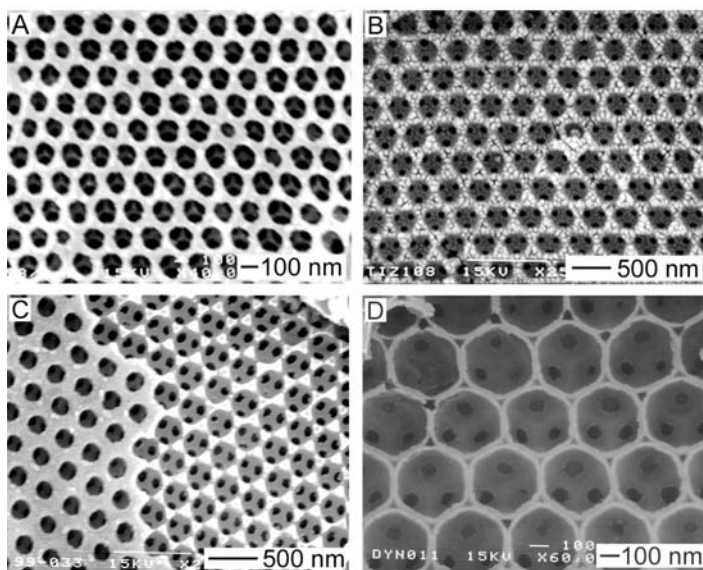


FIGURE 11.12 SEM images of inverse opals that were fabricated by templating (A) a UV-curable organic polymer, (B) a sol-gel precursor to SnO_2 , (C) a sol-gel precursor to SiO_2 , and (D) a sol-gel precursor to TiO_2 against opaline lattices of polystyrene beads. The polymer beads have been selectively removed through etching with toluene.

Templating against three-dimensional opaline arrays of spherical colloids has been successfully applied to the fabrication of inverse opals from a variety of materials, including organic polymers, ceramic materials, inorganic semiconductors, and metals.⁹²⁻¹⁰⁶ Fabrication based on this new approach is remarkable for its simplicity, and for its fidelity in transferring the structure from the template to the replica. The size of air balls or the periodicity of an inverse opal can be precisely controlled and readily tuned by changing the size of the spherical colloids. There is no doubt that a similar approach is extendible to many other functional materials. The only requirement seems to be the availability of a precursor that can infiltrate into the void spaces among colloidal spheres without significantly swelling or dissolving the template colloids (usually made of an organic polymer or silica). Some gaseous precursors have also been incorporated into this process.¹⁰⁷⁻¹¹¹ At present, the smallest spherical colloids that have been successfully used in this method are around 35 nm in diameter;¹¹² the lower limit to the particle size that can be incorporated into this technique has not been completely established.

Figure 11.12A shows the SEM image of a polymeric inverse opal that was fabricated by filling the opaline template with a photocurable polymer to polyurethane, followed by cross-linking the precursor with UV light and selective removal of the polystyrene beads in toluene.⁹³ The top surface of this inverse opal is characterized by a hexagonal array of circular pores through which the structures underneath can also be clearly observed. Inverse opals of inorganic materials such as ceramics can be obtained by templating sol-gel precursors against opaline lattices of polymer beads. In these cases, the initial precursor solution can completely fill the void spaces within the template. Upon hydration and subsequent evaporation of the alcohol, the inorganic oxide often forms thin coatings around the spherical colloids. Figure 11.12B shows an SnO_2 inverse opal formed by templating against a three-dimensional opaline lattice of 400-nm polystyrene beads.¹¹³ As illustrated by this image, this inverse opal has a periodic structure complementary to that of the original template. Windows into the adjacent spherical void spaces are observed where the close-packed particles were in contact in the original opaline lattice. Figure 11.12C and D show the SEM

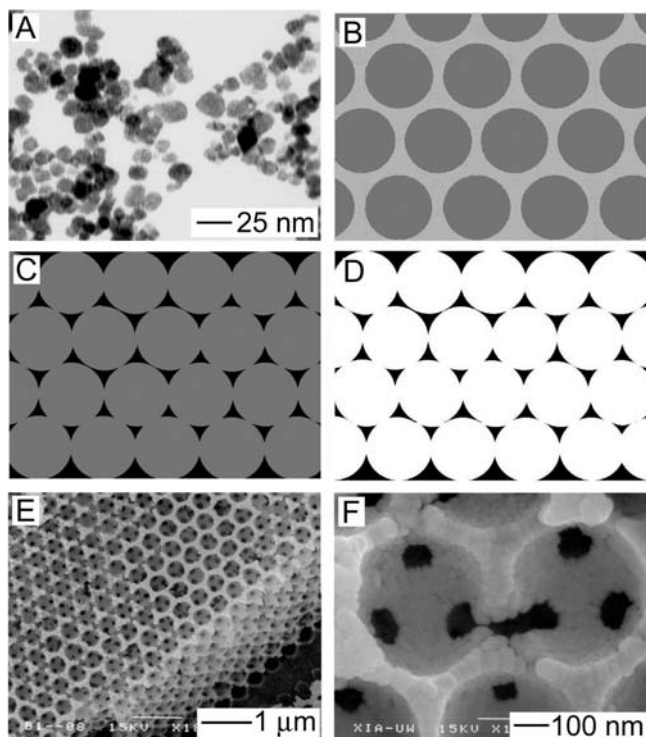


FIGURE 11.13 (A) The TEM image of magnetite nanoparticles contained in Ferrofluid EMG 308. (B–D) Schematic illustration of the hierarchical self-assembly process that was used to generate magnetite inverse opals by templating the magnetite nanoparticles against cubic-close-packed lattices of polystyrene spheres, followed by selective removal of the spheres. (E, F) SEM images of a magnetite inverse opal that were fabricated by templating against a three-dimensional opaline lattice made of 480-nm polystyrene beads. These two images indicate that the air balls are interconnected to each other and that the void spaces among the closely packed polymer spheres are filled by the magnetite nanoparticles with a volume fraction close to 26%.

images of two more examples of inverse opals that were fabricated by templating sol–gel precursors to SiO_2 and TiO_2 against opaline lattices of 480-nm polystyrene beads.¹¹³

11.5 HIERARCHICAL SELF-ASSEMBLY OF COLLOIDAL PARTICLES

Templating against opaline lattices of spherical colloids represents a general approach to the fabrication of macroporous materials (or inverse opals) with long-range ordered structures. The major problem associated with the infiltration method described in Section 11.4.5 is the difficulty in achieving a dense, complete filling of the void spaces among the colloidal particles. Hierarchical self-assembly overcomes this problem by crystallizing spherical colloids in a dispersion medium that contains the desired material in the form of nanoscale particles.¹¹⁴ During this self-assembly process, the nanoparticles can be simultaneously packed into a dense solid around the spherical colloids when these spherical colloids organize themselves into an opaline lattice. This process can lead to the formation of more uniform and better-controlled inverse opals over relatively larger areas than those generated by infiltrating the three-dimensional opaline lattice with a liquid or gaseous precursor. In this hierarchical self-assembly approach, the only requirement seems to be that the desired material can be supplied as suspensions of nanometer-sized particles. The size of these nanoparticles can be as large as one tenth of the diameter of the spherical colloids. Thanks to many years of efforts, almost all kinds of solid materials (including metals, semiconductors, and

dielectrics) can now be readily processed into nanoparticles using various chemical or physical methods.¹¹⁵⁻¹²⁰ In this regard, the hierarchical self-assembly approach described in this section may provide a simple, convenient, and practical route to inverse opals made of various functional materials.

Several groups have demonstrated the capability and feasibility of this hierarchical assembly approach by templating nanoparticles of titania,¹²¹ silica,¹²² or gold¹²³ against three-dimensional opaline lattices made of polystyrene beads or silica spheres. More recently, we have extended the scope of this approach to fabricate inverse opals whose photonic properties could be addressed or manipulated with an external magnetic field (Figure 11.13).¹²⁴ In this demonstration, monodispersed polystyrene beads were assembled into an fcc array (Figure 11.13B) in an aqueous ferrofluid (EMG 308, Ferrofluidics, Nashua, NH) that contained magnetite particles with sizes <15 nm (see Figure 11.13A for a TEM image). When the solvent evaporated, this crystalline array was condensed into a cubic-close-packed lattice (Figure 11.13C), with the magnetite nanoparticles precipitating out as a dense, continuous solid within the void spaces among the polystyrene beads. The filling fraction of magnetite nanoparticles could be conveniently changed in the range of 0 to 26% by controlling the ratio between the concentrations of spherical colloids and nanoparticles. The entire process could be completed within a relatively short period of time because the nanoparticles had already been placed around the spherical colloids and no transport of the material through the mesoscale pores was involved. When the spherical colloids were selectively removed through calcination at an elevated temperature or wet etching in a solvent, an inverse opal of magnetite was obtained (Figure 11.13D).

Figure 11.13E shows the SEM image of an inverse opal that was fabricated by self-assembling 480-nm polystyrene beads in the presence of magnetite nanoparticles. The templates have been removed through a calcination process.¹²⁴ This image indicates the existence of long-range order in all three dimensions of space. It was possible to generate such highly ordered structures over areas as large as several square centimeters. Although cracks might be formed during the sample drying and/or calcination processes as a result of volume shrinkage, single crystalline domains with sizes up to several hundred square micrometers could be easily obtained using this approach. Figure 11.13F shows a blowup view of this sample, suggesting that the void spaces among polymer beads had been filled with a dense structure of magnetite nanoparticles. Because each spherical pore was connected to adjacent pores underneath it through three small “windows,” we could conclude that the polymer beads were in a closely packed three-dimensional lattice.

11.6 CONCLUDING REMARKS

Monodispersed spherical colloids represent a class of building blocks that can be routinely assembled into well-defined aggregates by confining against physical templates. The availability of colloidal aggregates having well-controlled shape, dimension, and structures will provide an opportunity to experimentally probe the optical, hydrodynamic, and aerodynamic properties of colloidal particles characterized by very complex morphologies. It will also be interesting to investigate the interactions between these colloidal aggregates to achieve a better understanding on this matter. In addition, the ability to generate hybrid colloidal particles should make it possible to design some experiments that cannot be performed using colloidal particles with homogeneous surface properties. At the current stage of development, it is still not clear whether the TASA process can be eventually extended to the nanoscale (<100 nm). Based on what we have observed so far, the answer to this question seems to depend on a number of parameters that still need to be fully evaluated and optimized (e.g., densities of the spherical colloids and the solvent, temperature, surface tension, and viscosity of the dispersion medium; sign and density of charges on the surfaces of templates and colloidal particles; and rate at which the liquid slug moves). All these parameters ultimately determine the direction of net force exerted on the particles (i.e., the gravitational force, Brownian

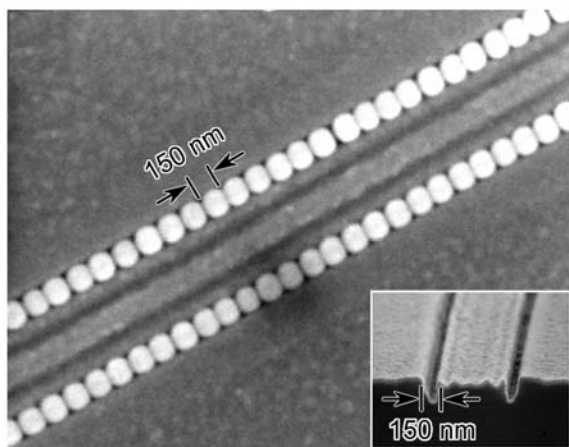


FIGURE 11.14 The SEM image of two linear chains self-assembled from 150-nm polystyrene beads. These polymer beads represent the smallest building blocks that have been successfully incorporated into the TASA process. The inset shows an SEM image of the template (a parallel array of trenches that were 150 and 150 nm in width and depth, respectively) that was fabricated using near-field optical lithography with a binary phase-shift mask.

motion, attractive capillary interactions, and hydrodynamic shear flow). Each of these forces plays a certain role in determining the yield of a TASA process, as well as the smallest colloids that can effectively work as the building blocks. We have started to address this issue in our research, and the major limitation seems to be our ability to fabricate small templates with well-controlled dimensions and well-defined shapes. Figure 11.14 shows a recent demonstration from our group, which has pushed the size of spherical colloids to the scale of ~ 150 nm. In this demonstration, the templates (a parallel array of trenches that were ~ 150 nm in width and ~ 150 nm in depth) were fabricated using the near-field optical lithographic method (with an elastomeric stamp as the binary phase-shift mask).¹²⁵ This demonstration indicated that it was still possible to organize polymer beads as small as ~ 150 nm into linear chains using the present method. We believe some modifications to the assembly procedure and development of new materials should be useful when smaller colloids are to be exploited.

Monodispersed spherical colloids also provide a class of building blocks that can be readily assembled into three-dimensional periodic structures such as opaline lattices and inverse opals. Self-assembly with spherical colloids represents a flexible and cost-effective route to three-dimensional microfabrication, and is remarkable for its small investment as compared with that required by the more familiar clean-room methods commonly used in microfabrication. The feature size of these highly ordered three-dimensional structures can also be easily varied in a well-controlled way to cover an extremely broad range that spans from a few nanometers to several hundred micrometers. The ability to generate such periodic structures with varying feature sizes should allow us to obtain useful functionalities not only from the constituent materials but also from the long-range ordering that characterizes these structures. For example, both colloidal arrays and inverse opals can be exploited as a platform to fabricate novel types of optical or electrooptical devices such as photonic crystals and smart diffractive sensors.¹²⁶

Although spherical colloids will continue to play a predominant role in the colloid science, they are not necessarily the best option for all fundamental studies or real-world applications that are associated with colloidal particles. They cannot, for example, exactly model the interactions between and hydrodynamic behaviors of colloidal particles with irregular morphologies.¹²⁷ They can only provide a very limited set of crystal structures when they are used as building blocks to form periodic arrays. Theoretical studies have also indicated that they are not well suited as the

building blocks in generating photonic crystals with complete band gaps due to degeneracy in the photonic band structure caused by the spherical symmetry of the lattice points.¹²⁸ In this regard, the aggregates of spherical colloids (described in Section 11.3) will provide immediate advantages over spherical precursors in applications that require lattices with lower symmetries and higher complexities. It will be interesting to integrate the research described in Sections 11.3 and 11.4 into a unified theme, in an effort to obtain three-dimensional crystalline lattices from nonspherical building blocks.

ACKNOWLEDGMENTS

This work has been supported in part by the AFOSR-MURI program, a Career Award from the National Science Foundation (DMR-9983893), a Research Fellowship from the Alfred P. Sloan Foundation, a Fellowship from the David and Lucile Packard Foundation, a New Faculty Award from the Dreyfus Foundation, and the Washington Technology Center. B.G. thanks the Center for Nanotechnology at the University of Washington for an IGERT Fellowship funded by the NSF (DGE-9987620). Y.Y. thanks the Center for Nanotechnology for a Student Fellowship Award supported by the University of Washington.

REFERENCES

1. Hunter, R.J., *Introduction to Modern Colloid Science*, Oxford University Press, Oxford, 1993.
2. Russel, W.B., *The Dynamics of Colloidal Systems*, University of Wisconsin Press, Madison, Wisconsin, 1987.
3. Everett, D.H., *Basic Principles of Colloid Science*, Royal Society of Chemistry, London, 1988.
4. Russel, W.B., Saville, D.A., and Scholwaller, W.R., A survey of colloidal dispersions, in *Colloidal Dispersions*, Batchelor, G.K., Ed., Cambridge University Press, New York, 1989, 1–20.
5. Poehlein, G.W., Ottewill, R.H., and Goodwin, J.W., Eds., *Science and Technology of Polymer Colloids*, Vol. II, Martinus Nijhoff Publishers, Boston, 1983.
6. Matijević, E., Preparation and properties of uniform size colloids, *Chem. Mater.*, 5, 412, 1993.
7. Matijević, E., Uniform inorganic colloid dispersions. Achievements and challenges, *Langmuir*, 10, 8, 1994.
8. Piirma, I., Ed., *Emulsion Polymerization*, Academic Press, New York, 1982.
9. Iler, R.K., *The Chemistry of Silica*, Wiley-Interscience, New York, 1979.
10. Larsen, A.E. and Grier, D.G., Like-charge attractions in metastable colloidal crystallites, *Nature (London)*, 385, 230, 1997.
11. Murray, C.A. and Grier, D.G., Colloidal crystals — solid particles suspended in fluid form ordered arrays with unusual and useful physical properties, *Am. Sci.*, 83, 238, 1995.
12. Pieranski, P., Colloidal crystals, *Contemp. Phys.*, 24, 25, 1983.
13. van Megan, W. and Snook, I., Equilibrium properties of suspensions, *Adv. Colloid. Interface Sci.*, 21, 119, 1984.
14. Grier, D.G., Ed., From Dynamics to Devices: Directed Self-Assembly of Colloidal Materials, a special issue in *MRS Bull.*, 23, 21, 1998.
15. Gast, A.P. and Russel, W.B., Simple ordering in complex fluids, *Phys. Today*, December, 24, 1998.
16. Dinsmore, A.D., Crocker, J.C., and Yodel, A.G., Self-assembly of colloidal crystals, *Curr. Opinion Colloid Interface*, 3, 5, 1998.
17. Xia, Y. et al., Monodispersed colloidal spheres: old materials with new applications, *Adv. Mater.*, 12, 693, 2000.
18. Carlson, R.J. and Asher, S.A., Characterization of optical diffraction and crystal structure in monodisperse polystyrene colloids, *Appl. Spectrosc.*, 38, 297, 1984.
19. Sanders, J.V., Color of precious opal, *Nature (London)*, 204, 1151, 1964.
20. Photonic Crystals, a special issue in *Adv. Mater.*, 13, 361–452, 2001.
21. Ball, P., *The Self-Made Tapestry: Pattern Formation in Nature*, Oxford University Press, New York, 1999.

22. Klug, A., From macromolecules to biological assemblies, *Angew. Chem. Int. Ed. Engl.*, 22, 565, 1983.
23. Isaacs, L. et al., Self-assembling systems on scales from nanometers to millimeters: design and discovery, in *Supramolecular Technology*, Reinhoudt, D.N., Ed., John Wiley & Sons, New York, 1999, 1–46.
24. Bates, F.S., Polymer-polymer phase behavior, *Science*, 251, 898, 1991.
25. Lehn, J.-M., Perspectives in supramolecular chemistry — from molecular recognition towards molecular information processing and self-organization, *Angew. Chem. Int. Ed. Engl.*, 29, 1304, 1990.
26. Philp, D. and Stoddart, J.F., Self-assembly in natural and unnatural systems, *Angew. Chem. Int. Ed. Engl.*, 35, 1154, 1996.
27. Reinhoudt, D.N., Ed., *Supramolecular Technology*, John Wiley & Sons, New York, 1999.
28. Stöber, W., Fink, A., and Bohn, E., Controlled growth of monodisperse silica spheres in the micron size range, *J. Colloid Interface Sci.*, 26, 62, 1968.
29. Wirth, M.J., Fairbank, R.W., and Futunmbi, H.O., Mixed self-assembled monolayers in chemical separations, *Science*, 275, 44, 1997.
30. Bishop, A.R. and Nuzzo, R.G., Self-assembled monolayers: recent developments and applications, *Curr. Opin. Colloid Interface Sci.*, 1, 127, 1996.
31. Bain, C.D. and Whitesides, G.M., Modeling organic surfaces with self-assembled monolayers, *Angew. Chem. Int. Ed. Engl.*, 28, 506, 1989.
32. Neeves, A.E. and Birnboim, M.H., *J. Opt. Soc. Am. B.*, 6, 787, 1989.
33. Quaroni, L. and Chumanov, G., Preparation of polymer-coated functionalized silver nanoparticles, *J. Am. Chem. Soc.*, 121, 10642, 1999.
34. Mecking, S. and Thomas, R., Core-shell microspheres of a catalytically active rhodium complex bound to a polyelectrolyte-coated latex, *Adv. Mater.*, 12, 953, 2000.
35. Mandal, T.K., Fleming, M.S., and Walt, D.R., Production of hollow polymeric microspheres by surface-confined living radical polymerization on silica templates, *Chem. Mater.* 12, 3481, 2000.
36. Ohmori, M. and Matijević, E., *J. Colloid Interface Sci.*, 150, 594, 1992.
37. Liz-Marzan, L.M., Giersig, M., and Mulvaney, P., Homogeneous silica coating of vitreophobic colloids, *Chem. Commun.*, 731, 1996.
38. Liz-Marzan, L.M., Giersig, M., and Mulvaney, P., Synthesis of nanosized gold-silica core-shell particles, *Langmuir*, 12, 4329, 1996.
39. Caruso, F., Caruso, R.A., and Mohwald, H., Nanoengineering of inorganic and hybrid hollow spheres by colloidal templating, *Science*, 282, 1111, 1998.
40. Caruso, F. et al., Hollow titania spheres from layered precursor deposition on sacrificial colloidal core, *Adv. Mater.*, 13, 740, 2001.
41. Velev, O.D., Lenhoff, A.M., and Kaler, E.W., A class of microstructured particles through colloidal crystallization, *Science*, 287, 2240, 2000.
42. Huck, W.T.S., Tien, J., and Whitesides, G.M., Three-dimensional mesoscale self-assembly, *J. Am. Chem. Soc.*, 120, 8267, 1998.
43. Tien, J., Terfort, A., and Whitesides, G.M., Microfabrication through electrostatic self-assembly, *Langmuir*, 13, 5349, 1997.
44. Aizenberg, J., Braun, P.V., and Wiltzius, P., Patterned colloidal deposition controlled by electrostatic and capillary forces, *Phys. Rev. Lett.*, 84, 2997, 2000.
45. Chen, K.M. et al., Selective self-organization of colloids on patterned polyelectrolyte templates, *Langmuir*, 16, 7825, 2000.
46. Yin, Y. and Xia, Y., Self-assembly of monodispersed colloidal spheres into complex aggregates with well-defined sizes, shapes, and structures, *Adv. Mater.*, 13, 267, 2001.
47. Yin, Y. et al., Template-assisted self-assembly: a practical route to complex aggregates of monodispersed colloids with well-defined sizes, shapes, and structures, *J. Am. Chem. Soc.*, 123, 8718, 2001.
48. Yin, Y., Lu, Y., and Xia, Y., A self-assembly approach to the formation of asymmetric dimers from monodispersed spherical colloids, *J. Am. Chem. Soc.*, 123, 771, 2000.
49. Yin, Y., Lu, Y., and Xia, Y., Self-assembly of monodispersed spherical colloids into 1D chains with well-defined lengths and structures, *J. Mater. Chem.*, 11, 987, 2001.
50. Lu, Y., Yin, Y., and Xia, Y., A self-assembly approach to the fabrication of patterned, two-dimensional arrays of microlenses of organic polymers, *Adv. Mater.*, 13, 34, 2001.

51. Xia, Y., Gates, B., and Yin, Y., Building complex structures from monodisperse spherical colloids, *Aust. J. Chem.*, 54, 287, 2001.
52. Lu, Y. et al., Growth of large crystals of monodispersed spherical colloids in fluidic cells fabricated using non-photolithographic methods, *Langmuir*, 17, 6344, 2001.
53. Gates, B., Park, S.H., and Xia, Y., Tuning the photonic band-gap properties of crystalline arrays of polystyrene beads by annealing at elevated temperatures, *Adv. Mater.*, 12, 653, 2000.
54. Mazur, S., Beckerbauer, R., and Buckholz, J., Particle size limits for sintering polymer colloids without viscous flow, *Langmuir*, 13, 4287, 1997.
55. Kralchevsky, P.A. and Nagayama, K., Capillary forces between colloidal particles, *Langmuir*, 10, 23, 1994.
56. Lu, Y., Yin, Y., and Xia, Y., Fabrication of three-dimensional photonic crystals with nonspherical colloids as the building blocks, *Adv. Mater.*, 13, 415, 2001.
57. Chia, S. et al., Patterned hexagonal arrays of living cells in sol-gel silica films, *J. Am. Chem. Soc.*, 122, 6488, 2000.
58. Míguez, H. et al., Photonic crystal properties of packed submicrometric SiO₂ spheres, *Appl. Phys. Lett.*, 71, 1148, 1997.
59. Astratov, V.N. et al., Photonic band gaps in 3D ordered fcc silica matrices, *Phys. Lett. A*, 222, 349, 1996.
60. Dushkin, C.D. et al., Colored multilayers from transparent submicrometer spheres, *Langmuir*, 9, 3695, 1993.
61. Lazarov, G.S. et al., Nagayama, K., Formation of two-dimensional structures from colloidal particles on fluorinated oil substrate, *J. Chem. Soc. Faraday Trans.*, 94, 2077, 1994.
62. Dimitrov, A.S. and Nagayama, K., Continuous convective assembling of fine particles into two-dimensional arrays on solid surfaces, *Langmuir*, 12, 1303, 1996.
63. Jiang, P. et al., Single-crystal colloidal multilayers of controlled thickness, *Chem. Mater.*, 11, 2132, 1999.
64. Jiang, P. et al., The fabrication and bandgap engineering of photonic crystals, *Adv. Mater.*, 13, 389, 2001.
65. Park, S.H., Qin, D., and Xia, Y., Crystallization of meso-scale particles over large areas, *Adv. Mater.*, 10, 1028, 1998.
66. Park, S.H. and Xia, Y., Crystallization of meso-scale particles over large areas and its application in fabricating tunable optical filters, *Langmuir*, 15, 266, 1999.
67. Gates, B., Qin, D., and Xia, Y., Assembly of nanoparticles into opaline structures over large areas, *Adv. Mater.*, 11, 466, 1999.
68. Park, S.H., Gates, B., and Xia, Y., A three-dimensional photonic crystals operating in the visible region, *Adv. Mater.*, 11, 462, 1999.
69. Xia, Y., Gates, B., and Park, S.H., Fabrication of three-dimensional photonic crystals for use in the spectral region from ultraviolet to near infrared, *IEEE J. Lightwave Technol.*, 17, 1956, 1999.
70. Mayoral, R. et al., 3D long-range ordering in an SiO₂ submicrometer-sphere sintered superstructure, *Adv. Mater.*, 9, 257, 1997.
71. van Winkle, D.H. and Murray, C.A., Layering transitions in colloidal crystals as observed by diffraction and direct-lattice imaging, *Phys. Rev. A*, 34, 562, 1986.
72. Pieranski, P., Strzelecki, L., and Pansu, B., Thin colloidal crystals, *Phys. Rev. Lett.*, 50, 900, 1983.
73. Nesper, S. et al., Finite-size effects on the closest packing of hard spheres, *Phys. Rev. Lett.*, 79, 2348, 1997.
74. Takano, K. and Hachisu, S., Pressure of kirkwood-alder transition in monodisperse latex, *J. Chem. Phys.*, 67, 2604, 1977.
75. Bertone, J.F. et al., Thickness dependence of the optical properties of ordered silica-air and air-polymer photonic crystals, *Phys. Rev. Lett.*, 83, 300, 1999.
76. Li, Z.-Y. and Zhang, Z.-Q., Fragility of photonic band gaps in inverse-opal photonic crystals, *Phys. Rev. B*, 62, 1516, 2000.
77. Joannopoulos, J.D., Villeneuve, P.R., and Fan, S., Photonic crystals: putting a new twist on light, *Nature (London)*, 386, 143, 1997.
78. Ozbay, E. et al., Defect structures in a layer-by-layer photonic band-gap crystal, *Phys. Rev. B*, 51, 13961, 1995.

79. Noda, S., Two- and three-dimensional photonic crystals in III-V semiconductors, *MRS Bull.*, August, 618, 2001.
80. Gates, B. and Xia, Y., Photonic band-gap properties of opaline lattices of spherical colloids doped with various concentrations of smaller colloids, *Appl. Phys. Lett.*, 78, 3178, 2001.
81. Murray, M.J. and Sanders, J.V., Close-packed structures of spheres of two different sizes, *Philos. Mag. A*, 42, 721, 1980.
82. Hachisu, S. and Yoshimura, S., Optical demonstration of crystalline superlattices in binary mixtures of latex globules, *Nature (London)*, 283, 188, 1980.
83. Kaplan, P.D. et al., Entropically driven surface phase separation in binary colloidal mixtures, *Phys. Rev. Lett.*, 72, 582, 1994.
84. Kiely, C.J. et al., Spontaneous ordering of bimodal ensembles of nanoscopic gold clusters, *Nature (London)*, 396, 444, 1998.
85. Salvarezza, R.C. et al., Edward-Wilkinson behavior of crystal surfaces grown by sedimentation of SiO₂ nanospheres, *Phys. Rev. Lett.*, 77, 4572, 1996.
86. Palberg, T. et al., Grain size control in polycrystalline colloidal solids, *J. Chem. Phys.*, 102, 5082, 1995.
87. van Blaaderen, A., Ruel, R., and Wiltzius, P., Template-directed colloidal crystallization, *Nature (London)*, 385, 321, 1997.
88. van Blaaderen, A.V. and Wiltzius, P., Growing large, well-oriented colloidal crystals, *Adv. Mater.*, 9, 833, 1997.
89. Lin, K.-H. et al., Entropically driven colloidal crystallization on patterned surfaces, *Phys. Rev. Lett.*, 85, 1770, 2000.
90. Dinsmore, A.D. and Yodh, A.G., Entropically confinement of colloidal spheres in corners on silicon substrates, *Langmuir*, 15, 314, 1999.
91. Kim, E., Xia, Y., and Whitesides, G.M., Polymer microstructures formed by moulding in capillaries, *Nature (London)*, 376, 581, 1995.
92. Velev, O.D. et al., Porous silica via colloidal crystallization, *Nature (London)*, 389, 447, 1997.
93. Park, S.H. and Xia, Y., Fabrication of three-dimensional macroporous membranes with crystalline lattices of polymer beads as templates, *Chem. Mater.*, 10, 1745, 1998.
94. Holland, B.T., Blanford, C.F., and Stein, A., Synthesis of macroporous minerals with highly ordered three-dimensional arrays of spheroidal voids, *Science*, 281, 538, 1998.
95. Velev, O.D. et al., Microstructured porous silica obtained via colloidal crystal templates, *Chem. Mater.*, 10, 3597, 1998.
96. Wijnhoven, J.E.G.J. and Vos, W.L., Preparation of photonic crystals made in air spheres in titania, *Science*, 281, 802, 1998.
97. Braun, P.V. and Wiltzius, P., Electrochemically grown photonic crystals, *Nature (London)*, 402, 603, 1999.
98. Vlasov, Y.A., Yao, N., and Norris, D.J., Synthesis of photonic crystals for optical wavelengths from semiconductor quantum dots, *Adv. Mater.*, 11, 165, 1999.
99. Jiang, P. et al., Template-directed preparation of macroporous polymers with oriented and crystalline arrays of voids, *J. Am. Chem. Soc.*, 121, 11630, 1999.
100. Gates, B., Yin, Y., and Xia, Y., Fabrication and characterization of porous membranes with highly ordered three-dimensional periodic structures, *Chem. Mater.*, 11, 2827, 1999.
101. Kulinowski, K.M. et al., Porous metals from colloidal templates, *Adv. Mater.*, 12, 833, 2000.
102. Jiang, P. et al., Preparation of macroporous metal films from colloidal crystals, *J. Am. Chem. Soc.*, 121, 7957, 1999.
103. Park, S.H. and Xia, Y., Macroporous membranes with highly ordered and three-dimensionally interconnected spherical pores, *Adv. Mater.*, 10, 1045, 1998.
104. Ramanov, S.G., Fokin, A.V., and La Rue, R.M., Stop-band structure in complementary three-dimensional opal-based crystals, *J. Phys. Condens. Matter*, 11, 3593, 1999.
105. Deutsch, M., Yurii, A.V., and Norris, D.J., Conjugated-polymer photonic crystals, *Adv. Mater.*, 12, 1176, 2000.
106. Wang, D. and Caruso, F., Fabrication of polyaniline inverse opals via templating ordered colloidal assemblies, *Adv. Mater.*, 13, 350, 2001.
107. Zakhidov, A.A. et al., Carbon structures with three-dimensional periodicity at optical wavelengths, *Science*, 282, 897, 1998.

108. Blanco, A. et al., Large-scale synthesis of a silicon photonic crystal with a complete three-dimensional bandgap near 1.5 micrometres, *Nature (London)*, 405, 437, 2000.
109. Scott, R.W.J. et al., Tin dioxide opals and inverted opals: near-ideal microstructures for gas sensors, *Adv. Mater.*, 13, 1468, 2001.
110. Míguez, H. et al., Photonic bandgap engineering in germanium inverse opals by chemical vapor deposition, *Adv. Mater.*, 13, 1634, 2001.
111. Vlasov, Y.A. et al., On-chip natural assembly of silicon photonic bandgap crystals, *Nature (London)*, 414, 289, 2001.
112. Johnson, S.A., Ollivier, P.J., and Mallouk, T.E., *Science*, 283, 963, 1999.
113. Zhong, Z. et al., Preparation of mesoscale hollow spheres of TiO₂ and SnO₂ by templating against crystalline arrays of polystyrene beads, *Adv. Mater.*, 12, 206, 2000.
114. Yang, P. et al., Hierachically ordered oxides, *Science*, 282, 2244, 1998.
115. Fendler, J.H., Atomic and molecular clusters in membrane mimetic chemistry, *Chem. Rev.*, 87, 877, 1987.
116. Bawendi, M.G., Steigerwald, M.L., and Brus, L.E., The quantum mechanics of larger semiconductor clusters ("quantum dots"), *Annu. Rev. Phys. Chem.*, 41, 477, 1990.
117. Weller, H., Quantized semiconductor particles: a novel state of matter for materials science, *Adv. Mater.*, 5, 88, 1993.
118. Alivisatos, A.P., Semiconductor nanocrystals, *MRS Bull.*, August, 23, 1995.
119. Schmid, G. and Chi, L.F., Metal clusters and colloids, *Adv. Mater.*, 10, 515, 1998.
120. Siegel, R.W., Creating naphase materials, *Sci. Am.*, December, 74, 1996.
121. Subramania, G. et al., Optical photonic crystals fabricated from colloidal systems, *Appl. Phys. Lett.*, 74, 3933, 1999.
122. Subramanian, G. et al., Ordered macroporous materials by colloidal assembly: a possible route to photonic bandgap materials, *Adv. Mater.*, 11, 1261, 1999.
123. Tessier, P.M. et al., Structured metallic films for optical and spectroscopic applications via colloidal crystal templating, *Adv. Mater.*, 13, 396, 2001.
124. Gates, B. and Xia, Y., Photonic crystals that can be addressed with an external magnetic field, *Adv. Mater.*, 13, 1605, 2001.
125. Li, Z.-Y., Yin, Y., and Xia, Y., Optimization of elastomeric phase masks for near-field photolithography, *Appl. Phys. Lett.*, 78, 2431, 2001.
126. Holtz, J.H. and Asher, S.A., Polymerized colloidal crystal hydrogel films as intelligent chemical sensing materials, *Nature (London)*, 389, 829, 1997.
127. Li, Z.-Y., Wang, J., and Gu, B.-Y., Full band gap in fcc and bcc photonic band gap structure: nonspherical atom, *J. Phys. Soc. Jpn.*, 67, 3288, 1998.
128. Xia, Y., Gates, B., and Li, Z.-Y., Self-assembly approaches to three-dimensional photonic crystals, *Adv. Mater.*, 13, 409, 2001.

12 Thermally Sensitive Latex Particles: Preparation, Characterization, and Application in the Biomedical Field

Abdelhamid Elaissari

CONTENTS

- 12.1 Introduction
 - 12.2 Synthesis of Reactive Thermally Sensitive Latex Particles
 - 12.2.1 Kinetic Study
 - 12.2.1.1 The Effect of Initiator
 - 12.2.1.2 The Effect of Temperature
 - 12.2.1.3 The Effect of the Cross-Linker Agent
 - 12.2.1.4 Functionalization Studies and Operating Methods
 - 12.2.1.5 Polymerization Mechanism
 - 12.3 Colloidal Characterization
 - 12.3.1 Morphology
 - 12.3.2 Effect of Temperature on Hydrodynamic Particle Size
 - 12.3.3 Electrokinetic Study
 - 12.3.4 Volume Phase Transition Temperature (T_{VPT})
 - 12.3.5 Colloidal Stability
 - 12.4 Immobilization of Biomolecules
 - 12.4.1 Protein Adsorption
 - 12.4.1.1 Effect of Temperature on the Adsorption of Protein onto Poly(NIPAM) Particles
 - 12.4.1.2 Effect of Ionic Strength on the Adsorption of Protein onto Poly(NIPAM)
 - 12.4.1.3 Desorption Study
 - 12.4.2 Adsorption of Nucleic Acids
 - 12.4.2.1 Adsorption Kinetic
 - 12.4.2.2 Influence of pH and Ionic Strength
 - 12.4.2.3 Desorption Study of Preadsorbed Nucleic Acids
 - 12.4.3 Amplification of Nucleic Acids
 - 12.5 Conclusion
 - 12.6 Acknowledgment
- References

12.1 INTRODUCTION

Polymer latex particles are widely used as a solid support in numerous applications and especially in the biomedical field, because of the existence of various polymerization processes (emulsion, dispersion, microemulsion, etc.) for preparing latex that is well defined in terms of particle size, reactive groups, surface charge density, colloidal stability, etc. Since 1986, precipitation polymerization of acrylamide and methacrylamide derivatives (water-soluble monomers) has been found to be a convenient method for producing submicronic, functionalized thermally sensitive latex hydrogel particles, as reported by Pelton and Chibante.¹ Since then, thermally responsive microgel latex particles have played a particular and considerable role in academic research and industrial applications. In academic research, studies are mainly focused on the polymerization mechanism and colloidal characterization in dispersed media. From an application point of view, stimuli-responsive microgels have been principally explored in drug delivery as a carrier in therapy.

The implication of such stimuli-responsive particles as a solid polymer support of biomolecules in the biomedical field is probably due to various factors: (1) easiest to prepare via precipitation polymerization (hydrogel particles) or a combination of emulsion and precipitation polymerizations (core-shell particles), (2) the colloidal properties are related to the temperature and to the medium composition (i.e., pH, salinity, surfactant etc.), (3) the adsorption and the desorption of antibodies and proteins are principally related to the incubation temperature, (4) the covalent binding of proteins onto such hydrophilic and stimuli-responsive particles can be controlled easily by temperature, and, finally, (5) the hydrophilic character of the microgel particles is an undeniably suitable environment for immobilized biomolecules.

The main objective of this chapter is to report on the preparation and characterization of thermally sensitive particles, and the pertinent aspects that should be considered before their utilization as a polymer support in the biomedical field. This is followed by an examination of the preparation of such hydrophilic thermally sensitive latex particles bearing reactive groups. Subsequently, the colloidal characterizations that are to be taken into consideration are presented. Finally, the chapter concludes by presenting and illustrating recent applications of thermally sensitive polymer colloids as solid supports in the biomedical field.

12.2 SYNTHESIS OF REACTIVE THERMALLY SENSITIVE LATEX PARTICLES

Over the last 20 years, precipitation polymerization leading to the preparation of thermally sensitive hydrogel latexes has been widely reported on and discussed. The first thermally sensitive linear polymer base, using *N*-isopropylacrylamide (NIPAM), was reported by Heskins and Guillet² in 1968. The linear homopolymer obtained exhibits a low critical solubility temperature (LCST) of 32°C, corresponding to a dramatic change in the solubility parameters. In fact, below the LCST the polymer is totally soluble in the aqueous phase, whereas above the LCST the solution exhibits phase separation induced by polymer precipitation (coil to globule transition; [Figure 12.1](#)).

In addition, the LCST of thermosensitive polymer has been widely studied using different physical methods — including turbidity or optical density ([Figure 12.2](#)), fluorescence, dynamic light scattering, and calorimetric measurements — to demonstrate the relationship between the polymer properties and solvent conditions, as reported by Schild³ in a very thorough review concentrated on poly(NIPAM). In the case of charged thermally sensitive polymers, the pH should always be considered when the determination of LCST is investigated. In fact, the presence of charged groups (i.e., ionic comonomer) increases the LCST, whereas the existence of hydrophobic parts induces a decrease in the LCST. In general, the increases in added salts induce the modification of the water structure surrounding the isopropyl groups (in the case of NIPAM), which dramatically influences the LCST values and consequently leads to a decrease in of the measured transition temperature. Furthermore, the LCST can be controlled by the addition of salt or polymer compositions and structures by adding ionic groups or hydrophobic compounds.

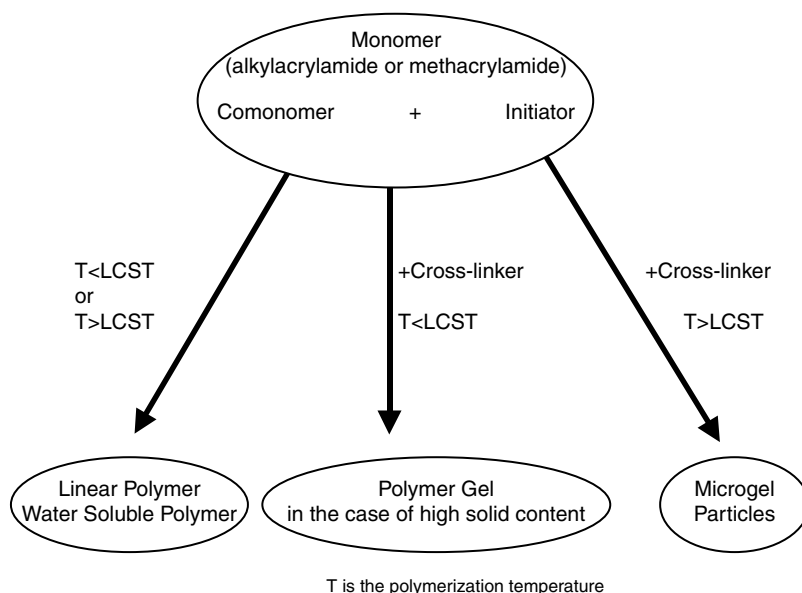


FIGURE 12.3 Schematic diagram illustrating the preparation of thermally sensitive materials.

sake of homogeneity at this stage, only latexes prepared using water-soluble cross-linkers are reported.

12.2.1 KINETIC STUDY

To prepare stable microgel particles, the polymerization should always be higher than the LCST of the corresponding homopolymer (or copolymer). In fact, without the precipitation of the formed chains (or low cross-linked chains) during the polymerization process, no real particles can be obtained. For example, the lower critical polymerization temperatures (LCPT) in the case of NIPAM, NIPMAM, and NEMAM monomers are 65, 70, and 80°C, respectively. The observed LCPT is related to the properties of the formed oligomers (chain light, molecular weight, composition, and charge distribution). This point is clearly illustrated in the polymerization mechanism described below, but has not been properly established experimentally.

Water-soluble alkylacrylamide or alkylmethacrylamide monomer conversion during the polymerization process can be easily determined or followed using both gas chromatography and $^1\text{H-NMR}$ techniques. According to the high reactivity of the water-soluble cross-linkers (i.e., MBA) generally used and the low concentration used in the polymerization recipe, only the main monomer conversion can be easily followed as a function of polymerization time. For most alkyl(metha)-acrylamide monomers studied, the polymerization kinetic was generally found to be rapid. In fact, only 30 min was needed to reach total conversion in the case of NIPAM/MBA/V50 (Figure 12.4) or KPS (polymerization temperature from 60 to 80°C)⁷ and 120 min in the case of NIPMAM/MBA/KPS (polymerization temperature from 60 to 80°C).⁵ The difference in polymerization rate between NIPAM and NIPMAM is related to the high propagation rate constant (k_p) for NIPAM compared to NIPMAM,^{8,9} as well as for the known reactivity of alkylacrylamides compared to alkylmethacrylamides derivatives ($k_p \sim 18000$ l/mol/s for acrylamide^{10,11} and $k_p \sim 800$ l/mol/s for methacrylamide¹² at 25°C).

The detailed analysis of particle size vs. polymerization time and conversion is one of the best methodologies generally used in polymerization in dispersed media to highlight particle evolution during the polymerization process. The diameter of hydrogel particles (NIPMAM/MBA/KPS at 70°C)⁵ vs. (conversion)^{1/3} reported in Figure 12.5 was a linear relationship, reflecting the fact that the number of particles remained constant and no new particles were formed during the polymerization

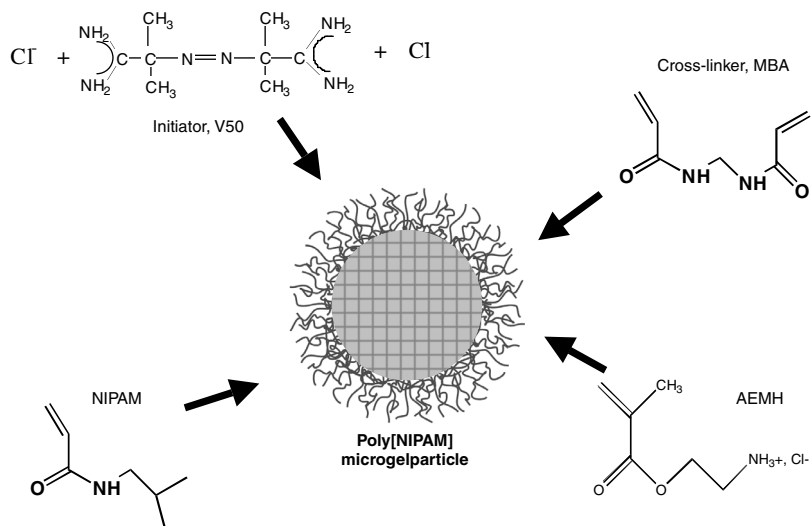


FIGURE 12.4 Schematic representation of batch preparation of functionalized thermally sensitive poly(NIPAM) microgel particles. NIPAM(1g)/MBA(<10% w/w)/V50(0.1 w/w%). The preparation of such poly(alkylacrylamide) particles can only be performed for low solid content, generally less than 5% w/v. V50: 2-2' azo-bis amidinopropane dihydrochloride, MBA: methylene bis acrylamide, AEMH: amino-ethyl methacrylate hydrochloride.

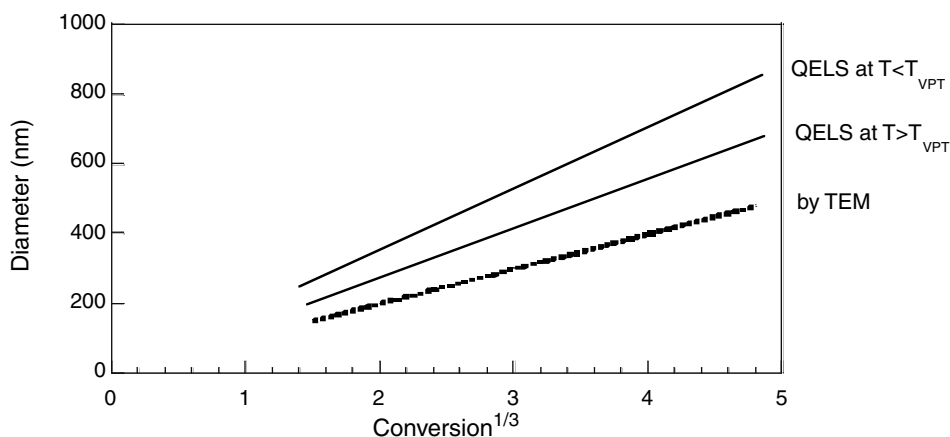


FIGURE 12.5 Illustration of hydrogel particle size vs. conversion in the case of classical alkylacrylamide monomers. See Duracher's work for experimental data with NIPAM monomer. (Adapted from Duracher, D. et al., *J. Polym. Sci. A Polym. Chem.* 37, 1823–1837, 1999.)

process. In fact, the particle size (R_h) is related to the particle number (N_p) and the polymer mass (m , i.e., polymer conversion) by assuming the constancy of the particle density during the polymerization process.

$$R_h \approx N_p^{-1/3} \cdot m^{1/3} \quad (12.1)$$

The observed behavior was confirmed by scanning electron microscopy (SEM) analysis of the particle size distribution vs. polymerization time, as illustrated in Figure 12.6. The utilization of

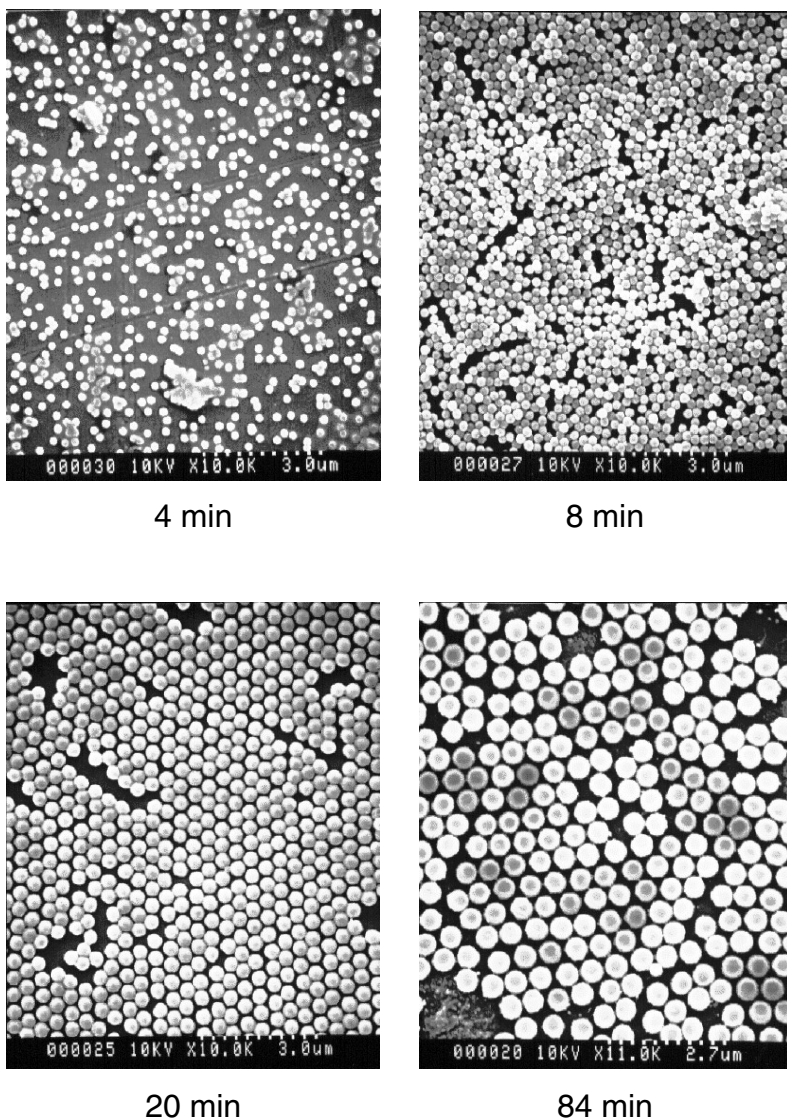


FIGURE 12.6 SEM images of poly(NIPMAM) particles at different polymerization times. (From Duracher, D. et al., *J. Polym. Sci. A Polym. Chem.* 37, 1823–1837, 1999. With permission.)

the investigations described above of both particle size vs. conversion^{1/3} and size distribution vs. time using transmission electron microscopy (TEM) or SEM are related to the difficulty in determining (or estimating) particle number concentrations induced by the swollen property of the microgels.

12.2.1.1 The Effect of Initiator

There are few reports on the influence of the initiator on the precipitation polymerization but as expected, the polymerization rate (Figure 12.7) increases together with the initiator concentration, as is often the case in emulsion polymerization. This behavior is attributed to an increase in the polymerization loci. It is interesting to note that an increase in the initiator concentration leads to an increase in the water-soluble polymer formation (oligomers bearing low molecular weight) and

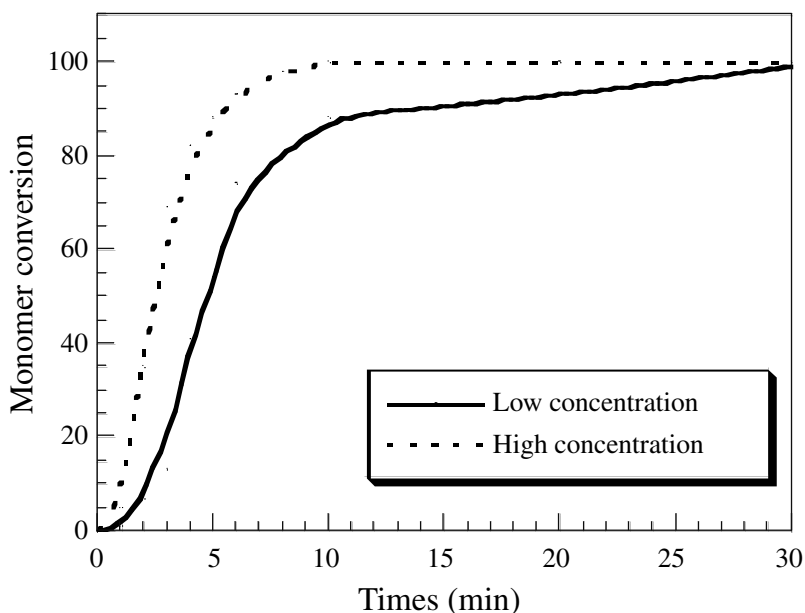


FIGURE 12.7 Monomer conversion vs. polymerization time for two initiator concentrations. (Example for poly(NIPAM) particles: polymerization temperature $T = 70^{\circ}\text{C}$, $[\text{NIPAM}] = 48.51$ mmol, $[\text{MBA}] = 3$ mmol, $[\text{V50}] = 0.1$ (—) to 1 mmol (-----) for total volume = 250 ml. (Adapted from Meunier, F., Ph.D. thesis, 1996.)

to a decrease in the final hydrodynamic particle size. The polymerization rate (R_p) is related to the initiator concentration $[I]$ using the low-scale representation:

$$R_p \approx [I]^a \quad (12.2)$$

For example, $a = 0.18$ for NIPAM/MBA/KPS at 70°C (Figure 12.8), and $a = 0.4$ in the case of emulsion polymerization. With such a complex system, it is more appropriate to consider the relationship between the number of particles (N_p) and the reactants concentration, then:

$$N_p \approx [M]^a [I]^b [\text{CL}]^c \quad (12.3)$$

where $[M]$ is the monomer, $[\text{CL}]$ is the cross-linker agent, and a , b , and c are the scaling exponents. The particle number cannot be easily determined without a drastic approximation.

12.2.1.2 The Effect of Temperature

The influence of temperature on precipitation polymerization was also studied^{5,7} and was found to be similar to the effect of the initiator (Figure 12.9). In fact, the increase in temperature leads to an increase in the decomposition rate of the initiator, which enhances the polymerization loci, as discussed above and described by the following rate decomposition equation:

$$N_{\text{dec}} = [I](1 - e^{-k_d t}) \quad (12.4)$$

where k_d is the decomposition rate constant of the initiator at a given temperature, $[I]$ is the initial concentration of initiator, and N_{dec} is the amount of decomposed initiator after a given time (t) and at a given temperature.

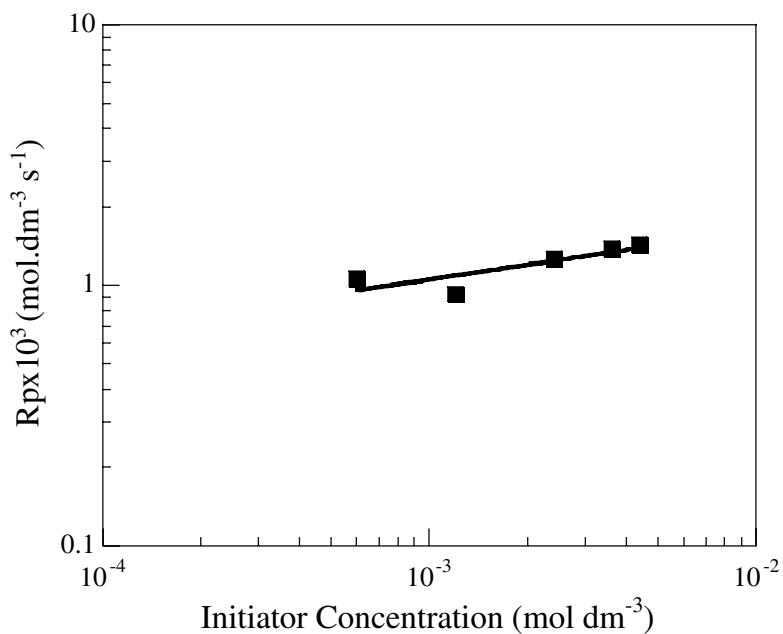


FIGURE 12.8 Dependence of polymerization rate on the initiator concentration in log-log scale. Temperature = 70°C, [NIPAM] = 48.51 mmol, [MBA] = 3 mmol, total volume = 250 ml. ($R_p \approx [I]^{0.18}$, [I]: V50 initiator concentration). (Adapted from Meunier, F., Ph.D. thesis, 1996.)

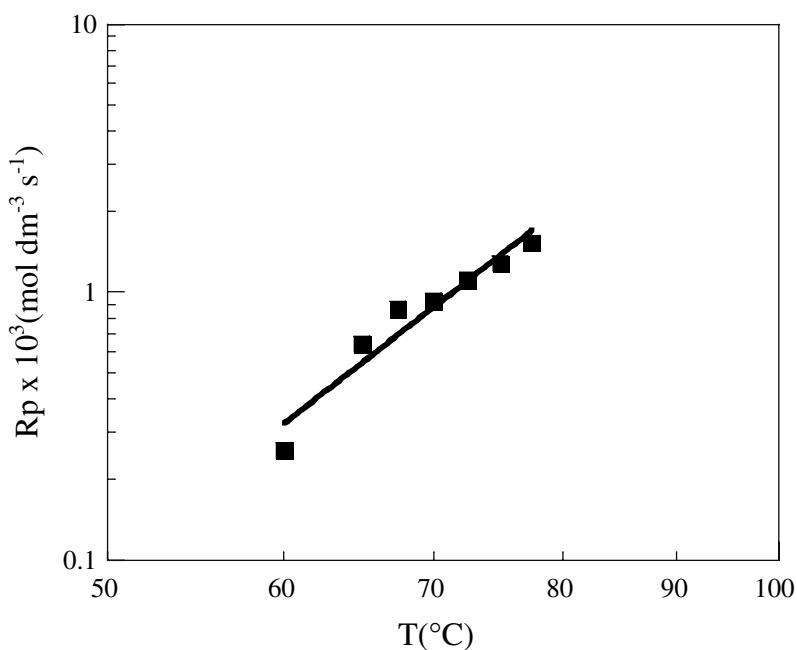


FIGURE 12.9 Polymerization rate vs. polymerization temperature in semi-log scale. [NIPAM] = 48.51 mmol, [I] = 0.3 mmol (V50), [MBA] = 3 mmol, total volume = 250 ml. (Adapted from Meunier, F., Ph.D. thesis, 1996.)

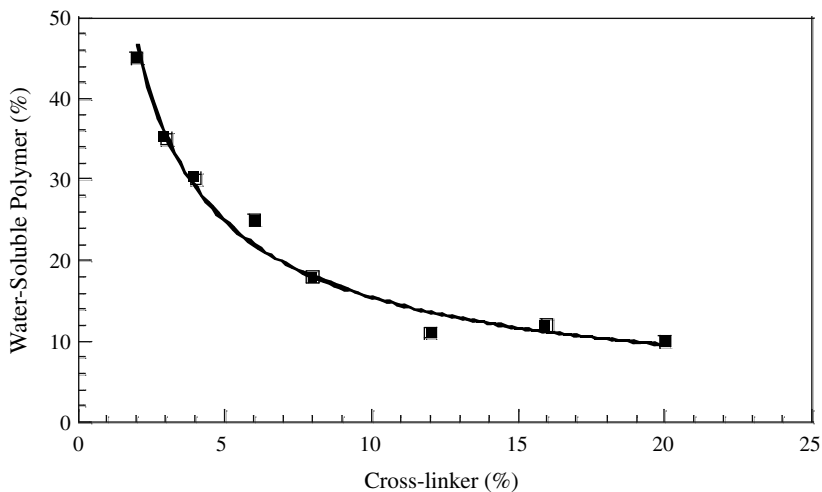


FIGURE 12.10 Effect of MBA (2 to 20% w/w) on water-soluble polymer formation using NIPMAM (1 g) monomer and KPS (2% w/w) initiator, polymerization temperature 70°C. (From Duracher, D. et al., *J. Polym. Sci. A Polym. Chem.* 37, 1823, 1999. With permission.)

It is important to note that the polymerization temperature of alkyl(meth)acrylamide in aqueous media should be above the LCST of the corresponding linear polymer, and high enough to favor the precipitation process of the formed water-soluble oligomers. The temperature also affects the final particle size: a low temperature results in a large particle size. Furthermore, the temperature affects the reactivity of each reactant, including the main monomer, initiator, and cross-linker agent. In fact, in the case of emulsion polymerization, the instantaneous rate of polymerization R_p is related to the propagation rate coefficient, the monomer concentration (M), the average number of radicals per particle (\bar{n}), and the number of latex particles N_p (which is connected to the rate radical generation $N_p \approx \rho^{0.4}$) as expressed by the following equation:

$$R_p = k_p[M]\bar{n}N_p \quad (12.5)$$

in which k_p is the rate coefficient for propagation of the monomer (M).

12.2.1.3 The Effect of the Cross-Linker Agent

The cross-linker agent has a marked and drastic effect on particle formation. It is needed in the polymerization recipe to favor particle formation by cross-linking the precipitated poly(N-alkyl-acrylamide) chains that generate the nucleation step. The increase in the cross-linker agent concentration in the batch polymerization recipe leads to a reduction in the final amount of water-soluble polymer (Figure 12.10). In addition, the water-soluble cross-linker agent was found to affect the polymerization rate and the final particle size⁵ to a small extent, and the swelling ability of the particles to a greater extent. In accordance with the higher reactivity of the water-soluble cross-linkers (such as MBA) generally used in such precipitation polymerization, the final structure of hydrogel particles was found to have a gradient composition (looser and looser from the core to the shell), as evidenced by Guillermo et al.¹³ during an investigation of the transverse relaxation of protons using the NMR technique. The internal structure of the particle vs. cross-linker concentration can be schematically illustrated as shown in Figure 12.11.

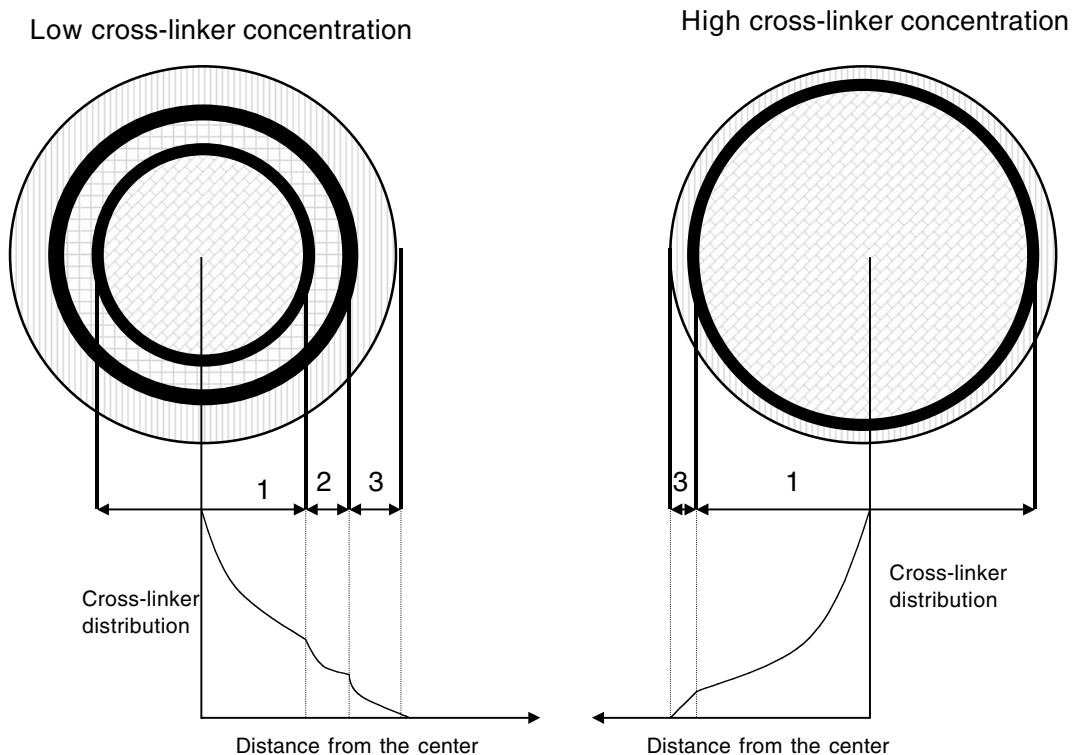
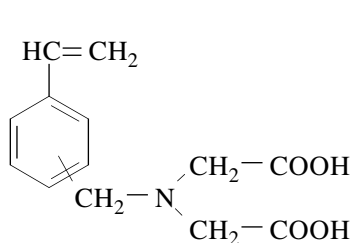


FIGURE 12.11 Schematic illustrations of hydrogel particles as a function of cross-linker concentration. (1) Highly cross-linked part, (2) medium cross-linked phase, and (3) low cross-linked shell.

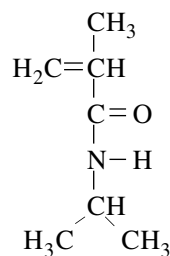
12.2.1.4 Functionalization Studies and Operating Methods

A large number of processes have been developed during the last decade, permitting the synthesis of reactive latexes and the functionalization of prepared polymer particles with specific properties:

- **Batch polymerization:** Polymerizations performed in a closed reactor, with all the ingredients introduced at the beginning of a single step. This method, apart from certain exceptions, is of little interest, as a large part of the functional monomer is consumed, providing substantial quantities of water-soluble polymers that disturb nucleation and the final stabilization of the particles.
- **Semicontinuous addition methods:** These are very useful for copolymerizations requiring control of homogeneous compositions at the level of the chain and the particle. Variable composition gradient processes permit the introduction of the functional monomer to a suitable conversion, favoring incorporation on the surface or inside the particles.
- **Multistage polymerizations:** These methods include the deferred addition of an ionic comonomer (constituting the basic latex), favoring a highly efficient surface functionalization.
- **Seed functionalization:** These methods consist of the functionalization of a latex seed by a monomer or monomer mixture. This often permits surface incorporation to be increased, and is well adapted to formulating controlled charge density model colloids.
- **Postreaction on reactive latexes:** This process is very useful for modifying the functionality of given latex if it cannot be obtained directly.

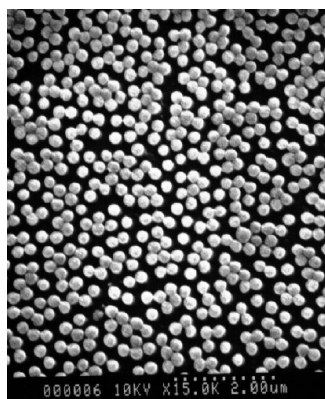


IDA

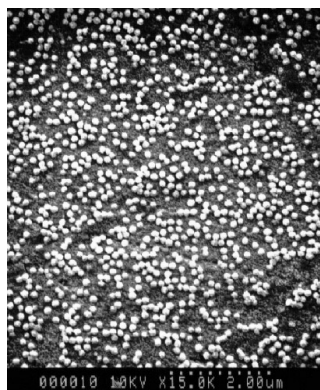


NIPMAM

FIGURE 12.12 Structure of *N*-(vinylbenzylimino)-diacetic acid (IDA) and *N*-isopropylmethacrylamide (NIPMAM).



0% IDA



2% IDA

FIGURE 12.13 SEM images of the final particles using the same scale. (From Duracher, D. et al., *Macromol. Symp.*, 150, 297, 2000. With permission.)

The preparation of functionalized thermally sensitive microgel particles has not been sufficiently investigated, as only a few works have been reported. The first systematic work on the preparation of functionalized poly(NIPAM) hydrogel particles was studied using NIPAM/MBA/AEMH (aminoethylmethacrylate hydrochloride) in a batch polymerization process, and was first reported by Meunier et al.⁹ (Figure 12.4) and then by Duracher et al.¹⁴ during an investigation of the effect of *N*-vinylbenzylimino diacetic acid (IDA) on the polymerization of NIPMAM/MBA/KPS (Figure 12.12). The effect of the charged functional monomer on the precipitation polymerization of such alkylacrylamide and alkylmethacrylamide monomers (i.e., NIPAM and NIPMAM) was found to resemble the effect of the ionic (or water-soluble) monomer on the emulsion polymerization of styrene, for instance. In fact, the increase in the functional monomer concentration leads to rapid polymerization, high polymerization conversion (>95%), low particle size (Figure 12.13), and high water-soluble polymer formation.

In addition to batch functionalization, the shot-grow process was also performed to prepare amino-containing thermally sensitive poly(NIPAM) hydrogel¹⁹ and core-shell (polystyrene core and poly(NIPAM) shell) particles.¹⁵ The results revealed a good functionalization yield with a non-negligible amount of water-soluble polymer formation.

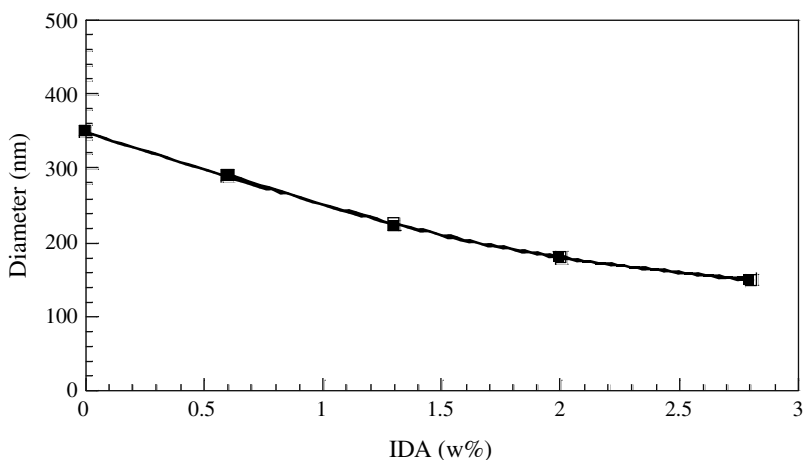


FIGURE 12.14 Effect of functional monomer on hydrodynamic particle diameter measured by quasi-elastic light scattering (QELS) at 20°C. (From Duracher, D. et al., *Macromol. Symp.*, 150, 297, 2000. With permission.)

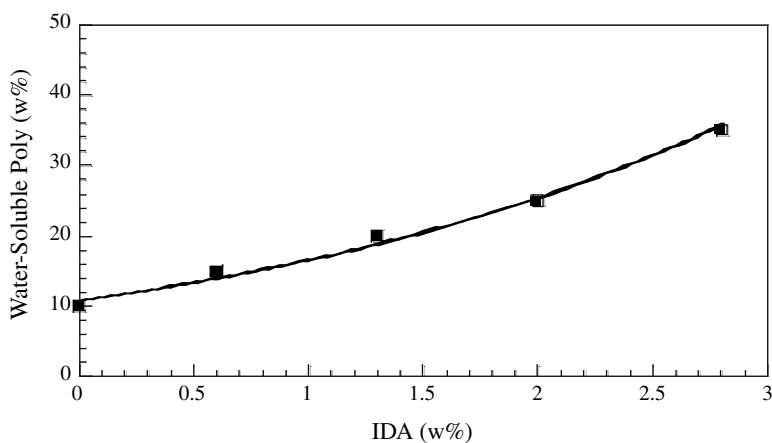


FIGURE 12.15 The wt% water-soluble polymer formation (WSP) vs. functional monomer concentration. (From Duracher, D. et al., *Macromol. Symp.*, 150, 297, 2000. With permission.)

As in the case of emulsion polymerization, an increase in the functional monomer concentration leads to a reduction in the final hydrodynamic particle size and enhanced water-soluble polymer formation, as illustrated in Figures 12.14 and 12.15 for batch polymerization of (NIP-MAM/MBA/IDA/KPS). The reduction in particle size vs. functional monomer has been attributed to the enhancement of precursor formation and the number of stable particles which rapidly become the polymerization loci.

12.2.1.5 Polymerization Mechanism

After examination of the role of each reactant implied in the polymerization of water-soluble *N*-alkylacrylamide and *N*-alkylmethacrylamide monomer in the presence of the water-soluble cross-linker agent and radical initiators, the polymerization mechanism of this system in the preparation of thermally sensitive microgel submicron particles can be presented and detailed as follows (Figure 12.16).

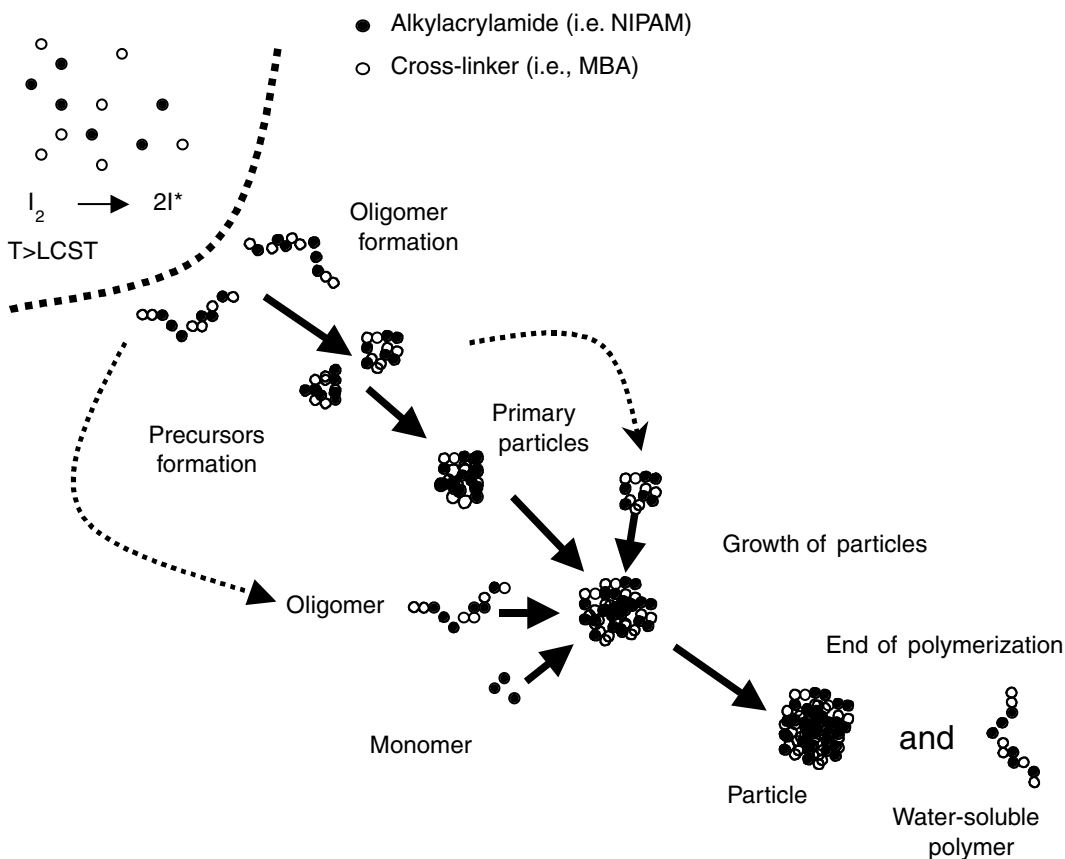


FIGURE 12.16 Schematic illustration of precipitation polymerization mechanism of water-soluble *N*-alkylacrylamide and *N*-alkylmethacrylamide monomer derivatives.

Water-phase polymerization. Before adding the water-soluble initiator, the medium is totally homogeneous and relatively limp, even at the polymerization temperature. After adding the initiator, the polymerization requires a low induction period (t^*) (generally less than 3 min in the case of NIPAM/MBA/KPS or V50 system using recrystallized reactants), probably due to the presence of oxygen traces in the aqueous phase. Above the t^* period, the decomposed initiator leads to rapid formation of oligomers. The oligomer concentration is principally governed by the initiator decomposition rate and efficiency.

Nucleation step. The nucleation period is mainly due to the precipitation of the oligomers formed when the critical chain lengths (or molecular weight and composition) are reached or when the cross-linked chains start to precipitate. In fact, the SEM (see Figure 12.6) analysis of the particle size and size distribution reveals rapid and narrow particle distribution formation (i.e., generally in less than 5 min in the case of NIPAM/MBA/KPS and NIPAM/MBA/V50 systems). In accordance with highly reactive water-soluble cross-linkers such as MBA, it may be assumed that the first oligomers contain a significant amount of the cross-linker agent of primary particles.

Growth of particles. After the rapid nucleation period, the polymerization of the residual monomer may take place at various points (i.e., water phase, on the surface of the formed particle, and in the swelled parts of the particles). In fact, the partition of the monomer between the water phase and polymer particles should be considered: (1) polymerization in the water phase leads to the formation of small oligomers which can be cross-linked on the formed particles when there is

a sufficient residual cross-linker agent concentration, and (2) the possible polymerization of the monomer in the swollen state. When the cross-linker agent is totally consumed, the oligomers formed contribute to water-soluble polymer formation. The water-soluble polymer formed may originate from the desorption of chains adsorbed onto the particles when the dispersion is cooled (temperature $< T_{\text{VPT}}$ or $< \text{LCST}$), or from low-molecular-weight chains that are highly water soluble even above the LCST of the considered homopolymer.

12.3 COLLOIDAL CHARACTERIZATION

The aim of this analysis stage is to obtain qualitative and quantitative information on particle morphology, particle size and size distribution, surface polarity, assessment of the localization of the functional monomer introduced into the reaction system, and colloidal stability before any application in the biomedical field. In addition, it is vital to purify polymer particles before colloidal characterization, by separating the particles from impurities originating from polymerization reactants (these are mostly traces of the initiator, residual monomers, and water-soluble polymer). There is now a whole arsenal of techniques whose multiple applications are well referenced. As for separation methods, the most important and frequently used are centrifugation, serum replacement, magnetic separation in the case of magnetic latexes, and ultrafiltration. Dialysis and ionic exchanges on mixtures of cationic and anionic resins deserve mention among the purification methods. In the case of hydrophilic thermally sensitive microgel particles, centrifugation can be used without any irreversible aggregation risk. In fact, the aggregated particles are easily dispersible in an aqueous medium simply by stirring after the centrifugation step (at high speed and low duration).

12.3.1 MORPHOLOGY

The morphological characterization of structured latexes is a fundamental aspect of their study, because (1) it provides very useful information on the nature of the mechanisms that regulate the formation of the particle, and (2) knowledge of the organization of the polymer within the particle is the essential foundation for the theoretical interpretation of the behavior of the resulting latex films (mechanical properties, permeability, etc.). From this perspective, there are a great many techniques that require examination to eliminate artifacts and incorrect conclusions deduced from their use.

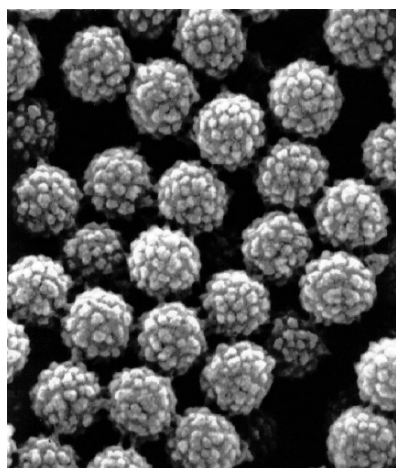
Various methods have been reported and published. Of these methods, electronic microscopy is still preferred for studying structured latexes, as improvements in observation techniques (sample preparation, introduction of selective marking of one of the components) permit direct and increasingly refined analysis of polymers inside particles.

SEM can also be used for both surface morphology and particle size and size distribution, as illustrated in [Figure 12.17](#) for thermally sensitive polystyrene core-cross-linked poly(NIPAM) shells. In addition, atomic force microscopy (AFM) can be used for investigating colloidal particle morphology, as reported by Duracher et al.¹⁵ In fact, atomic force microscopy leads to rapid and complementary information on particle morphology in a dried state.

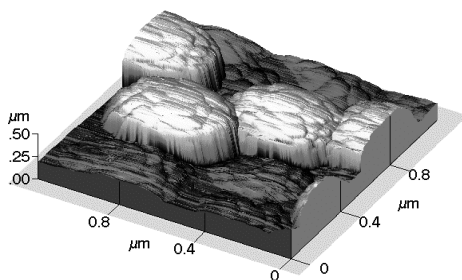
12.3.2 EFFECT OF TEMPERATURE ON HYDRODYNAMIC PARTICLE SIZE

The mean hydrodynamic diameter (D_h) was calculated from the diffusion coefficient measurement, which, in the high dilution limit of negligible particle–particle interactions, is calculated by using the Stokes–Einstein equation.

$$D = \frac{kT}{3\pi\eta D_h} \quad (12.6)$$



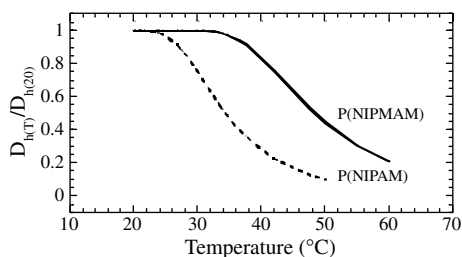
(SEM)



(AFM)

FIGURE 12.17 SEM and AFM of polystyrene (core)-cross-linked poly(NIPAM) shell microspheres. (From Duracher, D. et al., *Colloid Polym. Sci.*, 276, 219, 1998. With permission.)

Below the T_{VPT}
 $\chi_{12}=0$, in good solvent



Above the T_{VPT}
 $\chi_{12}>0.5$, in poor solvent



FIGURE 12.18 Reduced particle size of poly(NIPAM) and poly(NIPMAM) as a function of temperature using QELS at 1 mM NaCl. $D_{20^\circ\text{C}}$ and $D(T)$ are the hydrodynamic particle size at 20°C and at a given temperature (T), respectively.

where D is the diffusion coefficient, k the Boltzmann constant, T the absolute temperature, and η the viscosity of the medium. Light scattering technology (QELS) is generally suitable for low particle sizes (i.e., diameter $<1 \mu\text{m}$). For polystyrene latex particles bearing low charges density and hydrophobic surface, the particle size does not generally depend on temperature, pH, and salinity. However, in the case of hydrophilic and poly(N-alkylacrylamide) derivatives, particle size and swelling ability are affected by the solvent quality of the dispersion medium, temperature, pH, and salinity. By way of illustration, the particle size for various types of particle — poly(NIPAM) and poly(NIPMAM) — as a function of temperature is reported in Figure 12.18.

This decrease (in particle size vs. T) is more marked in the case of large particles (with low cross-linking properties), due to the pronounced size difference below and above the volume phase transition temperature (T_{VPT}) between the shrunken and the extended state. In addition, the effect of temperature is more marked in the case of total hydrogel microspheres compared to the core-shell particles, as illustrated in Figure 12.18. The behavior observed has already been reported by many authors with regard to poly(NIPAM) microgel particles, and attributed to the breaking of hydrogen bonds between polymer network and water molecules during the heating process, which

induces a decrease in hydrodynamic particle size. Such light scattering experiments can provide two major pieces of information concerning the dispersion: (1) the effect of temperature on particle size (i.e., volume phase transition domain) and (2) the swelling ability of the considered colloidal particles. The swelling ratio calculated from the hydrodynamic particle size above and below the volume phase transition temperature reflects the cross-linking density of the particle but not the cross-linker distribution, as recently reported by Guillermo et al.¹³ using the NMR technique described in Section 12.2.1.3 (see Figure 12.11). To compare the swelling capacity of the microgel particles (or core-shell latexes) with different functional monomer concentrations, charge densities, and internal structures, the swelling ratio (S_w) was introduced and defined by the following equation:

$$S_w = \frac{V}{V_c} \quad (12.7)$$

where V and V_c represent the particle volume calculated from the hydrodynamic radius as determined by QELS and V_c represents the collapsed volume above the volume phase transition temperature.

12.3.3 ELECTROKINETIC STUDY

The surface charge density of the charged thermally sensitive latexes can be determined using classical methods, such as conductimetry, potentiometry, chemical reaction, NMR, and infrared, etc. The investigation of electrophoretic mobility vs. pH and temperature can also be considered a key point for the analysis of surface charge density variation. In fact, the electrophoretic mobility of thermally sensitive microgel particles is drastically affected by the medium temperature. The decrease in particle size, and subsequent increase in surface charge density, results in an increase in electrophoretic mobility, as expressed by the following relationship between (μe) and particle size (R_h):

$$\mu e \approx \frac{Ne}{4\pi\eta R_h^2 \kappa} \quad (12.8)$$

where N is the number of charged groups per particle of hydrodynamic radius R_h , e is the electron charge, κ is the reciprocal of Debye length thickness, and η is the viscosity of the medium.

As illustrated in Figure 12.19, the reduced electrophoretic mobility increased together with the temperature, irrespective of the nature of the surface charge. Such behavior is related to the surface charge density vs. temperature. The amplitude of the measured transition in the electrokinetic property was more marked for low cross-linked thermosensitive particles (i.e., high swelling ability). The electrokinetic study of such thermally sensitive particles needs particular attention to demonstrate the location of charges implicated in electrophoretic mobility and explain the relationship between the volume phase transition temperature (T_{VPT}) and the electrokinetic transition temperature (T_{EKT}).

12.3.4 VOLUME PHASE TRANSITION TEMPERATURE (T_{VPT})

The volume phase transition temperature of thermally sensitive particles can be determined using various methods and techniques: fluorescence study,¹⁶ light scattering, differential scanning calorimetry, and turbidity measurement.

The easiest way to determine the LCST in the case of thermally sensitive linear polymer is to investigate the turbidity (τ) of the medium or the optical density (OD) variation as a function of temperature ($\tau = 2.303 \text{ OD}/L$, where L is the length of the sample in cm). This turbidity method

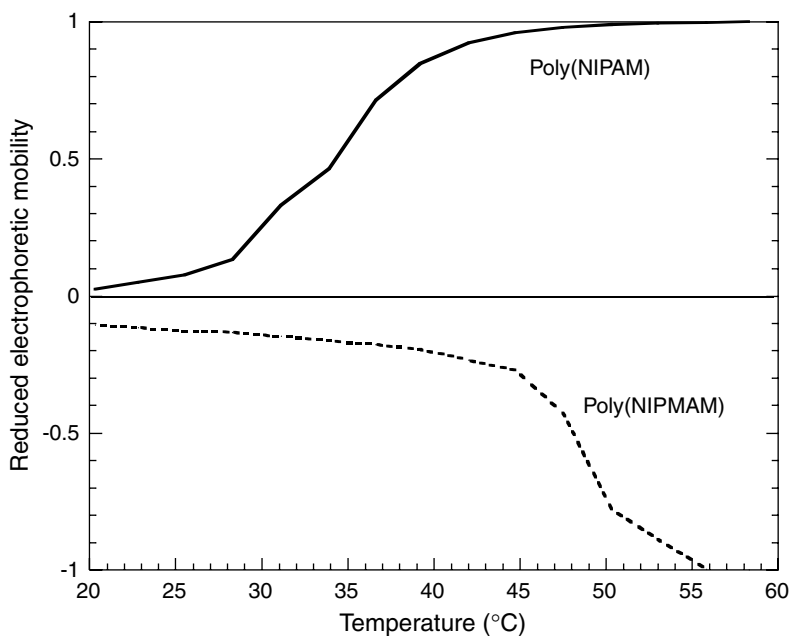


FIGURE 12.19 Reduced electrophoretic mobility ($\mu_e/\mu_{e,\max}$) of cationic poly(NIPAM) and anionic poly(NIPAM) microgel latexes as a function of temperature ($10^{-3}M$ NaCl). $\mu_{e,\max}$ is measured far from the electrokinetic transition temperature (T_{EKT}).

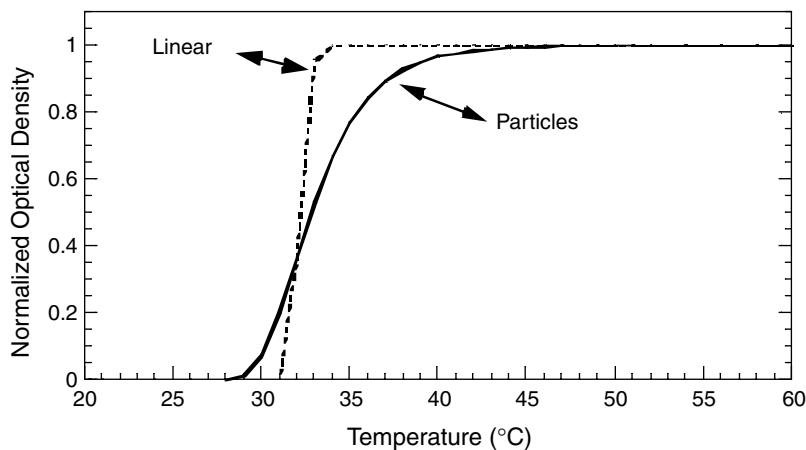


FIGURE 12.20 Normalized optical density vs. temperature for both linear and microgel poly(NIPAM) polymer (for highly diluted polymer and low-salinity concentration).

has been adapted to the hydrogel particles and defined as the maximum of the $\delta OD/\delta T$ curve vs. temperature.

The normalized optical density variation as a function of the temperature of linear and microgel poly(NIPAM) is illustrated in Figure 12.20. The normalized optical density increases with increases in temperature for both linear thermally sensitive polymer and microgel particles. Such behavior is related to change in the refractive index of the polymer (ϵ_p). In fact, below the volume phase transition temperature, the polymer is highly hydrated (i.e., $\epsilon \sim \Phi \cdot \epsilon_{\text{water}} + (1 - \Phi) \cdot \epsilon_p$, Φ is the water

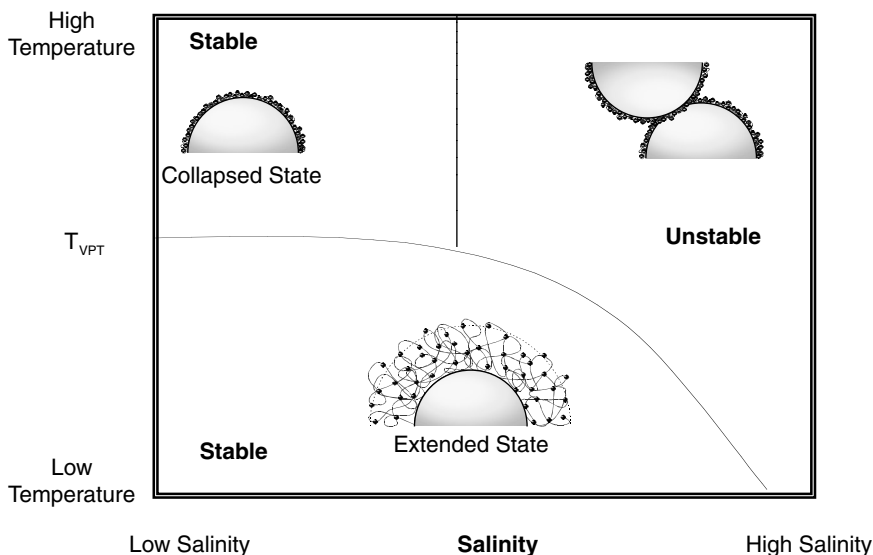


FIGURE 12.21 Schematic illustration of the colloidal stability of thermally sensitive particles as a function of temperature and salinity.

fraction in the polymer, here $\Phi \sim 1$). When the temperature increases, the polymer refractive index increases (decrease in $\Phi \rightarrow 0.3$) leading to a rise in the turbidity of the medium.

All the determined volume phase transition temperatures of hydrogel or core-shell bearing thermally sensitive polymer particles are in a broad range compared to the LCSTs. The volume phase transition temperature of thermally sensitive particles is also dependent on the internal structure (i.e., polymer composition, cross-linker density, and distribution in the particle).

12.3.5 COLLOIDAL STABILITY

The colloidal stability of thermally sensitive latex particles is related to both temperature and salinity. In fact, in the case of linear *N*-alkylacrylamide- or methacrylamide-based polymers, the increase in temperature leads to the precipitation of polymer chains discussed above (see [Figure 12.1](#)). In addition, the increase in salinity reduces the LCST of the considered polymer in water. The effects presented above (temperature and salinity) for linear polymer are also available for microgel and core-shell thermally sensitive particles. The increase in salinity reduces the volume phase transition temperature (T_{VPT}) and, with a high salinity medium, the colloidal stability may be affected and the aggregation process may take place as illustrated in [Figure 12.21](#) in which the colloidal stability domains are depicted vs. salinity and temperature. The critical coagulation concentration (CCC) of such a system is high below the volume phase transition temperature in which the particles are in an extended state and sterically stabilized. However, above the volume phase transition temperature, the CCC is low, proving that the particles are electrostatically stabilized. In addition, this behavior is reversible to a certain extent by cooling the dispersion and reducing the salt concentration.

12.4 IMMOBILIZATION OF BIOMOLECULES

Before dealing with the adsorption of biomolecules (proteins and nucleic acids) onto latex particles, we should recall certain aspects (which will not be defined here) of the adsorption of macromolecules on solid–liquid interfaces. Biomolecules are complex macromolecules in nature, which in

a polar solvent (usually water) bear a large number of ionized or ionizable functions. The adsorption of macromolecules onto solid surfaces should be well defined before presenting and discussing results. A macromolecule is adsorbed when, after a given contact period with the solid surface, at least one of its sites (or units) is fixed to the support surface. In the biomedical field, the adsorption of biomolecules onto solid phases is undesirable in most cases, but desirable in some. It is of paramount importance to understand the driving forces involved in this interaction process.

In biomedical diagnostics, the adsorption of biomolecules was generally investigated to control their covalent binding onto reactive supports. In fact, when the affinity between a given macromolecule and solid support is poor (i.e., low adsorbed amount), the chemically grafted amount is generally negligible. The adsorption process was also studied using biological molecules as a theoretical model for establishing or verifying new theories. Recently, the adsorption of biomolecules (nucleic acids, proteins etc.) has been investigated using both thermally sensitive magnetic¹⁷ and nonmagnetic colloids to concentrate molecules (DNA, RNA, and proteins) and thereby increase the sensitivity of biomedical diagnostics. In fact, the nonspecific concentration of biomolecules before the specific detection of the target is one of the most promising technologies and methodologies for the enhancement of biomedical diagnostics.

The utilization of classical polystyrene particles or hydrophobic latexes for protein concentrations can induce undesirable phenomena such as protein denaturation and low concentration yields, on account of the high adsorption affinity between both species which may lead to a low desorbed amount. In addition, the use of such hydrophobic colloids in the polymerase chain reaction (PCR) of nucleic acid amplification step generally leads to total inhibition of the enzymatic reaction. The inhibition phenomena can be attributed to the denaturation of enzymes adsorbed in large numbers onto hydrophobic colloids. The utilization of hydrophilic and highly hydrated latex particles (irrespective of temperature) is the key to solving this problem by suppressing the inhibition of enzyme activity. The purpose of this stage is then to focus on the potential application of thermally responsive poly(NIPAM) particles for both protein and nucleic acid concentrations.

12.4.1 PROTEIN ADSORPTION

The adsorption of proteins and antibodies onto thermally sensitive negatively charged particles was first investigated and reported by Kawaguchi et al.,¹⁸ and was found to be temperature dependent. Protein adsorption is low below the volume phase transition temperature of the hydrogel particles, and high above the T_{VPT} . This observed behavior has been principally attributed to hydrophobic adsorption processes above the T_{VPT} , corresponding to the hydrophobic property of linear poly(NIPAM) polymer. The adsorption of proteins onto such thermally sensitive hydrogel particles has not been thoroughly researched.

12.4.1.1 Effect of Temperature on the Adsorption of Protein onto Poly(NIPAM) Particles

The effect of temperature on the adsorption of proteins and antibodies onto classical polymer latexes, i.e., polystyrene, poly(MMA), etc., was found to be negligible at low temperatures ($T < 50^{\circ}\text{C}$). However, the effect of temperature on the adsorption process was principally investigated in the case of stimuli-responsive polymer particles such as poly(NIPAM) microgels and core-shell particles with thermally sensitive shells. In this area, the effect of temperature on poly(NIPAM) microgel particles was found to be negligible below the T_{VPT} when the poly(NIPAM) particles were highly hydrated (amount of water: ~80 wt%). But, when the temperature was increased, the amount of protein adsorbed increased dramatically. The observed behavior was discussed with regard to both hydrophobic and electrostatic interaction. The hydrophobic interaction was attributed to the dehydration of the poly(NIPAM) microgel particles and to the hydrophobic property of linear homopoly(NIPAM) above the LCST. The electrostatic interaction was explained by the increases in surface charge density caused by the shrinkage of the particles at higher temperatures.

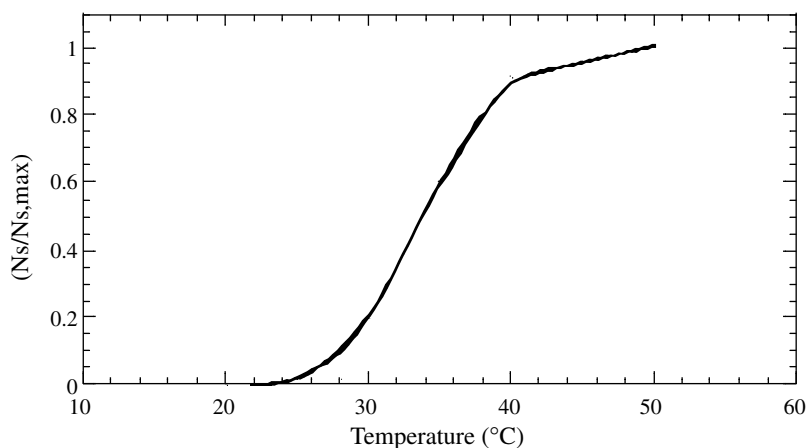


FIGURE 12.22 Reduced amount ($N_s/N_{s,max}$) of HIV-1 capsid P24 protein adsorbed onto thermally sensitive polystyrene core-cationic cross-linked poly(NIPAM) shell as a function of temperature (at pH 6.1, 10 mM phosphate buffer). (Adapted from Duracher, D., Ph.D. thesis, 1999.)

The adsorption process can more likely be attributed to electrostatic interaction. In fact, the increase in temperature raises the surface charge density on the thermally sensitive particle, as evidenced by electrophoretic mobility vs. temperature. In addition, the amount of water is at least close to 30% above the volume phase transition temperature. This adsorption profile (reduced adsorbed amount vs. temperature, as reported in Figure 12.22) is generally observed when the adsorption temperature is well controlled in the case of attractive electrostatic interactions and only the plateau is drastically affected by the pH, salinity, and surface charge density.

12.4.1.2 Effect of Ionic Strength on the Adsorption of Protein onto Poly(NIPAM)

The effect of ionic strength on the adsorption of protein onto poly(NIPAM) is more complex than was expected. In fact, salinity affects not only electrostatic interactions but also the colloidal properties of such thermally sensitive particles: (1) the increase in ionic strength leads to a reduction in particle size induced by lowering the volume phase transition temperature (i.e., the LCST of linear thermally sensitive polymer decreases as the salinity of the medium increases) and (2) salinity affects the degree of attractive and repulsive electrostatic interactions. As a result, the adsorption of proteins onto thermally sensitive microgel particles is generally and dramatically reduced as salinity increases, irrespective of temperature, as illustrated below for BSA (Figure 12.23) and HIV-1 capsid P24 protein (Figure 12.24) adsorption onto poly(NIPAM) particles.

Because the adsorption of proteins onto such thermally sensitive particles is salinity and pH dependent, the adsorption can be assumed to be governed principally by electrostatic interactions rather than hydrophobic adsorption process as generally reported. In any case, in view of these results, the driving forces in adsorption of proteins onto thermally sensitive hydrogel particles are debatable, and further research is necessary to demonstrate the driving forces involved in the adsorption process.

12.4.1.3 Desorption Study

In accordance with the reversibility of the colloidal properties of thermally sensitive particles, the adsorption of proteins is also found to be reversible in the same cases. In fact, 90% of adsorbed protein can be desorbed just by lowering the temperature (i.e., from above to below the volume phase transition temperature). The hydration processes of the particles lead to a reduction in adsorption affinity, which favors the desorption process (Figure 12.25). Furthermore, the desorbed

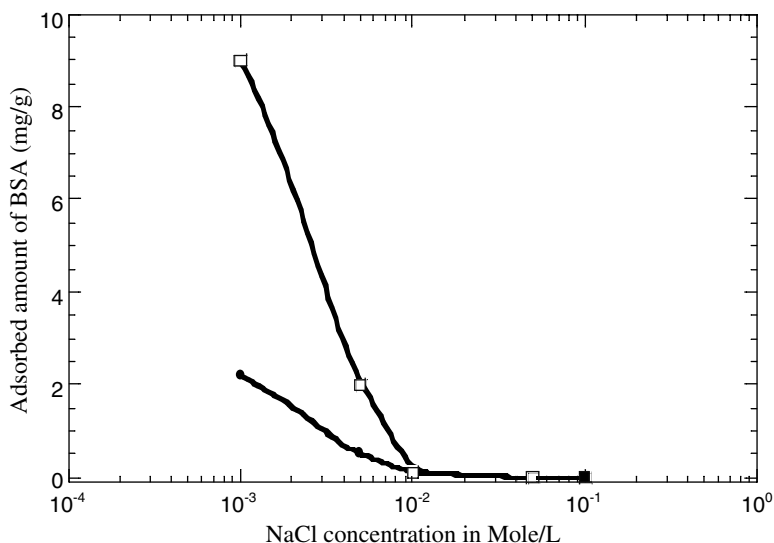


FIGURE 12.23 Effect of ionic strength and temperature on the adsorption of BSA onto cationic poly(NIPAM) latex at pH 4.6 at 20°C (●) and 40°C (□). (Adapted from Duracher, D., Ph.D., thesis, 1999.)

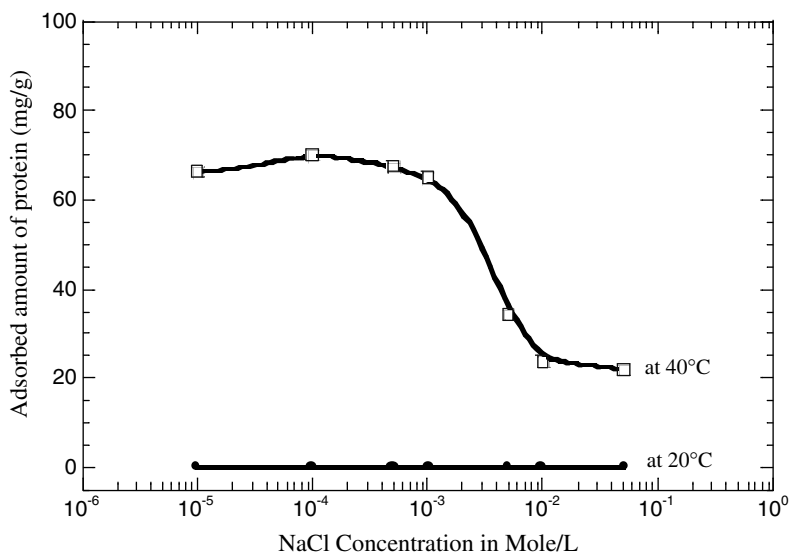


FIGURE 12.24 Effects of electrolyte concentration [NaCl] on modified HIV-1 capsid P24 protein adsorption onto cationic thermally sensitive core-shell microspheres at 40°C, pH 6.1 at 20°C (●) and 40°C (□). (Adapted from Duracher, D., Ph.D., thesis, 1999.)

amount of protein can be increased by reducing the adsorption affinity through changing the pH and salinity levels. The amount of residual adsorbed (or the nontotal desorption) is closely related to the adsorption time and to the protein nature. In fact, the more the incubation time (above the T_{VPT}) is increased, the more the desorbed amount (below the T_{VPT}) is reduced.

Such behavior can be explained as follows when batch adsorption is performed above the volume phase transition temperature: (1) the mechanical entrapment of protein molecules in the interfacial shell layer due to the poly(NIPAM) tentacles (octopus-like adsorption process) and

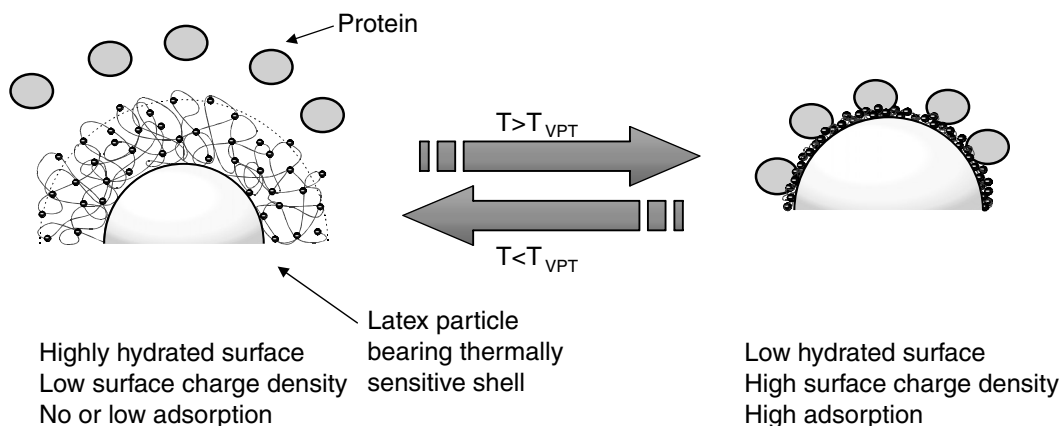


FIGURE 12.25 Schematic representation of protein adsorption and desorption as a function of temperature.

(2) the possible reformation of adsorbed protein occurring during the incubation phase. Consequently, the tangible interpretation of the protein adsorption and desorption processes should take account of the colloidal particle properties (i.e., cross-link density, charge distribution, and hydrophilic–hydrophobic balance) and the protein characteristics (flexibility, charge density, distribution of hydrophobic domains, etc.).

12.4.2 ADSORPTION OF NUCLEIC ACIDS

In recent years, numerous studies have been performed on the adsorption of nucleic acids onto colloidal particles. The adsorption of such polyelectrolytes has mainly been investigated using oligodeoxynucleotides (single-stranded DNA fragments, ssDNA), and there are only a few works dedicated to the adsorption of DNA or RNA macromolecules.²⁰ In the biomedical field, much attention has focused on the extraction, purification and concentration of nucleic acid molecules (DNA and RNA) from any microbial lysate or biological sample containing a complex mixture of proteins, nucleic acids, lipids, and membrane fragments, using appropriate colloidal particles. To achieve this, various colloids have been used, including macroporous silica beads, polystyrene magnetic latexes, and, more recently, thermally sensitive (magnetic and nonmagnetic) particles.

12.4.2.1 Adsorption Kinetic

As for highly charged polyelectrolytes, the adsorption of nucleic acids onto oppositely charged poly(NIPAM) microgel particles is pH, salinity, and charge density dependent. In fact, adsorption is rapid (Figure 12.26), with the attractive electrostatic forces increased by decreasing the pH (in the case of cationic particles), increasing the surface charge density,²¹ or lowering the ionic strength of the adsorption medium. As a general tendency, the adsorption kinetics profile of nucleic acids onto highly charged thermally sensitive poly(*N*-isopropylacrylamide) microgel particles bearing cationic groups (amines and amidines) can be illustrated as below. In the case of ssDNA fragment adsorption onto cationic polystyrene latexes,²¹ the surface coverage rate V_a :

$$V_a = d\theta/dt \quad (12.9)$$

V_a is deduced from the initial slope of the reduced adsorbed amount ($\theta = N_s/N_{s,\max}$) vs. time, and was found to be a linear variation as a function of surface charge density²¹ $V_a \approx \sigma(C/cm^2)$ (Figure 12.27).

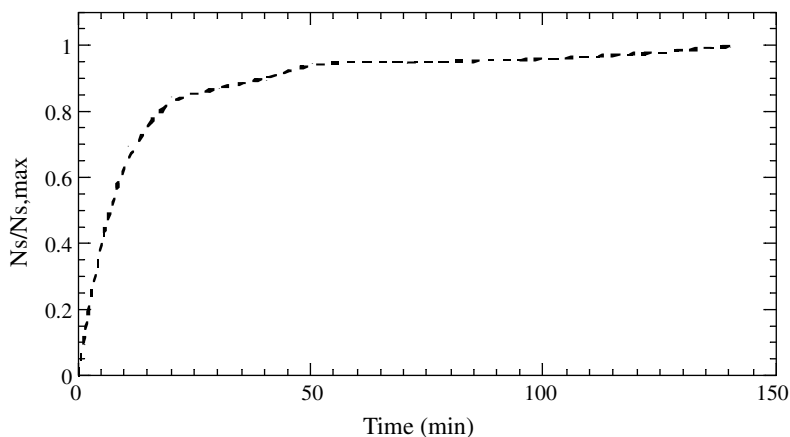


FIGURE 12.26 The reduced adsorbed amount ($\theta = N_s/N_{s,max}$) as a function of time with 0.1 mg/ml of poly-thymidylic acid at 20°C and a 10 mM phosphate buffer of pH 5.2. Adsorption equilibrium is generally attained during the first 10 min.

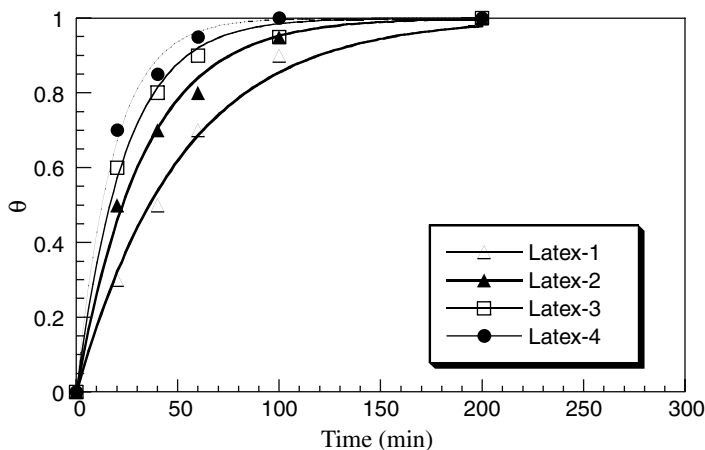


FIGURE 12.27 The reduced adsorbed amount ($\theta = N_s/N_{s,max}$) as a function of time with 0.1 mg/ml of poly-thymidylic acid on cationic polystyrene latexes at 20°C and a 10 mM phosphate buffer of pH 5.2. $\sigma_{\text{Latex-1}} < \sigma_{\text{Latex-2}} < \sigma_{\text{Latex-3}} < \sigma_{\text{Latex-4}}$. σ is the surface charge density. (From Elaissari, A. et al., *J. Colloid Interface Sci.*, 202, 2252, 1998. With permission.)

12.4.2.2 Influence of pH and Ionic Strength

As expected for charged systems, the adsorption of nucleic acids onto latexes is drastically influenced by both salt concentration and pH. The adsorbed amount decreases when the pH value of the incubation medium is increased. In fact, increases in the pH value mainly affect the concentration of the charges involved in the interaction process between negatively charged nucleic acids and cationic charges of the latex particles.

Meanwhile, an increase in the salinity of the dispersed medium leads to a reduction in the attractive electrostatic interactions. In addition, salinity drastically affects the solvency of the thermally sensitive polymers, as mentioned above. An increase in the electrolyte concentration

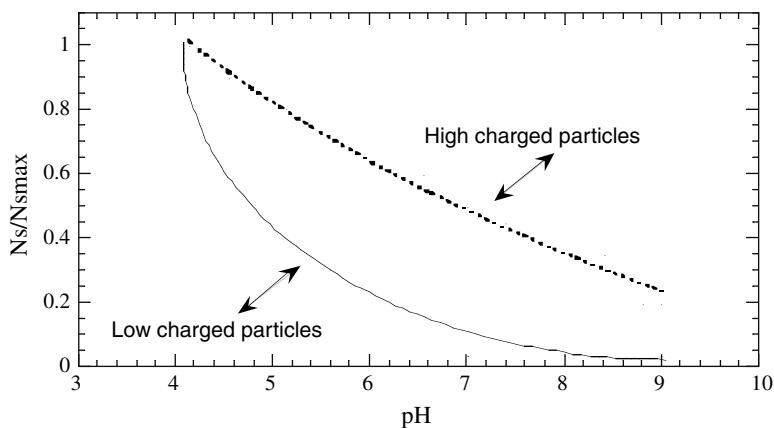


FIGURE 12.28 The reduction adsorbed amount of nucleic acids onto high cationic polystyrene latexes and low cationic poly(NIPAM) microgel particles as a function of pH at 20°C and $10^{-3}M$ ionic strength. (From Ganachaud, F. et al., *Langmuir*, 13, 701, 1997. With permission.)

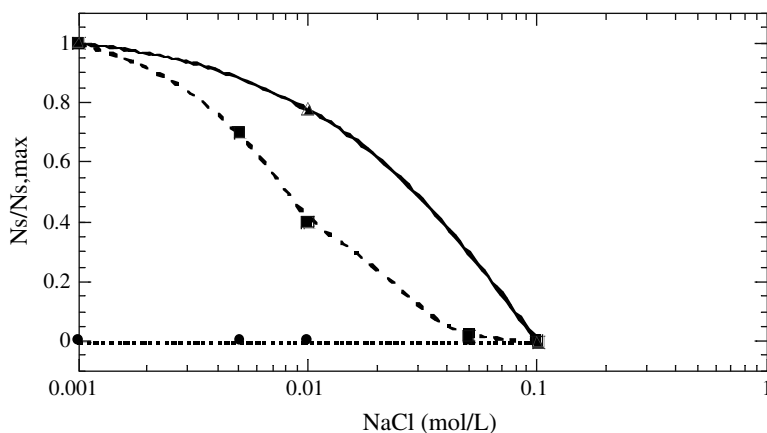


FIGURE 12.29 The reduction adsorbed amount of nucleic acids onto (amidine groups $5 \mu\text{mol/g}$, ●) and amine (amine and amidine groups, $14 \mu\text{mol/g}$, ■) poly(NIPAM) microgel particles²⁶ and (amine and amidine groups 5) thermally sensitive magnetic bearing poly(NIPAM) shells¹⁷ as a function of NaCl concentration (at pH 4.5 and at 20°C). (From Elaissari, A. et al., *J. Magn. Magn. Mater.*, 225, 127–133, 2001 and Delair, T. et al., *Colloids Surf. A Phys. Chem. Eng. Aspects*, 153, 341–353, 1999. With permission.)

leads to an increase in the Flory–Huggins²² interaction parameter between the polymer and water, resulting in reduced poly(*N*-alkylacrylamide) solvency. Consequently, the amount of nucleic acids adsorbed onto the cationic poly(NIPAM) microgel particles is reduced, as has been widely reported for the adsorption of polyelectrolytes onto oppositely charged solid supports. The attractive electrostatic interactions are the driving forces in the adsorption process of DNA, RNA, and ssDNA^{23,24} onto oppositely charged polymer supports. The variation of the quantity of nucleic acids adsorbed onto cationic thermally sensitive poly(NIPAM) latex particles as a function of both pH and ionic strength are shown in Figures 12.28 and 12.29, respectively.

As for classical polyelectrolytes, the adsorption of oligodeoxyribonucleotides (ssDNA) is basically related to the ssDNA adsorption energy, as described by the following equation:

$$N_s = k \cdot C_{\text{eq}} \cdot e^{(-n \cdot \Delta G)} \quad (12.10)$$

where N_s is the adsorbed amount, k is a constant characterizing the studied system, n is the polymerization degree (i.e., number of bases, for example, *dT35*, $n = 35$) and ΔG is the adsorption energy per monomer (per base). The adsorption energy in the case of nucleic acids/polymer particles is the sum of hydrophobic adsorption energy ($\Psi_{\text{hydrophobic}}$) attributed to the stacking adsorption process (ssDNA/negatively charged polystyrene latex) and electrostatic adsorption energy ($\Psi_{\text{electrostatic}}$) related to the charge–charge interaction.

$$n\Delta G = \Psi_{\text{hydrophobic}} + \Psi_{\text{electrostatic}} \quad (12.11)$$

In the case of such hydrophilic thermally sensitive microgel particles, the hydrophobic adsorption can be totally neglected and the electrostatic term can be described by the following relationship:

$$n\Delta G = \Psi_{\text{electrostatic}} \approx \sigma_{\text{ssDNA}} \cdot \sigma_{\text{latex}} \quad (12.12)$$

where σ_{ssDNA} and σ_{latex} are the charge density of ssDNA and latex particles, respectively. The charge density of ssDNA fragment and the surface charge density of latex particles can be approximately expressed as follows:

$$\sigma_{\text{ssDNA}} \approx \frac{n|e|}{L} \quad (12.13)$$

$$\sigma_{\text{latex}} \approx \frac{\epsilon\kappa\zeta}{4\pi} \quad (12.14)$$

where L is the chain length of a given ssDNA, ζ is the zeta potential of latex particles, κ is the inverse of double layer thickness, and ϵ is the dielectric constant. In the pH range generally investigated in the adsorption study, the σ_{ssDNA} is negatively charged, whereas the σ_{latex} is pH dependent, as evidenced by any electrokinetic study (zeta potential vs. pH). The electrostatic adsorption energy is thus expected to vary linearly with respect to the latex surface charge density leading to linear variation of $\log(N_s)$ vs. latex surface charge density or zeta potential as evidenced by Elaissari et al.²⁵

12.4.2.3 Desorption Study of Preadsorbed Nucleic Acids

In practice, there is a thermodynamic balance in the adsorption process between the macromolecules adsorbed and those free in the solution. This balance can be shifted in one direction or the other; adsorption is favored by changing the nature of the solvent (pH, ionic strength, temperature, etc.) or by increasing the number of adsorption sites, while desorption is generally favored by diluting the free macromolecules or by introducing competitive species.

Desorption is often considered a slow phenomenon, although its rate can be significant. If the molecule is adsorbed at several sites, there is little chance of it being desorbed. On the other hand, if adsorption occurs via a single contact point, there is competition with neighboring molecules. Vroman²⁸ showed that the higher the number of adsorption sites on the surface, the greater the free adsorption of energy and the higher the probability of low exchange rates.

The release of preadsorbed nucleic acid onto cationic thermally sensitive latexes was generally investigated to purify and concentrate such biomolecules (i.e., adsorption in a few milliliters from a large volume and desorption in a few liters). Desorption can be performed by changing the pH or salinity level, or by adding a caotropic agent. According to the adsorption process of such highly

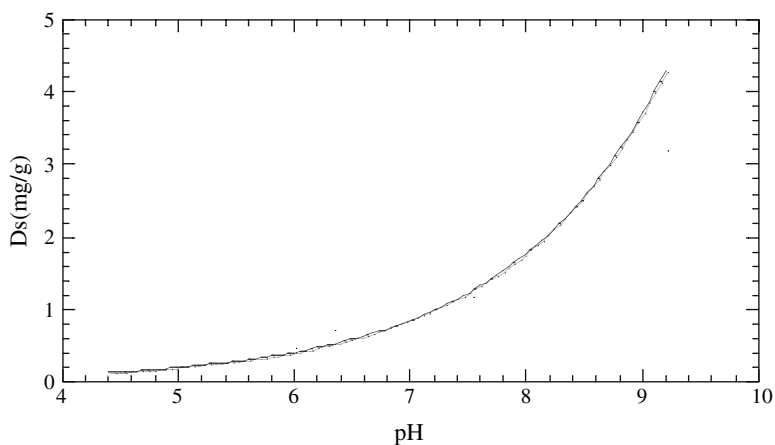


FIGURE 12.30 The effect of pH on the desorption of preadsorbed nucleic acid molecules onto cationic thermally sensitive magnetic latex particles. Adsorption was performed using 10 mM phosphate buffer, pH ~ 5.2, 10^{-3} M NaCl at 20°C, with an incubation time of 180 min. (From Elaissari, A. et al., *J. Magn. Magn. Mater.*, 2001. With permission.)

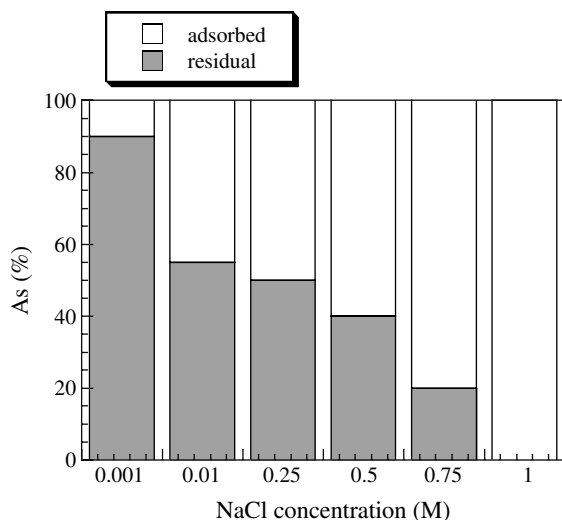


FIGURE 12.31 Effect of NaCl concentration on desorption of RNA from poly(NIPAM) latex at pH 9.2 and 20°C. The adsorbed amount of RNA at pH 4.6, 20°C, and 10^{-2} M ionic strength was 17 mg/g. (From Elaissari, A. et al., *J. Biomater. Sci. Polym.*, 10, 403, 1999. With permission.)

charged polyelectrolytes, which is mainly governed by electrostatic interaction, desorption can be intuitively favored by increasing the incubation pH of the medium to reduce the attractive forces, as shown in Figure 12.30 (i.e., reduction in the surface charge density of the polymer support), or by increasing salinity to screen the intensity of the attractive electrostatic interactions (Figure 12.31).

12.4.3 AMPLIFICATION OF NUCLEIC ACIDS

In biomedical diagnostics, the amplification of captured or adsorbed nucleic acids using the classical PCR method is one of the targets various biological applications. The enzymatic amplification of desired nucleic acids is often performed after the desorption or release step. Thanks to hydrophilic,

highly hydrated magnetic and nonmagnetic latex, direct amplification of adsorbed nucleic acid molecules onto the particles¹⁷ is now possible.

The inhibition of adsorbed nucleic acids after the desorption process can be attributed to the following factors: (1) the possible release of undesirable impurities originating from the particles, such as bare iron oxide nanoparticles, ferric or ferrous ions, surfactant, etc., and (2) the desorption of adsorbed inhibitor initially present in the biological sample under study.

The inhibition of direct amplification of adsorbed nucleic acids on the colloidal particles could be due to the factors mentioned above, and also to (1) high affinity between the enzymes and the particles, and (2) the nature of the support (high hydrophobicity, noncoated iron oxide, or denaturing domains), as well as the high concentration of colloidal particles in the PCR medium.

12.5 CONCLUSION

This chapter covers the preparation, characterization, and biomedical application of thermally sensitive particles. Thermosensitive hydrogel is prepared by precipitation polymerization of *N*-alkylacrylamide or *N*-alkylmethacrylamide as a principal water-soluble monomer, a water-soluble cross-linker (for example, *N*-methylenebisacrylamide) and an initiator (such as azobis-amidinopropane derivatives, potassium persulfate, or basically any charged initiator). The core-shell latexes are produced by a combination of emulsion and precipitation polymerization, such as preparation of polystyrene core and poly(*N*-isopropylacrylamide) shell or encapsulation of colloidal seed using alkylacrylamide derivatives. During the elaboration of such stimuli-responsive particles, various aspects should be considered: (1) a water-soluble cross-linker is needed, (2) the polymerization temperature should be higher than the LCST of the corresponding linear polymer, (3) a water-soluble polymer is produced (which can be controlled by monitoring the polymerization conditions). The polymerization mechanism has been clearly discussed and well illustrated, but the nucleation step remains questionable and requires further work.

The colloidal characteristics of *N*-alkylacrylamide- or *N*-alkylmethacrylamide-based particles are temperature related. In fact, the swelling ability, charge density, charge distribution, hydrophilic–hydrophobic balance, hydration and dehydration properties, particle size, surface polarity, colloidal stability, water content, turbidity, and electrokinetic and rheological properties are indiscernibly temperature dependent. Such polymer particles can be used as a stimuli-responsive model for the investigation of colloidal properties and for theoretical studies.

As can be seen from this chapter, the adsorption and desorption of proteins and nucleic acids can be monitored by controlling the key point governing the driving forces involved in the adsorption process.

The adsorption of proteins onto charged thermally sensitive particles is greatly affected by the incubation temperature. Protein adsorption onto highly hydrated thermosensitive particles below the volume phase transition temperature is negligible. However, the affinity and the amount of protein increase together with the temperature, revealing the complex adsorption process. Desorption is easily favored by cooling the temperature and controlling the adsorption time. In addition, the adsorption and desorption processes are pH, time, and ionic strength dependent.

The adsorption process of nucleic acids onto such cationic hydrophilic thermally sensitive colloids is governed by the attractive electrostatic interaction as the driving forces. The adsorption of DNA, RNA, and ssDNA are related to the surface charge density and accessible adsorption sites. The desorption of preadsorbed nucleic acid molecules onto polymer particles is favored by reducing the attractive electrostatic interactions by altering the pH and the salinity of the medium. Such hydrophilic particles can be used for specific adsorption and concentration of nucleic acids from any biological sample containing a complex mixture (proteins, lipids, membrane fragments, etc.). In addition, colloidal particles bearing hydrophilic and cross-linked thermally sensitive shells can be used directly in nucleic acid amplification processes (i.e., PCR) without any inhibition phenomena. The potential application of hydrophilic, cationic thermally sensitive particles is summarized [Figure 12.32](#).

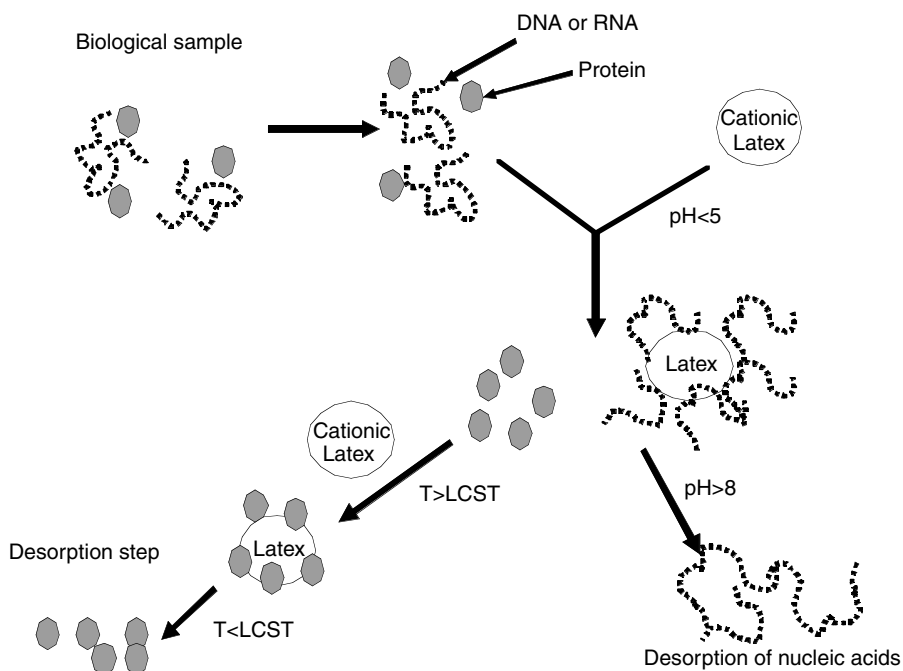


FIGURE 12.32 Stimuli-responsive colloidal particles for biomolecules isolation and concentration.

12.6 ACKNOWLEDGMENT

This chapter is personally dedicated to Dr. Christian Pichot on his retirement from CNRS. I worked with Dr. C. Pichot for more than ten years, enjoying successful joint research and collaboration in the chemistry of support groups in CNRS-bioMrieux's research unit. In addition, I would like to express my gratitude to Dr. F. Meunier, Dr. D. Duracher, and Dr. T. Taniguchi for their help and scientific contributions.

REFERENCES

1. Pelton, R.H. and Chibante, P., *Colloids Surf.*, 20, 247–256, 1986.
2. Heskins, M. and Guillet, J.E., *J. Macromol. Sci. Chem.*, A2 (8), 1441–1455, 1968.
3. Schild, H.G. *Prog. Polym. Sci.* 17, 163–249, 1992.
4. Hoshino, F. et al., *Polym. J.*, 19 (2), 241–247, 1987.
5. Duracher, D., Elaissari, A., and Pichot, C., *J. Polym. Sci. A Polym. Chem.*, 37, 1823–1837, 1999.
6. Hazot, P. et al., *Macromol. Symp.*, 150, 291–296, 2000.
7. Meunier, F., Ph.D. thesis, 1996.
8. Wu, X. et al., *Colloid Polym. Sci.*, 272, 467–477, 1994.
9. Meunier, F., Elaissari, A., and Pichot, C., *Pol. Adv. Tech.*, 6, 489–496, 1995.
10. Dainton, F.S. and Tordoff, M., *Trans. Faraday Soc.*, 53, 499, 1957.
11. Currie, D.J., Dainton, F.S., and Watt, W.S., *Polymer*, 6, 451, 1965.
12. Dainton, F.S. and Sisley, W.D., *Trans. Faraday Soc.*, 59, 1369, 1963.
13. Guillermo, A. et al., *J. Polym. Sci. B Polym. Phys.*, 38(6), 889–898, 2000.
14. Duracher, D. et al., *Macromol. Symp.*, 150, 297–303, 2000.
15. Duracher, D. et al., *Colloid Polym. Sci.*, 276, 219–231, 1998.
16. Castanheira, E.M.S. et al., *Langmuir*, 15(20), 6712–6717, 1999.
17. Elaissari, A. et al., 225, 127–133, *J. Magn. Magn. Mater.*, 2001.
18. Kawaguchi, H., Fujimoto, K., and Mizuhara, Y., *Colloid Polym. Sci.*, 270, 53–57, 1992.

13 Nucleic Acid–Dependent Enzymatic Reactions in Conventional Liposomes and Giant Vesicles

Thomas Oberholzer

CONTENTS

- 13.1 Introduction
 - 13.2 Enzymatic Reactions in Conventional Liposomes
 - 13.2.1 Strategies for Carrying Out Enzymatic Reactions Involving Nucleic Acids in Conventional Liposomes
 - 13.2.1.1 Strategy I
 - 13.2.1.2 Strategy II
 - 13.2.1.3 Strategy III
 - 13.2.1.4 Other Strategies
 - 13.2.2 Procedures for the Entrapment of Water-Soluble Enzymes and Substrate Macromolecules in Conventional Liposomes
 - 13.2.3 Case Study of the Polymerase Chain Reaction inside Conventional POPC Liposomes
 - 13.2.4 Studies with Entrapped Enzymes and External Addition of Substrate Molecules
 - 13.3 Enzymatic Reactions in Giant Vesicles
 - 13.3.1 Formation of GV's and Operational Methodology
 - 13.3.2 Enzymatic Reactions in GV's
 - 13.4 Concluding Remarks and Outlook
- References

13.1 INTRODUCTION

Although liposomes have been investigated for almost 40 years,¹ only relatively few attempts have been made to perform enzyme-catalyzed reactions in these compartments. This is surprising considering the large number of investigations that have been carried out in other artificial compartments, such as microemulsions, single water in oil (W/O) emulsions, and multiple emulsions (for review see References 2 through 6). The reasons for this are manifold: In contrast to all sorts of emulsions, the preparation of liposomes is relatively complicated; liposomes are not thermodynamically stable; their production requires energy; and the way in which they have been prepared influences their physical properties such as size or lamellarity. In addition, the entrapment of larger molecules such as enzymes or nucleic acids in liposomes is far from being trivial; special techniques

have to be applied to bring about sufficient yields of these macromolecules in the aqueous pool of liposomes (for an overview of these techniques, see Reference 7).

On the other hand, liposomes permit us to mimic cells much better than all other artificial compartments. With their inner aqueous pools that form a perfect boundary with the external medium, liposomes resemble cells or cell organelles much more closely than other artificial compartments.

Liposomes can be divided into two main classes: Conventional liposomes — small unilamellar liposomes (SUVs), large unilamellar liposomes (LUVs), and multilamellar vesicles (MLVs) (see Reference 8) — and giant vesicles. The former aggregates, the conventional liposomes, have sizes between 25 nm and 10 μm and their aqueous pools are typically in the range of 50 to 200 nm. In contrast to these relatively small aggregates, giant liposomes are aggregates that are often larger than 10 μm and can be visualized by conventional optical microscopy. Giant liposomes were described for the first time by Reeves and Dowben⁹ in 1969. Among the several methods that allow the preparation of giant vesicles, such as slow rehydration of lipid films, dialysis, or reverse phase evaporation, one of the most efficient methods for the preparation of uni- or oligolamellar giant vesicles has been turned out to be electroformation, first described by Angelova and Dimitrov in 1986.¹⁰

This chapter focuses on studies that describe enzymatic reactions occurring in the aqueous pools of conventional liposomes or giant vesicles; among all the reactions that have been performed within such aggregates, this chapter summarizes enzymatic reactions that are nucleic acid dependent (various polymerase reactions and protein synthesis) and are, therefore, also relevant to the origin of life.

13.2 ENZYMATIC REACTIONS IN CONVENTIONAL LIPOSOMES

13.2.1 STRATEGIES FOR CARRYING OUT ENZYMATIC REACTIONS INVOLVING NUCLEIC ACIDS IN CONVENTIONAL LIPOSOMES

Of the various strategies for conducting enzymatic reactions in liposomes involving nucleic acids, three strategies are discussed here because these strategies have also been applied and their results published in the literature.

13.2.1.1 Strategy I

All ingredients are present in the reaction mixture, which is added to a lipid film, and liposomes are prepared containing all macromolecules (enzymes and DNA or RNA templates) as well as all substrate molecules (nucleotides, for example). Consequently, this procedure has to be performed very quickly; otherwise, the enzymatic reaction would mainly occur outside the liposomes and a distinction between product molecules synthesized inside from those produced outside and entrapped later would be difficult to draw. After the formation of liposomes, the enzymes outside the liposomes have to be inhibited by potent inhibitors (inhibitors that do their job even in the presence of substantial amounts of phospholipids) or the liposomal dispersion has to be treated by digestive enzymes. This strategy has basically been applied in the case of the RNA replication by Q β replicase inside oleic acid/oleate liposomes¹¹ and in the case of the polymerase chain reaction (PCR) inside POPC or POPC/PS liposomes.¹² In the former case, EDTA was added after the formation of the liposomes to inhibit the non-entrapped enzymes (and the kinetics was followed after addition of the EDTA molecules), in the latter case, the non-entrapped DNA template molecules were digested by DNase I before the temperature was raised to 95°C and the polymerization started.

13.2.1.2 Strategy II

Liposomes are formed by rehydration of a lipid film at temperatures below 4°C. The substances to be entrapped are added to the aqueous solution; consequently, formation of vesicles and entrapment occur simultaneously. After this preparation period, inhibitor molecules are added to the external medium that block all enzymes that have not been entrapped, before the suspension is extruded through filters with appropriate pore sizes. One main drawback of this strategy is that it can only be applied with lipids that have their main transition temperature T_m below 0°C. This technique has basically been applied for the synthesis of poly(Phe) in liposomes.¹³

13.2.1.3 Strategy III

Only the macromolecules are entrapped during the period of liposome formation. In the case of enzymatic reactions with nucleic acids, enzymes and DNA/RNA template or oligonucleotide primer molecules are entrapped in the liposomes; the substrate molecules, such as the nucleotides, are added later. Because phospholipid bilayers are practically impermeable to most molecules, the phospholipid bilayers have to be made more permeable by increasing their normal permeability. The normal permeability of phospholipid bilayers to nucleotide triphosphates is too low to entrap substantial amounts in their water pool for a further detection of product molecules. Several methods have been applied to increase the permeability and to load conventional liposomes from the outside with nucleotide substrates.¹⁴⁻¹⁷ The advantage of this strategy is that the preparation of the liposomes need not be performed as fast as possible. The crucial point when applying this strategy is that non-entrapped enzymes/nucleic acids have to be separated from the liposomes almost entirely. This is often problematic when liposomes and larger nucleic acids such as plasmid DNAs are present.

13.2.1.4 Other Strategies

Of course, other strategies are conceivable and have also been suggested in the literature. Here, we could mention methods that derive from the classical reverse phase evaporation¹⁸ or formation of liposomes by dialysis.^{19,20} Another conceivable and proposed (but as yet never applied for such complex enzymatic reactions) approach would be one involving two preparations of liposomes containing, for example, enzyme in the first preparation and nucleic acids/substrate molecules in the second preparation. Then, a fusion process would have to be induced that would create one new compartment containing all the required molecules in the same aqueous pool.

13.2.2 PROCEDURES FOR THE ENTRAPMENT OF WATER-SOLUBLE ENZYMES AND SUBSTRATE MACROMOLECULES IN CONVENTIONAL LIPOSOMES

As mentioned above, one of the most critical points when carrying out enzymatic reactions inside liposomes involving nucleic acids is the entrapment efficiency of macromolecules. The question is whether enough macromolecules can be entrapped in a single liposome so that an individual liposome can host at least one enzyme and one template nucleic acid molecule. (It should be kept in mind that the concentrations of enzymes or nucleic acids can often not be increased too much.)

Among the various methods that can be applied to entrap macromolecules inside liposomes, those methods have to be selected that increase the entrapment efficiency substantially and lead to an entrapment efficiency that is higher than the entrapment yield that results from vesicles prepared by dispersing a lipid film with subsequent extrusion (VET method, see Reference 7). Entrapment of macromolecules by the VET method is quite inefficient; the likelihood that one liposome could contain enzyme as well as nucleic acid template molecule is very low.

Unfortunately, there are few studies available in which a systematic comparison of the encapsulation efficiency depending on the entrapment method has been reported. Therefore, experiments

were performed to find the best encapsulation procedure for nucleic acids. Monnard et al.²¹ compared the main three methods for entrapping nucleic acids in relatively monodisperse liposomes, namely, reverse phase evaporation (REV), dehydration/rehydration (DRV), and entrapment by several freeze/thaw cycles (FAT-VET), all of them with a subsequent extrusion step. As was demonstrated, all three methods entrapped longer nucleic acid molecules at a much higher efficiency than the entrapment by simple dispersion of a lipid film with subsequent extrusion. Among the investigated methods, FAT-VET resulted in the highest encapsulation yields. Especially, when a liposomal dispersion with a relatively narrow size distribution was produced by classical extrusion techniques, freeze/thaw cycles turned out to be the best method for encapsulating nucleic acids.

13.2.3 CASE STUDY OF THE POLYMERASE CHAIN REACTION INSIDE CONVENTIONAL POPC LIPOSOMES¹²

Carrying out a complex DNA polymerase reaction such as the PCR by thermostable DNA polymerases in liposomes was a particular challenge: the liposomes had to exhibit a high stability even at temperatures between 90 and 95°C. In addition, there had to be at least one enzyme molecule and one template DNA molecule, as well as several shorter oligonucleotide molecules present in a single compartment. The fact that such a complex polymerase reaction could be performed inside liposomes is a good advertisement for the above-defined Strategy I. Because no polymerase activity can be measured before melting the double-stranded DNA, the liposome preparation and entrapment techniques can be performed simultaneously without fear of producing product molecules outside the vesicles during this preparation period.

In fact, all ingredients were added to a lipidic film and the resulting dispersion was treated by freeze/thawing. Afterward, the dispersion was extruded through filters with a pore size of 400 nm. The extruded dispersion was then treated with high amounts of DNase I for several hours, before the non-entrapped material was removed by spin column gel permeation chromatography. The fractions containing turbid material were then combined and the liposomes were subjected to 25 temperature cycles. For a determination of the newly synthesized DNA, the liposomes were destroyed by adding sodium cholate and the DNA was isolated and analyzed by polyacrylamide gel electrophoresis (Figure 13.1).

This case study permitted us to show that even relatively complex biochemical reactions can be performed inside liposomes, even if they have to be carried out at temperatures between 55 and 95°C. On the other hand, these experiments also demonstrated the main difficulty when working with conventional liposomes: the likelihood that an individual liposome can host all ingredients is relatively small. At the concentrations of plasmid DNA and DNA polymerase applied for the presented PCR experiments in liposomes, the probability that an average-sized liposome (having a diameter of 180 nm, as evaluated by freeze-fracture electron microscopy) may contain both enzyme and DNA template was calculated to be <0.5%. In addition, inside such a model average-sized liposome there were enough nucleotides present so that three to four newly synthesized DNA molecules could be produced. These calculations also confirmed why the yield of obtained product was relatively modest. And they demonstrated that, for the design of a better microreactor model, it was inalienable that substrate molecules could be added externally.

13.2.4 STUDIES WITH ENTRAPPED ENZYMES AND EXTERNAL ADDITION OF SUBSTRATE MOLECULES

Several attempts by other groups as well as in our laboratory have aimed at the design of a liposomal microreactor. According to the above-described Strategy III, this would be a liposome containing macromolecules (enzymes/nucleic acids) while the substrate molecules, in these cases monomers, are added from the external milieu. Once the monomeric substrate molecules have crossed the bilayer, they are recognized by their enzymes and incorporated into larger, nonpermeable, polymers. In this way, a “perfect liposomal microreactor” is designed.

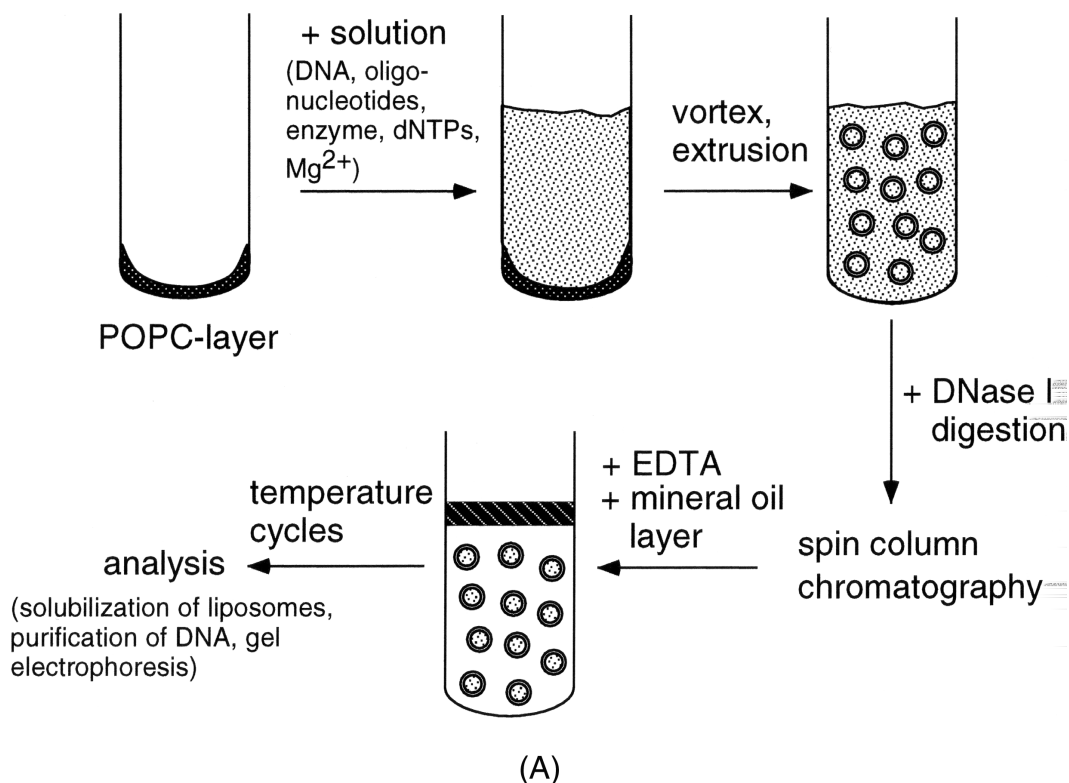


FIGURE 13.1 (A) Schematic representation illustrating the experimental procedure for PCR in conventional liposomes.¹² (B) PCR reaction in POPC (lanes 1–3) or POPC/PS (90:10; lanes 4, 5) liposomes. All the ingredients required for PCR were entrapped in the appropriate liposomes. The dispersion was treated with DNase I to digest the non-entrapped DNA template and the liposomes were purified by gel filtration chromatography. The fractions containing turbid material were then combined as indicated and subjected to 12 cycles at 60°C/72°C/95°C, before the liposomes were solubilized and the DNA was analyzed on a 7.5% acrylamide gel. Lanes 6–8 show the corresponding control experiments. To test whether the fact that the leakage of 2 to 3% of the entrapped material could be responsible for a PCR outside liposomes, all ingredients (without the DNA polymerase and DNA template) were added to a film and liposomes were prepared. After digestion with DNase I and isolation of the liposomes by gel filtration chromatography, the DNA polymerase/DNA template molecules were added externally and the liposomal dispersion was subjected to 12 temperature cycles. (From Oberholzer, T. et al., *Chem. Biol.*, 2, 677–682, 1995. With permission from Elsevier Science.)

Several years ago, Chakrabarti et al.¹⁴ described for the first time such a polymerization of RNA inside DMPC vesicles by polynucleotide phosphorylase. In these experiments, ADP was added externally to the enzyme-containing vesicles (this enzymatic reaction does not require template nucleic acids for initiation) and incubated at 23°C, the main phase transition temperature of DMPC. Because of these gel-to-liquid crystalline transitions of the bilayer, the vesicles could take up ADP from the external milieu, and the enzyme could produce poly(A). On the other hand, the enzyme could not leak out because of its size. Similar experiments were also carried out in our group by Walde et al.¹⁵ Here, the vesicles consisted of a single-chain amphiphile (oleic acid/oleate) that forms vesicles at a pH of about 8.0. ADP was shown to permeate across the oleic acid/oleate membrane and was incorporated inside the vesicles by polynucleotide phosphorylase to poly(A).

More recent studies showed that liposomes from POPC (a double-chain amphiphile, 1-palmitoyl-2-oleoyl-phosphatidylcholine) could also be utilized for such experiments. In these studies, the liposomes containing the enzyme were made semipermeable by adding sodium cholate, a well-described detergent. By using this technique, liposomes containing the appropriate enzyme (and template if

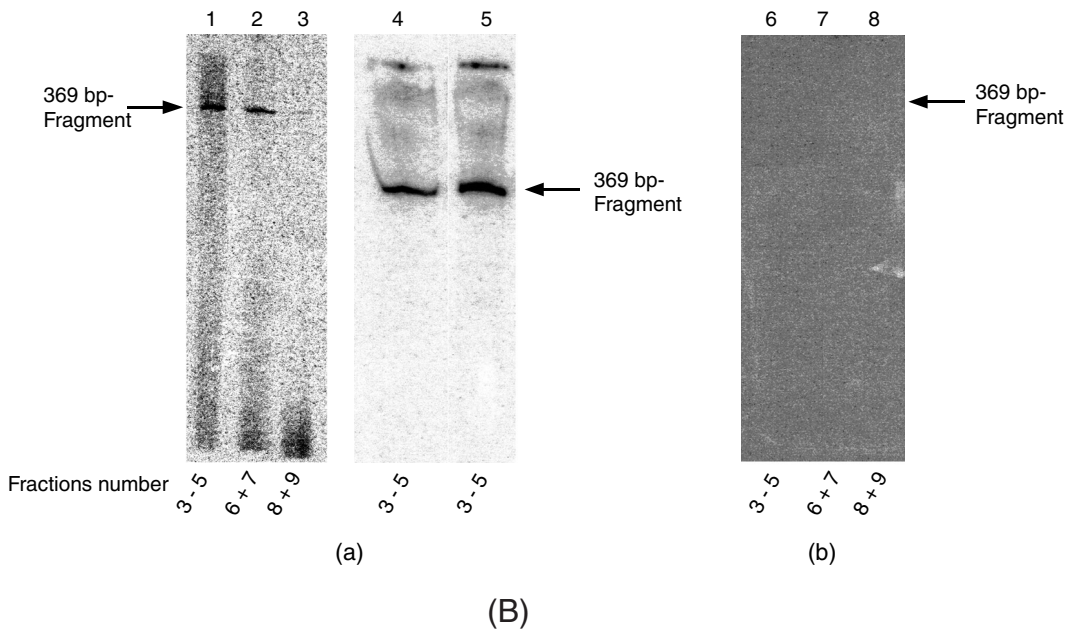


FIGURE 13.1 (continued)

necessary) were permeabilized by adding cholate. The resulting mixed phospholipid–cholate bilayer could take up the substrate molecules from the outside; however, the encapsulated macromolecules remained inside.

With this methodology, it was demonstrated in a first attempt that glycogen can be synthesized by glycogen phosphorylase with the monomers added from the outside.¹⁶ In this study, two macromolecules had to be entrapped in the same liposome: the enzyme glycogen phosphorylase and glycogen as an initiator. To be sure that no glycogen synthesis occurred outside the liposomes, aberrant amyloglucosidase, an enzyme that degrades glycogen, was added outside the liposomes (Figure 13.2). One difficulty when working with phospholipid–cholate systems is that an overconcentration of cholate could lead to the solubilization of liposomes and, consequently, to a release of once entrapped enzyme. Because the experiment was designed in such a way that a “short-term” overconcentration could not be totally excluded, in control experiments some glycogen was added together with the substrate molecules to the external medium. Even under these conditions, no relevant amount of glycogen was synthesized outside the liposomes, which is proof that an eventual release of encapsulated glycogen phosphorylase/glycogen due to an overconcentration of cholate had no effect.

In a recent study, Treyer et al.¹⁷ demonstrated that also poly(A) could be synthesized by polynucleotide phosphorylase inside POPC vesicles with the substrate molecules ADP added from the external medium. Again, the membrane was made semipermeable by adding cholate.

13.3 ENZYMATIC REACTIONS IN GIANT VESICLES

13.3.1 FORMATION OF GVs AND OPERATIONAL METHODOLOGY

A totally different approach is described in this section; here enzymatic reactions are performed in giant vesicles (GVs) with diameters of 30 to 100 μm . The GVVs are formed by a method described by Angelova and Dimitrov,^{10,22} called the electroformation method. This method is singular in the sense that the formed GVVs remain in contact with the platinum electrode (the site where they are formed), a fact that is crucial for further experimentation. Of course, these GVVs cannot be considered

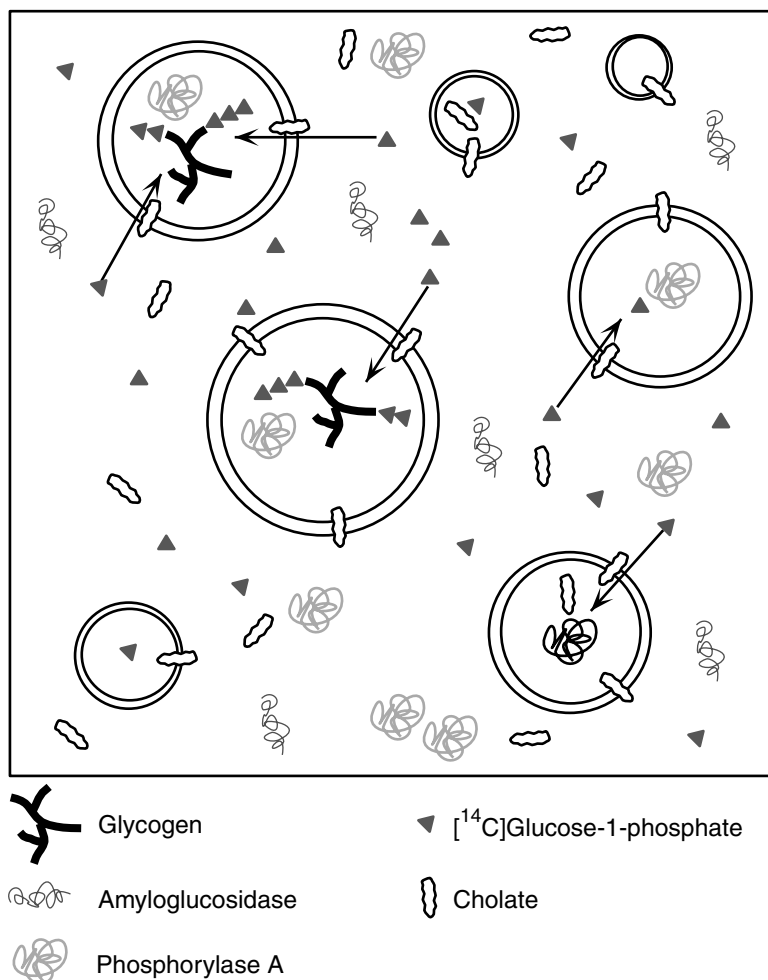


FIGURE 13.2 Schematic illustration of the elongation of glycogen by phosphorylase a in POPC/cholate liposomes.¹⁶ Phosphorylase a and glycogen were entrapped in POPC liposomes; then amyloglucosidase was added externally to digest the non-entrapped glycogen. After an incubation of 1.5 h at 37°C, cholate was added to produce mixed POPC/cholate liposomes before glucose-1-phosphate was loaded from the outside. (From Oberholzer, T. et al., *Biochem. Biophys. Acta*, 1416, 57–68, 1990. With permission.)

“normal” unilamellar phospholipid structures; instead, the fact that the GVs remain in connection with other lipid layers and with the electrode seems to indicate that the structures of these GVs formed during the period of growth in the electric field are more complex. However, there is no detailed information on lamellarity and structure of these GVs. What is known is that these GVs form lipid protrusions called tethers.²³ For our aims, performing enzymatic reactions in liposomes, it is important for further experimentation that these GVs form closed compartments.

Some years ago, we began in our laboratory to inject substances into these GVs formed by electroformation, while still in contact with the electrode.^{24,25} These results showed that these GVs permit the injection of hydrophilic substances into the aqueous pool of a selected GV. In this way, substances such as proteins or nucleic acids were loaded into a micropipet, the micropipet was positioned close to the selected GV, then the GV was punctured, and the substances were injected by blasts of air. Depending on the quality of the micropipet and the chemical property of the loaded substance, different pressures were necessary to push the substance into the GV. Once the substance

to be injected was inside the selected GV, the micropipet could be drawn back without measurable loss of injected substance. Obviously, the GV membranes reseal after the micropipet is removed. Injection experiments with macromolecules such as nucleic acids or proteins reveal that a macromolecule, once inside the GV, remains encapsulated. A loss of fluorescence can normally not be measured with these kinds of macromolecules.²⁵⁻²⁷

Among the macromolecules that have been successfully injected (and their fluorescence followed with time) are fluorescent proteins (the green fluorescent protein), enzymes (nucleases, phospholipases), RNAs and plasmid DNAs, and even large nucleoprotein particles such as ribosomes. To make these injected substances visible requires working with fluorescent dyes, which is also the main limitation of this technique. For nucleic acids there are many well-known dyes that specifically bind to their targets. For our experiments, YO-PRO-1 was selected in most cases because this dye turned out to be very sensitive for all kind of nucleic acids — DNA, mRNA, tRNA, or nucleoprotein complexes. Nucleotides, however, do not lead to a substantial increase in the background fluorescence. In addition, YO-PRO-1 can be added at concentrations that allow us to follow enzymatic reactions inside liposomes. Whether a particular solution containing nucleic acids is injected by one single injection or three injections results in a significantly distinct fluorescent GV. In this way, it could be shown that under standard conditions, no saturation with YO-PRO-1 is reached, a prerequisite for following enzymatic reactions involving nucleic acids in GVs. The reason that no saturation of injected nucleic acid with YO-PRO-1 can be detected is that YO-PRO-1 — even if the molecule is positively charged — can permeate across the GV membrane. Consequently, YO-PRO-1 can be added to the external medium at concentrations that normally permit further injection experiments. This means that there is a 1-ml pool containing YO-PRO-1 (normally at a concentration of 1 μM) outside the selected GV; the amount of injected nucleic acid, even if relatively concentrated, is so low that saturation with YO-PRO-1 can be detected. The only difficulty is that when injecting higher amounts of nucleic acids, we have to wait for some time before enough YO-PRO-1 can permeate across the bilayer and find its target molecule. Therefore, it may take some time for the final level of fluorescence to be reached.

13.3.2 ENZYMATIC REACTIONS IN GVs

The advantage of GVs over conventional liposomes for carrying out enzymatic reactions inside the compartment is obvious: GVs allow a direct observation by light microscopy. Consequently, for enzymatic reactions involving nucleic acids, an increase or decrease of nucleic acid can be followed by the change in their YO-PRO-1 fluorescence. One problematic point in carrying out enzymatic reactions in GVs is the injection procedure, because it is relatively time-consuming. Depending on the liquid applied, the backloading of the micropipet itself can take several minutes. Therefore, care has to be taken to prevent an enzymatic reaction from occurring in the micropipet instead of inside the GV.

Therefore, the experiments were designed in a way that the enzymatic reaction could only begin in the GV. There were basically two different strategies for performing these experiments: (1) multiple loading of the selected GV with different substances and (2) loading of the macromolecules into the selected GV by microinjection and addition of the substrate molecules from the external medium. Because nucleotide triphosphates are the substrate molecules for enzymes such as polymerases, the GV membranes had to be made semipermeable. Their “inherent” permeability toward nucleotides was too low for enzymatic reactions to be carried out in this way.

Very recently, the synthesis of mRNA by T7 RNA polymerase was carried out in GVs.²⁶ In a first attempt, the reaction was performed using the above-described multiple loading method. First, the plasmid DNA carrying a T7 promoter sequence was loaded into a micropipet and injected into the selected GV. Then, the GV was incubated for a longer period until the fluorescence intensity became “stable,” before in a second injection all the other ingredients required for this polymerase reaction were injected (enzyme, nucleotides, Mg^{2+} ions). It could be shown that by applying this

methodology, a complex biochemical reaction can be performed; however, these attempts also revealed that the double injection of the same GV is often problematic and time-consuming. In many cases, it turned out that a second injection into the GV loaded with DNA was not possible. For example, this was the case if the vesicle became too mobile after the injections of the plasmid DNA. The selected GV containing the DNA could be visualized by its fluorescence; however, when touched by a second micropipet, it could avoid the mechanical stress and moved away (something that happened seldom during injecting for the first time). It can be assumed that this “instability” was caused by the mechanical treatment of the selected GV with the micropipet. How the injected substance plays a role in these problems is under debate; however, a role of the injected substance cannot be totally excluded.

In an attempt to improve the above-described methodology, new experiments were designed aiming at reducing the injection procedure to a single injection of all macromolecules, while the smaller substrate molecules and the required salt ions/buffer molecules were externally loaded. Unfortunately, it turned out that with GVs sodium cholate could not be used, because the GVs did not remain stable in aqueous solutions containing reasonable concentrations of sodium cholate. And at very low concentrations of cholate, no effect of cholate on the permeability could be detected. Therefore, other molecules had to be found.

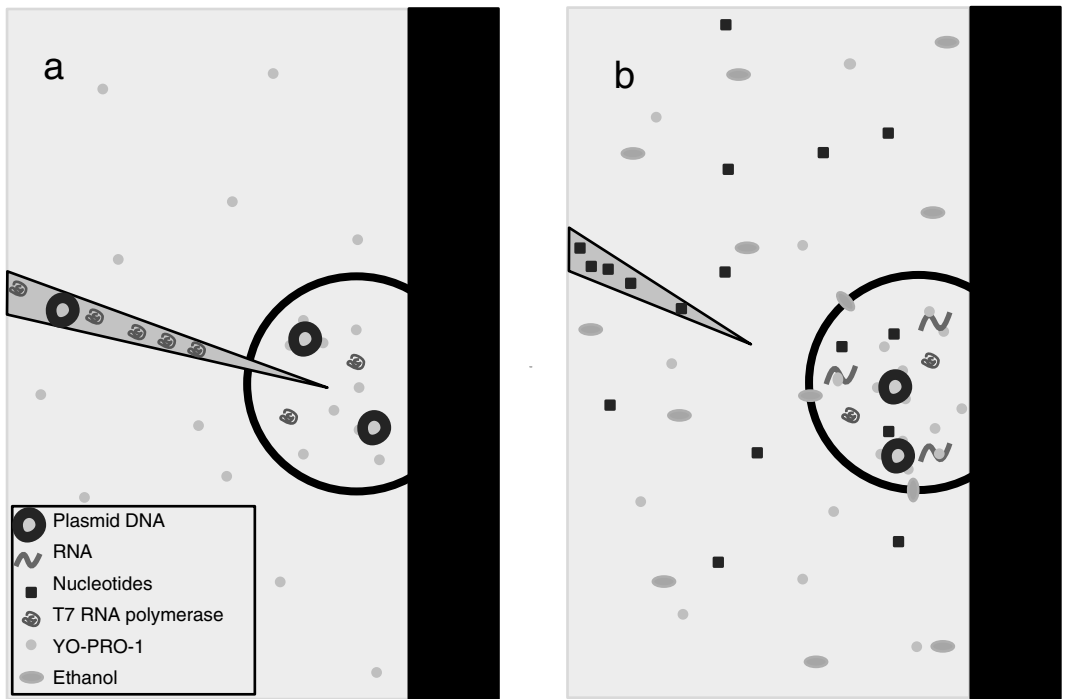
Ethanol was the molecule of choice. There are many studies available describing the effects of ethanol on the stability, structure, and permeability of conventional liposomes. The generally accepted view is that ethanol does induce the formation of interdigitation when liposomes are composed of phospholipids with two saturated acyl chains such as dimyristoyl-PC or dipalmitoyl-PC. Consequently, the permeability behavior of such liposomes changes upon formation of these interdigitated regions, presumably because clusters with interdigitated lipids coexist with non-interdigitated lipids, and at these interfaces the permeation of molecules is facilitated.

Unfortunately, there are only few data available describing the effects of ethanol on conventional liposomes composed of molecules with mixed-chain fatty acids, such as POPC. The few permeability studies seem to demonstrate that the effect of ethanol on such liposomes might be low. And with GVs, there is (to the best of my knowledge) only one study that has been published demonstrating the effect of ethanol on the GV bilayers.²⁸ In this study it was shown that high concentrations of ethanol induce shape transformations of GV formed by electroformation and it was assumed that the stability of these GVs might be negatively influenced.

To observe whether GVs could be loaded with nucleotides, a series of experiments was carried out demonstrating that GVs could take up, in an “ethanol-dependent” way, molecules such as Ca^{2+} ions or fluorescent nucleotide triphosphates. In a further attempt, the “loadable” microreactor could now be designed: macromolecules required for mRNA synthesis by the T7 RNA polymerase (the T7 RNA polymerase and the plasmid DNA) were injected into a selected GV and YO-PRO-1 was added externally. After the fluorescence intensity (caused by the DNA template) became stable, ethanol was added and the GVs were allowed to stand for another period. Then ribonucleotides were added with a micropipet in the vicinity of the selected GV and the increase in the fluorescence intensity was followed with time (Figure 13.3). The quantification of the fluorescence increase showed that the fluorescence increased from a starting normalized value of 100 to a value after 40 min of about 220. The corresponding control experiment carried out under the same conditions but in the absence of T7 RNA polymerase shows only a modest increase in fluorescence.

13.4 CONCLUDING REMARKS AND OUTLOOK

The above presented experiments with the mRNA synthesis by T7 RNA polymerase can be considered as a first step toward the design of a loadable microreactor. It could be shown that the entrapped macromolecules are able to take up the externally added monomers and incorporate them into newly synthesized polymers. Of course, the mRNA synthesis is, from a biological point of



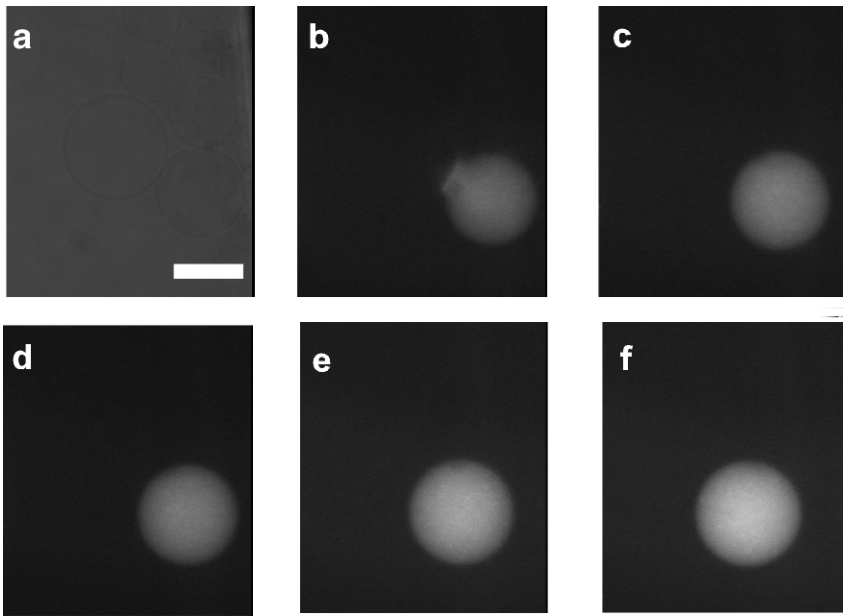
(A)

FIGURE 13.3 mRNA synthesis by T7 RNA polymerase in giant vesicles.²⁶ (A) Schematic representation of the injection procedure. In a first step (a) the enzyme T7 RNA polymerase and the plasmid pWMT7-EGFP (a plasmid containing the EGFP gene under the control of the T7 promoter) are injected into a selected GV. Then (b), ethanol is added and nucleotides are microinjected into the surrounding environment. Ethanol makes the GVs more permeable to nucleotides; thus they can permeate across the GV membrane. (B) Demonstration of the time course of the increase in fluorescence of the YO-PRO-1/nucleic acid complex due to the increased nucleic acid concentration inside the selected GV. (a, b) Before addition of nucleotides; (c) 3 min, (d) 12 min, (e) 22 min, (f) 32 min after the addition of nucleotides. Scale = 50 μm . (c) Quantification of the fluorescence intensities. (C) Kinetics of the increase in fluorescence by the T7 RNA polymerase (filled squares, initial value normalized to 100). The open squares show the same experiment in the absence of T7 RNA polymerase.

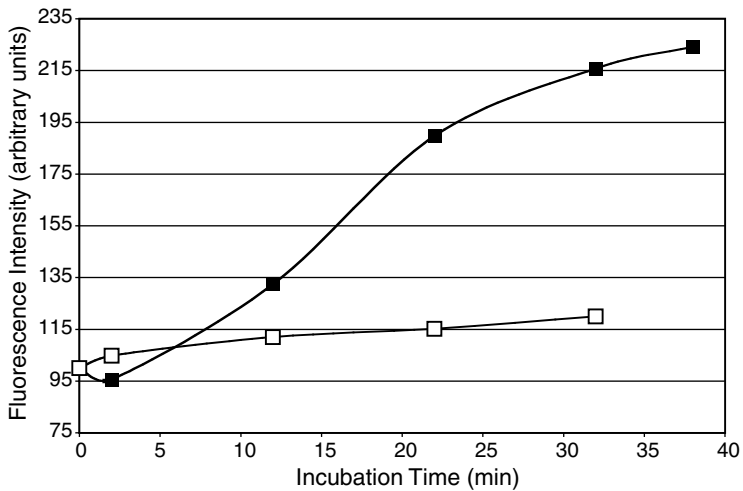
view, only the first step; future experiments have to be performed aiming at the synthesis of proteins. First attempts have been made; however, it turned out that to carry out protein synthesis in GVs is “much more complicated” than the synthesis of mRNA by T7 RNA polymerase.

One reason for this might be that the T7 RNA polymerase requires only Mg^{2+} to be able to work; even at relatively low ion concentrations that enzyme does have a reasonable activity. Contrast this to the protein synthesis; here the minimal salt concentration is much more delicate than it is in the case of T7 RNA polymerase. And the formation of GVs in higher concentrations of salt is quite limited. This leads to a situation where very concentrated solutions should be injected, a procedure that often turns out to be impossible because these solutions can clog the micropipet.

Another reason for these conceptual difficulties is that the commercially available kits for carrying out protein synthesis cannot be diluted many times (without losing most of their activity). This in contrast to the situation with T7 RNA polymerase, which can be injected at concentrations that are much higher than that required in aqueous solution. Therefore, we have to find methodologically new ways to load the GVs with all the ingredients required for protein synthesis and keep the GVs stable under those conditions.



(B)



(C)

FIGURE 13.3 (continued)

REFERENCES

1. Bangham, A.D., Physical structure and behavior of lipids and lipid enzymes, *Adv. Lipid Res.*, 1, 65–104, 1963.
2. Luisi, P.L. et al., Reserve micelles as hosts for proteins and small molecules, *Biochim. Biophys. Acta*, 947, 209–246, 1988.
3. Martinek, K. et al., Micellar enzymology: its relation to membranology, *Biochim. Biophys. Acta*, 981, 161–172, 1989.

4. Scheper, T., Enzyme immobilization in liquid surfactant membrane emulsions, *Adv. Drug Delivery Sys.*, 4, 209–231, 1990.
5. Tawfik, D.S. and Griffiths, A.D., Man-made cell-like compartments for molecular evolution, *Nature Biotech.*, 16, 652–656, 1998.
6. Doi, N. and Yanagawa, H., STABLE: protein-DNA fusion system for screening of combinatorial protein libraries *in vitro*, *FEBS Lett.*, 457, 227–230, 1999.
7. Walde, P. and Ichikawa, S., Enzymes inside lipid vesicles: preparation, reactivity, and applications, *Biomol. Eng.*, 18, 143–177, 2001.
8. New, R.R.C., *Liposomes — A Practical Approach*, Oxford University Press, New York, 1990.
9. Reeves, J.P. and Dowben, R.M., Formation and properties of thin-walled phospholipid vesicles, *J. Cell. Physiol.*, 73, 49–60, 1969.
10. Angelova, M.I. and Dimitrov, D.S., Liposome electroformation, *Faraday Discuss. Chem. Soc.*, 81, 303–311, 1986.
11. Oberholzer, T. et al., Enzymatic RNA replication in self-reproducing vesicles: an approach to a minimal cell, *Biochem. Biophys. Res. Commun.*, 207, 250–257, 1995.
12. Oberholzer, T., Albrizio, M., and Luisi, P.L., Polymerase chain reaction in liposomes, *Chem. Biol.*, 2, 677–682, 1995.
13. Oberholzer, T., Nierhaus, K.H., and Luisi, P.L., Protein expression in liposomes, *Biochem. Biophys. Res. Commun.*, 261, 238–241, 1990.
14. Chakrabarti, A.C. et al., Production of RNA by a polymerase protein encapsulated within phospholipid vesicles, *J. Mol. Evol.*, 39, 555–559, 1994.
15. Walde, P. et al., Oparin's reactions revisited: enzymatic synthesis of poly(adenylic acid) in micelles and self-reproducing vesicles, *J. Am. Chem. Soc.*, 116, 7541–7547, 1994.
16. Oberholzer, T. et al., Enzymatic reactions in liposomes using the detergent-induced loading method, *Biochim. Biophys. Acta*, 1416, 57–68, 1990.
17. Treyer, M., Walde, P., and Oberholzer, T., Permeability enhancement of lipid vesicles to nucleotides by use of sodium cholate. Basic studies and application to an enzyme-catalyzed reaction occurring inside the vesicles, *Langmuir*, 18, 1043–1050, 2002.
18. Szoka, F., Jr., and Papahadjopoulos, D., Procedure for preparation of liposomes with large internal aqueous space and high capture by reverse-phase evaporation, *Biochemistry*, 75, 4194–4198, 1978.
19. Schurtenberger, P. et al., Preparation of monodisperse vesicles with variable size by dilution of mixed micellar solutions of bile salt and phosphatidylcholine, *Biochim. Biophys. Acta*, 8, 111–114, 1984.
20. Ollivon, M. et al., Vesicle reconstitution from lipid-detergent mixed micelles, *Biochim. Biophys. Acta*, 1508, 34–50, 2000.
21. Monnard, P.-A., Oberholzer, T., and Luisi, P.L., Entrapment of nucleic acids in liposomes, *Biochim. Biophys. Acta*, 1329, 39–50, 1997.
22. Angelova, M.I. and Dimitrov, D.S., A mechanism of liposome electroformation, *Prog. Colloid Polym. Sci.*, 76, 59–67, 1988.
23. Mathivet, L., Cribier, S., and Devaux, P.F., Shape change and physical properties of giant phospholipid vesicles prepared in the presence of an ac electric field, *Biophys. J.*, 70, 1112–1121, 1996.
24. Wick, R. et al., Microinjection into giant vesicles and light microscopy investigation of enzyme mediated vesicle transformations, *Chem. Biol.*, 3, 105–111, 1996.
25. Bucher, P. et al., Giant vesicles as biochemical compartments: the use of microinjection techniques, *Langmuir*, 14, 2712–2721, 1998.
26. Fischer, A., Franco, A., and Oberholzer, T., Giant vesicles as microreactors for enzymatic mRNA synthesis, *ChemBioChem*, in press.
27. Oberholzer, T. and Fischer, A., Microinjection of macromolecules in giant vesicles prepared by electroformation, in *Giant Vesicles*, P.L. Luisi and P. Walde, Eds., John Wiley & Sons, New York, 2000.
28. Angelova, M.I. et al., Shape transformations of giant unilamellar vesicles induced by ethanol and temperature variations, *Colloids Surf.*, 149, 201–205, 1999.

14 Scattering and Absorption of Light by Particles and Aggregates

C.M. Sorensen

CONTENTS

- 14.1 Introduction
 - 14.2 Small Particles
 - 14.2.1 Polarization Considerations
 - 14.2.2 The Rayleigh Differential Scattering Cross Section
 - 14.2.3 The Rayleigh Total Scattering Cross Section
 - 14.2.4 The Rayleigh Absorption Cross Section
 - 14.2.4.1 Scattering, Absorption, and Extinction
 - 14.2.5 Rayleigh–Debye–Gans Scattering
 - 14.3 Spheres of Arbitrary Size: The Mie Theory
 - 14.3.1 The Mie Differential Scattering Cross Sections
 - 14.3.1.1 The Mie Guinier Regime
 - 14.3.1.2 The Mie Ripples
 - 14.3.2 The Mie Total Scattering Cross Section
 - 14.4 Fractal Aggregates
 - 14.4.1 Scattering and Absorption by Fractal Aggregates
 - 14.4.2 The Structure Factor
 - 14.4.3 The Structure Factor of an Ensemble of Polydisperse Aggregates
 - 14.5 Examples
- Acknowledgments
- Appendix 14.A: Cross Sections
- 14.A.1 The Differential Cross Sections
 - 14.A.2 The Total Cross Section
 - 14.A.3 Efficiencies
- Appendix 14.B: The Scattering Wave Vector
- References

14.1 INTRODUCTION

The goal of this chapter is to give a brief yet comprehensive description of scattering and absorption of light by spherical particles of arbitrary size and aggregates of these particles that have the fractal morphology. This chapter has been updated from its previous appearance in 1997, most significantly with a new vision of various patterns in Mie scattering from spheres discovered since then. I have refrained from derivation but have tried to give a physical interpretation of the results I quote. Exact equations for scattering and absorption are given, but the emphasis is placed not on the equations

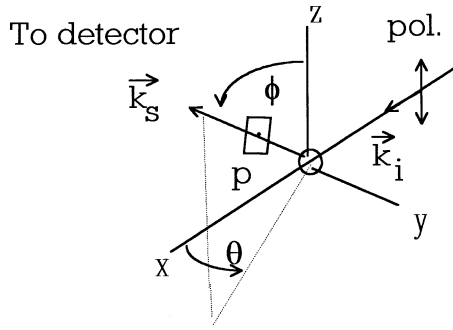


FIGURE 14.1 Geometry of scattering for an incident wave from the negative x -axis with propagation direction defined by the incident wave vector \vec{k}_i and with polarization (pol.) parallel to z . Light is scattered to the detector in the direction of the scattering wave vector \vec{k}_s . Scattered polarization will be in the direction of the projection of the incident polarization onto the plane p , which is perpendicular to the detector direction.

themselves but instead on the “features,” i.e., important functional dependencies, relation to other forms, cardinal points, etc. and on their graphical representation. Hence, I hope I have given the reader a user’s guide to light scattering and absorption that will provide a broad yet well-connected perspective, which can then serve as a frame of reference for deeper studies of a particular nature.

14.2 SMALL PARTICLES

Small is relative. The length scale of light is its wavelength λ ; hence, a small particle has all its dimensions small compared to λ . The simplest case, which is considered here, is a spherical particle of radius a . We may then define the size parameter as $\alpha = 2\pi a/\lambda$ which is a dimensionless ratio of the two length scales involved.

14.2.1 POLARIZATION CONSIDERATIONS

Since its advent, the light source of choice for light scattering studies of colloids and aerosols has been the laser. This source is almost always polarized in the vertical plane. Thus, we do not directly discuss the case of unpolarized or natural light, such as that obtained from an ordinary lightbulb or the sun, incident upon the scatterers. This can be an important situation, especially in nature, but its rules can be inferred from the incident light polarized case, which we discuss here, and it can also be found in earlier work.¹⁻³

Consider a light wave traveling in the positive x direction incident upon a particle at the origin as drawn in Figure 14.1. The direction of propagation is described by the incident wave vector \vec{k}_i with magnitude

$$|\vec{k}_i| = 2\pi/\lambda \quad (14.1)$$

where λ is the wavelength of the light in the medium. There are two independent linear polarizations, and we initially consider light polarized along the z axis. To relate this to typical laboratory situations we will call the z axis vertical, and the x - y plane the horizontal, scattering plane. Light can be scattered by this particle in any direction described by the scattered wave vector \vec{k}_s in Figure 14.1. We consider elastic scattering; hence,

$$|\vec{k}_s| = |\vec{k}_i| \quad (14.2)$$

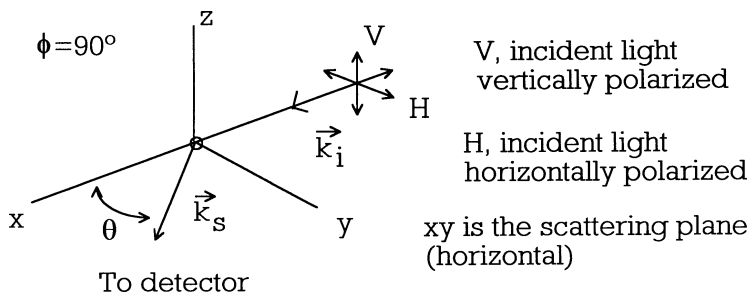


FIGURE 14.2 Typical scattering arrangement in which light is incident from the negative x axis with either (or both) horizontal or vertical polarization. Scattered light is detected in the horizontal, xy , scattering plane at a scattering angle of θ .

Because these magnitudes are equal, we represent each simply by k . Note that $\alpha = ka$.

For particles small compared to the wavelength we can now describe the polarization of the scattered light to be in the direction of the projection of the incident polarization onto a plane perpendicular to \vec{k}_s . This projection yields the amplitude of the scattered field to be proportional to $\sin \phi$; hence the scattered intensity is

$$I_{\text{scat}} \propto \sin^2 \phi \quad (14.3)$$

Most experiments are confined to the scattering plane; hence, $\phi = 90^\circ$, as drawn in Figure 14.2. The angle θ is the scattering angle; $\theta = 0$ is forward scattering. We now consider incident light with either polarization vertical, V , or horizontal, H . The scattered light can be detected through a polarizer set in either the V or H directions. Thus, four scattering arrangements can be obtained described by the scattered intensities as

$$I_{VV}, \quad I_{VH}, \quad I_{HV}, \quad \text{and} \quad I_{HH} \quad (14.4)$$

where the first subscript describes the incident polarization, the second the detected polarization of the scattered light. I_{VV} is the most common scattering arrangement, and it is the one we describe in the rest of this chapter.

For particles small compared to the wavelength, these four intensities are dependent on θ in simple ways. Larger particles yield more complex functionalities but bear the imprint of the simple functionalities of their smaller brethren. The polarization rule above and the concept of projection embodied in Equation 14.3 can be used to infer the four intensities. The most common scattering arrangement measures I_{VV} , which is independent of θ , hence isotropic in the scattering plane. The projection rule implies $I_{VH} = I_{HV} = 0$, and $I_{HH} \propto \cos^2 \theta$. Figure 14.3 shows both a polar and Cartesian plot of these functionalities.

14.2.2 THE RAYLEIGH DIFFERENTIAL SCATTERING CROSS SECTION

Rayleigh first presented a description of light scattering and adsorption from small particles. The conditions for Rayleigh scattering are¹⁻³

$$\alpha \ll 1 \quad (14.5a)$$

$$m\alpha \ll 1 \quad (14.5b)$$

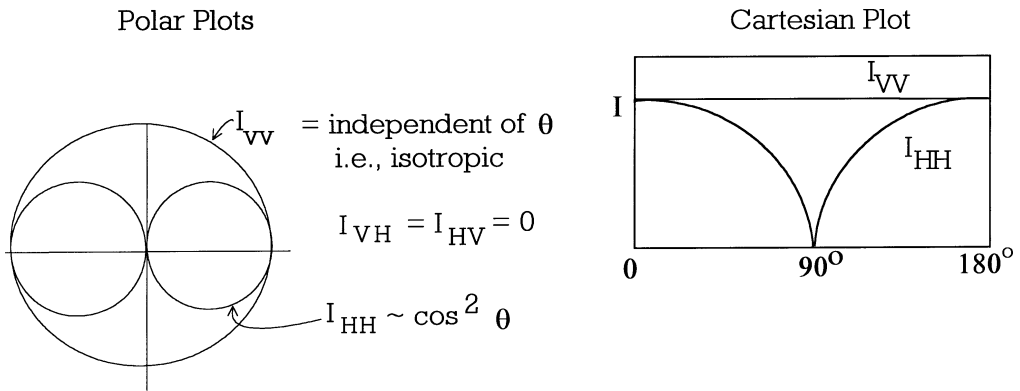


FIGURE 14.3 Polar and Cartesian plots of Rayleigh scattering for both I_{VV} and I_{HH} .

Then the differential scattering cross section is

$$\frac{d\sigma}{d\Omega} = k^4 a^6 \left| \frac{m^2 - 1}{m^2 + 2} \right|^2 \quad (14.6a)$$

$$= \frac{16\pi^4 a^6}{\lambda^4} \left| \frac{m^2 - 1}{m^2 + 2} \right|^2 \quad (14.6b)$$

For some elementary elaboration on the meaning of the differential scattering cross section, the reader is referred to Appendix 14.A at the end of this chapter. Simply put, the scattered intensity is proportional to the differential scattering cross section. Thus, by Equation 14.A4

$$I_{VV} = \frac{k^4 a^6}{r^2} \left| \frac{m^2 - 1}{m^2 + 2} \right|^2 I_o \quad (14.7)$$

Often the term involving the refractive index, the Lorentz term, is abbreviated as $F(m) = |(m^2 - 1)/(m^2 + 2)|^2$. This makes Equation 14.6a simply

$$\frac{d\sigma}{d\Omega} = k^4 a^6 F(m) \quad (14.8)$$

A simple dimensionality argument can be made for the length functionalities in Rayleigh scattering. Since the particle is very small compared to the wavelength of light, the phase of the incident light is uniform across the volume of the particle; i.e., all subvolumes of the particle see the same phase. Furthermore, again since the particle is so small, the light scattered to the detector from all subvolumes of the particle has the same phase. Thus, the total scattered field at the detector is directly proportional to the particle volume, V_{part} . Intensity is field amplitude squared, thus $I \propto V_{\text{part}}^2$. To determine the cross section realize that it has units of length squared. The argument above implies the cross section is proportional to V_{part}^2 , which is length to the sixth power. Thus, a factor of length to the inverse fourth power is missing. There are only two length scales in the problem, particle size and optical wavelength, λ . Particle size has already been used with V_{part}^2 . Thus, to achieve the proper units for cross section, a factor of λ^{-4} must be included to yield a cross section proportional to $\lambda^{-4} V_{\text{part}}^2$ a result consistent with Equation 14.8.

There are a number of important features to make note of for Rayleigh scattering:

1. The scattering is *independent of θ* ; i.e., it is isotropic in the scattering plane. $I_{\text{VH}} = I_{\text{HV}} = 0$, and $I_{\text{HH}} = I_{\text{VV}} \cos^2 \theta$, as drawn in [Figure 14.3](#).
2. The λ^{-4} dependence: Blue light scatters more than red. (This is often associated with the blue of the sky and the red of the sunset,⁴ but other factors are involved here including the fact that in perfectly clean air (no particles) scattering occurs from small, thermodynamic fluctuations in the air density.)
3. The strong size dependence of a^6 is proportional to the particle volume squared, V_{part}^2 .

Feature 3 leads to the *Tyndall effect*,² which describes the increased scattering from an aggregating colloid or aerosol of constant mass. Consider that the total scattering from a particulate system of Rayleigh scatterers of n particles per unit volume has the proportionality

$$I_{\text{scat}} \propto nV_{\text{part}}^2 \quad (14.9)$$

If the only growth process in the system is aggregation, the mass is neither created nor destroyed. Thus, the mass density is constant; hence, nV_{part} is constant. On the other hand V_{part} increases during aggregation. Rewriting Equation 14.9 as

$$I_{\text{scat}} \propto nV_{\text{part}} \cdot V_{\text{part}} \quad (14.10)$$

shows that the scattered intensity increases proportional to V_{part} as the system aggregates. This is the Tyndall effect.

14.2.3 THE RAYLEIGH TOTAL SCATTERING CROSS SECTION

Integration of the differential cross section over the complete solid angle of 4π yields the total cross section, Equations 14.A5 and 14.A6. We consider the scattering arrangement in [Figure 14.1](#) with incident light polarized in the vertical direction to find

$$\sigma = \int \frac{d\sigma}{d\Omega} d\Omega \quad (14.11a)$$

$$= \frac{d\sigma}{d\Omega} \int_0^{2\pi} d\theta \int_{-1}^1 \sin^2 \varphi d(\cos \varphi) \quad (14.11b)$$

$$= \frac{8\pi}{3} \frac{d\sigma}{d\Omega} \quad (14.11c)$$

We can say that the factor $8\pi/3$ comes from integration of the polarization. Equations 14.8 and 14.11c yield

$$\sigma_{\text{scat}} = \frac{8\pi}{3} k^4 a^6 F(m) \quad (14.12)$$

Thus, the scattering efficiency, $Q = \sigma/\pi a^2$ (Equation 14.A7), is

$$Q_{\text{scat}} = \frac{8}{3} \alpha^4 F(m) \quad (14.13)$$

Note that the condition for Rayleigh scattering to hold is $\alpha \ll 1$; thus Equation 14.13 implies that Rayleigh scatterers are not very efficient; i.e., it scatters a lot less than its geometric cross section would imply.

14.2.4 THE RAYLEIGH ABSORPTION CROSS SECTION

The Rayleigh absorption cross section is

$$\sigma_{\text{abs}} = -\frac{8\pi^2 a^3}{\lambda} \text{Im} \left(\frac{m^2 - 1}{m^2 + 2} \right) \quad (14.14)$$

where Im means imaginary part. We use the notation $\text{Im}[(m^2 - 1)/(m^2 + 2)] = E(m)$. Then the absorption efficiency is simply

$$Q_{\text{abs}} = -4\alpha E(m) \quad (14.15)$$

As for scattering, a simple dimensionality argument can be made for the absorption cross section. Since the particle is very small, the wave completely penetrates the volume of the particle. Hence, all subvolumes of the particle absorb equally to imply $\sigma_{\text{abs}} \propto V_{\text{part}}$. To make the units match we divide by the only other length scale of the system, the wavelength, to yield $\sigma_{\text{abs}} \propto \lambda^{-1} V_{\text{part}}$.

Features of Rayleigh absorption are as follows:

1. Absorption has different dependencies with λ and a than scattering

$$\begin{aligned} \sigma_{\text{scat}} &\propto \lambda^{-4} a^6 \\ \sigma_{\text{abs}} &\propto \lambda^{-1} a^3 \\ &\left(\text{a factor of } (a/\lambda)^3 \right) \end{aligned}$$

2. If m is real, there is no absorption.

14.2.4.1 Scattering, Absorption, and Extinction

When light passes through a medium containing particles, it is attenuated. This attenuation is called extinction and is described by an exponential decrease of the intensity as it passes through the medium:

$$I_{\text{trans}} = I_0 e^{-\tau x} \quad (14.16)$$

where I_{trans} is the intensity of the light transmitted after passing a distance x through the medium, and τ is the turbidity of the medium. The turbidity is related to the number density of particles n and their individual extinction cross section σ_{ext} by

$$\tau = n\sigma_{\text{ext}} \quad (14.17)$$

Extinction is due to both scattering, which removes light from the incident path, and absorption, which converts the light into other forms of energy (e.g., heat),

$$\sigma_{\text{ext}} = \sigma_{\text{abs}} + \sigma_{\text{scat}} \quad (14.18)$$

These facts are true for particles of all sizes, not just Rayleigh scatterers. From the discussion above two notable features arise:

1. If m is real, extinction is solely due to scattering

$$\sigma_{\text{ext}} = \sigma_{\text{scat}} \quad (14.19)$$

2. If m is complex and if the size parameter is small, $\alpha < 1$, e.g., Rayleigh scatterers, then Equations 14.13 and 14.15 imply $\sigma_{\text{abs}} \gg \sigma_{\text{scat}}$. Hence,

$$\sigma_{\text{ext}} \approx \sigma_{\text{abs}} \quad (14.20)$$

14.2.5 RAYLEIGH–DEBYE–GANS SCATTERING

The equations for Rayleigh scattering are derived under the assumption that the phase of the incident electromagnetic wave does not change across the particle. This is achieved by assuming the size of the particle to be small compared to $\lambda/2\pi$, hence the condition $\alpha \ll 1$ for spheres. This condition can be relaxed somewhat if the phase across the particle changes only negligibly relative to the phase change in the surrounding medium. Thus, a factor of $m - 1$ is involved as well as the length scale λ and the size of the particle.

The conditions for Rayleigh–Debye–Gans scattering are as follows:

$$|m - 1| \ll 1 \quad (14.21a)$$

$$\rho = 2\alpha|m - 1| \ll 1 \quad (14.21b)$$

The parameter ρ in Equation 14.21b is called the *phase shift parameter* and represents the difference in phase between a wave that travels through a particle directly across its diameter and one that travels the same distance through the medium.

Note that condition 14.21b allows for very large particles, i.e., $\alpha > 1$, so long as m is close enough to unity to satisfy the condition.

The Rayleigh–Debye–Gans differential scattering cross section in the scattering plane for vertically polarized light (Figure 14.1) is

$$\frac{d\sigma}{d\Omega_{\text{RDG}}} = \frac{d\sigma}{d\Omega_R} \left[\frac{9}{u^6} (\sin u - u \cos u)^2 \right] \quad (14.22)$$

where

$$u = 2\alpha \sin \theta/2 \quad (14.23a)$$

or

$$u = qa \quad (14.23b)$$

In Equation 14.22 the subscripts RDG and R denote Rayleigh–Debye–Gans and Rayleigh. In Equation 14.23b q is the *scattering wave vector* to be discussed below.

Notable features of Rayleigh–Debye–Gans scattering are as follows:

1. At $\theta = 0$ the cross section equals the Rayleigh cross section.
2. The scattering is larger in the forward direction and this anisotropy increases with increasing size.

The Rayleigh–Debye–Gans absorption cross section is equal to the Rayleigh absorption cross section.

14.3 SPHERES OF ARBITRARY SIZE: THE MIE THEORY

The Rayleigh and Rayleigh–Debye–Gans theories of scattering and absorption represent solutions to Maxwell’s equations in which approximations could be made due to small size and small index of refraction. For an arbitrary particle these approximations cannot be made; hence, Maxwell’s equations must be solved exactly. Various symmetries, dependent on the shape of the particle, make this task more tractable, and the most symmetric, hence simplest, is that of a homogeneous sphere, to which this discussion is limited. Mie first presented these solutions and the term *Mie scattering* is often applied to the general description of scattering from a homogeneous sphere of arbitrary size.¹⁻³

Mie’s solutions are complex enough to keep us from quoting them here. Moreover, their complexity does not allow for easy physical interpretation. Recently, we have used a graphical analysis to discern patterns in the Mie results that allow for a straightforward description of the angular scattering dependence.⁵⁻⁷

14.3.1 THE MIE DIFFERENTIAL SCATTERING CROSS SECTIONS

Figure 14.4a shows an example of Mie scattering for an index of refraction $m = 1.05$ and a variety of sizes expressed as the size parameter α . The normalized intensity $I(\theta)/I(0)$ vs. θ is plotted. A series of bumps and wiggles are seen with some periodicities, but with no particular coherent pattern. Curves for the larger $m = 1.50$ in Figure 14.5a are even more complex. The scattering angle θ , although conveniently measured in the laboratory, is not the best parameter for plotting the data. This complexity can be reduced if plots are made with the scattering wave vector q rather than the scattering angle θ . The scattering wave vector, derived in Appendix 14.B, is given by

$$q = 4\pi\lambda^{-1} \sin \theta/2 \quad (14.24)$$

Its physical significance is that the inverse, q^{-1} , is the length scale of the scattering experiment. This means that the scattering is sensitive to structures greater than q^{-1} , but it cannot “see” structures smaller than q^{-1} . Any universal character in the Mie curves should be revealed if the differential scattering cross section is plotted vs. the ratio of the two length scales involved: the radius of the particle a and the length scale of the scattering experiment q^{-1} . This ratio is the dimensionless product qa and both Figures 14.4a and 14.5a are replotted in Figures 14.4b and 14.5b as a function of qa .

At small qa a nearly universal “forward scattering lobe” is seen. Near $qa \sim 1$, the falloff is approximately described by the Guinier equation, $I(q)/I(0) \sim 1 - q^2a^2/5$ (see below). The enhanced backscattering, the “glory,” visible in plots with $m = 1.50$, shows no particular pattern but is compressed into spikes in the large qa part for each size parameter α . The key features are the envelopes of these plots. Figures 14.4b and 14.5b include lines that roughly describe these envelopes. For small size parameter α the envelope is described by a -4 slope, hence $(qa)^{-4}$; for larger α two slopes are seen to imply $(qa)^{-2}$ crossing over to $(qa)^{-4}$; and for $m = 1.50$ the envelope is dominated by a -2 slope although a -4 slope is visible at large qa .

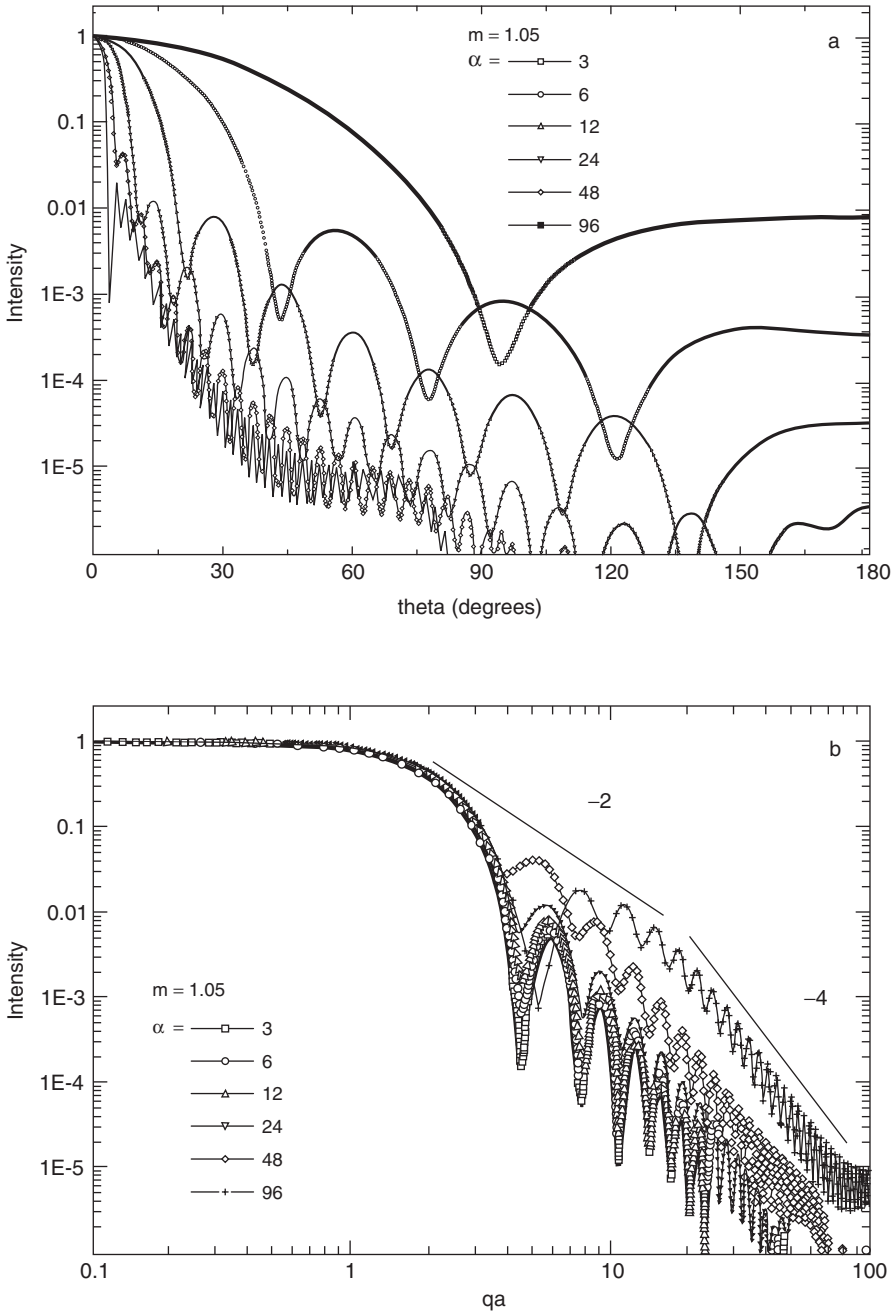


FIGURE 14.4 (a) Normalized Mie scattering curves as a function of scattering angle for spheres of refractive index $m = 1.05$ and a variety of size parameters; and (b) same as (a) but plotted vs. qa . Lines with slope -2 and -4 are shown. (From Sorensen, C.M. and Fischbach, D.F., *Opt. Commun.*, 173, 145, 2000. With permission.)

A complete picture comes together in Figure 14.6, where the envelopes for a wide range of phase shift parameters are plotted. We find that the envelopes are universal functions of the phase shift parameter ρ ; that is, m may vary and α may vary, but if $\rho = 2\alpha|m - 1|$ is the same, the envelopes of the Mie scattering curves lie together. With this, the picture in Figure 14.6 starts at $\rho = 0$, which is the RDG limit. As the phase shift parameter increases, the $(qa)^{-4}$ envelope moves up and away

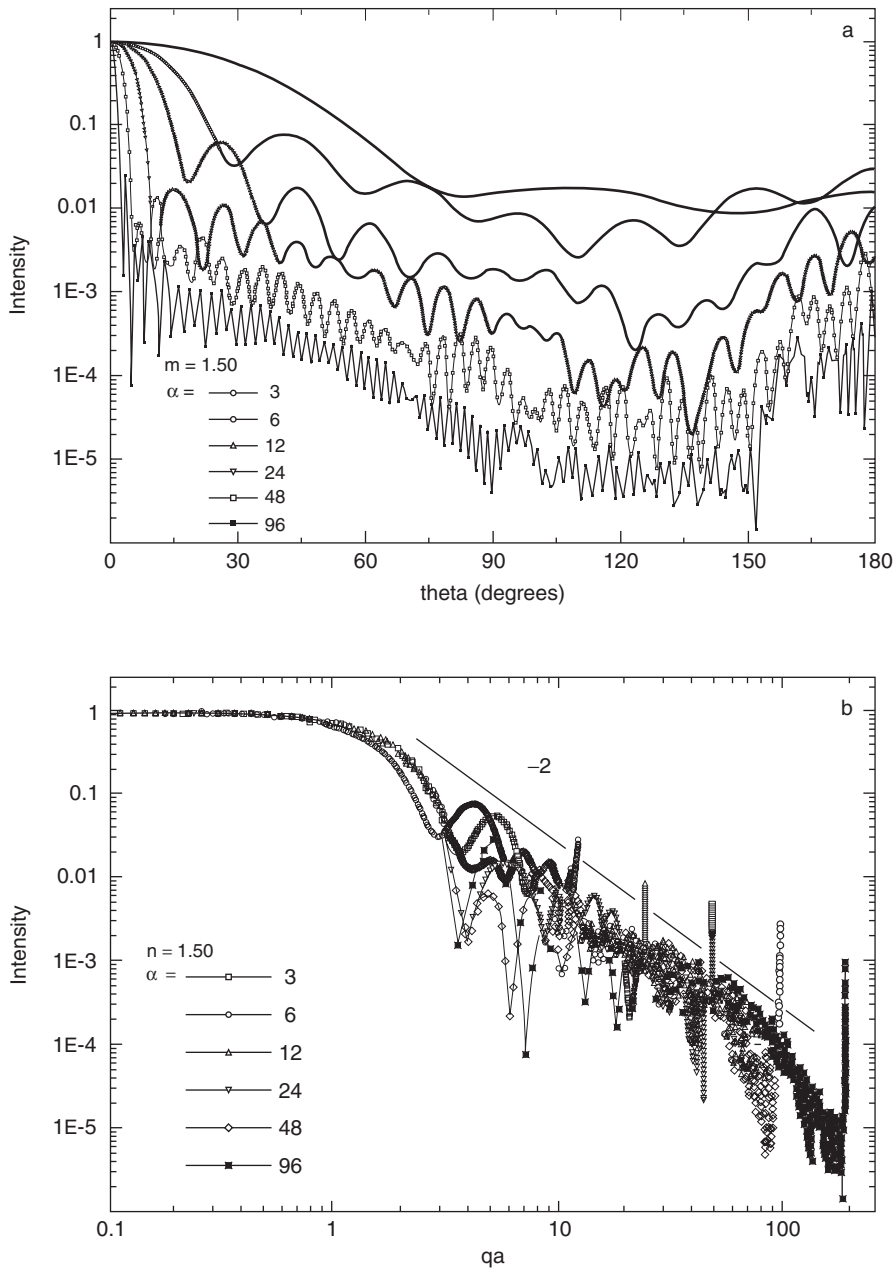


FIGURE 14.5 (a) Normalized Mie scattering curves as a function of scattering angle for spheres of refractive index $m = 1.50$ and a variety of size parameters; (b) same as (a) but plotted vs. qa . Line with slope -2 is shown. (From Sorensen, C.M. and Fischbach, D.F., *Opt. Commun.*, 173, 145, 2000. With permission.)

from the RDG limit at $9(qa)^{-4}$. However, it appears that this upward evolution is bounded from above by a universal $(qa)^{-2}$ power law with a coefficient approximation equal to two. Thus, some envelopes, such as those for $\rho = 12, 24, 48,$ and 96 have two power law regimes: $(qa)^{-2}$ and $c(qa)^{-4}$, where $c > 9$. Empirically, we find the crossover between these two power laws occurs approximately at $qa \approx \rho^{-1}$, but this varies slowly with α as evidenced by the lack of overlap in the $(qa)^{-4}$ regime for large ρ . We remark that past evaluation of Mie scattering has emphasized the importance of the size parameter α , we now see that the phase shift parameter is also quite significant. In

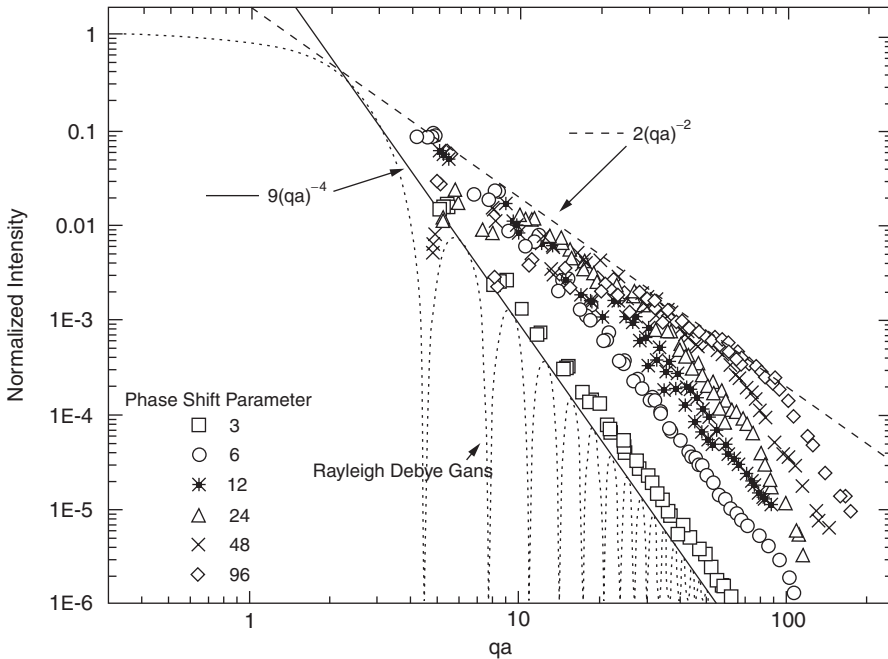


FIGURE 14.6 The envelopes of the normalized Mie scattering curves for a wide range of size parameters and refractive indices vs. qa . Curves with the same phase shift parameter ρ fall together. As the phase shift parameter increases from zero, the curves depart from the Rayleigh–Debye–Gans limit. Lines representing $9(qa)^{-4}$ and $2(qa)^{-2}$ indicate small ρ and large ρ limits, respectively, for these curves. (From Sorensen, C.M. and Fischbach, D.F., *Opt. Commun.*, 173, 145, 2000. With permission.)

summary, if we ignore the ripples and the glory, Mie scattering displays three power law regimes with approximate boundaries as

$$I \propto (qa)^0 \quad \text{when } qa < 1 \quad (14.25a)$$

$$\propto (qa)^{-2} \quad \text{when } 1 < qa < \rho \quad (14.25b)$$

$$\propto (qa)^{-4} \quad \text{when } qa > \rho \quad (14.25c)$$

The behavior of Equations 14.25 is illustrated in [Figure 14.7](#).

Recognize that the ripple structure that we have ignored by considering only the envelopes will in an experiment be washed out by any modest particle size polydispersity of geometric width of 20% or more.⁸

14.3.1.1 The Mie Guinier Regime

The region of crossover between the functionalities of Equations 14.25a and b is called the Guinier regime and for $\rho \rightarrow 0$ is described by

$$\frac{d\sigma}{d\Omega} = \left(\frac{d\sigma}{d\Omega} \right)_R \left(1 + \frac{1}{3} q^2 R_g^2 \right) \quad (14.26)$$

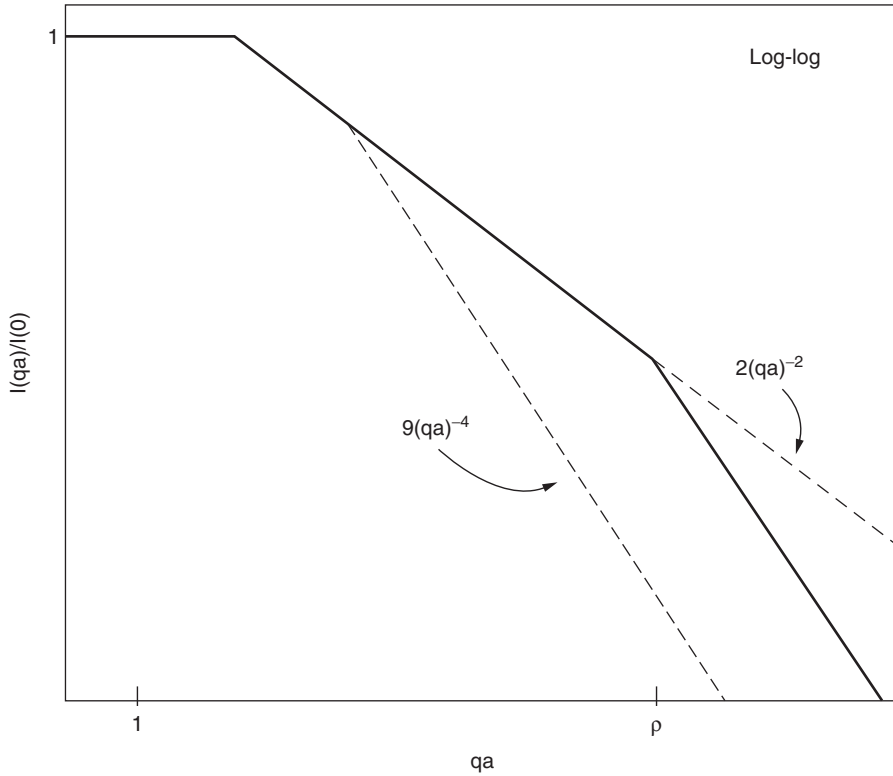


FIGURE 14.7 Schematic diagram of the envelopes of the Mie scattering curves for homogeneous, dielectric spheres (i.e., ignoring the ripple structure). Dashed lines are for the RDG limit at $\rho=0$ with slope -4 and the $\rho \rightarrow \infty$ limit with slope -2 . Solid line is the envelope for an arbitrary phase shift parameter ρ .

In Equation 14.26 R_g is the radius of gyration of the scattering object, which can have any shape. If spherical, $R_g = \sqrt{3/5} a$. We have found⁶ for spheres that Equation 14.26 must be modified when $\rho > 1$ to

$$\frac{d\sigma}{d\Omega} \sim \left(1 + \frac{1}{3} q^2 R_{g,G}^2 \right) \quad (14.27)$$

In Equation 14.27 the Rayleigh cross section is lost; i.e., at $q = 0$ ($\Theta = 0$) the sphere no longer has its Rayleigh cross section. Also in Equation 14.27 is $R_{g,G}$, which we call the “Guinier regime determined radius of gyration.”⁶ Only when $\rho = 0$ does $R_{g,G} = R_g$. Otherwise, it follows a quasi-universal behavior with ρ depicted in Figure 14.8. Note that as $\rho \rightarrow \infty$ $R_{g,G} = 1.12 R_g$, the Fraunhofer diffraction limit. Importantly, use of a Guinier analysis with Equation 14.27 and Figure 14.8 allows for a simple yet accurate experimental measurement of the particle R_g , hence geometric radius a .

14.3.1.2 The Mie Ripples

The ripple structure that we have ignored by considering only the envelopes displays ρ -dependent structure as well. We will use the symbol δ_{qa} to designate the spacing between consecutive ripples when intensity is plotted vs. qa , and δ_θ when plotted vs. θ . We find⁷

$$\delta_{qa} = \pi \text{ for } \rho \leq 5 \quad (14.28a)$$

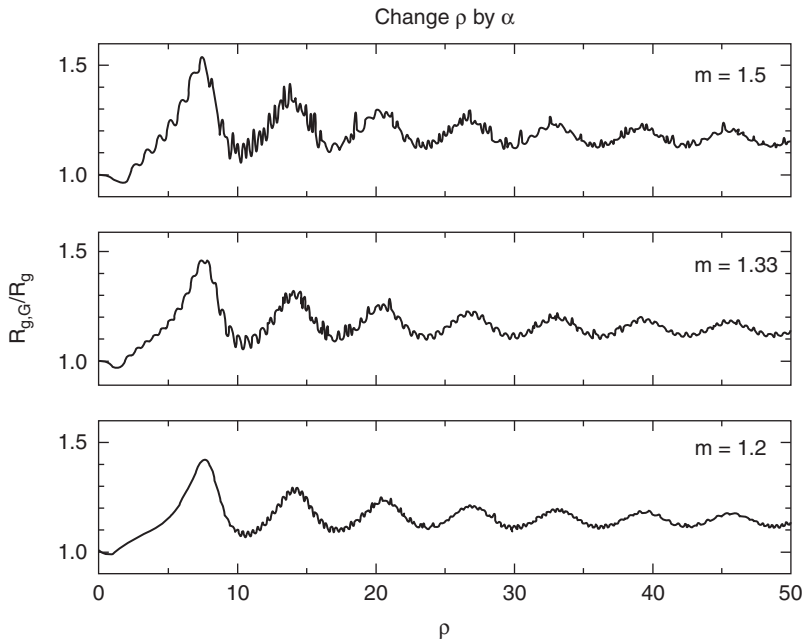


FIGURE 14.8 The ratio of the Guinier inferred to real radius of gyration, $R_{g,G}/R_g$, vs. phase shift parameter ρ for spheres with three different refractive indices. The size parameter $\alpha = kR$ was varied to vary ρ . (From Sorensen, C.M. and Shi, D., *Opt. Commun.*, 178, 31, 2000. With permission.)

$$\delta_{qa} = \pi \cos \theta \text{ for } \rho \gtrsim 5 \quad (14.28b)$$

Equation 14.28b is equivalent to

$$\delta_{\theta} = \pi/\alpha \text{ for } \rho \gtrsim 5 \quad (14.28c)$$

Physical explanation for this ripple structure and functionality has not yet been given. Equation 14.28c suggests that for highly monodisperse systems a measurement of the ripple spacing would yield the particle size.⁹⁻¹¹

In summary, features of Mie scattering may be listed as follows:

1. The functionality of the envelopes as depicted in [Figure 14.7](#) and described by Equation 14.25.
2. A modified Guinier regime exists as described by Equation 14.27 and Figure 14.8.
3. Ripples visible in systems with very narrow size distributions are described by Equation 14.28 and may afford a size measurement through Equation 14.28c.

14.3.2 THE MIE TOTAL SCATTERING CROSS SECTION

[Figure 14.9](#) plots the total scattering cross section as a function of the size parameter. This plot shows the general features but does not show the ripple structure and resonances also known to exist.¹⁻³ Features of the Mie scattering efficiency include the following:

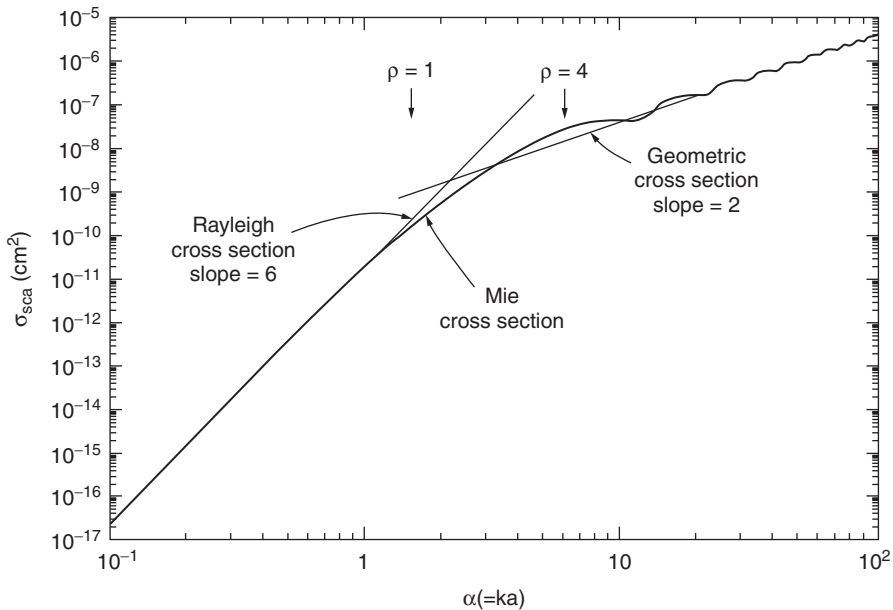


FIGURE 14.9 Total scattering cross section for a spherical particle with $m = 1.33$. (From Sorensen, C.M., *Aerosol Sci. Tech*, 35, 241, 2001. With permission.)

1. Again, for small particles $\sigma \sim a^6$. This crosses over to a “geometric” $\sigma \sim a^2$ behavior near $\rho \approx 1$.
2. A peak in the efficiency for scattering, $Q = \sigma/\pi a^2$ (see Appendix 14.A.3), near $\rho \approx 4$. For example, if $m = 1.33$ the peak is near $\alpha \approx \lambda$.
3. The geometric limit of the cross section (i.e., as $\alpha = kR \rightarrow \infty$) is $2\pi a^2$, twice the geometric cross section. This result is, at first, surprising because if we consider only the shadow, $\sigma = \pi a^2$. However, edge diffraction also contributes an additional πa^2 .

14.4 FRACTAL AGGREGATES

The general problem of scattering and absorption by an aggregate of particles can be very complex. Much of the complexity is due to the difficulty in formulating the electromagnetic wave solution for a system that lacks symmetry and contains many scattering centers. An additional problem lies in that aggregates can potentially represent an infinite number of different arrangements of constituent particles. Because we have little use for an infinite number of electromagnetic solutions, we need the ability to describe classes of aggregates and quantify their features in a manner related to the scattering and absorptive behavior. The past decade and a half has seen the development of the fractal concept for quantitative description of many aggregates that form in nature.¹²⁻¹⁶ The scattering and absorption by fractal aggregates is now fairly well known, has an extensive literature,¹⁷⁻²⁴ and is describable in terms of the quantified fractal parameters. It is the optical properties of these fractal aggregates that is the subject of the rest of this chapter.

A fractal is an object that displays scale invariant symmetry; that is, it looks the same when viewed at different scales. Any real fractal object will have this scale invariance over only a finite range of scales. One important consequence of this symmetry is that the density autocorrelation function will have a power law dependence, which can be written as

$$C(r) = \langle \rho(\vec{r}_o) \rho(\vec{r}_o + \vec{r}) \rangle \quad (14.29)$$

$$= Ar^{D-d} h(r/\xi); \quad r > a \quad (14.30)$$

Equation 14.29 defines the density correlation function $C(r)$, where $\rho(\vec{r})$ is the density of material at position \vec{r} , and the brackets represent an ensemble average. In Equation 14.30, A is a normalization constant, D is the fractal dimension of the object, and d is the spatial dimension. Also in Equation 14.30 are the limits of scale invariance, a at the smaller scale defined by the primary or monomeric particle size, and at the larger end of the scale $h(r/\xi)$ is the cutoff function that governs how the density autocorrelation function (not the density itself) is terminated at the perimeter of the aggregate near the length scale ξ . As the structure factor of scattered radiation is the Fourier transform of the density autocorrelation function, Equation 14.30 is important in the development below.

Another important property of fractal aggregates is that their mass scales with their size raised to the fractal dimension power. For a naturally occurring aggregate, apparently random to the eye, size is difficult to define in terms of the typically ragged border and anisotropic shape. Thus, a convenient measure of size that can be precisely quantified is the radius of gyration, R_g , defined as

$$R_g^2 = \frac{\int \rho(\vec{r})(\vec{r} - \vec{r}_{cm})^2 d\vec{r}}{\int \rho(\vec{r}) d\vec{r}} \quad (14.31)$$

In terms of the correlation function we may show that R_g is given by

$$R_g^2 = \frac{1}{2} \int r^2 C(r) d\vec{r} \quad (14.32)$$

In Equation 14.31 \vec{r}_{cm} is the position of the aggregate center of mass. The radius of gyration is a root-mean-square radius, which is often a useful point of view. Given R_g , a fractal of N monomers or primary particles obeys

$$N = k_o \left(R_g / a \right)^D \quad (14.33)$$

Perhaps the most common aggregation process is diffusion-limited cluster aggregation (DLCA) for which $D = 1.75$ to 1.80 . With experimentation on soot aggregates we have found $k_o = 1.23 \pm 0.07^{25}$ and 1.66 ± 0.4 .²⁶ With simulations, we have found $k_o = 1.19 \pm 0.1^{27}$ and 1.30 ± 0.07 .²⁸

14.4.1 SCATTERING AND ABSORPTION BY FRACTAL AGGREGATES

To lowest order the scattering and absorption cross sections for a fractal aggregate of N monomers with radius a are simply related to the monomer cross sections as follows.²⁴

$$\sigma_{abs}^c = N \sigma_{abs}^m \quad (14.34)$$

$$\frac{d\sigma^c}{d\Omega} = N^2 \frac{d\sigma^m}{d\Omega} S(q) \quad (14.35)$$

The superscripts c and m designate cluster and monomer, respectively. $S(q)$ is the static structure factor of the cluster which is the Fourier transform of the cluster, density autocorrelation function, and hence it contains information regarding the cluster morphology. The structure factor has the asymptotic forms $S(0) = 1$ and $S(q) \sim q^{-D}$ for $q \gg R_g^{-1}$.

The simple forms of Equations 14.34 and 14.35 have physical interpretation. Equation 14.34 implies that the absorption is independent of the state of aggregation; the monomers absorb independently. Equation 14.35 implies that the scattering at small q from N monomers is also independent of the state of aggregation; the N scattered fields add constructively to yield the N^2 dependence of the intensity. Equations 14.34 and 14.35 are under the assumption that the effects of intracluster multiple scattering within a cluster can be neglected. This assumption is particularly labile for $D > 2$ because such clusters are not “geometrically transparent;” that is, their projection onto a two-dimensional plane would fill the plane. Other factors that can lead to multiple scattering effects are large a (or, better, its size parameter α) N , and m .²² Current knowledge (see below) indicates that Equations 14.34 and 14.35 are quite good for monomer $\alpha \lesssim 0.3$, $D < 2$, and most values of m .

Recently, based on an analysis by Farias et al.²⁹ and our own experimental test of Equation 14.35,³⁰ we have concluded that a phase shift parameter for the cluster aggregate can be defined as

$$\rho^c = 2kR_g |m - 1| \lesssim 3 \quad (14.36)$$

When $\rho^c \lesssim 3$, Equation 14.35 should hold quite well ($\sim 10\%$).

The general behavior of $S(q)$ is shown in [Figure 14.10](#). Important features include the following:

1. A scattering angle-independent Rayleigh regime where the cross section is N^2 times the monomer Rayleigh cross section.
2. A Guinier regime near $q \sim R_g^{-1}$, which is expressed as

$$\frac{d\sigma^2}{d\Omega} = N^2 \frac{d\sigma^m}{d\Omega} \left(1 - \frac{1}{3} q^2 R_g^2 \right) \quad (14.37)$$

This dependency on $q^2 R_g^2$ holds for any morphology, and Equation 14.37 can be used to measure the cluster R_g .

3. A power law regime at $q > R_g^{-1}$, where $S(q) \sim q^{-D}$. This can be used to measure D .
4. The regime for which $q > a^{-1}$, where the length scale of the scattering experiment can resolve below the fractal scaling regime and see the individual monomers. In this regime $S(q) \sim q^{-4}$, which is known as Porod’s law. This feature is not included in Equation 14.35 but may be included by multiplying Equation 14.35 by the form factor, i.e., the normalized differential cross section, for the monomer.

It is worthwhile to compare these features with those listed above for scattering from a homogeneous sphere of arbitrary size, i.e., Mie scattering. Both fractal aggregates and Mie scatterers display a Rayleigh regime in which no angle dependence occurs. In each there follows, with increasing angle, a Guinier regime, which can yield an experimental measurement of R_g . After that follows a power law regime or regimes for which considerable differences appear (e.g., Mie ripples) but which are similar because of the decreasing power law with q . Finally, the possibility of enhanced backscattering for fractal aggregates, in analogy to that seen for spheres, has not to my knowledge been explored.

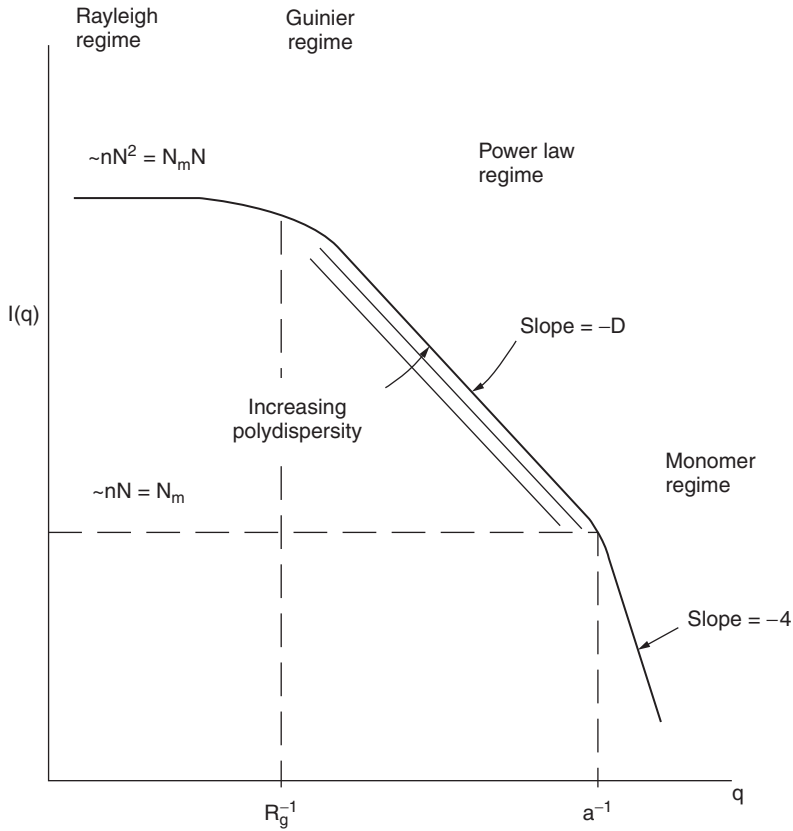


FIGURE 14.10 Schematic of the general behavior of the structure factor for a fractal aggregate with fractal dimension D , radius of gyration R_g , and monomer radius a . (From Sorensen, C.M., *Aerosol Sci. Tech*, 35, 241, 2001. With permission.)

14.4.2 THE STRUCTURE FACTOR

The structure factor and the density autocorrelation function are Fourier transform pairs; thus,

$$S(q) \propto \int C(r) e^{i\vec{q}\cdot\vec{r}} d^3 r \quad (14.38)$$

Knowledge of one implies knowledge of the other. As sure as Bragg scattering measures the structure of a crystal in q space, so too the structure factor of a cluster measured optically represents the structure cluster in q space.

Some useful general notions of how the structure factor depends on the structure of the object from which it scatters can be obtained by considering the density profile, not the correlation function, of the object as a function of radial distance r . This is depicted in Figure 14.11. A particle or cluster with uniform density and a sharp boundary (Figure 14.11a) is a homogeneous sphere and hence its scattering profile is its structure factor $p < 1$. It is the sharp boundary that causes the ripples and the uniform density the causes the q^{-4} envelope (at small p). If the boundary is smoothed to a finite width, the ripples become less severe and with increasing boundary width eventually disappear. If the density is not uniform but instead decreases with increasing r (Figure 14.11b), the power law describing the $qR_g > 1$ q -dependence will decrease from q^{-4} to, if fractal, q^{-D} , $D < 3$.

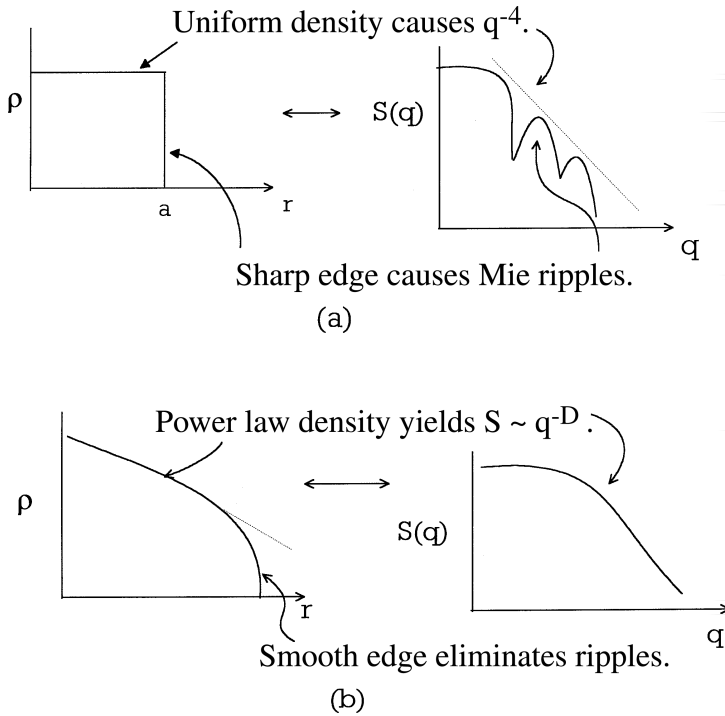


FIGURE 14.11 Examples of qualitative relations between particle or aggregate morphology, as described by the radial density profile, ρ vs. r , and the structure factor.

To gain more than a qualitative notion on how the structure factor is related to the structure of the object, an exact form for the correlation function must be given. A fractal object (cluster) will have $C(r) \sim r^{D-d}$ as in Equation 14.30. Beyond that, it is crucial to know the form of the correlation function cutoff function $h(r/\xi)$.³¹⁻³³ This function must decrease faster than any power law to effectively cut off the power law of $C(r)$.

The early work¹⁷⁻¹⁹ in this area assumed that $h(r/\xi)$ was an exponential:

$$h(r/\xi) = Ae^{-(r/\xi)} \quad (14.39)$$

The advantages of this function are (1) its simplicity, (2) an analytical form for $S(q)$ can be calculated, and it (3) is consistent with scattering from a fluid near the critical point. Given Equation 14.38 a relation between R_g and ξ can be determined and the structure factor can be calculated.

An important quality of the structure factor for the exponential cutoff is that for $D = 2$ it reduces to the so-called Fisher–Burford formula for light scattering from a critical fluid:³⁴

$$S(q) = \left(1 + \frac{1}{3} q^2 R_g^2\right)^{-1} \quad (14.40)$$

which is often generalized for D near 2 to

$$S(q) = \left(1 + \frac{2}{3D} q^2 R_g^2\right)^{-D/2} \quad (14.41)$$

The beauty of these equations is their simplicity, but care must be taken because, it appears, that the exponential cutoff and these equations are incorrect for DLCA fractal aggregates.

Another reasonable form for the cutoff is the Gaussian

$$h(r/\xi) = Ae^{-(r/\xi)^2} \quad (14.42)$$

A cutoff based on physical reasoning is the overlapping spheres cutoff, so named because calculation of $C(r)$ depends on how the spherical densities, $\rho(r)$, overlap.³⁵ We remark that Equations 14.39 and 14.42 can be generalized to

$$h(r/\xi) = Ae^{-(r/\xi)^\beta} \quad (14.43)$$

with β any positive, nonzero value. Mountain and Mulholland²¹ found $\beta = 2.5 \pm 0.5$ consistent with their computer-generated clusters with $D = 1.8$.

In our laboratory we have attempted to discern which structure factor, hence which cutoff function, describes reality the best. In one study³¹ we fit structure factor measurements from soot aggregates in a premixed CH_4/O_2 flame to the exponential, Gaussian, and Mountain and Mulholland forms, i.e., Equation 14.43 with $\beta = 1, 2,$ and 2.5 . If no polydispersity was included in the fit, $\beta = 1$ worked the best. However, with any reasonable polydispersity, $\beta = 1$, the exponential, failed completely. Both $\beta = 2$ and 2.5 worked well, with $\beta = 2$, the Gaussian, yielding the best result.

In another study, soot from the same flame was thermophoretically captured and examined via transmission electron microscopy (TEM).²⁵ The correlation function of soot clusters was determined and the cutoff function extracted from that. Once again, the $\beta = 1$ exponential failed completely. The best cutoff was the overlapping spheres, which is edifying given its physical origin. However, the $\beta = 2$ Gaussian worked very well failing only when $h(r/\xi)$ had decreased by a factor of 100.

Thus, a sharp cutoff is highly recommended over the exponential cutoff. Recently, we have reconsidered these issues with regard to the single cluster structure factor and concluded that it is best described by^{24,36}

$$S(q) = 1 - \frac{1}{3}q^2R_g^2, \quad qR_g \lesssim 1 \quad (14.44a)$$

$$= C(qR_g)^{-D}, \quad qR_g > 1 \quad (14.44b)$$

In Reference 36 we have found the sharp cutoffs all imply $C = 1.0 \pm 0.1$. Equation 14.44 is consistent with the form first proposed by Dobbins and Megaridis.³⁷ However, Equation 14.44 is not to be used to fit real data because they neglect the effects of polydispersity, which we consider below.

14.4.3 THE STRUCTURE FACTOR OF AN ENSEMBLE OF POLYDISPERSE AGGREGATES

Any real experiment detecting scattered radiation from an ensemble of fractal aggregates will involve a polydisperse (in cluster size) ensemble. Aggregates are a result of aggregation, which always gives a finite width to the cluster size distribution. This polydispersity causes the shape of the observed structure factor to be different from that of the structure factor of any single cluster in the distribution.^{36,38} The single cluster structure factor, dependent on the cutoff and D , was described above. Now we follow Reference 36 to consider how the shape is modified by a distribution in cluster sizes. The modifications will occur in both the Guinier and power law regimes.

In general, the effective structure factor for an ensemble of aggregates can be written as

$$S_{\text{eff}}(q) = \int N^2 n(N) S[qR_g(N)] dN / \int N^2 n(N) dN \quad (14.45)$$

where $n(N)$ is the size distribution, i.e., the number of clusters per unit volume with N monomers per cluster. The number of monomers per cluster and the cluster radius of gyration are related by Equation 14.33.

To compute the results of Equation 14.45 applied to Equation 14.44, we define the i th moment of the size distribution

$$M_i = \int N^i n(N) dN \quad (14.46)$$

Note that the moment is an average and could also be written as \bar{N}^i or $\langle N^i \rangle$. Equation 14.45 yields

$$S_{\text{eff}}(q) = 1 - \frac{1}{3} q^2 R_{g,z}^2, \quad qR_{g,z} \leq 1 \quad (14.47a)$$

$$= C C_p (qR_{g,z})^{-D}, \quad qR_{g,z} \geq 1 \quad (14.47b)$$

In Equations 14.47 we have the z -averaged radius of gyration:

$$R_{g,z}^2 = a^2 k_o^{-2/D} \frac{M_{2+2/D}}{M_2} \quad (14.48)$$

Obviously, $R_{g,z}$ can be determined from the slope of $S(q)$ or $S(q)^{-1}$ vs. q^2 graph of the data, as we illustrate below. In Equation 14.47b we have what we have called the polydispersity factor C_p ,

$$C_p = \frac{M_1}{M_2} \left(\frac{M_{2+2/D}}{M_2} \right)^{D/2} \quad (14.49)$$

To calculate C_p we need the analytical form of the size distribution.

It is well established that an aggregating system develops a self-preserving, scaling distribution given by^{39,40}

$$n(N) = Ax^{-\tau} e^{\alpha x} \quad (14.50)$$

where x is the relative size

$$x = N/s \quad (14.51)$$

s is a mean size and A and α are constants. Note that size in this context is the aggregation number, N . The exponent τ is a measure of the width of the distribution with large τ implying a broad distribution. This scaling form is valid when $x > 1$, with the small x form different. As scattering strongly weights the large end, i.e., $x > 1$, of the distribution, the small x has little effect on the properties of scattering from an ensemble of aggregates and hence can be ignored.

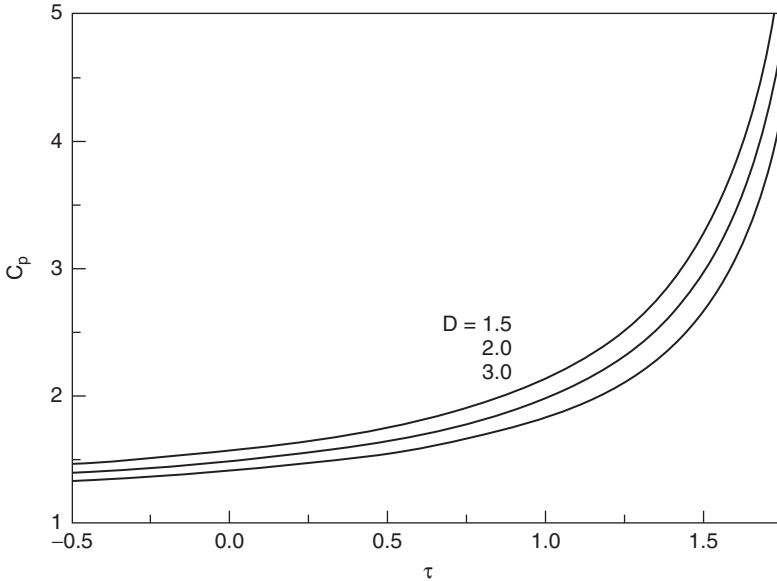


FIGURE 14.12 Polydispersity factor C_p for the large $qR_{g,z}$ power law regime of the structure factor $S(q) = cC_p(qR_{g,z})^{-D}$ for an ensemble of clusters as a function of the width parameter τ of the scaling size distribution for three values of the fractal dimension D . (From Sorensen, C.M. and Wang, G.M., *Phys. Rev. E*, 60, 7143, 1999. With permission.)

Other forms for the size distribution of aggregates exist, but caution must be exercised in their use. For example, the intuitive lognormal distributions are frequently used in the literature. However, we have shown⁴¹ that these distributions yield erroneous values for distribution moments higher than the second when compared with the exact scaling distribution. For the second moment and lower, the distributions agree well. Because scattering involves higher moments, such as $M_{2+2/D} \approx M_3$ for $D \approx 2$, it is erroneous to use the lognormal distribution for light scattering analysis.

We find the polydispersity factor to be

$$C_p = \frac{1}{2-\tau} \left[\frac{\Gamma(3-\tau+2/D)}{\Gamma(3-\tau)} \right]^{D/2} \quad (14.52)$$

where $\Gamma(x)$ is the gamma function. In Figure 14.12 we graph C_p as a function of the width parameter τ for a variety of fractal dimensions D . We find C_p in general to be significantly greater than unity.

In summary, return to Figure 14.10, which schematically illustrates all the quantitative aspects of the structure factor. In fitting data from a real system it is best to analyze the Guinier regime first. Equation 14.47a implies that the inverse normalized (to $q = 0$) scattered intensity is a linear function of q^2 , i.e.,

$$I(0)/I(q) = \left(1 + \frac{1}{3} q^2 R_{g,z}^2 \right) \quad (14.53)$$

Such a plot has a slope of $R_{g,z}^2/3$. With $R_{g,z}$ determined by this Guinier analysis, Equation 14.47b implies that at large q , ideally $qR_{g,z} \gtrsim 5$, the normalized scattered intensity will obey

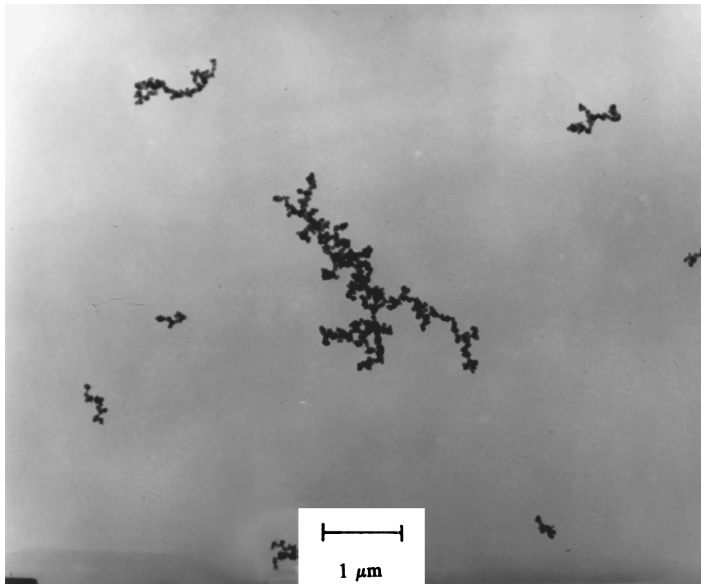


FIGURE 14.13 TEM micrograph of soot collected from an C_2H_2 /air diffusion flame.

$$I(q)/I(0) = CC_p R_{g,z}^{-D} q^{-D} \quad (14.54)$$

Thus, a log-log plot will have a slope of $-D$ and an intercept related to $CC_p R_{g,z}^{-D}$, or, as shown below, the product $I(q)/I(0)(qR_{g,z})^D$ will be constant at large $qR_{g,z}$ and equal to $CC_p \approx C_p$ (note, $S(q) = I(q)/I(0)$). Using $C = 1.0 \pm 0.1$ and the measured $R_{g,z}$ and D , C_p can be extracted to yield, through Figure 14.12 or Equation 14.52, a measure of the cluster size polydispersity.

Finally, one question that might arise is how the q^{-D} behavior for an aggregate transforms to q^{-4} as $D \rightarrow 3$ from below. Jullien⁴² has studied this question for both the exponential and Gaussian cutoffs. For the exponential cutoff there is an inflection in $S(q)$ after the Guinier regime. For q less than this inflection the negative slope on a $\log S(q)$ vs. $\log q$ plot is greater than D and approaches 4 as $D \rightarrow 3$. For q greater than the inflection q the negative slope is equal to D . As $D \rightarrow 3$ the inflection q goes to infinity. For the Gaussian cutoff a noticeable hump appears in $\log S$ vs. q as $D \rightarrow 3$. This hump has an exponential form: $\exp[-q^2 R_g^2/3]$. At larger q , the curve inflects and begins q^{-D} behavior; i.e., the slope is $-D$. As $D \rightarrow 3$ the inflection point goes to infinity leaving the exponential.

14.5 EXAMPLES

Figure 14.13 shows a TEM image of soot clusters sampled from an acetylene-in-air diffusion flame. Analysis shows these clusters are fractals with $D \approx 1.8$ and $a = 23$ nm (thus for $\lambda = 514.5$ nm $\alpha = 0.28$). This is typical of carbonaceous soot formed in a variety of flames.

Examples of optical structure factor measurements from aerosol soot fractal aggregates are shown in Figures 14.14 and 14.15. Figure 14.13 is for scattering from soot in a uniform, premixed flame of methane and oxygen.⁴³ As the height above burner increases from 8 to 20 mm, the scattering goes from isotropic to angle dependent. Figure 14.16 shows the inverse scattered intensity, normalized to the intensity scattered at zero angle, vs. wave vector squared for the data in Figure 14.14. The linearity is in accord with the Guinier formula (Equation 14.53), and the slope is $R_g^2/3$. This is a very convenient way to determine the average R_g for any system of scatterers and is the essence

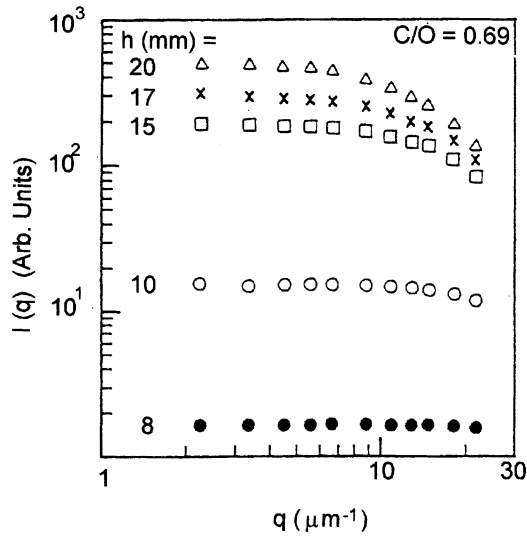


FIGURE 14.14 Optical structure factors for soot aggregates in a premixed CH_4/O_2 flame at various heights above the burner.

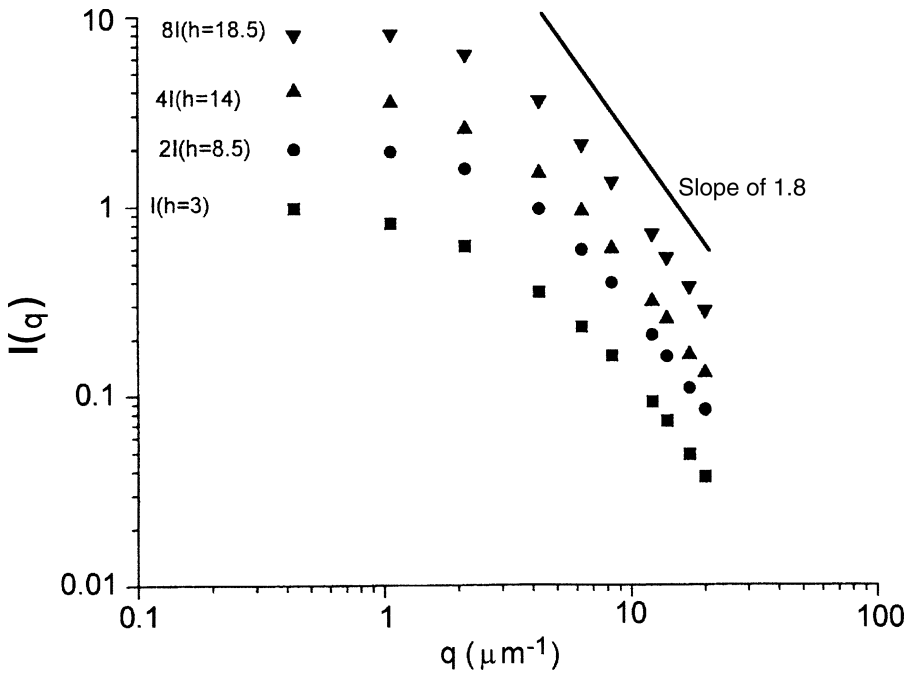


FIGURE 14.15 Optical structure factors for a $\text{C}_2\text{H}_2/\text{air}$ diffusion flame at various heights above the burner.

of the Zimm plot of biophysics.⁴⁴ We have also shown that the curvature of these plots in the regime of $qR_g \geq 1$ can be used to measure size distribution width.⁴⁵

Figure 14.15 shows data for $R_g = 0.5 \mu$ which, because of this large size, has qR_g sufficiently large so that the asymptotic q^{-D} dependence can be seen. A good rule of thumb is that the power law regime does not begin until $qR_g \geq 5$; hence, data below this limit should not be used in an asymptotic analysis for D (i.e., finding D from the slope of $\log S(q)$ vs. $\log q$).

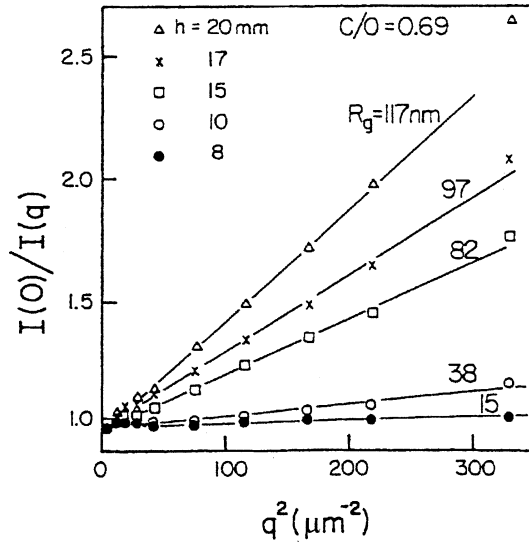


FIGURE 14.16 Guinier analysis of structure factor data in Figure 14.15. By Equation 14.53 I^{-1} vs. q^2 yields straight lines with slope $R_g^2/3$.

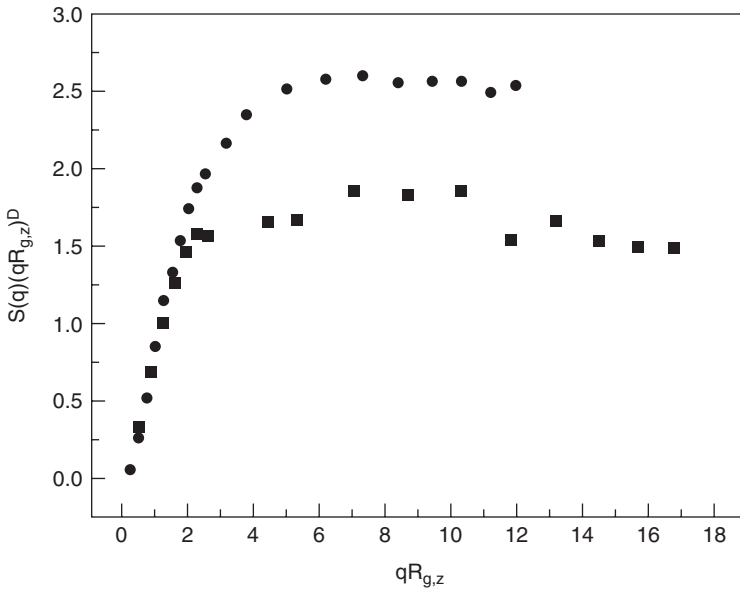


FIGURE 14.17 $(qR_{g,z})^D S(qR_{g,z})$ plotted vs. $qR_{g,z}$ for an aerosol (squares) and a colloid (circles). The constant level at large $qR_{g,z}$ is, by Equation 14.54, equal to CC_p . (From Sorensen, C.M. and Wang, G.M., *Phys. Rev. E*, 60, 7143, 1999. With permission.)

Figure 14.17 shows experimental data³⁶ for an aerosol with $D = 1.7$ (DLCA) and a colloid with $D = 2.15$, where we can see different levels at large $qR_{g,z}$, hence different C_p values, hence different degrees of polydispersity as parameterized by τ .

For soot or any other strongly absorbing material with a complex refractive index a complete morphological characterization to determine average R_g , N , a , and D can be made with *in situ* light scattering.⁴¹ The technique involves combining optical structure factor measurements and absolute

scattering and extinction measurements. From Equations 14.8 and 14.35, the scattered intensity at small angles such that $S(q) = 1$ is

$$I_{\text{scat}} = nN^2k^4a^6F(m) \quad (14.55)$$

From Equations 14.14, 14.34, 14.17, and 14.20 the turbidity is

$$\tau = nN4\pi ka^3E(m) \quad (14.56)$$

A ratio eliminates n ; thus,

$$\frac{I_{\text{scat}}}{\tau} \cdot \frac{4\pi}{k^3} = Na^3F(m)/E(m) \quad (14.57)$$

Measurement of absolute I_{scat} is achieved via calibration of scattering from gases or liquids of known Rayleigh ratio²⁴ with knowledge of the particle refractive index. Equation 14.57 allows for determination of the volume equivalent sphere radius:

$$R_v^3 = Na^3 \quad (14.58)$$

Now consider Equation 14.33

$$N = k_o \left(R_g/a \right)^D \quad (14.33)$$

Equations 14.33 and 14.43 can be solved for N or a in terms of the measurable R_v , R_g , and D ,

$$a = \left(R_v^3/k_o R_g^D \right)^{1/(3-D)} \quad (14.59a)$$

$$N = k_o^{3/(3-D)} \left(R_g/R_v \right)^{3D/(3-D)} \quad (14.59b)$$

Uncertainties arise from three sources; the value of k_o , the index of refraction, and, not shown above, correction to Equations 14.59 for a polydisperse system. The reader should consult the literature for a more detailed explanation.^{24,41}

ACKNOWLEDGMENTS

This work has been supported by grants from the National Science Foundation and the National Institute of Standards and Technology.

APPENDIX 14.A: CROSS SECTIONS

14.A.1 THE DIFFERENTIAL CROSS SECTIONS

The differential scattering cross section, $d\sigma/d\Omega$ describes the power scattered, P_{scat} , per unit solid angle, Ω , (watts/steradian) for an incident intensity (watts/meter²) I_o :

$$\frac{P_{\text{scat}}}{\Omega} = \frac{d\sigma}{d\Omega} I_o \quad (14.A1)$$

Thus, the units of $d\sigma/d\Omega$ are meter²/steradian.

The scattered intensity is the scattered power per unit area of detection:

$$I_{\text{scat}} = P_{\text{scat}}/A \quad (14.A2)$$

The solid angle subtended by the detector a distance r from the scatterer is

$$\Omega = A/r^2 \quad (14.A3)$$

Thus, from Equations 14.A1, 14.A2, and 14.A3, we obtain

$$I_{\text{scat}} = I_o \frac{d\sigma}{d\Omega} \frac{1}{r^2} \quad (14.A4)$$

We obtain the well-known $1/r^2$ dependence due to the geometry of space as described by Equation 14.A3.

14.A.2 THE TOTAL CROSS SECTION

The total scattering cross section is found by integration of the differential cross section over the complete solid angle:

$$\sigma = \int_{4\pi} \frac{d\sigma}{d\Omega} d\Omega \quad (14.A5)$$

This integral must include polarization effects (see main text). The differential element $d\Omega$ in three dimensional Euclidean space is

$$d\Omega = d\theta d(\cos \varphi) \quad (14.A6)$$

(see [Figure 14.1](#) for the polar coordinates θ and φ).

14.A.3 EFFICIENCIES

The scattering or absorption efficiency is a dimensionless ratio of the either total cross to the projected, onto a plane, area of the scatterer:

$$Q_{\text{scat or abs}} = \frac{\sigma_{\text{scat or abs}}}{A_{\text{proj}}} \quad (14.A7)$$

For a sphere of radius a

$$A_{\text{proj}} = \pi a^2$$

These quantities are physically intuitive because they compare the optical cross section to the geometric cross section. If light were not a wave, e.g., solely a particle, the sum of the scattering and absorption efficiencies would be unity.

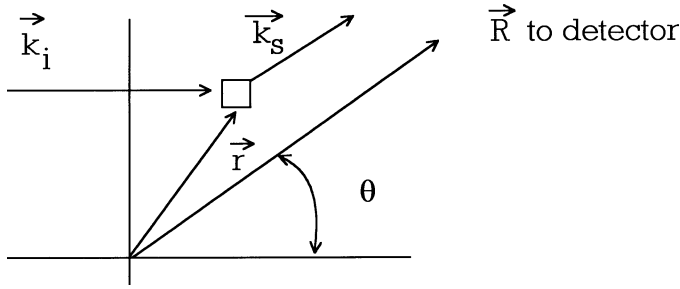


FIGURE 14.18 Light with incident wave vector \vec{k}_i scatters from an element at \vec{r} into a direction \vec{k}_s directed toward the detector at scattering angle θ and great relative distance.

APPENDIX 14.B: THE SCATTERING WAVE VECTOR

Consider a scalar electromagnetic field with incident wave vector \vec{k}_i incident upon a scattering element at \vec{r} as in Figure 14.18. The incident field at \vec{r} is

$$E_i \propto e^{i\vec{k}_i \cdot \vec{r}} \quad (14.B1)$$

where we keep track of phase information only. The field scatters toward the detector in the direction \vec{k}_s where \vec{k}_s is the scattered wave vector. We assume elastic scattering, i.e.,

$$|\vec{k}_i| = |\vec{k}_s| = \frac{2\pi}{\lambda} \quad (14.B2)$$

the field at the detector, which is at \vec{R} , is

$$E(\vec{R}) \propto E(\vec{r}) e^{i\vec{k}_s \cdot (\vec{R} - \vec{r})} \quad (14.B3)$$

Substitution of Equation 14.B1 into 14.B3 yields

$$E(\vec{R}) \propto e^{i\vec{k}_s \cdot \vec{R}} e^{i(\vec{k}_i - \vec{k}_s) \cdot \vec{r}} \quad (14.B4)$$

The second term of Equation 14.B4 shows that the phase at the detector is a function of the position of the scattering element and the vector

$$\vec{q} = \vec{k}_i - \vec{k}_s \quad (14.B5)$$

This vector \vec{q} is called the *scattering wave vector*. Its direction is in the scattering plane from \vec{k}_s to \vec{k}_i as shown in Figure 14.19. From Figure 14.19 and the elasticity condition, Equation 14.B2, the magnitude of \vec{q} is

$$q = 2k_i \sin \theta/2 \quad (14.B6a)$$

$$= 4\pi\lambda^{-1} \sin \theta/2 \quad (14.B6b)$$

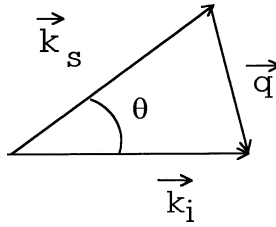


FIGURE 14.19 Relationship between the incident \vec{k}_i and scattered \vec{k}_s wave vectors, the scattering angle θ and the scattering wave vector \vec{q} .

where θ is the scattering angle.

The importance of q is that its inverse, q^{-1} , represents the length scale of the scattering experiment. This follows from the second term in Equation 14.B4, which cannot be written as

$$e^{i\vec{q}\cdot\vec{r}} \tag{14.B7}$$

As we have seen, Expression 14.B7 gives the phase at the detector due to a scattering element at \vec{r} . The scattering due to an object will be the sum of such terms, weighted by the scattering density, over the extent of the object. The key point is that during this sum, the phase expression Equation 14.B7 will not vary significantly if the range of \vec{r} is small compared to q^{-1} . Thus, the scattered phase is not sensitive to the overall extent of the object. We might say that the scattering cannot “see” the object.

Application of this concept to scattering for a particle of extent a implies that if $a \ll q^{-1}$, i.e., $qa \ll 1$, the scattering cannot see the morphology of the particle. Furthermore, if q varies but qa remains less than unity there will be no dependence on q , i.e., no scattering angle dependence. This is the Rayleigh regime for any size particle.

Another consequence of the phase term (Equation 14.B7) is that if $qa \ll 1$, the fields from the scattering elements add coherently. For an object in three dimensions this coherent addition occurs for all three dimensions, and the three dimensions add coherently. Thus, the scattered field will be proportional to the amount of matter in the object, which is proportional to the volume V of a dense particle or the number of monomers per cluster, N , of a ramified object. Since intensity is the field squared, we obtain V^2 or N^2 dependencies.

In summary, q^{-1} is the length scale or resolution limit of a scattering experiment. Therefore, the dimensionless product qa , where a is a measure of the extent of an object, determines the boundary of the Rayleigh regime:

$$\begin{aligned}
 qa \ll 1, \quad I &\sim V^2 \text{ or } N^2 \quad \text{not a function of } \theta, \text{ the Rayleigh regime} \\
 qa > 1, \quad I &= I(\theta)
 \end{aligned}$$

REFERENCES

1. van de Hulst, H.C., *Light Scattering by Small Particles*, Dover, New York, 1981.
2. Kerker, M., *The Scattering of Light and Other Electromagnetic Radiation*, Academic Press, New York, 1969.
3. Bohren, C.F. and Huffman, D.R., *Absorption and Scattering of Light by Small Particles*, John Wiley & Sons, New York, 1983.
4. Minneart, M.G.J., *Light and Color in the Outdoors*, Springer-Verlag, New York, 1993.
5. Sorensen, C.M. and Fischbach, D.F., Patterns in Mie scattering, *Opt. Commun.*, 173, 145, 2000.

6. Sorensen, C.M. and Shi, D., Guinier analysis for homogeneous dielectric spheres of arbitrary size, *Opt. Commun.*, 178, 31, 2000.
7. Sorensen, C.M. and Shi, D., Patterns in the ripple structure in mie scattering, *JOSA*, 19, 122, 2002.
8. Rieker, T.P. et al., Particle size distribution inferred from small-angle x-ray scattering and transmission electron microscopy, *Langmuir*, 15, 638, 1999.
9. Maron, S.H. and Elder, M.E., Determination of latex particle size by light scattering I. Minimum intensity method, *J. Colloid Sci.*, 18, 107–118, 1963.
10. Pierce, P.E. and Maron, S.H., Prediction of minima and maxima in intensities of scattered light and of higher order tyndall spectra, *J. Colloid Sci.*, 19, 658–672, 1964.
11. Kerker, M. et al., Determination of particle size by the minima and maxima in the angular dependence of the scattered light. Range of validity of the method, *J. Colloid Sci.*, 19, 193–200, 1964.
12. Mandelbrot, B., *The Fractal Geometry of Nature*, Freeman, San Francisco, CA, 1983.
13. Forrest, S.R. and Witten, T.A., Long-range correlations in smoke-particle aggregates, *J. Phys. A*, 12, L109, 1979.
14. Family, F. and Landau, D.P., Eds, *Kinetics of Aggregation and Gelation*, North-Holland, Amsterdam, 1984.
15. Stanley, H.E. and Ostrowsky, N., Eds., *On Growth and Form*, Nijhoff, Boston, 1986.
16. Jullien, R. and Botet, R., *Aggregation and Fractal Aggregates*, World Scientific, Singapore, 1987.
17. Berry, M.V. and Percival, I.C., Optics of fractal clusters such as smoke, *Opt. Acta*, 33, 577, 1986.
18. Freltoft, T., Kjems, J.K., and Sinha, S.K., Power-law correlations and finite-size effects in silica particle aggregates studied by small-angle neutron scattering, *Phys. Rev. B*, 33, 269, 1986.
19. Teixeira, J., in *On Growth and Form*, Stanley, H.E. and Ostrowsky, N., Eds., Nijhoff, Boston, 1986.
20. Martin, J.E. and Hurd, A.J., Scattering from fractals, *J. Appl. Cryst.*, 20, 61, 1987.
21. Mountain, R.D. and Mulholland, G.W., Light-scattering from simulated smoke agglomerates, *Langmuir*, 4, 1321, 1988.
22. Nelson, J., Test of a mean field theory for the optics of fractal clusters, *J. Mod. Opt.*, 36, 1031, 1989.
23. Singham, S.B. and Borhen, C.F., Scattering of unpolarized and polarized light by particle aggregates of different size and fractal dimension, *Langmuir*, 9, 1431, 1993.
24. Sorensen, C.M., Light scattering from fractal aggregates. A review, *Aerosol Sci. Tech.*, 35, 241, 2001.
25. Cai, J., Lu, N., and Sorensen, C.M., Analysis of fractal cluster morphology parameters: structural coefficient and density autocorrelation function cutoff, *J. Colloid Interface Sci.*, 171, 470, 1995.
26. Sorensen, C.M. and Feke, G.D., The morphology of macroscopic soot, *Aerosol Sci. Tech.*, 25, 328, 1996.
27. Sorensen, C.M. and Roberts, G., The prefactor of fractal aggregates, *J. Colloid Interface Sci.*, 186, 447, 1997.
28. Oh, C. and Sorensen, C.M., The effect of monomer overlap on the morphology of fractal aggregates, *J. Colloid Interface Sci.*, 193, 17, 1997.
29. Farias, T.L., Koylu, U.O., and Carvalho, M.G., Range of validity of the Rayleigh–Debye–Gans theory for optics of fractal aggregates, *Appl. Opt.*, 35, 6560, 1996.
30. Wang, G.M., and Sorensen, C.M., Experimental test of the Rayleigh–Debye–Gans theory for light scattering by fractal aggregates, *Appl. Opt.*, submitted.
31. Sorensen, C.M., Cai, J., and Lu, N., Test of structure factors for describing light scattering from fractal soot aggregates, *Langmuir*, 8, 2064, 1992.
32. Pearson, A. and Anderson, R.W., Long-range pair correlation and its role in small-angle scattering from fractals, *Phys. Rev. B*, 48, 5865, 1993.
33. Yanwei, Z. and Meriani, S., Scaling functions for the finite-size effect in fractal aggregates, *J. Appl. Cryst.*, 27, 782, 1994.
34. Schaefer, D.W. et al., Fractal geometry of colloidal aggregates, *Phys. Rev. Lett.*, 52, 2371, 1984.
35. Hurd, A.J. and Flower, W.L., *In situ* growth and structure of fractal silica aggregates in a flame, *J. Colloid Interface Sci.*, 122, 178, 1988.
36. Sorensen, C.M. and Wang, G.M., Size distribution effect on the power law regime of the structure factor of fractal aggregates, *Phys. Rev. E*, 60, 7143, 1999.
37. Dobbins, R.A. and Megaridis, C.M., Absorption and scattering of light by polydisperse aggregates, *Appl. Opt.*, 30, 4747, 1991.

15 Application of Scanning Probe Microscopy (Scanning Tunneling Microscopy and Atomic Force Microscopy) in Colloid and Surface Chemistry

K.S. Birdi and D.T. Vu

CONTENTS

- 15.1 Introduction
 - 15.2 Description of STM and AFM Apparatus
 - 15.2.1 Scanning Tunneling Microscope Apparatus
 - 15.2.2 Atomic Force Microscope Apparatus
 - 15.2.3 Sample Preparation Procedures
 - 15.2.3.1 Langmuir–Blodgett and SAM Films
 - 15.2.3.2 Biopolymer Sample Preparation Methods
 - 15.2.3.3 Solution Evaporation or Spray
 - 15.2.3.4 STM and AFM Analyses of Electron Microscope Grids
 - 15.2.4 Calibration and Image Analysis of STM and AFM
 - 15.3 Lipidlike Molecules on Solids
 - 15.3.1 Collapsed Lipid Monolayers
 - 15.3.1.1 Magnesium-Stearate Films
 - 15.3.1.2 Cholesterol and Oxidized Cholesterol (Cholestane) Films
 - 15.3.2 Lipid Assemblies as Langmuir–Blodgett Films
 - 15.3.3 STM and AFM Studies of Diverse Molecules on Solids
 - 15.4 Biopolymer Structures by STM and AFM
 - 15.5 Crystal Structures by STM and AFM
 - 15.5.1 Crystal Structures of Small Molecules
 - 15.5.2 Macromolecule Crystals by STM and AFM
 - 15.6 STM and AFM Studies under Fluids
 - 15.7 Measurement of Attractive and Repulsive Forces by Atomic Force Microscope
 - 15.8 Diverse Applications of STM and AFM
- References

15.1 INTRODUCTION

In science, just as in any other area, some inventions are more important than others. The last part of the 20th century saw large surge in the development of techniques for surface and colloid chemists. In fact, these developments indicate that there is no end to this trend regarding the vast expansion in the sensitivity and level of information; therefore, in this chapter we explain some of these exciting new developments to the reader. Regarding the level of sensitivity the human aim is to achieve information at molecular scale, i.e., nm (10^{-9} m).

Typical of all human experience, *seeing is believing*, so the microscope has attracted much interest for many decades. All these inventions, of course, were basically initiated on the principles laid out by the telescope (as invented by Galileo) and the light-optical microscope (as invented by Hooke).^{1a} Actually, no other scientific techniques have contributed so much to the scientific development in biology, medicine, and material science as the different microscopy techniques.

One element that the earlier microscopes lacked was a three-dimensional parameter. All kinds of molecular interactions between a solid and its environment (gas or liquid or solid) can take place initially only via the surface molecules of the interface. It is obvious that when a solid or liquid interacts with another phase, knowledge of the molecular structures at these interfaces is of interest. The term *surface* is generally used in the context of gas–liquid or gas–solid phase boundaries, whereas the term *interface* is used for liquid–liquid or liquid–solid phases. Furthermore, many fundamental properties of surfaces are characterized by morphology scales of the order of 1 to 20 nm ($1 \text{ nm} = 10^{-9} \text{ m} = 10 \text{ \AA}$).

Generally, the basic issues that should be addressed for these different interfaces are as follows:^{1b}

- The appearance of the molecules of a solid surface and how it differs from the appearance of the bulk molecules; in the case of crystals, kinks and dislocations
- Adsorption on solid surfaces, which requires the same information about the structure of the adsorbates and the adsorption site and configurations
- Solid–adsorbate interaction energy, which is also required, as is known from Hamaker theory²
- Molecular recognition in biological systems (active sites on the surfaces of macromolecules)
- Self-assembly monolayer structures at interfaces
- Semiconductors
- Microsensors

Depending on the sensitivity and experimental conditions, the methods of surface microscopy are many and varied.³

Generally, the study of solid surfaces is dependent on understanding not only the reactivity of the surface but also the underlying structures that determine that reactivity. Understanding the effects of different morphologies may lead to a process for enhancement of a given morphology and hence to improved reaction selectivities and product yields.

Atoms or molecules at the surface of a solid have fewer neighbors as compared with atoms in the bulk phase, which is analogous to the liquid surface, as described here; therefore, the surface atoms are characterized by an unsaturated, bond-forming capability and accordingly are quite reactive. In fact, surface atoms should be treated by using physical analyses different from those used for bulk solid molecules. Until a decade ago electron microscopy and some other similarly sensitive methods provided some information about the interfaces,³ although there were always some limitations inherent in all the techniques, which needed improvement. A decade ago, the best electron microscope images of globular proteins were virtually all little more than shapeless blobs. However, these days, due to relentless technical advances, electron crystallography is capable of

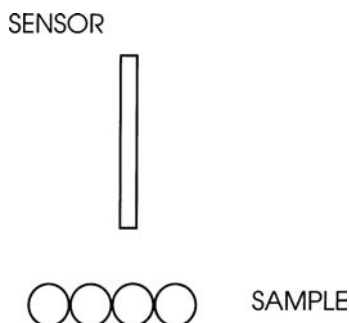


FIGURE 15.1 Sensor (tip/cantilever/optical device) movement in $x/y/z$ direction with nanometer sensitivity (controlled by piezomotor) over a solid surface (gas–solid or liquid–solid).

producing images at resolutions close to those attained by x-ray crystallography or multidimensional nuclear magnetic resonance (NMR). However, x-ray images can only be obtained under extreme conditions, rather than ambient. To improve on some of the limitations of the electron microscope, newer methods were needed. About two decades ago, a new procedure for molecular microscopy (scanning probe microscope, SPM) was invented and is delineated here.

The basic method was merely to be able to move a tip over the solid surface with a *sensor* with molecular sensitivity in both the longitudinal and height direction (Figure 15.1). This gave almost a new dimension — in the nanometer ($\text{nm} = 10^{-9} \text{ m} = 10 \text{ \AA}$) range — to surface chemical research, which was much needed at this stage. As a result of these developments, the last decade has a new aspect of science; nanotechnology. There were originally invented two types of microscopes: scanning tunneling microscopes (STM) and atomic force microscopes (AFM).

The STM was invented by Binnig and Rohrer in 1982 (for which they were awarded the Nobel prize in 1986).⁴⁻⁸ Later, the AFM was developed based on the principles of the STM but with resolving surface structures for both nonconducting and conducting materials.

The invention of the STM was in fact a true revolution in the fields of surface science and microscopy. After extremely high atomic resolution was achieved on clean semiconductor and metal surfaces, further studies were carried on surfaces that were covered with molecules, to observe structural information.

STM and AFM have both proved to be powerful tools for obtaining information on the packing order of molecular adsorption on a surface.⁹⁻¹²

Data obtained from STM images can be useful in providing information on the relative importance of molecule–molecule and molecule–substrate interactions, as well as the types of forces responsible for the packing order at the surface. This is useful in such applications as epitaxial growth of thin films, chromatography, lubrication, and microelectronics fabrication, each of which involves interactions between molecules on a surface and can be investigated by these procedures.

Regarding biological material analysis, prior to STM and AFM methods, the specimens were generally analyzed by the scanning electron microscope (SEM).^{13,14} The main objectives of the preparation methods have been based on stabilizing the specimen, preventing shrinkage and other artifacts during the dehydration, and rendering the sample electrically conductive. In some cases, water was replaced by other fluids such as glycerol or triethylene glycol, with the possibility of artifacts. These requirements are not necessary in STM and AFM methods. The samples could be analyzed under ambient conditions without any additional drying or treatment.

At this stage in the literature, we find that both STM and AFM can operate for fluids,¹⁵ which is technically impossible by electron microscope. This means that, for the first time in history, molecular dimensional analyses of surfaces and molecules situated at surfaces can be carried out in a liquid. This most important discovery in surface science instrumentation allows us to see

TABLE 15.1
Areas of Application for the STM
and AFM (and other SPMs)

Lipid monolayers (as Langmuir–Blodgett films)
Different layered substances on solids
Self-assembly structures at interfaces
Solid surfaces
Langmuir–Blodgett films
Thin-film technology
Interactions at surfaces of ion beams/laser damage
Nanoetching and lithography, nanotechnology
Semiconductors
Mineral surface morphology
Metal surfaces (roughness)
Microfabrication techniques
Optical and compact discs
Ceramic surface structures
Catalyses
Surface adsorption (metals, minerals)
Surface manipulation by STM/AFM
Friction force microscope (FFM)
Polymers
Biopolymers (peptides, proteins, DNA, cells, virus)
Vaccines
Microsensors

molecules in fluids, hitherto impossible with any electron microscope. Additionally, we can obtain images “live” and the adsorption of gas molecules on solid surfaces has also been investigated by STM. Based on these principles, a variety of SPMs are now being developed.

This is the most dramatic development because surface features from interatomic spacing to fractions of a millimeter can be studied with the same instrument. The various systems that have been analyzed by both STM and AFM are many and varied (Table 15.1). Additionally, surface force microscopes (SFM) allow the possibility of measurement of interfacial forces (at nanometer distances).

15.2 DESCRIPTION OF STM AND AFM APPARATUS

15.2.1 SCANNING TUNNELING MICROSCOPE APPARATUS

Basically, the STM consists of two conducting electrodes that are separated by some isolator, which forms a barrier for the electrons inside the electrodes (Figure 15.1). If the barrier is thin enough, electrons can pass through it by a quantum-mechanical process called tunneling. The tip is mounted within an array of piezoelectric elements that control its position in three dimensions. Piezoelectric materials contract or expand when a voltage is applied to them. (Conversely, they also generate small currents when flexed or compressed.) In STM instruments, these elements are usually made of a very stiff ceramic, so that the movements induced by the voltage may be smaller than a tenth of a nanometer. This allows the extremely fine control necessary for successful imaging and manipulation at the atomic and molecular level.

This current is extremely sensitive to the distance between the tip and the surface, increasing exponentially as the tip nears the surface. Because the current increases rapidly as the distances

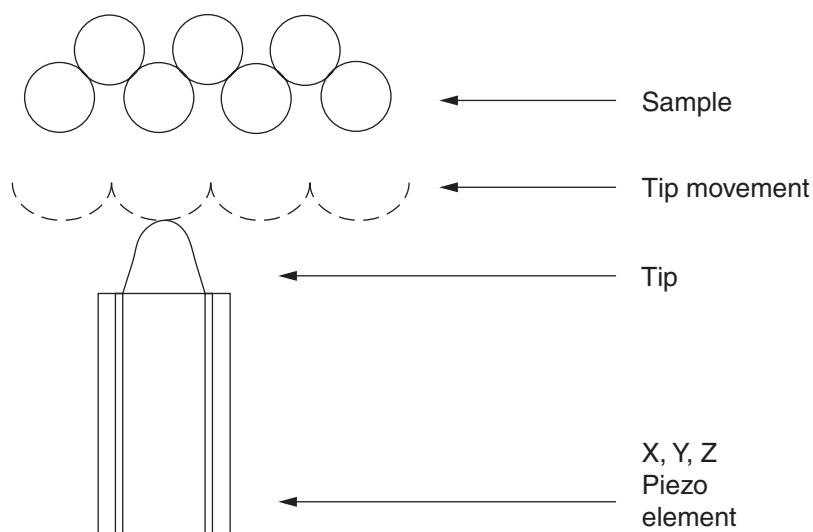


FIGURE 15.2 STM tip movement and setup in a commercially available instrument of piezomotor control on the solid surface.

decrease, very small changes — less than a tenth of a nanometer — in the position of the tip can be detected when it is close to the surface. In an STM, the barrier is a gap of 1 nm.

STM is based on the principle that a probe, made of tungsten (W) or platinum–iridium (Pt-Ir) alloy, scans the surface of a sample with the help of a piezoelectric device¹⁶ (Figure 15.2) at a distance 5 to 10 Å (0.5 to 1 nm).

This apparatus provides extremely fine positional control in all three dimensions, allowing the tip to be brought within a few atomic diameters — on the order of 1 nm — of the surface of the sample to be investigated. At such tiny distances, the electron clouds of the atoms in the tip begin to overlap with those of the atoms on the surface of the sample. When a voltage is applied, quantum effects allow electrons to “tunnel” across the gap, creating a small but detectable current. At very small distances of separation, the wave functions of molecules at the surface of the sample and the tip overlap.

If a bias voltage is applied to the sample, an electron tunneling current flows between the two phases. The tunneling current between the conductive sample and the tip is measured as a function of the distance traveled in the x and y directions. The direction of the electron flow depends on the sign of the bias applied to the sample. Measurement of the current is sensitive to the order of magnitude to resolve atomic or molecular corrugations on the surface of the sample. This allows us to obtain information of the surface at the atomic resolution. The interaction between the probe tip and the sample varies exponentially with the distance between the sample and the most extreme tip on the probe. Thus, in the case of STM, the atom at the tip of the probe allows the tunneling current to pass through. In a recent study^{16b} the energy exchange processes occurring in the tunneling microscope were described. The image is obtained as data in three-dimensional file, generally an IMG file. It can be treated in two-dimensional or three-dimensional image forms. This image file can be converted into other image files such as TIF, BMP, or JPG. There exist also many other software programs that can extensively treat these image files. For example, the images can be smoothed by using various extrapolation techniques. It is thus obvious that image analysis becomes an extensive analytical process.

The resolution in the image, which is only a surface or subsurface image, is defined both in the vertical direction and laterally on the plane of the sample. The magnitude of resolution can be achieved in the range of a fraction of 1 Å (10^{-10} m = 0.1 nm). Obviously, the size and shape of the

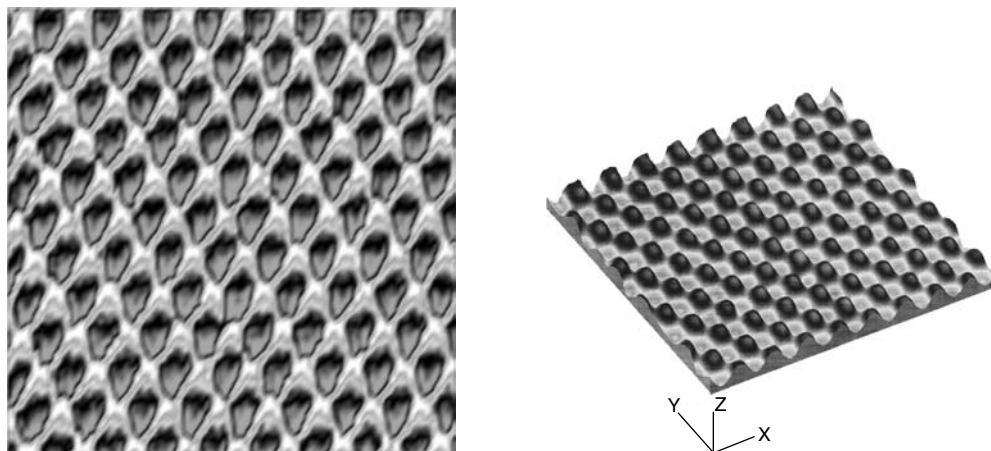


FIGURE 15.3 A two-dimensional ($23.2 \times 23.2 \text{ \AA}$) and a three-dimensional image of HOPG by STM 17 ($25.6 \times 25.6 \times 2.19 \text{ \AA}$).

probe tip will determine the lateral resolution. The tip moves at $\sim 10 \text{ \AA/V}$ applied to a translator. Typically, a lead zirconate–lead titanate (PZT) polycrystalline ceramic is used.

A typical STM image of graphite (highly oriented pyrolytic graphite, HOPG) is given in Figure 15.3. The two-dimensional and three-dimensional images are given. All STM and AFM studies generally use HOPG to control and calibrate. In all cases such images have been consistently reported in the literature. A detailed surface analysis of HOPG has been given in a recent study.¹⁷ The molecular resolution achieved by STM and the three-dimensional capability are the most useful aspects of this method. The morphology of objects in three dimensions provides much more useful information than hitherto available by electron microscopes.

Despite its capabilities, the STM has very real limitations as well. Because its operation depends on the flow of current, however minute, it can only be used to image conducting materials — generally crystals of metals and semiconductors. But many materials for which scientists would like to obtain detailed information, such as biological molecules, are nonconducting. Furthermore, while it probes the electron cloud structure of the surface with great precision, the STM reveals little or nothing about other important properties of the sample. Since it is only seeing an “electronic” surface, for example, it cannot distinguish very well, if at all, between atoms of different elements within a compound material.

It was found that the apparent corrugation is dependent mainly upon the tunneling resistance, which is defined by the ratio of bias voltage to tunneling current and which is expected to have a maximum of about 0.3 nm on a freshly cleaved surface. The surface of graphite has a layer structure in which each layer is composed of carbon atoms in a honeycomb arrangement. The distances between the carbon atoms were found to be 0.246 nm (2.46 \AA) and 0.142 nm (1.42 \AA). Adjacent layers were separated by 0.335 nm .

STM studies under ultrahigh vacuum (UHV/STM) have been carried out in many recent investigations.¹⁸

In general an image is obtained in an image file format. This is data in three-dimensional form. Most SPMs have software that can handle these image files, such that two-dimensional and three-dimensional images can be analyzed. The images can be also converted to other image files, such as TIF, BMP, or JPG. The image data can be transformed into TIFF files. These three-dimensional data can be analyzed using other suitable software programs that can interpolate data points. Many other software programs can be applied to make further analyses as needed.

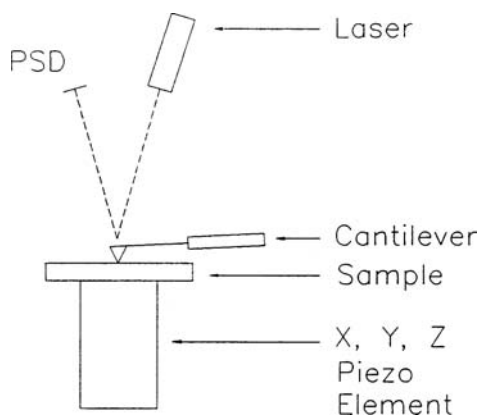


FIGURE 15.4 AFM cantilever movement over a solid surface.

15.2.2 ATOMIC FORCE MICROSCOPE APPARATUS

After some years it became necessary to modify STM to allow investigations of nonconducting surfaces. Based on the same principles as STM, the AFM was later developed for nonconducting solid surfaces.¹⁹ Thus, AFM can operate on both conducting and nonconducting surfaces. A cantilever scans the solid surface (similar to STM) and the deflection of the cantilever is detected by the reflection of a laser beam (Figure 15.4). An Si_3N_4 cantilever of approximately 200- μm length and a spring constant of 0.06 or 0.12 N/m are generally used. In many AFM instruments, the deflections of the tip are measured optically by bouncing a laser beam off the top of the cantilever; minute changes in the light path are measured with a photodiode. An alternative method employs a piezoresistive element in the cantilever itself, which generates a small voltage as it is flexed, in proportion to the magnitude of the deflection. The advantage of this arrangement is that the detection mechanism can be integrated directly into the microfabricated cantilever.

Because the AFM relies on actual contact rather than current flow to sense the nature of the sample surface, it can be used to probe nonconducting materials: biological molecules, organic materials, polymers, ceramics, and insulating materials like glass or diamond. Resolutions achieved by AFM probes vary according to the sample material: with hard substances like crystals or ceramics, it can achieve atomic resolutions of about 0.1 to 0.2 nm — comparable to the STM. With softer, less rigid materials like biological molecules, resolution drops to about 5 nm, and only the general shapes of the molecular surfaces can be determined. This still provides extremely useful information about such molecules, however. Recently, much research has been carried out on improving the shape of the cantilever. In simple terms, AFM is similar in principle to early record players, where the movement of a sharp needle in the groove reproduced the sound.

The interaction forces, attractive or repulsive, as small as few nanonewtons ($\text{nN} = 10^{-9}$ N) between the cantilever and the sample can be measured. The biggest advantage of AFM is that most samples can be investigated in their natural state, including biological samples (even in an aqueous environment), which is otherwise impossible by electron microscope methods. In the case of a repulsive force procedure, the tip physically touches the sample (with a sensitivity of nN force) and traces across the sample without damaging the morphology. In AFM, the sample moves under the cantilever, which is the main reason that the resolution by AFM is somewhat less than that of STM. The images of HOPG are almost of the same resolution as those obtained by STM; however, the resolution is highly dependent on the characteristics of the sample (i.e., surface texture and even the degree of hydration), as well as on sample preparation. This latter point has not been settled completely, and we should be careful in reaching any conclusions at this stage.

In general, the AFM is operated under a constant-force mode which incorporates optical beam deflection for sensing the cantilever motion. Usually the forces exerted are in the range of 0.5 to 0.1 N (force constant of the cantilever used is 0.06 N/m). The AFM is calibrated by using graphite and grating samples in the x - y direction. The height axis has been calibrated by using such collapsed lipid monolayers as the Langmuir–Blodgett (LB) film.²⁰

The spring constant of the cantilever must be measured directly, as the calculated values may not be too reliable.²¹ The spring constant, k_{spring} , for a beam, with Young's modulus E_y , loaded on the end with a rectangular cross section is given as

$$k_{\text{spring}} = E_y w_{\text{width}} / 4 \left(t_{\text{thickness}} / L_{\text{length}} \right)^3 \quad (15.1)$$

where w_{width} , $t_{\text{thickness}}$, and L_{length} are the beam width, thickness, and length, respectively. The calculation of k_{spring} becomes difficult when cantilevers of a thickness < 1 mm are used, due to the above relation. A simple method for measuring the spring constant uses a procedure where the static deflection of the cantilever under the force of a known mass is used.

The cantilever with the tip senses surface forces arising from various interactions (van der Waals, electrostatic, hydration) between the tip and the sample. When the force curve is initiated at a point where the tip and the sample are far apart, the magnitude of surface forces (acting between the tip and sample) are negligible, and thus there is no deflection of the cantilever. As the sample is raised toward the tip, a variety of attractive and repulsive forces interact and deflect the cantilever. This region is called the noncontact region, as described in the following. AFM thus provides information about the surface morphology, as well as about the surface forces at nanometer distances. More recently, new scanning near-field optical microscopes (SNOM-AFM) have been developed.²² This microscope should be very useful for biological systems.

15.2.3 SAMPLE PREPARATION PROCEDURES

As is well known from the current electron microscopy literature, sample preparation is the basic determining factor for obtaining high-resolution images. Accordingly, we may use the same well-known procedures for both STM and AFM analyses. Some well-known procedures will be given in the following. However, the main difference between these two different microscopic techniques is that latter method allows us to operate under ambient laboratory conditions.

15.2.3.1 Langmuir–Blodgett and SAM Films

The transfer of monolayers to solid surfaces is a very useful procedure, which results in the well-known LB films. In the study of lipids and biopolymers, the LB layers are prepared according to standard literature procedures.²³ Transfer of a lipid or biopolymer monolayer is generally performed at a low speed of 1 cm/min at a constant surface pressure of the lipid film. The substrate used for the transfer can be a freshly cleaved HOPG or any other suitable material (gold sample, mica, etc.). Self-assembly monolayer (SAM) films have been obtained by adsorption of alkyl sulides on gold surfaces.^{1a}

15.2.3.2 Biopolymer Sample Preparation Methods

Analyses of DNA have been made as follows. Mica was soaked in magnesium acetate solution (2 h)²⁴ and thereafter sonicated in water. After drying in air, a drop (10 μ l) of DNA solution (50 to 300 ng per 20 ml) was applied. DNA was also investigated after fixing on gold surfaces by 2-dimethylamino-ethanethiol.²⁵ Images of entire plasmid molecules were obtained. The helix structure was clearly visible in these images.

15.2.3.3 Solution Evaporation or Spray

In most cases, only a very dilute solution (~1 mg/l) was applied as a drop (few microliter) to the substrate (HOPG or mica or other suitable material) and STM/AFM was carried out after the evaporation of the solvent (overnight). The aqueous solutions of proteins or peptides were determined by this method. Because the volume of sample that can be used is so minute, the chance of finding particles by microscopy may be vanishingly small. A procedure was developed where a drop of protein or virus solution was used. The graphite sample was barely allowed to touch the surface of the drop, and a monolayer of material (biopolymers, virus, cells) was attached to the graphite.

15.2.3.4 STM and AFM Analyses of Electron Microscope Grids

In the author's laboratory, the grids used for the electron microscope have been analyzed by AFM and by STM (if a conducting layer is present). In fact, this procedure allows comparison of these different techniques. However, the STM and AFM provide three-dimensional images, which are more useful. In one case, the virus of AIDS was studied. Because the virus is destroyed under grid formation, we can safely study these by STM or AFM under ordinary laboratory conditions.^{1b}

15.2.4 CALIBRATION AND IMAGE ANALYSIS OF STM AND AFM

It is obvious that the calibration of SPMs is very critical and essential when considering atomic scale resolution. The calibration of STM and AFM in the *x-y* direction is accomplished using HOPG or suitable grids available commercially. The calibration in the *z* direction has been a somewhat more difficult problem. At this stage, the best procedures are based on the following:

1. Use of gold samples with steps of one layer of gold
2. Use of lipid layers deposited as LB films or as SAM films²⁰
3. Use of macromolecules with known dimensions^{20b}

There are also other procedures, but these are not as well documented. These procedures are delineated in this chapter. The image analysis is quite varied and covers a wide range of possibilities. Filtering techniques include both high and low frequency as well as two-dimensional Fourier transform filtering. Scrupulous preparation and extreme care yield excellent images.

Summarizing, the resolution of these different instruments varies, as does the information that can be obtained with each. Each offers a specialized window on the atomic and molecular world; each also involves special difficulties in interpreting the images obtained. One of the greatest problems in proximal probe imaging and manipulation of atoms and molecules lies in the difficulty in obtaining tips of consistent shape and known character. Even the tiniest variations in tip shape and composition — often a matter of just a few atoms — can cause variations in the results obtained.

As time has passed since the invention of these instruments, however, the collective expertise of the research community involved in proximal probe studies has increased enormously. Steady progress has been made in learning how to produce more uniform tips of consistent shape and character. Our knowledge of the basic phenomena involved in STM and AFM tip interactions with sample surfaces has become more comprehensive, as have our skills in interpreting the results obtained by these instruments.

Despite their limitations, and despite the difficulties in making sense of the images obtained, proximal probes have added greatly to our capabilities to explore atomic and molecular-scale realms. More recently, they have also begun to provide us with the means to carry out precise, controlled manipulation of atoms and molecules.

15.3 LIPIDLIKE MOLECULES ON SOLIDS

In the literature, many studies have been carried out on long-chain hydrocarbon molecule adsorption on graphite surfaces as a model system for determining the forces responsible for the adsorption processes.²⁶⁻²⁸ Thermodynamic analysis has indicated that the hydrocarbon molecules adsorb with high affinity to graphite surfaces and that the heat of adsorption increases with chain length,²⁸ which suggests that the alkane molecules are adsorbed with their long axis parallel to the graphite surface, as also confirmed by STM studies.²⁹⁻³¹

STM can distinguish molecules when found as mixed structures at surfaces. This was shown in a study,³² where the adsorption of mixed 1:1 triacontane/tricontanol mixtures in solutions were investigated by STM. STM images of 1-docosanol, 1-docosanethiol, didocosyl disulfide, and 1-chlorooctadecane have been compared on HOPG substrate.³² The images showed bright spots arising from sulfur (S) atoms. This suggests that S atoms in STM images can be used as a chromophore. This shows that STM can not only distinguish between molecules but also show differences within the same molecule.

The alcohol region was seen as “zigzags” and the alkane region as “straight” rows. Experiments were carried with tunneling conditions as -1200 mV and 60 Pa. The data for a mixture of 1:10 were obtained. STM images of 1-docosanol, 1-docosanethiol, didocosyl disulfide, and 1-chlorooctadecane on graphite were investigated in another report.³³ That both the S–H and S–S groups appear bright in the STM images indicates that the presence of an S atom on graphite gives rise to a higher tunneling current when the tip scans as compared to the current over a carbon (C), oxygen (O), or chlorine (Cl) atom. This finding might be useful in using S atoms as chromophores. This also shows that STM can see differences between the same molecule.

The resonance and environmental fluctuation effects in STM currents through adsorbed molecules have been analyzed.³⁴ AFM has also been used to modify structurally lipid bilayers in a controlled procedure.³⁵ The images showed that after the lipid tubule was scratched, the molecules rearrange after some time (24 h).

15.3.1 COLLAPSED LIPID MONOLAYERS

All lipids when spread on an aqueous interface form stable monomolecular films.²³ The stability of these self-assemblies is dependent on the lipid molecular structure. These monolayers have been used to investigate two-dimensional assemblies, to make organized arrays, and to model more complex biological membrane structures. As described elsewhere, a lipid film on compression exhibits a collapsed state, followed by a change in compressibility (i.e., the slope of the surface pressure vs. area isotherms changes).²³ In most cases, a drop in the surface pressure, π , is observed. This collapsed state is described as arising from the movement of the bilayer to slide over the monolayer. The magnitude of π remains constant until the surface is completely covered by a trilayer (or multilayer). After this state, the π again rises but with a somewhat lower compressibility. The collapsed state has hitherto remained much neglected, since we had no direct or indirect information on the exact molecular structures. The equilibrium near the collapsed state exists between a monolayer and a multilayer (most likely a trilayer).²⁰

The oleyl lecithin molecule was spread on water to give collapsed structures.^{1b} The AFM image was taken of these films after transfer to HOPG (Figure 15.5). The vesicle-like structure is clearly visible.

15.3.1.1 Magnesium-Stearate Films

The structure of collapsed lipid monolayers has not been investigated at the molecular scale. AFM studies²⁰ of collapsed monolayers on HOPG clearly showed steps of heights that correspond to the trilayer of Mg-(stearate)₂

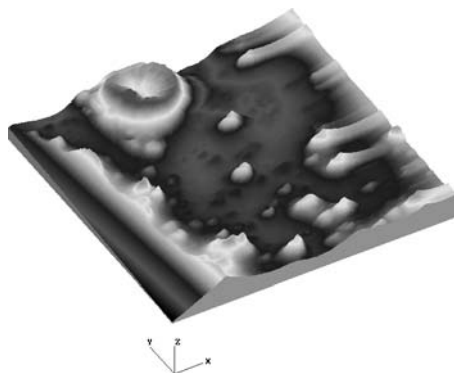


FIGURE 15.5 Collapsed three-dimensional AFM images of oleyl lecithin; see text for details ($90000 \times 90000 \times 2070 \text{ \AA}$).

MONOLAYER/BILAYER/TRILAYER

The step heights have magnitudes that correspond to the molecular dimensions of the lipid molecule. It is of interest to mention here that a clean graphite substrate (HOPG) does not show such step images. These studies were carried out by using a commercially available AFM (DME A/S, Denmark).

The AFM analysis showed that the collapsed film has broken up into islands due to mechanical handling. However, the large parts are perfect in structure. This information is useful when such LB films are to be used for the electronics industry or biosensors.

The height analysis shows that these films consist of multilayers, as the height is consistently 70 \AA . This value is much larger than the fully extended chain of $\text{Mg}-(\text{stearate})_2$, found to be 23 \AA from molecular modeling. These studies showed that indeed a trilayer (step height/length of the molecule = $70 \text{ \AA}/23 \text{ \AA} = 3$ layers) is formed as an LB film after the collapsed state. This finding agrees with the proposed structure. The morphology also indicates that the trilayer is a perfect state. This means that there exists an equilibrium between the monolayer and collapsed state. It will be shown below that the equilibrium is dependent on the lipid molecule. This structure can thus be used as a means for calibration of the AFM apparatus.

During these measurements, no damage was observed to the LB films by the probe tip. However, changes in AFM pictures are sometimes observed in those cases where the tip distance from the substrate has decreased, i.e., under increased resolution conditions, which may give rise to a closer tip separation from the substrate.

15.3.1.2 Cholesterol and Oxidized Cholesterol (Cholestane) Films

AFM was used to investigate whether a series of related molecules could be analyzed when present as SAM. The system chosen was the cholesterol molecule. The molecule cholesterol is a very important biological lipid. A cholesterol molecule with one hydroxyl group is known to oxidize into a variety of structures. These oxidized cholesterol products play an important role in many biological diseases, such as blood clots. The AFM data of the collapsed film of cholesterol (when spread on the surface of water) shows that two-dimensional crystallization takes place with very characteristic butterfly shapes.^{1b} This shows, for the first time in the literature, that not all lipid monolayers collapse to give a transition from monolayer to trilayer. This shows that the collapsed state may be a two-dimensional crystal phase.

The step height analysis of these two-dimensional cholesterol crystals gives 90 Å, which corresponds to six layers of cholesterol (90 Å/length of cholesterol molecule = 15 Å). This is different from what is seen for the collapsed films of Mg-(stearate)₂, as is well known from monolayer surface pressure vs. area isotherms.²³

The AFM software includes a program to calculate the area percent of any image. By comparing the percent area occupied in three dimensions we can estimate the number of molecules in any given image. From area analysis of the image (as obtained from AFM software), we can calculate the number of cholesterol molecules in each “half-butterfly.” The number of cholesterol molecules in this two-dimensional six-layer was found to be approximately 60×10^6 molecules (10^{-16} mol!). In this calculation, the area per molecule of cholesterol was assumed to be 40 \AA^2 (as found from the surface pressure vs. area isotherm).^{1b} This is a new kind of application of AFM as an analytical tool whereby the detection of very small amounts of materials can be carried out.²⁰

Cholesterol Butterfly ... six-layer ... 60×10^6 molecules

This observation shows that a two-dimensional crystal with a very narrow size distribution will self-assemble into ordered structures. The explanation is that cholesterol molecules are able to self-assemble under the influence of the molecular forces to form such nanocrystals. Regarding the self-assembly characteristics, a range of molecules with amphiphile characteristics possess this property.

Cholestane (as formed after oxidation of cholesterol molecule) collapsed films²⁰ show two step heights. These steps correspond to trilayers (length of cholestane $\times 3 = 50 \text{ \AA}$) and six layers (100 Å). This indicates that in the collapsed state the trilayer is able to form higher order two-dimensional crystals, i.e., six layers. These analyses show that in the collapsed monolayers of different lipids the following phase equilibria (with equilibrium constant, K) exist:^{20b}

Lipid	Phase Equilibria in the Collapsed Lipid Monolayer	
Mg-stearate	Monolayer = Trilayer;	$K = (\text{trilayer})/(\text{monolayer})$
Cholesterol	Monolayer = Hexalayer;	$K = (\text{hexalayer})/(\text{monolayer})$
Cholestane	Monolayer = Trilayer;	$K1 = (\text{trilayer})/(\text{monolayer})$
	Monolayer = Hexalayer;	$K2 = (\text{hexalayer})/(\text{trilayer})$

The molecules that form stable monolayers at the liquid interface are thus found to exhibit self-assembly characteristics. The differences between collapsed lipid phases (two-dimensional crystals) are easily seen from the surface pressure vs. area isotherms of lipids.²³ It is thus found that such AFM analyses now provide complete three-dimensional structures, which can be useful in explaining these differences in the collapsed states. Analyses of the stabilizing forces in such monolayer assemblies as van der Waals forces have been given elsewhere.^{23,35} The phase equilibria of oxidized lipids in bilayers is known to be of much interest in the biology. It is important to remark that in the literature monolayer structures have been studied where fluorescent probes have been added. The AFM studies are not mixed with such probes, as the latter might affect the phase equilibrium. Furthermore, the breakup of collapsed lipid monolayers is detected by AFM, which will be useful for other, more complicated systems. These results show that AFM can be applied to diagnostics of diseases known to be related to cholesterol oxidation. These studies have shown for the first time the high sensitivity with which AFM can be applied to biological systems.

Since the two-dimensional packing of the monolayer on the aqueous subphase can differ from that observed after transfer as a LB film to a solid substrate, the molecular packing in the film in the two systems must be known. AFM studies of crystallite formation in LB films have been reported in regard to cadmium-arachidate monolayers.^{20d}

15.3.2 LIPID ASSEMBLIES AS LANGMUIR–BLODGETT FILMS

Domain structures of phospholipid monolayer LB films were investigated by AFM.³⁶ The domain structures of phospholipids (di-palmitoyl-phosphatidylcholine, DPPC) were studied as LB films.

15.3.3 STM AND AFM STUDIES OF DIVERSE MOLECULES ON SOLIDS

C₆₀ molecules were investigated by STM.³⁷ The diameter of C₆₀ was found to be 1.1 nm. The STM image of C₆₀ multilayer growth at 300K was investigated.

Solid surfaces have been found to exhibit fractal morphology.³⁸ A study of the quality and accuracy of the methods based on frequency analysis for the fractal characterization of solid surfaces was carried out by STM.³⁹ The study was based on computer simulation of images of fractal surfaces. Measurement of the fractal character of a surface in the microscope range has specific problems. The most important is that the images of a given solid surface arise from the projections of the surface topography in which the vertical dimension is unknown, whereas from both STM and AFM we can obtain the vertical dimensions.

Carbon fiber surfaces were analyzed by STM and compared with HOPG.⁴⁰ The AFM measurements of FeOCl have been shown to compare well with the literature values of the *a*, *b*, *c* lattice constants.⁴¹

The STM tip is known to exert some force on the adsorbate, which requires the fixing of adsorbed molecules on the substrate. By covalently attaching porphyrin to a gold substrate, STM images were obtained.⁴¹ The interaction of such small molecules as H₂ and O₂ with copper (Cu) and nickel (Ni) surfaces has also been investigated by using STM.⁴²

15.4 BIOPOLYMER STRUCTURES BY STM AND AFM

The biological activity of proteins and enzymes is strongly dependent on the molecular configuration. Such macromolecular structures as helical, beta-sheet, and random-coil are well-defined, three-dimensional structures. Although electron microscopy has been very useful in determining such structures, the advent of STM and AFM has added much information in recent years.⁴³ In fact, the very first picture of DNA by STM was a highly acclaimed result.⁴⁴

Adenine and thymine molecules when placed on graphite were investigated by STM, and the two molecules could be easily distinguished (thymine contains a single hexagonal ring and the adenine molecule has a double-ring structure).⁴⁵ These results led to the possibility of using STM and AFM for obtaining the sequence of DNA.

Furthermore, in some cases the need for three-dimensional protein structures becomes urgent, as with the bacterial proteins (cholera toxin) that are known to produce the disease cholera. These investigations have been ongoing since 1977 using protein crystals and x-ray diffraction methods.⁴⁶ This knowledge is essential to produce new kinds of vaccines.

AFM has thus become a well-established and valuable tool in the three-dimensional topographical analysis of biopolymers.⁴⁷⁻⁵³ The three-dimensional structure of most biopolymers is within a range of 4 to 10 nm (40 to 100 Å) in lateral dimension by 1 to 5 nm (10 to 50 Å) in height. Unfortunately, in this size range, the finite size of the probe tip leads to relatively large systematic enlargements. However, this observation needs more extended investigation at this stage.

Images of poly(γ -benzyl-glutamate) (PBLG) were obtained by STM.⁵¹ These images reveal details of the molecular structures with the α -helical conformation as expected. Images by STM were compared with the Macro-Model and these agreed with the images of STM.

Globular features were reported from studies of catalase by using STM⁵⁴ studies. Catalase molecules could be observed from STM images. Molecular resolution images of β -helices were obtained by AFM studies of pentadecavaline films.^{55a} The repeat distance of 1.1 nm was obtained.

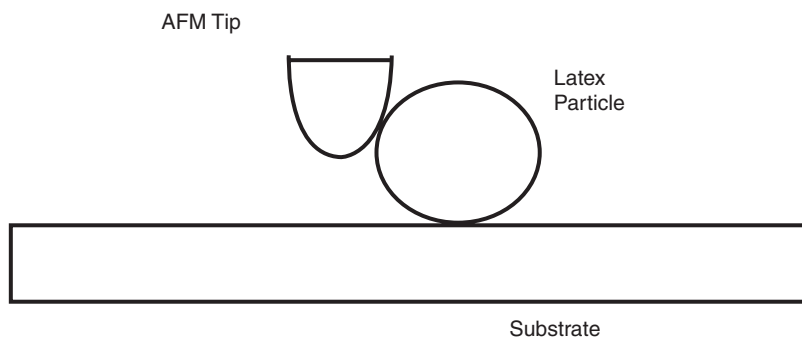


FIGURE 15.6 Tip shape and image and molecule relationship (schematic).

The molecular configuration of isotactic PMMA as LB films was investigated by STM.^{55b} The analysis showed that the polymer was present as a closely packed, well-ordered arrangement with helical and linear chain mixed configuration.^{55b}

AFM images⁵⁶ of the von Willebrand factor, which is a plasma glycoprotein, in hemostasis and thrombosis of blood were reported. The size of the glycoprotein as measured by AFM was some two to three times larger than that reported by electron microscopy. Other authors have also reported similar divergences for other systems, which may be ascribed to such factors as ambient humidity.

Antibody–membrane interactions have been studied by STM/AFM.^{57a} This is a particular system where such information as the nature of the attachment points and the bond strengths can be estimated.

The shape of the AFM tip is intimately related to the lateral enlargement phenomenon because of simple, hard-surface geometric considerations and because sources of interactive forces are distributed over the tip surfaces as well as the sample surface. Furthermore, some effects of the asymmetry of the tip on images has also been reported.^{56b} The tip surface molecule situation is depicted in Figure 15.6. It is obvious that no simple conclusion can be expected from such systems, because the images will be related to many different factors. There have been reported some studies on the effect of the shape and sharpness of the tip on the images.

SHAPE OF TIP ...

SHAPE OF SURFACE MOLECULES ...

IMAGE OF MOLECULE ...

It is generally accepted that at this stage no clear analyses can be given of the relation between the shape of the tip and the image of the molecule. More systematic and extensive studies are needed to understand fully the image and the tip surface molecule dependence at this stage. The biggest need at this stage is to provide the theoretical analyses that could provide extensive data on these observations.

Biological cell membranes are mainly made up of lipids and proteins. It is therefore obvious that such mixed model systems should be investigated. Mixed monolayers of hemoglobin, ovalbumin, xanthan, and virus with Mg-(stearate)₂ collapsed films have been studied as LB films on graphite.^{20,23} This provides a means of investigating biopolymers as found in their biological environment in the cell lipid-bilayer medium.

The hemoglobin protein molecule (a tetramer with molecular weight of 68,000) and ovalbumin (molecular weight of 40,000) were found to remain as small clusters on the collapsed lipid film.²⁰ The presence of protein molecules is easily observed from the light shaded spots. The step heights

were found to be ~ 50 Å. This corresponds to the diameters of these molecules. The size of the cluster varied, and under higher magnification we could barely see the outline of each molecule. However, preliminary data as shown here suggest that some ten molecules are involved in each cluster. At this stage, the method is not sensitive enough to provide better resolution. Work is in progress to improve this by using other cantilevers (i.e., sharp edged) and better equipment stability (for vibrations, etc.). However, the size of the cluster is indicative of protein–protein interactions in the monolayer. There seems to be some kind of higher-order aggregation in these two-dimensional structures. As far as we know, there has been no report previously of the cluster formation in the literature.

Xanthan (biopolymer), produced by the fermentation broth of the bacterium *Xanthomonas campestris*, is a polysaccharide that has been used in different industrial applications (food, tertiary oil recovery, pharmaceuticals). The xanthan molecule consists of a linear cellulose backbone, with links between the β -D-glucose residue, with a three-sugar side chain attached to every second glucose. This gives rise to a macromolecule with ionic characteristics and a comblike polymer. The xanthan structure results²⁰ showed a very characteristic morphology. The xanthan molecules ($\sim 10^6$ mol wt) are found to be arranged as linear-shaped structures (while globular proteins, e.g., hemoglobin and ovalbumin, are present as aggregates). This corresponds to clusters of xanthan molecules. The radius of gyration has been reported in the range of 80 to 90 nm. Furthermore, these structures have broken away from the lipid film. It is well known that the xanthan molecule (due to its high molecular weight) gives rise to very high viscosity in aqueous media. This means that xanthan must be aggregated in a state different from that of other proteins, such as hemoglobin and ovalbumin. These differences thus show the sensitivity of AFM. Furthermore, xanthan forms some compact gel-like structures (the so-called fish-eye). These images might be related to the fish-eye characteristic aggregation phenomena.

Immunoglobulin G (IgG) was investigated by STM.^{57b} IgG is a molecule consisting of two heavy chains (50,000 mol wt each) and two light chains of 25,000 each. These chains are known to be arranged in the form of a Y shape. The length and width of each arm from x-ray data are reported to be 8.5×6 nm. The height of the molecule is reported to be 4 nm. The IgG images showed dimensions of $7 \times 9 \times 4$ nm³, in agreement with both the x-ray and transmission electron microscopy (TEM) data. High-resolution images indicated the Y shapes. These data convincingly demonstrated that STM can provide images that are consistent with other microscopy data. No distortion or damage from the tip was observed.

The milk protein, casein, is known to form aggregates (casein micelles). The AFM image of casein placed on HOPG⁵⁸ is given in Figure 15.7. The size of the aggregates is found to be highly monodisperse, which shows the capability of applying AFM to such aggregate equilibria studies. The size analyses is as follows

Diameter = 1980 Å
Maximum height = 200 Å
Step height = 60 Å (= diameter of casein)

The data require further analysis at a higher resolution. However, the steps as observed in these images indicate that casein aggregates (micelles) are present under these conditions. The step height is almost equal to the known diameter of the casein molecule (~ 50 Å). This means that the aggregate consists of ~ 900 casein molecules. These images also show that the tip has apparently no effect on the resolution. This is noticed from the sharpness of the edges in the images. The magnitude of the maximum height corresponds to three molecules.

However, these observations clearly show that the molecular dimensions found for casein confirm the valid dimensions by AFM. This conclusion has been contested in the literature and therefore requires further analysis before it can be resolved satisfactorily.

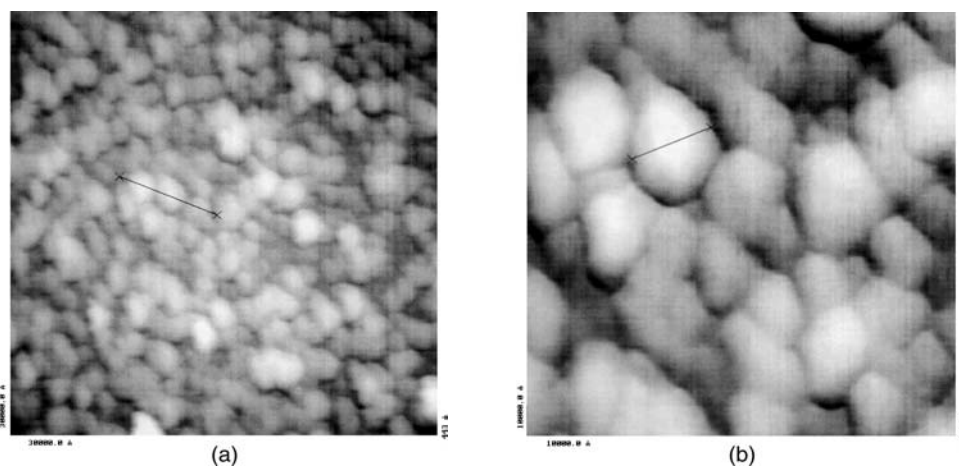


FIGURE 15.7 AFM image of casein placed on HOPG.⁵⁸ Scan sizes: (a) 30,000 × 30,000 Å; (b) 10,000 × 10,000 Å. Step height = 60 Å.

In virus–cell fusion, the mechanisms are not quite as well established at this stage. The very first step is the penetration of the surface protein into the cell membrane; therefore, a large number of investigations are being carried out by AFM whereby the molecular picture might be elucidated. A virus, *Moloney*, when studied on lipid films, showed that the particles prefer to orient at the edges of the collapsed lipid film.²⁰ The step height analysis shows that the virus has a diameter of 527 Å. This agrees with the electron microscope literature data.^{59,60} The geometric interparticle orientation provides information about the forces of interactions. In other words, different virus would exhibit different orientation images. Because membrane proteins have been found to be very difficult to crystallize, this procedure could be useful in studying the three-dimensional structures of such biopolymers. Virus particles tend to accumulate when suspended in water to concentrate at its surface with air.^{20a} This allows us to attach virus particles to substrates to obtain sharp images.

AFM has been used to study the morphology of neurons.⁶¹ It was also mentioned that with the AFM method we can image structures with diverse dimensions in a single scan without changing the focus (as required by the electron microscope).

STM topographs of xanthan gum, pipette-deposited and spray-deposited onto HOPG, and mica substrate were reported.⁶² A 10 μl solution of xanthan at a concentration of 10 mg/ml was deposited on HOPG and allowed to dry under ambient conditions. The topographs showed entangled molecules forming a dense network across the substrate surface. The diameter of strands varied from 6 to 16 nm.

The degree of miscibility of polymers will play an important role in biological and technology systems. The miscibility is dependent on the entropy, which results from the mixing of polymer chains. The mixing generally gives rise to a positive Gibbs free energy of mixing, thus giving phase separation. In drug delivery systems using the polymer erosion method, the AFM method was used to investigate these systems.^{63a} Degradations of the thin-film blends of polysebacic anhydride and polylactic acid were investigated.

Cell fusion peptides were investigated by AFM.^{63b} The peptides from different viruses were used: HIV-GP41; the protein responsible for influenza virus fusion, hemagglutinin HA-peptide; SFV. All peptides were dissolved in DMSO (0.01 mg/ml) and a 10 μl sample was placed on HOPG. After evaporation overnight of the solvent, the samples were analyzed. The morphology of the peptide SFV (SFV69) was as follows. The diameter of the molecule is ~20 Å, which agrees⁶⁴ with the molecular weight of 20,000. The different peptides show different morphological images (Figure 15.8). The SFV image shows the following dimensional analysis:

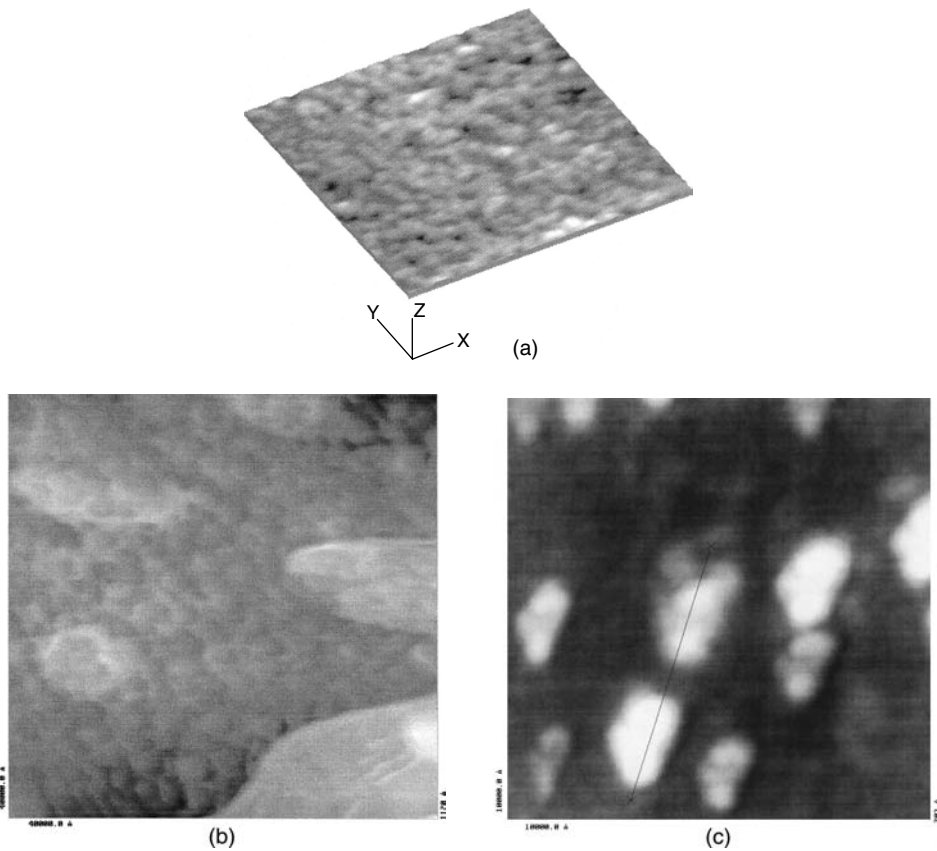


FIGURE 15.8 AFM images of fusion peptides:⁶³ (a) HA; (b) HIV-GP41; (c) SFV (see text for details).

Step height = 20 Å

Length = 2000 Å = 2000 Å/step height (20 Å) = 100 peptide molecules

This finding is in agreement with the data for lysozyme, as described below. The length corresponds to an aggregate of 100 peptide molecules. The differences in these images between peptides are shown, then, to be related to the amino acid composition and sequence.

The differences in the morphology of these peptides can be ascribed to their hydrophobicity characteristics.^{63a} These studies also indicate that the effect of solvent on the polymer configuration can be investigated by AFM studies. This observation is important in the studies of cell fusion mechanisms. It is well accepted that virus fusion starts by a step height triggering the integral membrane protein to change conformation, thus exposing a hydrophobic domain that can mix with the lipid bilayer of the cell membrane.

It has been argued that AFM or STM should principally provide the same kind of morphological features as reported by electron microscopy,^{63a} which may depend both on the radius (or rather the shape) of the tip, as well as on the geometry and the physicochemical state of the biological material (for example, adsorbed water). The less corrugated the objects are, the less important is the actual tip shape. This is found for near-atomic resolution images in the case of LB films. In the case of STM, better resolution can be obtained by averaging the signal-to-noise ratio.

Recently there has been much interest in the ability to precisely position and orient biological molecules on engineered nanofabricated substrates thus enabling technology critical to the long-term goal of integrating biomolecular motors with nanoelectromechanical systems. In some

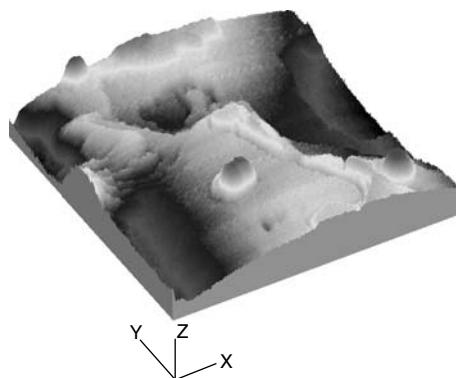


FIGURE 15.9 AFM image of mixed system of SDS + PEO ($20000 \times 20000 \times 440 \text{ \AA}$).

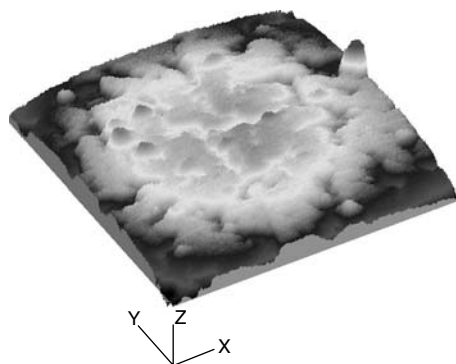


FIGURE 15.10 AFM image of mixed system of SDS + gelatin ($45000 \times 45000 \times 351 \text{ \AA}$).

cases electron beam lithography and nanoimprinting techniques were used to produce arrays of nickel dots (50 to 200 nm diameter). The technique of fluorescence (of microspheres attached to the subunit) and AFM of these arrays has demonstrated precise positioning, spacing, and orientation of individual F1-ATPase molecules.^{65b}

It is now well established that the biophysical analysis of a variety of enzymes shows that many act as nanoscale biological motors. In these studies the force generation and size scale of these biomolecular motors have been reported to be compatible with nanofabricated structures.

The precision attachment of individual F1-ATPase biomolecular motors on the nickel dot arrays was demonstrated using two different methods. The attachment of F1-ATPase–microsphere complexes was examined using epifluorescence microscopy, demonstrating attachment of the complexes in specific array patterns. It was also found that F1-ATPase molecules did not attach to all dots in the array. The AFM imaging of nickel dot (60 to 600 nm in diameter, 4 to 20 nm high) arrays produced by e-beam lithography demonstrated the presence of individual F1-ATPase molecules (14 nm high and 8 nm in diameter) on the nickel dots. These images showed that apparent diameter of the F1-ATPase molecules was 30 to 50 nm due to AFM tip–F1-ATPase convolution.

Mixed detergent (sodium dodecyl sulfate, SDS) + polymers (polyethylene oxide, PEO; gelatin) were investigated using AFM.^{1b} The images of mixed SDS + PEO are given in Figure 15.9. These images were taken after the evaporation of a drop of solution (10 μl) was dried on HOPG. It is seen that polymer clusters are clearly visible. Similar kinds of images were obtained in the case of SDS + gelatin (Figure 15.10). This shows the useful application to such mixed systems. It is hoped that more detailed image analyses will provide information on such detergent binding to polymers.

15.5 CRYSTAL STRUCTURES BY STM AND AFM

A characteristic of many solids is their crystalline state, i.e., a crystal is a solid bounded by faces meeting in definite angles. Except in the so-called regular system of crystals (cube, octahedron, etc.), the properties of a crystalline solid, such as elasticity, thermal conductivity, refractive index, etc. are different in different directions. The application of AFM to the studies of crystal structures has been of much interest. In the following we will give a few examples of such investigations.

15.5.1 CRYSTAL STRUCTURES OF SMALL MOLECULES

Crystals (macro- and nanodimensional) are generally formed from solutions as the concentration of the solute becomes oversaturated. It thus is interesting to study these crystals by STM and AFM, which has been done in recent years.^{66,67} The smallest particles (atoms, ions, molecules) that make up a crystal and thus also delineate the surface have specific electric, magnetic, and mechanical properties, which can be registered by STM and AFM. Using this procedure, an anthracene crystal surface was investigated. The images showed the 001 face of the anthracene crystal, and the molecular size of 4.7 Å was clearly seen. The x-ray data give a size of 5 Å. Further, the influence of functional modification (CH₂, CO, CN₂) of the alkylated anthrone derivatives of the structures of their two-dimensional crystals were investigated by STM.⁶⁶

STM of galena and surface oxidation and sorption of aqueous gold were reported in a recent study.⁶⁸ The calcite precipitation mechanisms were investigated by AFM.⁶⁹ The crystals of proteins are difficult to obtain but are prerequisite for any kind of electron microscopic analysis. Because all protein molecules are composed primarily of 25 different amino acids, it was useful to determine the crystal structure of each amino acid by AFM. A solution of amino acid of concentration 0.01 mg/ml was used. A 10- μ l drop was placed on HOPG and after evaporation overnight AFM measurements were carried out.⁷⁰ Different images of various amino acids were investigated.

It was concluded that AFM provides much useful information regarding the crystal formation of amino acids from aqueous solutions. Differences are observed between the various amino acids. As is well known, amino acids in an aqueous environment are classified, among other properties, as:

- Charged
- Hydrophobic
- Neutral

as determined by the side chain group.^{23,71,72} In other words, the solubility of different amino acids in water would be different, as was also found. The evaporation of water molecules leads to the formation of crystals. The shape of crystals thus would be expected to be related to the water + amino acid interaction properties.

Further, we can conclude from these image analyses that there are basically two kinds of crystal forms:

1. Sharp-edged crystal form (proline, phenylalanine, threonine, valine, lysine)
2. Rough-edged form (ornithine, dl-serine, tyrosine, tryptophan)

It also seems that the crystals of the hydrophobic (less hydrating) amino acids (e.g., phenylalanine, proline, alanine, valine) are more sharp-edged than the polar amino acids (glycine, cysteine, ornithine). This may suggest that as water evaporates the hydrophobic nature of the amino acid determines the crystal formation. This further suggests that the protein crystal formation would be expected to be related to the polar/apolar nature and may provide useful information on protein crystal formation. The self-assembly characteristics are obviously different in these amino acids, as expected. It is important to recognize that the water–amino acid interaction, as found from heat

of solution data, determines the overall property of a given protein from its sequence. These crystal images would thus help in understanding these water-binding mechanisms. The nucleation growth and molecular-packing structures of guanine and adenine on graphite have been investigated by STM and AFM.^{70b} These studies show for the first time that nanocrystal structures can be investigated by using AFM in three-dimensional images.

15.5.2 MACROMOLECULE CRYSTALS BY STM AND AFM

Protein crystal structures were also investigated by STM.⁶⁶ Protein crystals are known to be unstable in a dry atmosphere. The water content is ~43%. Lysozyme was therefore precipitated from an electrolyte-free aqueous solution (either with ethanol or polyethylene glycol).

The dimension found is 37 Å upward and 79 Å sideways. This gives the size of the lysozyme as 37 × 79 Å. This is in contrast to the x-ray data; however, the tetragonal unit cell of lysozyme^{73a} gives for eight molecules the dimensions:

$$\begin{aligned}a &= b = 79.1 \text{ \AA} \\c &= 39.1 \text{ \AA}\end{aligned}$$

These STM data agree with the lattice constant for the eight molecules. Similar data for other proteins have been observed.^{73b}

Lamellar crystals of poly(oxyethylene) (POM; molecular weight = 90,000 g/mol) grown from solvent bromobenzene were found to form hexagonal shapes.⁷⁴ The crystal height was 8.5 nm. High-resolution AFM images of polyethylene crystalline lamellae gave a pitch height of 0.26 nm and interchain spacing as 0.50 nm.⁷⁴ These data agree with x-ray diffraction data.

In a recent study, simultaneous measurements were carried out using SEM and AFM^{75a} of polystyrene particles with diameters of 144 and 55 nm. The SEM images showed two-dimensional crystals, which were hexagonally arranged. The 144-nm particles were identical according to SEM. The AFM images of 38- and 12-nm particles were somewhat diffuse as compared to SEM. This observation requires further investigation. The spherulitic morphology of isotactic polypropylene has been investigated by AFM.^{75b}

The AFM method was used to study some biopolymers, such as DNA on mica, etc.,⁷⁶⁻⁸² however, the resolution of AFM is known to be limited by the sharpness of the tip, and interpretation of the image has been related to the geometry of the tips.⁸³ For example, due to the finite radius of the tip, AFM images of DNA are on average seven times broader than the known 2-nm (20 Å) width of DNA. This kind of result requires the description of the resolution of AFM images, especially when comparing images of AFM with electron microscopy.

AFM images of some solid surfaces might be subject to artifacts such as the broadening of structures and ghost images of tips due to the finite size and shape of the contacting probe. This means that the shape or radius of the tip used in AFM measurements should be known. One procedure that might be of much use is if the tip happens to leave a scratch on the soft lipid substrate⁸³ (Figure 15.11).

Synthetic membranes as used for filtration and microfiltration were analyzed by STM;⁸⁴ 80-nm pores were observed. The three-dimensional crystals — Ca-adenosine triphosphatase (Ca-ATPase) — of the calcium pump from sarcoplasmic reticulum were imaged by AFM.⁸⁵

15.6 STM AND AFM STUDIES UNDER FLUIDS

For all kinds of everyday systems, we would like to have knowledge of the molecular information of interfaces (e.g., gas–solid, solid–liquid). STM and AFM can be modified with a so-called fluid cell, which allows us to measure almost any kind of fluid.

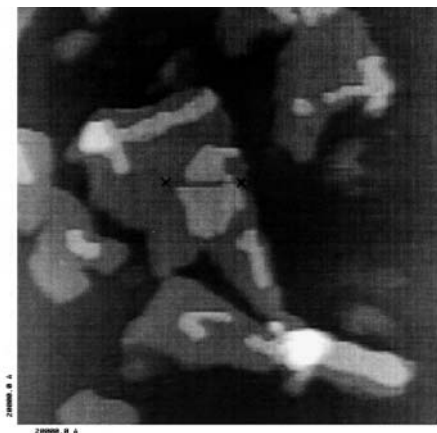


FIGURE 15.11 AFM image with the scratch from the cantilever. The three-dimensional analyses of the scratch is an image of the tip shape.

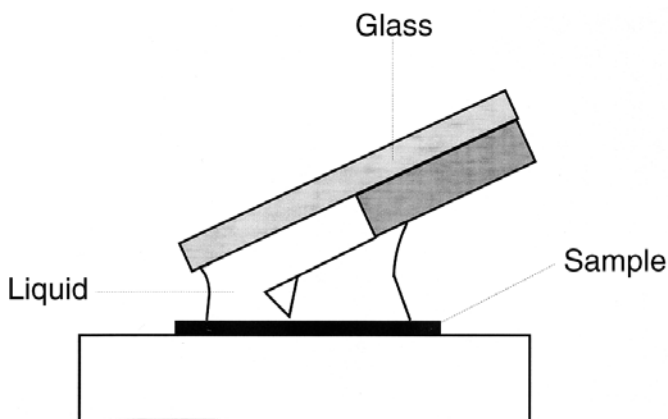


FIGURE 15.12 A simple fluid cell with glass slide in an AFM. (From Birdi, K.S., *Handbook of Surface and Colloid Chemistry*, CRC Press, Boca Raton, FL, 1997.)

STM can be modified, as described in the literature.^{86,87} The tip is covered by some suitable insulator, except at the end of the tip through which the tunneling current is measured. A rather simple method of modifying the commercially available AFM is shown in Figure 15.12. The principle is to glue a glass slide just over the cantilever. A drop of fluid is then added under the glass plate such that the sample is covered ($10\ \mu\text{l}$ is often enough volume). The laser beam can pass through the glass slide and the fluid in order for AFM to operate under fluids. The main disadvantage is that the fluid evaporates slowly, and leads to distortions in the image. However, considering its simplicity, we can manage it quite successfully. It is easy to change the composition of the fluid, as the amount of fluid used is of the order of $10\ \mu\text{l}$. In the author's laboratory this procedure has allowed us to obtain many useful images by AFM. Another method⁸⁸ is shown in Figure 15.13. For some of the apparatus, such cells are now commercially available. Some of the cells allow us to change the solution composition under measurement. In a recent study, living renal epithelial cells in an aqueous environment were studied by AFM.⁸⁸

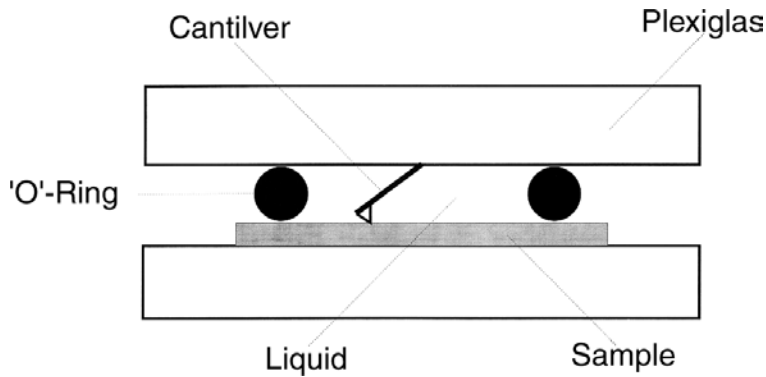


FIGURE 15.13 Schematics of the AFM fluid cell. The O-rings are used to contain the fluid.

15.7 MEASUREMENT OF ATTRACTIVE AND REPULSIVE FORCES BY ATOMIC FORCE MICROSCOPE

The physical description of all kinds of molecular interactions are based on the magnitude of the distance between two bodies. Furthermore, all physical forces are related to the distance of separation, especially at nanometer scale, i.e., molecular dimension.

As two bodies approach each other, at very close distances (nanometer range), there exists attractive (van der Waals) and repulsive (Coulombic) forces. van der Waals forces acting between two different phases have attracted the attention of various investigators; however, experimental measurement of these forces at very small distances (nm) has not been easy. These are measured by the surface-force apparatus (SFA) by using direct force. In the literature are studies⁸⁹⁻⁹² using two curved mica surfaces.

Recently, AFM⁹²⁻⁹⁷ has been used to measure these hydrophobic forces. AFM has many advantages over SFA. Almost any kind of surface can be used. Furthermore, these force curves can be obtained both in air and fluids.

The theoretical analysis is carried out as follows. The relation between the attractive force, F , and two mica surfaces of curvature, R , is given as⁸⁹

$$F/R = C_1 \exp[-H/D_1] + C_2 \exp[-H/D_2] \quad (15.2)$$

where H is the closest distance of approach, C_1 and C_2 are parameters characterizing the magnitudes of short- ($H < 10$ nm) and long-range hydrophobic forces, respectively. However, the hydrophobic forces may also be given as a power law:

$$F/R = -K_h / [6H^2] \quad (15.3)$$

where K_h is the only fitting parameter, also called the Hamaker constant⁹⁸ (Table 15.2).

Hamaker theory is based on pairwise additivity of interactions: i.e., it assumes that the total interaction is just the sum of the interaction between pairs of molecules. However, the neighboring molecules will moderate the interaction between any molecule pair. Interaction between fluctuating dipoles is instantaneous. The electromagnetic wave set up by the moving electrons travels at a finite rate. When the wave reaches a neighboring molecule that is farther than ~ 10 nm away, the original electronic state of the molecule might have changed. The interaction between the molecules will be reduced.

TABLE 15.2
Magnitude of Hamaker Constant⁹⁸
for Various Substances Immersed
in Water (20°C)

Solid	Hamaker Constant (J)
Polyhexafluoropropylene	2×10^{-22}
Paraffin wax	2×10^{-22}
Polyethylene	2×10^{-21}
Polystyrene	5×10^{-21}
Copper	1.4×10^{-20}
Silver	2.5×10^{-20}
Anastase (TiO ₂)	3.5×10^{-20}
Iron	4×10^{-20}
Graphite	5×10^{-20}
Silica	6×10^{-20}
Mercury	1.3×10^{-19}

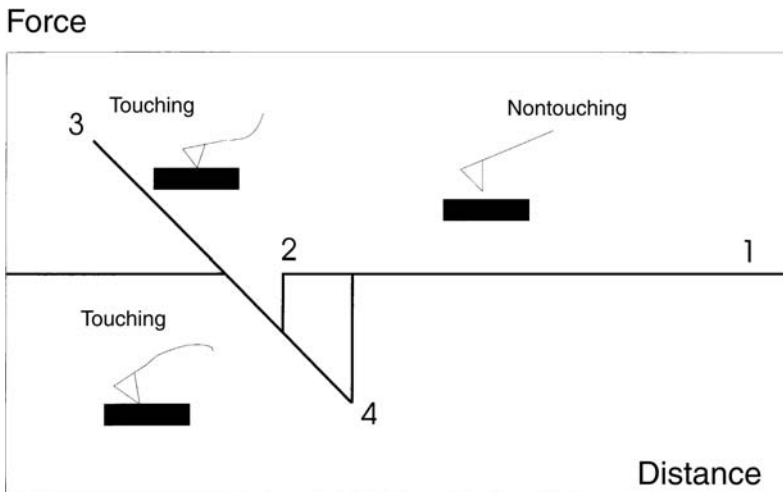


FIGURE 15.14 Force vs. distance (between tip and sample) schematic curve. Sample is at a large distance at position 1, and the tip is nontouching, while it has contact (touching) in positions 2, 3, and 4.

The interaction between particles falls off more rapidly if the particles are farther than ~10 nm apart; e.g., the interaction is proportional to H^{-3} (where H is the separation distance) instead of H^{-2} , when $H \sim 10$ nm or more. This is known as the retardation effect.⁹⁹

The hydrophobic forces were described as arising from various interactions — for example, an entropy increase resulting from a rearrangement of the configuration of the water molecules.

The tip and sample interaction is depicted in Figure 15.14. The data of such studies⁹⁷ have been reported on silica surfaces. These measurements showed the deflection of the cantilever between the silica plate and the glass sphere coated with octadecyltrichlorosilane. It is of interest to note that AFM is a very sensitive molecular force microscope. The forces measured by AFM are of the order of 10,000 to 100,000 times lower than an insect (~1 mg) sitting on a surface!

At very large distances, there is no interaction between the tip and the sample, and the force vs. curve is a straight line (as depicted in Figure 15.14 by 1–2). Although electrostatic interactions will have some effect even at large distances, these can be measurable at some intermediate distance. As the distance becomes shorter, the attractive van der Waals forces at position 2 (Figure 15.14) make the tip jump into contact with the sample. This distance would be determined by properties of the sample and the tip and the Hamaker constant. The repulsive forces become active as the distance becomes shorter. During the retraction cycle, the adhesive forces maintain the contact at position 4. The AFM operation can be maintained between positions 3 and 4.

In the noncontact mode, the net force detected is the attractive force between the tip and the substrate. On the other hand, in the contact mode, the net force measured is the sum of the attractive and repulsive forces.

In the field of surface science and interfaces, it is well known that acid–base interactions play an important role for a large number of phenomena, such as adhesion on polymers, polishing, etc.^{99,100} The oxide surfaces in an aqueous solution become charged due to amphoteric dissociation of surface M-OH groups. The Brønsted acidity or basicity of an oxide surface can be characterized by the point-of-zero charge (pzc), which corresponds to the pH value required to achieve zero net surface charge.

The surface of an oxide can also be characterized by the isoelectric point (iep) corresponding to the pH at which the zeta potential is zero. If there is no specific adsorption of ions other than H or OH, the magnitude of iep is equal to pzc.

In general, we determine the magnitude of pzc and iep by electrophoretic or potentiometric titration methods.¹⁰¹ In some cases, these data have been obtained by using the streaming potential measurements.¹⁰² In a recent study, the wetting properties of silanated surfaces were investigated by AFM.^{103a} Also, the force measurement on hydrogel was measured by AFM.^{103b}

It is thus seen that a variety of interfacial forces can be investigated by using AFM. In the noncontact mode, we mainly estimate the van der Waals forces (image resolution ~10 nm). On the other hand, the ionic repulsion forces are measured in the contact mode. These studies thus would provide an understanding of the interaction forces (attractive and repulsive) in much greater detail. It is seen that by AFM we can determine the magnitude of distance of separation at which two bodies jump into contact. The exponential and power laws have been found to fit the experimental force curves.

15.8 DIVERSE APPLICATIONS OF STM AND AFM

The ultimate aim of nanotechnology is the development of self-assembling molecular-scale devices that can themselves perform specific, precisely controlled operations at the molecular and atomic level. Current methods using natural molecular machines — proteins, enzymes, antibodies, and the like — or synthetic molecular forms still rely to a large degree on bulk processes. They provide us with rudimentary devices that operate at the molecular and atomic level, but at present they lack the precision and positional control required to develop more advanced nanotechnologies.

Oddly enough, the devices that currently provide us with the most precise and most specific control at the molecular and atomic level are macroscopic instruments operating on laboratory bench tops: STM and AFM.

In recent decades, the areas of application of SPMs has increased rapidly. Because this subject is becoming very large only a few examples will be delineated here. The STM and AFM microscopes allow us to manipulate the sensor (STM = tip, AFM = cantilever) at a distance of the order of nanometers (Å) from the substrate under ambient conditions. This means that we can develop so-called nanotechnology products if we could control the movement of the sensor within this range of separation. In the following some major developments are mentioned; however, as the possibilities are many, the list is not complete due to space considerations and the rapid rate at which advances are being made.

Another use of AFM and STM technology that has been investigated is nanolithography.^{105,106} This is carried out by increasing the force applied to the cantilever; the surface can then be scraped,

leaving behind a rectangular depression that corresponds to the scanning area.¹⁰⁶ In the literature, more results have been reported using this procedure.

STM studies of mercury sessile drops have been reported in a recent study.¹⁰⁷ In another report, a general procedure of manipulating atoms on solid surfaces by the help of a tip in an STM was described.¹⁰⁸

An atomic switch has been realized by using the principles of STM, according to a recent report.¹⁰⁹ A multiple photochemical switching device has been described by using an LB method consisting of molecules with switching, transmission, and working units.¹¹⁰ It was shown that by using different switching units to assemble the device, its conductivity could be controlled by four different types of light irradiation. The potentiodynamic STM analysis of iodide chemisorption on Au(100) has been reported.¹¹¹

The phenomenon of metal surface reconstruction has been investigated, whereby the top atomic layer assumes ordered structures that differ markedly from the bulk-phase crystal lattice.¹¹² STM has been useful in obtaining real-space/time insight into the local structural changes associated with surface reconstruction.¹¹³

The capacitance of a substance determines the ability to add electrons, or to extract them. STM exhibits stepwise charging (Coulombic staircase), which is expected for such materials as metal films. Single molecules (liquid crystals) have also been found to exhibit this incremental charging behavior.^{114a} Various early attempts at using STM and AFM for atomic and molecular manipulation were reported.^{114b} As knowledge of the forces involved and phenomena observed during STM and AFM imaging accumulated, it soon became apparent that these instruments could also be used to manipulate atoms and molecules. It was obvious that the electric field forces generated by the STM and the actual force of contact exerted on the sample surface by the AFM could and often did affect the structure of the sample. The question was, could these alterations and modifications be controlled? And if so, could they be carried out in a more precise, selective manner? Researchers began experimenting almost as soon as the instruments themselves became available.

Simple manipulation experiments were reported on deposition and etching. Initial attempts to effect controlled changes at the atomic and molecular level were often quite simple, even crude. The level of control over the attempted alterations was low, and the results often inconsistent. One of the earliest unambiguous attempts was reported with much success.^{114b} Using a tungsten STM tip, it was possible to create small, stable features on a clean germanium surface with short voltage pulses. These features were just 0.8 nm across, and 0.1 to 0.2 nm high. The conclusion was that germanium atoms picked up from the surface by the STM tip during imaging scans were transferred back to the surface in small clusters during each pulse. This conclusion was bolstered by the fact that the tip could be “charged” with germanium atoms by touching it to the surface, and then depositing them elsewhere with a pulse. These tiny but distinct features could then be “read” by the STM in a low-voltage scanning mode.

A method was described that permitted study of the electrochemical behavior of a single molecule by using the principles of STM and the scanning electrochemical microscope.^{115a} The STM was used to investigate the electro-oxidation of phenoxide to oligophenol on gold in alkaline solutions.^{115b}

In some recent studies creating ordered structures at molecular scales has been attempted. However, even these examples, involving alterations of single molecules, do not yet approach the sort of precision, consistency, or positional control that would be required in the construction of molecular devices. Moreover, these methods often rely on fairly high energy events to destroy chemical bonds and split molecules, but they do not yet provide very reliable ways of putting atoms and molecules together with strong stable bonds. Over the last few years, however, significant progress has been made in this direction. A number of these experiments have demonstrated the capability of using the STM and AFM to create precise, well-ordered arrangements of atoms and molecules of a specified and reproducible design. One well-known example succeeded in using a tungsten STM tip to position 35 xenon atoms on a nickel surface to spell out “IBM,” demonstrating

a rudimentary ability to manipulate the basic building blocks of most materials to form orderly patterns.^{115c} Furthermore, the researchers were also able to create linear arrays of xenon atoms and other arrangements. Similar results were reported involving carbon monoxide molecules on a platinum surface.^{115d} However, no stable bonds were formed in either set of experiments.

STM and AFM methods can be used as a nanoscale quantitative analysis tool for materials on surfaces (e.g., pollution control). This was mentioned earlier where 60×10^6 cholesterol molecules were estimated in the image. The lower limit in detection by AFM or STM is theoretically one atom or molecule (i.e., 10^{-23} mol!). This means that quantitative analysis has an extreme lower limit for detection, which is important in pollution control, etc. where very small amounts must be monitored. On this subject of the nanoanalytical application of both STM and AFM much remains to be studied. It is obvious that in the future of nanochemistry will develop based on such nanosystem studies. The nanocrystal studies of amino acids as described above are also another area that will develop based on these procedures.

In a recent report,^{115c} a procedure for writing and reading by STM at a nanoscale was described. The substrate used was gold and an electrochemical cell.

A modified type of AFM, called a friction-force microscope (FFM), has been described.^{115,116a} This method was shown to be able to distinguish between fluorocarbons and hydrocarbons on a phase-separated LB film. This shows that although AFM has proven useful for imaging organic thin films on an atomic scale, the technique can also provide useful information about the composition of molecules, as well as their conformation.

In a recent study the nanotribological properties of C_{60} and C_{70} films on graphite were reported.^{116b} C_{60} molecules were observed on graphite to grow in a monolayer form, whereas C_{70} molecules grew in a bilayer form. The shear stress between a C_{60} monolayer and graphite was approximately 0.2 GPa. In these C_{60} films, a change of tip motion, from one-dimensional stick-slip to two-dimensional zigzag stick-slip with decrease of a loading force, appears. Furthermore, the mechanical properties of fullerenes have been of much interest in the field of materials science. C_{60} and C_{70} solids have been suggested to be good lubricant materials because of their nearly spherical shape and low surface strength.^{116b} The nanotribological properties of the C_{60} islands on KCl using frictional force microscopy (FFM) were described. The different scanning directions of a C_{60} surface were carried out. The effect of water adsorption on the C_{60} films was found to give a lower frictional force, indicating that C_{60} molecules rotate or translate at the surface. This suggested that the C_{60} films exhibit various behaviors depending on the loading force, scanning direction, and relative humidity. Furthermore, the growth mode of C_{60} and C_{70} films on graphite using AFM and FFM, and we focus on the nanotribological properties of C_{60} and C_{70} films.

The C_{60} and C_{70} films on HOPG and KCl were also investigated after being prepared by evaporation from a BN crucible. The temperatures of their substrates during evaporation were kept at range of 150 to 200°C. Normal and lateral forces were measured simultaneously under argon atmosphere at room temperature using a commercially available instrument. The scan speed was 0.13 m/s. A rectangular silicon cantilever with a normal spring constant of 0.05 N/m was used. Zero normal force is defined as the position at which the cantilever is not bent. AFM images of C_{60} and C_{70} islands on a KCl surface were obtained. These images showed the C_{60} and C_{70} islands, which form parallel to a KCl substrate. It was found that the island growth takes place in cases where an intermolecular interaction is stronger than a molecule–substrate interaction, as reported in previous studies.^{116b}

From these studies it was concluded that C_{60} – C_{60} and C_{70} – C_{70} interactions are stronger than C_{60} –KCl and C_{70} –KCl interactions, respectively. The AFM images of C_{60} and C_{70} films on a graphite surface in the initial stage of growth were studied. The height of the C_{60} films in the middle of images was approximately 1 nm, exhibiting a monolayer. The high-resolution FFM image of the C_{60} monolayer exhibited a periodicity of 0.9 nm, which indicated a zigzag motion along the scanning direction of the C_{60} monolayer.

Thus, the existence of the monolayer exhibits epitaxial growth on graphite, as shown by other investigators.^{116b} The growth of this monolayer indicates that C₆₀ molecules grow on graphite such that the hexagonal face of a C₆₀ molecule pairs with the hexagonal face of the second graphite layer, so as to continue the natural stacking of the graphite. The height of the C₇₀ films in the middle of the image was about 2 nm, exhibiting a bilayer, which indicated that no C₇₀ monolayer on graphite exists in these systems. Because the hexagonal face in a C₇₀ molecule does not situate on the top of its ellipsoid, it may not always be stable to pair with the hexagon face of the graphite in a monolayer manner.

A procedure has been described to perform *fast time-resolved* experiments with STM.¹¹⁷ As already seen, STM is the only method that can be carried out based on localized quantum mechanical tunneling of electrons between the sample and the tip. This procedure offers an observed resolution of the molecules in the three-dimensional domain. The fourth dimension has been suggested to be also possible by this method, which relates to the atomic timescale.

The estimated intrinsic timescale for tunneling across the junction between the sample and the tip has been estimated to be of the order 10 fs (10⁻¹⁵ s) or less. It was suggested that, in order for the time-resolved STM to be useful, it must be possible to relate the shape of the time-resolved current to the time dependence of the underlying processes.

Another interesting almost *nanodevice* was created¹¹⁸ in the form of an extremely tiny electrochemical “battery.” A voltage pulse from an STM tip was used to form a small pit in a graphite surface bathed in a dilute solution of silver. This provided a nucleation site for the formation of a small pillar of silver. A solution of copper was then introduced, and an additional pulse effected the formation of a similar copper pillar. “Immediately following the deposition of copper metal on the surface,” their report states, “the volumes of both copper and silver structures begin to change.” The copper migrates via an electrochemical reaction through the solution to plate the silver structures, discharging a minute current in the process. While interesting, it is difficult to see how the current generated could be harnessed in a useful fashion, and in any case the device only “functions” for about 45 min.

Much of the research into STM manipulation of silicon and other semiconductor surfaces, including the experiments described earlier, is aimed toward the long-term goal of creating molecular-scale electronic devices. Research¹¹⁹ indicates that atomic and molecular-scale structures exhibiting circuit-like behaviors such as the tunnel-diode effect can be constructed. Many researchers working in the field hope to develop single-electron tunneling (SET) transistors, and eventually transistor arrays as part of functional computing devices. However, a question that will have to be addressed, if working SET devices are ever to be created, is whether the energy dissipation of electron tunneling in the sort of high-density arrays envisioned by many researchers in this field will exceed levels that make such devices practical. The tunneling of even a single electron dissipates a relatively large amount of energy at the molecular scale.

Another line of STM manipulation research that has attracted similar interest is the construction of quantum electronic structures (atomic and molecular-scale features that constrain electron movement in one, two, or three dimensions). Recent reports offer some preliminary indication that such structures may also eventually be employed to construct molecular-scale electronic devices.¹²⁰

REFERENCES

1. a) Laidler, K.J., *The World of Physical Chemistry*, Oxford University Press, Oxford, 1995. b) Birdi, K.S., Ed., *Handbook of Surface and Colloid Chemistry*, CRC Press, Boca Raton, FL, 1997.
2. Adamson, A.W., *Physical Chemistry of Surfaces*, 5th ed., John Wiley & Sons, New York, 1990.
3. Christmann, K., *Introduction to Surface Physical Chemistry*, Steinkopff-Verlag, New York, 1991.
4. Binnig, G., Gerber, C.H., and Weibel, E., *Phys. Rev. Lett.*, 49, 57, 1982.
5. Binnig, G. and Rohrer, H., *Surf. Sci.*, 126, 236, 1983.

6. Binnig, G. et al., *Phys. Rev. Lett.*, 50, 120, 1983.
7. Binnig, G., Quale, C.F., and Gerber, C., *Phys. Rev. Lett.*, 56, 930, 1986.
8. Binnig, G. et al., *Europhys. Lett.*, 3, 1281, 1987.
9. Garcia, N., in *Proc. First Int. Conf. Scanning Tunnelling Microscopy*; Garcia, N., Ed., *Surf. Sci.*, 181, 1987; Hansma, P.K., Ed., *Tunneling Spectroscopy*, Plenum Press, New York, 1982.
10. Feenstra, R.M., Proceedings of the Second International Conference on Scanning Tunnelling Microscopy, *J. Vac. Sci. Technol.*, A6, 259, 1988; Sarikaya, M., *Ultramicroscopy*, 47, 1, 1992.
11. van de Leemput, L.E.C. and van Kempen, H., *Rep. Prog. Phys.*, 55, 1165, 1992.
12. Frommer, J., *Angew. Chem. Int.*, 31, 1298, 1992.
13. Parsons, E. et al., *J. Microsc.*, 174, 59, 1993.
14. Falk, R.H., *Scanning Electron Microsc.*, 1980, 79, 1980.
15. Marti, O., Drake, B., and Hansma, P.K., *Appl. Phys. Lett.*, 51, 484, 1987; Drake, B. et al., *Science*, 243, 1586, 1989.
16. a) Avouris, P., *J. Phys. Chem.*, 94, 2246, 1990; Sexton, B.A., in *Surface Analysis Methods in Materials Science*, O'Conner, D.J., Sexton, B.A., and Smart, R.C., Eds., Springer-Verlag, Berlin, 1992; Peachey, N.M. and Eckhardt, C.J., *Micron*, 25, 27, 1994; Jorgensen, J.F., Scanning Probe Microscopy, Ph.D. thesis, Danish Technical University, Lyngby, Denmark, 1993. b) Xu, J.B. et al., *Appl. Phys. A*, 59, 155, 1994.
17. Iri, T., Shiba, H., and Nishikawa, H., *Jpn. J. Appl. Phys.*, 31, 1441, 1992.
18. Wang, C. et al., *J. Phys. Chem.*, 99, 8216, 1995.
19. Meyer, E., *Prog. Surf. Sci.*, 41, 3, 1992.
20. a) Birdi, K.S. and Vu, D.T., *Langmuir*, 10, 623, 1994. b) Birdi, K.S. et al., *Surf. Coatings Technol.*, 67, 183, 1994; Johnson, R.P.C. and Gregory, D.W., *J. Microsc.*, 171, 125, 1993. c) Roberts, G.G., Ed., *Langmuir-Blodgett (LB) Films*, Plenum Press, New York, 1990; Kajiyama, T. et al., *Langmuir*, 10, 1297, 1994; Bordi, A.F. and Paradossi, G., *J. Phys. Chem.*, 99, 274, 1995. d) Schwartz, D.K., Viswanathan, R., and Zasadzinski, J.A.N., *J. Phys. Chem.*, 96, 10444, 1992.
21. Senden, T.J. and Ducker, W.A., *Langmuir*, 10, 1003, 1995.
22. Muramatsu, H. et al., *Near Field Optics-3*, EOS Topical Meeting, Vol. 8, Brno, Czech Republic, May 9-11, 1995; Egawa, A., *J. Microsc.*, 194, 325, 1999; Fischer, U.C., *J. Microsc.*, 202, 53, 2001.
23. Birdi, K.S., *Lipid and Biopolymer Monolayers at Liquid Interfaces*, Plenum Press, New York, 1989; Birdi, K.S., *Self-Assembly Monolayer (SAM) Structures*, Plenum Press, New York, 1999; Sparr, E. et al., *Langmuir*, 17, 164, 2001.
24. Hansma, H.G. et al., *Science*, 256, 1180, 1992; Murakami, M., *J. Biochem. Biophys. Methods*, 44(1), 31, 2000.
25. Allison, D.P. et al., *J. Vac. Sci. Technol. A*, 11, 616, 1993.
26. Findenegg, G.H., *J. Chem. Soc. Faraday Soc.*, 69, 1069, 1973.
27. Findenegg, G.H., *J. Chem. Soc. Faraday Soc.*, 68, 1799, 1972.
28. Groszek, A.J., *Proc. R. Soc. (London)*, a314, 473, 1970.
29. Yeo, Y.H., McGoigal, G.C., and Thomson, D.J., *Langmuir*, 9, 649, 1993.
30. Buchholz, S. and Rabe, J.P., *Angew. Chem. Int.*, 31, 189, 1992.
31. Yachoboski, K. et al., *Ultramicroscopy*, 42, 963, 1992.
32. Venkataraman, B., Breen, J.J., and Flynn, G.W., *J. Phys. Chem.*, 99, 6608, 1995; Venkataraman, B. et al., *J. Phys. Chem.*, 99, 8684, 1995.
33. Venkataraman, B. et al., *J. Phys. Chem.*, 99, 8684, 1995.
34. Kuznetsov, A.M., Sommer-Larsen, P., and Ulstrup, J., *Surf. Sci.*, 275, 52, 1992.
35. Brandow, S.L. et al., *Biophys. J. Biophys. Soc.*, 64, 898, 1993.
36. Yang, X.M. et al., *Appl. Phys. A*, 59, 139, 1994.
37. Li, Y.Z. et al., *Science*, 253, 429, 1991; Howells, S. et al., *Surf. Sci.*, 274, 141, 1992.
38. Birdi, K.S., *Fractals in Chemistry, Geochemistry and Biophysics*, Plenum Press, New York, 1994.
39. Anguiano, E., Pancorbo, M., and Aguilar, M.J., *Microscopy*, 172, 223, 1993.
40. Donnet, J.B. and Qin, R.Y., *Carbon*, 30, 787, 1992.
41. a) Pieczko, M.E. and Breen, J.J., *Langmuir*, 1412, 11, 1995. b) Luttrull, D.K. et al., *Langmuir*, 8, 765, 1992.
42. Stensgaard, I. et al., *Surf. Sci.*, 269, 81, 1992.
43. Lal, R. and John, S.A., *Am. J. Phys. Cell Phys.*, 266, C-1, 1994.
44. Arscott, P.G. et al., *Nature (London)*, 339, 484, 1989.
45. Balhorn, R., *Scanning Microsc.*, 5, 625, 1991.

46. Gibbons, A., *Science*, 253, 382, 1991.
47. Blackford, B.L., Jericho, M.H., and Mulhern, P.J., *Scanning Microsc.*, 5, 907, 1991.
48. Rees, W.A. et al., *Science*, 260, 1646, 1993.
49. Hansma, H.G., Sinsheimer, R.L., and Groppe, J., *Scanning Microsc.*, 15, 296, 1993.
50. Ohnische, S. et al., *Biophys. J.*, 65, 573, 1993.
51. Breen, J.J. and Flynn, G.W., *J. Phys. Chem.*, 96, 6825, 1992.
52. de-Grooth, B.G., and Putman, C.A., *J. Microsc.*, 168, 239, 1992.
53. Wilson, D.L. et al., *Langmuir*, 11, 265, 1995.
54. F. Leggett, G.J. et al., *Langmuir*, 9, 2356, 1993.
55. a) Kim, J.-J. et al., *Thin Solid Films*, 244, 700, 1994. b) Weisenhorn, A.L., Rohmer, D.U., and Lorenzi, G.P., *Langmuir*, 8, 3145, 1992; Li, L. et al., *Macromolecules*, 34, 316, 2001.
56. a) Eppell, S.J., Zypman, F.R., and Marchant, R.E., *Langmuir*, 9, 2281, 1993; Li, L. et al., *Macromolecules*, 34, 316, 2001. b) Vesenja, J., Miller, R., and Henderson, E., *Rev. Sci. Instrum.*, 65, 2249, 1994; Henderson, E., *Prog. Surf. Sci.*, 46, 39, 1994.
57. a) Mulhern, P.J. et al., *Scanning Tunneling Microscope-91. Conference, Ultramicroscopy*, 1992; Third International Conf. on AFM, Hamburg, July, 2000. b) Tang, S.L. and McGhie, A.J., *Langmuir*, 12, 1088, 1996.
58. Birdi, K.S. and Vu, D.T., submitted.
59. Wilschut, J. and Hoekstra, D., *Membrane Fusion*, Marcel Dekker, New York, 1991.
60. Andersen, K.B. and Skov, H., *J. Gen. Virol.*, 70, 1921, 1989.
61. Umemura, K., Arakawa, H., and Ikai, A., *J. Vac. Sci. Technol.*, B(12, 3), 1470, 1994.
62. Wilkins, M.J. et al., *J. Microsc.*, 172 (3), 215, 1993.
63. a) Sahesheff, K.M. et al., *Langmuir*, 11, 3921, 1995. b) Lewerenz, H.J. et al., *AIDS Res. Hum. Retroviruses*, 8, 1663, 1992. c) Birdi, K.S. and Vu, D.T, submitted.
64. van Holde, K.E., *Physical Biochemistry*, Prentice-Hall, Englewood Cliffs, NJ, 1990.
65. a) White, J.M., *Science*, 258, 917, 1992. b) Bachand, G.D. et al., *Nano Lett.*, 1, 42, 2001.
66. Littke, W., Haber, M., and Guntherodt, H.-J., *J. Cryst. Growth*, 122, 80, 1992.
67. Burrows, P.E. et al., *Appl. Phys. Lett.*, 61(20), 2417, 1992.
68. Eggleston, C.M. and Hochella, M.F., *Science*, 254, 983, 1991.
69. Dove, P.M. and Hochella, M.F., *Geochim. Cosmochim. Acta*, 57, 705, 1993.
70. a) Birdi, K.S. and Vu, D.T., *Probe Microsc.*, 1, 99, 1997. b) Tao, N.J. and Shi, Z., *J. Phys. Chem.*, 98, 1464, 1994.
71. Tanford, C., *The Hydrophobic Effect*, John Wiley & Sons, New York, 1980.
72. Chattoraj, D.K. and Birdi, K.S., *Adsorption and the Gibbs Surface Excess*, Plenum Press, New York, 1984.
73. a) Blake, C.C.F. et al., *Nature (London)*, 196, 1173, 1962. b) Ratcliff, G. and Erie, D., *J. Am. Chem. Soc.*, 123, 5632, 2001.
74. Nisman, R., Smith, P., and Vansco, J.G., *Langmuir*, 10, 1667, 1995.
75. a) Eng, L.M. et al., *Appl. Phys.*, A59, 145, 1994; Yoshimura, H., Ebina, S., and Nagayama, K., *Langmuir*, 11, 1711, 1995. b) Schonhen, H., Sneuvy, D., and Vansco, G.J., *Polym. Bull.*, 30, 567, 1993.
76. Henderson, E., *J. Microsc.*, 167, 77, 1992.
77. Thundat, T. et al., *J. Vac. Sci. Technol. A*, 10, 630, 1992.
78. Mosser, G. and Brisson, A., *J. Electron Microsc. Technol.*, 18, 387, 1991.
79. Bustamante, C.J. et al., *Biochemistry*, 31, 22, 1992.
80. Hansma, H.G. et al., *Nucleic Acids*, 20, 3585, 1992.
81. Vesenka, J. et al., *Ultramicroscopy*, 42, 1243, 1992.
82. Thundat, T. et al., *Scanning Microsc.*, 16, 903, 1992.
83. a) Wilson, D.L. et al., *Langmuir*, 11, 265, 1995. b) Birdi, K.S. and Vu, D.T., submitted.
84. Chahboun, A. et al., *J. Membr. Sci.*, 67, 295, 1992; Ton-That, C., Shard, A.G., and Bradley, R.H., *Langmuir*, 16, 2281, 2000.
85. Lacapere, J.-J., Stokes, D.L., and Chatenay, D., *Biophys. J.*, 63, 303, 1992.
86. Putman, C.A.J. et al., *Langmuir*, 8, 3014, 1992.
87. Song, J.P. et al., *Surf. Sci.*, 296, 299, 1993.
88. Oberleithner, H. et al., in *Seminars in Renal Physiology*, Lang, F., Ed., S. Karger, Basel, 1994.
89. Derjaguin, B.V. and Kusakov, M., *Acta Physicochim. U.R.S.S.*, 10, 25, 1939.

90. a) Israelachvili, J.N., *Intermolecular and Surface Forces*, Academic Press, London, 1985. b) Israelachvili, J.N. and Pashley, R.M., *Nature (London)*, 300, 341, 1982. c) Pashley, R.M. et al., *Science*, 229, 1088, 1985. d) Herder, P.C., *J. Colloid Interface Sci.*, 134, 336, 1990. e) Shubin, V.E. and Kekicheff, P., *J. Colloid Interface Sci.*, 155, 108, 1993; Meagher, L. and Pashley, R.M., *Langmuir*, 11, 4019, 1995; Parker, J.L. and Attard, P., *J. Phys. Chem.*, 96, 10398, 1992.
91. Xu, Z. and Yoon, R.-H., *J. Colloid Interface Sci.*, 1, 34, 427, 1990.
92. Butt, H.-J., *Biophys. J.*, 60, 1438, 1991; Butt, H.-J. and Guckenberger, R., *Ultramicroscopy*, 46, 375, 1992.
93. Ducker, W.A., Senden, T.J., and Pashley, R.M., *Langmuir*, 8, 1831, 1992.
94. Hoh, J.H. and Engel, A., *Langmuir*, 9, 3310, 1993.
95. Cleveland, J.P. et al., *Rev. Sci. Instrum.*, 64, 403, 1993.
96. Rabinovich, Y.A.I. and Yoon, R.-H., *Langmuir*, 10, 1903, 1994; Costa, C.A.R. et al., *Langmuir*, 17, 189, 2001.
97. Friedbacher, G., Prohaska, T., and Grasserbauer, M., *Mikrochim. Acta*, 113, 179, 1994.
98. Hough, D.B. and White, L.R., *Adv. Colloid Sci.*, 14, 3, 1980; Bargeman, D., and van Voorst Vader, F.J., *Electroanal. Chem. Interfacial Electrochem.*, 37, 45, 1972; Fowkes, F.W., *Ind. Eng. Chem.*, 56(12), 40, 1964.
99. Lin, X.-Y., Creuzet, F., and Arribart, H., *J. Phys. Chem.*, 97, 7272, 1993; Hugel, T. et al., *Macromolecules*, 34(4), 1039, 2001.
100. Fowkes, F.M., *J. Adhes. Sci. Technol.*, 1, 7, 1987.
101. Sprycha, K., *J. Colloid Interface Sci.*, 127, 1, 1989.
102. Bousse, L. et al., *J. Colloid Interface Sci.*, 147, 22, 1991.
103. a) Barrat, A. et al., *Europhys. Lett.*, 20(7), 633, 1992. b) Wigren, R., Design of SFM, Thesis, Linkoping University, Sweden, 1996.
104. a) Quate, C.F., in *Scanning Tunnelling Microscopy and Related Methods*, Rohrer, H., Behm, R.J., and Garcia, N., Eds., Kluwer, Dordrecht, 1990. b) Schimmel, T.H., Fuchs, H., and Lux-Steiner, M., *Phys. Status Solidi. A*, 131, 47, 1992.
105. McCarley, R.L., Hedricks, S.A., and Bard, A.J., *J. Phys. Chem.*, 96, 10089, 1992; Sugimura, H., and Nakagiri, N., *Langmuir*, 11, 3623, 1995.
106. Bruckner-Lea, C.J. et al., *Langmuir*, 9, 3612, 1993.
107. Thompson, D., *J. Microsc.*, 152, 627, 1988; Whitman, L.J. et al., *Science*, 251, 1206, 1991.
108. Eigler, D.M., Lutz, C.P., and Rudge, W.E., *Nature (London)*, 352, 600, 1991.
109. Tachibana, H. et al., *Appl. Phys. Lett.*, 61, 2420, 1992.
110. Gao, X. and Weaver, M.J., *J. Phys. Chem.*, 97, 8685, 1993.
111. van Hove, M.A. et al., *Adv. Quantum Chem.*, 20, 1, 1989.
112. Gao, X. and Weaver, M.J., *J. Phys. Chem.*, 97, 8685, 1993; Tao, N.J. and Lindsay, S.M., *J. Appl. Phys.*, 70, 5141, 1991.
113. Nejhoh, H., *Nature (London)*, 353, 640, 1991.
114. a) Fan, Fu-R., F., Bard, A.J., *Science*, 267, 871, 1995. b) Yang, R., Evans, D.F., and Hendrickson, W.A., *Langmuir*, 11, 211, 1995; Becker, R.S. and Tao, N.J., *Nature (London)*, 325, 419, 1987. c) Richard, K.M. and Gewirth, A.A., *J. Phys. Chem.*, 99, 12288, 1995.
115. a) Foster, J., Atomic imaging and positioning, in *Nanotechnology: Research and Perspectives*, Crandall and Lewis, Eds., MIT Press, Cambridge, MA, 1992, the First Foresight Conference on Nanotechnology, Palo Alto, October 1989; b) Overney, R.M., Meyer, E., and Frommer, J., *Nature (London)*, 359, 133, 1992; Drexler, K.E., *Nanosystems: Molecular Machinery, Manufacturing and Computation*, John Wiley & Sons, New York, 1992; James, P.J. et al., *Langmuir*, 17, 349, 2001; Frank, B.P. and Belfort, G., *Langmuir*, 2001. c) Eigler, D. and Schweizer, E.K., *Nature (London)*, 344, 524, 1990. d) Stroschio, J.A. and D.M. Eigler, *Science*, 254, 1319, 1991.
116. a) Nunes, G. and Freeman, M.R., *Science*, 262, 1029, 1993. b) Okita, S. and Miura, K., *Nano Lett.*, 1, 101, 2001; Skulason, H. and Frisbie, C.D., *Langmuir*, 16, 6294, 2000.
117. Goldsbury, C., *J. Struct. Biol.*, 131(3), 171, 2000.
118. Li, W., Chander, M., and Patrin, J.C., *J. Phys. Chem.*, 96, 6529, 1992.
119. Lyo, I.W. and Avouris, P., *Science*, 245, 1369, 1989; Bedrossian, P., Bloomfield, V.A., and Evans, D.F., *Nature (London)*, 342, 258, 1989.
120. Crommie, M.F., *Science*, 262, 218, 1993; Aono, M., *Science*, 258, 586, 1992.

16 Thermodynamics of Polymer Solutions

Georgios M. Kontogeorgis

CONTENTS

- 16.1 Introduction
- 16.2 Group-Contribution Methods for Estimating Properties of Pure Polymers
 - 16.2.1 Introduction to the Group-Contribution Principle
 - 16.2.2 Methods for Estimating the Density of Polymers
 - 16.2.2.1 The van Krevelen Method
 - 16.2.2.2 The GCVOL Method
 - 16.2.3 The Solubility Parameter of Polymers
 - 16.2.3.1 Definitions
 - 16.2.3.2 Methods for Estimating the Solubility Parameters
 - 16.2.3.3 Methods for Estimating the Hansen Solubility Parameters
- 16.3 Basic Concepts and Models in Polymer Thermodynamics
 - 16.3.1 Phase Equilibria Principles Applied to Polymers
 - 16.3.2 Thermodynamic Databases for Polymers
 - 16.3.3 Classical Models for Polymer Solutions
 - 16.3.3.1 The Solubility Parameter Method and the Hansen Plots
 - 16.3.3.1.1 Heat of Mixing and Solubility: Application to Nonpolar Systems
 - 16.3.3.1.2 The Hansen Plots: Extension to Polar and Hydrogen Bonding Systems
 - 16.3.3.2 The Flory–Huggins Model
 - 16.3.3.2.1 Selecting Solvents with the Flory-Huggins Model
 - 16.3.3.2.2 Other Rules of Thumb Based on the Flory-Huggins Model
 - 16.3.3.3 Summary of Rules of Thumb for Predicting Polymer–Solvent Miscibility
- 16.4 The Free-Volume Models
 - 16.4.1 The Free-Volume Concept
 - 16.4.2 Group-Contribution Free-Volume Activity Coefficient Models
 - 16.4.2.1 The UNIFAC-FV Model
 - 16.4.2.2 The Entropic-FV Model
 - 16.4.3 Results
 - 16.4.4 More Recent Approaches in the Free-Volume Term
- 16.5 Cubic Equations of State for Polymers
 - 16.5.1 General
 - 16.5.2 Cubic Equations of State

- 16.5.2.1 Cubic Equations of State for Pure Compounds
- 16.5.2.2 Extension of Cubic Equations of State to Mixtures
 - 16.5.2.2.1 Van der Waals One-Fluid and Related Mixing Rules
 - 16.5.2.2.2 EoS/ G^E Mixing Rules
- 16.5.2.3 Results and Discussion
- 16.6 The SAFT Equation of State
 - 16.6.1 Model Description
 - 16.6.2 Results and Discussion
- 16.7 Discussion of the Models
 - 16.7.1 Why So Many Models for Polymer Systems?
 - 16.7.2 Results for Athermal Polymer Solutions
 - 16.7.3 Results for Nonpolar and Slightly Polar Systems — Vapor Liquid Equilibria
 - 16.7.4 Results for Nonpolar and Slightly Polar Systems — Liquid–Liquid Equilibria
 - 16.7.5 Results for Water-Soluble Polymers and Other Hydrogen Bonding Systems
 - 16.7.6 Results for Polymer Blends
 - 16.7.7 Results for Copolymer Solutions
 - 16.7.8 Swelling — The Effects of Crystallinity and Cross-linking (Sorption, SLLE)
 - 16.7.9 Polymer–Mixed Solvent Systems
 - 16.7.10 Concluding Remarks and Future Challenges

List of Abbreviations

Acknowledgments

References

16.1 INTRODUCTION

Polymer thermodynamics plays an important role in a large number of processes and the design of many different products that are based on polymers. In these applications, knowledge of phase equilibria is crucial for systems involving polymer solutions and polymer blends. We mention here a few examples of such applications:

1. Many polymerizations and processes in polymer industry are conducted in solutions or emulsions, where the polymer is dissolved (or dispersed) in a liquid. Separation processes are required after the end of polymerization to removing unreacted monomers, colorants, by-products, toxic compounds, and other additives added during the production of the polymer.¹
2. In the paint/coatings industry, a polymer is in most cases dissolved in a solvent (or mixture of solvents), which devolatilize during the drying of the paint. In this case, finding the best solvent (mixture) is crucial to meet both property and health–environmental regulations, e.g., reducing the volatile organic compound (VOC) content and on developing water-based (organic-free) paints. Moreover, during the process of drying/curing, the solvents evaporate and the original single-phase system may exhibit phase separation. This can result in eventual failures of the paint systems, as has been observed, e.g., for ink formulations.² Knowledge of phase equilibria as a function of temperature, concentration, and possibly other factors (e.g., polymer molecular weight) is required for developing expert formulation systems. The calculation of evaporation rates requires the solvent activities in polymeric systems, as well.^{3,4} Finally, after the curing process

has been completed, the polymer is often cross-linked. Understanding of the swelling and sorption phenomena caused by water uptake and other external factors (gases, etc.) is important in the protection of the coatings.^{5,6} It is interesting to note that in many applications, such as those related to the ship-coating industry, inorganic polymeric materials are employed, e.g., tin-based antifouling paints.

3. Recent physicochemical methods for recycling polymer waste are based on a technique called *selective dissolution*.⁷ According to this method, the mixture of polymers is first dissolved in a suitable solvent (often different for each polymer) and then the polymers are recovered with the use of a proper antisolvent. Knowledge of ternary polymer–solvent–antisolvent liquid–liquid equilibria can facilitate the design of this process.⁸
4. The compatibility of polymer blends has been a subject of much interest. Polymer blends are systems with two (or more) polymers, most of which are incompatible (immiscible). Finding “compatible” polymer pairs is an important task in the design of such advanced materials.⁹ Moreover, several new polymeric materials with interesting properties involve novel structures, which go beyond the well-known ones (linear, branched, cross-linked, and network). Such novel structures, e.g., starlike polymer and dendrimers may require new concepts for selecting proper solvents and generally for understanding their solubility behavior.^{10,11}
5. Flexible polymeric pipes are often used toady, e.g., from the North Sea and other major oil- and gas-producing areas for the transporting of hydrocarbons on the seabed and from the seabed to the surface. A fundamental requirement concerning the design of flexible high-pressure pipes is the maintenance of their structural integrity during the specified lifetime to minimize the risk of pollution or uncontrolled discharge of combustible, explosive, and/or toxic fluids. Therefore, efficient design of such offshore flexible pipes requires knowledge of the solubility, diffusion, and permeability of gases in these solid polymers at the high temperatures and pressures involved under typical field conditions.¹² The area of gas solubilities in both molten and solid polymers has received increased interest over the last years, as can be seen by both the many theoretical works presented and the large number of experimental data collected.¹³ Both conventional and new exciting applications are reported, where gas/polymer phase equilibria is of relevance. Of the classical applications, we can mention the production of polyethylene, which is performed at high pressures and where the solubility of the ethylene in polyethylene is required for the design.¹ Moreover, from a less conventional point of view, the use of CO₂ as a user-friendly solvent has found widespread use for many polymer-related applications including those involving paints and coatings, as described in both the open and the patent literature.^{14–16}
6. Colloidal dispersions and other related systems are present in many applications, e.g., in paints and coatings and detergents. Here, phase equilibrium and surface phenomena are equally important. A unified representation of such phenomena, e.g., of adhesion phenomena and liquid–liquid equilibria with the same model/concepts is of interest. Thermodynamic models can be used to calculate certain surface properties such as surface tension.² In addition, properties such as the solubility parameters can be equally well employed for bulk and surface thermodynamic properties.¹⁷
7. A very important phenomenon, of interest to both the polyvinyl chloride (PVC) industry and the paints/coatings industry, is the migration (with time or during drying/curing of coatings) of plasticizers (and other similar substances such as curing agents) from polymers (coatings). The plasticizers are compounds such as phthalates, benzoates, etc., which decrease the glass transition temperature of the polymer, thus making it useful for practical applications. It has been shown, however, that with time they tend to migrate to the surface of the material.¹⁸ There may be several explanations for the migration

phenomenon. Thermodynamics may be of relevance in this discussion. One of the key requirements for the plasticizers is that they are completely miscible with PVC (or the other polymers that are inserted). However, several investigations¹⁹⁻²¹ have raised doubts about this “complete miscibility,” especially at higher temperatures and plasticizer content. The problem has not been as yet resolved and understood and this is an area of apparent social significance, where polymer thermodynamics can be of assistance.

8. In applications related to biotechnology, polymeric materials appear very often. A common example is the use of the so-called aqueous two-phase systems for the separation of proteins and other biomolecules.^{1,22,23} These systems comprise water and two water-soluble polymers such as polyethylene glycol and dextran and form two liquid phases in which the biomolecules are distributed. Salts may be also added. In this case, knowledge of the liquid–liquid equilibria of a very complex system comprising one or two polymers, water, salt, and biomolecules is required for design of this extraction technique.

The above represent only a very small sample of applications, based on our own experience and contacts with industry in Denmark. Many more applications exist.

This chapter presents the basics of polymer thermodynamics and some important thermodynamic models, which can be useful for the design/understanding of the processes and the products discussed above and many others.

Section 16.2 will discuss the concept and importance of the group-contribution (GC) approach in estimating two polymer properties, which are relevant for polymer solutions and blends: the density and the solubility parameter. The GC technique is employed in several of the thermodynamic models discussed later in the chapter.

Section 16.3 reviews the basics of polymer thermodynamics, discusses the differences compared to thermodynamics of systems having only low-molecular-weight compounds, and finally gives an overview of the Flory–Huggins model, which has been considered one of the cornerstones of polymer thermodynamics.

Sections 16.4 through 16.6 discuss three types of “advanced” thermodynamic models, each of which has its merits and limitations. These (and other) approaches are compared in Section 16.7 for a large number of real-life applications. We have not attempted to include in our discussion all possible models and theories that can be potentially used for polymers. We feel that this would have been impossible considering the space limitations of a single chapter and confusing as well. Several models — mostly other than the ones considered here — have been recently reviewed elsewhere.¹ We have selected three promising approaches:

1. The free-volume activity coefficient models (Section 16.4)
2. The cubic equations of state (Section 16.5)
3. The Statistical Associating Fluid Theory (SAFT) (Section 16.6)

These three approaches have found widespread application to a large variety of systems and equilibria types ranging from vapor–liquid equilibria for binary and multicomponent polymer solutions, blends, and copolymers, liquid–liquid equilibria for polymer solutions and blends, solid–liquid–liquid equilibria, and solubility of gases in polymers, to mention only a few. In some cases, the results are purely predictive; in others interaction parameters are required and the models are capable of correlating (describing) the experimental information. In Section 16.7, we attempt to summarize and comparatively discuss the performance of these three approaches. We attempt there, for reasons of completion, to discuss the performance of a few other (mostly) predictive models such as the group-contribution lattice fluid²⁴ and the group-contribution Flory²⁵ equations of state, which are not extensively discussed separately.

16.2 GROUP-CONTRIBUTION METHODS FOR ESTIMATING PROPERTIES OF PURE POLYMERS

16.2.1 INTRODUCTION TO THE GROUP-CONTRIBUTION PRINCIPLE

Many properties of pure polymers (and of polymer solutions) can be estimated with group contributions (GC). Examples of properties for which (GC) methods have been developed are the density, the solubility parameter, the melting and glass transition temperatures, as well as the surface tension. Phase equilibria for polymer solutions and blends can also be estimated with GC methods, as we discuss in Section 16.4 and 16.5. Here we review the GC principle, and in the following sections we discuss estimation methods for the density and the solubility parameter. These two properties are relevant for many thermodynamic models used for polymers, e.g., the Hansen and Flory–Huggins models discussed in Section 16.3 and the free-volume activity coefficient models discussed in Section 16.4.

The GC method is based on the assumption that the properties of molecules can be estimated using “additive rules” from the values of the corresponding groups of which they are composed. For example, *n*-hexane (CH₃–(CH₂)₄–CH₃) can be considered to have two CH₃ and four CH₂ groups. Similarly, butanone has one CH₃, one CH₂, and one CH₃CO group. If the group values are known for a specific property *F*, then the total value of the property for the whole molecule is often expressed by a general additive rule of the form:

$$F = \sum_i n_i F_i \quad (16.1)$$

or similar additive equations.

In Equation 16.1 n_i is the number of groups of type *i* and F_i is the corresponding group value. In some cases, F_i values are also a function of temperature for temperature-dependent properties such as the volume and the vapor pressure. For several properties, the general GC equation has a more complicated form than that indicated by Equation 16.1.

The GC methodology has been applied to many properties and for both low-molecular-weight compounds and polymers. Several mixture properties, such as activity coefficients, have also been predicted with group contributions, e.g., the UNIFAC model by Fredenslund et al.^{26,27} In his excellent book, van Krevelen²⁸ gives an overview of the application of group contribution methods to several properties of pure polymers, including also mechanical and other properties.

The great advantage of the group-contribution method is its simplicity: although there may be many thousands of different molecules (and mixtures), the corresponding number of groups is significantly smaller (no more than 100 or so). Thus, instead of knowing the parameter values of a specific property for thousands of molecules, it suffices to know the group parameters for a much smaller number of groups. Two remarks, which may in some cases be considered as limitations, should be kept in mind:

1. The GC methodology is a very useful technique leading to good results in many cases. However, it is an approximation, based often on a bit unjustified distinction of the molecule into groups. For some properties, such as for density, GC methods perform much better than for others, e.g., melting point. Specific molecules are assigned as separate groups (e.g., methanol) because further distinction is not possible, if good results are to be obtained. Problems can also be expected for multifunctional groups and where more than one polar groups are close to each other (e.g., in alcohols and acids with more than one OH and COOH groups or for hydroxy acids). However, despite these problems,

the GC principle is often used for property calculations for specific molecules and also, in the reverse way, for selecting suitable compounds having a required set of properties. The latter technique is called computer-aided product design.^{29,30}

2. The exact definition of groups may change from method to method. In some cases, even two different methods for the same property can have different definitions for the groups. In other cases, and for the same GC method, a particular molecule can be divided into groups in two different ways that may yield different results. These points are discussed further later in this chapter.

16.2.2 METHODS FOR ESTIMATING THE DENSITY OF POLYMERS

Experimental density data are now available for many polymers.^{31,32} However, the number of polymers (and copolymers) of interest is much greater than the number of those for which data are available. For some of those polymers, the density can be estimated via one of the GC methods discussed below.

16.2.2.1 The van Krevelen Method

van Krevelen²⁸ suggested the following equations for estimating the volume of polymers using group contributions and based on their physical state (amorphous, glassy, crystalline):

1. For amorphous polymers:

$$V_a = V_w(1.30 + 10^{-3}T) \quad (16.2)$$

2. For glassy polymers:

$$V_g = V_w(1.30 + 0.5510^{-3}T_g + 0.4510^{-3}T) \quad (16.3)$$

3. For completely crystalline polymers:

$$V_c = V_w(1.30 + 0.4510^{-3}T) \quad (16.4)$$

In Equations 16.2 through 16.4, T is the temperature in K, T_g is the glass transition temperature in K, and V_w is the van der Waals volume of the molecule.

The van der Waals volume, originally introduced by Bondi, is defined as the actual volume of the molecule and can be easily estimated using GCs via Equation 16.1 (where $F = V_w$) and the parameter tables available in many references.^{26,27,33} In these tables, which has been originally developed for the UNIFAC model for activity coefficients, the van der Waals volume is given in terms of a dimensionless parameter R_k . The group van der Waals volumes can be estimated from the R_k values as follows:

$$V_w = R_k \times 15.17 V_w \quad \text{in cm}^3/\text{gmol} \quad (16.5)$$

16.2.2.2 The GCVOL Method

The group-contribution volume (GCVOL) method has been proposed by Elbro et al.³⁴ and has the advantage, over the van Krevelen method, that it can be used (with the same parameter table) for low-molecular-weight compounds (“solvents”), for oligomers, and for polymers. The method is based on GCs according to the equations:

$$V = \sum_i n_i V_i \quad (16.6)$$

$$V_i = A_i + B_i T + C_i T^2 \quad (16.7)$$

Later, Tsimbanogiannis et al.³⁵ extended the GCVOL method to cover some additional groups (COOH, COH) and corrections for cyclo-compounds and allenes. The A_i , B_i , and C_i group parameters from both publications are collected in [Table 16.1](#).

The group parameter table of GCVOL covers fewer groups compared to the van Krevelen method (the latter covers most existing groups). Thus, the van Krevelen method can be applied to a much wider range of groups compared to GCVOL. The GCVOL method is under continuous development and improvement, and more groups may appear in the future.

More recently, Constantinou et al.³⁶ developed an alternative GC method for the density of polymers (restricted to 25°C). An important feature of the works by Elbro et al.³⁴ and Constantinou et al.,³⁶ over that of van Krevelen,²⁸ is that these authors showed that the same consistent GC method can be applied to the prediction of density for low-molecular-weight compounds (solvents), oligomers, and polymers.

The performance of the GCVOL method is quite satisfactory, with a typical deviation around 2%, often better than the older GC method proposed by Fedors.³⁷ Very good results are also obtained for the density of copolymers, as shown by Bogdanic and Fredenslund.³⁸ A comparison with the van Krevelen method for a number of polymers is shown in [Table 16.2](#). These results obtained from recent publications^{39,40} illustrate the importance of choosing different group definitions for the same polymer.

The van Krevelen method should be used in those cases where the deviation with GCVOL is over 6% (polyisobutylene, polyvinyl propionate) and for those polymers for which the GCVOL group parameters are not available. The density of polymers is important in many calculations. Several of the free-volume activity coefficient models discussed in Section 16.4 require the densities of polymers (and solvents) as input. We will see then that certain models are quite sensitive to the values of the densities employed. Moreover, polymer density data are often employed in equations of polymers for obtaining the pure polymer parameters.

16.2.3 THE SOLUBILITY PARAMETER OF POLYMERS

16.2.3.1 Definitions

The solubility parameter is a very important property in science and has found widespread use in many fields and not just in the study of polymer–solvent thermodynamics. It is connected to the Flory–Huggins model as well, as explained in Section 16.3.3.2, but can also be used independent of it, as discussed in Sections 16.3.3.1 and 16.3.3.3. Several handbooks and reference books provide extensive lists of solubility parameters of numerous chemicals.^{17,41–43} The solubility parameter is defined as

$$\delta = \sqrt{\frac{\Delta E^{\text{vap}}}{V}} \quad (16.8)$$

where V is the liquid molar volume and ΔE^{vap} is the internal energy of vaporization, which is equal to the heat of vaporization minus RT (the product of gas constant and temperature). This quantity has been traditionally named the cohesive energy. The solubility parameter is universally denoted with the symbol δ from the first letter of the Greek word $\delta\iota\alpha\lambda\upsilon\tau\omicron\tau\eta\tau\alpha$ (pronounced: dialitotita) which means solubility. The solubility parameters of solvents can be measured by direct experimental

TABLE 16.1
Group Parameter Values for the GCVOL Method of Estimating the Density of Polymers, Solvents, and Oligomers (Equation 16.7)

Group	A (cm ³ /mol)	10 ³ B (cm ³ /mol K)	10 ⁵ C (cm ³ /mol K ²)	Ref.
CH ₃	18.960	45.58	0	34
CH ₂	12.520	12.94	0	34
CH	6.297	-21.92	0	34
C	1.296	-59.66	0	34
ACH	10.090	17.37	0	34
ACCH ₃	23.580	24.43	0	34
ACCH ₂	18.160	-8.589	0	34
ACCH	8.295	-31.86	0	34
ACC	7.369	-83.60	0	34
AC	3.65	-15.27	0	111
CH ₂ =	20.630	31.43	0	34
CH=	6.761	23.97	0	34
C=	-0.3971	-14.10	0	34
Correction for allenes =C=	14.1610	-58.082	16.86	35
Correction for cyclopentanes	19.8947	-103.645	30.38	35
Correction for cyclohexanes	21.9038	-105.403	25.07	35
C≡CH	27.8327	-28.813	18.49	35
CH ₂ OH	39.460	-110.60	23.31	34
CHOH	40.920	-193.20	32.21	34
COH	37.8699	-287.098	48.97	35
ACOH	41.200	-164.20	22.78	34
COOH	40.0107	-94.367	18.33	35
CH ₃ CO	42.180	-67.17	22.58	34
CH ₂ CO	48.560	-170.40	32.15	34
CHCO	25.170	-185.60	28.59	34
CHO	12.090	45.25	0	34
CH ₃ COO	42.820	-20.50	16.42	34
CH ₂ COO	49.730	-154.10	33.19	34
CHCOO	43.280	-168.70	33.25	34
COO	14.230	11.93	0	34
ACCOO	43.060	-147.20	20.93	34
CH ₃ O	16.660	74.31	0	34
CH ₂ O	14.410	28.54	0	34
CHO	35.070	-199.70	40.93	34
CO	30.120	-247.30	40.69	34
CH ₂ Cl	25.290	49.11	0	34
CHCl	17.400	27.24	0	34
CCl	37.620	-179.10	32.47	34
CHCl ₂	36.450	54.31	0	34
CCl ₃	48.740	65.53	0	34
ACCl	23.510	9.303	0	34
Si	86.710	-555.5	97.90	34
SiO	17.410	-22.18	0	34

TABLE 16.2
Comparison of the Performance of the GCVOL and
van Krevelen Methods in Predicting the Densities
for Several Polymers

Polymer	T Range (K)	GCVOL	van Krevelen
Poly(ethylene oxide)	360–490	3.6	3.1
Poly(ϵ -caprolactone)	373–421	1.2	0.6
Poly(vinyl acetate)	308–373	4.9	1.1
Poly(methyl acrylate) ^a	310–493	11.8	3.0
Poly(methyl acrylate) ^b	310–493	5.7	3.0
Poly(ethyl acrylate) ^a	310–493	6.7	0.8
Poly(ethyl acrylate) ^b	310–493	7.3	0.8
Poly(methyl methacrylate)	387–432	1.2	9.0
Poly(ethyl methacrylate)	386–434	1.8	4.2
Poly(butyl methacrylate)	307–473	2.0	2.2
Average		3.5	3.0

Note: The numbers shown are the mean percentage deviations between experimental (from the Tait equation) and predicted volumes over the temperature range shown.

^a The subgroup CHCOO is used in GCVOL.

^b The subgroups CH and COO are used in GCVOL.

Source: Lindvig, Th., et al., *Fluid Phase Equilibria*, 663, 194–197, 2002. With permission.

measurements using this definition (Equation 16.8). However, polymers are not volatile and they degrade long before reaching their vaporization temperatures. Their solubility parameters are experimentally assessed via various indirect methods (especially swelling and viscometric studies). This often results in different values of the solubility parameters of polymers, as shown in Table 16.3. van Krevelen²⁸ lists a range of values of solubility parameters for each polymer, indicating that the lower limit is usually the most reliable.

Traditionally, solubility parameters are given in $(\text{cal}/\text{cm}^3)^{1/2} = \text{Hildebrand}$, in honor of the founder of the regular solution theory, Joel Hildebrand. Now, they are more commonly listed in $(\text{MPa})^{1/2} (= 1 (\text{J}/\text{cm}^3)^{1/2})$. The solubility parameters were originally defined in conjunction with the regular solution theory, as discussed in Section 16.3.3.1.

16.2.3.2 Methods for Estimating the Solubility Parameters

In the absence of experimental data, the solubility parameters of both solvents and polymers can be estimated via GC methods. Two of the most widely used methods are those by Hoftyser–van Krevelen and by Small, both cited and discussed by van Krevelen.²⁸ The two methods are similar but are based on somewhat different assumptions.

1. *The Hoftyser–van Krevelen method:* These researchers proposed group values for the cohesive energy, i.e., for the ratio $\Delta E^{\text{vap}}/V$. The total cohesive energy is estimated from the group values via Equation 16.1. Then the solubility parameter is estimated from the definition, Equation 16.8.
2. *The Small method:* Small proposed an additive method for the so-called *molar attraction constant F*:

TABLE 16.3
Solubility Parameters of Some Polymers from Different Sources

Polymer	δ_d	δ_p	δ_h	δ (total value)	Ref.
Poly(butyl methacrylate)	15.9	5.5	5.9	17.8	17
	18.0	8.4	3.1	20.1	200
	17.7	5.8	4.0	19.1	200
	17.7	1.2	6.2	18.8	201
Poly(ethyl methacrylate)	16.5	8.7	5.0	19.3	17
	17.6	9.6	2.5	20.2	67
	18.1	6.0	3.3	19.4	200
	17.5	1.3	7.1	18.9	201
Poly(methyl acrylate)	17.1	1.5	8.4	19.1	201
Poly(methyl methacrylate)	18.6	10.5	7.5	22.6	17
	19.1	6.5	3.9	20.5	200
	15.6	10.5	5.2	19.5	202
Poly(vinyl acetate)	17.6	2.2	4.0	18.2	17
	20.9	11.3	9.6	25.6	67
	17.6	8.0	6.6	20.4	203
	15.7	11.4	7.8	20.9	202

$$F_i = \sqrt{E_{\text{coh},i} V_i} \quad (16.9)$$

Small considered that the F quantity of Equation 16.9 shows better “additive” characteristics than the cohesive energy. The total molar attraction constant is calculated from Equation 16.1 and the solubility parameter is calculated from the equation:

$$\delta = \frac{F}{V} \quad (16.10)$$

Comments:

- Both methods are approximately equally accurate (within 10% in most cases).
- Fedors^{28,37} had proposed a less accurate method, which, however, has the advantage of having a very extensive group parameter table. It can be therefore employed in those cases where the two other methods cannot be applied due to lack of parameters.
- An indirect method to estimate the solubility parameter is via a predictive equation of state model⁴⁴ suitable for polymers.

16.2.3.3 Methods for Estimating the Hansen Solubility Parameters

The Danish scientist Charles Hansen proposed an extension of the solubility parameter concept, which is particularly suitable for solubility assessments for strongly polar and hydrogen bonding fluids. He identified three contributions to the cohesive energy and thus to the solubility parameter, one stemming from nonpolar (dispersion or van der Waals forces, d), one from (permanent) polar (p), and one from hydrogen bonding forces (h). He suggested that these three effects contribute additively to the cohesive energy density (i.e., the ratio of the cohesive energy to the volume):

$$E_{coh} = E_d + E_p + E_h \quad (16.11)$$

Therefore, using Equation 16.11, the total solubility parameter is estimated from the equation:

$$\delta = \sqrt{\delta_d^2 + \delta_p^2 + \delta_h^2} \quad (16.12)$$

Thus, the solubility parameter may be thought of as a vector in a three-dimensional d - p - h space. The above equation provides the magnitude of this vector. Each solvent and each polymer can be characterized by the three “solubility parameter increments” $\delta_d, \delta_p, \delta_h$.

Hansen has presented extensive tables with the solubility parameter increments (d, p, h). In his recent book,¹⁷ he has collected an extensive compilation of such values. van Krevelen²⁸ proposed GC methods for all three increments according to the equations:

$$\begin{aligned} \delta_d &= \frac{\sum_i F_{di}}{V} \\ \delta_p &= \sqrt{\frac{\sum_i F_{pi}^2}{V}} \\ \delta_h &= \sqrt{\frac{\sum_i E_{hi}}{V}} \end{aligned} \quad (16.13)$$

Due to the uncertainty in the way Hansen parameters are estimated, different values have been proposed for polymers, as shown in Table 16.3. The way the Hansen method is used for solubility calculations is given in Section 16.3.3.1.

16.3 BASIC CONCEPTS AND MODELS IN POLYMER THERMODYNAMICS

16.3.1 PHASE EQUILIBRIA PRINCIPLES APPLIED TO POLYMERS

Many industrial separation processes are based on phase equilibria. By this we mean that the various components of the mixtures present in the (vapor, liquid, solid) phases are in equilibrium. This is a dynamic equilibrium and equal numbers of components are being transferred continuously from one phase to the other; thus the concentrations at equilibrium do not change. To design the separation processes in industry, e.g., finding the height and number of trays of a distillation column, we need to know the concentrations at equilibrium at any temperature and pressure.

In theory, the problem was solved more than 100 years ago by Gibbs who found that at equilibrium, a property termed *fugacity* is, for each component, equal at all phases (for example, here denoted as a and b):

$$f_i^a = f_i^b \quad i = 1, 2, \dots, N \quad (16.14)$$

Equation 16.14 (or the equivalent with chemical potentials) is the starting point in phase equilibria calculations.

The most important type of phase equilibrium in (nonpolymer related) industry is, for many applications, the vapor–liquid equilibria (VLE). For the polymer industry, liquid–liquid, and liquid–solid equilibria are equally important.

Equation 16.14 can be equivalently written for VLE in terms of the fugacity coefficients (Φ_i):

$$y_i \Phi_i^V = x_i \Phi_i^L \quad i = 1, 2, \dots, N \quad (16.15)$$

where y is the vapor phase mole fraction and x is the liquid phase mole fraction. The phase equilibrium (Equations 16.14 or 16.15) is applied to all components in the mixture.

These fugacities or fugacity coefficients are functions of pressure (P), temperature (T), volume (V) and composition (x_i or y_i):

$$RT \ln \frac{f_i}{x_i P} = \int_V^\infty \left(\frac{\partial P}{\partial n_i} \Big|_{T, V, n_j} - \frac{RT}{V} \right) dV - RT \ln \frac{PV}{RT} \quad (16.16)$$

n_i is the number of moles of component i and R is the ideal gas constant. Equation 16.16 is general. No assumptions whatsoever are involved. This general equation follows from the mathematical analysis of phase equilibria by Gibbs. It is valid at any condition (temperature, pressure, and concentration) and can be solved provided that a suitable mathematical function of pressure–volume–temperature and concentration is known for every fluid and every mixture of fluids:

$$P = P(V, T, x, y) \quad (16.17)$$

This mathematical function, Equation 16.17, is called an equation of state (EoS).

Thus, the phase equilibrium problem can be solved and proper design of separation processes in industry can be accomplished if suitable functions of the type of Equation 16.17 are available; that is, if suitable “equations of state” are available. This provides the definition of the problem: to find general equations of state that can be applied for many different types of fluid and fluid mixtures including polymer solutions and blends and over broad condition spectra (temperatures, pressure, and concentrations). Finding a suitable equation of state is an ongoing problem in applied thermodynamics, a problem whose solution has been sought for the last 100 years by physicists, chemists, mathematicians, and chemical engineers working closely together. Many reviews on equations of state have been published, the most recent one by Wei and Sadus.⁴⁵

From the 19th century until our times, we see an endless number of efforts to develop suitable functions of the type of Equation 16.17. This quest is almost unlimited and has resulted in a enormous number of potential equations of state. Many equations of state are included in the commercial simulators and some can also be applied to polymers. Some of these will be discussed in Sections 16.5 and 16.6.

Despite the generality of phase equilibrium Equations 16.14 through 16.16, satisfactory results and thus proper design of industrial processes depend very much on whether an appropriate equation of state is available as well as accurate methods for determining its parameters. The description of the vapor phase poses many fewer problems than the liquid (and solid) phases. Several equations of state are very accurate for the vapor phase but occasionally not so for the liquid phase, especially for complex fluid mixtures. It would thus be interesting to describe the two phases with different concepts (models). This has led to the so-called γ - Φ approach. According to this approach, for vapor–liquid phase equilibria Equation 16.15 can be approximated at low pressures:¹

$$y_i \Phi_i^V P = x_i \gamma_i P_i^{\text{sat}} \quad (16.18)$$

where P_i^{sat} is the vapor pressure of pure component i . In Equation 16.18, the liquid phase fugacity is described through a parameter, which is called an activity coefficient and is universally denoted with the Greek letter γ . This is a correction for nonideality compared to Raoult's law of ideal solutions:

$$P = x_i P_i^{\text{sat}} \quad (16.19)$$

Solutions with compounds having similar sizes, shapes, and intermolecular forces form ideal solutions, e.g., hexane/heptane, heptanol/hexanol. In these cases the activity coefficient is (close to) unity. For most solutions that do not include polymers, however, the activity coefficient differs significantly from unity and it is usually higher than one, but it can be also lower than one in some specific cases when strong hydrogen bonding or other association effects are present, e.g., chloroform–acetone.

The γ - Φ approach is applicable only at low pressures. Like equations of state, activity coefficient models are also mathematical functions, however, of only temperature and concentration. Because in many applications related to polymer solutions, e.g., in paints and coatings industry, low pressures are involved, Equation 16.18 is a useful approximation. If, furthermore, it is assumed that the vapor phase, which typically contains only the volatile components (solvents), is ideal, then Equation 16.18 can be further simplified:

$$y_i P = x_i \gamma_i P_i^{\text{sat}} \quad (16.20)$$

The key property of Equation 16.20 is γ_i , the *activity coefficient*, which represents the deviation of the solution from the ideal state (Raoult's law, where $\gamma_i = 1$). Polymer solutions are highly nonideal systems and in most cases the activity coefficients have values much lower than unity. This implies that negative deviations from Raoult's law are observed as, for example, is shown in [Figure 16.1](#); the pressure of the solution is lower than the one calculated by Raoult's law. This characteristic highly nonideal behavior of polymer solutions distinguishes them from “normal” solutions, which typically exhibit positive deviations. However, and even in the absence of strong energetic interactions, for the polymeric solutions large negative deviations are observed. This is a demonstration that entropic effects, which in many cases can be ignored for nonpolymeric solutions, are dominant for polymer solutions.

For binary solvent–polymer systems, and since the vapor phase can be considered to contain pure solvent (the polymer is nonvolatile), Equation 16.20 can be simplified to give the following expression for the equilibrium pressure of the solution:

$$P = x_1 \gamma_1 P_1^{\text{sat}} \quad (16.21)$$

The molar activity coefficient γ_i , shown in Equations 16.20 and 16.21, is not always a suitable quantity in polymer thermodynamics. Molar activity coefficients can reach very low values, especially at very high polymer molecular weights. More convenient is the weight fraction activity coefficient (Ω_1), which is the ratio of the activity to the weight fraction:

$$\Omega_1 = \frac{\alpha_1}{w_1} = \frac{x_1 \gamma_1}{w_1} \quad (16.22)$$

or the volume fraction activity coefficient based on volume fractions (ϕ_i):

$$\Gamma_1 = \frac{\alpha_1}{\phi_1} \quad (16.23)$$

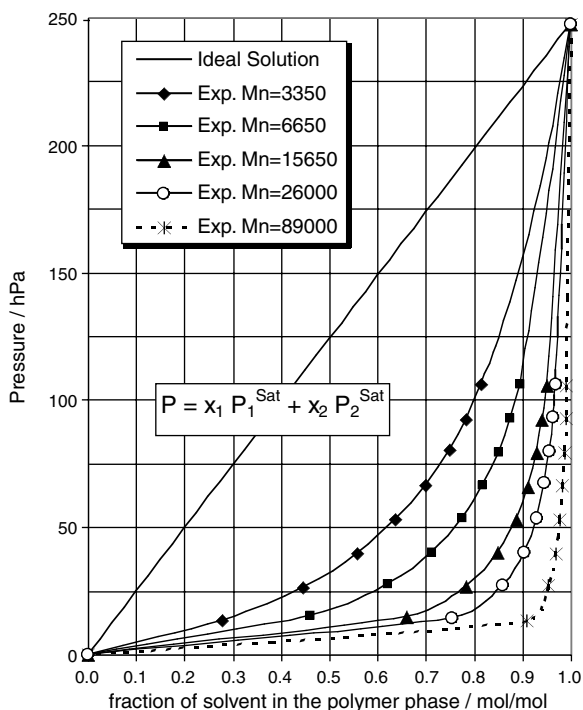


FIGURE 16.1 Polymer solutions exhibit negative deviations from Raoult's law; demonstration for the system *n*-hexane/polydimethylsiloxane at various polymer molecular weights. (From Dohrn, R. and Pfohl, O., *Fluid Phase Equilibria*, 15, 194–197, 2002. With permission.)

Because in several practical cases concerning polymer–solvent systems, the “solvent” is only present in very small (trace) amounts, the so-called infinite dilution activity coefficients are important. On a molar and weight basis, they are defined as follows:

$$\begin{aligned} \gamma_i^\infty &= \lim_{x_i \rightarrow 0} \gamma_i \\ \Omega_i^\infty &= \lim_{w_i \rightarrow 0} \Omega_i \left(\frac{x_i \gamma_i}{w_i} \right) \end{aligned} \quad (16.24)$$

The weight-based infinite dilution activity coefficient Ω_1^∞ , which can be determined experimentally, is also a very useful quantity for selecting good solvents. Low values (typically below 6) indicate good solvents, whereas high values (typically above 10) indicate poor solvents according to rules of thumb discussed by several investigators.^{5,46,47} This method for solvent selection is particularly useful for the following reasons:

- It avoids the need for direct liquid–liquid measurements.
- The existing database of solvent infinite dilution activity coefficients is quite large, using the convenient gas chromatographic technique. These data are stored in two databases, which are also available in computerized form from DECHEMA and DIPPR.^{31,48}
- In the absence of experimental data, existing thermodynamic models (such as the Flory–Huggins, the Entropic-FV, and the UNIFAC-FV discussed later) can be used to predict the infinite dilution activity coefficient.

TABLE 16.4
Choice of Suitable Solvents Using the Ω_1^∞ -Rules
of Thumb for PBMA Systems

Solvent	s/ns	E-FV	U-FV	GC-FI
Hexane	ns	7.1	7.0	10.7 ^a
<i>n</i> -Octane	ns	6.7	6.3	10.4 ^a
<i>n</i> -Decane	ns	6.5	6.0	10.7 ^a
<i>n</i> -Dodecane	ns	6.6	6.0	11.3 ^a
<i>n</i> -Hexadecane	ns	6.8	6.1	13.2 ^a
Toluene	s	3.2 ^a	4.4 ^a	4.7 ^a
Xylene	s	2.3 ^a	3.6 ^a	5.7 ^a
Methylene dichloride	s	3.3 ^a	2.5 ^a	3.0 ^a
Chloroform	s	1.9 ^a	2.1 ^a	1.7 ^a
Carbon tetrachloride	s	2.2 ^a	2.2 ^a	2.9 ^a
Ethylene dichloride	s	3.5 ^a	3.0 ^a	—
Trichloroethylene	s	2.5 ^a	2.9 ^a	33.9
Chlorobenzene	s	2.5 ^a	3.0 ^a	3.0 ^a
<i>O</i> -Dichlorobenzene	s	1.3 ^a	2.5 ^a	2.7 ^a
Acetone	s	10.9 ^b	14.2 ^b	11.1 ^b
MEK	s	8.4 ^b	10.5 ^b	8.2 ^b
MIBK	s	6.3	7.7	5.7 ^a
Acetophenone	s	8.1 ^b	9.3 ^b	8.6 ^b
Ethyl acetate	s	6.7	6.7	60.3
Butyl acetate	s	5.3 ^a	5.1 ^a	31.4
Diethyl ether	s	5.2 ^a	5.8 ^a	11.6 ^b
THF	s	3.8 ^a	4.0 ^a	—
1,4-Dioxane	s	4.1 ^a	4.4 ^a	159.4
Methanol	ns	43.7 ^a	57.7 ^a	35.7 ^a
Ethanol	ns	29.2 ^a	31.3 ^a	17.3 ^a
1-Butanol	ns	18.1 ^a	17.1 ^a	8.1 ^b
Cyclohexanol	ns	24.3 ^a	20.1 ^a	3.0
Ethylene glycol	ns	277.8 ^a	—	15947.0
Propylene glycol	ns	212.6 ^a	—	1879.2
1,3-Butanediol	ns	158.5 ^a	—	525.5
Glycerol	ns	294.6 ^a	—	2282.4
Isopropanol	ns	23.4 ^a	21.6 ^a	10.6 ^a
Isobutanol	s	19.0 ^b	17.9 ^b	7.9
Diethylene glycol	ns	240.1 ^a	—	2470.4
Dipropylene glycol	ns	127.9 ^a	945.7	287.8
Nitromethane	ns	16.7 ^a	17.2 ^a	—
1-Nitropropane	s	4.7 ^a	5.2 ^a	—
<i>N,N</i> -Dimethylformamide	s	3.8 ^a	—	—

Note: E-FV = Entropic-FV; U-FV = UNIFAC-FV; GC-FI = GC-Flory;
s = Solvent and ns = nonsolvent (experimental information).

^a Agreement with rule of thumb

^b Disagreement with rule of thumb

Source: Modified from Lindvig, Th. et al., *AIChE J.*, 47 2573, 2001.

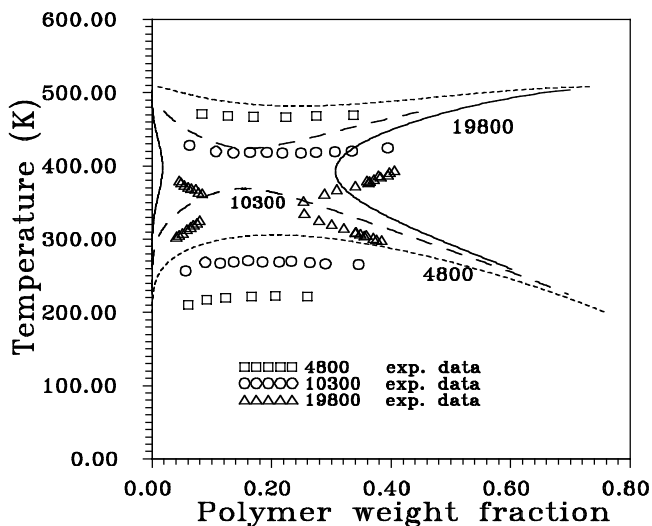


FIGURE 16.2 Experimental and predicted LLE diagram for the system polystyrene/acetone at three polymer molecular weights (4800, 10300, and 19800). The points are the experimental data and the lines are the predictions with the model Entropic-FV. (From Kontogeorgis, G.M. et al., *Ind. Eng. Chem. Res.*, 34, 1823, 1995. With permission.)

In the typical case today, existing models perform much better for VLE and activity coefficient calculations than directly for liquid–liquid equilibria (LLE) calculations. Table 16.4 shows an example of such model/computer-aided decisions in choosing proper solvents for poly(butyl methacrylate) (PBMA), a polymer employed in paints and coatings. The thermodynamic models UNIFAC-FV, Entropic-FV, and GC-Flory, which are described later, are used for obtaining the infinite dilution activity coefficient in this case. We can see that, with few exceptions, these models in combination with the rule of thumb mentioned above can identify suitable solvents for PBMA among a large list of chemicals. Elbro⁴⁶ showed that the above rule correctly predicted the solubility/nonsolubility tendency of a large number of organic compounds in two isomers of PBMA (polymers of interest to paints).

Liquid–Liquid Equilibria

For mixtures of low-molecular-weight compounds only, it can be stated that “mixing is the rule” and “the presence of two liquid phases is the exception.” The contrary typically occurs for polymer solutions, for which the presence of two liquid phases is evidenced very often. Figure 16.2 presents a classical example, the extensively studied acetone/polystyrene system at three different polymer molecular weights. The most important features of polymer–solvent LLE can be discussed based on this graph:

1. LLE strongly depends on the temperature and the molecular weight. Typically, two LLE areas are observed, one at low temperatures (UCST = upper critical solution temperature) and one at high temperatures (LCST = lower critical solution temperature). LCST is typically observed at temperatures between the boiling point and the critical temperature of the solvent.
2. As a general rule, the higher the polymer molecular weight, the less miscible are the polymer and the solvent, or in other words the greater the LLE region (the area shown below the curves).
3. A third type of phase diagram, such as the one shown for molecular weight equal to 19,800, is called hourglass type and has been observed for only a few systems. Most polymer solutions only exhibit the UCST and LCST behavior. As the temperature increases for UCST and as the temperature decreases for LCST, the difference between

two subsequent critical solution temperatures decreases. Thus, at very high molecular weights the UCST and LCST seem to converge to a single value, which is termed the *theta temperature*. Two theta temperatures (one corresponding to UCST and one to LCST) typically exist and are rigorously defined as:

$$\begin{aligned}\Theta_U &= \lim_{M \rightarrow \infty} \text{UCST} \\ \Theta_L &= \lim_{M \rightarrow \infty} \text{LCST}\end{aligned}\tag{16.25}$$

Theta temperatures have been tabulated for many systems, including several containing mixed solvents,⁴¹⁻⁴³ and define the ultimate limit of solubility. A very rough estimate of the theta temperatures based on the solvent and polymer solubility parameters can be made using an equation proposed by Fox:⁵¹

$$\begin{aligned}\Theta &= \frac{375}{0.225\delta_{\text{pol}} - 1} (\delta_{\text{pol}} - \delta_{\text{solv}}) \quad \text{if } \delta_{\text{solv}} \leq \delta_{\text{pol}} \\ \Theta &= \frac{175}{0.225\delta_{\text{pol}} - 1} (\delta_{\text{solv}} - \delta_{\text{pol}}) \quad \text{if } \delta_{\text{solv}} \geq \delta_{\text{pol}}\end{aligned}\tag{16.26}$$

- There is another type of phase diagram encountered in some polymer solutions, where the LCST lies below the UCST. This is called closed-loop and appears for polymer solutions where hydrogen bonding effects are dominant such as polyethylene glycol/water and polyvinyl alcohol/water (Figure 16.4).
- The existence of UCST is typically attributed to the energy differences between polymer and solvent and of LCST to the so-called free-volume effects, which are due to the differences in size and free-volume between polymer and solvent. Free-volume effects are small for nonpolymeric solutions and are discussed in conjunction with free-volume-based activity coefficient models in Section 16.4. The LCST was first discovered by Freeman and Rowlinson⁵² only about 40 years ago, but is now considered to be a universal phenomenon of polymer–solvent systems at high temperatures. In some cases, it is not observed if the polymer degrades before reaching the LCST.

In the case of LLE, Equation 16.15 is often written in the following form:

$$(\gamma_i x_i)^a = (\gamma_i x_i)^b \quad i = 1, 2, \dots\tag{16.27}$$

or more generally in terms of the fugacity coefficients:

$$(\Phi_i x_i)^a = (\Phi_i x_i)^b \quad i = 1, 2, \dots\tag{16.28}$$

where a and b represent the two liquid phases.

Equations 16.27 and 16.28 imply that LLE can be calculated if a suitable model for the activity coefficient (or an equation of state) is available.

According to thermodynamics, complete miscibility is achieved if

$$\left(\frac{\partial^2 \Delta G}{\partial \phi_1^2} \right)_{T,P} \geq 0\tag{16.29}$$

If a system is miscible, then $\Delta G < 0$ (the Gibbs energy of mixing is negative), but the second derivative criterion, Equation 16.29, offers a more rigorous criterion for miscibility. At the critical solution temperature (onset of two-phase appearance) the following equations hold:

$$\frac{\partial^2 \Delta G}{\partial \phi_2^2} = \frac{\partial^3 \Delta G}{\partial \phi_2^3} = 0$$

or

$$\frac{\partial \ln \alpha_1}{\partial \phi_2} = \frac{\partial^2 \ln \alpha_1}{\partial \phi_2^2} = 0 \quad (16.30)$$

The second set of equations is particularly useful if an activity coefficient model (an equation for the activity coefficient γ or the activity α) is known.

16.3.2 THERMODYNAMIC DATABASES FOR POLYMERS

Extensive databases for thermodynamic polymer properties are now available:

1. *Pure polymer densities*: Experimental data for a number of polymers are correlated via the Tait equation and are summarized in the DIPPR Polymer Project.³¹ Recently, an extensive compilation of polymer densities (using the Tait equation) has been presented by Rodgers.³² The Tait equation is a five-parameter correlation of the density of polymers as a function of both temperature and pressure. It provides an excellent correlation over extended temperature and pressure ranges.
2. *Polymer and solvent solubility parameters*: The most extensive compilation is provided in the recent book by Hansen¹⁷ and in the handbooks by Barton.^{41,42}
3. *Polymer–solvent VLE*: Vapor–liquid data, both at intermediate concentrations and at the infinite dilution of the solvent, are available in two extensive databases: DECHEMA and DIPPR Polymer Project.^{31,48} These databases are also available in electronic form. The data are restricted to single solvent systems and often cover various temperatures. A more recent compilation of VLE has been published by Wohlfarth.⁵³ Basically low-pressure VLE data are available. Very few high-pressure VLE data exist for polymer–solvent systems (with nongaseous solvents), e.g., the work by Surana et al.⁵⁴
4. *Polymer–solvent LLE*: Many data are stored in the two above-mentioned databases.^{31,48} In DECHEMA, data are only cited as LCST/UCST temperatures and restricted to single solvents. The DIPPR project provides the full binodal curves and in addition ternary LLE data for some few systems (mostly with polystyrene) with two solvents are reported.

Very limited data are available for solid–liquid–liquid equilibria (SLLE) for semicrystalline polymer–solvent systems (a list is presented by Harismiadis and Tassios⁵⁵).

Particularly evident is the lack of systematic reports on polymer–mixed solvents data (VLE or LLE) in the open literature, especially in form of full-phase equilibrium measurements. Most experimental studies for mixed solvent systems have been reported by Chinese and Japanese investigators^{56,57} and only a few by other investigators.^{58,59} Data are often reported simply as “soluble/nonsoluble” or as “theta temperatures” (critical solution temperature at infinite polymer molecular weight). Several reported polymer–mixed solvent data concern supercritical fluid applications (e.g., polypropylene/pentane/CO₂,⁶⁰ and PEG/CO₂/cosolvent⁶¹) and bioseparations,^{62–65} especially for systems related to the partitioning of biomolecules in aqueous two-phase systems, which contain PEG and dextran. A recent review for data on solubility of gases in glassy polymers is also available.¹³

Very extensive data are available for polymer blends (including UCST/LCST behavior, heats of mixing, etc.), but, to our knowledge, these are not systematically reviewed in any current database.

The original publications should be consulted and this may occasionally be a problem, as data are often presented in graphs and other forms with difficulties in conversion and interpretation.

16.3.3 CLASSICAL MODELS FOR POLYMER SOLUTIONS

16.3.3.1 The Solubility Parameter Method and the Hansen Plots

16.3.3.1.1 Heat of Mixing and Solubility: Application to Nonpolar Systems

The crucial concept in determining miscibility in thermodynamics is the Gibbs free energy of mixing:

$$\Delta G^{\text{mix}} = \Delta H - T\Delta S \quad (16.31)$$

A negative value implies that a solvent–polymer system forms a homogeneous solution; i.e., the two components are miscible (necessary but not sufficient criterion for miscibility).

Because the contribution of the entropic term ($-T\Delta S$) is always negative due to the positive entropy of mixing, it is the heat of mixing term that determines the sign of the Gibbs energy.

The heat of mixing term can be obtained from various theories. One valid possibility for nonpolar systems is the regular solution theory, introduced by Joel Hildebrand, which employs the concept of the solubility parameter. For a binary solvent(1)–polymer(2) system, the heat of mixing is given according to the regular solution theory:

$$\Delta H = \varphi_1\varphi_2V(\delta_1 - \delta_2)^2 \quad (16.32)$$

where φ_i is the so-called volume fraction of component i . This is defined via the mole fractions x_i and the molar volumes V_i as (binary systems)

$$\varphi_i = \frac{x_i V_i}{x_i V_i + x_j V_j} \quad (16.33)$$

According to regular solution theory (Equation 16.32), the heat of mixing is always positive. The regular solution theory is strictly valid for nonpolar/slightly polar systems, without any specific interactions. For systems with specific interactions (hydrogen bonding), the heat of mixing can be negative; Equation 16.32 does not hold.

According to Equations 16.31 and 16.32, if a solvent and polymer have the same solubility parameters, the heat of mixing is zero and they are thus miscible at all proportions. The smaller the solubility parameter difference, the larger the tendency of miscibility. Many empirical rules of thumb have been proposed based on this observation. Seymour⁶⁶ suggests that if the difference of solubility parameters is below 1 to 1.8 (cal/cm³)^{1/2}, then polymer and solvent are miscible.

A note on the classification of polymer solutions:

Most polymer solutions are typically highly nonideal; i.e., both an expression for the entropy and the enthalpy of mixing need to be known. However, a few nonpolar solutions where the repeating unit of the polymer is structurally similar to the solvent (e.g., polyethylene/alkanes, polystyrene/benzene, polyvinyl acetate/ethyl acetate) can be considered to be athermal; i.e., the heat of mixing is approximately zero. These polymers and solvents have, in agreement with Equation 16.32, the same or very similar solubility parameters. Thus, experimental phase equilibrium data for athermal polymer solutions can help checking expressions for the entropy of mixing. For the regular solutions, e.g., benzene/heptane, carbon monoxide/methane, only an expression for the heat of mixing need be developed; the entropy of mixing has the ideal value. Finally, ideal solutions, e.g., hexane/heptane,

ethanol/propanol, have the ideal value for the entropy of mixing and zero enthalpy of mixing. From this discussion, it is understood that even the simplest nonpolar polymer solutions are nonideal due to a nonideal value of the entropy of mixing.

16.3.3.1.2 The Hansen Plots: Extension to Polar and Hydrogen Bonding Systems

Hansen observed that when the solubility parameter increments of the solvents and polymers are plotted in three-dimensional plots, then the “good” solvents lie approximately within a sphere of radius R (with the polymer located in the center). Because three-dimensional plots are a bit cumbersome to use, two alternative simplified ways are often employed.

The first is to employ the Hansen equation:

$$\sqrt{4(\delta_{d1} - \delta_{d2})^2 + (\delta_{p1} - \delta_{p2})^2 + (\delta_{h1} - \delta_{h2})^2} \leq R \quad (16.34)$$

where 1 denotes the solvents and 2 the polymer. The quantity under the square root is the distance between the solvent and the polymer. Hansen found empirically that a universal value 4 should be added as a factor in the dispersion term to approximately attain the shape of a sphere. This universal factor has been confirmed by many experiments. Hansen¹⁷ recently attempts to provide a theoretical justification for this value.

The second way is to employ two-dimensional plots. Several such plots have been used. For example, Hansen⁶⁷ shows $\delta_p - \delta_h, \delta_h - \delta_d, \delta_p - \delta_d$ plots for polystyrene and poly(vinyl acetate). Interestingly enough, the sphere is now reduced to a circle and the good solvents lie within the circle. Poor solvents lie outside. The method is satisfactory but approximate, and deviations are also observed.

Another possibility is the use of $\delta_v - \delta_h, \delta_v = \sqrt{\delta_d^2 + \delta_p^2}$ plots suggested by van Krevelen.²⁸ With few exceptions good solvents lie within the circle of radius R , which mathematically can be expressed as

$$\sqrt{(\delta_{v1} - \delta_{v2})^2 + (\delta_{h1} - \delta_{h2})^2} \leq R \quad (16.35)$$

The justification for this plot lies in the fact that, of the three solubility parameter increments, the dispersion parameter varies the least and, via this average way, it can be treated together with the polar increment. The hydrogen bonding increment is very important and it is thus accounted for separately in Equation 16.35.

The Hansen method is very valuable. It has found widespread use particularly in the paints and coatings industry, where the choice of solvents to meet economical, ecological, and safety constraints is of critical importance.⁶⁸ It can explain cases in which polymer and solvent solubility parameters are almost perfectly matched, yet the polymer will not dissolve. The Hansen method can also predict cases where two nonsolvents can be mixed to form a solvent. Still, the method is approximate, it lacks the generality of a full thermodynamic model for assessing miscibility, and it requires some experimental measurements. The determination of R is typically based on visual observation of solubility (or not) of 0.5 g polymer in 5 cm³ solvent at room temperature. Given the concentration and the temperature dependence of phase boundaries, such a determination may seem a bit arbitrary. Still the method works out pretty well in practice, probably because the liquid–liquid boundaries for most polymer–solvent systems are fairly “flat.”

16.3.3.2 The Flory–Huggins Model

The Flory–Huggins (FH) model is a famous expression for the activity coefficient (generally for the Gibbs free energy of mixing) proposed in the early 1940s by Flory⁶⁹ and Huggins,⁷⁰ almost at

the same time and independently (working a continent apart). They were the first to realize that the main contribution to the activity coefficient should stem from “entropic” effects (differences in size, shape, and free-volume between the polymer and the solvent) rather than from “energetic” (enthalpic) effects. They, thus, proposed first an expression for the entropy of mixing to which they subsequently added a simple van-Laar type (random-mixing) energetic term. For a binary system, the total Gibbs energy of mixing is written:

$$\frac{\Delta G}{RT} = n_1 \ln \phi_1 + n_2 \ln \phi_2 + \chi_{12} n_1 \phi_2 \quad (16.36)$$

The first term of Equation 16.36 is due to “combinatorial” effects and is derived from lattice theory. The second energetic term is of a rather empirical nature and includes only the adjustable parameter of the model, the so-called FH interaction parameter χ_{12} .

In Equation 16.36 volume fractions are used. Alternatively, ϕ_i can be defined as segment fraction, if in Equation 16.36 the segment or van der Waals volumes R_i are used instead of the molar volumes.

Originally, it was assumed that the FH interaction parameter was a constant, characteristic for each polymer–solvent pair. In this case, it can be proved based on thermodynamics that the FH equation for the activity coefficient of a solvent in a binary solvent(1)–polymer(2) system is

$$\ln \gamma_1 = \ln \frac{\phi_1}{x_1} + 1 - \frac{\phi_1}{x_1} + \chi_{12} \phi_2^2 = \ln \frac{\phi_1}{x_1} + \left(1 - \frac{1}{r}\right) \phi_2 + \chi_{12} \phi_2^2 \quad (16.37)$$

where r is the ratio of the polymer volume to the solvent volume V_2/V_1 (approximately equal to the degree of polymerization).

The FH theory can be extended to multicomponent systems but (at least) one χ_{12} -value is required per binary. It has been shown that, unfortunately, the FH parameter is typically not a constant and should be estimated from experimental data. Usually it varies with both temperature and concentration, which renders the FH model useful only for describing experimental data. It cannot be used for predicting phase equilibria for systems for which no data are available. Moreover, when fitted to the critical solution temperature, the FH model cannot yield a good representation of the whole shape of the miscibility curve with a single parameter.

Accurate representation of miscibility curves with the FH model is possible using suitable rather complex equations for the temperature and the concentration dependence of the FH parameter:⁷¹⁻⁷³

$$\frac{\Delta G}{RT} = \sum_i x_i \ln \phi_i + g_{12} \phi_1 \phi_2 \quad (16.38)$$

$$g_{12} = B(\phi)C(T) = (a + b\phi_2) \left(1 + \frac{c}{T} + dT + e \ln T\right)$$

The parameters of such equations (a, b, c, d, e) have no apparent physical significance, they cannot be generalized, and are specific for each polymer–solvent system. Thus, the FH model cannot be used for predictions. Other researchers, e.g., Koningsveld and Kleintjens,⁷⁴ have suggested more sound expressions for the FH dependence on concentration, which also require experimental data specific for each polymer–solvent system:

$$g_{12} = a + \frac{b(1-c)}{(1-c\phi_2^2)} \quad (16.39)$$

High and Danner³¹ found that the Koningsveld–Kleintjens expression (Equation 16.39) is superior to the polynomial series in correlating and extrapolating concentration-dependent FH interaction parameters.

Another problem of the combinatorial term of the model is that it predicts complete miscibility for athermal polymer solutions. This is not in agreement with the general observation of the LCST for even nonpolar (athermal) polymer solutions, as we mentioned previously. However, even the more recent combinatorial expressions, which are discussed in Section 16.4, suffer from this deficiency.

Accurate results with the FH model can only be obtained if equations like 16.38 or 16.39 are used for estimating the FH parameter. Still, for some practical cases, a reasonable value of the FH parameter can be obtained, by combining the FH and regular solutions theories, using the solubility parameters of the compounds via the equation:

$$\chi_{12} = \chi_s + \chi_h = 0.35 + \frac{V_1}{RT} (\delta_1 - \delta_2)^2 \quad (16.40)$$

Equation 16.40, without the empirical 0.35 term, is derived from the regular solution theory. The constant 0.35 is added for correcting for the deficiencies of the FH combinatorial term. These deficiencies become evident when comparing experimental data for athermal polymer and other asymmetric solutions to the results obtained with the FH model. A consistent underestimation of the data is observed, as discussed extensively in the literature,^{1,82} which is often attributed to the inability of the FH model for accounting for the free-volume differences between polymers and solvents or between compounds differing significantly in size such as solutions of *n*-alkanes with very different chain lengths. The term, which contains the “0.35 factor,” corrects in an empirical way for these free-volume effects. However, and although satisfactory results are obtained in some cases, we cannot generally recommend Equation 16.40 for estimating the FH parameter. Moreover, for many nonpolar systems with compounds having similar solubility parameters, the empirical factor 0.35 should be dropped.

16.3.3.2.1 Selecting Solvents with the Flory-Huggins Model

The FH model has found over the last 60 years extensive use both in research and in industrial practice. Very extensive compilations of the FH parameters are available^{41,42} and there is much familiarity with them, as was also the case in the industry with the parameters of the Wilson equation for nonpolymeric systems.

One practical implication of the FH model, which has been used in the industry for miscibility studies (choosing suitable solvents), comes from thermodynamic stability analysis of the model. Applying the stability Equations 16.30 to the FH model, the critical values of the FH interaction parameter and of the concentration are found:

$$\begin{aligned} \chi^{\text{crit}} &= \frac{1}{2} \left[1 + \frac{1}{\sqrt{r}} \right]^2 \\ r &= \frac{V_2}{V_1} \\ \phi_2^{\text{crit}} &= \frac{1}{1 + \sqrt{r}} \end{aligned} \quad (16.41)$$

For high molecular-weight polymer–solvent systems, the polymer critical concentration is close to zero and the interaction parameter has a value close to 0.5. Thus, a good solvent (polymer soluble in the solvent at all proportions) is obtained if $\chi_{12} \leq 0.5$, whereas values greater than 0.5 indicate poor solvency. Since we mentioned that the model is only an approximate representation of the physical picture and that the FH parameter is often not a constant at all, this empirical rule is certainly subject to some uncertainty. Nevertheless, it has found widespread use and its conclusions are often in good agreement with experiment.

Since 1980 polymer thermodynamics has been developed considerably and, to date, models are available that are suitable for at least satisfactory calculations of VLE and, qualitatively, also for LLE. Some of these methods are models for the activity coefficient, which are modifications of the FH equation. These modifications use a similar to FH but better combinatorial/free-volume expression and a local-composition-type energetic term such as those found in the UNIQUAC and UNIFAC models. Models like the UNIFAC-FV and the Entropic-FV are discussed in Section 16.4.

16.3.3.2.2 Other Rules of Thumb Based on the Flory-Huggins Model

Based on the FH model, several techniques have been proposed for interpreting as well as for correlating experimental data for polymer systems. We cite here some of the most useful of these approaches:

The Schultz–Flory (SF) Plot

Schultz and Flory⁷⁵ have developed, starting from the FH model and Equation 16.41, the following expression, which relates the critical solution temperature (CST), with the theta temperature and the polymer molecular weight:

$$\frac{1}{\text{CST}} = \frac{1}{\Theta} \left[1 + \frac{1}{\Psi} \left(\frac{1}{\sqrt{r}} + \frac{1}{2r} \right) \right] \quad (16.42)$$

where $\Psi (= 1/2 - \chi_s)$ is the entropic parameter of the FH model (see Equation 16.40) and r is the ratio of molar volumes of the polymer to the solvent. This parameter is evidently dependent on the molecular weight of the polymer. The SF plot can be used for correlating data of critical solution temperatures for the same polymer–solvent system, but at different polymer molecular weights. This can be done, as anticipated from Equation 16.42 because the plot of $1/\text{CST}$ with the quantity in parentheses in Equation 16.42 is linear. The SF plot can be also used for the following:

- Predicting CST for the same system but at molecular weights different from those used for correlation
- Calculating the theta temperature and the entropic part of the FH parameter
- Correlating CST/molecular weight data for both the UCST and LCST areas; apparently, different coefficients are needed

Based on Equation 16.42, the somewhat simpler direct dependency of CST with the polymer molecular weight (MW) is often used for correlating purposes:

$$\frac{1}{\text{CST}} = \frac{1}{\Theta} \left[1 + \frac{C}{\sqrt{\text{MW}}} \right] \quad (16.43)$$

The FH Parameter–Solubility Parameter Relationship

Starting from Equation 16.40, the following expression can be derived that links the FH parameter to the solubility parameters of both the solvent and the polymer:

$$\left(\frac{\delta_1^2}{RT} - \frac{\chi}{V_1} \right) = \left(\frac{2\delta_2}{RT} \right) \delta_1 - \left(\frac{\delta_2^2}{RT} + \frac{\chi_s}{V_1} \right) \quad (16.44)$$

Equation 16.44 can be used in the following way: If experimental data for the FH parameter are available, e.g., via chromatographic measurements for a series of systems with the same polymer in different solvents, then from the linear plot depicted by Equation 16.44, the solubility parameter of the polymer can be estimated. Solubility parameters of the solvents are known from direct experimental measurements. Thus, Equation 16.44 represents one of the various indirect methods for estimating polymer solubility parameters.

16.3.3.3 Summary of Rules of Thumb for Predicting Polymer–Solvent Miscibility

Based on the properties and concepts introduced above (activity coefficient, FH parameter, and solubility parameter), we summarize here the rules of thumb that have been proposed and extensively used in the literature for roughly selecting good solvents for specific polymers.

Thus, a chemical (1) will be good solvent for a specific polymer (2), or in other words the two compounds will be miscible if one (or more) of the following “rules of thumb” are valid:^{28,66}

1. If the polymer and the solvent have “similar hydrogen bonding degrees”:

$$|\delta_1 - \delta_2| \leq 1 - 1.8 \left(\frac{\text{cal}}{\text{cm}^3} \right)^{1/2} \quad (16.45)$$

2. If the polymer and the solvent have very different hydrogen bonding degrees:

$$\sqrt{4(\delta_{d1} - \delta_{d2})^2 + (\delta_{p1} - \delta_{p2})^2 + (\delta_{h1} - \delta_{h2})^2} \leq R$$

where R is the Hansen solubility parameter sphere radius.

3. $\chi_{12} \leq 0.5$ (the lower the FH parameter value, the greater the miscibility, or in other words the greater the solvency capacity of a specific chemical). Values much above 0.5 indicate nonsolvency.
4. $\Omega_1^\infty \leq 6$ (the lower the infinite dilution activity coefficient of the solvent, the greater the solvency of a chemical). Values of the infinite dilution activity coefficient above 10 indicate nonsolvency. In the intermediate region, it is difficult to conclude if the specific chemical is a solvent or a nonsolvent.

16.4 THE FREE-VOLUME MODELS

The FH model provides a first approximation for polymer solutions. As shown, both the combinatorial and the energetic terms need substantial improvement. Many authors have replaced the random van-Laar energetic term by a nonrandom local-composition term such as those of UNIQUAC, NRTL, and UNIFAC models. The combinatorial term should be extended/modified to account for the free-volume differences between solvents and polymers.

Two particularly interesting semipredictive extensions of the FH model that account for non-randomness have been reported:

1. Gottlieb and Herskowitz⁷⁶ used UNIFAC to estimate the concentration dependency of the FH interaction parameter for some PDMS solutions. The results were quite satisfactory. However, they did that by equating Equation 16.37, which assumes a constant FH parameter, with UNIFAC. This approach can be, at best, considered approximate.
2. Vetere⁷⁷⁻⁷⁹ proposed combining the FH equation (empirically modified to account for free-volume effects) with the NRTL expression for the energetic effects. The two NRTL parameters were correlated with the solubility parameters of the components. The relative importance of the combinatorial and residual contributions was analyzed and satisfactory results (for both VLE and LLE) are obtained for some binary systems, including aqueous polymer solutions. This recent approach is under development.

The improvement of the energy term of the FH equation is important. Local-composition terms like those appearing in NRTL, UNIQUAC, and UNIFAC models provide such an improvement. In addition, however, “free-volume” effects should be incorporated into the combinatorial term. The free-volume concept is discussed in Section 16.4.1 and some models that incorporate both free-volume and local composition effects are discussed in Sections 16.4.2 through 16.4.4.

16.4.1 THE FREE-VOLUME CONCEPT

The free-volume (FV) concept has a special importance in polymer thermodynamics. FV is the volume allocated to the molecules for movement when their own volume is subtracted. Patterson,⁸⁰ in his excellent review on FV, offers a qualitative description of the relationship between FV and polymer solubility. Elbro⁴⁶ demonstrated, using a simple definition for the FV (Equation 16.46), that the FV percentages of solvents and polymers are different. It is exactly these differences in FV (or expansivities), which were ignored in early theories like the famous FH equation. In the typical case, the FV percentage of solvents is greater (40 to 50%) than that of polymers (30 to 40%). There are two exceptions to this rule: water and PDMS.^{46,81,82} Water has lower FV than other solvents and closer to that of most polymers, and PDMS has a quite higher FV percentage, closer to that of most solvents. LCST is, as expected, related to the FV differences between polymers and solvents. As shown by Elbro,⁴⁶ the larger the FV differences, the lower the LCST value (the larger the area of immiscibility). For this reason, PDMS solutions have LCST, that are located at very high temperatures.

It may be difficult to formulate a rigorous mathematical expression of FV, fully consistent with the above physical picture. Bondi⁸³ stated, “every author defines the free-volume as what he wants it to mean.” This may very well be true. Thus, various expressions have been proposed for the FV. Some of them are employed in the development of activity coefficient models for polymer solutions.

One of the simplest and most successful equations is

$$V_f = V - V^* = V - V_w \quad (16.46)$$

originally proposed by Bondi⁸³ and later adopted by Elbro et al.⁸² and Kontogeorgis et al.⁵⁰ in the so-called Entropic-FV model (described in Section 16.4.2.2). According to this equation, FV is just the “empty” volume available to the molecule when the molecule’s own (hard-core or closed-packed V^*) volume is subtracted from the total volume.

Even the hard-core volume is a quantity difficult to define and various approximations are available for V^* . Elbro et al.⁸² suggested taking $V^* = V_w$, i.e., equal to the van der Waals volume, which is obtained from the group increments of Bondi and is tabulated for almost all existing groups in the UNIFAC tables. Wilson⁸⁴ stated that, in the liquid phase, it would be expected that the “real” hard-core volume (minimum volume in the fluid state) might be a bit (around 14%) larger than the molecule’s actual closed packed volume, e.g., $V^* = 1.14 V_w$. This and other arguments related to the physical meaning of the hard-core volume have been used recently⁸⁵ in the development

of improved FV expressions for polymer solutions, which employ Equation 16.46 as basis, but with V^* values higher than V_w .

Other similar FV equations have been proposed, e.g., the following Flory:

$$V_f = (V^{1/3} - V_w^{1/3})^{3.3} \quad (16.47)$$

This equation (although it does not literally correspond to volume) was later used by several investigators⁸⁶⁻⁸⁸ for phase equilibria in both polymeric and other asymmetric nonpolymeric systems with satisfactory results. Especially, Coutinho et al.⁸⁷ found that Equation 16.47 was superior to Equation 16.46 for solid–liquid equilibrium calculations for largely asymmetric alkane solutions.

16.4.2 GROUP-CONTRIBUTION FREE-VOLUME ACTIVITY COEFFICIENT MODELS

The GC concept has received great attention for the prediction of activity coefficients during the last 30 years. It has been applied to many different types of properties of pure compounds, as shown in Section 16.2, but also for phase equilibrium calculations for mixtures. Especially well known is the UNIFAC equation^{1,26,27} for the activity coefficient. The UNIFAC model is available in several modified forms, e.g., by Larsen et al.⁸⁹ and Gmehling and Weidlich.⁹⁰ These modified UNIFAC models contain, unlike the original UNIFAC, temperature-dependent interaction parameters.

The original UNIFAC model ignores the FV differences between solvents and polymers and, as a consequence, it highly underestimates the solvent activities in polymer solutions.^{49,50,82} On the other hand, the various modified UNIFAC versions are also inadequate for polymer solutions. Although their combinatorial terms are more satisfactory for alkane systems, they fail completely for polymer–solvent systems, and as shown⁸⁶ they significantly and systematically underestimate the solvent activities. Although these UNIFAC models are not adequate for polymer solutions, the problem seems, however, to lie more on the combinatorial term rather than the residual (energetic) term. In other words, improvements are required especially for describing the FV effects, which are dominant in polymer solutions.

Over the last 20 years or so many GC methods have been developed for polymer solutions. GC models proposed for polymer solutions (and blends) can be roughly divided into two types:

1. UNIFAC-based FV models
2. Equations of state (cubic and noncubic)

We consider the activity coefficient models in this section and the equations of state in the next.

The strong point of the GC technique for mixtures is that using a relatively small number of (group) interaction parameters, properties can be estimated for a very large number of different systems. Evidently, due to their nature, the GC technique is recommended and often applied to polymers. In the typical case, problems are expected for isomers and highly complex compounds with several “functional groups.”

Several reviews and comparisons of various models have been published.⁹¹⁻⁹⁶ In their recent and more industrially oriented review, Bokis et al.⁹¹ mention the UNIFAC, UNIFAC-FV,⁴⁹ FH, and SAFT models as the ones currently available in the ASPEN polymer software. Of these, the first two are based on GCs.

16.4.2.1 The UNIFAC-FV Model

Various modifications and extensions of the classical UNIFAC approach to polymers have been proposed. All these approaches attempt to include the FV effects, which are neglected in the

UNIFAC combinatorial term. All employ the energetic (residual) term of UNIFAC. The first of this type of models is the UNIFAC-FV by Oishi and Prausnitz:⁴⁹

$$\ln \gamma_i = \ln \gamma_i^{\text{comb}} + \ln \gamma_i^{\text{res}} + \ln \gamma_i^{\text{fv}} \quad (16.48)$$

The combinatorial and residual terms are obtained from the original UNIFAC. An additional term is added for the FV effects. An approximation but at the same time an interesting feature of UNIFAC-FV and the other models of this type is that the same UNIFAC group-interaction parameters, i.e., those of original UNIFAC, are used. No parameter estimation is performed. The FV term used in UNIFAC-FV has a theoretical origin and is based on the Flory equation of state:

$$\ln \gamma_i^{\text{fv}} = 3c_i \ln \left[\frac{\left(\frac{v_i^{-1/3} - 1}{v_m^{-1/3} - 1} \right)}{\left(\frac{v_i}{v_m} - 1 \right)} \right] - c_i \left[\left(\frac{v_i}{v_m} - 1 \right) \left(1 - \frac{1}{v_i^{-1/3}} \right)^{-1} \right] \quad (16.49)$$

where the reduced volumes are defined as

$$\begin{aligned} \bar{v}_i &= \frac{v_i}{bV_{i,w}} \\ \bar{v}_m &= \frac{x_1 v_1 + x_2 v_2}{b(x_1 V_{1,w} + x_2 V_{2,w})} \end{aligned} \quad (16.50)$$

In Equation 16.50, the volumes v_i and the van der Waals volumes are all expressed in cm^3/mol . v_i is the mole fraction.

In the UNIFAC-FV model as suggested by Oishi and Prausnitz⁴⁹ the parameters c_i ($3c_i$ is the number of external degrees of freedom) and b are set to constant values ($c_i = 1.1$ and $b = 1.28$). The performance is rather satisfactory, as shown by many investigators,^{1,25,31,40,49,50,82,96} for a large variety of polymer–solvent systems. When referring to UNIFAC-FV in the rest of this section, the original version with constant b and c values is employed.

However, several authors have shown that better agreement is obtained in specific cases if these parameters are fitted to experimental data.^{93,97,98} Although in the case c and/or b are fitted to data the model is no more predictive, such fitting gives an additional flexibility to the UNIFAC-FV model.

Originally, the UNIFAC-FV model has been developed for solvent activities in polymers. It can be assumed that the model (Equations 16.48 through 16.50) is also valid for estimating the polymer activities. However, such an application of UNIFAC-FV is rather problematic.^{99,100} It has been shown⁸⁵ that the performance of UNIFAC-FV in predicting the activities of heavy alkanes in shorter ones is not very good. Sample results are shown in [Tables 16.5](#) and [16.6](#) for the activities of both the solvent and the heavy compound where comparison with other models is also provided. Such problems restrict the applicability of UNIFAC-FV to cases where only the solvent activity is needed. To our knowledge, UNIFAC-FV has not been tested for LLE in polymer solutions, where both the solvent and polymer activities are required.

16.4.2.2 The Entropic-FV Model

An approach similar to UNIFAC-FV but somewhat simpler, which can be readily extended to multicomponent systems and LLE, is the so-called Entropic-FV model proposed by Elbro et al.⁸² and Kontogeorgis et al.:⁵⁰

TABLE 16.5
Mean Percentage Deviations between Experimental and Calculated Activity
Coefficients of Solvents in Various Nearly Athermal Solutions

% AAD Infinite Dilution Conditions				
γ_i^∞ (Ω_i^∞ for polymers)	Entropic-FV	UNIFAC-ZM	UNIFAC-FV	Flory-FV
Short <i>n</i> -alkanes/long alkanes	8	7	15	20
Short branched, cyclic alkanes/long alkanes	10	7	17	20
Alkanes/polyethylene	9	10	23	19
Alkanes/polyisobutylene	16	27	12	38
Organic solvent/PDMS, PS, PVAc	20	22	29	26
Overall	13	15	19	25
% AAD Finite Concentrations				
	Entropic-FV	UNIFAC-ZM	UNIFAC-FV	Flory-FV
Alkanes/polyethylene, polypropylene	19	21	22	29
Short <i>n</i> -alkanes/polyisobutylene	5	24	17	35
Short <i>b</i> -alkane/polyisobutylene	20	41	8	24
Short <i>c</i> -alkane/polyisobutylene	4	5	3	3
Organic solvent/PDMS, PS, PVAc	7	10	19	6
Overall	11	20	14	19

Note: n = normal; b = branched; c = cyclic.

Source: Kouskoumvekaki, I. et al., *Fluid Phase Equilibria*, accepted for publication, 2002. With permission.

$$\ln \gamma_i = \ln \gamma_i^{\text{comb-fv}} + \ln \gamma_i^{\text{res}}$$

$$\ln \gamma_i^{\text{comb-fv}} = \ln \frac{\Phi_i^{\text{fv}}}{x_i} + 1 - \frac{\Phi_i^{\text{fv}}}{x_i} \quad (16.51)$$

$$\Phi_i^{\text{fv}} = \frac{x_i V_{i,\text{fv}}}{\sum_j x_j V_{j,\text{fv}}} = \frac{x_i (V_i - V_{wi})}{\sum_j x_j (V_j - V_{wj})}$$

As can be seen from Equation 16.51, the FV definition given by Equation 16.46 is employed.

The combinatorial term of Equation 16.51 is very similar to that of FH. However, instead of volume or segment fractions, FV fractions are used. In this way, both combinatorial and FV effects are combined into a single expression.

The combinatorial FV expression of the Entropic-FV model is derived from statistical mechanics, using a suitable form of the generalized van der Waals partition function.⁸²

The residual term of Entropic-FV is taken by the so-called “new-UNIFAC” model, which uses a linear-dependent parameter table:¹⁰¹

$$a_{mn} = a_{mn,1} + a_{mn,2}(T - T_o) \quad (16.52)$$

The new-UNIFAC represents the most recent version of the UNIFAC model developed at the Technical University of Denmark (Lyngby). The parameter table has been developed using the combinatorial term of the original UNIFAC model. As with UNIFAC-FV, no parameter reestimation has been performed. The same group parameters are used in the new-UNIFAC and in the Entropic-FV models.

TABLE 16.6
Mean Percentage Deviations between Experimental and Calculated
Activity Coefficients of Heavy Alkane Solutes in Alkane Solvents

% AAD Infinite Dilution Conditions, γ_2^∞	Entropic-FV	UNIFAC-ZM	UNIFAC-FV	Flory-FV
Symmetric long alkanes/short alkanes	36	53	47	10
Medium asymmetric long alkanes/short alkanes	34	54	48	12
Asymmetric long alkanes/short alkanes	44	61	54	37
Overall	38	56	50	20

% AAD Finite Concentrations, γ_2	Entropic-FV	UNIFAC-ZM	UNIFAC-FV	Flory-FV
Symmetric long alkanes/short alkanes	14	14	17	6
Medium asymmetric long alkanes/short alkanes	23	26	31	11
Asymmetric long alkanes/short alkanes	40	55	55	16
Overall	26	32	34	11

Source: Kouskoumvekaki, I. et al., *Fluid Phase Equilibria*, accepted for publication, 2002. With permission.

The UNIFAC-FV and Entropic-FV models are not the only extensions of UNIFAC to polymers. Similar models have been presented by Iwai and Arai^{102,103} and by Choi et al.¹⁰⁴ Choi's model is not based on UNIFAC but on ASOG. ASOG (Analytical Solution of Groups) is a predictive GC method for calculating activities, similar to UNIFAC, but which has not experienced the widespread use of UNIFAC. It is mostly employed in Japan. Besides this difference, the models of Arai and Choi contain an FV, which is different from that of Equation 16.49. These two models have been applied with success for some polymer–solvent systems but not for LLE.

A common feature of UNIFAC-FV, Entropic-FV, and other similar models is that they require the volumes of solvents and polymers (at the different temperatures where application is required). This can be a problem in those cases where the densities are not available experimentally and have to be estimated using one of the methods discussed in Section 16.2. Figure 16.3 shows that both UNIFAC-FV and Entropic-FV are rather sensitive to the density values used for the calculation of solvent activities. The UNIFAC-FV model, in particular, can be extremely sensitive if the free volume percentage of the polymer is very low.

Both UNIFAC-FV and Entropic-FV are GC models. This renders the models truly predictive, but at the same time very little flexibility is available if the performance of the models for specific cases is not satisfactory. An interesting approach is to employ the UNIQUAC expression for the residual term in Equation 16.51. This Entropic-FV/UNIQUAC model was originally suggested by Elbro et al.⁸² and has given very good results^{1,82} for polymer solutions if the parameters are obtained from VLE data between the solvent and the low molecular weight monomer (or the repeating unit of the polymer). The Entropic-FV/UNIQUAC model has been recently further developed and extended by several researchers^{1,105-107} to cover both VLE and LLE equilibria, and very satisfactory results were obtained as can be seen for typical systems in Figures 16.4 and 16.5. It has been demonstrated that the Entropic-FV/UNIQUAC approach can correlate both UCST/LCST and closed-loop behavior^{105,106} and even show the pressure dependency of critical solution temperatures (UCST and LCST).¹⁰⁷

16.4.3 RESULTS

Several FV models, e.g., the UNIFAC-FV models by Oishi and Prausnitz⁴⁹ and Iwai and Arai^{102,103} have been extensively applied to VLE/solvent activities in polymers and other asymmetric systems. However, these models have not been systematically applied to LLE and other types of equilibria

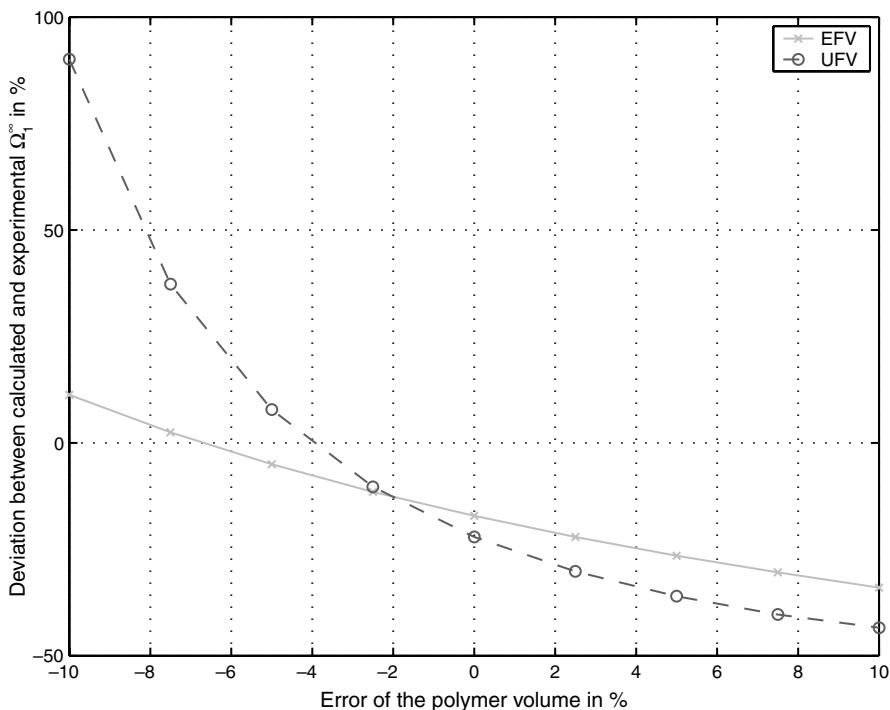


FIGURE 16.3 Influence of the volume on the deviations of activity coefficients for the system poly(methyl acrylate)/acetone at 393 K. Calculations with two free-volume are shown, EFV (Entropic-FV) and UFV (UNIFAC-FV). (From Lindvig, Th. et al., *Fluid Phase Equilibria*, 663, 189–197, 2002. With permission.)

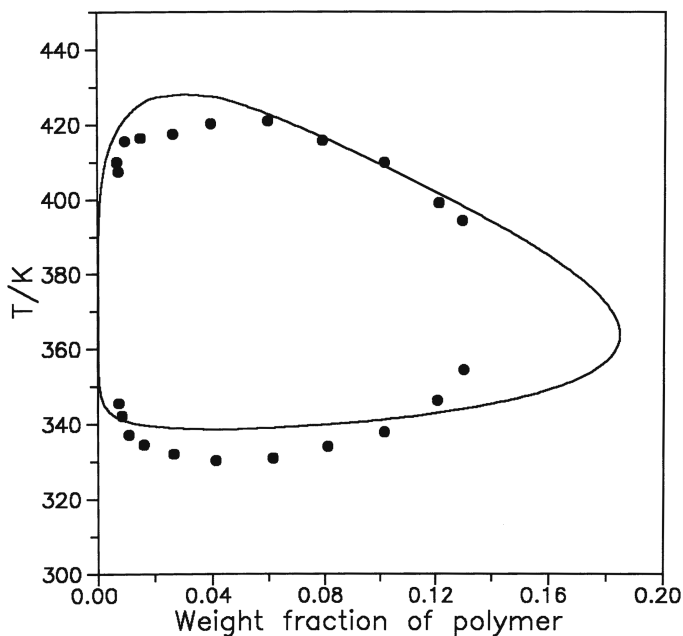


FIGURE 16.4 Correlation of LLE for the PVAL/water system with the Entropic-FV/UNIQUAC model. ● Exp. data ($M_n = 140000$ g/mol); — correlation. (From Bogdanic, G. and Vidal, J., *Fluid Phase Equilibria*, 173, 241–252, 2000. With permission.)

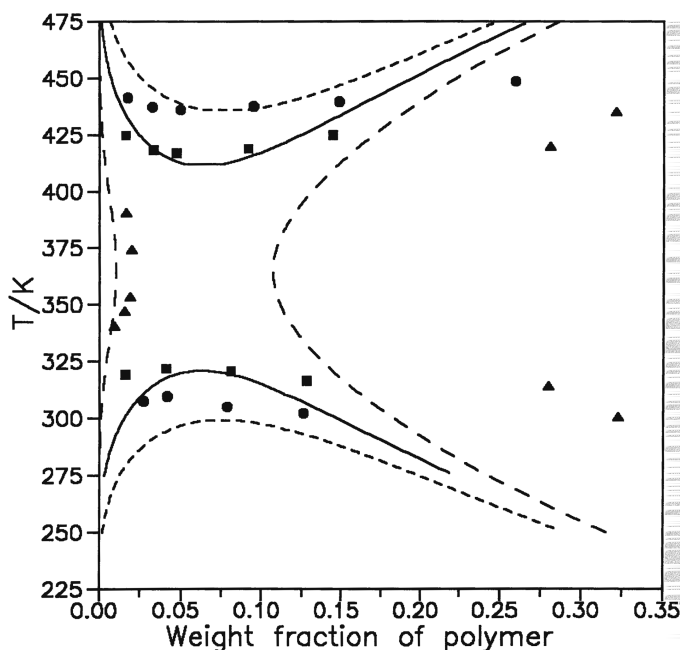


FIGURE 16.5 Correlation and prediction of LLE for the PBD/1-octane system with the Entropic-FV/UNIQUAC model. ■ Exp. data ($M_v = 65000$ g/mol), — correlation; ▲ Exp. data ($M_v = 135000$ g/mol), — prediction; ● Exp. data ($M_w = 44500$ g/mol), - - - prediction. (From Bogdanic, G. and Vidal, J., *Fluid Phase Equilibria*, 173, 241–252, 2000. With permission.)

for polymer solutions and blends. On the other hand, the Entropic-FV model has been applied to many types of polymer–solvent and polymer–polymer phase equilibria:

- VLE including infinite dilution conditions for binary polymer solutions^{50,86,94}
- SLE of asymmetric alkane solutions^{85–88}
- LLE for binary polymer solutions¹⁰⁸
- LLE for polymer blends¹⁰⁹
- VLE for copolymer–solvent systems³⁸
- SLLE for semicrystalline polymer–solvent systems⁵⁵
- VLE for a large variety of polar and hydrogen bonding systems¹¹⁰
- LLE for ternary polymer–solvent–solvent (and solvent–antisolvent) systems⁸
- VLE for paint-related polymer solutions including commercial epoxy resins^{39,40,111}
- VLE for ternary polymer–mixed solvent systems¹¹²

(The abbreviations for the various types of phase equilibria are as follows: VLE = vapor–liquid equilibria, LLE = liquid–liquid equilibria, SLLE = solid–liquid–liquid equilibria, SLE = solid–liquid equilibria.)

Some typical results are shown in [Figure 16.2](#) (LLE for PS/acetone), [Table 16.4](#) (infinite dilution activity coefficient for PBMA solutions in a variety of solvents), [Tables 16.5](#) and [16.6](#) (activity coefficients of low- and heavy-molecular-weight alkanes in asymmetric athermal–alkane solutions), [Table 16.7](#) (VLE for ternary polymer–solvent solutions), [Figure 16.6](#) (VLE calculations for systems containing the commercial epoxy resin Araldit), and [Table 16.8](#) (comparison of LLE results from various thermodynamic models).

Overall, we can conclude that Entropic-FV provides satisfactory predictions of solvent activities, even at infinite dilutions, when mixed solvents are present and for complex polar and hydrogen

TABLE 16.7
Prediction of Ternary Polymer–Solvent VLE with Predictive Models

System	Temperature, K	Solvent	%AAD			
			Entropic-FV	UNIFAC-FV	GC-Flory	GCLF
Based on Activities						
PMMA–butanone–acetone	308.15	Butanone	35	27	36	29
		Acetone	93	127	24	22
PMMA–toluene–butanone	308.15	Butanone	95	117	81	75
		Toluene	83	80	73	71
PS–chloroform–CCl ₄	323.15	Chloroform	18	8	147	32
		CCl ₄	42	37	164	83
PS–toluene–ethylbenzene	303.15	Toluene	6	5	32	14
		Ethylbenzene	11	11	18	7
PS–toluene–cyclohexane	303.15	Toluene	11	8	—	13
		Cyclohexane	4	7	—	9
PVAc–acetone–ethylacetate	303.15	Acetone	7	7	12	15
		Ethylacetate	10	13	19	9
PVAc–acetone–methanol	303.15	Acetone	12	11	25	17
		Methanol	10	9	10	9
Average			31	33	53	29
Average, excl first two systems			13	11	43	21
Average, excl first three systems			9	9	14	11
Based on Inactivities						
PMMA–butanone–acetone	308.15	Butanone	36	24	38	30
		Acetone	49	54	16	16
PMMA–toluene–butanone	308.15	Butanone	45	55	39	37
		Toluene	310	278	229	214
PS–chloroform–CCl ₄	323.15	Chloroform	13	6	71	23
		CCl ₄	17	24	136	310
PS–toluene–ethylbenzene	303.15	Toluene	7	5	32	16
		Ethylbenzene	15	15	26	9
PS–toluene–cyclohexane	303.15	Toluene	15	10	—	20
		Cyclohexane	7	9	—	14
PVAc–acetone–ethylacetate	303.15	Acetone	10	10	20	22
		Ethylacetate	12	16	22	10
PVAc–acetone–methanol	303.15	Acetone	15	13	32	22
		Methanol	30	25	21	19
Average			42	39	57	54
Average, excl first to systems			14	13	36	46
Average, exl first three systems			14	13	19	16

Note: Average absolute deviations between experimental and predicted solvent activities for ternary polymer–solvent systems. Predictions are shown with the Entropic-FV and UNIFAC-FV activity coefficient models as well as with two GC equations of state: GC-Flory and GCLF. Results are reported based on both the activities and the logarithms of the activities.

bonding systems including solutions of interest to paints and coatings. The model can be readily applied to LLE and SLE and is shown to predict all types of phase diagrams present in polymeric systems (UCST, LCST, hourglass-type). However, the results are more of qualitative than of quantitative value in most cases. In the cases of polymer blends, where FV effects are not very important, the model deviates substantially from experimental data, although it can predict the

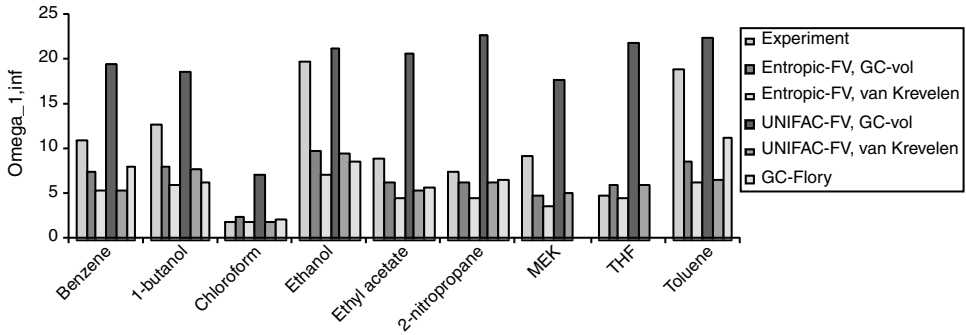
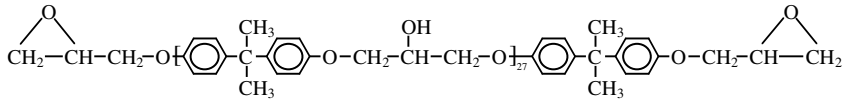


FIGURE 16.6 Molecular structure of the paint Araldit 488 and infinite dilution activity coefficients (Ω_1^∞) with various models for Araldit 488–solvent systems. Results are shown with the Entropic-FV and UNIFAC-FV activity coefficient models and the GC-Flory equation of state. The calculations with the two activity coefficient models are shown for two different values of the density of the polymer, predicted by the GC-VOL and van Krevelen models. (Modified from Lindvig et al., *AIChE J.*, 47(11), 2573–2584, 2001.)

TABLE 16.8
Prediction of LLE for Polymer–Solvent Systems with Various Thermodynamic Models

Polymer System	Molecular Weight	van der Waals	Entropic-FV	new-UNIFAC	GC-Flory
PS/acetone	4800	109	84	21	75
PS/acetone	10300	69	98	8	42
PS/cyclohexane	20400	10	38	62	—
PS/cyclohexane	37000	7	26	59	—
PS/cyclohexane	43600	1	24	63	—
PS/cyclohexane	89000	0	11	60	—
PS/cyclohexane	100000	0	15	62	—
PS/cyclopentane	97200	10	27	105	—
PS/cyclopentane	200000	7	12	103	—
HDPE/ <i>n</i> -butyl acetate	13600	102	10	82	72
HDPE/ <i>n</i> -butyl acetate	20000	118	22	97	70
HDPE/ <i>n</i> -butyl acetate	61100	128	29	107	71
PMMA/1-chloro butane	34760	2	53	—	—
PBMA/ <i>n</i> -pentane	11600	10	Hourglass	—	—
PBMA/ <i>n</i> -octane	11600	30	155	—	—

Note: Absolute difference (in K) between experimental and predicted UCST for several polymer solutions using various models (based on results from References 108 and 124). All results are predictions. The three last models are based on group contributions. The new-UNIFAC model is a combination of FH with the UNIFAC residual term. The predictions with the van der Waals equation of state are based on a very simple correlation of the interaction parameter with the molecular weight of the solvent alone presented in Reference 123.

PS: polystyrene; HDPE: high-density polyethylene; PMMA: poly(methyl methacrylate); PBMA: poly(butyl methacrylate).

UCST-type behavior. Compared with the other FV models, Entropic-FV may be considered as the most successful and widely used extension of UNIFAC to polymers. A more detailed discussion of the results as well as comparison with the other approaches are presented in Section 16.7.

16.4.4 MORE RECENT APPROACHES IN THE FREE-VOLUME TERM

Despite the overall successful performance of Entropic-FV and UNIFAC-FV models for a large number of systems and types of phase equilibria, it has been shown over the last several years by a number of researchers,^{87,88,94,113,114} that the combinatorial/FV terms of both the Entropic-FV and UNIFAC-FV models have a number of deficiencies:

1. The solvent activities in athermal polymer solutions are systematically underestimated, often by 10% (in the case of Entropic-FV) or more (for UNIFAC-FV). For athermal systems, the residual term is zero. Such an error cannot be entirely attributed to the small interaction effects present in such systems.
2. The activities of heavy alkanes in short-chain ones, available from SLE measurements, are in significant error, especially as the size difference increases. Because of the lack of experimental data on polymer activities, such SLE data can help in testing the applicability of the models at the nonsolvent concentration end (activities of polymers).
3. The performance of the models is rather sensitive to the values used for the polymer density.

To account for one or more of these deficiencies, a number of entropic formulas have been proposed over the last few years. Kontogeorgis et al.^{86,113} have proposed the following two modifications (p-FV, Chain-FV) of Entropic-FVs combinatorial/FV term:

p-FV:⁸⁶

$$\ln \gamma_i^{\text{comb-fv}} = \ln \frac{\Phi_i^{\text{fv}}}{x_i} + 1 - \frac{\Phi_i^{\text{fv}}}{x_i}$$

$$\Phi_i^{\text{fv}} = \frac{x_i (V_i - V_{i,w})^p}{\sum_j x_j (V_j - V_{j,w})^p} \quad (16.53)$$

$$p = 1 - \frac{V_{w,1}}{V_{w,2}}$$

Chain-FV:¹¹³

$$\ln \gamma_i^{\text{comb-fv}} = \ln \frac{\Phi_i}{x_i} + 1 - \frac{\Phi_i}{x_i} + c_i \ln \left(\frac{\Phi_i^{\text{fv}}}{\Phi_i} \right) + c_m \left(\frac{\Phi_i}{x_i} - \frac{\Phi_i^{\text{fv}}}{x_i} \right) \quad (16.54)$$

The p-FV model is an empirical modification of the Entropic-FV model (Equation 16.51). The Chain-FV formula can be theoretically derived from statistical mechanics (from the generalized van der Waals partition function) and it attempts to include rotational/vibrational effects. It is interesting to see that, as limiting cases, the Chain-FV model results in the FH equation when the FV (Φ_i^{fv}) and volume Φ_i fractions coincide and in Entropic-FV when $c_i = 1$.

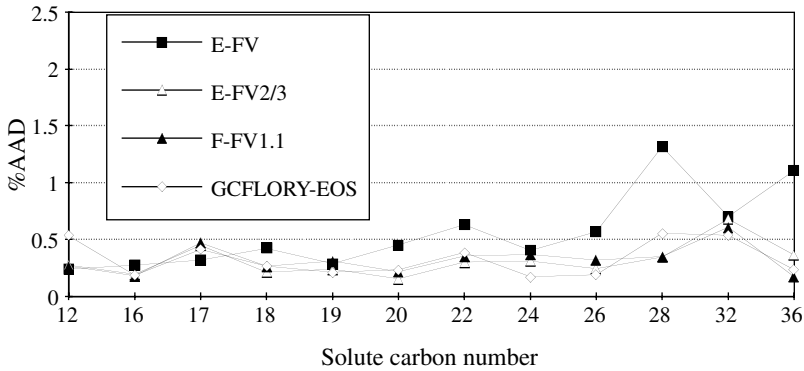


FIGURE 16.7 Average deviations in solid–liquid equilibrium calculations, as a function of the solute carbon number, for alkane systems using various FV models. E-FV is the Entropic-FV model. F-FV1.1 is the Flory-FV model using $c = 1.1$. GCFLORY EoS is the GC-Flory equation of state. (From Coutinho, J.A.P. et al., *Fluid Phase Equilibria*, 103, 23, 1995. With permission.)

Based on the FV definition adopted by Flory (Equation 16.47), the following so-called Flory-FV model has been proposed:⁸⁶⁻⁸⁸

$$\ln \gamma_i^{\text{comb-fv}} = \ln \frac{\Phi_i^{\text{fv}}}{x_i} + 1 - \frac{\Phi_i^{\text{fv}}}{x_i}$$

$$\Phi_i^{\text{fv}} = \frac{x_i V_{i,\text{fv}}}{\sum_j x_j V_{j,\text{fv}}} = \frac{x_i (V_i - V_{wi})^{3.3}}{\sum_j x_j (V_j - V_{wj})^{3.3}} \quad (16.55)$$

This model has been shown⁸⁷ to be particularly useful for SLE calculations for size-asymmetric alkane systems. A typical result is given in [Figure 16.7](#).

Finally, Voutsas et al.¹¹⁴ and Zhong et al.¹¹⁵ have proposed two combinatorial/FV formulas suitable for polymer solutions, which do not include the volume of the compounds:

R-UNIFAC:¹¹⁴

$$\ln \gamma_i^{\text{comb-fv}} = \ln \frac{\Psi_i}{x_i} + 1 - \frac{\Psi_i}{x_i} - \frac{z}{2} q_i \left(\ln \frac{\Phi_i}{\vartheta_i} + 1 - \frac{\Phi_i}{\vartheta_i} \right)$$

$$\Psi_i = \frac{x_i V_{wi}^R}{\sum_j x_j V_{wj}^R} \quad (16.56)$$

$$R = 0.9 \left(1 - \frac{V_{w,\text{small}}}{V_{w,\text{large}}} \right)$$

The segment and surface area fractions are given by the equations:

$$\Phi_i = \frac{x_i V_{wi}}{\sum_j x_j V_{wj}} \quad (16.57)$$

$$\vartheta_i = \frac{x_i q_i}{\sum_j x_j q_j} \quad (16.58)$$

Zhong et al.:¹¹⁵

$$\ln \gamma_i^{\text{comb-fv}} = \ln \frac{\Phi'_i}{x_i} + 1 - \frac{\Phi'_i}{x_i} - \frac{z}{2} q_i \left(\ln \frac{\Phi_i}{\vartheta_i} + 1 - \frac{\Phi_i}{\vartheta_i} \right) \quad (16.59)$$

The “modified” volume fraction is, for a solvent, given by the equation:

$$\Phi'_1 = \frac{x_1 V_{w1}}{x_1 V_{w1} + x_2 0.6583 V_{w2}} \quad (16.60)$$

The articles cited in this section also include investigations that compare the performance of these more recent FV equations for athermal systems. Although the database used in the various investigations is not always the same, this typically consists of solutions with components differing significantly in size but which do not exhibit energetic interactions. These nearly athermal systems are solutions of polyethylene and polyisobutylene with alkanes (only solvent activities are available), alkane solutions (where both the activity of light- and heavy-chain alkanes are available), polystyrene/ethylbenzene, polyvinyl acetate/vinyl acetate as well as “pseudo” experimental data for polymer activities generated with molecular simulation techniques.¹¹⁶

Some overall comparisons are provided in [Tables 16.5](#) and [16.6](#) (activity coefficients for alkane systems). The general conclusions that can be drawn based on these results and those presented in the various literature investigations are as follows (see also [Section 16.7](#)):

1. The activities of alkane solvents in either alkane or athermal polymer (PE, PIB) solutions are very satisfactorily predicted (much better than the Entropic-FV formula) by some of the modified equations cited above (Chain-FV, p-FV, R-UNIFAC). However, these models cannot be extended to multicomponent systems.¹¹⁷ This is apparently a serious limitation for these models.
2. Volume-based models perform better than those not including volume-containing terms.
3. The UNIFAC-FV expression (Equation 16.49), the first FV equation proposed, which is derived from the theory of Flory, is not as successful for athermal systems compared to more recent simpler equations. This may be due to the values of the parameters *b* and *c* employed in this model. Fitting these parameters may improve the performance of the UNIFAC-FV term. The results with this model seem particularly sensitive to the density values employed ([Figure 16.3](#)).
4. All models perform clearly less satisfactorily for the activities of heavy alkanes in short-chain ones, especially as the size asymmetry increases. Models without FV corrections such as UNIFAC, ASOG, and FH are particularly poor in these cases. Unfortunately, such activity coefficient measurements, which are used for testing the performance of the models for the activities of polymers, are scarce. Direct measurements for polymer

activities have not been reported. Molecular simulation studies can offer help in this direction. The Flory-FV model seems to be the best of these approaches, which at the same time has no restrictions for multicomponent systems.

16.5 CUBIC EQUATIONS OF STATE FOR POLYMERS

16.5.1 GENERAL

Equations of state offer a number of advantages over activity coefficient models; for example, they can be applied to both low and high pressures, for properties other than phase equilibria, and the density is not required as an input parameter. However, often they are more difficult to develop for complex fluids and mixtures than are activity coefficient models. Very many equations of state have been proposed for polymers; Section 16.7 discusses the reason. Recent reviews have been presented.^{1,91,118,119} We will not attempt to cover all the various approaches, but essentially discuss in detail only two of them, which seem promising for polymer solutions and blends: the cubic equations of state and the SAFT (Statistical Associating Fluid Theory) method.

Originally, basically noncubic equations of state, often with some theoretical background on statistical mechanics, have been proposed for polymer systems. To date, it is generally accepted that both cubic and noncubic equations of state can be used for correlating polymer–solvent equilibria. Orbey et al.¹²⁰ recently reviewed several cubic equations of state for polymers.

Another way to differentiate the various equations of state is based on their predictive capabilities; i.e., whether they can be used only as correlative models or for predicting phase equilibria as well. “Correlative models” can describe phase equilibria using one or more “interaction parameters,” which are typically determined from experimental data. If such parameters can be generalized or predicted from independent information, these models may fall into the category of “predictive models.” The distinction between correlative and predictive models is not always clear.

16.5.2 CUBIC EQUATIONS OF STATE

Cubic equations of state like the Soave-Redlich-Kwong (SRK) and Peng–Robinson (PR) equations have been traditionally employed in the oil and chemical industry. Although known from the early 1900s, until recently, cubic equations have not been extended to polymer solutions, mostly due to the alleged deficiencies of the van der Waals repulsive term for such systems. The first extension of cubic EoS to polymers was made as late as 1990 by Sako et al.¹²¹ The Sako et al. cubic equation of state was originally applied exclusively to the high-pressure polyethylene/ethylene system, but no subsequent articles presenting other applications appeared in the forthcoming years. However, the model was used in industry (Krooshof, G., 1999, personal communication) for the polyethylene and related high-pressure processes. It was only later, after 1994, that a large number of independent researchers have clearly shown that cubic equations of state can be applied to both polymer solutions and blends and for both VLE and LLE. Some of the most known efforts are as follows:

1. The van der Waals equation of state has been shown since 1994 by Kontogeorgis and co-workers to be successfully applied to polymer–solvent VLE,^{122,123} polymer–solvent LLE,^{124,125} Henry constants,^{126,127} and polymer blends.¹²⁸ The van der Waals–polymer project was carried out during the period 1994 to 1996 as a collaboration project between the Technical University of Denmark (Institut for Kemiteknik), Shell-Research (Amsterdam), and the Technical University of Athens (Greece).
2. The PR equation of state using the FH model with the Wong–Sandler mixing rules^{129,120} or combined with the Entropic-FV,¹³⁰ UNIFAC-FV,¹³¹ or ASOG-FV¹³² models in the mixing rule for the energy parameter or with other choices of mixing rules, such as the classical van der Waals one-fluid¹³³ or others.^{134,135}

3. The SRK equation of state has been also quite extensively applied, using activity coefficient models in the mixing rule for the energy parameter^{136,137} or mixing rules of the van der Waals one-fluid type.^{138,140}
4. Following the successes of the common cubic equations of state (van der Waals, SRK, and PR), the Sako equation of state has been “reevaluated” from some researchers, as shown by some recent applications.¹⁴¹⁻¹⁴⁶ In some of these recent efforts, an activity coefficient model suitable for polymers is employed in the mixing rule for the energy parameter.

In all the above efforts, two major directions for applying cubic equations of state can be identified:

1. As correlative models to describe phase equilibrium behavior provided experimental data are available. This approach is not useful for predictions but it is useful when accurate design is required (provided data are available).
2. Use as a predictive model via the “EoS/G^E” technique. This implies that an activity coefficient model is employed in the mixing rule for the energy parameter of cubic EoS.

In the following, we attempt to give a short unified representation of the various approaches, discussing the similarities and the differences of the various methodologies.

16.5.2.1 Cubic Equations of State for Pure Compounds

The cubic equations of state, which have been applied to polymer systems so far, are the van der Waals equation of state:

$$P = \frac{RT}{V-b} - \frac{a}{V^2} \quad (16.61)$$

the SRK equation of state:

$$P = \frac{RT}{V-b} - \frac{a}{V(V+b)} \quad (16.62)$$

the PR equation of state:

$$P = \frac{RT}{V-b} - \frac{a}{V(V+b)+b(V-b)} \quad (16.63)$$

and the Sako et al. equation of state:

$$P = \frac{RT(V-b+bc)}{V(V-b)} - \frac{a}{V(V+b)} \quad (16.64)$$

All the variables have the usual meaning; i.e., P is the pressure, T is the temperature, V is the molar volume, and R is the gas constant.

The van der Waals, SRK, and PR equations of state have only two parameters per pure fluid (a and b) that need to be estimated for solvents and polymers. The Sako et al. equation of state has three parameters. It can be shown that the Sako et al. repulsive term is essentially equivalent to the chain-free volume expression presented previously (Equation 16.54).

The a, b -values for solvents are estimated in the usual way, i.e., using the critical temperature, pressure, and acentric factor. However, for polymers critical property data are not available and, moreover, polymers are nonvolatile. Thus, all equation of state parameters need to be estimated from other types of data. Typically, densities, which are available over extended temperatures and pressures, are used. Different approaches have been proposed by various researchers:

1. Use of only two temperature-volume data at low pressures¹²²⁻¹²⁸
2. Use of extensive volumetric data over wide range of temperatures and pressures^{130,133}
3. Use of default values for the critical properties^{120,139}

In most approaches the vapor pressure of the polymer is set to a very low default value.

The estimated equation of state parameters seem to have some physical significance; e.g., they seem to be proportional to the polymer molecular weight.¹²² Moreover, it seems that the estimated b values represent a measure of the flexibility of polymer molecules; for many polymers and for different approaches, the parameter b is closely related to the van der Waals volume. Generally, the performance of these cubic equation of state in correlating volumetric (PVT) data, although it varies from model to model, is satisfactory considering the simplicity of the approach.

16.5.2.2 Extension of Cubic Equations of State to Mixtures

Irrespective of the functional form of the equation of state employed, two major methodologies have been employed for the extension to mixtures:

1. The use of the well-known van der Waals one-fluid or related mixing rules for the energy and co-volume parameters. These mixing rules require interaction parameters (especially in the energy term) and are employed for correlating experimental data.
2. The use of the so-called EoS/ G^E mixing rules, which were suggested in the early 1990s. This is a very powerful tool of applied thermodynamics, which permits a predictive use of cubic equations of state, when a GC (or other predictive) activity coefficient model is used for estimating the energy term of the equation of state. These methodologies are briefly reviewed in the next sections.

16.5.2.2.1 Van der Waals One-Fluid and Related Mixing Rules

These mixing rules are given by the equations:

$$a = \sum_i \sum_j x_i x_j a_{ij} \quad b = \sum_i \sum_j x_i x_j b_{ij} \quad (16.65)$$

They have been employed in the use of the van der Waals equation of state for polymers. They require combining rules for both the cross energy and cross co-volume parameters. Kontogeorgis et al.¹²² have employed the typically used geometric mean for the co-volume parameter, but they used the Berthelot rule for the cross-energy parameter:

$$a_{12} = \sqrt{a_1 a_2} \frac{b_{12}}{\sqrt{b_1 b_2}} (1 - L_{12}) \quad (16.66)$$

$$b_{12} = \frac{b_1 + b_2}{2}$$

L_{12} is the only interaction parameter of the equation of state. Generally it should be regressed from experimental data. Various correlations of the L_{12} parameter with the physical properties of the

system have been proposed for polymer solutions^{123,124} and blends.¹²⁸ Typically, different values are obtained from VLE and LLE data.

The equation for the cross-energy parameter a_{12} can be justified theoretically. It is based on the London theory for intermolecular forces combined with the Mie function for the intermolecular potential. We offer here a short derivation, as discussed recently.¹⁴⁷

The starting point for the derivation is the London equation for the cross-attractive intermolecular potential (Γ_{12}):

$$\Gamma_{12} = \sqrt{\Gamma_1 \Gamma_2} \left(\frac{2\sqrt{I_1 I_2}}{I_1 + I_2} \right) \quad (16.67)$$

and the Mie potential function:

$$\Gamma_{12} = \frac{m}{m-n} \left(\frac{m}{n} \right)^{\frac{n}{m-n}} \epsilon_{12} \left[\left(\frac{\sigma_{12}}{r} \right)^m - \left(\frac{\sigma_{12}}{r} \right)^n \right] \quad (16.68)$$

where I_i is the ionization potential of component i , ϵ_{12} is the molecular cross-energy parameter, σ_{12} is the molecular cross diameter, and r is the distance of the molecules.

Equation 16.67 is strictly valid for molecules exhibiting only dispersion forces, but its practical validity is considered to be greater. Inserting the attractive part of Equation 16.68 into Equation 16.67, we obtain:

$$\epsilon_{12} = \sqrt{\epsilon_1 \epsilon_2} \left(\frac{\sqrt{\sigma_1 \sigma_2}}{\sigma_{12}} \right)^n \left(\frac{2\sqrt{I_1 I_2}}{I_1 + I_2} \right) \quad (16.69)$$

A similar equation was first proposed by Hudson and McCoubrey and later by numerous researchers. Equation 16.69 is a general combining rule for the cross-energy parameter as a function of the molecular energy (ϵ) and size (σ) parameters. The exponent n is a characteristic of the potential function. The ionization potential term is often ignored. However, in some cases, as shown by Coutinho et al.¹⁴⁸ for CO₂/alkanes, the ionization term can be approximated using the co-volume parameters:

$$I \propto \frac{1}{\sigma^3} \Rightarrow \frac{2\sqrt{I_1 I_2}}{I_1 + I_2} \cong \left(\frac{\sqrt{b_1 b_2}}{b_{12}} \right)^{-1} \quad (16.70)$$

Equation 16.70 is not restricted to CO₂ systems but holds for other gas/alkane systems as well (CO, methane, ethane, hydrogen sulfide, etc.) and can be thus considered a reasonable approximation for some cases.

Using the proportionalities, relations between “microscopic” (ϵ, σ) and “macroscopic” properties,

$$\epsilon \propto \frac{a}{b} \propto T_c$$

$$\sigma^3 \propto b \propto V_c$$

and upon combining Equations 16.69 and 16.70, we arrive at the expressions for the cross-energy parameters, the cross-critical temperature ($T_{c_{12}}$):

$$T_{c_{12}} = \sqrt{T_{c_1} T_{c_2}} \left(\frac{\sqrt{V_{c_1} V_{c_2}}}{V_{c_{12}}} \right)^{\frac{n}{3}-1} \quad (16.71)$$

and the cross-energy parameter of cubic equations of state (a_{12}):

$$a_{12} = \sqrt{a_1 a_2} \left(\frac{\sqrt{b_1 b_2}}{b_{12}} \right)^{\frac{n}{3}-2} \quad (16.72)$$

By using Equations 16.71 and 16.72, the following simple expressions can be derived for the interaction parameter k_{ij} (correction to the geometric mean (GM) rule for the cross-critical temperature $T_{c_{12}} = \sqrt{T_{c_1} T_{c_2}} (1 - k_{ij})$ and the cross energy parameter $a_{12} = \sqrt{a_1 a_2} (1 - k_{ij})$):

$$k_{12} = 1 - \left(\frac{\sqrt{b_1 b_2}}{b_{12}} \right)^{\frac{n}{3}-2} \quad (16.73)$$

or

$$k_{12} = 1 - \left(\frac{\sqrt{V_{c_1} V_{c_2}}}{V_{c_{12}}} \right)^{\frac{n}{3}-1} \quad (16.74)$$

By using this analysis, various combining rules previously proposed in the literature can be deduced from different values for the exponent n of this general equation. For example, the GM rule typically employed in cubic equations of state is obtained for $n = 6$, while the Berthelot rule is reduced for $n = 3$. The value $n = 6$ corresponds to the widely used Lennard–Jones potential function. However, for asymmetric systems, several researchers have suggested that a value closer to $n = 3$ should be employed^{147,149}; e.g., Plocker et al.¹⁴⁹ suggested $n = 3.75$.

The fact that the GM rule is recovered for $n = 6$ (Lennard–Jones value) is an interesting result and offers some theoretical support for the GM rule. If the ionization potential term is ignored, as is usually done in the literature, then the GM rule is derived for $n = 3$, and the Berthelot for $n = 0$.

Other researchers^{134–136} have used other mixing rules similar to the van der Waals one-fluid rules. Some have been shown to yield improved results over the van der Waals one-fluid mixing rules.

16.5.2.2.2 EoS/ G^E Mixing Rules

The EoS/ G^E methodology is one of the novel successful concepts of applied thermodynamics and hundreds of papers have been published, especially over the last 10 years. The EoS/ G^E method is in fact a mixing rule for the energy parameter of cubic equations of state. In this mixing rule, via some matching procedure, the activity coefficient equation (G^E) of some known model, e.g., UNIFAC, NRTL, etc. is inserted. The starting equation used in the derivation is

$$\left(\frac{G^E}{RT} \right)_P^{\text{EoS}} = \left(\frac{G^E}{RT} \right)_P^{\text{model}*} \quad (16.75)$$

Equation 16.75 represents the basic principle (or starting point) in the development of the EoS/G^E models (mixing rules). The superscript * refers to the specific activity coefficient model used, e.g., UNIFAC or NRTL. For polymers, a suitable activity coefficient model such as the ones including FV effects should be used. The subscript P denotes that the equality of Equation 16.75 is valid at a certain pressure, which is called the “reference pressure.” Various choices have been proposed for the reference pressure. The most popular choices are the infinite and the zero reference pressures, but other choices have also been proposed.

The EoS/G^E method combines the best features of cubic equations of state and classical activity coefficient models. This is because, via this technique, at low pressures the behavior of the activity coefficient model is recovered. However, the model is also applicable at high pressures in a predictive way. It is important to note that existing parameter tables from, e.g., UNIFAC, UNIQUAC, etc. can be used. From the above it is understood that it is essential that the activity coefficient employed in the mixing rule should be as accurate as possible (at the low pressure limit).

Various EoS/G^E models have been proposed over the last several years for polymers. These models combine the SRK, the PR equation of state, or the Sako et al. cubic equation of state with FV activity coefficient models such as UNIFAC-FV, Entropic-FV, FH and the ASOG.

16.5.2.3 Results and Discussion

The various cubic equations of state have been quite extensively applied to polymer solutions and blends since 1990. More specifically:

1. The van der Waals equation of state was shown to:
 - Correlate, using a single parameter per binary system, binary polymer–solvent VLE and LLE (UCST). Of particular interest is the fact that the vdW EoS predicts a much flatter coexistence curve than the FH and other related models, in agreement with experimental evidence.
 - Correlate the LCST of binary polymer–solvents using a linearly temperature-dependent interaction parameter
 - Correlate the Henry’s constants of solvent–polymers (including gas–polymers) with a single parameter
 - Correlate the UCST of polymer blends with a single parameter per system. As with polymer solutions, a linearly temperature-dependent parameter is required for an accurate description of LCST.
2. The Sako et al. equation of state has been shown to:
 - Correlate the polyethylene/ethylene system
 - Describe the high-pressure binary and ternary polyolefin and copolymer (poly(ethylene-co-propylene)) systems
 - Correlate high pressure phase equilibria for certain polydisperse systems e.g., ethylene/poly(ethylene-co-vinyl acetate) and CO_2 /cyclohexane/polystyrene
3. The SRK and PR equations of state have been shown to:
 - Correlate polymer–solvent VLE better than the FH model, when the comparison is made using a single per binary interaction parameter
 - Correlate the high-pressure polyethylene/ethylene system
 - Correlate gas solubilities in various polymers — many different gases have been considered
 - Predict low-pressure VLE using various EoS/G^E mixing rules combined with activity coefficient models suitable for polymer solutions
 - Predict (using the modified Huron-Vidal *second order* (MHV2) mixing rule) the sorption of CO_2 in polyethylene glycol over extended pressure ranges
 - Predict (using EoS/G^E mixing rules) Henry’s law constants for different polymer solutions

4. The various EoS/ G^E mixing rules have been shown to be quite successful for binary polymer–solvent VLE, where they have been applied, since they reproduce (to a certain extent) at low pressures the behavior of a successful activity coefficient model for polymers. In addition, they are readily extended to high pressures as well, which is important in some polymer applications. Very few of these models have been extended to LLE, although reproduction of the behavior of the activity coefficient model incorporated (in the mixing rule) should be expected. Few applications to high pressures, where the true value of this approach would be appreciated, have been reported, e.g., the recent application of the SRK/MHV2 model to gas–solid polymer systems.¹³⁷ The limited investigation of the high-pressure applicability is partly explained by the lack of many high-pressure VLE data for polymer–solvent systems.

Finally, in the light of these extensive recent applications, an attempt to justify the use of cubic equations of state for polymer systems seems of interest. Traditionally, cubic equations of state had not been considered applicable to polymer systems because of alleged limitations of their functional form and especially the van der Waals–type repulsive term. We cite below two points that shed some light in why van der Waals–type equations may be applicable to asymmetric systems (e.g., alkane solutions with large size differences, polymer solutions):

1. The entropy of mixing of van der Waals–type equations, which is derived from the repulsive term, bears a remarkable functional similarity with that of explicit activity coefficient models, which are successfully applied to polymer solutions. Below are shown these equations for the van der Waals–type equation of state, the FH model and the Entropic-FV model (Elbro–Hildebrand term):

$$\begin{aligned} \frac{\Delta S^{\text{mix}}}{R} &= - \left(\sum_i x_i \ln \left(\frac{V_i - b_i}{V - b} \right) \right) && \text{van der Waals} \\ \frac{\Delta S^{\text{mix}}}{R} &= - \left(\sum_i x_i \ln \left(\frac{V_i^*}{V^*} \right) \right) && \text{FH} \\ \frac{\Delta S^{\text{mix}}}{R} &= - \left(\sum_i x_i \ln \left(\frac{V_i - V_{wi}}{V - V_w} \right) \right) && \text{Elbro – Hildebrand} \end{aligned} \quad (16.76)$$

In the FH formula, the characteristic volume V^* can be the molar volume or a specific hard-core volume of the molecule such as the van der Waals volume V_w . The last of the above equations is the Entropic-FV formula, discussed earlier (Equation 16.51). As shown, in the Entropic-FV model the van der Waals volume V_w is used, as a measure of the molecular volume with increments by Bondi. The Entropic-FV formula was shown to work satisfactorily for athermal polymer solutions and offers a substantial improvement over the FH term. The van der Waals repulsive term and the Entropic-FV form are functionally identical.

2. By using standard thermodynamics, the activity coefficient expression that corresponds to the van der Waals equation of state can be derived. When the van der Waals one-fluid mixing rules for the energy and co-volume parameters are employed, the van der Waals equation can be expressed as a sum of a combinatorial-FV and a regular solution term:

$$\begin{aligned}\ln \gamma_i &= \ln \gamma_i^{\text{comb-fv}} + \ln \gamma_i^{\text{res}} \\ &= \left(\ln \frac{\Phi_i^{\text{fv}}}{x_i} + 1 - \frac{\Phi_i^{\text{fv}}}{x_i} \right) + \left(\frac{V_i}{RT} (\delta_i - \delta_i)^2 \Phi_j^2 \right)\end{aligned}\quad (16.77)$$

$$\Phi_i^{\text{fv}} = \frac{x_i(V_i - b_i)}{\sum_j x_j(V_j - b_j)}$$

$$\delta_i = \frac{\sqrt{a_i}}{V_i}$$

Such an expression provides partial justification for the success of van der Waals-type equations for asymmetric polymer systems: the van der Waals equation is a sum of an improved FH (actually an FV) term and a regular solution energetic term. Furthermore, analysis of the contributions (attractive and repulsive) of cubic equations of state showed¹⁵⁰ that the classical (linear) combining rule for the co-volume parameter (Equation 16.66 for b_{12}) is the best choice for size asymmetric systems. This combining rule performs much better than the Lorentz and other combining rules for the cross-co volume parameter. Using this successful arithmetic mean rule for b_{12} , the combinatorial-FV term of the van der Waals equation of state is functionally identical to that of the Entropic-FV model.

16.6 THE SAFT EQUATION OF STATE

Very many noncubic equations of state have been proposed for polymers. Most of them are rather complicated and a few of them, such as several of the models discussed previously, are based on the GC concept, like the GC-Flory and the GCLF equation of state. Several of these equations of state are reviewed elsewhere,¹ and we will restrict here our presentation to one equation of state that is very promising for polymer systems and has already found widespread acceptance. This is the Statistical Associating Fluid Theory (SAFT).

The SAFT equation of state was proposed by Radosz, Gubbins, Jackson, and Chapman^{151,152} and is a model derived based on the perturbation theory of Weirtheim. SAFT is a noncubic equation with separate terms for the various effects (dispersion, polar, chain, hydrogen bonding). SAFT has already found extensive application in both polymer and oil industry, where different capabilities of the model have been exploited. In the oil industry, it is used for describing the complex multiphase equilibria of hydrogen bonding multicomponent systems, e.g., water-oil-alcohols (glycols). Several recent reviews of the SAFT equation of state are available,¹⁵³⁻¹⁵⁵ all of which present results for polymer solutions.

For polymer applications, SAFT has been extensively applied in industry (e.g., Exxon) mainly for polyolefin and related copolymer systems in both liquid solvents and supercritical fluids.¹⁵⁶⁻¹⁶⁰ Recently, a number of other applications have been reported:

- SLLE for some nonpolar polyethylene solutions¹⁶¹
- Polar polymer solutions¹⁶²⁻¹⁷⁴

One of the versions of SAFT, the so-called PC-SAFT developed by the group of Professor Sadowski,¹⁷⁵⁻¹⁷⁷ has been extensively applied to high-pressure polymer systems.

16.6.1 MODEL DESCRIPTION

The original SAFT equation of state is given by the equation:

$$Z = 1 + Z^{\text{seg}} + Z^{\text{chain}} + Z^{\text{assoc}} = 1 + m(Z^{\text{hs}} + Z^{\text{disp}}) + Z^{\text{chain}} + Z^{\text{assoc}} \quad (16.78)$$

where Z^{hs} , Z^{disp} , Z^{chain} , and Z^{assoc} account for the contributions to the compressibility factor of the hard-sphere repulsive interactions, the attractive dispersive interactions, the chain connectivity, and the hydrogen bonding. The parameter m is the number of segments per molecule. The various terms shown in Equation 16.78 are given by the expressions:

$$\begin{aligned} Z^{\text{hs}} &= \frac{4y - 2y^2}{(1 - y)^3} \\ Z^{\text{disp}} &= \sum_i \sum_j j D_{ij} \left(\frac{u}{kT} \right)^i \left(\frac{y}{0.74048} \right)^j \\ Z^{\text{chain}} &= (1 - m) \frac{2.5y - y^2}{(1 - y)(1 - 0.5y)} \\ Z^{\text{assoc}} &= \rho \sum_i x_i \sum_j x_j \sum_A \left[\left(\frac{1}{X^{A_j}} - \frac{1}{2} \right) \frac{\partial X^{A_j}}{\partial \rho_i} \right] \end{aligned} \quad (16.79)$$

The variables of Equations 16.79 have the following meaning:

- y is the packing fraction, a measure of the reduced density:

$$y = \frac{\pi N_{AV}}{6} \rho m d^3$$

- The temperature-dependent segment diameter d is related to the temperature-independent diameter σ via

$$\frac{d}{\sigma} = 1 - C \exp\left(\frac{-3u}{kT}\right)$$

- The hard-core volume v^* is related to the temperature-independent parameter:

$$v^* = \frac{\pi N_{AV}}{6\tau} \sigma^3$$

- u/k is the dispersion energy
- D_{ij} are universal constants

Two points should be noted here:

1. For the Z^{disp} term, various equations based on different theoretical considerations have been proposed.
2. For nonassociating systems, the Z^{assoc} term of Equation 16.78 is omitted.

In the association term of Equation 16.79, X^{A_i} is the mole fraction of the molecule i not bonded at site A, i.e., the monomer mole fraction. This is a function of density and of a property called “association strength.” X^{A_i} and the association strength between two association sites belonging in two different molecules ($\Delta^{A_i B_j}$) are defined as

$$X^{A_i} = \left(1 + \rho \sum_j \sum_{B_j} x_j X^{B_j} \Delta^{A_i B_j} \right)^{-1} \quad (16.80)$$

$$\Delta^{A_i B_j} = g(\rho) \left[\exp\left(\frac{\epsilon^{A_i B_j}}{RT}\right) - 1 \right] \sigma_{ij} \kappa^{A_i B_j}$$

where ϵ^{AB}/k is the association energy, κ^{AB} is the volume of association, and $g(\rho)$ is the radial distribution function. The association energy and volume are related to the enthalpy and entropy of hydrogen bonding.

The association and chain terms are obtained from the Wertheim theory. Recently,^{178,179} an expression for the association term has been presented. It is identical to that of the Wertheim theory, as cited by Chapman et al.,¹⁵² but mathematically significantly simpler.

The determination of X^A depends on the association scheme, i.e., the exact form of association, which is assumed for each hydrogen bonding (associating) molecule. Huang and Radosz¹⁵¹ present a table with association schemes for different types of associating molecules such as acids, alcohols, amines, and water. Different association schemes are typically required for the different molecules, and the table given by Huang and Radosz can be employed as a starting point in the establishment of the correct association scheme. The final choice, however, should be determined from a combination of intuition and experimental data.

The SAFT equation of state typically contains five pure compound parameters, which are estimated from both vapor pressure and liquid density data. These are the molecular size parameter m , the segment size parameter v^* , the segment energy parameter u^0/k , and the two association parameters: the association energy ϵ^{AB}/k and the association volume κ^{AB} .

For polymers, the parameters are estimated from volumetric (PVT) data. Alternatively, for polyolefins the parameters can be estimated by extrapolating the n -alkane parameters.

The repulsive, chain, and hydrogen bonding terms are extended to mixtures rigorously, and so mixing rules are needed only for the dispersion term of the equation. The van der Waals one-fluid mixing rules are used, which involve only one temperature-independent interaction parameter k_{ij} :

$$\frac{u}{kT} = \frac{\sum_i \sum_j x_i x_j m_i m_j \left[\frac{u_{ij}}{kT} \right] (v^*)_{ij}}{\sum_i \sum_j x_i x_j m_i m_j (v^*)_{ij}} \quad (16.81)$$

where the cross-co-volume is given by the Berthelot rule:

$$(v^*)_{ij} = \left[\frac{1}{2} \left\{ (v^*)_i^{1/3} + (v^*)_j^{1/3} \right\} \right]^3 \quad (16.82)$$

and the cross-energy parameter is given by the GM rule:

$$u_{ij} = \sqrt{u_i u_j} (1 - k_{ij}) \quad (16.83)$$

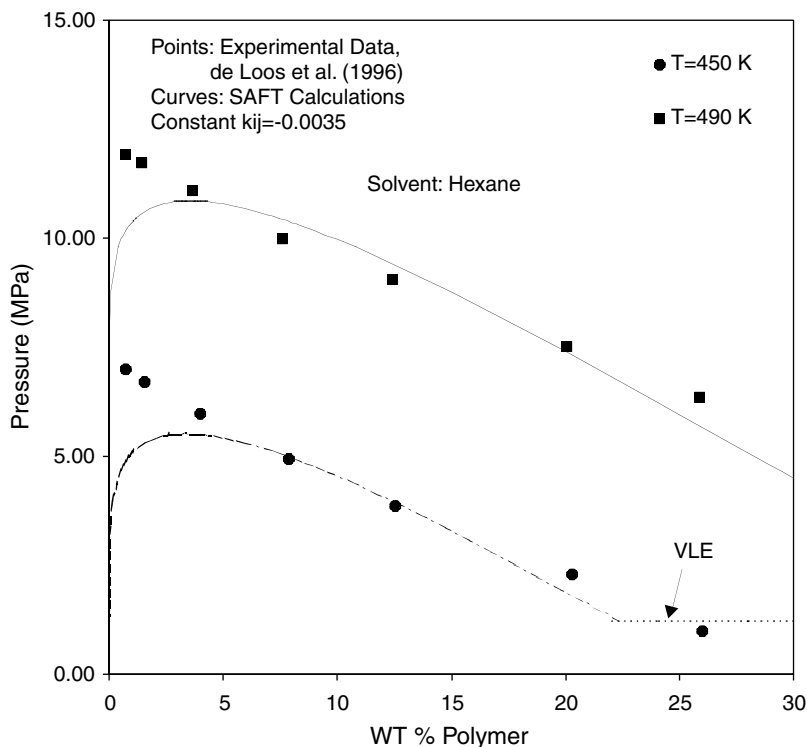


FIGURE 16.8 Cloud-point curves for the poly(ethylene-octene) ($M_n = 33000$)–hexane system from experiment points and the SAFT equation of state (curves). (From Jog, P.K. et al., *Ind. Eng. Chem. Res.*, 41(5), 887, 2002. With permission.)

Other mixing rules have been proposed for asymmetric systems,¹⁸⁰ such as water–hydrocarbons.

16.6.2 RESULTS AND DISCUSSION

Various modifications of the SAFT equation of state have been already proposed over the last several years. These have been presented in recent reviews.¹⁵³⁻¹⁵⁵ It is worth mentioning that in all these SAFT modifications different attractive terms are proposed, i.e., different terms for the Z^{disp} of Equation 16.78. The chain and association terms remain unchanged. SAFT is available in existing process simulators by Aspen Tech and Simulation Sciences, and it is used by several industries (examples of applications have been reported by Exxon Research and Engineering Company and Shell Oil Company). However, in these simulators, only the nonassociating contributions are incorporated. The SAFT equation of state has been extensively applied to nonpolymeric systems as well, including mixtures of hydrocarbons, water, alcohols, and phenols. A few applications to cross-associating systems, e.g., alcohol–water, have been also reported.

For polymer systems, most applications are related to the high-pressure polyethylene technology. Typical results are shown in Figures 16.8 through 16.13.

The most important conclusions from the various applications of the SAFT theory to polymer-containing systems are as follows:

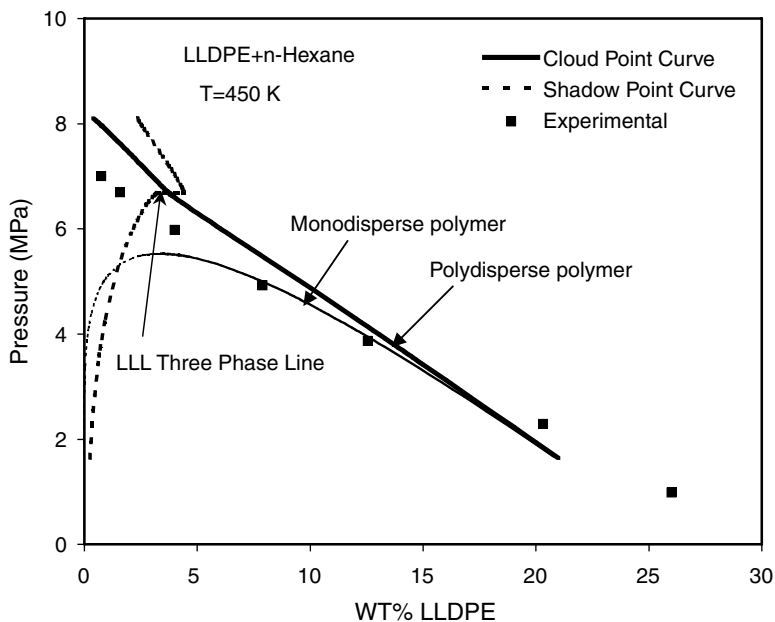


FIGURE 16.9 The cloud-point and shadow curves for poly(ethylene-octene)-hexane at 450 K from experiment (points) and the SAFT equation of state (curves). The dotted curve shows the composition of the incipient phase at the cloud point. Results for monodisperse and polydisperse polymer are included. (From Jog, P.K. et al., *Ind. Eng. Chem. Res.*, 41(5), 887, 2002. With permission.)

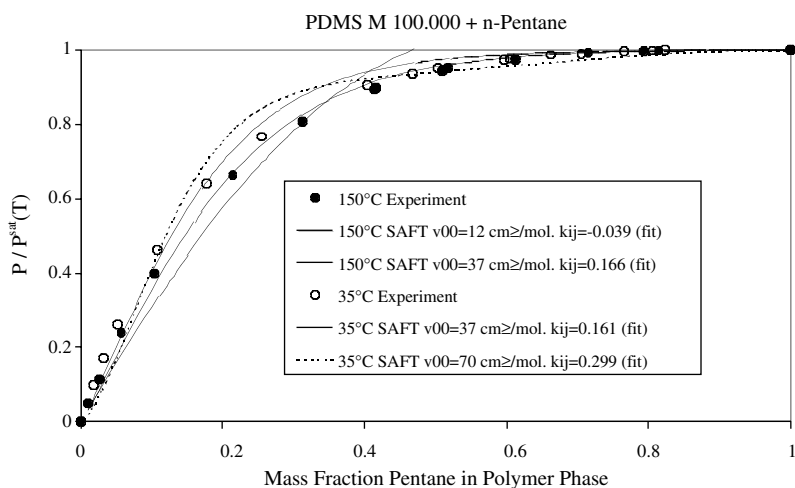


FIGURE 16.10 Pressure-composition phase diagram for the system polydimethylsiloxane (PDMS) — *n*-pentane with the SAFT equation of state. Using PDMS pure-component parameter sets, which reproduce the PDMS densities well, no acceptable reproduction of the binary equilibria is possible. (From Pfohl, O. et al., *Fluid Phase Equilibria*, submitted, 2001. With permission.)

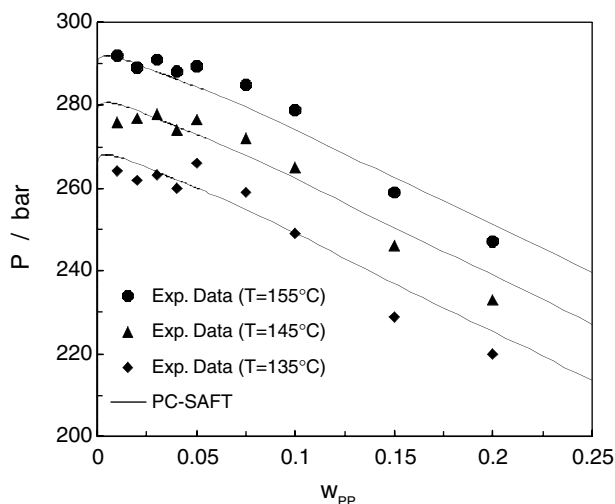


FIGURE 16.11 LLE of polypropylene (PP)–propane at three temperatures in a pressure–weight fraction plot. (PP: $M_w = 290$ kg/mol, $M_w/M_n = 4.4$). Comparison of experimental cloud points to PC-SAFT calculations ($k_{ij} = 0.0242$). The polymer was modeled using three pseudo-components. (From Tumakaka, F. et al., *Fluid Phase Equilibria*, 541, 194–197, 2002. With permission.)

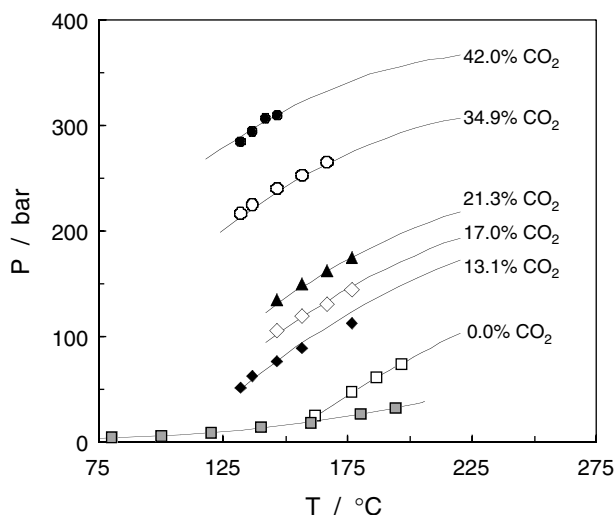


FIGURE 16.12 Cloud-point curve of polypropylene (PP)–n-pentane–CO₂ for various CO₂ contents. Initial polymer weight fraction $w_{pp} = 0.03$ (before the addition of CO₂). Comparison of experimental cloud points⁶⁰ to PC-SAFT calculations (PP–n-pentane: $k_{ij} = 0.0137$, PP–CO₂: $k_{ij} = 0.177$, n-pentane–CO₂: $k_{ij} = 0.143$). (From Tumakaka, F. et al., *Fluid Phase Equilibria*, 541, 194–197, 2002. With permission.)

1. Excellent description of high-pressure VLE and LLE of systems containing polyethylene and related polymers is obtained. Similarly, good results are obtained for the Henry's law constants for various solvents in polyethylene.
2. The SAFT model has not been applied to associating polymers or to systems containing hydrogen bonding solvents (alcohols, water, etc.). Investigations by numerous researchers show that the extension of SAFT to polar polymers may be difficult. Parameters for PDMS, PMMA, polycarbonates, and other polymers obtained by fitting volumetric data

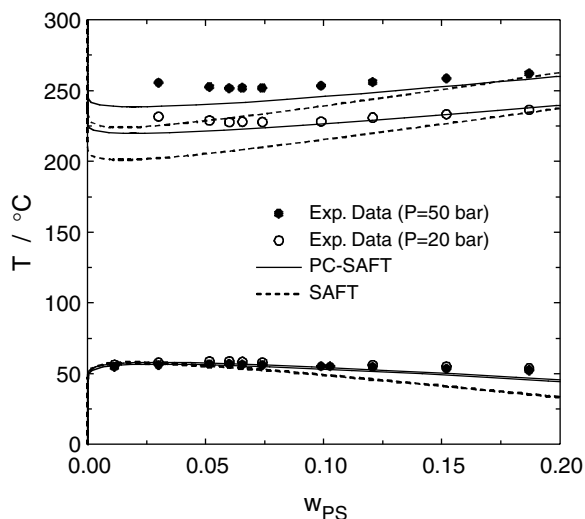


FIGURE 16.13 Liquid–liquid demixing of polystyrene (PS)–methylcyclohexane at pressures of 20 and 50 bar. (PS: $M_w = 405$ kg/mol, $M_w/M_n = 1.832$). Comparison of PC-SAFT ($k_{ij} = 0.007$) and SAFT ($k_{ij} = 0.023$) correlation results to experimental data. The polymer is modeled as monodisperse. (From Tumakaka, F. et al., *Fluid Phase Equilibria*, 541, 194–197, 2002. With permission.)

are not suitable for correlating phase equilibria. It is expected that significant effort is needed in the future for resolving this serious deficiency.

3. An extension of SAFT to systems containing electrolytes has appeared. However, the model has not as yet been extended to polyelectrolytes.
4. Limited comparisons of SAFT with other models have been reported. In a recent review, Kang et al.¹¹⁹ compared SAFT to the PR equation of state. Similar deviations are observed for the VLE of a few polymer–solvent systems investigated.
5. Several impressive applications of SAFT has been reported, such as the critical micellar densities for the PVAC-PTAN (a block copolymer)–CO₂ system and systems including telechelic polymers.

16.7 DISCUSSION OF THE MODELS

16.7.1 WHY SO MANY MODELS FOR POLYMER SYSTEMS?

Why have so many different models been developed for polymer systems? The situation could be easily considered confusing for the practicing engineer. Polymer solutions and blends are complicated systems: the frequent occurrence of LLE in many forms (UCST, LCST, closed loop), the significant effect of temperature and polymer molecular weight in phase equilibria, the FV effects, and other factors cause these difficulties. The choice of a suitable model depends on the actual problem and demands, especially the following:

- Type of mixture (solution or blend, binary or multicomponent)
- Type of phase equilibria (VLE, LLE, SLLE, gas solubility)
- Conditions (temperature, pressure, concentration)
- Type of calculations (accuracy, speed, yes/no answer, or complete design)

In their recent review paper, “Properly model polymer processes,” Bokis et al.⁹¹ from Aspen list the polymer models currently supplied in the ASPEN-Plus Process Simulator:

Activity Coefficient	Equations of State
Flory-Huggins	Sanchez-Lacombe
Polymer-NRTL	SAFT
UNIFAC-FV	Polymer-SRK

The performance of various models and their range of application have been discussed briefly throughout the chapter. We summarize and enhance this discussion here.

16.7.2 RESULTS FOR ATHERMAL POLYMER SOLUTIONS

Athermal polymer systems provide a very useful means for testing the “heart,” i.e., the combinatorial and FV terms of the various thermodynamic models. Several comparisons have been presented in the literature for such systems.^{85-88,96,110,113} The review by Lee and Danner⁹⁶ is quite thorough considering a large part of available VLE data for different types of polymer–solvent binaries (with nonpolar solvents, weakly polar and hydrogen bonding ones) and four different literature models (GCLF, UNIFAC-FV, Entropic-FV, GC-Flory). In their recent review, Pappa et al.,¹¹⁰ considered over 200 experimental data points for athermal polymer solutions at intermediate concentrations and about 100 points at infinite dilution and compared the Entropic-FV and Zhong–Masuoka models. They found that the Entropic-FV formula (Equation 16.51) yields lower error than the Zhong term (Equation 16.59), which, however, does not contain any volume terms (9% vs. 16%). Other literature comparisons⁸⁵⁻⁸⁷ also agree that the FV models with volume-containing terms perform better than those models requiring no volume information. Thus, Entropic-FV, Flory-FV, and related models provide a good basis for building a full thermodynamic model for polymers. More complicated FV terms such as the one derived from the Flory equation of state and used in UNIFAC-FV seem to offer no advantage over the simpler approaches. Moreover, more complicated FV terms seem to be more sensitive^{40,110-112} to the volume values employed compared with simpler FV equations. Typical results are shown in [Tables 16.5](#) and [16.6](#).

16.7.3 RESULTS FOR NONPOLAR AND SLIGHTLY POLAR SYSTEMS — VAPOR LIQUID EQUILIBRIA

Numerous results (predictions and correlations) are available for such systems.^{24,31,96} Many models perform satisfactorily even when pure predictions are considered. In a recent comparison, Pappa et al.¹¹⁰ showed that Entropic-FV performs better than the Zwong–Masuoka model (11% vs. 20%). In the review by Lee and Danner,⁹⁶ GCLF and Entropic-FV perform similarly for nonpolar systems (15%), but GCLF appears to perform better for the weakly polar systems. This is attributed to problems of the Entropic-FV model for systems containing polyacrylates and polymethacrylates with acetates. UNIFAC-FV has an average error of 23% for these types of systems and GC-Flory of 20%. Typical results are shown in [Table 16.4](#).

16.7.4 RESULTS FOR NONPOLAR AND SLIGHTLY POLAR SYSTEMS — LIQUID–LIQUID EQUILIBRIA

Some of the predictive models mentioned above, especially Entropic-FV (using either UNIFAC or UNIQUAC in the residual term), GC-Flory, and GCLF equations of state, have been applied to single solvent–polymer LLE, including both UCST and LCST calculations.^{105-108,185-187} Some typical results are shown in [Table 16.8](#) and [Figure 16.2](#). Each model has its strengths and weaknesses; possibly the Entropic-FV model is the most accurate, followed by GCLF. In particular, the combination of Entropic-FV + UNIQUAC seems very promising for predicting LLE at pressures and molecular weights other than those used in the parameter estimation¹⁰⁵⁻¹⁰⁷ ([Figure 16.5](#)). GC-Flory and GCLF perform better for LCST than for UCST. A difference of 10 to 30°C should be expected in the predictions. The performance of Entropic-FV is quite encouraging, as shown, for example, in [Figure 16.2](#) for PS/acetone, where it is shown that the model can predict all three different phase

equilibrium types (UCST, LCST, hourglass) and the molecular weight and temperature dependence of miscibility. The same observation is true for the Entropic-FV + UNIQUAC combination,¹⁰⁵⁻¹⁰⁸ with even better quantitative performance. The performance of Entropic-FV (when the UNIFAC model is used for the residual term) seems rather system specific, e.g., for polyethylene/octylphenols the difference in UCST is 5 to 10°C while for polyethylene/octanol it is approximately 40°C (Table 16.8).

A very interesting result is the correlative and predictive performance for the UCST of binary polymer solutions with the van der Waals equation of state.¹²⁴ Excellent correlation is achieved and reasonable prediction, using an extremely simple equation developed from athermal polymer–solvent VLE (which is simply a linear correlation of the interaction parameter with the molecular weight of the solvent). Two important comments can be made:

1. The van der Waals equation of state can successfully describe the UCST phase diagram over the whole temperature range with a single adjustable parameter. This is not possible with the FH and other related models, as discussed extensively in the literature.¹
2. A small change in the interaction parameter does not substantially change the phase diagram. For more complex models, e.g., GCLF, a very small change of the interaction parameter can cause significant changes in the phase diagram even a change from phase split to complete miscibility.¹⁸⁵

16.7.5 RESULTS FOR WATER-SOLUBLE POLYMERS AND OTHER HYDROGEN BONDING SYSTEMS

The PEG/water, PPG/water, and PVAL/water are among the most extensively studied water-soluble polymer solutions. These systems typically show a closed-loop phase behavior (Figure 16.4). Results for some ternary systems have been reported; many of these data are for PEG/Dextran/water and PEG/water/salts and related systems, which are important for separating biomolecules such as proteins. Only few data for PEG or other hydrogen bonding polymer with mixed water solvents have been reported.

The FH (and other similar) models can correlate such closed-type LLE behavior using a number (four to six) of adjustable parameters per binary system.⁶⁴ No predictions have been reported for such systems by other models.

Predictions have been provided for some hydrogen bonding systems, mostly for VLE, with a number of models. Pappa et al.¹¹⁰ report an average deviation of 26% (in VLE) with both Entropic-FV and Zhong–Masuoka models, which is higher than the deviations observed for nonpolar and polar systems. Lee and Danner's⁹⁶ comparison revealed that Entropic-FV is the best model for strongly polar solvents (23%), followed by GCLF (28%) and GC-Flory (31%). The classical FV model by Oishi and Prausnitz does not seem to be very successful for such complex systems (mean deviation 65%). In some recent investigations,^{40,111,112} several of these well-known GC models (Entropic-FV, UNIFAC-FV, GC-Flory) have been tested for VLE of paint-related systems. These are systems of polyacetates, polyacrylates, polymethacrylates, epoxies, and a variety of solvents (nonpolar, polar, hydrogen bonding, water). The performance of the models is overall similar, with the Entropic-FV and GC-Flory overall better than UNIFAC-FV in most situations, in agreement to the investigations reported earlier. Some typical results are shown in Figure 16.6 for systems including the commercial epoxy resin Araldit.

Novenario et al.^{187a} recently demonstrated the problems of several predictive models (UNIFAC-FV, cubic EoS/ G^E models) in predicting VLE for the PEG/water system.

The Entropic-FV/UNIQUAC combination has been shown^{105,106} to correlate successfully the PVAL/water and other systems exhibiting closed-loop behavior with temperature-dependent parameters (Figure 16.4).

16.7.6 RESULTS FOR POLYMER BLENDS

Such cubic equations of state as van der Waals correlate very satisfactorily the UCST-type behavior for polymer solutions, as shown by Harismiadis et al.¹⁰⁹ A generalized correlation of the interaction parameter of the van der Waals equation of state for polymer blends based exclusively on polystyrene blends has been presented.¹⁰⁹ By using this equation, the van der Waals equation of state can be used as a predictive tool for investigating the compatibility of polymer blends. Predictive GC thermodynamic methods such as Entropic-FV, GC-Flory, UNIFAC, and UNIFAC-FV perform rather poorly, at least from a quantitative point of view.^{99,109} Entropic-FV performs best among these models, on a qualitative basis. For semiquantitative predictions in polymer blends, the approach proposed by Coleman et al.⁹ is recommended.

16.7.7 RESULTS FOR COPOLYMER SOLUTIONS

Comparisons for copolymer systems are not extensive, although several VLE data for solvent-copolymers are available. Bogdanic and Fredenslund,³⁸ Pappa et al.,¹¹⁰ and Lee and Danner¹⁸⁸ have presented comparisons for such systems, using the models Entropic-FV, GC-Flory, Zhong-Masuoka, UNIFAC-FV, and GCLF. In their comparison, Pappa et al.¹¹⁰ found that both Entropic-FV and Zhong-Masuoka models perform similarly for these systems with a deviation around 20%. Similar overall performance for the Entropic-FV, GC-Flory, and UNIFAC-FV models was observed by Bogdanic and Fredenslund,³⁸ although the various models perform differently for specific copolymer systems. For example, the Entropic-FV model has problems in the presence of chloro groups. GCLF is also shown to be quite successful for a number of copolymer solutions in mostly nonpolar/slightly polar solvents.

16.7.8 SWELLING — THE EFFECTS OF CRYSTALLINITY AND CROSS-LINKING (SORPTION, SLLE)

When highly crystalline or cross-linked polymers are considered, e.g., paints after drying, rubbers, polyolefins, the effects of cross-linking and crystallinity should be considered because they affect the solubility. Cross-linking and crystallinity are often visualized as “similar” (in some sense) phenomena and are described with the same theories: crystalline regions are assumed to act as “physical or giant cross-links.” Crystalline and cross-linked polymers do not dissolve (with a few exceptions) in solvents but only swell. Swelling equilibria is thus important. To account for the crystalline/cross-linking effect, an additional factor (elastic term) is typically required in thermodynamic models. Two popular theories to account for this effect are the Flory-Rechner:¹⁸⁹

$$\ln \alpha_1^{el} = \frac{\rho_a V_1}{M_c} \phi_2^{1/3} \quad (16.84)$$

where

ρ_a = the density of the amorphous polymer

V_1 = the molar volume of the solvent

M_c = the molecular weight between cross-links

and the Michaels-Hausslein¹⁹⁰ equation:

$$\ln \alpha_1^{el} = \frac{V_1 \left[\Delta H_2^f \rho_a \left(\frac{1}{T} - \frac{1}{T_m} \right) \right] - \phi_1 + \chi \phi_1^2}{\left[3 / (2 f \phi_2) - 1 \right]} \quad (16.85)$$

where

T_m = the melting point temperature

f = the fraction of elastically effective chains in amorphous regions

As observed from these equations, both theories introduce at least one more extra parameter, which needs to be determined from experimental data: the molecular weight between cross-links M_c and the fraction of elastically effective chains f .

They have been combined with FV models^{6,191,192} and they have been applied to semicrystalline polymer–solvent systems. The results are satisfactory but they are not predictive: the M_c and f parameters should be estimated from experimental data. However, the swelling of cross-linked polymers can be estimated with such equations. In one of the very few works reported on the prediction of SLLE⁵⁵ for polymer solutions, the Entropic-FV and UNIFAC models have been compared for semicrystalline polymer–solvent systems. These two models are shown to yield similar results for SLLE.

16.7.9 POLYMER–MIXED SOLVENT SYSTEMS

Mixed solvent–polymer systems are very important for many practical applications, e.g., in the paints and coatings industry and for the separation of biomolecules using aqueous two-phase systems. However, very few models have been extended to ternary polymer–mixed solvent systems.

The solubility parameter theory has been applied extensively using a mixed value of the solubility parameter:

$$\delta = \sum_i \varphi_i \delta_i \quad (16.86)$$

Barton^{41,42} provides empirical methods based on solubility parameters for ternary solvent systems. All these methods provide only a qualitative idea on miscibility. The combination of regular solution theory and solubility parameters has been employed for predicting the partition coefficients of organic compounds between water and polystyrene¹⁹³ and between alcohols and polyolefins.¹⁹⁴ The results are useful to a first approximation.

Heil and Prausnitz¹⁹⁵ proposed an FH/UNIQUAC-type model, which has been applied to a number of ternary liquid–liquid PS–mixed solvent systems. Satisfactory results were obtained for the ternary systems using solely two parameters per binary. These results show the potential of local composition concept (UNIQUAC, UNIFAC) for multicomponent polymer systems. The required binary parameters were estimated from solvent–polymer VLE data.

A third interesting approach, presented by Blanks and Prausnitz,¹⁹⁶ is an extension of the FH equation to polymer–mixed solvents. The method employs an FH parameter calculated from the regular solution theory using separate contributions for the various effects: nonpolar, polar, hydrogen bonding. The authors apply the method to a single ternary system: poly(methyl methacrylate)/hexane/acetone at 25°C, where they found that it correctly predicts that the polymer is soluble in the mixed solvent as long as the volume fraction of acetone is greater than 0.55, which is in agreement with data by Billmeyer (personal communication to John Prausnitz, 1964).

Dee¹⁹⁷ applied the Flory equation of state to PS/cyclohexane/water, but the results are only of correlative value.

Recently,⁸ the Holten-Andersen et al.² and the Entropic-FV models were applied to LLE for polymer–mixed solvent, considering both solvent–solvent or solvent–antisolvent systems. The comparison was limited to eight PS–two solvent systems (benzene/acetone, benzene/methanol, methylcyclohexane/acetone, toluene/acetone, MEK/acetone, ethyl acetate/acetone, NNDMF/cyclohexane) and one PMMA system (with chlorobutane/butanol-2) for which full data are available. Qualitatively good results are obtained with both models, especially Entropic-FV (despite that all group interaction parameters were based on low-pressure VLE of nonpolymeric systems).

In another recent investigation,¹¹² a database for ternary VLE systems (polymer–mixed solvents) has been compiled and used for evaluating the performance of four GC models (Entropic-FV, UNIFAC-FV, GC-Flory, and GCLF). Some typical results are presented in Table 16.7. The performance of these predictive models, although somewhat inferior to the binary systems, can be considered quite satisfactory. The experimental measurements of solvent activities in mixed solvent–polymer systems are not easy and may often be associated with significant errors (J.M. Prausnitz, 2000, personal communication).

16.7.10 CONCLUDING REMARKS AND FUTURE CHALLENGES

Attempting to summarize in few words the current status in polymer thermodynamics, we could state the following:

1. Many databases (some available in computer form) and reliable GC methods are available for estimating many pure polymer properties and phase equilibria of polymer solutions such as densities, solubility parameters, glass and melting temperatures, and solvent activity coefficients.
2. Simple GC methods based on UNIFAC, containing corrections for the FV effects, satisfactorily predict the solvent activities and VLE for binary and ternary polymer solutions. They are less successful for the prediction of LLE if the parameters are based on VLE. They are much more successful if the parameters are based on LLE data. The combination of a simple FV expression such as that employed in the Entropic-FV model and a local composition energetic term such as that of UNIQUAC seems to be a very promising tool for both VLE and LLE in polymer solutions. We expect that such tools may find widespread use in the future for practical applications.
3. Simple cubic equations of state can correlate both VLE and LLE for polymer solutions and blends with a single interaction parameters. They can be combined with an activity coefficient model for predictive calculations using the so-called EoS/ G^E mixing rules. Applications of cubic equations of state to high pressures are so far limited to those shown for the Sako et al. cubic equation of state.
4. The SAFT model may prove to be a very successful tool in the future for polymer systems. The low-pressure and especially the high-pressure results for systems including solvents and nonpolar polymers (with emphasis on those of interest to the polyolefin industry) are very satisfactory. However, its failure to extend to polar systems represents so far a significant limitation of the model.
5. Most theoretical/modeling studies in polymer thermodynamics are limited to:
 - Organic polymers
 - Binary systems often involving monodisperse polymers and single solvents
 - Rather “simple” polymers (polyolefins, polystyrene, PVC, etc.)
 - VLE and activity coefficients
 - “Rules of thumb” estimates of miscibility (solubility parameters, theta parameters, etc.)

Some of the future challenges in the area of polymer thermodynamics will involve the following:

1. The correlation and prediction of phase equilibria of solutions containing polar and hydrogen bonding solvents and polymers
2. More emphasis on multicomponent systems including both mixed solvents, blend–solvent systems, as well as the effect of polydispersity
3. Better treatment of condensed phases especially LLE and SLE as well as water-soluble polymer systems and polyelectrolytes

4. Emphasis on high-pressure systems involving both the typical nonpolar and polar polymers
5. New directions such as description of “special materials” including those involving oligomers, copolymers, new structures (starlike and dendrimers), “inorganic” polymers (e.g., tin-based antifouling paints)
6. Proper account for the effects of crystallinity and cross-linking with special attention to swelling phenomena
7. Closer collaboration with industry, e.g., for testing existing theories for polymers with novel structures, for commercial polymers for which so far the structure is not revealed to academic researchers, and for many other applications of practical interest. Many industrial systems are much more complex than the systems studied in academia. Closer collaboration in the future between academia and the polymer and paint/adhesives industries may further help the advancements in the area of polymer thermodynamics in the coming years.

LIST OF ABBREVIATIONS

BR	butadiene rubber
CST	critical solution temperature
EAC	ethyl acetate
EoS	equation of state
FH	Flory–Huggins (model/equation/interaction parameter)
FV	free-volume
GC	group contribution (method/principle)
GC-Flory	group contribution Flory equation of state
GCLF	group contribution lattice fluid
GCVOL	group contribution volume (method for estimating the density)
LCST	lower critical solution temperature
LLE	liquid–liquid equilibria
PBMA	polybutyl methacrylate
PDMS	polydimethylsiloxane
PE	polyethylene
PEO	polyethylene oxide
PIB	polyisobutylene
PS	polystyrene
PVAC	polyvinyl acetate
PVC	polyvinyl chloride
SLE	solid–liquid equilibria
SLLE	solid–liquid–liquid equilibria
UCST	upper critical solution temperature
UNIFAC	universal functional activity coefficient (a method for estimating activity coefficients)
vdWlf	van der Waals one fluid (mixing rules)
VLE	vapor–liquid equilibria
VOC	volatile organic content

ACKNOWLEDGMENTS

The author gratefully acknowledges the financial support of J. Hempel Foundation and of the Danish Technical Research Council (STVF). Moreover, the author acknowledges the contributions of many colleagues who have offered useful material and advice/suggestions for this manuscript.

They are listed here in alphabetical order: Dr. Grozdana Bogdanic, Prof. Walter Chapman, Prof. Yan-Ping Chen, Prof. Joao Coutinho, Dr. Ralf Dohrn, Dr. Ioannis Economou, Dr. Vassilis Harismiadis, Dr. Gerard Krooshof, Prof. Masuoka; Mrs. Georgia Pappa, Prof. Gabriele Sadowski, Prof. Katsumi Tochigi, and Prof. Chongli Zhong.

Finally, my Ph.D. students Thomas Lindvig and Irene Kouskoumvekaki are greatly acknowledged for reading the manuscript and for providing results prior to publication.

REFERENCES

1. Prausnitz, J.M., Lichtenthaler, R.N., and Azevedo, E.G.D., *Molecular Thermodynamics of Fluid Phase Equilibria*, 3rd ed., Prentice-Hall International, Englewood Cliffs, NJ, 1999.
2. Holten-Andersen, J., *Physical Models and Coatings Technology*, Report T12-87, Scandinavian Paint and Printing Ink Research Institute, 1987; also presented at the International Conference in Organic Coatings Science and Technology, Athens, 1986.
3. Holten-Andersen, J., Heat balance and solvent balance in the drying of coatings, *J. O.C.C.A.*, 69(12), 324–331, 1986.
4. Holten-Andersen, J. and Hansen, C.M., Solvent and water evaporation from coatings, *Prog. Org. Coat.*, 11(3), 219, 1983.
5. Holten-Andersen, J. and Eng, K., Activity coefficients in polymer solutions, *Prog. Org. Coat.*, 16, 77, 1988.
6. Doong, S.J. and Ho, W.S., Sorption of organic vapors in polyethylene, *Ind. Eng. Chem. Res.*, 30, 1351–1361, 1991.
7. Kampouris, E.M., Diakoulaki, D.C., and Papaspyrides, C.D., Solvent recycling of rigid poly(vinyl chloride) bottles, *J. Vinyl Technol.*, 8(2), 79, 1986.
8. Pappa, G.D., Kontogeorgis, G.M., and Tassios, D.P., Prediction of ternary liquid-liquid equilibria in polymer-solvent-solvent systems, *Ind. Eng. Chem. Res.*, 36, 5461, 1997.
9. Coleman, M.M., Graf, J.F., and Painter, P.C., *Specific Interactions and the Miscibility of Polymer Blends*, Technomic, Lancaster, PA, 1991.
10. Mio, C. et al., Vapor-liquid equilibria for solutions of dendritic polymers, *J. Chem. Eng. Data*, 43, 541–550, 1998.
11. Lieu, J.G. et al., Vapor-liquid equilibria for dendritic-polymer solutions, *J. Chem. Eng. Data*, 44, 613–620, 1999.
12. Dandekar, A.Y. et al., Measurement of gas solubility in polymers using a high-pressure microbalance. Technical University of Denmark, Department of Chemical Engineering, Research Group IVC-SEP (internal publication), 2000.
13. Patterson, R. et al., IUPAC-NIST solubility data series 70. The solubility of gases in glassy polymers, *J. Phys. Chem. Ref. Data*, 28(5), 1255–1452, 1999.
14. Leitner, W., Designed to dissolve, *Nature (London)*, 405, May 2000.
15. Teja, A.S. and Eckert, C.A., Commentary on supercritical fluids: research and applications, *Ind. Eng. Chem. Res.*, 39, 4442–4444, 2000.
16. Perrut, M., Supercritical fluid applications: industrial developments and economic issues, *Ind. Eng. Chem. Res.*, 39, 4531–4535, 2000.
17. Hansen, C.M., *Hansen Solubility Parameters. A User's Handbook*, CRC Press, Boca Raton, FL, 2000.
18. Shashoua, Y., Permanence of plasticizers in polyvinylchloride objects in the museum environment, *Polymer Preprints*, 41(2), 1796–1797, 2000.
19. Su, C.S., Patterson, D., and Schreiber, H.P., Thermodynamic interactions and the properties of the PVC-plasticiser systems, *J. Appl. Polymer Sci.*, 20, 1025–1034, 1976.
20. Demertzis, P.G., Riganakos, K.A., and Akrida-Demertzi, K., Study of compatibility of PVC and polyester-type plasticizer blends by inverse gas chromatography, *Eur. Polym. J.*, 26(2), 137–140, 1990.
21. Demertzis, P.G., Riganakos, K.A., and Akrida-Demertzi, K., An inverse gas chromatographic study of the compatibility of food grade PVdC copolymer and low volatility plasticisers, *Polym. Int.*, 25, 229–236, 1991.
22. Prausnitz, J.M., Some new frontiers in chemical engineering thermodynamics, *Fluid Phase Equilibria*, 104, 1–20, 1995.

23. Prausnitz, J.M., Biotechnology: a new frontier for molecular thermodynamics, *Fluid Phase Equilibria*, 53, 439–451, 1989.
24. Lee, B.-C. and Danner, R.P., Prediction of polymer–solvent phase equilibria by a modified GC EoS, *AIChE J.*, 42, 837, 1996.
25. Bogdanic, G. and Fredenslund, Aa., Revision of the GC-Flory EoS for phase equilibria in mixtures with polymers. 1. Prediction of VLE for polymer solutions, *Ind. Eng. Chem. Res.*, 33, 1331, 1994.
26. Fredenslund, Aa., Gmehling, J., and Rasmussen, P., *Vapor-Liquid Equilibria with UNIFAC. A Group Contribution Method*, Elsevier, Amsterdam, 1977.
27. Fredenslund, Aa., Jones, R.L., and Prausnitz, J.M., Group contribution estimation of activity coefficients in nonideal liquid mixtures, *AIChE J.*, 25(1), 1086–1098, 1975.
28. van Krevelen, *Properties of Polymers. Their Correlation with Chemical Structure; Their Numerical Estimation and Prediction from Additive Group Contributions*, Elsevier, Amsterdam, 1990.
29. Gani, R., Nielsen, B., and Fredenslund, Aa., A group contribution approach to computer-aided molecular design, *AIChE J.*, 37(9), 1318, 1991.
30. Vaidyanathan, R. and El-Halwagi, M., Computer-aided design of high performance polymers, *J. Elastomers and Plastics*, 26, 277, 1994.
31. High, M.S. and Danner, R.P., *Polymer Solution Handbook*; DIPPR 881 Project. Design Institute for Physical Property Data, 1992.
32. Rodgers, P.A., PVT relationships for polymeric liquids: a review of equations of state and their characteristic parameters for 56 polymers, *J. Appl. Polym. Sci.*, 48, 1061, 1993.
33. Reid, R.C., Prausnitz, J.M., and Poling, B.E., *The Properties of Gases and Liquids*, 4th ed., McGraw-Hill, New York, 1987.
34. Elbro, H.S., Fredenslund, Aa., and Rasmussen, P., Group contribution method for the prediction of liquid densities as a function of temperature for solvents, oligomers, and polymers, *Ind. Eng. Chem. Res.*, 30, 2576, 1991.
35. Tsibanogiannis, I.N., Kalospiros, N.S., and Tassios, D.P., Extension of the GCVOL method and application to some complex compounds, *Ind. Eng. Chem. Res.*, 33, 1641, 1994.
36. Constantinou, L., Gani, R., and O’Connell, J.P., Estimation of the acentric factor and the liquid molar volume at 298 K through a new group contribution method, *Fluid Phase Equilibria*, 103, 11, 1995.
37. Fedors, R.F., A method for estimating both the solubility parameters and molar volumes of liquids, *Polym. Eng. Sci.*, 14(2), 147, 1974.
38. Bogdanic, G. and Fredenslund, Aa., Prediction of VLE for mixtures with co-polymers, *Ind. Eng. Chem. Res.*, 34, 324, 1995.
39. Hansen, A.F. and Hestkjær, L.L., *Phase Equilibria in Binary Polymer/Solvent Systems* [in Danish], B.Sc.thesis, Technical University of Denmark, Department of Applied Chemistry, 2001.
40. Lindvig, Th. et al., Phase equilibria for complex polymer solutions, *Fluid Phase Equilibria*, 189–197: 663, 2002.
41. Barton, A.F.M., *Handbook of Solubility Parameters and Other Cohesion Parameters*, CRC Press, Boca Raton, FL, 1983.
42. Barton, A.F.M., *CRC Handbook of Polymer–Liquid Interaction Parameters and Solubility Parameters*, CRC Press, Boca Raton, FL, 1990.
43. Brandrup, J. and Immergut, E.H., *Polymer Handbook*, John Wiley & Sons, New York, 1989.
44. Panayiotou, C., Solubility parameter revisited: an equation-of-state approach for its estimation, *Fluid Phase Equilibria*, 131, 21, 1997.
45. Wei, Y.S. and Sadus, R.J., Equations of state for the calculation of fluid phase equilibria, *AIChE J.*, 46(1), 169–196, 2000.
46. Elbro, H.S., *Phase Equilibria of Polymer Solutions — With Special Emphasis on Free Volumes*, Ph.D thesis, Department of Chemical Engineering, Technical University of Denmark, 1992.
47. Klein, J. and Jeberien, H.E., Chainlength dependence of thermodynamic properties of polyethylene (glycol), *Makromol. Chem.*, 181, 1237, 1980.
48. Wen, H., Elbro, H.S., and Alessi, P., *Polymer Solution Data Collection*, Dechema Chemistry Data Series, Frankfurt, 1991.
49. Oishi, T. and Prausnitz, M., Estimation of solvent activities in polymer solutions using a group-contribution method, *Ind. Eng. Chem. Process Des. Dev.*, 17(3), 333, 1978.

50. Kontogeorgis, G.M., Fredenslund, Aa., and Tassios, D.P., Simple activity coefficient model for the prediction of solvent activities in polymer solutions, *Ind. Eng. Chem. Res.*, 32, 362, 1993.
51. Fox, T.G., *Polymer*, 3, 111, 1962.
52. Freeman, P.I. and Rowlinson, J.S., Lower critical points in polymer solutions, *Polymer*, 1, 20, 1960.
53. Wohlfarth, C., *VLE Data of Binary Polymer Solutions*, Elsevier, Amsterdam, 1994.
54. Surana, R.K. et al., New technique to measure high-pressure and high-temperature polymer–solvent vapor–liquid equilibria, *Fluid Phase Equilibria*, 139, 361, 1997.
55. Harismiadis, V.I. and Tassios, D.P., Solid–liquid–liquid equilibria in polymer solutions, *Ind. Eng. Chem. Res.*, 35, 4667, 1996.
56. Tsuji, T. et al., VLE of the three ternary systems containing polyethylene glycol (PEG): methanol+water+PEG, ethanol+water+PEG, and 1-propanol+water+PEG, *Fluid Phase Equilibria*, submitted, 2001.
57. Wang, H., *J. East China University Sci. Technol.*, 23, 614–620, 1997.
58. Surana, R.K., Danner, R.P., and Duda, J.L., Diffusion and equilibrium measurements in ternary polymer–solvent–solvent systems using IGC, *Ind. Eng. Chem. Res.*, 37, 3203, 1998.
59. Tanbonliong, J.O. and Prausnitz, J.M., Vapour-liquid equilibria for some binary and ternary polymer solutions, *Polymer*, 38(23), 5775–5783, 1997.
60. Martin, T.M., Lateef, A.A., and Roberts, C.B., Measurements and modeling of cloud point behavior for PP/*n*-pentane and PP/*n*-pentane/carbon dioxide mixtures at high pressures, *Fluid Phase Equilibria*, 154, 241, 1999.
61. Mishima, K., Matsuyama, K., and Nagatani, M., Solubilities of PEGs in the mixtures of supercritical carbon dioxide and cosolvent, *Fluid Phase Equilibria*, 161, 315, 1999.
62. Diamond, A.D. and Hsu, J.T., Protein partitioning in PEG/dextran aqueous two-phase systems, *AIChE J.*, 36, 1017, 1990.
63. Kakisaka, K. et al., Partition coefficients of amino acids, peptides, and enzymes in Dextran/PEG/water aqueous two phase systems, *J. Chem. Eng. Jpn.*, 31, 991, 1998.
64. Kang, C.H. and Sandler, S.I., Phase behavior of aqueous two-polymer systems, *Fluid Phase Equilibria*, 38, 245, 1987.
65. Voros, N., Proust, P., and Fredenslund, Aa., Liquid-liquid equilibria of aqueous two-phase systems containing salts and polyethylene glycol, *Fluid Phase Equilibria*, 90(2), 333–353, 1993.
66. Seymour, R.B., *Plastics vs. Corrosives*, SPE Monograph Series, John Wiley & Sons, New York, 1982.
67. Hansen, C.M., *The Three-Dimensional Solubility Parameter and Solvent Diffusion Coefficient*, Ph.D. thesis, Technical University of Denmark, 1967.
68. Bentley, J. and Turner, G.P.A., *Introduction to Paint Chemistry and Principles of Paint Technology*, 4th ed. Chapman & Hall, London, 1998.
69. Flory, P.J., *J. Chem. Phys.*, 9, 660, 1941.
70. Huggins, M.L., *J. Chem. Phys.*, 15, 225, 1941.
71. Qian, C., Mumby, S.J., and Eichinger, B.E., Application of the theory of phase diagrams to binary polymer solutions and blends, *Polym. Preprints*, 31, 621, 1990.
72. Qian, C., Mumby, S.J., and Eichinger, B.E., Phase diagrams of binary polymer solutions and blends, *Macromolecules*, 24, 1655, 1991.
73. Bae, Y.C. et al., Representation of VLE and LLE for binary systems containing polymers: applicability of an extended Flory-Huggins equation, *J. Appl. Polym. Sci.*, 47, 1193, 1993.
74. Koningsveld, R. and Kleintjens, L.A., Liquid-liquid phase separation in multicomponent polymer systems. X. Concentration dependence of the pair-interaction parameter in the system cyclohexane-polystyrene, *Macromolecules*, 4, 637, 1971.
75. Schultz, A.R. and Flory, P.J., Phase equilibria in polymer–solvent systems. II. Thermodynamic interaction parameters from critical miscibility data, *J. Am. Chem. Soc.*, 75, 496, 1953.
76. Gottlieb, M. and Herskowitz, M., Estimation of the Flory-Huggins parameter for poly(dimethylsiloxane) solutions by the UNIFAC group contribution method, *Macromolecules*, 14, 1468, 1981.
77. Vetere, A., Rules for predicting vapor–liquid equilibria of amorphous polymer solutions using a modified Flory-Huggins equation, *Fluid Phase Equilibria*, 97, 43, 1994.
78. Vetere, A., An empirical method to correlate and to predict the VLE and LLE for binary amorphous polymer solutions, *Ind. Eng. Chem. Res.*, 37, 2864, 1998.

79. Vetere, A., An empirical method to predict LLE of binary polymer systems, *Ind. Eng. Chem. Res.*, 37, 4463, 1998.
80. Patterson, D., Review. Free volume and polymer solubility. A qualitative view, *Macromolecules*, 2, 672, 1969.
81. Rasmussen, D. and Rasmussen, P., Phase equilibria in aqueous polymer solutions, *Chem. Eng. Progr.*, February, 50, 1989.
82. Elbro, H.S., Fredenslund, Aa., and Rasmussen, P., A new simple equation for the prediction of solvent activities in polymer solutions, *Macromolecules*, 23, 4707, 1990.
83. Bondi, A., *Physical Properties of Molecular Crystals, Liquids and Glasses*, John Wiley & Sons, New York, 1968.
84. Wilson, G.M., Interpretation of Trouton's law in relation to equation of state properties. Equations of State, Theories and Applications, American Chemical Society Symposium Series 300, Washington, D.C, 1986.
85. Kouskoumvekaki, I., Michelsen, M.L., and Kontogeorgis, G.M., An improved entropic expression for polymer solutions, *Fluid Phase Equilibria*, accepted for publication, 2002.
86. Kontogeorgis, G.M. et al., Improved models for the prediction of activity coefficients in nearly athermal mixtures. Part I. Empirical modifications of free-volume models, *Fluid Phase Equilibria*, 92, 35, 1994.
87. Coutinho, J.A.P., Andersen, S.I., and Stenby, E.H., Evaluation of activity coefficient models in prediction of alkane SLE, *Fluid Phase Equilibria*, 103, 23, 1995.
88. Polyzou, E.N. et al., Assessment of activity coefficient models for predicting solid-liquid equilibria of asymmetric binary alkane systems, *Ind. Eng. Chem. Res.*, 38, 316-323, 1999.
89. Larsen, B.L., Rasmussen, P., and Fredenslund, Aa., A modified UNIFAC group-contribution model for the prediction of phase equilibria and heats of mixing, *Ind. Eng. Chem. Res.*, 26, 2274, 1987.
90. Gmehling, J. and Weidlich, U., *Fluid Phase Equilibria*, 27, 171, 1986.
91. Bokis, C., Orbey, H., and Chen C.-C., Properly model polymer processes, *Chem. Eng. Progr.*, April, 39, 1999.
92. Goydan, R., Reid, R.C., and Tseng, H-S., Estimation of the solubilities of organic compounds in polymers by group-contribution methods, *Ind. Eng. Chem. Res.*, 28, 445, 1989.
93. Fried, J.R., Jiang, J.S., and Yeh, E., Group-contribution methods in polymer thermodynamics, *Comput. Polym. Sci.*, 2, 95, 1992.
94. Kontogeorgis, G.M. et al., Equations of state and activity coefficient models for vapor-liquid equilibria of polymer solutions, *AIChEJ.*, 40, 1711, 1994.
95. High, M.S. and Danner, R.P., Application of the group contribution lattice-fluid EoS to polymer solutions, *AIChE J.*, 36, 1625, 1990.
96. Lee, B.-C. and Danner, R.P., Prediction of infinite dilution activity coefficients in polymer solutions: comparison of prediction models, *Fluid Phase Equilibria*, 128, 97, 1997.
97. Patwardhan, A.A. and Belfiore, L.A., Prediction of thermodynamic properties of polymer solutions by a group-contribution method, *J. Polym. Sci. B Polym. Phys.*, 24, 2743-2486, 1986.
98. Beret, S. and Prausnitz, J.M., *AIChE J.*, 21, 1123, 1975.
99. Belfiore, L.A., Patwardhan, A.A., and Lenz, T.G., Shortcomings of UNIFAC-FV to characterize the phase behavior of polymer-polymer blends, *Ind. Eng. Chem. Res.*, 27, 284-294, 1988.
100. High, M.S. and Danner, R.P., Prediction of solvent activities in polymer solutions, *Fluid Phase Equilibria*, 55, 1, 1990.
101. Hansen, H.K., Coto, B. and Kuhlmann, B., UNIFAC with Lineary Temperature-Dependent Group-Interaction Parameters, IVC-SEP Internal Report 9212, 1992.
102. Iwai, Y. and Arai, Y., Measurement and prediction of solubilities of hydrocarbon vapors in molten polymers, *J. Chem. Eng. Jpn.*, 22, 155, 1989.
103. Iwai, Y. et al., Measurement and prediction of solubilities of ethylbenzene vapor in styrene-butadiene rubbers, *J. Chem. Eng. Jpn.*, 23, 508, 1990.
104. Choi, J.S., Tochigi, K., and Kojima, K., Measurement and correlation of VLE in polymer solutions containing polystyrene with polymer ASOG, *Fluid Phase Equilibria*, 111, 143, 1995.
105. a) Bogdanic, G. and Vidal, J., A segmental interaction model for liquid-liquid equilibrium calculations for polymer solutions, *Fluid Phase Equilibria*, 173, 241-252, 2000. b) Bogdanic, G., The FV-UNIQUAC segmental interaction model for liquid-liquid equilibrium calculations for polymer solutions. Part 2. Extension to solutions containing polystyrene, *Fluid Phase Equilibria*, 4791, 1-9, 2001.

106. Panagou, E., Vidal, J., and Bogdanic, G., A segmental interaction model for LLE correlation and prediction — application to the poly(vinyl alcohol)/water system, *Polym. Bull.*, 40, 117, 1998.
107. a) Pappa, G.D. et al., Use of activity coefficient models for the correlation and prediction of miscibility in polymer/solvent and polymer/polymer systems, presented at the 3rd Greek Conference of Chemical Engineering, Athens, May 2001 [in Greek], 2001. b) Pappa, G.D., Voutsas, E.C., and Tassios, D.P., Liquid/liquid phase equilibrium in polymer–solvent systems: correlation and prediction of the polymer molecular weight and the pressure effect, *Ind. Eng. Chem. Res.* 40(21), 4654–4663, 2001.
108. Kontogeorgis, G.M. et al., Prediction of liquid–liquid equilibrium for binary polymer solutions with simple activity coefficient models, *Ind. Eng. Chem. Res.*, 34, 1823, 1995.
109. Harismiadis, V.I. et al., Miscibility of polymer blends with engineering models, *AIChE J.*, 42, 3170, 1996.
110. Pappa, G.D., Voutsas, E.C., and Tassios, D.P., Prediction of solvent activities in polymer solutions with simple group-contribution models, *Ind. Eng. Chem. Res.*, 38, 4975, 1999.
111. Lindvig, Th., Michelsen, M.L., and Kontogeorgis, G.M., Thermodynamics of paint related systems with engineering models, *AIChE J.*, 47(11), 2573–2584, 2001.
112. Lindvig, Th. et al., Phase equilibria for complex polymer solutions, poster presentation in the 9th International Conference on Properties and Phase Equilibria for Product and Process Design, Kurashiki, Japan, May 20–25, 2001, 2001.
113. Kontogeorgis, G.M. et al., Improved models for the prediction of activity coefficients in nearly athermal mixtures. Part II. A theoretically based G^E -model based on the van der Waals partition function, *Fluid Phase Equilibria*, 127, 103, 1997.
114. Voutsas, E.C., Kalospiros, N.S., and Tassios, D.P., A combinatorial activity coefficient model for symmetric and asymmetric mixtures, *Fluid Phase Equilibria*, 109, 1, 1995.
115. Zhong, C. et al., Improvement of predictive accuracy of the UNIFAC model for VLE of polymer solutions, *Fluid Phase Equilibria*, 123, 97, 1996.
116. Kontogeorgis, G.M., Voutsas, E.C., and Tassios, D.P., A molecular simulation-based method for the estimation of activity coefficients for alkane solutions, *Chem. Eng. Sci.*, 51, 3247, 1996.
117. Voutsas, E.C. and Tassios, D.P., On the extension of the p-FV and R-UNIFAC models to multicomponent mixtures, *Fluid Phase Equilibria*, 128, 271–272, 1997.
118. Condo, P.D. and Radosz, M., Equations of state for monomers and polymers, *Fluid Phase Equilibria*, 117, 1, 1996.
119. Kang, J.W. et al., Evaluation of equations of state applicable to polymers and complex systems, *Fluid Phase Equilibria*, 77, 194–197, 2002.
120. Orbey, H., Chen, C.-C., and Bokis, C.P., An extension of cubic equations of state to vapor–liquid equilibria in polymer–solvent mixtures, *Fluid Phase Equilibria*, 145, 169, 1998.
121. Sako, T., Wu, A.H. and Prausnitz, J.M., A cubic equation of state for high-pressure phase equilibria of mixtures containing polymers and volatile fluids, *J. Appl. Polym. Sci.*, 38, 1839, 1989.
122. Kontogeorgis, G.M. et al., Application of the van der Waals equation of state to polymers. I. Correlation, *Fluid Phase Equilibria*, 96, 65–92, 1994.
123. Harismiadis, V.I. et al., Application of the van der Waals equation of state to polymers. II. Prediction, *Fluid Phase Equilibria*, 96, 93–117, 1994.
124. Harismiadis, V.I. et al., Application of the van der Waals equation of state to polymers. III. Correlation and prediction of upper critical solution temperatures for polymer solutions, *Fluid Phase Equilibria*, 100, 63–102, 1994.
125. Saraiva, A. et al., Application of the van der Waals equation of state to polymers. IV. Correlation and prediction of lower critical solution temperatures for polymer solutions, *Fluid Phase Equilibria*, 115, 73–93, 1996.
126. Bithas, S. et al., Correlation and prediction of Henry constants for liquids and gases in five industrially important polymers using a CS-type correlation based on the van der Waals equation of state. Comparison with other predictive models, *Fluid Phase Equilibria*, 113, 79–102, 1995.
127. Bithas, S. et al., Henry constants in polymer solutions with the van der Waals equation of state, *Polym. Eng. & Science*, 36(2), 254–261, 1996.
128. Harismiadis, V.I. et al., Miscibility of polymer blends with engineering models, *AIChE J.*, 42(11), 3170–3180, 1996.
129. Orbey, N. and Sandler, S.I., VLE of polymer solutions using a cubic equation of state, *AIChE J.*, 40(7), 1203, 1994.

130. Kalospiros, N., and Tassios, D.P., Prediction of vapor–liquid equilibria in polymer solutions using an equation of state/excess Gibbs free energy model, *Ind. Eng. Chem. Res.*, 34, 2117–2124, 1995.
131. Tochigi, K., Futakuchi, H., and Kojima, K., Prediction of vapor–liquid equilibria in polymer solutions using the Peng–Robinson group contribution model, *Fluid Phase Equilibria*, 152, 209–217, 1998.
132. Tochigi, K., Prediction of vapor–liquid equilibria in nonpolymer and polymer solutions using an ASOG-based equation of state (PRASOG), *Fluid Phase Equilibria*, 144, 59–68, 1998.
133. Louli, V. and Tassios, D.P., Vapor–liquid equilibrium in polymer–solvent systems with a cubic EoS, *Fluid Phase Equilibria*, 168, 165–182, 2000.
134. Zhong, C. and Masuoka, H., Modeling of gas solubilities in polymers with cubic equations of state, *Fluid Phase Equilibria*, 144, 49, 1998.
135. Zhong, C. and Masuoka, H., A new mixing rule for cubic equations of state and its application to vapor–liquid equilibria of polymer solutions, *Fluid Phase Equilibria*, 123, 59, 1996.
136. Zhong, C. and Masuoka, H., Prediction of Henry’s constants for polymer-containing systems using the SRK equation of state coupled with a new modified UNIFAC model, *Fluid Phase Equilibria*, 126, 1, 1996.
137. De Melo, S.A.B. et al., Predictive methods for supercritical CO₂ sorption into polymers, presented at the 9th International Conference on Properties and Phase Equilibria for Product and Process Design, Kurashiki, Japan, May 20–25, 2001, 2001.
138. Bertucco, A. and Mio, C., Prediction of vapor–liquid equilibria for polymers with a group contribution equation of state, *Fluid Phase Equilibria*, 117, 18–25, 1996.
139. Orbey, H., Bokis, C.P., and Chen, C.-C., Polymer–solvent vapor–liquid equilibrium: equations of state vs. activity coefficient models, *Ind. Eng. Chem. Res.*, 37, 1567, 1998.
140. Orbey, H., Bokis, C.P., and Chen, C.-C., Equation of state modeling of phase equilibrium in the low-density polyethylene process: the Sanchez-Lacombe, Statistical Associating Fluid Theory, and the polymer–SRK equation of state, *Ind. Eng. Chem. Res.*, 37, 4481, 1998.
141. Tochigi, K., Kurita, S., and Matsumoto, T., Prediction of PVT and VLE in polymer solutions using a cubic-perturbed equation of state, *Fluid Phase Equilibria*, 158–160, 313, 1999.
142. Tochigi, K., Kojima, K., and Sako, T., Prediction of VLE in polymer solutions using EoS-group contribution model consistent with the second virial coefficient condition, *Fluid Phase Equilibria*, 117, 55–60, 1996.
143. Tork, T. et al., Modelling of high-pressure phase equilibria using the Sako–Wu–Prausnitz equation of state, Parts I and II, *Fluid Phase Equilibria*, 163, 61, 79, 1999.
144. Browarzik, C. and Kowaleski, M., Calculation of the cloud-point and the spinodal curve for the system methylcyclohexane/polystyrene at high pressure, *Fluid Phase Equilibria*, 451, 194–197, 2002.
145. Browarzik, C., Browarzik, D., and Kehlen, H., Phase equilibrium calculations for solutions of poly(ethylene-co-vinyl acetate) copolymers in supercritical ethylene using a cubic equation of state, *J. Super-crit. Fluids*, 20(1), 73–88, 2001.
146. Browarzik, D. and Kowalewski, M., Calculation of the stability and phase equilibrium in the system polystyrene + cyclohexane + carbon dioxide based on equations of state, *Fluid Phase Equilibria*, 163, 43–60, 1999.
147. Coutinho, J.A.P., Vlamos, P.M., and Kontogeorgis, G.M., General form of the cross-energy parameter of equations of state, *Ind. Eng. Chem. Res.*, 2000.
148. Coutinho, J.A.P., Kontogeorgis, G.M., and Stenby, E.H., Binary interaction parameters for nonpolar systems with cubic equations of state: a theoretical approach. 1. CO₂/hydrocarbons using the SRK equation of state, *Fluid Phase Equilibria*, 102, 31, 1994.
149. Plocker, U., Knapp, H., and Prausnitz, J.M., Calculation of high pressure vapor–liquid equilibria from a corresponding states correlation with emphasis on asymmetric mixtures, *Ind. Eng. Chem. Process Des. Dev.*, 17, 324, 1978.
150. Kontogeorgis, G.M. et al., A novel method for investigating the repulsive and attractive parts of cubic EoS and the combining rules used with the vdW1f theory, *Chem. Eng. Sci.*, 53, 541–552, 1998.
151. Huang, S.H. and Radosz, M., Equation of state for small, large, polydisperse and associating molecules, *Ind. Eng. Chem. Res.*, 29, 2284–2294, 1990.
152. Chapman, W.G. et al., New reference equation of state for associating fluids, *Ind. Eng. Chem. Res.*, 29, 1709–1721, 1990.

153. Paricaud, P., Galindo, A., and Jackson, G., Recent advances in the use of the SAFT approach in describing electrolytes, interfaces, liquid crystals and polymers, *Fluid Phase Equilibria*, 87, 194–197, 2002.
154. Economou, I.G., Statistical Associating Fluid Theory: a successful model for the calculation of thermodynamic and phase equilibrium properties of complex fluid mixtures, *Ind. Eng. Chem. Res.*, 41(5), 953–962, 2002.
155. Muller, E.A. and Gubbins, K.E., Molecular-based equations of state for associating fluids: a review of SAFT and related approaches, *Ind. Eng. Chem. Res.*, 40(10), 2193–2211, 2001.
156. Albrecht, K.L. et al., Phase equilibria of saturated and unsaturated polyisoprene in sub- and supercritical ethane, ethylene, propane, propylene and dimethyl ether, *Fluid Phase Equilibria*, 117, 84–91, 1996.
157. Chen, S.-J., Economou, I.G., and Radosz, M., Phase behavior of LCST and UCST solutions of branchy copolymers: experiment and SAFT modeling, *Fluid Phase Equilibria*, 83, 391–398, 1993.
158. Chen, S.-J. and Radosz, M., Density-tuned polyolefin phase equilibria. 1. Binary solutions of alternating poly(ethylene-propylene) in subcritical and supercritical propylene, 1-butene and 1-hexene. Experimental and Flory-Patterson model, *Macromolecules*, 25, 3089–3096, 1992.
159. Chen, S.-J., Economou, I.G., and Radosz, M., Density-tuned polyolefin phase equilibria. 1. Multi-component solutions of alternating poly(ethylene-propylene) in subcritical and supercritical olefins. Experimental and SAFT model, *Macromolecules*, 25, 4987–4995, 1992.
160. Gregg, C.J. et al., Phase behavior of binary ethylene-propylene copolymer solutions in sub- and supercritical ethylene and propylene, *Fluid Phase Equilibria*, 83, 375–382, 1993.
161. Pan, and Radosz, M., Modeling of SLE in naphthalene, normal-alkane and polyethylene solutions, *Fluid Phase Equilibria*, 155, 57, 1999.
162. Kinzl, M. et al., SAFT modeling of inert-gas effects on the cloud-point pressures in ethylene copolymerization systems: poly(ethylene-co-vinyl acetate)+vinyl acetate+ethylene and poly(ethylene-co-hexene-1)+hexene-1+ethylene with carbon dioxide, nitrogen or *n*-butane, *Ind. Eng. Chem. Res.*, 39, 541–546, 2000.
163. Lee, S.-H., Hasch, B.M., and McHugh, M.A., Calculating copolymer solution behavior with SAFT, *Fluid Phase Equilibria*, 117, 61, 1996.
164. Lora, M. and McHugh, M.A., Phase behavior and modeling of the poly(methyl methacrylate)-CO₂-methyl methacrylate system, *Fluid Phase Equilibria*, 157, 285–297, 1999.
165. Folie, B. and Radosz, M., Phase equilibria in high-pressure polyethylene technology, *Ind. Eng. Chem. Res.*, 34, 1501–1516, 1995.
166. Folie, B. et al., Phase equilibria of poly(ethylene-co-vinyl acetate) copolymers in subcritical and supercritical ethylene and ethylene-vinyl acetate mixtures, *Fluid Phase Equilibria*, 120, 11–37, 1996.
167. Wiesmet, V. et al., Measurement and modeling of high-pressure phase equilibria in the systems polyethylene glycol (PEG)-propane, PEG-nitrogen and PEG-carbon dioxide, *J. Supercritical Fluids*, 17, 1–12, 2000.
168. Koak, N., Visser, R.M., and de Loos, Th.W., High-pressure phase behavior of the systems polyethylene+ethylene and polybutene+1-butene, *Fluid Phase Equilibria*, 158–160, 835–846, 1999.
169. Lora, M., Rindfleisch, F., and McHugh, M.A., Influence of the alkyl tail on the solubility of poly(alkyl acrylates) in ethylene and CO₂ at high pressures: experiments and modeling, *J. Appl. Polym. Sci.*, 73, 1979–1991, 1999.
170. Colina, C.M., Hall, C.K., and Gubbins, K.E., Phase behavior of PVAC-PTAN block copolymer in supercritical carbon dioxide using SAFT, presented at the 9th International Conference on Properties and Phase Equilibria for Product and Process Design, Kurashiki, Japan, May 20–25, 2001, 2001.
171. Wu, C.-S., Tang, M., and Chen, Y.-P., Application of the GFD EoS on VLE calculations of polymer solutions, *Fluid Phase Equilibria*, 117, 26, 1996.
172. a) Wu, C.-S. and Chen, Y.-P., Calculation of vapor–liquid equilibria of polymer solutions using the SAFT equation of state, *Fluid Phase Equilibria*, 100, 103–119, 1994. b) Tsai, J.-C., Tang, M., and Chen, Y.-P., Prediction of VLE of polymer solutions by the GFD equation of state, *Fluid Phase Equilibria*, 158–160, 303–312, 1999.
173. Feng, W. et al., Calculation of vapor–liquid equilibria of high concentrated polymer solution by a modified SAFT equation of state, presented at the 9th International Conference on Properties and Phase Equilibria for Product and Process Design, Kurashiki, Japan, May 20–25, 2001, 2001.

174. Pfohl, O., Dohrn, R., and Riebesell, C., Measurement and calculation of phase equilibria in the system *n*-pentane + poly(dimethylsiloxane) at 35°C and at 150°C, *Fluid Phase Equilibria*, submitted for publication, 2001.
175. Gross, J. and Sadowski, G., Perturbed-chain SAFT: an equation of state based on a perturbation theory for chain molecules, *Ind. Eng. Chem. Res.*, 40, 1244–1260, 2001.
176. Sadowski, G., Mokrushina, L.V., and Arlt, W., Finite and infinite dilution activity coefficients in polycarbonate systems, *Fluid Phase Equilibria*, 139, 391–403, 1997.
177. Tumakaka, F., Gross, J., and Sadowski, G., Modeling of polymer phase equilibria using perturbed-chain SAFT, *Fluid Phase Equilibria*, 541, 194–197, 2002.
178. Yakoumis, I.V. et al., Prediction of phase equilibria in binary aqueous systems containing alkanes, cycloalkanes, and alkenes with the CPA EoS, *Ind. Eng. Chem. Res.*, 37, 4175, 1998.
179. Michelsen, M.L. and Hendriks, E., Physical properties from association models, *Fluid Phase Equilibria*, 180(1–2), 165–174, 2001.
180. Economou, I.G. and Tsionopoulos, C., Associating models and mixing rules in equations of state for water/hydrocarbon mixtures, *Chem. Eng. Sci.*, 52(4), 511–525, 1997.
181. Economou, I.G. and Donohue, M.D., Chemical, quasi-chemical and perturbation theories for associating fluids, *AIChE J.*, 37, 1875, 1991.
182. Kontogeorgis, G.M. et al., An equation of state for associating fluids, *Ind. Eng. Chem. Res.*, 35, 4310, 1996.
183. Jog, P.K., Garcia-Cuellar, A., and Chapman, W.G., Extensions and applications of the SAFT equation of state to solvents, monomers and polymers, *Fluid Phase Equilibria*, 158–160, 321–326, 1999.
184. Jog, P.K. and Chapman, W.G., Application of Wertheim's thermodynamic perturbation theory to dipolar hard sphere chains, *Mol. Phys.*, 97(3), 307–319, 1999.
185. Lee, B.-C. and Danner, R.P., GCLF EoS: prediction of LLE in polymer solutions, *AIChE J.*, 42, 3223, 1996.
186. Wang, W., Tree, D.A., and High, M.S., A comparison of lattice-fluid models for the calculation of the liquid–liquid equilibria of polymer solutions, *Fluid Phase Equilibria*, 114, 47–62, 1996.
187. a) Novenario, C.R., Caruthers, J.M., and Chao, K.-C., VLE of polymer+solvent mixtures by the chain-of-rotators EoS, *Ind. Eng. Chem. Res.*, 27, 1033, 1998. b) Saraiva, A., Bogdanic, G., and Fredenslund, Aa., Revision of the GC-Flory EoS for phase equilibria calculations in mixtures with polymers. 2. Prediction of LLE for polymer solutions, *Ind. Eng. Chem. Res.*, 34, 1835, 1995.
188. Lee, B.-C. and Danner, R.P., Application of the GCLF EoS to random co-polymer–solvent systems, *Fluid Phase Equilibria*, 117, 33, 1996.
189. Flory, P.J. and Rehner, J., Statistical mechanics of cross-linked polymer networks, *J. Chem. Phys.*, 11, 521, 1943.
190. Michaels, M.J. and Hausslein, R.W., Elastic factors controlling sorption and transport properties of polyethylene, *J. Polym. Sci. C*, 10, 61, 1965.
191. Yoo, J.S., Kim, S.J., and Choi, J.S., Swelling equilibria of mixed solvent/PDMS systems, *J. Chem. Eng. Data*, 44, 16, 1999.
192. Shim, J.J. and Johnston, K.P., Molecular thermodynamics of solute-polymer-supercritical fluids, *AIChE J.*, 37, 607–616, 1991.
193. Gavara, R., Hernandez, R.J., and Giacin, J., Methods to determine partition coefficients of organic compounds in water/polystyrene systems, *J. Food Sci.*, 61, 947, 1996.
194. Baner, A.L. and Piringir, O.G., Prediction of solute partition coefficients between polyolefins and alcohols using the regular solution theory and group contribution methods, *Ind. Eng. Chem. Res.*, 30, 1506, 1991.
195. Heil, J.F. and Prausnitz, J.M., Phase equilibria in polymer solutions, *AIChE J.*, 12, 678, 1966.
196. Blanks, R.F. and Prausnitz, J.M., Thermodynamics of polymer solubility in polar and nonpolar systems, *I&EC Fundam.*, 3, 1, 1964.
197. Dee, G.Y., The application of EoS theories to polar-nonpolar liquid mixtures, *J. Supercritical Fluids*, 4, 152, 1991.
198. Dohrn, R. and Pfohl, O., Thermophysical properties — industrial directions, *Fluid Phase Equilibria*, 15, 194–197, 2002.